

A11101 725742

NAT'L INST OF STANDARDS & TECH R.I.C.



A11101725742

/Mechanics of pneumatic tires
QC100 .U556 V122:1971 C.2 NBS-PUB-R 1971

GOVERNMENT
PUBLICATION



NBS MONOGRAPH 122

Mechanics of Pneumatic Tires

U.S.
DEPARTMENT
OF
COMMERCE

National
Bureau
of
Standards



FEB 15 1972

163146-Ref.

UNITED STATES DEPARTMENT OF COMMERCE • MAURICE H. STANS, *Secretary*U.S. NATIONAL BUREAU OF STANDARDS • LEWIS M. BRANSCOMB, *Director*

QC 100
U556
No. 122
1971

Mechanics of Pneumatic Tires

Samuel K. Clark, Editor

Department of Engineering Mechanics
University of Michigan
Ann Arbor, Michigan 48104

Prepared for the
Office of Vehicle Systems Research
Institute for Applied Technology
National Bureau of Standards
Washington, D.C. 20234



This Monograph was prepared in fulfillment of the
National Bureau of Standards Contract CST-386
funded by the
National Highway Traffic Safety Administration,
Department of Transportation,
through the NBS Interagency Agreement FH-11-6090.

National Bureau of Standards⁷¹ Monograph 122

Nat. Bur. Stand. (U.S.), Monogr. 122, 853 pages (Nov. 1971)
CODEN: NBSMA

Issued November 1971

Abstract

The pneumatic tire has been an integral part of automotive transportation almost since its inception, yet it remains a product whose characteristics are not easily predictable or comprehensible by conventional engineering techniques. This treatise is an attempt to provide a rational descriptive and analytical basis for tire mechanics. Chapters of this book are contributed by active research workers in the fields of rubber and textile properties, friction, material properties, tire stress problems, tire design and construction, vehicle skid and handling, and tire mechanical properties.

Key words: Friction; rubber; skid; tires; tire cord; tire contact; tire stress; tire structure; vehicles.

Library of Congress Catalog Card Number: 70-611535

Foreword

Without the pneumatic tire, the development of motor vehicle transport would not have been possible. The tire carries the load, absorbs road shocks, transmits engine power to the road, and steers and stops the vehicle.

The first patent describing a pneumatic tire was issued to R. W. Thomson in 1845, and the first practical pneumatic (bicycle) tire was made by J. B. Dunlop in 1888. Since that time, tires have been improved so that they can operate safely and efficiently at high speeds for sustained periods under large loads on wet and dry roads, in hot weather or cold, on unimproved dirt or gravel roads, or on the modern high speed turnpikes of the Federal highway system. Tires have been designed for dependable service on a wide variety of vehicles including aircraft and earthmovers.

The evolution of this complex product has been the result of much successful experimental and theoretical research carried out largely by the major tire manufacturers. Partly because much of this work has been considered proprietary, no previous book has given an overview of the state of knowledge of the mechanics of pneumatic tires. Because of its responsibility to the Department of Transportation for the development of a technical basis for tire safety performance standards, NBS stimulated the compilation of this book, and is pleased to make it available.

We hope that this volume will provide a comprehensive introduction to a subject central to the tire safety problem, and that it will help to establish reasonable, practical, and effective safety standards for use by those who are responsible for improving tire performance.

Lewis M. Branscomb, *Director*



Preface

This volume was conceived as an aid to the practicing engineer or research worker who has need of information concerning the mechanics of pneumatic tires. While a number of smaller and less comprehensive reviews of particular aspects of tire mechanics or technology have appeared in the last few years, particularly the excellent review by Hofferberth and Frank in 1968, there has none the less been no comprehensive evaluation of the field since Hadekel's work in 1952, nearly 20 years ago. Even in the case of Hadekel's report, attention was directed primarily to aircraft tires and the emphasis was somewhat more on the presentation of pertinent data rather than on a description of the theoretical side of the various problems.

A further reason for compiling such a volume as this lies in the chaotic state of the literature on tire mechanics. There is no single accepted source in the English speaking world which prints papers primarily concerned with tire mechanics. None of the technical societies are exclusively directed to this goal, so that worthwhile research contributions are to be found in a number of different journals, and in some cases papers are given orally at various meetings and then not published in permanent form. In addition, a great deal of the worthwhile literature appears in the German and Russian languages so that a research worker wishing to keep abreast of the field finds it necessary to scan a wide range of publications. For this reason comprehensive summary reviews are probably worthwhile and valuable if for no other reason than to bring together pertinent recent research references.

This book attempts to assess the current state of tire mechanics both theoretically and experimentally. It attempts to do so without avoiding or emphasizing either the mathematics or the physics which can be helpful and informative, or the reality of fact and experiment upon which all engineering is ultimately based. It does not claim to be without shortcomings, since there are undoubtedly valuable research papers which have missed the attention of the various authors. This is particularly true in the Russian and Japanese languages, where so few research workers have a reading familiarity. Nevertheless, the editor would appreciate notification of errors or omissions and will make every effort to accommodate them in subsequent editions.

The idea for this book was suggested to the editor by Dr. F. Cecil Brenner, Office of Vehicle Systems Research, National Bureau of Standards. Financial support for it was furnished by funds from the Department of Transportation, and the editor would like to acknowledge his debt to those two sources as being primarily responsible for making this volume possible.

Whatever success or failure this book achieves will be due almost entirely to two groups of people. The first is made up of the authors of the various individual chapters, who are identified publicly with their efforts. The second group, who will receive no such public recognition, have also contributed greatly and should be recognized here for their efforts in reviewing parts of the texts during its preparation. I would like to acknowledge such assistance from Ralph Paterson of Textile Fibers Laboratory, E. I. Dupont Company, Seymour Lippman of Uniroyal, Inc., Dr. Robert Harrington of B. F. Goodrich Research Laboratories, and Dr. F. S. Conant of Firestone Central Research Laboratories. Finally, special thanks should be given to Milton Platt and G. A. M. Butterworth of Fabric Research Laboratories, and to Donald Nordeen of the General Motors Corporation, for substantial efforts in the review of two of the chapters.

A great deal of effort was needed to bring the manuscripts from the various authors into a common format. This is not a simple matter in a book of this size, and I would like to express my thanks to Miss Elaine Beale and Mrs. Bertha Darrow of the National Bureau of Standards and to Dr. J. T. Tielking, consultant, for their diligence and care in this task.

Samuel K. Clark

Ann Arbor, Michigan
September, 1970

Contents

	Page
Foreword.....	III
Lewis M. Branscomb, Director, National Bureau of Standards, Washington, D.C. 20234	
Preface.....	v
Samuel K. Clark, University of Michigan, Ann Arbor, Michigan 48104	
Conversion of U.S. Customary Units to SI Units.....	x
Chapter 1. Material Characteristics.....	1
1.1. Rubber Structure and Properties.....	1
S. D. Gehman, formerly with The Goodyear Tire & Rubber Company, Akron, Ohio 44316 (now retired)	
Introduction.....	2
Composition of tire compounds.....	3
Technical evaluations of physical properties of tire compounds...	5
Rubber elasticity.....	14
Rubber viscoelasticity.....	23
Reinforcement of rubber with carbon black.....	32
1.2. Friction of Rubber.....	41
K. C. Ludema, Department of Mechanical Engineering, University of Michigan, Ann Arbor, Michigan 48104	
Introduction.....	42
Early phenomenological laws of friction vs. new information.....	43
Mechanical classes of tire and rubber friction.....	44
Rubber friction.....	45
Combined components of friction.....	54
1.3. Tire Cord Structure and Properties.....	63
Stanley Backer, Department of Mechanical Engineering, Massachusetts Institute of Technology, Cambridge, Massachusetts 02139	
Introduction.....	65
Cord geometry.....	65
Mechanics of tensile behavior of tire cords.....	111
Bending mechanics of twisted structures.....	191
1.4. Recent Developments with Tire Cords and Cord-to-Rubber Bonding.....	219
T. Takeyama and J. Matsui, Industrial Products Laboratory, Fibers and Textiles Research Laboratories, Toray Industries, Inc. Otsu, Japan	
Physical properties of tire cords.....	220
Rubber-to-cord bonding.....	265
Chapter 2. Properties of Cord-Rubber Laminates.....	307
Samuel K. Clark, Department of Engineering Mechanics, University of Michigan, Ann Arbor, Michigan 48104	
Elastic properties of cord reinforced rubber.....	308
Strength and failure mechanisms for cord reinforced rubber.....	341

CONTENTS – Continued

	Page
Chapter 3. Structure of the Tire	355
V. E. Gough, formerly with the Dunlop Company, Birmingham, Eng- land (now retired)	
General considerations.....	356
Pneumatic tire structure—general features.....	360
Flexible filament and soft matrix constructions.....	369
Tire construction methods.....	379
Cord path—practical factors determining selection.....	385
Calculation of cord length.....	386
Analysis of manufacturing methods by R vs $\cos \phi$ charts.....	390
Mechanism of load carrying—infinitely flexible membrane.....	392
Mechanism of load carrying—tire structure.....	398
Chapter 4. Tire Stress and Deformation	405
Joseph D. Walter, The Firestone Tire & Rubber Company, Akron, Ohio 44317	
Introduction.....	406
Analytical techniques.....	407
Experimental techniques.....	430
Principal notation.....	439
Chapter 5. The Contact Between Tire and Roadway	445
Samuel K. Clark, Department of Engineering Mechanics, University of Michigan, Ann Arbor, Michigan 48104	
Introduction.....	446
Contact area.....	447
Slip between tire and roadway.....	463
Contact pressures.....	471
Chapter 6. Skid Resistance and Directional Control	501
A. Schallamach, The Natural Rubber Producers' Research Associa- tion, Welwyn Garden City, Hertfordshire, England	
Introduction.....	502
Theory.....	502
Cornering and side force.....	508
Braking and circumferential slip.....	515
The speed dependence of rubber friction.....	518
Hydrodynamic effects on wet roads.....	520
The velocity dependence of the braking coefficient on wet roads.....	523
The effect of tread pattern and carcass construction on tire friction...	526
Tread compound effects on wet friction.....	531
Aquaplaning (hydroplaning).....	539
Winter tires.....	544
Chapter 7. The Tire as a Vehicle Component	545
H. C. A. van Eldik Thieme and H. B. Pacejka, Technological Uni- versity of Delft, Delft, The Netherlands	
Introduction.....	548
Straight line rolling experiments (H. C. A. van Eldik Thieme).....	553

CONTENTS – Continued

Chapter 7. – Continued

	Page
Cornering and camber experiments (H. C. A. van Eldik Thieme).....	631
Tire in-plane dynamics (H. B. Pacejka).....	695
Yaw and camber analysis (H. B. Pacejka).....	763
Index.....	841

Conversion of U.S. Customary Units to SI Units

The International System of Units (SI) was adopted by the Thirteenth General Conference on Weights and Measures, Sevres, France, October 15-17, 1968. Conversion factors for the units used here are given in the following table:

Physical quantity	U.S. Customary Unit	Conversion factor (*)	SI Unit
Length.....	inch	0.0254	meters (m)
Temperature.....	(°F + 459.67)	5/9	degrees Kelvin (K)
Force.....	lbf	4.448	newtons (N)
Density.....	lbm/ft ³	16.02	kilograms per cubic meter (kg/m ³)
Stress, Pressure..	psi = lbf/in ²	6895	newtons per square meter (N/m ²)
Torque.....	in-lbf	0.1130	meter-newtons (m · N)

*Multiply value given in U.S. Customary Unit by conversion factor to obtain equivalent value in SI Unit.

Prefixes to indicate multiple of units are as follows:

Prefix	Multiple
kilo (k)	10 ³
mega (M)	10 ⁶
giga (G)	10 ⁹
centi (c)	10 ⁻²
micro (μ)	10 ⁻⁶

In addition, certain engineering units which have come into common usage in Europe are rarely seen in English or American literature. Their conversion is summarized by the relations given below:

$$\begin{aligned}
 1 \text{ kp.} &= 1 \text{ kgf.} = 2.205 \text{ lbf.} \\
 1 \text{ bar} &= 10^5 \text{ N/m}^2 \\
 1 \text{ atmos. (Standard)} &= 1 \text{ kgf./cm}^2
 \end{aligned}$$

The standard acceleration due to gravity is taken to be 9.807 m/s².

CHAPTER 1

Material Characteristics

1.1. Rubber Structure and Properties

S. D. Gehman ¹

	Page
1.1.1. Introduction.....	2
1.1.2. Composition of tire compounds.....	3
1.1.3. Technical evaluations of physical properties of tire compounds.....	5
Stress-strain properties and evaluation of cure.....	5
Aging tests.....	9
Tear tests.....	10
Hardness.....	11
Dynamic tests.....	12
Flex cracking.....	12
Rubber abrasion tests.....	12
1.1.4. Rubber elasticity.....	14
Thermodynamic aspects.....	14
Molecular picture: elasticity of a rubber molecule.....	16
Elasticity of the molecular network.....	19
Strain energy representation of rubber elasticity.....	21
1.1.5. Rubber viscoelasticity.....	23
Molecular and model concepts of rubber viscoelasticity...	23
Viscoelastic relations between creep, stress relaxation, and complex dynamic modulus.....	26
Superposition principle.....	26
Time-temperature superposition principle.....	26
Dynamic properties.....	27
Energy losses in tires.....	31
1.1.6. Reinforcement of rubber with carbon black.....	32
References.....	37

¹ Formerly with The Goodyear Tire & Rubber Company, Akron, Ohio 44316.
(Retired. Present address: 214 Kenilworth Drive, Akron, Ohio 44313.)

1.1.1. Introduction

Pneumatic tires usually contain a variety of rubber compositions, each designed to contribute some particular factor to overall performance. Rubber compounds designed for a specific function will usually be similar but not identical in composition and properties, although in some cases there can be significant differences between compounds in tires of various types. The guiding principle in development of rubber compositions for tires is to achieve the best *balance* of properties for a particular type of tire service. Since a tire is a mechanical structure, a rubber component should be judged on how it functions in the system rather than on its individual properties or performance capabilities. Thus a rubber compound which did not adhere well to other tire components, or which required vastly different vulcanization conditions than other parts of the tire, could be useless in the tire even though it had excellent strength and other mechanical properties. Tire performance is the result of skill and experience in producing a mechanically harmonious structure of rubber compounds, fabric and adhesive, beads and other components which work together to give optimum service.

The principal functions of the rubber compositions in a tire are fairly obvious. The tread compound must provide wear resistance and be tough and resilient to minimize cuts, tears, and cracks, as well as to protect the tire body from bruising impacts. Low mechanical hysteresis loss in the tread is desirable since lower tire operating temperatures are advantageous. Good friction properties of the tire tread for all driving conditions are, of course, very important. In some cases optimum tread properties are obtained by using a cushioning compound between tread and tire body as additional protection against fabric bruises, thus making a "double layer" tread. This cushion can also serve, especially in retreading, as a bonding or transition layer between tread and body compounds. Intermediate hardness properties between those of tread and body are usually used in the cushion or breaker under the tread.

Tire body or carcass rubber compounds must form strong bonds to the adhesive-coated fabric. Their strength and durability should be adequate to insulate the cords and hold them in their paths. The rubber must, however, be soft enough to permit a slight change of cord angles when the tire is flexed. The body rubber serves as insulation between the fabric plies. Outstanding fatigue resistance is required of body compounds in order to withstand cyclic deformation. It is essential that they retain adequate physical properties and durability at the internal tire temperatures generated in service. Hence, low mechanical energy losses are needed for body compounds. There may be gradations in the properties of body compounds, with hardness usually diminishing somewhat from tread to cushion to top plies to inner plies.

In tubeless tires, a liner or coating on the inside ply retards diffusion

of inflating air into the fabric, and protects against ensuing ply separations.

Rubber compositions around the wire bead are called bead insulation, and give it geometric stability, shape it to fit the rim, and provide firm anchorage for the cords.

Finally, sidewall compounds must be especially durable in flexing and weathering, and be scuff and impact resistant to protect the body from curb impacts. The sidewall may include a decorative compound as a surface layer.

Processing requirements impose additional restraints on rubber compositions suitable for tires, so that the rubber technologist must consider many factors in compounding a rubber for a specific use.

1.1.2. Composition of Tire Compounds

Ingredients [1]² in tire compounds can be classified as: (1) the rubber which may be a single polymer or a blend of polymers [2, 3] and, with high molecular weight polymers, may include an extending oil [4-6]; (2) fillers, principally various types of highly-developed carbon blacks [7-9]; (3) relatively small additions of softeners, plasticizers, or reclaim rubber which serve principally as processing aids; (4) the chemical vulcanization system [10-12], which is likely to include two accelerators [13], sulfur, and a small amount of zinc oxide; (5) chemical protective agents, known as antioxidants and antiozonants [14, 15].

With such a wide variety of ingredients, the important mechanical properties for a given tire compound can usually be obtained from a number of different compositions. For example, modulus and hardness can be controlled by varying either the amount of carbon black, the amount of extender-oil or softener, the fineness and structure of the black, or the number of molecular crosslinks introduced during vulcanization. Thus even small advantages in cost, performance, and processing, which may only become apparent with extensive testing or service experience, become important factors in compound selection. No tire compound is ever final but is always subject to changes as test results and experience accumulate.

In the United States, in 1968, about 75 percent of the rubber being used in tires and tire products was synthetic [16], and of this about 73 percent was SBR (styrene-butadiene copolymers) [17], 21 percent was stereoelelastomer [17] and about 5 percent was butyl [18] or chlorobutyl rubber [19]. The latter is used for liners and inner tubes because of low air permeability and resistance to oxidative deterioration. The stereo rubber, *cis*-1,4-poly-butadiene, has come into wide use as a compounding ingredient which can improve durability of tire body compounds, can reduce groove cracking and can increase abrasion resistance of tire treads.

² Figures in brackets indicate the literature references at the end of this chapter.

Airplane tires have been the last stronghold of completely natural rubber tires, but synthetic rubber is now beginning to appear in them also.

Of the 30 or so standard types of carbon black, the HAF (High Abrasion Furnace) and ISAF (Intermediate Super Abrasion Furnace) types with their HS (High Structure) variants are currently used most extensively in tire treads. There is now a trend toward high structure blacks in treads, i.e., from ISAF black to HAF-HS. Relative use of HAF and ISAF in 1967 was about 68 percent and 32 percent respectively [20]. The high structure blacks are reported to give somewhat better wear and resistance to cracking and cut growth, along with improving processing of polymers used in treads. A physical description of these blacks is given in table 1.1.3. of this chapter.

Larger particle size carbon blacks, such as SRF, GPF, and FEF types are usually preferred for carcass compounds.

Representative tread and carcass compound recipes can be found in the rubber technical literature [2, 3] as can cushion or undertread formulations [21], wire bead insulation [22], and liner recipes [19].

For illustration a few recipes are given which are representative of tire compounds.

TABLE 1.1.1. *Tread-type formulations*

	Example A [23]	Example B [24]
OE-SBR ^a	89.38	96.00
BR ^b	35.00	30.00
Carbon black.....	^c 70.00	^d 70.00
Zinc oxide.....	3.00	4.00
Stearic acid.....	2.00	2.00
Antiozonant.....	^e 1.00	^f 1.50
Highly aromatic oil.....	19.63	24.00
Primary accelerator.....	^g 1.05	^h 1.20
Secondary accelerator.....	ⁱ 0.02
Sulfur.....	1.86	2.00
	222.94	230.70
Cure.....	40 min/ 293° F

^a Oil-extended styrene-butadiene copolymer; 100 parts polymer, 37.5 parts oil

^b *cis*-polybutadiene

^c HAF or ISAF types

^d HAF types

^e N-Cyclohexyl-N-phenyl-*p*-phenylenediamine

^f Aromatic secondary amine type

^g N-Oxidiethylene-2-benzothiazylsulfenamide

^h Sulfenamide type

ⁱ Diphenyl guanidine

TABLE 1.1.2. *Carcass-type formulations* [2]

	Truck tire body compound	Passenger tire body compound
Smoked sheet.....	25.00	25.00
Pale crepe.....	25.00	25.00
<i>cis</i> -BR.....	50.00	50.00
FEF Carbon black.....	40.00	35.00
Medium processing oil.....	8.00	8.00
Rosin oil.....	2.00	2.00
Wing-Stay 100.....	1.00	1.00
Stearic acid.....	2.00	2.00
Amax #1.....	.80	.80
Zinc oxide.....	5.00	5.00
Sulfur.....	2.50	2.50
Optimum cure.....	40 min/ 275° F	8 min/ 310° F

Simpler standard formulations are available for test and material specification purposes [25], and these, or similar ones, are often preferred for research studies on physical properties of rubber compounds.

1.1.3. Technical Evaluations Of Physical Properties Of Tire Compounds

Evaluation of the physical properties of rubber compounds for technical purposes proceeds by subjecting them to a battery of standard laboratory tests [26, 27]. Occasionally individual laboratories may deviate from these standard procedures, and may also use special tests and testing devices which they have found to be advantageous. However, the standard tests for rubber in the United States represent many years of testing experience [4]. International standardization of rubber tests is also well advanced and under constant development [28]. It should be realized that these standard tests, although they fulfill practical purposes in rubber technology, often involve combinations of several basic properties of rubber and hence are of limited general use. They usually do not furnish a very fundamental description of the physical properties, such as might be desired for research purposes.

Here we discuss very briefly the most important of these test procedures, and examine a few typical results when they are applied to tire compounds.

Stress-strain properties and evaluation of cure. The physical properties of any rubber compound depend upon the state of cure [10], that is, upon how far the chemical vulcanization reactions have been carried. Vulcanization introduces chemical crosslinks or bonds between the long chain polymer molecules. This crosslinked network is decisive for

the physical properties and is determined, for a given rubber compound, by vulcanization time and temperature. The traditional rule of thumb is that the vulcanizing time to reach a given level of a property, such as static modulus, is halved if vulcanization temperature is raised 18° F, and vice versa. Although this rule is still often adequate, a more precise description of the time-temperature dependence of vulcanization requires determination of the activation energy of vulcanization for each rubber compound [10, 29, 30].

The effect of cure on the physical properties of a rubber compound is usually determined by vulcanizing a series of test sheets for different times at the same temperature [25]. This may, of course, also be done at several temperatures if more thorough tests are desired. Dumbbell-shaped test specimens are cut from the sheets and static stress-strain curves taken [31].

Rubber stress-strain curves under static conditions are concave toward the load axis, i.e., strain hardening, except for a short portion near the origin. The concavity is accentuated by the occurrence of stress-induced crystallization in natural rubber at higher elongations [32, 33]. There is no yield point before failure, as is usual with metals. The curves in figure 1.1.1. represent approximately the effect of cure time on static stress-strain properties for a range of cures of a tread-type compound. Stress and tensile strength are calculated using the original cross-section area. In rubber technology, this stress is called modulus and is designated for a specific elongation, so that the 300 percent modulus for a rubber compound is the stress required to extend a strip to four times its original length. Volume changes are negligible [34], when rubber is strained, so that Poisson's ratio is assumed to be one-half.

Static modulus provides a convenient parameter to assess the temperature range in which elastomeric properties are exhibited. While this varies somewhat with individual polymers, in general the modulus of an elastomer varies with temperature as shown in figure 1.1.2. At low temperatures a hard or glassy character is evident. As temperature is raised the rubber passes through a transition region in which properties change rapidly. Rubber properties prevail over a range of temperatures above the transition temperature, and finally at yet higher temperatures viscoelastic or flow properties become important and predominate. It should be noted that properties other than modulus generally also show significant changes in passing from the glassy to the rubbery state.

At high temperatures and for long times, the flow properties of rubber are marked. Stress relaxation in this region can often be attributed to oxidative degradation. In the elastomeric region there is relatively little stress relaxation, and in this state the molecular network comes into equilibrium with applied stress, so that here the concept of modulus is valuable.

As shown in figure 1.1.1., modulus or stress at a given elongation increases, and breaking elongation decreases, as cure advances. This is almost invariably the case. Tensile strength usually goes through a maximum, although this is not always observed in a range of test cures. In some compounds a phenomenon known as reversion occurs and mod-

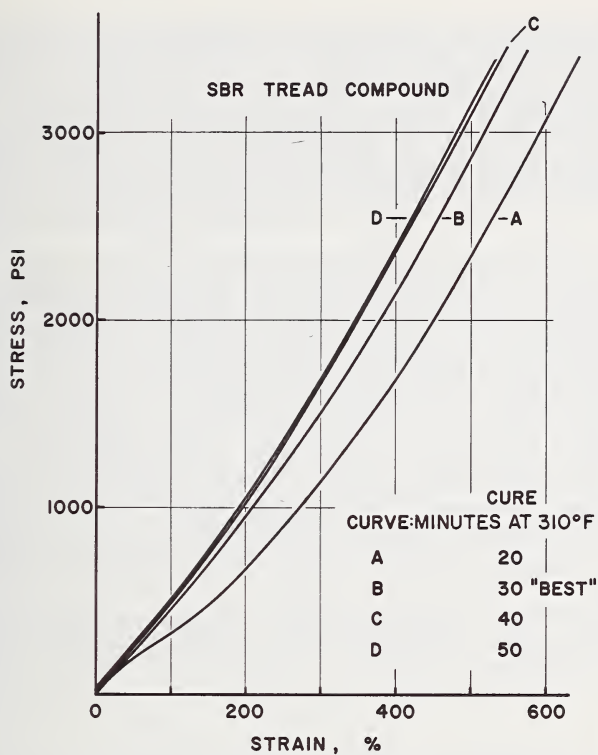


FIGURE 1.1.1. Variation of stress-strain curves with cure; data from reference [108].

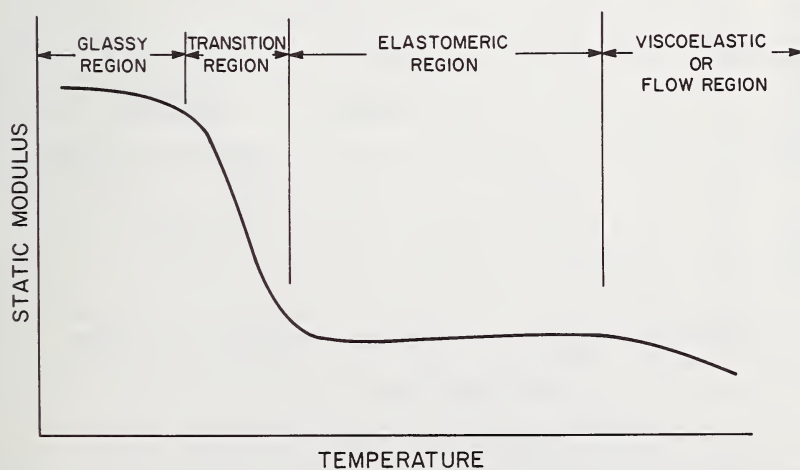


FIGURE 1.1.2. General variation of rubber modulus with temperature.

ulus, tensile strength, and breaking elongation all decrease with overcuring. Natural rubber is especially prone to this reversion. Stress-strain curves such as those shown in figure 1.1.1. are widely used in tire compound development to adjust cure rates and to insure that modulus, tensile strength, and breaking elongation of a compound fall inside a desired range. For tire tread compounds the usual tensile strength will be in the range 2500 to 4000 psi, 300 percent modulus in the range of 1000 to 1700 psi, and breaking elongation in the range of 400 to 600 percent.

Although such discrete test cures are traditional in the rubber industry, and are useful for evaluation of physical properties in relation to cure, various instruments are also used which furnish a continuous record of modulus or stiffness as cure progresses [30, 35]. Such data are very useful in showing how modulus develops, whether or not it reaches a flat plateau and whether or not there is reversion or decrease in modulus with overcure. Figure 1.1.3 illustrates these possibilities diagrammatically. The character of such a curve is determined by the polymer and the vulcanizing system [10]. The start of the curve is also significant, because it gives a measure of processing safety, that is, an indication of time-temperature conditions which the compound can endure in mixing, extrusion, etc., without excessive prevulcanization or "scorching".

Optimum or "best" cure for a rubber compound cannot in general be uniquely defined, since it depends upon the type of service and the par-

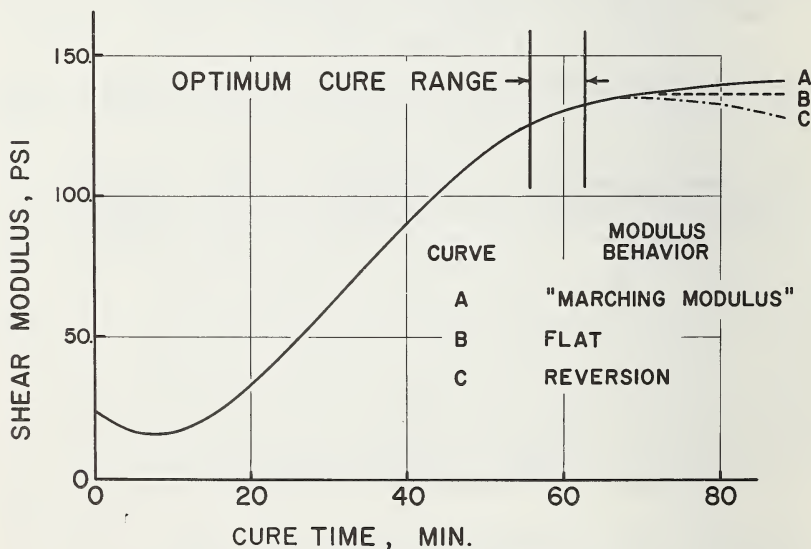


FIGURE 1.1.3. *Diagram of continuous cure curves.*

Curve A is representative for an SBR tread compound cured at 280° F; the term "marching modulus" indicates a slowly increasing modulus for long cure times.

ticular property, or properties, which should be optimized [36]. The cure designated "best" in figure 1.1.1 gives a balance of properties best suited by experience for tire tread service. There is usually a range of cures for which a vulcanizate would be expected to give about the same service performance, but large deviations from the best cure can be disastrous. Optimum cure time is usually found to be within the time required to obtain 90 to 95 percent of the rise in modulus, as shown by a curve such as in figure 1.1.3.

When a tire is cured, the time-temperature history will vary throughout the tire cross section since heat must flow into it from the mold and through the internal bladder used to form the tire. The thermal diffusivity of rubber is relatively low [37], so that the equivalent cure, i.e., minutes of cure expressed through calculation at a given reference temperature, may vary considerably between the outer surface and the interior point of least cure, even for a passenger tire. It is desirable to formulate tire compounds to compensate for this as much as possible, and to use vulcanization systems which provide "flat" cures, that is, cures such that physical properties tend to reach a plateau as vulcanization progresses. It is important to have a good, adequate cure at every point in the tire and yet to avoid excessive cure at any point.

Tire cures are originally determined by incorporating thermocouples at strategic points in the tire. Temperature is measured during vulcanization as a function of time. The production curing cycle is gotten by analysis of these time-temperature curves in relation to the vulcanizing characteristics of the compounds. Cure times for passenger car tires may be on the order of 20 minutes [38].

The state of cure of the rubber in a tire can probably be most conveniently examined or studied by equilibrium swelling measurements in benzene using small pieces of rubber cut from the tire [10]. The molecular crosslinks formed during vulcanization limit the swelling.

Aging tests. Physical properties of tire compounds, especially stress-strain properties, are also routinely examined in rubber laboratories after the rubber has been exposed to one or more accelerated aging tests [39]. These are usually run at elevated temperatures in order to simulate deterioration in service over a long period of time. Several of the tests are oven-aging tests under carefully controlled conditions, while others use a bomb filled with air or oxygen under pressure to further accelerate degradation.

Figure 1.1.4 gives an example of the effect of oven aging on the stress-strain curve of a tread compound. Although such results do not correlate perfectly with aging deterioration in service, they can be very helpful, especially with a background of experience, in anticipating whether or not a compound will be satisfactory in this respect. These aging effects are quite complicated [40, 41] as they depend on oxidative chemical reactions with the polymer [42, 43]. Hence they are very dependent both on the chemical nature of the polymer and on antioxidants in the compound recipes. In general, SBR is less sensitive to aging than natural rubber. The basic mechanism of degradation in these two rubbers appears to be quite different, SBR tending to harden on aging and natural

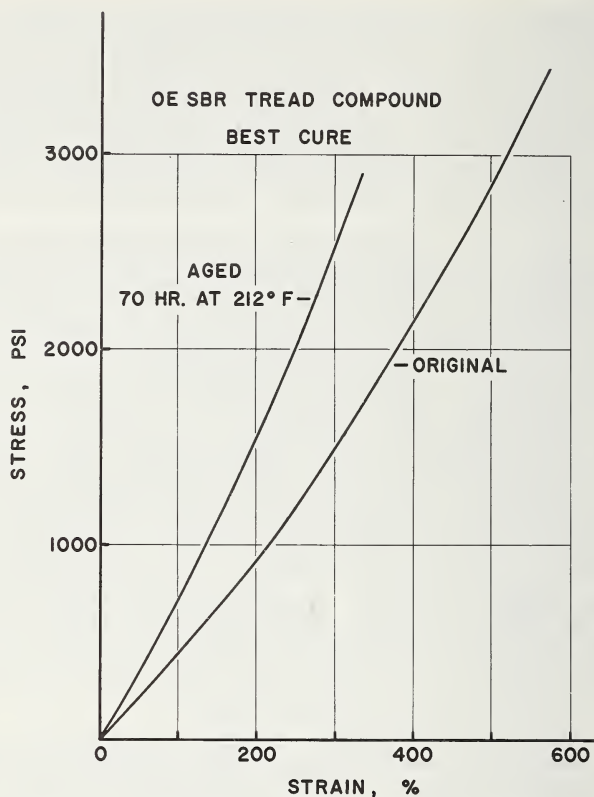
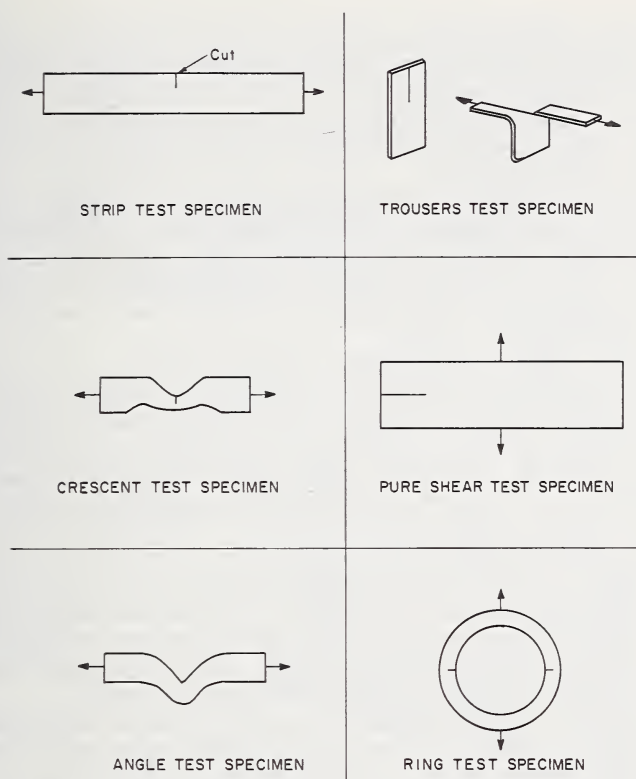


FIGURE 1.1.4. Effect of air-oven aging on stress-strain curve of the rubber compound of figure 1.1.1.

rubber to soften, reflecting, respectively, predominance of additional molecular crosslinks and chain scission, i.e., cutting of chain molecules into smaller molecules.

Effectiveness of antiozonants in rubber compounds is usually evaluated by outdoor exposure tests [44] and accelerated ozone tests [45], to promote the characteristic cracks which result from action of ozone on stretched rubber [46, 47].

Tear tests. Rubber tear tests [48] are designed to cause a high stress gradient at the end of a cut or notch in an angle or crescent shaped testpiece, which is pulled in a testing machine. Figure 1.1.5 illustrates various types of tear test specimens. Although tearing phenomena with rubber are most important and revealing in regard to mechanisms of rubber failure [49, 50], technical tear tests have very limited practical significance, probably because the notch effect is so complicated and difficult to control for rubber. Tear test values are reported as load per unit of specimen thickness. An SBR tread compound with tensile

FIGURE 1.1.5. *Tear test specimens.*

strength about 3000 psi might reasonably show a crescent tear strength of about 250 lb/in. In general, tear values tend to increase with greater tensile strength and breaking elongation but to decrease with higher modulus.

Hardness. Rubber hardness is an important quality control parameter. It is conveniently measured with a Shore *A* Durometer,³ a pocket instrument which has been standardized [51] but use of which often leaves much to be desired in the way of precision. This may be improved by mounting it in a rigid stand. The durometer uses a small, spring loaded indenter with a truncated conical point protruding from a flat base. When indenter and base are pressed against the rubber, the resulting spring deflection, which depends upon rubber hardness, is indicated by a pointer with a scale graduated from 0 (no hardness) to 100 (no indentation). Shore *A* hardness for rubber tread compounds is typically in the range of 50 to 65 units and for unfilled vulcanizates about 25 to 30.

³ Certain commercial products and instruments are identified in this book in order to specify adequately technical procedures. In no case does such identification imply recommendation or endorsement by the National Bureau of Standards, nor does it imply that the products or equipment identified are necessarily the best available for the purpose.

There are a variety of other hardness test instruments for rubber and a well-developed International Rubber Hardness Degree (IRHD) scale which agrees approximately with the Shore *A* Durometer scale [52, 53]. Indentation of thick rubber obeys the classical elasticity analysis of Hertz very well [54], and this gives a mechanism to relate elastic modulus to hardness measurements.

Dynamic tests. Many different test procedures are available to measure rubber stiffness and energy loss for relatively small cyclic deformations, often over ranges of temperature and frequency. These evaluations are especially pertinent for tire compounds because heat generation and temperature rise from rubber hysteresis losses are important factors in tire durability [55].

One of the oldest and still most widely used types of test for this purpose is a pendulum rebound test, in which a pendulum is released from a fixed height to strike a rubber block and then rebound [56]. Superiority or natural rubber or synthetic *cis*-1,4-polyisoprene in this test is pronounced. Percent rebound for SBR tread compounds will usually be in the range of 52 to 62 percent while that for comparable natural rubber compounds may be more than 70 percent. A falling ball instead of a pendulum is often used in a rebound test.

Free vibration tests [57] and forced nonresonant and resonant vibration tests are also found in great variety [58, 59]. These are used to measure dynamic modulus,⁴ internal friction,⁴ and resilience⁴ of rubber compounds. Reference [60] includes a useful table of storage⁴ and loss moduli⁴ for a wide variety of rubbers and other materials.

Energy losses in rubber may be evaluated by measuring the temperature rise when a block specimen is cyclically deformed in shear or compression or both. These rubber testers are called flexometers [61]. There are many limitations, however, on the usefulness and interpretation of such temperature rise data. Compression set of the rubber specimen after a flexometer test is usually also reported and is used in compound evaluations, especially for state of cure. Occasionally the tests are run to destruction.

Flex cracking. Initiation and growth of small cuts or tears in tire treads, especially in the pattern grooves and in tire sidewalls, are so significant for tire performance that much effort has been expended in developing laboratory tests to simulate and clarify these phenomena. Several testing machines and procedures have been standardized for such tests [62]. The DeMattia machine, where a specimen with a transverse groove is cyclically bent as shown in figure 1.1.6, is probably the most familiar of these. Results of such tests are sensitive to compounding factors such as type of elastomer, state of cure, and protective agents in the recipe [63].

Rubber abrasion tests. Laboratory abrasion tests are used in tread compound development because they provide inexpensive, rapid screening of experimental polymers and rubbers, in spite of the fact that correlations with roadwear have limited success. Two methods are

⁴ These terms are defined in the section on dynamic properties.

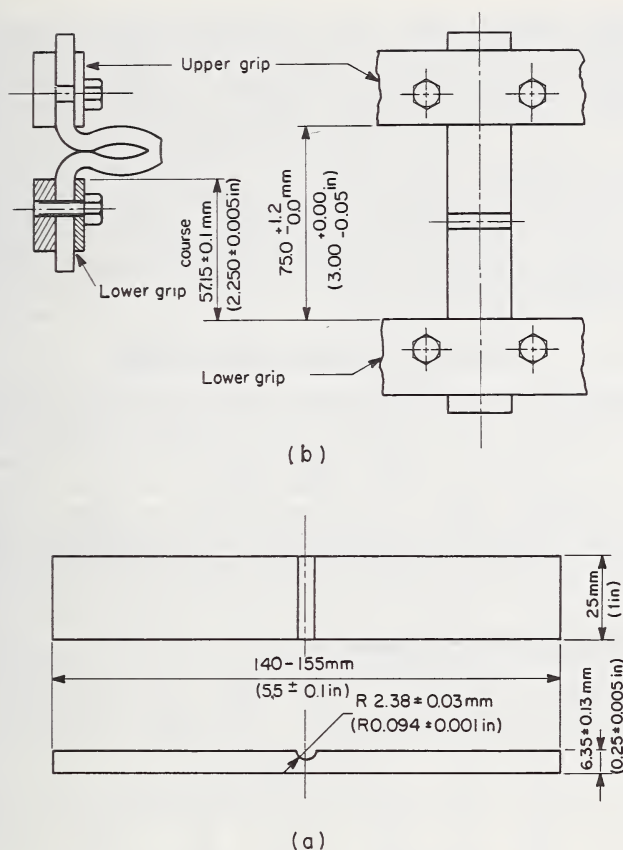


FIGURE 1.1.6.

(a) DeMattia testpiece. (b) Mounting of DeMattia testpiece.

given in ASTM Standards [64], the Dupont abrader where two rubber specimens are abraded against a revolving disk, and the Pico abrader in which the surface of the specimen is rubbed by revolving tungsten carbide knives under carefully controlled conditions. Much abrasion testing is also done with the Goodyear angle abrader [65], in which a specimen in the shape of a small rubber wheel is mounted at a slip angle and driven by a revolving abrasive wheel. A variation of this is the Lambourn [66] abrader, in which slip of the rubber wheel specimen is controlled by an electromagnetic brake so that tests can be run either at constant slip or constant transmitted power. Developments with Lambourn-type abraders have become quite sophisticated in efforts to secure correlations with road tests on different road surfaces and under different driving conditions [67].

It is widely recognized that the severity of abrasion, or rate of wear, is an important factor in abrasion testing. Rankings of a series of com-

pounds may change if rate of wear is changed. This introduces obvious complications in trying to correlate laboratory data with road wear, since severity of wear on the road depends on many factors including road surface, frequency of curves, amount of rain, braking and many others. The severity level of a laboratory abrasion test, that is, the amount of rubber removed per unit distance traveled, should presumably be comparable to that in road tests for best correlations. This may be very low, by American standards, in the order of 100 miles/mil⁵ of wear normally and 50 miles/mil or less for severe service. To reduce testing time, laboratory tests are usually accelerated and have much larger wear rates than road tests.

1.1.4. Rubber Elasticity

Thermodynamic aspects. Distinctive features of rubber elasticity are easy deformability or low modulus, enormous deformations, and rapid recovery when deforming forces are released. There is also more sensitivity to temperature than for many elastic materials. Figure 1.1.7 shows the dramatic effect of low temperatures on relative modulus of unfilled vulcanizates of several polymers. For any elastomer there is a range of temperatures over which transition occurs from a rubbery to

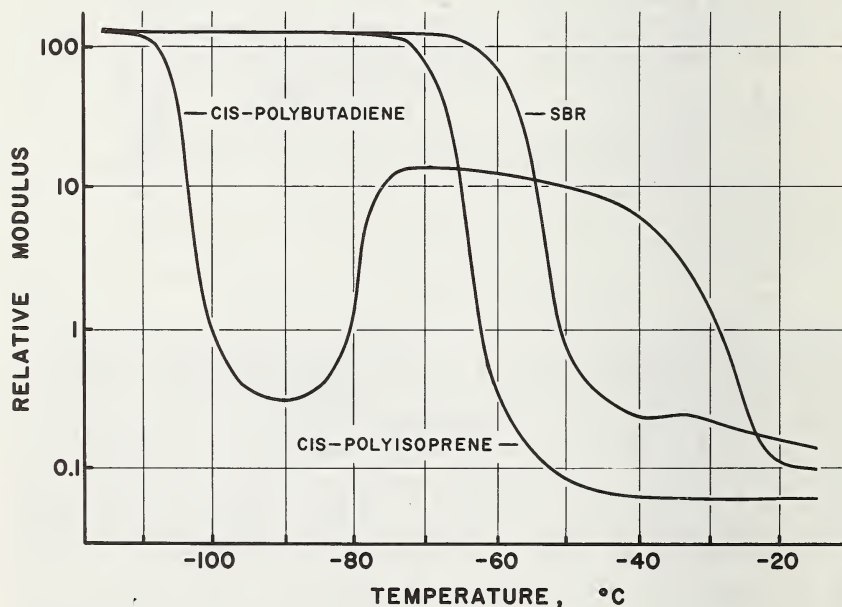


FIGURE 1.1.7. Effect of low temperatures on rubber modulus; data by ASTM method 1053-65, reference [4].

⁵ One mil equals .001 inch equals .0254 mm.

a glassy state, as shown in figure 1.1.2. This transition temperature range for SBR is from -60°C to -40°C , which is about as high as can be tolerated for a general purpose tire rubber. The curve for *cis*-polybutadiene in figure 1.1.7 is complicated by crystallization, which starts to affect the warming curve at about -95°C .

In the transition range from the glassy to the rubber state modulus falls rapidly with increasing temperature, but further temperature increase results in a slowly rising modulus. This rise was first observed in experiments by Gough, published in 1805, as a contraction when a rubber specimen stretched by a weight was heated. Joule, about 50 years later, studied thermoelastic phenomena exhibited by rubber and interpreted them in terms of the new science of thermodynamics then being developed by Kelvin. Treloar [72] gives a very good review of the thermodynamic fundamentals of rubber elasticity. For a reversible process, the first and second laws of thermodynamics provide,

$$dE = TdS + dW \quad (1.1.1)$$

in which E is internal energy of a system, T is absolute temperature, S is entropy, and W is work done on the system. At once there is a difficulty here because ordinary rubber deformations are not completely reversible. It is necessary to take special measures with any test specimens, such as solvent vapor treatments or prestretching them at an elevated temperature, in order to secure reversible deformations.

If the tensile force on a rubber strip is f , then the work done during an isothermal displacement dl is, neglecting small volume changes,

$$dW = fdl \quad (1.1.2)$$

and, with eq (1.1.1)

$$f = \left(\frac{\delta W}{\delta l} \right)_T = \left(\frac{\delta E}{\delta l} \right)_T - T \left(\frac{\delta S}{\delta l} \right)_T \quad (1.1.3)$$

Equation (1.1.3) resolves the force into two terms. The first arises from changes in internal energy and the second from entropy changes with changes in length.

By differentiation of eq. (1.1.3), it follows that

$$\left(\frac{\delta f}{\delta T} \right)_l = - \left(\frac{\delta S}{\delta l} \right)_T \quad (1.1.4)$$

so that eq (1.1.3) can be written

$$f = \left(\frac{\delta E}{\delta l} \right)_T + T \left(\frac{\delta f}{\delta T} \right)_l \quad (1.1.5)$$

Equation (1.1.5), in conjunction with eq (1.1.4), has been very important for understanding rubber elasticity because it allows experimental

evaluation of internal energy and entropy changes upon deformation. If the equilibrium force exerted by a stretched rubber strip held at constant length is measured and plotted as a function of temperature, the slope at any value of T is $\left(\frac{\delta f}{\delta T}\right)_l$, which eq (1.1.4) shows to be the entropy change per unit change in length for isothermal extension at T . The corresponding internal energy change $\left(\frac{\delta E}{\delta l}\right)_T$ is given by the intercept of the tangent with the zero T axis.

Careful experimental work of this type by Meyer and Ferri [68], Anthony, Caston, and Guth [69], Wood and Roth [70], Gee [71] and many others showed that over a considerable temperature range stress was closely proportional to absolute temperature, and this led to the conclusion that rubber elasticity resides principally in the entropy term of eq (1.1.5). There is an entropy decrease on extension and an increase on retraction, except:

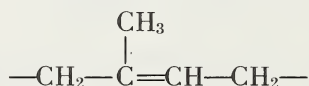
a. at very low elongations, below about 10 percent where a so-called thermoelastic inversion is observed due to thermal expansion obscuring the entropy effect

b. at large elongations, where high orientation and crystallization may occur.

Volume changes and internal energy effects, however, appear never to be entirely absent. This entropy basis indicates that rubber elasticity must have an entirely different molecular origin or mechanism than ordinary elasticity, where stresses increase the internal energy by increasing molecular or atomic spacings.

Molecular picture: elasticity of a rubber molecule. The unique thermoelastic behavior of rubber is related to molecular structure by the kinetic or statistical theory of rubber elasticity. The theory provides a very satisfactory explanation of what might be called the mainspring of rubber elasticity, but it involves idealizations which have restricted its quantitative application to very carefully controlled equilibrium experiments with suitable rubber compounds and limited elongations and temperatures. It can only be regarded as semiquantitative for rubber in real applications. Reasons for these deviations from the theory, however, are quite comprehensible in light of what is known from many sources concerning the molecular geometry and forces.

There is extensive evidence that a rubber is composed of long chain molecules, as shown in figure 1.1.8. The monomer repeating unit in the chain molecule of *cis*-polyisoprene or natural rubber is



while in *cis*-polybutadiene it is $-\text{CH}_2-\text{CH}=\text{CH}-\text{CH}_2-$. In SBR, styrene units amounting to about 23 percent by weight occur at random in the polybutadiene chain. Such molecules are flexible by virtue of rotation around the single bonds, except at low temperatures where packing becomes too close or crystallization may occur for the first two rubbers. They tend to assume haphazard or chance configurations because of thermal agitation of their segments. Most of these configurations will be very crumpled, so that a chain molecule can be extended by an external tensile force provided that interaction with its neighbors is not too strong. As temperature is lowered, this interaction increases until the typical low modulus and rubber elasticity are no longer present. This temperature influence is shown in figure 1.1.7.

Chemical composition of the molecules may vary widely provided that chain length, flexibility, and interactions all lie within ranges appropriate for rubber elasticity. In order to secure mechanical stability in such a molecular structure it is necessary to connect the chain molecules into a network by introducing chemical bonds or crosslinks between them during vulcanization. The chemical nature of the crosslinks is not relevant for the theory because they are idealized simply as network connections. The nature of the crosslinks is, however, technically important. The crosslinks cannot be too numerous, or flexibility of the network will suffer, but their number must be adequate to suppress plastic flow. To be more definite, rubber chain molecules having 1000 to 2000 monomer units per chain may very well have about 10 to 40 of these units crosslinked at random along a chain in a vulcanizate.

History of the kinetic theory of rubber elasticity, which dates back to about 1932, has been recounted by Treloar [72] and by Flory [73]. The theory has been thoroughly examined both experimentally and analytically and has been refined in many respects. Treloar gives an excellent exposition of developments up to about 1958, and a review article by

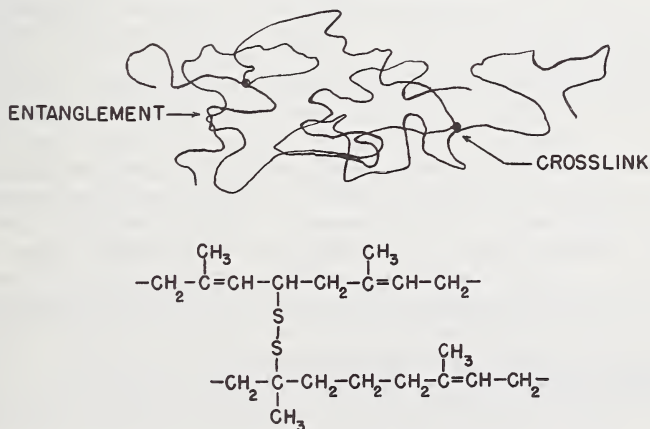


FIGURE 1.1.8. Diagram to illustrate concept of molecular structure of rubber.

Krigbaum and Roe [74] brings the subject up to recent years. Only a brief recapitulation of a few of the main features of the theory will be given here.

A single, long chain rubber molecule assumes random statistical configurations to the extent permitted by hindered bond rotations, fixed valence-bond angles,⁶ excluded volumes (since no two atoms can occupy the same space simultaneously), and intermolecular forces. Some of these effects can be accommodated in the theory, but in the first mathematical model the molecule is assumed to undergo random thermal fluctuations among all possible configurations of its n links, each of length l , just as if they were freely orienting. Thus the problem of describing the configurations is the random walk problem, and the configurations have analogies to the Brownian motion of a particle.

The distance between the ends of a chain, r , is called the displacement length, end-to-end distance, or simply the chain length. The distance measured along the chain is the chain contour length.

The distribution of chain lengths is Gaussian provided they are not extended more than about one-third of their fully extend length, nl .

This distribution is given by

$$P(r)dr = (4b^3/\pi^{1/2})r^2 \exp(-b^2r^2)dr. \quad (1.1.6)$$

In eq (1.1.6) $P(r)$ is the probability function for r and

$$b^2 = (3/2)/(nl^2). \quad (1.1.7)$$

The root mean square value of r is

$$(\bar{r}^2)^{1/2} = ln^{1/2}. \quad (1.1.8)$$

This shows at once that n must be large to account for rubber elongations, since the ratio of the average unstretched chain end separation to the fully extended chain length is $n^{-1/2}$. Higher molecular weights thus favor greater extensibility.

Equation (1.1.6) is for a freely orienting chain. For a real molecule, where valence angles are retained and rotation may be hindered, it is necessary to introduce the idea of an equivalent random chain and an equivalent random link. Length of the equivalent random link depends upon the chemical structure. Usually the equivalent link contains up to ten main chain bonds. For polyisoprene, Treloar estimated that there were 0.76 monomer units per random link. If a rubber network chain molecule, i.e., a chain between crosslinks, contains about 80 monomer units, or 105 freely orienting links, the ratio of fully stretched length to average unstretched end-to-end distance will be $(105)^{1/2} \approx 10.2$. This is adequate to account for rubber elongations.

According to the familiar Boltzmann relation the entropy of a system is proportional to the logarithm of the number of possible configurations.

⁶ For a paraffin chain molecule the angle between two adjacent bonds in the -C-C structure is 109.5°.

Hence from eq (1.1.6) the entropy S of a single chain molecule is

$$S = c - k \cdot b^2 \cdot r^2 \quad (1.1.9)$$

in which c is an arbitrary constant and k is Boltzmann's constant. It is apparent from eq (1.1.9) that the entropy decreases as r becomes larger, that is, as the molecule is stretched. The work required to increase r to $r + dr$ is

$$fdr = -T \frac{dS}{dr} \quad (1.1.10)$$

in which f is the stretching force on the molecule. From eq (1.1.9) $dS/dr = -2kb^2r$ so that

$$f = 2kTb^2r. \quad (1.1.11)$$

This is the average fluctuating statistical force exerted at the end of a stretched molecule. It is proportional to absolute temperature and to the value of r , the end-to-end distance, and it acts along the line of r .

Elasticity of the molecular network. A chain molecule reaching from one crosslink to another is called a network chain. The Gaussian distribution of eq (1.1.6) is assumed to apply to each network chain so that the entropy change for deformation of the network can be calculated by summing the entropy changes for all the chains in the network. In doing this the assumption is made that the deformation is affine, that is, the vector components of length of each chain are changed in the same ratio as the corresponding dimensions of the rubber specimen. Treloar [72] gives the entropy change ΔS of the network due to deformation as

$$\Delta S = -\frac{1}{2} Nk (\lambda_1^2 + \lambda_2^2 + \lambda_3^2 - 3) \quad (1.1.12)$$

in which N is the number of network chains per unit volume and λ_1 , λ_2 , and λ_3 are the principal extension ratios along the three mutually perpendicular axes of strain for a pure homogeneous strain. The extension ratio is defined as the ratio of the deformed to the undeformed length.

If the deformation is not accompanied by any change in internal energy the work of deformation, \mathcal{W} , is $-T\Delta S$, so that

$$\mathcal{W} = \frac{1}{2} NkT (\lambda_1^2 + \lambda_2^2 + \lambda_3^2 - 3) = \frac{1}{2} G (\lambda_1^2 + \lambda_2^2 + \lambda_3^2 - 3) \quad (1.1.13)$$

\mathcal{W} is the elastically stored free energy per unit volume and is known as the stored energy function.

In eq (1.1.13) G is the modulus of rigidity which in this simpler version of the theory depends uniquely on chain molecular weight through the relation

$$G = NkT = \rho RT/M_c. \quad (1.1.14)$$

Here ρ is the density of the rubber, R is the gas constant and M_c is the number-average network chain molecular weight. The theory thus provides a single elastic constant which is proportional to the degree of crosslinking.

To calculate the principal stresses from eq (1.1.13) it is assumed that volume changes can be neglected so that

$$\lambda_1 \cdot \lambda_2 \cdot \lambda_3 = 1 \quad (1.1.15)$$

Work done by the applied forces is

$$dW = f_1 d\lambda_1 + f_2 d\lambda_2 + f_3 d\lambda_3 \quad (1.1.16)$$

in which f_1 , f_2 , and f_3 are forces per unit initial *unstrained* area and act along the principal axes. Comparing dW obtained by differentiating eq (1.1.13) with dW in eq (1.1.16), after eliminating λ_3 from both by use of eq (1.1.15), and equating the coefficients of $d\lambda_1$ and $d\lambda_2$ gives the general stress-strain relations:

$$\lambda_1 f_1 - \lambda_3 f_3 - G(\lambda_1^2 - \lambda_3^2), \quad (1.1.17)$$

$$\lambda_2 f_2 - \lambda_3 f_3 = G(\lambda_2^2 - \lambda_3^2). \quad (1.1.18)$$

Equations (1.1.17) and (1.1.18) can be written in terms of principal stresses t_1 , t_2 , t_3 , defined as forces per unit area after straining, by use of relations such as $f_1 = t_1 \lambda_2 \lambda_3$, in the form

$$t_1 - t_3 = G(\lambda_1^2 - \lambda_3^2), \quad (1.1.19)$$

$$t_2 - t_3 = G(\lambda_2^2 - \lambda_3^2). \quad (1.1.20)$$

These equations give only the difference between two principal stresses, since eq (1.1.15) has introduced the indeterminacy of an arbitrary hydrostatic stress. This may be recognized by writing the principal stresses [72] as

$$t_1 = G\lambda_1^2 + p; \quad t_2 = G\lambda_2^2 + p; \quad t_3 = G\lambda_3^2 + p. \quad (1.1.21)$$

However, if one or more of the principal stresses is given, a unique solution can be obtained for the other two stresses provided that the extension ratios λ_1 , λ_2 , λ_3 are known. For uniaxial extension f_2 and f_3 both vanish, and $\lambda_2 = \lambda_3 = \lambda_1^{-1/2}$ so that from eqs (1.1.17) and (1.1.18), the rubber stress-strain relation is

$$f = G(\lambda - \lambda^{-2}). \quad (1.1.22)$$

Treloar carried out experiments to verify eqs (1.1.19) and (1.1.20) using simple extension, uniaxial compression, uniform two dimensional extension and shear deformation on natural rubber gum vulcanizates. He

found that these equations using the single physical constant G provided a fairly satisfactory first approximation to experimental results. However, deviations were observed both at moderate strains, where measured stresses tended to be lower than predicted, and at very high strains where they were larger than predicted. The effects at large strains are caused by failure of the Gaussian distribution, eq (1.1.6) to apply for large extensions of the chain molecules. This can be explained by non-Gaussian statistics [72].

Deviations at moderate strains have been attributed to inadequacy of the stored energy function using only a single constant. Krigbaum and Roe [74] analyze such deviations from the kinetic theory in detail, summarize the evidence that there are, in fact, appreciable energy changes in rubber deformations, and describe more recent attempts to test and refine this theory.

Correction terms have been introduced into the theory to account for free ends of chains which are not tied into the network and for chain entanglements which act as effective crosslinks [72, 73, 75, 76]. Fillers and crystallites seem to provide fixed attachment points for network chains and thus simulate to some extent the effects of additional crosslinks.

Strain-energy representation of rubber elasticity. The preceding sections have shown how thermoelastic phenomena, along with rubber and thermodynamic analysis, led to the kinetic or statistical theory of rubber elasticity. In turn, this leads to a description of rubber elasticity in terms of a stored energy function using a single elastic constant, called G in eq (1.1.13).

The stored-energy approach has been developed for rubber in an entirely phenomenological way, independent of any molecular theory, both by Mooney [77] and by Rivlin [78]. In applying the general elasticity theory for large deformations of incompressible, isotropic elastic materials, Mooney assumed a linear shear stress law consistent with kinetic theory. Rivlin showed that it was unnecessary, for many purposes, to assume any particular elastic law and that the elastic law could be determined experimentally through relations derived from the theory.

The strain energy per unit unstressed volume stored in a material is a function of the general components of strain at any point [79]. The stored-energy function is unaffected by coordinate transformations. The form of this function is as characteristic of the material as the stress-strain relation, with which, of course, it is closely connected. The nature of the stored energy function for a pure homogeneous strain completely determines the elastic properties of the material. The assumption of incompressibility simplifies the function, and is justified for rubber in practical terms because stresses required for changing the volume are so much larger than those required to change the shape.

It follows from this general theory for large elastic deformations of rubber [72, 79–81] that the stored energy \mathcal{W} is a symmetric function of the three principal extension ratios λ_1 , λ_2 , and λ_3 , and can be expressed

in terms of the three following strain invariants:

$$I_1 = \lambda_1^2 + \lambda_2^2 + \lambda_3^2, \quad (1.1.23)$$

$$I_2 = \lambda_1^2 \cdot \lambda_2^2 + \lambda_2^2 \cdot \lambda_3^2 + \lambda_3^2 \cdot \lambda_1^2, \quad (1.1.24)$$

$$I_3 = \lambda_1^2 \cdot \lambda_2^2 \cdot \lambda_3^2. \quad (1.1.25)$$

Assuming incompressibility, $I_3 = 1$, and λ_3 can be eliminated from eqs (1.1.23) and (1.1.24) so that W can be expressed in terms of two independent variables I_1 and I_2 , which in turn contain only λ_1 and λ_2 . This means, of course, that only two of the extension ratios can be varied independently.

The most general form of this stored energy function can be written [72]

$$W = \sum_{i=0}^{\infty} \sum_{j=0}^{\infty} C_{ij} (I_1 - 3)^i (I_2 - 3)^j \quad (1.1.26)$$

$(I_1 - 3)$ and $(I_2 - 3)$ are used in eq (1.1.26) instead of I_1 and I_2 so that W will be zero for zero strain.

The first term of the series, $i = 1, j = 0$, gives for W the form derived from the kinetic theory, eq (1.1.13) which gives a reasonably good first approximation to the rubber stress-strain relations.

Retention of the first two terms, $i = 1, j = 0$ and $i = 0, j = 1$ gives

$$W = C_1(I_1 - 3) + C_2(I_2 - 3) \quad (1.1.27)$$

This was the form derived by Mooney which, having two constants, provides better agreement with experimental data than eq (1.1.13).

From eq (1.1.27) for simple extension, the force f per unit initial cross section is derived as

$$f = 2 \left(\lambda - \frac{1}{\lambda^2} \right) \left(C_1 + \frac{C_2}{\lambda} \right). \quad (1.1.28)$$

Equation (1.1.28) is known as the Mooney-Rivlin equation. For simple shear,

$$t_\sigma = 2(C_1 + C_2)\sigma \quad (1.1.29)$$

in which t_σ is shear stress, σ shear strain and hence $2(C_1 + C_2)$ is the modulus of rigidity.

Equation (1.1.28) has been exhaustively tested and debated [72, 74, 79]. There is little question that it gives better agreement with experiments at moderate elongations than does eq (1.1.22) but the physical origin or significance of C_2 is obscure. Ciferri and Flory [82] showed that it decreased in value when better techniques were used to reach equilibrium strains, but it evidently does not vanish entirely and sometimes is quite appreciable [74].

Energy effects have been shown to make a substantial contribution to C_2 , but there are probably also entropy effects related to the orienting properties of particular network structures as affected by chain length distribution and chain packing [74]. The exact nature of this is still nebulous.

It would be necessary to retain more terms in eq (1.1.26) in order to account for the upward curvature in rubber stress-strain curves at high elongation. These occur because of limited chain extensibility.

A convenient way to test eq (1.1.28) experimentally is to plot $f/2 (\lambda - 1/\lambda^2)$ against $1/\lambda$. If the equation holds, a straight line will be obtained, the slope of which is C_2 while the intercept is C_1 .

1.1.5. Rubber Viscoelasticity

Viscoelasticity, or delayed response to stress change, of rubber compounds is especially important for tire performance because it is greatly enhanced by reinforcing carbon blacks. Equilibrium or reversible stress-strain relations from the kinetic theory become submerged in viscoelastic effects for such compounds. Tire deflections occur so rapidly that equilibrium conditions are not approached for the rubber deformations in tires. In general, rubber viscoelasticity becomes evident in a dependence of properties on rate of deformation, time-deformation history, and temperature dependence in excess of the relatively small kinetic theory effect, according to which the modulus should be proportional to absolute temperature. In recent years it has been found that tensile and tear strength mechanisms [83] and even abrasion processes for rubber compounds [84] are dominated by viscoelastic effects.

Figure 1.1.9 gives a diagram illustrating the delayed response of rubber in a creep test where a test specimen is loaded with a constant weight. There is a rapid deformation at the start followed by slow, gradual approach to an equilibrium deformation. When the weight is removed, there is a rapid retraction followed by a slow recovery which may never be complete, so that there is permanent set as well.

Figure 1.1.10 illustrates compressive stress-relaxation curves for an SBR tread-type compound, when a test specimen was subjected to constant compression. Rate of stress decay, i.e., time rate of change of stress at constant strain, for this compound evidently went through a minimum at about 78° F. Stress relaxation at moderate temperature is largely a physical phenomenon, but at elevated temperatures it is usually associated with chemical changes such as oxidation and degradation.

Molecular and model concepts of rubber viscoelasticity. The molecular basis for rubber viscoelasticity lies in viscous forces acting on the segments of a chain molecule as they move in response to an applied stress. Each segment is essentially drawn through a very viscous medium consisting of its neighbors, so that its motion is retarded and an appreciable time is required to adjust to a stress. Semiquantitative calculations based on such a molecular picture show that it is essentially correct [75].

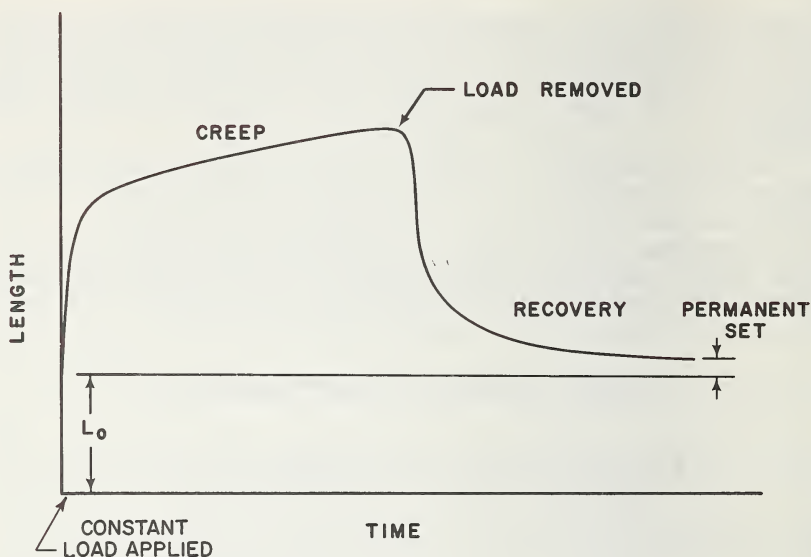


FIGURE 1.1.9. Typical deformation in creep, recovery, and permanent set.

The mathematical theory of linear viscoelasticity can be presented by an analysis of ideal spring-dashpot models to represent, respectively, the elastic and viscous components of the response of the material to stress. These models have been widely described [75, 85–87]. For stress relaxation, that is, decay of stress at constant strain, it is convenient for the model to consist of a large number of Maxwell elements in parallel

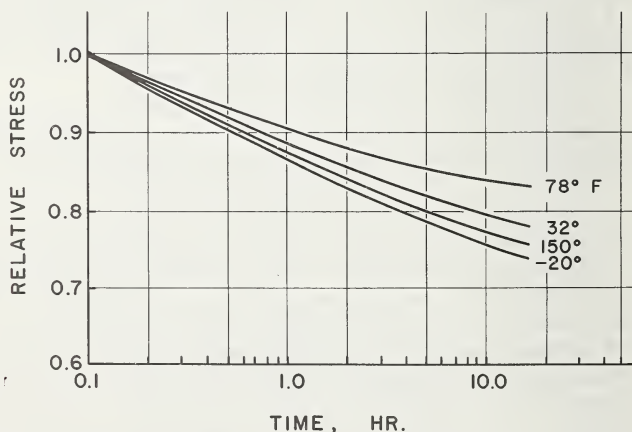


FIGURE 1.1.10. Compressive stress relaxation for an SBR tread compound under 30% compression.

such as shown in figure 1.1.11(a). For descriptions of creep Voigt-Kelvin elements in series are advantageous as shown in figure 1.1.11(b). Although any rubber viscoelastic curve, such as a creep or stress relaxation curve, can be matched by a suitable model with sufficient elements [88], this is entirely formal since the model elements cannot be identified with specific features of molecular or network structure. If the material does not truly display linear viscoelasticity, such complicated models cannot be expected to cover a wide range of behavior. For a Voigt-Kelvin element, stress on the unit at any time is the sum of the force arising from spring elongation and that from dashpot velocity, so that one may write

$$\sigma = E \cdot \epsilon + \eta \frac{d\epsilon}{dt}. \quad (1.1.30)$$

Response of a Voigt-Kelvin element to a constant load is [75]

$$D(t) = \epsilon/\sigma = (1/E) [1 - \exp(-t/\tau)]. \quad (1.1.31)$$

Using the element to represent a unit cube of material, ϵ in eqs (1.1.30) and (1.1.31) is the strain, $\frac{d\epsilon}{dt}$ the strain rate, σ the stress, E is Young's modulus and τ is the retardation time of strain. This latter quantity is defined as η/E , where η is the internal friction of the material, that is, the stress per unit strain rate. $D(t)$, or ϵ/σ , is called the creep compliance.

If there are a number of elements in a series model, as in figure 1.1.11(b), there will be a discrete spectrum of retardation times, and

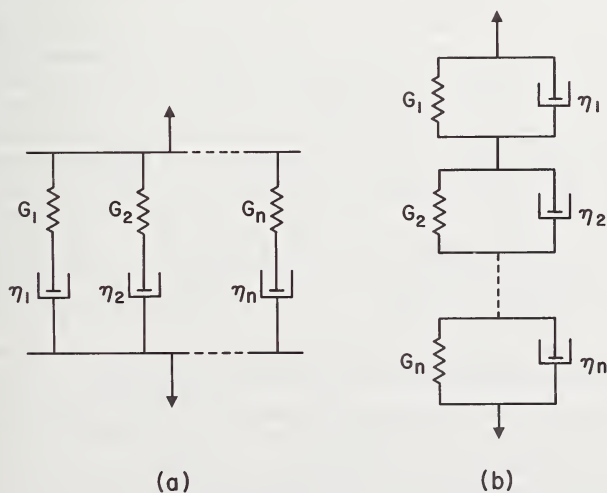


FIGURE 1.1.11. *Models for viscoelasticity.*

(a) Maxwell elements in parallel. (b) Voigt-Kelvin elements in series.

creep compliance will be given by a summation of the contributions to ϵ from the individual elements.

Viscoelastic relations between creep, stress relaxation, and complex dynamic modulus. When the mathematical summation described above is carried to the limit for a continuous distribution of retardation times of strain, the distribution function is known as the retardation spectrum of the material. The creep compliance is obtained from this distribution as an integral expression [88, 89]. Similarly, the relaxation modulus can be derived as an integral expression involving the distribution function of the relaxation times of stress, conveniently derived through a generalized Maxwell model, figure 1.1.11(a). The relaxation and retardation spectra are alternative ways of specifying the viscoelastic behavior of a vulcanizate. They are related by the mathematical theory of linear viscoelasticity [88, 90]. In theory, these spectra can be determined for a material which conforms to linear viscoelasticity from suitable stress relaxation or creep curves. This is usually done by approximation methods. Similarly, when the models are subjected to a sinusoidal driving force, the response can be calculated by properly formulated integrations of either of the distribution functions. Thus, in principle, any of these experimental methods, suitably applied, can be used to completely determine the viscoelastic response of a material to forces. For instance, data from a relaxation test can be used to calculate creep [91, 92].

Superposition principle. A basic assumption of linear viscoelasticity theory is that the material responds to stresses in the same way regardless of its past stress history. The effect of a change in stress can be superimposed on effects remaining from previous stresses. This principle permits the response to be calculated for variable applied forces [88, 90].

As with the kinetic theory, the linear theory of viscoelasticity provides a useful framework of reference from which to describe rubber properties. Unfortunately it is not truly descriptive of tire compounds which are filled with reinforcing carbon black. Reasons for this are apparent in light of the restrictions of the superposition principle. In the first place, aside from small shear stresses, rubber has a nonlinear stress-strain relation. In addition there is an irreversible deformation component, or permanent set, which can be described in particular cases by model elements but which cannot be well described for all deformations. Finally, in vulcanizates filled with reinforcing carbon black there appear to be stress-induced changes in internal structure associated with breaking or slipping of polymer bonds, polymer-filler bonds or filler-filler bonds. These tend to invalidate application of the superposition principle and hence the linear theory of viscoelasticity.

Time-temperature superposition principle. A very useful viscoelastic concept is that time and temperature are equivalent for describing viscoelastic behavior [75, 86, 89]. Thus a creep curve observed for short times at a given temperature is identical with one observed for longer times at a lower temperature, except that the curves are shifted on a logarithmic time axis. They can be superimposed once more by proper

scale changes on this axis. Similarly, portions of a creep curve or stress relaxation curve can be observed at different temperature, and these curve segments can then be shifted along the log-time axis to construct a composite curve or master curve, applicable for a given temperature, extending over many decades of time. Figures 1.1.12 and 1.1.13 from Bueche [75] illustrate this procedure for a plot of creep compliance against log-time. The shift factor for a curve segment is designated a_T , $\log a_T$ being the horizontal displacement necessary to allow it to join smoothly into the master curve. This is the factor by which the time scale is altered due to the difference in temperature, and is, of course, a function of temperature.

For exact work, there is also a small vertical shift, modulus values being multiplied by $T_0\rho_0/T\rho$ (or compliance values by the reciprocal ratio) to take account of the entropy effect of temperature on stress. T_0 and ρ_0 are absolute temperature and density, respectively, for standard conditions or for the master curve, and T and ρ apply for the curve segment which is to be shifted [86, 89].

It has been found [89] that for all linear viscoelastic materials over a limited temperature range horizontal shift factors are given by the empirical Williams-Landel-Ferry (WLF) equation:

$$\log a_T = \frac{-17.44(T - T_g)}{51.6 + (T - T_g)}. \quad (1.1.32)$$

T_g is the glass transition temperature of the material. Equation (1.1.32) provides quite satisfactory shift factors in the range $T_g < T < T_g + 120$ for all types of viscoelastic phenomena. Either Kelvin or Centigrade temperatures may be used in it. The applicability of eq (1.1.32) is often used as a criterion for whether a process, such as abrasion or tearing of rubber is viscoelastic in nature.

For tire deformations, this time-temperature equivalence principle implies that response of the rubber at high speeds will not be correctly evaluated with conventional laboratory stress-strain testing speeds at the same temperature, and that tire temperature and speeds should be taken into consideration. To estimate the order of magnitude of the effect, assuming tire temperature to be 25°C and $T_g = -70^\circ\text{C}$, eq (1.1.32) gives $\log a_T = -11.3$ for $T = 25^\circ\text{C}$ and for $T = 0^\circ\text{C}$, $\log a_T = -10.0$. Thus lowering the test temperature from 25°C to 0°C is roughly equivalent to increasing testing speed by a factor of $10^{1.3}$, or 20, say from 20 in/min. to 400 in/min.

In the same way, high frequency vibration response of the rubber at 25°C could be simulated by testing at 0°C with frequencies lowered by a factor of about 20. All this assumes that eq (1.1.32) is valid for tire compounds, which in general is not strictly so.

Dynamic properties. When a sinusoidal force is applied to a viscoelastic material, the viscous reaction causes a lag of strain behind stress, just as in a creep test, as illustrated in figure 1.1.14.

This phase lag is indicative of mechanical energy loss in each cycle,

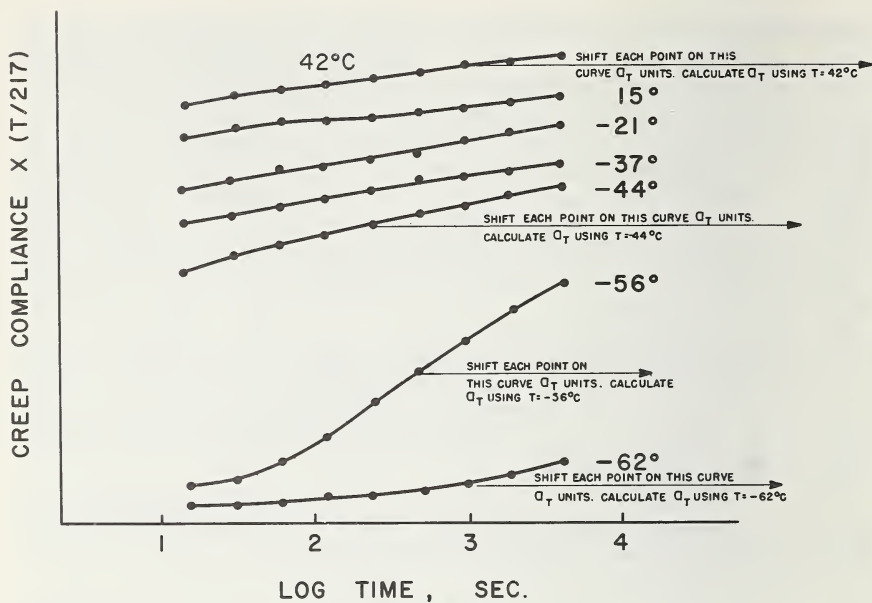


FIGURE 1.1.12. Plot of creep compliance vs. log time for a natural rubber vulcanizate at a series of temperatures [75].

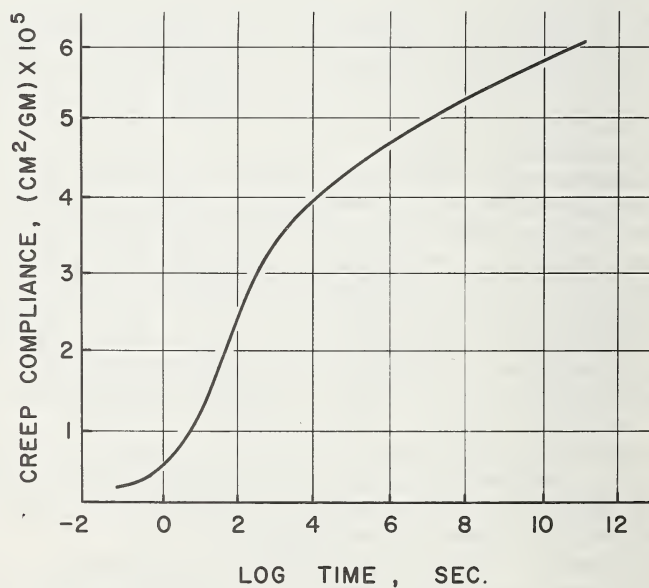


FIGURE 1.1.13. Master curve, constructed by horizontal shifting of curve segments of figure 1.1.12, giving creep compliance at -56°C , from reference [75].

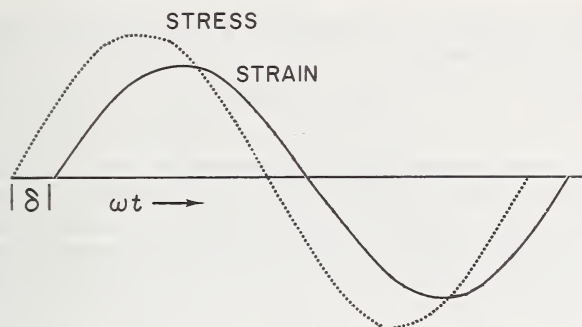


FIGURE 1.1.14. Diagram to illustrate phase lag of strain behind stress when a sinusoidal force acts on a rubber specimen.

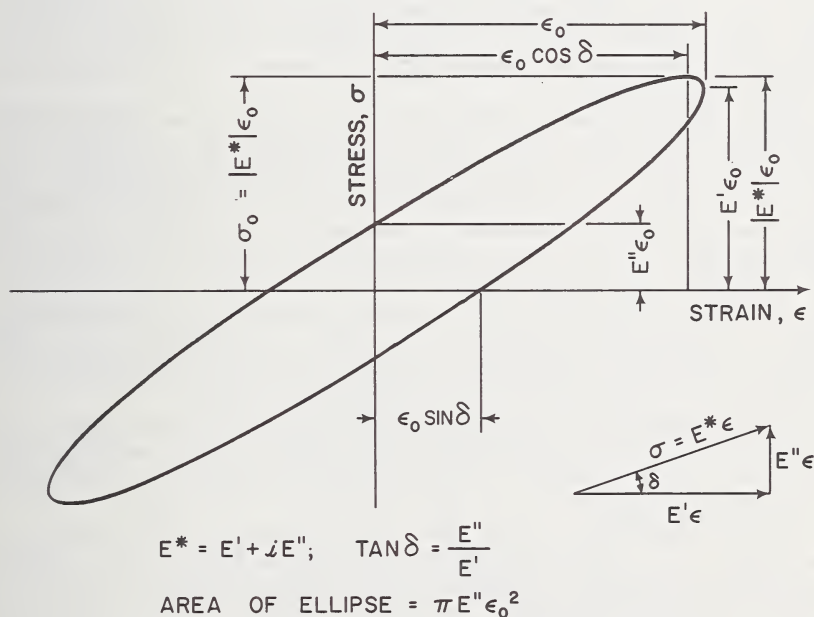


FIGURE 1.1.15. Hysteresis loop showing its relations to storage and loss moduli and the phase angle, δ .

this energy appearing as equivalent heat generation in the rubber. The amount of energy loss is given by the area of the hysteresis loop when stress in the material is plotted against strain, as shown in figure 1.1.15.

The dynamic modulus of a material is defined as a complex number whose real part is the ratio of the stress component in phase with the strain to the strain itself, while the imaginary part is the ratio of the stress component 90° out of phase with the strain to the strain itself. The latter

component, of course, is responsible for the energy losses. These relations are expressed by

$$G^* = G' + iG'' \quad (1.1.33)$$

in which G^* is the total complex shear modulus. The real component G' is called the storage modulus or the dynamic modulus, and G'' is the loss modulus. The complex Young's modulus is defined similarly and, assuming incompressibility, it is three times the complex shear modulus. $\tan \delta$, the tangent of the angular phase lag of strain behind stress is given by

$$\tan \delta = \frac{G''}{G'} \quad (1.1.34)$$

$\tan \delta$ is a basic parameter for expressing the energy losses relative to the energy stored. Losses in various dynamic test methods, such as rebound experiments or decay of free vibrations, can all be expressed in terms of $\tan \delta$ [93].

All of these dynamic properties such as G' , G'' , and $\tan \delta$, being viscoelastic in nature, show marked dependence on temperature and frequency. However, in a limited range of mechanical frequencies, from about five or ten to several hundred Hz and at temperatures well above the glass transition temperature T_g , the frequency dependence is rather flat. Storage and loss moduli decrease with increase in temperature, showing that viscoelastic effects dominate over the increase predicted by the kinetic theory. $\tan \delta$ also decreases with increase in temperature. This is a saving feature for tire compounds, since otherwise they would tend to run hotter and hotter in service rather than to approach an equilibrium temperature for a given operating condition.

To give some idea of numerical values, $\tan \delta$ for tread compounds will usually be found in the range 0.1 to 0.2 while dynamic modulus E' will range from 1500 to 2500 psi for low amplitude vibrations of about 60 Hz at room temperature.

Dynamic modulus for tread compounds exceeds the static modulus, sometimes by a factor of two or more, depending on the vibration conditions. It should be noted that the apparent Young's modulus for rubber determined by either dynamic or static tests in compression depends upon the shape of the test specimen unless the bearing surfaces are well lubricated. Thus the tread "buttons" in a tread pattern will be somewhat stiffer in compression on a road which is dry than when it is wet. Empirical shape factors [53, 94] such as the ratio of load area to free area are used to take this shape effect into account. The effect is somewhat larger for dynamic than for static tests [95].

Dynamic properties of tire tread compounds are further complicated by a marked dependence on amplitude [96], giving rise to nonlinear effects. Except for extremely small amplitudes [97], dynamic modulus decreases with increasing amplitude, slowly approaching an asymptotic value at high amplitudes. This gives rise to a skewed resonance curve as

shown in figure 1.1.16 obtained in this case by varying the mass of the system while holding excitation frequency constant. These effects are structural or thixotropic in character. However, for a steady forced vibration amplitude an equilibrium structure is soon reached so that there is a sinusoidal response without harmonics.

Energy losses in tires. Mechanical hysteresis losses in the rubber compounds and in the fabric of a tire result in a drag component manifesting itself in internal heat generation which is readily observed as an increase in tire temperature above ambient. Internal heat generation is especially severe for thick, heavy-duty tires. It limits speeds and loads at which such tires can operate, and it delayed the use of synthetic rubber in compounds for airplane, bus, truck, and off-the-road tires.

In comparing energy losses for rubber compounds it is necessary to specify the deformation circumstances. Hysteresis loss H per cycle per unit volume under sinusoidal displacement is [98]

$$H = \pi \sigma_0 \epsilon_0 \sin \delta. \quad (1.1.35)$$

Here σ_0 and ϵ_0 are stress and strain amplitude, respectively, and $\sin \delta = E''/|E^*|$.

If rubber compounds are compared at the same strain amplitude, $\sigma_0 = \epsilon_0 \cdot |E^*|$ and

$$H_\epsilon = \pi \epsilon_0^2 E''. \quad (1.1.36)$$

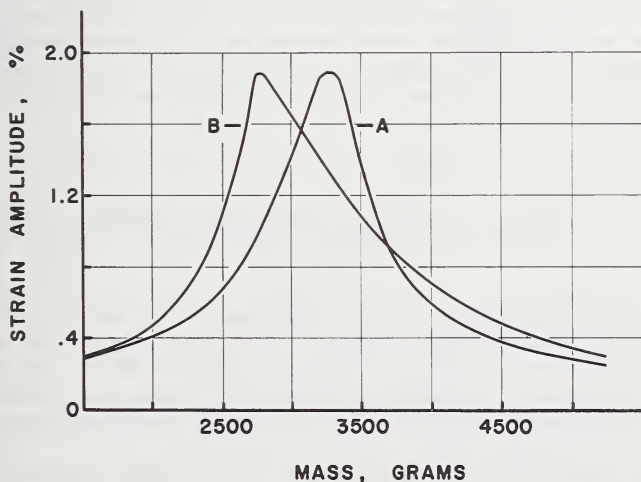


FIGURE 1.1.16. Curve A, resonance curve for a natural rubber unfilled vulcanizate, forced compressive vibrations, 60 Hz. Curve B, resonance curve for a tread compound showing distortion because of nonlinear response.

Constant amplitude driving force.

If they are compared at the same stress amplitude, $\epsilon_0 = \sigma_0/|E^*|$ and

$$H_\sigma = (\pi \sigma_0^2 E'')/|E^*|^2. \quad (1.1.37)$$

In both cases, energy loss is proportional to loss modulus. At constant stress cycle amplitude stiffer compounds have lower losses because the loss per cycle is inversely proportional to the square of the complex modulus.

Deformation conditions in a tire are so complicated that it is difficult to consider them to be purely constant stress amplitude or constant strain amplitude cycles. Amplitude of bending cycles in the tire tread and body do not depend much on compound modulus and so are approximately constant strain amplitude cycles. Compressive stress cycles of the tread itself are more like cycles at constant stress amplitude.

Detailed experimental analysis to determine contributions of individual tire components of a 9.00-20 truck tire to drag [98] showed that tread compression contributed 32 percent of the drag, tread bending 27 percent, body rubber 12 percent and cord system 29 percent.

The coefficient of rolling resistance of a tire, defined as the drag force to pull the free rolling tire divided by the vertical tire load, is related to power loss by the equation

$$R = \frac{P}{60 SL} \quad (1.1.38)$$

where R is the dimensionless coefficient of rolling resistance, P is power loss, ft-lb/min.; S is speed, ft/sec.; and L is tire load, lb. In dynamometer tests on 9.00-20 truck tires [99], power loss for a tire made with SBR compounds was about 1.5 times as large as that for a comparable tire made with natural rubber compounds. This is symptomatic of the problem which is encountered with heat generation in using synthetic rubber for heavy duty tires.

1.1.6. Reinforcement of Rubber With Carbon Black

Carbon black is unique in tire technology. The beneficiation which ensues from dispersing it in rubber is described by the ad hoc term "reinforcement." The carbon black/rubber system is very complex. It has been studied exhaustively [100, 101] and many factors have been shown to contribute to its effectiveness in tires. These include:

a. chemical aspects, such as effects on vulcanization reactions through adsorption of vulcanizing ingredients or through functional chemical groups or elements on the carbon black surface

b. physical or chemical adsorption of segments of the chain molecules

- c. physical bonding between carbon black particles resulting in carbon black chains and a reticulated structure
- d. microstress fields at the particles.

The complex interaction of these chemical, physical chemical, and physical effects has precluded any simple, definitive explanation of all of the phenomena. The fine carbon black particles are dispersed by high shearing forces in the thermoplastic rubber, where they tend to form a sort of loose, flocculated or reticulated structure because of their surface activity and mutual attractions. This structure is then interlaced by a network of rubber chain molecules crosslinked during vulcanization. The carbon black particles are fine enough and have sufficient surface activity to influence the rubber network structure profoundly, perhaps furnishing more or less stable junction sites which act like additional crosslinks to produce effects not observed with an ordinary, diluent type of filler [101, 102]. There is also a theory that the particles act to distribute the rubber network stresses [75]. One effect is to greatly increase the viscous forces on the chain segments of the rubber molecules as they move to accommodate to stresses.

Carbon black in rubber increases the modulus or hardness, as do all fillers. However, distinctive improvements are observed in strength properties such as tensile strength, tear strength and above all, in road-wear. On the other hand, mechanical energy losses, hysteresis loss and viscoelastic responses to forces are greatly augmented. It is now realized that these two broad characterizations of the effects of carbon black on physical properties are closely connected. All types of strength failures in rubber probably originate at small flaws and proceed by essentially a tearing process [50]. Viscoelastic mechanisms have been clearly demonstrated in tearing and abrasion of unfilled vulcanizates [103, 104], and are incorporated in current theories of rubber tensile strength [83]. Stress relaxation and creep reduce stress concentrations at the tip of a growing flaw or cut. This appears as increased strength. There is an additional strengthening mechanism with carbon black in that enhanced stresses at the particles produce molecular orientation or alignment, a sort of fibering, which blunts the tear tip and tends to divert the tear from a straight line course.

Carbon blacks are characterized by particle size, surface area, and structure. Particle size is measured from electron micrographs. Surface area is determined by iodine [105] or nitrogen adsorption. "Structure" measures the proclivity of a carbon black to form reticulated structures. It is evaluated by oil absorption tests [106] or measurement of packing volume under pressure. Manufacturing methods for carbon blacks are so advanced that they can now be produced commercially with practically any desired combination of these three characteristics. Table 1.1.3 summarizes ranges of these properties for carbon blacks used frequently in tires.

Figures 1.1.17 and 1.1.18 display the effect of carbon black loadings on tensile strength, pendulum rebound, breaking elongation, and hardness [108].

TABLE 1.1.3. *Description of several carbon blacks [107]*

Type	Av. particle diam, Å (Electron microscope)	Surface area, m ² /g (BET N ₂ adsorption)	Apparent sp. vol. at 734 psi, cc/g
HMF (High Modulus Furnace).....	460-660	30-45	1.20-1.46
FEF (Fine Extrusion Furnace).....	310-580	36-48	1.40-1.70
HAF (High Abrasion Furnace).....	260-350	62-88	1.45-1.60
ISAF (Intermediate Super Abrasion Furnace).....	175-275	95-135	1.45-1.75
SAF (Super Abrasion Furnace).....	140-270	120-145	1.55-1.75

Tensile strength usually goes through a broad maximum as carbon black loading increases, as does abrasion resistance. The level of 45-55 parts of black per hundred of rubber in tire treads, if not the optimum for wear in a particular compound, will generally represent the best balance between wear, resistance to tread cracking, heat generation, traction, etc., and give best overall performance.

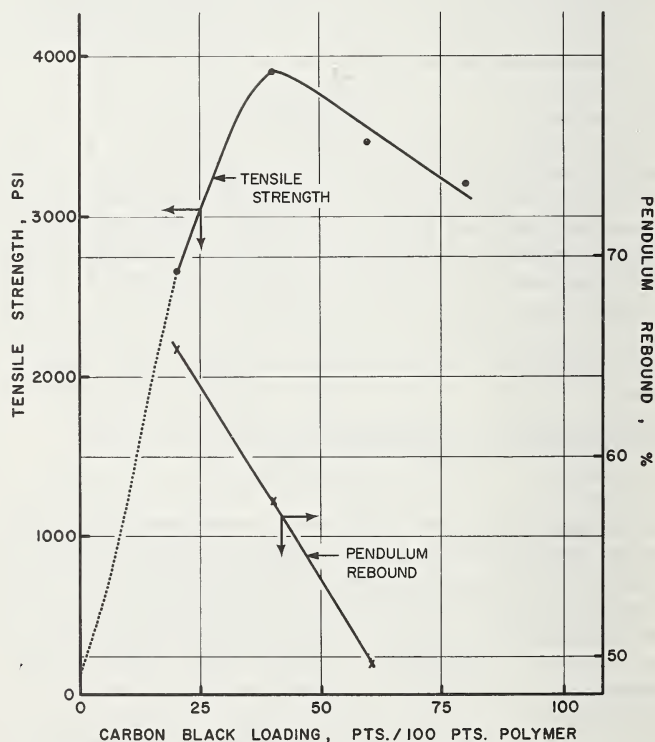


FIGURE 1.1.17. *Effect of loadings of ISAF carbon black in SBR-1500C on tensile strength and pendulum rebound.*

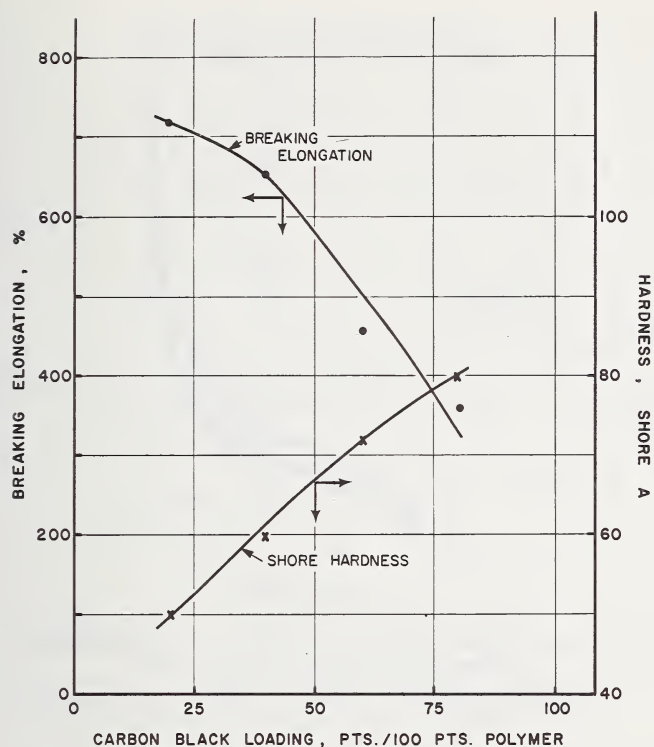


FIGURE 1.1.18. *Effect of loadings of ISAF carbon black in SBR-1500C on breaking elongation and hardness.*

Stress-strain curves for carbon black filled vulcanizates show pronounced stress softening [109, 110], that is, the rubber compound has a much lower modulus on the second extension than on the first, as shown in figure 1.1.19. This effect was widely studied and for a long time was thought to be an important characteristic of the reinforcement process. It is now known to be a much more general phenomenon [111, 112] and its significance for reinforcement has been obscured. This effect is obviously related to the fact that stable reproducible mechanical properties for tires are observed only after a "break-in" run.

Abrasion of rubber involves very complicated failure processes [50, 103], including softening and fatigue of a thin surface layer, probably associated also with oxidative deterioration and actual smearing under severe conditions, localized cutting and chipping from road asperities, and shearing off and rolling up of thin flakes of rubber from the surface. Carbon blacks have evolved largely from requirements to improve treadwear, and have been developed through tire experience and carefully controlled road tests. No one type of black can be optimum for the wide range of rubber compounds, tires, and service conditions.

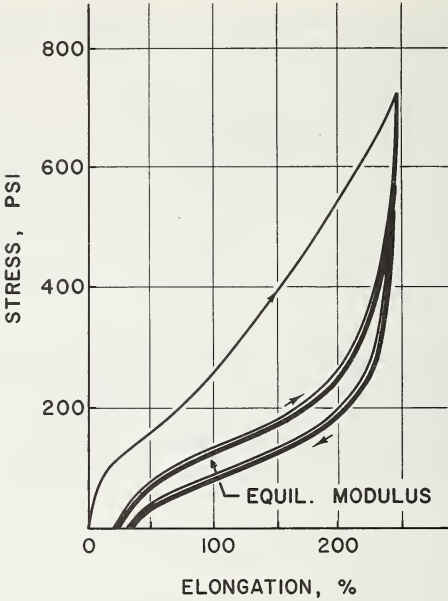


FIGURE 1.1.19. Stress-softening for a tread vulcanizate illustrating approach to an equilibrium hysteresis loop after many cycles.

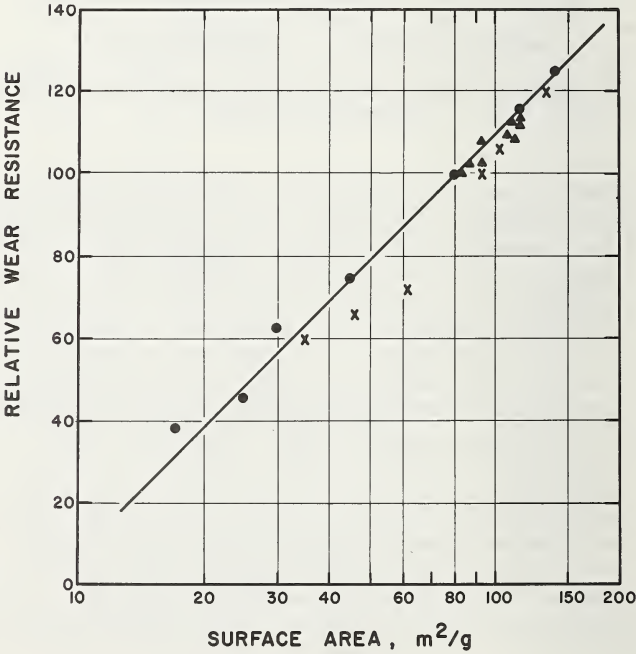


FIGURE 1.1.20. Correlation of treadwear with specific surface area of the carbon black. Data assembled by Studebaker [113] from several sources.

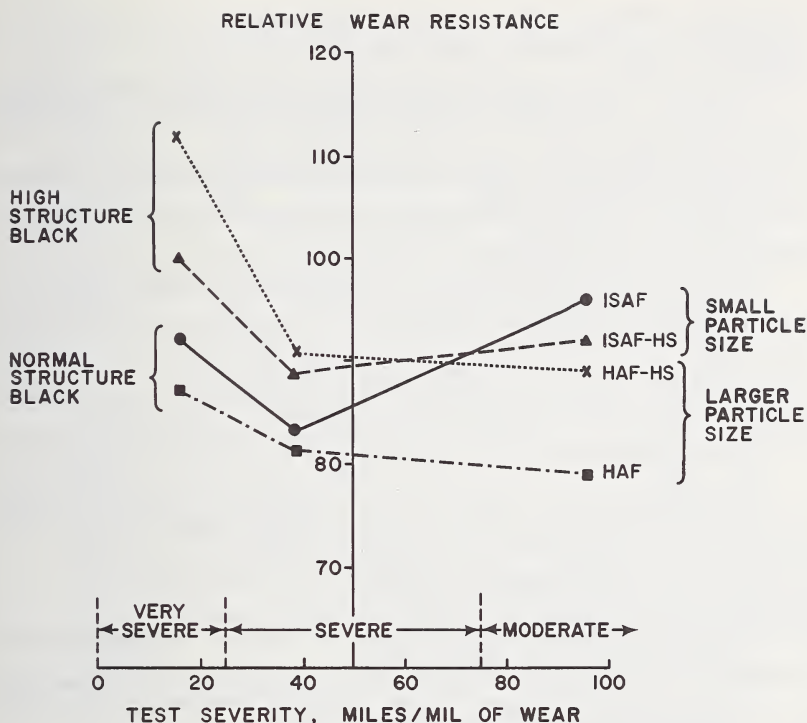


FIGURE 1.1.21. Relations between relative treadwear, particle size and "structure" of carbon black and severity of service [113].

A broad, general correlation exists between specific surface area of the carbon black and treadwear [113] as shown in figure 1.1.20. This emphasizes the importance of surface interactions between rubber and filler for good wear resistance. Figure 1.1.21, however, reflects experience showing that high structure in carbon black is especially advantageous for very severe service [113]. This is an indication of the present sophistication in development and use of carbon blacks in tire compounds.

References

- [1] Walker, Richard, ed., *Materials and Compounding Ingredients for Rubber and Plastics* (Rubber World, New York, N.Y. 1965).
- [2] Brown, R. J., et al., *Rubber World* **145**(2), 70 (1961); *Rubber Chem. Tech.* **35**(2), 546 (1962).
- [3] Sarbach, D. V., Hallman, R. W., and Cavicchia, M. A., *Rubber Age* **98**(11), 67 (1966).
- [4] 1967 Annual Book of ASTM Standards, Part 28, Rubber, carbon black, gaskets, Method D2226-65T, Description of types of petroleum extender oils, p. 992 (Am. Soc. Testing Mats., Phil., Penn.).

- [5] Storey, E. B., *Rubber Chem. Tech.* **34**(5), 1402 (1962).
- [6] Stout, W. J., and Eaton, R. L., *Rubber Age* **99**(12), 82 (1967).
- [7] Ref. [4], p. 844.
- [8] Snyder, J. W., and Leonard, M. H., *Carbon black*, chap. 8, *Introduction to Rubber Technology*, Morton, M., ed., p. 172 (Reinhold Publishing Corp., New York, N.Y., 1959).
- [9] Studebaker, M. L., *Rubber Chem. Tech.* **30**(5), 1400 (1957).
- [10] Alliger, G., and Sjöthun, I. J., eds., *Vulcanization of Elastomers* (Reinhold Publishing Corp., New York, N.Y., 1964).
- [11] Hofmann, W., *Vulcanization and Vulcanizing Agents* (Palmerton Publishing Co., New York, N.Y., 1967).
- [12] Bateman, L., et al., *Chemistry of vulcanization*, chap. 15, *The Chemistry and Physics of Rubber-Like Substances*, L. Bateman, ed., p. 449 (John Wiley & Sons, New York, N.Y., 1963).
- [13] Trivette, Jr., C. D., Morita, E., and Young, E. J., *Rubber Chem. Tech.* **35**(5), 1360 (1962).
- [14] Ambelang, J. C., et al., *Rubber Chem. Tech.* **36**(5), 1497 (1963).
- [15] Thornley, E. R., *Trans. Inst. Rubber Ind.* **40**, T1 (1964); *Rubber Chem. Tech.* **37**, 973 (1964).
- [16] *Rubber: Supply and distribution for the United States*, Current Industrial Reports, U.S. Dept. of Commerce, Bureau of the Census, Industry Div., Washington, D.C., Dec. 1967.
- [17] *Description of Synthetic Rubber and Latices* (International Institute of Synthetic Rubber Producers, Inc., New York, N.Y., Jan. edition 1968); Ref. [4], p. 1150.
- [18] Buckley, D. J., *Rubber Chem. Tech.* **32**(5), 1475 (1959).
- [19] Dudley, R. H., and Wallace, A. J., *Rubber World* **152**(2), 66 (1965).
- [20] Andrews, J., *Rubber Age* **99**(12), 53 (1967).
- [21] Hall, W. S., and Norman, D. T., *Rubber Age* **93**(1), 77 (1963).
- [22] *Vanderbilt News* **28**(4), 47 (1962); for other tire compound formulations see **31**(1), 11 (1965); **31**(2), 8 (1965); **32**(2), 7 (1967).
- [23] Kochmit, C. J., *Changing trends in tread type carbon blacks*, Paper presented at meeting of the ACS Division of Rubber Chemistry, Cleveland, Ohio, April 23-26, 1968; *Abstract in Rubber Age* **100**(3), 79 (1968).
- [24] Vance, R. M., and Burgess, K. A., *Laboratory tire groove cracking test*, Paper presented at meeting of ACS Division of Rubber Chemistry, Cleveland, Ohio, April 23-26, 1968; *Rubber Chem. Technol.* **41**(4), 1080 (1968).
- [25] Ref. [4], Method D15-66T, Sample preparation for physical testing of rubber products, p. 1.
- [26] Juve, A. E., *Physical testing*, chap. 19, p. 462, in Ref. [8].
- [27] Scott, J. R., *Physical Testing of Rubbers* (Palmerton Publishing Co., New York, N.Y., 1965).
- [28] *International Organization for Standardization Recommendations* (Listed in ISO Catalog (1967), USA Standards Institute, New York); also listed in Ref. [4], p. 1121.
- [29] Franck, A., Hafner, K., and Kern, W. F., *Kaut. Gummi Kunstst* **13**(12) WT 292 (1960); *Rubber Chem. Tech.* **35**(1), 76 (1962).
- [30] Gehman, S. D., and Ogilby, S. R. ASTM STP-383, *Continuous Measurement of the Cure Rate of Rubber* (Am. Soc. Testing Mats., Phil., Penn. 1965).
- [31] Ref. [4], Method D412-66, *Tensile testing of vulcanized rubber*, p. 200.
- [32] Gehman, S. D., *Chem. Revs.* **26**(2), 203 (1940).
- [33] Mandelkern, L., *Crystallization of Polymers* (McGraw-Hill Book Co., New York, N.Y., 1964).
- [34] Mullins, L., and Tobin, N. R., *Trans. Inst. Rubber Ind.* **33**(1), 2 (1957); *Rubber Chem. Tech.* **31**, 505 (1958).
- [35] ASTM tentative methods D2704, D2705, and D2706 on methods of measurement of curing characteristics. Should appear in future editions of Ref. [4].
- [36] Gehman, S. D., Maxey, F. S., and Ogilby, S. R., *Rubber Chem. Tech.* **38**(4), 757 (1965).
- [37] Gehman, S. D., *Rubber Chem. Tech.* **40**(1), 36 (1967).
- [38] Freeman, H. A., *Rubber Age* **90**(5), 779 (1962).
- [39] Ref. [4], Methods D454-53, D572-67, D573-53, D865-62.

- [40] Barnhart, R. R., and Newby, T. H., Antioxidants and antiozonants, chap. 6, p. 130, in Ref. [8].
- [41] Buist, J. M., Aging and Weathering of Rubber (W. Heffer & Sons, Cambridge, England, 1956).
- [42] Shelton, J. R., Rubber Chem. Tech. **30**(5), 1251 (1957).
- [43] Norling, P. M., Lee, T. C. P., and Tobolsky, A. V., Rubber Chem. Tech. **38**(5), 1198 (1965).
- [44] Ref. [4], Method D518-61, Resistance to surface cracking of stretched rubber compounds, p. 275.
- [45] Ref. [4], Method D1149-64, Accelerated ozone cracking of vulcanized rubber, p. 554.
- [46] Symposium on Effect of Ozone on Rubber, ASTM STP-229 (Am. Soc. Testing Mats., Phil., Penn., 1958).
- [47] Andrews, E. H., et al, Ozone attack on rubbers, chap. 12, p. 329, in Ref. [12].
- [48] Ref. [4], Method D624-54, Tear resistance of vulcanized rubber, p. 342.
- [49] Kainradl, P., and Handler, F., Kautschuk Gummi **12**, WT 239 (1959); Rubber Chem. Tech. **33**, 1438 (1960).
- [50] Gehman, S. D., Mechanism of tearing and abrasion of reinforced elastomers, chap. 2, Reinforcement of Elastomers, G. Kraus, ed., p. 23 (Interscience Publishers, Inc., New York, N.Y., 1965).
- [51] Ref. [4], Method D2240-64-T, Indentation hardness of rubber and plastics by means of a durometer, p. 1009.
- [52] Ref. [4], Method D1415-62T, International hardness of vulcanized natural and synthetic rubbers, p. 642.
- [53] Payne, A. R., and Scott, J. R., Engineering Design with Rubber, p. 122 (Interscience Publishers, New York, N.Y., 1960).
- [54] Waters, N. E., Brit. J. Appl. Phys. **16**, 557 & 1387 (1965); J. Inst. Rubber Ind. **1**(1), 51 (1967).
- [55] Coddington, D. M., Marsh, W. D., and Hodges, H. C., Rubber Chem. Tech. **38**(4), 741 (1965).
- [56] Ref. [4], Method D1054-66, Impact resilience and penetration of rubber by the rebound pendulum, p. 509.
- [57] Ref. [4], Method D945-59, Mechanical properties of elastomeric vulcanizates under compressive or shear strains by the mechanical oscillograph.
- [58] Gehman, S. D., Rubber Chem. Tech. **30**(5), 1202 (1957).
- [59] Ref. [4], Method D2231-66, Forced vibration testing of vulcanizates, p. 1003.
- [60] Harris, C. M., and Crede, C. E., eds., Shock and Vibration Handbook, Vol. 3, pp. 36-25 to 36-27 (McGraw-Hill Book Co., New York, N.Y., 1961).
- [61] Ref. [4], Method D623-62, Compression fatigue of vulcanized rubber, p. 334.
- [62] Ref. [4], Method D430-59, Dynamic testing for ply separation and cracking of rubber products, p. 227; Method D813-59, Resistance of vulcanized rubber or synthetic elastomers to crack growth, p. 410.
- [63] Beatty, J. R., Rubber Chem. Tech. **37**(5), 1341 (1964).
- [64] Ref. [4], Method D394-59, Abrasion resistance of rubber compounds, p. 190; Method D2228-63T, Abrasion resistance of rubber and elastomeric materials by the Pico method, p. 985.
- [65] Vogt, W. W., Ind. Eng. Chem. **20**, 303 (1968).
- [66] Lambourn, L. J., Trans. Inst. Rubber Ind., **4**, 210 (1928).
- [67] Davison, S., et. al., Rubber World **151**(5), 81 (1965); **151**(6), 79 (1965); Rubber Chem. Tech. **38**(3), 457 (1965).
- [68] Meyer, K. H., and Ferri, C., Helv. Chim. Acta **18**, 570 (1935).
- [69] Anthony, R. L., Caston, R. H., and Guth, E., J. Phys. Chem. **46**, 826 (1942).
- [70] Wood, L. A., and Roth, F. L., J. Appl. Phys. **15**, 781 (1944).
- [71] Gee, G., Trans. Faraday Soc. **42**, 585 (1946).
- [72] Treloar, L. R. G., The Physics of Rubber Elasticity, second edition (Oxford University Press, 1958).
- [73] Flory, P. J., Principles of Polymer Chemistry (Cornell University Press, Ithaca, New York, 1953).
- [74] Krigbaum, W. R., and Roe, R. J., Rubber Chem. Tech. **38**, 1039 (1965).
- [75] Bueche, F., Physical Properties of Polymers (Interscience Publishers, New York, N.Y., 1962).

- [76] Mullins, L., and Thomas, A. G., Theory of rubber-like elasticity, chap. 7, p. 155, in Ref. [12].
- [77] Mooney, M., J. Appl. Phys. **11**, 582 (1940).
- [78] Rivlin, R. S., chap. 10, vol. 1, Rheology: Theory and Application (5 vols.), F. R. Eirich, ed., p. 351 (Academic Press, New York, N.Y., 1956).
- [79] Varga, O. H., Stress-Strain Behavior of Elastic Materials; Selected Problems of Large Deformations (Interscience Publishers, New York, N.Y., 1966).
- [80] Rivlin, R. S., Phil. Trans. Roy. Soc. (London) **A241**, 379 (1948).
- [81] Blatz, P. J., Rubber Chem. Tech. **36**(5), 1450 (1963).
- [82] Ciferri, A., and Flory, P. J., J. Appl. Phys. **30**, 1498 (1959).
- [83] Halpin, J. C., Rubber Chem. Tech. **38**(5), 1007 (1965).
- [84] Schallamach, A., Rubber Chem. Tech. **41**(1), 209 (1968).
- [85] Alfrey, Jr., T., Mechanical Behavior of High Polymers, Vol. 6 of High Polymers (Interscience Publishers, New York, N.Y., 1948).
- [86] Tobolsky, A. V., Properties and Structure of Polymers (John Wiley & Sons, New York, N.Y., 1960).
- [87] Flügge, W., Viscoelasticity, (Blaisdell Publishing Co., Waltham, Mass., 1967).
- [88] Leaderman, H., chap. 1, vol. 2 of Rheology: Theory and Application (5 vols), F. R. Eirich, ed., p. 1 (Academic Press, New York, N.Y., 1958).
- [89] Ferry, J. D., Viscoelastic Properties of Polymers (John Wiley & Sons, New York, N.Y., 1961).
- [90] Gross, B., Mathematical Structure of the Theories of Viscoelasticity (Hermann & Cie, Paris, France, 1953); J. Appl. Phys. **18**, 212 (1947); **19**, 257 (1948); **22**, 1035 (1951).
- [91] Hopkins, I. L., and Hamming, R. W., J. Appl. Phys. **28**(8), 906 (1957).
- [92] Aklonis, J. J., and Tobolsky, A. V., J. Appl. Phys. **36**(11), 3483 (1965).
- [93] Gehman, S. D., Rubber Chem. Tech. **30**(5), 1202 (1957).
- [94] Kimmich, E. G., India Rubber World **103**(3), 45 (1940).
- [95] Gehman, S. D., J. Appl. Phys. **11**(6), 402 (1943).
- [96] Gui, K. E., Wilkinson, Jr., C. S., and Gehman, S. D., Ind. Eng. Chem. **44**, 720 (1952).
- [97] Payne, A. R., Dynamic properties of filler-loaded rubbers, chap. 3, p. 69, in Ref. [50].
- [98] Collins, J. M., Jackson, W. L., and Oubridge, P. S., Trans. Inst. Rubber Ind. **40**, 239 (1964); Rubber Chem. Tech. **38**(2), 400 (1965).
- [99] Stiehler, R. D., et al., Proc. Intern. Rubber Conf., p. 73, Washington, D.C., 1959.
- [100] Kraus, G., ed., Reinforcement of Elastomers (Interscience Publishers, Inc., New York, N.Y., 1965); Rubber Chem. Tech. **38**(5), 1070 (1965).
- [101] Parkinson, D., Reinforcement of Rubbers, Monograph of the Inst. Rubber Ind. (London, 1957).
- [102] Bueche, A. M., J. Polymer Sci. **25**, 139 (1957).
- [103] Schallamach, A., Rubber Chem. Tech. **41**(1), 209 (1968).
- [104] Greensmith, H. W., Mullins, L., and Thomas, A. G., Strength of rubbers, chap. 10, p. 249, in Ref. [12].
- [105] Ref. [4], Method D1510-65, Iodine adsorption number of carbon black, p. 710.
- [106] Ref. [4], Method D2414, Dibutyl phthalate absorption number of carbon black, p. 1044.
- [107] Studebaker, M. L., Compounding with carbon black, chap. 12, p. 319, in Ref. [50].
- [108] Data from Goodyear Tech Book for the Chemical Process Industry, The Goodyear Tire & Rubber Co., Chemical Div., Akron, Ohio 44316.
- [109] Dannenberg, E. M., and Brennan, J. J., Rubber Chem. Tech. **39**(3), 597 (1966).
- [110] Kraus, G., Childers, C. W., and Rollmann, K. W., J. Appl. Polymer Sci. **10**, 229 (1966); Rubber Chem. Tech. **39**(5), 1530 (1966).
- [111] Trick, G. S., J. Appl. Polymer Sci. **3**(8), 252 (1960).
- [112] Harwood, J. A. C., Mullins, L., and Payne, A. R., J. Appl. Polymer Sci. **9**, 3011 (1965); Rubber Chem. Tech. **39**(4), 814 (1966).
- [113] Studebaker, M. L., Rubber Chem. Tech. **41**(2), 373 (1968).

1.2. Friction of Rubber

K. C. Ludema ¹

	Page
1.2.1. Introduction.....	42
1.2.2. Early phenomenological laws of friction vs. new information.....	43
1.2.3. Mechanical classes of tire and rubber friction.....	44
1.2.4. Rubber friction.....	45
1.2.5. Combined components of friction.....	54
Dry friction.....	54
Wet friction.....	56
Rubber properties.....	57
Longitudinal and lateral tire slip and slide.....	57
References.....	61

¹ Department of Mechanical Engineering, University of Michigan, Ann Arbor, Michigan 48104.

1.2.1. Introduction

The efficiency and convenience of the automobile is to a great extent due to the use of rubber tires. The frictional properties of rubber make relatively high forces available for accurately controlling road vehicles within the reaction capability of most drivers.

As with most consumer materials, rubber was not developed from first principles to fulfill a defined need. Rather, it existed for other purposes, and it was adapted and developed for use as a tire tread material. Understanding of rubber properties lags behind its public use. The existence of its high friction is known to almost everyone, but the method of controlling the friction is known to only a few. Again, the performance of tires is known in detail by many, but the origin or fundamental cause of rubber friction is not completely known by anyone.

A major impediment to the understanding of tire frictional performance is the lack of adequate, broad, and clearly expressed laws of rubber friction. Total tire performance is acknowledged in a number of publications [1, 2]² to be the summation of tire carcass properties plus the frictional behavior of the tread elements at and near the tire road interface. Considerable study is being directed toward general tire behavior related to the "comfort" dynamics of vehicles. However, basic work in friction mechanisms is lagging far behind. There is no lack of conceptual models of the basic friction process or of tire behavior. However, research and testing in these topics is done under such restricted conditions as to seriously compromise the applicability of the results to broader practical conditions. As a result there are many gaps in our knowledge, and there are several research conclusions that are not yet well recognized as being relevant to tire friction.

Another problem is the ambiguity in the use of terminology in describing tire friction processes. This probably arises from the general tendency to define all ratios of traction force to normal force as the coefficient of friction, whether sliding occurs or not.

This paper is addressed to these two problems as well as to the task of bringing research conclusions to bear upon practical tire behavior. The starting point is a section on the classical laws of friction, followed by a section on terminology of the mechanical classes of friction. Then follows a new delineation of the basic mechanisms or components of rubber friction. The emphasis will be upon what is well established without a detailed analysis of various points of view. The references cited are not necessarily supportive of the statements of this paper but rather should be used as a source where more can be found on the particular topic.

² Figures in brackets indicate the literature references at the end of this chapter.

1.2.2. Early Phenomenological Laws of Friction Versus New Information

To the practicing automotive or tire engineer a knowledge of the fundamentals of rubber friction is important for a general understanding of observed data. The main interest has been to make preliminary estimates of the kinds of maneuvers and stopping distances which can be accomplished under given conditions. In this general area, the literature has been prone to rely somewhat heavily on classical descriptions of friction.³

The most popular source of statements on frictional behavior is the French engineer C. A. Coulomb (1736–1806). His popularity is a curious state of affairs since Coulomb was neither the first to publish, nor were his explanations of the cause of friction correct. The French architect G. A. Amontons (1663–1705) published many of the same conclusions, and the Englishman J. D. Desaguliers (1683–1744) was the first to connect dry friction with interface “cohesion”. The latter view has been repeatedly confirmed since the time of Desaguliers, although it is now referred to as the adhesion theory of friction.

However, Amontons and Coulomb were both careful observers and both came to essentially the same conclusions. Both used the common engineering materials of their day—building stone, metals, wood, and earth. The simplest of their conclusions are the best known, and may be summarized in the statements:

- “1. A higher force is required to begin sliding than to perpetuate sliding (i.e., the static coefficient of friction is greater than the kinetic value).

Furthermore, the coefficient of friction of a sliding pair is:

2. independent of applied load,
3. independent of sliding speed,
4. independent of nominal area of contact, and
5. dependent on the nature of the materials in contact.”

These statements are incomplete for describing frictional phenomena in general and particularly misleading when applied to the friction of tire rubber on road. Coulomb himself had a broader view than many moderns who quote him. However in the last few years many new and definitive conclusions concerning rubber friction have been published. It is now possible to see that the simple categories listed in these classical laws are not entirely separable. For example, the applied load and the nominal area of contact interact to produce a nominal contact stress. Since surfaces are rarely smooth one would expect that there might be varying local contact pressures, different from the average, and these would be controlled by the geometric features of the interface roughness, and by the material properties. Thus a change in any of these variables

³ For a very interesting historic account of the early work on friction see chapter 24 of reference [3].

may (an usually does) influence sliding friction. New information also suggests a connection between the stick-slip phenomenon and the effect of sliding speed on rubber friction. All of these effects vary as a function of other factors such as the damping loss in the rubber and the quantity of contaminant, including moisture, in the contact region.

In view of the complex interaction of the variables mentioned above we will not proceed with a point by point modification of Coulomb's (or Amontons') law. Rather we will begin with more fundamental observations and attempt to synthesize real tire behavior.

1.2.3. Mechanical Classes of Tire and Rubber Friction

The following list of five friction processes and a definition of terms is offered in the interest of reducing the ambiguity surrounding the use of the words "coefficient of friction."

a. The classical coefficient of friction, μ , is defined [3] as being equal to F_s/W , where F_s is the force, tangent to the contact surface, applied to a solid slider to initiate or maintain sliding and W is the force, normal to the contact surface, holding the sliding elements in contact. This latter is the wheel load in the case of tires. Thus

$$\mu \equiv \frac{F_s}{W}$$

b. Where no sliding occurs at any point, a force tangent to the contact surface, F , may be applied to a perfectly rigid slider producing a uniform tractive stress τ at the interface. We define $F/W = \theta$, and obviously the maximum values of F and θ are given by $F_{\max} = F_s$ and $\theta_{\max} = \mu$.

c. A force F_p , tangent to the contact surface, may be applied to a *flexible* slider such as a *non-rotating* tire, producing a nonuniform distribution of tractive stress τ at the interface. This may occur where the nominal contact stress is nonuniform and/or where elastic constraints on the interfaces are nonuniform. Using the findings of Mason [4], we can state that a very small value of tangential force will produce slip over at least a small part of the interface. F_p thus always produces partial slip. As the value of F_p increases, a greater fraction of the interface slips. We define $F_p/W \equiv \phi$ and obviously F_p and ϕ_p at full slip equals F_s and μ , respectively.

d. A force F_r is required to roll a loaded tire on a level surface. When control forces are not applied, this mode of operation is referred to as free rolling. F_r is usually considered to be due to all of the hysteresis losses in a deflecting tire, which results in moving the center of pressure toward the leading edge of the contact patch. However, from the work Reynolds and others [5], it is apparent that even in free rolling

of a cylinder tractive stresses and sometimes slip may be induced in the contact region. In addition, for tires, tractive stresses are developed in the contact path because distortion is required to change the curved surface of the tire to conform to the flat road surface. For any complete model of the tire-road interface friction, these tractive stresses must be superimposed upon the tractive stresses caused by forces other than F_r .

e. A control force F_c , either braking, traction, or lateral, may be applied to a *rotating* tire. In this case, the tractive stress and slip distributions in the contact region are more complex than described in paragraph (c) above. This case is the subject of a number of papers [6, 7]. The point to be made here is that $(F_c)_{\max}/W$ is often referred to as the coefficient of friction, confusing it with μ .

During braking, as the rotating wheel is slowed toward complete slip, an increasing fraction of the contact patch slips. In this case, F_c approaches F_s , and this is a result of increasing relative speed between the tire carcass and road surface. On the other hand, F_p approaches F_s as a result of the distance of movement of the center of mass of the slider, a very different mechanism.

It is apparent that the operation of a tire at high slip will be directly influenced by the frictional properties of the tire rubber. It has been found that [8] various frictional conditions can influence tire elastic because behavior at small values of slip as well, where carcass deflections usually control tire behavior. On the other hand, tire carcass properties strongly influence the frictional behavior of tread elements, particularly by way of controlling tire-road contact pressure and local slip velocities. Because of these interactions, it is imperative that tire performance studies include detailed considerations of friction as well as of tire deformation and normal pressure distribution.

One common method of acknowledging the combination of the several events in the contact patch is to describe tire friction in terms of three functional categories. They are dry friction, wet friction, and hydroplaning [6, 7, 9]. The role of the road surface is often included under the description, smooth, polished, abrasive, rough, well-drained, etc. The tire may be characterized as being with or without tread and in some instances the tread material is given. Unfortunately, none of these descriptions is adequate for a frictional characterization of a particular tire on a particular road in a particular environment. A more fundamental approach follows.

1.2.4. Rubber Friction

For rubbing systems in general, there are several factors that contribute to sliding resistance. The friction of tire rubber on practical surfaces can be divided into at least four components, or causes. The naming of these four components is arbitrary to some extent, and they are here separated in terms of friction force, F , rather than the coefficient

of friction μ :

$$F_{\text{total}} = F_{\text{ad(hesive)}} + F_{\text{def(ormation)}} + F_{\text{vis(cous)}} + F_{\text{tear(ing)}}$$

and each component is defined below. Each component is distinctive as shown by simple experiments. Each component varies in a different way, and affects tire performance in a different way, with variation in contact stress, sliding speed, temperature, tire material, road surface profile, etc. The several components of friction will first be described individually, for clarity. In later paragraphs, the likely balance of the components will be discussed in relation to a real tire.

The existence of the adhesive, or dry, component of rubber friction is verified, and values are measured, by sliding a rubber specimen on a carefully cleaned, smooth surface, such as glass. Such experiments show that a thin smooth film of rubber about 100 \AA^4 thick is deposited and remains attached to the mating surface. The sliding retardation force varies considerably with contact pressure, sliding speed, and temperature and is consistent with the view that the value of F_{ad} is dependent on the viscoelastic mechanical properties of the polymer [10, 11].

When a sliding body leaves a thin film or track, a friction test may be merely a shear test. If this is the case, then F_{ad} depends on bulk mechanical properties of the polymer and not on adhesion kinetics. Other authors [12-14] are of the opinion that adhesion kinetics is responsible for either a part of, or the entire, adhesive frictional behavior. In their view, the rate of making and breaking bonds controls the magnitude of F_{ad} . Apparently they assume that the bonds that form also break at the original interface.

One observation at least may be explained by surface kinetics, and that is the need to slide rubber a few inches before a steady state value of friction is measured. On the other hand, this may also be due to the existence of surface films.

Whether F_{ad} is controlled by adhesion kinetics or bulk mechanical properties may in the end be a moot point. There is a possibility that these two properties may be derived from the same source.

In any case, there is general agreement that F_{ad} varies with sliding speed and temperature as shown in figure 1.2.1. The plotted master curve (a) is from reference [10] for an acrylonitrile-butadiene tire material with a t_g (glass transition temperature) of -20° C (-4° F). The curves are shifted using the WLF transform to show friction at various temperatures.

The location of the peak of the friction curves can be predicted from the glass transition temperature of the rubber. For SBR rubber with $t_g \simeq -45^\circ \text{ C}$ (-49° F), for example, the friction maxima at the temperatures designated in figure 1.2.1 would be shifted nearly two

⁴ \AA - Angstrom units, 10^{-8} cm .

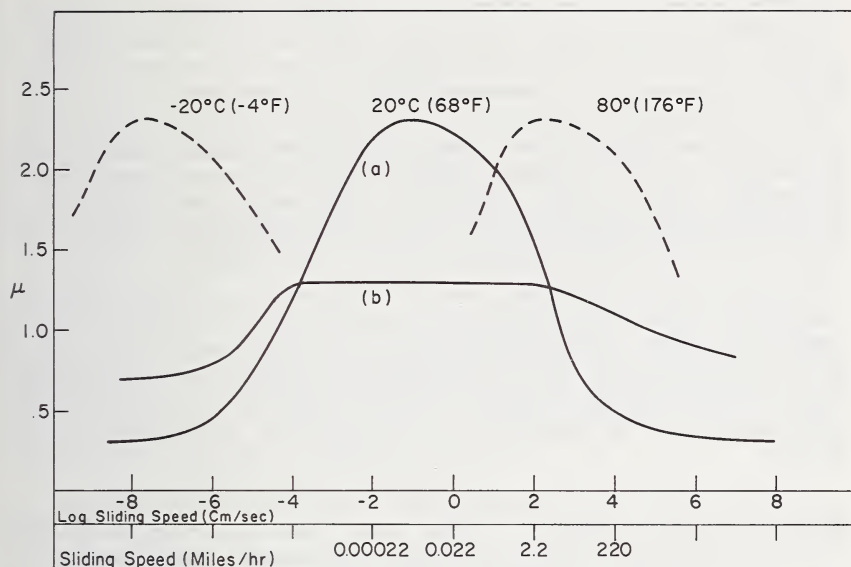


FIGURE 1.2.1. Coefficient of sliding friction plotted against sliding speed in cm./sec. and miles per hour.

Curve (a) is the master curve for acrylonitrile-butadiene (unfilled) at 20° C (68° F). Positions of curve (a) shifted to -20° C (-4° F) and 80° C (176° F) are shown. Curve (b) is for acrylonitrile-butadiene containing 50 parts of high abrasion furnace carbon particles [11].

orders of 10 to the right on the velocity scale. In the same manner, natural rubber with $t_g = -60^\circ \text{C}$ (-76°F) would have the peaks of the curves shifted nearly three orders of 10 to the left.

The main point to be gotten from figure 1.2.1 is that it appears that in practice friction most often decreases as sliding speed increases. However, tire-road slip causes surface heating which was not accounted for in figure 1.2.1. Heating will modify the effect of sliding speed, by an amount unknown at this time.

These curves "imply" that friction should increase as the ambient temperature increases. In practice, this is not found to the extent shown in figure 1.2.1 and the cause of this discrepancy is not known. Perhaps the reason lies in the fact that other mechanisms besides the adhesive component of friction are important in most real conditions. It should be noted that practical values of μ are not as high as shown in figure 1.2.1. The reason for this is also not known.

The values plotted in figure 1.2.1 are for kinetic or dynamic coefficient of friction μ_k . It is tempting to extrapolate the curves to zero velocity to find the static value, μ_s . It would appear that μ_s is smaller than μ_k , which is opposite to general expectations. The problem most likely lies in identifying μ_s with absolute zero velocity, which may be reasonable for some sliding systems involving more rigid materials. However, it is easy to see that in order to achieve a practical sliding

speed from zero velocity one passes through low velocities and possibly through the velocity range where high values of μ are measured. Thus the value of μ which must be supplied to start sliding can be higher than the value of μ to maintain sliding. The literature is not always clear on where the transition or peak value occurs on the velocity scale. Reference [15] reports a few test results showing a nearly linear decrease in μ with increasing sliding speed, with emphasis on common automobile speeds. Hurry and Prock [16] report an increase in μ with increasing sliding speed, but only up to speeds of 10 ft/min. (≈ 0.1 mph). There is no conflict between these two sets of data.

Friction induced vibrations are often caused by materials exhibiting reduced friction with an increase in speed. Such vibrations are often attributed to the "stick-slip phenomenon," which occurs in cases where μ_s is greater than μ_k . These vibrations are initiated by random disturbances either at sliding interface or in the machinery driving the friction experiment, and the frequency is determined by the dynamics of the system.

Standing vibrations are never found to occur at sliding speeds less than that at peak values of μ (fig. 1.2.1). Vibrations occur to the right of the peak and the vibrations are the more severe where the slope of the curve is steepest. Careful analysis of vibration data shows that in many cases the vibrations produce an oscillation in sliding speed between two finite values, and both values are to the right of the peak of the curve. This cannot be called the "stick-slip phenomenon"!

The entire explanation for friction induced vibration is not to be found in the adhesion component of friction. More of the topic will be found in the later discussion on the viscous component of friction.

The adhesion component of friction has been shown repeatedly [3] to result from strong interface bonding at the small local sites of contact between two surfaces. If bond strength is the same wherever bonds exist, the force that resists sliding is proportional to the total of all of the minute areas of contact. A number of factors control this true area of contact. We could expect that the true area of contact of two atomically smooth surfaces would be equal to the nominal area of contact and μ would be very high. However, for the usual surface which is very rough on the atomic scale, contact would be limited to the highest protrubances on the surfaces. The resulting true area of contact will depend upon details of the surface profile, the magnitude of the average contact pressure and certain properties of the materials. Estimates of true contact area are available for two classes of material behavior. For materials that yield plastically the total true area of contact A is

$$A = \frac{K_1 W}{3Y} \quad (1.2.1)$$

where W is the load per nominal unit area, Y is the yield strength of the material, and K_1 is a factor of proportionality. For elastomers on rough surfaces represented by an array of hemispheres we obtain the area of

contact from the Hertz contact stress equations:

$$A = K_2 \frac{Wr}{E} \quad (1.2.2)$$

where r is the radius of the hemispheres, E is the modulus of elasticity of the rubber, and K_2 is a factor of proportionality. The values of K_1 and K_2 vary with a number of conditions including surface roughness. For example, if surface roughness is represented by an array of spheres, an eight-fold decrease in the population density of spheres will decrease A by one-half.

From eq (1.2.2) above it can be seen that the adhesive μ is proportional to (average contact pressure)^{2/3}. This is observed in rubber and other elastic materials, as shown in figure 1.2.2 [17]. Again, it is known that μ is proportional to (1/rubber hardness)^{2/3} on dry surfaces. More general conclusions on this subject can be reached after discussion of the remaining components of rubber friction.

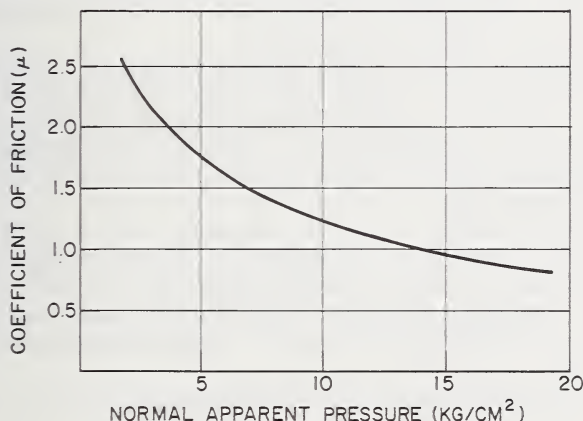


FIGURE 1.2.2. Coefficient of friction vs. normal apparent pressure [17].

F_{def} is a retardation force available when sliding a rubber specimen on perfectly lubricated surfaces with smooth bumps or protuberances [3]. The retardation force is due to the partial irreversibility of deformation, i.e., damping loss of the rubber caused by passage of the bumps or protuberances. This component of friction is not significant until there is sliding. The need to attribute F_{def} to the damping loss of tread rubber is not often disputed. Attempts have been made to connect *dry* frictional behavior with the damping properties of rubber. More work is required to resolve this point.

Damping loss varies with frequency of deformation as shown schematically in figure 1.2.3. It is reasonable to expect that sliding over a regular array of bumps produces a vibration in the rubber, the frequency

of which would be related to sliding speed. Where the bumps are 1/4 inch (0.6 cm.) diameter spheres and the rubber is acrylonitrile-butadiene with $t_g \approx -20^\circ\text{C}$ (-4°F), the retardation force due to damping alone varies with sliding speed as shown in figure 1.2.4.

If topographical features of a real road are included, it is possible to synthesize a more general deformation component loss curve. The large texture of a road surface is approximated by the 1/4 inch (0.6 cm.) diameter spheres just mentioned [18]. A second finer level of texture exists which has a radius of about two orders of 10 less than the course texture. Finally, a third very fine level of texture exists at about three to four orders of 10 less than the course texture. The friction performance of the three textures is shown in figure 1.2.5 together with the approximate theoretical maximum value of $F_{\text{def}} \approx 0.16$ for a very high loss rubber.

If in the place of discrete steps in texture size we assume a continuous distribution, a very broad curve could be plotted as shown by curve *a* in figure 1.2.6. On the other hand, if one range of texture size is missing from the road surface, the retardation force curve could be altered as shown by curve *b* in figure 1.2.6. This curve represents an alteration of the fine texture of figure 1.2.5, as occurs on polished roads. This effect is more fully described below.

Curve *b* of figure 1.2.6 may also serve as a basis for explaining the decrease in wet friction as temperature increases. The curves in figure 1.2.6 shift to the right with an increase in temperature, which has the effect of lowering F_{def} at moderate to slow sliding speeds. The effect is found by measurement to be the greatest on well-polished roads, which also fits the curves of figure 1.2.6.

An interesting finding is that the maximum friction coefficient available from the deformation component of friction depends upon the population density of the fine protuberances on the road surface. For example, for most tire rubber, with an average tire-road contact pressure of 30 psi, $F_{\text{def}} \approx 0.07 W$ when sliding over a tight-packed array of spheres,

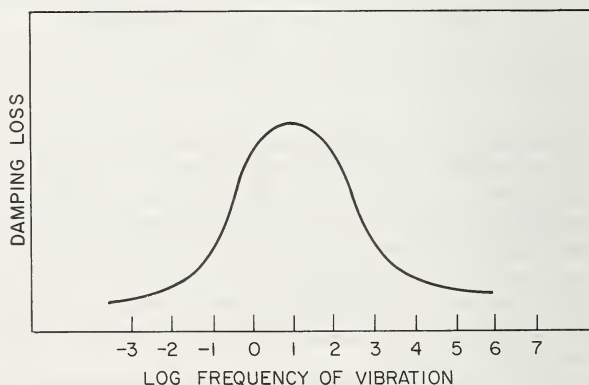


FIGURE 1.2.3. Typical curve for damping loss as a function of log frequency of vibration from a vibrating reed test.

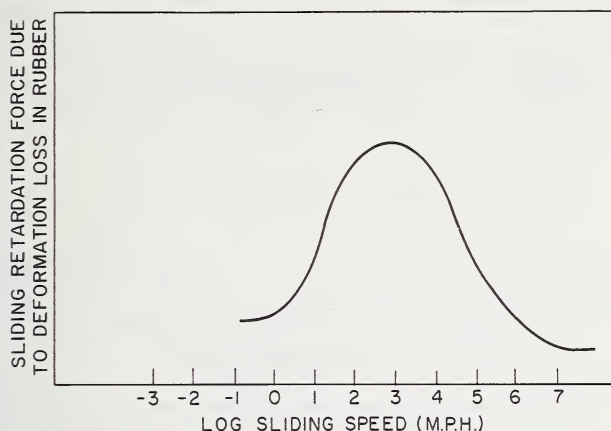


FIGURE 1.2.4. *Sliding retardation force due to damping loss in rubber when sliding over an array of sphere $\frac{1}{4}$ in. (0.6 cm.) diameter.*

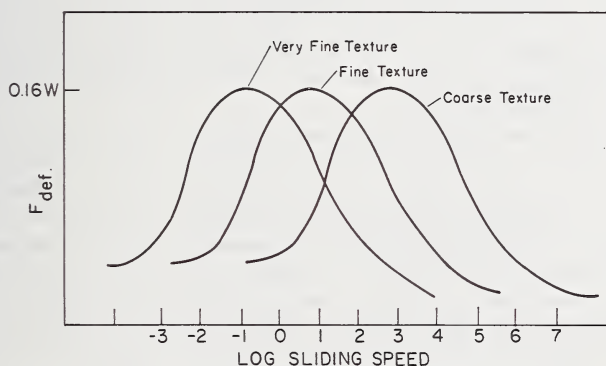


FIGURE 1.2.5. *Schematic representation of the sliding retardation force due to damping loss in a high loss rubber when sliding over a three order array of spheres, $b = \frac{1}{4}$ in. (0.6 cm.), $b \times 10^{-2}$, $b \times 10^{-3.5}$.*

The three textures are not known to produce equal effects.

while $F_{\text{def}} \approx 0.09 W$ when sliding over the same array with alternate spheres removed. The theoretical maximum $F_{\text{def}} \approx 0.16 W$, as previously indicated.

The deformation component of friction is difficult to separate from other components on complex surfaces. However, in spite of the low theoretical maximum value of $\mu = 0.16$, this could be the primary friction mechanism at high sliding speeds on films of water. It would be expected that F_{def} would be primarily influenced by the damping loss (rebound) properties of the rubber. This has been found to be true

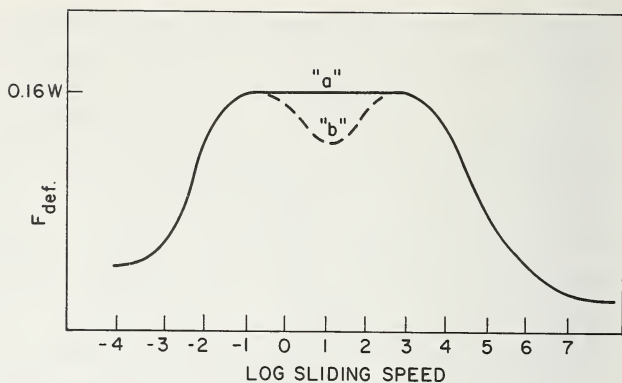


FIGURE 1.2.6. Sliding retardation force due to damping loss in a high loss rubber sliding on "a", a surface of a continuous distribution i.e., continuous effectiveness of sphere sizes within the range of figure 1.2.4, and "b" with size 6×10^{-2} missing.

for tires on wet roads although the effect of rubber hardness confused the picture to some extent [19].

Increased rubber hardness would have the effect of increasing contact pressure and when contact pressure is increased by increasing the load, F_{def} increased [18]. On the other hand, harder rubber often has lower damping loss (higher rebound) which could more than offset the effect of contact pressure.

The viscous component of friction force F_{vis} is defined to take account of the existence of a layer of either adsorbed or liquid species between the tire and the road surfaces. It is presumed that this layer is thick enough to significantly reduce direct bonding, or adhesion, of the tire rubber to the road material. The uniqueness of the viscous component can be demonstrated by rubbing a rubber slider on a glass that has been carefully cleaned and exposed to water vapor. A high friction force may be measured on this glass surface, with F approaching $W/2$. In this experiment, there is probably no F_{def} to confuse the picture because of the smoothness of glass, and no thin film of rubber remains attached to the glass.

It would appear that the experiment described above, producing $F \approx W/2$, is one extreme example of a fluid film. However, this may, in fact, be the most common condition of tire-road contact, due to the adsorption of water vapor on tire and road surfaces.

The thickness of these adsorbed water films is not known. The closest approximation can be made from the work on water adsorption on lime-soda glass, a material of the same class as some road stones [20]. A surface water film, apparently of 105A (0.4×10^{-6} in.) thick, may persist in a dry atmosphere at 23°C (41°F), and 55 \AA thick at 215°C (390°F). Very likely much thicker films would exist at lower temperatures and higher relative humidities. In addition, when two mating surfaces each have an adsorbed film, the total separating film is still thicker. More careful work is needed in this area.

When water films exceed a few tens of molecules in thickness we may expect the following competing events to occur. The normal load on the rubber will eject or squeeze out the liquid film allowing the rubber to approach the mating solid. The Stefan equation describes this situation [21],

$$t = \frac{3\pi\eta R^4}{4f} \left[\frac{1}{h_2^2} - \frac{1}{h_1^2} \right] \quad (1.2.3)$$

where f is the force applied to a circular disc of radius R . The initial film thickness h_1 of a fluid of viscosity η is reduced to a thickness h_2 in time t . Where viscosity, velocity, and separation h_1 are large and contact pressure is small, conditions are favorable for maintaining complete separation of the rubber slider from the mating surface. On the other hand, increasing rubber hardness would be expected to produce thin water films and therefore higher viscous drag force.

The condition from which the Stefan equation was derived is that of nonsliding contact. Where sliding occurs and where the rubber slider has a rounded leading edge, the rubber will tend to slide over the top of the liquid film. There is as yet no rigorous mathematical expression for this behavior. However we may approximate it by slipper bearing action. Such hydrodynamic lift occurs over a larger fraction of tire surface as sliding speed increases. Hydrodynamic lift must be distinguished from aquaplaning or hydroplaning of a tire. The latter is due to insufficient squeezing out of water film in the time of contact of each tread element. This may explain why a rolling tire can hydroplane at a high linear speed, spin down to a stop, and restart only after a considerable decrease in linear speed.

It should be noted that if the leading edge of the rubber slider is sharp, hydrodynamic lift may be partially averted, although there will be no "wiping" or drying of the road surface. A water film persists in approximate accord with the Stefan equation. In the real case, the leading edges are not sharp, and, in fact, the contact stress near the edge is less than the average stress over the contact area. Furthermore, the road surface geometry is as important to the problem of local hydrodynamic lift as is the tire surface geometry.

A complete and formal description of the viscous effects in rubber friction is not possible at this time. The difficulty does not lie with the classical basic equations that govern film thickness. Rather, difficulties arise in finding meaningful quantities to put into the equations. For example, a satisfactory mathematical description of mating surface geometries has not yet been developed [22].

Another important unknown quantity is the description of the appropriate properties of the film separating the rubbing surfaces. A thin film of lubricant may behave as a fluid of greater apparent viscosity than the bulk viscosity [21]. This effect is thought to be due to the nature of the bond between a liquid and solid, which is manifested by the tenacity with which liquids remain adsorbed to a solid. There is some criticism of this view, but it appears to be a criticism of form rather than substance.

Other recent work shows an opposite effect [23]. Electrical double layers in an electrolytic liquid film between rubber and glass were observed to maintain a larger equilibrium separation between the sliders than can be accounted for by viscous or inertia effects. Thus, a value of F_{vis} was measured for a fluid film thicker than normal for the contact stress, producing a very low value of $\mu=0.04$ without hydrodynamic lift.

In principle, at least, F_{vis} can be sliding speed dependent in such a way as to encourage frictional vibrations. The proper conditions are achieved by rounding the edges of rubber elements so that hydrodynamic lift increases with velocity. These conditions are apparently met when a tire slides on a wet polished concrete surface. A high frequency vibration (squeal) can be heard, particularly at speeds below 15 mph, and it originates in the tread region of the tire.

F_{tear} is a component of friction which takes account of the observation that some solid surfaces tear particles from the rubber. These particles usually do not remain attached to the mating surface, and this mechanism can occur on contaminated surfaces where values of μ may be low. In some cases, where values of μ are high, it is easy to explain the tearing of particles from a rubber surface by high traction stress, in combination with contact stresses, which cause fracture in the rubber. Likewise, it could be argued that F_{tear} is already accounted for under one of the other three components of friction. On the other hand, the deformation and thick film viscous components of friction would not ordinarily be expected to produce large wear fragments.

1.2.5. Combined Components of Friction

The operation of tires on roads involves some combination of the several mechanical classes and components of friction. Research has not yet reached the stage where it is possible to mathematically express either the distribution of slip velocities in the contact patch, or the traction stress distribution due to the components of friction on tire and road surfaces of undefined surface geometry. It will therefore be necessary to qualitatively describe some of the events in the contact patch under various operating conditions, and to further define some terms. In these descriptions, very many details are omitted, in the interest of maintaining the broader and more unifying view.

Dry Friction

Dry friction is one phenomenological category of tire operation that is thought to be simple, and it usually produces high friction. In fact, it is a wide range of conditions. A common but probably inaccurate assumption is that dry friction involves primarily the adhesive component of friction. Several interesting coincidences seem to bear this out, but the situation is far from resolved. For example, begin with curve *a* of figure 1.2.1 for dry friction of an unfilled rubber where a film of rubber

was not left on the glass surface. Reference [11] shows the peak value of friction for the same rubber at nearly the same sliding speed as that of reference [10], in an experiment that produced a thin film of rubber attached to the glass. Reference [10] also reports data for carbon filled tire rubber, which is a curve that overlaps the curves of figure 1.2.1 except that the peak of the curve is replaced by a plateau showing a maximum sliding coefficient of friction near 1.2, a value that has been reported for tires on dry roads. On the other hand, a μ of 1.2 is not proof of the adhesion component of friction alone. Reference [11] measures a maximum μ of 3.2, but reference [23] shows a value in excess of 10. It is likely that these differences are due to complex surface films.

A "dry" surface may be covered with adsorbed water up to the limit of invisibility at about 500 \AA ($2 \times 10^{-6} \text{ in.}$) or $\frac{1}{2}$ micron thick. A reduction in braking friction is possible on surfaces exposed to cool moist air without a visible water film [24]. This could be true with a 500 \AA thick film.

The tenacity of thin water films is surprisingly high. Water is usually not completely removed by the local pressures in the tire contact patch. From eq (1.2.3), for a local contact pressure of 250 psi, a vehicle speed of 30 mph and a water viscosity of one centipoise ($1.45 \times 10^{-6} \text{ Reyn.}^5$), and $R = 10^{-3} \text{ cm.}$ ($0.4 \times 10^{-3} \text{ in.}$), a water film of $5 \times 10^{-6} \text{ cm.}$ ($2 \times 10^{-6} \text{ in.}$) is squeezed to $1.2 \times 10^{-6} \text{ cm.}$ thick in the time of local contact of the tire on the road. Thin films or more viscous films would thin proportionately less in the same time.

It can be estimated, using the simple Newtonian viscosity equation for drag force per unit wetted area, $f = \eta v / h_0$, that the viscous drag of a water film of about 10^{-6} cm. thick between two flat surfaces may produce F_{vis} in excess of $0.25 W$ at a sliding speed in the order of 1 mph. For thinner films or higher velocities, F_{vis} would be higher. This line of reasoning ends with the comment that $(F_c)_{\text{max}}$ for tires does not often exceed W , in which case $\mu = 1$. Conversely, it has not been proven that some penetration of the water film [21] does not occur on very sharp asperities, thus producing some adhesion friction. However, it is not necessary to invoke adhesive friction to account for the high values of tire traction measured on so-called dry surfaces.

At larger slip velocities, such as during braking or severe cornering, the thin water film would probably be heated and possibly boiled away to produce more adhesive friction. A simple calculation shows that where $F \approx 0.5W$, average contact pressure is 30 psi, and due account is taken of the heat of adsorption of water to glass, adiabatic heating, and boiling of a water film 10^{-6} cm. ($0.4 \times 10^{-6} \text{ in.}$) thick takes place by rubbing a distance of from one to two inches. Thus, for a typical automobile tire a slip of about 15 percent would boil such a water film away. For larger slip ratios or for thinner water films, the water would be removed in the leading part of the slip region in the contact patch, producing dry or adhesive friction over the remainder of the contact patch. Traction stresses could, therefore, decrease as slip velocities increase (see

⁵Reyn. — Reynolds units, lbf · sec/in.².

fig. 1.2.1), the opposite of what would be expected if a viscous film were to persist. Under still more severe conditions, the surface temperature of the rubber could reach the softening or reversion temperature where rubber is easily removed from the tire surface [26].

Wet Friction

Wet friction covers a range of conditions from visible wetness to standing water. In this case, the balance between the various friction components is strongly influenced by tire rolling speed.

A rolling tire can be viewed as a device that places tread elements on top of a water film, applies a load for a period of time and then reverses the process [27]. During the time of loading the tread element sinks toward the condition of static dry contact, without achieving this end.

Therefore, through the contact excursion there is an increasing viscous drag force potential, which is not realized until there is a slip. In principle, separating the tire-road surfaces should require a force, limited by cavitation and peeling. This force would have the effect of an additional small force holding the tire near the road.

When slip occurs, there may be sufficient hydrodynamic lift to decrease viscous drag. It is reasonable to expect that this effect should be greatest as the slip ratio of a tire increases toward complete sliding.

For instantaneous water film thickness of 10^{-3} cm. (0.4×10^{-3} in.) between flat surfaces, viscous drag forces are negligibly small even at 100 mph sliding speed. This type of statement begs the question of how much total water on a road surface produces an effective water film 10^{-3} cm. thick, because of several factors. If each sinking element can freely expel water from the pressure surfaces, it will sink in a viscous manner, ignoring inertia effects. If it cannot do so, it, together with neighboring elements in the same situation, becomes a single operating element with an increased effective value of R in eq (1.2.3). In the extreme, all elements in the contact region might operate together, with a value of R that properly represents contact between an entire contact patch and a rough road surface. This situation is often described as the cause of hydroplaning [28]. When hydroplaning occurs, the viscous drag forces are very small and appropriate directional control forces are not achieved.

In practice, a water film much deeper than 10^{-3} cm. is required to achieve very small friction forces [7]. Most road surfaces consist of protuberances or projections rising above the average surface plane. A sinking element will sink more slowly when approaching one of these projections than will a nearby element located over a valley, if water can be expelled. Thus, the road surface contour is to some extent impressed upon the tire surface. This is called draping [29]. For a sliding tire the impressions move parallel with the surface with some loss of energy. Thus, there can be a useful F_{def} even though F_{vis} may be very small. When the water film over the larger projections becomes less than 10^{-3} cm., the second order or fine projections [30, 31] will begin to be impressed upon the tire surface, which will produce a higher traction potential. For thinner water films, $\approx 10^{-5}$ cm. (0.4×10^{-5} in.) the full F_{def} potential is equal to the viscous drag at 10 mph producing F_{total}

$\approx 0.4 W$. Thinner water films would expose the very fine projections but their exposure does not enhance tire traction. It is apparent that a simple tire friction test does not reveal the fundamental causes of friction.

Rubber Properties

There is no tire rubber that produces high friction on all surfaces, under all conditions. The effect of base polymer and of compounding ingredients on frictional properties appears to depend upon a number of other conditions describing the sliding process, including the nature of the opposing surface, the lubrication, and the load. For example, increasing carbon black content has been reported to increase friction coefficient on an abrasive surface but to decrease it on a smooth surface at low loads.

Soft compounds usually give higher coefficients of friction than do harder compounds on smooth surfaces under low loads. In line with this observation the effect of rubber plasticizer is to produce softer rubber, while increased state of cure produces harder rubber and lower friction.

The effect of rubber hardness on its frictional properties is complicated by a reduction in hardness of the rubber layer in immediate contact with the opposing surface as a result of severe mechanical flexure during sliding [32]. The hardness of a layer of filled rubber in immediate contact with an abrasive surface is very close to that of an unfilled rubber. For tires, any effect of hardness increase, caused by addition of fillers, on frictional force must therefore be attributed to the effect of the properties of the rubber below the surface layer. It is well known that these substrate or bulk properties can be important, since in comparing the friction of thick and thin rubber membranes on ice the thin specimens exhibited consistently lower coefficients of friction than did the thicker ones.

The influence of rubber properties is complex. However, in summary, it can be said that the choice of base polymer and of the ingredients used in compounding can affect frictional properties not only through their influence on such physical characteristics as hardness, damping loss [19], and surface roughness, but also by changes in chemical adhesion and the ease of surface contaminations through bleeding of pigments or adherence of extraneous contaminants. Furthermore, the compounding necessary to achieve maximum friction may need to be specific to the opposing surface. In view of the several constraints on the practical range of tire rubber properties the available range of friction is not large. By far the most important variables are the nature of the road surface and the tread pattern.

Longitudinal and Lateral Tire Slip and Slide

The frictional forces between a tire and road vary with the amount of deviation from straight line free rolling operation. For the classical rigid wheel rolling on a flat plane any slip whatsoever is complete sliding. However, the flexible tire structure can deviate from straight line free rolling without complete sliding at the tire-road interface. Although the

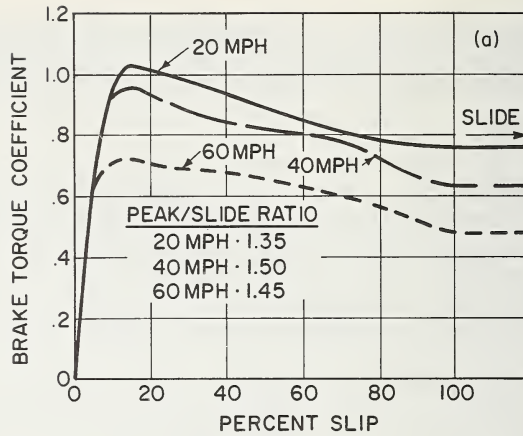


FIGURE 1.2.7a. Brake torque coefficient vs. slip—wet asphalt [33].

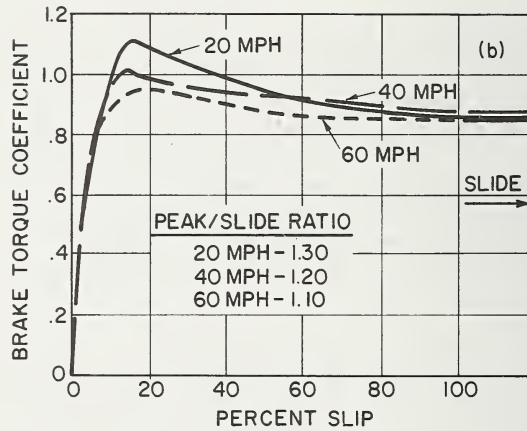


FIGURE 1.2.7b. Brake torque coefficient vs. slip—dry asphalt [33].

exact mechanics of this behavior have not been worked out the results are well known. Some are summarized below.

The behavior of the tire in braking is shown in figure 1.2.7 [33]. The data are presented in terms of brake torque coefficient and percent slip. The brake force coefficient is a value which is, to within a few percent, the ratio of braking force to normal load. Percent slip is defined as

$$\frac{W_r - W_t}{W_r} (100) = \text{percent slip}$$

where W_r = rotational speed of a free rolling reference wheel and W_t = rotational speed of the test wheel.

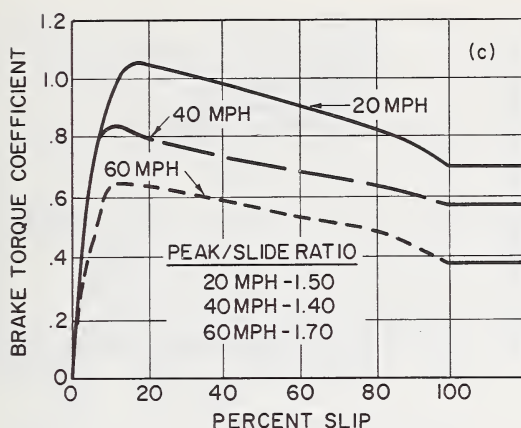


FIGURE 1.2.7c. Brake torque coefficient vs. slip — wet portland concrete [33].

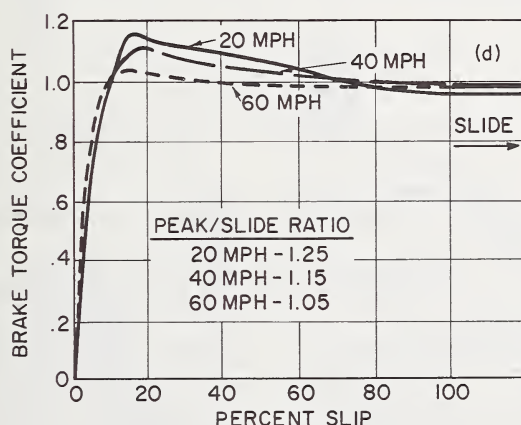


FIGURE 1.2.7d. Brake torque coefficient vs. slip — dry portland concrete [33].

The behavior of the tire in side slip can be seen in figure 1.2.8, giving data for a number of tires, road surfaces, and vehicle speeds [34]. Data for combined braking and side slip are found in the same paper. However, a clearer picture of combined effects are found in figure 1.2.9 [35].

Several attempts have been made to mathematically express the forces available in all possible directions and degrees of slip. This usually takes the form of a "friction circle" or "friction ellipse." In the case of an assumed friction circle, one hopes that it would be possible to predict total behavior from a simple braking test. Unfortunately, available data [34] do not show this to be practical. An expression of the form $R^2 = B^2 + S^2$ is often used, where R is the resultant horizontal force, B is the braking force, and S is the side force. There is not a detailed dis-

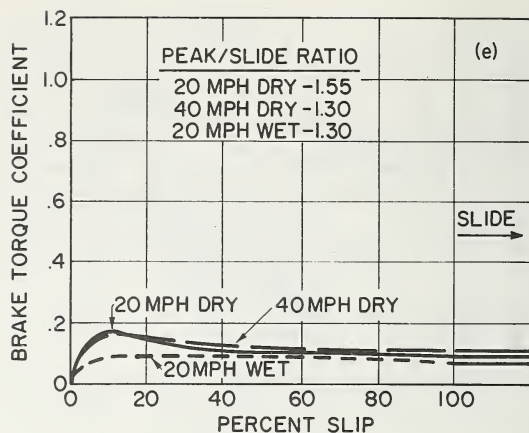


FIGURE 1.2.7e. Brake torque coefficient vs. slip - ice [33].

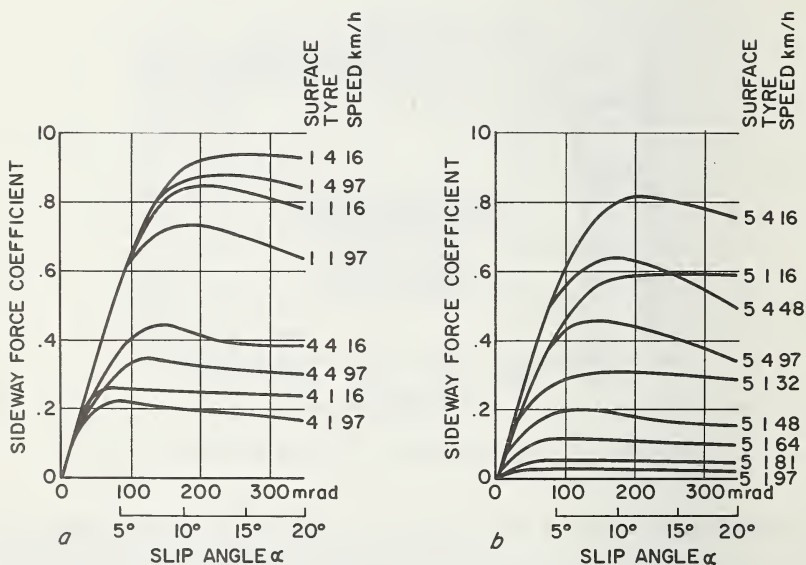


FIGURE 1.2.8. Effect of slip angle on sideways force coefficient [34].

cussion of this topic in hand. It would be surprising if a single simple expression of the above form could be applied to all cases. For example, the effect of speed on the above expression is known to depend on tread design. Furthermore, it makes some difference whether the data used are peak values of braking force and side force, or sliding values. Speculation on this subject may be near an end since the advent of high quality test devices [35] to measure force values at all combinations of braking and side slip.

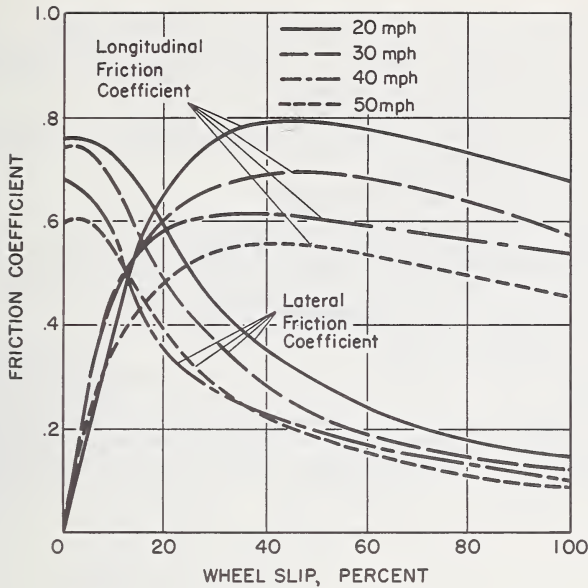


FIGURE 1.2.9. Friction coefficient vs. wheel slip [35].

References

- [1] Julian, M. A., *Revue Generale du Caoutchouc* **36** (10), (1959).
- [2] Gough, V., and French, T., *Proc. First International Skid Prevention Conf.*, Charlottesville, Va., 1959, p. 189.
- [3] Bowden, F., and Tabor, D., *Friction and Lubrication of Solids*, Vol. 2, (Oxford Univ. Press, New York, 1964).
- [4] Mason, W. P., *ASLE Trans.* **2** (1), 39 (1959).
- [5] Ref. [3], p. 288.
- [6] Maycock, G., *Proc. IME* **180-2A** (4), 122 (1956-66).
- [7] Allbert, B., and Walker, J., *Proc. IME* **180-2A** (4), 105 (1956-66).
- [8] Daube, J., *La Technique Routiere* **4** (1), 4 (1959).
- [9] Leland, T., and Taylor, R., *J. Aircraft* **2** (2), 72 (1965).
- [10] Grosch, K., *Proc. Roy. Soc.* **A274**, 21 (1963).
- [11] Ludema, K., and Tabor, D., *Wear* **9**, 329 (1966).
- [12] Schallamach, A., *Wear* **6**, 375 (1963).
- [13] Savkoor, A., *Wear* **9**, 66 (1966).
- [14] Bartenev, G., and Elkin, A., *Wear* **8**, 8 (1965).
- [15] Krempel, G., *A. T. Z.* **69** (1), 128 (Jan. 1967), *A. T. Z.* **69** (8), 1334 (Aug. 1967).
- [16] Hurry, J. A., and Prock, J. D., *India Rubber World* **128**, 619 (1953).
- [17] Atach, D., and Tabor, D., *Proc. Roy. Soc.* **246**, 539 (1958).
- [18] Ludema, K., and Lee, C. S., *ASME Paper No. 69-LUB-20* (1969).
- [19] Bevilacqua, E., and Percarpio, E., *Rubber Chem. Tech.* **41** (4), 832-894 (Sept. 1968).
- [20] Holland, L., *Properties of Glass Surfaces* (John Wiley & Sons, Inc., New York, 1964).
- [21] Cameron, A., *Principles of Lubrication* (John Wiley & Sons, Inc., New York, 1966).
- [22] Moore, D., *Wear* **13**, 381 (1969).
- [23] Roberts, A., and Tabor, D., *Nature* **219**, 1122 (1968).
- [24] Leland, T. J. W., *Proc. 9th Stapp Car Crash Conf.*, p. 383, University of Minnesota, 1966.

- [25] Sabey, B. E., Brit. Granite and Whetstone Fed. J., 7 (Autumn, 1965).
- [26] Nybakken, G., Staples, R., and Clark, S., Laboratory Experiments on reverted rubber friction, Tech. Report 7 (Office of Research Administration, The University of Michigan, Ann Arbor, Mich., Oct. 1968).
- [27] Moore, D. F., Research Trends, p. 8 (Spring-Summer 1966).
- [28] Horne, W., and Dreher, R., NASA TN D-2056 (National Aeronautics and Space Administration, Washington, D.C. (1963).
- [29] Moore, D. F., Wear **8**, 245 (1965).
- [30] Wehner, B., Der Bauingenieur **10** (1) (1965).
- [31] Schulze, K. H., Strasse und Autobahn **10** (10), 379 (1959).
- [32] Schallamach, A., Rubber Chem. Tech. **27**, 439 (1954).
- [33] Goodenow, G., Kolhoff, T., and Smithson, F., SAE Paper No. 680137, 13 (Jan. 1968).
- [34] Holmes, K. E., and Stone, R. D., Symposium on Handling of Vehicles Under Emergency Conditions, Inst. Mech. Engrs., Jan. 8, 1969, p. 81.
- [35] Dugoff, H., and Brown, B. J., Instrumentation for measuring tire shear forces, SAE Paper No. 700093 (Jan. 1970).
- [36] Davisson, J. A., SAE Paper No. 700093 (Jan. 1970). Annual Meeting, Detroit, Mich., Jan. 1968).
- [37] Dillard, J., SAE Paper No. 970A (SAE 1968 Annual Meeting, Detroit, Mich., Jan. 1968).
- [38] Kummer, H. W., and Meyer, W. E., Tentative skid-resistance requirements for main rural highways, Nat. Coop. Hwy. Res. Program Report 37, Highway Research Board, NAS, Washington, D.C. 20418, 1967.

1.3. Tire Cord Structure and Properties

Stanley Backer ¹

	Page
1.3.1. Introduction.....	65
1.3.2. Cord geometry.....	65
1.3.2.1. Definitions.....	65
1.3.2.2. Geometric models: singles yarns.....	67
1.3.2.3. Geometric models: plied yarns.....	73
1.3.2.4. Experimental observations of plied yarn structures.....	87
Singles yarn retraction.....	88
Plied yarn retraction.....	93
Helix angles.....	96
Cross sections.....	100
Migration.....	101
1.3.3. Mechanics of tensile behavior of tire cords.....	111
1.3.3.1. An introduction to the mechanics of simple yarn structure.....	111
1.3.3.2. Analyses of tensile behavior of continuous filament singles yarn.....	117
The case of pure fiber tension and idealized geometry.....	117
The case with transverse forces.....	121
The case with large extensions.....	125
Yarn analysis using an energy method.....	127
Analyzing the role of fiber uniformity.....	129
1.3.3.3. Experimental observations of singles yarn tensile behavior.....	139
1.3.3.4. Analysis of tensile behavior of continuous fila- ment plied yarns and cords.....	153
Simple fiber tension and idealized geometry.....	153
Plied yarn analysis using an energy method.....	162
Analysis of the role of singles yarn variability in plied yarn mechanics.....	166
Cord behavior in compression.....	172
1.3.3.5. Observations of plied yarn behavior in tension and compression.....	175

¹Mechanical Engineering Department, Massachusetts Institute of Technology, Cambridge, Massachusetts 02139.

	Page
Tensile behavior.....	175
Effect of temperature on tensile mechanical properties.....	182
Effect of strain rate on tensile mechanical properties.....	183
Compression and buckling.....	186
Spectrum of stress strain properties	186
Effect of lubricants.....	190
1.3.4. Bending mechanics of twisted structures.....	191
1.3.4.1. Geometry of bent yarns.....	191
1.3.4.2. Bending rigidity of twisted yarns (with no friction).....	196
1.3.4.3. Bending rigidity of twisted yarns (with friction)...	205
References.....	213

1.3.1. Introduction

The textile cord reinforced rubber system which we call a tire differs in many respects from the classical composite material discussed so intensively in the current literature [1, 2].² For the tire is, in fact, a structure whose form and composition vary from point to point according to design. Likewise, its reinforcing cords are placed in specific regions and in different orientations. The levels of strength and stiffness of the reinforced rubber tire fall well below those of the usual composite. On the other hand, the ratio of breaking stress of the reinforcing textile fiber to that of the rubber matrix is higher than for most fiber strengthened composites. This ratio is approximately 50 for the reinforced rubber tire [3].

The reinforcing element in a tire is, in itself, a structure with numerous filament components organized in a geometrical array with a view towards enhancing the translation of filament properties into optimum in situ tire cord performance. And, finally, the filament itself has been shown in recent studies to possess an internal structure at the microscopic as well as at the molecular level [4, 5, 6].

The uniqueness of tire reinforcement design is covered in chapter 3 of this monograph. Likewise, the analytical treatment of those portions of the tire which can be approximately considered as uniform composite material will be found in chapter 2. This chapter will emphasize still another of the cited differences between the tire and the more usual composite. It will consider the structural geometry of textile tire cords and will illustrate the interaction of this geometry with the mechanical properties of the component filaments to influence cord behavior. This treatment is but a part of the general subject of structural mechanics of fibers, yarns and fabrics which has received considerable coverage in the textile literature of the last 25 years. The consolidation and review of such material by Hearle [7] is recommended for more detailed study.

1.3.2. Cord Geometry

1.3.2.1. Definitions

Engineers attempting for the first time to use textile components as structural elements are frequently confused by the uniqueness and ambiguity of terms used to describe textile materials and processes. The presence of such ambiguity can frequently be traced to the develop-

²Figures in brackets indicate the literature references at the end of this chapter.

ment of textile language during the early part of the industrial revolution when communication and transport between communities were limited. Thus the developing industries in towns or local regions not distant in a modern sense, often coined entirely different terms for the same concept. This trend was accentuated by the complete separation of different parts of the industry, say that dealing with cotton and that dealing with wool.

The confusion experienced by outside users of textiles has likewise plagued the professionals working in the industry, particularly in their efforts to develop information storage and retrieval systems. And of late, considerable progress has been made in cooperative efforts to foster a universal textile language [8, 9].

The selected group of definitions which follows is listed according to U.S.A. terminology and is limited to the structures and processes associated with tire cords [9, 10, 11].

Cord: two or more *plied* yarns twisted together in one operation (also called a cable yarn).

Count (yarn): a number to indicate linear density of yarn systems, either in mass per unit length or length per unit mass.

Denier: a specific count system often used for filament (as contrasted to staple) yarns. It is the weight in grams of 9000 meters of the yarn.

Drawing (filament): extending a polymeric filament beyond its yield point thereby attenuating its cross section, and increasing its modulus and its internal orientation. Generally, filament assemblies are drawn prior to twisting.

Fiber: a unit of matter characterized by flexibility, fineness, and high ratio of length to thickness.

Filament: a fiber of infinite length (as compared to short staple fibers).

Filament Yarn: a yarn comprised of filaments of indefinite length.

Helix Angle: angle between a fiber segment as it lies in a yarn and the corresponding segment of the yarn axis, or the angle between a single yarn segment as it lies in a plied yarn and the corresponding segment of the plied yarn axis.

Packing Factor (Yarn): the relative packing of fibers or filaments in a yarn structure expressed as the ratio of fiber cross sectional area to corresponding yarn cross section.

Plied Yarn: a yarn in which two or more single yarns are twisted together in one operation.

Staple Yarn: a yarn comprised of relatively short (1 to 5 inches) staple fibers.

Stretching (Cord): extending a cord structure under controlled conditions to increase its mechanical properties, its dimensional stability, and its uniformity from cord to cord.

Tenacity: the maximum specific stress developed in a tensile test taken to rupture, often expressed in g.p.d. or grams per denier. (Notice the dimension of tenacity is that of length, and g.p.d. is a measure of how many 9000 meter lengths of itself which the yarn will support.)

Tex: a specific decimal count system. It is the weight in grams of 1000 meters of a yarn.

Twist: the spiral disposition of the component(s) of a yarn which is usually the result of relative rotation of the extremities of the yarn(s), expressed as turns per unit length of the twisted structure.

Yarn: a continuous length of assembled staple fibers or filaments, often twisted together in one operation.

In the tire industry the element of textile reinforcement is called a tire cord. And in the early 1900's the twisted cotton reinforcement structure then used was a true cord according to the above definitions, for it was made by cabling together several plied yarns. And each plied yarn was made by twisting together several singles staple yarns. With the introduction of filament rayon cords in 1938, then nylon in 1947, and polyester in 1962, the structure was modified and it became in effect a two or a three ply yarn. This reminder that today's tire cord is a plied yarn in textile terms is intended as a guide to information retrieval in the textile literature as should be clear from the appended reference titles.

1.3.2.2. Geometric Models: Singles Yarns

The single filament yarn has been assigned the simplest geometrical model based on the assumptions that (1) the yarn and its component filaments are uniform in dimensions along their length, (2) each filament of the yarn lies in a helical path, rotating around the yarn axis at the same rate (expressed in turns per unit length of that axis), (3) each filament helix has a constant radius. Thus the yarn is composed of rings of filaments and all the filaments of a single ring lie in equal helices.

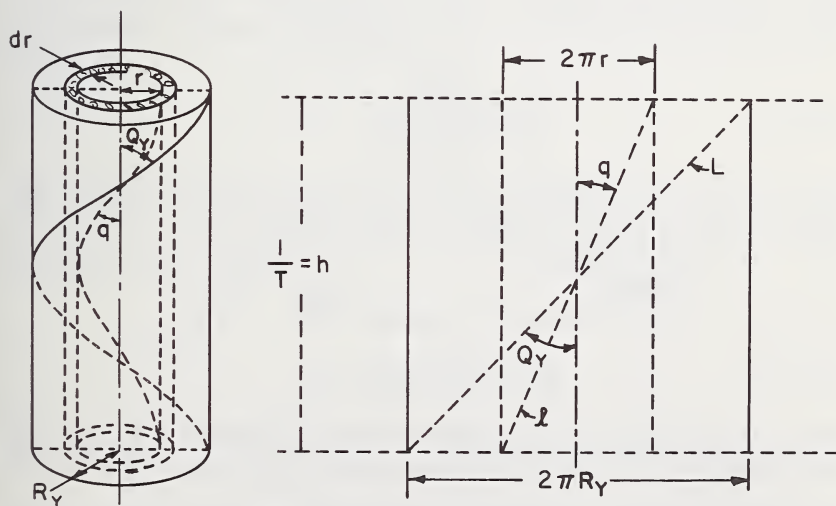


FIGURE 1.3.1. Geometric model of singles yarn.

The form of the model is illustrated in figure 1.3.1 where, according to Hearle [7],

R_y = singles yarn radius,

r = radius of helix containing a particular fiber,

T = yarn twist, in turns per unit length,

$h = 1/T$ or the length of one turn of twist,

Q_y = surface angle of twist, i.e., the helix angle of the outermost ring of filament helices,

q = corresponding helical angle at radius r ,

l = length of fiber in one turn of twist at radius r ,

L = length of fiber in one turn of twist at radius R_y

Clearly, the length of the central fiber in the model is h . And from the developed surfaces of the cylindrical rings, it follows that,

$$l^2 = h^2 + 4\pi^2 r^2 \quad (1.3.1)$$

$$\tan q = 2\pi r T \quad (1.3.2)$$

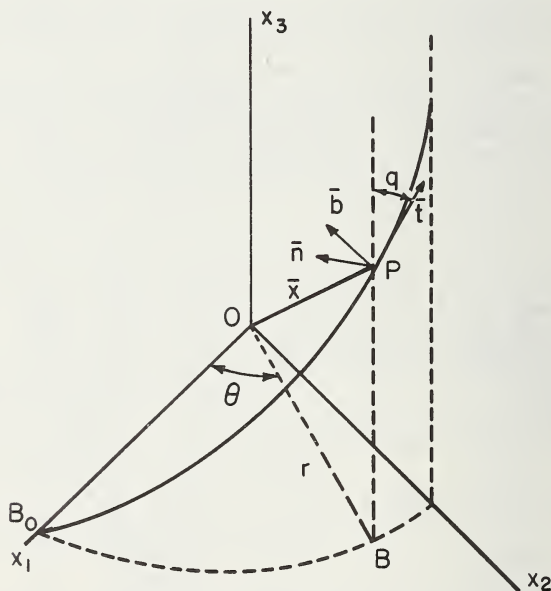


FIGURE 1.3.2. Single helix.

Now, redrawing the single helix in Cartesian coordinates in figure 1.3.2, we locate the point P at an arbitrary point on the helix and note that,

B = the vertically projected base point from P to the horizontal plane x_1ox_2 ,

θ = the rotation of OB from the starting point along ox_1 ,
 s = the distance along the helix path from B_0 to P ,
 q = the helix angle formed between \bar{t} and the vertical,
 \bar{t} = the unit tangent vector along the helix path at P ,
 \bar{n} = the principal normal of the helix path at P ,
 \bar{b} = the binormal of the helix path at P ,
 \bar{x} = position vector from O to P .

The coordinates of point P are seen to be:

$$x_1 = r \cos \theta \quad (1.3.3)$$

$$x_2 = r \sin \theta \quad (1.3.4)$$

$$x_3 = r \theta \cot q \quad (1.3.5)$$

and

$$s = r \theta \operatorname{cosec} q. \quad (1.3.6)$$

From Frenet;

$$\frac{d\bar{x}}{ds} = \bar{t} \quad (1.3.7)$$

$$\frac{d\bar{t}}{ds} = k\bar{n} \quad (1.3.8)$$

$$\frac{d\bar{b}}{ds} = -\tau\bar{n} \quad (1.3.9)$$

where k is the curvature of the helix path and τ is the geometric torsion of the helix path. The classical texts in differential geometry carry through from equations (1.3.3) to (1.3.9) to expressions for curvature and torsion, i.e.:

$$k = \frac{\sin^2 q}{r}, \quad \tau = \frac{\sin 2q}{2r} \quad (1.3.10)$$

two important relationships in the structural mechanics of yarns, which indicate that the individual filament paths in a twisted yarn possess both curvature and torsion. Now, substituting in (1.3.10) for the value of r taken from (1.3.2),

$$k = 2\pi T \sin q \cdot \cos q, \quad (1.3.11)$$

$$\tau = 2\pi T \cos^2 q. \quad (1.3.12)$$

For the inside central fiber whose $q = 0$,

$$k_i = 0,$$

$$\tau_i = 2\pi T \text{ radians/unit length,}$$

while for the outermost fiber with maximum helix angle Q_y ,

$$k_o = 2\pi T \sin Q_y \cdot \cos Q_y, \quad (1.3.13)$$

$$\tau_o = 2\pi T \cos^2 Q_y. \quad (1.3.14)$$

Thus, the central fiber possesses a path-torsion equivalent to the yarn twist, and this geometric torsion is reduced in the outermost fiber by the factor $\cos^2 Q$, while the central fiber path is straight at the center and maximally curved at the outer layer. It turns out that the geometric torsion calculated above is equal to the mechanical twist felt by each fiber in the yarn (about its own axis) if it is assumed that the process of twisting starts with a cylindrical array of parallel untwisted fibers and all fibers are grasped at one end and rotated together around the yarn axis. Likewise, the path curvature determined from (1.3.10), (1.3.11), and (1.3.13) all reflect the mechanical curvature of the fibers themselves.

This is one caution to be observed in converting from the fiber-path parameters k and τ to the actual curvature k_a and twist τ_a of the fibers. If the parallel components arrayed for simultaneous twisting into a higher order structure are already pretwisted, then the quantities determined from (1.3.10), (1.3.12) and (1.3.14) represent only the differences in local twist from the initial state of the component to the in situ configuration in the higher order structure.

It is unlikely that single filaments will have a pretwist prior to their combination into a twisted yarn. Singles yarn being ply twisted are usually pretwisted, and hence their changes in local twist will be reflected by (1.3.10), (1.3.12) and (1.3.14).

The assumptions lying behind the model illustrated in figure 1.3.1 lead to the conclusion that the central filament in a given turn is shorter than the outer filaments. Observations of short segments of yarns show that this indeed is the case. But this means that the filament path which is short in one yarn segment is likely to be longer in the next segment along the yarn axis. For the condition of equal filament velocity input to the twisting operation requires that over a long length of yarn each filament has equal path length. Which is to say, if a filament path is relatively short at one point along the yarn, it will be compensatingly longer at another point. Of course, the local path lengths of a filament will vary if the filament migrates from helix radius to helix radius, and this is precisely what occurs in the conventional twisting process. This kind of migration will be considered briefly at a later point.

Another phenomenon can be anticipated from knowledge of the varying path lengths of filaments at a given yarn segment. And that is the contraction which takes place in the parallel assembly of filaments as they are twisted. Since in figure 1.3.1, only the center filament lies in a straight line, most of the filaments occupy longer paths than the axis of the twisted yarn. Hearle [7] suggests that the pretwisted, precontracted length of a given yarn segment is equal to the average length of the filaments in that segment, and indicates a direct procedure of calculating this average.

Viewing figure 1.3.1, it can be shown that the number of fibers dn which lie in the indicated cylindrical ring of radius r , thickness dr , and helix angle q is

$$dn = (N2\pi r) \cos q dr \quad (1.3.15)$$

where N is the fiber packing number per unit area perpendicular to the fiber axes. From eq (1.3.1) it can be shown that

$$\frac{dr}{dl} = \frac{l}{4\pi^2 r} \quad (1.3.16)$$

Now, from figure 1.3.1,

$$\cos q = h/l \quad (1.3.17)$$

whence from eqs (1.3.15-17)

$$\frac{dn}{dl} = \frac{dn}{dr} \frac{dr}{dl} = \frac{Nh}{2\pi} \quad (1.3.18)$$

Since dn/dl is constant, it follows that the variation of n with l is linear and that the average \bar{l} is simply the average of the maximum and minimum fiber path lengths in the given segment, i.e.,

$$\bar{l} = \left(\frac{h}{2} \right) (1 + \sec Q) \quad (1.3.19)$$

and, as Hearle points out, the retraction incurred during twisting is

$$R_e = (\bar{l} - h)/\bar{l} = \tan^2 \left(\frac{Q}{2} \right) \quad (1.3.20)$$

which shows the numerical relationship of table 1.3.1.

TABLE 1.3.1. Yarn contraction (after Hearle)

Outside twist angle Q	Retraction R_e
0	0
10	.008
20	.031
30	.072
40	.132
50	.217

Calculations according to eq (1.3.20) predict well the twisting behavior of continuous filament yarns, according to Hearle, who warns, however, that deviations can occur if the yarn twists irregularly or if there is

permanent straining of the outer filaments or if buckling of the center filaments occurs. (See also Kilby, 1959 [12].)

The twist multiplier, T.M., is technologically a more useful quantity for calculating the retraction, R_e . Twist multiple is the product of the yarn twist and the square root of the direct yarn count (say denier, D). For a yarn denier of D , the weight of a 9000 meter length is

$$D = \frac{\pi R_y^2}{v_y} \cdot 9000 \cdot 100 \quad (1.3.21)$$

where v_y is the specific volume of the yarn expressed in cubic cm. per gram weight. Thus, as stated above

$$\text{T.M.} = T_s \sqrt{D} \quad (1.3.22)$$

From eq (1.3.2) and eqs (1.3.21–22) one can express the relationship between twist multiplier (in the denier system) and outside helix angle of the yarn, as:

for denier system:

$$\tan Q_y = 0.00373 \sqrt{v_y} (\text{T.M.})_d \quad (1.3.23)$$

and for the tex system [7]:

$$\tan Q_y = 0.0112 \sqrt{v_y} (\text{T.M.})_x \quad (1.3.24)$$

The determination of v_y is best made by an optical method, either examining the yarn profile, or its cross section. The cross sectional method, although requiring painstaking techniques, gives more information for it permits measurement of specific volume, cross sectional shape, packing factor, and variation in these parameters.

The specific volume of the yarn is dependent on the specific volume of the fiber and on the degree of packing of the fibers. The packing fraction ψ is defined by Hearle [7] as

$$\psi = \frac{v_f}{v_y} \quad (1.3.25)$$

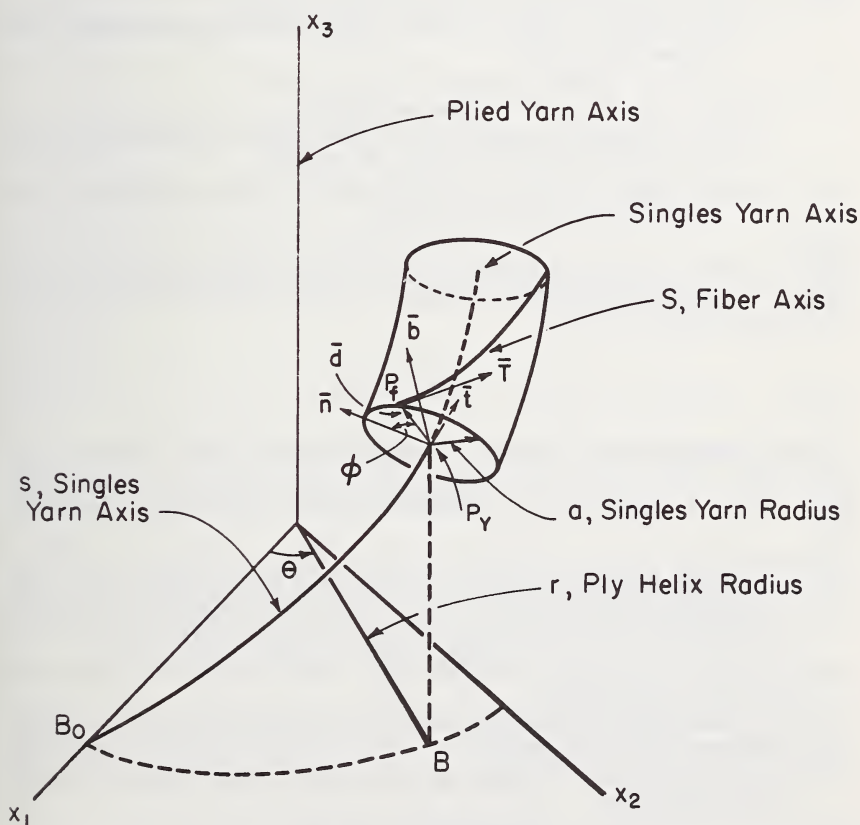
and is shown to vary from 0.3 for certain staple fiber yarns to as high as 0.9 for a highly twisted nylon filament yarn. The theoretical value for hexagonal close packing is 0.91. Specific volumes of fibers vary from 1.1 for polypropylene to 0.4 for glass, with rayon at 0.66, polyester at 0.72, and nylon at 0.88. Specific volumes of filament yarns are shown by Hearle [7] to decrease with twist, starting at levels of 2.65 for polyester and 3.12 for nylon at very low twist levels and dropping just below 1.00 at very high twists. Conversely, the packing factor of the low twist yarns in question was about 0.25 and this increased to 0.75 for the highly twisted polyester and 0.89 for the corresponding nylon.

Under extreme conditions of temperature and tension it may be expected that the hexagonal packing factor of 0.91 (for round fibers) can be exceeded where the lateral pressures between fibers caused lateral distortion of their cross sections and the yarn cross section approaches a solid polymeric section.

1.3.2.3. Geometric Models: Plied Yarns

The twisting of two or more singles yarns together to form a plied yarn is similar in many geometric aspects to the twisting of two or more filaments to form a single yarn. Instead of the fiber following the helical path B_0P in figure 1.3.2, it is now the singles yarn axis which lies along B_0P_y . And the curvature, K , and torsion, τ , calculated according to eq (1.3.10) now refer to the bending and torsion of the singles yarn.

What happens to the original fiber helix in the singles as it is bent and twisted into the plied structure can be followed in terms of differential

FIGURE 1.3.3. *Plied yarn geometry.*

geometry. In figure 1.3.3 the singles yarn length, s , is now shown lying along the helix $B_o P_y$ and the yarn section through P_y is shown to contain the principal normal, \bar{n} , and the binormal, \bar{b} . The helix tangent \bar{t} lies perpendicular to the singles yarn section at P_y . The position vector \bar{x} connects the arbitrary point P_y of the helix with the coordinate system center. A point P_f marks where the fiber "S" lying in the yarn "s", intersects the yarn cross section containing to point P_y on the singles yarn axis.

The Frenet relations necessary for further analysis are:

$$\frac{d\bar{y}}{dS} = \bar{T}, \quad (1.3.26)$$

$$\frac{d\bar{T}}{dS} = K\bar{N} \quad (1.3.27)$$

where \bar{y} = the position vector of point P_f (not shown),

S = the distance along the fiber path, which twists around the singles yarn helix,

\bar{T} = the unit tangent vector to the fiber at P_f ,

K = the curvature of the fiber at point P_f ,

\bar{N} = the principal normal of the fiber path at P_f (not shown),

\bar{d} = the vector joining the points P_y and P_f ,

ϕ = the angle between \bar{n} and \bar{d} and it locates any given fiber in the yarn cross section at P_y .

Now ϕ is taken to be proportional to θ , for as the yarn turns around the ply axis by θ , the fibers rotate around the singles axis by ϕ . The constant of proportionality is λ , i.e.,

$$\lambda = \frac{\phi}{\theta} \quad (1.3.28)$$

The objective of the following summary analysis after Schwarz [13] and Treloar [17] is to provide expressions for specific parameters to define the interaction between filament geometry and singles geometry, i.e.,

- (1) the angle, α , between the filament axis and the singles yarn axis at any point, i.e., between \bar{t} and \bar{T} . This is the local helix angle of the fiber as it lies in the singles yarn (see eq (1.3.44) below);
- (2) the length of a single turn of fiber around the plied singles yarn (see eq (1.3.47) below);
- (3) the contraction of the plied yarn as it is twisted from the singles (see eqs (1.372-76) below);
- (4) the curvature K of the fiber as it lies in the plied singles yarn (see eq (1.3.92) below).

The value of these expressions will become obvious in the sections

which follow and which treat the subject of the mechanics of twisted structures.

Now, back to the Frenet equations for the tangent vectors \bar{t} and \bar{T} , we can write

$$\bar{t} = \frac{d\bar{x}}{ds} = \frac{d\bar{x}}{d\theta} \frac{d\theta}{ds}, \quad (1.3.29)$$

$$\bar{T} = \frac{d\bar{y}}{dS} = \frac{d\bar{y}}{d\theta} \frac{d\theta}{dS}. \quad (1.3.30)$$

In this form lies the suggestion that if \bar{x} and \bar{y} can be expressed as functions of θ , they can be differentiated and simply multiplied by $d\theta/ds$ and $d\theta/dS$ respectively to provide expressions for \bar{t} and \bar{T} . Then from

$$\bar{t} \cdot \bar{T} = \cos \alpha \quad (1.3.31)$$

we have α .

Now \bar{x} is expressed as a function of θ in eqs (1.3.3-5). Similar treatment of \bar{y} is a bit more complicated for

$$\bar{y} = \bar{x} + \bar{d} \quad (1.3.32)$$

and, assuming very small fiber diameters,

$$\bar{d} = a \cos \phi \cdot \bar{n} + a \sin \phi \cdot \bar{b} \quad (1.3.33)$$

$$\bar{n} = -\cos \theta \cdot \bar{x}_1 - \sin \theta \cdot \bar{x}_2 \quad (1.3.34)$$

$$\bar{b} = \sin \theta \cos Q \cdot \bar{x}_1 - \cos \theta \cos Q \cdot \bar{x}_2 + \sin Q \cdot \bar{x}_3 \quad (1.3.35)$$

whence

$$y_1 = r \cos \theta - a \cos \theta \cos \lambda \theta + a \cos Q \sin \theta \sin \lambda \theta \quad (1.3.36)$$

$$y_2 = r \sin \theta - a \sin \theta \cos \lambda \theta - a \cos Q \cos \theta \sin \lambda \theta \quad (1.3.37)$$

$$y_3 = r \theta \cot Q + a \sin Q \sin \lambda \theta \quad (1.3.38)$$

The x_1 , x_2 , and x_3 coordinates of \bar{x} and the y_1 , y_2 , y_3 coordinates of \bar{y} are then differentiated with respect to θ and multiplied by $d\theta/ds$ and $d\theta/dS$ respectively. Now the value of $d\theta/ds$ is obtained from eq (1.3.6):

$$\frac{d\theta}{ds} = \frac{\sin Q}{r} \quad (1.3.39)$$

however, the value $d\theta/dS$ must be determined from the differential geometric expression

$$\frac{dS}{d\theta} = \sqrt{\sum_{i=1}^{i=3} \frac{dy_i}{d\theta} \cdot \frac{dy_i}{d\theta}} \quad (1.3.40)$$

The θ derivatives of eqs (1.3.36–38) supply the terms under the square root and lead to the expression

$$\frac{dS}{d\theta} = [r^2 \operatorname{cosec}^2 Q + a^2 \lambda^2 + a^2 \cos^2 \lambda \theta + a^2 \cos^2 Q \sin^2 \lambda \theta - 2ra \cos \lambda \theta + 2a^2 \lambda \cos Q]^{1/2}. \quad (1.3.41)$$

Now the x_1 , x_2 and x_3 components of \bar{T} are:

$$\frac{dy_1}{d\theta} [\quad]^{1/2}; \frac{dy_2}{d\theta} [\quad]^{1/2}; \frac{dy_3}{d\theta} [\quad]^{1/2} \quad (1.3.42)$$

and

$$\cos \alpha = \bar{t} \cdot \bar{T} = [t_1 \cdot T_1 + t_2 \cdot T_2 + t_3 \cdot T_3] \quad (1.3.43)$$

whence from eqs (1.3.3–5), eq (1.3.29), eqs (1.3.36–39), and eqs (1.3.41–43) we can derive after Chow and Schwarz [13]

$$\tan \alpha = \frac{a\lambda + a \cos Q}{r \operatorname{cosec} Q - a \sin Q \cos \lambda \theta} \quad (1.3.44a)$$

which leads to determination of α , the local helix angle of the fiber as it lies in the singles yarn as it lies in the ply yarn. On the other hand, the angle between the local filament axis and the ply yarn axis, β , is $Q + \alpha$ and there is merit in developing an expression for the angle, β_0 , between the outermost filament of the singles yarn and the ply yarn axis, in terms of other ply yarn parameters. This was done by Treloar in a relationship consistent with eq (1.3.44a):

$$\tan \beta_0 = \frac{r + a(1 + \lambda \cos Q)}{r \cot Q - a\lambda \sin \alpha} \quad (1.3.44b)$$

or, in other terms,

$$\tan \beta_0 = \frac{(1 + a/r) \tan Q + a\tau_s(C_1)}{1 - a\tau_s(C_1) \tan Q} \quad (1.3.44c)$$

where C_1 is the ratio of the singles yarn length per unit filament length (prior to plying) to the ply yarn length per unit filament length (after plying). τ_s is the twist (expressed in radians) of the singles yarn prior to plying. Discussion of C_1 follows later, after eq (1.3.71) below.

The general view of the state of torsional balance in a plied yarn (i.e. dimensional stability with respect to untwisting where all external restraints are removed) has in the past been correlated with the occurrence of parallel alignment of the outside filament of the singles yarn with the ply yarn axis, i.e., when β_0 equals zero. Schwarz [13] and Treloar [17] have both treated this special case. But Freeston et al. [14–15] emphasize that recovery from torsional strains is an important factor to be included in consideration of balance in low-singles low-ply twist yarns. While for high-singles high-ply twist yarns bending and

bending recovery, as well as friction, become important variables in consideration of ply yarn balance.

By integrating eq (1.3.41) from θ values of 0 to 2π , we obtain the fiber length as it lies in the singles, which, in turn, lies in the ply, for one turn of ply twist. From (28) we note that ϕ will have rotated through $\lambda 2\pi$ while θ rotates 2π . Thus the fiber path length for a single turn of ϕ will be $1/\lambda$ that for a single turn of θ .

The integration of eq (1.3.41) was shown by Chow [16] for $\theta = 0$ to $\theta = 2\pi$, to be:

$$S_\theta = 2\pi \operatorname{cosec} Q [r^2 + a^2 \sin^2 Q (\lambda + \cos Q)^2]^{1/2} \quad (1.3.45)$$

when the following condition is met, i.e.

$$\sin^2 Q + \left(\frac{r}{a}\right) < \sqrt{2 \left(\frac{r}{a}\right)^2 + (\lambda + \cos Q)^2 \sin^2 Q} \quad (1.3.46)$$

and thus for $\phi = 0$ to $\phi = 2\pi$, the length of a single turn of fiber around the plied singles yarn is:

$$S_\phi = \frac{2\pi}{\lambda} \operatorname{cosec} Q [r^2 + a^2 \sin^2 Q (\lambda + \cos Q)^2]^{1/2} \quad (1.3.47)$$

which is in agreement with Treloar's [17] eq (20).

Still another useful expression given by Chow is the length of fiber (in a singles lying in a plied yarn) per unit length of the plied axis. Taking T_p as the turns of ply twist per unit length of ply axis, the fiber length is simply

$$S_p = 2\pi T_p \operatorname{cosec} Q [r^2 + a^2 \sin^2 Q (\lambda + \cos Q)^2]^{1/2}. \quad (1.3.48)$$

From these expressions (1.3.45 and 1.3.48) Chow [16] determines the "crimp" of the fiber as it lies in the higher order structure—first, the "crimp" of the fiber related to the singles yarn axis C_{fs} ; second, the fiber "crimp" related to the ply yarn axis C_{fp} :

$$C_{fs} = \frac{S_\theta - 2\pi r \operatorname{cosec} Q}{2\pi r \operatorname{cosec} Q}$$

$$C_{fs} = \frac{1}{r} \{ [r^2 + a^2 \sin^2 Q (\lambda + \cos Q)^2]^{1/2} - r \} \quad (1.3.49)$$

and then

$$C_{fp} = \frac{S_p - 1}{1}$$

$$C_{fp} = 2\pi T_p \operatorname{cosec} Q [r^2 + a^2 \sin^2 Q (\lambda + \cos Q)^2]^{1/2} - 1 \quad (1.3.50)$$

as later reported by Schwartz [13, 18].

Using eq (1.3.2), i.e., $\tan Q = 2\pi r T_p$, the form of eq (1.3.50) can be so altered as to show

$$\sec Q (C_{fs} + 1) = C_{fp} + 1. \quad (1.3.51)$$

As Chow suggests, eqs (1.3.49–50) can be used in the design of plied yarns, cords, and cables, for they indicate the required length of the primary components per unit length of structures. Equation (1.3.49), for example, indicates how much filament is needed per unit length of singles yarn (as it lies in the plied yarn). Equation (1.3.50) indicates how much filament is needed per unit length of the plied yarn. And it follows that the crimp of the singles as it lies in the ply is

$$C_{sp} = \sec Q - 1 \quad (1.3.52)$$

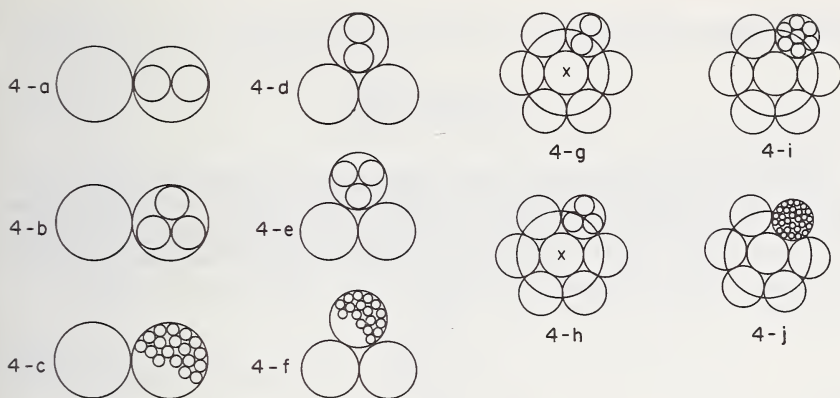
As Schwarz [18] points out, these equations for crimp reflect directly the extension which will take place upon untwisting of the various structures. And the contraction, or retraction, expected upon twisting is

$$R_e = \frac{C}{C + 1} \quad (1.3.53)$$

where C may be C_{fs} , C_{fp} or C_{sp} . Clearly, insertion of C_{fp} in eq (1.3.53) is a measure of contraction of filament length to the final ply length and of C_{sp} is a measure of contraction of singles length to the final ply length. The use of C_{fs} in eq (1.3.53) has less technological significance than does C_{fp} or C_{sp} .

The principal drawback of these determinations of contraction and extension is their dependence on a , the radius of the secondary helix. The quantity a signifies, in terms of our technological example, the radius of the singles yarn as it lies in the ply. For the case of a singles yarn whose fiber diameter is small compared to the singles yarn diameter, the quantity a approximates the radius of the secondary helical path of the fibers lying in the outer ring of the singles yarn cross section, as shown in figure 1.3.3.

Clearly, a fiber lying in the singles yarn of figure 1.3.3 at a radius of $(1/2a)$ or $(1/3a)$ will have a different crimp and retraction calculated according to eq (1.3.50) or eqs (1.3.52–53) than the fiber at the radius a . It is only when a single value of a is used that the indicated equation (1.3.53) for retraction can be used in a technological sense, and figure 1.3.4 illustrates such cases, particularly figures 1.3.4*a, b, d, e, g, h*. With the exception of the central singles yarns of figures 1.3.4*g, h* (marked x), all the other singles yarn of these figures exhibit the same helix radius, r , and within these singles, the filaments all exhibit the same secondary helix angle α . The same is true for figure 1.3.4*i*, except for the core singles and the core filament in the singles. In contrast, the secondary helical radii a of figures 1.3.4*c, f, j* all vary from fiber ring to fiber ring, within each singles yarn.

FIGURE 1.3.4. *Plied yarns constructions.*

In short, direct application of eq (1.3.53) can be made in the cases of figures 1.3.4a, b, d, e, and possibly to cases 1.3.4g, h, i, but under no circumstances to 1.3.4c, f, j. Unfortunately, cases 1.3.4c, and f are of great technological importance both in apparel textiles and in industrial textiles, such as tire cords; and it is necessary to apply the path averaging techniques for calculation of retraction in multifilament singles yarns. This procedure was reported by Treloar [17], who assumed that the number of filaments crossing unit area normal to the yarn (singles) axis, m , is constant over the cross section. Treloar also showed that the results which follow from this assumption are similar to those following from the assumption of constant packing density of the filaments in the section normal to the *filament axes* as shown in eqs (1.3.15–20) above.

Treloar started with the component of length of the filament along the singles yarn axis (first considered to be straight) and showed that for a unit length of filament at a radius r , the axial component l_r is:

$$l_r = [1 + (2\pi r T_s)^2]^{-1/2}. \quad (1.3.54)$$

It follows that the total axial component of the unit length filaments in the cylindric shell of thickness dr and radius r , is:

$$2\pi m r [1 + (2\pi r T_s)^2]^{-1/2} dr. \quad (1.3.55)$$

Then the mean axial length of the twisted singles yarn, \bar{l}_a , formed from unit length of the (straight, untwisted) filaments is shown to be:

$$\bar{l}_a = \left(\frac{2}{R_y^2 (2\pi T_s)^2} \right) [(1 + R_y^2 (2\pi T_s)^2)^{1/2} - 1] \quad (1.3.56)$$

where R_y is the singles yarn radius.

The singles yarn retraction R_e is, by definition,

$$R_e = 1 - \bar{l}_a \quad (1.3.57)$$

and it can be shown that

$$R_e = \tan^2 \left(\frac{Q}{2} \right) \quad (1.3.20)$$

as stated above.

Treloar determines the ply yarn contraction by calculating the mean length of the singles axis per unit filament length, then resolves this quantity along the ply axis through multiplication by $\cos Q_p$ (Q_p is the ply helix angle). But to calculate the singles yarn axis length, it is useful to obtain a more tractable expression for λ . Thus from eq (1.3.28)

$$\lambda = \frac{d\phi}{d\theta} \quad (1.3.58)$$

and

$$\frac{d\phi}{d\theta} = \frac{d\phi}{ds} \cdot \frac{ds}{d\phi} \quad (1.3.59)$$

From figure 1.3.3, it follows that

$$\lambda = \frac{d\phi}{ds} \cdot r \operatorname{cosec} q \quad (1.3.60)$$

or

$$\phi = \frac{\lambda s}{r \operatorname{cosec} q} \quad (1.3.61)$$

Now going back to eq (1.3.47) and integrating from $\phi = 0$ to $\phi \gg 2\pi$ we have

$$S_\phi = \frac{\phi}{\lambda} \operatorname{cosec} Q [r^2 + a_1^2 \sin^2 q (\lambda + \cos Q)^2]^{1/2} \quad (1.3.62)$$

$$= \frac{s}{r} [r^2 + a_1^2 \sin^2 q (\lambda + \cos Q)^2]^{1/2}$$

where a_1 is the radius of the secondary helix. Now for the length of singles yarn axis (as it lies in the ply) per unit of filament length, l_r , one can show

$$l_{rp} = \frac{s}{S_\phi} = \left[1 + a_1^2 \left(\frac{\lambda + \cos Q}{r \operatorname{cosec} Q} \right)^2 \right]^{-1/2} \quad (1.3.63)$$

It turns out that the quantity in the parentheses has special meaning as will be seen shortly. The total twist of the singles yarn as it lies in the ply yarn is:

$$T'_{fsp} = T'_s + T'_{sp} \quad (1.3.64)$$

where T'_{fsp} is the twist per unit length along the singles yarn axis as it lies in the ply yarn. T'_s is the twist of the singles prior to plying (calculated per unit length along the singles axis corrected for the change in singles axis length which occurs during plying and T'_p is the twist of the

singles yarn axis around the ply axis per unit length along the singles yarn axis as it lies in the ply. Thus,

$$2\pi T'_{fsp} = \frac{d\phi}{ds} + \tau_{sp} \quad (1.3.65)$$

where τ_{sp} is the torsion of the singles axis as it lies in the primary helix. Stated another way, the total twist (in radians) τ_{fsp} of the filament constituting the secondary helix in figure 1.3.3 is

$$\tau_{fsp} = \frac{d\phi}{ds} + \tau_{sp} \quad (1.3.66)$$

Since from eqs (1.3.61) and (1.3.10)

$$\begin{aligned} \frac{d\phi}{ds} &= \frac{\lambda}{r \operatorname{cosec} q} \quad \text{and} \quad \tau_{sp} = \frac{\sin q \cos q}{r} \\ \tau_{fsp} &= \frac{\lambda}{r \operatorname{cosec} q} + \frac{\sin q \cos q}{r} \\ \tau_{fsp} &= \frac{\lambda + \cos q}{r \operatorname{cosec} q} = 2\pi T'_{fsp} \end{aligned} \quad (1.3.67)$$

where eq (1.3.67) is the quantity in the parentheses of eq (1.3.63). In other words,

$$l_{rp} = [1 + a_1^2 (2\pi T'_{fsp})^2]^{-1/2} \quad (1.2.68)$$

an expression similar to eq (1.3.54), which following the sequence of eqs (1.3.55–56) provides an expression for the mean singles yarn axial length (as it lies in the ply yarn) formed by unit length of the (straight, untwisted filaments)

$$\bar{l}_{ap} = \frac{2}{(2\pi a T'_{fsp})^2} [(1 + (2\pi a T'_{fsp})^2)^{-1/2} - 1] \quad (1.3.69)$$

where a is the radius of the singles yarn as it lies in the ply yarn.

Now Treloar shows that from eq (1.3.69) one may deduce that

$$2\pi a T'_{fsp} = \frac{2(1 - \bar{l}_{ap})^{1/2}}{\bar{l}_{ap}} = a\tau_{fsp} \quad (1.3.70)$$

Now eq (1.3.64) can be rewritten as

$$\tau_{fsp} = 2\pi T_s \left[\frac{\bar{l}_a}{\bar{l}_{ap}} \right] + \tau_{sp} = \tau_s \left[\frac{\bar{l}_a}{\bar{l}_{ap}} \right] + \tau_{sp} \quad (1.3.71)$$

where \bar{l}_a/\bar{l}_{ap} is the correction factor applied to the original singles twist

to account for the additional contraction or extension in the singles axial length due to plying. Note that this correction factor appears in eq (1.3.44c) as the term C_1 . T_s is the singles yarn twist based along its straight (preplied) axis and τ_s is T_s expressed in radians rather than turns. Now in eq (1.3.56) \bar{l}_a is seen as a function of τ_s , i.e., $F(a, \tau_s)$, using a in lieu of R_s . This leads to

$$\frac{2(1 - \bar{l}_{ap})^{1/2}}{\bar{l}_{ap}} = \frac{a\tau_s F(a, \tau_s)}{\bar{l}_{ap}} + a\tau_{sp} \quad (1.3.72)$$

which can be solved for \bar{l}_{ap} , as reported by Riding [19].

$$\bar{l}_{ap} = \{-(2 + cu) + 2(1 + cu + u^2)^{1/2}\}/u^2 \quad (1.3.73)$$

where

$$c = a\tau_s F(a, \tau_s) \quad (1.3.74)$$

see eq (1.3.56) and

$$u = \frac{a}{r} \sin Q \cos Q.$$

Using eq (1.3.73) one now determines the average length, L , of the ply yarn axis per unit length of filament.

$$L = \bar{l}_{ap} \cos Q \quad (1.3.75)$$

and by definition the retraction of the ply yarn is

$$R_{ep} = 1 - L \quad (1.3.76)$$

Treloar treated the case of the two ply yarn where $r = a$ presenting a somewhat simplified reduction of eq (1.3.73).

Stansfield [20] also developed expressions for singles yarn contraction upon twisting, for the plied yarn contraction in twisting, and for the plied yarn helix angle developed in plying. However, he used a geometrical model different than that of Chow, Schwarz and Treloar.

The earlier models were based on the concept of a singles yarn whose axis followed a right circular helix. This helix is generated by a radial vector, r , advancing along the straight ply yarn axis and rotating perpendicular to it. A secondary helix comprising the individual filament of the singles yarn, twists around the singles yarn axis as it lies in the ply and its path is generated by a radial vector, a , advancing along the singles yarn axis and rotating perpendicular to it. Thus, the singles yarn section shown in figure 1.3.3 at P_y is perpendicular to the singles axis.

Stansfield's model, figure 1.3.5, differs from the above in that the secondary vector rotates in a plane *perpendicular* to the *ply yarn axis*. And the path of the filament is described as an epi-helix with coordinates

differing from those of eqs (1.3.36–38) as follows:

$$y_1 = r \cos \theta - a \cos \phi \cos \theta + a \sin \phi \sin \theta \quad (1.3.77)$$

$$y_2 = r \sin \theta - a \cos \phi \sin \theta - a \sin \phi \cos \theta \quad (1.3.78)$$

$$y_3 = r \theta \cot Q \quad (1.3.79)$$

Note that the r and a and the sign of the angle ϕ in Treloar's and Stansfield's expressions are altered to agree with the nomenclature of models of Chow as in figure 1.3.3. And from eqs (1.3.77–79), Riding [19] derived the following expression for the singles yarn axis as it lies in the plied yarn,

$$\bar{l}_{ap} = [-(2 + cw) + 2(1 + cw + w^2)^{1/2}]w^2 \quad (1.3.80)$$

where $w = a/r \sin Q$. Riding [19] points out that eq (1.3.80) is equivalent to eq (1.3.73), except that $\sin Q$ is substituted for $\sin Q \cos Q$. And thus

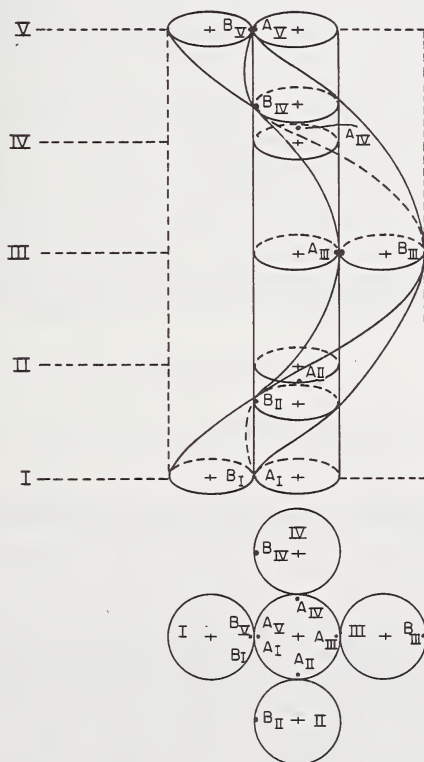


FIGURE 1.3.5. Geometrical model of Stansfield for a plied yarn construction.

at low ply twists, the two expressions give numerically close predictions.

Gracie [21] objects to the treatment of yarn contraction upon twisting according to the method of Treloar. For as he points out, the selection of a unit length of a filament at a given radius from the yarn center and the averaging of its projected length along the yarn axis with the projected lengths of other unit filament lengths at other radii is based on limited model conditions. It "implies that in a length L_o of untwisted yarn, the filaments acquire on twisting a range of axial lengths from L_o (at the center) downwards, i.e., the yarn acquires a profiled end or ends. This can then be related to the case of a real yarn by imagining filament migration as a practical mechanism which over a fairly long sample, equalizes the axial lengths, but is of sufficient long period that it may be neglected in retraction and volume considerations." Gracie feels this approach is in error "because it uniquely fixes the retraction ratio without including the condition that the volume of the material is the same before and after twisting."

Gracie [21] further points out that the derivation of eq (1.3.19) by Hearle, is based on the constancy of N in eq (1.3.15), i.e., the constancy across the yarn section of the number of fibers per unit area perpendicular to the *fiber axes*. This, in turn, implies a constancy of packing factor ϕ across the yarn section and therefore a constancy of yarn volume before and after twisting. In contrast, Treloar's assumption of a constant number of fibers per unit area perpendicular to the *yarn axis*, over the yarn section, implies a low packing factor at the yarn center and a high packing factor at the outside of the yarn. (It should be noted that if packing factors are not constant across the twisted yarn section, the higher factors would be intuitively expected at the yarn center and lower packing at the periphery.)

Employing the Treloar assumption regarding packing factor, Gracie shows that in a unit length of twisted yarn, the number of filaments dM in an arbitrary annulus (where M is the total number of filaments in the yarn) is,

$$dM = 2\pi r dr / \pi R_y^2 \quad (1.3.81)$$

and the total length of the filaments in the unit length of singles (twisted) yarn is,

$$\int_0^{\sqrt{1 + (2\pi T_s r)^2}} dM = \frac{2M}{3(2\pi T_s)^2 R_y^2} \{ [1 + (2\pi T_s R_y)^2]^{3/2} - 1 \} \quad (1.3.82)$$

The average filament length, \bar{L} , is then the expression (1.3.82) divided by M , which differs somewhat from the expression for \bar{l}_a of eq (1.3.56) derived on the assumption of constant packing factor across the yarn and before and after twisting. Gracie points out that values of \bar{l}_a based on these two expressions (1.3.82)/ M and (1.3.56) differ very little at low twist levels, e.g. by 0.98 percent at a twist of $2\pi R_y T_s = 1.0$ and 3.7 percent at $2\pi R_y T_s = 3.0$.

However, he points out, there is a much larger error in twisted radius R_y because the packing factor ϕ is highest at the outside with Treloar's assumption. At most, $\phi = 0.90$ at the outside, hence for $2\pi R_y T_s = 1.0$, ϕ at the center is 29.3 percent lower than at the outside and the twisted radius is 17.4 percent higher than for constant packing factor case (as per Hearle). Gracie gives the example of low levels of twist as $(2\pi R_y T_s)^2 = 1.0, 3.0, 8.0$, which actually represent the cases of outside helix angles $Q > 45^\circ$, hardly a low twist level. But he concludes that eq (1.3.82) is more awkward to deal with than eq (1.3.56) and therefore utilizes eq (1.3.56) in his further analysis, leading to the following expressions of value in yarn structural mechanics. First, the retraction ratio follows from substitution of $T_s = LT_b$ in eq (1.3.56),

$$\frac{1}{\bar{L}} = [1 - (T_b 2\pi R_{yt})^2]/4 \quad (1.3.83)$$

where \bar{L} is the average length of filament in a unit length of a singles twisted yarn. It corresponds to \bar{l}/h and can be easily related to retraction R_e of eq (1.3.20). T_b is the basic twist, defined by Gracie as the twist per unit of *untwisted* length. R_{yt} is the radius of the twisted yarn as contrasted to R_{yu} , the radius of the yarn before twisting.

Substituting in eq (1.3.56) the requirement for constancy of yarn volume during twisting

$$R_{yt}^2 = L P_{yu}^2 \quad (1.3.84)$$

$$L = 1 + (2\pi T_b R_{yu})^2/4 \quad (1.3.85)$$

and then substituting in eq (1.3.83) he writes:

$$L = \frac{2}{(2\pi T_b R_{yu})^2} \{1 \pm [1 - (2\pi T_b R_{yu})^2]^{1/2}\} \quad (1.3.86)$$

which can be rewritten as,

$$\frac{1}{L} = \frac{1}{2} \{1 \pm \sqrt{1 - (2\pi T_b R_{yu})^2}\} \quad (1.3.87)$$

Now from eq (1.3.83) Gracie points out that $2\pi T_b$ cannot exceed $2/R_{yt}$ and from eq (1.3.86) $2\pi T_b$ cannot exceed $1/R_{yt}$. Stated somewhat differently, $1/T_b$ must exceed $(2\pi R_{yt})/2$ and also it must exceed $(2\pi R_{yu})$, i.e., the average length filament in one turn of the twisted yarn must exceed half the circumference of the twisted yarn. It must also exceed the circumference of the untwisted yarn. If T_b is increased beyond these limits, then snarling of the singles yarn is induced. Snarling due to lateral jamming of the singles in plied yarn is also considered by Gracie, who shows that for an m -ply yarn, the maximum ply twist N_m must be

$$aN_m \leq \frac{1}{2} \left[\frac{1}{m^2} - \frac{a^2}{\pi^2 r^2} \right]^{1/2} \quad (1.3.88)$$

where a is the radius of the singles yarn and r is the radius of the helix formed by the singles yarn as it lies in the ply yarn.

For practical purposes we note eq (1.3.85) as the expression useful for calculating retraction which occurs during twisting when the singles twist (nominal) and the original (pretwisted) yarn radius is known, while eq (1.3.87) serves for prediction of retraction if the basic twist and the original (untwisted) yarn radius are known. Finally, one may predict the yarn radial enlargement from the requirement of constancy of yarn volume during twisting, i.e., from eq (1.3.84).

$$\left(\frac{R_{yt}}{R_{yu}}\right)^2 = [1 + \pi^2 R_{yu} T_s] \quad (1.3.89)$$

which may also be derived from Platt's [24] eq (3) and shown equivalent to his eq (7).

The fourth objective in the above summary analysis of cord geometry was to provide an expression for the curvature K of the fiber as it lies in the plied singles yarn. To derive K one may start with eq (1.3.27), then differentiate the components of \bar{T} in eq (1.3.42) with respect to θ and multiply by the $d\theta/dS$ of eq (1.3.41). The dot product of the results should give the expression for K^2 . But this expression turns out to be unmanageable and an approximate expression for K can be obtained by considering fiber curvature in the singles yarn as this yarn is bent in an imagined plane to a curvature corresponding to $\sin^2 Q_p/r_h$ where Q_p is the helix angle and r_h the helix radius which the singles yarn axis follows in the actual plied yarn.

For the case of bending a singles yarn in a plane, Backer [80] has shown that eq (1.3.41) reduces to

$$\frac{dS}{d\theta} = [(a \cos \lambda\theta - r)^2 + a^2 \lambda^2]^{1/2} \quad (1.3.90)$$

where r is the radius of curvature into which the yarn is bent, and eq (1.3.27) becomes

$$K\bar{N} = \frac{d\bar{T}}{d\theta} \frac{d\theta}{dS} = \frac{d}{d\theta} \left[\frac{d\bar{y}}{d\theta} \frac{1}{\sqrt{u}} \right] \frac{d\theta}{dS} \quad (1.3.91)$$

where \bar{N} is the principal normal of the fiber path and u is the quantity in brackets in eq (1.3.90). By taking the product $K\bar{N} \cdot K\bar{N}$ one obtains with $g = r/a$:

$$K = \sqrt{\frac{(\cos \lambda\theta - g)^2 + \lambda^4 + 2\lambda^2 \cos \theta (\cos \lambda\theta - g) + 4\lambda^2 \sin^2 \theta - \lambda^2 \sin^2 \lambda\theta (\cos \theta - g)^2}{a[(\cos \lambda\theta - g)^2 + \lambda^2]}} \quad (1.3.92)$$

which simplifies greatly for the inside, outside, and middle filaments, to:

$\phi = 0$ (inside)

$$K = \frac{[(1-g) + \lambda^2]}{a[(1-g)^2 + \lambda^2]} \quad (1.3.93)$$

$\phi = \pi$ (outside)

$$K = \frac{[(1+g) + \lambda^2]}{a[(1+g)^2 + \lambda^2]} \quad (1.3.94)$$

and

$\phi = \frac{\pi}{2}$ (middle)

$$K = \frac{\sqrt{\frac{g^4}{g^2 + \lambda^2} + \lambda^4 + 4\lambda^2}}{a(g^2 + \lambda^2)} \quad (1.3.95)$$

Now the radius of curvature r in eq (1.3.90) is set equal to $r_h/\sin^2 Q_p$, the curvature realized in the ply helix, and g in eqs (1.3.93–95) becomes $r_h/a \sin^2 Q_p$, where a is the singles yarn axis. In the two ply yarn $r_h = a$ (with no flattening) and g then becomes $1/\sin^2 Q_p$. On the other hand, λ becomes $2\pi r_h T'_{fsp}/\sin Q_p$ where T'_{fsp} is the twist per unit length of the singles yarn axis as it lies in the ply yarn (see eq 1.3.64).

1.3.2.4. Experimental Observations of Plied Yarn Structures

In the decade of the 50's a fair number of papers appeared in the textile literature on the subject of plied yarn structures and properties. Many of these papers reported experimental results to establish the validity of various geometrical relationships, such as those discussed above. In general, it was argued that the theoretical relationships which provided predictions of geometric parameters closest to those observed in experiment were the most valid. And it was suggested that close agreement between theory and experiment followed from selection of the most realistic model and from suitable analytical logic.

As it turned out, the early experimental results reported contained little information concerning experimental methods of studying yarn geometry. Later papers included such experimental details, and showed that test data tended to vary with conditions of experiment as much as did predictions based on analysis rooted in different geometrical models. It was not surprising therefore to note the conclusions of several writers that when experimental factors closely match the model conditions which form the basis of a given analysis, then experiment and theory are generally in close agreement. And wide variations between theory and experiment follow from observed experimental violations of model assumptions.

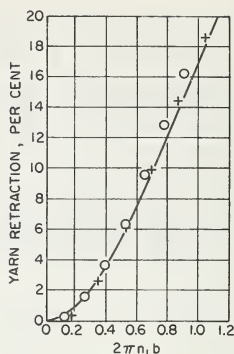


FIGURE 1.3.6. Yarn retraction, calculated from eqs (1.3.56) and (1.3.57) after Treloar [17].
 $R_y T_s = n, b$.

○ = Courtauld's data
 + = Dunlop data

Singles Yarn Retraction

The retraction, R_e , was, in a derivation by Treloar, shown to equal $(1 - \bar{l}_a)$ in eq (1.3.57), where

$$\bar{l}_a = \frac{2}{x^2} [(1 + x^2)^{1/2} - 1] \quad (1.3.56)$$

where x is $2\pi R_y T_s$. And Treloar reported singles yarn contraction data furnished by Courtaulds and by Dunlop to check the prediction of eq (1.3.56) and eq (1.3.57) as shown in figure 1.3.6. In plotting the experimental results it was noted that the yarn radius R_y varied somewhat with T_s and so an average value of R_y was used for graphing. The theoretical curve had no adjustable parameter, and so the agreement was considered very good. On the other hand, Hearle shows some variation from fiber to fiber contraction ratios $C_y = \bar{l}/h$, where by dividing eq (1.3.19) by h we have:

$$C_y = \frac{\bar{l}}{h} = \frac{(1 + \sec Q)}{2} \quad (1.3.19)$$

Figure 1.3.7 shows the experimental values of contraction ratio, C_y , for viscose, Tenasco nylon and acetate plotted against twist angle, Q_y . The theoretical curve, $\frac{1}{2} (\sec Q_y + 1)$ vs. Q_y falls amidst the experimental data, with the high denier Tenasco yarn showing an excessively high contraction ratio and two of the acetate yarns significantly low values compared to eq (1.3.19). The remaining yarns contracted at levels close to those predicted by eq (1.3.19).

Tattersall [22] reports the results of twisting contraction tests run under "static" twisting conditions where the entire yarn segment is twisted at once by one revolving clamp, while the other clamp is free to slide longitudinally, but not to rotate. He shows that the agreement

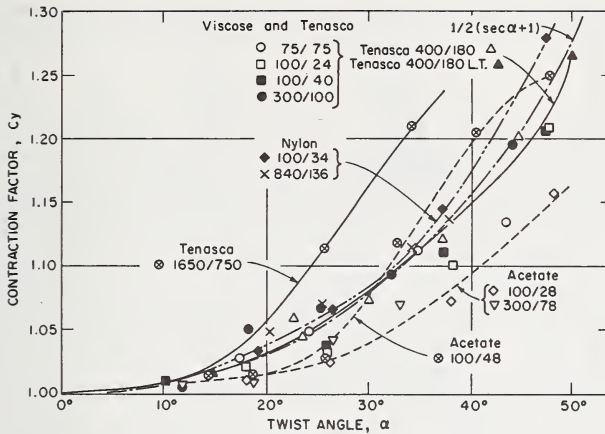


FIGURE 1.3.7. Comparison of contraction factors, Hearle et al. [7].

between experimentally measured retraction R_e and predicted values is not as good as for the Dunlop and Courtaulds data reported by Treloar, but shows that the test data can be made to fit the theoretical curve by multiplying the radius by a suitable factor, or by selecting a proper tension at which to conduct the tests (see fig. 1.3.8a). He also noted that surface treatments such as prewashing the yarn in petroleum ether or applying a spinning oil did not influence the results. Finally, he pointed to the occurrence of kinks at intervals of 1 cm. which became progressively worse as the twist was increased.

Tattersall [22] recognized the difference in conditions for "static" twisting a yarn and simultaneously measuring its contraction at progressively higher twists as against dynamically twisting a yarn in a commercial upwister to a given twist level, then untwisting it in the

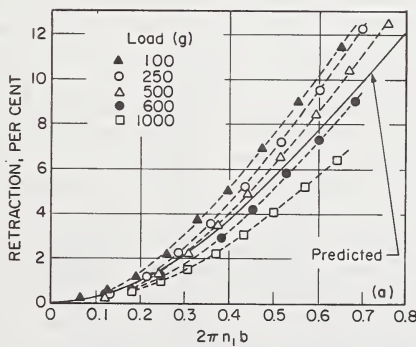


FIGURE 1.3.8a. Retraction as function of twist in 1650 denier Tenasco yarn under various tensions, after Tattersall [22]. $R_y T_s = h, b$.

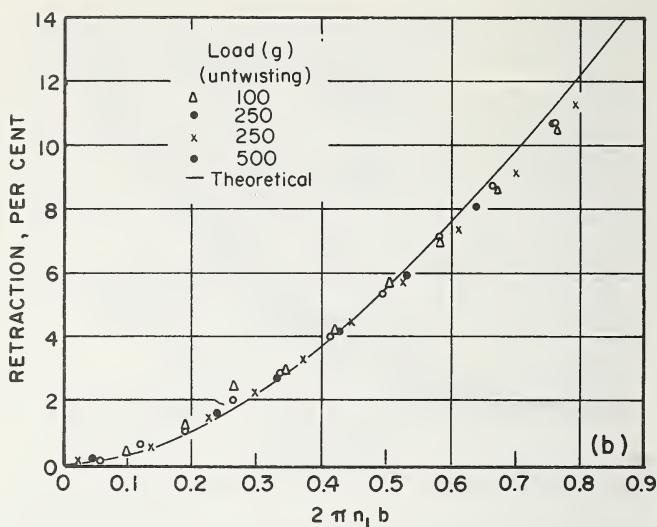


FIGURE 1.3.8b. Retraction determined from untwisting of up-twisted 1650 denier Tenasco yarn, after Tattersall [22].

laboratory tester while measuring its elongation at progressively higher levels of untwist. He reasoned that in the commercial twister, the redistribution of filaments required by the theory could occur, in contrast to the restrictions of the static twisting method. In his untwisting vs retraction measurements on a commercially twisted 1650 denier Tenasco yarn, Tattersall showed excellent agreement with theory (according to eqs (1.3.56–57)) at several levels of untwisting tension (see fig. 1.3.8b).

Riding [23] studied further the variables discussed by Tattersall, and used the same instrument to twist, then untwist the same yarn at various tension levels, while measuring twist retraction. He found that the twist-untwist process was perfectly reversible at low tensions, but at high tensions, permanent straining of the outer filaments occurred as evidenced in microscopic examination of the yarn and in the dropping of the untwist retractions to negative values, during the final stages of untwisting. Riding then designed a laboratory twister which was comprised of a rotating head which continuously fed new portions of untwisted yarn into the twist zone and a rotationally fixed head which fed the twisted yarn to a down stream windup. He then ran a series of twist-retraction experiments with “twisting zones” of 1, 4, 8, and 40 inches, and found that all twist-retraction curves were very close and in close agreement with Treloar’s eqs (1.3.56–57). Riding used experimentally observed values of R_y to calculate the retractions, reading the appropriate value of R_y from a mean value curve of R_y vs. twist.

Stansfield [20] showed that eq (1.3.56) can be written simply as:

$$\pi R_y T_s = \frac{1}{\bar{l}_a} \sqrt{1 - \bar{l}_a} \quad (1.3.96)$$

and he plotted experimental values of the right hand side of eq (1.3.96) versus T_s in figure 1.3.9a. His data were based on static twist tests at a fixed tension. The resulting straight line had a slope equal to πR_y , and this value of R_y was used to calculate \bar{l}_a on the basis of eq (1.3.56). The agreement between theoretical and experimental contraction was shown to be excellent in Stansfield's figure 1.3.6. But, as Riding points out, one may obtain different predictions of $R_e = (1 - \bar{l}_a)$ from eq (1.3.56) depending on what values of R_y are used. Stansfield's values of R_y obtained from the slope of figure 1.3.9a were, according to Riding [23], much larger than those observed in actual experiment. And Riding in figure 1.3.9b shows the variation in R_e vs. $2\pi R_y T_s$ when: (a) individual measured values of R_y are used (giving excessive retraction over the theoretical value), (b) the mean of the measured value of R_y is used, giving a small improvement, and (c) the hypothetical value of R_y , in excess of measured values, but giving good agreement with the prediction of eqs (1.3.56-57). Clearly, both Riding and Stansfield have used experimentally derived values of yarn radius to obtain improved predictions

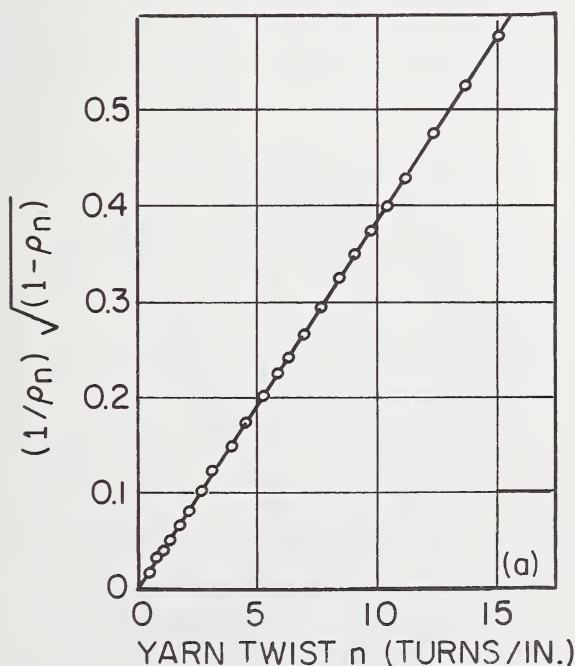


FIGURE 1.3.9a. Graph of $(1/\rho_n)\sqrt{1-\rho_n}$ against yarn twist n , after Stansfield [20]. $\rho_n = \bar{l}_a$.

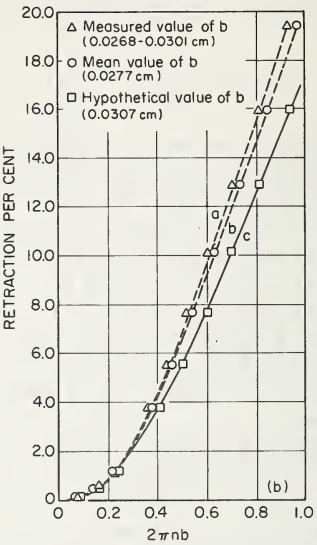


FIGURE 1.3.9b. Variation of retraction with different values of hypothetical radius, after Riding [23]. $R_y=b$.

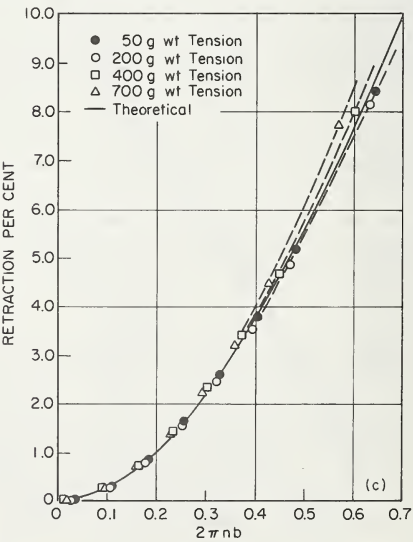


FIGURE 1.3.9c. Effect of tension on retraction of 1650 denier Tenasco, after Riding [23].

from eq (1.3.56), but Stansfield has used that average value of R_y which satisfies eq (1.3.96) which is simply another form of eq (1.3.56) in order to show good agreement with eq (1.3.56). Stansfield shows good agreement of predicted values of R_e for statistically twisted yarns. Riding shows poor agreement of predicted values of R_e (using actually measured values of R_y) with experimental values of statically twisted yarns (his fig. 1a), but very good agreement with experimental values of continuously (dynamically) twisted yarns (fig. 1.3.9c). This agreement is seen to hold for a wide range of twisting zone lengths (his fig. 6) over a wide range of twisting tensions (fig. 1.3.9c) and yarn deniers (his fig. 9). We prefer Riding's approach to the subject of retraction.

Plied Yarn Retraction

The calculation of plied yarn length per unit of initially straight filament has been based on the determination of singles yarn contracted length \bar{l}_a at initial twist, followed by a modification of singles yarn length \bar{l}_{ap} as it is somewhat backtwisted during plying according to eq (1.3.73). And the projection of this helically formed singles on the plied yarn axis provides the desired quantity $L = \bar{l}_{ap} \cos Q$ as in eq (1.3.75). The reduced form of eq (1.3.73) (shown by Treloar in his equation (40) for a two ply yarn) has been calculated in conjunction with eq (1.3.75) and the results plotted by Treloar in figure 1.3.10, while in figures 1.3.11a and 1.3.11b are plotted theoretical and experimental contraction ratios for the Dunlop yarns (at various singles yarn twist). It is clear that while the general features of the observed retraction curves are predicted by the theory, the quantitative values are considerably different.

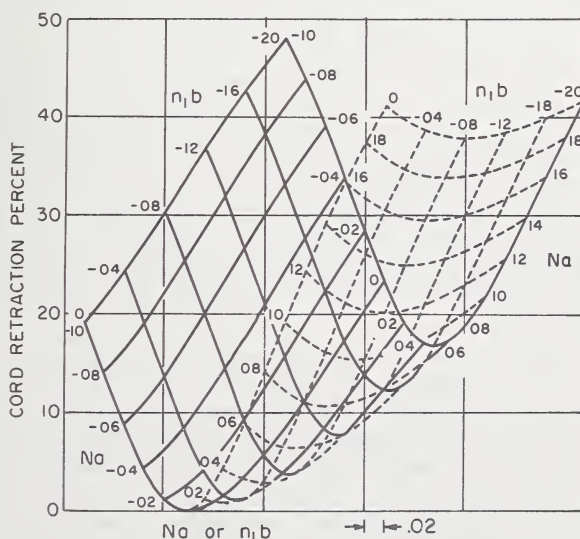


FIGURE 1.3.10. Theoretical retraction data for two-ply cord, after Treloar.

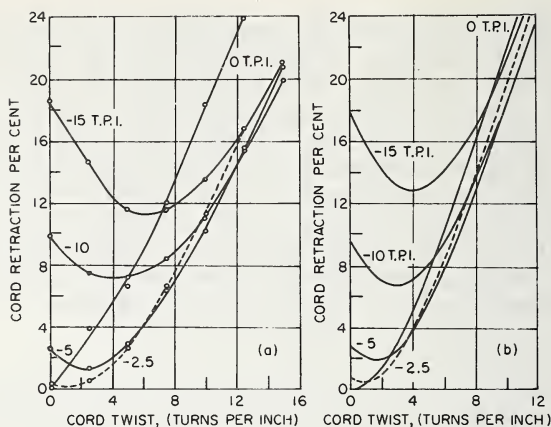


FIGURE 1.3.11. (a) Experimental cord retraction vs. cord twist curves. Parameter, single yarn twist (Dunlop). (b) Theoretical cord retraction vs. cord twist curves. Parameter, single yarn twist.

The theoretical curves of figure 1.3.11 were calculated using the observed average value of a , the singles yarn radius, over the range of twists, and the radius of the ply helix, r , was taken equal to a . Treloar felt that changes in ply yarn radius with ply twist could have accounted for much of this discrepancy. Accordingly, he recalculated the retraction for one set of yarns using measured values of ply yarn diameter and assuming $a = r = \text{observed diameter}/4$. The result showed considerable improvement in the theory vs. experimental agreement, suggesting that variations in actual cord diameter played an important role in experimental retractions during plying.

Tattersall, figure 1.3.12, conducted retraction tests on two ply yarn (2×1650 den. Tenasco) and compared experimental with theory. His experiments included (a) "static" twisting of the singles followed by "static" plying, (b) continuously twisted (on an uptwister) singles yarns which were then statically twisted in the laboratory to form a plied yarn and (c) uptwisted singles which were then uptwisted to form a two-ply yarn. The poor agreement he obtains for case (a) is similar to that reported by Treloar for the Dunlop results. The cases (b) and (c) still show considerable divergence from the theoretical, but are much closer to it than is case (a).

Stansfield [20], as in the case of singles yarn retraction, runs preliminary cord static twisting tests and plots the results of $\tan Q$ vs. T_p over a range of 0 to 15 turns/inch. The relationship is linear over a large part of the test range. He then uses the average (hypothetical) singles radius, \bar{a} , obtained as before from preliminary singles static twisting tests, and the measured value of Q versus T_p to calculate expected ply yarn retracted lengths for different ply twists according to his ply retraction equations which Riding [19] has rederived as in eq (1.3.80). The agreement between Stansfield's theory and experimental results (see

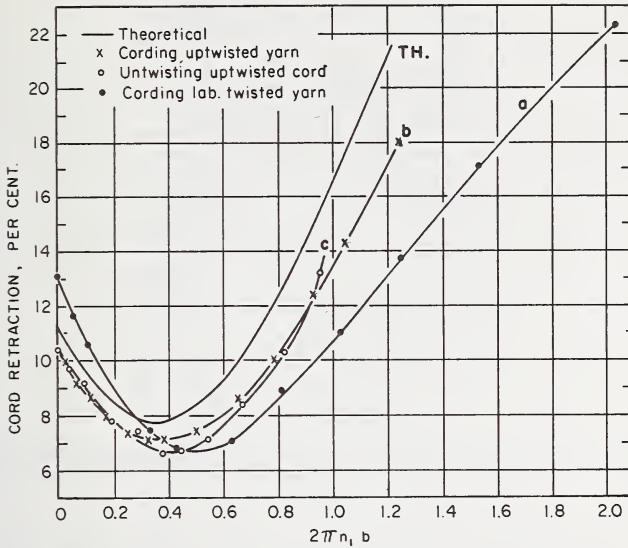


FIGURE 1.3.12. Retraction on twisting of two-ply cord (2×1650 den. Tenasco). After Tattersall [22].

his fig. 8) is excellent, but his method is still one of preliminary fitting of the experimental data to derive data for final calculation and may be expected to give improved agreements so long as the general shape of the theoretical curves are correct. As was pointed out by Riding [19], the retraction equations derived from Treloar's geometric model and from Stansfield's models are very similar and give numerically close predictions at low ply twists.

Riding [19] measured the ply yarn axial length, L , per unit filament length at different ply twists, by several techniques and found significant differences in the L vs. T_p curves for the same ply yarns, according to the test method used. He made up individual ply yarns at several ply twist levels on a commercial up-twister and then unplied the yarn and untwisted one of the singles to obtain readings at the beginning and end only—considered to be the most reliable method. He then took commercially (continuously) twisted singles and statically twisted (plied) them on the Tattersall trolley twister, measuring plied yarn length vs. ply twist on the same specimen. He also took a commercially produced plied yarn, twisted to the level of $T_p = 5$ turns/inch and statically untwisted it, measuring ply yarn length (on a single specimen) vs. residual ply twist. The results of the three methods were significantly different as shown in figure 1.3.13. The deviation of the “static plying” data was attributed to the restriction on de-migration of the filaments in the singles yarn due to the relatively high pressure of the singles against each other in the plied structure and causation of spurious ply yarn lengths at each ply twist. The serious deviation of the “static unplying” test was at-

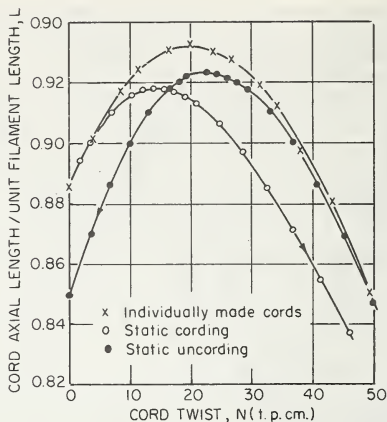


FIGURE 1.3.13. *Contracted cord length for different experimental techniques. Two-fold 1650 denier Tenasco (-4.88 t.p.cm. $= -12.40$ t.p.i.) after Riding [19].*

tributed to the static retwisting of the singles during the unplying operation—which, in effect, created unreal singles-in-ply yarn lengths and spuriously effected ply yarn and lengths at each ply yarn twist. Riding also observed the effect of tight vs. loose singles readings during his untwisting tests.

Helix Angles

The simple relationship between the tangent of the helix angle and the turns of twist in a simple helix, as expressed in eq (1.3.2) should apply equally for the case of a filament helix in a twisted singles and for a singles yarn helix as it lies in a plied yarn. Treloar [17], however, shows that the angle of the singles in the plied yarn (cord helix angle in his terminology) varies as a function of the original singles twist, as well as of the ply twist. The data shown in figure 1.3.14 indicate lower ply helix angles at any given ply twist when the singles twists are larger. This dependence is not consistent with the theory, and it is suggested by Treloar that the deviation might be connected with variations in ply diameter with ply twist. On the other hand, it might be argued that the ply diameters at two or three turns per inch of ply should be larger for the case of the 10 TPI and 12 TPI (prior) singles twist than for the 0 TPI prior singles twist and thus eq (1.3.2) suggests that angle q will increase with the increase in the radius, r , of the singles yarn helix. The data, however, show it to decrease for the pretwisted singles specimens.

Actually, the simplicity of the geometric expression for the primary helix angle is misleading when applied to a plied yarn, for while the ply twist can be accurately measured, the determination of the helix radius for the singles of the ply is virtually impossible. For, according to Riding [19], the singles axis is actually a mathematical line within the singles and it is possible to measure only the angles which the edges of the

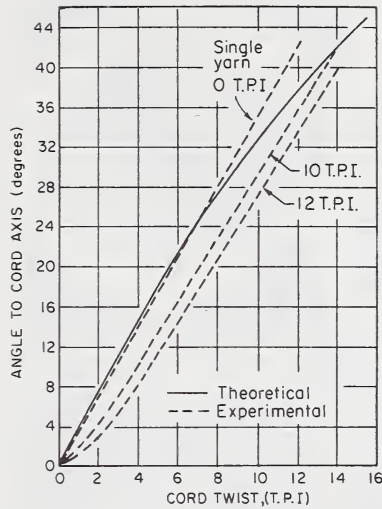


FIGURE 1.3.14. *Cord helix angles, after Treloar [17].*

singles, as seen in profile, make with the ply axis. One must know more about the actual shape of the singles cross section as it lies in the ply. This need is conveyed in figure 1.3.15 in which Riding shows the significant flattening which takes place in a two-ply yarn and in a three-ply yarn. It is seen that flattening in a seven-ply yarn is negligible, but in terms of tire cords it is the lower ply structures which are most widely used. Riding, accordingly, determines the helix radius by two methods: (1) by assuming the singles axis to lie midway across the section, and (2) by assuming it lies at the centroid of the flattened circles of figure 1.3.15 (one side flattening for the two-ply yarn, two side flattening for the three-ply). And with these two values he calculates the singles (in ply) helix angle and compares it with observed angles at various twists for two-, three-, and seven-ply yarns. In figure 1.3.16a, the two-ply yarn shows some departures at the higher ply twists. Considerably more departure of observed from calculated values occur in his three-ply sample. However, Riding's data for the seven-ply yarn lies close on to his predicted values as shown in figure 1.3.16b, as one might expect for the more controlled geometry of the seven-ply structure.

The local angle, α , between a filament following a secondary helix in a singles of a ply and the axis of that singles is predicted by eq (1.3.44a). But measurement of this quantity is more difficult than one would initially expect. The angle in question represents the difference in local direction of the filament axis and of the corresponding local segment of the singles yarn axis. Chow [13] has calculated the error introduced into measurement of the outer filament direction by misalignment of the observer's microscope. Riding has underscored the difficulty in accurately locating the local singles yarn axis, particularly with regard to its effective helix

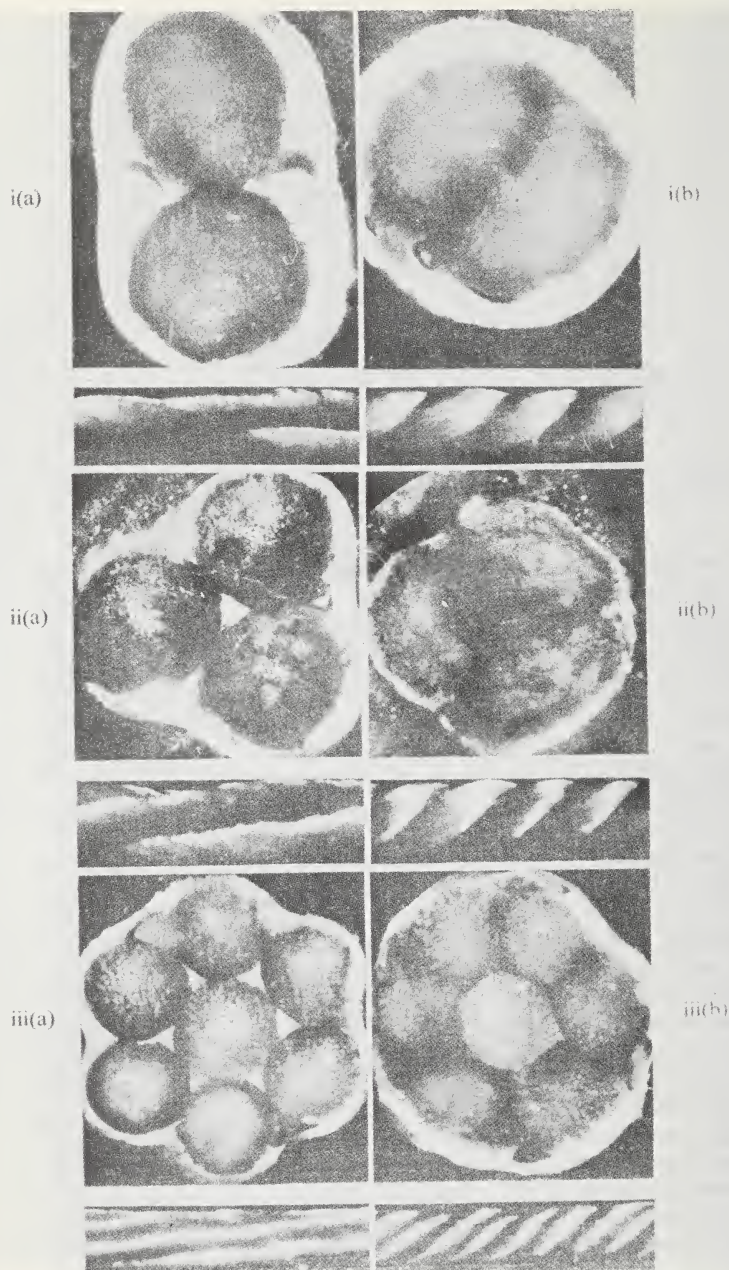


FIGURE 1.3.15. Cross section of cords, after Riding [19].

- (i) Two-fold 1650-den Tenasco - 4.88 t.p.cm. initial
(a) + 0.42 t.p.cm (b) + 4.96 t.p.cm.
- (ii) Three-fold 1650-den Tenasco - 4.62 t.p.cm. initial
(a) + 0.59 t.p.cm. (b) + 3.51 t.p.cm.
- (iii) Seven-fold 550-den Tenasco - 7.78 t.p.cm. initial
(a) + 0.60 t.p.cm. (b) + 3.44 t.p.cm.

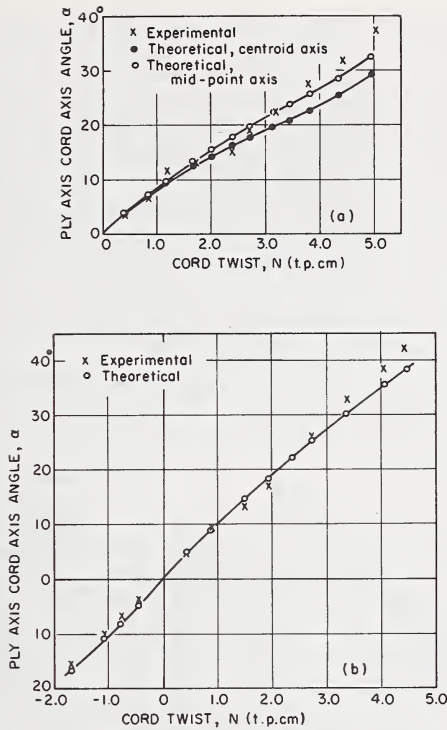


FIGURE 1.3.16.

(a) Cord helix angle, after Riding [19].

(b) Cord helix angle, after Riding [19].

Two-fold 1650 denier Tenasco.
 $n_1=4.88$ t.p.c.m. $= -12.40$ t.p.i.

Seven-fold 550 denier Fortisan H.
 $n_1=-7.0$ t.p.c.m. $= -20.09$ t.p.i.

radius, r . Thus with uncertainties relating to measured values on both sides of eq (1.3.44a) it is not surprising to find differences in direct measurements vs. calculated values of α .

Treloar has calculated [17] the angle α for a particular sized plied yarn and has measured corresponding α 's over a range of ply twists. His data presented in figure 1.3.17 evidences serious experimental departures from the predicted relationship.

Gracie [21] who has developed a modified expression for the outside filament angle, compares its calculated prediction to the Dunlop data shown in figure 1.3.17. He reports that the agreement is not very good, though somewhat better than for Treloar's calculations.

Riding, on the other hand, has used eq (1.3.44b) to calculate values of β_o (angle between the outside filament axis and the plied yarn axis) for two-, three- and seven-ply structures. His experimental values for the two-ply yarn depart significantly from the predicted values, but the difference between theory and experiment lessen considerably for the

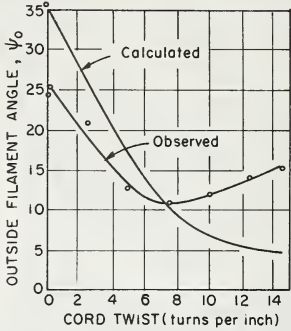


FIGURE 1.3.17. *Calculated and observed filament angles, after Treloar [17].*

$n_1 = -10 \text{ t.p.i.}$ $b = 0.0110 \text{ in.}$

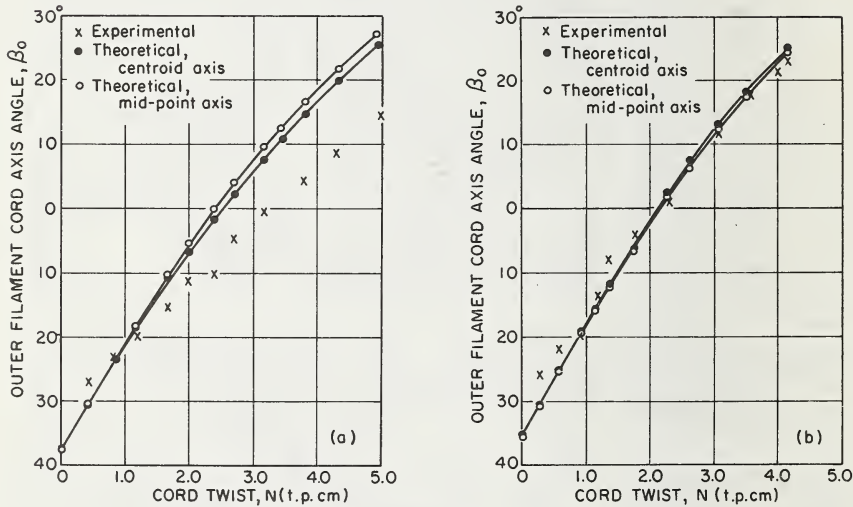


FIGURE 1.3.18.

(a) *Outer filament angle, after Riding [19].* (b) *Outer filament angle, after Riding [19].*

Two-fold 1650 denier Tenasco. Three-fold 1650 denier Tenasco.
 $n_1 = -4.88 \text{ t.p.cm.} = -12.40 \text{ t.p.i.}$ $n_1 = -4.62 \text{ t.p.cm.} = -11.73 \text{ t.p.i.}$

three- and seven-ply structures. In view of the experimental difficulties which he so carefully evaluates, Riding considers the overall agreement between curves in figure 1.3.18*a, b* as satisfactory—in other words, eq (1.3.44*b*) is reasonably well backed by experiment.

Cross Sections

Riding, in figure 1.3.15, shows the cross sections of two-, three- and seven-ply yarns before and after plying and the degree of flattening of

each singles component, as it lies in the plied yarns, is quite evident. Extreme flattening is seen in the two-ply structure and negligible flattening in the seven-ply structure. Hearle [7] shows a case of extreme flattening (his fig. 2.16) of a two-ply hot stretched yarn in which hexagonal distortion of individual fiber cross sections is also evident. But it is Hamilton [25] who provides the most comprehensive picture of changes in yarn diameters and bulk densities under conditions of thread flattening. Although his work related to singles yarns, it does include both filament and staple yarn. And in figure 1.3.19, Hamilton shows the change in flattened cross sectional width and depth of yarns wound under tension around a slender mandrel with varying degrees of twist. A logical extension of Hamilton's data can be considered for the cross sectional distortion of the singles lying in a ply, provided that the radius of curvature of the singles helix is substituted for the radius of the mandrel of Hamilton's test equipment. The analytical prediction of singles distortion in the ply is a problem of considerable complexity.

Migration

The ideal geometric models discussed earlier in this chapter are suitable for calculation of incremental structure and local mechanical behavior. But the requirement of filament continuity and the practicality of equivalent filament feed rates into the twisting zone necessitate the interchange of filaments between helical rings, so that the filament which occupies a central position at one point along the yarn must move to an outer position at a subsequent point. And filaments in outer rings at one point move inward further down the yarn. Such lateral movement, as contrasted with the circumferential movement associated with conventional twist, has been termed migration, and a great deal has been written about it. Hearle [7], for example, devotes a

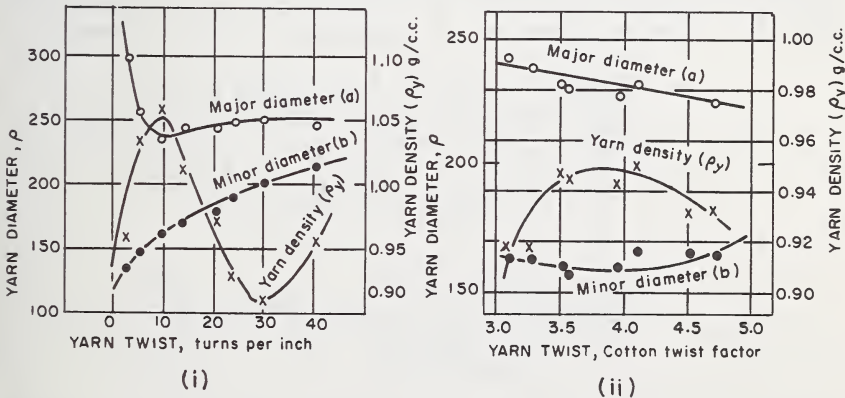


FIGURE 1.3.19. Effect of twist on yarn cross section, after Hamilton [25].

(i) Filament yarn
(ii) Staple yarn

full chapter to the subject, and El Behery [26] has written a useful review article on the topic.

Because of the availability of Hearle's consolidated treatment of the subject of migration, we will give only limited space to its consideration. But, at the same time, it must be stressed that lateral migration is a recognized, analyzed and experimentally verified aspect of twisted yarn structure, and it must be kept in mind in treating special fiber assemblies such as the singles and plied filament yarns as are in use today for tire reinforcement. The subject can be treated as a phenomenon inherent in twisted structures and studied on a geometric basis, both in theory and experiment. It can also be studied on a mechanistic basis, relating fiber properties, yarn structure, and processing conditions to fiber movement within the yarn cross section during twisting.

Hearle discusses the geometry of ideal migration in which the filament "migrates regularly and uniformly from the outside to the center of the yarn and then back to the outside, in such a way that the density of packing of fibers in the yarn is constant throughout the yarn." He divides the yarn into cylindrical zones with increments of radius dr and from the requirement that the length of fiber crossing each zone is proportional to the volume of the zone, demonstrates a linear relationship between the square of the relative radial position of a filament $(r/R_y)^2$ and the distance along the filament S . A corresponding relationship is shown to exist, for ideal migration, between $(r/R_y)^2$ and the length, z , along the yarn axis, and is seen in figure 1.3.20 to approximate linearity.

Treloar [27] reports a more rigorous analysis of ideal migration, which shows an approximately linear relationship between r^2 and z for low twists and low rates of migration, but also indicates the imaginary form of the relationship at small values of r/R , i.e., near the yarn axis.

Observation of migration behavior starting with Morton [28] and proceeding with Hearle [7], Gupta [29], Treloar [30], Riding [31], El-Shiekh [32], and Marzoli [33] has shown that migration behavior occurs, although, as Hearle points out, in a somewhat irregular manner.

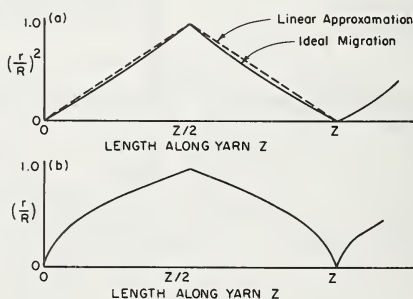


FIGURE 1.3.20. Migration envelopes for yarn with twist angle of 40° , plotted against length along yarn, after Hearle's figure 34 [7].

- (a) Variation of r^2 with Z .
 (b) Variation of r with Z .

Much has been written about experimental techniques for determining fiber migration in twisted structures and about computational methods for presenting and analyzing the observations of migration. Morton and Yen [28] used a dyed tracer fiber against the background of undyed fibers and made their observations in a medium of matching refractive index. A mirror placed at 45° below the yarn being observed provided simultaneous images corresponding to yarn views at right angles. Chaikin [34, 35] et al. prepared radioactive wool fibers and employed the techniques of autoradiography and shadowgraphy in measurement of fiber configuration and longitudinal strain. Block [36, 37] et al. embedded yarn in a soft polymer, microtomed it and examined the placement of blended fibers within the cross section of the yarn as a basis for observing and measuring longitudinal, radial and rotational distribution of fibers. Hamilton [38] similarly cross sectioned blended yarns as a basis for characterizing the radial distribution of fibers by a migration index. It remained for Bunting [39] to automate the microtoming and photographing of successive yarn sections and playing back the results in motion picture form to permit visual conception of the migrating and interlacing movement of individual filaments along the yarn length. Finally, the simplest method of measuring migration behavior is the direct observation of a seven (or lesser element) ply yarn with one color distinguishable ply. For here, as Hearle [7] points out, the absence of the distinguishable ply from the surface of the yarn means it is occupying the central position of the plied yarn. El-Shiekh [32] and Marzoli [33] have used this direct observation as their primary technique.

The results of these migration studies can be illustrated in innumerable examples. Hearle's [7] diagram best illustrates the phenomenon in figure 1.3.21 where comparison is made between the projection of a fiber path of an ideal structure versus one of a migrating fiber path. One may take measurements of the x coordinates of the fiber path from figure

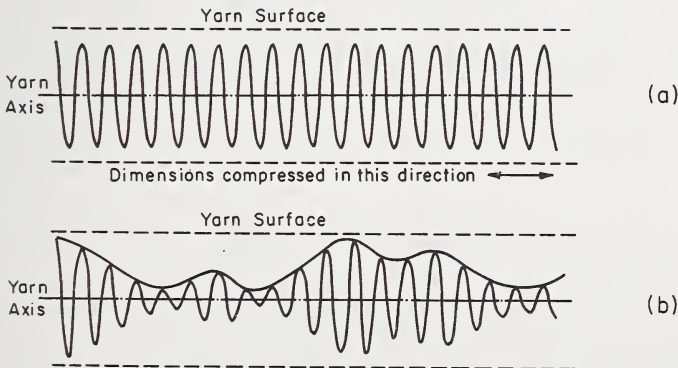


FIGURE 1.3.21. (a) Projection of the path of a fiber forming part of an idealized yarn structure. (b) Projection of the path of a fiber migrating over the yarn cross section. (From Gupta, 1963.)

1.3.21 and simultaneously measure the y coordinates (point for point) from a projection at right angles (to that of the fig. 1.3.21). Squaring and summing the x and y values to give the local helix radius r permits the experimenter to plot r/R versus the length along the yarn, as done by Morton in examples given by Hearle [7] in figure 1.3.22a. Data of this sort can be replotted as in figure 1.3.22b for an ideal fiber, two typical normal fibers and a wild fiber. The differences are striking and can be used to study the effect of processing and fiber variables such as the position of fibers upon entering the twist zone, the fiber modulus and the effect of trailing fiber ends. Such graphs can also show up variations in density of fiber packing across the yarn section.

Hearle [7] has studied fiber migration in spun rayon yarn with emphasis on mean fiber position, RMS deviation of fiber position, mean migration intensity, equivalent migration frequency, and the coefficient of variation of each of these parameters. And he reports little effect of

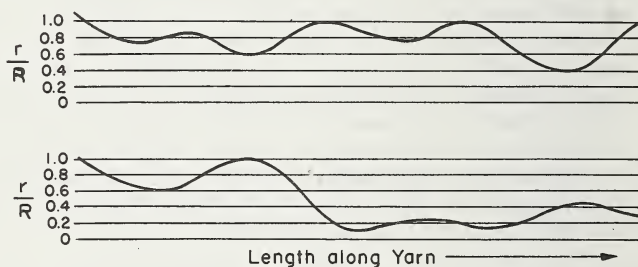


FIGURE 1.3.22a. Examples of helix envelope showing arbitrary zone boundaries, after Morton, 1956.

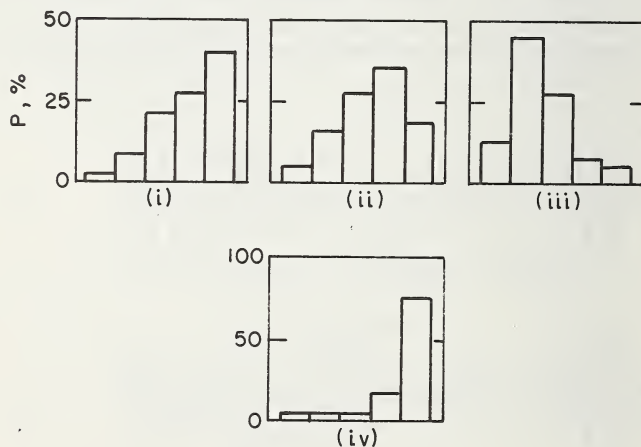


FIGURE 1.3.22b. Zonal distributions for individual fibers.

- (i) ideal.
- (ii), (iii) typical normal fibers.
- (iv) wild fiber.

twisting tension on migration during ring spinning of staple rayon yarns. But migration intensity and frequency increase significantly with twist—in fact, he reports “the ratio of migration frequency to twist frequency is almost constant, with a migration cycle corresponding to about four turns of twist.” The reduction of C.V. values for the above parameters as twist increases is taken to indicate a more regular migration pattern at higher twists. Finally, Hearle points out the presence of a long term drift (or migration) corresponding in period to the twist in the roving from which the yarn was spun—corrected for the draft employed during spinning. This long term drift is superposed on the short term migration discussed above.

The migration of filaments during the twisting of multifilament yarns is, of course, more pertinent to the subject of tire cords, and considerable effort has been expended on this topic. Riding [40], Hearle and Gupta [41], Treloar [27], El-Shiekh [32], and Marzoli [33] have studied filament migration in multifilament or multi-ply yarns, and their results are pertinent to tire cord problems. Riding [40] analyzed the migration of radial position of individual filaments in a twisted yarn by calculating a serial correlation coefficient, r_s , for pairs of r/R values separated by s intervals along the yarn length. A correlogram is then plotted (r_s versus s) for a given yarn. Hearle [7] summarizes this work and illustrates the different correlograms obtained for: (1) constant radial position, (2) regular migration, (3) random variation, and (4) a combination of regular and irregular variation. Riding studied migration in different types of twisting devices and found that the correlogram of up-twisted yarn generally gave the appearance of a damped oscillation with a well-defined periodicity. Ring twisted yarn correlograms generally reflected irregular variation of migration patterns. Controlled changes in yarn denier, filament denier and twisting tension did not appear to have consistent effects on the migration pattern and frequency (obtained from the correlogram). However, the producers' twist present in the yarn before the experimental twisting (to a fixed twist level) was observed to correlate directly and significantly with the correlogram frequency. Further work on continuous filament yarns, reported by Hearle and Gupta [41], also showed the correlogram frequency was very close to the frequency of producers' twist. But the equivalent migration frequency calculated by Hearle [7] was greater than that determined by the correlogram method. Both “equivalent migration frequency” and “mean migration intensity” increase with higher twists, but decrease with higher tensions of twisting according to Hearle [7].

Some confusion may arise from the fact that the producers' twist (or for the purpose of the experiment, the pretwist of the yarn) appears to govern migration frequency in some instances and the conditions of twisting, i.e., twist level and twisting tension, significantly affect migration frequency in other instances. Part of the confusion may lie in the use of different measures of migration frequency, but a large part of the difference in yarn structure may have real mechanical and structural origins. As Hearle [7] points out, there are two different mechanisms of twisting and twist migration, each of which may dominate in a given case—or both may be active at one time.

There is the "Tension Mechanism", first proposed by Morton, and quantified by Hearle and Merchant [42] for the case of the seven-ply yarn. The mechanism is based on the assumption that during twisting the external six singles yarns will bear the major portion of the twisting tension. The central yarn, on the other hand, will tend towards slackness since it is being fed into the twist zone at the same velocity as the other six yarns, but its in situ path length is less than that of the six helically disposed singles in the outer ring. The assumption is made that when the central yarn tension falls to zero (and even into compression by an amount X , representing the degree of buckling necessary to initiate migration) then one yarn in the external ring, carrying $1/6$ of the twisting tension will move to the central position, displacing the yarn originally in that place. At this instant, one of the six outer yarns is at zero tension, and the others are at $1/6$ of twisting tension. The central yarn is also, for an instant, at $1/6$ of twisting tension. Then as twisting proceeds, the central yarn accumulates increments of excess length relative to the central path length of the plied yarn, and its tension starts to fall, eventually reaching zero tension (and beyond) at which time buckling is initiated and a second migration is underway. While this was taking place, the slack yarn which had moved to the outer ring, then starts to build up in tension, since it now follows a longer helical path. Its rate of tension buildup is assumed to equal the rate of tension fall off of the central yarn.

Quantitization of this descriptive mechanism is provided by Hearle [7] who shows that the length along the ply yarn for which one singles remains in the central position z_c is

$$Z_c = L(\cos q + T_y/6\gamma) \left\{ \ln \left[1 + \frac{T_y \sec q}{6\gamma(1 - \cos q) - T_y} \right] + \frac{\gamma x}{\gamma(1 - \cos q) - T_y/6} \right\} \quad (1.3.97)$$

where L is the free length of yarn in the twisting zone,

q is the helix angle of the singles in the plied yarn,

γ is the tensile spring constant of the singles,

T_y is the twisting tension of the plied yarn,

x is the fractional excess of yarn in the free zone necessary to initiate buckling.

There are, Hearle points out, two migrations for each occasion that a yarn occupies the central position and each yarn should be in the central position $1/7$ of the total time. Thus, the average migration per 100 cm. for one of the seven singles involved is $200/7Z_c$. And it is seen that migration frequency will vary in a prescribed manner with twist angle, q , tension T_y , free length, L , in the twist zone and the buckling parameter, x . Only x has to be determined experimentally by trial calculations of the average effective migrations per singles yarn per 100 cm., and comparing the results with experimental observations as in figure 1.3.23.

El-Shiekh [32] examined the geometric configuration of a ribbon of seven equispaced singles moving into the twist zone and calculated

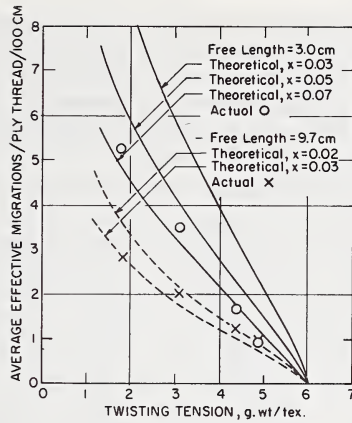


FIGURE 1.3.23. *Experimental and theoretical results obtained by Hearle and Merchant (1962) for twisting of seven-ply structure.*

X is the degree of buckling needed for migration.

the amount of central element slack, x , necessary to initiate migration from center to outer ring. He assumed that the slack central yarn would be caught up in the external yarns, thus initiating the interchange, when the axis of the nearest external yarn intersected the surface of revolution of the revolving slack yarn. This calculation removed the need for experimental determinations of x and led to quite reasonable agreement between theory and experiment as shown in figure 1.3.24. Its applicability is, of course, limited to the geometry of an open ribbon of sepa-

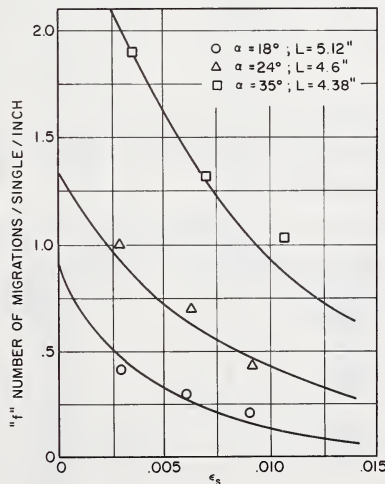


FIGURE 1.3.24. *Variation of frequency of migration with twist angle, α , and yarn tensile strain, E_s .*

rated elements. Contact and crowding of the filaments as occurs in real twisting of multifilament yarns makes such a determination most difficult—in fact, the entire procedure of calculating migration frequency becomes extremely complex when the simple geometry of the limited-ply yarn gives way to the real conditions met in twisting of commercial yarns.

Yet, in viewing the successive cross sections of the twisting zone in a seven monofil ply as in figures 1.3.25*a*, *b*, one learns a great deal which can apply to the real twisting process. In figure 1.3.25, El-Shiekh shows seven monofil *S* twisted at five TPI under a constant tension of 200g. In figure 1.3.25*a*, the twist triangle was embedded when monofil #1 was slack, while #6 was slack in figure 1.3.25*b*. The slack element can be readily detected in both cases, and it is seen to end up as the central element of the plied yarn. The different location of the twist point is easily observed, generally in a position near the center of gravity of the tensioned yarn, i.e., it moves from the slack yarn. Note that subtwisting takes place between groups of components before formation of the final structure—in fact, one monofil in each case is seen to join the plied yarn only at the last moment.

The lasting effect on migration frequency of producers' twist in the case of Riding [40] and of roving twist in the case of Hearle [7] is seen by Hearle to be the result of a second mechanism of twisting quite unlike

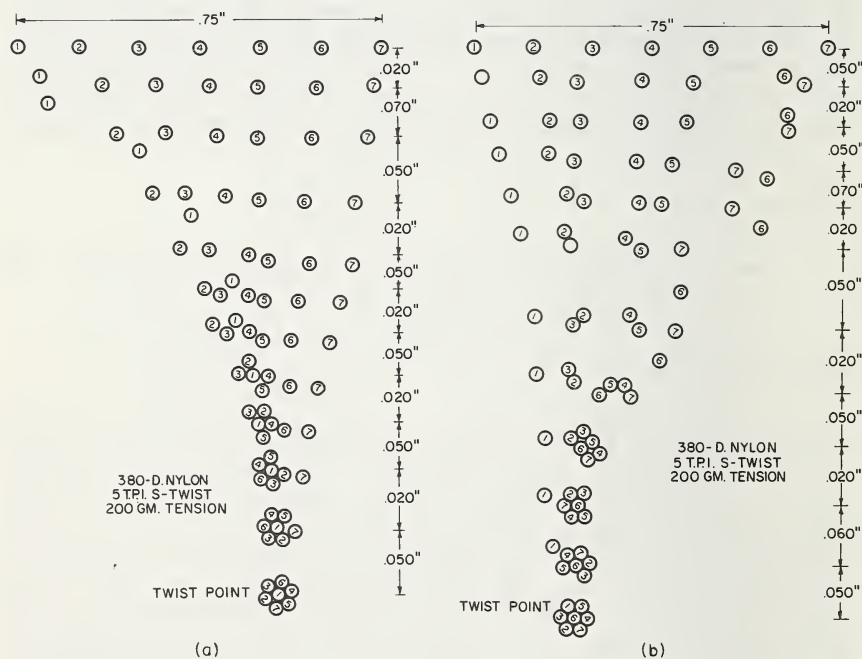


FIGURE 1.3.25. Filament positions in the twist triangle (development of slack).

that dictated by the tensile motivation of migration during cylindrical twisting. Hearle [7] terms the second twist form as ribbon twisting. The geometry of simple twisting of a ribbon is shown in figure 1.3.26a and the formation of a wrapped ribbon by bending on a skew is shown in figure 1.3.26b. According to Hearle [7] both theory and experiment indicate that a flat rubber strip will seek the twisted form of figure 1.3.26a at lower twists, but the wrapped form of figure 1.3.26b at higher twists.

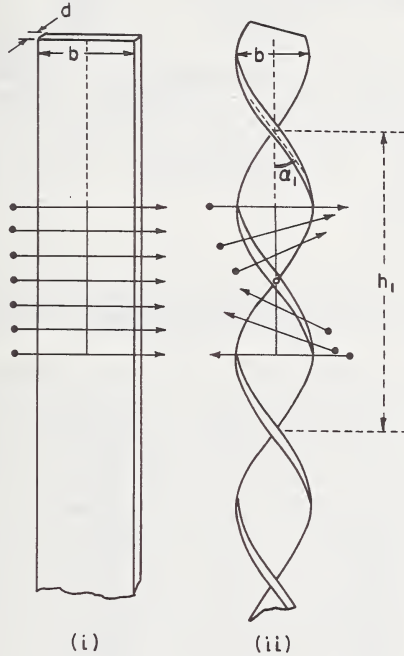


FIGURE 1.3.26a. Geometry of simple twisting of ribbon of width b and thickness a to a twist angle α , and period h , after Hearle and Bose, 1966.

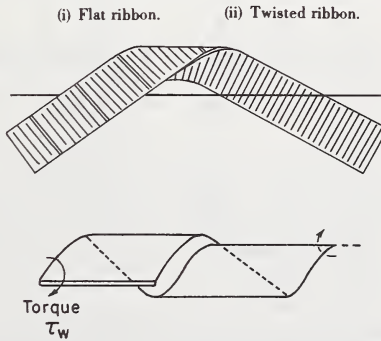


FIGURE 1.3.26b. Formation of a wrapped ribbon by bending on a skew, due to the action of the torque τ_w .

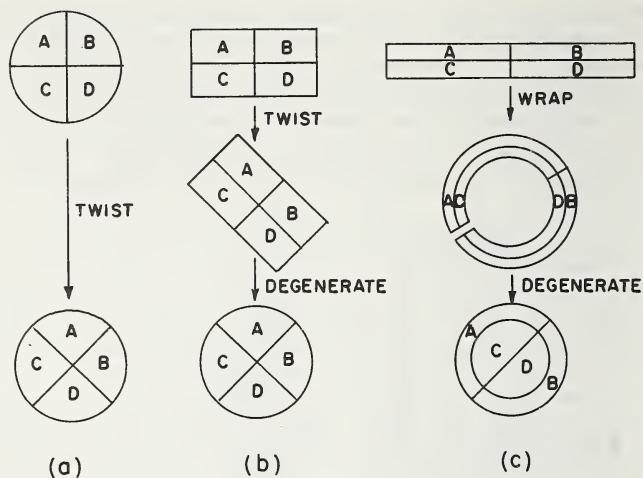


FIGURE 1.3.27. (a) *Cylindrical twisting*, (b) *Twisted ribbon form*, (c) *Wrapped ribbon form* (Hearle and Bose, 1966).

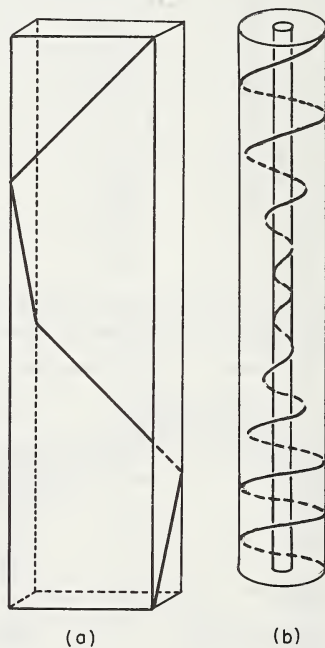


FIGURE 1.3.28. (a) *Schematic representation of ribbon-form of yarn, with filament twisting round due to producer's twist*. (b) *The same yarn twisted into a wrapped form, and hence showing migration*.

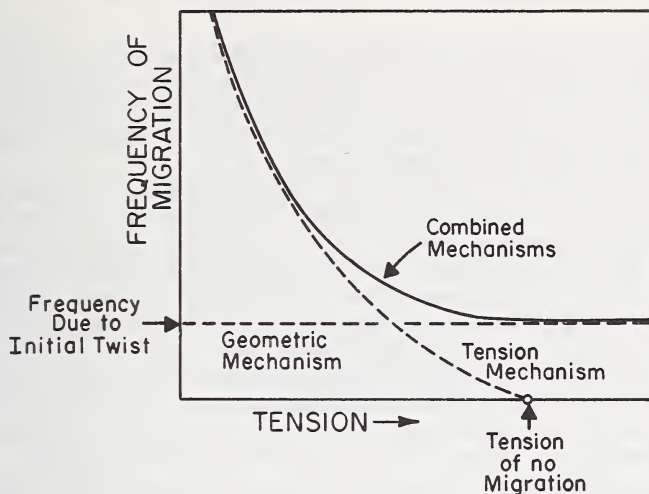


FIGURE 1.3.29. Variation of frequency of migration with twisting tension resulting from a combination of mechanisms. (Hearle, Gupta, and Goswami, 1965).

There is an intermediate region in which both forms exist together. If, however, the twisting ribbon is made of individual separated filaments, the form of figure 1.3.26a will not be a stable one, and the structure will degenerate to a form similar to that obtained in cylindrical (conventional) twisting as discussed above. Hearle provides an excellent summary of the structural form which will occur in twisting, as shown in figure 1.3.27, which reflects the influence of twist form on expected filament migrations of the different kinds of twisting and migration patterns and pinpoints the relationship between migration period and producers' twist period (corrected for contraction) on the basis of the wrapped ribbon structure as shown in figure 1.3.28. Finally, Hearle concludes that the combination of the two mechanisms will show the relationship of migration frequency and twist tension as in figure 1.3.29.

1.3.3. Mechanics of Tensile Behavior of Tire Cords

1.3.3.1. An Introduction to the Mechanics of Simple Yarn Structure

The prediction and observation of the tensile behavior of singles twisted yarn has been covered so effectively by Hearle [7] that any attempt at developing a comprehensive treatment of this topic in the current chapter would be highly repetitive. It is our purpose to focus on the mechanics of tensile behavior of higher order structures, i.e., tire cords and plied yarns. However, to dive into this topic without a summarization of the analysis and experimental observations on singles yarns would leave the reader at considerable disadvantage, and so some repetition must be endured.

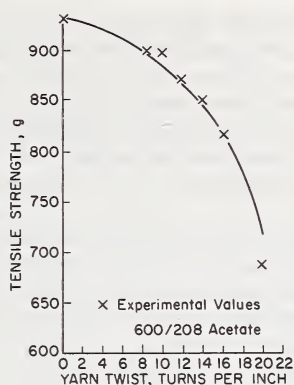
As a start we use the introductory treatment to simple yarn mechanics recently prepared by Backer [7]. In approaching the subject we have the choice of following papers published on a chronological basis, or we can consider the literature in the order of logical development of subject matter. We take the latter course.

Consider a series of fibers infinitely long, uniform in cross section, and uniform in mechanical properties. The fibers are twisted together so as to form a series of uniform helices, with each fiber lying on a helix of fixed radius (and staying at that radius). Each fiber has properties constant along its length; each fiber is similar to its neighbor in geometry and in mechanical properties. We assume that there is no interaction between the fibers and we consider each fiber element to be so slender that it can withstand only tensile forces along its axis. This is the background of Platt's [43] initial development in yarn mechanics. Gégauff [44] attempted a similar approach early in the century, but his work was not brought to light until some years later by Hearle [45].

Platt's approach was as follows. Assume that when a yarn is stretched, each fiber in that yarn has a fixed geometric location identifiable by its inclination angle relative to the yarn axis. A given stretch for the yarn causes fiber strains which differ from position to position. The fiber strain at any location equals the product of the yarn extension and the cosine squared of the helix angle of the fiber. From the stress-strain curve given for the fiber we can determine the tensile force which will develop along its axis as a result of the strain imposed. The contribution of this force to the normal stress acting on the cross section of the yarn at that location is equal to the product of the axial stress in the fiber and the cosine squared of its helix angle. One now considers this stress acting on a small increment of area and integrates the resulting incremental force over the cross section of the yarn for all fibers.

Once this integration process is undertaken, we have an expression for the tensile load or tensile resistance which the yarn puts up to axial stretch at a given level of strain. But the prediction of when the yarn will break depends on the criteria for failure. One may decide that the yarn will break when the fiber in the position of maximum strain reaches its own breaking strain. This fiber lies at the yarn center with a zero helix angle. If we know the fiber elongation at rupture, we can then assume that the yarn breakdown will initiate at this same strain and from the expression developed by Platt for the tensile resistance of the yarn to strain, we can calculate the breaking strength of the yarn. An analytical expression for this breaking strength will be a function of the properties of the fiber and the geometry of the yarn, exemplified by its twist and radius. Figure 1.3.30 shows a plot of yarn strength calculated from Platt's expression and also determined experimentally at various twist levels. For this calculation Platt assumed that the twist angle did not change significantly with yarn extension, nor did the radius of the yarn decrease during the test.

Later, Platt [46] dealt with the questions of helix angle change and lateral yarn contraction. He concluded that lateral contraction plays a secondary part in the overall efficiency of strength translation of fibers

FIGURE 1.3.30. *Yarn strength vs. twist.*

into yarns for helix angles less than thirty degrees. He also concluded that his first assumption—that of negligible effect of helix angle changes—was valid for most textile yarns.

Up to this point both Gégauff and Platt had neglected transverse forces. And in considering spun yarns they treated only the cases where the twist level was high enough to prevent slippage of the fibers. So the analysis was essentially that for continuous filament yarns, even though applied to both filament and spun yarns. Hearle [45] treated the case of both tensile and transverse or lateral forces. His first report was restricted to small strains and provided for no lateral contraction. Later Hearle et al. [47] took lateral contraction and transverse forces into account in arriving at expressions for the tensile behavior of twisted filament yarns. For a full treatment of this subject, see Hearle [7].

It is interesting to note that Galileo [48] showed some interest in the transverse forces between fibers in a yarn as he attempted to explain to a friend how “fibers, each not more than two or three cubits in length, so tightly bound together in the case of a rope one hundred cubits long” would require a great force to break them. “Can you not hold a hempen fiber,” he writes, “so tightly between your fingers that I, pulling by the other end, would break it before drawing it away from you? Certainly you can. And now when the fibers of hemp are held not only at the ends, but are grasped by the surrounding medium throughout their entire length, is it not manifestly more difficult to tear them loose from what holds them than to break them? But in the case of rope, the very act of twisting causes the threads to bind one another in such a way that when the rope is stretched with a great force, the fibers break rather than separate from each other. At the point where a rope parts the fibers are, as everyone knows, very short, nothing like a cubit long, as they would be if the parting of the rope occurred, not by the breaking of the filament, but by their slipping one over the other.”

Galileo also concerned himself with the nonuniformity of filament strength along its axis. However, by faulty reasoning, he arrived at the

wrong conclusion concerning the effect of weak spots in a long rope and, as he said, "How can you therefore maintain that the long rope is weaker than the short one. Give up then this erroneous view which you share with very many intelligent people." The treatment of nonuniformity in yarns was taken up by a highly intelligent individual, F. T. Peirce [49] whose pioneering work on the weak link theory for textile yarns serves as reference in numerous current researches on the failure of engineering structures.

Platt [50] found that it was necessary, in many practical applications, to deal with fibers which varied considerably in their stress-strain properties. His assumption of uniformity of mechanical properties had to be set aside and the nonuniformity or variation of stress-strain characteristics of the fiber became another parameter to be included in the analysis. Platt's reasoning was roughly as follows. If one takes ten natural fibers and compares their individual stress-strain curves, it is evident that their rupture does not occur all at one point of extension. A frequency distribution of the rupture extension of the individual fibers can be determined and is shown in figure 1.3.31 in normalized form. The objective of the analysis is to treat the idealized single yarn geometry without the assumption of uniformity. If now the normal frequency distribution is converted into a cumulative distribution and inverted, that is, subtracted from the quantity 1, we have in effect a measure of the relative number of fibers which will not have broken at any given extension. Note that we are referring here to fiber extension. For the most simple case, that of parallel untwisted fibers, fiber extension and bundle extension are the same.

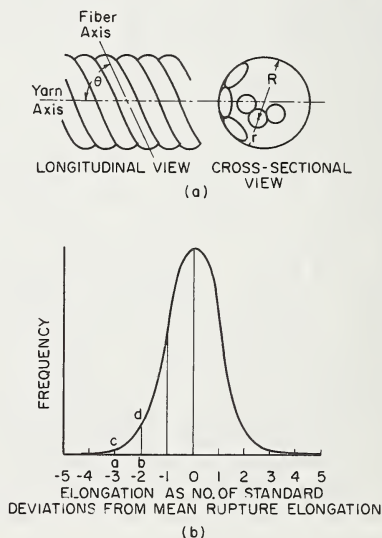


FIGURE 1.3.31. (a) *Idealized singles yarn geometry.* (b) *Standardized normal distribution curve of rupture elongation.*

Treating this simple case of parallel fibers, Platt sets the bundle strength equal to the product of the average fiber resistance to a given strain (taken from the average stress-strain curve) times the number of fibers active at that moment. The fiber stress-strain curve can be considered linear or taken in any form that can be expressed mathematically. The plot of percentage of unbroken fibers in figure 1.3.32a can also be expressed mathematically. And thus an expression is available for the tensile resistance of the bundle at any given strain.

The fact that fibers start to rupture part way along in a bundle test and continue to rupture until the entire assemblage is broken is accounted for by the ever-reducing percentage of unbroken fibers shown in figure 1.3.32a. If this bundle resistance is calculated on a point by point basis, it does not matter whether the stress-strain curve of the average fiber is linear or not. In fact, a more realistic form of the fiber stress-strain curve consists of two linear portions first, the so-called elastic region, and the second with a reduced slope, the so-called plastic region. The second region is of more importance if we are considering the rupture of a bundle of parallel or even twisted fibers and this region

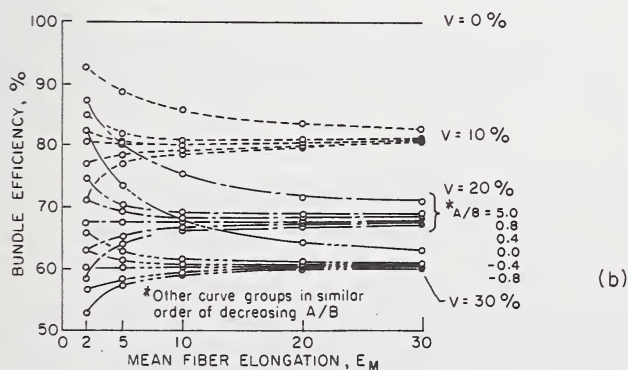
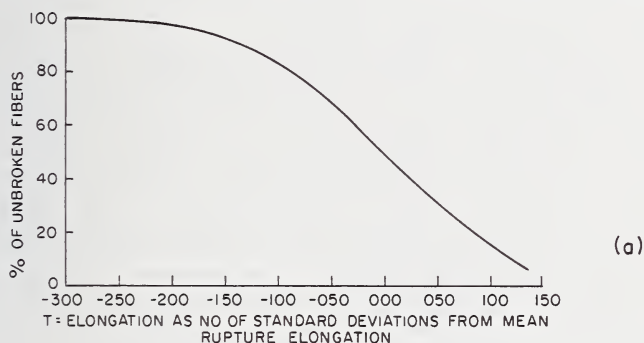


FIGURE 1.3.32. (a) Unbroken fibers vs. strain. (b) Bundle efficiencies, with coefficient of variation V as a parameter, after Platt.

may be characterized in terms of its slope B and its intercept A . Now if one takes the three parameters: (1) average rupture strain for the fiber population, (2) coefficient of variation of the fiber strain (which dictates the breadth of the frequency distribution pictured in fig. 1.3.31*b*), and (3) the rheological properties of the fiber (expressed as the ratio A over B), one can determine the transmission of fiber properties into maximum bundle resistance to extension.

The function representing tensile resistance of the bundle is simply differentiated with respect to strain and its derivative is set equal to zero to establish the maximum resistance. If this maximum, i.e., the breaking strength, is compared to the breaking strength summation of the individual fibers, tested separately, one develops a measure of relative bundle efficiency. It is this relative bundle efficiency which is plotted in figure 1.3.32*b* by Platt. Note that the bundle efficiency is a hundred percent where the coefficient of variation, v , is zero. As the coefficient of variation increases to 10, then 20, then 30 percent, the bundle efficiency for a given mean fiber elongation and ratio of intercept to slope (A/B) decreases significantly. The efficiencies are highest for the high A over B ratios, indicating that a stress-strain curve with a high flat plateau will provide maximum bundle efficiency. It is noted also that as the mean fiber elongation is increased, the bundle efficiency may go up or go down, depending upon the stress-strain properties of the fiber.

Physically what these data say is that if the fiber stress-strain curve is quite flat in the region of rupture, it does not matter whether some of the fibers in the bundle are breaking at the left-hand side of the flat plateau while others are breaking way over to the right-hand side, at much higher elongations, and some are breaking in the middle. The point is that they are all up on the plateau closely corresponding to their maximum load capacity and therefore at the moment of bundle rupture, they are very nearly contributing their maximum support to the bundle. And the bundle as a result will tend to have a high strength efficiency.

Platt has superimposed the analysis for the varying fiber stress-strain properties on the analysis for the idealized singles yarn geometry (fig. 1.3.31*a*) and thus has extended the treatment of twisted yarn mechanics to include the practical case of highly variable fibrous material. This work represents a significant contribution to the structural theory of textile materials. Note also that this approach permitted the treatment of nonelastic fibers, that is to say, it allowed for a change in the slope of the stress-strain curve and dealt with the behavior of the fiber in its region of rupture. To generalize the treatment one need but express mathematically the resistance of a fiber population to an average strain, and further express the variation in the rupture strain for the fiber population. Finally, one must convert from average fiber assembly strain to, the local fiber strain, depending upon its geometric configuration. Then by integrating the force contribution of the unbroken fibers in each region of the assembly to the axial tension in the assembly, one can determine the total resistance of the structure. Differentiating this total resistance with respect to strain and equating the derivative to zero permits calculation of the strength of the structure.

This treatment does not include the effect of lateral compression of individual fibers within the structure, and it does not provide for the contraction of the structure itself. These two elements were dealt with in Hearle's later studies (Hearle et al. [47]). Consideration of lateral contraction or the Poisson effect was essential in the development of a fiber web theory for nonwovens, for it was quite obvious that bonded fiber webs contracted significantly in the lateral direction as a result of longitudinal stresses. It is interesting to note that the analysis of the stress-strain behavior of nonwovens (Backer and Petterson [51]) followed the general pattern established by Platt in his analysis of twisted structures, with fiber inclination angles replacing fiber helix angles.

The principal difference between the analytical treatment of the nonwoven and that of the twisted structure is the fact that the inclination angle follows a statistical function in the nonwoven, while in the twisted structure it is determined simply from the yarn twist and the distance of the fiber from the center of the yarn. The expression for resistance of a nonwoven to extension in a longitudinal direction contains terms relating to the angular distribution of the fibers, to the fiber modulus and to the contraction ratio of the structure. The latter quantity is unknown, but it may be calculated by equating the stresses developed in the lateral direction during a longitudinal pull to zero. This expression for the lateral stress similarly consists of the fiber modulus, its angular distribution in the structure, and the contraction ratio. Equating this expression to zero leads to a solution for the Poisson ratio expressed solely in terms of the geometry of the structure. The Poisson ratio of a nonwoven is indeed independent of the properties of its fibrous material; it is actually a structural parameter, but it can be used as a basic property of nonwovens considered as orthotropic sheet materials, as shown by Backer and Petterson [51] and Petterson and Backer [52]. One can now imagine the wrapping of a web of nonwoven material into a cylindrical roll to form a three-dimensional structure for which calculations of lateral contraction occurring during application of longitudinal axial tensions can be made.

A formal listing of papers on the theory of tensile properties of twisted continuous filament yarns, furnished in Hearle's [7] table 4.1, provides the serious student of this subject with the "must" reading of the structural mechanics of tire cord.

1.3.3.2. Analyses of Tensile Behavior of Continuous Filament Singles Yarn

The Case of Pure Fiber Tension and Idealized Geometry

Platt [43] assumed an ideal geometry for the singles continuous filament yarn as pictured in figure 1.3.31a, with all component filaments round in cross section and uniform in properties and geometry along their length. Each filament maintains a fixed helical path, within the yarn with constant helix radius, curvature and helix angle. Packing density

is also constant along the yarn length. The forces acting on the fiber of figure 1.3.33a can be characterized as:

- a. a tensile force, p_r , along the fiber axis,
- b. a shear force, v , acting in the fiber cross section,
- c. a bending moment, m ,
- d. a torsional moment, t ,

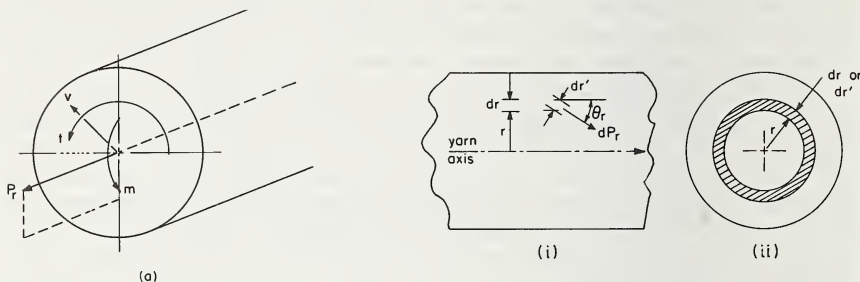


FIGURE 1.3.35.

- (a) General stresses in fibers. (b) (i) Longitudinal view of yarn.
(ii) Cross-section view of yarn.

Platt sets v , t , and $m=0$ and, neglecting forces acting on the longitudinal surfaces between fibers, treats the components of p_r , the force acting axially along the fibers, so as to develop a relationship between P , the tensile force on the yarn, and the properties of the filaments as well as their geometric arrangement. From the simple geometry of a helix (with helix angle q , radius r and twist T)

$$\tan q = 2\pi r T \quad (1.3.2)$$

and the force relationship for the ring of Figure 33b

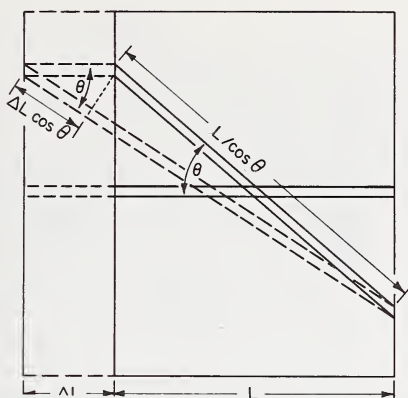
$$dp_r = \sigma_f 2\pi r dr \cos q \quad (1.3.98)$$

where σ_f is the tensile stress acting along the axis of the fibers of the ring. Platt expresses the yarn tension, P , as:

$$P = 2\pi \int_{r=0}^R \sigma_f r \cos^2 q dr \quad (1.3.99)$$

Now, using the relationship between the applied yarn strain $\Delta L/L = \epsilon_y$ and the axial fiber strain ϵ_f derived from the condition of small strains from the geometry of figure 1.3.34, i.e.,

$$\epsilon_f = \epsilon_y \cos^2 q \quad (1.3.100)$$

FIGURE 1.3.34. *Deformations in twisted yarns.*

and the identity:

$$\cos^2 q = \frac{1}{1 + \tan^2 q} \quad (1.3.101)$$

one obtains for the fiber whose generalized stress strain relationship is of the form

$$\sigma_f = a + b\epsilon_f \quad (1.3.102)$$

the expression for yarn tensile resistance to an imposed axial yarn strain of ϵ_y

$$P = 2\pi \int_{r=0}^R (a + b\epsilon_y \cos^2 q) r \cos^2 q dr \quad (1.3.103)$$

which Hearle [7] illustrates can be integrated and reduced to the simple expression when the constant a vanishes

$$P = (\pi R^2 \phi) E_f \epsilon_y \cos^2 Q \quad (1.3.104)$$

where the packing factor ϕ has been introduced to permit a proper substitution of the fiber tensile modulus E_f for b in eq (1.3.102). Actually, Hearle shows the quantity $1/v_y$ (v_y = specific volume of the yarn) in lieu of ϕ in eq (1.3.104) and expresses the specific stress and fiber modulus in units of [g-wt/(g per cm.)] equal to $10^{-5} \cdot \text{g-wt/tex}$. We chose to report eq (1.3.104) with the packing factor ϕ , the ratio for fiber area A_f to yarn cross sectional area A_y , or πR_y^2 , and with the fiber modulus E_f as well as the stresses σ_f and σ_y expressed in units of force per unit cross-sectional area. Care must be taken in use of the correct units for whatever equation is used.

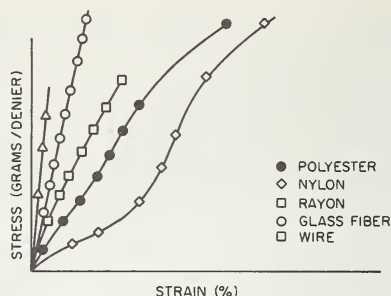


FIGURE 1.3.35. *Stress-strain characteristics of high tenacity yarns*

To reach the simple form of eq (1.3.104) the quantity a is taken as zero for simplification, i.e., the stress-strain curve of the fiber is a simple linear relationship starting at the 0-0 origin. Such a simplification is satisfactory for such tire cord materials as wire, glass fiber, or rayon as shown in figure 1.3.35, but the polyester yarn would no doubt require the full form of eq (1.3.102) for its post yield region. The form of the nylon curve suggests a more exacting expression than that of eq (1.3.104).

As Hearle [7] points out, the specific yarn stress multiplied by its solid cross-sectional area equals the yarn tensile load, P , i.e.,

$$\sigma_y(\pi R^2 \phi) = P \quad (1.3.105)$$

and, by definition, the yarn tensile modulus E_y

$$E_y = \frac{\sigma_y}{\epsilon_y} \quad (1.3.106)$$

whence, from eqs (1.3.104-106),

$$E_y = E_f \cos^2 Q$$

a simple relationship shown in reasonable agreement with experimental results. Recall that Q is the outside helix angle.

Platt reasoned that since the fiber strain at the yarn center equals the axial strain of the yarn, then initial rupture will take place in the central fiber, and, following on this event, there occurs a rapid progressive rupturing of all remaining filaments and the yarn breaks. While this chain of events is observed in certain yarns, where catastrophic failure occurs as a result of almost instantaneous rupture propagation, it is by no means universal, as is seen, for example, in Platt's later work [50] on cordage structures. Here variations in the rupture strain levels of the component fibers are shown to slow down the propagation of the initial fiber rupture in the yarn structure. In other instances, the propagation of failure is observed to depend on yarn twist levels, on blend ratio (of a two component yarn), on friction and on relative fiber properties in a blend. More will be said about this later.

The Case With Transverse Forces

The importance of lateral forces in affecting load transfer from fiber to fiber of a staple fiber (spun) yarn was recognized as far back as Gallileo [48] and many researchers in yarn mechanics have incorporated the effect of transverse forces on fiber and yarn behavior for twisted structures. For example, Gurney [53] developed a relationship between yarn strength, twist, lateral contraction ratio and fiber stress strain properties. Sullivan [54] determined the strength of staple fiber yarns by analyzing the lateral pressure distribution across the yarn and its contribution to axial stress transfer between fibers and to strength development. Machida [55] analyzed the lateral pressure in blended yarns under tension as a means of predicting the critical fiber length during yarn rupture. Grosberg [56] et al. calculated the lateral pressure distribution in a low twist sliver during extension as a means for predicting sliver strength.

Hearle [45, 47] provided the most complete treatment of the case of yarn strength taking into account transverse forces. His procedure was to establish first a more complete relationship between filament strain and yarn strain

$$\epsilon_f = \epsilon_y (\cos^2 q - \mu_y \sin^2 q) \quad (1.3.108)$$

where μ_y is the contraction ratio (or Poisson's ratio) of the yarn, i.e., the ratio of transverse, radial contraction ϵ_{yt} resulting from an axial extension, ϵ_{ya} .

$$\mu_y = -\epsilon_{yt}/\epsilon_{ya} \quad (1.3.109)$$

It is worth noting that Petterson [57] started with the same expression in analysis of the load extension properties of a nonwoven web taking lateral contraction into account. Assuming linearly elastic fiber behavior, Hearle then established the generalized stress strain relationship for the fiber as:

$$\epsilon_{fa} = \frac{\sigma_{fa}}{E_{fa}} - 2\mu_{at} \frac{\sigma_{ft}}{E_{ft}} \quad (1.3.110)$$

where: ϵ_{fa} is the axial fiber strain,

σ_{fa} is the axial fiber stress, σ_{ft} is the transverse fiber stress assumed by Hearle to be equal in both radial and circumferential directions,

E_{fa} is the fiber modulus in the axial direction, and

E_{ft} is the fiber modulus in the transverse directions,

μ_{at} is the Poisson's ratio of the fiber, i.e., the ratio of resultant axial strain to lateral strain.

In a later paper, Hearle and El-Behery [58] actually measured the ratio of transverse to applied pressure (where the applied pressure is lateral

$$\chi = \frac{3}{4} \cos^2 q [1 + (l/L)^2] - \frac{1}{2} [1 + \ln (l/L)] \quad (1.3.116)$$

$$g = \frac{3}{4} \cos^2 q [1 - (l/L)^2] + \frac{1}{2} \ln (l/L) \quad (1.3.117)$$

plotted in figure 1.3.37, where l , L are the filament lengths at radius r and R respectively. Hearle [45] then develops an expression for the mean normalized axial stress on the yarn resulting from an imposed small elastic axial yarn strain. This normalized mean axial stress is a useful quantity, for when it is multiplied by the axial stress which would occur in a parallel set of similar fibers and by the area (or count, depending on the units in which the modulus is expressed) it leads to a prediction of yarn tension for a given axial yarn strain. This same quantity equals the ratio of yarn axial tensile modulus to fiber tensile modulus. Hearle [7] provides a most useful table (his table 4.2) showing calculated yarn stress parameters for twisted systems with outside helix angles varying from 0 to 50° and with μ_{ta} varying from -0.25 to +0.50. The parameters calculated include the normalized axial fiber stress at the yarn center as well as the normalized transverse stress at the center, and also the mean normalized tension for $\mu_y = 0$ and 0.5 respectively. The simple parameter, $\cos^2 Q$, is seen to predict reasonably well the values which are obtained by the more sophisticated analyses at outside helix angles below 30°. Above 30° the predictions of $\cos^2 Q$ are increasingly in disagreement with the more rigorous analyses, with differences as high as 30 percent at 40° and over 50 percent at 50°.

Finally, it is worth noting the simplified expressions which have been derived for lateral pressures by others corresponding to eq (1.3.115,7). Machida [55], for example, used the typical free body diagram such as pictured in figure 1.3.36 to obtain the equation for force equilibrium in

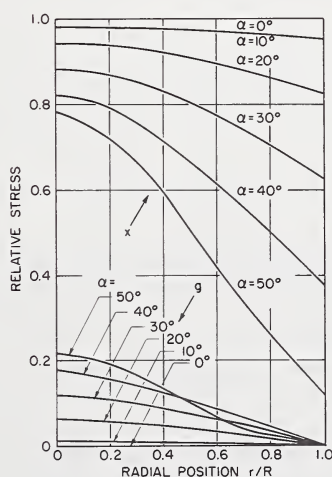


FIGURE 1.3.37. Variation of stress with radial position in yarn.

the radial direction. His basic relationship, obtained after neglecting higher order terms, was

$$\frac{\delta\sigma_t}{\partial r} = \frac{-E_{fa}\epsilon_y \cos^2 q \sin^2 q}{r} \quad (1.3.118)$$

which, when integrated, led to the following approximate expressions:

$$\sigma_{tr} = \sigma_{tc} \left[1 - \left(\frac{r^2}{R^2} \right) \right] \quad (1.3.119)$$

$$\sigma_{tc} = \frac{E_{fa}\epsilon_y \sin^2 Q}{2} \quad (1.3.120)$$

or

$$\sigma_{tr} = \frac{E_{fa}\epsilon_y \sin^2 Q}{2} \left[1 - \left(\frac{r}{R} \right)^2 \right] \quad (1.3.121)$$

where σ_{tr} is the lateral (radial) stress at radius r and σ_{tc} is the lateral pressure at the center of the yarn. Considering eq (1.3.104) and taking ϕ , the packing, as unity, we have:

$$\sigma_{tc} = 2\pi PT^2 \quad (1.3.122)$$

$$\sigma_{tr} = 2\pi PT^2 \left[1 - \left(\frac{r}{R} \right)^2 \right] \quad (1.3.123)$$

where P is the tensile load acting along the yarn axis and T is the yarn twist. Now the average pressure over the yarn is obtained from integration of:

$$\bar{\sigma}_t = \frac{1}{\pi R^2} \int_0^R \sigma_t 2\pi r dr \quad (1.3.124)$$

leading to:

$$\bar{\sigma}_t = \frac{\sigma_{tc}}{2} = \pi PT^2 \quad (1.3.124a)$$

Grosberg [56] derived eq (1.3.124a) along the way of predicting resistance to fiber slippage in a low twist sliver. Sullivan derived an expression similar to eq (1.3.122) but in his analysis the effective lateral pressure did not fall to zero at points close to the yarn surface.

It is interesting to note that multiplication of eq (1.3.117) by $E_{fa}\epsilon_y$ provides an expression for σ_{tr} which shares many of the characteristics of eq (1.3.121), as would be shown if one were to plot the parabolic drop in pressure from center to outside of the yarn. At the yarn center, eq (1.3.117) differs from eq (1.3.120) by the constant $3/4$ versus $1/2$. Yet it is useful to have the rule of thumb which states that for a given yarn

tensile strain ϵ_y and a given fiber modulus E_f , the average tension along the yarn axis will vary as the $\cos^2 Q$ and the average (or central) lateral pressure will vary as $\sin^2 Q$.

The Case with Large Extensions

Considering the fact that many yarns in commercial usage, particularly of synthetic fibers, have rupture strains between 15 and 30 percent, it would seem desirable that large extension analysis be introduced in studies of yarn breaking strength. On the other hand, one might question the importance of breaking strength as a quality parameter for textile materials. Certainly, in the case of conventional yarn usage, bending and mild tensile action often predominate, at strain levels of a few percent. Nonetheless, in matters relating to processing efficiency textile yarns are still judged on tensile strength qualities, among others, and the importance of the strength and rupture energy of tire cord is universally acknowledged.

Hearle [7] has derived more rigorous expressions for local fiber strains as a function of yarn tensile strain and yarn geometry. And he reports

$$\epsilon_{fa} = \epsilon_y (\cos^2 q_1 - \mu_y \sin^2 q_1) - \frac{3}{2} \epsilon_y^2 (1 + \mu_y)^2 \sin^2 q_1 \cos^2 q_1 \quad (1.3.125)$$

where q_1 is the local helix angle in the strained yarn, and μ_y is the contraction ratio of the yarn. Note that eqs (1.3.108) and (1.3.125) have the same first term. And if $\mu_y = 0$, this first term equals eq (1.3.100), for the case of no lateral contraction.

For constant volume deformation Hearle [7] derives:

$$\epsilon_{fa} = \epsilon_y (\cos^2 q_1 - \frac{1}{2} \sin^2 q_1) - 3\epsilon_y^2 \sin^2 q_1 (\cos^2 q_1 - \frac{1}{8} \sin^2 q_1) \quad (1.3.126)$$

and in his calculations for eqs (1.3.100), (1.3.108), (1.3.125), and (1.3.126) he shows that suitable accuracy is obtained in using eqs (1.3.100), and (1.3.108) up to 10 percent yarn extensions. But with yarn extensions of 30 percent it is reasonable to use eqs (1.3.125) and (1.3.126) above. Finally, he notes that the difference between use of $\mu_y = 0$ and the use, at high strains, of the more exact constant volume expression, is small except at strains of 30 percent and helix angles above 25° .

For the case of large extension, and lateral contraction, Hearle suggests substitution of eqs (1.3.125), and (1.3.126) in the equations for yarn force prediction, i.e., (1.3.99) through (1.3.104). And he normalizes the non-Hookean stress-strain curve:

$$\frac{\sigma_f}{\sigma_{fb}} = a' + b' \epsilon_f \quad (1.3.127)$$

where σ_{fb} is the rupture stress of the fiber. Then eq (1.3.127) is combined with eqs (1.3.125), (1.3.126), and (1.3.99) through (1.3.104) to obtain detailed expressions for yarn specific stress, normalized to fiber tenacity

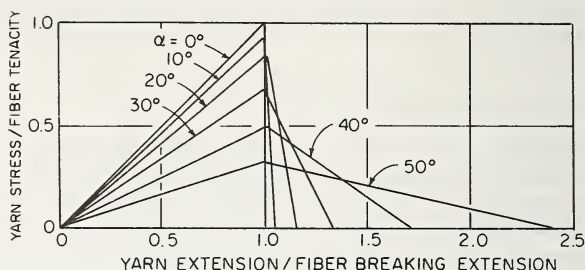


FIGURE 1.3.38. Theoretical stress-strain curves of yarns assuming Hooke's Law, and regarding broken regions as merely inoperative, after Hearle [7].

as a function of the stress-strain parameters a and b and the geometry of the yarn. Note, the yarn stress expressions furnished by Hearle for large extensions with lateral yarn contraction and non-Hookean behavior are equations for the stress-strain curves of the yarn up to the point of first fiber rupture, which Hearle states will occur at the centermost fiber at yarn strain, $\epsilon_y = \epsilon_{fb}$, the rupture strain of the fiber. Beyond this point, Hearle reasons, the yarn will rupture catastrophically or, if the broken regions are merely considered inoperative, the stress strain curve will sink linearly as shown in figure 1.3.38. Note that the above stress analysis has not been extended by Hearle to provide for the effect of transverse forces, although the latter combined problem is treated by energy methods.

There is, however, an interesting sidelight to the treatment of transverse pressure under conditions of large strains. It has been considered by Machida, and shows the introduction of eq (1.3.102) into the differential equation for lateral pressure, as well as for axial yarn tension. Solving for the center pressure, he obtains

$$\sigma_{tc} = \frac{a}{2} \ln (1 + \tan^2 Q) + \frac{b}{2} \epsilon_y (\sin^2 Q) \quad (1.3.128)$$

$$P = \frac{a}{4\pi T^2} \ln (1 + \tan^2 Q) + \frac{b\epsilon_y}{4\pi T^2} (\sin^2 Q) \quad (1.3.129)$$

hence

$$\sigma_c = 2\pi T^2 P \quad (1.3.122)$$

the same expression shown above to apply in the case of Hookean materials. But in treating the high end of the stress strain curve, one must take into account the effect of ϵ_y on T , the twist at a given yarn strain. If T_0 is the original yarn twist,

$$T = \frac{T_0}{1 + \epsilon_y} \quad (1.3.130)$$

whereupon for a yarn load elongation curve of

$$P = A + B\epsilon_y \quad (1.3.131)$$

substitution into eq (1.3.122), differentiating P with respect to ϵ_y and equating to 0 gives the ϵ_y at which σ_{tc} is maximum, which turns out to be

$$\text{for } \sigma_{tc} \text{ maximum, } \epsilon_y = 1 - 2\left(\frac{A}{B}\right) \quad (1.3.132)$$

Thus, for yarns with varying load elongation curves as in figure 1.3.39a, the central pressure versus yarn elongation curves will vary as in figure 1.3.39b, with maximum pressure occurring at $\epsilon_y = 0$ for case (4) and way off the graph to the right for $A = 0$. It is interesting to note that σ_{tc} has the same values at 25 percent strain since from figure 1.3.39a we note that all four load elongation curves converge at 25 percent strain.

Yarn Analysis using an Energy Method

Treloar and Riding [59] turned to one of the energy methods for the prediction of the load-extension relationship of a twisted yarn. There are three theorems related to elastic energy, as Den Hartog states [60]. theorems of "virtual work", of "Castigliano" and of "least work". Den Hartog points out that the theorem of virtual work is applicable to non-Hookean materials so long as no energy is dissipated in heat. Castigliano's theorem does not hold for nonlinear materials, nor does the theorem of least work. The theorem of virtual work states that "if an elastic body in equilibrium is given a small displacement or deformation, then the work done by all external forces acting on the body equals the increase in elastic energy U stored in the body." (For a recent review of energy methods, see Oravas and McLean [67].) Stated simply,

$$dU = P_n d\delta_n$$

or

$$\frac{\partial U}{\partial \delta_n} = P_n \quad (1.3.133)$$

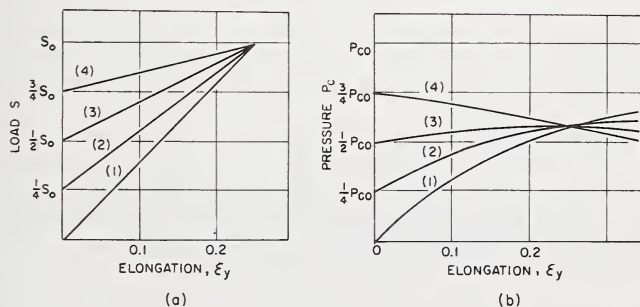


FIGURE 1.3.39. (a) Assumed load-elongation curves for different yarns. (b) Central pressure vs. yarn elongation curves.

where the elastic strain energy U is expressed entirely in terms of displacements δ of the body.

Treloar and Riding [59], using the method of virtual work, treat a filament material whose stress-strain properties are represented by the general function

$$\sigma_f = \psi(\lambda) \quad (1.3.134)$$

where σ_f is the force per unit original area along the fiber axis and λ is the extension ratio $l/l_o = 1 + \epsilon_f$. The work performed in stretching a unit of filament to λ_{fr} is

$$W_f = \int_1^{\lambda_{fr}} \psi(\lambda) d\lambda \quad (1.3.135)$$

which equals the elastic strain energy U stored in the unit volume. Now the increment of strain energy in the increment of yarn volume $2\pi r_o dr_o$ is

$$dU = 2\pi\phi r_o dr_o \int_1^{\lambda_{fr}} \psi(\lambda) d\lambda \quad (1.3.136)$$

where λ_{fr} is the filament extension ratio at the radius r , ϕ converts the increment of yarn volume to an increment of fiber volume and the radius, r_o , is measured in the unstrained condition. The total energy in a unit length (when unstrained) of yarn is then

$$U = 2\pi\phi \int_0^{R_o} \left[\int_0^{\lambda_{fr}} \psi(\lambda) d\lambda \right] r_o dr_o \quad (1.3.137)$$

Differentiating eq (1.3.137) with respect to the yarn axial extension ratio λ_y as in eq (1.3.133) should then provide the axial yarn force at any extension ratio, and as Treloar shows after some manipulation,

$$P = 2\pi\phi \int_0^{R_o} \psi(\lambda_{fr}) \frac{\partial \lambda_{fr}}{\partial \lambda_y} r_o dr_o \quad (1.3.138)$$

where $\psi(\lambda_{fr})$ is in units of stress based on the unstrained cross sectional area, i.e., nominal or engineering stress rather than true stress based on strained cross-sectional area.

Comparing eq (1.3.138) and Platt's eq (1.3.103), one is tempted to designate the quantity $(a + b\epsilon_y \cos^2 q)$ as equivalent to $\psi(\lambda_{fr})$ and the quantity $\cos^2 q$ as equivalent to $\delta\lambda_{fr}/\delta\lambda_y$, which they are if $\mu_y = 0$. But, for the case which takes lateral pressure into account and yarn volume is constant during straining (also ϕ , constant), Treloar shows

$$R^2 = R_o^2/\lambda_y \quad (1.3.139)$$

$$r^2 = r_o^2/\lambda_y \quad (1.3.140)$$

where R vs. R_o and r vs. r_o are the radial positions after and before yarn straining. In a yarn of unstrained unit length the length of a filament at helix angle q_{ro} is $\sec q_{ro}$ and the length of the corresponding filament in the strained state of the yarn (yarn extension ratio being λ_y) is $\lambda_y \sec q_r$. From eq (1.3.2) and eq (1.3.140), Treloar shows the filament extension ratio to be

$$\lambda_{fr} = \lambda_y \frac{\sec q_r}{\sec q_{ro}} = \lambda_y \frac{(1 + \lambda_y^{-3} \tan^2 q_{ro})}{(1 + \tan^2 q_{ro})} \quad (1.3.141)$$

Now, by definition,

$$\lambda = 1 + \epsilon \quad (1.3.142)$$

so Treloar substituted eq (1.3.142) in eq (1.3.141), expanded and retained only first order terms in ϵ to give

$$\epsilon_f = \epsilon_y \left(\frac{1 - \tan^2 q_o/2}{1 + \tan^2 q_o} \right) \quad (1.3.143)$$

where the quantity in the parentheses is seen to be the $\delta\lambda_{fr}/\delta\lambda_y$ of eq (1.3.138).

Now, for the case of small strains,

$$\psi(\lambda_f) = E_f(\lambda_f - 1) = E_f\epsilon_f \quad (1.3.144)$$

whereupon substituting eqs (1.3.144) and (1.3.143) into eq (1.3.138) Treloar reports the nominal average stress σ_y of the yarn (in g/denier of the unstressed yarn corresponding to the case where ψ and E are expressed in similar units).

$$\bar{\sigma}_y = E_f\epsilon_y \left[\frac{3}{4} \cos^2 Q - 3 \cot^2 Q \log \sec Q + \frac{1}{4} \right] \quad (1.3.145)$$

which is shown to be equivalent to Hearle, El Behery, and Thakur's [47] results as corrected [61] for the stress analysis at small strains, in which lateral pressure is taken into account. And Treloar shows that reductions of modulus at yarn twists "which are not too large" are about 50 percent greater on the above theory than in the case of Platt's theory.

Analyzing the Role of Fiber Uniformity

All of the tensile behavior analysis discussed in detail above was predicated on the constancy of fiber properties, both along each fiber and between fibers. However, some reference was made earlier to Platt's [50] treatment of the case in which fiber properties varied from fiber to fiber, and this section is intended to summarize the results of his analysis. But first we note that variable fiber behavior in tension may follow from variable fiber geometry, or from actual variation in specific local properties such as fiber modulus, or breaking stress, or breaking strain. And the source of variation may lie in differences between fibers,

each of which is uniform in geometry and properties along its length. Or, it may derive from variation along the length of each of the fibers. Chaikin [62] was concerned with the effect of nonuniform cross-sectional area (along a fiber length) on the stress-strain-time behavior of the fiber. This was the case of a series loading of a nonuniform specimen, whereas Platt's study was occupied with the case of parallel loading of fibers with properties varying from fiber to fiber.

Chaikin [62] showed that the strain over the entire length l_o subjected to load P is

$$\epsilon = \frac{l - l_o}{l_o} = \frac{1}{l_o} \int_0^{l_o} f\left(\frac{P}{A(z)}\right) dz \quad (1.3.146)$$

where z is the position along the fiber axis, $A(z)$ is the local cross-sectional area, and f is a known function.

Now,

$$\int_0^{l_o} dz = l_o$$

hence from eq (1.3.146)

$$\epsilon = \bar{f}\left(\frac{P}{A(z)}\right) \quad (1.3.147)$$

where \bar{f} is the mean value of $f\left(\frac{P}{A(z)}\right)$ over the length of the unstrained specimen. Chaikin goes on to indicate that for the strain-stress distribution with the form

$$\text{Strain} = B (\text{stress})^n \quad (1.3.148)$$

where B is constant and $n > 0$, the strain for the uniform specimen, ϵ_u , and the strain for the nonuniform cross section, ϵ_n , become:

$$\epsilon_u = BP^n \left[\frac{1}{\bar{A}(z)} \right]^n \quad (1.3.149)$$

$$\epsilon_{nu} = BP^n \left[\frac{1}{A(z)} \right]^n \quad (1.3.150)$$

and for the cases of a truncated cone whose end radii are in the ratio of 2 to 1 and a cylinder whose cross-sectional area is equivalent to that of the cone, the ratio of strains at a given axial load, P , is:

$$\frac{\epsilon_{nu}}{\epsilon_u} \simeq 2.5 \text{ for } n = 3; \quad \frac{\epsilon_{nu}}{\epsilon_u} \simeq 1.17 \text{ for } n = 1.$$

For the case where the cross-sectional area of the specimen is normally distributed with a mean \bar{A} and standard deviation, σ_A , and where the coefficient of variation σ_A/\bar{A} is 20 percent

$$\frac{\epsilon_{nu}}{\epsilon_u} = 1.33 \text{ for } n = 3; \quad \frac{\epsilon_{nu}}{\epsilon_u} = 1.04 \text{ for } n = 1.$$

Chaikin goes on to treat the effect of specimen nonuniformity on stress-strain properties of certain fibers, on the creep behavior under constant load, and on stress relaxation behavior at constant extension.

The case where variation in tensile behavior is noted from fiber to fiber was treated by Platt [24, 50]. His first case was that of variable property fibers subjected to tensile strain in parallel, without interaction between filaments. The bundle load, P_b , in such a case is simply the sum of the loads on individual fibers P_1, P_2, \dots, P_n , i.e.,

$$P_b = P_1 + P_2 + P_3, \dots, P_n \quad (1.3.151)$$

or

$$P_b = N_f \bar{P} \quad (1.3.152)$$

where N_f is the number of fibers and \bar{P} the average fiber load. Now, if all the fibers in the bundle had been tested independently for their individual load-elongation curves, it would be possible to calculate an average load \bar{P} for any given strain, ϵ_f , and by plotting \bar{P} against ϵ_f an average stress-strain curve could be obtained. If \bar{P} is calculated on the basis of the number of unbroken fibers at a given ϵ_f , it is possible to extend the average load extension curve over the entire range of strains. Likewise, if $(N_f n_u) = N_{fu}$, the number of unbroken fibers, is substituted in eq (1.3.152) and P is the average load on the unbroken fibers taken from the average load elongation curve, then eq (1.3.152) is valid in the region where fiber rupture is taking place.

The same data used to obtain the average load elongation curve for the fibers can be used to calculate average breaking load, average breaking elongation, and standard deviations of these parameters. The variation in breaking load can be attributed to variation in material properties or in fiber geometry (such as cross section). Since the case treated was for independent parallel filaments, Platt was concerned primarily with the variation encountered in fiber rupture strain. As indicated in section 1.3.3.1 above, he showed a normalized frequency distribution for fiber rupture elongations in figure 1.3.31, then drew a general curve (fig. 1.3.32a) of the percent unbroken fibers versus ϵ_f (from the cumulative distribution of broken fibers versus ϵ_f).

The following power series was used as an approximation to the curve of figure 1.3.32a:

$$n_u = 100(0.496 - 0.442t - 0.0979t^2) \quad (1.3.153)$$

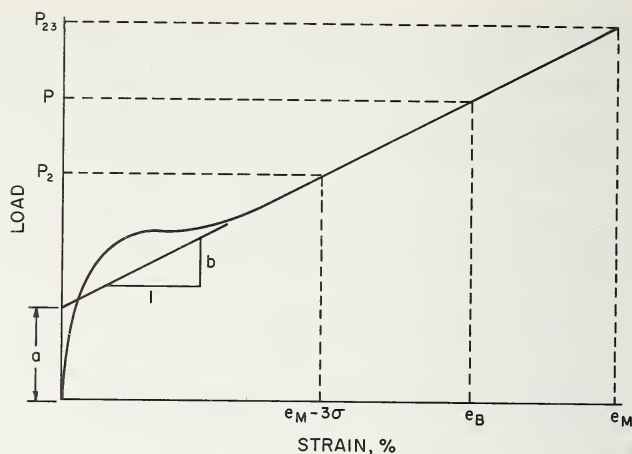


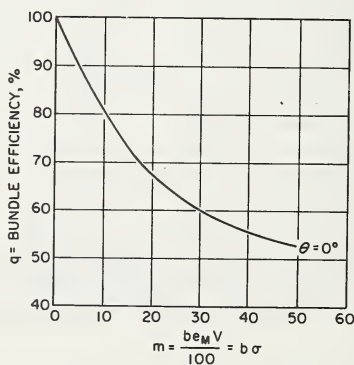
FIGURE 1.3.40. Average load strain curve, after Platt [50].

where t is the number of standard deviations of strain from the mean rupture strain (as plotted in figure 1.3.31). By definition, then,

$$\nu_\epsilon = (\sigma_\epsilon / \epsilon_m) 100, \quad (1.3.154)$$

$$t = \frac{\epsilon_b - \epsilon_m}{\sigma_\epsilon} \quad (1.3.155)$$

where ϵ_b is the elongation of the bundle, ϵ_m is the mean elongation to rupture in the fiber population and σ_ϵ is the standard deviation of the rupture strain of the fiber population. Since $(\sigma_\epsilon / \epsilon_m) 100$ is the coefficient of variation, ν_ϵ , of rupture strain of the fibers, it follows that eq (1.3.153)

FIGURE 1.3.41. Bundle efficiency vs. parameter $m = be_m V / 100$, after Platt [50].

can be expressed as a function of ϵ_b , ϵ_m and v_ϵ . Now rewriting eq (1.3.152) as

$$P_b = N_f n_u \bar{P} \quad (1.3.156)$$

and expressing n_u as a function of the above variables via eq (1.3.153) the load P_b is differentiated with respect to ϵ_b , the bundle strain, and the derivative set equal to zero. This permitted determination of the bundle strain ϵ_b at which the bundle load was maximum, and this value of ϵ_b was substituted into eq (1.3.156) to obtain the maximum value of P_b . The average load-elongation curve of figure 1.3.40 was expressed as

$$P = b \left(\frac{a}{b} + \epsilon_b \right) \quad (1.3.157)$$

which can be rewritten in terms of v_ϵ , ϵ_m , ϵ_b , and a/b , the ratio of intercept to slope. The results of the calculated maximum bundle loads expressed as a percent of the product of number of fibers and the average breaking load is plotted in figure 1.3.32b and reflects the efficiency of translation of average fiber strength into bundle strength. Platt [50] later shows that parallel bundle efficiency can be expressed in terms of a single parameter m , where

$$m = \frac{b\epsilon_m v_\epsilon}{100} = \frac{b\sigma_\epsilon}{100} \quad (1.3.158)$$

as plotted in figure 1.3.41. He points out that while this simple relationship applies only to the case of untwisted structures, nonetheless except for extreme cases of high twist and large changes in ϵ_m , a lower value of m indicates a better translational efficiency in any structure. Finally, a study is made of the effect of the shape of the elongation to rupture frequency curve compared to the results obtained with the Gaussian distribution of figure 1.3.31. It was found that considerable departure from normality of the distribution could be suffered with only small deviations in the number of unbroken fibers with increase in strain.

Basically, the above analyses had not been intended for treatment of twisted structures. Meanwhile, in the relationships expressed in eqs (1.3.103) and (1.3.104), Platt had assumed that "all fibers in the yarn are bearing load hence (they) are valid only for yarn elongations less than those necessary to cause the lowest elongation fiber to rupture. For these low elongations yarn characteristics such as modulus, extension, and energy absorption are independent of variability." To combine the statistical and geometric (twist) approaches, Platt modified eq (1.3.155) so that ϵ_b , the bundle strain, read $\epsilon_y \cos^2 q$, the strain of the fiber lying in the helix at radius r . Then, introducing this modification in eq (1.3.153) to give n'_u and using the linear fiber stress-strain relationship, $(a + b\epsilon_f)$, he rewrote eq (1.3.103) as

$$P = 2 \int_0^R \pi b \left(\frac{a}{b} + \epsilon_y \cos^2 q \right) \cos^2 q \frac{n'_u}{100} r dr \quad (1.3.159)$$

where n'_u is a function of ϵ_y , $\cos^2 q$, ϵ_m , and ν_ϵ . From eq (1.3.159) Platt determined specific maximum values of P for different values (a/b), ν_ϵ , and $Q(=\theta)$, and expressed them as a ratio of the average assembly strength when tested one component at a time. This ratio, as plotted in figure 1.3.42, is the strength efficiency of the yarn—combining the effects of yarn structure and component variability. It is worth noting that the effect of the stress-strain relationship, (a/b), is a dominant one when the mean rupture elongation is small ($\epsilon_m=2$ percent) as shown in figure 1.3.42a. This is true even when the fibers are perfectly uniform, i.e., $\nu_\epsilon=0$. But the a/b effect becomes less important at $\epsilon_m=10$ and 20 percent as shown in figures 1.3.42b, c. The variability effect, however, is shown as a major contributor to loss of yarn strength efficiency even at helix angles below 20° . For example, for c.v.'s of $\nu_\epsilon=10$ percent, the fibers with ϵ_m 's of 10 percent and 20 percent lose about 20 percent of their strength efficiency in low twist yarns, and for $\nu_\epsilon=20$ percent the loss exceeds 30 percent as seen in figures 1.3.42b, c, and d. The implication of these graphs is worth studying in any application of textile fibers, natural or synthetic, into mechanical systems.

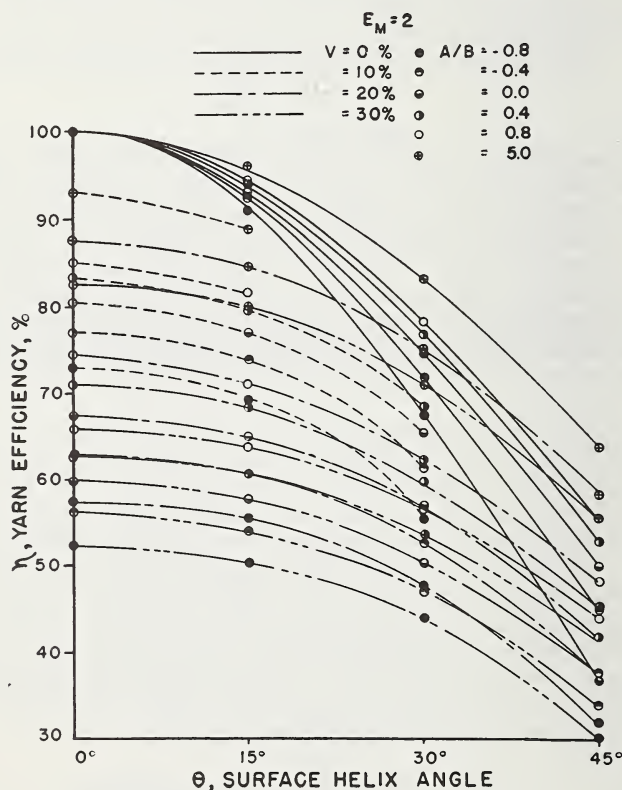
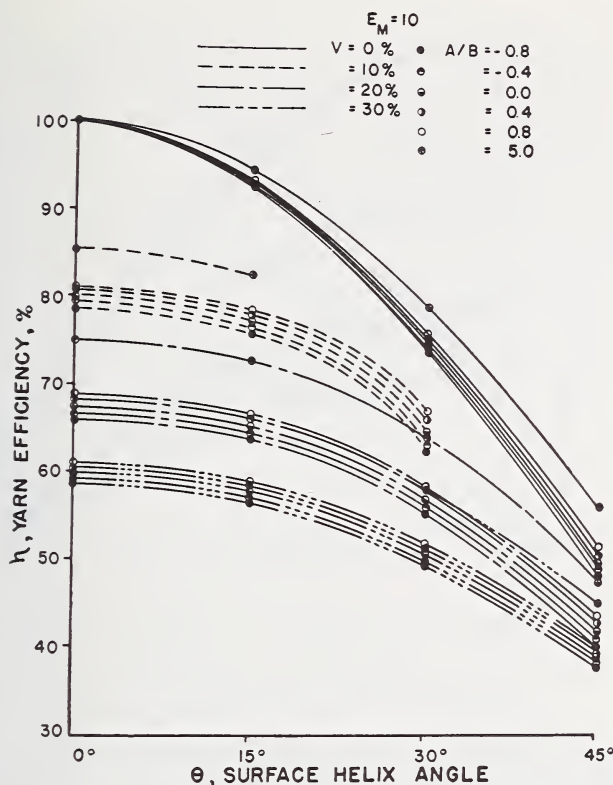
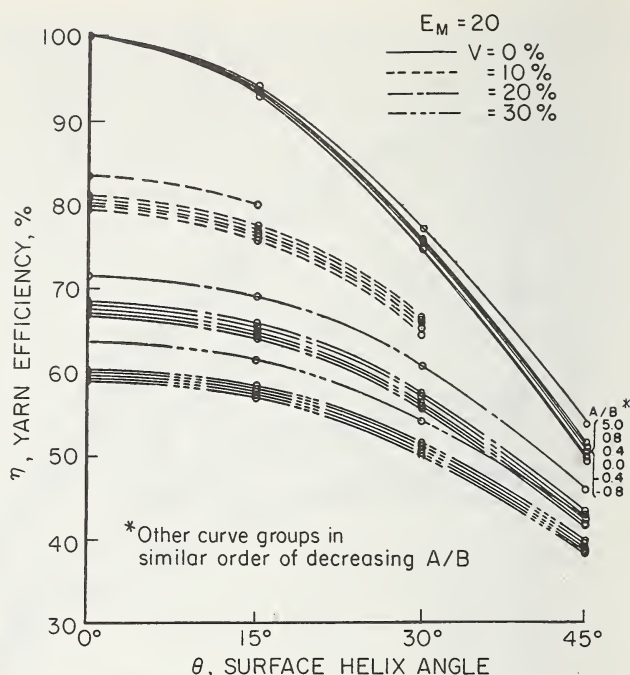


FIGURE 1.3.42a. Yarn efficiency vs. helix angle ($E_m=2$).

FIGURE 1.3.42b. Yarn efficiency vs. helix angle ($E_m = 10$).

The variability of mechanical properties along the length of a single fiber was the subject of Peirce's early studies [49] and the effect of the variability of a fiber's geometry along its length on the average mechanical properties of that fiber was treated by Chaikin [62] as discussed above. In contrast, Daniels [64], Rosen [65] and Scop and Argon [66] have considered the statistics of failure of fiber bundles. The latter two, working in the field of composite materials and laminates, have assumed a failure model based on a chain-link scheme. Scop [66] pictures the parallel bundle failure model as shown in figure 1.3.43, with N vertical sheets (or elements) and n horizontal links (or strips). If δ is the vertical length of each link, then for a model L in length, $n = L/\delta$.

Scop assumes that if a single vertical element (sheet or filament) breaks, its failure is limited to a very small region in the neighborhood of the break. Beyond this region, the vertical element is still useful for carrying its fraction of the load, as the glue sets up shear tractions along both sides of the sheet. The stress in the sheet thus increases from zero at the break and at some distance d on either side of the break it reaches its maximum value, equal to the average applied stress. Thus, the

FIGURE 1.3.42c. Yarn efficiency vs. helix angle ($E_m = 20$).

presence of the glue limits a single vertical element break to a region $\delta = 2d$. And δ is taken as the length of the link in the chain-link model. Clearly, rupture of the entire assembly does not occur when one vertical element or sheet breaks. It does not even occur when each of the elements has broken somewhere along its length, but only when each of the vertical components has broken at the same horizontal strip. (Thus the analysis does not allow for inclined propagation of a rupture, such as is often observed in yarns or in fabric structures.)

Scoop defines $\xi(\sigma)$ as the flaw stress distribution, equal to the number of cracks (or weak spots) per unit area (in a sheet of given thickness) with a strength $\leq \sigma$. In practice $\xi(\sigma)$ is determined by experiment. (For a yarn or a fiber, repeated tensile tests on a given length would do it, breaking the original, then the two broken segments, then four segments, etc. The curve $\xi(\sigma)$ vs. σ is obtained by integrating the strength frequency distribution curve for the yarn. This method assumes that a given rupture level is not affected by previous loadings. If it is, the strength distribution may be obtained by successive testing of many very small specimens.)

Knowing $\xi(\sigma)$ one may then determine the cumulative strength distribution $Q_s(\sigma)$ for individual sheets. This function has the form

$$Q_s(\sigma) = 1 - e^{-WL\xi(\sigma)} \quad (1.3.160a)$$

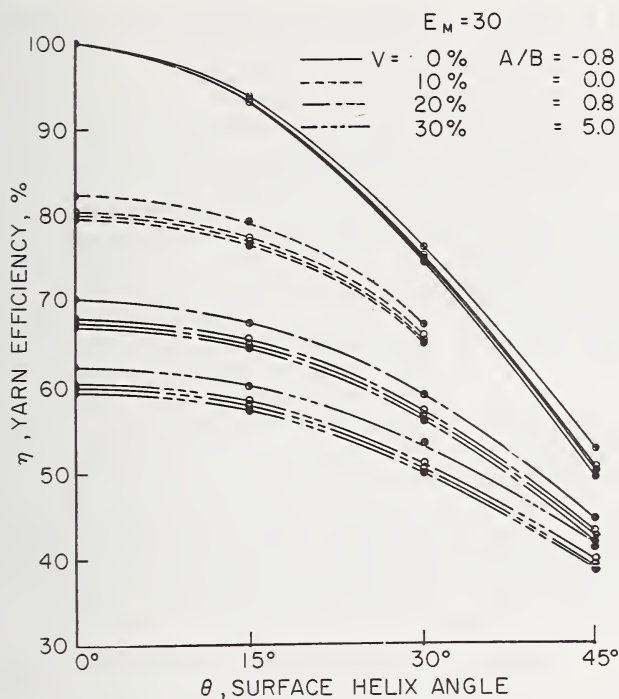
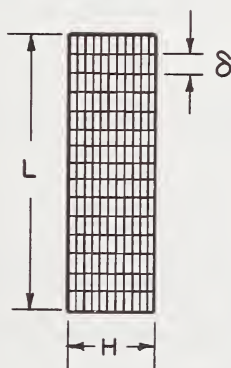

 FIGURE 1.3.42d. Yarn efficiency vs. helix angle ($E_m = 30$).


FIGURE 1.3.43. Failure model.

where W is the width of a sheet and L is its length. If a shorter length such as δ be substituted for L in the above equation, then $Q_s(\sigma)$ is the probability that a single sheet (or fiber) one link, δ , in length will fail when the local stress $\leq \sigma$. Now, consider a horizontal strip or link, δ in length, as shown in figure 1.3.43 which consists of N parallel segments,

δ in length. It remains to calculate the cumulative strength distribution $F(\sigma)$ for all the N elements in parallel in the link, δ . This is not a simple calculation, for one "must take into account all the possible ways that the N sheets can fail within the strip and compute the probability of failure in each of the failure modes. In statistical terms, each of the failure modes represents an event which is mutually exclusive so that $F(\sigma)$ equals the sum of the probabilities of failure in each of the failure modes." Scop shows that for N sheets in a strip δ long there are a total of 2^{N-1} possible failure modes. For the case of $N=3$ a simple example serves to illustrate the implications of the theory. At any given externally applied stress the local stress in each parallel element is σ_0 . If one of the three elements breaks, the stress, σ_1 , in the remaining two becomes $3/2\sigma_0 = \sigma_1$ and if two of the three elements are broken, the stress, σ_2 , in the third becomes $3\sigma_0 = \sigma_2$. The modes are then: (1) all three elements breaking at a stress $\leq \sigma_0$, which can happen in only one way; (2) two sheets break at a stress $\leq \sigma_0$ and the third sheet breaks between σ_0 and σ_2 , which event can happen three ways, i.e., with one each of the sheets possibly outlasting the σ_0 level; (3) one of the sheets fails at a stress $\leq \sigma_0$ and the remaining two fail at a stress between σ_0 and σ_1 , which event can happen three different ways; and (4) one of the sheets breaking below σ_0 , one between σ_1 and σ_2 , which event can happen $N!$ or six ways.

The probability $F(\sigma)$ that this single (bundle) link will fail at a stress $\leq \sigma_0$ is a function of $Q(\sigma_k)$, for the single (sheet) links, where

$$Q(\sigma_k) = 1 - e^{-\frac{wt}{\tau} \left(\frac{N}{N-k} \right) \sigma_0 \xi(\sigma_k)} \quad (1.3.160b)$$

Equation (1.3.160b) is obtained from eq (1.3.160b) by substituting δ for L and using the relationship between the local stress, the sheet thickness and the adhesive stress between sheets, i.e.

$$\delta\tau = \sigma t \quad (1.3.160c)$$

Finally, the stress redistribution factor is used to redefine σ_0 after the k th break among the N sheets

$$\sigma_k = \frac{N}{N-k} \sigma_0 \quad (1.3.160d)$$

and the value of $F(\sigma)$ for the given example becomes:

$$\begin{aligned} F(\sigma) = & Q^3(\sigma_0) + 3Q^2(\sigma_0)[Q(\sigma_2) - Q(\sigma_0)] \\ & + 3Q(\sigma_0)[Q(\sigma_1) - Q(\sigma_0)]^2 \\ & + 6Q(\sigma_0)[Q(\sigma_1) - Q(\sigma_0)][Q(\sigma_2) - Q(\sigma_1)] \end{aligned} \quad (1.3.160e)$$

reflecting the summation of probabilities of all possible modes of failure of the three sheets across the strip or (bundle) link δ in length.

Looking along the entire laminate, or bundle, one determines the

cumulative strength distribution function $G(\sigma)$

$$G(\sigma) = 1 - [1 - F(\sigma)]^n \quad (1.3.160f)$$

where n is the number of links in the chain. As Scop points out, $g(\sigma) = dG(\sigma)/d\sigma$ is the strength distribution function of the laminate, i.e., $g(\sigma)d\sigma$ is the probability that the laminate fails when the external stress lies between σ and $\sigma + d\sigma$.

It is emphasized that the above treatment assumes that when a single element is broken, its prebreak stress is distributed uniformly over the remaining parallel elements. The likelihood that this occurs in filament bundles is questionable and it may be expected that fibers in the neighborhood of the first break will suffer greater overloading than those far removed from the scene of the first rupture.

Scop and Argon [66] have carried the study further to allow for determination of a stress enhancement factor, K_r , (where the subscript r stands for the number of adjacent fractures to be bridged by the two bonding elements). And this factor was used to modify the stress levels in statistical determinations such as those described above. Modified stress levels for elements in the vicinity of the broken elements were calculated for two conditions; (1) the plastic matrix, and (2) the elastic matrix.

1.3.3.3. Experimental Observations of Singles Yarn Tensile Behavior

The validity of the geometric factor $\cos^2 Q$ as a basis for predicting translation of fiber properties into yarn properties was checked at an early stage. Tensile strength as predicted by eq (1.3.104) with the rupture strain of the fiber substituted for ϵ_y was shown by Platt to be in close agreement with experimental values as reported in figure 1.3.30. Likewise, the eq (1.3.107) prediction of the relative yarn tensile modulus, E_y/E_{fg} , was checked experimentally by Hearle [7] and found to give reasonable results over a range of twists as shown in figure 1.3.44, although it was clear that a more extensive analysis based on eqs (1.3.116) and (1.3.117) provided an improved correlation between theory and experiment. This latter analysis took into account the effect of lateral yarn pressure and Poisson contraction of both fiber and yarn. And for the cases plotted in figure 1.3.44, both fibers and yarns were assumed to deform with constant volume ($\mu_u = \mu_{ta} = 0$) which permitted simplification by Hearle of the expression for relative yarn modulus to

$$\frac{E_y}{E_f} = F(Q, \mu_{ta}, \mu_y) = \frac{1}{4} + \frac{9}{4} c^2 + \frac{3c^2}{(1-c^2)} \ln c \quad (1.3.161)$$

where c is $\cos Q$. Equation (1.3.161) plotted as the lower curve in figure 1.3.44 appears to be closer to the center of the data spread while eq (1.3.107) lies more or less along the upper bounds of the experimental results.

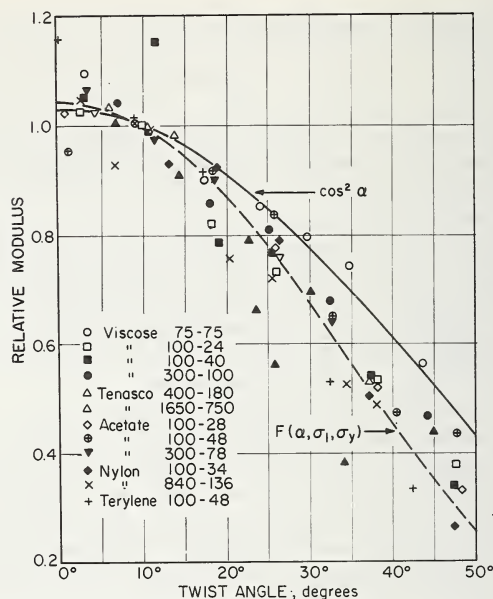


FIGURE 1.3.44. Comparison of experimental values of modulus with theoretical relations.

Hearle's [7] treatment of large extensions has been referred to briefly and his more rigorous expressions for strain have been reported in eqs (1.3.125) and (1.3.126). The approximation to the non-Hookean region of the fiber stress strain curves was given in eq (1.3.127) and these were developed to obtain expressions for normalized specific yarn stress as a function of fiber stress strain parameters a and b and of yarn geometry. Hearle's laboratory studies, however, led him to the conclusion that there is not very good quantitative experimental confirmation of his theories developed for large extensions.

It turns out that tensile tests over the full range of yarn extension can be best predicted by the energy method of Treloar as, for example, via eq (1.3.138). In testing a number of yarns, Treloar and Riding [59] and, later, Riding and Wilson [68] showed close agreement between eq (1.3.138) and experiment for high tenacity rayon (see fig. 1.3.45a), nylon (fig. 1.3.45b), low tenacity polyester (fig. 1.3.45c), high tenacity polyester (fig. 1.3.45d), triacetate and Teflon. (Their method required the knowledge of the geometric parameters of twist and yarn radius measured in the unstrained state of the yarn. Since R_0 was somewhat difficult to measure directly, it was calculated from yarn retraction during twisting, as previously done by Riding [23]). "It is found, however, that for Fortisan and high tenacity Terylene there is serious disagreement between experimental and calculated curves, for which there is no obvious explanation," according to Riding et al. [68], but a quick look at one of these "serious disagreements" for high tenacity polyester (in fig. 1.3.45d) shows that the discrepancies occur at $\tan Q$ (or α) values of .66 and .78.

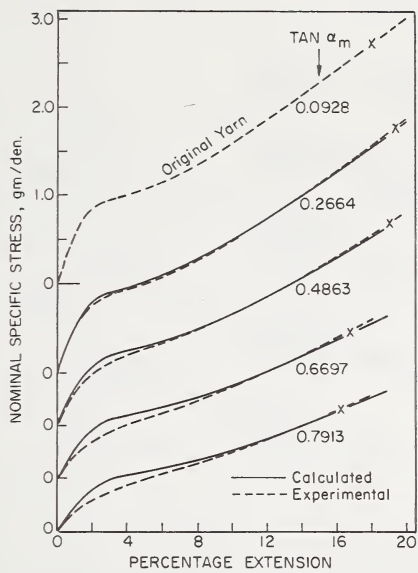


FIGURE 1.3.45a. Experimental and calculated stress-strain curves for yarns with various twists (represented by $\tan \alpha_m$).

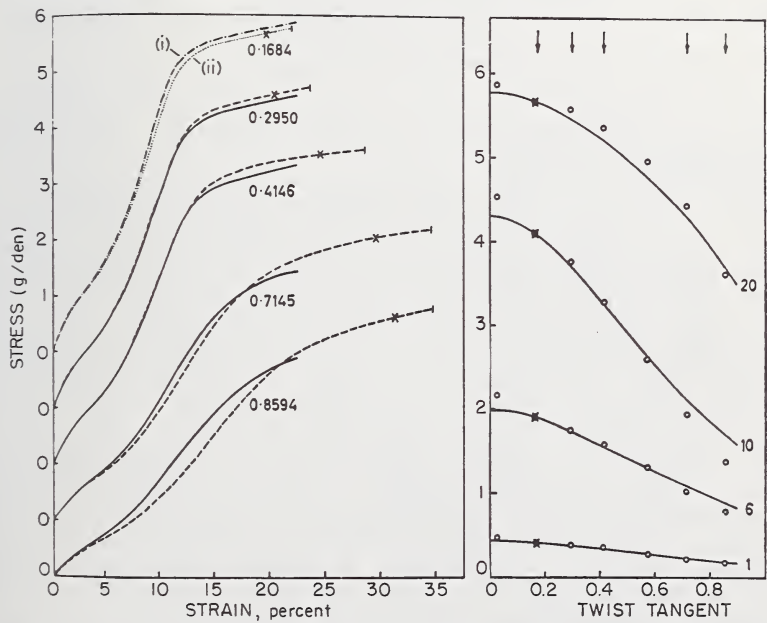


FIGURE 1.3.45b. Comparison of theoretical and experimental stress strain curves, after Riding and Wilson, 1965.

Numbers on curves are values of $\tan \alpha$.

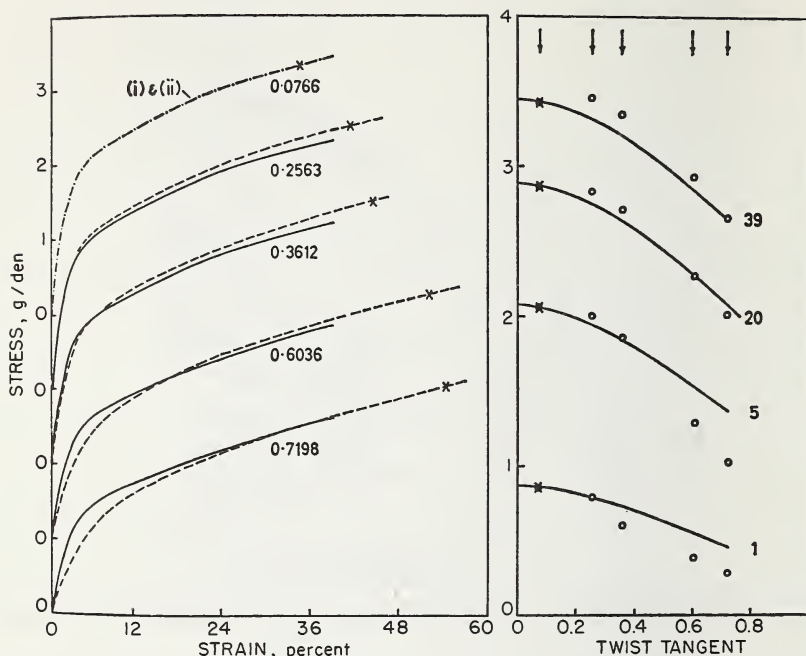


FIGURE 1.3.45c. Comparison of theoretical and experimental stress strain curves, after Riding and Wilson, 1965.

Numbers on curves are values of $\tan \alpha$.

At $\tan Q = .39$ and less, the agreement is quite good, i.e., at outside helix angles of 21° and less.

At this point it is worth referring to a few studies reported in the literature on experimental determination of fiber properties such as those required for the prediction of yarn tensile (and bending) behavior. While studies of fiber tensile properties, such as tensile modulus, breaking tenacity, breaking elongation and, indeed, the entire fiber stress strain curve, are too numerous to mention, published data on compressive moduli, and Poisson's ratio of textile fibers are limited. Backer [69] and Miles [70] measured the initial modulus of compression of nylon monofilaments. Some work has been reported on the tensile vs. compressive moduli of keratin, but most of the fiber studies as such have compared the tensile modulus with the bending modulus (in effect, a composite value relating to tensile and compressive moduli). A most useful report has been given by Elder [71] on the tensile, compressive, and also bending moduli of nylon, polyethylene, polypropylene, saran and polyester monofilaments. In general, Elder found that the initial modulus of these many monofilaments in tension, compression, and bending showed little variation, i.e., they were fairly constant in all deformation modes. The monofilaments which he tested were shown to be reasonably well oriented.

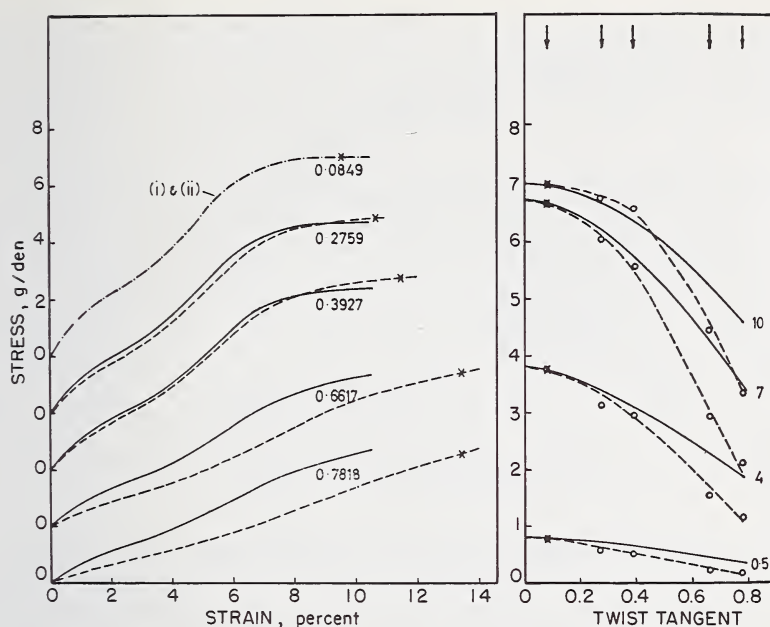


FIGURE 1.3.45d. Comparison of theoretical and experimental stress strain curves, after Riding and Wilson, 1965.

Numbers on curves are values of $\tan \alpha$.

There are also a few papers reporting tests of the Poisson's ratio of textile fibers. Higuchi and Takai [72] tested nylon 6 fishing line and found that the ratio was .385 to .386 for longitudinal strains up to 11 to 13 percent. Beyond that point, the Poisson's ratio goes as high as 0.446 at the rupture point. Frank and Ruoff [73] obtained the average of .392 as a Poisson's log ratio for nylon at a log strain of 6 percent. Their results may be considered in agreement with the above.

The prediction of twisted yarn properties relating to rupture is most difficult for a number of reasons. As has been pointed out above in the discussion on migration, the conditions of twisting significantly affect the degree of migration, the level of local strains during twisting, the extent of local filament recovery and/or buckling and the retraction of the yarn itself. Thus, one encounters a varying stress history from fiber to fiber within a given yarn structure, as well as a significant difference in local geometry for yarns which are nominally the same, i.e., with the same fiber composition, the same twist, and the same yarn count.

The simplest prediction of breaking strength is expressed in eq (1.3.104), based on the assumption of ideal yarn geometry (no migration) and all fibers at zero stress when $\epsilon_y = 0$. It is further assumed that the yarn will rupture completely when $\epsilon_y = \epsilon_{fr}$, where ϵ_{fr} is the fiber rupture strain. All of these assumptions are frequently observed to be violated, yet Platt shows excellent agreement between eq (1.3.104) and experiment in figure 1.3.30. And Hearle shows good agreement in figure

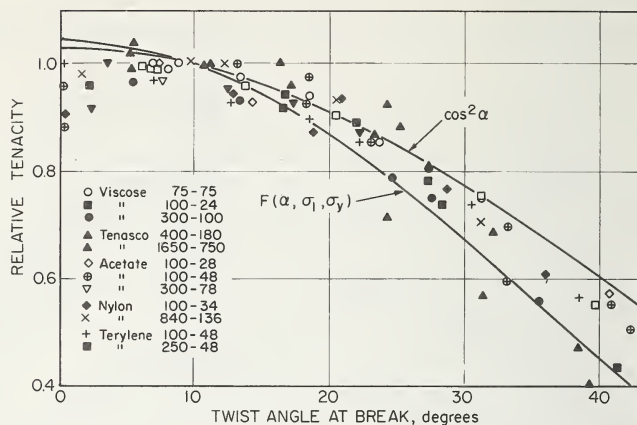


FIGURE 1.3.46. Comparison of experimental value of tenacity with theoretical expressions, modified from Hearle et al., 1961.

1.3.46, between measured relative tenacities and $\cos^2 Q$ as Q (or α) varies. But this time, a significant improvement in prediction of breaking strength is not observed as he uses eqs (1.3.116), (1.3.117), and (1.3.161), taking into account lateral yarn pressures and both fiber and yarn lateral contraction at constant volume. So, it appears that the simple model of yarn tensile behavior is very close to reality in a number of cases insofar as tensile strength of yarns is concerned. Yet it is worthwhile looking at other behavioral developments which follow from the simple model to see if these modes of behavior are frequently observed in practice.

First, the simple model and its fiber strain/yarn strain relationship of eq (1.3.100) suggest that when the yarn is extended, first fiber failure will take place at the yarn center, then rupture will take place in the fibers of the first ring about the center, the second ring, and so on. It is difficult to demonstrate this mode of rupture in a simple filament yarn, since, as Platt predicted, the twisted filament yarn tends to rupture precipitously once the first break takes place. Hearle [7], on the other hand, has shown that by varying yarn twist and the gage length of the yarn specimen being tested, he can arrest the process of rupturing mid-way. But detection of the specific mode of rupture initiation and propagation thereafter is difficult.

Backer, Monego and Machida [74] have shown the use of mechanical tracer elements as a means of studying rupture mechanisms in continuous filament twisted structures. They have worked with model plied structure, twisted under "no migration" conditions of 91 singles yarns. The bulk of the singles were 70/34 polyester filament yarns, and the tracer yarns were 79's cotton, dyed various colors for identification. Because of the low rupture elongation of the cotton (≈ 8 percent) compared to the 30-35 percent rupture elongation of the polyester, the cotton was prone to rupture at an early stage without leading to total

failure of the surrounding Dacron. The technique also permitted study of propagation of the rupture from cotton to cotton tracer, and even from cotton to polyester. And the tracers were used to confirm experimentally the distribution of strain and of lateral pressure through the twisted model as it was extended axially.

A fairly simple system was used to record the location and frequency of component breaks at each extension level for each gross model. A series of parallel lines was drawn in groups corresponding to the number of components in each ring of the model cross section. These lines are shown in figures 1.3.47*a-c*. Each group is arranged symmetrically about the center line or axis of the model. The lines were then numbered arbitrarily from right to left. Thus, each numbered line corresponds to a numbered position in the cross section of the model shown in figure 1.3.47*d*. It now becomes a simple matter to identify the location of the cotton component by numbering the appropriate cross sectional location as in figure 1.3.47*d*. The unmarked locations represent polyester yarn positions for the given specimen. In recording breaks in the component yarns, one places a horizontal mark on the appropriate line at a longitudinal position corresponding to the location of the actual break in the actual 8-inch gauge length. Six and often eight strain levels were used in the test program and break counts were made after each test. A few sample results follow.

Figure 1.3.47 shows data taken in tests of a 2-cotton/89-polyester component model with the cotton located at positions #8 and #52, as shown in figure 1.3.47*d*. The twist multiple was 2.19. After extension of the model yarn to the 11 percent level, component #52, located in the second ring from the core, evidenced five breaks in its 8-inch gauge length, while component #8 in the fifth or outer ring showed no breaks, as seen in figure 1.3.47*a*. (In another similar specimen examined after a 7 percent extension, the cotton yarn one ring from the core showed but three breaks.) When another specimen of the material containing cotton components #8 and #52 was extended to 15 percent, it evidenced 19 breaks in #52 and two breaks in #8, as shown in figure 1.3.47*b*. Figure 1.3.47*c*, representing the effects of 25 percent extension, shows the presence of 44 breaks in #52 and 13 in #8. These results and data taken from tests at other strains are plotted as (dotted and solid) vertical lines on the actual stress strain curve shown in figure 1.3.47*d*. Thus, figure 1.3.47*d* provides a complete history of rupture propagation superposed on the load elongation curve of the material, and permits the reader to judge the interaction between local rupture and total yarn resistance to further extension. Better examples of this interaction are given in figures 1.3.48-50, for figure 1.3.47*d* shows little effect of the rupture of only two cotton components on the overall load elongation behavior of the model. Rather, these two components have served, in effect, as mechanical tracers.

As mechanical tracers, components #52 and #8 show in figure 1.3.47 that the model yarn break does initiate in the more centrally located low elongation component. Secondly, they clearly illustrate the dependence of multiple break frequency on location, hence on local strain level and

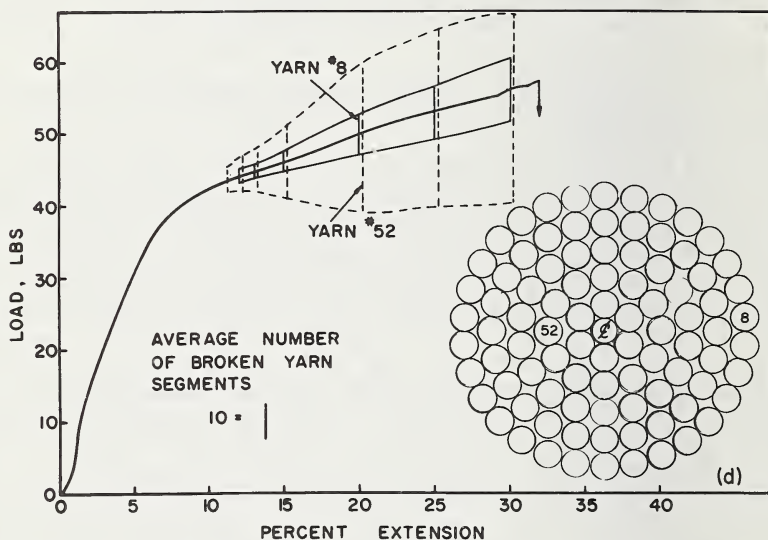
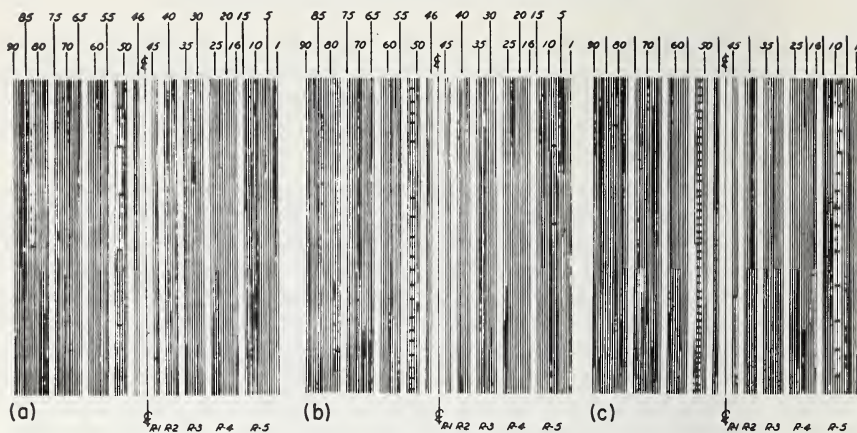


FIGURE 1.3.47. Diagram of break location in a 2-cotton/89-polyester component yarn model.

- (a) At 11% extension.
(b) At 15% extension.

- (c) At 25% extension.
(d) Composite plot of yarn load-elongation and break frequency.

on local pressures. For component #52 breaks in multiple before #8 breaks even once; further, #52 breaks far more frequently than #8 at all levels of model strain.

The presence of multiple breaks along a single cotton tracer illustrates the invalidity of the assumption that a broken fiber in a yarn ceases to contribute to yarn strength. For even though the cotton tracer fails a

few times (as did yarn #8 in figure 1.3.47b, it is subjected to the full level of the yarn strain at positions removed from the broken end. This buildup in local stress (or strain) from zero at the position of the break to the average yarn strain at a given radius, occurs through a frictional mechanism such that

$$\sigma_f = \mu \sigma_t l_s \quad (1.3.162a)$$

where σ_f is the fiber tension, μ the fiber coefficient of friction, σ_t the lateral force per unit fiber length and l_s the slip distance from the broken end. Thus, if σ_f equals the stress in the unaffected parts of the yarn, it is likely that yarn #8, for example, can rupture elsewhere as the yarn is further extended. And this is what we observe in figure 1.3.47c.

Now, if $\sigma_{f, \text{rup}}$ is the average rupture tension of the fiber (or tracer component), it follows that the minimum length into which the tracer element can be broken is

$$l_{\min} = 2\sigma_{f, \text{rup}} / \mu \sigma_{tr} \quad (1.3.162b)$$

For a fixed value of μ between the tracer element and the yarn matrix we will then expect that the frequency of breaks will be proportional to the local pressure in the yarn. Machida [55] used eqs (1.3.123) and (1.3.162) to calculate the minimum lengths of the tracer segments in such models as described above. The agreement which he found between the predicted minimum lengths and the measured lengths served to validate eqs (1.3.123) and (1.3.162) and underscore the importance of lateral stress transfer of load between ruptured elements in the yarn and the surrounding matrix.

The tracer yarn method is used with the expectation that rupture of the cotton will not affect the load elongation behavior of the remaining yarn. But the technique can be modified so that the proportion of the tracer element is increased to such an extent that the tracer participates in true rupture of the yarn. At this stage it is no longer a tracer, but a full fledged blend component. But even though the model system is now a blended one, it can provide mechanistic illustration for the single fiber twisted filament yarn. For now the low elongation fiber element can be considered to represent that portion of a uni-fibered yarn which was overstrained during twisting, either due to excessive overall spinning tension or due to restriction of the stress relieving mechanism of filament migration. With this application in mind, the range of examples becomes unlimited.

Take, first, the case of a low twist 40-cotton element model whose tensile behavior is shown in figure 1.3.48. One notices here that the initial rupture of the centrally located cotton components is soon propagated to many of the other cotton yarns in the same vicinity. And this failure concentration appears to loosen the model structure to the extent that the cotton contribution to yarn strength is lost. This is seen as a severe drop in load in the load-extension curve of figure 1.3.48d for the model (with a 2.17 twist multiple). Figures 1.3.48a-c shows the break history at 8 percent, 12 percent, and 30 percent extensions. The

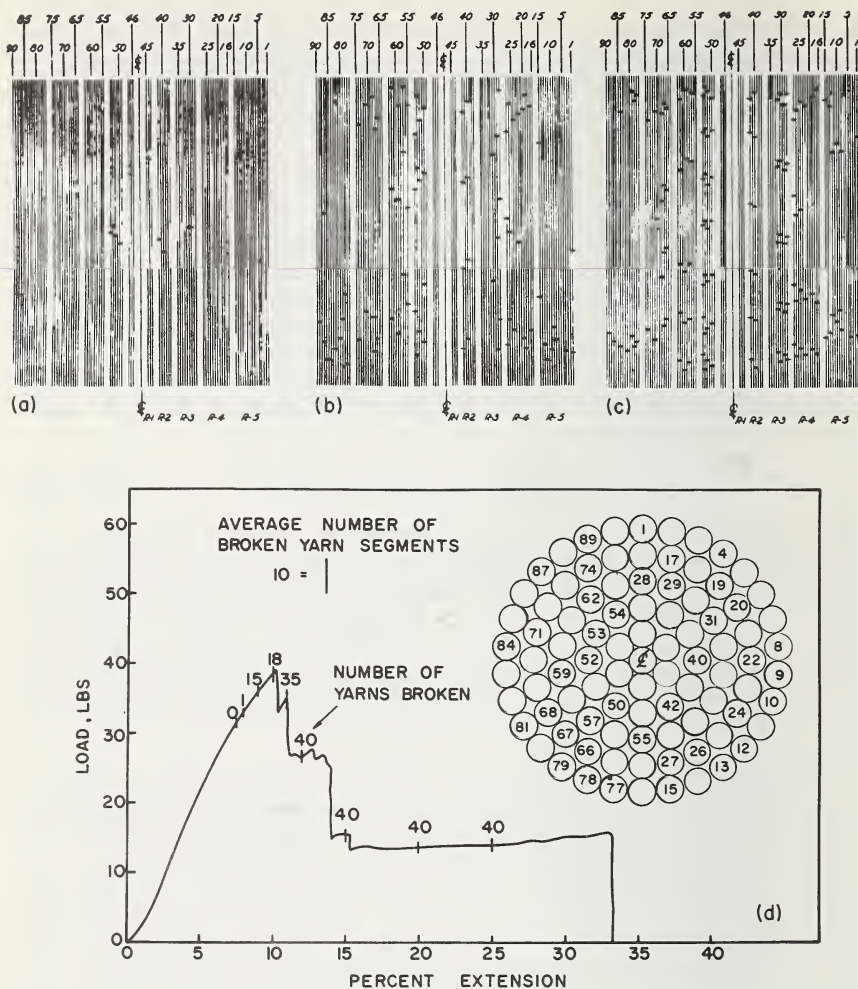


FIGURE 1.3.48. Diagram of break location for a low twist (2.17 TM) yarn with 40-cotton/49-polyester composition.

- (a) At 8% extension. (c) At 30% extension.
(b) At 12% extension. (d) Composite plot of yarn load-elongation and break frequency.

small number of breaks per yarn in figures 1.3.48c and 1.3.48d versus those shown in figures 1.3.47c and 1.3.47d for comparable model strains is significant; for it confirms the fact that the matrix of the 40-cotton component model of 2.17 twist multiple has loosened up upon initial rupture of its cotton elements and cannot grip them sufficiently to cause their breakage into shorter segments.

If the twist of the 40-cotton component model is increased from 2.17 to 3.26 twist multiple, the initiation of rupture of a few inner cotton

components is followed by rapid, concentrated, propagation of the break to most of the cotton yarns in that region. At this point, the load shed so precipitously by the cotton exceeds the additional load-bearing capacity of the polyester and the entire model fails in a manner characteristic of a 100 percent cotton model. The remaining elongation of the polyester is not realized, as is seen in figure 1.3.49*d*. The concentration of the break propagation is seen in figures 1.3.49*a-c* for extension steps of 11 percent, 12 percent and 13 percent.

In a case where extreme straining takes place in the outer fibers during twisting, resulting in their reduction in ϵ_{fr} , the model pictured in figure 1.3.50 is appropos—or the case where the central fibers were buckled, hence their effective ϵ_{fr} was increased. In figure 1.3.50 we note the

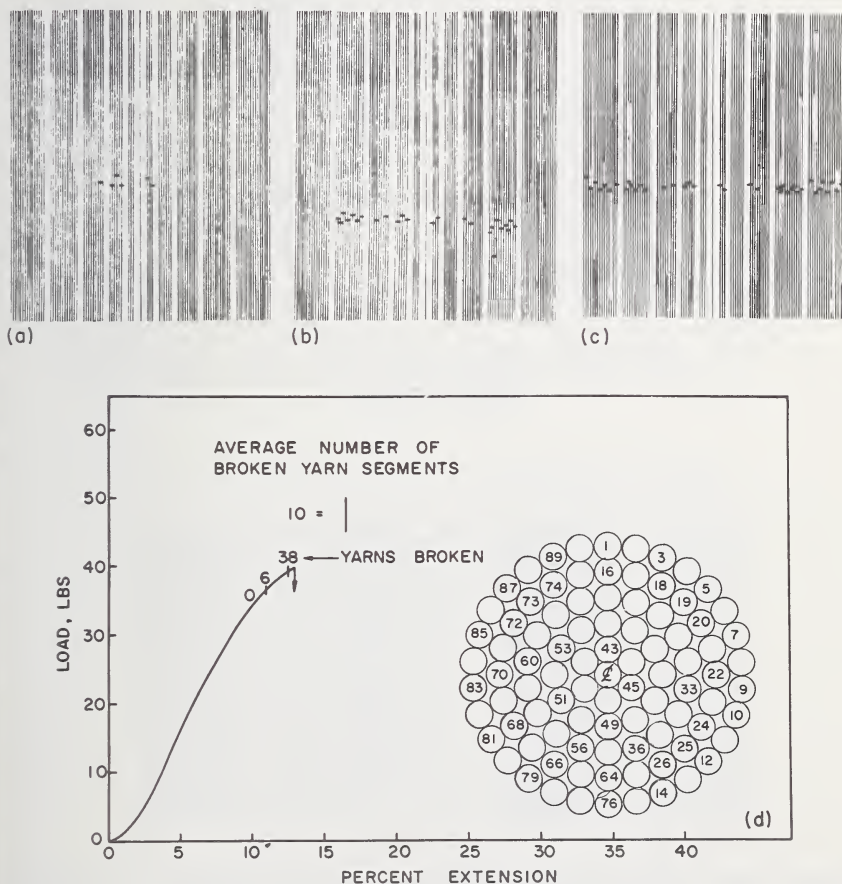


FIGURE 1.3.49. Diagram of break location for a medium twist (3.26 TM) yarn model with 40-cotton/49-polyester composition.

- (a) At 11% extension.
(b) At 12% extension.

- (c) At 13% extension.
(d) Composite plot of yarn load-elongation and break frequency.

low elongation fiber in the outer two rings and observe their early rupture at about 10 percent. But with their first rupture pictured in figure 1.3.50a, the lateral pressure in the cotton sheath was completely relieved and there was no further gripping to effect subsequent breakage. The result was a significant drop in tensile load of the model, and from the elongation of 10 to 33 percent, the model behaved like a 100 percent high elongation yarn of reduced size.

In still another case where the low elongation elements were located

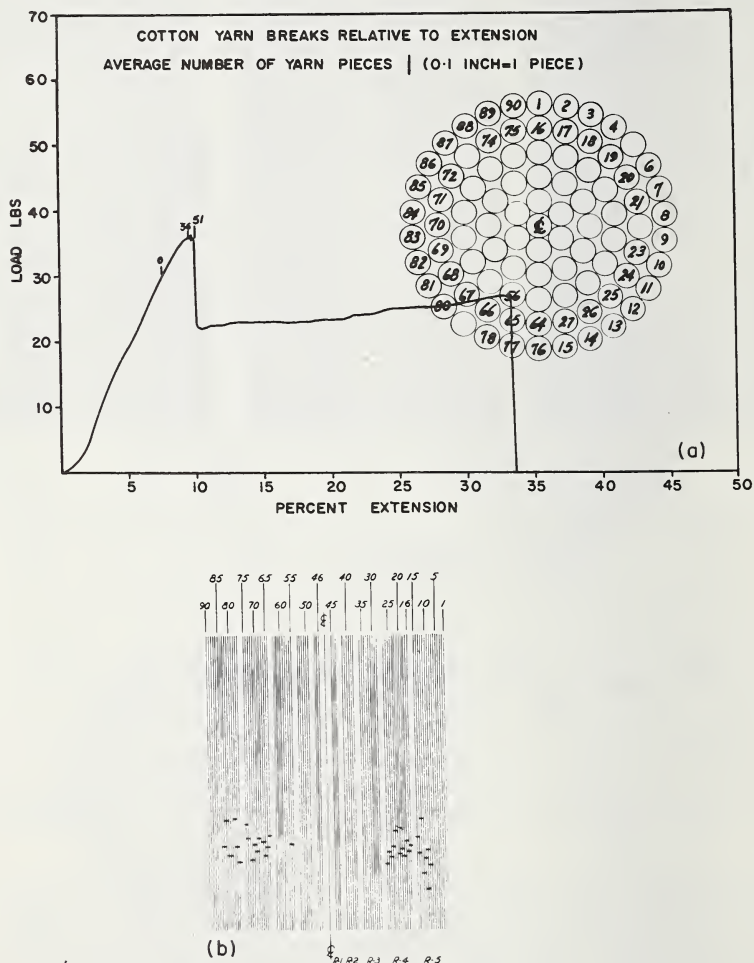


FIGURE 1.3.50. Diagram of break location for a cotton-dacron yarn model where extreme straining of the outer fibers was induced during twisting.

Composition 56% cotton, 44% dacron with 2.17 TM.

(a) Composite plot of yarn load-elongation and break frequency.

(b) Diagram of break location at 10% extension.

asymmetrically in the model structure of figure 1.3.51, the first rupture quickly spread to the adjacent regions of the cotton as seen in figure 1.3.51b. But the model's strain levels were not high enough to rupture the remaining high elongation (polyester) elements. Yet, the low elongation elements remained gripped in the high elongation matrix. As a result there was no major drop in the model tension at 10 percent extension, and the tension increased slightly as the model was extended further to 30 percent while the low elongation element was ruptured many times as seen in figure 1.3.51c.

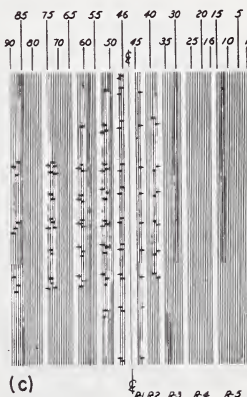
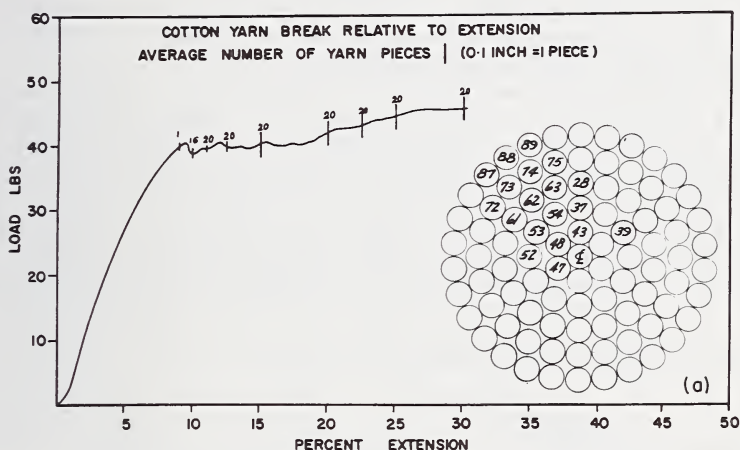


FIGURE 1.3.51. Break location for a 22% cotton-78% dacron yarn model with asymmetrically located low elongation elements. $TM=1.09$.

- (a) Composite plot of yarn load-elongation and break frequency.
- (b) Diagram of break location at 10% extension.
- (c) Diagram of break location at 15% extension.

Finally, it is shown in figure 1.3.52 that twist strongly influences the load transfer and rupture propagation and thus, by affecting component independence, it significantly affects the level of tensile strength, the reaching of (or failure to reach) full fiber extension potential, the overall shape of the stress strain curve and its general slope and, finally, the work to tensile rupture. Figure 1.3.52*a* shows the load elongation curves of the 100 percent Dacron model, 1.3.52*b* the 56/44 cotton/Dacron model, and 1.3.52*c* the 100 percent cotton model. It should be emphasized that the likelihood of multiple stage rupture (i.e., with sudden partial load relief during a constant elongation test) is increased at lower twists. But it is also increased as the elongations to rupture of the filament components differ either due to processing history or to original material selection and placement.

Hearle [7] reported test results on 100 den. nylon yarns at various twist levels and illustrates the occurrence of multiple filament breaks at zero twist levels, but at twists of 10 to 70 turns/inch, the ruptures were singular, sudden and "clean." He also showed the effect of sample gauge length on the shape of the stress strain curve and on the mode of rupture propagation. The transition from a complete to a partial sharp break is not only dependent on gauge length, but also on speed of jaw separation. And he observes that "the change from one mechanism to

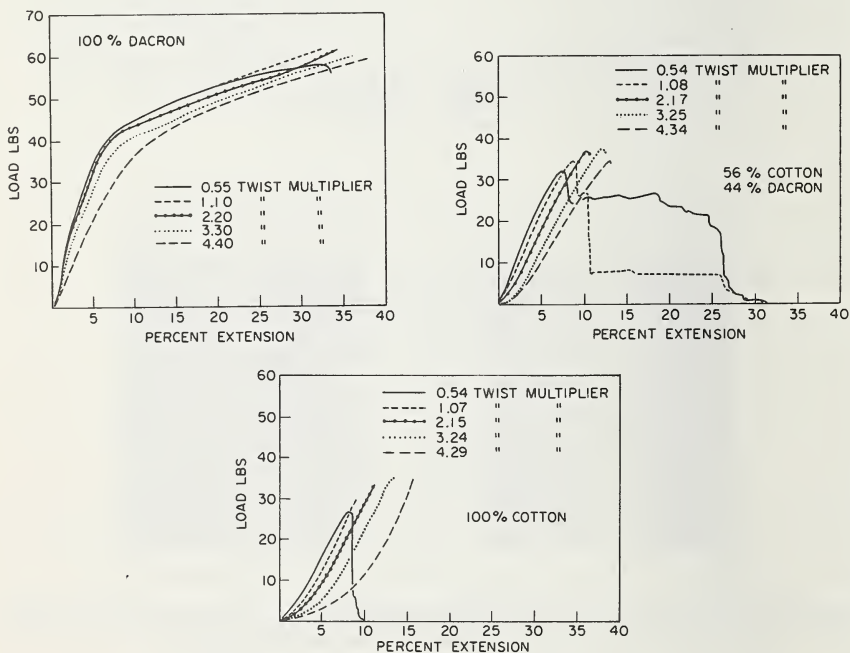


FIGURE 1.3.52. (a) Load-elongation curves for 100% dacron model yarn. (b) Load-elongation curves for 56% cotton/44% dacron model. (c) Load-elongation curves for 100% cotton model.

the other as the gauge length is altered is due to the amounts of elastic energy stored in the shorter specimen being less, and insufficient to complete the breakage. Similarly, in the slower tests, the stored elastic energy will have decreased due to stress relaxation."

Hearle [7] hypothesizes five modes of break propagation for the partial break phenomenon: (1) break starting at center, moving out symmetrically to stop partway through the yarn; (2) break starting at outside, then moving in symmetrically half-way; (3) break starting at center, then moving outward in one-half of the yarn; (4) break starting at one side only, in the outer ring, then moving in to the center; (5) break starting half-way out from the center at one point, then spreading over half the yarn. He then provides convincing mechanistic arguments as to twisting conditions and yarn structures which will cause these various modes to occur, and proceeds to relate the departure of yarn structure from the ideal model to the variation of yarn rupture behavior with twist. Specifically, consideration is given to the change in breaking extension with twist for various fibers, including viscose rayon, acetate, nylon and polyester. And the effects of filament buckling, twist-process fiber deformation, and migration on breaking elongation are analyzed. Finally, a report is given of the influence of twisting tensions and twisting machine types on yarn load-elongation properties.

The inescapable conclusion is that the properties of a yarn cannot be predicted solely from a knowledge of its fiber content, and yarn geometry, but that the complete processing history must be included.

1.3.3.4. Analysis of Tensile Behavior of Continuous Filament Plyed Yarns and Cords

Simple Fiber Tension and Idealized Geometry

Platt, Klein, and Hamburger have made significant contributions in the use of stress analysis for the prediction of tensile properties of ideal yarn geometries [43] and also in use of rupture statistics to predict the breaking strength of nonuniform fiber bundles and yarns [50]. Their studies were later extended to the cases of cordage strands and ropes [63] where the more complex geometry of plied yarns became an essential part of their analyses. Their later starting point was eq (1.3.159) which applies to the singles yarn, taking into account the translation of fiber strength into yarn strength on the basis of inherent fiber properties and yarn geometry. The factor n'_u accounts for the effect of fiber variability. It will be given consideration after the simple effects of geometry have been dealt with below.

Starting back with a simple structured plied yarn as pictured in figure 1.3.4c or 1.3.4f and figure 1.3.3, it is seen that the contribution of each singles yarn to the plied yarn load is

$$P_p = P_y \cos Q_p \quad (1.3.163)$$

where P_p is the tensile load along the plied yarn axis, P_y is the tensile

load along the singles yarn axis and Q_p is the helix angle of the plied yarn. For the plied yarn eq (1.3.2) is simple

$$\tan Q_p = 2\pi T_p R_p \quad (1.3.164)$$

where T_p is the ply yarn twist and R_p is the plied yarn helix radius (corresponding to r in figure 1.3.3). For the case of noncircular singles (as they lie in the plied yarn) Platt [63] defines R_p as the distance from the center of the plied yarn to the center of mass of the given singles yarn.

Platt then assumed the same expression to hold for the helix angle, α_{yp} , of any fiber in the singles yarn as it lies in the ply.

$$\tan \alpha_{yp} = 2\pi T_{yp} a_y \quad (1.3.165)$$

where T_{yp} is the number of turns per unit length of the singles as it lies in the ply, and a_y is the radius of the singles. Clearly, from eq (1.3.44a) we note that α_{yp} will vary from the side of the singles bend to the outside (that is as ϕ or $\lambda\theta$ varies), but Platt points out that the use of eq (1.3.165) over (1.3.44a) introduces negligible error in the results of the mechanical analysis.

A factor of more importance to the mechanical analysis is the creation of excess fiber lengths in the case where the plying twist works directly to reduce the number of turns in the singles yarn as it lies in the ply. (Of course, if the original twist direction of the singles yarn coincides with that of the ply twist, the local singles twist will be increased during plying. But the conventional twisting procedure, certainly for tire cords, is to use opposite singles and ply twists so as to effect torque balance, and this procedure will reduce the original singles twist.)

Since T_p is the ply turns per unit length of plied axis, then $T_p \cos Q_p$ is the ply turns per unit length of singles axis as it lies in the ply and eq (1.3.165) can be rewritten as

$$\tan \alpha_{yp} = 2\pi(T_{yo} - T_p \cos Q_p)a_y \quad (1.3.166)$$

where T_{yo} is the original turns per unit length of the original singles yarn. Remember that the original singles yarn helix angle α_{yo} is related to the original yarn twist, T_{yo} , via its tangent as per eq (1.3.165). Platt assumes that the change in singles twist during plying does not affect the singles axis length. Further, the fibers lying at the center of the singles have zero helix angle both before and after plying, hence their length remains constant. However, the helix length of a fiber lying at a local radius, a , and at an original singles helix angle of α_o , per unit length of the singles yarn axis, is

$$l_f = \frac{1}{\cos \alpha_o} = \left[1 + 4\pi^2 a^2 T_{yo}^2 \right]^{1/2} \quad (1.3.167)$$

and if the singles yarn has been formed with the simple ideal geometry (no migration and no local fiber average strains), it can be said that this

helix length l_f is equal to the unstrained length of that particular fiber. If, due to plying, the local helix angle changes as per eq (1.3.165) and the singles yarn axial length does not change, then the *helix path length* for that same fiber (of eq (1.3.167)), per unit length of singles yarn is $1/\cos \alpha$ or $\sqrt{1+4\pi^2 a^2 T_{yp}^2}$. The difference between the original fiber length and the new "in situ" helix length is the excess of fiber length, or crimp caused by the local untwisting of the singles during plying, which is seen to be the difference between the reciprocals of the singles helix angle cosines before and after plying.

Now let Δl_f be the total fiber *path* extension resulting from an extension Δl_y of the singles yarn axis. From eq (1.3.100) it follows that

$$\Delta l_f = \Delta l_y \cos \alpha \quad (1.3.168)$$

but only a portion of this fiber helical extension comes from actual load bearing extension $(\Delta l_f)_p$ of the fiber. The rest comes from taking up the fiber crimp, thus

$$(\Delta l_f)_p = \Delta l_f - l_y \left(\frac{1}{\cos \alpha_0} - \frac{1}{\cos \alpha} \right) \quad (1.3.169)$$

which can be expressed in terms of load bearing strain of the fiber $(\epsilon_f)_p$

$$(\epsilon_f)_p = \epsilon_y (\cos \alpha) (\cos \alpha_0) - \left(1 - \frac{\cos \alpha_0}{\cos \alpha} \right) \quad (1.3.170)$$

If the reader will check eq (1.3.159), it will be noted that $\epsilon_y \cos^2 q$ represents (in the reasoning leading to its derivation) the load bearing strain of the given fiber which, in terms of eq (1.3.170), is $(\epsilon_f)_p$. Thus, one may substitute $(\epsilon_f)_p$ of eq (1.3.170) for $\epsilon_y \cos^2 q$ of eq (1.3.159) to formulate an expression for the tensile resistance of the yarn, P_y , to a given yarn extension ϵ_y . And if ϵ_y of the singles equals $\epsilon_p \cos^2 Q_p$ of the plied yarn, then summation of the P_y 's from eqs (1.3.170) and (1.3.159) and use of eq (1.3.163) will allow calculation of plied yarn tensile resistance P_p to a plied yarn strain ϵ_p .

Because of the improbability of integrating eqs (1.3.159) and (1.3.170) Platt employed a piecewise summation to obtain approximate solutions for several specific cordage structures. He did this by dividing the singles yarn cross section into five parts by inscribing four circles with radii of $(a_y/5)$, $2(a_y/5)$, $3(a_y/5)$ and $4(a_y/5)$. Then for a given value of ϵ_y , he calculated $(\epsilon_f)_p$ for each ring from eq (1.3.170) and from eqs (1.3.165) and (1.3.166) determined α_0 and α for each ring. From the calculated value of $(\epsilon_f)_p$ and the fiber stress-strain curves, he calculated the axial load of the fibers in each ring (or in simplified form from eq (1.3.157)). And with knowledge of $(\epsilon_f)_p$, ϵ_m and ν_ϵ he used eq (1.3.153) to determine n_u , the fraction of unbroken fibers in each ring. Finally, he summed the axial tensile contributions of the fibers in each ring, to obtain the total tensile resistance of each singles yarn. This, in turn, was converted to plied yarn tension via eq (1.3.163). The entire pro-

cedure was then repeated at successively higher values of ϵ_p , until a maximum value of P_p was obtained. This maximum tensile resistance of the fiber assembly was divided by the product of the average strength of each fiber and the number of fibers to give the strength efficiency, as was done earlier for preparation of figure 1.3.42 for the original yarns.

If the excess fiber lengths occurring in the singles yarns as a result of plying are neglected, the strength efficiencies can be more easily determined for twisted singles and plied yarns of the "parallel bundle" type, i.e., wherein each single traces the same geometric path (as in the case of two-ply or three-ply structures). One need only apply the results of figures 1.3.42a-c, using eq (1.3.166) to convert values of T_{yo} and T_p to the surface helix angle, α_{yp} (or θ) of the singles yarn as it lies in the ply for entry into the graphs of the figure, then using $\cos Q_p$ to convert from singles efficiencies to ply yarn efficiencies. The results of these conversions are shown in figures 1.3.53a-d. The graphs express the theoretical yarn efficiency η as a function of $T_p a_y$ (or, as marked, $N_p R_y$). The curves plotted are for constant values of $(T_{yp} + T_p) a_y$ (indicated as $(N_{yp} + N_p) R_y$). Thus, one enters the graph at the product $T_p a_y$, then selects the desired $T_{yp} a_y$ and adds it to $T_p a_y$. This sum determines the proper curve intersection with the vertical at $T_p a_y$, and one reads off the resultant efficiency η at the intersection. For these calculations it has been assumed that there is no variability between rupture elongations of the singles yarns. However, the calculations do take into account the variation, V , in elongation at rupture of the individual fibers constituting the singles yarns. The a/b characteristic of the fiber stress-strain curve is also accounted for, along with the mean elongation to rupture of the fibers.

Checking the many assumptions in the above analyses, Platt et al. [63] show that the in situ singles-in-plied-yarn helix angles calculated from eq (1.3.165) are quite close to those calculated from the more rigorous equations of Chow [16]. The major percentage difference between the

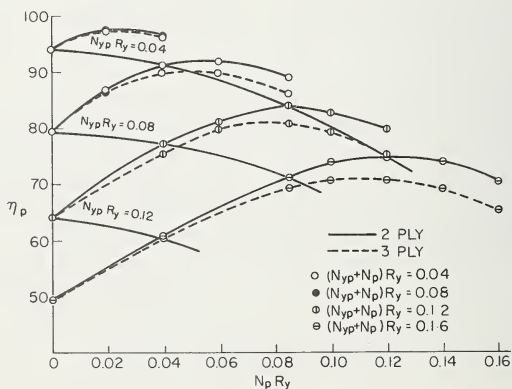


FIGURE 1.3.53a. Theoretical plied yarn efficiency. Yarn rupture elongation variability=0.

Fiber properties: $V=0$, $a/b=0$.

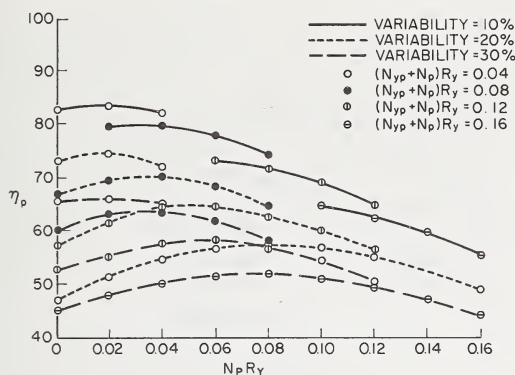


FIGURE 1.3.53b. *Theoretical three-ply yarn efficiency. Yarn rupture elongation variability = 0.*

Fiber properties: $a/b = 5$, $e_m = 10\%$.

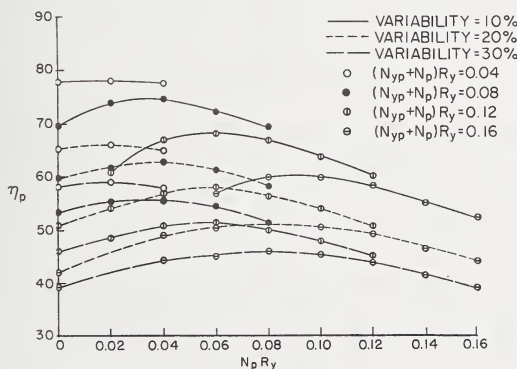


FIGURE 1.3.53c. *Theoretical three-ply yarn efficiency. Yarn rupture elongation variability = 0.*

Fiber properties: $a/b = 0$, $e_m = 10\%$.

two calculated values occurs at low values of α_{yp} where differences are of small importance. Further, these differences decrease as Q_p decreases. Platt [63] also compared the required path length of a fiber in a plied yarn per unit length of the plied yarn, l_{fp} , expressed as

$$l_{fp} = \frac{1}{(\cos Q_p) (\cos \alpha_{yp})} \quad (1.3.171)$$

with the corresponding Chow expression using Chow's more rigorous equation for α_{yp} , and Platt reports that the differences in calculated excess lengths are small over the range of practical singles and plied yarn twists.

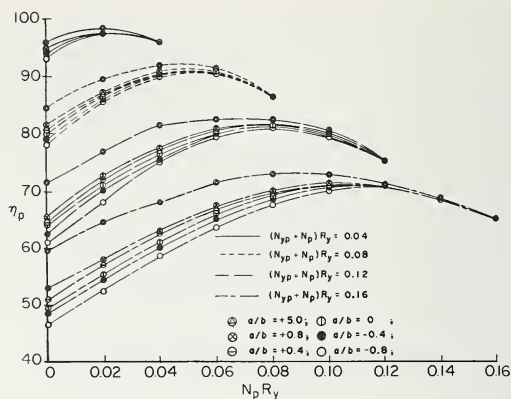


FIGURE 1.3.53d. *Theoretical three-ply yarn efficiency. Yarn rupture elongation variability = 0.*

Fiber properties: $V=0$, $e_m=5\%$.

Finally, Platt compared his simplified expression for fiber strain, ϵ_f ,

$$\epsilon_f = \epsilon_p \cos^2 Q_p \cos^2 \alpha_{yp} \quad (1.3.172)$$

with a more rigorous expression derived from Chow's analysis:

$$\epsilon'_f = \sqrt{\frac{(1 + \epsilon_p)^2 + \tan^2 Q_p}{1 + \tan^2 Q_p}} \times \frac{\sqrt{1 + \left[\frac{\tan \alpha}{1 + \epsilon_p \cos^2 Q_p} - \frac{a_y}{r_p} \frac{(1 + \epsilon_p) \tan Q_p}{(1 + \epsilon_p)^2 + \tan^2 Q_p} \right]^2}}{\sqrt{1 + \left[\tan \alpha - \frac{a_y}{r_p} \frac{\tan Q_p}{1 + \tan^2 Q_p} \right]^2}} - 1 \quad (1.3.173)$$

and found that values calculated from the two equations differ little in the ranges calculated. The values calculated via eq (1.3.172) represent average strains. It is interesting to note, however, that Chow's equations can be used to calculate local strains, within a single helix, as were calculated by Backer [80] in his study of local strains incurred during the bending of twisted yarns. Platt et al. shows that for a case of average helix strain of 7.5 percent calculated via eq (1.3.172) the local strains ranged from 4.7 at $\phi = \pi$ to 11.5 percent (at $\phi = 0$). It is worth recording their comments concerning the factors which tend to mitigate the severity of these local conditions.

"(1) If local differences in strain are admitted, then local differences in excess lengths must also be considered, and the high excess length regions occur just when high strain would be predicted, i.e., at $\phi = 0$;

(2) any freedom of motion of fibers whatsoever would tend to equalize strains, and some freedom of motion must exist; (3) any distortion of the yarn from circularity will tend to remove excess lengths, and by a direct extension of this reasoning it is easy to see that unequal strains along the length of a given fiber will cause an equalizing distortion. These distortions can occur either before or during the loading of the structure, or at both times. Distortions before loading can occur as the result of the presence of excess lengths. Such distortions tend to alter the local fiber radii of curvature considerably from that for circular yarns. The local strains are critically dependent upon local radii of curvature, whereas the average strains are not so dependent. Examples of distortion under loading, for a circular cross section yarn with no excess lengths, would be: (a) local flattening in the region of high fiber strain, (b) higher freedom of fiber relative motion in the region of low fiber strain, with the attendant opportunity of fiber length travel to the region of high fiber strain. Both mechanisms will equalize fiber strain. Thus, differences in local strain may safely be considered negligible, and the average values used."

Platt concludes from experimental strength and rupture elongation results "that large differences in strains do not exist, since large differences would produce much lower strand and rope efficiencies and elongations than those observed." Further comment on this point will be saved for discussion of experimental results on lubricated versus non-lubricated yarns in tension.

Paul [75] likewise used the stress analysis approach for prediction of tensile properties of yarns, twines and ropes possessing ideal geometry. In his survey of the literature in the mechanics of twisted structures he focusses on the differences between wire ropes, yarns and twines and fiber ropes. He treats the idealized three strand rope model, starting with the geometry of the strands before and after laying onto the rope structure and considers the influence of the laying process on strand twist (during which strand twist can be varied independently of rope twist during the laying process). He also considers the bending strains in rope twines after rope manufacture.

Paul then stretches the rope model theoretically and calculates local strand elongation as well as local rope twine elongation. He does consider the effect on local strains of lateral contraction during rope extension. The yarn force-strain diagram is then used to convert local strains to local forces. Then the sum of the axial components of yarn and strand forces provides the calculation of average rope tension at each level of rope elongation. His computations were conducted on a CDC 1600 computer. Paul carried out sufficient computations so as to predict the full load elongation curves of rope structures with various geometries, various material stress strain properties, and differing "foreturn" levels (in the rope laying process). He then calculated the theoretical breaking strength as that which occurred when the most highly strained components of the system reached their rupture elongation, as did Platt in his earlier paper [43].

In contrast to the more complex treatments used by Platt [50] [63]

and, later, by Paul [75] on plied yarn, cord, strand, and rope structures of "cordage fibers" and even wire, Symes [76] proposes a greatly simplified approach for nylon (continuous filament) tire cords. His theory does not assume any particular form of cord geometry. But, rather, on the basis of measured values of cord tex (count) and of filament properties, he predicts cord breaking load, extension at break, and contraction on heating. He focuses on the concept of average cosines-of-inclination-angles for the individual filament as it lies in the cord, and this permits significant simplification of the treatment—for it obviates the consideration of the singles yarn and its geometry. Symes' treatment follows (with his symbols converted, where possible, to those used earlier in this chapter):

- β_o = inclination of filament to the axis of the unstrained cord,
- β_s = inclination of filament to the axis of the strained cord,
- ϵ_f = tensile extension of filament (fractional),
- ϵ_c = tensile extension of cord (fractional),
- D_f = sum of filament counts (in tex),
- D_c = cord count (in tex),
- ϵ_{fc} = contraction of filament (from heating),
- ϵ_{cc} = contraction of cord (from heating),
- l_f = filament length,
- l_c = cord length.

Symes assumed that all filaments in the cord would behave alike, that all filaments have the same average inclination angle and are strained to the same degree in relationship to the cord strain. He further assumed, as did Platt above, that the strain along a given filament would be uniform, implying freedom of longitudinal slippage. Finally, he considered that no change in volume would take place during straining of the cord.

Considering a segment δl_f of the filament before straining, and its projection on the cord axis δl_c . Then

$$\delta l_c = \delta l_f \cos \beta_o \quad (1.3.174)$$

and the mean value of $\cos \beta_o$ is defined

$$\overline{\cos \beta_o} = \frac{\int \cos \beta_o dl_f}{\int dl_f} \quad (1.3.175)$$

$$\text{whence} \quad \overline{\cos \beta_o} = \frac{l_c}{l_f} = \frac{D_f}{D_c} \quad (1.3.176)$$

For the strained configuration eq (1.3.174) becomes

$$(1 + \epsilon_c) \delta l_c = (1 + \epsilon_f) \cos \beta_s \delta l_f \quad (1.3.177)$$

or

$$(1 + \epsilon_{tc}) \cos \beta_o = (1 + \epsilon_{tf}) \cos \beta_s \quad (1.3.178)$$

It remains to determine how β_o changes to β_s with cord strain ϵ_{tc} . If a short straight length of fiber, l_f , starts from the point A in figure 1.3.54

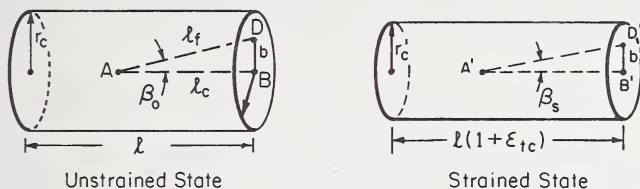


FIGURE 1.3.54. Assumed geometry of cord extension.

and goes to D , while AB is drawn so as to lie parallel to the cord axis (in the unstrained state), then for the strained state AD becomes $A'D'$ and AB becomes $A'B'$. The tangents of the angle β_o between AB and AD and angle β_s between $A'B'$ and $A'D'$ are

$$\tan \beta_o = \frac{b}{l_c}; \quad \tan \beta_s = \frac{b'}{l'_c(1 + \epsilon_{tc})} \quad (1.3.179)$$

where l_c is the length of cord axis corresponding to AB in the unstrained state. Now b' will relate to b as r'_c is to r_c , where r'_c is the radius of the strained cord and r_c that of the unstrained cord. From the assumption of constant volume

$$\pi l_c r_c^2 = \pi l'_c (1 + \epsilon_{tc}) r'_c{}^2 \quad (1.3.180)$$

or

$$\frac{r'_c}{r_c} = (1 + \epsilon_{tc})^{-1/2} = \frac{b'}{b} \quad (1.3.181)$$

and combining eqs (1.3.179) and (1.3.181) we obtain:

$$\tan \beta_s = \tan \beta_o (1 + \epsilon_{tc})^{-3/2} \quad (1.3.182)$$

which when combined with eq (1.3.178) gives:

$$\frac{(1 + \epsilon_{tf}) \cos \beta_s}{\cos \beta_o} = \left(\frac{\tan \beta_o}{\tan \beta_s} \right)^{2/3} \quad (1.3.183)$$

Equation (1.3.183) is rearranged to read:

$$\sin \beta_s \cos^{1/2} \beta_s = (1 + \epsilon_{tf})^{-3/2} \sin \beta_o \cos^{1/2} \beta_o \quad (1.3.184)$$

in which Symes has expanded the sines and cosines as power series

and multiplied them together. Then, neglecting cubes and higher powers, he shows

$$\beta_s = \beta_o (1 + \epsilon_{tf})^{-3/2} \quad (1.3.185)$$

which for ϵ_{tf} of 0.15 and $\beta_o \leq 0.75$ radians gives as error ≤ 3.5 percent when compared with eq (1.3.184). Substituting eq (1.3.185) in eq (1.3.178)

he obtains

$$(1 + \epsilon_{tc}) = (1 + \epsilon_{tf}) \{ \sec \beta_o \cos [\beta_o (1 + \epsilon_{tf})^{-3/2}] \}. \quad (1.3.186)$$

Equation (1.3.186) can be used directly to predict cord breaking strain if the value of filament breaking strain is substituted for ϵ_{tf} and if the bracketed function $\{ \}$ in eq (1.3.186) is a linear, or nearly linear, function of $\cos \beta_o$ for the β_o 's expected in the cord, thus permitting the use of $\cos \beta_o$ from eq (1.3.176). In terms of yarn count before and after twisting eq (1.3.186) becomes

$$(1 + \epsilon_{tc}) = (1 + \epsilon_{tf}) (D_c/D_f) \cos [(1 + \epsilon_{tf})^{-3/2} \cos^{-1} D_f/D_c] \quad (1.3.187)$$

For a case of thermal contraction in the cord, where ϵ_{cf} is the filament contraction or shrinkage and ϵ_{cc} the cord contraction,

$$(1 - \epsilon_{cc}) = (1 - \epsilon_{cf}) \sec \beta_o \cos [\beta_o (1 - \epsilon_{cf})^{-3/2}] \quad (1.3.188)$$

Symes considers that the contribution that an inclined tension loaded component makes to the cord is $P \cos \beta$. If $\overline{\cos \beta_s}$ is the average cosine of the angle of inclination of the filament at the instant at break, then the breaking strength of the cord is simply the breaking strength of the component yarns times $\overline{\cos \beta_s}$. Thus

$$P_{cr} = n_y P_{yr} \cos [\beta_o (1 + \epsilon_{tfr})^{-3/2}] \quad (1.3.189)$$

where ϵ_{tfr} is the rupture strain of the fiber and P_{cr} and P_{yr} are the breaking strengths of the cord and yarn component respectively. There are n_y yarn components. And since the \cos function in eq (1.3.189) is found to be very nearly linear in $\cos \beta_o$, it is reasonable to use $\overline{\cos \beta_o}$ obtained from eq (1.3.176). The strength efficiency η_c of the plied yarn or cord is the strength P_{cr} of the cord divided by the sum of the singles strength $n_y P_{yr}$, hence

$$\eta_c = \frac{P_{cr}}{n_y P_{yr}} = \cos [(1 + \epsilon_{tfr})^{-3/2} \cos^{-1} (D_f/D_c)] \quad (1.3.190)$$

Plied Yarn Analysis using an Energy Method

Treloar extended his earlier use of energy methods [59] in deriving the stress-strain properties of continuous filament yarns to the case of multi-

ply cords [77]. As he stated, the essential features of the theory were (1) "that it enables the whole of the stress strain curve of the twisted yarn to be predicted from a knowledge of the stress-strain curve of the filament material," (2) that its calculations based on strain energy of filaments in the whole structure, are simpler than for the case of stress-analysis, and (3) that its use of numerical methods permits direct use of the full stress-strain curve of the fiber without the need for simplification. This same approach was then applied to the somewhat more complex geometry of plied yarns and so-called tire cord structures with two, three, and seven components. The two- and three-ply structures correspond to Platt's [63] parallel bundle case and will be considered below. The seven-ply yarn, a special case with center yarn behaving differently than the six sheath yarns, has been treated by Treloar [77] and Platt, as well [63], but we will not consider it at this time.

Going back to the singles yarn analysis, using the energy method, we note in eq (1.3.138) that r_o represents the distance of a given filament from the singles yarn axis and $\delta\lambda_{fr}/\delta\lambda_y$ represents the change in filament extension ratio at r_o with change in yarn extension. Equation (1.3.138) reflects the force P required to extend the singles yarn axis to an extension ratio λ_y and was obtained by differentiating the total strain energy (per unit length of unstrained singles yarn) which developed in the yarn extended to λ_y , as expressed by U of eq (1.3.137).

If the tensile strain energy developed in the singles yarn as it lies in the plied yarn is indicated by U_{sp} and λ_{sp} is the extension ratio of that singles as the plied yarn is extended λ_p , then the expression corresponding to eq (1.3.138) for the tension in the singles, P_{sp} is:

$$P_{sp} = \frac{\delta U_{sp}}{\delta \lambda_{sp}} = 2\pi\phi \int_0^{R_{spo}} \psi(\lambda_{fr}) \frac{\delta \lambda_{fr}}{\delta \lambda_{sp}} r_o dr_o \quad (1.3.191)$$

where ϕ is the usual packing factor. Since U_{sp} is based on the unit length of the singles as it lies in the ply, the U_p , the strain energy per unit length of the plied yarn axis (i.e., tire cord axis) is simply

$$U_p = U_{so} \sec Q_{po} \quad (1.3.192)$$

(that is, for one of the singles components). The tension contribution of this one component along the plied yarn axis is then

$$P_p = \frac{dU_p}{d\lambda_p} = \sec Q_{po} \frac{dU_{sp}}{d\lambda_p} = \sec Q_{po} \frac{dU_{sp}}{d\lambda_{sp}} \frac{d\lambda_{sp}}{d\lambda_p} \quad (1.3.193)$$

Combining eqs (1.3.191) and (1.3.193) gives:

$$P_p = 2\pi\phi \sec Q_{po} \frac{d\lambda_{sp}}{d\lambda_p} \int_0^{R_{spo}} \psi(\lambda_{fr}) \frac{\delta \lambda_{fr}}{\delta \lambda_{sp}} r_o dr_o. \quad (1.3.194)$$

To complete the analysis it is necessary to express the quantities $d\lambda_{sp}/d\lambda_p$

and $\delta\lambda_{fr}/\delta\lambda_{sp}$ in terms of directly measurable parameters, as is done in the paragraphs to follow. Recall that the total plied yarn force at extension λ_p is obtained by multiplying eq (1.3.194) by the number of parallel structured components or plies.

Treloar assumed that extension of the singles in the plied yarn takes place at constant volume, hence

$$R_{sp} = R_{spo}/\lambda_{sp}^{1/2} \quad (1.3.195)$$

where R_{sp} is the radius of the extended singles as it lies in the plied yarn. For a two-ply yarn, the radius of the ply helix R_p would be R_{sp} and for a three-ply yarn, $2R_{sp}/\sqrt{3}$. This assumes no flattening of the singles during plying or during ply extension. Since, as is seen in figure 1.3.15, flattening is to be expected, the ply helix radius R_p is taken as an independent measurable parameter. It is assumed, however, that R_{sp}/R_p is independent of strain, i.e., the shape of the ply axis is unchanged during cord extension. Thus

$$R_p = R_{po}/\lambda_{sp}^{1/2} \quad (1.3.196)$$

Now

$$\tan Q_{po} = 2\pi R_{po} T_{po}, \quad (1.3.197)$$

and in the strained state

$$\tan Q_p = 2\pi R_p T_p = \frac{\tan Q_{po}}{\lambda_p \lambda_{sp}^{1/2}}. \quad (1.3.198)$$

The ratio of the strained singles yarn axis as it lies in the ply to the unstrained singles yarn as it lies in the ply is

$$\lambda_{sp} = \lambda_p \frac{\sec Q_p}{\sec Q_{po}} \quad (1.3.199)$$

and from the above it is shown that

$$\lambda_p^2 = \lambda_{sp}^2 \sec^2 Q_{po} - \frac{\tan^2 Q_{po}}{\lambda_{sp}} \quad (1.3.200)$$

By differentiation of eq (1.3.200) one can obtain $d\lambda_{sp}/d\lambda_p$, one of the key quantities required for solution of eq (1.3.194). It remains now to determine a suitable expression for $\delta\lambda_{fr}/\delta\lambda_{sp}$ in eq (1.3.194).

When a straight singles yarn with an original local twist, expressed in radians as $2\pi T_s$, is ply twisted into a multiple structure, its local twist as it lies in the ply must be corrected for the change in singles axis length (due to plying) and for the geometric torsion of its ply-helical path. These corrections are expressed simply as

$$2\pi T_{spo} = 2\pi T_{so} \frac{l_{so}}{l_{spo}} + \frac{\sin Q_{po} \cos Q_{po}}{R_{po}} \quad (1.3.201)$$

where the subscript o refers to the unstrained state. For the strained state

$$\begin{aligned} 2\pi T_{sp} &= 2\pi T_{so} \frac{l_{so}}{l_{sp}} + \frac{\sin Q_p \cos Q_p}{R_p} \\ &= \frac{2\pi T_{so} l_{so}}{\lambda_{sp} l_{spo}} + \frac{\sin Q_p \cos Q_p}{R_p} \end{aligned} \quad (1.3.202)$$

Making use of the above expressions Treloar showed the last term of eq (1.3.202) could be expressed as a function of Q_{po} , R_{po} , and λ_{sp} from which he showed

$$2\pi T_{yp} = \frac{1}{\lambda_{sp}} \left[\frac{2\pi T_{so} l_{so}}{l_{spo}} + \frac{\sin Q_{po}}{R_{po}} \left(1 - \frac{\sin^2 Q_{po}}{\lambda^3} \right)^{1/2} \right] \quad (1.3.203)$$

Now from eq (1.3.56) l_{so} is

$$l_{so} = \frac{2}{(2\pi T_{so})^2 R_s^2} \{ [1 + (2\pi T_s R_s)^2]^{1/2} - 1 \}. \quad (1.3.204)$$

He then showed that l_{spo} can be expressed in directly measurable parameters as:

$$l_{spo} = \frac{1}{u_1^2} [2 (1 + 2\pi T_{so} R_{so} l_{so} u_1 + u_1^2)^{1/2} - (2 + 2\pi T_{so} R_{so} l_{so} u_1)] \quad (1.3.205)$$

where

$$u_1 = \left(\frac{R_{so}}{R_{spo}} \right) \sin Q_{po} \cos Q_{po}. \quad (1.3.206)$$

Now we proceed further towards an expression for $\delta\lambda_{fr}/\delta\lambda_{sp}$, noting that in accordance with previous notations the local helix angle between filament axis and singles yarn axis as it lies in the ply is originally α_o and α for the strained state. Let S_o and S be the unstrained and strained length of a filament at a radius distance r (measured from the singles yarn axis). Then

$$S_o = \sec \alpha_o \quad (1.3.207)$$

$$S = \lambda_{sp} \sec \alpha \quad (1.3.208)$$

therefore the filament extension ratio λ_{fr} is

$$\lambda_{fr} = \lambda_p \frac{\sec \alpha}{\sec \alpha_o} \quad (1.3.209)$$

and from the constant volume assumption

$$R_{sp} = R_{spo}^2 / \lambda_p. \quad (1.3.210)$$

From the identities:

$$\sec^2 \alpha_o = 1 + 4\pi^2 T_{spo}^2 R_{spo}^2 \quad (1.3.211)$$

$$\sec^2 \alpha = 1 + 4\pi^2 T^2 R_{sp}^2 \quad (1.3.212)$$

and using eqs (1.3.201) and (1.3.203), Treloar obtains

$$\lambda_{fr}^2 = \lambda_{sp}^2 \frac{1 + \frac{R_{spo}^2}{\lambda_{sp}^3} \left[\frac{2\pi T_{so} l_{so}}{l_{sp}} + \frac{\sin Q_{po}}{R_{po}} \left(1 - \frac{\sin^2 Q_{po}}{\lambda_{sp}^3} \right) \right]}{1 + R_{spo}^2 \left[\frac{2\pi T_{so} l_{so}}{l_{sp}} + \frac{1}{R_{po}} \sin Q_p \cos Q_p \right]^2}. \quad (1.3.213)$$

From eq (1.3.213) one obtains $\delta \bar{\lambda}_{fr} / \delta \lambda_{sp}$ required for solution of eq (1.3.194). Treloar emphasizes that in the above treatment the curvature of the singles lying in the ply is taken into account in deriving values of the singles axial length in the ply and its helix torsion, but the effects of this curvature are omitted in derivation of filament strain.

Analysis of the Role of Singles Yarn Variability in Plied Yarn Mechanics

Platt et al. [63] point out that "variability of elongation to break among singles yarns in a plied yarn cannot, in general, be treated in the same manner as variability among fibers in a yarn." They present a method of predicting the effect of variability on the strength of small groups of fibers or yarns, and use the method to define the minimum size of a sample for which the large sample method developed earlier may be used. The method can be applied directly to cords and plied structures where all the components considered follow parallel (though helical) paths. Note that the ply helix angle serves as a geometric factor for strength efficiency calculations, but it does not enter in the statistical determinations.

Consider a population, say, of singles yarns each of which has a somewhat different stress strain behavior than the others. By testing the population one obtains a distribution of singles' elongation at rupture. Now, form a plied yarn from two or more of these singles and attempt to predict rupture behavior of the plied yarns. Clearly, the lowest elongation singles will govern the occurrence of the component break in the plied yarn, and it can be said with certainty "that the mean load for the first break in each component will also be very nearly the mean maximum load." It is therefore important that one knows the distribution of first unit breaks for various bundle or plied yarn sizes.

Platt [63] considered the population of singles with a mean rupture elongation \bar{l}_m and a normal distribution of elongations to break with a C.V. = V . He defined the probability of any unit breaking at an elongation in excess of the normalized extension t as

$$p = \frac{1}{2\pi} \int_t^{\infty} f(t) dt \quad (1.3.214)$$

where $f(t)$ is the relative frequency of break at (t) . Now h is defined as the relative frequency of 1st unit break at elongation t . If n parallel component units are strained to t , then the probability of having $n-1$ components unbroken is p^{n-1} . An the probability that the other component shall have just ruptured is $f(t)$, therefore for one rupture and no others at t , the probability, h , is

$$h = f(t)p^{n-1} \quad (1.3.215)$$

By assigning various values to t and using eqs (1.3.214) and (1.3.215) Platt was able to obtain the distribution of first unit breaks for various plied yarn sizes and these are plotted in figure 1.3.55a. The mean value for t in each of these curves is plotted versus n in figure 1.3.55b. This mean value is equivalent to an efficiency value, Platt points out, if one uses a linear approximation to the stress strain curve. That is, using the value of t from figure 1.3.55b, one may read off the load on the linear curve corresponding to the indicated t , then divide this by the mean breaking load of the components to give the strength efficiency of the plied yarn (still to be corrected for Q_p).

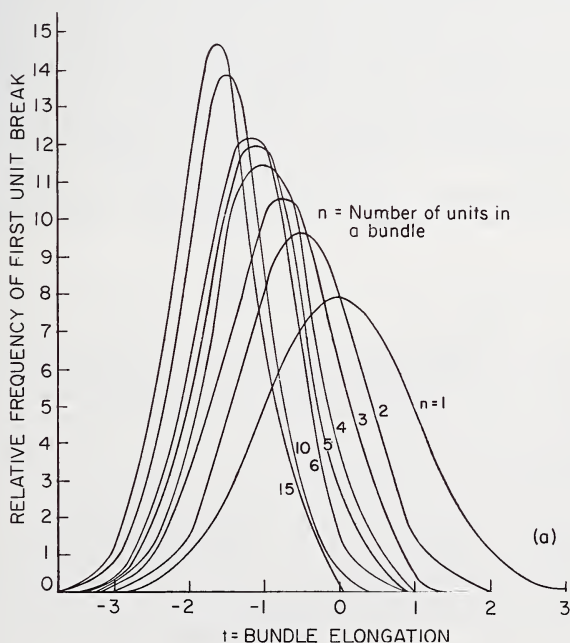


FIGURE 1.3.55a. Distribution of first unit rupture in a bundle vs. bundle elongation.

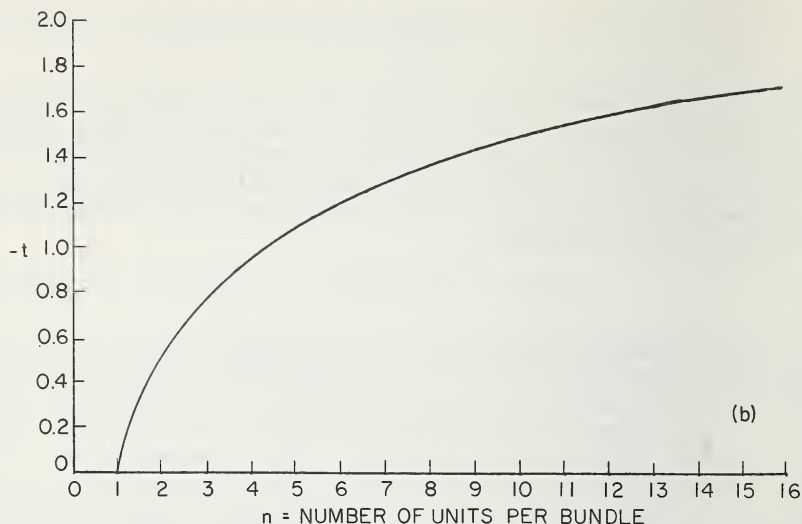


FIGURE 1.3.55b. Mean value of t vs. bundle size n for first unit break.

Platt uses various values of $m = b\sigma_\epsilon = b\epsilon_m V$ described earlier eq (1.3.158) together with the t values at first break in figure 1.3.55b to calculate efficiency versus bundle size for $m = 10, 20$, and 30 as shown in figure 1.3.56. Note the solid lines joining the crosses are the efficiencies to be expected for different sized "parallel" groups whose tensile resistance does not exceed the bundle load at the occurrence of first break. Note also the effect of b times σ_ϵ or of m on the shape of first break efficiency curves.

As long as the number of parallel components in the structure is small, there is a "very low probability of ever attaining a higher load than that

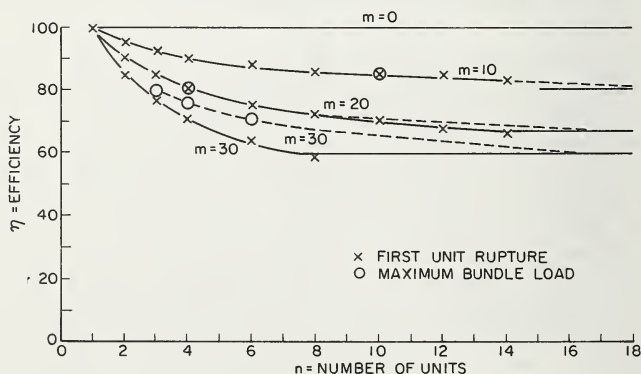


FIGURE 1.3.56. Yarn efficiency vs bundle size n .

reached when the first unit broke (except in cases of very high variability). Conversely, if n is very large, say 100, the maximum bundle load will almost certainly not be reached until several units have been ruptured." The factors defining attainment of maximum load in the latter case were formulated analytically by Platt et al. [63] as follows:

Assume that at extension t , the first of n units breaks and also that the load in the bundle never subsequently exceeds the level it reached at this instant, i.e., $ng(t_1)$, where $g(t_1)$ is the tension per unit at the strain t_1 . This means that the instant before the second unit breaks, $g(t_2)$, the maximum tension achievable in the unbroken units at strain t_2 is determined from the relationship $(n-1)g(t_2) = ng(t_1)$. And the limiting load, $g(t_3)$, at the occasion of the third break is $(n-2)g(t_3) = ng(t_1)$, etc. for t_4, t_5, \dots . Thus, if t_1 is selected arbitrarily and the average stress-strain function $g(t)$ is known, one can then calculate all t_i 's from the above relationships. It is also possible to treat the case where the maximum load occurs at the second break, or at the third break, etc., Platt's treatment is summarized below.

The probability of any unit breaking in the elongation interval t_{i-1} to t_i (where $t_0 = -\infty$) is:

$$p_i = \int_{t_{i-1}}^{t_i} f(t) dt = \frac{1}{2\pi} \int_{t_{i-1}}^{t_i} e^{-t^2/2} dt \quad (1.3.216)$$

where values of this definite integral are to be found in probability handbooks. For the case of maximum load occurring at the first break, it is desired to plot a curve of relative frequency versus t . This can then be done for maximum load at second break, etc. Towards this end $h(t)_l$ is defined as the relative frequency of occurrence of a maximum bundle load at t when the l th unit breaks at t . From probability theory, Platt points out, the probability of various combinations of events occurring in a total of n events is designated by the term

$$Ap_1^{q_1} p_2^{q_2} \dots p_n^{q_n} \quad (1.3.217)$$

where

$$\sum_{i=1}^n q_i = n \quad (1.3.218)$$

Here p_1 is the probability of event #1 (rupture of any unit between t_0 to t_1) occurring in a single test or run, p_2 is the independent probability that event #2 (rupture of any unit between t_1 and t_2) will occur in a single test. The exponents q_1, q_2 , etc. indicate how many times event #1 and event #2 occur in the particular combination of n events designated by eq (1.3.217). As stated, the numerical value of eq (1.3.217) is the probability of occurrence of that particular combination of q_1, q_2, \dots, q_n values. It is worth repeating that p_1 is the probability of a unit breaking in the strain interval t_0 to t_1 and p_2 , the probability of a unit breaking in the interval t_1 to t_2 , etc. The expression eq (1.3.217) is seen to be the individual terms in the expansion of

$$(p_1 + p_2 + \dots + p_n)^n \quad (1.3.219)$$

To determine $h(t)_1$, the relative frequency of occurrences of a maximum bundle load when the first unit breaks, one must multiply the relative frequency $f(t_1)$ of any unit breaking at t_1 by the "*probability of the existence of a breaking array among the remaining units such that the first break at t_1 is a maximum.*" A modification of eq (1.3.219) is necessary to deal with the breaking array among units remaining after the first unit has broken. The necessary expression is seen to be

$$(p_2 + p_3 + \dots + p_n)^{n-1} \quad (1.3.220)$$

and product is

$$h(t)_1 = Cf(t_1)(p_2 + p_3 + \dots + p_n)^{n-1} \quad (1.3.221)$$

where C is a normalizing constant such that the total probability is unity. It can be shown that certain terms of the expansion in eq (1.3.221) must be discarded to meet the conditions of having the load at first break be the maximum load as well. This restriction can be seen to be equivalent to the condition

$$\Sigma q_i > (k-1), \quad k=2, 3, \dots, n \quad (1.3.222)$$

In short, eq (1.3.222) specifies the "necessary and sufficient conditions such that each of the terms of the expansion satisfies the assumption of maximum bundle load being attained at first-unit break." Thus, to determine the $h(t)_1$ curve involves: (a) "selection of a series of arbitrary values of t_1 and the corresponding values of $f(t_1)$ "; (b) for each value of t_1 so chosen, the determination of the corresponding limiting values of t_2, t_3 , etc. from the $g(t)$ equalities previously described; (c) the determination of p_2, p_3 , etc. from the probability integral for each value of t_1 and its corresponding t_2, t_3 , etc."; (d) the evaluation of the expansion terms of eq (1.3.221) retaining only those in accordance with condition eq (1.3.222).

Platt suggests that the function $h(t)_1$ can be plotted as a curve of strength versus t_1 . The strength is the product of n (the total number of units in the bundle) and the load per unit $g(t_1)$. For the case where the load elongation curve of the units is a straight line passing through the origin,

$$g(t) = \frac{Vt}{100} + 1 \quad (1.3.223)$$

where $g(t)$ is expressed as a fraction of mean load per unit. The average \bar{t} is taken by inspection from the curve of $h(t)_1$ vs. t_1 leading to the average bundle load, $\bar{g}(t_1)$. Thus, the maximum bundle loads resulting from these average bundle loads of first unit ruptures is $ng(t_1)$.

In a similar way one formulates all values of $h(t)_l$ as shown for $l=2$ and 3:

$$h(t)_2 = Cf(t_2)(p_1 + p_3 + p_4 + \dots + p_n)^{n-1} \quad (1.3.224)$$

$$q_1 = 1; \sum_{i=3}^k q_i \geq (k-2), \quad k = 3, 4, \dots, n \quad (1.3.225)$$

$$h(t)_3 = Cf(t_3)(p_1 + p_2 + p_4 + p_5 + \dots + p_n)^{n-1} \quad (1.3.226)$$

$$q_1 = 0; q_1 + q_2 = 2; \sum_{i=4}^k q_i \geq k-3 \quad k = 4, 5, \dots, n. \quad (1.3.227)$$

Values of $h(t)_1$ and $h(t)_2$ can be plotted as curves of frequency vs. bundle break as done in figure 1.3.57. The strength here is the product of the number of intact units times the appropriate $g(\bar{t})$. Thus, for first break maximum, then second break, then third break maxima, we have:

$$\overline{ng(t_1)}; (n-1)\overline{g(t_2)}; (n-2)\overline{g(t_3)}, \text{ etc.} \quad (1.3.228)$$

Taking \bar{t}_1 and \bar{t}_2 from curves as in figure 1.3.57 and using eq (1.3.223) where V is given, one calculates a weighted mean breaking strength of the bundle where each unit breaking load (first unit break maximum, second unit break maximum, etc.) is weighted by the relative area of its $h(t)_i$ curve and by the number of units as yet unbroken. The areas under each of the $h(t)$ curves representing the relative number of all bundle breaks which produce maximum load at first break, at second unit break, etc. The sum of the areas is then the total number of breaks.

Dividing the weighted mean breaking load of the bundle by the mean strength of the individual units times the number of units, n , is normally the procedure for determining the breaking efficiency of the bundle.

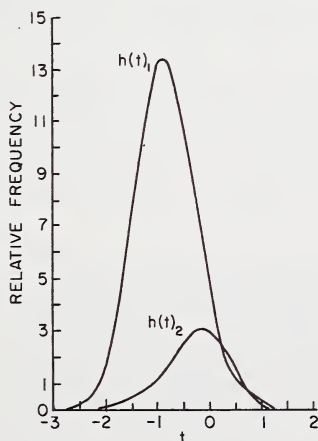


FIGURE 1.3.57. Relative frequency of maximum bundle load vs. t , for $n=4$, $m=20$.

But in the procedure described above the $g(t)$ according to eq (1.3.223) is the fraction of mean load per unit, hence the efficiency concept is introduced automatically.

The bundle breaking efficiencies have been calculated by Platt et al. for different values of n and m according to the above procedure and plotted in figure 1.3.56. The calculations were first based on first unit break values, then on maximum bundle loads. It is seen that as n becomes smaller, the efficiency can be best characterized by the first unit break efficiency. As n reaches about 15 an infinite sample can be assumed insofar as these calculations are concerned.

Finally, we point to the similarity of the approach taken by Platt [63] and later by Scop [66] in considering the probabilities of rupture in succeeding units following failure of the first unit, i.e., the similarity of eq (1.3.160e) and eq (1.3.217). Yet there were differences, one treating load transfer, the other strain variation. It is clear that Scop went beyond considering the initial break and its subsequent lateral propagation to occur in one chain link comprised of many parallel units. For he also treated the probability of rupture of other links in the system. In short, in Scop's system, the failure of a single parallel unit at one link did not rule out its strength contribution at another link location above or below the original location. In Platt's analysis, a single unit break ruled out any subsequent contribution by that unit. As we know from other evidence, such as that shown in figures 1.3.47-52 inclusive, the broken unit in a large sample of parallel twisted elements can continue to participate in resistance to subsequent extension, but this continued participation is dependent on lateral pressures, frictional conditions and strength reserves at the local region of break propagation.

Cord Behavior in Compression

Considering the early emphasis put on the compressive part of the fatigue cycle in testing of tire cord, it is surprising that work was not initiated earlier on the simple axial compressive behavior of tire yarns and cords. So much has been done, as indicated in this chapter, on the tensile properties of fibers, yarns, and cords. The difficulty, of course, was in the matter of procedure for compression testing of yarns or, most specifically, in the arrangement of the mechanical boundaries in a given test. A similar difficulty was encountered in measurement of the axial compressive properties of fibers and the planar compressive properties of fabrics.

In 1963 Clark [79] studied the plane elastic characteristics of cord-rubber laminates and deduced that the modulus of elasticity of the cords was much greater in tension than in compression, although the compressive modulus of the twisted cords was not found to be insignificant, and such cords were observed to carry appreciable compressive loads when properly encased in rubber and when prevented from buckling.

Wood and Redmond [78] two years later ran similar tests while emphasizing the role of cord geometry in determining compressive behavior. Their analytical approach is summarized briefly below with symbols changed to match terminology of this chapter.

Viewing a single filament helix loop (in a yarn) with helix radius r , twist T , and helix angle q , Wood considers the filament axial strain ϵ_{fc} which occurs as a result of an applied compressive strain, ϵ_{yc} , with an allowed lateral strain of ϵ_{yt} . His primary relationship between lateral strain and twist is seen to be equivalent to eq (1.3.108)

$$\epsilon_f = \epsilon_y (\cos^2 q - \mu_y \sin^2 q) \quad (1.3.108)$$

where

$$\mu_y = \epsilon_{yt} / \epsilon_{yc}$$

If buckling is considered to take place before any appreciable filament strain takes place, then $\epsilon_f = 0$ and

$$\epsilon_{yt} = \epsilon_{yc} / \tan^2 q \quad (1.3.229)$$

A plot of $\epsilon_{yt} / \epsilon_{yc}$ versus T in figure 1.3.58 shows the powerful effect of twist on lateral yarn strain (remember, $\tan q = 2\pi rT$).

Wood then views the longitudinal compression of a tire cord embedded in rubber stock taking into account the axial fiber compressive forces, the lateral pressures of the laterally expanding yarn, the pressures of the rubber, and most important, the geometry of the cord structure. The relationships of the lateral expanding pressures to the axial fiber compressive force are the same as those used initially to relate lateral contractive pressures to axial fiber tensile forces (as in eq (1.3.118)). Starting with the average compressive force, f , on each of N filaments in a yarn, he proposes a level of lateral pressure, p

$$\frac{Nf(2 \sin^2 q)}{d_y (\cos q) (d_y)} = \frac{2Nf}{d_y^2} \frac{(\pi T d_y)^2}{[1 + (\pi T d_y)^2]^{1/2}} \quad (1.3.230)$$

where d_y is the yarn diameter, T the yarn twist, q the helix angle of the filaments and f the compressive (axial) force in each filament.

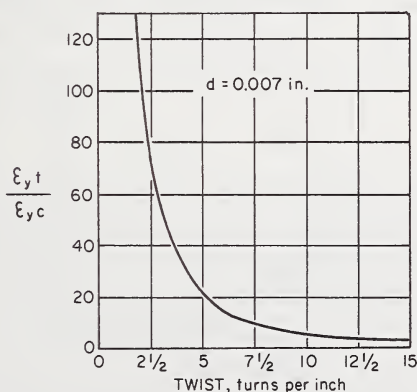


FIGURE 1.3.58. Lateral yarn strain per unit imposed longitudinal cord strain vs. twist.

Through a succession of simplifying assumptions (which warrant close examination) Wood arrives at a relationship between the lateral pressure, p , developed through yarn expansion in contact with the surrounding rubber hole and the local strain levels, i.e.,

$$p = \frac{E_r(\epsilon_t + \epsilon_l)}{2} \quad (1.3.231)$$

where ϵ_l is the longitudinal tensile or compressive strain of the cord-rubber assembly, and ϵ_t is the transverse spreading of the filaments, with E_r being the effective rubber modulus (or spring constant acting against transverse spreading of the filaments). The filament compressive stress-strain curve is simply

$$f = -E_f \epsilon_f \quad (1.3.232)$$

whence

$$\frac{f}{\epsilon_l E_f} = \frac{[1 + (\pi T d_y)^2]^{1/2} [1 - (\pi T d_y)^2]}{[1 + (\pi T d_y)^2]^{3/2} + \frac{4NE_f}{d_y^2 E_r} (\pi T d_y)^4} \quad (1.3.233)$$

and

$$\frac{\epsilon_t}{\epsilon_l} = \frac{[1 + (\pi T d_y)^2]^{3/2} + \frac{4NE_f}{d_y E_r} (\pi T d_y)^2}{[1 + (\pi T d_y)^2]^{3/2} + \frac{4NE_f}{d_y^2 E_r} (\pi T d_y)^4} \quad (1.3.234)$$

Values of eq (1.3.233) and eq (1.3.224) are plotted against turns per inch, T , of the yarn for arbitrary values of $d_y 2\pi/d_y^2 E_f$ and E_r (corresponding to his experimental data). See figure 1.3.59. From the figure it is seen that as twist increases, the resistive force per unit of longitudinal strain falls off significantly, leading to the expectation of lower modulus in high twist embedded cord systems. This reduction is much larger than that expected in a tensile modulus variation with twist. And if filament modulus in compression is actually lower than that in tension, it may be

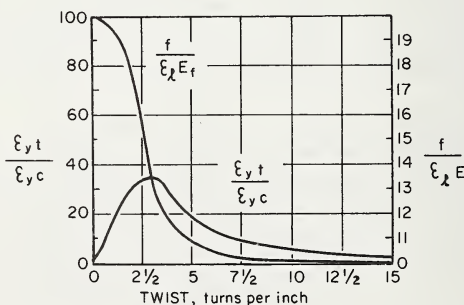


FIGURE 1.3.59. Theoretical curves showing filament stress and folding separation vs. twist. See eqs (1.3.233) and (1.3.234).

expected that the compressive softening with twist of the embedded cord will be even greater.

Wood does observe the occurrence of buckling in his compressive tests on embedded cord, but he provides no insight as to its mechanism. Actually, the buckling of fiber assemblies has received more attention of late in connection with studies of fabric aesthetics, but it still remains for someone to work out the specific mechanics of compressive buckling of a twisted structure embedded in an elastomeric matrix. We can only refer at present to several recent studies which deal with various phases of the problem. The work on buckling of fabrics, taking into account elastic behavior and inter-fiber friction is summarized by Grosberg [7] and, more recently, by Olofsson [81, 82], Sadowsky et al. [83] treat the buckling of microfibers in composite materials. Haringx [84] dealt with compressive buckling of helical springs, which in a way simulate the structure of a two- or three-ply yarn, and he also considers the effect of lateral elastic restraints. Amirbayat and Hearle [85] have studied the buckling of reinforcing fibers in an elastomeric matrix as a result of repeated flexing accompanied by slippage. And, finally, Menzies [86] has treated the buckling of twisted structures under the combined influence of torsion and tension. He was able to show the usefulness of the classical torsional buckling relationship for an elastic rod as applied specifically to the case of a twisted strand, i.e.,

$$M_t^2 = 4EIP + \frac{4(EI\pi)^2}{(L)^2} \quad (1.3.235)$$

where M_t is the torque at buckling, EI is the bending rigidity of the yarn, P is the tensile load on the yarn, L is the yarn length between torsional jaws. Menzies attempted to derive an effective EI on the basis of yarn geometry and fiber properties, but the full success of such an effort must await further results in the elastic-viscoelastic-friction treatment of bending in twisted fiber assemblies. Some review of progress in this latter area will be given in the following section.

1.3.3.5. Observations of Plied Yarn Behavior in Tension and Compression

Tensile Behavior

In presenting quantitative data on the stress strain properties of yarns and cords, one generally includes breaking tenacity, elongation at rupture, initial (tangent modulus), secant modulus and energy to rupture—all based on a first time load elongation test in uniaxial tension. The major part of the analysis incorporated in this chapter is directed toward this limited view of the stress strain behavior of raw, that is non-dipped, tire cord. It is hoped that the survey of mechanics here recorded, provides the reader with starting concepts and directions of analysis useful in treating the geometry of twisted structures and the interaction of fiber properties with said geometry as it determines the

stress-strain properties of the raw cord. We will say something about other stress-strain properties at the end of this section, but for now we focus on the more common properties of strength, elongation and modulus.

Mechanical properties may be listed in table form with separate columns for the structural variables of yarn counts, diameter, singles twists and ply twists, and this was done at an early date by Gurney et al. [87] for tire cords made of cotton. A most extensive series of experimental studies were undertaken during the period 1931 to 1943 by Coulson and Dakin [88] (although not published until 1957) on the mechanical properties of plied yarns—again cotton. They provide extensive tabular data for 20s/2, 30s/2, 40s/2, 45s/2, 60s/2, and 80s/2 ply yarns, but unfortunately, the material is in staple form and has application to continuous filament tire cord yarns, only in limited regions of singles and ply twist. Yet it is instructive to provide a graphical picture of the effect of structural variables on mechanical properties of staple plied yarns as is done in figure 1.3.60. Here we see a topological plotting of tenacity and elongation at rupture at different singles and ply twists for 42s/2 cotton (1 $\frac{1}{8}$ " carded). The maximum tenacity of 1.55 grams/grex occurs at a singles TM of 4.0 and ply twist of 30 and the tenacity slopes off as one moves southeast, south, southwest or west from the tenacity summit, as reflected in the solid isotenacity lines. The isoelongation

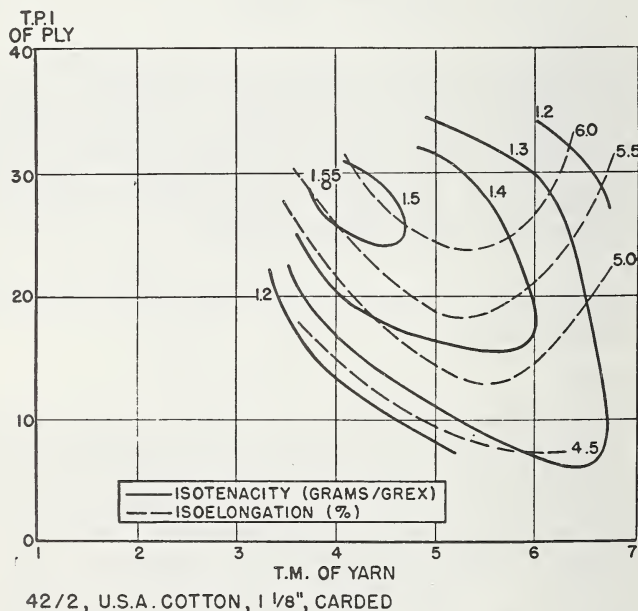


FIGURE 1.3.60. Tenacity and elongation at rupture as a function of twist multiple of the yarn and turns per inch of the ply for 42s/2 cotton.

lines likewise reflect a positive slope as one moves up vertically, although the data do not reflect a distinct summit of elongation values.

The work of Platt et al. [50, 63] on cordage fibers was referred to at length in earlier discussions of singles and plied yarn mechanics, for their studies emphasized the interaction between fiber properties (including variability) and structural geometry. The following data reveal their success in predicting efficiencies of cordage yarns and cords based on the analyses of this chapter. Their experiments had to do with such yarns as abaca, henequen and sansevieria and therefore cannot be directly applied to the continuous filament rayon or nylon. But the good agreement obtained in the following table between theoretically calculated and experimentally determined efficiencies underwrites the validity of the mechanics and statistical treatment reported by Platt.

The tabular results that follow were obtained by determining the pertinent fiber data, picking points off the curves in figures 1.3.42a-c and comparing theoretical strength efficiencies with the experimental results.

TABLE 1.3.2. *Comparison of theoretical and experimental efficiencies*

Yarn type	e_m	a/b	v	θ	Yarn Efficiencies	
					Theoret.	Experim.
	(%)		(%)	deg	(%)	(%)
Blended abaca	3.00	- 0.73	22	16.5	54.0	56 \pm 3
	3.00	.73	24	20.0	50.0	50 \pm 3
	3.00	.73	31	24.5	47.0	43 \pm 3
	3.00	.73	32	29.4	42.0	38 \pm 3
Abaca strand yarns	3.00	2.10	24	14.0	62.0	64 \pm 3
	3.00	1.51	24	18.0	58.5	56 \pm 2
	3.00	0.91	24	24.0	52.5	50 \pm 2
Henequen	5.00	2.10	20	22.0	59.0	63 \pm 1
	5.00	2.10	20	28.0	54.0	56 \pm 2
	5.00	2.10	20	35.0	45.0	39 \pm 3
Sansevieria	3.00	0.00	30	17.0	55.5	56

It should be pointed out that certain corrections were necessary for calculation of either theoretical or experimental efficiencies shown above. These included corrections for oil pickup, for twist take-up in the yarns, and for mean fiber strength (as against stress at mean fiber elongation).

In another set of calculations Platt determined the efficiencies of translation of Manila Abaca fiber strength into bundles containing a small number of units. The theoretical efficiencies taken from figure 1.3.56 are compared below with experimental efficiencies and show reasonable agreement.

TABLE 1.3.3. *Efficiency of strength translation of manila abaca fibers*

Number of fibers in bundle	Efficiencies	
	Theoretical	Experimental
2	90	88.3 \pm 7
3	81	81.0 \pm 5
7	73	76.0 \pm 8
15	68	69.8 \pm 7.5

Platt summarizes all his information on the structure and efficiencies of abaca strands (in effect, a multi-ply yarn) in the following cited table:

TABLE 1.3.4. *Comparison and theoretical and experimental strand efficiencies*

Strand code	Cosine strand helix angle	Strand efficiency		
		No excess length	Excess length	Experimental
		%	%	%
SSS	0.931	40.7	37.4	41.4 \pm 2
SSM	.897	35.5	32.1	37.1 \pm 2
SSH	.880	34.3	29.8	31.0 \pm 2
SMS	.945	38.3	33.6	40.6 \pm 3
SMM	.917	37.7	31.2	43.5 \pm 2
SMH	.878	33.1	26.6	29.6 \pm 2.5
SHS	.943	34.6	31.4	31.8 \pm 2
SHM	.942	34.5	31.4	33.2 \pm 5.5
SHH	.931	33.7	30.7	33.4 \pm 6

It was pointed out that Symes [76] took a greatly simplified approach for nylon tire cords, in analyses covered by eqs (1.3.174–190). He emphasized the effect of changes in cord denier (or tex) to indicate changing radii, helix angles, and structure. And in eq (1.3.187) he related cord strain to fiber tensile strain, in eq (1.3.189) cord strength to rupture strain of the fiber and in eq (1.3.188) cord contraction to filament shrinkage in heating. Figures 1.3.61a–d show the agreement between theory and experiment—shown to be good except in the prediction of elongation to rupture. Symes states of the latter that “Experimental extensions are higher than the predicted values by 3 or 4 percent (strain). Most surprising is the lack of agreement between the low twist, low tex, extension of cord at break and the extension of the yarns extracted from the cords. The difference is perhaps due to structural or coil looseness in the cord, that is, the filaments in the cord when the cord is inserted in the clamp

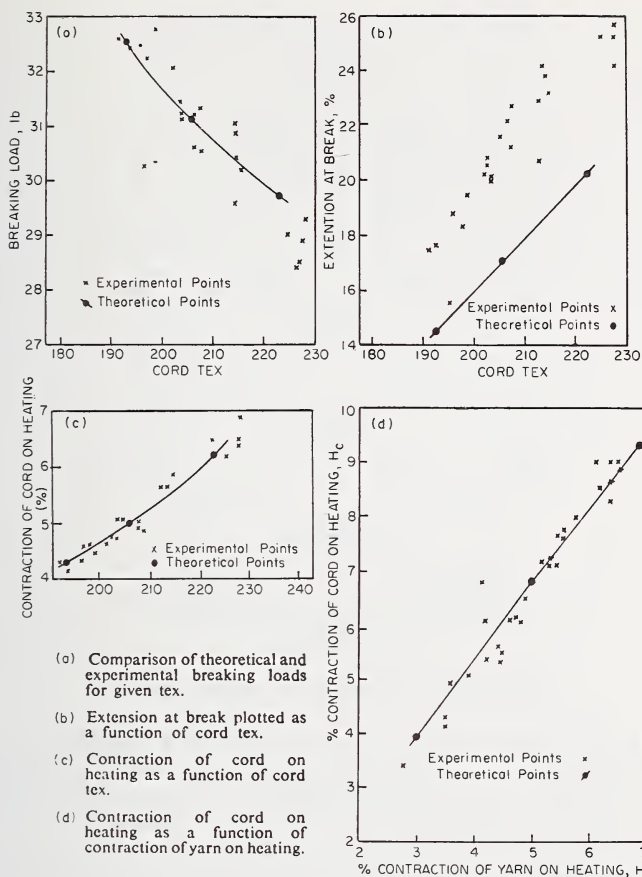


FIGURE 1.3.61. Strength, elongation, and contraction experiments.

for tensile testing are not straightened to the same extent as when testing yarn. Higher tensions when making the cords might reduce extensions of the cord or give a better fit than that shown."

The use of energy method to analyze the tensile stress strain properties of multiple yarns was reported by Treloar [77] following on his earlier work with continuous filament singles yarn [59]. Experimental verification of the cord, or multiple yarn analyses was provided by Riding [90]. Recall that Treloar expressed the load on the ply yarn P_p in eq (1.3.194) as a function of the fiber stress strain curve $[\psi(\lambda_{fr})]$, the helix angle of the ply (Q_{po}), the position of the fiber in the singles (r_o), and the change ratio of singles strain to ply strain, and fiber strain to singles strain. The latter two ratios had to be developed separately from eqs (1.3.200) and (1.3.213) respectively. Thus, eq (1.3.194) becomes the vehicle for predicting the ply yarn load at any given ply yarn extension.

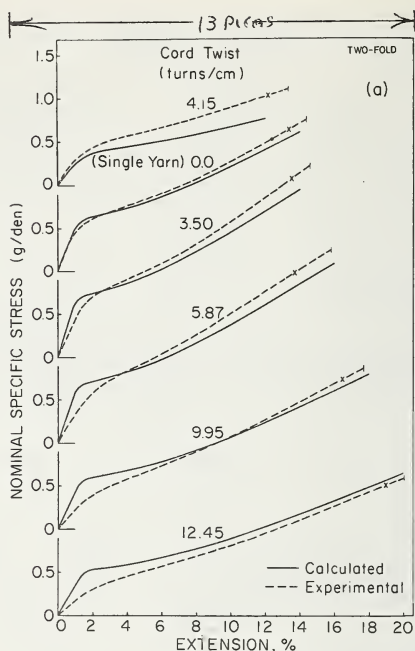


FIGURE 1.3.62a. Stress-strain curves: two-fold.

It says nothing about breaking loads or breaking extensions—but can be used to predict the full load elongation curve of the ply yarn in the “unbroken” region. Riding did just this for a two-ply, a three-ply, and a seven-ply yarn, with good agreement between theory and experiment, as shown in figure 1.3.62 for the two- and three-ply. Equal agreement was observed for the seven-ply, not shown. The mean breaking point determined experimentally is shown on the broken curves with a cross. It was observed, however, that relatively low values of the experimental curves (versus the calculated ones) occurred at low strains, and particularly for high twists. As Riding points out, this difference was also observed in comparison with theory and experiment on singles yarns, hence it is not surprising to find the effect occurring again in cords made from the singles. The unfortunate feature is the focus of the difference on the slope of the curves; in other words, on the initial tensile modulus, the parameter so important to the engineer working with tire structures.

Riding [90] replotted the curves of figure 1.3.62 as shown in figure 1.3.63 (only for case of two-ply yarns). This form should be more useful in tire studies.

The reader should be aware from earlier discussions in this chapter that data such as that plotted in figures 1.3.62 and 1.3.63 can be misleading unless full details are provided of the experimental techniques for measuring singles and plied yarn structure. Riding provides such details; unfortunately, many other reports in this field do not. He de-

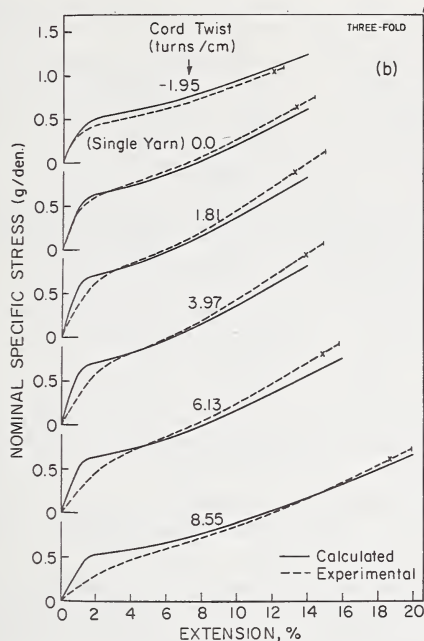


FIGURE 1.3.62b. Stress-strain curves: three-fold.

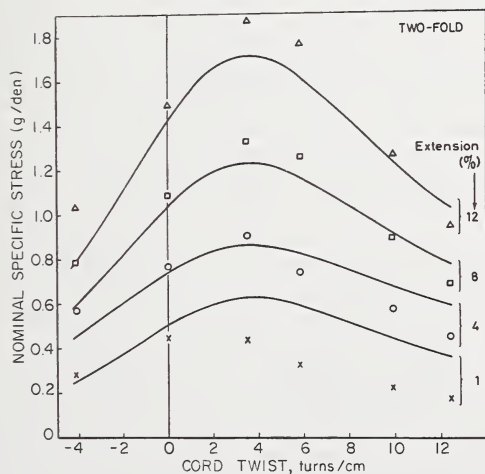


FIGURE 1.3.63. Nominal specific stress vs. cord twist: two-fold.

termines (see fig. 1.3.9b, also see eq (1.3.96)) the yarn radius indirectly from measurements of retracted length per unit filament length. Singles twists are determined on 30 specimens of the singles yarn. The mean

stress strain curve of the original yarn was obtained from 20 tests. The basic parameters to be determined in the two- and three-ply cords are the cord twist and the ply axis radius. Since it is virtually impossible to obtain satisfactory direct measurement of the ply axis radius, Riding uses instead an "effective" radius, defined as the radius required to give a calculated value of cord retraction in agreement with an observed value for corresponding, measured values of cord or ply twist.

A note of caution pertains to the determination of the stress strain properties of the fiber as it lies in the singles, or of the singles as it lies in the ply. Any prediction of strength translation into higher order twisted structures must take into account changes in fiber properties which occur as a result of the twisted (and winding) operation. Riding [91] has shown "that the twisting of a viscose rayon yarn followed by a subsequent detwisting, produces a reduction in tenacity and extensibility of the constituent filaments, and that the magnitude of this effect is influenced by the type of twisting machine, twisting tension, amount of twist, and the number of times the operation is repeated, but is unaffected by the time for which the yarn remains in the twisted state." He has also shown that this effect was caused by a form of filament surface damage, produced by inter-filament contact. We cannot provide a corresponding reference concerning loss in filament tensile properties due to twisting of other tire cord materials, such as nylon or the polyesters, yet this factor must be kept in mind in any attempt to predict yarn or cord properties on the basis of single filament stress-strain curves.

Effect of Temperature on Tensile Mechanical Properties

The change in filament properties due to damage incurred during twisting is only the first of many variations in filament behavior which must be taken into account in predicting cord strength and elongation. The most obvious change which must be dealt with is the influence of temperature on mechanical properties of the basic filament. At first, one must consider the effect of tire running temperature on the properties of the fiber, hence of the cord. Then consideration must be given to the effect of temperatures during cord stretching treatments and, finally, to the effect of temperatures of vulcanization. Takeyama et al. [89] have provided an excellent survey of the literature of tire cord materials and treatments and there is no point of repeating their extensive reporting of heat effects on tire cord behavior. But for convenience, we reproduce one of their summary curves in figure 1.3.64, which shows the effect on breaking strength and energy of temperatures ranging from 100–300° F, with both low speed tests and high speed tests. At low testing speeds it is noted that decreases in strength and breaking energy of nylon are more rapid than those of rayon and polyester. At high testing speeds decreases in strength and breaking energy of nylon are greater than those of rayon and polyester. In fact, rayon shows an increase in breaking energy with temperature. To be sure, in the absence of full identification of the types of rayon, nylon, polyester and glass involved in the experiments reported by Takeyama in figure

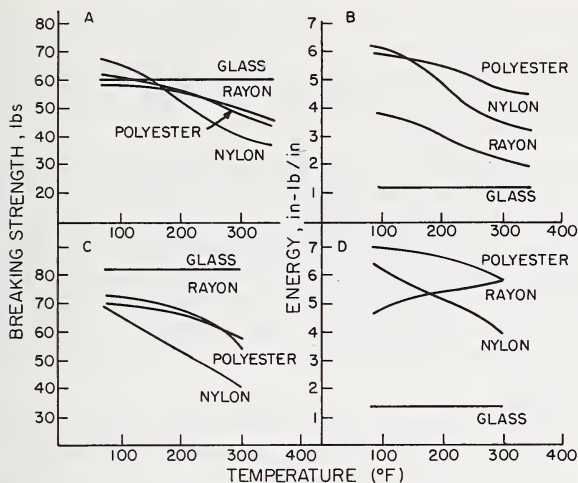


FIGURE 1.3.64. Effect of temperature on breaking strength and energy. A and B: low speed test. C and D: high speed test.

1.3.64, and in the absence of full data as to dipping or stretching conditions, caution in ranking fiber behavior is necessary.

Effect of Strain Rate on Tensile Mechanical Properties

The influence of strain rates on the mechanical behavior of individual filaments is a subject to itself, and it is to be expected that an increase in testing speed which will significantly affect the stress-strain curve of the individual filament will correspondingly change the mechanical behavior of the plied yarn or cord. And presumably the same analyses leading to prediction of plied yarn properties, as covered in this chapter, will prevail provided that the altered filament stress-strain properties are inserted in the equations used in the prediction of cord behavior.

From experience we know that fiber modulus will generally increase as the strain rate goes up and elongation to rupture will go down (for most filament materials) at higher testing speeds. But another factor to be considered is the effect of higher testing speeds on the slope of the stress-strain curve in the region of filament rupture. Platt et al. [50] analyzed the effect of this slope on conversion of fiber properties into bundle, or yarn properties. And Takeyama [89] refers to the effect of this "latter curve" slope on the yarn to cord conversion efficiency for polyester yarns—the higher the slope of the upper part of the stress-strain curve, the lower becomes the conversion efficiency. What influence strain rate has on the "latter curve" slope is evident in the many stress-strain curves reported by Krizik et al. [92] at strain rates of 0.33, 2025 and 2775 percent per second. Of particular interest is their data showing the effect of strain rate on the loop strength efficiency of several textile yarns—for here the role of "latter curve" slope and slope change with strain rate is of utmost importance.

Of course, yarn history, particularly that of drawing, will influence the shape of the stress-strain curve, hence the conversion efficiency in tire cords. Takeyama discusses the effect of polyester drawing on conversion efficiency as shown in figure 1.3.65. The interaction with ply twist factor is quite evident.

An important reference text on the impact, or high speed testing of fibers, yarns and fabrics was written by Lyons [94]. Lyons provides an historical review of instrumentation developed in this special field of testing, including the falling weight devices, the rotary disk methods, ballistic methods and the more recently developed pneumatic and hydraulic apparatus. He summarizes the theories of deformation and rupture under high-speed impact and reports considerable experimental data on fibers, yarns, cords, ropes, woven cloth, and special body armor fabrics.

A good collection of impact data is provided by Hall [95] who studied the impact behavior of various fibers at strain rates of 330 sec^{-1} and at $8.3 \times 10^{-3} \text{ sec}^{-1}$ for low twist yarns. A sampling of his data taken from Takeyama is provided below.

TABLE 1.3.5. *Effect of rate of extension on mechanical properties of various yarns*

Yarn	Extension breaking		Tenacity		Initial modulus		Energy to rupture		Critical velocity
	Low*	Hi**	Low	Hi	Low	Hi	Low	Hi	
Nylon 900	20.1	12.7	84.9	110.0	510	1900	87.1	67.5	360
Nylon 300	20.5	13.8	60.6	93.1	360	700	71.7	59.7	350
Nylon 100	30.4	13.7	48.2	65.4	350	1400	103.0	51.7	260
H. T. Enkalon	26.8	15.3	73.9	90.8	320	1500	88.0	56.5	290
Tenasco 105	15.2	10.5	35.6	50.5	900	1800	29.8	32.8	190
Textile Tenasco	19.2	15.5	26.1	39.5	730	1700	28.1	39.1	220
Standard Rayon	23.2	19.6	18.9	29.8	400	1200	27.8	38.9	210
Ulstron	19.7	14.6	78.9	82.8	1080	1100	98.5	75.9	270
Polypropylene multifil	54.0	16.5	43.0	65.1	610	1100	193.0	69.8	300
Courlene X3	19.7	7.5	37.4	63.0	640	1300	57.6	25.7	210
H. T. Terylene	12.8	7.3	60.8	77.7	1290	2000	54.5	34.4	220
M. T. Terylene	31.0	17.6	41.4	43.9	900	1900	98.0	67.5	150

*Low = $8.3 \times 10^{-3} \text{ sec}^{-1}$ strain rate.

**Hi = 330 sec^{-1} strain rate.

Lothrop worked with dipped rayon and nylon cords, measuring tensile properties as a function of temperature and rate of extension. His data are shown below in table form. According to Takeyama, for both oven dried rayon and nylon, breaking strengths (measured by Lothrop) decrease as temperature increases at a given rate of extension [96].

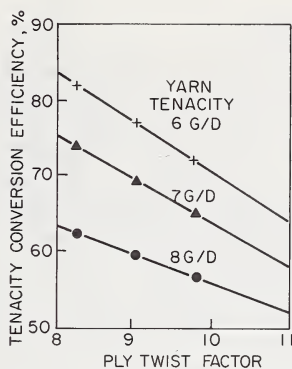


FIGURE 1.3.65. Effect of yarn drawing on tenacity conversion efficiency for polyester.

TABLE 1.3.6. Breaking characteristics* of dipped rayon and nylon cords as a function of temperature and rate of extension

Strain rate %/sec	Item	Rayon					Nylon				
		Cond., °F	Oven-dried, °F				Cond., °F	Oven-dried, °F			
		75	75	150	225	300	75	75	150	225	300
1	A	32.3	35.0	31.9	27.8	24.0	28.3	29.2	24.0	21.1	16.7
	B	13.5	10.2	10.4	10.8	11.3	19.9	20.8	18.9	20.5	22.2
	C	2.45	2.08	1.94	1.69	1.51	2.50	2.69	1.92	1.93	1.82
1000	A	38.5	41.7	40.0	36.6	33.0	32.9	33.4	29.1	25.2	21.3
	B	13.8	10.4	11.4	12.5	13.5	17.6	21.1	20.9	21.1	21.3
	C	3.24	2.66	2.70	2.78	2.75	2.80	3.12	2.59	2.51	2.05
3000	A	39.2	43.6	40.6	38.3	36.3	34.6	33.4	29.2	25.1	22.2
	B	14.2	10.4	12.7	13.3	14.2	18.5	20.6	20.1	19.5	20.5
	C	3.17	2.76	3.07	3.08	3.12	2.83	2.94	2.58	1.98	1.91
6000	A	41.0	44.0	42.2	40.3	38.1	35.3	34.7	29.3	26.3	22.4
	B	13.7	10.3	12.4	13.3	15.0	17.5	21.0	19.8	19.5	19.0
	C	3.21	2.55	3.07	3.18	3.32	2.75	3.01	2.35	2.18	1.79

*Breaking characteristics

A = strength, lb

B = elongation, %

C = energy, in. lb/in. of cord.

Compression and Buckling

We now briefly turn to observed axial compressive behavior of tire cords so as to complement earlier discussion on the mechanics of compression. Wood [78] has attempted an analysis of the structural interaction of tire cords subjected to axial compression and his experiments bear out the shape of his predictions in a general way. Figure 1.3.66a shows the effect of twist on the lateral/longitudinal strain ratio in compression. The theory is indeed different than the experimental values at twists below five T.P.I. The effect of twist on the compressive stress-strain curve is shown in figure 1.3.66b, while the effect of twist on compression modulus of cords in rubber is shown in figure 1.3.66c. An added comparison between rubber embedded cord behavior in tension versus compression is provided by Clark [79] in figure 1.3.67 for rayon cords. He reports similar data for embedded nylon cords, reflecting higher moduli in tension than in compression. Finally, it is worth noting the appearance of twisted, embedded structures subjected to axial compression. Wood used a transparent rubber slab for his compression tests and was able to show two distinct mechanisms of cord compression. First, at low twists he observed distinct cord zig-zag buckling. He reported that when the cord reinforced rubber slab was bent for the first time, it exerted a large resistance, which suddenly decreased as the low twist cords collapsed and buckled. At the point at which the cords buckled, adhesion breakdown occurred, this being so marked that it was actually heard as the slab was first bent. In regions of high twist, cord buckling became less pronounced and eventually disappeared. At this twist level and above, separation of the cord plies was observed, with each of the singles forming the plied yarn compressing in a manner similar to that of a spiral spring. This expansion of cord diameter during compression was also noted by Busby et al. [93].

The buckling pictured by Wood was a sudden, catastrophic one, localized in nature and occurring primarily at low twists. In general, however, buckling takes place in twisted structures in a well-defined relationship, as per eq (1.3.235), between torque and axial load. And Menzies found the form of the experimental relationship was linear for Manila cordage as shown in figure 1.3.68 and as expected from eq (1.3.235). But the difference in behavior of his samples as against Wood's was that torsional buckling was a gradual process whereby the straight-axis of the twisted structure assumed a helical configuration, then the helix localized into a loose loop, which then tightened on itself. The end point was one of complete local distortion and strain concentration, such that when the specimen was straightened and tested again, early buckling would reoccur at the same position.

Spectrum of Stress Strain Properties

As pointed out above, the stress strain properties most often reported in the textile literature include breaking tenacity, elongation at rupture, initial modulus and energy to rupture. In the analyses cited in previous section 1.3.3.4, numerous methods are presented for calculating the conversion of these properties from fiber to cord structures. And in the

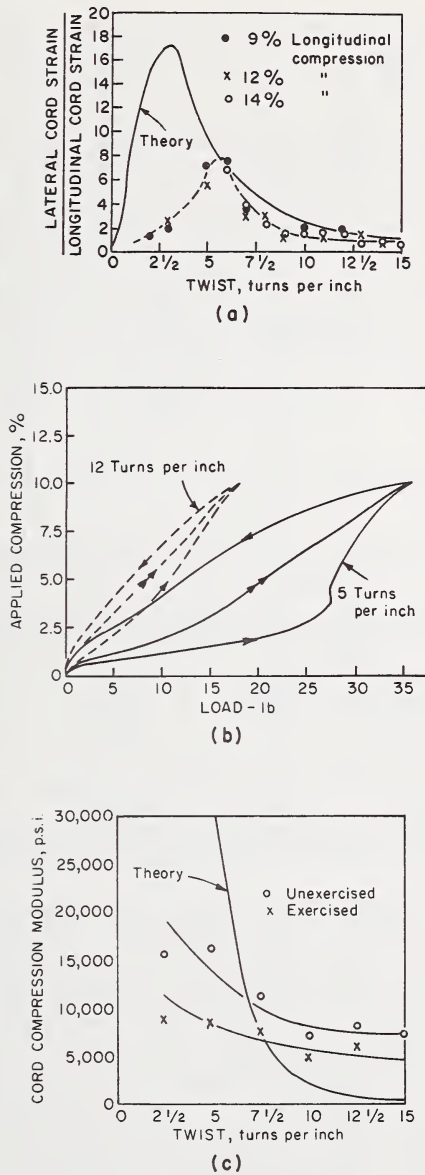


FIGURE 1.3.66. Cord compression characteristics.

- (a) Lateral cord strain per unit longitudinal strain vs. cord twist.
 (b) Compression-load curves for rubber blocks containing 30 rayon cords.
 (c) Compression modulus of cord in rubber.

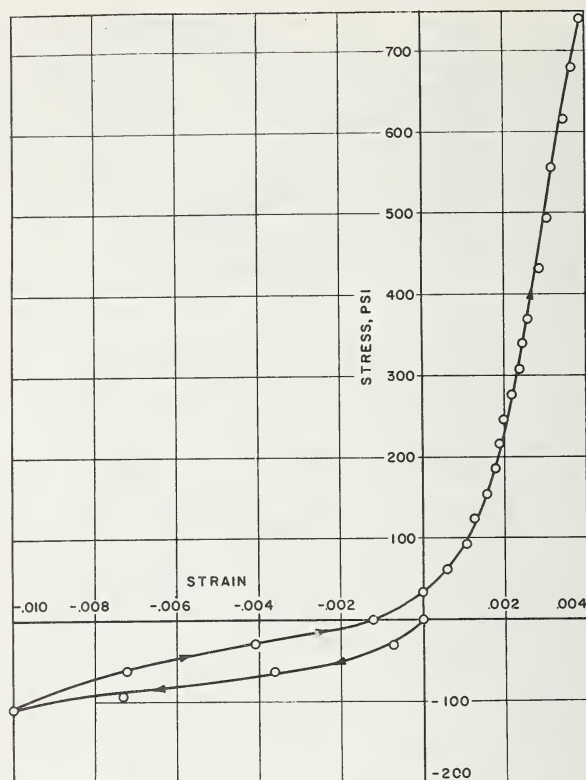


FIGURE 1.3.67. Continuous stress-strain curve through compression and into tension for rayon cords embedded in rubber. Stress based on total cross-sectional area of specimen.

section 1.3.3.5 on Observations of Plied Yarn Behavior in Tension and Compression, considerable numerical data on cord properties are provided under each of the above-named principal properties. The data serve two purposes, first to validate the analytical methods, as well as the geometric assumptions on which they were based and, second, to furnish the technologist or engineer with experimentally determined quantities as a basis for product design. But the tire manufacturer and the fiber producer responsible for improving cord quality cannot function without considerably more information concerning cord behavior. Knowledge of a range of stress-strain properties is necessary, including creep, flatspot index, shrinkage impact toughness, and fatigue. These additional properties constitute but a small part of the more than fifty stress-strain properties listed in the *Thesaurus of Textile Terms* [8], yet they add immeasurably to the challenge of developing analytical methods for predicting or designing total tire cord mechanical behavior. We will make no effort to deal with these topics at present, since they are covered so recently in Takeyama's treatment [89] and we simply extract pertinent summary data in the following table based on work by Schroeder and Prettyman [97] (see Takeyama also).

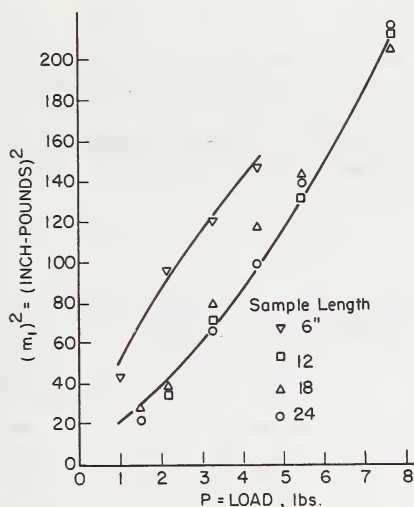


FIGURE 1.3.68. Buckling torsion of twisted structure.

TABLE 1.3.7.

Cord construction	Rayon (current) 1650D/2 12 × 12	Nylon 840/D2 12 × 12	Nylon (modified)	Polyester 840D/2 12 × 12
	2200D/3 8.5 = 8.5	1260D/2 10 × 10	840D/2 12 × 12	1260D/2 10 × 10
Tenacity, gpd.	4.5	7	6.5	6
Elongation at break, %	9	21	15	13
Initial modulus gpd	60	27	40	70
Creep, %	3	4	3	2
Shrinkage, %	0.6	6	7	7
Flatspot Index, mills	50	170	115	50
Impact toughness, erg/cm D	225	525	400	375
C-F fatigue min	400	1400	600-1200	500
Adhesion, lbs min	100	90	70	65
Aging, %	70	95	70-95	70

Effect of Lubricants

Takeyama [89] et al. point out that the yarn to cord tenacity conversion efficiency of rayon cords is quite low and therefore the choice of tire cord lubricant is important. They point out that a lubricant which decreases the friction coefficient of the yarn and improves the conversion factor (as shown in the accompanying table) has to be developed.

TABLE 1.3.8. *Correlation of cord strength with yarn friction coefficient*

Specimen 1650/2 rayon	Friction coefficient		Bone dry strength per 100 denier
	Static	Dynamic	
A	0.207	0.197	263
B	.200	.184	266
C	.160	.150	272
D	.132	.158	280
E	.107	.144	296
F	.118	.133	306

Roder [98], who originally reported the above data, points out that the manner of twisting of the cord will likewise have significant effect on cord strength, but with regard to finish, he feels that a low static coefficient will help each filament in the yarn find its equilibrium position during cord twisting, which leads to maximum strength in the cord. If one reviews the possible effects of friction between fibers on the ease of migration during twisting, on the ease of singles flattening and cord radius reduction, on the ease of longitudinal slippage of fibers during the bending of the singles inherent in the plying operation, and on the ease of longitudinal fiber slippage to accommodate varying strain levels along a single filament during axial tensioning of the cord, then it is easy to understand the results of Roder's experiments. It remains, however, to determine which, of the above-named mechanisms, fiber to fiber friction affects to the greatest degree, at least insofar as breaking strength is concerned.

Finally, it may be expected that lubricants should show a far greater effect on the bending rigidity, as against tensile strength, of fiber assemblies whose bending is accompanied by so much fiber slippage. And this bending rigidity, in turn, should play an important role in matters of flex fatigue and fatigue in general. This leads directly to the topic of bending mechanics of twisted structures, a subject which has received considerable attention in the textile literature of the last five years.

1.3.4. Bending Mechanics of Twisted Structures

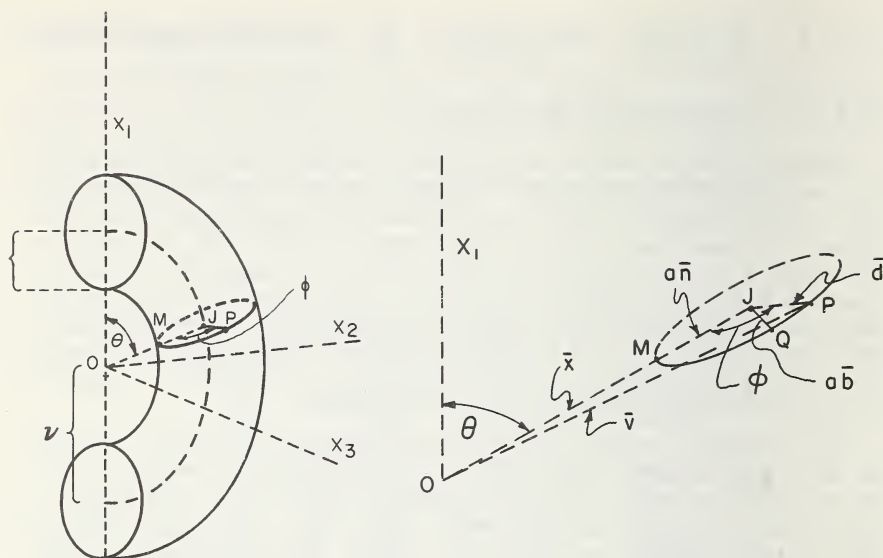
1.3.4.1. Geometry of Bent Yarns

Anyone who has seen a tire in action is aware of the fact that extensive bending takes place in the "footprint" region. Depending on where the cord is located, it may be in tension, in compression, and/or in a bend. It follows that during the full rotation of the tire the cord experiences a tension-compression flex cycle, the magnitude of which is controlled by the deflection of the tire. The frequency is, of course, dictated by the speed of the vehicle, with the average tire rotating about 800 times per mile, or for a speed of 60 mph, at 800 cycles per minute. As Kovac [10] points out, the average passenger tire will be subjected to about 20 million flex cycles during its lifetime.

The bending of twisted structures has been given very little attention in the textile literature before the 1950's, although civil engineers have been concerned with bending mechanics of wire rope used in heavy construction. And in the late 1940's such authors as Czitary [99] and Wyss [100] published reports on the subject. More recently, the topic has been considered by Lutchansky [101] in connection with problems on bent submarine cables.

Tovey's [102] excellent review article is a good starting point for review of the textile literature on the subject of bending and bending recovery—a subject of great interest in the commercial market as it is related to the fabric qualities of wrinkle resistance. Hamburger et al. [103] were concerned with the analysis of bending strains in yarns at the fabric crease, and they proposed that average bending strains be computed with the assumption of freedom of motion between fibers. They showed that experimental recoveries from tensile strain calculated for bent structures correlated well with experimental bending recoveries of creased fabrics. This led to the conclusion that tensile strains in bent fabrics were of the order of only a few percent, even though the yarns concerned were being bent around themselves—an exercise which should produce outer-fiber strains of the order of 50 percent if the fibers were restricted from slipping past one another. At a later date, Platt, Klein and Hamburger [14] examined the structural behavior of singles yarns in bending, using a more rigorous analysis to predict bending rigidity of the twisted structure on the basis of bending, as well as twisting moments of the individual fibers. This approach warrants further consideration. And still later, they [104] used a similar approach to the mechanics of torque development in a singles yarn system.

Backer [80, 105] emphasized the geometric aspects of bent yarn mechanics, and as was seen in eqs (1.3.90) through (1.3.95), showed that the differential geometry of the double helix could be greatly simplified if the helix angle of the primary helix angle went to $\pi/2$. Thus the primary helix became instead a planar circle, and the singles yarn assumed the form of a torus as shown in figure 1.3.69. The vector treatment then followed the course of eqs (1.3.32) to (1.3.44) above, except that Q became

FIGURE 1.3.69. *Torus form of bent yarn.*

$\pi/2$ and all equations were somewhat shortened. In particular eq (1.3.44a) became

$$\tan \alpha = \frac{a\lambda}{r - a \cos \lambda \theta} \quad (1.3.236)$$

remembering that $\lambda\theta = \phi$ is the angle shown in figure 1.3.69 locating the fiber position at P in the yarn cross section. When $\phi = 0$, we have the fiber at the inside of the bend, and when $\phi = \pi$, the fiber is at the outside of the bend. At $\phi = \pi/2$, the fiber is at the pseudo-neutral plane of the yarn. For these particular fibers the local helix angles are:

$$\text{for } \phi = 0, \quad \tan \alpha_b = \frac{a\lambda}{r - a} = \frac{\lambda}{r/a - 1} \quad (1.3.237)$$

$$\text{for } \phi = \pi/2, \quad \tan \alpha_o = \frac{a\lambda}{r} = \frac{a2\pi rT}{r} = 2\pi aT \quad (1.3.238)$$

$$\text{for } \phi = \pi, \quad \tan \alpha_t = \frac{a\lambda}{r + a} = \frac{\lambda}{r/a + 1} \quad (1.3.239)$$

since λ can be shown equal to $2\pi rT$. Note that $2\pi aT$ is equal to the tangent of the original helix angle of the unbent yarn, hence no change in helix angle takes place at the pseudo-neutral plane during bending of a singles yarn. However, considerable change is seen to take place at the top and bottom of the bend. This is quickly seen if we take the case of a yarn bending around itself, i.e., where $r = 2a$, which simplifies

the expressions for $\tan \alpha$ to: λ at the bottom, $\lambda/2$ at the middle (equal to the tangent of the unbent yarn helix angle) and $\lambda/3$ for the top as reflected in figure 1.3.69. Notice the heavy horizontal line drawn along the center of the yarn in figure 1.3.70a. The yarn is then bent concavely upward (plane of curvature perpendicular to the paper) and the inside of the bend is seen to experience a significant increase in helix angle as seen in figure 1.3.70b. In figure 1.3.70c, one views the top of the yarn bend, which evidences a reduction in helix angle. As a result of these helix angle changes, the originally connected horizontal heavy line segments of figure 1.3.70a are rotated, each around its center point, as shown in figures 1.3.70b and 1.3.70c, and clearly the separation which is now shown between the ends of these segments represents relative slippage between fibers, δ_s , calculated to be

$$\delta_s = 2\rho_f(\cot \alpha - \cot \alpha_o) \quad (1.3.240)$$

where ρ_f is the fiber radius, α_o is the original helix angle and α is the local helix angle in the bent state. The drawings of figure 1.3.70 were presented by Backer [80] and actual photographs were furnished later [112]. These changes in local helix angle take place every time a yarn is bent. And they are present in the singles yarns bent and twisted in the ply configuration of a plied yarn, as shown in figure 1.3.71. Here for the case of a three-ply nylon yarn, the high helix angles at the inside of the bend and the low helix angles at the outside of the bend are evidenced by the low and high degree of fiber sectional ellipticity in these two locations.

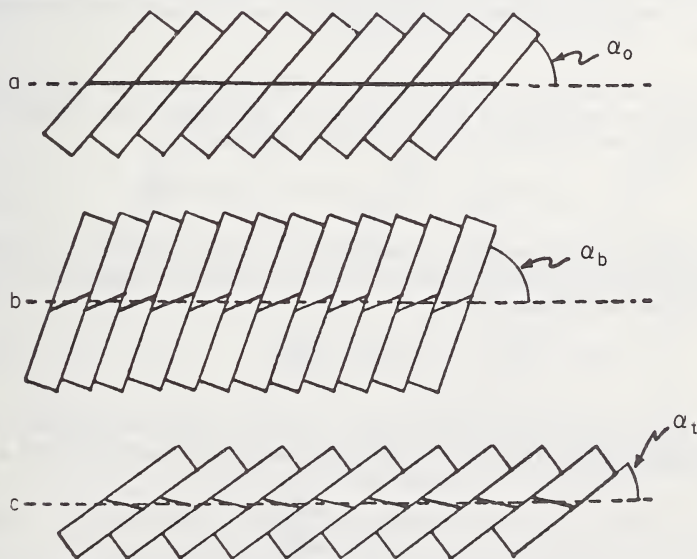


FIGURE 1.3.70. Change in local helix angle due to yarn bending.

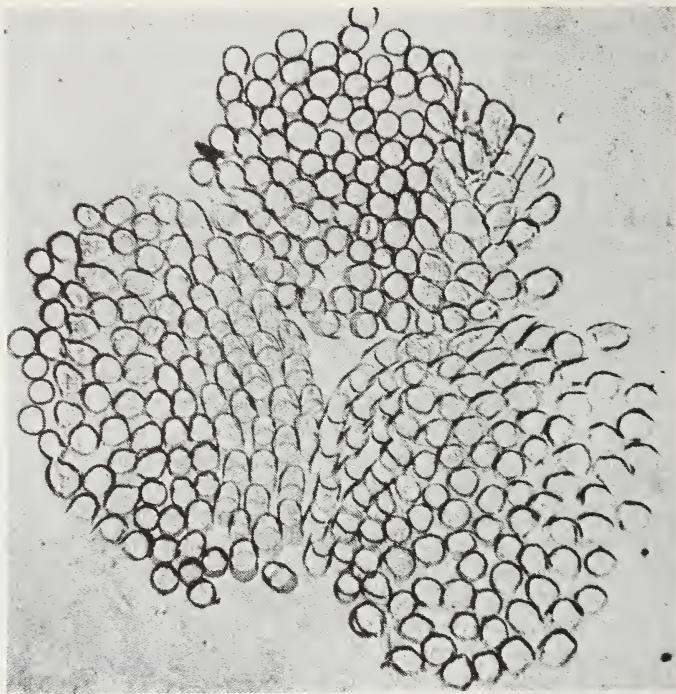


FIGURE 1.3.71. Cross section of three-ply, 102-filament nylon yarn. Note that fibers at the center of the ply lie at a steep angle with the ply axis, as evidenced by their elliptical appearance. (Courtesy of E. R. Schwarz [13]).

One of the more interesting parts of this study on bent yarn geometry [80] was the analysis of local strains in the bent yarn. Starting with eq (1.3.41) it was possible to show for $Q = \pi/2$ that

$$dS = [(r - a \cos \lambda \theta)^2 + a^2 \lambda^2]^{1/2} d\theta \quad (1.3.241)$$

If no slippage of the fiber is permitted to occur because of frictional constraint, then the local strain of the fiber lying in the angular increment $d\phi$ when the yarn is bent is

$$\epsilon_f = \frac{dS - dS_0}{dS} \quad (1.3.242)$$

where dS is the length of that fiber segment after bending and dS_0 is the length before bending. Noting that from the geometry of the unbent yarn

$$\sin \alpha_0 = \frac{ad\phi}{dS_0} \quad (1.3.243)$$

and for the bent yarn

$$\lambda = 2\pi rT = \frac{r}{a} \tan \alpha_0 \quad (1.3.244)$$

where α_0 is the helix angle of the given fiber in the unbent yarn. Thus eq (1.3.242) becomes:

$$\epsilon_f = \sqrt{\frac{(r/a - \cos \phi)^2 + \lambda^2}{(r/a)^2 + \lambda^2}} - 1 \quad (1.3.245)$$

reflecting zero strain at $\phi = \pi/2$, the pseudo-neutral axis. Values of ϵ_f are plotted against ϕ in figure 1.3.72 as ϕ varies from 0 to 180° . Symmetry conditions apply in the range $180^\circ < \phi < 360^\circ$. The parameter r/a varies from 1.5 to 2.5, the normal range of diameter variation encountered in ordinary woven textile structures. (But in ordinary ply structures the effective r/a for high twist two-ply yarns with helix angles of 30° would be of the order of 4.0 and even higher for lower ply twists. Thus fiber bending strains in straight plied yarns would be still lower than those pictured in the right hand graph of fig. 1.3.72). In each of the three diagrams of figure 1.3.72 the range of curve slopes from maximum to minimum correspond to $\lambda = .5, .75, 1.00$, and 1.25 respectively. Remember that λ for a given r/a is proportional to $\tan \alpha_0$, the helix angle of the unbent yarn.

In short, the analysis suggests that for yarn bending in the absence of fiber slippage, the fiber strains will be zero at the neutral plane and will increase nonlinearly away from the neutral axis. If $\lambda = 0$, i.e., the original yarn twist is 0, then eq (1.3.245) becomes the expression for the fiber strain, ϵ_{fp} , in a parallel bundle with no freedom of slippage.

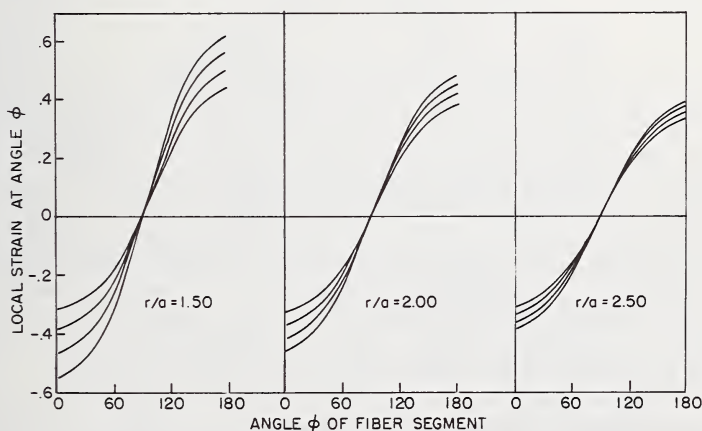


FIGURE 1.3.72. Local fiber strain caused by yarn bending, assuming no freedom of motion between fibers.

In each of the three diagrams of figure 1.3.2, the range of curve slopes from maximum to minimum correspond to $\lambda = .5, .75, 1.00$, and 1.25, respectively.

$$\epsilon_{fp} = \frac{r/a - \cos \phi}{r/a} - 1 = \frac{a \cos \phi}{r} = \frac{c}{r} \quad (1.3.246)$$

where c is the distance of a given fiber from the neutral axis and r is the radius of curvature. This is, of course, the simple formula for bending strain in an elastic prismatic beam bent to small curvatures. If $\lambda = (r/a) \tan \alpha$ is substituted in eq (1.3.245), then ϵ_f becomes:

$$\epsilon_f = \sqrt{(1 - \epsilon_{fp})^2 \cos^2 \alpha + \sin^2 \alpha} - 1 \quad (1.3.247)$$

At the same time [80] it was shown that length of the fiber helix before and after bending of the yarn is constant, which means that the average strain of the fiber above the neutral axis just equals that of the fiber below the neutral axis, except for the sign, i.e., tensile above and compressive below. The yarn system will then attempt to cancel this fiber strain (and hence fiber stress) differential along a given fiber by slipping material from the compressive region into the tensile region. This material interchange does not take place in the simple prismatic elastic beam—it occurs, however, in all twisted (nonbonded) structures, because of the direct connection along the same fiber element in the two zones strained in compression and tension respectively. If complete freedom of motion exists, the slippage will be complete and the average strains will subside, with only the bending strains within each fiber remaining. If ΔS is the difference in path length in the outer and inner parts of the bent yarn fiber loop, the following expression is obtained:

$$\frac{\Delta S}{2} = \int_{\phi=\pi/2}^{\phi=\pi} dS - \int_{\phi=0}^{\phi=\pi/2} dS \quad (1.3.248)$$

or

$$\frac{\Delta S}{2} = \frac{2ar}{\lambda(a^2\lambda^2 + r^2)^{1/2}} - \frac{2a^5r\lambda}{3(\sqrt{a^2\lambda^2 + r^2})^5} \quad (1.3.249)$$

then it can be easily demonstrated that the slippage of fiber from bottom to top of the bend, past the neutral axis is half of eq (1.3.249) or $\Delta S/4$. The first term of eq (1.3.249) is plotted in figure 1.3.73 and it is seen that this approximate value of $\Delta S/2$ drops rapidly when λ increases. To convert the value of $\Delta S/2$ in figure 1.3.73 it is necessary to multiply by r , expressed in the same units as “ a ” and “ T ”. For fixed radius of bend, r , and a fixed twist, T , the slippage decreases as “ a ” becomes smaller and vice versa. Slippage of this nature must be calculated in order to determine the amount of work which will be expended due to friction during bending of a twisted yarn. More will be given about this later.

1.3.4.2. Bending Rigidity of Twisted Yarns (with no Friction)

Generally speaking, the work to bend a twisted structure will depend on its material modulus E_f , its geometry, and, in the case of partial slippage, the friction between its elements. Putting slippage friction

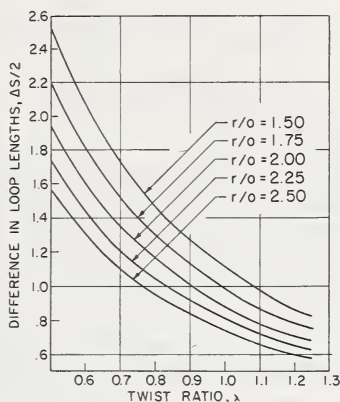


FIGURE 1.3.73. Difference in path length of upper and lower parts of the fiber loop indicated as a function of r/a and λ .

Here r is taken as the unit of length, and $\Delta S/2$ is expressed in terms of this unit.

aside, the analysis of the contribution of geometry and material properties is somewhat more extensive than the prediction of tensile properties alone. Consider first the case of complete constraint, i.e., no longitudinal slippage along the fiber axes. Assuming that plane sections of the yarn remain plane during bending, it is noted in eq (1.3.246) that ϵ_{fp} in a parallel bundle with no freedom of slippage is $c/r = (a \cos \phi)/r$. For the case of a twisted yarn of radius a , bent to the radius of curvature r , the strain ϵ_f in a fiber lying at an angle q , is

$$\epsilon_f = \epsilon_{fp} \cos^2 q = \frac{a \cos \phi \cos^2 q}{r} \quad (1.3.250)$$

and for $\sigma_f = E_f \epsilon_f$, it follows that the force dP_y resulting from the stress σ_y normal to the yarn axis acting on an element of yarn sectional area $dA_y (= a d\phi da)$ is:

$$dP_y = \sigma_y dA_y = \frac{E_f a \cos \phi \cos^4 q}{r} \cdot a d\phi da \quad (1.3.251)$$

The corresponding element of bending moment is

$$dM_b = cdP_y = \frac{E_f a^3 \cos^2 \phi \cos^4 q}{r} d\phi da \quad (1.3.252)$$

which is first integrated for ϕ or the limits 0 to 2π and then for a or the limit 0 to a_y , where a_y is the radius of the yarn. Thus, Backer showed that when the packing factor was unity, [105]

$$M_b = \frac{E_f \pi a_y^4 \gamma}{r} \left\{ \frac{\ln \sec^2 Q - \sin^2 Q}{2 \tan^4 Q} \right\} \quad (1.3.253)$$

$$= \frac{E_f I_y}{r} 4M_a$$

$$\text{where } M_a = \left\{ \frac{\ln \sec^2 Q - \sin^2 Q}{2 \tan^4 Q} \right\}$$

which for small Q becomes

$$M_b = \frac{E_f I_y}{r} (2 \cos^2 Q) \quad (1.3.254)$$

Equation (1.3.253) above was independently derived by Platt [14] to permit prediction of yarn bending rigidity from fiber properties and actual numbers of fibers in the yarn N_f . Thus, rather than writing the $E\pi a_y^4$ of eq (1.3.253) above, he utilized the fiber cross-sectional area, A_f , and the number of fibers, N_f , so that

$$E\pi a_y^4 \rightarrow N_f E_f A_f a_y^2 \left(\frac{a_y^2}{a_{y0}^2} \right) \quad (1.3.255)$$

where a_{y0} was the cross-sectional area of the untwisted yarn (with no change in packing factor, ϕ , as a result of twisting). The expression for the ratio of the twisted yarn radius to the untwisted yarn radius (i.e., a_y/A_{y0}) was shown to be [107]

$$\left(\frac{a_y}{a_{y0}} \right)^2 = \frac{\tan^2 Q \cos Q}{2(1 - \cos Q)} \quad (1.3.256)$$

An equivalent expression was derived independently [105]. Remembering the definition of $\phi (= \Sigma A_f/A_y)$, one can show

$$E\pi a_y^4 \rightarrow E\pi \phi a_y^4 \quad (1.3.257)$$

leading to the suggestion that ϕ be included in both eqs (1.3.253) and (1.3.254).

The response of yarns with complete freedom of relative fiber motion was treated by Platt [14] in considerable detail. If the fiber segment located at position ϕ and helix radius r is considered bent to a curvature K_f as a result of yarn bending, then the required bending moment vector for such a fiber configuration would lie along the binormal, \hat{b} , to the fiber at the given segment. The component of this bending moment vector perpendicular to the plane of yarn bending represents the contribution of the given fiber to resistance to yarn bending and is seen to be δM_{yb} where

$$\delta M_{yb} = E_f I_f K_f \cos q \cos \phi \quad (1.3.258)$$

or for the fibers in the incremental area dA_y where

$$dA_y = a \cdot da \cdot d\phi \quad (1.3.259)$$

and the number of fibers in the dA_y is

$$dN_f = \frac{N_f(adad\phi) \cos q}{\pi a_{y0}^2} \quad (1.3.260)$$

where a_{y0} is the radius of the yarn before twisting, with $\phi = \text{constant}$ during twisting. Whereupon dM_b per incremental area dA_y is obtained through the product of eqs (1.3.259) and (1.3.260). K_f may be obtained from eq (1.3.92). But Platt has elected to treat K_f vectorially, thus eliminating the need for the terms $\cos q \cos \phi$ in eq (1.3.92). For in the cartesian system $\bar{i}, \bar{j}, \bar{k}$ where \bar{k} is the unit vector corresponding to the x_3 direction in figure 1.3.69, the "yarn bending" component of the binormal fiber bending vector $K_f \bar{b}$ is simply its \bar{k} component. Platt thus obtains the expression for K_{fk} :

$$K_f \cos q \cos \phi = K_{fj} = [(a \cos \phi - r)^2 + a^2 \lambda^2 (1 + \sin^2 \phi) - ar \lambda^2 \cos \phi] u^{-3/2} \quad (1.3.261)$$

where $u = (a \cos \phi - r)^2 + a^2 \lambda^2$; $\lambda = (r/a) \tan Q$. Then, combining eqs (1.3.258-261), he integrates through ϕ and a to obtain for the bending rigidity of the yarn (with approximations)

$$\begin{aligned} (EI)_{\text{yarn}} &= M_{by} r \text{ (with freedom to slip)} \\ &= N_f E_f I_f \left[\frac{2 \ln \sec^2 Q - 3 \sin^2 Q + (1 - \cos^4 Q)}{\tan Q} \right] \left(\frac{a_y}{a_{y0}} \right)^2 \end{aligned} \quad (1.3.262)$$

which can be shown to equal:

$$(EI)_{\text{free yarn}} = N_f E_f I_f \left[(4M_a \tan^2 Q + \cos^4 Q) \left(\frac{a_y}{a_{y0}} \right)^2 \right] \quad (1.3.263)$$

Now, comparing eqs (1.3.253) and (1.3.263), we note that the bending rigidity of the "no fiber slip" yarn is that of the no twist no slip yarn corrected by the factor $4M_a$. The free fiber slip yarn has a bending rigidity equal to that of a zero twist "free slip" yarn corrected by the bracketed quantity in eq (1.3.263). It can be shown that with freedom of fiber slippage

$$(EI)_{\text{free yarn}} = \frac{E_f I_y}{N_f} \left[(4M_a \tan^2 Q + \cos^4 Q) \left(\frac{A_f}{A_y} \right) \right] \quad (1.3.264)$$

where A_f is the collective (nontwisted) fiber cross-sectional area, and A_y is the twisted yarn cross-sectional area. Thus, it appears that the rigidity of the free to slip twisted yarn is related to that of the "not free to slip" untwisted yarn:

$$\frac{(EI)_{\text{free}}}{(EI)_{\text{not free}}} = \frac{\left[(4M_a \tan^2 Q + \cos^4 Q) \left(\frac{A_f}{A_y} \right) \right]}{N_f} \quad (1.3.265)$$

For $Q = 30^\circ$, $A_f/A_y = .75$, the ratio is about $.6/N_f$. If $N_f = 1$, which means there is no slippage, the reduction in stiffness is about 40 percent. If $Q = 30^\circ$ and $N_f = 100$, clearly the reduction in rigidity is influenced by the factor of 100 and the relative loss due to twist is small by comparison.

Platt points out that if the yarn being bent has been "set" after twisting, then the curvatures incurred during yarn bending do not determine local bending moments but, rather, they are determined by the changes in fiber curvature from the straight yarn state to the bent yarn state. Now, if the yarn has been relaxed after twisting, there is a likely effect on the fiber modulus, therefore a new quantity E'_f must be introduced to the above equations. Platt has calculated the effect of yarn relaxation on bending rigidity of a singles yarn, leaving aside the modulus effect from setting, and concludes that "aside from its possible effect on changing fiber modulus, relaxation of fiber bending stresses during yarn twisting diminishes yarn bending rigidity. The effect is slight, ranging from no effect at zero twist to 4.3 percent at a surface helix angle of 35° ."

The effect of torsional moments (acting on individual fibers) on the bending moment of the yarn has been treated by Platt. For while the k components of the fiber torques, M_t , are seen to cancel out in the twisted, straight, yarn and additional fiber torque is cancelled out by local fiber rotation in a "free to slip" bent yarn, yet unrelaxed torque due to yarn twisting can have an effect on bending rigidity of that yarn. Platt has carried through an analysis similar to the above, this time taking fiber torque components; and he concludes that for fiber torsional rigidity equal to or less than fiber bending rigidity, the effect of fiber torque on bending rigidity is relatively small and since for most drawn synthetics it is .2 to .3, it can be safely neglected in such cases.

Finally, Platt has looked at the important question of "clustering"—defined as the joint action of groups of fibers acting thereby as single fibers. The two cases of complete freedom of motion, and complete restraint of slippage are, of course, extremes which do not occur often in the application of fibers in textile systems. In most cases, there is some slippage with frictional, but not total, restraint and such instances fall between the extremes discussed above. The clustering phenomenon represents another case between the extremes wherein some fibers are free to slip (without friction) and others are totally restrained from slipping in groups or clusters. The effect of clustering is similar to using fewer heavy (high denier) filaments as contrasted to more low denier filaments in yarns of the same total denier. The analysis of bending rigidities of yarns containing clustered fibers does require determination of bending rigidities of the individual clusters. And since the cross section of the clusters is noncircular, and the sectional moment of inertia depends on cluster orientation, Platt assumes a random distribution of orientations and calculates an average moment for insertion in

the above equations. Clustering significantly effects the bending rigidity of a yarn and if x is the number of fibers in a cluster, then the bending rigidity of the clustered yarn is approximately x times the rigidity for the "completely free to slip" yarn. If the entire yarn is clustered, i.e., $x = N_f$, then its bending rigidity is N_f times the bending rigidity of the "completely free to slip" yarn. Geometric effects aside, this is shown in eq (1.3.265).

Zorowski [106] took an alternate approach to the "cluster" condition in the bending of continuous filament yarns. He assumed either complete fiber freedom to slip or complete restraint in various parts of a yarn cantilever. The "no slip" region is shown as cross-hatched in figure 1.3.74 and is seen to cover the entire cross section of the cantilever for a length l_o from its free end. In the region at a distance x from the free end, where $l_o < x < l$, there was an elliptical central core of no slip fibers, surrounded by free slip fibers. The minimum radius of the ellipse was R , and its maximum radius was $R_o = R_y$, the nominal radius of the round yarn.

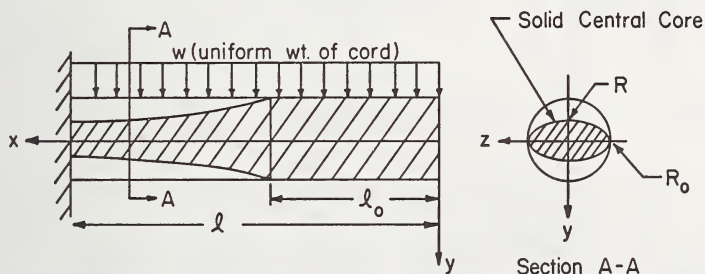


FIGURE 1.3.74. Proposed equivalent bending model of Zorowski [106].

For the cantilevered homogeneous isotropic beam bent under the action of its own weight, one would expect an end deflection of δ

$$\delta = \frac{wl^4}{8EI} \quad (1.3.266)$$

where w is the weight per unit length. This relationship is based on small deflection theory but Zorowski points out that it is actually within 16 percent of agreement with large deflection theory for δ/l ratios up to 0.5. It would indicate that δ/l should vary linearly with l^3 . Actual tests by Zorowski on cantilevered 840 denier, two-ply yarns of different fiber deniers are reported in figure 1.3.75 which does indicate a linear relationship for δ/l up to values of 0.5 to 0.6. But, as seen in the insert of figure 1.3.75, the curves do not go through the origin. Determining the slope, m , from figure 1.3.75, where $m = l^3/\delta/l$, one obtains the bending rigidity (EI_b) from:

$$EI_b = \frac{mw}{8} \quad (1.3.267)$$

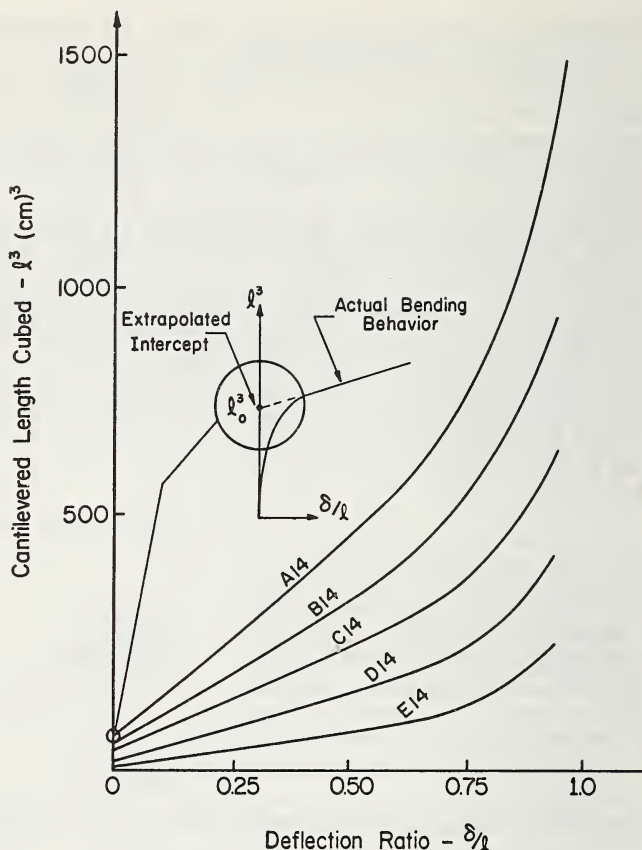


FIGURE 1.3.75. Characteristic results from bending tests.

Now from the definition of the conditions of complete freedom and complete restraint

$$EI_o = NE_f \frac{\pi r^4}{4}; (EI)_\infty = E_i \frac{\pi R_y^4}{4} \quad (1.3.268)$$

and as was shown above

$$(EI)_o = \frac{1}{N} (EI)_\infty \quad (1.3.265)$$

Using eqs (1.3.267) and (1.3.268), Zorowski reports that for selected plied yarns (cords) the measured $(EI)_b$ were 5 to 20 times the zero friction rigidity. However, the infinite friction rigidity is an order of magnitude 30 to 200 times the measured value. And the infinite friction rigidity was N times the rigidity of zero friction case since both were calculated from eq (1.3.268).

Zorowski assumed that difference between zero friction fiber strain and infinite friction fiber strain which exists at the position $x = l_o$ will be constant over the region $l_o < xl$. The maximum strain for the ∞ friction case at l_o is

$$\epsilon_{\infty}|_{l_o} = \frac{yM}{EI} = \frac{R_y}{E_f} \left(\frac{4}{\pi R_y^4} \right) \frac{wl_o^2}{2} = \frac{2w}{E_f \pi} \left(\frac{l_o^2}{R_y^3} \right) \quad (1.3.269)$$

while the zero friction maximum strain is:

$$\epsilon_f|_{l_o} = \frac{2w}{E_f \pi N_f} \left(\frac{l_o^2}{r^3} \right) \quad (1.3.270)$$

where N_f is the number of fibers. Rewriting eqs (1.3.269) and (1.3.270) for $l_o < x < l$ and letting the strain difference be constant at each location, i.e.,

$$(\epsilon_{\infty} - \epsilon_f)_x = (\epsilon_{\infty} - \epsilon_f)_{l_o} \quad (1.3.271)$$

Zorowski showed R as a function of x :

$$\left(\frac{Ry}{R} \right)^2 = \left(\frac{l_o}{x} \right)^2 (1 - \sqrt{N_f} + \sqrt{N_f}) \quad (1.3.272)$$

which provides the equivalent dimensions of a nonhomogeneous property beam for which gravity deflections of a cantilever are to be calculated. He then applied strain energy principles and the unit load method of deflection analysis to determine the end deflection of the cantilever beam of figure 1.3.74. The deflection δ , is then:

$$\delta = \frac{1}{2} \int_0^l \frac{wx^3}{\beta E_f I} \cdot dx \quad (1.3.273)$$

where $I = N_f I_o$ for $0 < x < l_o$

$$= N_f I_o \left(\frac{R}{R_y} \right)^3 \text{ for } l_o < x < l$$

and the factor β is the geometric factor developed by Platt as described above. Substituting eq (1.3.272) into eq (1.3.273) provided an expression for δ as a function of fiber properties and yarn geometry. Then calculating from eq (1.3.267) and from $m = l^4/\delta$,

$$(EI)_b = \frac{mw}{8} \simeq \frac{wl^4}{8\delta} \quad (1.3.274)$$

Using the calculated value of δ , Zorowski showed

$$\frac{(EI)_b}{(EI)_o} \approx \frac{N_f \beta}{K} \quad (1.3.275)$$

where K was a function of l , l_o and N_f . Using eq (1.3.275), Zorowski compared theoretical deflection curves and those measured in the cantilever test in figure 1.3.76. The agreement between experiment and theory was not as good as might be desired, he concluded, but the general characteristics of the observed behavior are reproduced and the numerical magnitudes are not completely out of line.

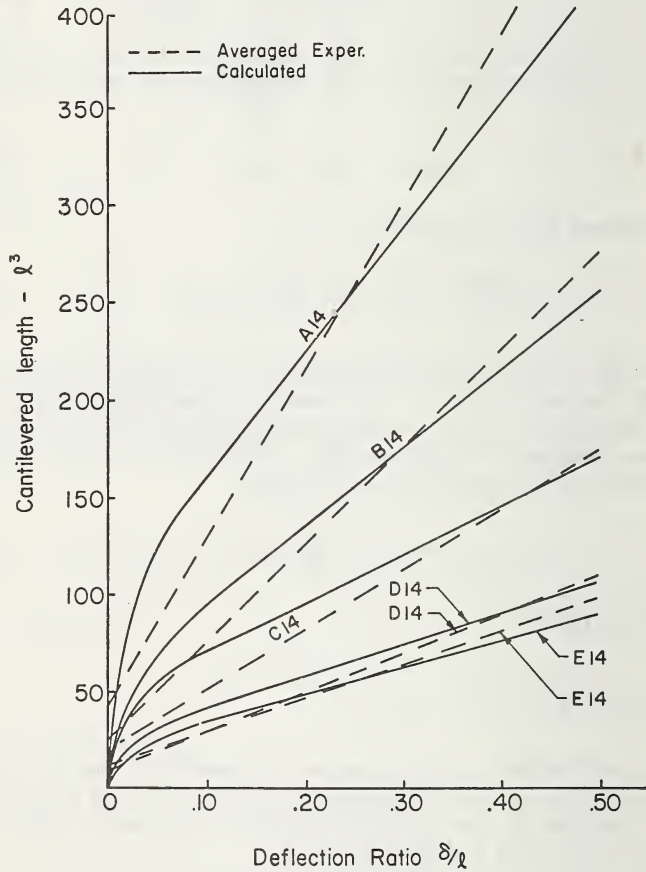


FIGURE 1.3.76. Comparison between predicted and experimental bending behavior.

1.3.4.3. Bending Rigidity of Twisted Yarn (with Friction)

An early attempt to include the role of friction in the analysis of bending rigidity of twisted yarns was that of Mellen [107] et al. who considered the case of a ring of cords helically wound around an inflated cylinder. The cords were, in effect, the reinforcing elements required to prevent excessive expansion during inflation of the cylinder. Since the inflated cylinder was intended for incorporation into a fully pressurized suit for space walking, it was necessary to minimize the change in cylinder dimensions with inflation, and at the same time to reduce the bending rigidity of the inflated cylinder.

If the reinforcing cords are considered to have a tensile modulus infinitely greater than the modulus of the material of the cylinder, and if they are wrapped equally in sets of right hand and left hand helices, it can be shown that they will assume an equilibrium helix angle of 35° . The assumption is then made that the cylinder does not flatten during bending, a reasonable condition for small curvatures, but one which has been observed to fail at large curvatures.

Now viewing the wrap reinforced bent cylinder in figure 1.3.77 we consider two cases: (1) where cord stress develops with no cord slippage along the cylinder surface, and (2) where the cord wrapping does slip, as indicated in figure 1.3.77, along its length. For the case of no slippage, we can show that the bending moment M_b for an applied curvature $K = 1/\rho$, is:

$$M_b = 2 \int_0^\pi J \sigma_l w R d\lambda = 2 \int_0^\pi J (E_c \epsilon_c \cos^2 Q) (R \cos \lambda) R d\lambda \quad (1.3.276)$$

where $1/J$ is the helical separation of the cords, $J \sigma_l$ is the longitudinal stress along the cylinder axis provided by the tensile force σ_c in the cord, ϵ_c is the tensile strain of the cord and ρ , w , Q , R and λ are geometric parameters as shown in figure 1.3.77. Since the inclined cord strain is related to the longitudinal strain by the factor $\cos^2 Q$ and the longitudinal strain is w/ρ or $R \cos \lambda/\rho$, eq (1.3.276) becomes

$$M_b = \frac{2 J E_c R^3 \cos^4 Q}{\rho} \int_0^\pi \cos^2 \lambda d\lambda = \frac{2 J E_c R^3 \cos^4 Q (\pi/2)}{\rho} \quad (1.3.277)$$

It was reasoned that since the local strain at the neutral plane is zero from eq (1.3.245) or from eq. (1.3.247), the stress there would also be zero, while it would be maximum at λ (or ϕ) = 0 or π (fig. 1.3.72). Thus, if no slippage occurred, the local stress of an Hookean cord would be pictured in figure 1.3.78, with σ_c as a function of l , (as per fig. 1.3.77, or s in fig. 1.3.2). To prevent slippage, $d\sigma/dl$ must not exceed μN where μ is the coefficient of friction, and N is the normal force between cord and cylinder per unit length of cord. Since μN can be assumed constant, one can expect that

$$\sigma_c = \mu N l = E_c \epsilon_c \quad (1.3.278)$$

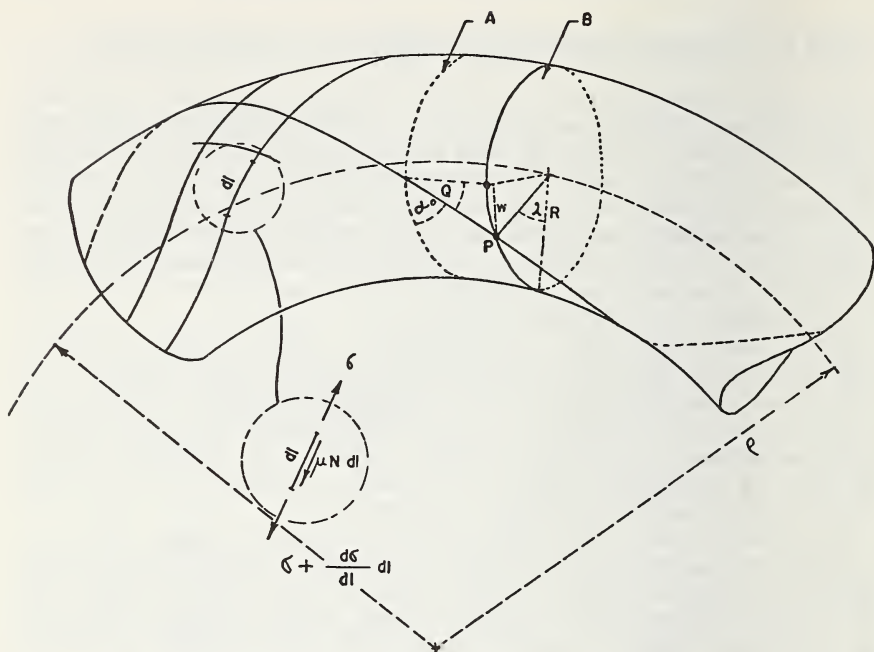


FIGURE 1.3.77. Geometry of wrap-reinforced bent cylinder.

Since l in figure 1.3.77, or s in figure 1.3.2 is a function of λ , as shown in figure 1.3.78, or ϕ , of figure 1.3.2, one can use eq (1.3.278) to plot a "slippage allowable" ϵ_c versus ϕ in figure 1.3.78, and for small curvatures this will be a straight line passing through the origin. Thus, as the cylinder is first bent, the ϵ_{local} versus ϕ curve will be dictated by the no slip condition as in figure 1.3.78. But as the curvature, $1/\rho$, increases, the no slip curve rotates counterclockwise until it contacts the "slip allowable" curve. Since the slope of the "no slip" curve cannot exceed that of the "slip allowable" curve, then the change in the actual ϵ_{local} versus ϕ curve can be thought of as a "freezing" or flattening of the "no slip" curve against the straight "slip allowable" curve. Wherever the flattening or freezing takes place, local slippage will be present. And from the shapes of the curves of figure 1.3.78, it will be expected that slippage will first take place at the neutral axis at $\lambda = \pi/2$, then propagate both upward and downward to values of $\lambda\theta$, or $\phi = 0, \pi$ respectively. Note this is the λ of figure 1.3.78.

If now, l is zero at $\lambda = \pi/2$, it follows for low curvatures that l can be taken as $(\lambda - \pi/2)R/\sin Q$ and it can be shown from eqs (1.3.276) and (1.3.277) that the bending moment incurred for an applied curvature of $1/\rho$ is:

$$M_b = \int_0^\pi 2J[\mu N(\lambda - \pi/2)R/\sin Q] \cos^2 Q (R \cos \lambda) R d\lambda \quad (1.3.279)$$

$$= J\mu NR^3 \cos^2 Q / \sin Q$$

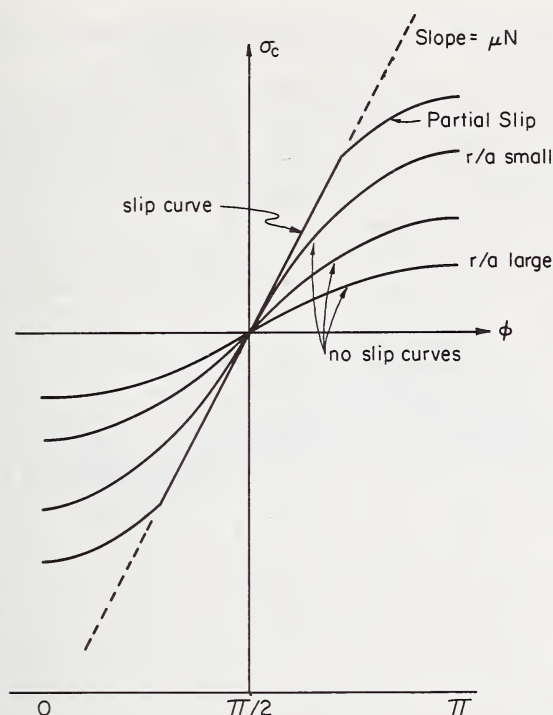


FIGURE 1.3.78. Local fiber stress caused by yarn bending, corrected for slip, as a function of angle ϕ of fiber segment.

which, surprisingly, shows M_b to be independent of E_c , the cord modulus, and even independent of ρ , the radius of curvature of the cylinder. In short, for the conditions assumed, the M_b versus K curve will be flat and at a level independent of E_c ; rather, its level will be dependent on the cord frequency, J , the cube of the cylinder radius, and the product of coefficient of friction μ and normal pressure N . Note that the K or $1/\rho$ region considered here was the one in which slippage was propagated throughout the structure. At smaller K 's we would expect partial slippage and partial restraint as shown in figure 1.3.78. At still smaller K 's we would expect complete restraint. There was no effort made in this early study to consider the very lower curvature cases, nor to consider the contribution of cylinder tensile-compressive modulus to the bending moments at "all slip" curvatures, nor the contributions of the bending rigidities of the slipping cord to overall assembly rigidity in the "all slip" curvature region. (Clearly, the contribution of the cylinder modulus and of the EI of the cords will be dependent on K , hence the total M_b versus K curve would no longer be flat in the all slip region,

but this is hindsight based on results of subsequent multilayer beam bending studies.)

Treatment of a multifilament yarn in bending calls for a more realistic model than that of figure 1.3.77 and the obvious requirement is for the introduction of multiple helical layers of fibers, with slippage between layers or cylindrical rings during bending. But since the direction of slippage must be in opposite directions, at the top and bottom of each layer of fibers, it follows that eq (1.3.278) must be expressed in terms of δN , the normal pressure differential across each fiber. As is seen from eq (1.3.123) N or σ_{tr} is larger at the inside surface of each ring than the outside surface, when the yarn is under some tension during bending. Hence from eq (1.3.123) one can express δN as a function of radial position r and of fiber diameter δr and integrate dM_b once again as in eq (1.3.279) to provide the frictional bending moment in a twisted yarn when bent under tension as, for example, in the case of a cord running over a pulley, or the bending of a tire cord in an inflated tire. The form of the expression for the predicted frictional moment obtained by this stress analysis method agrees with the moment predicted by the work methods to be discussed below, specifically with eq (1.3.288). It is interesting to note that the "work" solution for bending behavior of the multilayered twisted structure with friction actually preceded the stress analysis solution for bending of a multifilament yarn while in the case of tensile properties the stress analysis treatments preceded the energy treatments.

Using as a model yarn a series of straight circular filaments stacked in layers so as to form a rectangular cross-sectional bundle, it has been shown [110] that the local slippage, S , between layers pressed together by a pressure p (per unit fiber length) is a source of work loss, W_f , during bending, i.e.,

$$W_f = \int_{-l/2}^{l/2} \frac{f_f w S}{d_f} dx \quad (1.3.280)$$

where f_f is the friction per unit fiber length constant throughout and equal to $\mu p d_f$ (p the lateral pressure being constant throughout the model), w is the layer width, d_f the fiber diameter, and x the length from the fiber center. The local slippage, S , between fibers for the model shown in figure 1.3.79 is shown to be

$$S = d_f k x \quad (1.3.281)$$

where k , the layer curvature, is constant throughout the model. Substituting eq (1.3.281) into eq (1.3.280) and integrating, we have the frictional work loss at a single interface

$$W_f = \frac{f_f w k l^2}{4} \quad (1.3.282)$$

From beam theory it is shown that the work to bend one layer to a curvature k (not considering friction, but only elastic forces) is

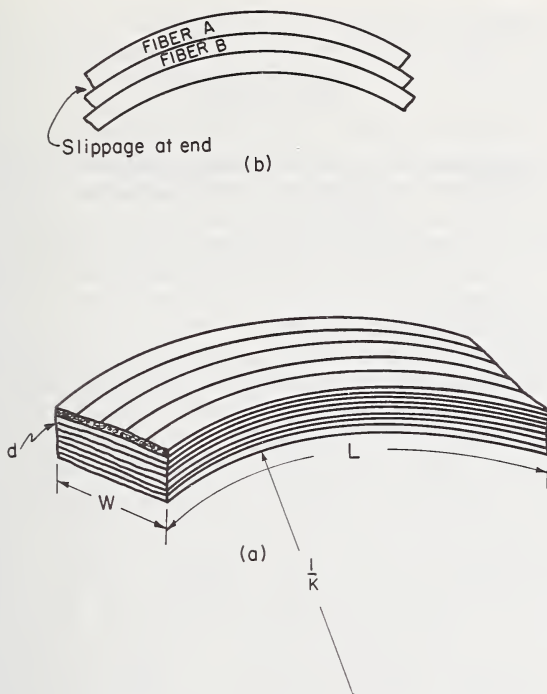


FIGURE 1.3.79. (a) Simplified model of yarn bending. (b) Slippage between layers of fibers.

$$W_e = \frac{E\pi d^3 w l k^2}{128}, \quad (1.3.283)$$

since I_{layer} equals $I_f w/d_f$, i.e., $\pi d_f^3 w/64$. The sum of W_f and W_e is the total work W_t to bend each layer to curvature k . From eq (1.3.282) it is seen that W_f is linear in k , i.e., dW_f/dk is constant. Now, if M_f is the moment required to do the frictional work,

$$dW_f = M_f d\theta = M_f(l) dk \quad (1.3.284)$$

hence M_f is constant and equal to $\frac{f w l}{4}$. From eq (1.3.283) W_e is seen linear in k^2 hence M_e is directly proportional to k , as one would expect for elastic behavior. Thus, the total bending moment M_T can be shown as:

$$M_T = M_f + M_e = \frac{d_f f w l}{4} + \frac{E\pi d_f^3 w k}{64} \quad (1.3.285)$$

where f is the frictional shear stress between fiber layers ($=d_{ff}$). If V is the total vertical force spread uniformly between fiber layers, eq

(1.3.285) can be expressed as:

$$M_f = \frac{1}{4} V \mu d_f \quad (1.3.286)$$

as was shown independently by Grosberg [108] and by Popper [109].

From eq (1.3.285), one anticipates a bending moment versus curvature curve as shown in figure 1.3.80. The recovery portion of the curve results from the change in sign of the second term of eq (1.3.285) during unloading. Clearly, the final recovery (at zero moment) from the applied curvature will be reduced as the frictional moment increases relative to the elastic rigidity of the layered system.

Popper [109] takes special pains to analyze the initiation of slippage in a layered beam, showing that it must start at the center of the beam at a local region where vertical shear force and bending moment prevail, and then it will propagate longitudinally into the region of pure bending moment. Grosberg [108] and Popper [109] independently analyze the forces required to maintain yarns in the crimped configuration of a woven fabric, considering that the total normal force between warp and filling yarns is equal to the sum of the normal forces necessary to bend each of the fibers comprising the yarn. An important element of the analysis has to do with the fact that the pressure between fibers in each yarn set is maximum at the fabric center, but it decreases linearly with each fiber layer (say in a rectangular cross section yarn) until the last interface where the interfacial normal pressure is simply enough to keep the outside fiber layer bent. Grosberg [108] makes the important point that the force between yarn sets in a fabric should not be calculated on the

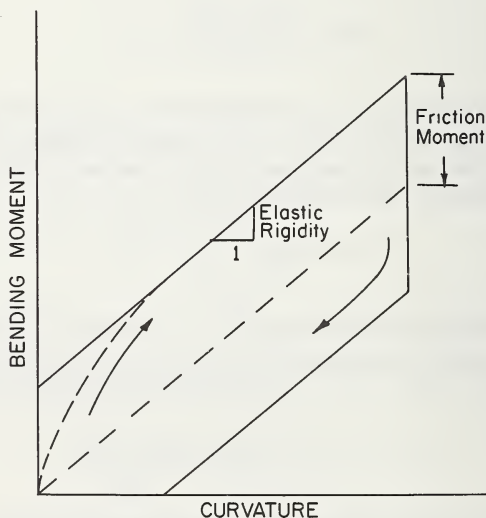


FIGURE 1.3.80. *Effect of sliding friction on moment-curvature relation.*

basis of the in situ curvatures of the fibers in the fabric, but rather on the difference in curvatures between the fibers as they lie in the yarn in the fabric and the same fibers as they lie in the yarn removed from the fabric. This use of curvature change serves to account for yarn bending relaxation after weaving or that due to setting treatments.

Popper [109, 111] then shows that when a twisted yarn, with a constant normal force between fibers, is bent, the friction moment, M_f , is

$$M_f = \frac{2}{\pi^2} \mu n_i N_i d_f \frac{L_t}{2} \quad (1.3.287)$$

where n_i is the normal force per length at each fiber interface, N_i is the number of fiber interfaces, and $L_t/2$ is the length of fiber in half a turn of twist. Note that $L_t/2$ corresponds to the characteristic length l in the M_f term of eq (1.3.282). The similarity of the expressions is obvious. Popper [111] treated the case of bending a yarn subjected to axial tension. The pressure distribution between fibers was taken according to Machida [55] (eq (1.3.123)). This pressure distribution was then translated into a normal force per unit length on each fiber interface and this was combined with the relative fiber motions to give the work loss. The essential difference between this analysis and the cases for the layered beams or square fiber area with constant pressure between layers is that in this case the work loss varies with radial position. For this reason, the total frictional work loss involves summing the work losses throughout the structure after correcting for the differences in number of interfaces at each radial position. The resulting frictional moment is approximated by Popper [109] as

$$M_f = 4R_y^2 \phi_y \mu P T \quad (1.3.288)$$

where ϕ_y is the yarn packing factor and P is the axial tension on the yarn. And it is interesting to note that eq (1.3.288) can be obtained from eq (1.3.277), taking into account the indicated pressure distribution resulting from the axial tension P and calculating the tension build up along each yarn due to the incremental friction. This incremental friction follows from the incremental resultant of normal pressure forces at one sliding surface of each fiber.

In terms of predicting the bending moment resulting from bending a yarn to a known curvature, the Popper method of determining eq (1.3.288) is more direct, but as is the case with energy, and work methods, it loses some of the detail of the stress analysis method. In particular, if we wish to calculate the local force which builds up along a fiber in a yarn, due to slippage friction (with a known pressure distribution from layer to layer) we can do so simply by using eq (1.3.278). And this knowledge will permit a determination of the local fiber stress and strain level, which when compared with tensile (or if available, compressive) recovery data for the fiber, will permit calculation of yarn bending recovery taking elastic behavior, friction, and also viscoelastic behavior into account. Of equal importance, the knowledge of

local fiber stress and strain levels will permit the use of fatigue data based on straight fibers and low twist yarns to predict fiber fatigue incurred during the bending of highly twisted structures. Clearly, much more work remains to be done in this problem area.

As a final comment on the mechanics of bending fiber assemblies, we present in figure 1.3.81 a diagrammatic summary of the different strain distributions which can occur in the cases of: (1) complete freedom to slip; (2) no freedom to slip; (3) frictional resistance to slippage. While numerous experimental data have been reported on the substance of these analyses, we include but one set by Popper [111], (fig. 1.3.82) showing a comparison between theoretical and measured deflection curves for a layered beam with constant pressure between all layers. Here the stiffness, i.e., the vertical load V per unit deflection, is plotted against the position of loading γ along the beam. The value of γ is 0 at the free end of the multilayered cantilever, whose layers slip with constant friction.

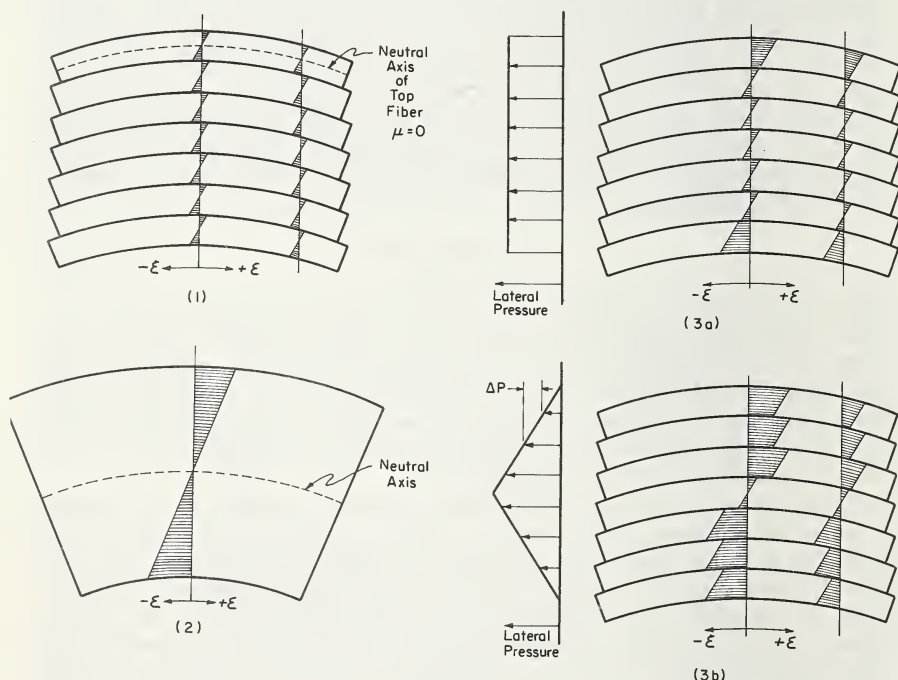


FIGURE 1.3.81. Diagrammatic summary of different possible strain distributions.

1. Complete freedom to slip.
2. No freedom to slip.
3. (a) Constant pressure at all interfaces.
(b) Constant pressure change across each layer.

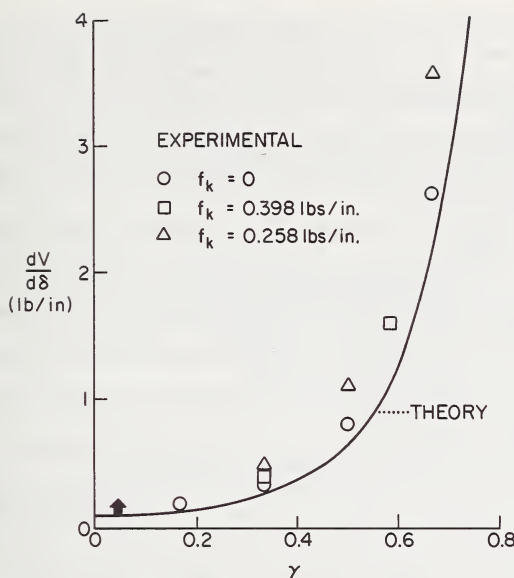


FIGURE 1.3.82. Multi-layer beam stiffness vs. position of load.

References

- [1] Journal of Composite Materials, Technomic Publishing Company, Inc., Stamford, Connecticut.
- [2] Fiber Science and Technology, Elsevier Publishing Company, Barking, England.
- [3] Kersker, T. M., Kovac, F. J., and Dague, M. F., Engineering of Textiles for Tire Composites, Paper presented at the American Institute of Chemical Engineers meeting, March 1969, New Orleans, Louisiana.
- [4] Hearle, J. W. S., The Structural Mechanics of Fibers, Journal of Polymer Science: Part C, No. 20, pp. 215-251 (1967).
- [5] Van Veld, R. D., Morris, G., and Billica, H. R., Morphology of man made fibers, Journal of Applied Polymer Science **12**, 2709-2724 (1968).
- [6] Centola, G., Supermolecular structure and fiber properties, Journal of the Textile Institute **59**, 445-456 (1968).
- [7] Hearle, J. W. S., Grosberg, P., and Backer, S., The Structural Mechanics of Fibers, Yarns, and Fabrics, (Wiley-Interscience, New York, 1969).
- [8] Backer, S., and Valko, E. I., Thesaurus of Textile Terms, Covering Fibrous Materials and Processes, (M.I.T. Press, Cambridge, Massachusetts, 1969).
- [9] Textile Terms and Definitions, (The Textile Institute, 5th Edition, 1963, Manchester, England).
- [10] Kovac, F. J., Tire Reinforcing Systems, (University of Akron Lecture Series, Second Edition, 1969).
- [11] Linton, G. E., The Modern Textile Dictionary, (Little, Brown, and Company, Boston, 1954).
- [12] Kilby, W. F., The retraction of twisted continuous filament yarns, Journal of the Textile Institute **50**, T673-687 (1959).
- [13] Schwarz, E. R., Twist structure of plied yarns, Textile Research Journal **20**, 175-179 (1950).

- [14] Platt, M. M., Klein, W. G., and Hamburger, W. J., Some aspects of bending rigidity of singles yarns, *Textile Research Journal* **29**, 611-627 (1959).
- [15] Freeston, W. D., Platt, M. M., and Butterworth, G. A. M., Torsional recovery of filaments and single yarns and plied-yarn balance, *Textile Research Journal* **36**, 12-30 (1966).
- [16] Chow, Tseng-yeh, Some Aspects of the Geometry of Yarn Structure, M.S. Thesis, M.I.T., Cambridge, Massachusetts, 1948.
- [17] Treloar, L. R. G., The geometry of multi-ply yarns, *Journal of the Textile Institute* **47**, T348-368 (1956).
- [18] Schwarz, E. R., Certain Aspects of Yarn Structure, *Textile Research Journal* **20**, 175-179 (1950).
- [19] Riding, G., A study of the geometrical structure of multi-ply yarns, *Journal of the Textile Institute* **52**, T366-381 (1961).
- [20] Stansfield, G. J., The geometry of twisted multi-filament structures, *British Journal of Applied Physics* **9**, 133-139 (1958).
- [21] Gracie, P. S., Twist geometry and twist limits in yarns and cords, *Journal of the Textile Institute* **51**, T271-288 (1960).
- [22] Tattersall, G. H., An experimental study of yarn geometry, *Journal of the Textile Institute* **49**, 295-304 (1958).
- [23] Riding, G., An experimental study of the geometrical structure of singles yarns, *Journal of the Textile Institute* **50**, T425-442 (1959).
- [24] Platt, M. M., Klein, W. G., and Hamburger, W. J., The Applied Mechanics of Yarn Structures as Influenced by Yarn Geometry and Inherent Fiber Properties, *Congres International des Sciences Appliquees a l'Industrie Textile*, 75th Anniversary Celebration Communication No. 20.
- [25] Hamilton, J. B., A direct method for measuring yarn diameters and bulk densities under conditions of thread flattening, *Journal of the Textile Institute* **50**, 655-672 (1959).
- [26] El Behery, H. M., Study of theories of fiber migration, need for more fundamental approach and further studies, *Textile Research Journal* **38**, 321 (1968).
- [27] Treloar, L. R. G., A migrating-filament theory of yarn properties, *Journal of the Textile Institute* **56**, 359-380 (1965).
- [28] Morton, W. E. and Yen, K. C., Arrangement of fibres in fibro yarn, *Journal of the Textile Institute* **43**, 60 (1952).
- [29] Gupta, B. S., Ph.D. Thesis, University of Manchester, 1963.
- [30] Treloar, L. R. G., and Riding, G., Migrating filament theory: apparent variation of twist with radial position, *Journal of the Textile Institute* **56**, 381-388 (1965).
- [31] Riding, G., Filament migration in single yarns, *Journal of the Textile Institute* **55**, 9 (1964).
- [32] El-Shiekh, A. H. M., On the Mechanics of Twist Insertion, Sc.D. Thesis, M.I.T., Cambridge, Massachusetts, 1965.
- [33] Marzoli, P., On the Mechanics of Fiber Migration, M.S. Thesis, M.I.T., Cambridge, Massachusetts, 1965.
- [34] Hickie, T. S., and Chaikin, M., The configuration and mechanical state of single fibers in woolen and worsted yarns, *Journal of the Textile Institute* **51**, 1120-1129 (1960).
- [35] Chaikin, M., Baird, K., Stutter, A. G., and Curtis, J., *Proc. Inst. Wool Textile Research Conference*, Australia, E-168, 1955.
- [36] Bloch, M. G., M.S. Thesis, M.I.T., Cambridge, Massachusetts, 1954.
- [37] Coplan, M. J., and Bloch, M. G., A study of blended woolen structure, *Textile Research Journal* **25**, 902-922 (1955).
- [38] Hamilton, J. B., The radial distribution of fibers in blended yarns, *Journal of the Textile Institute* **49**, 411-423 (1958).
- [39] Bunting, W. W., Compact Interlaced Yarn, U.S. Patent 2,985,995, May 30, 1961.
- [40] Riding, G., Filament migration in singles yarns, *Journal of the Textile Institute* **55**, T9-17 (1964).
- [41] Hearle, J. W. S., and Gupta, B. S., Migration of fibers in yarns, *Textile Research Journal* **35**, 788 and 885 (1965).
- [42] Hearle, J. W. S., and Merchant, V. B., Interchange of position among components of a seven-ply structure, *Journal of the Textile Institute* **53**, 537-552 (1962).
- [43] Platt, M. M., Mechanics of elastic performance of textile materials, Part III: Some

- aspects of stress analysis of textile structures—continuous filament yarns, *Textile Research Journal* **20**, 1–15 (1950).
- [44] Gégauff, G., *Bull. Soc. Ind. Mulhouse* **77**, 153 (1907).
- [45] Hearle, J. W. S., The mechanics of twisted yarns, the influence of transverse forces on tensile behavior, *Journal of the Textile Institute* **49**, 389–408 (1958).
- [46] Platt, M. M., A note on certain relationships between yarn and fiber strain, *Textile Research Journal* **24**, 132–134 (1954).
- [47] Hearle, J. W. S., El Behery, H. M. A., and Thakur, V. M., Mechanics of twisted yarns: theoretical developments, *Journal of the Textile Institute* **52**, 197–220 (1961).
- [48] Galileo, Galilei, *Dialogues Concerning Two New Sciences*, Leyden (1638) translated by A. De Salvio and A. Fabaro, Evanston, Illinois, (1914).
- [49] Peirce, F. T., *Journal of the Textile Institute* **17**, 355 (1926).
- [50] Platt, M. M., Klein, W. G., and Hamburger, W. J., Mechanics of elastic performance of textile materials, Part IX: Factors affecting translation of certain mechanical properties of cordage fibers into cordage yarns, *Textile Research Journal* **22**, 641–667 (1952).
- [51] Backer, S., and Petterson, D. R., Some principles of nonwoven fabrics, *Textile Research Journal* **30**, 704–711 (1960).
- [52] Petterson, D. R., and Backer, S., Mechanics of nonwovens: orthotropic behavior, *Textile Research Journal* **33**, 809–816 (1963).
- [53] Gurney, H. P., Distribution of stresses in cotton products, *Journal of the Textile Institute* **16**, 269–289 (1925).
- [54] Sullivan, R. R., A theoretical approach to the problem of yarn strength, *Journal of Applied Physics* **13**, 157–167 (1942).
- [55] Machida, K., *Mechanics of Rupture of Blended Yarns*, M.S. Thesis, M.I.T. Cambridge, Massachusetts, 1963.
- [56] Grosberg, P., and Smith, P. A., The strength of slivers of relatively low twist, *Journal of the Textile Institute* **57**, 15–23 (1966).
- [57] Petterson, D. R., *On the Mechanics of Non Woven Fabrics*, Sc.D. Thesis, M.I.T., Cambridge, Massachusetts, 1958.
- [58] Hearle, J. W. S., and El-Behery, H. M. A., The transmission of transverse stresses in fiber assemblies, *Journal of the Textile Institute* **51**, 164–171 (1960).
- [59] Treloar, L. R. G., and Riding, G., A theory of the stress strain properties of continuous filament yarns, *Journal of the Textile Institute* **54**, 156–170 (1963).
- [60] Den Hartog, J. P., *Advanced Strength of Materials*, pp. 212–234 (McGraw-Hill Book Company, New York, 1952).
- [61] Treloar, L. R. G., and Hearle, J. W. S., Mechanics of twisted yarns, a correction, *Journal of the Textile Institute* **53**, T446–T448 (1962).
- [62] Kenny, P., and Chaikin, M., Stress strain time relationships of non-uniform textile materials, *Journal of the Textile Institute* **50**, 18–40 (1959).
- [63] Platt, M. M., Klein, W. G., and Hamburger, W. J., Mechanics of elastic performance of textile materials, Part XI: Factors affecting the translation of certain mechanical properties of cordage fibers and yarns into cordage strands and ropes, *Textile Research Journal* **24**, 907–939 (1954).
- [64] Daniels, H. E., The statistical theory of the strength of bundles of thread, *Proceedings of the Royal Society (London)* **183A**, 405 (1945).
- [65] Rosen, B. W., Tensile Failure of Fibrous Composites, *J.A.I.A.A.* **2**, 985 (1964).
- [66] Scop, P. M., and Argon, A. S., Statistical theory of strength of laminated composites, *Journal of Composite Materials*, Part I **1**, 92–99 (1967), Part II **3**, 30–47 (1969).
- [67] Oravas, G. A., and McLean, L., Historical development of energetical principles in elastomechanics, Part II: From Cotterill to Prange, *Applied Mechanics Reviews* **19**, 919–933 (1966).
- [68] Riding, G., and Wilson, N., The stress strain properties of continuous filament yarns, *Journal of the Textile Institute* **56**, 205–214 (1965).
- [69] Backer, S., Compressional behavior of textile fibers, *Textile Research Journal* **30**, 405–407 (1960).
- [70] Miles, J. B., Compressional behavior of textile fibers, *Textile Research Journal* **30**, 408–409 (1960).
- [71] Elder, H. M., The tensile, compressive, and bending moduli of some monofilament materials, *Journal of the Textile Institute* **56**, 8–14 (1965).

- [72] Higuchi, K., and Takai, H., Stress strain diagram, Young's modulus and Poisson's ratio of textile fibers, *Journal of the Textile Machinery Society of Japan*, **7**, 4-12 (1961).
- [73] Frank, F. I., and Ruoff, A. L., A method of measuring Poisson's ratio of fibers, *Textile Research Journal* **28**, 213-217 (1958).
- [74] Backer, S., Monego, C. J., and Machida, K., Mechanisms of tensile rupture in blended yarns, *Journal of the Textile Institute* (in press).
- [75] Paul, W., Untersuchungen über das Kraft-Dehnungsverhalten dreilitzger Seile aus synthetischen Fasern, Dissertation (Doktor-Ingenieur), Technischen Hochschule, Hannover, 1967.
- [76] Symes, W. S., The prediction of cord properties, *Journal of the Textile Institute* **50**, 241-248 (1959).
- [77] Treloar, L. R. G., The stress-strain properties of multi-ply cords, Part I: Theory, *Journal of the Textile Institute* **56**, 477-488 (1965).
- [78] Wood, J. O., and Redmond, G. B., Tyre cord behaviour under compressive stress, *Journal of the Textile Institute* **56**, 191-204 (1965).
- [79] Clark, S. K., The plane elastic characteristics of cord rubber laminates, *Textile Research Journal* **33**, 295-313 (1963).
- [80] Backer, S., The mechanics of bent yarns, *Textile Research Journal* **22**, 668-681 (1952).
- [81] Olofsson, B., The rheology of textile fabrics, Chapter 9 of *Rheology* Vol. 5, Edited by Eirich, F. R. (Academic Press, New York and London, 1969).
- [82] Olofsson, B., *Studies of Deformation and Recovery Properties of Textile Materials*, Doctoral Thesis, Chalmers Technical University, Gothenberg, Sweden, 1968.
- [83] Sadowsky, M. A., Pu, S. L., and Hussain, M. A., Buckling of microfibers, ASME Paper 67-WA/APM-4 (American Society of Mechanical Engineers, New York City, 1967).
- [84] Haringx, J. A., On Highly Compressible Helical Springs and Rubber Rods and Their Application for Vibration Free Mountings, Doctoral Thesis, Technical University of Delft, Netherlands, 1947.
- [85] Amirbayat, J., and Hearle, J. W. S., Properties of unit composites, *Fiber and Science Technology* **2**, 123-154 (1969).
- [86] Menzies, W. C., Buckling of Twisted Textile Structures, M.S. Thesis, Department of Mechanical Engineering, M.I.T., Cambridge, Massachusetts, 1951.
- [87] Gurney, H. P., and Davis, E. H., The elastic properties of yarns with special reference to tire cords, *Journal of the Textile Institute* **21**, 463-480 (1930).
- [88] Coulson, A. F. W., and Dakin, G., Doubled yarns, Parts I to V, *Journal of the Textile Institute* **48**, 203-232, 233-257, 258-292, 293-320, 321-332 (1957).
- [89] Takeyama, T., and Matsui, J., Recent developments with tire cords and cord to rubber bonding, *Rubber Reviews*, Division of Rubber Chemistry of the American Chemical Society **42**(1), 159-256 (1969).
- [90] Riding, G., The stress strain properties of multiple cords, Part II: Experimental, *Journal of the Textile Institute* **56**, 489-497 (1965).
- [91] Riding, G., The effect of yarn twist on filament properties, *Journal of the Textile Institute* **56**, 109-120 (1965).
- [92] Krizik, J. G., Mellen, D. M., and Backer, S., Dynamic Testing of Small Textile Structures and Assemblies, Final Report, QMC R and D Center, Natick, Massachusetts, TD-93-1961.
- [93] Busby, W. J., and Reeves, E. V., *Proceedings of the Fourth Rubber Technology Conference*, 1962 (p. 217).
- [94] Lyons, W. J., *Impact Phenomena in Textiles* (M.I.T. Press, Cambridge, Massachusetts, 1964).
- [95] Hall, I. H., *Journal of Applied Polymer Science* **8**, 237 (1964).
- [96] Lothrop, E. W., *Applied Polymer Symposium*, No. 1, 111 (1965).
- [97] Schroeder, W. A. and Prettyman, *Rubber Age* **99**, 72 (1967).
- [98] Röder, H. L., The relation between fiber friction and the behavior of fibers and yarns during processing, *Journal of the Textile Institute* **46**, 84-100 (1955).
- [99] Czitary, E., On the bending strains of wire cables, *Asterreichisches Ingenieur Archiv* **1**, 342-350 (1947).
- [100] Wyss, Th., Einfluss der sekundären Biegung und der inneren Pressungen auf die

- Lebenselaner von Stahldraht-Litzenseilen mit Hanfseele, Schweiz-Bauzeitung Nr. 14, 15, and 16 (1949).
- [101] Lutchansky, M., Axial stresses in armor wires of bent submarine cables, ASME Paper No. 68-WA/DE-1 (ASME Headquarters, New York City, 1968).
- [102] Tovey, H., Wrinkle resistance and recovery from deformation, Textile Research Journal **31**, 185 (1961).
- [103] Hamburger, W. J., Platt, M. M., and Morgan, H. M., Some aspects of elastic behavior at low strains, Textile Research Journal **22**, 695 (1952).
- [104] Platt, M. M., Klein, W. G., and Hamburger, W. J., Mechanics of elastic performance of textile materials, Part XIII: Torque development in yarn systems: Singles Yarn, Textile Research Journal **28**, 1-14 (1958).
- [105] Backer, S., An Analysis of the Deformation Mechanisms of Textile Structures under Varying Conditions of Stress, Sc. D. Thesis, Department of Mechanical Engineering, M.I.T., Cambridge, Massachusetts, 1953.
- [106] Zorowski, C. F., and Chen, C. S., Cantilever bending behavior of continuous filament cords, Textile Research Journal **35**, 529-538 (1965).
- [107] Mellen, O. M., Backer, S., and Park, B. J., Research on Materials for use in a Full Pressure Suit, WADD Technical Report 60-311, M.I.T., Cambridge, Massachusetts, 1960.
- [108] Grosberg, P., Mechanical properties of woven fabrics, Part II: Bending of woven fabrics, Textile Research Journal **36**, 205-211 (1966).
- [109] Popper, P. G., Bending of Fiber Assemblies, Report TD-153-66, Fibers and Polymers Division, M.I.T., Cambridge, Massachusetts, 1966. [U.S.D.A. Grant 12-14-100-7650 (72)].
- [110] Popper, P. G., The Effect of Friction on the Bending Behavior of Textile Materials, Report TD-106-62, Fibers and Polymers Division, M.I.T., Cambridge, Massachusetts, 1962 (unpublished). [Monsanto Company Project.]
- [111] Popper, P. G., Bending of Fiber Assemblies, Sc.D. Thesis, Mechanical Engineering Department, M.I.T., Cambridge, Massachusetts, 1966.
- [112] Backer, S., Zimmerman, J., and Best-Gordon, H. W., The interaction of twist and twill direction as related to fabric structure, Textile Research Journal **26**, 87-107 (1956).

1.4. Recent Developments with Tire Cords and Cord-to-Rubber Bonding

T. Takeyama¹ and J. Matsui¹

	Page
1.4.1. Physical properties of tire cords	220
1.4.1.1. Introduction.....	220
1.4.1.2. High tenacity rayons	221
1.4.1.3. High tenacity nylons	225
1.4.1.4. Polyester cord.....	238
1.4.1.5. Fiber glass cord	241
1.4.1.6. Steel wire cord.....	243
1.4.1.7. Miscellaneous cords.....	244
1.4.1.8. Comparative analysis of various tire cords.....	244
1.4.1.9. Impact resistance of tire cords.....	246
1.4.1.10. Fatigue resistance of tire cords.....	253
1.4.1.11. Effects of twist on cord properties	261
1.4.2. Rubber-to-cord bonding.....	265
1.4.2.1. Introduction.....	265
1.4.2.2. Outline of bonding methods.....	266
1.4.2.3. Adhesive treatment of nylon and rayon—RFL treatment.....	274
1.4.2.4. Polyester to rubber bonding.....	279
1.4.2.5. Adhesive treatment of miscellaneous tire cords...	290
1.4.2.6. Evaluation of adhesion.....	291
References	299

¹ Industrial Products Laboratory, Fibers and Textile Research Laboratories, Toray Industries, Inc., Otsu, Japan.

1.4.1. Physical Properties of Tire Cords

1.4.1.1. Introduction

The first pneumatic tire was made in 1888 by J. B. Dunlop with Irish flax as the reinforcing material. This fiber was one of the strongest at that time. It was gradually replaced by cotton, since Irish flax was expensive. Cotton tire fabrics in the early stages, about 1910, were plain fabrics. As requirements imposed by the severity of tire operating conditions increased, these fabrics were gradually replaced by the present tire cord fabrics, which were first devised by J. F. Palmer in 1892.

Prior to World War II, cotton was the sole textile used to any large extent in pneumatic tires. However, this cotton tire cord fabric also failed to meet requirements imposed by increasing severity of tire operations, so that tire engineers began to consider man-made fibers.

The first rayon tire cord tenacity was about two grams per denier, and was produced in 1923. Du Pont started to manufacture high tenacity rayon, Cordura, in 1933 [1]² and Courtaulds also started to manufacture high tenacity rayon, Tenasco, in 1936 [1], but by 1940 high tenacity rayons had only a small portion of the total tire cord market. In the late 1940's, use of high tenacity rayon tire cords increased rapidly in the United States and Europe. In Japan, rayon truck tires were first manufactured in 1951 [2-3]. Initially rayon cords were used only for truck tires. The rayon cord tire had improved carcass performance and its life was increased 30 to 60 percent [2-3]. This improvement of tire quality was utilized more for truck tires than for passenger car tires. Increased power of automobile vehicles, however, gave birth to troubles in rayon cord (truck) tires. New, tougher materials were required for tire cords, especially for heavy duty tires.

In 1947, nylon cords (nylon 66) were examined as reinforcing materials for truck tires in the United States, and it was confirmed that nylon truck tires have excellent properties, especially under severe operating conditions. In the late 1950's, rayon cords were gradually replaced by nylon cords, especially in the United States.

Japanese tire manufacturers made extensive efforts to use nylon 6 for tire cords. Nylon 6 was available from domestic suppliers (nylon 66 was more costly) and nylon 6 tires, when post cure inflation was used, showed no difference from nylon 66 tires in practice [2], [3]. Mass production of nylon tires in Japan started in 1958. In the first five years, 60 percent

² Figures in brackets indicate the literature references at the end of this chapter.

of all tire cords had been replaced by nylon cords. In 1967 nylon cords were used for 90 percent of the tires made in Japan.

In Europe, rayon cord still has a large portion of the tire cord market.

Goodyear started to produce polyester tires for passenger car service in 1962. In 1969, production of polyester tires has rapidly increased in the United States, and polyester cord has become very important in the field of the original equipment tires for passenger cars.

Mass production of polyester tires in Japan started in 1967 and their production is gradually increasing.

In the United States, most polyester cords are used in fiber glass belted-bias construction tires, whereas in Japan they are used as reinforcing elements for bias construction tires.

Steel cords, which made their appearance in France in 1936, have been used extensively in Europe in radial tires.

Glass fiber cords, one of the most promising types for the belt ply of radial tires or belted-bias tires, recently appeared in tires in the United States.

1.4.1.2. High Tenacity Rayons

For more than thirty years, high tenacity rayons have been used as tire cords. The tenacity of the first rayon tire cord in 1923 was only two grams per denier as previously mentioned. In the 1930's, commercial production of high tenacity rayons, Cordura and Tenasco started in the United States and in England, respectively. Tenacity of these cords was about 2.3 grams per denier.

Thereafter, tenacity and durability of rayon cords was improved and super series rayons, e.g. Super I, Super II and Super III were developed. More recently, newer types of rayon cords, compressed rayon Dynacor [4-6] and extra high modulus rayon were developed [7].

The improvement of cord tenacity of rayons is illustrated in figure 1.4.1 [8]. Cord tenacity of rayon now has reached five grams per denier or higher.

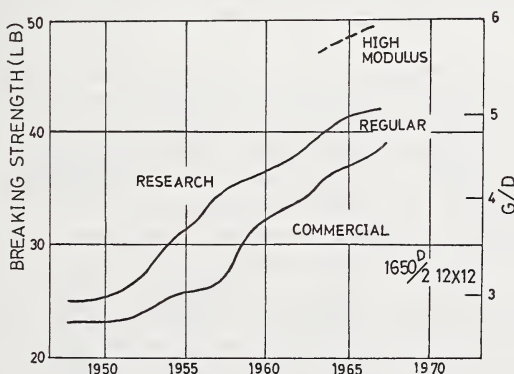


FIGURE 1.4.1. Evolution of rayon tire cord strength.

In spite of nylon's and polyester's assault, rayon cords still keep their position in the original equipment market for passenger car tires in the United States and Europe. In Japan, however, the future of rayon tire cords is not promising.

The production process for high tenacity rayons differs in several respects from that for regular rayons. High tenacity rayons have to be made denser and more uniform in fine structure than regular rayons.

High quality wood pulp, and high quality, homogeneous viscose solutions are usually used in the production of high tenacity rayons.

The degree of polymerization of cellulose in the production of high tenacity rayons ranges from 400 to 600, which is considerably greater than that of regular rayon, 300. A higher concentration of carbon disulfide and sodium hydroxide, and lower concentration of cellulose are employed to improve the solubility of viscose.

The high yarn strength can be obtained upon application of stretch at high temperature.

Cox [9] first found that some additives (retardants) in the spinning bath were effective for this purpose. These modifications by retardants became very important in the production of super series rayons. These retardants have the effect of retarding the regeneration of the cellulose from the xanthate and of increasing the tenacity of the fiber [1]. Filament cross section obtained by this method is circular and more uniform, as demonstrated by absence of skin and core regions, which can be seen in cross sections for earlier high tenacity rayons. Many reports were published on the effects of retardants on regeneration and coagulation mechanisms. It was explained that these retardants react with zinc ions to form stable colloidal chelate compounds, suppress diffusion of the coagulant and then slow down the rate of regeneration.

Yarn-to-cord tenacity conversion efficiency of rayon cords is quite low. Therefore, choice of cord lubricant is important. A lubricant, which decreases the friction coefficient of the yarn and improves the yarn-to-cord tenacity conversion, has to be developed [10-11], see table 1.4.1 [10].

Detailed investigations of fine structure of super high tenacity rayon filaments show that while overall change in total crystallinity is very

TABLE 1.4.1. *Correlation of cord strength with yarn friction coefficient [10]*

Specimen (1650/2 rayon cords)	Yarn friction coefficient		Bone-dry strength per 100 denier
	Static	Dynamic	
A	0.207	0.197	263
B	.200	.184	266
C	.160	.150	272
D	.132	.158	280
E	.107	.144	296
F	.118	.133	306

small, the average crystallite size has been reduced. Thus, a fine, even textured filament permits the load to be distributed more evenly across its structural elements.

Internal structure of a rayon filament is simply expressed in terms of lateral order distribution [12–15] which can be measured by accessibility of the cellulose internal structure to various chemicals, e.g., esterification by formic acid, dissolution by alkali solutions and so on. Skin or less-ordered regions can be dissolved by alkaline solution more easily than core or ordered regions.

The change of lateral order distribution in super series rayon filaments is illustrated in figure 1.4.2 [16]. The improvement of super series rayons explained by change of the lateral order distribution to a low ordered, narrow distribution.

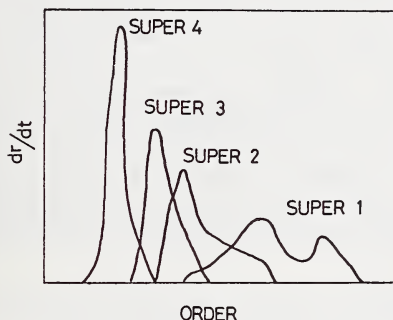


FIGURE 1.4.2. Change of lateral order distribution of super series rayons.

Dynacor rayon (compressed rayon [3–4]): Dynacor rayon, manufactured by all Tyrex members, has the same chemical composition as conventional rayon tire cord, but differs in physical characteristics and in the way it is processed. It is made of low modulus, high tenacity and twisted greige yarn dipped at minimum tension in a standard RFL (Resorcinol Formaldehyde Latex) adhesive and immediately stretched 15 percent prior to drying.

This processing technique increases dip penetration into the cord. Stretching aligns the filaments and compacts the bundle. Physical locking-in of the dip and uniform stress distribution among the several thousand individual filaments in the cord are obtained. In addition, it is said that longitudinal air wicking, considered by many tire experts to be a major cause of ply separation, is reduced to a minimum and cord-to-rubber bonding made more durable. Equally important, this cord is claimed to cost no more than regular rayon and requires little or no modification of processing equipment.

Performance results together with indoor wheel tests [3] are claimed to indicate that this rayon cord has greatly improved resistance to ply separation, and that in the accelerated test for tread separation, Dynacor tires run three to four times longer than regular rayons, with separations generally occurring at a rubber to rubber interface.

Extra high modulus rayon [5]: Extra high modulus rayon is a polynosic type of filament yarn. Extra high modulus rayon yarn has a tenacity of more than 9 g. per denier bone dry and approximately 8.5 g. per denier in the conditioned state. Elongation at break, 4 to 5 percent bone dry and 5 to 6 percent conditioned, is extremely low, while wet strength reaches 7 g. per denier and wet elongation at break only 6 percent.

Young's modulus is very high, see figure 1.4.3 [7], and its temperature dependence is low. This indicates dimensional stability for extra high modulus rayon in tire construction, particularly for radial ply tires. Effects of twist on cord strength of Super III rayon and extra high modulus rayon are indicated in figure 1.4.4a [7]. The curve for Super III indicates increase in strength to 22 kg. in the twist range of 20 to 40 turns per 10 cm., followed by a downward trend because of increasing conversion losses. With low-extension, extra high modulus rayon cord, the curve starts out at 26 kg. and then shows a steady downward trend over the entire range represented to reach 15 kg. In one range of twist extra high modulus rayon cord has a greater breaking load than Super III, while in the higher range the breaking load of Super III is superior.

Results of the Firestone flex fatigue test are illustrated in figure 1.4.4b [7]. The shape of the curve shows that higher cord twist can increase fatigue resistance. A twist level of approximately 47 turns per 10 cm. gives an optimum balance between pre- and post-flexing strength.

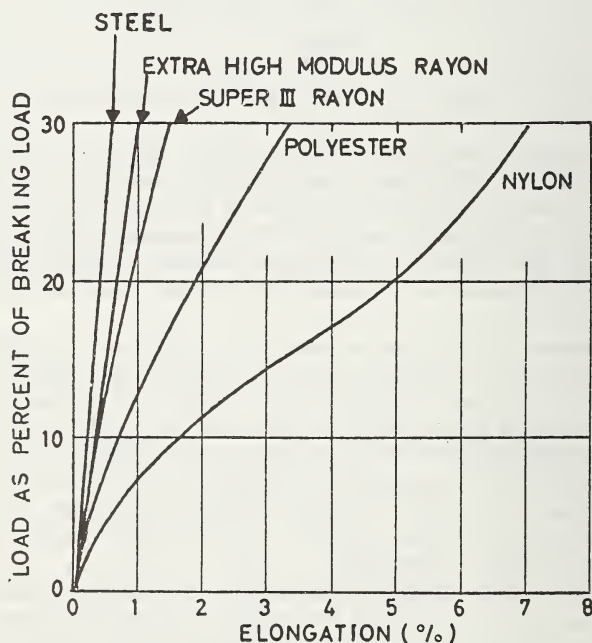


FIGURE 1.4.3. Comparison of stress-strain curves of extra high modulus rayon and other cords.

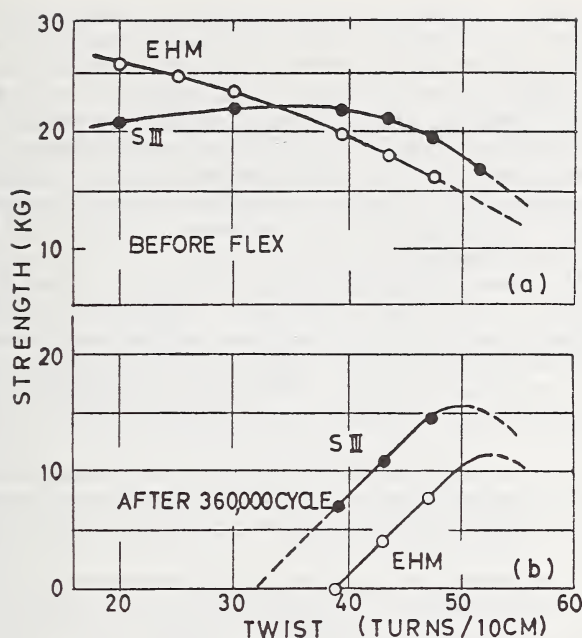


FIGURE 1.4.4. Effect of twist on cord tensile strength and fatigue resistance of Super III rayon and extra high modulus rayon [7].

(a) Tensile strength vs. twist.

(b) Residual tensile strength after flexing with Firestone Flex Tester vs. twist.

The curve for extra high modulus rayon cord shows great similarity to that for Super III, except that retained strength at all twist levels is 5 kg. lower. In the commercial twist range, breaking loads both before and after the flex test are lower with extra high modulus rayon than with Super III. Use of this low-extension rayon cord for conventional tire construction seems out of the question. On the other hand, its high strength and low elongation may make extra high modulus rayon cord a choice for reinforcing belts in radial ply tires, where it is not subjected to such severe flex compression.

1.4.1.3. High Tenacity Nylons

Nylon cord is the strongest tire cord. In the standard twist construction 840D/2, 47×47 (turns per 10 cm.), the cord strength of current nylon 6 and nylon 66 are 8 g. per denier and 7.5 g. per denier, respectively.

As compared with rayon cords, nylon cords give much longer tire life, particularly when used in heavy duty truck tires. For this reason, nylon cord was initially applied in heavy duty truck tires and then was gradually adopted for light truck tires and replacement tires for passenger cars. Up to now, nylon tires are the largest fraction of automobile

tires, especially in Japan and the United States. Almost all nylon cords used in Japan are nylon 6. On the other hand, nylon 66 cords have a greater portion of the nylon cord market in the United States. Nylon 6 cord differs slightly from nylon 66 cord in regard to tire cord characteristics. Nylon 6 cord has greater tenacity, is more economical and more shock resistant than nylon 66 cord. Nylon 6 cord balances so well with carcass compounds that dynamic adhesion fatigue is highly improved [2]. Furthermore, Allied Chemical stated their nylon 6 tire cord, Caprolan, has better heat aging resistance, adhesion to rubber, and flex fatigue resistance than nylon 66 [1].

On the other hand, nylon 66 has better thermal stability than nylon 6 due to polymer melting point difference. Thermal shrinkage at fairly high temperatures such as tire curing temperatures is greater than for nylon 66, figure 1.4.5 [17]. This requires minor changes in processing conditions in manufacturing tires with nylon 6 cord. Higher stretch rate must be applied in the heat treating process for nylon 6 cords due to low modulus.

Nylon 6 loses tensile strength more than nylon 66 during high temperature cures. Accordingly, nylon 6 cord requires lower tire curing temperatures or enough cooling when the tire is removed from the mold.

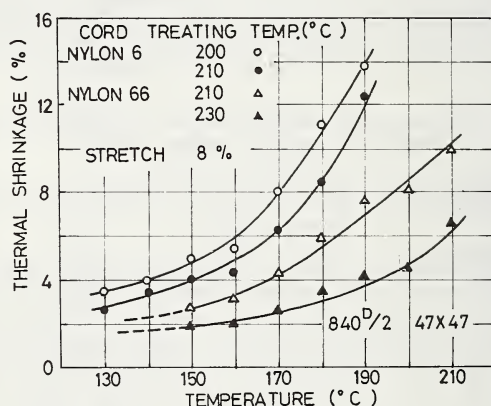


FIGURE 1.4.5. Thermal shrinkage of nylon 6 and 66 tire cords as a function of temperature.

840 D/2 (47 × 47 turns/10cm.) [17].

Nylon 6 and nylon 66 in common show flat spotting phenomena and lower modulus than rayon and polyester. Many efforts have been made to improve these properties, but all of them failed to achieve commercialized materials.

The improvement of strength is one of the currently important problems of nylon cord. The tenacity of recently developed nylon tire yarn has reached ten grams per denier or higher [276].

Nylon monofilaments are currently under investigation for tire service [276].

To obtain high tensile strength, higher molecular weight polymer is used and a higher draw ratio. Tensile strength increases progressively with increasing molecular weight but dimensional stability of greige and treated cord decrease at high temperature. Therefore, molecular weight has to be selected to obtain the best balance of tensile strength and dimensional stability. Hot stretching at a higher temperature and other means to improve dimensional cord stability [18-21] are adopted in production processing of the yarn, e.g. multistep stretching, stretch and relax, etc.

Heat aging resistance is also an important property for tire service. Various additives are usually used in yarn production to improve aging resistance of the tire cord.

Thermal degradation of nylon cord in hot air decreases tensile strength. This change becomes important at temperatures reached in heat setting cords and in operating tires [22-24].

Decrease in tensile strength runs parallel to reduction in length of polyamide chains, reduction in the number of primary amine end groups and increase in the number of carboxyl end groups.

In order to improve heat and oxidation degradation properties, various additives are used before or after polymerization. These additives are often organic, e.g. some amines, some phenols, some haloaromatic acids, diarylamine-ketone condensation products, 2-mercepto benzimidazole and so on. Sometimes they are inorganic, e.g. phosphorous compounds and sometimes metals and their compounds, e.g. copper and its salts, organotin compounds, cobalt chelating compounds and so on [22-23].

There are many reports concerned with heat treatment of nylon cords and dipping and heat-stretching machines for tire cords or fabrics [17, 27-32].

Nylon cords, or more generally, thermoplastic fiber cords, must be dipped and heat stretched to improve dipped cord properties, e.g. to improve tensile properties, to reduce growth, (to increase Young's modulus and to decrease creep), to improve dimensional stability, and to impose cord-to-rubber bondability. A wide variety of single- and multiple-step treatments have been adopted by various tire and fiber producers. Typical heat-treatment machines are diagrammed in figures 1.4.51 to 1.4.54.

Cord or fabric treating conditions used by the tire industry at large vary somewhat. Yet, within this variance, cords or fabrics produced under different conditions all serve the precise purpose of the individual company.

Table 1.4.2 shows examples of variations that exist in conditions for treating nylon 66 cords [30].

We discuss the effect of treating conditions on the physical properties of nylon 66 according to Du Pont's data [27].

Figure 1.4.6a [27] shows the change in breaking strength that occurs in a single step process as net stretch is increased.

Cold growth, heat shrinkage, and heat shrinkage tension are also dependent upon net stretch as shown in figure 1.4.6b [27]. Heat shrinkage increases with increasing net stretch up to a point, after which little

further change is seen. On the other hand, shrinkage tension increases in a fairly linear manner with increasing net stretch at least to 20 percent net stretch.

TABLE 1.4.2. *Nylon 66 processing conditions for drying zone and single, dual or triple zone treatment* [30]

Company	Time	Temp.	Tension, lb/cord	Stretch	Residual H ₂ O, %	Tenacity, lb
Drying conditions						
A	1.5 min	270° F	1	1%	1%	24-26
B	2.5 min	240° F	0.75	1%	1%	24-26
C	3.5 min	180° F	0.5	1.5%	7-10%	23-25
Heat set conditions						
A	20 sec	425° F	10	12-14%	0%	29-30
B	30 sec	410° F	10	10-12%	0%	28-29
C	45 sec	390° F	10	10-12%	0%	27-28
Normalizing conditions						
A	20 sec	400° F	?	8%	0%	30
B	30 sec	370° F	?	8%	0%	30
C	30 sec	350° F	?	7%	0%	29
Reheat stretch conditions						
A	20 sec	425° F	?	12-16%	0%	31.5
B	30 sec	410° F	?	12-15%	0%	31.0
C	Does not use triple zone treatment					

Basis—840/2 nylon 66—Type 700.

Temperature levels for nylon 6 materials are approximately 30° to 40° below the nylon 66 values shown.

Figure 1.4.6c [27] shows the results for a two-step process chosen to give the same net stretch as the optimum one-step, with considerably better heat shrinkage. Heat shrinkage tension does not improve. There are patents on similar processes [33].

Our similar results with nylon 6 are shown in figure 1.4.7 and table 1.4.3 [17, 32].

Good dimensional stability can be obtained by heat treating at high temperature.

Drying conditions are also important. Loss of tensile strength in the heat stretching process is marked when water in the cord has not been removed sufficiently in a dryer. This loss, however, can be avoided by adopting a predip process (water dip prior to RFL dip [34]).

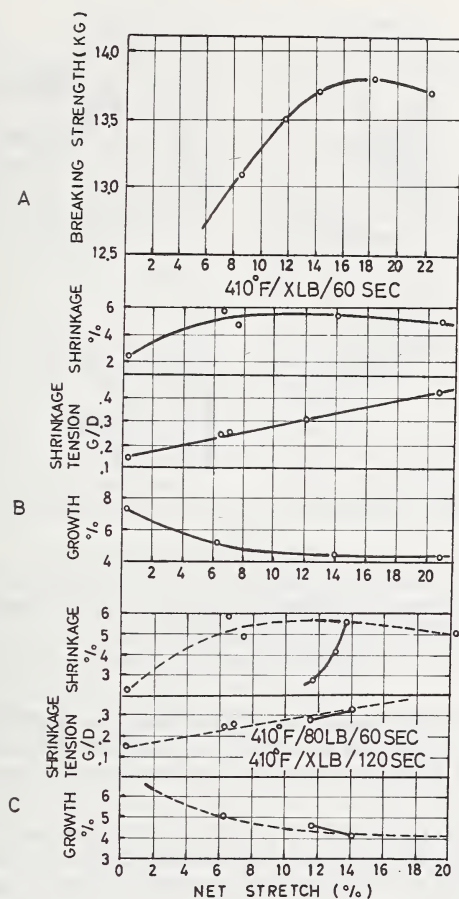


FIGURE 1.4.6. (a) Correlation between net stretch and breaking strength for nylon 66 cords (single step stretching) [27]. (b) Correlation between net stretch and cord stability for nylon 66 (single step stretching) [27]. (c) Correlation between net stretch and cord stability for nylon 66 (two step stretching) [27].

TABLE 1.4.3. Correlation between stretch and thermal shrinkage for nylon 6 cord; two step stretching [17, 32]

1st Stretch, %	2nd Stretch, %	Total stretch, %	Elongation at 4.5 kg, %	Thermal shrinkage, %
4	4	8	9.5	4.0
6	2	8	9.4	3.8
8	0	8	9.4	3.7
10	-2	8	9.3	3.2
12	-4	8	9.5	2.8
14	-6	8	9.6	2.7

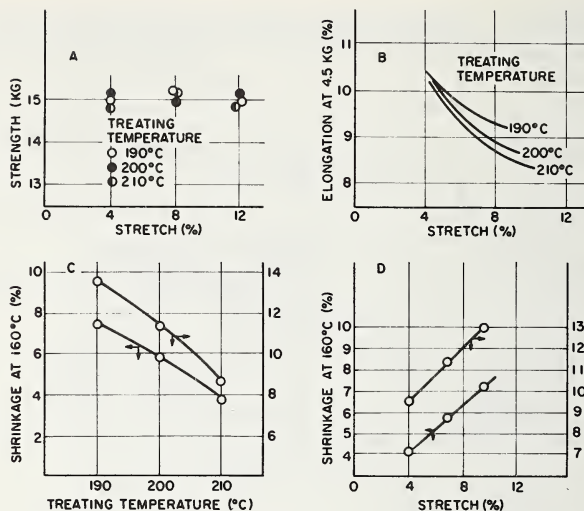


FIGURE 1.4.7. (a) Correlation between stretch and cord strength for nylon 6 [17-32]. (b) Correlation between stretch and elongation at 4.5 kg. for nylon 6 [17-32]. (c) Correlation between stretch and thermal shrinkage for nylon 6 [17-32]. (d) Correlation between treating temperature and thermal shrinkage for nylon 6.

840 D/2, 47×47 turns/10 cm. [17-32].

Among heat treating machines other than the usual types mentioned above, a fluid bed process is worthy of mention [35]. This process, in which small glass beads are used as the heating medium, was developed in England.

In high temperature curing of nylon tires, particularly nylon 6 tires by the Bag-O-Matic process, it is considered important to improve the thermal stability of the tire cord to withstand the curing conditions. Loss of strength is more serious in the portion around the bead than at the crown.

Figure 1.4.8 indicates Pieper's result [36], in which strength loss of nylon 6 is compared with that of nylon 66. Strength loss of nylon 6 is greater than that of nylon 66, particularly at high curing temperatures. However, adoption of cooling before removing from the mold is effective in avoiding the strength loss. We also have examined loss of strength in tire cures with nylon 6, using a steel mold like Reagan and Sabos [37], to simulate the typical actual shrinking behavior of cord which is expected in a tire curing process [38]. The test diagrams of shrinkage are shown in figure 1.4.9.

Strength loss and thermal shrinkage in the curing process are illustrated in figures 1.4.10 and 1.4.11, respectively.

From these results, it was concluded that strength loss of the cord is largely to be attributed to rapid shrinkage when the work is removed from the mold at high temperature and that a slow shrinkage of about 10 percent, which the cord suffers during the curing process, has little

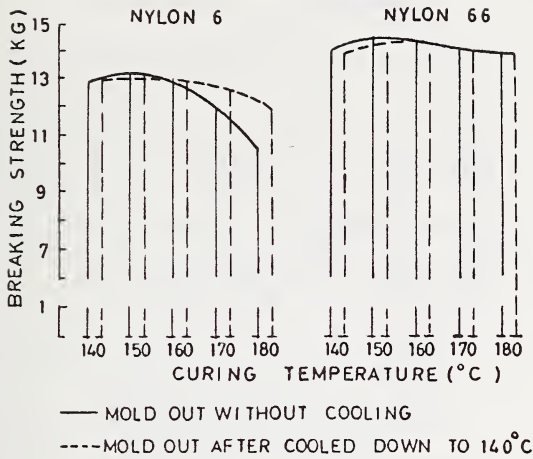


FIGURE 1.4.8. *Strength loss of nylons in vulcanization.*

840 D/2, 50 × 50 turns/10 cm. [36].

effect on strength. Therefore, it is advisable to cool the cord and then remove it from the mold. These phenomena have also been confirmed by actual tire curing experiments. The strength loss of the cord is also affected by heat treating conditions of cord.

Molecular mechanisms of strength loss with (rapid) thermal shrinkage have been studied by various investigators. Dismore and Statton [39] concluded from their study on nylon 66 that strength loss with thermal shrinkage at high temperature is related to introduction of folded chains.

Fujimoto stated that there were good correlations between strength loss with shrinkage at high temperature and the 002 lattice spacing of crystalline regions or their change with thermal shrinkage as shown in

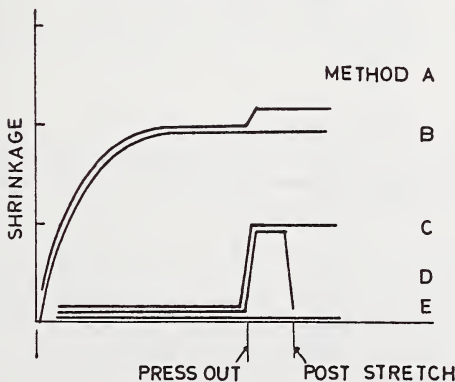


FIGURE 1.4.9. *Laboratory test diagrams of shrinkage used for evaluating strength loss in curing.*

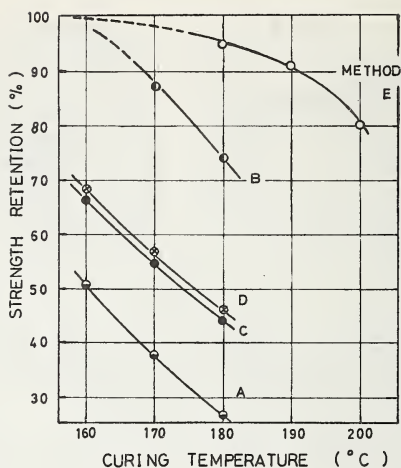


FIGURE 1.4.10. *Strength retention of nylon 6 (T-781S) after curing as a function of curing temperature.*

figures 1.4.12a and 1.4.12b [40]. Furthermore he stated that when strength loss was great, a large number of filaments were ruptured with sharp edges inclined approximately 35 degrees to the fiber axis. There was a good correlation between strength loss and number of bias breaks, figure 1.4.13. From these experimental results, he suggested that mechanisms of strength loss of thermal shrinkage and fatigue failure have something in common as will be mentioned later.

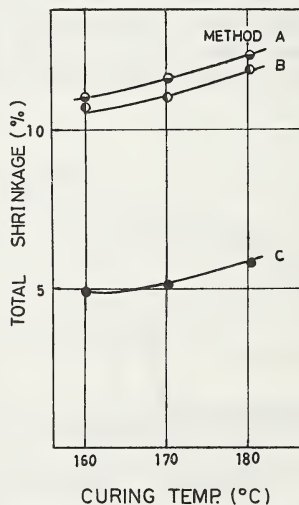


FIGURE 1.4.11. *Total shrinkage of nylon 6 (T-781S) through curing cycle.*

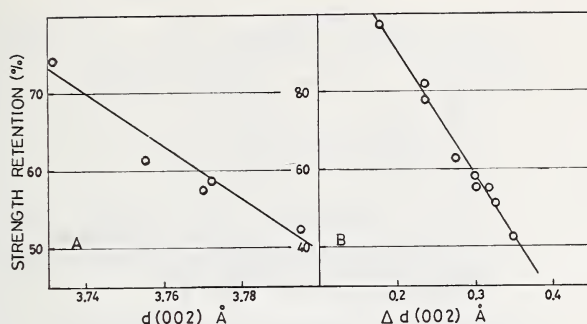


FIGURE 1.4.12. Strength retention of nylon 6 after curing as a function of lattice spacing and change of lattice spacing [40].

- (a) Strength retention vs. lattice spacing.
(b) Strength retention vs. change of lattice spacing.

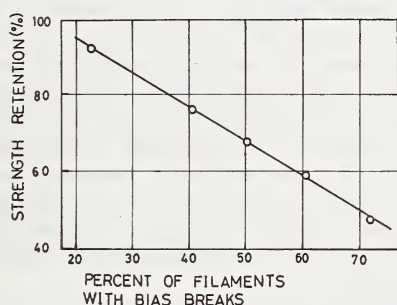


FIGURE 1.4.13. Strength retention as a function of bias filament breaks [40].

Mechanisms of flatspotting: It is generally assumed that the tire cord is primarily responsible for flatspotting, in spite of other variables [41–42] in tire construction and manufacture which affect flatspotting. Therefore, almost all articles which deal with test methods or mechanisms of flatspotting are based on the viscoelastic behavior of the component fiber.

Some papers have dealt with laboratory tests on cords (or yarns) to simulate the phenomenon of flatspotting in tires as affected by choice of tire cord [43–51]. Other papers have been concerned with quantitative measurement of flatspotting in tires on indoor wheels [52–53].

Here, we will consider how tire cords behave in tire service. Figure 1.4.14 shows the deformation of a tire under load. Cord strain in the footprint is smaller than in other parts. All volume elements of the tire, however, spend an equal time in the footprint during a revolution; their average strain per revolution is the same. This situation no longer exists after the tire stops. When the tire comes to rest under load after long running which raised the tire temperature, the volume elements in the footprint cool to ambient temperature under less strain than other ele-

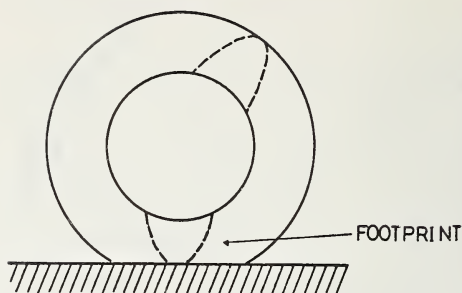


FIGURE 1.4.14. *Deformation of tire under load.*

ments. When the tire starts to rotate again, persistence of this strain difference causes the flatspot. As the tire rolls and consequently is heated, this difference decreases with time and eventually becomes negligible. The qualitative phenomena can be investigated in the laboratory; the conditions which we examined are illustrated in figure 1.4.15 [54].

Two cords are used in the experiments. First, they are given thermal and mechanical conditioning steps to approximate vulcanization. Thereafter, these cords are given a thermal and mechanical history to simulate the behavior of cords in actual tire operation; one cord represents a cord located in the footprint when the tire was brought to rest and the second cord represents a cord in other parts of the tire.

The difference between A and B, see figure 1.4.15, is an index of the magnitude of flatspotting.

Finally, to simulate the run-out of flatspotting, both cords are reheated.

Tippett explained the magnitude of flatspotting in terms of the difference in Young's modulus of the cord at tire operating temperature and at room temperature [44]. He concluded that magnitude of flatspotting is proportional to $(1/M_H) \times [1 - (M_H/M_R)]$, where M_H is Young's modulus at tire operating temperature and M_R is Young's modulus at room temperature.

Flatspotting becomes large when the operating temperature exceeds the glass transition temperature T_g of the cord, because then $(1/M_H) [1 - (M_H/M_R)]$ becomes large rapidly.

Relationships between flatspot index and tire operating temperature, which were examined by Papero and co-workers, are illustrated in figure 1.4.16 [46]. In both cases, nylon and polyester flatspot indices increase rapidly when tire operating temperature exceeds the T_g of the cord.

Flatspot index decreases as cord T_g increases, as shown in figure 1.4.17 [54]. Moisture regain of the cord also has important effects on the flatspot index of water sensitive cord because absorbed moisture lowers the T_g of the cord, figure 1.4.18 [54]. The flatspot index rapidly increases, then passes through a maximum and finally decreases with moisture content. Reduced flatspot nylon, modified by blending of aromatic polyamide, is claimed to exhibit good flatspotting resistance at low humidity but loses its merit at high humidity.

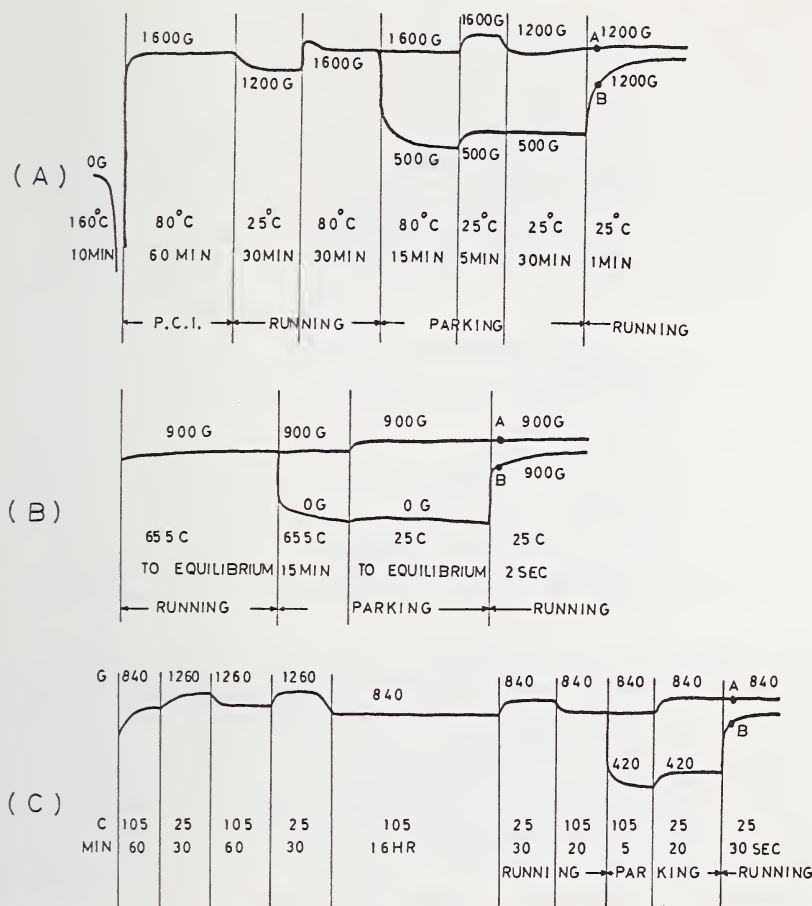


FIGURE 1.4.15. Laboratory testing methods for flatspot index of cords [54].

- A. Du Pont method.
 B. Modification of Goodyear method.
 C. Modification of Allied method.

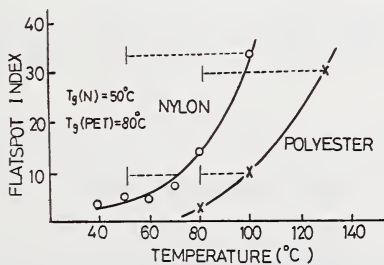


FIGURE 1.4.16. Flatspot index as a function of running temperature [46].

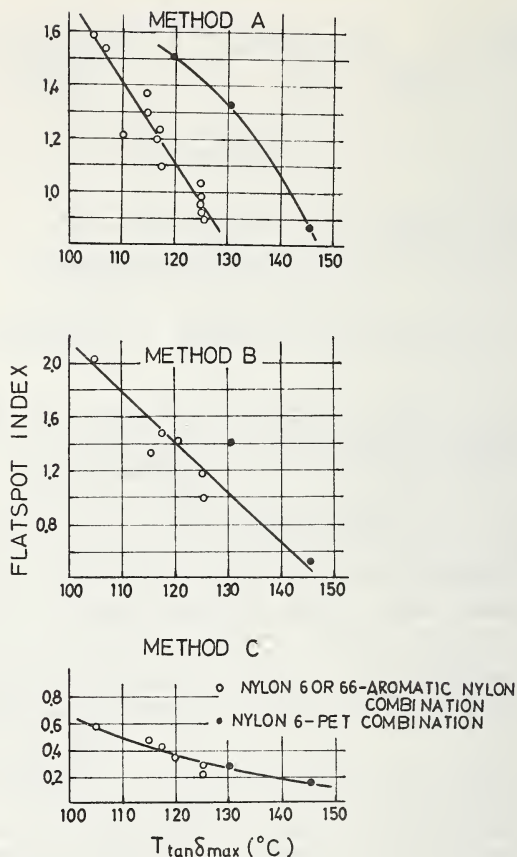


FIGURE 1.4.17. Flatspot index as a function of $T(\tan \delta_{max})$ (as measure of T_g) [54].

Reduced flatspot nylons:

(1) Diisocyanate crosslinked nylon [55]

Cipriani and co-workers found that short, vapor phase treatments with diisocyanates, particularly tolylene diisocyanate, produced nylon 6 with greatly improved flatspotting resistance, without undesirable side effects.

(2) Cyanuric chloride crosslinked nylon [56]

It was reported that treatment with cyanuric chloride improved the high temperature properties and flatspotting resistance of nylon 6 cord.

(3) N-44 [48], [57-59]

N-44 is Du Pont's reduced flatspot nylon, a melt blend yarn of nylon 66 and aromatic polyamide. The process is disclosed in Du Pont's patents

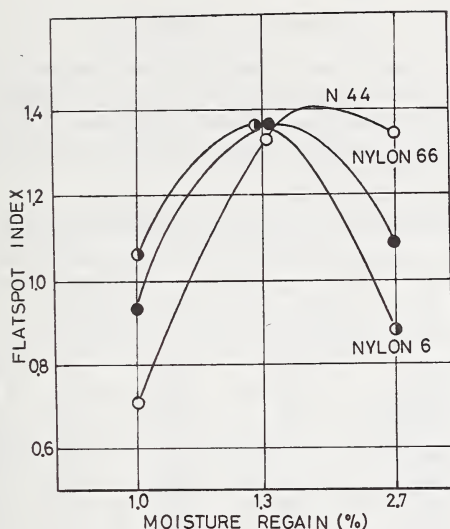


FIGURE 1.4.18. Flatspot index as a function of moisture regain [54].

for blending aromatic polyamide, T_g of which is higher than 140°C , with aliphatic polyamide, e.g. nylon 6 and nylon 66 to improve flatspotting resistance. A typical example of an aromatic polyamide is polyhexamethylene isophthalamide (6I). This blend yarn loses its good properties at high humidity. In another Du Pont patent, it is mentioned that use of an aromatic polyamide made from *t*-butyl isophthalamide or from polymethylene diamine having a longer polymethylene chain than hexamethylene diamine, is effective in overcoming this demerit at high humidity.

(4) X-88 [60]

Monsanto's X-88 nylon is nylon 66 modified by aromatic polyamide based on terephthalic acid.

(5) EF-121 [46, 49, 57]

Allied Chemical's EF-121 nylon is a melt blend yarn of 30 percent polyethylene terephthalate and 70 percent nylon 6.

(6) NF-20 [57, 61]

Firestone's NF-20 nylon is said to be a block copolymer of polyamide and polyester.

(7) Merged fiber [62]

Kovac and co-workers investigated merged fibers of various materials. They reported that the merged fiber combination of nylon-polyester is very effective in flatspotting resistance without undesirable side effects, as shown in table 1.4.4.

(8) Aromatic polyamides

Aromatic polyamides which have high melting and glass transition temperatures, are excellent in their resistance to high temperature and flatspotting. Typical examples of these aromatic polyamides are poly (*m*-phenylene isophthalamide) (Nomex [63]) and poly (hexamethylene terephthalamide) (6T fiber [64]).

TABLE 1.4.4. *Cord properties of merged fibers* [62]

	Cord	Tenacity,	Durability,	3% Modulus,	DS ^a	FS ^b
		<i>g/denier</i>	<i>kc</i>	<i>lb</i>		
Polyester	1000/2	7.3	500	9.5	2.2	0.35
Rayon/PE	1650/1000	5.0	410	11.4	2.1	0.35
Rayon	1650/2	4.1	290	17.7	2.0	0.40
Nylon/PE	840/1000	7.0	520	6.8	3.5	0.50
Nylon	840/2	7.3	500	3.3	7.3	0.90
Glass fiber/PE	3040/2000	6.0	150	14.0	0.9	0.10
Glass fiber	1520/2	9.1	50	40.0	0.0	0
Nomex/PE	1200/1000	6.5	450	10.0	2.0	0.35
Nomex	1200/2	5.8	400	4.2	1.9	0.38

^a Dimensional stability^b Flatspot.

1.4.1.4. Polyester Cord [65-69]

Almost all polyester yarns used in the tire industry are filament yarns of polyethylene terephthalate.

As rayon and polyamide dominate the tire cord market an improved reinforcing material is expected to meet the requirements imposed by increasing severity of tire operating conditions. A fiber, to be a satisfactory tire cord material, must possess a rather special, balanced combination of properties.

Polyester's high modulus and low elongation reduce tire deformation and growth under service conditions and lead to better high speed performance and tread wear, reduced tread cracking and better steering characteristics. In addition, polyester's dimensional stability allows manufacturing a more uniform tire.

High strength or tenacity is required to provide adequate carcass strength and in this respect, nylon is superior to current commercial polyester, which in turn is superior to rayon.

Polyester is considerably superior to rayon in fatigue resistance. In summary, polyester yarns have a better balance of fundamental properties for efficient use in modern tires than does rayon, and will replace a large portion of rayon cord in the future.

Recently, Dunlop U. K. announced that they were introducing an all polyester radial tire utilizing polyester macrofilament yarn in the belt [274].

Differences in production processes for high tenacity polyester yarn from those for regular polyester yarns are explained below. To improve the tenacity of cords, molecular weight of yarns and draw ratio in the production of the yarn are important factors. Intrinsic viscosity, IV, (a measure of molecular weight) of current tire yarn is 0.8 to 0.95, while that of regular polyester yarn is under 0.6. Draw ratio in tire yarn production is also much higher than that in regular yarn production.

Draw ratio in the production of the yarn has a large effect on both yarn tenacity and the yarn-to-cord tenacity conversion efficiency. As can be seen in figure 1.4.19 [65], the results effectively demonstrate the lower conversion efficiency of the higher tenacity materials. This decrease in conversion efficiency eventually reaches such proportions (as yarn tenacity is increased by increasing yarn draw ratio) that cord tenacity actually begins to decrease in spite of higher starting yarn tenacities, figure 1.4.20 [65].

The slope of the upper part (near the breaking point) of the stress-strain curve significantly affects yarn-to-cord conversion efficiency [34, 65, 70]. The higher the slope of the upper part of the stress-strain curve the lower becomes the conversion efficiency. This tendency is explained in terms of homogeneity of stress distribution in the cord by twist theory [71]. The slope of the upper part of the stress-strain curve is greatly affected by the draw ratio in the production of yarn, but other factors are also significant.

Tenacity of the cords can be increased without increasing the slope of the final part of the stress-strain curve or decreasing the yarn-to-cord conversion efficiency by increasing the molecular weight.

Using a suitable lubricant, which decreases the static friction coefficient of the yarn, is also effective for improving the yarn-to-cord conversion efficiency, as in the case of rayon.

Furthermore, heat aging resistance and hydrolytic resistance of the yarn are important factors. To improve heat aging resistance the diethylene glycol content of yarn must be reduced to a low level. On the other hand, as the carboxyl end group content decreases hydrolytic resistance increases [34, 73-75].

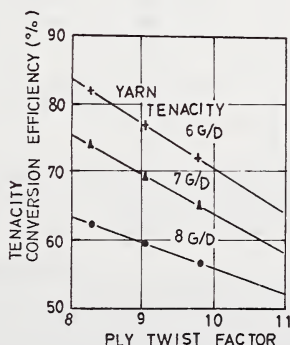


FIGURE 1.4.19. Effect of yarn drawing on tenacity conversion efficiency for polyester [65].

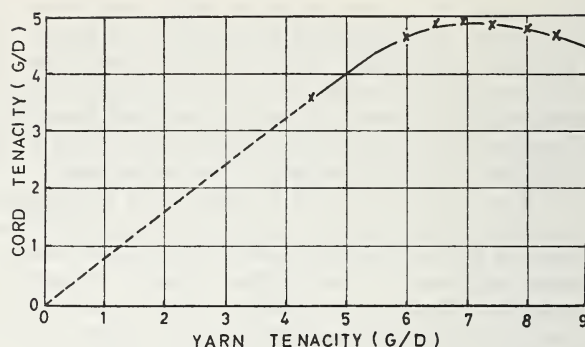


FIGURE 1.4.20. Cord tenacity vs. base yarn tenacity for 1100 D/2, 51 \times 51 turns/10cm. polyester cords [65].

Heat treating conditions of polyester cords have a pronounced effect on their properties. The heat treatment temperature of polyester cord is considerably higher than that of nylon or rayon. Stretch rate for polyester is considerably lower than that for nylon. Typical heat treating conditions of polyester cords are compared with those of nylon and rayon cords in table 1.4.5 [38]. In the case of polyester cord, fatigue resistance is particularly sensitive to the heat treatment.

TABLE 1.4.5 Comparison of Typical Heat Treating Conditions for Rayon, Nylons, and Polyester [38]

	Set temperature		Net stretch
	$^{\circ}\text{C}$	$^{\circ}\text{F}$	%
Passenger tire			
Rayon	155-165	310-329	1.5-3.0
Nylon 6	205-210	401-410	5.0-9.0
Nylon 66	220-230	428-446	4.0-7.0
Polyester	235-245	455-473	0-4.0
Truck tire			
Nylon 6	207-212	404.6-413.6	6.0-10.0

Aitken and co-workers reported that although stretching ratio affects the fatigue rating, treating temperature is the single most important factor in achieving high fatigue rating with polyester tire cord, table 1.4.6 [65].

They concluded from their results shown in table 1.4.7 [65] as follows; strength retention of the cords after heat treatment is best for the highest IV samples, which increases the advantage of high IV material over low IV material. This effect is most marked at high heat-treating temperatures. The higher the cord IV, the higher the fatigue rating

which can be achieved. A reduction in Mallory rating occurs at all IV levels when treating temperatures are taken to 490° F. High IV cords suffer less than low IV cords in this respect, however.

At 450° F, the Mallory ratings of the low IV samples exceed those of the high IV samples. At the two higher temperatures investigated, 475° F and 490° F, this effect is reversed.

In our experiments dealing with higher molecular weight (0.85 and 0.95 IV) yarn, rather high temperature heat treating may give a good fatigue rating and good dimensional stability but results in low strength cord and in a stiff fabric, which may cause difficulties during tire building [34].

TABLE 1.4.6. *Optimization of heat-treating conditions for polyester cord* [65]

	Oven temperature, ^a °F	Heat treatment		Mallory fatigue rating, kc
		First oven stretch, %	Second oven stretch, %	
A	400	3	0	11
B	400	5	-2	12
C	450	3	+2	24
D	450	5	-2	48
E	475	4	0	134
F	475	4	-3	196

^a 2/1100, 13 × 13 cord made from Type 24 "Terylene" yarn. Dwell time 90 sec in all cases.

TABLE 1.4.7. *Effect of IV and treating conditions on treated cord properties for polyester* [65]

Yarn IV	Greige breaking load, lb	Treating temperature, °F	Breaking load retained, %	Mallory fatigue rating, kc
0.60	28	490	76	8
		475	86	132
		450	92	122
		490	81	21
0.69	30	475	87	159
		450	95	61
		490	85	97
		475	91	175
0.73	31	450	95	23

1.4.1.5. Fiber Glass Cord

Simply stated, the most important problem of fiber glass cord is effective use in multifilament structures of superior single filament properties shown in table 1.4.8 [76]. Characteristically, single-filament properties are reduced by more than one-half when formed into strands or yarns.

Early developments showed that excellent flex life of single-filaments disappeared when they were combined as a cord.

For years, many attempts have been made to solve these problems. Phenol formaldehyde, elastomeric materials and more recently, some of the organo-silicon compound coatings were found to be effective to improve these properties.

Some inorganic coatings such as metals were also effective in improving abrasion resistance and flex life of multifilament glass fiber structures. However, lack of rubber-to-cord adhesion and insufficient filament-to-filament stress transfer resulted in unsatisfactory performance.

TABLE 1.4.8. *Physical properties of single filaments of glass and of organic fibers* [76]

	Glass ECG ^a	Rayon T-130	Nylon T-A05	Polyester T-52
Tensile strength ultimate, psi...	500,000	79,000	126,000	139,000
Tenacity at break, gpd.....	15.32	4.05	8.65	7.89
Ultimate elonga- tion, %.....	4.76	11.74	19.93	14.92
Modulus, gpd....	322	35	43	53
1000 psi.....	10,500	680	630	940
Toughness, gpd...	0.365	0.312	1.05	0.720
psi.....	11,900	6,100	15,300	12,800

^a Sp. gr., 2.55; elastic recovery, 100%; softening point, 1555° F; coefficient of thermal expansion (°F), 2.8×10.6 ; and water absorbency, 0.3%.

Various surface finishes were investigated to improve glass-to-rubber adhesion. A combination system of a compatible surface finish and an RFL was also developed as an impregnation material to improve filament to filament abrasion. With these developments it becomes possible to maintain single filament properties in impregnated multifilament glass cord, table 1.4.9 [76].

To achieve the aging characteristics associated with glass filaments, a melt was formulated in which oxides of boron, aluminum, and magnesium were combined with silicon dioxide, table 1.4.10 [76]. At present this aluminum-boron-silicate composition, known as E glass, is used for tire cord.

E glass has a three dimensional, completely crosslinked structure. The structure consists of a continuous silicon dioxide network with some silicon atoms from other networks forming oxides such as aluminum.

TABLE 1.4.9. *Physical properties of cords of glass and organic fibers [76]*

	Glass ECG-150 10-1A/0	Glass ECG-150 10-1A/3	Rayon T-130 1650/2	Nylon T-130 840/2	Polyester T-52 1100/2
Tensile strength (ultimate), psi.....	407,000	365,000	94,000	122,000	104,000
Tenacity at break, gpd.....	12.47	11.17	4.79	8.37	5.86
Ultimate elongation, %.....	4.83	4.84	9.8	19.3	18.5
Toughness, gpd.....	0.302	0.254	0.296	0.696	0.560
psi.....	9,900	8,300	5,800	10,200	9,900
Modulus, gpd.....	259	231	49	43	32
1000 psi.....	8,450	7,540	960	630	570
Breaking strength, lb..	79	219	39.1	33.2	32.1
Impact resistance, (ft/lb $\times 10^{-4}$)/denier..	3.95	2.75	1.87	4.08	3.41
Diameter, mils.....	17	35	26	21	24
Number of filaments...	2,040	6,120	8,000	280	500
Specific gravity (fiber).	2.55	2.55	1.53	1.14	1.38

TABLE 1.4.10. *E glass formulation [76]*

Silicon dioxide.....	52-56%
Calcium oxide.....	16-25%
Aluminum oxide.....	12-16%
Boron oxide.....	8-13%
Sodium and potassium oxide...	0-1%
Magnesium oxide.....	0-6%

Glass cord seems to be a promising material for belt ply cord for radial tires and belted-bias tires [80-84].

1.4.1.6. Steel Wire Cord [85-89]

The principal use of wire cord tires is in truck and bus tires and in some cases for off-the-road tires. Mileage in most cases is high.

The wire cord tire differs not only in cord properties but also in construction of the carcass plies and in method of tire manufacture. Conventional tire designs are used in some cases, but the wire characteristics allow radial ply construction.

Typical cord constructions currently used are illustrated in figure 1.4.21. Wire cord has high strength, extremely high modulus and high fatigue resistance.

Most wire cords are brass or zinc plated to improve cord-to-rubber bonding. This is done in the production process of the cord wires by continuous electrolytic methods after the wire has been drawn.

The wire is usually wound on convenient spools and is shipped to tire companies in a package containing a desiccant.

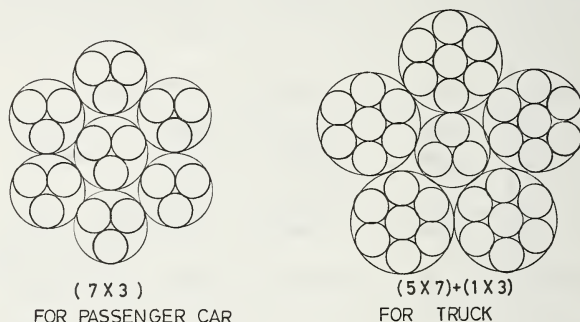


FIGURE 1.4.21. *Typical cord constructions of steel wires.*

1.4.1.7. Miscellaneous Cords

In addition to the cords mentioned above, Vinylon [16a], polyolefins, and polycarbonate [90] are being investigated as tire reinforcing materials.

Vinylon is used to some extent in bicycle tires but not in automobile tires because of inferior heat aging resistance.

Kurashiki Rayon has recently developed a new type of high modulus, high tenacity PVA filament yarn, which could be good material for the belt ply of radial tire [275].

Among polyolefins, polypropylene fiber is also being examined for bicycle tires [91] but its future as tire cord material does not seem to be promising because of poor high temperature properties and rubber-to-cord bondability.

1.4.1.8. Comparative Analysis of Various Tire Cords

A number of articles have appeared which are concerned with comparative analysis of various tire cords. The results which are summarized in table 1.4.11 were reported by Schroeder and Prettyman [92]. In increasing order of tenacity and breaking elongation are rayon, polyester, modified nylon and nylon. Rayon and polyester have higher initial moduli than do either of the nylons. Rayon possesses greater thermal stability than polyester and nylon. Rayon and polyester have higher flatspotting resistance than nylons. Nylon shows a definite superiority for both impact toughness and compression-flex fatigue resistance. Adhesion tests place

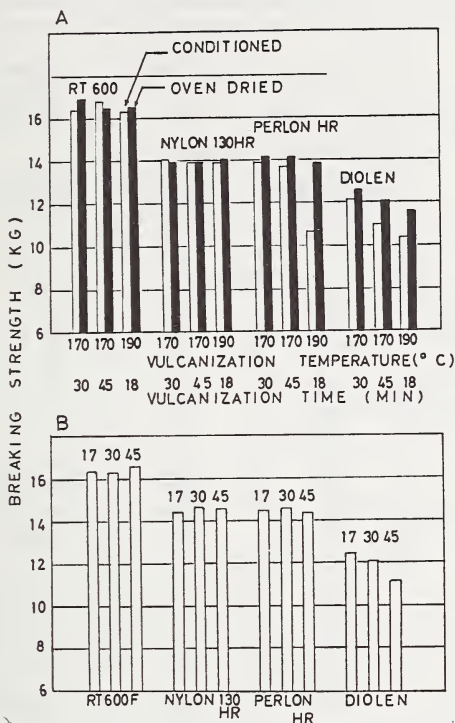


FIGURE 1.4.22. Comparison of strength loss in vulcanization [93].

RT 600F is rayon, 1650 D/2, 47.2×47.2 turns/10cm. Nylon 130HR is nylon 66, 840 D/2, 48×48 turns/10cm. Perlon HR is nylon 6, 840 D/2, 48×48 turns/10cm. Diolen is polyester, 1000 D/2, 50×50 turns/10cm.

(A) Effect of moisture on strength loss of cords in vulcanization.

(B) Effect of vulcanization time, 17, 30 and 45 min. on cord strength; Vulcanization temperature, 170° C; Conditioned at normal humidity.

rayon on top, followed in order by nylon, modified nylon, and polyester, although all are at a high level with modern dip systems.

We can conclude from these results that any current commercial cord cannot satisfy all cord properties required.

Schroeder and Prettyman also indicated the desired directions for cord properties as shown in table 1.4.12.

Daimler investigated the strength loss of various tire cords during tire curing under various conditions as shown in figure 1.4.22 [93].

For both rayon and nylon 66, no serious strength loss was observed under any condition investigated. Nylon 6 loses strength when it is allowed to shrink rapidly under high temperature, high humidity conditions, because of physical causes. On the other hand, polyester loses its strength because of hydrolysis at high temperature and high humidity. Strength loss of polyester depends greatly upon curing time, while that of nylon 6 does not.

TABLE 1.4.11. *Physical properties of various tire cords [92]*

	Rayon (current)	Nylon	Nylon (modified)	Polyester
Cord construction	1650 D/2, 12 × 12 2200 D/3, 8.5 × 8.5	840 D/2, 12 × 12 1260 D/2, 10 × 10	840 D/2, 12 × 12	840 D/2, 12 × 12 1260 D/2, 10 × 10
Tenacity, gpd.....	4.5	7	6.5	6
Elongation at break, %....	9	21	15	13
Initial modulus, gpd.....	60	27	40	70
Creep, %.....	3	4	3	2
Shrinkage, %.....	0.6	6	7	7
Flatspot Index, mils.....	50	170	115	50
Impact toughness, erg/cm · D.....	225	525	400	375
C-F fatigue, min.....	400	1400	600-1200	500
Adhesion, lbs/in.....	100	90	70	65
Aging, %.....	70	95	70-95	70
Esthetic rating of tires				
Flatspot.....	Par	Even
Roughness.....	Par	++	++	Even
Ride.....	Par	Even
Noise, smooth road.....	Par
Noise, brick road.....	Par
Handling.....	Par	Even	Even	Even

Furthermore, strength loss of polyester was affected by the rubber recipe; some amines, some moisture sensitive fillers, and thiuram accelerators in a rubber compound degrade polyester cords [34, 94].

Ebert [7] also compared various textile cords with steel cord as the reinforcing material for the belt ply of radial tires, see table 1.4.13.

Extra high modulus rayon and steel are promising materials for this purpose from the viewpoint of initial modulus.

Some polyesters also seem to be acceptable.

1.4.1.9. Impact Resistance of Tire Cords [95-99]

Impact failure of tires and tire cords, which will be considered here, is one of several failures that may occur in high speed operations. In general, impact resistance of a tire is determined either by road or simulated road tests, or has been inferred from laboratory tests at low speeds and room temperature.

Road tests are difficult and expensive and are limited in their ability to provide specific technical information for the design and modification of the design of tires. It is expected from the well-known behavior of

TABLE 1.4.12. *Characteristics of super-goal tire cord* [92]

Property	Level suggested	Tire-responses reduced
Tenacity: 75°F to 400°F.....	High	Impact breaks, heat breaks, heat buildup, high speed failure.
Elong. at break.....	High	Impact breaks.
Tensile modulus.....	High to medium	Flatspotting, growth, high speed failure. Impact breaks, flex failure, roughness.
Bending modulus.....	Low	Flex failure, roughness.
Creep.....	Low	Growth, tread wear, sidewall checking, tread cracking, high speed failure, flatspotting, tire dimension and uniformity variations.
Thermal shrinkage.....	Low to high	Tread concavity, bead distortion uniformity variations. High speed failure.
Flatspotting index.....	Low	Flatspotting.
Impact toughness.....	High	Impact breaks.
Flex fatigue resistance.....	High	Flex breaks.
Adhesion.....	High	Tread and ply separation.
Heat aging resistance.....	High	Impact breaks, heat breaks, flex breaks.

polymers that deflections, breaking forces, and breaking energies under high speed, high temperature conditions will differ greatly from those determined at low speeds and room temperature.

Laboratory impact tests of tires and tire cords are important as a design base for modern high speed tires.

Many superior laboratory methods of testing impact resistance of tires and tire cords have been proposed but we will not discuss them in detail here.

Hall [95] investigated the impact behavior of various fibers at a very high rate of straining, 330 sec.⁻¹, and at a normal rate, 8.3×10^{-3} sec.⁻¹, for a range of lightly twisted yarns covering all commercially important fiber forming polymers. Details of his experimental results are given in table 1.4.14. From these data, we see that at the high rate, breaking stress is always greater and with one exception, breaking extension less than at normal rates. Energy to rupture increases with rate for wet spun fibers and with one exception and decreases for thermoplastic fibers. Similar experiments performed with three of the yarns highly twisted,

TABLE 1.4.13. *Physical properties of cords for radial tire construction* [7]

		Elongation at 20% of breaking load	Adhesive power	Impact energy	Bending life	Bending stiffness	Heat growth
		%	tons	cm · kg	cycles	cm · g	%
Steel	1	0.4	7	230	40	1,400	0.2
EHM	2	0.7	16	450	1,900	80	0.3
	3	0.5	15	700	1,000	60	0.3
Rayon	4	0.5	18	730	1,500	100	0.4
	5	0.9	14	1,700	10,000	25	0.9
Polyester	6	1.0	1,800	4,200	700	0.5
	7	1.1	20	1,600	5,200	140	0.5
	8	1.9	14	1,400	5,600	30	0.5
Nylon	9	5.0	19	1,800	26,500	17	0.2

the data of which are given in table 1.4.15 and 1.4.16 [95], showed that ranking of the yarns according to a particular property could be altered by insertion of twist.

Lothrop [96] determined the tensile properties of rayon and nylon cords as a function of temperature and rate of extension. His testing equipment was designed and built to be capable of measuring the properties of tire cords over a range of temperature from 75° to 300° F at rates of extension of 1000 percent to 6000 percent/sec. (10 to 60 sec.⁻¹).

His complete data for treated rayon and nylon cords are summarized in table 1.4.17. Characteristically, for both oven-dried rayon and nylon, breaking strength decreases as temperature increases at a given rate of extension. Likewise, for a given temperature, breaking strength increases as rate of extension increases. For oven-dried nylon cord, breaking elongation is reasonably constant throughout the complete range of testing conditions. Oven-dried rayon, on the other hand, shows an increase in breaking elongation with increase in temperature as well as with increase in testing speed so that the maximum breaking elongation was observed at a temperature of 300° F and a rate of extension of 6000 percent/sec. (60 sec.⁻¹).

Breaking energy of the oven-dried nylon cord decreases with increasing rate of extension at the lower test temperature but not at the higher test temperatures.

Breaking energy of oven-dried rayon decreases with increasing temperature at low rate of extension but increases with increasing temperature at high rates of extension.

Recently, Lothrop published another report [97], which confirmed the

TABLE 1.4.14 Effect of rate of extension on breaking properties of various yarns [95]

Yarn	Poly- mer type	Breaking Extension, %		Tenacity, g/tex		Initial modulus, g/tex		Energy to rupture, joule/g		Critical velocity, m/sec	Sensitivity to strain rate ^a		
		8.3×10^{-3} sec ⁻¹	330 sec ⁻¹	8.3×10^{-3} sec ⁻¹	330 sec ⁻¹	8.3×10^{-3} sec ⁻¹	330 sec ⁻¹	8.3×10^{-3} sec ⁻¹	330 sec ⁻¹		A	B	C
Nylon 900	GG	20.1	12.7	84.9	110.0	510	1900	87.1	67.5	360	142	37	-23
Nylon 300	GG	20.5	13.8	60.6	93.1	360	700	71.7	59.7	350	89	33	-17
Nylon 100	GG	30.4	13.7	48.2	65.4	350	1400	103.0	51.7	260	117	55	-50
H. T. Enkalon	G	26.8	15.3	73.9	90.8	320	1500	88.0	56.5	290	153	43	-36
Enkalon	G	46.8	22.1	38.9	50.4	240	500	132.0	71.7	350	69	53	-46
Tenasco 105	R	15.2	10.5	35.6	50.5	900	1800	29.8	32.8	190	99	31	+10
Textile Tenasco	R	19.2	15.5	26.1	39.5	730	1700	28.1	39.1	220	115	19	+39
Standard rayon	R	23.2	19.6	18.9	29.8	490	1200	27.8	38.9	210	90	16	+40
Polynosic S.C. 28	R	7.7	7.0	27.5	46.3	1040	2300	12.2	20.2	180	101	9	+66
Tricel	ACE	37.1	23.0	10.4	14.6	340	1200	29.4	29.8	110	99	16	+1.4
Ulstron	PP	19.7	14.6	78.9	82.8	1080	1100	98.5	75.9	270	22	26	-23
Polypropylene multifil	PP	54.0	16.5	43.0	65.1	610	1100	193.0	69.8	300	76	70	-64
Polyethylene multifil	PE	23.8	7.4	39.9	69.8	770	1200	76.3	27.8	220	114	64	-64
Courlene X3	PE	19.7	7.5	37.4	63.0	640	1300	57.6	25.7	210	121	62	-55
H.T. Terylene	PET	12.8	7.3	60.8	77.7	1290	2000	54.5	34.4	220	57	75	-37
M.T. Terylene	PET	31.0	17.6	41.4	43.9	900	1900	98.0	67.5	150	52	43	-31
Courtelle	AN	33.9	22.1	25.0	27.4	530	1400	47.3	49.4	170	119	35	+4.4
Acrilan-16	AN	40.9	29.2	20.9	28.6	490	900	57.5	65.5	210	85	19	+14
B.H.S.	VC/AN	17.8	15.7	39.6	54.8	570	1500	31.3	46.1	280	109	12	+47
Aeress	VC/AN	24.1	18.7	21.2	36.8	640	1300	31.5	48.1	210	127	22	+53
Human hair		50.4	41.9	17.1	20.9	380	600	52.2	60.4	250	61	17	+16
Silk		16.2	16.7	31.6	47.8	550	1500	35.1	61.8	230	80	-3.1	+76
Saran 3:1 draw ratio		66.9	18.4	9.6	16.8	70	500	50.3	20.9	170	226	73	-59
Saran 3.6:1 draw ratio		15.2	13.1	15.2	26.8	73	400	11.5	19.3	180	227	14	+68
Vinal F.O.	PVA	13.9	10.8	58.4	85.0	1440	4100	41.5	53.6	290	129	22	+29

^aIf t_h were the stress at a given strain at the high rate; t_n were the stress at the same strain at the normal rate; e_h were the breaking strain at the high rate; e_n were the breaking strain at the normal rate; E_h were the energy to rupture at the high rate; and E_n were the energy to rupture at the normal rate; then Column A = $100(t_h - t_n)/t_n$ averaged over the whole curve, Column B = $100(e_h - e_n)/e_n$, and Column C = $100(E_h - E_n)/E_n$.

TABLE 1.4.15. *Effect of rate of extension on breaking properties of twisted yarns* [95]

Material	Tenacity g/tex		Breaking extension, %		Energy to rupture, joule/g		Initial modulus, g/tex		Critical velocity, m/sec
	330 sec ⁻¹	8.3×10 ⁻³ sec ⁻¹	330 sec ⁻¹	8.3×10 ⁻³ sec ⁻¹	330 sec ⁻¹	8.3×10 ⁻³ sec ⁻¹	330 sec ⁻¹	8.3×10 ⁻³ sec ⁻¹	
Standard rayon twisted	19.0	11.8	24.8	22.4	28.8	15.5	200	250	210
Standard rayon untwisted	29.8	18.9	19.6	23.2	38.9	27.8	1200	490	210
Nylon 100 twisted	42.1	39.1	21.1	38.0	48.4	90.0	300	160	300
Nylon 100 untwisted	65.4	48.2	13.7	30.4	51.7	103.0	1400	350	260
M.T.Terylene twisted	33.5	34.8	18.9	40.5	45.8	97.8	900	340	230
M.T.Terylene untwisted	55.4	41.4	17.6	31.0	83.4	98.0	2400	900	190

TABLE 1.4.16. *Percentage change in tensile properties on twisting*

Material	Tenacity		Breaking extension		Energy to rupture		Initial modulus	
	330 sec ⁻¹	8.3 × 10 ⁻³ sec ⁻¹	330 sec ⁻¹	8.3 × 10 ⁻³ sec ⁻¹	330 sec ⁻¹	8.3 × 10 ⁻³ sec ⁻¹	330 sec ⁻¹	8.3 × 10 ⁻³ sec ⁻¹
Standard rayon	-36	-38	+27	-3	-26	-44	-80	-50
Nylon 100	-36	-19	+54	+25	-6	-13	-80	-27
M.T. Terylene	-26	-16	+7	+31	-32	0	-51	-62

TABLE 1.4.17. *Breaking characteristics of dipped rayon and nylon cords as a function of temperature and rate of extension* [96]

Ratio of extension of sample, %/sec	Breaking characteristics	Rayon				Nylon					
		Cond., °F 75	Oven-dried, °F			Cond., °F 75	Oven-dried, °F				
			75	150	225		300	75	150	225	300
1	Strength, lb Elongation, % Energy, in. lb/in. of cord	32.3 13.5 2.45	35.0 10.2 2.08	31.9 10.4 1.94	27.8 10.8 1.69	24.0 11.3 1.51	28.3 19.9 2.50	29.2 20.8 2.69	24.0 18.9 1.92	21.1 20.5 1.93	16.7 22.2 1.82
1000	Strength, lb Elongation, % Energy, in. lb/in. of cord	38.5 13.8 3.24	41.7 10.4 2.66	40.0 11.4 2.70	36.6 12.5 2.78	33.0 13.5 2.75	32.9 17.6 2.80	33.4 21.1 3.12	29.1 20.9 2.59	25.2 21.1 2.51	21.3 21.3 2.05
3000	Strength, lb Elongation, % Energy, in. lb/in. of cord	39.2 14.2 3.17	43.6 10.4 2.76	40.6 12.7 3.07	38.3 13.3 3.08	36.3 14.2 3.12	34.6 18.5 2.83	33.4 20.6 2.94	29.2 20.1 2.58	25.1 19.5 1.98	22.2 20.2 2.91
6000	Strength, lb Elongation, % Energy, in. lb/in. of cord	41.0 13.7 3.21	44.0 10.3 2.55	42.2 12.4 3.07	40.3 13.3 3.18	38.1 15.0 3.32	35.3 17.5 2.75	34.7 21.0 3.01	29.3 19.8 2.35	26.3 19.5 2.18	22.4 19.0 1.79

above results by tire plunger tests at high rates and high temperatures. He used a test machine which consisted of a pneumatic gun for propelling the plunger at an inflated tire, mounted in a temperature-controlled cabinet, and photoelectric devices for measuring plunger velocity. The minimum kinetic energy required to cause failure of the tire fabric is taken as a measure of carcass breaking energy. Data on rayon and nylon cord tires indicate that the breaking energy of a tire is dependent on both speed and temperature and that the relationship between energy, speed, and temperature depends on the cord-reinforcing material. As a result, it is impossible to predict the relative impact resistance of tires under service conditions on the basis of laboratory test results obtained with the standard static plunger test, in which the plunger penetrates the tire at 2 in/min. at room temperature.

A comparison of data obtained on 7.75-14, two-ply rayon and nylon cord tires at three different speeds is shown in figure 1.4.23.

O'Neil, Dague, and Kimmel [98] also reported test results which include results of an individual cord impact test and three dynamic tire tests using a pendulum, a ballistic plunger, and resiliometer bruise.

Figure 1.4.24 shows the stress-strain curves of the four cord materials used.

Effects of temperature on strength and breaking energy of these cords at low speed are shown in figure 1.4.25a and 1.4.25b, respec-

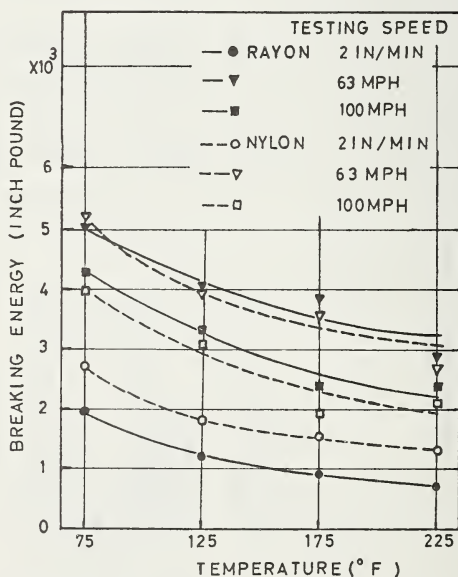


FIGURE 1.4.23. Breaking energy of 7.75-14, two-ply, rayon and nylon cord tires as a function of temperature.

Speed: 2 in/min., 63 mph, and 100 mph.

tively. Decreases in strength and breaking energy of nylon are more rapid than those of rayon and polyester.

Effects of temperature on strength and breaking energy of these cords at high speed are shown in figures 1.4.25c and 1.4.25d, respectively. Also in this case, decreases in strength and breaking energy of nylon are greater than those of rayon and polyester. On the other hand, rayon shows an increase in breaking energy with temperature.

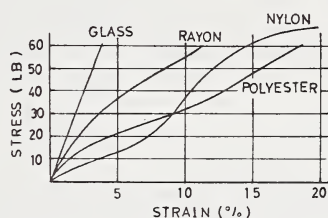


FIGURE 1.4.24. Stress-strain curve, low speed, 12 in/min. [98].

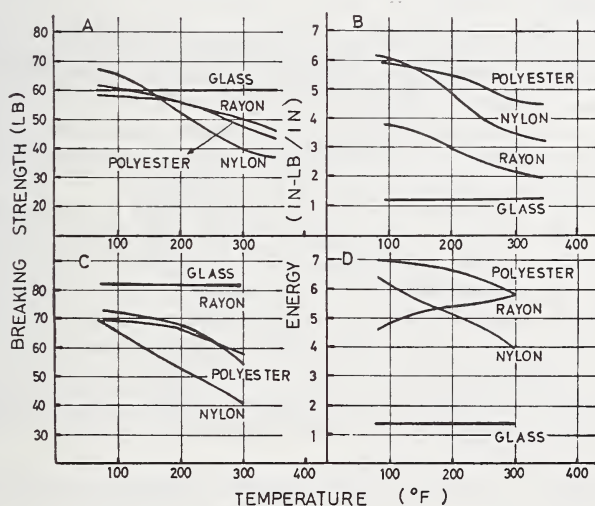


FIGURE 1.4.25. Effects of temperature on breaking strength and energy [98].

A and B. Low speed test. C and D. High speed test.

They also examined the impact resistance of tires. Table 1.4.18 shows the comparison between the low speed test and the high speed tests. The nylon cord tire has the highest failure energy at low speed, and the polyester cord tire has the highest value at high speed.

1.4.1.10. Fatigue Resistance of Tire Cords

Fatigue resistance of tire cord is an important property but difficult to assess. A variety of cord fatigue tests and laboratory tire wheel tests

TABLE 1.4.18. *Plunger, Pendulum, and projectile tests of tires* [98]

	Rayon	Nylon	Polyester
Plunger (slow) (I) energy, in-lb	2260	3450	3120
Pendulum (impact) energy, in-lb	9160	3390	3900
change over (I), %	+ 40	- 2	+ 25
Projectile (impact) energy, in-lb	3470	3600	4430
change over (I), %	+ 53	+ 4	+ 42

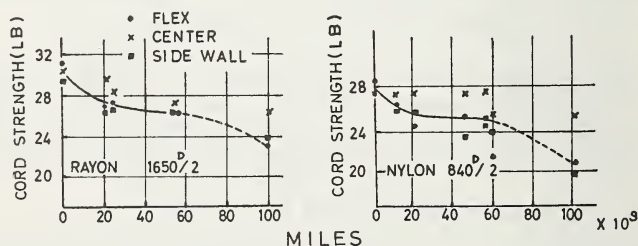
are currently available for evaluating relative tire durability. However, none of these tests can be considered adequate for characterization of road performance and therefore, in the last analysis, a road durability test is required.

Numerous papers are concerned with fatigue resistance of tire cord; some give phenomenological treatments of fatigue under cyclic tension [99-103], biaxial rotation [104] or flexing of cords in air [101, 105-109], some present statistical treatments of fatigue phenomena [110-112], [108*d*, e.g.], and others are treatments of fatigue under compressive or flexing conditions in rubber blocks or in actual tires.

Here, we will be mainly concerned with fatigue in rubber blocks or in the tire itself, which is most important for durability of tires.

Various views on the mechanism of cord fatigue in tires have been presented in the literature and diverse opinions have clearly indicated need for further research. For example, Williams and co-workers [113] concluded that cords in tires lose their strength linearly with mileage due to broken filaments. On the other hand, Entwistle and co-workers, and Klein and co-workers [114], see figure 1.4.26, said [115] that cords did not become progressively weaker until failure but fail suddenly by an undefined catastrophic process.

Fatigue failure of cords in tires generally occurs at special localized points. Williams and co-workers [113], and Patterson and Anderson

FIGURE 1.4.26. *Cord strength as a function of tire miles, taxi fleet test* [114].

reported that cords lose their strength more rapidly in inner plies than in outer plies. Klein and co-workers [114] also reported from tests of Tyrex rayon and nylon cord tires, that cord strength loss is greater in the flexing or side wall region than in the crown or center region, figure 1.4.26.

Patterson and Anderson [115] found that strength loss of nylon cords in tires was affected by the direction of tire rotation and the direction of cord bias and that cords in opposite sidewalls of tires lost strength at markedly different rates. Strength loss was higher for the half of the cord that led into the load bearing region of tire as it rotated (leading half) than for the other half of the cord (trailing half), as shown in figures 1.4.27 and 1.4.28 [115].

Two regions of high strength loss were found in each tire sidewall by breaking short segments of cords; at the shoulder, and at a point about two inches above each bead. Figure 1.4.29 [115] shows breaking strength at these points in first-ply cords from unfailed tires as a function of miles run on the test wheel. The point of lowest cord strength, in the range from 12,000 to 18,000 miles where tire failures began to occur, is shown to be in the leading shoulder. However, tire failures were always in the sidewall about two inches above the bead. This seemed to indicate that tires do not fail where the cords are weakest.

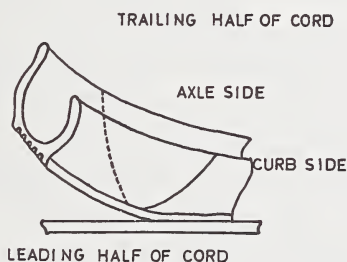


FIGURE 1.4.27. Identification of cord sections to side wall and rotation direction [115].

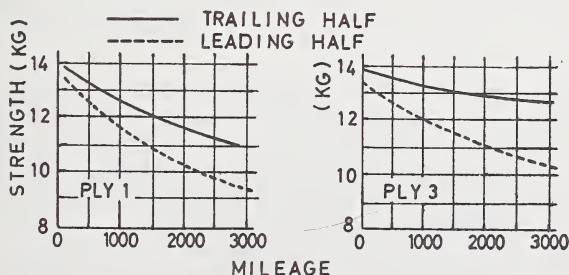


FIGURE 1.4.28. Cord Strength as a function of tire miles at test [115].

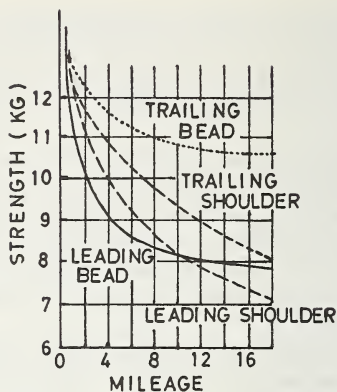


FIGURE 1.4.29. Average breaking strength of sections of first ply cords [115].

Patterson [116] concluded from the above discussions and microscope examination of broken ends of cords, that fatigue failures in nylon filaments were mainly related to cyclic flexing associated with compressive loading of inner ply cords.

In addition to the above fatigue failure of cords, it is generally accepted that cord-to-rubber adhesion failure [114] and rubber failure [117] play an important part in fatigue failure of tires. The general levels of adhesion (as measured by the stripping test) before and after a long run are shown in figure 1.4.66. Highest adhesion loss is observed in the region of maximum compressive flexing.

Microscope examination of broken ends of cords from failed nylon 66 tires showed a large number of filaments broken at a certain angle to the fiber axis [115, 116]. Polyester and nylon 6 filaments showed similar bias ruptures [115, 118–120].

Bias breaks are most prevalent at the point of cord rupture but are also found occasionally along the entire cord length. Patterson and Anderson stated that the number of bias ruptured filaments in flex tested tires increased linearly with severity of fatigue damage to the cord, see figure 1.4.30 [115]. These bias breaks were not produced by tensile loading of filaments.

Patterson dealt with the mechanism of bias rupture in another paper [116], a number of tests being run on filaments and cords to produce bias rupture.

A variety of tensile loading conditions applied to single filaments failed to produce bias ruptures. These results indicated that possibly unique or complex loading conditions were imposed on cords during flexing in a tire. To establish what these conditions might be, an investigation was made of the behavior of cords in transparent rubber under a variety of loading circumstances.

Examination of the cords during alternate tension and compression showed that the filaments undergo bending and sometimes buckling when in compression. The severity of bending increased with reduc-

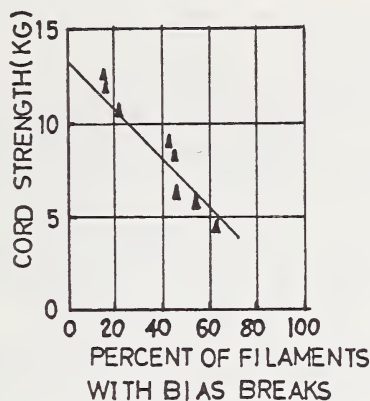


FIGURE 1.4.30. Cord strength as a function of percent of bias filament breaks [115].

tion of twist. Similar results were also obtained by Wood and Redmond [121]. The observed increase in filament bending at low twist and the accompanying poorer fatigue resistance indicated that bias filament ruptures might not depend on the complex stress associated with a twisted structure but more directly on simple bending associated with compressive loading of the specimens.

This hypothesis was tested with Mallory and Goodrich Disk Fatigue Testers. These tests established conclusively that bias rupture was produced by simple bending.

Further investigation showed that bias rupture began at the compression side of the bend in filaments subjected to repeated cyclic bending. Similar findings were indicated for ductile metal.

Fujimoto [40] investigated the correlation between fatigue life and molecular structure of nylon 6. He found that fatigue life in compressive loading decreased linearly with the second moment of the NMR peak of the noncrystalline part, and then concluded that long fatigue life is to be attributed to weak intermolecular interaction and mobility of molecules in amorphous regions, see figure 1.4.31*a*. Furthermore, he mentioned that fatigue life decreased linearly with lattice spacing d (002), see figure 1.4.31*b*, and suggested that mechanisms of fatigue failure and strength loss in the curing process, as mentioned before, have something in common.

Each tire company has its own methods of assessing tire cord fatigue resistance. Laboratory machines designed to examine fatigue resistance of cords fall into two groups; those flexing cords with air as medium and those flexing cords in rubber. Among typical examples of the former, there are cyclic tension types (e.g., U.S. Rubber Fatigue Tester, Du Pont Dynamically Balanced Tester [103] and Goodrich Tension Vibrator [102] and flexing types, e.g. Goodrich Flexing Tester [106].

Dillon classified these test methods according to the types of applied stress or strain as figure 1.4.32 [122].

Of the latter group, generally regarded as the more important, there

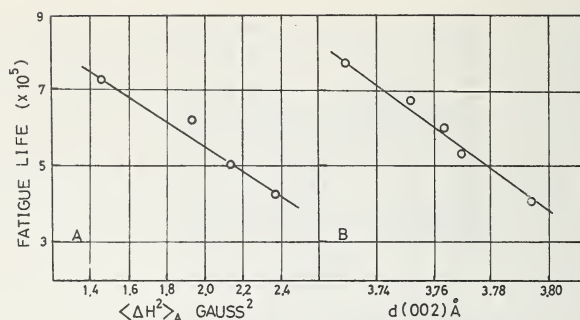


FIGURE 1.4.31. (A) Fatigue life of nylon 6 as a function of second moment of NMR peak for amorphous region. (B) Fatigue life of nylon 6 as a function of lattice spacing $d(002)$ [10].

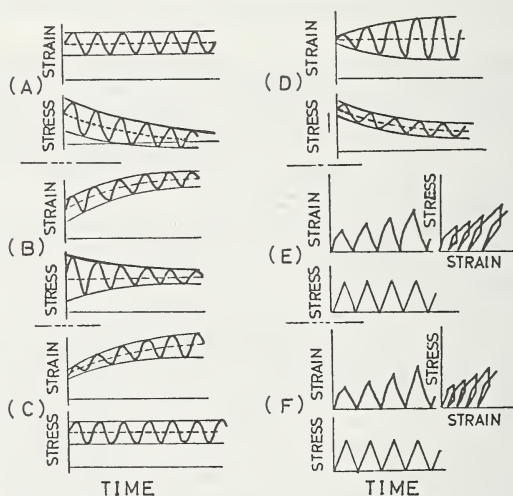


FIGURE 1.4.32. Classification of cyclic tension fatigue tests [122].

are several methods, as we will mention below; Mallory Tube [123–125], U.S. Rubber Tube [124], Goodrich Disk [124–127], Firestone Compression Flex [124–125], Dunlop and De Mattia Flex [128–131].

(1) Mallory Tube Test

The testpiece is a rubber hollow cylinder in which the cords to be tested run parallel to each other and to the axis of the test cylinder and are arranged to have the required number per inch.

The flexing principle is illustrated in figure 1.4.33. The test tube is bent and tightly clamped on two spindles of the flexer. Thereafter, air pressure inside the tube is increased and then the horizontal spindle is rotated. Cords in the tube undergo alternatively compression and tension.

The number of revolutions until failure is the measure of fatigue resistance.

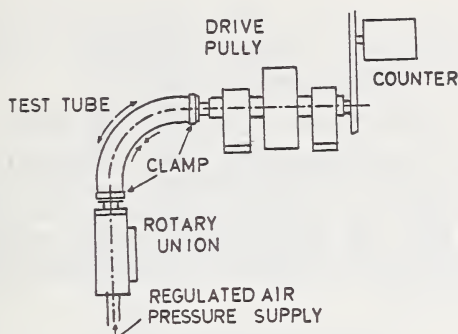


FIGURE 1.4.33. Schematic drawing of Mallory Tube Fatigue Tester.

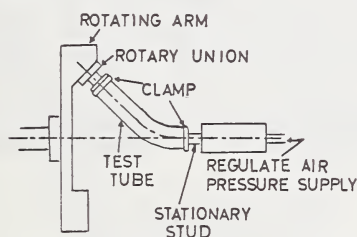


FIGURE 1.4.34. Schematic drawing of U.S. Rubber Tube Fatigue Tester.

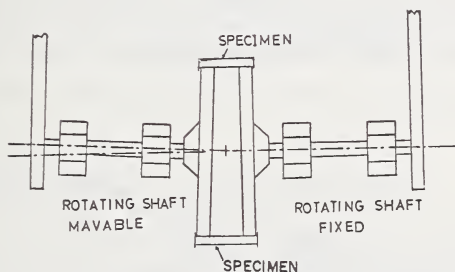


FIGURE 1.4.35. Schematic drawing of Goodrich Disk Fatigue Tester.

(2) U.S. Rubber Tube Test

This method is basically similar to the Mallory Tube Test but the flexing principle differs somewhat, as shown in figure 1.4.34.

(3) Goodrich Disk Test

The flexing principle is illustrated in figure 1.4.35. The testpieces are rectangular rubber blocks in which test cords run parallel to the long axis. The testpieces are firmly secured into the periphery of two canted disks, the cords passing cross the gap between them. When these disks

are motor driven, each cord in a rubber block suffers simple longitudinal extension and compression. Strength loss after a certain number of revolutions is examined to evaluate the cords.

(4) Firestone Compression Flex Test

The testpiece is a rubberized belt which contains two plies of cords in parallel planes, one ply of test cords and the other of steel cords.

Compressive fatigue is produced by flexing the testpiece over a spindle, figure 1.4.36. The inextensibility of the steel ply causes the layer of rubber itself and the spindle to be compressed and the tire cords are situated in this layer.

(5) Dunlop Fatigue Test

Essentially, the testpiece is an endless belt made up of five plies of rubberized cord. Counting from the inside, the second and fifth plies are comprised of the cords to be tested, these cords running along the length of the endless belt and being arranged in the required number per inch. The belt is tensioned between two pulleys as shown in figure 1.4.37. The test usually consists of running belts for known times, then extracting the cords from the two test plies and measuring their breaking strength.

(6) De Mattia Flex Test

The testpiece is a rubber block, in which the cords to be tested run parallel to each other and to the long axis of the block. The testpiece is firmly clamped on the two heads of a De Mattia Flex Tester which is usually used in rubber flex fatigue tests, figure 1.4.38. The test consists of flexing the rubber blocks and measuring their residual strength.

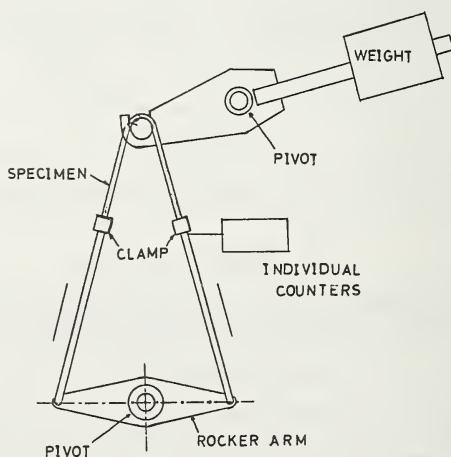


FIGURE 1.4.36. Schematic drawing of Firestone Compression Fatigue Tester.

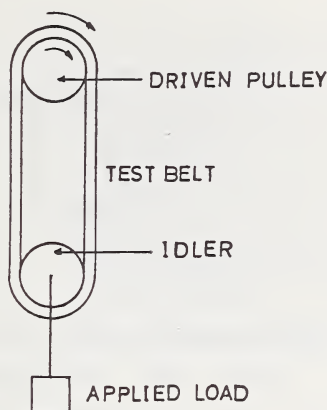


FIGURE 1.4.37. Schematic drawing of Dunlop Fatigue Tester.

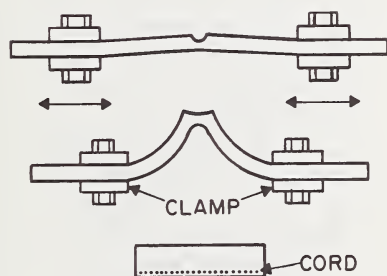


FIGURE 1.4.38. Schematic drawing of De Mattia Flex Fatigue Tester.

1.4.1.11. Effects of Twist on Cord Properties

Many papers have been published dealing with effects of twist on cord properties, some are theoretical, others experimental.

Tire and tire cord producers throughout the world do not agree on which twist gives the best results. Some of them choose a symmetrical twist and others prefer an asymmetrical twist.

They also adopt different twists for different materials; usually polyester cords are twisted more highly than nylon cord. Generally speaking, as twist increases, cord strength, initial modulus, and fatigue resistance in cyclic tension decrease, while elongation at break, rupture energy, and fatigue resistance in compression increase.

Kemnitz and co-workers have reported extensive studies on rayon cord dealing with effects of twist on cord properties. Figures 1.4.39 to 1.4.46 [132] show their experimental results. Cord construction was 1100D/2.

The effects of twist on strength were observed when the ratio of

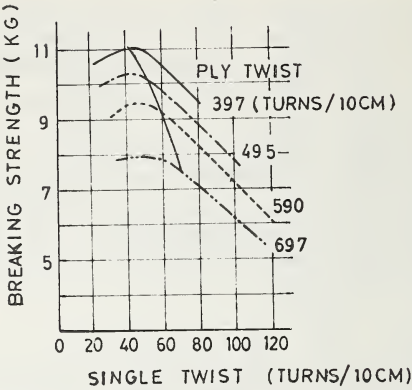


FIGURE 1.4.39. *Effect of twist construction on breaking strength of raw cords [132].*

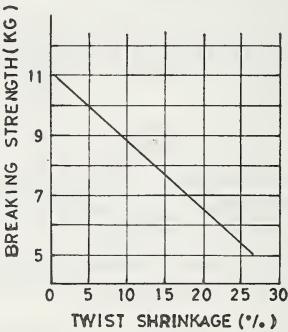


FIGURE 1.4.40. *Breaking strength of cord as a function of twist shrinkage [123].*

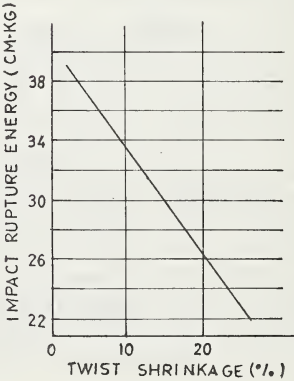


FIGURE 1.4.41. *Impact rupture energy as a function of twist shrinkage [132].*

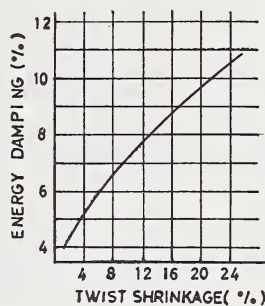


FIGURE 1.4.42. Energy damping as a function of twist shrinkage [132].

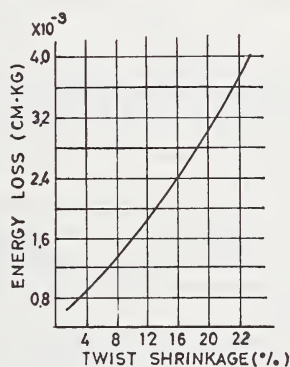


FIGURE 1.4.43. Energy loss as a function of twist shrinkage [132].

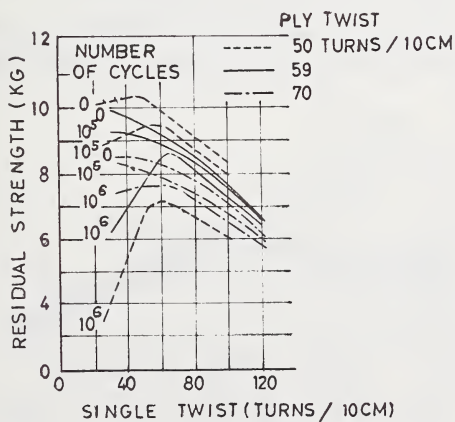


FIGURE 1.4.44. Residual strength after 10^5 and 10^6 cycles of flexing (De Mattia Tester) [132].

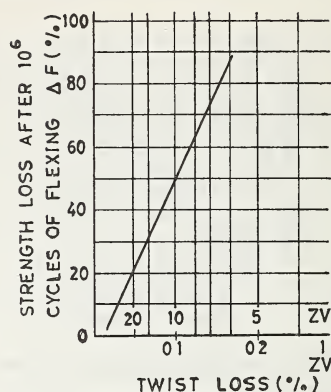


FIGURE 1.4.45. Correlation between strength loss after 10^6 cycle of flexing and twist loss [132].

ply and cord twist was not equal to unity. Cord strength is indicated as a function of twist shrinkage in figure 1.4.40.

In figure 1.4.41, rupture energy is shown as a function of twist shrinkage. Figures 1.4.42 and 1.4.43 show the relationship between dynamic properties and twist shrinkage.

These cord properties were stated to be uniquely determined by a simple function of twist shrinkage in the range examined. In figure 1.4.44, effects of twist construction on fatigue resistance are shown as residual cord strength measured after a known period of flexing on the De Mattia Flex Tester.

The relationship between residual strength after a known period of flexing, ΔF , and twist loss of cord ZV (Zwirn Verlust) are indicated in figure 1.4.45.

ΔF decreases linearly with ZV and the optimum residual strength is obtained by suitably balancing ΔF with ZV.

Figure 1.4.46 also shows the relationship between amount of twist and cord strength after flexing with number of load cycles as a parameter

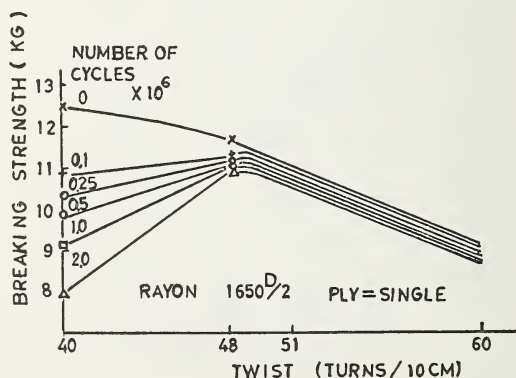


FIGURE 1.4.46. Residual strength of cord after flexing on De Mattia Tester as a function of ply twist and cycles of flexing [132].

[72, 133]. Twist construction was symmetrical twist of 1650D/2. Obviously the symmetrical twist 49 turns per 10 cm. reached its peak strength already after application of few load cycles. Similar results have also been obtained with Disk Fatigue Tests and tire fleet tests [113], figure 1.4.47.

Furthermore, it is well known that fatigue resistance measured by the Mallory Tube Test also increases with amount of twist in the ordinary twist range [65, 66].

Fujimoto stated that fatigue life in cyclic tension decreases with the amount of twist in the ordinary twist range, while flexing and compressive fatigue life increase, figure 1.4.48 [134].

1.4.2. Rubber-to-Cord Bonding

1.4.2.1. Introduction

Composite rubber and textile products are a considerable portion of all rubber products. For example, in Japan new rubber consumed for tires, belts, hose, and coated fabric was about two-thirds of the total

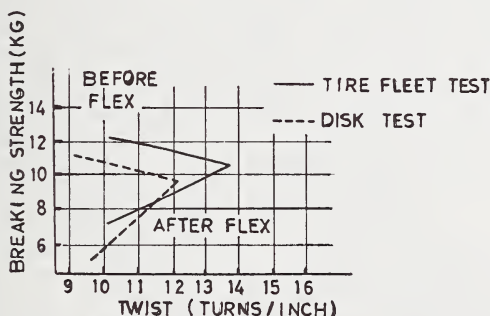


FIGURE 1.4.47. Effect of twist on cord strength before and after flexing in actual tire and Goodrich Disk test [113].

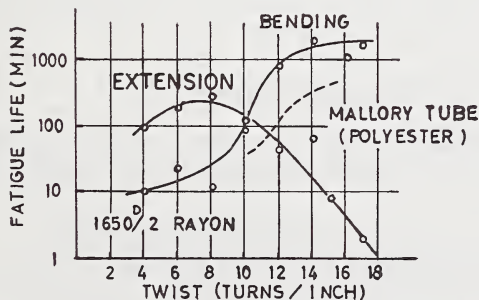


FIGURE 1.4.48. Fatigue life of cord as a function of twist [134].

new rubber consumption in 1967. Particularly, new rubber consumption for tires reached about half the total.

Adhesion is an important factor in using textile materials together with rubber, as are the individual properties of each material. The roles of adhesion may be: (1) to give desirable properties, (2) improve durability, and (3) maintain the shape of the composite material.

Tires, conveyer belts, and transmission belts are used under severe conditions, and a very high level of adhesion is required. In general, strong adhesion is obtained through adhesive treatment of the textile or through addition of bonding agents to the rubber compound. Hose and coated fabric do not require such high adhesion. Therefore the mechanical keying effect of textile to rubber gives sufficiently good results for these uses. Though several methods are available to bond textiles to rubber, it is necessary to select an adequate method according to the raw materials and the application.

For instance, looking back upon the progress of tire cord adhesion, in the early period (1890–1920's) cotton was used with no adhesive treatment or with rubber cement treatment. As loads, horsepower, and operating speeds of automobiles increased, needs grew for stronger and cooler running tires. Therefore rayon filament was introduced. Rayon has good mechanical properties, but lacks adhesion. Initially, reclaimed rubber-casein-latex adhesive was tried to improve this defect, but it failed to satisfy the requirements of the tire industry. Thereafter, studies of adhesives based on latex and thermosetting resin progressed, and led to finding resorcinol-formaldehyde-latex adhesive, commonly called RFL. RFL has met the requirements for modern tires, and has gotten wide acceptance in the tire industry since 1935. In 1947 nylon 66 was introduced as a tire reinforcing material in the United States. RFL adhesive is also effective with nylon. At present this adhesive is used extensively for bonding rubber to rayon and nylon cord. In 1936 (for the first time) steel wire cord tires were produced in France. Adhesion of wire can be gotten by zinc or brass plating. Recently polyester fibers and glass fibers have been used in the tire industry. From the rubber side, natural rubber has been gradually replaced by synthetic rubber and new materials, such as *cis*-1,4-polybutadiene and ethylene propylene rubber, have been introduced in the rubber industry. New adhesives and new methods have been developed to bond these new materials satisfactorily.

1.4.2.2. Outline of Bonding Methods

Methods of rubber to textile bonding should be varied according to the application. It is convenient to divide the methods into the following three groups:

- (1) adhesion based on mechanical keying effects,
- (2) adhesive treatment of textile material,
- (3) addition of bonding agents to rubber compound.

Each of the methods is explained briefly in this section, and details

of adhesive treatments of rayon, nylon, polyester, and other tire cords will be described later.

Mechanical interlocking, which is brought about by protruding fiber ends or fabric openings, has an important role in rubber to textile bonding. Borroff and Wake investigated the function of staple fiber in adhesion [135-136]. The fabric tested was a five-end satin weave which consisted of rayon filament as warp and a staple yarn-filament yarn combination as weft. Fabrics were coated with a rubber cement, and then vulcanized in an oven. Adhesion was measured by the direct tension method. As shown in table 1.4.19, bond strength is remarkably affected by amount of staple yarn as well as type of rubber cement and kind of textile material. The effect of staple yarn may be due to mechanical keying around the protruding fiber ends.

Also, rubber to textile adhesion varies with the nature of the weave. Adhesion to a fabric woven from continuous filament yarn is related to its interfacial surface area. Differences in surface area can be secured by differences in weave. The dependence of adhesion on interfacial surface area is obvious from the results shown in figure 1.4.49 [137].

Use of very bulky yarn enables rubber to bond to fabric without any adhesive treatment [138]. In this case adhesion may be brought about through an anchoring effect of little loops formed by the air bulking method. Also insertion of coarse fabrics into rubber is effective for reinforcing the composite material. This method is applicable to materials which are difficult to bond since rubber bridge formation through openings of the coarse fabric contributes to adhesion. For example reinforcement of silicone diaphragms has been achieved by insertion of multiple layers of nylon nets into the rubber plate, since silicone rubber is a favorable raw material because of its chemical and heat resistant properties, but it is very difficult to bond to textiles.

Rubber cement adhesives: Rubber cement adhesives have been employed, preferably in the belt and coated fabric industries. These adhesives are based on rubber solutions to which very reactive chemicals are added just prior to use. Preferred reactive chemicals are polyisocyanates such as diphenylmethane diisocyanate, tolylene diisocyanate, or triphenylmethane triisocyanate. Commonly used solvents are inert organic solvents, such as gasoline, toluene, halogenated hydrocarbons, or ethyl acetate. A high level of adhesion is obtained by immersing a textile material into rubber cements of low concentration or spreading with doughs of high concentration. The adhesive treated textile is then dried in an oven, and vulcanized with rubber compound. Immersion is suitable for cotton and rayon. Spreading is preferred for nylon and polyester [139]. This method is simple and available for every textile material including cotton, rayon, nylon, and even polyester [139-140]. By choosing suitable rubber compounds this method is available not only for natural rubber, but also for polychloroprene, nitrile rubber, etc.

It has been recognized from general experience that triisocyanate is more effective. However, Meyrick and Watts [141] reported that the effect on adhesion was much the same for di- and triisocyanate. Adhesion is affected by drying conditions after immersion. As shown in figure 1.4.50,

TABLE 1.4.19. *Results of direct tension tests* [135]

Cement	Weft Bond strength, lb/in ²								
	Rayon			Acetate			Nylon		
	Cont. fil.	20% staple	80% staple	Cont. fil.	20% staple	80% staple	Cont. fil.	20% staple	80% staple
Natural rubber	88	130	165	79	117	139	75	143	240
Polychloroprene	121	136	154	106	121	145	103	169	251
Nitrile rubber	77	134	154	90	121	139	62	130	192

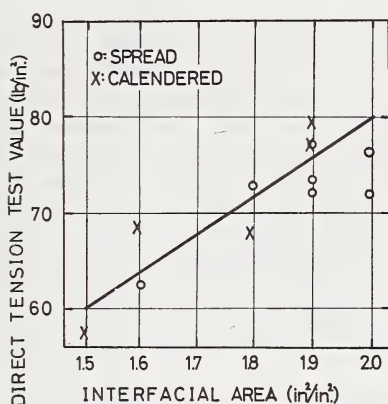


FIGURE 1.4.49. Relationship between interfacial surface area and adhesion [137].

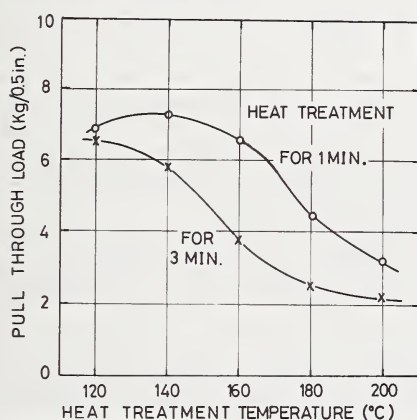


FIGURE 1.4.50. Effect of heat treatment conditions on adhesion [34].

long dwell time or too high oven temperature is detrimental [34]. In general, severe heat treatment causes much crosslinking of the rubber component in the adhesive. Hence, miscibility of adhesive with the unvulcanized rubber to be bonded decreases, and adhesion decreases. Optimum conditions should be determined empirically.

However, use of this adhesive is limited by the following disadvantages: (1) necessity for solvent recovery, (2) danger of fire, (3) toxicity, (4) long-drying time, and (5) sensitivity to moisture and short life. The isocyanate group—NCO is easily decomposed by moisture and loses its activity as an adhesive. Blocked isocyanates have been used instead of free isocyanates to improve this defect [142–143].

RFL adhesives: If latex alone is employed as an adhesive, good rubber to textile adhesion cannot be obtained because of lack of active groups in the latex and weak tensile properties of the adhesive coating film. Addition of a resin was studied to improve the mechanical prop-

erties of latex film. The reclaimed rubber-casein-latex system initially used provided improved adhesion, but failed to satisfy requirements of today's automobile tire [144]. Next, several thermosetting resins were used for this purpose. Phenol formaldehyde [145], urea formaldehyde [146], aniline formaldehyde [147], and ketone formaldehyde resins [146], were patented. Among them, resorcinol formaldehyde resin was selected to be used as an aqueous adhesive incorporated into latex because of its superior adhesion and ease of processing [148].

RFL is useful to bond rubber to textiles, such as rayon, nylon 6, nylon 66, Vinyon and easy-to-adhere types of polyester i.e., Trevira GPA, Diolen, DSP and Diolen V75 [93, 149, 150]. Also, RFL is used as a base for polyester adhesives. By suitable choice of the latex component, RFL provides good adhesion for many kinds of rubber as described later.

A typical RFL treatment will be outlined below. The tire cord or tire fabric is immersed in an RFL dipbath, and squeezed by passing through a squeeze roll unit, vacuum unit, or beater to adjust pickup of adhesive. Then the fabric is introduced into an air oven where drying and baking of the RFL is accomplished. Heat treatment is indispensable for nylon and polyester to give the preferred tire cord properties. Baking of RFL can be done at the same time. Widely accepted dipping machines for cord and fabric are illustrated in figures 1.4.51 through 1.4.54 [151]. A predip unit is included in this equipment. Water predip before RFL immersion is widely accepted to improve physical properties of dipped cords [151-152].

Double dipping systems are often employed for polyester. Polyester tire fabric is initially immersed in the first dip solution which consists, for example, of aqueous polyepoxide solution, and heat treated. This treated fabric is then passed through the second dip solution which is RFL, and heat treated again. A new dip equipment which includes two dip units and two heat treatment zones has been introduced. An example of this type equipment was described by Kersker and Kovac of Goodyear [66]. A lucid review on the dipping machine was presented by C. A. Litzler [277].

The treated cord or fabric may be stored a long time if it is sealed in black polyethylene film to shut out light. It is said that addition of wax [201] or ketene dimer [202] to RFL results in good resistance to lowering of adhesion during storage.

Mechanism of rubber to cord bonding through RFL adhesive will be outlined below. Although there have been numerous opinions concerning the nature of the fiber to rubber bond, only a few papers have been published about this problem. It is generally recognized that there are two primary considerations, nature of the RFL to fiber bond and nature of the RFL to rubber bond.

The nature of the fiber plays the most important role in RFL treatment of tire cords. In practice it has been recognized that rayon and nylon tire cords are easy to bond to rubber by RFL treatment, but with polyester cord this is extremely difficult. This should be attributed to the nature of the polymer structures. Rayon and nylon contain reactive

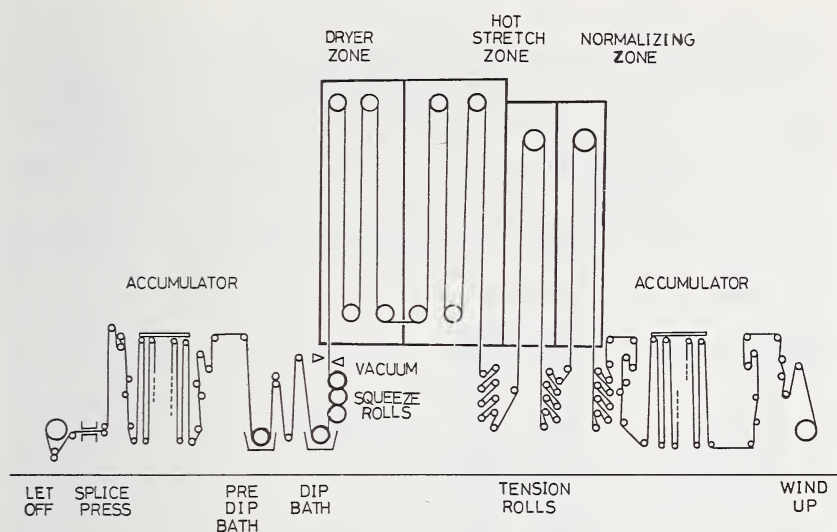


FIGURE 1.4.51. Schematic drawing of Ross fabric type heat set equipment [151].

groups such as hydroxy groups $-OH$ and amide groups $-CONH-$. But polyester has a less reactive structure, and it does not have so-called active hydrogen in the polymer chain. It was also suggested that ability for hydrogen bonding of polyester is less than that of polyamide [153]. Iyengar and Erickson deduced that lower adhesion of polyester is attributed to inaccordance of the solubility parameter of polyester with resorcinol [278].

There are many opinions on how RFL functions with rayon and nylon: hydrogen bonding between phenolic hydroxy groups in RFL resin and electronegative groups in fibers, condensation reaction be-

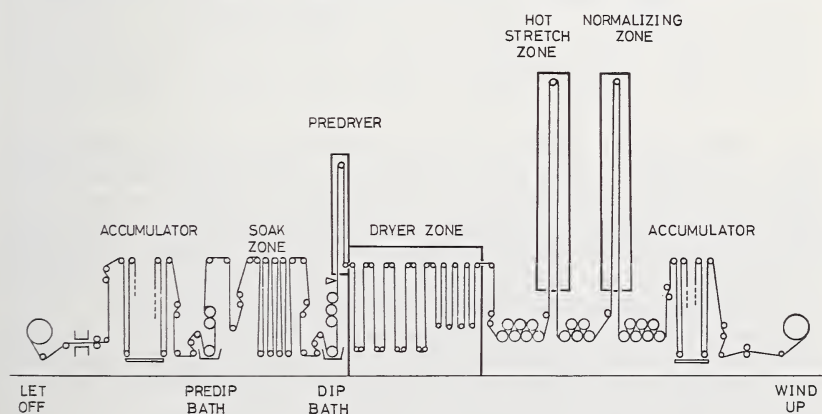


FIGURE 1.4.52. Schematic drawing of Litzler fabric type heat set equipment [151].

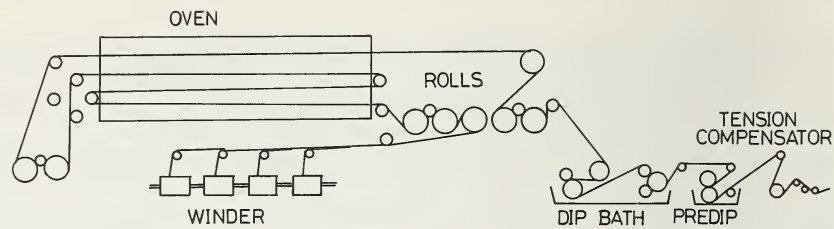


FIGURE 1.4.53. Schematic drawing of Kidde cord type heat set equipment.

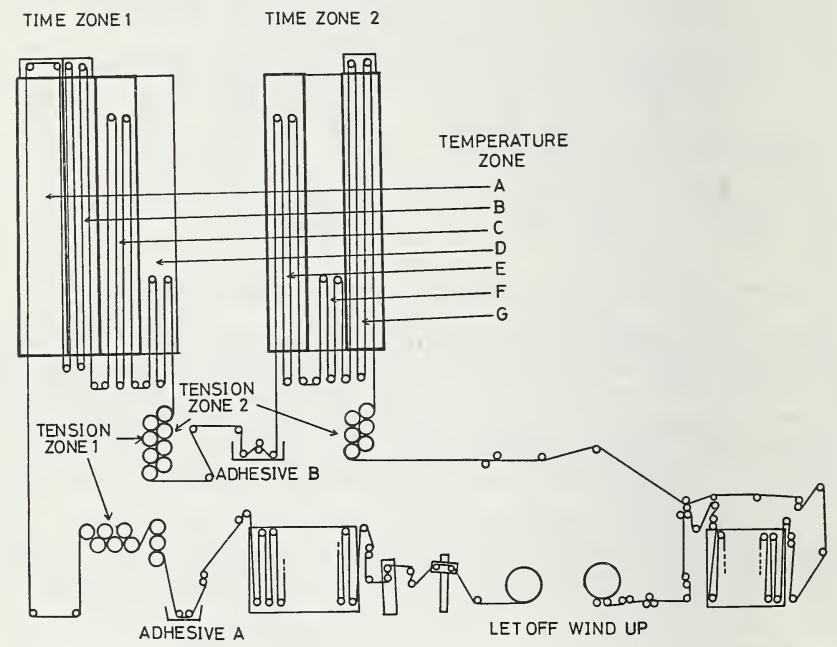


FIGURE 1.4.54. Schematic drawing of Goodyear continuous double dip equipment.

tween methyl group of RF resin and active hydrogen in the fiber, dipole-dipole interaction, molecular entanglement [152–157]. However, the evidence has been insufficient for any of these bonding mechanisms to gain wide acceptance. Also many opinions have been presented for the rubber to RFL bond: interdiffusion between RFL and rubber, covulcanization of carbon-carbon double bonds in RFL with rubber, ionic interaction, chemical reaction between RF resin and rubber [158–162].

Rubber to textile adhesion can also be achieved by addition of bonding agents to the rubber compound, thus eliminating adhesive treatment of textile materials. Isocyanate derivatives have been used for this purpose [163], but more widely accepted chemicals are combinations of resorcinol and formaldehyde donors [164], such as hexamethylenetetramine or

paraformaldehyde. Many modifications of this method have been patented. For example, trimethylolnitromethane [165], trimethylolacetaldehyde [166], or hexamethylmelamine [164] are used. Encapsulation of formaldehyde donors is also patented [167].

By addition of resorcinol formaldehyde donors to the rubber compound the best adhesion can be obtained even with untreated nylon and rayon. But good results are not obtained for polyester. However polyester to rubber bonding by this system is markedly improved by polyepoxide pretreatment. Easy-to-adhere polyesters, such as Diolen DSP or V75, bond very well, according to the Bayer's test results [168]. On the other hand, addition of *p*-chlorobenzoquinone together with resorcinol and formaldehyde donor can be used to bond conventional polyester (without pretreatment) to rubber [169]. The complex forming property of chlorobenzoquinone with aromatic compounds may function in the specific action with polyester [170].

On the rubber side, silica enhances adhesion. A typical tire carcass formulation may contain 40 phr³ carbon black. To use these systems with this rubber, 15 phr of silica are added and the carbon black is reduced to 25 phr to keep the total filler loading the same. Optimum amounts of other components are 2.5 phr resorcinol and 1.5 phr hexamethylenetetramine. According to Bayer's test results, the effect of silica is evident.

TABLE 1.4.20. *Bond strength of a typical fire hose compound with and without suitable bonding additives*

Additives, phr				Bond strength, kg/25 mm			
Carbon black	Silica ^a	Resorcinol	Formaldehyde donor ^b	Cotton	Rayon	Nylon	Polyester
60	2.7	1.5	1.1	1.0
60	2.5	2.5	4.6	2.5	3.3	2.3
30	30	3.8	3.2	2.4	2.4
30	30	2.5	2.5	8.6	15.8	17.5	5.6

^a Vulcasil S.

^b Bonding Agent 7110.

At present these methods are used in manufacturing conveyer belts, transmission belts, hose, and footwear. Pittsburgh Plate Glass, Degussa, and Bayer are all making efforts to develop these systems and they are working with rubber companies to use these adhesives for tires.

It is not well understood why these systems work. Resorcinol and the formaldehyde donor form resorcinol-formaldehyde resin in rubber. The resin may combine with both rubber and textile as described before.

³ phr = parts per hundred rubber.

Besides the above methods, addition of resorcinol and azomethynes [171], resorcinol-aldehyde polymer and azodioxycyclooctane [172], methylene donor and acceptor to the rubber compound are patented [173]. Recently many practical details of the method have been disclosed [279-281].

1.4.2.3. Adhesive Treatment of Nylon and Rayon—RFL Treatment

Many factors are known to affect the bond strength secured with RFL adhesives. For example, composition of RFL, method of RFL preparation, amounts of adhesive applied to cords, its distribution on the cord, heat treatment after dipping, method of storing dipped cord, composition of rubber compound, and vulcanization conditions may be factors affecting the cord to rubber bonding. Participation of each factor is explained in the following sections.

RFL adhesives are usually prepared by reacting resorcinol and formaldehyde under alkaline conditions prior to addition to latex. The mixture of RFL resin solution and rubber latex is further aged before use. An example of RFL preparation is as follows [174].

Sodium hydroxide, resorcinol, and formaldehyde are dissolved successively in water. After complete solution is effected, a reaction takes place which should be allowed to continue for six hours at 25°C.

<i>Resin solution</i>	
Water	238.4 g
Resorcinol	11.0
Formalin, 37%	16.2
Sodium hydroxide	0.3

The RFL recipe should be varied with the textile material. The following formulations have been found to give optimum adhesion with rayon and nylon.

<i>Fabric</i>	<i>Rayon</i>	<i>Nylon</i>
Gentac latex, 41%	52.5 g	428.0 g
SBR latex, 40%	215.0
RF solution, 6.5%	284.0	465.0
Water	467.8	107.0

The recommended maturing condition for the above RF-latex mixtures is six hours at 25°C.

Precondensation of RF resin is, however, not indispensable when synthetic latex is used [154].

Also resorcinol-formaldehyde precondensate, such as Penacolite resin of Koppers Co., is available to prepare RFL [159]. Adhesive is prepared by successively mixing the following components:

Water	407.7 g
Sodium hydroxide, 10% aq. sol.	8.0
Penacolite resin R2170, 75%	26.7
Formalin, 37%	20.3
Vinylpyridine latex, 40%	250.0

The mixture should be aged 18 to 20 hours before use.

Adhesion is affected by the composition of RFL and maturing conditions. Resorcinol to formaldehyde ratio, pH of solution, concentration, maturing time and temperature have an effect on the structure and molecular weight of resorcinol formaldehyde resin. Choice of latex component is very important on the viewpoint of affinity of RFL for rubber. Latex to resin ratio is also influential in adhesion. Strength of RFL film and balance of affinity to both fiber and rubber depend on L/RF resin ratio.

Nowadays, the composition of RFL for nylon and rayon has been decided empirically. R/F is in a range of $\frac{1}{2}$ to $\frac{1}{4}$ in molar ratio, and L/RF resin is in $\frac{1}{5}$ to $\frac{1}{15}$ in weight ratio of solid components. The most widely accepted latex component for natural rubber and/or SBR compound is vinyl pyridine-styrene-butadiene terpolymer latex. In some cases, mixture of vinyl pyridine latex with SBR latex on natural rubber latex is used [34, 154, 159, 176-194].

Adhesion is affected by conditions of dipping and of heat treatment after dipping.

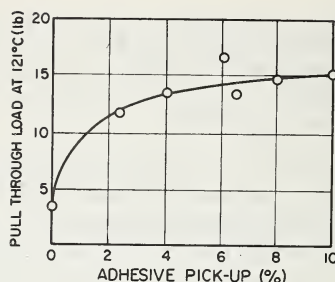
Effect and control of RFL pickup: Pickup of adhesive on a cord and penetration conditions of the adhesive into the cord interior affect adhesion. From general experience, bonding strength increases with pickup of adhesive. It is, however, important to consider not total pickup, but effective pickup since penetrated RFL does not contribute to adhesion. It is observed by microscopic inspection of a cross section that RFL penetrates into the cord interior to a certain extent.

Penetration may be controlled by squeezing conditions [154], concentration of RFL, viscosity of RFL, cord tension in the dipping bath [195], and presence of water predip. However, the contribution of penetration of RFL to adhesion has never been quantitatively analyzed.

The dependence of adhesion on RFL pick-up was reported in many papers.

Adhesion increases gradually with pickup and reaches a saturation point. An example is shown from Dietrick [159], and illustrated in figure 1.4.55. Too much pickup should be avoided because the amount of adhesive affects stiffness of the cord [197]. Also a pickup level should be decided upon by balancing cost against adhesion level. It is generally recognized that an adequate level of RFL pickup is from 6 to 8 percent of the cord weight.

Pickup level is affected by the kind of textile material, textile lubricant, concentration and viscosity of adhesive solution, and conditions of squeezing. Looking at the kind of textile material, nylon takes up the adhesive with more difficulty than rayon because of its hydrophobic nature. Polyester has still less pickup than nylon. A comparison for

FIGURE 1.4.55. *Effect of adhesive pick-up on pull through load* [159].

rayon and nylon is shown in table 1.4.21 [154]. If dipping is done under the same conditions where concentration of RFL and squeeze pressure is held constant, rayon cord has more RFL pickup, and adhesion is superior to that of nylon cord. Concentration of adhesive should be changed with the textile material to adjust the pickup level. For example, it is recommended that suitable concentrations for nylon and rayon are 20 and 12 percent respectively [174].

TABLE 1.4.21. *Relationship between squeeze conditions and pickup* [154]

Latex RFL	RFL conc., %	Squeeze roll, lb	Rayon		Nylon	
			Pickup, %	Pull-through load, lb	Pickup, %	Pull-through load, lb
Butyl latex	12.5	0	8.5	17.2	3.3	11.4
	12.5	15	2.2	14.5	2.8	10.7
	12.5	35	3.5	12.5	2.2	10.6
SBR latex	0	7.3	26.4	3.2	17.7
	15	4.9	23.9	2.9	15.9
	35	3.7	19.2	2.5	14.2

Even if the textile material is the same, different lubricants cause different pickups and different bond strengths. Gillman and Thoman [198] reported on this problem using the casein-latex adhesive system with rayon tire cord. When effects of waxy ester and sulfonated oil are compared, hydrophilic cord lubricated with sulfonated oil has higher pickup than hydrophobic waxy ester cord. Materials that have been used in tire cord lubricants are white mineral oil, petroleum sulfonate, triglyceride, ethoxylated and sulfonated derivatives, and so on. Generally, two or more of these materials are blended to produce a proprietary formulation. Petroleum sulfonate is often used to enhance cord to rubber adhesion [199]. The dependence of adhesion on lubricants is, however, a very complicated phenomenon, and cannot always be explained solely by the hydrophile-hydrophobe nature of the lubricants.

Also, pickup level depends on the adhesive concentration and squeeze conditions as shown in table 1.4.22. Change of concentration is more effective than change of squeezing conditions.

TABLE 1.4.22. *Effect of hydrophilic nature of lubricants on adhesive pickup and adhesion*

Adhesive conc., %	Viscosity at 25 °C, cp	Waxy ester on cord		Sulfonated oil on cord	
		Pickup, %	Adhesion, lb	Pickup, %	Adhesion, lb
5	1.67	0.4	7.8	1.7	9.0
7.5	1.94	0.5	8.0	2.6	10.6
10.0	2.46	0.8	8.1	3.9	10.9
12.5	3.53	1.2	9.4	6.1	12.2
15.0	8.36	1.9	10.9	8.4	13.8
17.5	26.5	2.5	11.0	9.5	14.1
20.0	57.2	5.9	12.0	22.0	17.4
22.5	83.5	21.1	14.8	46.3	19.8

Effect of heat treatment after dipping: Heat treatment conditions should be decided from the kind of textile material, adhesive composition, and procedure for the condensation reaction of the RF resin. Since each heat treatment equipment has its own heat efficiency, it is impossible to establish identical heat treatment conditions. Roughly saying, commonly accepted conditions are:

Rayon	155° to 165° C	2 to 3 min.
Nylon 6	205° to 210°	0.5 to 1 min.
Nylon 66	220° to 230°	0.5 to 1 min.

During heat treatment, a highly crosslinked structure is formed in RFL and strong interaction between adhesive and textile is achieved. Weak heat treatment causes the RFL coating to have inferior tensile properties and there is lack of interaction with the textile. Strong treatment impairs compatibility with the rubber. Both over- and under-

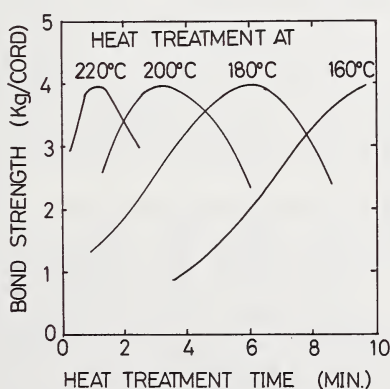


FIGURE 1.4.56. *Variation of adhesion with heat treatment conditions.*

heat treatments are undesirable for adhesion. These features are shown in figure 1.4.56. Iyengar reported the similar results on nylon 66 and 6, [282].

Examples of heat treatments used by United States tire manufacturers for nylon 66 tire fabric were given in a previous section, table 1.4.2.

During the subsequent processes in building tires, rubber-to-cord adhesion is affected by calendering temperature and vulcanization conditions, but mostly by composition of the rubber compound.

To obtain a high level of adhesion, it is important for rubber and the adhesive on the cord to have an opportunity for contact. The opportunity relates to fluidity of the rubber compound during processing. For example, adhesion increases with rising rubber temperature in the calendering process. However, at too high temperatures, cross-linking of the rubber proceeds with passage of time, and its fluidity gradually decreases. Too high calendering temperature causes rather inferior adhesion for this reason [203]. The opportunity for interaction also depends on time of contact. As scorch time of the compound indicates the time which it is fluid, opportunity for contact can be represented as a function of scorch time. Dependence of adhesion on scorch time with various rubber compounds is shown in figure 1.4.57, [204]. The rubber compound with a long scorch time, that is, with high probability of contact, showed high adhesion in both static and dynamic evaluations.

Adhesion is associated not only with opportunity of contact, but also with polarity of the rubber compound. Polarity of a compound may be varied by choice of rubber and filler. It has been stated that higher adhesion attained by substituting channel black for furnace black was primarily due to surface polarity of the channel black [204]. Rubber compounds with highly polar silica filler showed a very high level of adhesion if they were compounded to have a very long scorch time. Iyengar suggested that long scorch time and high polarity were two requirements for development of good adhesion.

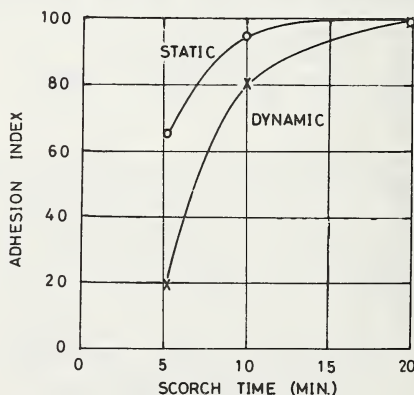


FIGURE 1.4.57. Variation of adhesion with scorch time of rubber compounds [204].

When adhesion is at a very high level, it is observed that a test specimen in the pull-through test is broken by failure of the rubber. In these cases, pull-through value is determined by the properties of the vulcanizate. Meyrick and Watts reported on this problem using rubber compounds with various fillers. They found that there was some relationship between hardness and modulus (stiffness) of the vulcanizate and adhesion level [141].

The properties of vulcanized rubber are, of course, affected by vulcanization conditions. Adhesion is also affected by these conditions. If adequate properties of the unvulcanized rubber are secured by adjustment of the cure cycle high adhesive strength is obtained even at high vulcanization temperatures [34].

1.4.2.4. Polyester to Rubber Bonding

The potential of polyester fiber as a tire reinforcing material was recognized as described before, but its use has been delayed by lack of a suitable bonding method. This situation has, however, been improved by introduction of new adhesive systems such as the double dip system. Nowadays, use of polyester tire fabrics is increasing steadily in the United States and Japan.

Looking back on the progress of polyester to rubber adhesion, attempts were first made to modify existing RFL adhesives. But this approach proved inadequate because the adhesion between fiber and RFL was insufficient [66]. Poor adhesion may be due to reduced ability to form hydrogen bonds [153], lack of reactive hydrogen in the polyester molecule, and its hydrophobic nature [205]. Therefore many efforts have been made to secure a high level of adhesion both by improvement of the fiber and improvement of the adhesive.

Modification of polyester fiber can be attained by solvolysis besides copolymerization or blended spinning. Immersing the polyester fiber in alkaline solution causes it to undergo hydrolysis and many hydroxyl groups and carboxyl groups are produced on the surface [206]. These groups give sites for the condensation reaction and hydrogen bonding with RF resin. Contribution of sodium hydroxide pretreatment of the polyester to rubber adhesion is obvious from results shown in figure 1.4.58. Only ten seconds immersion in 20 percent aqueous sodium hydroxide solution at 65°C produced Terylene tire cord to rubber bonding after RFL treatment [207].

Amines are available too. In this case, amide and hydroxyl groups are formed on the polyester surface [206, 208]. Too long immersion causes somewhat decreased adhesion [34]. This phenomenon may be caused by deterioration of the surface layer of the cord.

The polyethyleneimine-RFL double dip system of N. V. Onderzoeking Inst. Res. may be based on aminolysis [209]. Polyethyleneimine contains primary amino groups to the extent of about 30 percent of the total amino groups [210]. These primary amino groups attack ester links, and polyethyleneimine is combined tightly at the polyester surface. Imino-HN-

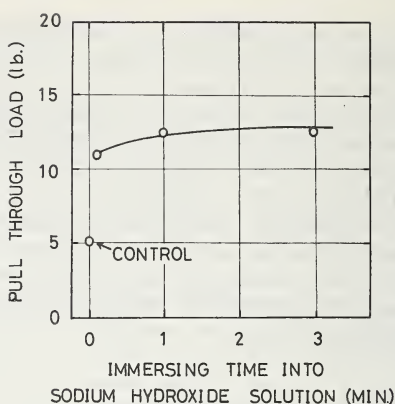


FIGURE 1.4.58. *Effect of fiber immersion in sodium hydroxide solution on rubber to Terylene adhesion after RFL treatment.*

and amino-NH₂ groups in polyethyleneimine may have the same affinity for RFL as do the hydroxyl groups of rayon.

Pretreatment by aqueous solution of a carboxyl-group-containing polymer such as polyacrylic acid was also proposed [211].

Now these solvolysis methods have been abandoned because adhesion is not sufficient in practice, and there is strength loss of the fiber.

Several new adhesives have been found as the result of major efforts. These adhesives may be classified as follows by the nature of the functional material.

- (1) Isocyanates, blocked isocyanates
- (2) Ethyleneureas
- (3) Modified polyvinylchloride
- (4) Polyepoxides
- (5) N3, Pexul

In this section, details of each method will be explained.

Isocyanate rubber cement is useful in polyester to rubber bonding as described before. The isocyanate group, -NCO, has a specific action for both polyester and rubber. Once polyester is treated by isocyanate, which is used as an organic solution, adhesion to rubber is facilitated remarkably after RFL treatment. The process and experimental results with this method are shown in what follows [141].

Polyester cord → Polyisocyanate in organic solvent → Drying → RFL Treatment

Resulting strength of adhesion

Isocyanate/RFL double dip system	36.3 lb/in.
RFL single dip system	8.8 lb/in.

Bond strength also depends on pH of the RFL. Satisfactory adhesion can be achieved over a pH range of 9.8 to 10.7.

A further interesting feature is that cord treated with polyisocyanate can be stored for prolonged periods under laboratory conditions, e.g. six months, without fear of loss of adhesion. Patents were issued for these methods [185, 186, 212]. They are simple and superior for adhesion, but requirements of solvent recovery and ventilation, as well as toxicity, limit their wide acceptance in the tire industry. Another drawback is its sensitivity to water. Since isocyanates react easily with water and lose their activity [213], they cannot be used in an aqueous adhesive system as is. Stabilization against water is accomplished by encapsulation [214], dimerization [215-218], or blocking of isocyanate [215]. Utilization of blocked isocyanates is commoner. Phenol is widely accepted as a blocking agent. Phenol blocked isocyanate is not decomposed further in water, and regenerates free isocyanate when it is heated at 140 to 170°C. Some blocked isocyanates are sold on the market, for example, phenol blocked diphenylmethane diisocyanate is marketed by DuPont as Hylene MP.

The adhesive solution is prepared by mixing ball-milled Hylene MP, latex, and thickener. A mixture of Hylene MP and RFL is also a good adhesive for polyester [219-224].

Ethyleneurea is a derivative of an isocyanate, but does not act as an isocyanate generator [225]. Ethyleneurea is prepared through the addition reaction of ethyleneimine to isocyanate.

Originally ethyleneureas were used as an adhesive for wood [226], or were incorporated into rubber cement as a bonding agent of cellulose fiber or polyamide fiber to rubber [142, 143]. Application of ethyleneureas for polyester-to-rubber bonding was developed by Japanese tire manufacturers and fiber producers [222, 227-231]. They are available for both single and double dip systems. A single dip system combined with RFL was, however, developed purposefully.

As low-priced isocyanates are limited to tolylenediisocyanate and diphenylmethane diisocyanate, only aromatic ethyleneureas have practical significance. They are insoluble in water and settle out easily.

Several ways have been developed to improve mechanical stability of the resulting dip solution such as addition of thickener, introduction of methylol groups into ethyleneureas [232], and so on [231]. With the thickened dip system, maturing conditions of the RF resin should be very carefully controlled to avoid gelation of the dip solution [233-234].

Bond strength also depends on the heat treatment [34]. The ethyleneurea-RFL single dip system had been developed in Japan, but it did not find practical use in the tire industry because of poor dynamic performance at tire operating temperatures and inferior adhesion with high vulcanization temperatures. As to the action of ethyleneurea with polyester, Timmons speculated that it functioned the same as isocyanates, i.e., isocyanate should be regenerated from ethyleneurea [240]. But this does not seem to be correct since ethyleneurea changes thermally to an isomerized product or a polymer, but never dissociates to an isocyanate and ethyleneimine [225]. Kigane's concept that the

adhesion is dependent on reaction of polyester polymer chain ends and aziridine rings is fairly acceptable [235].

In 1958 a new aqueous double dip system was invented at CIL (Canadian Industries Limited) [236, 237]. The first dipping solution is coded TR-5, and consists essentially of a poly(vinylchloride) latex and a reactive polyamide. The TR-5 emulsion is nontoxic and its composition is as follows:

Geon 151 (PVC 50% emulsion).....	40.0
Versamide 125.....	5.0
Diethylphthalate.....	12.0
Catanac SP.....	4.0
Triton X-100.....	0.6
Acetic acid.....	0.3
Isopropanol.....	2.8
Water.....	60.0

Versamide 125 is a low molecular weight polyamine resin containing many free amino groups.

High speed emulsifying equipment and specialized techniques are required to prepare TR-5. Since recommended solid pickup of TR-5 is 0.5 percent concentration, the above concentrated TR-5 solution is diluted 7:1 with water just prior to use. The second dipping solution is RFL as commonly applied to rayon and nylon.

Adhesion depends on the heat treatment, especially after the first dipping, see figure 1.4.59. Relatively low temperature heat treatment, 150° C, after the second dipping gives satisfactory results [238]. This process was used in some commercial polyester tire production in Canada, but it did not find wide use. It is said that lack of wider acceptance was caused by the necessity of using special techniques in preparing a stable emulsion and by stiffness of the dipped cord [240].

The original use of polyepoxide for rubber to polyester bonding is found in patents secured by N. V. de Bataafsche Petroleum and Shell Development. Many other systems have been developed from these systems. They may be classified into three groups shown in the following schemes, see figures 1.4.60-1.4.62.

Group 1: The adhesive is composed of polyepoxide, hardener, and latex. This class is exemplified by using the TRL-12 system of Du Pont [69]. First dip composition is the following mixture:

Glycidylether of glycerin.....	12.5 g
Lauryl sulfate.....	0.5 g
Water.....	125 cc
Gentac, 41%.....	50 g

Second dip solution is prepared by mixing the following components:

Metaphenylenediamine.....	6.3 g
Water.....	138 cc
Gentac, 41%.....	195 g

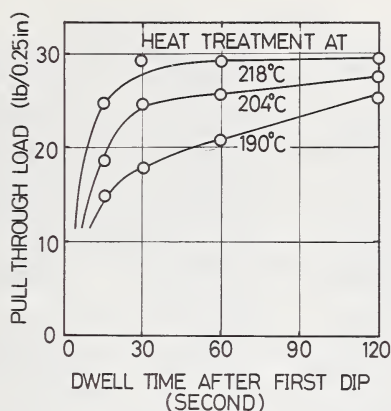


FIGURE 1.4.59. Effect of heat treatment condition after first dipping on adhesion.

polyester cord is immersed in the first dip solution and then heat treated at 232°C for 1.5 minutes. This treated cord is immersed in the second bath and heat treated at 232°C for 1.5 minutes again. While the cord treated only with the first dip shows relatively poor adhesion, 2 lb., the doubly dipped cord has strong adhesion, 10 lb. This double dip system is superior to the D-15 blocked isocyanate system for adhesion as shown in table 1.4.23. Drawbacks are lower adhesion at high temperature and difficulty of handling in subsequent processing because of stickiness of the dipped cord.

Group 2: All methods are double dip systems in which the first dipping solution is a mixture of polyepoxide and hardener, and the second is

GROUP 1

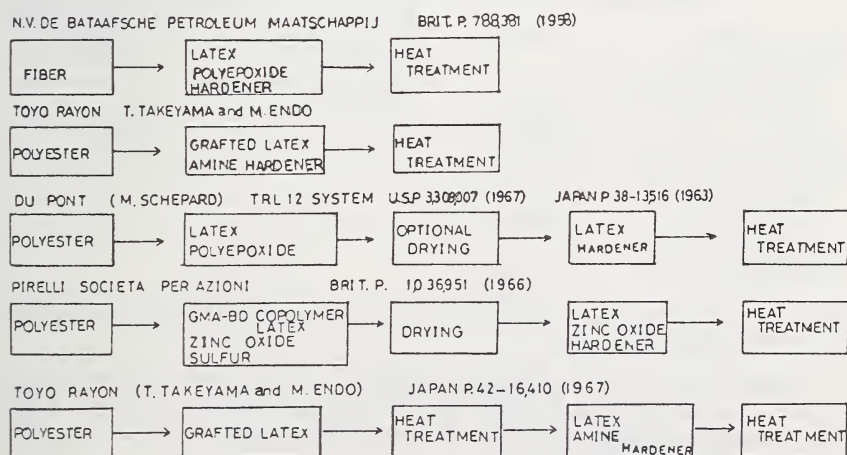


FIGURE 1.4.60. Flow sheet of dipping methods, Group 1 systems.

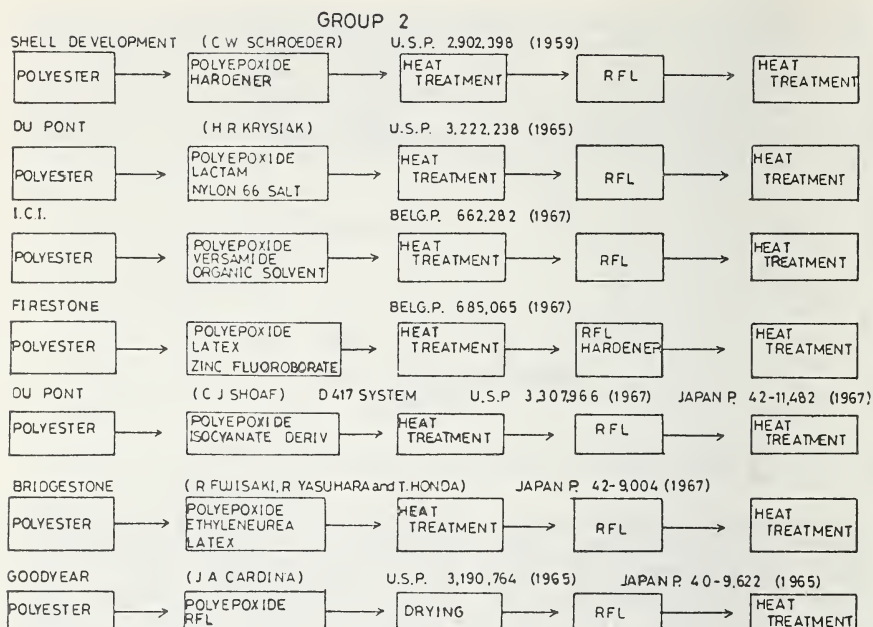


FIGURE 1.4.61. Flow sheet of dipping methods, Group 2 systems.

RFL. The D417 system of Du Pont containing isocyanate as hardener is a typical example of this class. The composition of each dipping solution is tabulated as follows [261]:

First bath		Second bath	
Triton X-100.....	0.4 cc	Resorcinol.....	73.7 g
Phenol blocked		Formalin, 37%.....	40.0
diphenyl methane		Vinyl pyridine latex,	
diisocyanate.....	16.0 g	41%.....	148
Water.....	400 cc	Water.....	480
Diethylaminoethyl			
methacrylate,			
0.5% aq. sol.....	25 cc		
Glycidylether of			
glycerine.....	4.8 cc		

Heat treatment after immersion in the first and second dip solutions was 218° C for 45 seconds.

A series of test was conducted varying the proportion of the polyepoxide and isocyanate from 0:100 to 100:0. Results are shown in figure 1.4.63. For comparison ethylenediamine was used as a hardener. The results are shown on the same graph.

GROUP 3

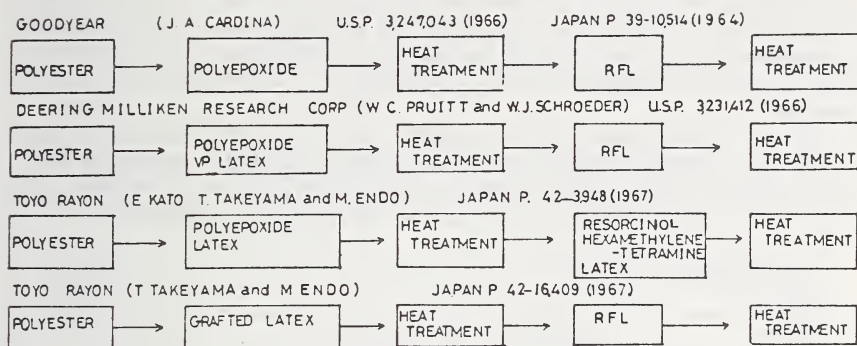


FIGURE 1.4.62. Flow sheet of dipping methods, Group 3 systems.

TABLE 1.4.23. Comparison of dip systems

Test method	Dip	TRL-12		Isocyanate	RFL
	Rubber	NR	SBR	SBR	SBR
Pull-through load, lb/0.25 in					
Cold		28.8	22.0	19.3	16.0
Hot		10.8	9.5	7.4	6.0
Strip force, lb		4.2	7.9	6.3	1.5

It is well known that proper combination of the isocyanate and polyepoxide increases the adhesion, and amine hardener is less effective under these experimental conditions.

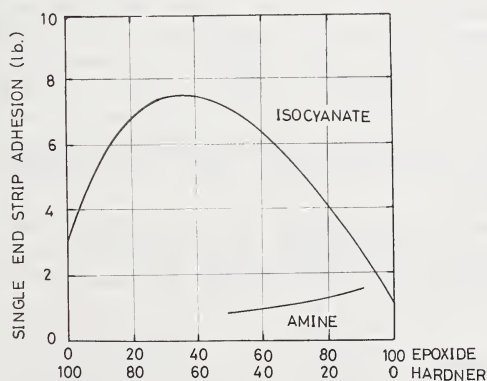


FIGURE 1.4.63. Effect of polyepoxide to hardener proportion on adhesion.

Although this system has many disadvantages such as requiring a double dip, necessity of a time consuming ball-milling process, settling out tendency of the dispersion, and lack of good dynamic performance at high temperatures required for use in tires [65], many tires have been built using this system, and it still provides a commercially available method.

Group 3: This class is also a double dip system. Polyepoxide is used in the first dipping solution without hardener, and the second is RFL. An example of this class is Deering Milliken's process. Polyester cord is passed through the first dip solution. The recipe is as follows:

Vinyl pyridine latex, 41%.....	125 g
Eponite 100 ^a	31.2
Petrowet.....	1.25
Water.....	312

^a Eponite 100 is diglycidyl ether of glycerine (Shell).

Wet pickup is adjusted to give 3.3 percent solid pickup by passing through a squeeze roll unit. The dipped cord is then passed into a heat treatment oven at 232° C for 96 seconds. The resulting tacky cord is immersed in an RFL bath and heat treated again at 230° C for 120 seconds with slight stretching. The second dipping solution is RFL which is prepared by maturing the following composition for 96 hours at room temperature:

Resorcinol.....	45 g
Formalin, 37%.....	22
Water.....	219
Isopropanol.....	5.8
Vinylpyridine latex, 41%.....	144
Sodium hydroxide, 10%	Optional amount to adjust pH to 9 to 9.3

The resulting cord is substantially free of stickiness and processes well. Adhesion of this doubly treated cord to rubber is excellent. Table 1.4.24 gives the adhesion obtained at each step of this process. In this method the adhesion depends upon the composition of the first dip solution and the heat treatment. The proper range of concentration of polyepoxide gives a high level of adhesion as shown in figure 1.4.64. Higher temperature treatment is preferable to give a high level of adhesion. This correlation is common to most methods utilizing the polyepoxide. The following results shown in figure 1.4.65 were obtained with Deering Milliken's method.

A similar correlation is found with the polyepoxide-Versamide/RFL double dip system of ICI ⁴ (Belg. 662,282) and with the D417 system, i.e., polyepoxide-isocyanate/RFL double dip system of Du Pont [261].

⁴ Imperial Chemical Industries.

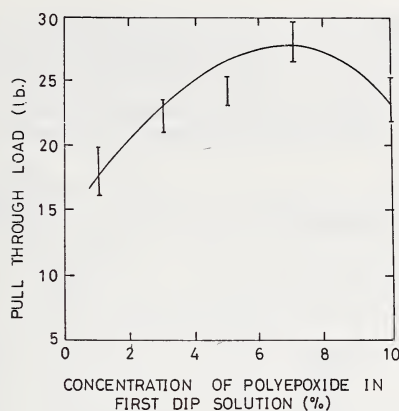


FIGURE 1.4.64. *Effect of concentration of polyepoxide in first dipping solution on adhesion.*

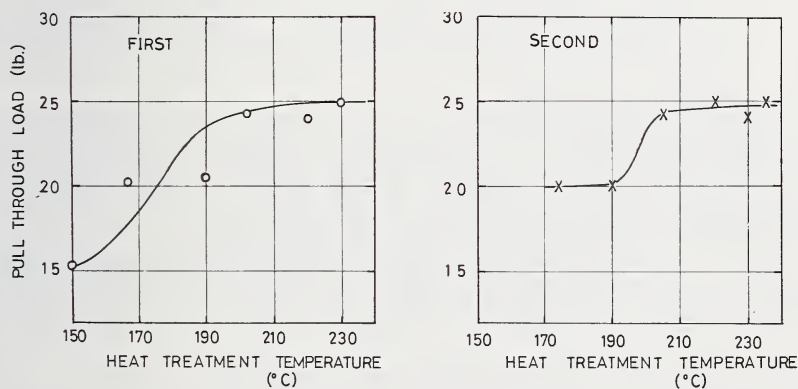


FIGURE 1.4.65. *Effect of heat treatment temperature on adhesion of Deering Milliken's system.*

TABLE 1.4.24. *Comparison of adhesion at each step of Deering Milliken's system*

Step	Pull-through load, lb
Untreated	0 to 4
Only first dipped	14 to 16
Only second dipped	10 to 12
Doubly dipped	27

TABLE 1.4.25. *Effect of heat treatment on polyester cord to rubber adhesion*

Polyepoxide-Versamide/RFL system			
First temp, °C	Time, sec Pull-through load, kg/6.35 mm		
	20	45	90
205°	7.12	7.53
234°	5.44	8.71	10.57
246°	7.85	9.53
260°	9.85	10.70	11.66

The most popular epoxide for this purpose is glycidyl ether of glycerine since it is easy to handle because of its water solubility. But it is necessary to have regard for the life of the dipping solution because the epoxide groups gradually undergo hydrolysis in an aqueous solution, and activity drops by half in a week [34].

Compositions of RFL used for the second dip solution are either the same for nylon and rayon or a special one for polyester. RF resin of lower formaldehyde content is found in several patents for this purpose although a lower formaldehyde RFL is inadequate for nylon and rayon. Examples of special recipes are shown in table 1.4.26.

Recently easy-to-adhere type polyester yarns have appeared in West Germany such as Trevira GPA [150], Diolen DSP [93] and V75 [149]. Cords or fabrics of this type polyester give a good rubber to textile ad-

TABLE 1.4.26. *Examples of RFL recipes for the second dip solution*

	A	B	C
Resorcinol/formaldehyde molar ratio	1/0.66	1/0.68	1/0.73
Latex solid/RF solid weight ratio	3.3/1	1.7/1	2.2/1
Resorcinol	48.4	10.3	10.0
Formalin, 37%	23.3	50.5	54
VP latex, 40%	505	646
SBR latex, 40%	445
Sodium hydroxide, 10%	6	Optional amount
Water	463	330	200
Source	Goodyear U.S. 3,247,043	Deering Milliken U.S. 3,231,412	Du Pont U.S. 3,307,966

hesion with the same RFL treatment as nylon or rayon. RFL treated Diolen DSP cable cord (1000D3/3) gives a pull-through load of over 20kg/cm., but the normal type only 10kg/cm. A comparison of two Diolen types using two vinylpyridine latexes for the RFL component, and two adherent rubber compounds is shown in table 1.4.27.

TABLE 1.4.27. *Comparison of two Diolen types* [93]

Type of Diolen	Pull-through load, kg/cm					
	DSP				Normal	
	A		B		A	
	Kind of VP latex		Kind of rubber		Kind of rubber	
	R	D	R	D	R	D
Heat treated at 175 °C	15	22	23	25	8	10
Heat treated at 195 °C	16	22	26	29	7	9

The manufacturing process for these modified polyesters is not disclosed. Deducing the method from patents of Glanzstoff-Fabriken [241], it is supposed that undrawn polyester fiber is treated with a spinning preparation which contains lubricant agents, polyepoxide, and amine hardener, then stretched and heat treated at the same time. Since existing dipping equipment can be employed for these polyesters, demand for them will grow if adhesion is satisfactory for tire cords.

This trend has been followed by fiber makers of the United Kingdom, Canada, and Japan. Little of Millhaven presented information at the Akron meeting in 1970 that T 790, an easy-to-adhere type of polyester, shows satisfactory adhesion even in tests at elevated temperatures. [274].

CIL has developed a new polyester to rubber adhesive system [65, 240-246]. It was called N3 and consisted of a reaction product of triallylcyanurate, resorcinol, and formaldehyde of the following composition.

Resorcinol.....	100 parts
Triallylcyanurate	24
Red lead catalyst.....	0.25
Formalin, 37%.....	28
Water.....	400
Ammonium hydroxide, 28%	28

N3 is available both for single dip and double dip processes. It is also applicable to nylon.

Resorcinol to formaldehyde ratio of the RFL used with N3 affects the adhesion of polyester to rubber, see table 1.4.28. For this adhesive system high heat treatment temperature is necessary. Typical conditions

TABLE 1.4.28. *Effect of RFL composition on adhesion with the N3-RFL single dip system*

	A	B	C
Gentac latex, 41%	53.0	29.2	58.5
SBR latex, 41%	7.3
Resorcinol	3.1	2.1	5.0
Formalin, 37%	4.9	3.4	2.8
Sodium hydroxide, 5%	5.7	3.7
Water	33.3	54.3	33.7
Pull-through load, lb/0.25 in Rubber compound			
A	15	17	23
B	22	22	^a 27
C	12	19	19

^a Rubber failure.

are drying at 104° C for 120 seconds and heat treatment at 254° C for 45 seconds. Addition of sodium carbonate or diethylenetriamine to the N3-RFL mixture results in better adhesion after less severe heat treatment. Bonding force also depends on adhesive pick-up and preferable pick-up is in a range of 5 to 7 percent on the weight of cord.

ICI has developed a new single dip adhesive system. The additive is called Pexul, formerly H7, and the dip solution is prepared by mixing Pexul with RFL of a special recipe. The composition of Pexul has not been disclosed, but it can be surmised to be 2,6-*bis*-(2,4'-dihydroxyphenyl-methyl)-4-chlorophenol from the patent literature [248]. The working mechanism may be sorption of Pexul into polyester.

There are several single dip adhesives which could be attributed to sorption to polyester other than N3 and Pexul. They are furfural modified resorcinol formaldehyde latex of AKU⁵ [247], alkylated resorcinol formaldehyde latex [278], and I-RFL of Toray [25].

1.4.2.5. Adhesive Treatment of Miscellaneous Tire Cords

Steel Wire Cord: A special method has been used to bond rubber to steel wire cord. A high level of adhesion can be obtained by vulcanizing the rubber compound in contact with brass or zinc plated steel cord. Most tire wire is plated at the wire mill, after drawing, by continuous electrolytic methods. Amount of brass and zinc on the wire is controlled in the ranges of 4 to 8 g/kg. and 2 to 3 g/kg., respectively. It is mentioned that the preferable brass composition is 70 percent copper and 30 percent zinc [249]. Choice of the type of plating is decided by the nature of the rubber compound. And it is said that adhesion is affected by ingredients of the rubber compound [250, 283-286].

Besides the plating method, addition of isocyanate or halogenated rubber adhesives to the rubber compound is also employed [113].

⁵ Algemene Kunstzijde Uni.

Glass Fiber: Glass fiber cord is pretreated with an adhesive prior to treating with RFL or rubber cement [87, 77]. The pretreatment is applied during the fiber forming process in combination with a variety of lubricants which give improved fiber properties, especially abrasion resistance, to glass fiber. Since unsaturated silanes such as vinylsilane are effective for bonding glass to rubber, the pretreatment agent may contain such a compound [251–252].

Polypropylene: Polypropylene to rubber bonding is one of the most difficult problems in this field. Several methods are patented. For example, polyepoxide/RFL double dip was claimed to be effective [253]. Adhesion of polypropylene for isocyanate rubber cement is improved by graft polymerization of vinylacetate, followed by hydrolysis [254]. It is mentioned that polypropylene to ethylene propylene rubber bonding is attained simply by vulcanization together if a peroxide curing system is used [255].

Vynylon: Vynylon is made bondable to rubber by the same treatments as for nylon or rayon. Since Vynylon has a very hydrophilic nature, easy penetration of RFL adhesive into the fiber interior causes stiffening of the dipped cord. Addition of water-repellent agents to RFL is used to reduce this tendency [256]. Also pretreatment of Vynylon by softeners, a type of surfactant, is effective for softening the dipped cord [257].

1.4.2.6. Evaluation of Adhesion

Adhesion has been evaluated by both tire tests and laboratory methods. In both cases, measurements of the bonding strength and observation of the failed state are important to judge the level of adhesion. And since adhesion falls gradually during tire operation, it is necessary to simulate a change of adhesion with running of the tire. To meet the requirements, static measurements, dynamic measurements, and combinations of them have been developed. However, there is no method of satisfactory evaluation on a laboratory scale.

Klein and co-workers [114] stated that stripping adhesion decreased with mileage, and the highest adhesion loss occurred in the region of maximum flexing (between 3.5 and 4 inches along the cord from the center of the tire), figure 1.4.66.

Kenyon [258] mentioned that deterioration of adhesion of rayon tires after running is greater than for nylon tires. Also, reduction of adhesion of Ply 1 to 2 is greater than that of Ply 3 to 4 on four-ply tires.

Eccher [117] investigated the failed state by microscopic observation of tire cross sections. He reported that damage was concentrated in the zone beneath the tire shoulder, and consisted of rubber tears and separation between cord and rubber.

Numerous methods have been proposed to estimate tire cord to rubber adhesion. They are briefly explained here.

Static Tests

Pull-through type tests; H, T, and U-tests: Adhesion is represented by the force required to pull an embedded cord through and out of a

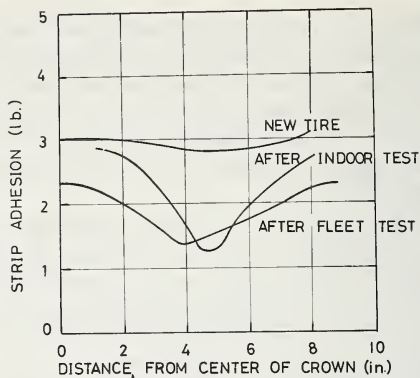


FIGURE 1.4.66. Deterioration of adhesion after fleet test and indoor wheel test.

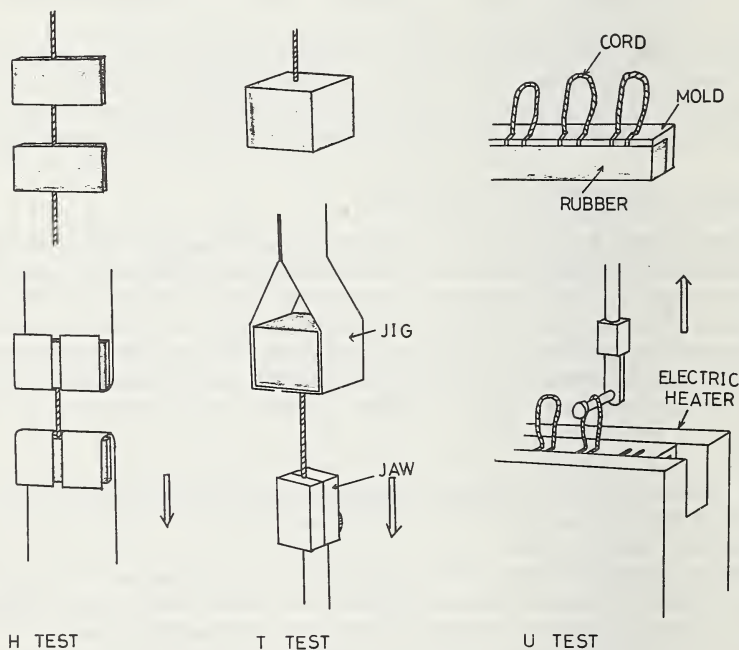


FIGURE 1.4.67. Test specimens and testing features of pull-through type test.

rubber block in the H-test, T-test, and U-test. The various test names come from the shapes of the test specimens, and are used only for convenience, see figure 1.4.67.

In these methods, the force is affected by embedded length of cord, rate of loading, and temperature [258–259]. Measurement is frequently at 110° to 130° C since temperature in a running tire may be this high.

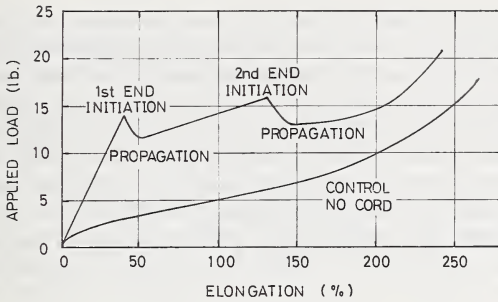


FIGURE 1.4.68. "I" test stress-strain curve compared with control sample with no cord [154].

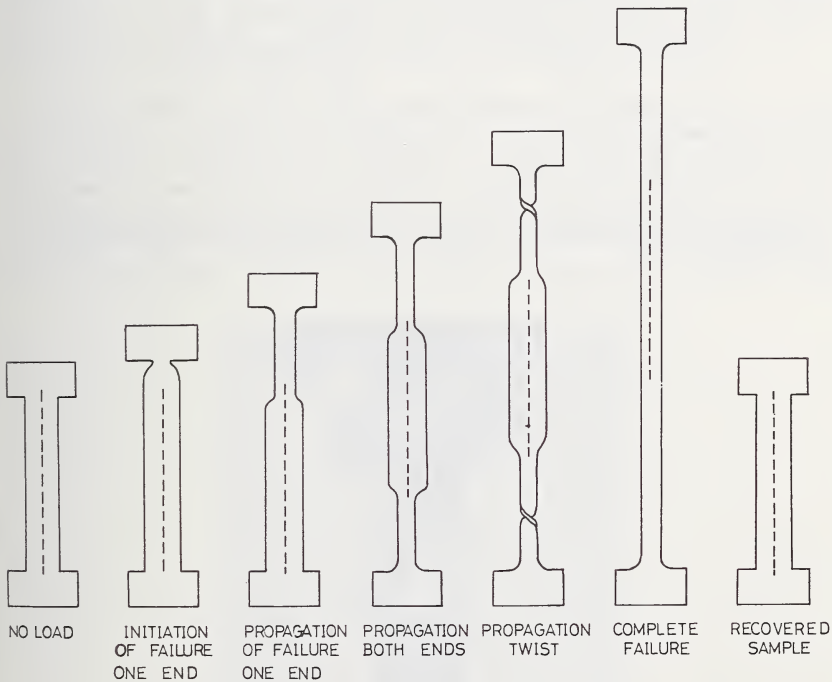


FIGURE 1.4.69. Distortion of "I" test specimen during load application [154]. Dotted line is the cord.

I-test: The I-test is made by pulling both ends of an I-shaped test specimen in which a sample cord is embedded as shown in figure 1.4.68. The cord is represented by a dotted line. The force-deflection curve is recorded. Adhesion is represented by the second peak force of figure 1.4.69. Distortion of the I-test specimen during loading is shown in figure 1.4.68 [154].

Pop-test: The pop-test is made by compressing a cylindrical rubber test specimen in which a sample cord is embedded in the middle as shown in figure 1.4.70. The test specimen is deformed on application of load, from shape A to B. When failure of adhesions occurs, appearance of the specimen changes to C or D. Adhesion is represented by the compression force required to deform the test specimen to the C or D stage [260].

Cord stripping test: A form of stripping cord adhesion test is practiced in Du Pont, the Single End Strip Adhesion (SESA) Test [261]. The force necessary to strip the cord from a rubber sheet is determined and is reported as pounds force per single end of cord. The test arrangement is shown in figure 1.4.71.

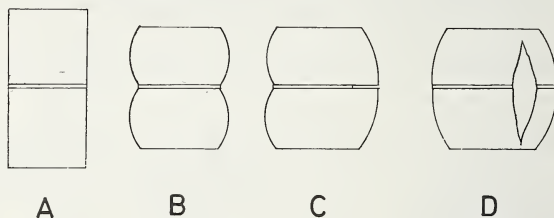


FIGURE 1.4.70. Deformation of Pop test specimen during load application [260].



FIGURE 1.4.71. Testing arrangement for Single End Strip Adhesion test.

Fabric stripping test: Adhesion of tire fabric and belting duck is evaluated by stripping a two-ply specimen which is a sandwich structure of rubber cover-test fabric-inner rubber-test fabric-rubber cover [262–263]. In evaluating tire fabric, high cord end counts are used to minimize rubber bridge formation. The force is also affected by thickness of the inner rubber and rate of loading [264]. This method has been adopted to estimate the level of adhesion in tire carcasses. Timmons [240] suggested that visual inspection of strips frequently correlated with the appearance of cords in tires after high speed tire testing. The testing arrangement is shown in figure 1.4.72.

Dynamic: Adhesion gradually deteriorates with repeated deformation. Dynamic evaluation of adhesion is made by counting cycles of deformation to reach a limiting value. Testing equipment is commonly designed to cut off when bonding force reaches a specific value. Type of deformation may be classified as: (1) compression, (2) shearing, (3) dynamic strip, and (4) flexing.

Compression type [265–266]: A test specimen is repeatedly compressed as illustrated in figure 1.4.73. The test cord is under tension by means of a weight. When the test specimen is compressed the rubber to cord interface is subjected to shear force. Adhesion deteriorates with compression cycles, and failure occurs when the bonding force becomes less than the weight suspended on the cord. The Goodrich Flexometer has been conveniently used for this purpose. Besides, the Goodrich Disk



FIGURE 1.4.72. Testing arrangement for two-ply strip test.

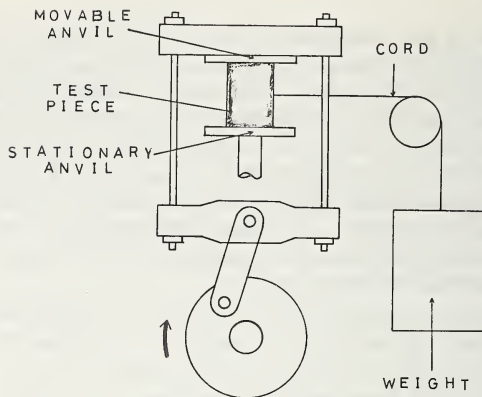


FIGURE 1.4.73. *Principle of Compression Adhesion Tester.*

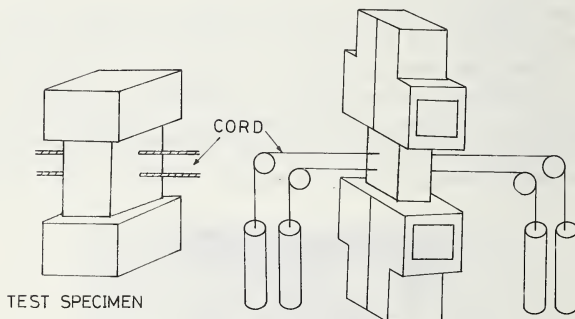


FIGURE 1.4.74. *Schematic drawing of Compression-Extension Type Tester and test specimen.*

Fatigue Tester is available, in which the specimen is subjected to both compression and extension [267]. Compression-extension deformation may be used with the equipment diagrammed in figure 1.4.74 [268]. A test cord is embedded in the middle of a dumbbell shaped test specimen. In these tests, failure occurs just inside the rubber where there is severe heat degradation. Therefore, it is said that these methods are inadequate to examine adhesion [195]. This method is available not only for cord but also for fabric [269-270].

Shearing type: Continuous vibration is applied to a rubber specimen as illustrated in figure 1.4.75. This is an example of this type testing equipment, the Dynamic Shear Adhesion (DSA) Tester. Adhesion is represented by cycles to failure of the cord-to-rubber bond and this is automatically recorded [204].

Dynamic strip type: In the case of tire fabrics or belting ducks, a two-ply strip testpiece is subjected to continuous vertical vibration under a certain weight. Adhesion is expressed by cycles required to strip a unit

length. This type of equipment has been on the market and called a Scott Tester, see diagram in figure 1.4.76.

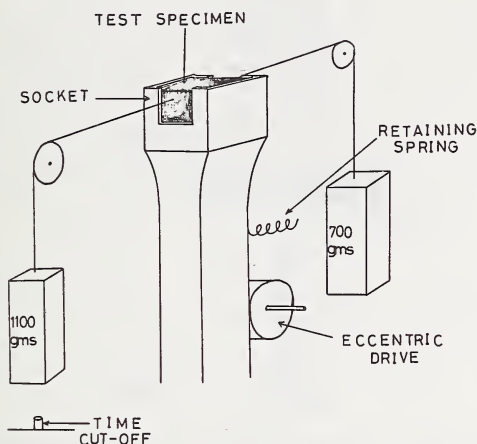


FIGURE 1.4.75. Schematic drawing of Dynamic Shear Adhesion Tester.

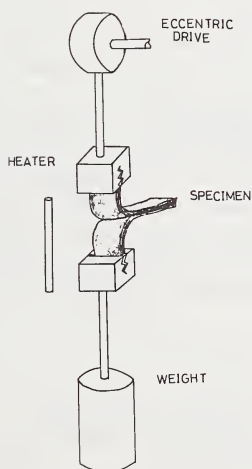


FIGURE 1.4.76. Schematic drawing of Dynamic Strip Adhesion Tester (Scott Tester).

Flexing type: Dipped cord to be evaluated is embedded in a cylindrical rubber specimen. Flexing is by deformation of the specimen between a stationary anvil and a plunger, see figure 1.4.77 [271]. Compression deformation can be given to the specimen at the same time by adjustment of the position of the stationary anvil. An alternative flex adhesion fatigue testing equipment was proposed. The test strap has a

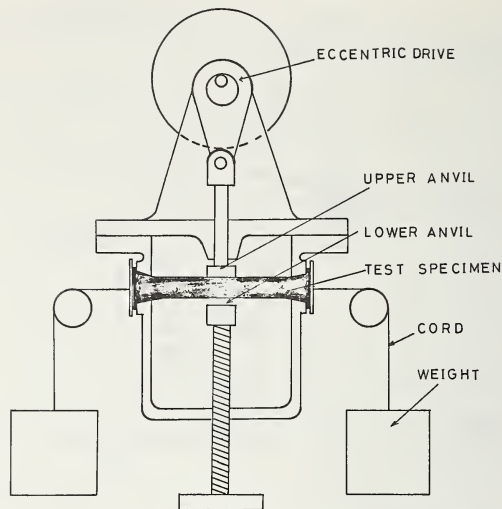


FIGURE 1.4.77. *Principle of Dynamic Flex Adhesion Tester.*

band of cords passing longitudinally through the middle. Affixed at one end to a stationary mounting, the strap passes horizontally from there to a pair of little rollers which are mounted in a reciprocating carriage. The strap follows a sigmoidal path around the rollers, and continues horizontally to its free end on which hangs a weight. Figure 1.4.78 gives a schematic view of the equipment. Adhesion is evaluated by a comparison of pull-through load before and after flexing [272].

In evaluating fabrics, the test specimen is built as a two-ply sandwich structure. Compressive fatigue is produced by flexing it over a spindle. The principle is illustrated in figure 1.4.79 [125, 209, 273]. Adhesion is estimated by either comparison of strip adhesion before and after flexing or cycles for ply separation [200].

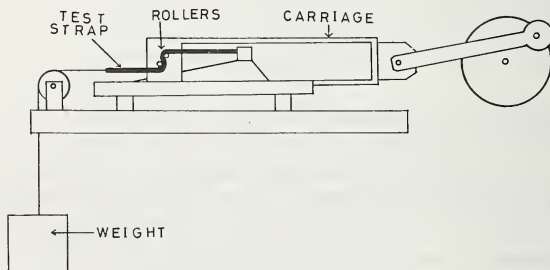


FIGURE 1.4.78. *Schematic side view of Roller Flex Adhesion Tester.*

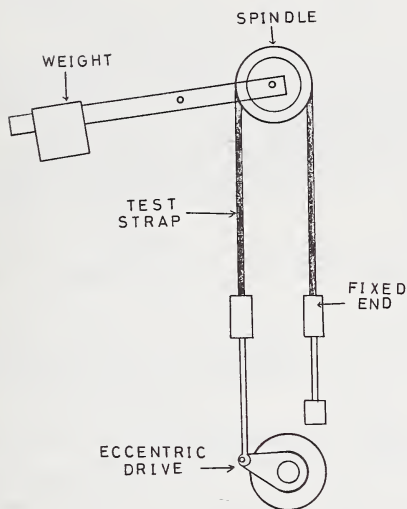


FIGURE 1.4.79. Schematic drawing of Belt Flex Type Dynamic Adhesion Tester.

References

- [1] Moncrief, R. W., *Man-Made Fibers*, p. 234 (John Wiley & Sons, New York, 1963).
- [2] Matsudaira, N., *Kaut. Gummi Kunstst.* **19**, 156 (1966).
- [3] Matsudaira, N., *J. Soc. Rubber Ind. Japan* **39**, 289 (1966).
- [4] Ewald, G. W., *Rubber Age* **98**(3), 57 (1966).
- [5] *Chem. Eng. News* **43**(37), 41 (1965).
- [6] *Chem. Week* **97**(24) (1965).
- [7] Ebert, A., *Kaut. Gummi Kunstst.* **18**, 372 (1965); *Rubber World* **152**(6), 98 (1965).
- [8] Curley, J. B., *Rubber World* **156**(6), 58 (1967).
- [9] Cox, N. L., U.S. Patent 2,536,014 (1950).
- [10] Röder, H. L., *J. Textile Inst.* **46**, p84 (1955).
- [11] Warzee, M., and Quintelier, G., *J. Textile Inst.* **46**, p123 (1955).
- [12] Howsman, J. A., and Sission, W. A., in *Cellulose and Cellulose Derivatives*, Part I, Ed. E. Ott, p. 254 (Interscience Publishers, New York, 1964).
- [13] Maeda, H., *J. Soc. Textile Cellulose Ind. Japan (Sen-i Gakkaishi)* **12**, 6 (1956); *Kobunshi (High Polymer, Japan)* **4**, 413 (1955); **7**, 261 (1958).
- [14] Sobue, H., and Fukuhara, S., *J. Chem. Soc. Japan, Ind. Chem. Section* **59**, 990 (1956); **60**, 323 (1957).
- [15] Mitsubishi, Y., and Maeda, H., *J. Soc. Textile Cellulose Ind. Japan (Sen-i Gakkaishi)* **18**, 1049 (1962).
- [16a] Recent Development in Tire Yarns, American Enka Corp., 1963.
- [16b] Fukuhara, S., *Kobunshi (High Polymer, Japan)* **17**, 7 (1968).
- [16c] Fukahara, S., *J. Soc. Rubber Ind. Japan* **40**, 39 (1967).
- [17] Mukoyama, E., *J. Textile Machinery Soc. Japan, Proc.* **20**, 706 (1967).
- [18] Chemstrand, Fr. 1,323,811 (1968); Belg. 615,991 (1962).
- [19] Du Pont, Brit. 811,349 (1959); Brit. 889,144 (1962).
- [20] Monsanto, Brit. 955,903 (1964).
- [21a] Toyo Rayon, Japan 42-25, 502 (1967).
- [21b] Toyo Rayon, Japan, 42-27, 572 (1967).

- [22] Hattori, H., *Kobunshi (High Polymer, Japan)* **11**, 481 (1962).
- [23] Hattori, H., *Kobunshi (High Polymer, Japan)* **12**, 615 (1963).
- [24] d'Albignac, J., *J. Soc. Dyers Colour.* **82**, 389 (1966).
- [25] Rochas, P., and Martin, J. C., *Bull. Inst. Textile France*, No. 83, 41 (1959).
- [26] For example, Sharkey, W. H., *J. Am. Chem. Soc.* **81**, 3000 (1959).
- [27] Howe, D. E., *Du Pont Tire Yarn Tech. Rev.*, p. 5 (1957); Patterson, R. G., McCrea, H. H., and Howe, D. E., *Rubber World* **138**, 409 (1958).
- [28] Howe, D. E., *Du Pont Tire Yarn Tech. Rev.*, p. 7 (1960).
- [29] Bolmeyer, J. W., *Du Pont Tire Yarn Tech. Rev.*, p. 5 (1958).
- [30] Litzler, C. A., Southern Rubber Group, Dallas, Texas (Feb. 22, 1963); *Rubber World* **148**(2), 68 (1963).
- [31] Toyo Rayon, *Toray Tire Cord News*, No. 3 (1966).
- [32] Toyo Rayon, *Toray Tire Cord News*, No. 4 (1967).
- [33] Firestone, *Brit.* 809,916 (1959); *Brit.* 822,809 (1959); U.S. 2,955,344 (1960); U.S. 2,955,345 (1960).
- [34] Toyo Rayon, unpublished data.
- [35] Goy, R. S., and Möring, P. L. E., *Trans. Inst. Rubber Ind.* **40**, 176 (1964); Goy, R. S., E. S., *Textile Inst. Ind.* **5**, 220 (1967); Goy, R. S., and Möring, P. L. E., *Rubber World* **152**(3), 67 (1965).
- [36] Pieper, E., *Kaut. Gummi Kunstst.* **16**, 18 (1963).
- [37] Reegen, S. L., and Sabo, J., *J. Appl. Polymer Sci.* **2**, 337 (1959).
- [38] Toyo Rayon, *Toray Tire Cord News*, No. 5 (1968).
- [39] Dismore, P. F., and Statton, W. O., *J. Polymer Sci.* **C13**, 133 (1966).
- [40] Kujimoto, K., and Fukuda, K., *Annual Meeting of the Society of Rubber Industry, Japan, Fukuoka, Japan, May 16, 1968*.
- [41] Hechert, D. H., *Du Pont Tire Yarn Tech. Rev.*, p. 14 (1959).
- [42] Mihell, W. G., *Du Pont Tire Yarn Tech. Rev.*, p. 37 (1958).
- [43] Howard, W. H., and Williams, M. L., *Rubber Chem. Tech.* **40**, 1139 (1967).
- [44] Tipetts, E. A., *Textile Research Institute, 36th Annual Meeting, New York, April 1, 1966*.
- [45] Rye, G. W., and Martin, J. E., *Rubber World* **149**(1), 75 (1963).
- [46] Papero, P. V., Winckhofer, R. C., and Oswald, H. J., *Rubber Chem. Tech.* **38**, 999 (1965).
- [47] Claxton, W. E., Forster, M. J., Robertson, J. J., and Thurman, G. R., *Textile Res. J.* **36**, 903 (1966).
- [48] Du Pont, *Brit.* 918,637 (1963); Japan 40-17,083 (1965).
- [49] Allied Chemical, *Belg.* 675,292 (1965); South Africa 918,637 (1963).
- [50] Monsanto, *Belg.* 665,541 (1965).
- [51] U.S. Rubber, *Brit.* 893,386 (1965).
- [52] Swanson, J. M., *Du Pont Tire Yarn Tech. Rev.*, p. 37 (1958).
- [53] Brownlee, J. L., and Perry, E., *Rubber Chem. Tech.* **40**, 1147 (1967).
- [54] Mukoyama, E., and Takeyama, T., *Kobunshi (High Polymer, Japan)* **17**, 14 (1968).
- [55] Cipriani, C., Papero, P. V., and Morre, M. S., *J. Appl. Polymer Sci.* **10**, 601 (1966).
- [56] *Chemiefasern* **16**, 421 (1966).
- [57] *Chem. Week* **98**(10), 35 (1966).
- [58] Du Pont, U.S. 3,220,456 (1965); Japan, p. 41-7889 (1966).
- [59] Du Pont U.S. 3,258,049 (1965).
- [60] *Chem. Eng. News* **43**(37), 41 (1965).
- [61] Firestone, U.S. 3,378,602 (1968).
- [62] Kovac, F. J., Rye, G. W., and Dague, M. F., *Ind. Eng. Chem. Prod. Res. Develop.* **2**, 279 (1963).
- [63] McCune, L. K., *Textile Res. J.* **32**, 762 (1962).
- [64] Sprague, B. S., and Singleton, R. W., *Textile Res. J.* **35**, 999 (1965).
- [65] Aitken, R. G., Griffith, R. L., Little, J. S., and McLellan, J. W., *Rubber World* **151**(5), 58 (1965).
- [66] Kovac, F. J., and Kersker, T. M., *Textile Res. J.* **34**, 69 (1964).
- [67] Kovac, F. J., and McMillen, C. R., *Rubber World* **152**(5), 83 (1965).
- [68] Ishizaki, S., *J. Textile Machinery Soc. Japan* **20**, 696 (1967).
- [69] Craig, R. A., *Du Pont Tire Yarn Tech. Rev.*, p. 21 (1960).
- [70] Du Pont, Japan 41-7892 (1966).
- [71] For example, Manabe, T., *J. Textile Machinery Soc. Japan* **8**, 685 (1955).

- [72] Kemnitz, G., *Kaut. Gummi* **12**, WT270 (1957).
- [73] Du Pont, Japan 37-5821 (1962).
- [74] Ravens, D. A. S., and Ward, I. M., *Trans. Faraday Soc.* **57**, 150 (1961).
- [75] Ravens, D. A. S., *Polymer* **1**, 375 (1960).
- [76] Marzocchi, A., and Gagnon, R. K., *Rubber World* **156**(5), 55 (1967).
- [77] Marzocchi, A., and Leary, D. E., *Am. Dyestuff Reporter* **54**, 870 (1965).
- [78] Marzocchi, A., and Rooney, M. J., *J. Polymer Sci.* **C19**, 227 (1967).
- [79] Wilson, J. B., *Rubber Plastics Age* **45**, 525 (1964).
- [80] Welch, F. G., *Rubber World* **156**(5), 60 (1967).
- [81] Ralph, F. W., *Rubber Age* **99**(9), 59 (1967).
- [82] *Rubber Age* **100**(2), 100 (1968).
- [83] *Rubber World* **154**(1), 34, 37 (1966).
- [84] *Rubber Age* **98**(4), 86 (1966).
- [85] Ryckebosch, F., *Trans. I.R.I.* **38**, 79 (1962).
- [86] Beckaert Steel Cord Technical Information.
- [87] Litzler, C. A., *Rubber World* **141**, 229 (1959).
- [88] Josifek, C. W., *Kaut. Gummi* **19**(3), 160 (1966).
- [89] Miles, D. C., *Rubber Plastic Age* **45**, 521 (1964).
- [90] *Chem. Eng. News* **42**(4), 21 (1964).
- [91] *Rubber Digest (Japan)* **17**(10), 146 (1965).
- [92] Schroeder, W. A., and Prettyman, I. B., *Rubber Age* **99**(1), 72 (1967).
- [93] Daimler, B. H., *Kaut. Gummi Kunstst.* **18**, 15 (1965).
- [94] Du Pont, Brit. 1,106,920 (1968).
- [95] Hall, I. H., *J. Appl. Polymer Sci.* **8**, 237 (1964).
- [96] Lothrop, E. W., *Appl. Polymer, Symp. No. 1*, 111 (1965).
- [97] Lothrop, E. W., *Appl. Polymer Symp. No. 5*, 53 (1967).
- [98] O'Neil, K. B., Dague, M. F., and Kimmel, J. E., *Appl. Polymer Symp. No. 5*, 41 (1967).
- [99] Lyons, W. J., *Textile Res. J.* **32**, 448 (1962); **32**, 553 (1962).
- [100] Prevorsk, D. C., and Lyons, W. J., *Textile Res. J.* **35**, 110 (1965); **35**, 217 (1965); Lyons, W. J., and Prevorsk, D. C., *Textile Res. J.* **35**, 1109 (1965); Lyons, W. J., and Ribnick, A. S., *Textile Res. J.* **37**, 1014 (1967).
- [101] Wilson, M. W., *Tappi* **43**, 129 (1960).
- [102] Lessig, E. T., U.S. 2,240,505 (1941); Busse, W. F., Lessig, E. T., Loughborough, D. L., and Larrick, L., *J. Appl. Phys.* **13**, 715 (1942).
- [103] Rosevear, W. E., and Waller, R. C., *Textile Res. J.* **19**, 633 (1949).
- [104] Lyons, W. J., *Textile Res. J.* **32**, 750 (1962).
- [105] Lessig, E. T., U.S. 2,291,086 (1942).
- [106] Budd, C. B., and Larrick, L., U.S. 2,488,761 (1949); Budd, C. B., *Textile Res. J.* **21**, 174 (1951).
- [107] Noshi, H., Murata, A., and Hirata, Y., *J. Textile Machinery Soc. Japan* **15**, 46 (1962).
- [108] (a) Fujino, K., Noshi, H., and Amau, M., *J. Textile Machinery Soc. Japan* **6**, 626 (1953); (b) Fujino, K., Noshi, H., and Yuse, M., *ibid.* **8**, 254 (1955); (c) *ibid.* **8**, 254 (1955); (d) Fujino, K., Noshi, H., and Shiomi, A., *ibid.* **9**, 164 (1956); (e) *ibid.* **9**, 334 (1956); (f) *ibid.* **9**, 378 (1956); (g) *ibid.* **10**, 689 (1957); (h) Fujino, K., Noshi, H., and Matsubayashi, F., *ibid.* **11**, 100 (1958).
- [109] Mitome, N., Manabe, T., and Tojima, T., *J. Textile Machinery Soc. Japan* **9**, 97 (1956); **9**, 248 (1956).
- [110] Frank, F., and Singleton, R. W., *Textile Res. J.* **34**, 11 (1964).
- [111] Prevorsk, D. C., and Lyons, W. J., *Textile Res. J.* **34**, 881 (1964); **34**, 1040 (1964).
- [112] Noshi, H., Fujimoto, H., and Yoshida, T., *J. Textile Machinery Soc. Japan* **14**, 256 (1961).
- [113] Williams, K. R., Hannell, J. W., and Swanson, J. M., *Ind. Eng. Chem.* **45**, 796 (1953).
- [114] Klein, W. G., Platt, M. M., and Hamburger, J. J., *Textile Res. J.* **32**, 393 (1962); *Tappi* **43**, 657 (1960).
- [115] Patterson, R. G., and Anderson, R. K., *Rubber Chem. Tech.* **38**, 832 (1965).
- [116] Patterson, R. G., *Rubber Chem. Tech.* **39**, 1382 (1966).
- [117] Eccher, S., *Kaut. Gummi Kunstst.* **19**, 299 (1966); **19**, 372 (1966).
- [118] Mieck, K.-P., and Lauchner, W., *Faserforsch. Textiltechn.* **16**, 16 (1965).
- [119] Miyamoto, S., Washimi, Y., and Fujimoto, N., *J. Soc. Rubber Ind. Japan* **38**, 48 (1965).

- [120] Miyamoto, S., Washimi, Y., Nagai, H., and Fujimoto, N., *J. Soc. Rubber Ind. Japan* **39**, 53 (1966).
- [121] Wood, J. O., and Redmond, G. B., *J. Textile Inst.* **56**, T191 (1965).
- [122] Dillon, J. H., Fatigue phenomena in high polymers, in *Advances in Colloid Science*, Vol. III, Ed. Mark, H., p. 219 (Interscience Publishers, New York, 1950).
- [123] Mallory, G. D., U.S., 241,524 (1946).
- [124] ASTM Standards, Part 24, Textile Materials, Method D885-64, Appendix, In-rubber fatigue determination of textile tire cords, p. 175 (American Society for Testing and Materials, Philadelphia, 1967).
- [125] Kenyon, D., *Proc. I.R.I.* **11**, 67 (1964).
- [126] Wilson, M. W., *Textile Res. J.* **21**, 47 (1954).
- [127] Noshi, H., and Shiroguchi, T., *J. Textile Machinery Soc. Japan* **16**, 828 (1963).
- [128] Mieck, K.-P., *Faserforsch. Textiltechn.* **10**, 578 (1959).
- [129] Kainradl, P., and Handler, F., *Faserforsch. Textiltechn.* **11**, 408 (1960).
- [130] Kern, W., *Kaut. Gummi* **8**, WT195; WT233 (1955).
- [131] Mieck, K.-P., *Plaste Kaut.* **7**, 344 (1960).
- [132] Kemmnitz, G., and Espanion, G., *Chemiefasern* **16**(3), 182 (1966).
- [133] Kemmnitz, G., *J. Appl. Polymer Sci.* **6**, 373 (1962).
- [134] Fujimoto, S., *J. Textile Machinery Soc. Japan* **18**, P57 (1965).
- [135] Borroff, E. M., and Wake, W. C., *Rubber Chem. Tech.* **23**, 500 (1950).
- [136] Wake, W. C., *Proc. I.R.I.* **1**, 176 (1954).
- [137] Wake, W. C., *Trans. I.R.I.* **35**, 159 (1959).
- [138] Du Pont, U.S. 3,314,847 (1967).
- [139] ICI Rubber Chemicals Literature, No. 31, Vulcabond TX for rubber to textile bonding.
- [140] Gatetovskaya, N. L., and Belyaeva, N. V., *Sov. Rubber Tech.* **24** (7), 26 (1965).
- [141] Meyrick, T. J., and Watts, J. T., *Proc. I.R.I.* **13**, 52 (1966).
- [142] Hodogaya Kagaku, Japan 32-8192 (1957).
- [143] Kaneko, T., Japan 30-1895 (1955); Japan 31-1692 (1956).
- [144] For example, Gardner, E. R., and Williams, P. L., *Rubber Chem. Tech.* **23**, 698 (1950).
- [145] Du Pont, U.S. 2,128,229 (1938).
- [146] Du Pont, U.S. 2,211,959 (1940).
- [147] Du Pont, U.S. 2,211,948 (1940).
- [148] For example, Thoman, R., and Gilman, H., *Trans. I.R.I.* **25**, 105 (1949).
- [149] Daimler, B., *Kaut. Gummi Kunstst.* **20**(3), 159 (1967).
- [150] *The Daily News Record*, Aug. 17, 1965.
- [151] Tsuji, T., and Torigoe, M., *Setchaku (Adhesion and Adhesives, Japan)* **8**, 847 (1964).
- [152] Wilson, M. W., *Tappi* **43**(2), 129 (1960).
- [153] Patterson, H., *Adhesive Age* **6**(9), 38 (1963).
- [154] Miller, A. L., and Robison, S. B., *Rubber World* **137**, 397 (1957).
- [155] Moul, H., in *Handbook of Adhesives*, Ed., Skeist, I., p. 495 (Reinhold Publishing Corp., New York, 1962).
- [156] Greth, A., *Angew. Chem.* **51**, 719 (1938).
- [157] Rawe, A., and Fitko, C., *J. Polymer Sci. A-1* **4**, 2533 (1966).
- [158] Basin, V. E., Berlin, A. A., and Uzina, R. V., *Sov. Rubber Tech.* **21**(9), 12 (1962).
- [159] Dietrick, M. I., *Rubber World* **136**, 847 (1957).
- [160] Boguslavskii, D. B., et al, *Sov. Rubber Tech.* **21**(12), 15 (1962).
- [161] Hultzsch, K., *Kunstst.* **37**, 43 (1947).
- [162] van der Meer, S., *Rubber Chem. Tech.* **18**, 853 (1945).
- [163] For example, *Farbenfabriken Bayer*, Japan 31-2961 (1956).
- [164] *Chem. Eng. News* **46**(18), 40 (1968).
- [165] U.S. Rubber, Japan 42-19923 (1967); U.S. 3,364,100 (1968).
- [166] U.S. Rubber, Japan 42-19924 (1967).
- [167] Dunlop Rubber, Japan 42-23081 (1967).
- [168] *Farbenfabriken Bayer brochure*, Bonding agent 7110, 1967.
- [169] Continental Gummi, German 1,228,799 (1966).
- [170] Foster, R., Hammick, D. L., and Parsons, B. N., *J. Chem. Soc.* **1956**, 555.
- [171] U.S. Rubber, Japan 40-28938 (1965).
- [172] U.S. Rubber, Japan 41-12743 (1966).
- [173] Goodyear Tire and Rubber, Belg. 675,166 (1966); Belg. 675,202 (1966).

- [174] General Tire brochure, Gentac.
- [175] Wake, W. C., in *Adhesion and Adhesives*, Vol. 2, 2nd ed., Eds. Houwink, R., and Salomon, G., p. 418 (Elsevier Publishing Co., New York, 1967).
- [176] Doyle, G. M., *Trans. I.R.I.* **36**, 177 (1960).
- [177] Dubrisay, R., and Papault, R., *Compt. Rend.* **215**, 348 (1942).
- [178] Le Bras, J., and Piccini, I., *Ind. Eng. Chem.* **43**, 381 (1951).
- [179] Uzina, R. V., et al., *Sov. Rubber Tech.* **20**(7), 18 (1961).
- [180] Levitin, I. A., et al., *Sov. Rubber Tech.* **21**(1), 41 (1962).
- [181] Stedry, P. J., *Ind. Eng. Chem.* **43**, 2372 (1951).
- [182] van Giles, G. E., *Polymer Preprints* **8**(1), 508 (1967).
- [183] Du Pont, *Brit.* 1,106,920 (1968).
- [184] Esso, *Brit.* 803,182 (1958); *Brit.* 823,282 (1959); *Brit.* 861,814 (1961).
- [185] Burlington, U.S. 3,240,659 (1966).
- [186] Burlington, U.S. 3,240,649 (1966).
- [187] Stamicarbon, Belg. 680,492 (1966).
- [188] Dunlop Rubber, U.S. 3,268,386 (1966).
- [189] Du Pont, U.S. 3,276,948 (1966).
- [190] Farbwerke Hoechst, Japan 42-17642 (1967).
- [191] Montecatini, Japan 42-23632 (1967); *Brit.* 1,071,528 (1967).
- [192] Reeves, L. W., *Rubber World* **132**, 764 (1955).
- [193] Reeves, E. V., *Adhesive Age* **6**(3), 28 (1963).
- [194] Hannel, J. W., *Du Pont Tire Yarn Tech. Rev.*, p. 27 (1958).
- [195] James, D. I., Wake, W. C., *Trans. I.R.I.* **39**, 103 (1963).
- [196] FMC Corporation, Japan 42-6668 (1967).
- [197] Murphy, R. T., Baker, L. M., and Reinhardt, Jr., R., *Ind. Eng. Chem.* **40**, 2292 (1948).
- [198] Gillman, H., and Thoman, R., *Ind. Eng. Chem.* **40**, 1237 (1948).
- [199] Turner, J., Cohen, N., and Janow, S., *Rubber World* **153**(3), 67 (1965).
- [200] Kigane, K., *Teijin Times* **38**(2), 36 (1968).
- [201] Nippon Rayon, Japan 42-15765 (1965).
- [202] Nippon Rayon, Japan 41-12228 (1966).
- [203] Maizels, M. G., and Raevskii, V. G., *Sov. Rubber Tech.* **19**(6), 16 (1960).
- [204] Iyengar, Y., *Rubber World* **148**(6), 39 (1963).
- [205] Garetovskaya, N. L., and Belyaeva, N. V., *Sov. Rubber Tech.* **24**(7), 20 (1965).
- [206] Ludewig, H., *Polyesterfasern, Chemie und Technologie*, Chap. 11 (Akademie-Verlag, Berlin, 1965).
- [207] RABRM, *Brit.* 804,005 (1958).
- [208] Zahn, H., and Pfeifer, H., *Polymer* **4**, 429 (1963).
- [209] N. V. Onderzoecking Inst. Res., Japan 40-1713 (1965); Belg. 612,198 (1962).
- [210] Leibnitz, E., Könnecke, H., Gawalek, G., *J. Prakt. Chem.* **6**, 289 (1958).
- [211] ICI, Belg. 663,578 (1966).
- [212] ICI, Japan 35-13125 (1960); *Brit.* 816,640 (1959).
- [213] For example, Shkapenko, G., Gmitter, G., Gruber, E., *Ind. Eng. Chem.* **52**, 605 (1960).
- [214] Farbwerke Hoechst, Japan 41-12109 (1966).
- [215] Bayer, O., *Angew. Chem.* **A59**(9), 257 (1947).
- [216] Tanabe, T., et al., *Kogyo Kagaku Zasshi (J. Chem. Soc., Japan, Ind. Chem. Sec.)* **66**, 821 (1963).
- [217] Farbwerke Hoechst, Belg. 656,656 (1965); Belg. 672,260 (1966).
- [218] Yokohama Rubber, Japan 42-784 (1967).
- [219] Thompson, W. L., and Parke, L. W., *Rubber World* **138**, 588 (1958).
- [220] Du Pont, U.S. 2,994,671 (1961).
- [221] Du Pont, *Instruction Manual for D-15*, 1957.
- [222] Teijin, Japan 38-13236 (1963).
- [223] Goodyear Tire and Rubber, Japan 40-21429 (1965); U.S. 3,268,467 (1968); Japan 40-10723 (1965); U.S. 3,226,276 (1966).
- [224] Toyo Rayon, Japan 38-20961 (1963).
- [225] Iwakura, Y., Nabeya, A., and Nishiguchi, T., *Yuki Gosei Kagaku Kyokai Shi (J. Soc. Organic Synthetic Chem. Japan)* **26**, 101 (1968).
- [226] Iwakura, Y., in *Setchaku, High Polymer Series 1*, p. 185 (High Polymer Soc. Japan ed., Maruzen, 1965).

- [227] Toyo Rubber, Japan 42-2896 (1967).
- [228] Toyo Rayon, Japan 42-2275 (1967); Japan 40-26548 (1965).
- [229] Teijin, Japan 37-3123 (1962); Japan 37-3124 (1962).
- [230] Toyo Spinning, Japan 42-543 (1967).
- [231] Takeda Pharmacy, Japan 42-8221 (1967); Japan 42-541 (1967); Japan 42-860 (1967).
- [232] Teijin, Japan 39-10513 (1964); Japan 40-28937 (1965); Japan 41-5260 (1966); Brit. 953,415 (1964), U.S. 3,235,333 (1967); I.C.I. Belg. 674,529 (1966).
- [233] Teijin, Japan 40-922 (1967).
- [234] Mitsuboshi Belt, Japan 40-16135 (1965).
- [235] Kigane, K., Japan 38-20956 (1963).
- [236] Little, J. S., Can. Textile J. **78**(19), 57 (1961).
- [237] Canadian Industries Ltd., Japan 36-5740 (1960); U.S. 3,051,594 (1962); Brit. 867,187 (1961); German 1,259,093 (1968).
- [238] Chapman, R., Rubber Plastic Age **47**, 769 (1966).
- [239] ICI, Manual for Pexul, The use of pexul for bonding terylene to rubber, 1967.
- [240] Timmons, W. D., Adhesive Age **10**(10), 27 (1967).
- [240a] Law, C., Rubber World, **158**(4), 43 (1968).
- [241] Vereingte Glanzstoff-Fabriken, Brit. 1,025,310 (1966); U.S. 3,297,467 (1967); Brit. 1,035,299 (1916); Japan 42-19921 (1967); Brit. 1,025,309 (1966); U.S. 3,297,468 (1967); Brit. 1,035,220 (1966); Japan 42-19922 (1967); Brit. 1,012,935 (1966); Brit. 1,026,221 (1966).
- [242] Canadian Industries Ltd., U.S. 3,318,750 (1967).
- [243] ICI, Belg. 674,528 (1966).
- [244] Smolin, E., and Rapoport, L., The Chemistry of Heterocyclic Compounds, S-Triazines and Derivatives, p. 400 (Interscience Publishers, New York, 1955).
- [245] Clampitt, B. H., German, D. E., and Galli, J. R., J. Polymer Sci. **27**, 515 (1958).
- [246] Saunders, J. H., and Frish, K. C., Polyurethanes Chemistry and Technology, Part 1, p. 116 (Interscience Publishers, New York, 1962).
- [247] Algemene Kunstzijde Uni, Fr. 1,481,392 (1967); Belg. 682,153 (1966).
- [248] ICI, Belg. 688,424 (1967); Fr. 1,496,951 (1967); Neth. 6,614,669 (1967); Belg. 688,425 (1967).
- [249] Wake, W. C., Reference [175], p. 413.
- [250] For example, Hicks, E., and Lyon, F., Rubber Chem. Tech. **40**, 1607 (1967).
- [251] Vanderbilt, B. M., and Clayton, R. E., Rubber Chem. Tech. **38**, 379 (1965).
- [252] Esso, U.S. 3,307,967 (1967).
- [253] Toyo Rayon, Japan 42-3947 (1967).
- [254] Toyo Rayon, Japan 42-542 (1967).
- [255] Montecatini, Japan 42-26830 (1967).
- [256] Kurashiki Rayon, Japan 36-7742 (1961); Japan 37-12119 (1962).
- [257] Mitsuboshi Belt, Japan 36-7742 (1961).
- [258] Kenyon, D., Trans. I.R.I. **38**, 165 (1962).
- [259] Wood, J. O., Rubber Chem. Tech. **40**, 1014 (1967).
- [260] Lessig, E. T., and Compton, J., Rubber Chem. Tech. **19**, 223 (1946).
- [261] Du Pont, U.S. 3,307,966 (1967).
- [262] JIS K-6301-1962, Physical Testing Methods for Vulcanized Rubber.
- [263] ISO Recommendation R36, Rubber Chem. Tech. **31**(1), xxi (1958).
- [264] Barroff, E. M., Elliot, R., and Wake, W. C., Rubber Chem. Tech. **25**, 391 (1952).
- [265] Uzina, R. V., Gromova, L. S., Rubber Chem. Tech. **32**, 898 (1959).
- [266] Gardner, E., and Williams, P., Trans. I.R.I. **24**, 284 (1949).
- [267] Kenyon, D., Trans. I.R.I. **40**, 67 (1964).
- [268] Khromov, M. K., Reznikovskii, M. M., and Lazareva, N. K., Sov. Rubber Tech. **21**(6), 25 (1962).
- [269] Levitin, I. A., Korablev, Yu. G., Kornev, A. E., and Babitskii, B. L., Rubber Chem. Tech. **32**, 889 (1959).
- [270] Tsydik, M. A., Lukomskaya, A. I., and Slonimskii, G. L., Rubber Chem. Tech. **33**, 42 (1960).
- [271] Pittman, G. A., and Thornly, E. R., Trans. I.R.I. **25**, 116 (1949).
- [272] Lyons, W. J., Anal. Chem. **23**, 1255 (1951).
- [273] ASTM Standards, Part 28, Rubber; Carbon Black; Gaskets, Method D430-59. Dynamic testing for ply separation and cracking of rubber products, p. 233 (American Society for Testing and Materials, Philadelphia, 1968).

- [274] Little, J. S., Akron Rubber Group Symp., Akron, Ohio (Jan. 23, 1970).
- [275] Kawai, K., Akron Rubber Group Symp., Akron, Ohio (Jan. 23, 1970).
- [276] Hannell, J. W., Akron Rubber Group Symp., Akron, Ohio (Jan. 23, 1970).
- [277] Litzler, C. A., Akron Rubber Group Symp., Akron, Ohio (Jan. 23, 1970).
- [278] Iyengar, Y., Erickson, D. E., J. Appl. Polymer Sci. **11**, 2311 (1967).
- [279] Creasey, J. R., and Wagner, M. P., Rubber Age **100**(10), 72 (1968).
- [280] Creasey, J. R., Russel, D. B., and Wagner, M. P., Rubber Chem. Tech. **41**(5), 1300 (1968).
- [281] Rawe, A., and Fitko, C., J. Polymer Sci. A1 **4**, 2533 (1966).
- [282] Iyengar, Y., J. Appl. Polymer Sci. **13**, 353 (1969).
- [283] Adler, O. E., Adhesive Age **12**(1), 30 (1969).
- [284] Hicks, A. E., and Lyon, E., Adhesive Age **12**(5), 21 (1969).
- [285] Sexsmith, F. H., Adhesive Age **13**(5), 21 (1970).
- [286] Sexsmith, F. H., Adhesive Age **13**(6), 31 (1970).



CHAPTER 2

Properties of Cord-Rubber Laminates

Samuel K. Clark ¹

	Page
2.1. Elastic Properties of Cord Reinforced Rubber.....	308
2.2. Strength and Failure Mechanisms for Cord Reinforced Rubber.....	341
References.....	351

¹ Department of Engineering Mechanics, University of Michigan, Ann Arbor, Michigan 48104.

2.1. Elastic Properties of Cord Reinforced Rubber

The increased use of more sophisticated structural configurations in pneumatic tires during the last few years has resulted in a greater interest in the elastic properties of cord-rubber laminates. Much of the reason for this may be found by considering the basic nature of redundant structures, in which the loads carried by individual cords are in part determined by the elastic characteristics of the entire system. In such situations, a knowledge of elastic characteristics becomes important to good structural design practice. As a second reason for increased attention to the elastic properties of such materials, one might cite the body of work which is now developing in the general area of filamentary reinforcement of materials. A knowledge of elastic characteristics is important in obtaining optimum reinforcement properties, and such studies inevitably lead to a clearer understanding of the internal stress states of all reinforced materials. One result of this research is that much of the work done in the areas of fiberglass and whisker reinforcement has increased the general understanding, in a broad way, of the action of cord reinforced rubber. The main aspects of the problems are similar, although major differences exist in the structure of the reinforcement itself and in the fact that in many reinforced elastomers the cords are anchored to some relatively rigid structural member.

The elastic properties of cord-rubber materials are understood today much better than they were even 10 or 15 years ago. General reviews which describe various aspects of current knowledge have been published by Hashin [1],² Hofferberth and Frank [2], and by Clark [3].

Historically, the role of material properties in pneumatic tire design and analysis has been approached in three distinct ways:

a. First, the anisotropic nature of such materials may be completely ignored, and all tire structures treated as membranes whose stresses are determined entirely from membrane equilibrium considerations. This is a statically determinate shell approach, and in some regions tire stresses, and cord loads, may be found rather accurately by this technique when loadings are simple, such as in the case of inflation of a tire. However, proper elastic properties are necessary for adequate stress determinations near edges or boundaries in all shell problems, and in the case of a pneumatic tire it is necessary to know the material characteristics in order to find stresses near the bead and in the sidewall.

In more complex loadings where bending is an important factor, such as in deflecting a tire against a flat surface, the elastic properties of the material are needed for estimation of cord loads, and an isotropic approximation is not adequate.

Quite apart from stress analysis problems, which are always governed by force and moment equilibrium and hence can sometimes be less

² Figures in brackets indicate the literature references at the end of this chapter.

dependent on material properties, all deformation characteristics of cord-rubber structures are entirely determined by their elastic constants so that an isotropic approximation might be characterized as a very crude one in most cases.

b. An interesting and unique attempt to calculate cord loads in a cord-rubber structure has been provided by Rivlin and his co-workers [4-6] and by Adkins [7-11]. They both utilize the concept of an inextensible net made up of the reinforcing textile cords in a normal cord-rubber structure, with the assumption that in such a net the cross-over points between cords in adjacent lamina act as knots which do not slip. This analysis has much to recommend it. Basically, in most situations, the reinforcing textile cords do indeed carry a major share of the tire structural loads. Thus neglect of the surrounding rubber matrix is not generally serious, although situations exist when the surrounding rubber can contribute substantially to the load carrying ability of the composite, as has recently been discussed by Clark and Dodge [12]. The mathematics of such cord networks is interesting, and represents a fertile field for the applied mathematician. Its most important contribution is undoubtedly as a stress analysis tool, where many solutions are now known. However, it has not been possible to use it to obtain the elastic constants of cord-rubber composites since the absence of the rubber characteristic results in a completely rigid structure.

c. A third and somewhat later general approach to the elastic properties of cord-rubber laminates utilizes the overall elastic stiffnesses of both the cords and rubber treated as a two-dimensional orthotropic material. This requires that the concentrated cords and distributed rubber be viewed over dimensions much greater than the cord spacing, so that the average elastic modulus of a single lamina may be obtained, as opposed to the local or microscopic modulus which varies widely with position. The primary reason for this is that it is difficult to mathematically describe the large variations which exist in elastic stiffness of a cord-rubber laminate. It is much more convenient to work with an average property.

Basically a single ply or lamina of cord-rubber material may first be considered in terms of its constituent properties. These are discussed in detail elsewhere in this volume, but it is worthwhile to review the fact that for large deformations both the cord and rubber properties are highly nonlinear as well as visco-elastic. For example, quasi-static force extension curves for a typical rubber are given in figure 2.1 for large extension ratios, while for small strains in rubber the force extension characteristic is essentially linear as shown in figure 2.2. Stress-strain curves for typical tire cord materials are given in figure 2.3. From these, it might be concluded that a nonlinear theory would be necessary to completely describe the action of combined cord in rubber, and this is undoubtedly true for large strain. For small strains, which fortunately are the primary condition in tire usage, material characteristics are much more linear. This is illustrated in figure 2.4, where a stress-strain curve for rayon cords

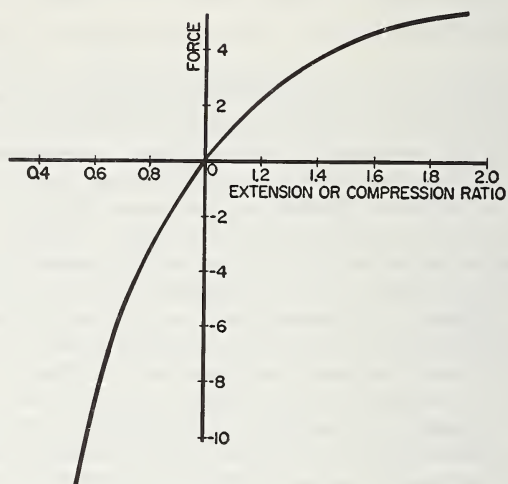


FIGURE 2.1. *Force-extension ratio for a typical rubber.*

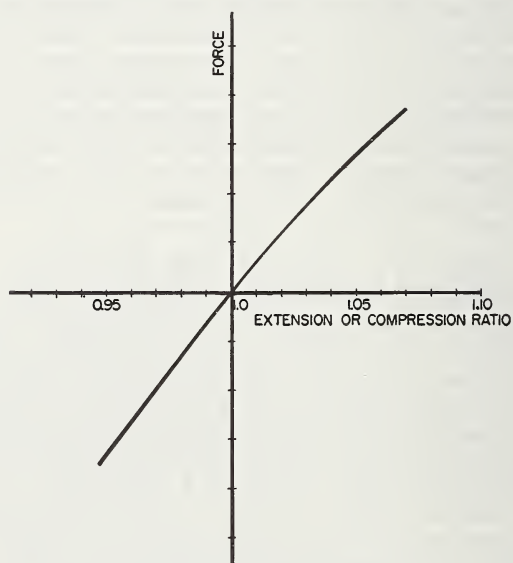
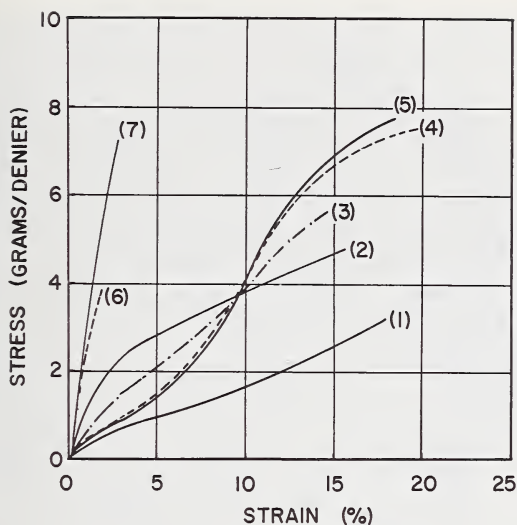


FIGURE 2.2. *Region near origin of force-extension ratio curve for rubber.*



- | | |
|---------------|--------------|
| (1) RAYON | (5) NYLON-66 |
| (2) NOMEX | (6) STEEL |
| (3) POLYESTER | (7) GLASS |
| (4) NYLON-6 | |

TESTED AT 70°F., 65% R.H.

INSTRON - 100% STRAIN RATE

Courtesy of FABRIC RESEARCH LABORATORIES, INC.

FIGURE 2.3. *Stress-strain characteristics of typical tire cords.*

imbedded in rubber is given, where here the direction of tensile stress is parallel to that of the cords. Aside from the soft stretch portion at very low loads, the cord action may be approximated by considering the stress-strain curve to be linear. One might thus hope to treat cord-rubber laminates as linearly elastic materials.

Before attempting to examine the elastic properties of laminates made up of a number of plies of cord-rubber sheets, it is first necessary to review the basic characteristics of a single layer of such material. It is common to align a parallel series of evenly spaced textile cords, and to calender these with unvulcanized rubber, in such a way as to form a single layer of cord reinforced material as illustrated in figure 2.5a. This figure shows each of the reinforcing cords as a circle, although in actuality the cord is somewhat irregular in shape. It is made up of a multiplicity of filaments twisted into singles yarns (strands) and two or three of these are then twisted in the opposite direction, for balance, to form the cord.

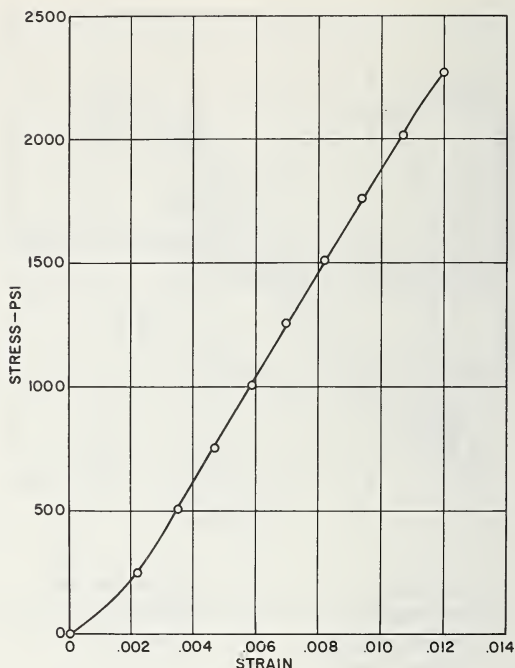


FIGURE 2.4. *Stress-strain curve in tension of rayon cords embedded in rubber, where stress is based on total cross-section area of specimen.*

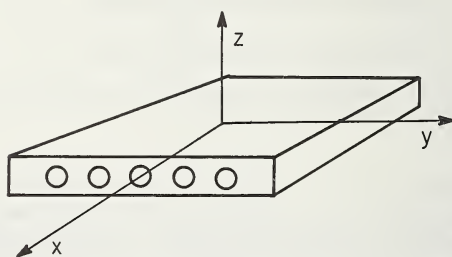


FIGURE 2.5a. *End view of a series of parallel textile cords embedded in rubber.*

Prior to calendering with rubber, the cords are usually passed through a dip which promotes adhesion to the rubber. One may visualize each of the reinforcing cords as a complex twisted structure made of many monofilaments having this irregular cross section shape, and being imbedded in rubber which encases the cords completely in order to prevent mechanical chafing of one cord against another. This is shown in the photograph of figure 2.5b. Due to the complexity of such a structure, the prediction of the elastic characteristics of such a single lamina is in itself a difficult job. Fortunately, the cord diameter and spacing are almost always small compared with typical dimensions of a pneumatic tire, so

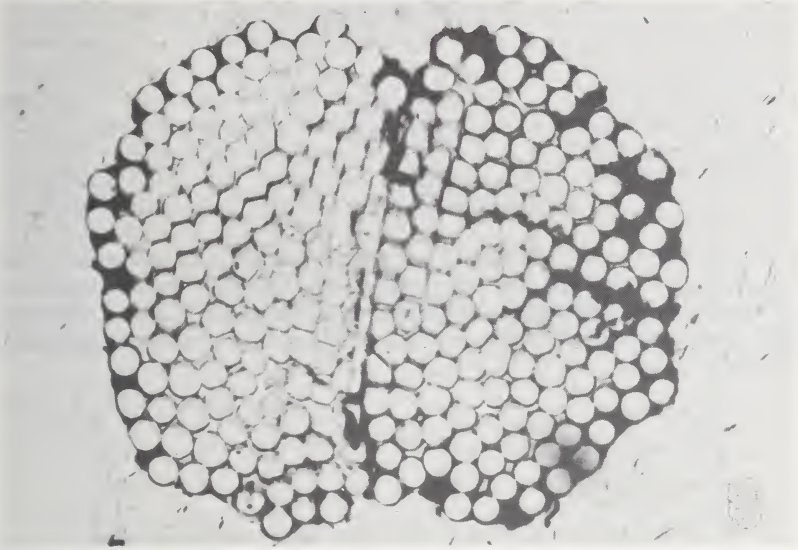


FIGURE 2.5b. *End view of a single textile cord.*

that the average elastic properties will suffice in many structural applications.

Such a sheet as shown in figure 2.5a may be further idealized considering it to be essentially a two-dimensional orthotropic body, where the properties through the thickness are taken to be isotropic. This simplifies discussion of the elastic properties considerably, and is not particularly restrictive since most structures associated with pneumatic tires have very small bending rigidity, compared to their membrane rigidity. This means that the coupling of plane tension to twist is very weak in most cord-rubber laminates, and can safely be neglected. This is not the case for general filamentary or fiber reinforced materials, since when the matrix is of sufficient stiffness and monofilament reinforcement is used, then tensile and compressive moduli are about equal and the coupling between plane effects, such as tension and shear, and bending effects, such as twist and curvature change, may be significant.

Insofar as the two-dimensional orthotropic properties of the sheet are concerned, primary interest usually centers on determining the elastic characteristics in the so-called principal directions, which in figure 2.5a are given as the x and y directions. For such a definition one may utilize either a direct or inverted form of Hooke's law, as given alternately by eqs (2.1) and (2.2).

$$\begin{aligned}\sigma_x &= C_{xx}\epsilon_x + C_{xy}\epsilon_y, \\ \sigma_y &= C_{xy}\epsilon_x + C_{yy}\epsilon_y, \\ \sigma_{xy} &= C_{ss}\epsilon_{xy}.\end{aligned}\tag{2.1}$$

$$\begin{aligned}\epsilon_x &= \frac{\sigma_x}{E_x} - \frac{\sigma_y}{F_{xy}}, \\ \epsilon_y &= \frac{\sigma_y}{E_y} - \frac{\sigma_x}{F_{xy}}, \\ \epsilon_{xy} &= \frac{\sigma_{xy}}{G_{xy}}.\end{aligned}\tag{2.2}$$

The fact that the same constant C_{xy} appears in both the first and second of eqs (2.1), and similarly the constant F_{xy} in the first and second of eqs (2.2) may be demonstrated by drawing upon the single-valued character of the strain energy stored in such a sheet. This has been derived in the literature [14].

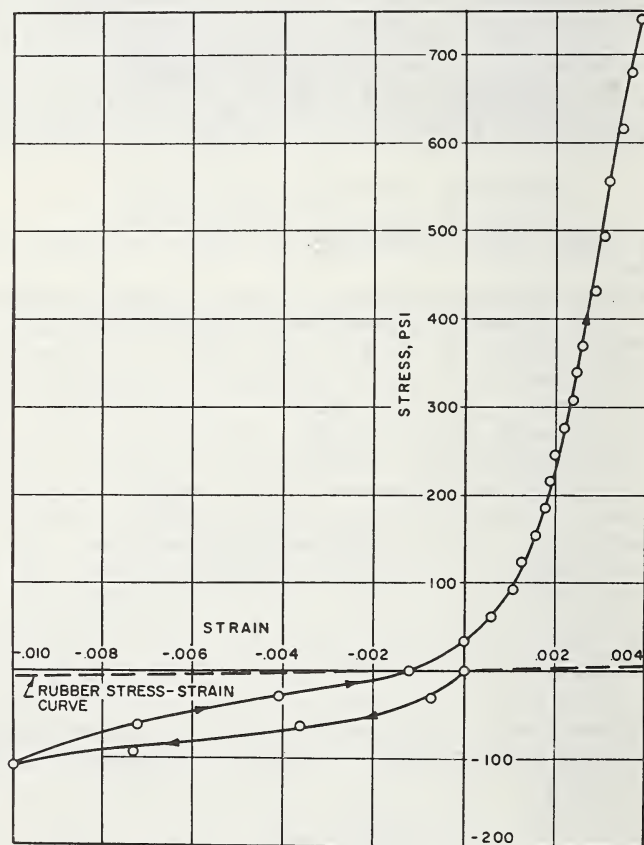


FIGURE 2.6. Continuous stress-strain curve through compression and into tension for rayon cords embedded in rubber.

Stress based on total cross-section area of specimen.

The use of such a law as given in eqs (2.1) or (2.2) is only valid if the materials involved are linearly elastic. In some applications this is almost self evident, such as in whisker reinforced metallics and ceramics, and fiber reinforced plastics. In the case of cord reinforced rubber this is not nearly so assured, and experimental data must be used as confirmation. Typical experimental data from Clark [3] is given in figures 2.6 and 2.7. From these it is seen that such a mathematical simplification is only justified under the following conditions.

- a. The cord is loaded in tension at all times.
- b. The value of the cord tension is large enough so that the region near the origin, commonly called the soft stretch region, is not encountered.
- c. Viscoelastic effects are ignored.

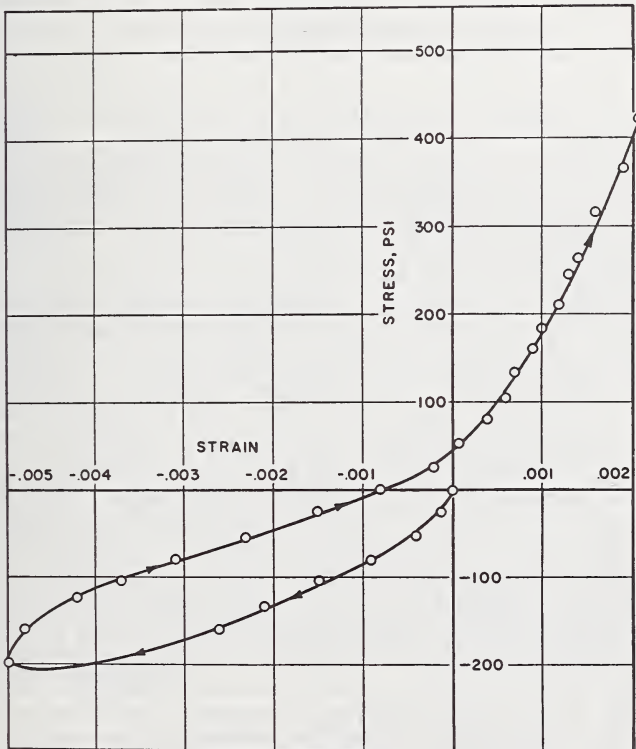
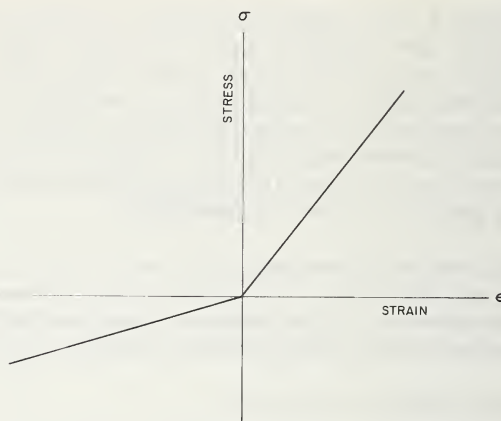


FIGURE 2.7. Continuous stress-strain curve through compression and into tension for nylon cords embedded in rubber.

Stress based on total cross-section area of specimen.



Bi-linear Stress Strain Curve

FIGURE 2.8. *Idealized bilinear stress-strain curve.*

Unless these conditions are fulfilled, typical stress strain curves such as shown in figures 2.6 and 2.7 indicate that some other more complex structural model for a tire cord must be chosen. It has been suggested that a bilinear model, such as shown in figure 2.8, would be appropriate but little evidence appears in the literature that such a model has been useful for analysis for practical problems.

In reviewing the implications of experimental data such as shown in figures 2.6 and 2.7, and associated idealizations such as shown in figure 2.8, it should be noted that the textile cords used in both figures 2.6 and 2.7 will carry appreciable compressive loads, since the stiffness of the associated rubber predicts only negligible compressive resistance. The specimens in question were thick-walled hollow cylinders made from ordinary pneumatic tire carcass material. The contribution to stress or load of the surrounding rubber is shown, and it is seen that the textile cords carry surprisingly large loads in compression. When a twisted textile cord is compressed, it tends to deform as a spiral spring, each ply yarn behaving as a monofilament. The lower the helix angle of the plied structure, the greater the initial radial growth during compression. This structural growth leads to a very high structural Poisson's ratio of the cord structure (not the cord filaments) when the cord is compressed. The compressive resistance is attributable to the rubber, the proximity of neighboring cords and the pressure normal to the laminate resisting cord growth. In any event this type of response leads one to conclude that even for small strains it would be necessary to consider twisted cords in rubber as being represented by a bilinear stress strain curve as a first approximation, as shown in figure 2.8, for all cases where cord tension could not be maintained. The practical effect of this is to force the description of the elastic constants of the single sheet of cord rein-

forced rubber into two distinct parts, one in which the cords are in tension and another in which the cords are in compression. This would appear to be the idealization of greatest benefit, and in the event that one wished to work in both tension and compression regions there will be just twice as many elastic constants applicable to a cord reinforced rubber sheet as to a sheet of wood or fiberglass reinforced plastic. Thus, eqs (2.1) and (2.2) actually have counterparts in the compressive region so that, as a first idealization, eight elastic constants actually exist for each laminated cord-rubber ply, four constants pertaining to conditions in cord tension while the other four pertain to conditions of cord compression.

In view of the similarity of the mathematics for each case, i.e., tension and compression, further discussion will be restricted to a single set of equations, since the form for the other set is identical.

The four constants C_{ij} in eqs (2.1) represent the stiffness of the composite material in the x and y directions, while the constants E_x , E_y and G_{xy} in eqs (2.2) are the conventional Young's moduli in x and y directions and the conventional shear modulus of the material along x - y boundaries, and the quantity F_{xy} represents a so-called cross-modulus of the material. From this point of view some authors have preferred eqs (2.2) as a standard form, since the conventional elastic constants appear directly in it, while other authors have used eqs (2.1). A complete discussion of the fundamentals of anisotropic elasticity is given in the book of Hearmon [15].

It would be desirable to be able to calculate either set of elastic constants given in eqs (2.1) or (2.2) in terms of the elastic properties of the textile cord and its surrounding rubber matrix. Theoretical methods for calculating the elastic constants of multi-phase materials have been published by Hashin and Rosen [16], and other similar methods have been reviewed by Hashin [1], based on energy principles to establish upper and lower bounds for elastic constants. These principles have not proved to be of much practical value since they do not bound the constants closely enough for the type of constituents being considered here.

However, from this has resulted a generalization of the so-called law of mixtures which has validity when fiber and matrix have the same Poisson's ratios. One of the difficulties of applying this type of theory to a cord-rubber structure is the noncontinuous nature of the cord itself, and due to the large values of possible cord contraction there may be substantial differences between the contraction characteristics of the cord and its surrounding rubber. The law of mixtures has been utilized by Whitney [17] in computing the elastic modulus E_x parallel to the cord direction in a sheet of material reinforced by parallel cords. This results in the expression

$$E_x = E_c \cdot \lambda + E_R(1 - \lambda) \quad (2.3)$$

where E_c represents cord modulus, E_R represents rubber modulus, and λ is the fraction of the cross sectional area occupied by the cord, this cross section being taken at right angles to the cord direction. This type

of expression may hold well for tension loads in the cords, but probably breaks down when the cords are in compression since then the effective cord Poisson's ratio becomes very large, much larger than that for rubber.

The other elastic characteristics of a single sheet of parallel cords imbedded in rubber are not so easily obtained. Methods of determining them on a semi-empirical basis have been investigated by both Ekvall [18] and by Clark, Field, and Dodge [13]. Both of these later attempts utilize simple volumetric fraction proportioning of the individual elastic constants of the constituent materials, and were partly successful by this approach. The elastic modulus parallel to the cord reinforcement direction can be predicted quite well by such principles, so that eq (2.3) is usually accurate enough. It is considerably more difficult to calculate the modulus E_y , referring to deformation at right angles to the direction of cord reinforcement. Shear modulus G_{xy} of the lamina shown in figure 2.5a is also difficult to predict. Test data reported in reference [19] seems to imply that a basic difficulty in calculating the elastic constant G_{xy} of a single ply involves the unknown role of the shearing deformation of the textile cord reinforcement itself. This test data was obtained using thick-walled tubes, with cords parallel to the tube centerline, tested in torsion accompanied by pre-tension in the longitudinal direction. The specimen is shown in figure 2.9. During such a test the cord length will not change, at least for relatively small deformations, so that the cords are exposed to pure shear. Apparently such a textile cord can contribute substantially to shear deformation, and this fact must be taken into account in constructing any simple theory for calculation of the overall shear property. It is difficult to visualize the contribution to shearing deformation of the twisted textile cord and it is difficult to include this factor into a stiffness proportioning scheme. Finally, the elastic constant F_{xy} is obtained by considering contraction of the sheet in the y direction due to the extension in the x direction. Experiments designed to determine values of F_{xy} for various combinations of cord-rubber sheets indicate that the cords themselves apparently participate strongly in the process of contracting at right angles to their axial direction under tension load. Attempts to measure such effects have shown that the effective Poisson's ratio of normal textile cord materials used for pneumatic tires is about 0.7, as reported by Budd [20] for tension measurements, but

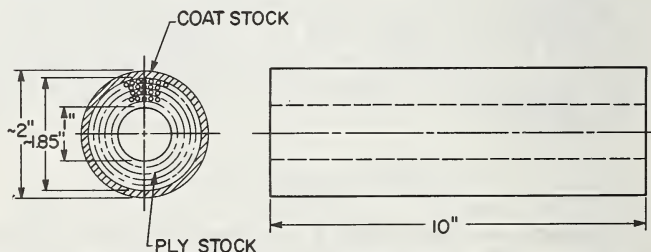


FIGURE 2.9. Test specimen used to determine cord shear properties.

can reach high values for cords in compression. Platt and Butterworth [37] report a Poisson's ratio of 3.3 for a two-ply nylon tire cord in rubber compressed to 15 percent strain.

While such a semiempirical approach allows one to predict single sheet elastic constants over a limited range, it gives little insight into the possibilities of optimum reinforcement or into the basic mechanisms of load carrying.

As an illustration of elastic constants of a single ply of tire material, table 2.1 gives experimental values taken from a set of experiments from reference [19]. Tables 2.2 and 2.3, taken from the same source, give measured values of E_y and G_{xy} for similar tire materials. It may be seen from table 2.1 that the simple approximation of considering the entire stiffness to be furnished by the reinforcing cords is quite good,

TABLE 2.1. *Comparison of measured and calculated values of E_x*

Type of cord	End count n	Ply thickness h	$(AE)_c$ (measured)	E_x^*	E_x (measured)	Error, %
Rayon	16	0.054	338	100,000	92,000	8
Rayon	25	.035	371	265,000	271,000	2
Rayon	14	.074	493	93,000	87,000	7
Nylon	34	.029	92	10,800	10,800	0
Nylon	16	.058	93.5	26,000	26,000	0
Nylon	33	.042	107	81,000	75,000	7
Rayon	34	.030	209	236,000	250,000	6
Rayon	34	.032	209	236,000	176,000	34
Nylon	15	.034	263	116,000	98,000	18
Nylon	15	.030	263	131,000	100,000	31

n ~ cords per inch measured perpendicular to cord direction.

h ~ ply thickness in inches.

$(AE)_c$ ~ product of the cord area and cord modulus, outside the "soft-stretch" region. This is measured by determining the total spring rate of a cord, in lbs. per inch, and then dividing by the length of this cord in inches.

E_x^* calculated using eq (2.3) with $E_R = 416$ psi.

E_x measured in tension on a strip specimen 1 inch wide and 12 inches long.

TABLE 2.2. *Measured values of E_y*

Type of cord	End count n	Cord diameter d	Ply thickness h	E (E_{Rubber})	E_y (Measured)
Rayon	25	0.032	0.059	416	2021
Nylon	28	.026	.047	416	1300
Nylon	29	.021	.037	416	1134
Nylon	29	.021	.036	416	1134
Rayon	25	.026	.042	416	1145
Rayon	32	.021	.040	416	1514

TABLE 2.3. *Experimental values of G_{xy}*

Cord material	Cord diameter, d	Cord spacing, s	Ply thickness, h	Rubber shear modulus, G_R	G_{xy} measured experimentally
Rayon	0.028	0.034	0.039	275	470
Rayon	.028	.034	.039	275	442
Rayon	.028	.034	.039	275	447
Rayon	.028	.034	.039	275	431
Rayon	.029	.041	.039	406	553
Rayon	.029	.041	.039	406	573
Nylon	.028	.033	.039	275	472
Nylon	.028	.033	.039	275	439
Nylon	.026	.033	.039	275	463
Nylon	.021	.029	.027	406	569
Nylon	.021	.029	.027	406	578
Wire	.032	.123	.071	406	446
Wire	.031	.123	.071	406	438

since it gives results not far removed from measurement. On the other hand, such a simple approach for calculating modulus E_y and the shear modulus G_{xy} is obviously not possible, and considerable work needs to be done in this area in order to provide rational expressions for these quantities.

A number of important references bear on the problem of predicting the elastic characteristics of a multiplicity of cord reinforced lamina bonded together. A direct approach to such a complex structure was published by Hofferberth [21] in which an attempt was made to decompose forces into vector components lying parallel to the reinforced cords, and to allow these cords to carry the component loads. From such an analysis, Hofferberth was able to predict certain characteristics of the elastic constants which appear to agree in a general way with the experimental evidence obtained from other sources, but Hofferberth himself gives no experimental evidence to validate his theoretical development.

A very general discussion of the composite properties of filament-resin systems has been given by Herrmann and Pister [22]. However, the models which Herrmann and Pister use are primarily concerned with multiple layers of parallel cords, which does not generally correspond to the case with cord-rubber laminates.

The elastic properties of plywood have many similarities in theory to the elastic properties demonstrated by cord reinforced rubber laminates, with the exception of the fact that normally the compressive modulus of wood does not differ much from its extension modulus, so that the problem of the bilinear representation does not exist in wood as it does in textile cord reinforced rubber. The plywood problem has been extensively studied and is thoroughly reviewed in the work of Hoff [23] and in a recent report from the Forest Products Laboratory of the

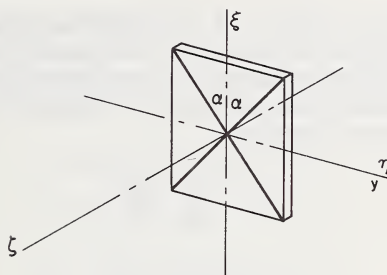


FIGURE 2.10. Schematic view of a small section of two-ply laminate.

U.S. Department of Agriculture [14]. From such a background, it is not difficult to construct a theoretical prediction of the elastic characteristics of symmetric cord-rubber laminates provided that the elastic properties of a single sheet or lamina of the material are known. In what follows, a brief review will be given of such a theory.

Attention here will be centered on layered, or laminated, structures built up by bonding together plane sheets of rubber-coated fabric. In the case of pneumatic tires this fabric is simply a series of parallel tire cords. In addition, the class of laminated structure considered here is that of a two-ply combination in which the cords are separated angularly in the two plies by an included angle 2α , as shown in figure 2.10. In that illustration, the heavy diagonal lines representing typical textile cords are shown being bisected by the coordinate axes ξ and η , two arms of the orthogonal ξ , η , ζ system.

For the present, attention will be confined to those structures in which stresses in the ζ direction are negligibly small compared with those in the ξ and η directions. This assumption will generally be true for bodies that are large in the ξ and η directions compared to their thickness in the ζ direction.

While discussion here is limited to the characteristics of a two-ply system, the ideas and techniques developed allow fairly easy extension to any number of plies provided that the structure remains orthotropic as defined below.

Neglecting effects through the thickness of the two-ply structure (ζ direction), one may define an orthotropic material as one possessing two planes of symmetry at every point. For example, in figure 2.10, the planes of symmetry are $\zeta-\eta$ and $\zeta-\xi$. From this it is seen that not only will the two-ply construction be orthotropic, but so will a multi-ply construction made up of a series of similar two-ply structures, and so will a number of special cases such as illustrated in figure 2.11. In figure 2.10,

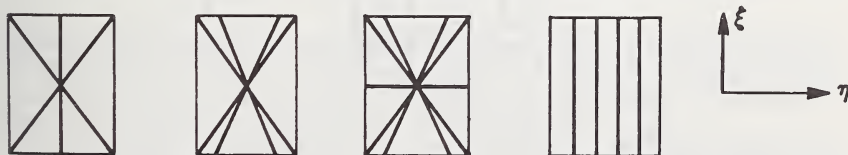


FIGURE 2.11. Typical orthotropic laminates.

it may be seen that ξ and η are principal directions, in that normal stresses applied in these directions do not produce shearing distortion, nor do applied shearing stresses in these directions result in normal distortion. A convenient general form for Hooke's law about principal axes for such orthotropic material is

$$\begin{aligned}\epsilon_{\xi} &= \frac{\sigma_{\xi}}{E_{\xi}} - \frac{\sigma_{\eta}}{F_{\xi\eta}}, \\ \epsilon_{\eta} &= \frac{\sigma_{\eta}}{E_{\eta}} - \frac{\sigma_{\xi}}{F_{\xi\eta}}, \\ \epsilon_{\xi\eta} &= \frac{\sigma_{\xi\eta}}{G_{\xi\eta}},\end{aligned}\tag{2.4}$$

where E_{ξ} , E_{η} , $F_{\xi\eta}$, and $G_{\xi\eta}$ represent the four orthotropic elastic constants of such a laminate. These equations may be used in the structural analysis of devices made from such materials.

In order to determine the four elastic constants just mentioned, it is necessary to consider the construction of each individual ply making up the laminate. The laminate is formed by embedding a series of parallel, straight cords lying in a plane into a sheetlike matrix of more elastic material. This is illustrated in figure 2.12. It is seen that maximum and minimum moduli of elasticity are to be found in the x and y directions and that this single sheet is also orthotropic about x and y , with resulting elastic constants E_x , E_y , F_{xy} , and G_{xy} . These are assumed to be known. Generally they would be associated with a state of tension in the cords. However, they could be associated with cord compression as previously discussed.

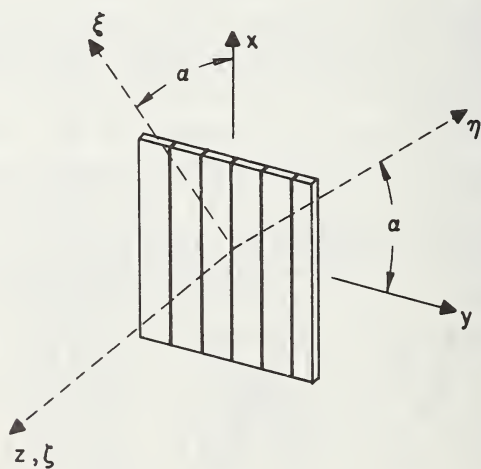


FIGURE 2.12. Schematic view of a single ply of cord embedded in rubber.

The generalized form of Hooke's law may be written for the sheet of figure 2.12 using the stresses as independent variables with respect to any desired coordinate axes, as shown in eqs (2.5). These are basic to this development and will be treated in some detail.

$$\begin{aligned}\epsilon_{\xi} &= a_{11}\sigma_{\xi} + a_{12}\sigma_{\eta} + a_{13}\sigma_{\xi\eta}, \\ \epsilon_{\eta} &= a_{21}\sigma_{\xi} + a_{22}\sigma_{\eta} + a_{23}\sigma_{\xi\eta}, \\ \epsilon_{\xi\eta} &= a_{31}\sigma_{\xi} + a_{32}\sigma_{\eta} + a_{33}\sigma_{\xi\eta}.\end{aligned}\tag{2.5}$$

Reference [19] derives expressions for the elastic constants a_{ij} as functions of the angle of inclination α of the ξ - η axes with respect to the x - y axes, and of the orthotropic elastic constants of a single sheet E_x , E_y , F_{xy} , and G_{xy} . These expressions are

$$\begin{aligned}a_{11} &= \frac{\cos^4 \alpha}{E_x} + \frac{\sin^4 \alpha}{E_y} + \left(\frac{1}{G_{xy}} - \frac{2}{F_{xy}} \right) \sin^2 \alpha \cos^2 \alpha, \\ a_{22} &= \frac{\sin^4 \alpha}{E_x} + \frac{\cos^4 \alpha}{E_y} + \left(\frac{1}{G_{xy}} - \frac{2}{F_{xy}} \right) \sin^2 \alpha \cos^2 \alpha, \\ a_{33} &= 4 \left(\frac{1}{E_x} + \frac{1}{E_y} + \frac{2}{F_{xy}} \right) \sin^2 \alpha \cos^2 \alpha + \frac{(\cos^2 \alpha - \sin^2 \alpha)^2}{G_{xy}}, \\ a_{21} = a_{12} &= \left(\frac{1}{E_x} + \frac{1}{E_y} - \frac{1}{G_{xy}} \right) \sin^2 \alpha \cos^2 \alpha - \frac{\sin^4 \alpha + \cos^4 \alpha}{F_{xy}}, \\ a_{31} = a_{13} &= \frac{2 \cos^3 \alpha \sin \alpha}{E_x} - \frac{2 \sin^3 \alpha \cos \alpha}{E_y} \\ &\quad - \left(\frac{1}{G_{xy}} - \frac{2}{F_{xy}} \right) (\cos^2 \alpha - \sin^2 \alpha) \sin \alpha \cos \alpha, \\ a_{32} = a_{23} &= \frac{2 \sin^3 \alpha \cos \alpha}{E_x} - \frac{2 \cos^3 \alpha \sin \alpha}{E_y} \\ &\quad + \left(\frac{1}{G_{xy}} - \frac{2}{F_{xy}} \right) (\cos^2 \alpha - \sin^2 \alpha) \sin \alpha \cos \alpha.\end{aligned}\tag{2.6}$$

Equations (2.5) and (2.6) now allow the properties of an orthotropic sheet (for example, one ply of cords embedded in a matrix) to be predicted in any direction ξ - η at an angle α with the cord direction x . This knowledge can be used to construct a two-ply structure.

Consider now a sheet of the type shown in figure 2.12 but inclined at some angle α to the axes ξ - η . This is illustrated in figure 2.13. Imagine

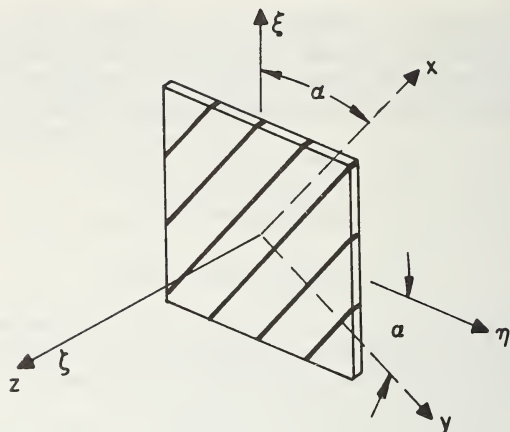


FIGURE 2.13. Single ply of cord embedded in rubber at angle α to the vertical ξ axis.

that this sheet is extended in the ξ and η directions by means of normal stresses acting on the edges. Since the orthotropic axes x and y do not coincide with the ξ - η axes, this is not possible; distortions $\epsilon_{\xi\eta}$ will inevitably accompany the application of any set of normal stresses σ_{ξ} and σ_{η} . For that reason one must admit the existence of shearing stresses $\sigma_{\xi\eta}$ as necessary for distortionless extension of an element such as that of figure 2.13, where the reference and orthotropic axes are not the same. With this provision in mind, one may go directly to eqs (2.5) and presume no distortion under loading; that is, the loads will be adjusted to prevent distortion. Then, eqs (2.5) become

$$\begin{aligned}\epsilon_{\xi} &= a_{11}\sigma_{\xi} + a_{12}\sigma_{\eta} + a_{13}\sigma_{\xi\eta}, \\ \epsilon_{\eta} &= a_{21}\sigma_{\xi} + a_{22}\sigma_{\eta} + a_{23}\sigma_{\xi\eta}, \\ \epsilon_{\xi\eta} &= a_{31}\sigma_{\xi} + a_{32}\sigma_{\eta} + a_{33}\sigma_{\xi\eta} = 0.\end{aligned}\tag{2.7}$$

From these it may be seen that the only stress which is not independent can be chosen to be $\sigma_{\xi\eta}$ since it can be expressed in terms of σ_{ξ} and σ_{η} from the last of eqs (2.7), and this expression can then be substituted into the first two of eqs (2.7). On doing this, one obtains

$$\sigma_{\xi\eta} = -(a_{31}/a_{33})\sigma_{\xi} - (a_{32}/a_{33})\sigma_{\eta},\tag{2.8a}$$

$$\epsilon_{\xi} = [a_{11} - (a_{13}a_{31}/a_{33})]\sigma_{\xi} + [a_{12} - (a_{13}a_{32}/a_{33})]\sigma_{\eta},\tag{2.8b}$$

$$\epsilon_{\eta} = [a_{21} - (a_{23}a_{31}/a_{33})]\sigma_{\xi} + [a_{22} - (a_{23}a_{32}/a_{33})]\sigma_{\eta},\tag{2.8c}$$

where $\sigma_{\xi\eta}$ is the stress that must be furnished from some external source to obtain a distortionless extension. In view of the previously determined symmetry $a_{12}=a_{21}$, $a_{13}=a_{31}$, $a_{32}=a_{23}$, it is seen by comparison of this set of equations with eqs (2.4) that

$$\begin{aligned} E_{\xi} &= [a_{11} - (a_{13}^2/a_{33})]^{-1}, \\ E_{\eta} &= [a_{22} - (a_{23}^2/a_{33})]^{-1}, \\ F_{\xi\eta} &= -[a_{12} - (a_{13}a_{23}/a_{33})]^{-1}. \end{aligned} \quad (2.9)$$

In connection with eqs (2.9), if one were to return to eqs (2.6) and utilize the compression characteristics E'_x , E'_y , etc., a completely different set of constants a'_{11} , a'_{22} , etc. would exist, and this would result in a set of moduli E'_{ξ} , E'_{η} , and $F'_{\xi\eta}$ completely different from those using the elastic constants associated with tension.

It is now necessary to consider the last elastic constant $G_{\xi\eta}$. Two different possible shear moduli $G_{\xi\eta}$ exist, one associated with all cords in compression and the other with all cords in tension. These two cases may be worked out in a very straightforward way and will be presented here.

To obtain the $G_{\xi\eta}$ associated with either cord compression or cord tension, it is necessary to postulate an extension-free distortion, or pure distortion $\epsilon_{\xi\eta}$, which occurs as the result of the proper application of the stresses σ_{ξ} , σ_{η} , and $\sigma_{\xi\eta}$. Equations (2.4) become, when applied to this case,

$$\begin{aligned} \epsilon_{\xi} &= a_{11}\sigma_{\xi} + a_{12}\sigma_{\eta} + a_{13}\sigma_{\xi\eta} = 0, \\ \epsilon_{\eta} &= a_{21}\sigma_{\xi} + a_{22}\sigma_{\eta} + a_{23}\sigma_{\xi\eta} = 0, \\ \epsilon_{\xi\eta} &= a_{31}\sigma_{\xi} + a_{32}\sigma_{\eta} + a_{33}\sigma_{\xi\eta}. \end{aligned} \quad (2.10)$$

The first two of these may be used to express σ_{ξ} and σ_{η} in terms of $\sigma_{\xi\eta}$. This results in

$$\begin{aligned} \sigma_{\eta} &= -\frac{a_{23} - (a_{12}a_{13}/a_{11})}{a_{22} - (a_{12}^2/a_{11})} \sigma_{\xi\eta} \\ \sigma_{\xi} &= \left[\frac{a_{12}}{a_{11}} - \frac{a_{23} - (a_{12}a_{13}/a_{11})}{a_{22} - (a_{12}^2/a_{11})} - \frac{a_{13}}{a_{11}} \right] \sigma_{\xi\eta} \end{aligned} \quad (2.11)$$

and finally these may be used to obtain

$$G_{\xi\eta} = \left\{ -a_{31} \left[\left(\frac{a_{12}}{a_{11}} \right) \left(\frac{a_{12}a_{13} - a_{11}a_{23}}{a_{11}a_{22} - a_{12}^2} \right) + \frac{a_{13}}{a_{11}} \right] + a_{23} \left[\frac{a_{12}a_{13} - a_{11}a_{23}}{a_{11}a_{22} - a_{12}^2} \right] + a_{33} \right\}^{-1}. \quad (2.12)$$

Equations (2.9) and (2.12) are extremely important as they allow the elastic constants of an orthotropic structure to be calculated in any

direction as a function of the terms $a_{11}, a_{22}, \dots, a_{33}$. These, in turn, are determined completely by the elastic properties of the single sheet in the directions of the orthotropic axes, that is, parallel and perpendicular to the cord directions, as well as the angular orientation of the sheet. As mentioned previously, eq (2.12) represents both the possible shear moduli of a laminated orthotropic structure. It can be used to represent the shear modulus for those structures where all cords are either in tension or compression, depending on whether a_{ij} or a'_{ij} is used.

It is seen that the elastic properties given by eqs (2.9) and (2.12) are identical to the elastic properties of the compound orthotropic structure of figures 2.10 and 2.11 provided that the two plies which make up figure 2.10 are identical in all respects, and provided that provisions are made for obtaining the necessary shear and normal stresses such as given by eqs (2.8a) and (2.11). In general, it must be considered that these necessary shear and normal stresses are provided by the bond between adjacent plies in a laminated multi-ply structure, and that these stresses may be used to define the load intensities acting on the adhesives linking the plies together.

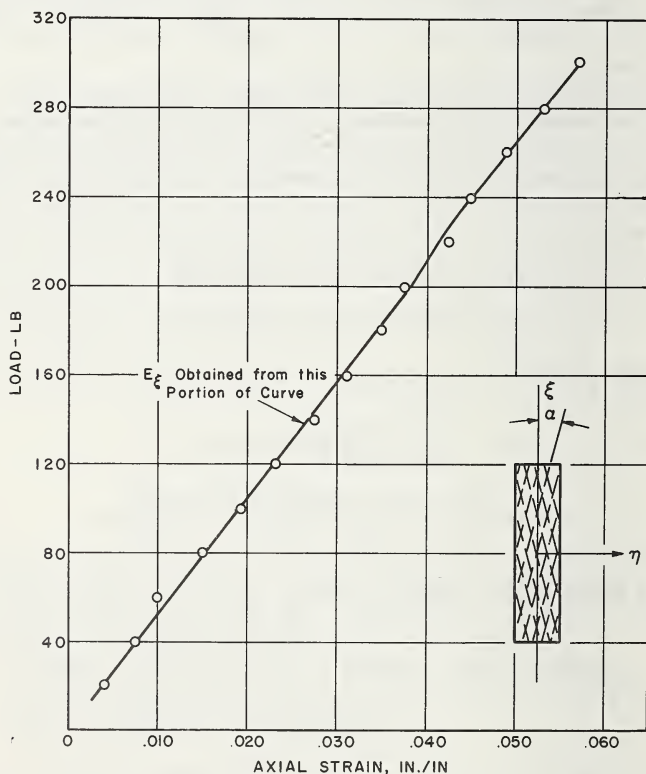


FIGURE 2.14. Typical load-axial strain curve for a cylindrical tube subjected to axial tension.

Reference [19] gives comparisons between calculated and measured values of such elastic constants for a series of four-ply cylinders made up of rayon cord reinforced rubber. The construction of these cylinders was orthotropic, in that alternate plies were oppositely directed at the same angle with respect to the centerline of the cylinder. Such specimens were tested under various combinations of internal pressure and end load, and the resulting stress-strain curves were surprisingly linear. An example of one of these is given in figure 2.14, from which it may be seen that the resulting composite body exhibits linear stress-strain relationships to within a close approximation, and hence elastic constants for such structures are meaningful.

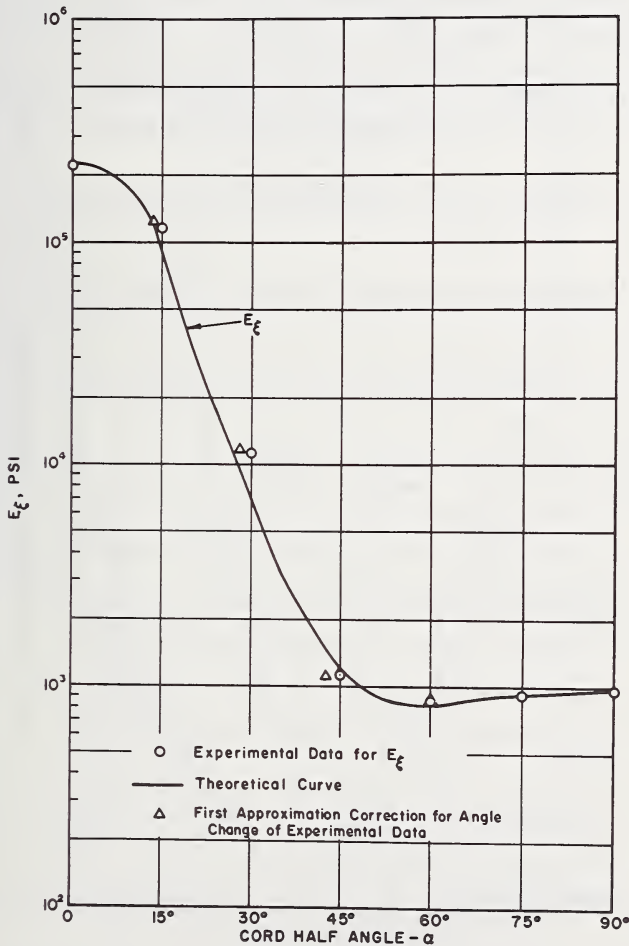


FIGURE 2.15a. Modulus E_ξ as predicted from eq (2.9) vs. cord half-angle α , along with experimental values for E_ξ .

A comparison between the modulus E_ξ in the axial direction of the cylinder, as predicted from eqs (2.9) and as measured on the rayon cord-rubber cylinders, is given in figure 2.15a while a similar comparison for the so-called cross modulus $F_{\xi\eta}$ is given in figure 2.15b. In connection with figure 2.15b it is interesting to note that as the half-angle between textile cords in adjacent plies is increased, the imposition of pure tensile loads on the cylinder eventually causes compressive forces to be set up in the reinforcing cords. In the absence of any cord preload, this means that at this particular point, which occurs at approximately 56° , one must begin to think in terms of the compression elastic properties.

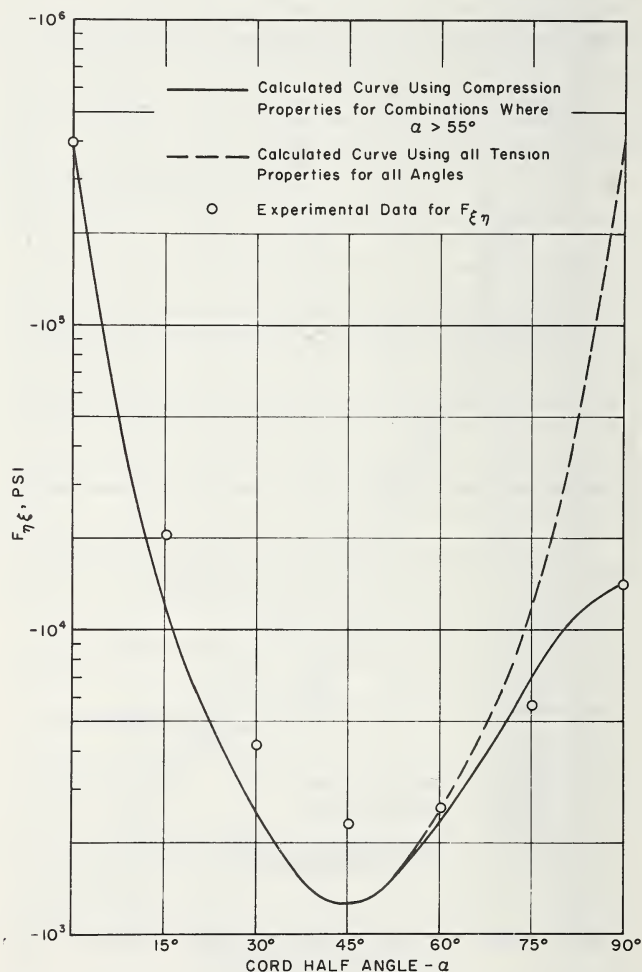


FIGURE 2.15b. Modulus $F_{\xi\eta}$, as predicted from eq (2.9), vs. cord half-angle α , along with experimental values for $F_{\xi\eta}$.

This has been done in figure 2.15b and the resulting plot actually illustrates the tension and compression portions blended together. This demonstrates very clearly the necessity for utilizing all eight elastic constants of such cord-rubber laminates when conditions require, since it is clear from figure 2.15b that calculations made on the basis of tension characteristics alone would not correspond to experiment.

One of the basic elastic constants used in describing the elasticity of homogeneous isotropic materials is the ratio between the lateral and the axial strain caused by an axial stress. This quantity, called Poisson's ratio, has a value ranging from approximately 0.1 to 0.5 for most ordinary materials, with rubber having a value very close to 0.5. One may physically associate the property of infinite bulk modulus, or incompressibility, with the value of Poisson's ratio of 0.5 for an isotropic body. As has been pointed out previously, a cord-rubber combination is not homogeneous nor is it isotropic. It is not, therefore, surprising to find cord-rubber combinations exhibiting values of Poisson's ratio outside those ordinarily obtained from homogeneous materials possessing isotropy. In fact, link-

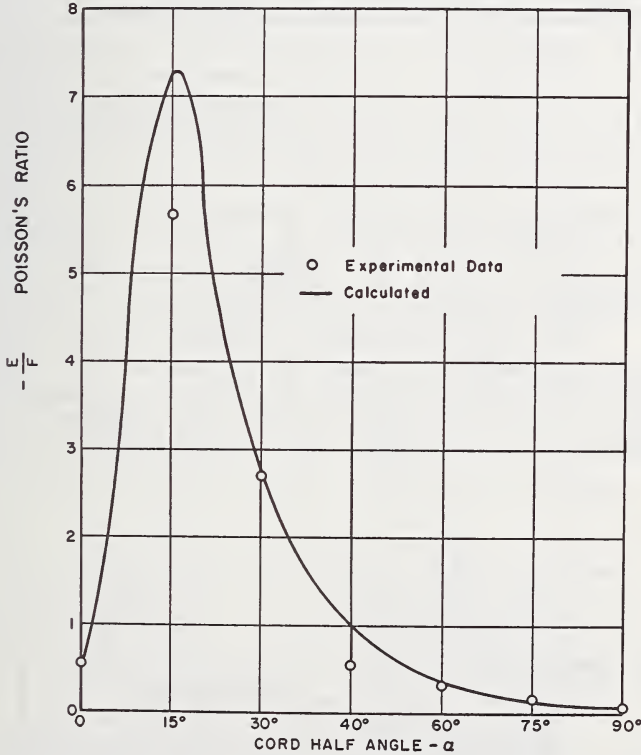


FIGURE 2.16. Poisson's ratio as predicted from eq (2.9), vs. cord half-angle α , along with experimental values for Poisson's ratio.

ages or structures can be arranged in such a way that their overall effective Poisson's ratio is large, and could easily be 5 or 10. It is probably more correct in this case to consider the combination of monofilaments into singles strands, the strands into cord, and the cord in rubber as a structure rather than as a continuum. As an example, previously quoted, Platt and Butterworth [37] report a Poisson's ratio of 3.3 for a two-ply nylon tire cord in rubber compressed to a 15 percent axial strain.

Poisson's ratio may be obtained in terms of the notation used here by taking the ratio $E_{\xi}/F_{\xi\eta}$, which is the ratio of lateral to axial strain. This has been calculated from the experimental data in reference [19] and is given as a function of the cord half-angle in figure 2.16. Again, a comparison is made between experimental data and the theoretically predicted Poisson's ratio using eqs (2.8) and (2.11). The results indicate that the corresponding shapes of the curves are at least of the same type. It is interesting to note that Poisson's ratios in excess of 1 are possible and have been observed. This means that at the proper cord angles, a tubular cord-rubber specimen will contract more in its diameter than it will elongate when subjected to a tensile load in the axial direction. This is undoubtedly the physical basis of the well-known Chinese finger puzzle, as well as various gripping devices derived from it.

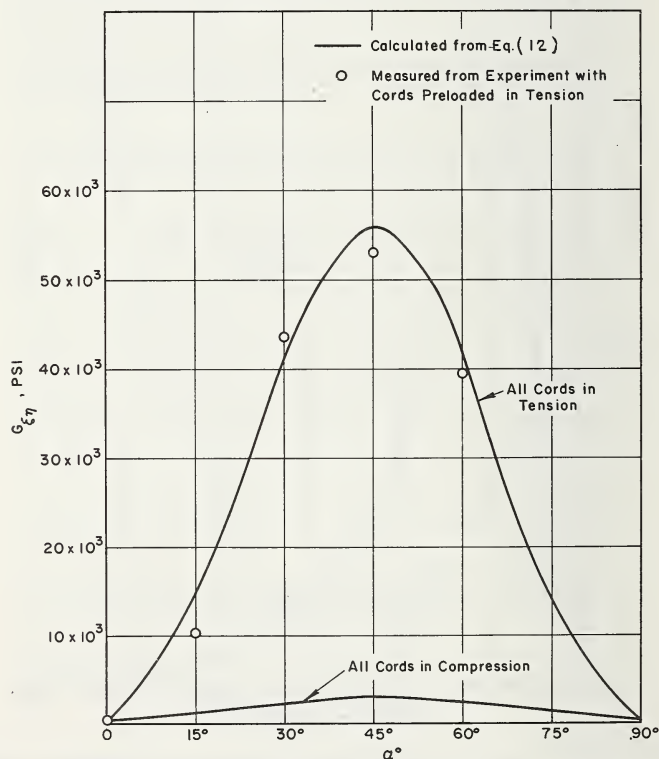


FIGURE 2.17. Shear modulus $G_{\xi\eta}$, as predicted from eq (2.12), vs. cord half-angle α , along with experimental values for $G_{\xi\eta}$.

Torsion tests of cylindrical tube specimens have also been reported over a range of half-angles from 0° to 60° where all cords were preloaded into tension. The results of these experiments are compared in figure 2.17 with calculations made on the basis of eq (2.12). It may be seen that the agreement between the experimental data and the calculations is acceptable. It should also be noted that in figure 2.17 the calculated value of shear modulus, assuming all cords to be in a state of compression, is also presented for comparative purposes. This condition results in shear stiffnesses considerably lower than obtained when all cords are in a state of tension.

Reference [24] shows that the elastic constants of a symmetric laminated series of sheets may be expressed in dimensionless form in terms of a single dimensionless parameter E_x/G_{xy} , and also in terms of the cord angle of the individual lamina with respect to the principal axis of elasticity. This is accomplished by making simple approximations for the four elastic constants of a single sheet of cord reinforced rubber, on an elementary strength of materials basis, and by using these approximations to obtain numerical values of some of the ratios of elastic constants. This particular simplification has only been worked out for textile and wire cords embedded in rubber and may not be particularly appropriate for fiberglass-epoxy or other materials. From such an approximation the elastic constants of a multi-ply orthotropic structure may be determined and plotted as a function of the cord half angle α and the single numerical quantity E_x/G_{xy} , representative of the degree of anisotropy of a single sheet of material used in the laminate. This analysis also assumes that all sheets used in the laminate are identical, although in a more general case this need not be so. It should be noted that the ratio E_x/G_{xy} is convenient to represent the characteristics of a single sheet of material since this ratio takes on a value of 3 for an isotropic incompressible material. Values for this ratio as high as nearly 10^4 have been measured for twisted wire cords reinforcing rubber. The notation used here is illustrated in figure 2.18.

Reference [24] shows that for those cases where all plies of the multi-ply laminate are loaded in such a way that their cords are in tension, or alternately, when all plies are loaded in such a way that their cords are in compression, then exact expressions for the moduli of the

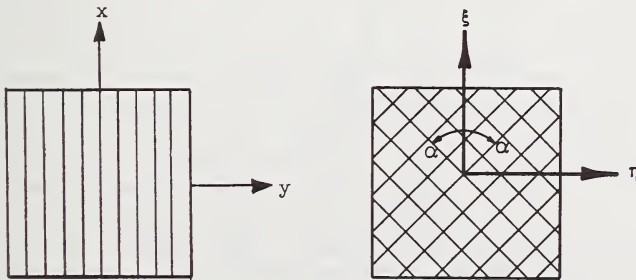


FIGURE 2.18. Left, single sheet of fabric; right, even number of laminated fabric sheets.

resulting orthotropic structures can be found. These moduli are expressed in terms of the cord half angle α and the four elastic constants of a single sheet of the material used in forming the laminate. Figure 2.19 gives values of the dimensionless extension ratio E_ξ/G_{xy} for such laminates over a wide range of anisotropies, while figures 2.20 and 2.21 give similar dimensionless information concerning the cross modulus and the shearing modulus of such laminated structures.

It is seen that cord angles play a most dominant role in the variation of these elastic constants. In particular, the variation of extensional modulus E_ξ with cord angle is extremely steep. This indicates that there might be many situations in which a laminated structure can be used to control the elastic characteristics over a wide range.

In most applications for pneumatic tires, the loadings are such that the material constants are those associated with cord tension. Occa-

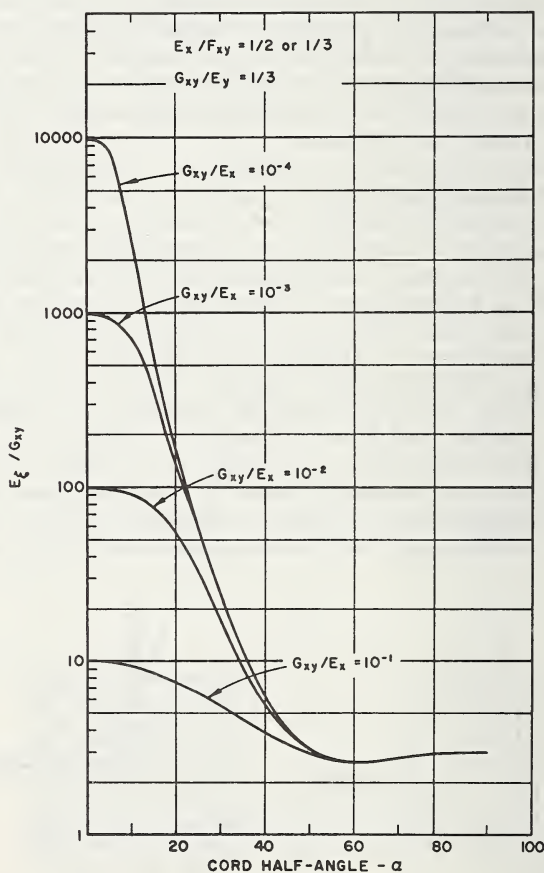


FIGURE 2.19. E_ξ/G_{xy} vs. half-angle α for various values of G_{xy}/E_x .

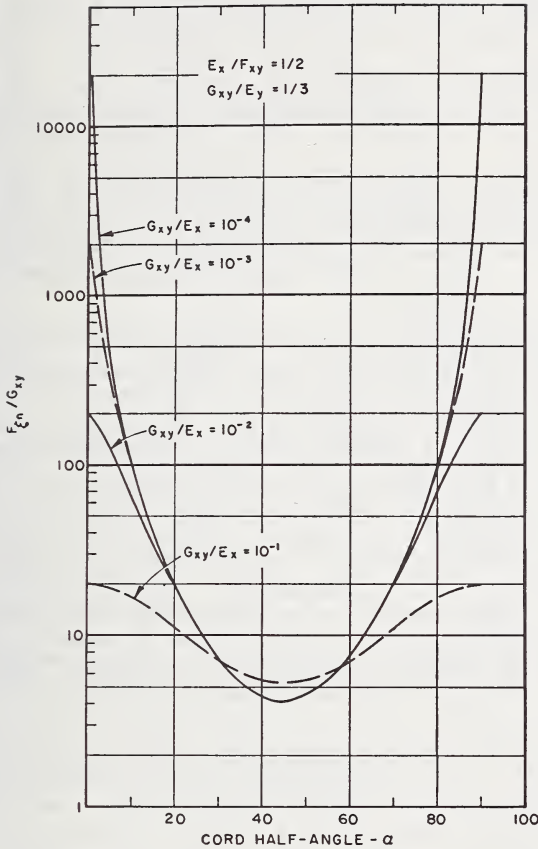


FIGURE 2.20. $F_{\xi\eta}/G_{xy}$ vs. half-angle α for various values of G_{xy}/E_x .

sionally, under large tire deflections, cord compression appears in the tire sidewall and the elastic constants defining the stiffness then take on values appropriate to this, as previously discussed. Under both large deflection and significant tractive effort or braking force, tire sidewalls can wrinkle. Insofar as is known there is no systematic technique in the literature for defining the conditions under which this occurs, but recently Stein and Hedgepeth [25] have proposed methods for analyzing partly-wrinkled structures, and have shown that membrane structures retain much of their stiffness at loads substantially above the load at which wrinkling first occurs.

The stiffness of cord rubber laminates in which cord layers take on three or more different directions is of importance in the design of breakers or belts for the tread band reinforcement of tires. With this application in mind, such elastic properties have been studied by

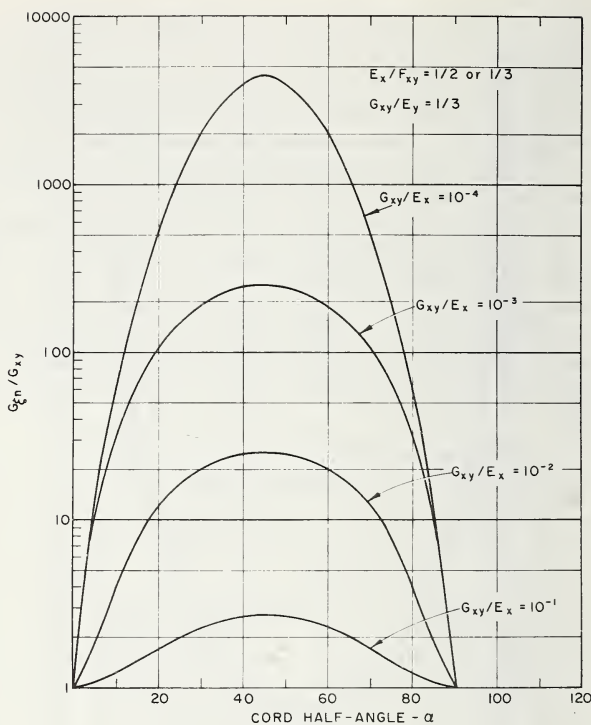


FIGURE 2.21. $G_{\xi\eta}/G_{xy}$ vs. half-angle α for various values of G_{xy}/E_x .

Gough [38] and co-workers. They propose a method of analysis in which one takes a rectangular sample of finite dimensions and applies a tensile strain e_1 parallel to one axis and in the plane containing the cords. It is then supposed that there must be a complementary strain e_2 in the perpendicular direction, also in the cord plane. Tensions in the cords are then deduced from the magnitude of e_1 and e_2 , and the cord angle. It is assumed that the component in the e_2 direction of the cord tension is balanced by the stress in the rubber in the same direction, since no external forces are presumed to be applied in the e_2 direction. This condition allows e_2 to be eliminated from the equations. The contribution to the total force in the e_1 direction made by the effects of the rubber and by the cord tension is then computed, and from this value and the strain e_1 the equivalent Young's modulus is obtained.

Such a computation is based on the following assumptions:

- (a) That the long edges of the sample remain straight and parallel as if the sample is part of an infinite sheet.

- (b) That strain is homogeneous throughout rubber and cord, so that the strain in either part is identical with the strain of the whole.
- (c) That the stress along the cord length is proportional to the cord modulus, but that the cords behave as part of the rubber in shear and transverse stresses.
- (d) That the finite thickness of the cords does not in itself influence complementary stresses in the calculations, although it is taken into account when computing the sectional area of the rubber and cord in both principal directions.

In carrying out such an analysis, one must account for the additional physical facts imposed by the type of structure to be encountered. For example, in the construction of pneumatic tires it is common that the structure be symmetric, or nearly symmetric. Within that restriction, and presuming similar but oppositely directed cord angles $\pm \alpha$, an additional cord at an angle of zero is often considered to form the third direction of a three directional cord system. The two bias cord plies may have a different modulus from the single zero degree ply, and the ratio of these moduli is an important new parameter which must appear in any computation of elastic stiffness of the plane sheet. The product of cord end count and cord modulus may be used as a measure of the local stiffness density in each lamina or ply, measured parallel to the cord direction. The ratio of these stiffness densities may be thought of as an overall cord stiffness density ratio for a typical three-directional composite. It is clear that composites of four or more directions could become even more complex, and most interest is centered on the symmetric cases of these possible combinations.

Gough [38] has computed elastic stiffness characteristics for a number of four-ply combinations, a few of which are shown in figures 2.22, 2.23 and 2.24. Similar computations may be done to estimate the effect of breaker angle and modulus on stiffness of the breaker region of tires, and these are illustrated in figure 2.25. Reference [38] also gives plots of stiffness of breakers using cords in three directions. Once again the need is demonstrated for the presence of a pair of low angle layers, in the region of 20° , for maximum stiffness.

Due to the difficulties of presenting information on multi-ply structures in concise form, considerable additional work could very well be done in the area of bringing to the tire designers simple and concise information on the elastic stiffness of various cord angle and cord density ratio combinations. Along this line, Gough and co-workers studied tire to ground forces and movements of the tire elements across the ground, using as a model for the tire an elastic beam on an elastic foundation. From such studies, they deduced that treadwear is minimized if the edge-wise stiffness of the tread band region is maximized. From such studies, one may conclude that low crown angles and tread reinforcement insure high beam stiffness, as might be expected, but they also show the rather unexpected conclusion that maximum beam stiffness may be contained

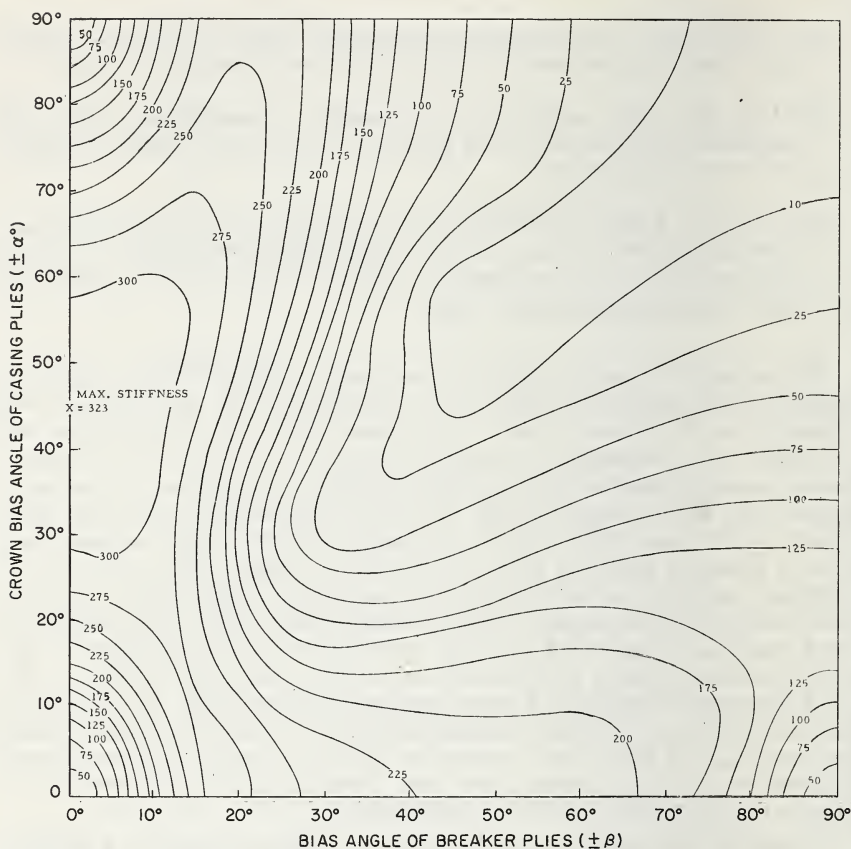


FIGURE 2.22. Crown stiffness of tires with a 4-ply rayon casing and 2-ply breaker of ply stiffness $(E_c A_n)/T = 15,000 \text{ lb/in}^2$.

by other than zero angle breaker plies, as illustrated most clearly in figure 2.23.

The role of the individual reinforcing cord in load carrying is not well understood in dealing with the elastic properties of cord reinforced rubber. Hedgepeth [26] has shown that sudden failure of one cord in an array of parallel cords can result in dynamic load overshoot of neighboring cords by a factor of about 1.25. Clark and Reid [27] have examined the nature of the cord loads in the neighborhood of a broken cord by means of a small cord force transducer inserted into one cord in the center of a strip of parallel cords. This strip was placed in a state of tension. The load in the instrumented cord was measured, and then the

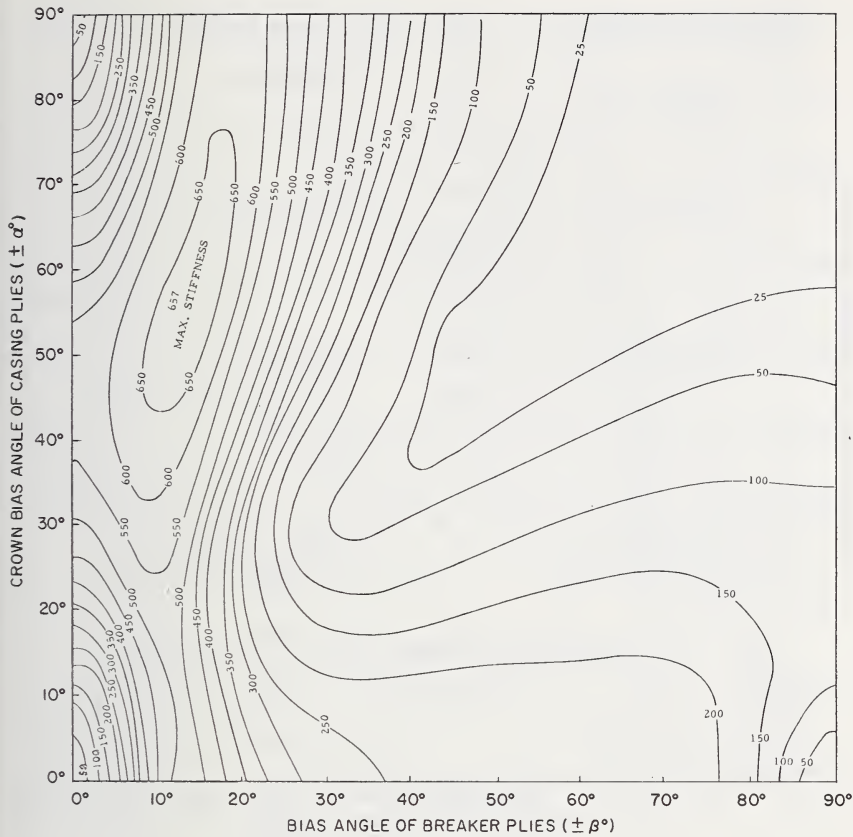


FIGURE 2.23. Crown stiffness of tires with a 4-ply rayon casing and 2-ply breaker of ply stiffness $(E_c A_n)/T = 40,000 \text{ lb/in}^2$.

instrumented cord was cut, first at a great distance from the location of the force transducer and then closer and closer to it. After each cut, cord load was again measured, and from this one could obtain information on the way in which cord load is built-up along the cord from its free end. This information is summarized in figure 2.26, where it is shown that for the typical tire carcass materials used here about 1 inch of cord length is needed before the cord carries most of its intended load.

Weiner and Gogos [28] have studied the damping characteristics of cord rubber laminates by means of sinusoidal excitation in bending of a specimen which is pretensioned. Their results were presented in the form of curves showing the Q -factor, which may be interpreted for simple

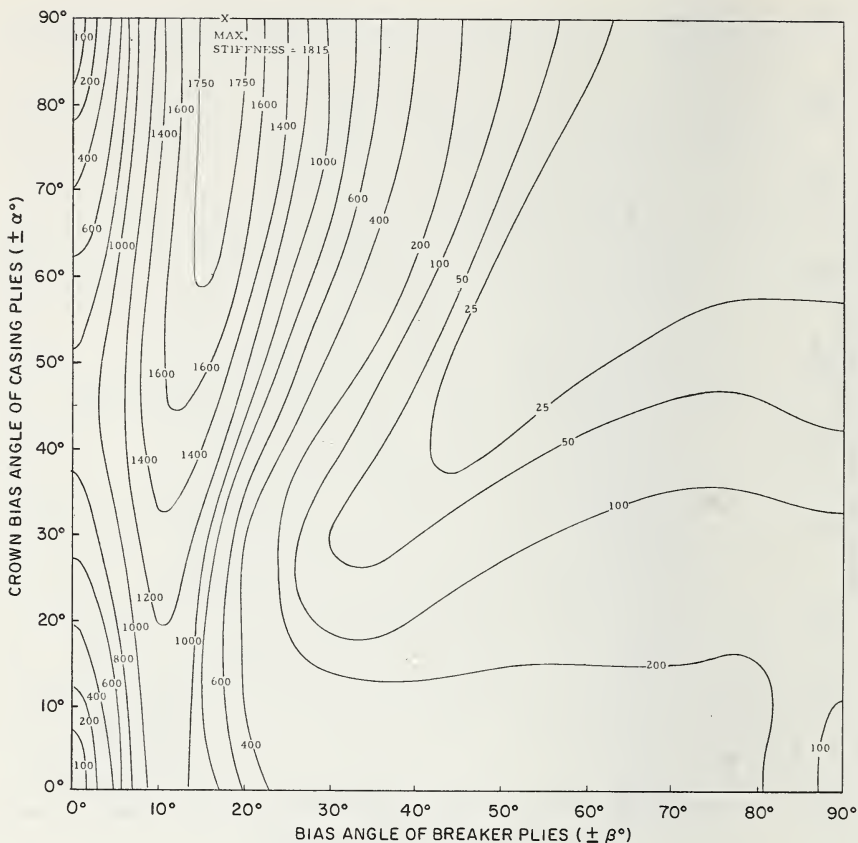


FIGURE 2.24. *Crown stiffness of tires with a 4-ply rayon casing and 2-ply steel breaker of ply stiffness $(E_c A_n)/T = 123,000 \text{ lb/in}^2$.*

harmonic motion in terms of the dimensionless damping ξ by means of the relation

$$Q = \frac{1}{2\xi}$$

Their conclusions generally were that the damping of such bending waves in fabric reinforced rubber appears to be caused primarily by energy loss in shear, and that such loss characteristics tended to increase rather markedly with the frequency above a level of about 100 Hz.

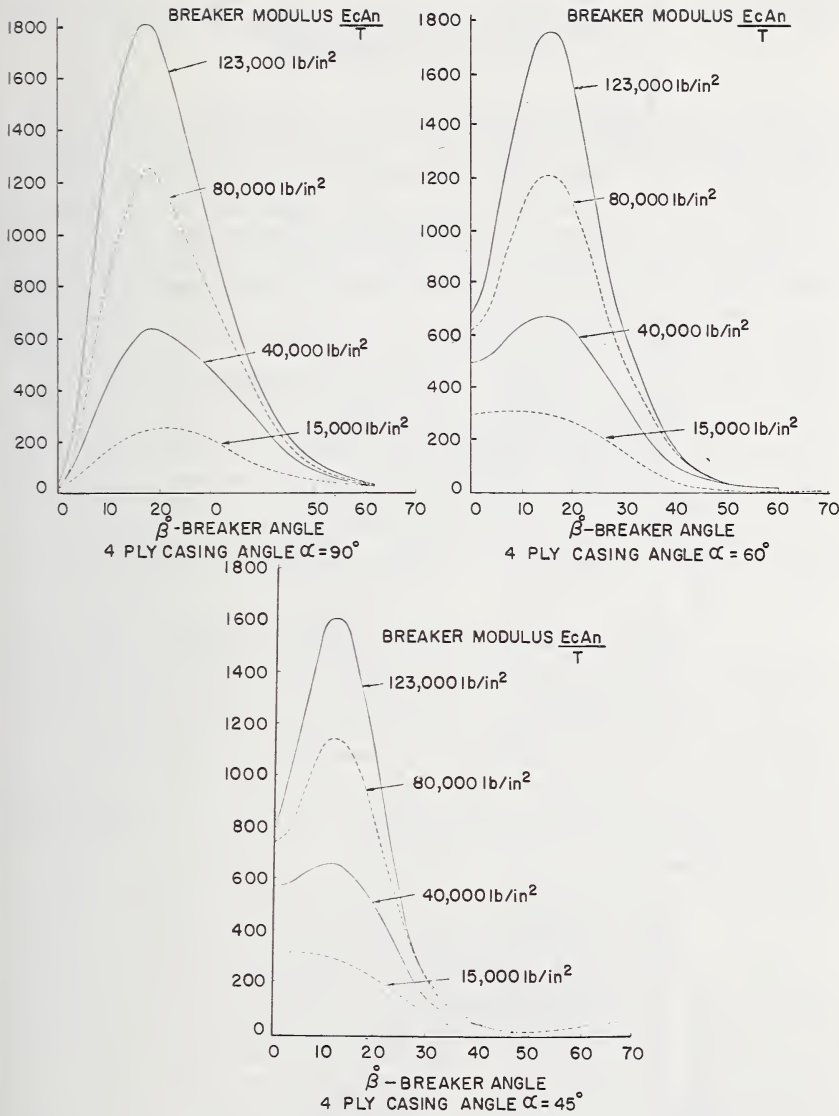


FIGURE 2.25. *Effect of breaker angle and modulus on stiffness of breaker region of cross bias cover.*

Some of their results are shown in figure 2.27, while the influence of membrane tension on energy dissipation in damping is shown more clearly in figure 2.28.

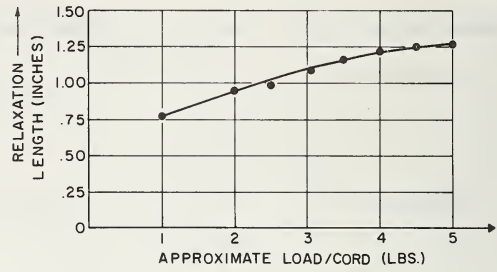


FIGURE 2.26. Transducer load vs. distance of load transducer from free end of cord.

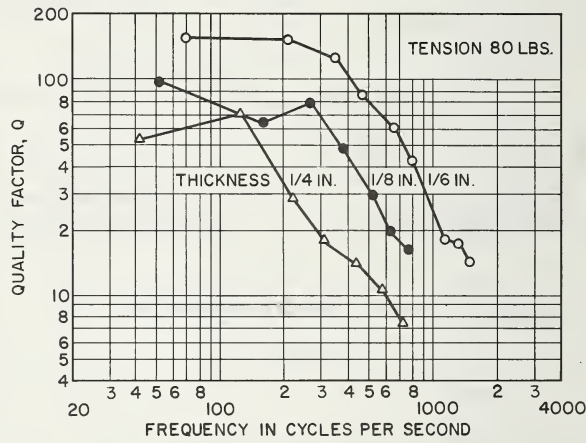


FIGURE 2.27. Q of fabric-reinforced rubber specimens with two plies of cord as a function of rubber thickness.

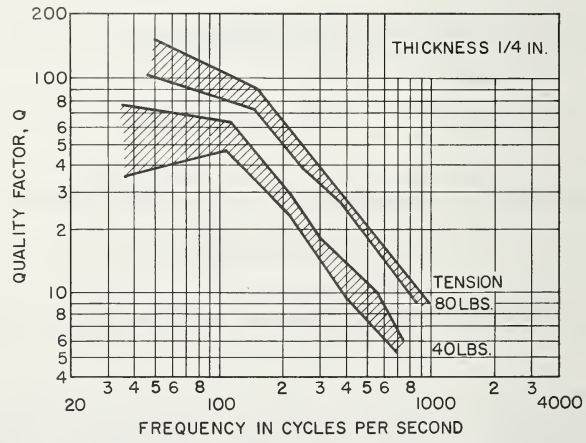


FIGURE 2.28. Q of fabric-reinforced rubber specimen with one ply of cord as a function of tension.

2.2. Strength and Failure Mechanisms for Cord Reinforced Rubber

The failure mechanisms of cord reinforced rubber are extremely complex and have recently been the subject of considerable active research. For purposes of application to pneumatic tires, most of the emphasis lies on the fatigue failure characteristics of these materials, since service requirements demand that a pneumatic tire undergo a very large number of loading cycles. This inevitably forces the tire designer to proportion the carcass textile reinforcement in such a way that ultimate static strength is many times the inflation pressure or the applied load. Large static factors of safety are the rule in tire design.

When ultimate tensile strength is to be calculated, most approximations consider that cord failure results when cord loads reach a tensile value equal to that which they exhibit in simple direct tension tests. In other words, ultimate strength of cord reinforced rubbers is equivalent to cord strength uninfluenced by the surrounding rubber, so that the rubber neither increases nor decreases the ultimate tensile strength of the cord. To that extent the cord-rubber system may be thought of as uncoupled in regard to ultimate strength. For example, bursting of a tire due to inflation would be predicted on a cord tension basis without regard to presence of the rubber.

The more common loading environment involves the fatigue characteristics of cord reinforced rubber, and here the situation is much more complex. First of all, it is necessary to recognize that the complete cord reinforced rubber system consists of three phases: first, the textile cord itself, secondly, the adhesive which is applied to the cord surface in order to promote adhesion to the rubber, and finally the surrounding rubber matrix. Details of the rubber and cord characteristics are given in previous chapters of this volume, but it should be noted that the cord is made of a multiplicity of filaments which are first twisted to form a strand, followed by the twisting in opposite directions of two or more strands to form a cord. For purposes of pneumatic tire construction two and three strand cords are the most commonly used.

Since many service failures seem to occur as a result of fatigue, a great deal of attention has been directed to mechanisms of tire fatigue failure. In order to describe such mechanisms, it is probably best to do so in some systematic order roughly paralleling that which would occur in an actual tire. For such a description, one may draw upon the work of Eccher [29], Patterson and Anderson [30], Patterson [31], Uzina and Basin [32], Butterworth, Davis, and Platt [33]. A number of other authors and references will be cited in addition, but the basic mechanism of fatigue failure as it is now understood is well delineated by these authors.

First of all, two primary concepts regarding fatigue failure should be stated clearly:

- a. For cord reinforced rubber, the so-called fatigue failure is, in fact,

a system failure in which the failure is initiated at or very close to the cord-adhesive-rubber interface.

b. A normal fatigue process, such as occurs in metals, does not exist for the cord-adhesive-rubber combination as a whole. However, there exist fatigue mechanisms both for the rubber and for the rubber to adhesive bond, which then directly or indirectly act on the strength of the fabric.

The actual initiation of the processes which precede the fatigue failure of a cord reinforced elastomer has been studied by Eccher [29], by use of the Mallory tube test and by microscopic examination, and by Uzina and Basin [32], using fluorescence analysis as well as photomicrography. Uzina and Basin studied dipped viscose, Nylon 6, cotton and polyamide cords under fatigue conditions and observed the following forms of initial failure on tires which had been run to the point of obvious ply separation:

a. Cord separation accompanied by a considerable part of the adhesive adhering to the rubber, coupled with some adhesive remaining on the cord. Such a mechanism clearly indicates separation occurring within the adhesive layer, but is cohesive in nature.

b. Separation in which a thin film of the adhesive remains attached to the rubber, while in some areas a portion of the rubber remains with the adhesive. This type of separation is much closer to a separation along the adhesive-rubber boundary than type a., and can be termed a composite separation. It is also cohesive in nature.

c. Separation occurring without traces of adhesive film being left on the rubber or of rubber on the cord. Consequently, this separation occurs cleanly at the adhesive-rubber interface and is purely adhesive in nature.

Some of the details of such a cord-rubber-adhesive system are presented here. Table 2.4 gives typical penetration depths for RFL³ dipped cords.

Eccher [29] found by photomicrography that both Mallory test tubes as well as examination of tires implied very similar types of failure initiation.

Butterworth, Davis and Platt [33] have accumulated extensive evidence to show that the types of failures just described are promoted and accelerated when the cord is forced to carry compression in the pneumatic tire structure. Their studies agree with those of Patterson [31], and both authors report that compressive loading of typical tire cord structures in transparent rubber allows one to clearly observe the strain concentra-

³RFL is the common abbreviation for resorcinol-formaldehyde-latex, which is the basic tire cord adhesive. Most commercial adhesives use this as a basis for more sophisticated, proprietary adhesives.

TABLE 2.4. *Depth to which latex-resorcinal-formaldehyde compositions penetrate various cords when dipped*

	Viscose	Nylon	Cotton
Cord diam. (mils*)	35	20	35
Radial dip penetration in fiber diameters	4	3	4
Radial dip penetration (mils)	1.9	3.54	2.8
Fiber diam. (mils)	0.485	1.18	0.7

*1 mil = 0.001 inch.

tion effects of compressive forces on the cord-rubber interface. In particular, the reentrant angle caused by the twisting of the several strands together to form the cord seems to be a point of particularly high strain concentration, and a point which is prone to initiate adhesive system failure under compressive loads. Cord degradation resistance is determined by the ability of the surrounding rubber matrix to control the compressive axial deformation of the cord. Where the adhesive interface fails, this control is lost and filaments traversing the reentrant angle in the cord geometry tend to buckle in an uncontrolled manner. This leads to severe relative deformation between the surrounding rubber matrix and the cord structure. This relative deformation increases in severity because, with continued cycling, the cord geometry opens up (reduction in cord packing factor) leading to increased filament buckling and an increased interaction with the matrix. A reduction in cord packing factor leads to the induction of higher tensile strains in filament lengths having a low angle of inclination to the cord axis—mainly filaments on the external surface of the cord. Test data in general indicates that cord fatigue is greatly dependent upon the presence of compressive stresses in the cord, as reported by Illingworth [35].

Following the initial failure somewhere in the cord-adhesive-rubber system, present evidence points toward the occurrence of increased relative motion between the cord and rubber, as well as among the cord filaments themselves. This may result in chafing or rubbing of the cord filaments against one another, with the consequent possibility of initiating sites of microscopic mechanical damage on the surface of the individual filaments. Patterson [31] has studied this in some detail and concludes that the mechanism of filament rupture in the fatigue of individual nylon monofilaments is directly traceable to the presence of some small surface defect. Such a defect serves as an initiator of fatigue failure, which then propagates due to alternating bending of the monofilament. Patterson found that if the imperfection occurs at the point of maximum compression in bending, the fatigue life of a monofilament was greatly decreased. Simple bending seems to account for the mechanism

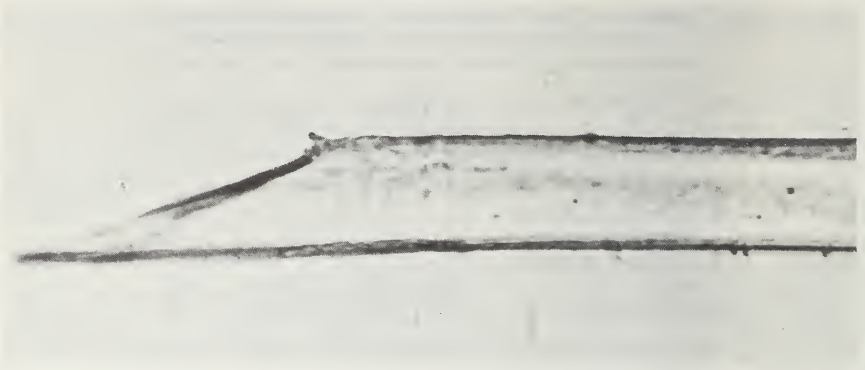


FIGURE 2.29. *Bias ruptured filament.*

of failure since the appearance of broken filaments taken from pneumatic tires and broken filaments fatigued in bending are essentially identical. Figure 2.29 shows an enlargement of a filament taken from a tire after some running.

This same problem has recently been studied by Platt and Butterworth. They conclude that the creation of a filament buckle and the location

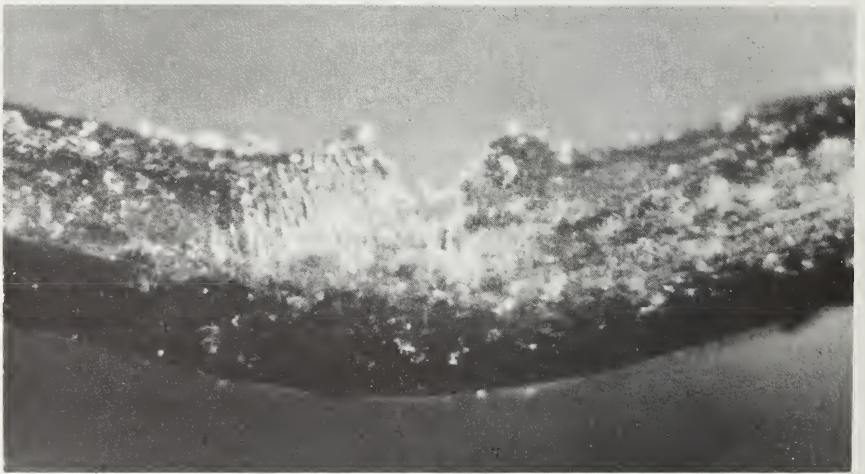


FIGURE 2.30a. *Filament failure modes. (Courtesy of Fabric Research Laboratories, Inc.)*

Failure initiated on inside of bend flex zone. Nylon monofilament whose diameter is equivalent to a standard 2 ply nylon cord ~ 20 mils.

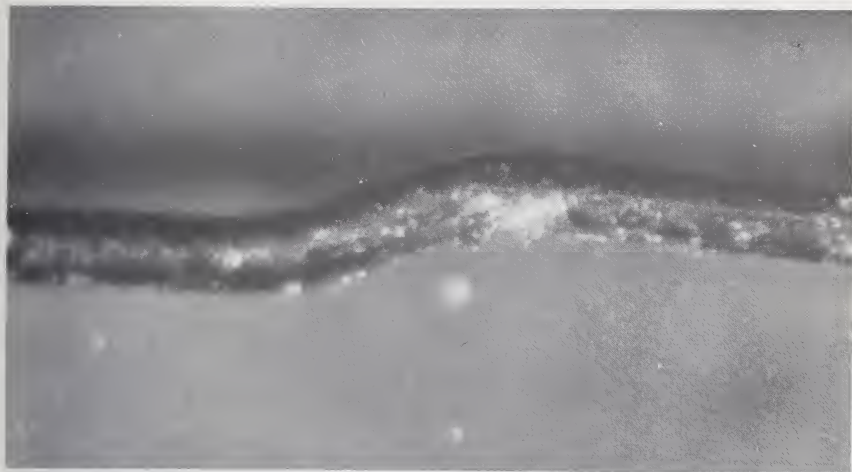


FIGURE 2.30b. *Filament failure modes. (Courtesy of Fabric Research Laboratories, Inc.)*

Two bend buckle of 20 mil nylon monofilament.

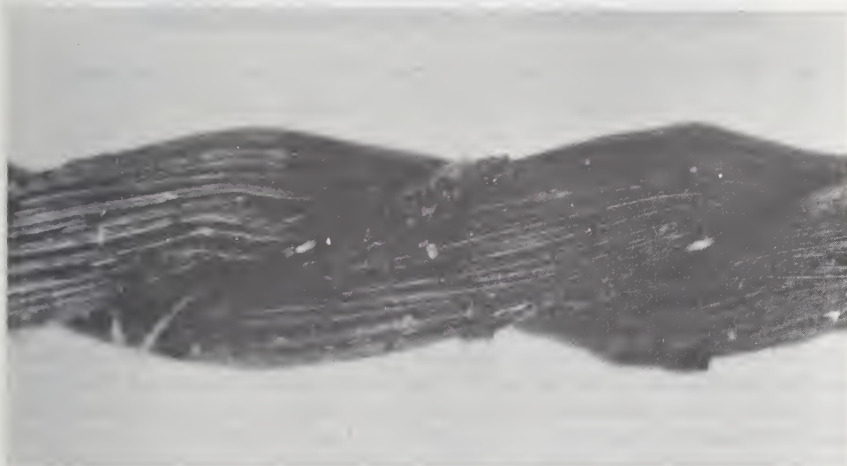


FIGURE 2.30c. *Filament failure modes. (Courtesy of Fabric Research Laboratories, Inc.)*

Partially failed nylon tire cord. Degraded in rubber on Goodrich test machine.

3 percent tension
15 percent compression

cyclic axial
cord strain

Note inception of filament buckle failure at cord ply line.

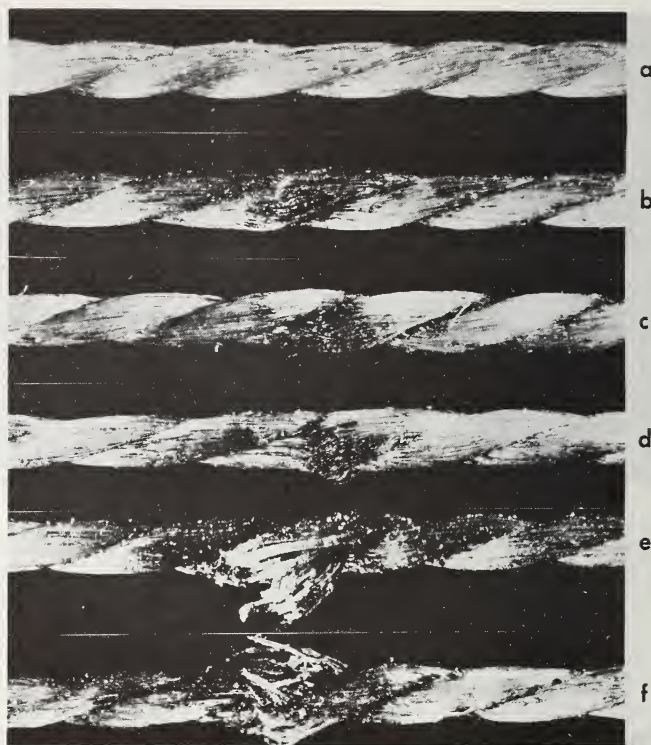


FIGURE 2.30d. *Filament failure modes.* (Courtesy of Fabric Research Laboratories, Inc.)

Failure sequence in two-ply dipped and stretched nylon tire cord.

of the buckle angles is determined by the position of the element of filament, its degree of association with neighboring filaments and tri-axial stress state to which it is subjected. They conclude that it is unlikely that *all* filament failures are initiated by a defect of a filament leading to a buckle failure. They observed that when monofilaments of diameter equivalent to a conventional tire cord are subjected to simulated tire use, the monofilament tends to buckle in fashion similar in shape and character to buckles noted in individual filaments taken from fatigued tire cords. Such buckles are illustrated in figure 2.30. In particular, the two angle buckle shown there failed initially on the compression side of the buckle but ultimately failed in tension.

The process of tire degradation therefore apparently involves failure first at the surface of the cord, by one of the three forms proposed by Uzina and Basin, allowing detachment of the cord from the surrounding



FIGURE 2.30e. *Filament failure modes.* (Courtesy of Fabric Research Laboratories, Inc.)

20 mil nylon monofil, failure in rubber, induced by tensile and compressive strain cycling.

rubber. This is followed, according to Butterworth, Davis, and Platt [33], by mechanical working of the cord leading to a reversion of its tensile properties to those of the undipped, unstretched cord. Failure of individual filaments next occurs, in a sequential fashion, finally leading to total cord failure. This hypothesis seems to be in accord with the experimental evidence obtained by studying the characteristics of tires which have been run on both road and test wheels, since most observations have found that tire cords which have lost a fraction of their strength, due to monofilament fracture in fatigue also exhibit reduced adhesive bond strength to the surrounding rubber, as measured by strip-out tests.

The process of cord degradation goes forward by means of individual monofilament fatigue fracture. The nature of this process is clearly statistical and is not well understood. Patterson and Anderson [30] carried out an extensive study of the residual strength of nylon tire cords in tires which had been run on test wheels, while similar studies on rayon cords in highway service have been carried out by Klein, Platt, and Hamburger



FIGURE 2.30f. *Filament failure modes.* (Courtesy of Fabric Research Laboratories, Inc.)

Partially failed nylon tire cord.

[36]. Both authors conclude that cord strength does not linearly degrade with mileage. As a matter of fact, it is this particular area which represents one of the substantially unknown regions in the process of tire cord degradation, since both these studies indicate that after an initial, relatively rapid loss of cord strength there follows a long period in which the rate of loss is rather small. Typical data are shown in figures 2.31 and 2.32. The reason for this initial loss is as yet uncertain, but it has been postulated that it is due to physical and geometric rearrangement. Even in fatigue-failed tires, cords adjacent to the failure are in general of normal strength. It must be concluded that the cord failure process, once initiated, is somehow catastrophic and runs a rapid course, similar to the effects found in propagation of a fatigue crack in metals.

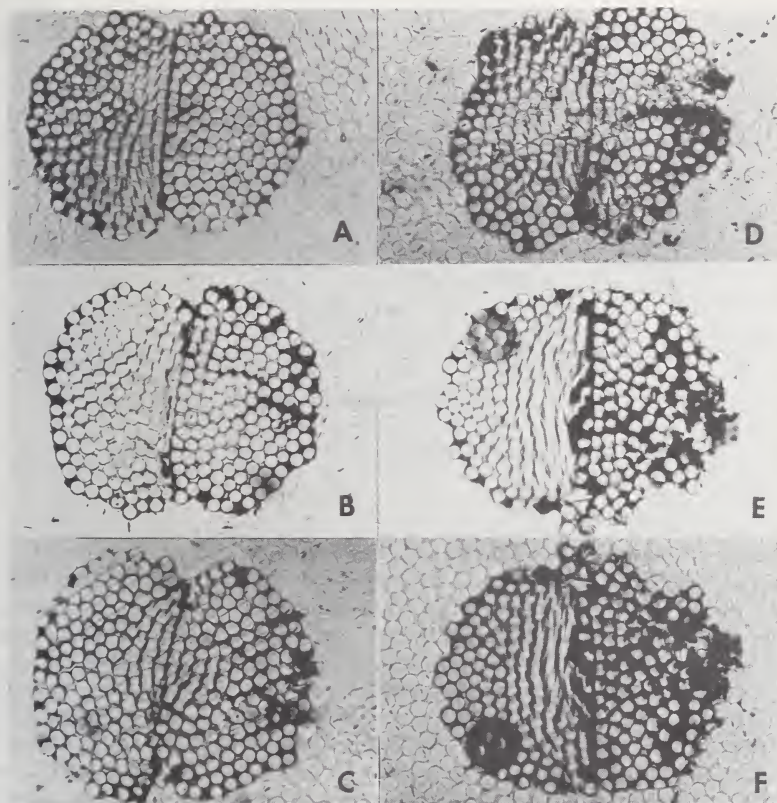


FIGURE 2.30g. Filament failure modes. (Courtesy of Fabric Research Laboratories, Inc.)

Cord cross section photomicrographs. Failure sequence A-F.

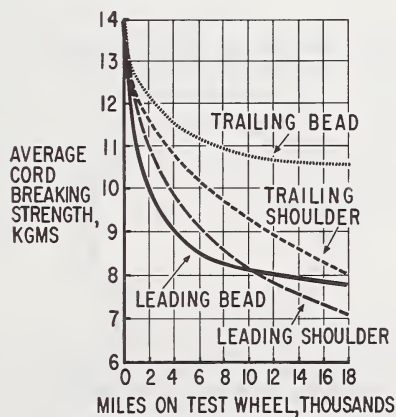


FIGURE 2.31. Average breaking strength of sections of first-ply cords.

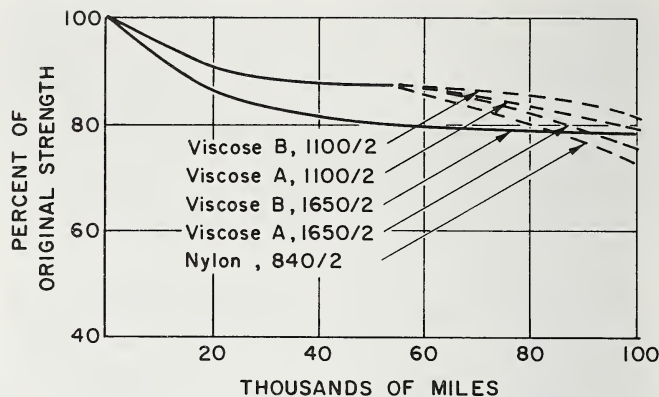


FIGURE 2.32. Percent residual cord strength vs. tire mileage.

There are substantial differences between cord failure rates in different parts of the tire. Patterson and Anderson report the most critical regions to be at the shoulder and shortly below the turn-up region, as shown in figure 2.33, and further depends on the direction of the cord with respect to the tire direction of motion, as previously shown in figure 2.31.

Eccher [29] has discussed in some detail the use of various tests, and particularly the Mallory tube test, as a mechanism for simulating the behavior of the tire materials in service insofar as such fatigue characteristics are concerned. He concludes that the Mallory test, which uses a tube bent through a 90° arc, held under internal pressure and rotated at high speed, is valuable in reproducing cord-adhesive-rubber system failure similar to those observed in tires. A sketch of the Mallory appa-

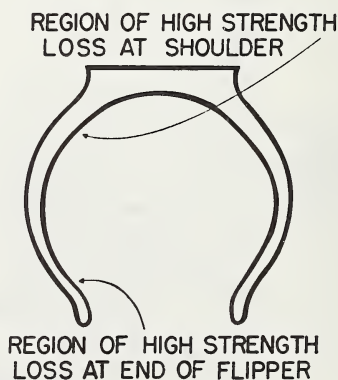


FIGURE 2.33. Locations of maximum cord damage in tire after flexing test.

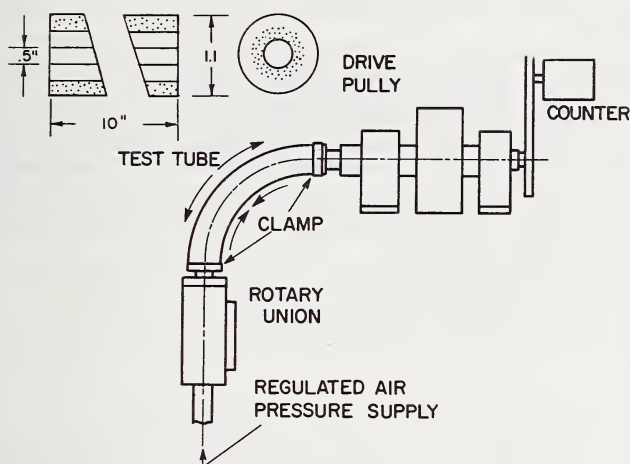


FIGURE 2.34. Sketch of Mallory tube test.

ratus is shown in figure 2.34. A number of other test devices have been designed to induce cord fatigue, and since this is an area related but not particularly pertinent to tire mechanics, the reader is again referred to Eccher [29] for a more thorough discussion of various test methods.

Once a cord has failed, the loss of strength throws additional load to neighboring cords in such a way that under favorable conditions an adhesive separation of one of the types previously mentioned may begin in the neighboring cord, followed by individual filament rupture and eventual cord tensile fracture. Under sufficiently severe loads this process can result in the propagation of a failure.

Finally, it might be of some brief interest to indicate the magnitude of the problem of fatigue failure of tire materials. This can only be estimated roughly, but the data of Starks [34], taken on the British Motorway M.1 in 1962-63, showed that the percentage of total tire failures was caused almost exactly half by puncture and half by burst, the latter representing a fatigue failure of some sort or another. Therefore, the question of the fatigue of cord reinforced rubber is not only complex but very practical indeed.

References

- [1] Hashin, Z., Theory of mechanical behavior of heterogeneous media, *Appl. Mech. Rev.* **17** (1), 1-8 (1964).
- [2] Frank, F., and Hofferberth, W., Mechanics of the pneumatic tire, *Rubber Chem. Tech.* **40** (1), 271-322 (Feb. 1967).
- [3] Clark, S. K., A review of cord-rubber elastic characteristics, *Rubber Chem. Tech.* **37** (5), 1365-1390 (Dec. 1964).

- [4] Rivlin, R. S., Plane strain of a net formed by inextensible cords, *J. Ratl. Mech. Anal.* **4**, 951 (1955).
- [5] Rivlin, R. S., Networks of inextensible cords, *Nonlinear Problems of Engineering*, W. F. Ames, ed. (Academic Press, New York, 1964).
- [6] Genensky, S. M., and Rivlin, R. S., Infinitesimal plane strain in a network of elastic cords, *Arch. Ratl. Mech. Anal.* **4**, 30-34 (1959).
- [7] Adkins, J. E., Large elastic deformations, *Progress in Solid Mechanics*, Vol. II, I. N. Sneddon and R. Hill, eds. (North Holland Publishing Co., Amsterdam, 1961).
- [8] Adkins, J. E., Cylindrically symmetrical deformations of incompressible elastic materials reinforced with inextensible cords, *J. Ratl. Mech. Anal.* **5**, 189 (1956).
- [9] Adkins, J. E., Finite deformation of materials exhibiting curvilinear aeolotropy, *Proc. Roy. Soc. A* **229**, 119 (1955).
- [10] Adkins, J. E., Finite plane deformation in thin elastic sheets reinforced with inextensible cords, *Phil. Trans. Roy. Soc. (London)* **A249**, 125 (1956).
- [11] Adkins, J. E., and Rivlin, R. S., Large elastic deformations of isotropic materials, X: reinforcement by inextensible cords, *Phil. Trans. Roy. Soc. (London)* **A248**, 201 (1955).
- [12] Clark, S. K., and Dodge, R. N., A comparison of net and continuum theory for cord reinforced laminates, *Textile Res. J.* **38** (9), 931 (Sept. 1968).
- [13] Clark, S. K., Dodge, R. N., and Field, N. L., Calculation of the elastic constants of a single sheet of rubber-coated fabric, Report 02957-13-T, (Office of Research Administration, The University of Michigan, Ann Arbor, Mich., Oct. 1961).
- [14] Stress-strain relations in wood and plywood considered as orthotropic materials, Rept. No. 1503 (U.S. Dept. of Agriculture, Forest Products Laboratory, Forest Service, Madison, Wisc., March 1956).
- [15] Hearmon, R. F. S., *An Introduction to Applied Anisotropic Elasticity* (Oxford University Press, London, 1961).
- [16] Hashin, Z., and Rosen, B. W., *J. Appl. Mech.* **31**, 223 (1964).
- [17] Whitney, J. M., Basic mechanics of fiber reinforced composite materials, *Textile Res. J.* **37**, 1056-1062 (Dec. 1967).
- [18] Ekvall, J. C., Elastic properties of orthotropic monofilament laminates, *ASME Paper No. 61-AV-56*, (1961).
- [19] Clark, S. K., The plane elastic characteristics of cord-rubber laminates, *Textile Res. J.* **33**, 295 (1963).
- [20] Budd, C. B. (Private communication).
- [21] Hofferberth, W., The elasticity law for composite rubber-textile bodies, *Gummi Asbest* **9**, 240 (1956).
- [22] Herrmann, L. R., and Pister, K. S., Composite properties of filament-resin systems, *ASME Paper No. 63-WA-239*, (1963).
- [23] Hoff, N. J., The strength of laminates and sandwich structural elements, Chapt. 1, *Engineering Laminates*, A. G. H. Dietz, ed. (John Wiley and Sons, New York, 1949).
- [24] Clark, S. K., Internal characteristics of orthotropic laminates, *Textile Res. J.* **33**, 935 (1963).
- [25] Stein, Manuel, and Hedgepeth, J. M., Analysis of partly wrinkled membranes, *NASA TN D-813* (National Aeronautics and Space Administration, Washington, D.C., July 1961).
- [26] Hedgepeth, J. M., Stress concentrations in filamentary structures, *NASA TN D-882* (National Aeronautics and Space Administration, Washington, D.C., May 1961).
- [27] Clark, S. K., and Reid, F. R. (Unpublished data).
- [28] Weiner, F. M., and Gogos, C. M., *Rubber Chem. Tech.* **34** (1), 158 (1961).
- [29] Eccher, S., Typical damage in Mallory tubes and tire carcasses, *Rubber Chem. Tech.* **19**, 299 (1966).
- [30] Patterson, R. G., and Anderson, R. K., Fatigue failure in nylon reinforced tires, *Rubber Chem. Tech.* **38** (4) (Nov. 1965).
- [31] Patterson, R. G., Mechanics of bias filament rupture in fatigue of nylon, *Rubber Chem. Tech.* **39** (5) (Dec. 1966).
- [32] Uzina, R. V., and Basin, V. E., Study of the nature of failure in the system cord-adhesive-rubber, *Sov. Rubber Tech.* **19**, 27-33 (July 1960).
- [33] Butterworth, G. A. M., Davis, S. J., and Platt, M. M., The response of nylon tire cord in rubber systems to cyclical strain (Fabric Research Laboratories, Inc., unpublished report).

- [34] Starks, H. J. H., Tyre failures in accidents on the motorway M. 1 in 1962-63, *Inst. Auto. Assess.* **17** (1), 17-25 (1966).
- [35] Illingworth, J. W., *J. Textile Inst.* **44**, 328 (1953).
- [36] Klein, W. G., Platt, M. M., and Hamburger, W. J., Cord fatigue in fleet tested tires (Fabric Research Laboratories, Dedham, Mass.).
- [37] Platt, M. M., and Butterworth, G. A. M. (Private communication).
- [38] Gough, V. E., Stiffness of cord/rubber constructions, *Kautschuk und Gummi*, **20**, 469-482 (Aug. 1967).



CHAPTER 3

Structure of the Tire

V. E. Gough ¹

	Page
3.1. General considerations.....	356
3.2. Pneumatic tire structure—general features.....	360
3.3. Flexible filament and soft matrix constructions.....	369
3.4. Tire construction methods.....	379
3.5. Cord path—practical factors determining selection.....	385
3.6. Calculation of cord length.....	386
3.7. Analysis of manufacturing methods by R vs. $\cos \phi$ charts...	390
3.8. Mechanism of load carrying—infinitely flexible membrane...	392
3.9. Mechanism of load carrying—tire structure.....	398
References.....	404

¹ Formerly with the Dunlop Company, Birmingham, England (Retired. Present address: Croyde, Devon, England.)

3.1. General Considerations

That the function of a tire is to transmit the forces which drive, brake, and guide the vehicle as well as to carry the load is now accepted by all—it is, of course, the only component of the vehicle which makes contact with the road surface. Also, it is now being recognized that the tire not only has to absorb local road surface irregularities over a wide range of types of road materials but also has to provide a vibration-free motion on smooth roads comparable with that given by a circular solid wheel on a perfectly straight guideway. There is a conflict in these differing requirements. Flexibility is required for the absorption of road rugosity. Constancy of effective dimensions is needed for the exacting requirements of constant axle height, straight line motion and uniformity of effective rolling radius on a flat, smooth road as illustrated in figure 3.1. This conflict is further heightened by the fact that basically a pneumatic tire structure is a surface of revolution, usually of curved cross section in a radial plane, and consequently is a surface of double curvature. A surface of double curvature is, from a geometrical point of view, a non-developable surface and yet it must deform to give an area of contact on a plane road surface.

These conflicting geometric and mechanical requirements demand that a vehicle tire is either:

- a. a solid tire made to a high geometrical precision from relatively low modulus, highly elastic material capable of substantial deformation, or
- b. a gas inflated envelope with certain exacting requirements to be met.

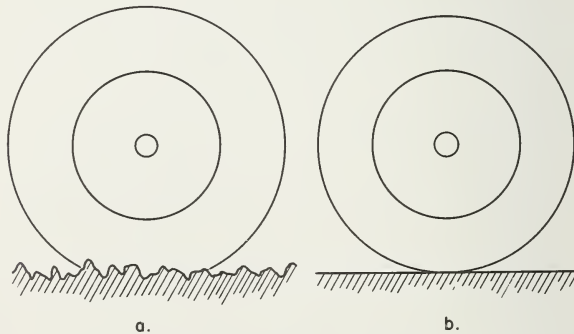


FIGURE 3.1. *Conflicting requirements which a tire has to meet.*

- (a) ability to absorb surface irregularities—this requires flexibility.
- (b) constant axle height and effective rolling radius on smooth roads—this requires uniformity, and is most easily obtained with a rigid wheel.

It will be seen later that this envelope of double curvature usually is an anisotropic hollow structure made of flexible filaments of high modulus material such as textiles, metal or glass, embedded in and bonded to a matrix of low modulus material such as rubber or a rubber-like polymer. The orientation of the filaments in this envelope has to be such as to meet certain contrasting structural requirements. These are:

- a. no appreciable change of size upon inflation,
- b. an ability to envelop obstacles without sustaining damage,
- c. the ability to deform from a surface of double curvature to a plane surface, and
- d. enough rigidity to develop substantial forces in any direction.

It is this type of structure in which we are interested.

Inflated shell structures having surfaces of double curvature made solely of a single isotropic material have in the past failed to meet all of the several requirements outlined above. The capability of having a long fatigue life when continuously flexed from a surface of double curvature to a flat surface and back again—and at the same time having adequate structural rigidity to carry the vehicle load and resist the drive, brake and side force for a practical automobile, and also at the same time providing a constant dimensional size nearly independent of the inflation pressure, have not been met by an isotropic thin or thick shell of materials yet known.

Uninflated thin shell structures of double curvature made from high modulus materials such as metals or the semi-rigid or rigid plastics, including all known forms of high modulus polymers, have not been practical since the necessary flat contact cannot be developed without stressing the material beyond its yield point or at least to the point where fatigue life is very short.

The same limitations apply to open frame structures, unsupported by gas inflation, made from a single material or a combination of materials, as anyone who has had experience in designing spring wheel alternatives to the pneumatic tire will agree. Such structures can, however, be designed to meet the requirements associated with low gravitational fields, e.g., moon vehicles. Consider the design of a tire-like space frame consisting of a series of steel rings of appropriate dimensions for use on an automobile on earth, such as shown in figure 3.2. It is found that either the rings are thin enough to be capable of deflecting the required amount but can only carry a trivial load, or, they are stiff enough to carry a useful load but too stiff to change their shape to a flat one without exceeding the yield point or fatigue stress limits of the metal or other material being used. Practically the only type of spring wheel design to get further than the drawing board stage is a series of helical springs supporting a chain belt or flexible ring as shown in figure 3.3. This is a sort of solid tire in which the low modulus material is replaced by suitably fashioned high

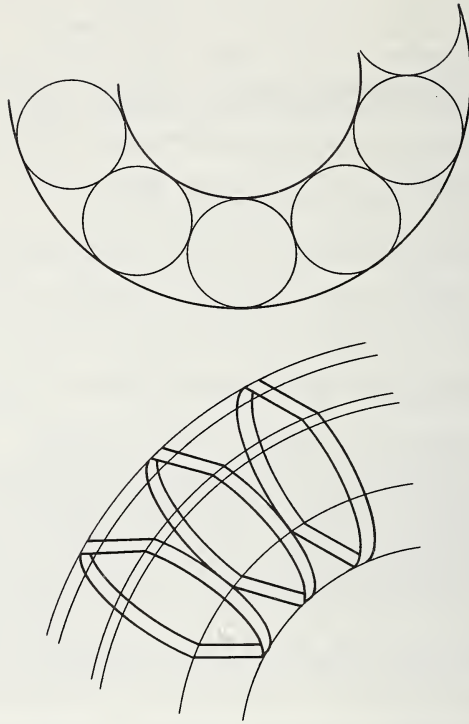


FIGURE 3.2. *Space frame and spring wheels built of steel hoops in any configuration can be designed for either load requirement or deflection requirement, but not both for a practical earth vehicle.*

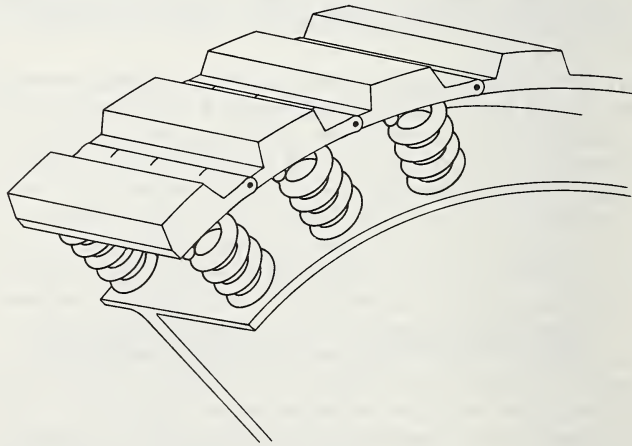


FIGURE 3.3. *One form of spring wheel surviving initial tests, but which does not compete with pneumatic tires.*

modulus material to get a long length of metal torsion bar in the space available. Such devices have, however, never seriously challenged even solid rubber tires, let alone the pneumatic tire.

Consideration of these various concepts and designs may seem to be somewhat removed from the structure of a pneumatic tire, but they have some relevance to the fact that a pneumatic tire casing is a practical working device precisely because it is comprised of high modulus flexible filaments embedded in and bonded to a low modulus matrix. Such an anisotropic shell structure, although unable to carry much load by itself, can carry substantial loads when inflated by a gas under pressure, and can still meet the geometric and mechanical requirements stated earlier. One reason for this is that the ground contact pressure within the contact patch is primarily determined by the pressure of the gas inflating the tire structure, so that the load carried by the tire is not limited by the conflict of material properties in the same way as it is in the case of the solid rubber tire. In the case of the solid tire the entire load is carried by only a small fraction of the total tire volume, in fact, to a first approximation it is carried by a volume made up of the tire cross-sectional area times the length of the contact patch. To carry a greater load at no greater tire stress requires a wider, heavier tire. The total weight of the tire is thus approximately the ratio of the tire periphery to the contact patch length multiplied by the weight of the material being locally stressed. In a pneumatic tire, on the other hand, such a calculation is not pertinent since load carrying ability is controlled by contact patch area and inflation pressure. Increasing inflation pressure contributes negligibly to tire weight.

All these points and several others lead to the fundamental importance of the character of the structure of the pneumatic tire.

Before describing in outline the character of the pneumatic tire structure it must be stated that full or complete mathematical analyses of these structures in the form of closed functions are unattainable precisely because of the highly redundant nature of the structure.

Useful analyses, usually approximate in character, of a number of aspects of major importance are possible. This is so in spite of the fact that the relevant mechanics problems are usually considered difficult subjects, such as finite deformation of a nondevelopable surface of revolution, nonlinear elastic and time dependent or nonlinear hysteretic properties of the materials, and added complexity due to anisotropy of the basic structure. The problems are also fundamentally difficult because of the fact that the final structure is highly redundant, even if none of these effects were present, and all materials were linear and the law of superposition was applicable.

The fact that the pneumatic tire is essential to the basis of twentieth century living and that innumerable forms, types, and ranges of sizes are manufactured on a mass production basis without any noticeable competition from alternative devices shows that tire designers have succeeded in producing viable and efficient product designs using the simple but theoretical analyses or concepts which are available to them.

The objective in this chapter is to try to examine the fundamentals of

why the pneumatic tire is made from filaments embedded in a lower modulus matrix and to point out the principles of the consequences of this fact, along with the fact that the structure requires gas inflation to be an effective load carrying device. It is not intended to discuss current design rules and practice.

3.2. Pneumatic Tire Structure—General Features

A pneumatic tire has certain essential structural elements. The most important is the casing or carcass made up of many flexible filaments of high modulus cord, of natural textile, synthetic polymer, glass fibre, or fine hard drawn steel embedded in and bonded to a matrix of low modulus polymeric material, usually natural or synthetic rubber.

The flexible high modulus cords are usually disposed as multi-filament layers. One, two, or more such layers of parallel cords are used according to the design requirements. The number of layers is decided in the first instance by the tire type, the tire size and the inflation pressure to be used. The first commercially successful tires were made from woven fabric as shown in figure 3.4a, and even sheet leather was proposed in the first recorded design. It was only when layers of parallel cords, not woven, were introduced that tire endurance life reached a reliable level and adequate tire performance could be taken for granted. This is shown in figure 3.4b. Although the principle is well established that cords in a given layer must be in one direction only, and cords in another direction must be in another layer or ply, the parallel cords in a ply are frequently connected by light weight wefts, see figure 3.4c. These fine wefts are not

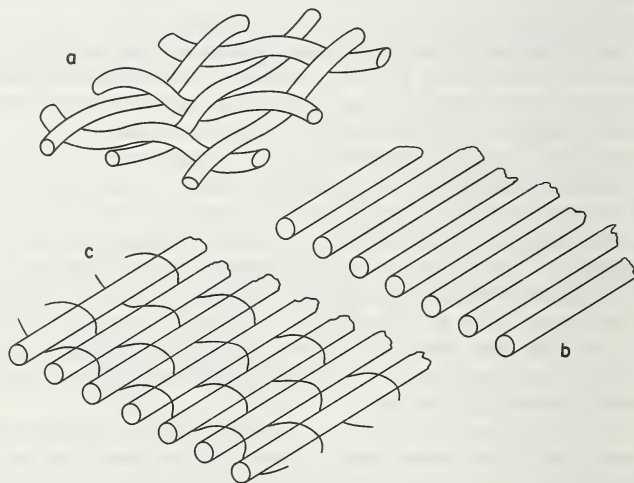


FIGURE 3.4. *Filament arrangements which have been used successfully in pneumatic tires, at one time or another.*

- (a) Woven cord (obsolete).
- (b) Weftless cord.
- (c) Cord material with light wefts.

stress carrying members and serve only to hold the cords in their appropriate relationship during manufacturing processing. The need for these wefts is principally during any dipping or adhesion treatment prior to rubbering, and during the feed stage of the rubbering process on the calender. It is essential that the direction of the wefts are not diverted substantially from their normal direction of lying at right angles to the main cords of the ply during these process stages because, during the subsequent shearing within the ply which occurs during the shaping stage of tire manufacture, the wefts could damage or take a position so as to cause damage to develop during tire life. Sometimes to avoid this problem the wefts are so designed that they fracture during the tire shaping process during manufacture.

It would appear that a continuous ring like a hose would make a suitable tire construction, provided that the tubular tire was so attached to the wheel on which it is mounted that it could not roll off the wheel under the action of sideforce. While constructions of this type have been made for some special applications, these constructions do not form the basis of ordinary pneumatic tires. There are several reasons for this. During the long period of time when all tires had a separate inner tube to contain the inflating gas—and also for the quite large numbers of tires still of this type—it was and is essential that the tire casing can be demounted from the rim of the wheel to enable the inner tube to be fitted and to allow

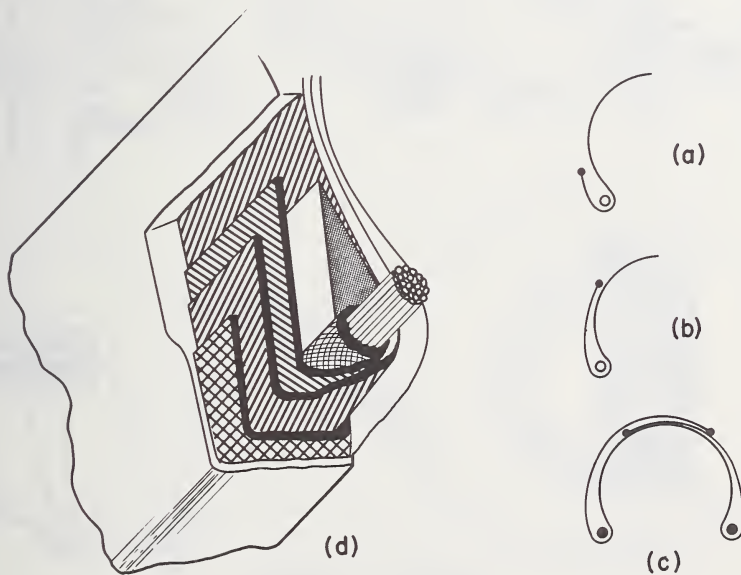


FIGURE 3.5 *Essentials of bead construction.*

- (a) Low turn-up construction.
- (b) High turn-up construction.
- (c) Overlap construction.
- (d) Detail of a typical bead.

for repair after being punctured during road use. Manufacture of the normal demountable casing is far easier, better, and cheaper than any form of tubular tire. Specifically, a tubular tire has to be made substantially in its final shape so that molding and consolidation of the inner surface and plies of the tire are difficult. These layers are readily consolidated by the diaphragm or curing bag in the normal casing of the demountable tire—a device which cannot be employed in the manufacture of a tubular tire as it would be virtually impossible to remove from the finished tire. It is for these reasons that tubeless tires have the same type of demountable casing, although it might have been thought that puncture repair by plugs would cause a trend away from the conventional demountable casing towards the tubular type of tire.

Tubeless tires, that is tires which are designed for use without a separate (removable) inner tube, have a thicker inner lining inside and integral with the tire casing—usually of a material of low permeability.

In order that the tire casing can be demountably fitted to the wheel rim, the layers of the high modulus cords or filaments are turned around bead coils made of a number of turns of high tensile, hard drawn steel wire, located at the inner edge of the tire sidewalls as shown in figure 3.5.

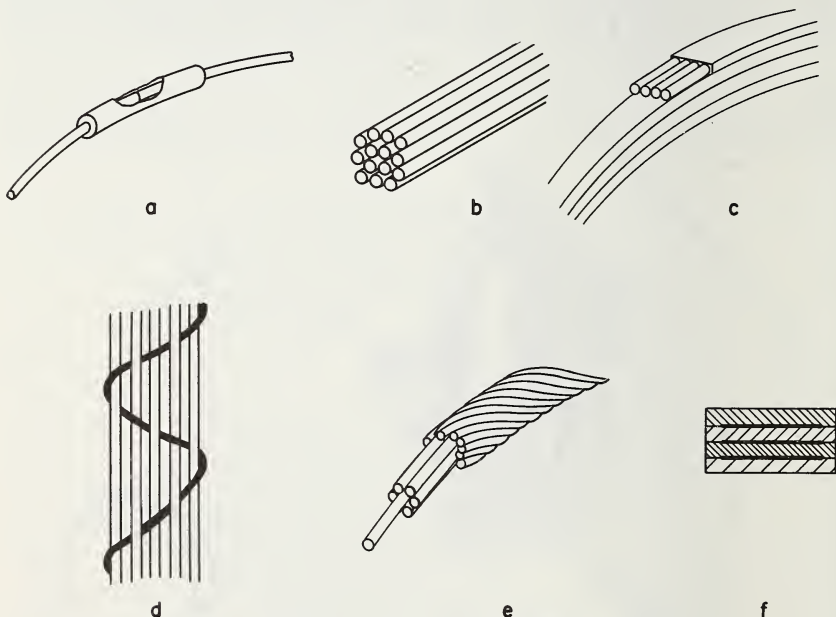


FIGURE 3.6. *Bead wires.*

- (a) Single bead wire for cycle tires.
- (b) Single wire wound to produce a multi-turn coil.
- (c) Tape of several wires wound in layers.
- (d) Multi-wire woven tape.
- (e) Cable bead.
- (f) Tape bead.

Although in cycle tires a single wire bead coil can be used, as in figure 3.6a, beads for pneumatic tires are usually comprised of many turns of hard drawn steel wire. There are several reasons for this fact. The wire-drawing process ensures that the tensile strength (100–150 tons/sq. in.) is several times that of the undrawn material. The multiple wire feature ensures a degree of flexibility essential to tires fitted on a well base or drop-center rim, and is a great help for ease of fitting and seating home on the rim base even for tires fitted on detachable flange or divided wheels, as shown in figure 3.7. The multiple wire bead coil can be made from an appropriate number of turns of one length of wire as in figure 3.6b, or an appropriate number of layers of a tape of several parallel wires embedded in hard rubber as in figure 3.6c, or an appropriate number of layers or turns of woven tape, in which the several main bead wires are held together by an interlacing wave-wound binding wire shown in figure 3.6d.

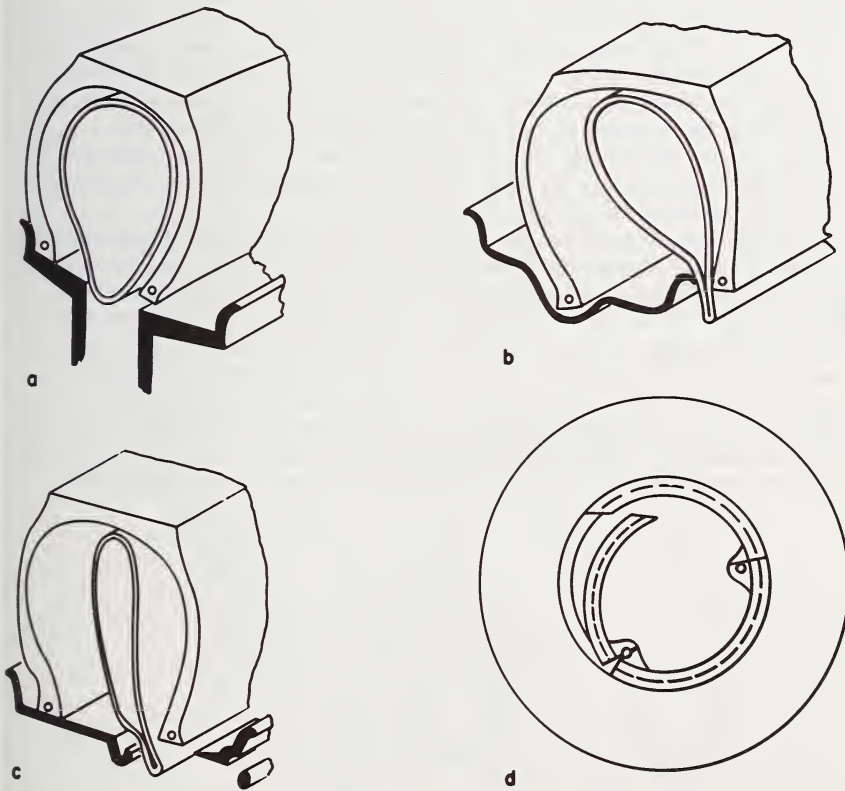


FIGURE 3.7. Means of demounting pneumatic tires and extracting or inserting inner tube.

- (a) Split or divided wheel.
- (b) Well in the rim base or drop center rim.
- (c) Demountable flange on the rim.
- (d) Collapsible rim.

All of these bead wire systems have the wires embedded in hard rubber, the wire having been treated to achieve a bond to the hard rubber, usually by a copper dipping process. The ends of the various wires in these multiple wire coils are not joined in any direct way; the overall strength of the bead is achieved by having an adequate overlap to ensure that the tension is built up through the adherence to the surrounding hard rubber and consequently to the adjacent layer of wires as indicated in figure 3.6c.

The single wire coil of a cycle tire is usually butt-welded to form a continuous loop and often the welded joint is reinforced by a thin sleeve soldered to the wire as in figure 3.6a.

Another form of multiple wire bead coil is the cable bead made from a single length of wire in which each layer of the winding is helically wound at the opposite hand to the immediately previous layer shown in figure 3.6c. This forms a more flexible type of bead than the other types of bead coils and it also makes the ply turn-ups easier.

Since the tension developed in the coils of the upper layers of the layered bead coils shown in figure 3.6e depends on the compression modulus of the intermediate layers of hard rubber, these coils may be under lower stress than the coils at the base of the bead. To minimize such effects when particularly strong beads of low bulk are required, beads have been made of hard drawn flat tape as in figure 3.6f.

Other forms of bead have been used at times in the past but they are of historic interest only, as they were either superseded by the wired-on type or they failed to replace the wire bead.

The tensions in the casing cords set up by the inflation pressure are resisted by the tension developed in the steel wire bead coil. The material in the bead which encases the steel wire coils is pressed against the rim flange of the wheel upon which it is mounted by the inflation pressure within the casing, some of this force being the axial component of the casing cord tensions due to the direction of the sidewall at the bead as shown in figure 3.8. This reaction between rim flange and tire bead enables traction and braking forces to be transmitted by friction between tire bead and rim flange. The magnitude of available traction or braking force is augmented by the radial pressure between tire bead base and

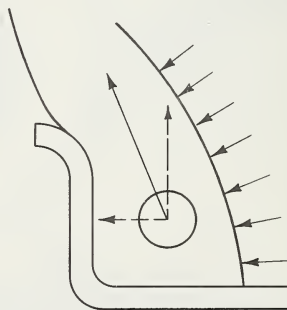


FIGURE 3.8. *Forces pressing bead against rim flange on the wheel to obtain driving and braking reactions.*

wheel rim seat due to the load on the tire and also by the use of an interference fit between bead and rim dimensions.

The height to which the plies are taken after they have passed round the bead coil can be low as in figure 3.5a, or high as in figure 3.5b, or the plies can extend across the crown as in figure 3.5c. In this case of crown overlap the plies can be arranged to give extra casing strength in the crown region compared with the sidewalls.

The choice between these alternatives rests on experience of fatigue life of tires in the field and to some extent on manufacturing considerations. In all cases where a number of plies finish in relatively close proximity the endings are staggered as in figure 3.5d, or a variant of this, so as to cause a gradation of the stress concentration and stress transfer to the main part of the plies. The integrity of the tire structure depends on the security of attachment of these ply ends to the main part of the plies, which form the tire casing, and this depends on the bond between the high modulus cords or filaments and the low modulus material in which the filaments are embedded, and the bond between the various layers of low modulus materials in that region of the tire.

The steel bead coils may have a canvas wrapping. The bead almost always has a form of packing above it to give a suitable path of return for the edges of the plies to the main part of the carcass, as in figure 3.9a. If this packing, or filler, or flipper as it is variously called, were absent the tension would not build up smoothly from zero at the end of the cords to the full value at the bottom edge of the plies of the inner part of the sidewall. If the plies were wrapped round the bead coil only without the filler being present, as in figure 3.9b, only the cranked portion, that is the portion wrapped round the bead coil, would be of use in resisting the

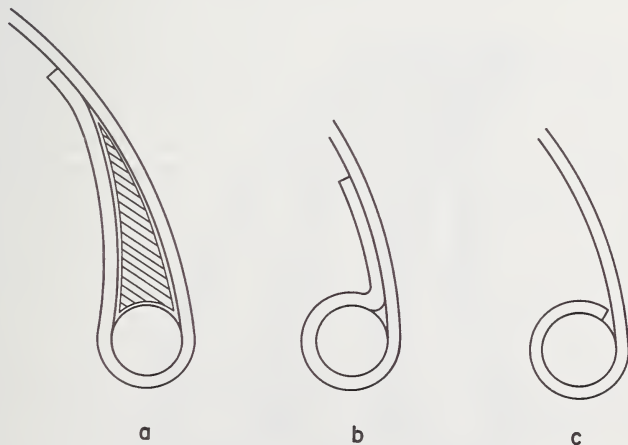


FIGURE 3.9. *Conventional layout to give filler with good return transition for ply end.*

- (a) Satisfactory design with filler.
- (b) Unsatisfactory design with no filler.
- (c) The effectively stressed part of design (b).

cord tensions, and the construction might as well be as in figure 3.9c. In this case the only way that the cord tensions would be resisted and the movement of the plies prevented would be by the stresses set up in the bead coil acting as a ring with a torsional moment applied along its periphery. The resisting moment and the torsional rigidity of even a solid ring, when loaded in this manner, is not great and consequently the usual multiple wire bead coil would be quite inadequate to resist the ply tension. Hence plies are turned up round the bead and passed across the bead filler to adhere to the main plies as in figure 3.9a.

In tires which have a large number of plies, two or even three bead coils are employed, with each bead usually having about the same number of plies around it as in figure 3.10. Multiple bead coils are not used in tires with less than eight to twelve plies and so they appear only in tires for trucks, earthmovers and aircraft.

The bead region commonly has a layer of textile material, such as woven fabric, wrapped around it before the outer rubber covering is applied. This is shown in figure 3.5d. The function of this chafer, as it is called, is to minimize the movements of the tire bead surface in contact with the steel rim flange in the region in which the tire cords are caused to move within the tire wall due to the application of the load on the road. In the area where the tire bulges due to load there are radial and longitudinal movements of the tire wall which are constrained by the chafer, and so abrasive wear is eliminated at this point. In some tire designs rubber chafers of appropriate hardness are suitable for this function.

In a large proportion of tire designs, security of the attachment of tire to rim is augmented by an interference between bead and rim diameters. This interference is always employed on tires fitted to one piece rims. It is essential for tubeless tires, to ensure an airtight seal between bead

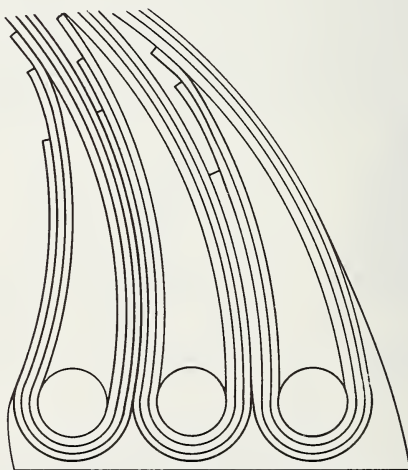
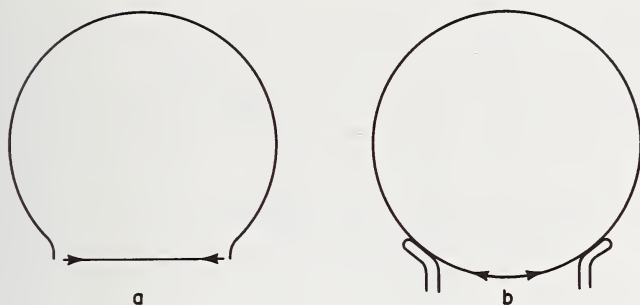


FIGURE 3.10. *Multiple bead coils for tires with a large number of plies.*

FIGURE 3.11. *Axial tension in rim base.*

- (a) Tire and wheel.
(b) Tubular tire.

and rim, and even with tube tires it is more necessary with modern wide base rims than it was in some of the earlier narrow rim widths, because of the relative magnitudes of the axial component of casing tension. The interference causes compression in the material under the steel bead coils, and this in turn sets up a tension in the coils which adds to the effects of inflation. Sometimes dimensions are so chosen that the tension in the bead coils due to interference fit is greater than that due to casing inflation tensions. In a large proportion of designs for low pressure tires, such as passenger car tires, the interference fit is so chosen that the tire has to be inflated to a pressure substantially higher than its operating pressure in order to elastically stretch the coils sufficiently to permit the bead to move up the seat. This ensures that the beads seat home against the rim flange during the fitting of the tire on the rim.

The axially outward component of the casing tensions press the bead against the rim flanges and set up a tension in the rim base, shown in figure 3.11a. In the little-used tubular tire design this tension would be taken either wholly or in part by the casing cords on the inner periphery of the toroid, as illustrated in figure 3.11b. However, it should be noted that tubular tire designs require anchorage points to the wheel, spaced apart as in the manner of the beads of the conventional form of tire. Without such anchorage points the tubular tire would roll sideways and so provide only low resisting forces to sideway drift on the road. It would in consequence have only poor guiding properties. The apparent digression to discuss the almost unused tubular tire design serves to draw attention to important aspects of the function of the bead and of the high modulus wire coils in the bead of the conventional tire.

Demounting of a conventional tire is made possible by either the provision of a well in the rim base, also known as drop center, or by the use of a detachable flange, or by having the wheel in a divided or split form. These are shown in figure 3.7.

The shape of the tire bead and rim on to which it fits can be divided into two main categories, the 5° and 15° taper rims shown in figure 3.12.

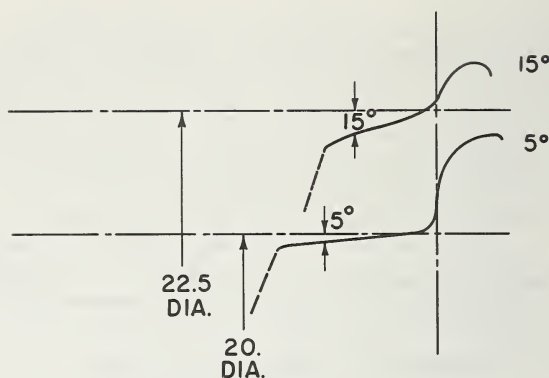


FIGURE 3.12. 5° and 15° taper rim flanges drawn in similar relation to the wheel axis of revolution.

The 15° taper rim design is the more recent design, having been introduced in medium size truck tires in the United States about 15 years ago. Variants of the more generally used 5° taper rim have existed in the past, since it developed from a cylindrical base, or 0° taper. There have been one or two examples in the truck tire range with a taper angle of 8° to 13° . Although such rims may still exist in service, the tires are designed for mounting on the 5° taper.

The flange height of the rim is higher for the 5° rim than for the 15° , and the tire beads have some necessary differing disposition or internal components. Tire sectional heights are shallower for the 15° rim than the 5° . For example, the 22.5 in. rim shown in figure 3.12 uses a tire of the same outer diameter as the 20 in. rim also shown there.

All tires in regular use have two equal size bead coils but there is no theoretical reason why the two bead coil diameters should not be different. One could produce technical arguments in favor of such designs, and in fact various tire designs of this type have been the subject of patents but none have gotten beyond the experimental stage. One practical objection against them, and an objection raised against any asymmetrical or directional tire feature, is that they have to be fitted one specific way. If the unequal rim diameter is coupled with a directional tread pattern feature then two different moulds and tire types are required for any given vehicle.

The technical arguments which have been put forward for the use of a smaller diameter bead seat on the side of the wheel away from the vehicle, and a larger diameter bead seat on the inner side are the lower risk of curb damage with a long sidewall on the outside, and greater diameter for the brake on the inside of the wheel. Further arguments stem from the fact that during cornering of a vehicle the wheels on the outside of the curved path, which are the ones which carry the greater load, are usually caused to camber by the suspension linkwork and this

camber is in the direction to increase the deflection of the outer sidewall of the tire, and hence to lessen the deflection of the inner sidewall, the terms inner and outer being in relation to the vehicle here. The fact that the tires on the inside of the curve are usually cambered so as to shorten the short inner wall more than the long outer wall of the same tire is not important, it is argued, since the load on this tire is lower and so the percentage deflection of the short inner wall of the tire on the inside of the curve need not be any greater than the percentage deflection of the longer outer wall of the tire on the outside of the curve. Even so, no such tires have gotten beyond experimental investigation.

So far, tire casing and beads have been discussed in a general descriptive way. The third important component of a tire is the tread.

The tread performs several functions. It is the only part of the tire to come into contact with the road surface. It provides a wear-resistant layer and also protects the casing. It provides frictional contact with the road sufficient to transmit driving, braking, and cornering forces. These frictional forces may reach a value equal to the load carried by the tire. The tire tread carries a pattern of such character and detail design as to ensure adequate removal of water and other contaminants from the road surface, so as to maintain an adequate level of frictional adhesion between tire and road over a wide range of operational conditions.

For tires intended for operation on soft ground, the character of the deformation of the ground and the laws of soil mechanics determine the form of the tread pattern.

The only type of material which has been successfully used as tread material is rubber or a rubber-like material, that is, a long chain molecular material or polymer of a modulus comparable with that of the matrix in which the filaments are embedded in the rest of the structure. The tread polymer has to be reinforced with suitable ingredients such as carbon black to obtain the required abrasion resistance but this is a subject in itself and will not be discussed here because detail changes in this material do not significantly alter the tire structure required. Experience in the development of spring wheel devices shows that rubber, natural or synthetic, has no competitor as a tread material.

These materials automatically give good friction on dry roads and some aid the achievement of good friction on wet roads. This will not be discussed here since it is covered elsewhere in this book.

3.3. Flexible Filament and Soft Matrix Constructions

Although the patent literature contains a wide variety of alternatives to the use of filaments or cords in tires, all commercially successful tires are now built as a series of layers of flexible high modulus cords encased in a low modulus rubber or rubber-like material, the cords in each layer being in a given path or direction and substantially equi-spaced and parallel.

A conventional cross bias casing or carcass is built of two or more, usually an even number, and most commonly four, layers of parallel cord filaments, the direction of the cords in a layer being at an angle to the principal axes of the tire. Half of the layers have the cords at a positive angle and half at a negative angle as shown in figure 3.13. Usually alternate layers have cords at the opposite hand, thus giving the cross bias effect between adjacent layers at all points in the tire as in figure 3.14a. However, tires have been made with adjacent layers of cords parallel. In the case of four-ply tires the middle two plies are parallel, and in the case of more than four plies, the ply arrangement is, say, *AABBAABB* etc, or, *ABBAABBA*. Some of these are shown in figures 3.14b and 3.14c. Tires have been made with an odd number of plies, and even tires with three plies have been commercially tried but they are the exception rather than the rule.

Usually the crown angle of the cords in the two directions are equal in magnitude. The crown angle is the angle between the path of the cord and the line along the tire periphery defined by the intersection of a plane at right angles to the axis of rotation of the tire and the highest point of the tire cross section, as shown in figure 3.15.

Tires of conventional cross bias construction are rarely made with a crown angle exceeding 38° . Lower angles are used, particularly when high speed or other special performance characteristics are to be achieved. Tires intended for vehicles on public roads are rarely less than 10° lower than the above figure, although tires with crown angles of

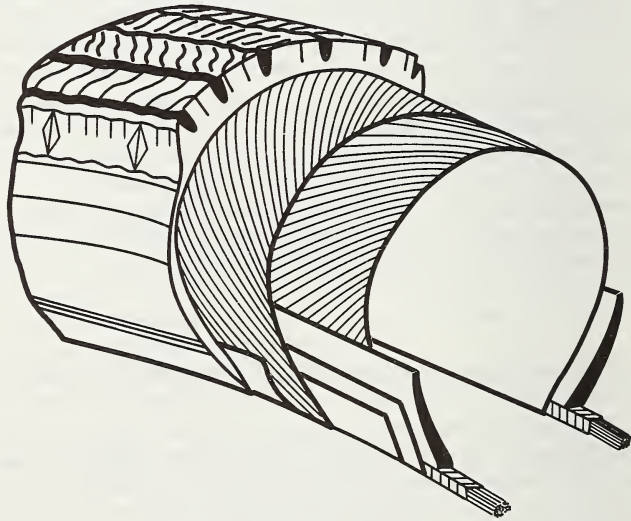


FIGURE 3.13. *Conventional cross-bias tire.*

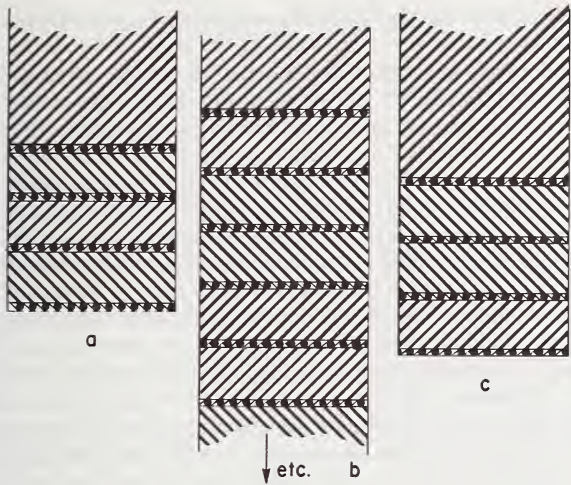


FIGURE 3.14. Cord ply arrangements.
(a) ABAB—the usual.
(b) ABBAA.
(c) ABBA.
(b and c are called parallel ply constructions.)

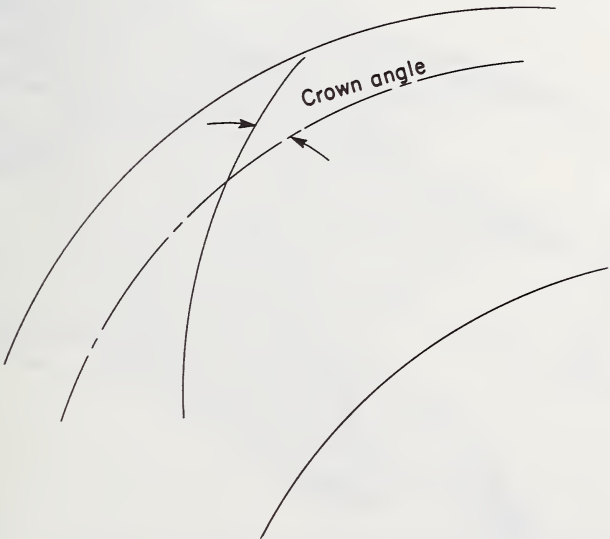


FIGURE 3.15. Cord crown angle.

the order of 20° lower may be used for very high speed vehicles restricted to use on tracks.

Conventional cross bias tires with a crown angle substantially higher than 38° , although capable of giving a good comfort, are not used because of the low cornering power and consequent poor guiding characteristics of such tires.

In order to give increased protection to the casing under the tread and/or to increase the casing strength in the crown region of a conventional cross bias tire, one or two layers of cords are sometimes incorporated substantially parallel to the cords in the other plies but extending only approximately the width of the tire tread. This is shown in figure 3.16. Such layers are called breakers. Sometimes the cord spacing in the breaker plies is greater than in the main plies, sometimes the spacing between layers is greater than between the main plies, and sometimes insulations of differing modulus are incorporated above, between, or below the breaker cords. These variants are decided from service experience and relate to the fatigue life rather than the mechanical behavior of the tire as a structure. A conventional tire of cross bias casing construction with a breaker of the same angle as the casing is not detectably different in mechanical behavior from a tire without a breaker but otherwise of similar construction, i.e., cord angle, number of plies, etc.

The above comments relate to the conventional cross bias tire, which has been used from the beginning of the automobile era. However, if the

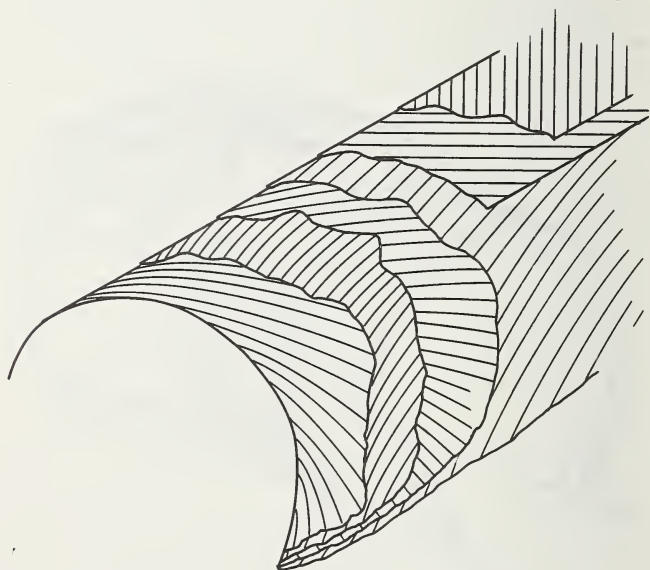


FIGURE 3.16. *Breaker layers in conventional cross-bias tire.*
The cords in the breaker layers are at the same crown angle as the casing cords.

cord angles in the breaker layers are substantially different from those in the main plies, and the breaker is made of either higher modulus cords than the casing or of more layers than the casing, then the breaker construction has an important bearing on the mechanical properties of the tire.

For about 20 years in Europe, and more recently in North America, tires of a construction very different from the cross bias construction have been produced and successfully used in large quantities. In these newer tires the cords or filaments in the casing are disposed in a radial, or substantially radial, direction giving a 90° bias or crown angle in relation to the axis of rotation of the tire. They also use a breaker or belt of several plies of cords fitted on top of the casing under the tread, and laid at various crown angles, two of the layers at least having a low crown angle of the order of 20° as shown in figure 3.17. These tires are commonly called radial tires although a more correct description is rigid breaker, radial ply tires. An alternative name is belted radial ply tires. The rigid breaker or belt is essential to the functioning of the tire. Without it a radial ply casing can become unstable. When inflated to a high pressure, determined by the magnitude of the slight irregularities in cord spacing, differing extension of the rubber between the cords at different points around the tire permits the cords to move out of a radial plane and the tire periphery develops into a series of severe buckles. Such an instability is to be expected if the comparison is made

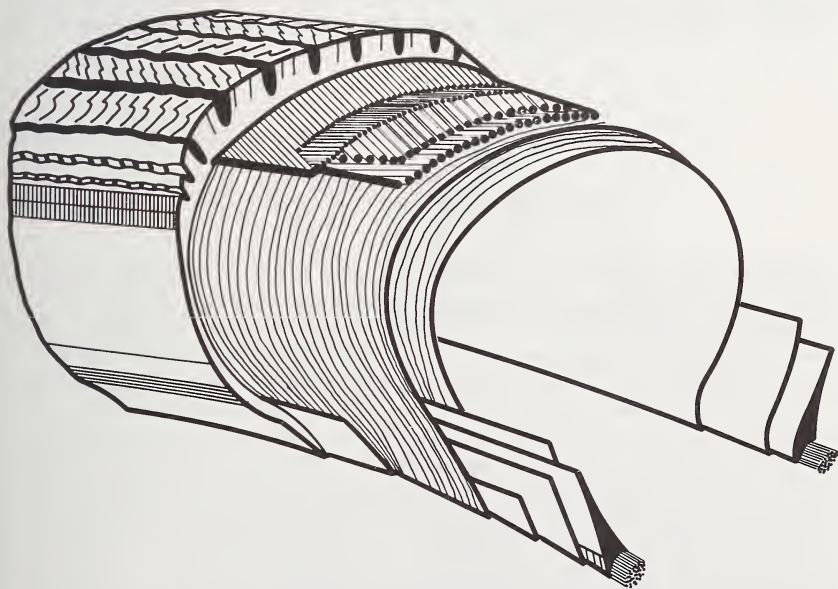


FIGURE 3.17. *Radial ply rigid breaker tire.*

with a tall pile of interspersed rubber and metal washers under compressive load.

The concept of a radial casing with a reinforcing band or belt on it in the crown region, although developed successfully only recently, is much older since a British patent dated 1913 describes a tire in which the reinforcing belt is placed under the casing cords. These early designs were never brought to a successful development state.

Tires are also made with low crown angle belts on conventional cross bias casings (of crown angles greater than that of the belt). Usually the cords in the belts of these tires are of higher modulus materials than the casing.

These belted-bias tires have at times been wrongly called semi-radial because of the common use of the term radial—ignoring the essential belt on the radial casing tire.

The objective of the belt or breaker of low cord angle is to provide rigidity to the tread against the distortions in the lateral direction which are set up during cornering, and so to reduce tread wear under this condition of use.

The conflict between a nondevelopable surface, such as a surface of revolution of curved cross section, which in consequence is a surface of double curvature, and a flat plane surface is an important factor in the decisions of designers to employ cords embedded in rubber for the tire structure.

The simplest tire-like form which can be expressed in simple geometry is a toroid. If the curved cap is flattened from its original shape to a flat plane without altering any other part of the tire periphery, as shown in figure 3.18, then the length along the surface is the direction of the

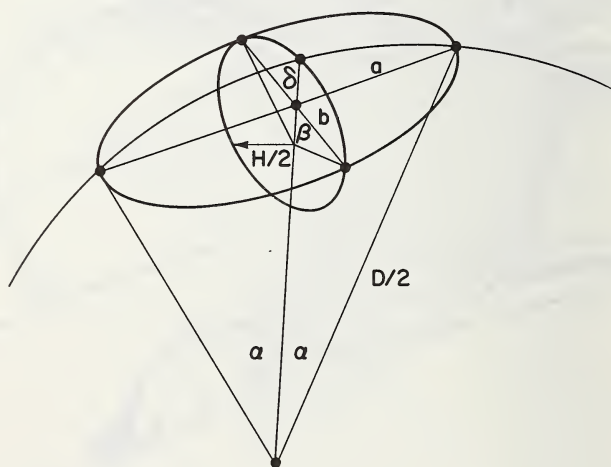


FIGURE 3.18. *Toroid in contact with flat plane.*

longer axis of the patch, originally αD , is compressed to a length $2a$. Now

$$a^2 = \delta(D - \delta)$$

and

$$\alpha = \sin^{-1} \left(\frac{2a}{D} \right).$$

Noting that

$$\frac{\sin^{-1} x}{x} = 1 + \frac{x^2}{6} + \frac{3x^4}{40} + \dots$$

and by putting

$$x = \frac{2a}{D}$$

we have

$$\frac{\text{Original length}}{\text{New length}} = \frac{\text{length along arc}}{\text{length along flat}} = \frac{\alpha D}{2a} = 1 + \text{Longitudinal Strain}$$

$$= 1 + \frac{2}{3} \frac{a^2}{D^2} + \frac{6}{5} \frac{a^4}{D^4} + \dots =$$

$$= 1 + \frac{2}{3} \frac{\delta(D - \delta)}{D^2} + \frac{6}{5} \frac{\delta^2(D - \delta)^2}{D^4}$$

$$\approx 1 + \frac{2\delta}{3D}.$$

Consideration of the dimensions across the patch leads to

$$\frac{\beta H}{2b} \approx 1 + \frac{2\delta}{3H} = 1 + \text{Transverse Strain}$$

It follows that the surface may undergo compression in both directions at all points in the area under discussion while simultaneously the size of the elliptical contact area of this patch is unaltered. It also follows that if the cap were flattened without compression in either of its principal axes, the outer edges of the elliptical patch must extend or tear.

In the case just discussed it was assumed that the part of the tire outside the contact patch is undisturbed. This might be the basis of a challenge that the example, as discussed, does not establish the point being made. It is not as can be seen by considering a sphere. If the structure under consideration were a sphere made of isotropic material, instead of a toroid, the contact patch would be circular, not elliptical. The actual circular contact patch (ignoring transition curves due to shell bending stiffness, which in an appropriate case can be considered to be a second order effect) will lie between that given by the intersection of

the sphere and the "contact plane" and a circle of diameter

$$\left(1 + \frac{2\delta}{3S}\right)$$

times as large, as shown in figure 3.19. The former corresponds to a hypothetical case in which all the distortion is in the cap or part of the shell within the contact patch, and there is no tension along the periphery of the contact patch. The latter case corresponds to the hypothetical case in which there is no radial compression in that part of the shell forming the cap or contact patch, but in this case the periphery of the patch is extended in the ratio $(1 + 2\delta/3S)$. This implies that the part of the sphere outside the contact patch is strained.

In the actual case the compressions and extensions will lie between zero and $2\delta/S$, and at least one of the strains will be of that order if another is near zero. If they are all of similar magnitude they will be of the order of $\delta/3S$. If the sphere diameter S is similar in magnitude to the diameter of the cross section of the toroid discussed above, and δ/S or δ/H is taken to be of a magnitude of acceptable tire operating deflection, i.e., 0.15 to 0.35, then the resulting strains are greater than any crystalline metallic material can withstand within its elastic range or fatigue limit.

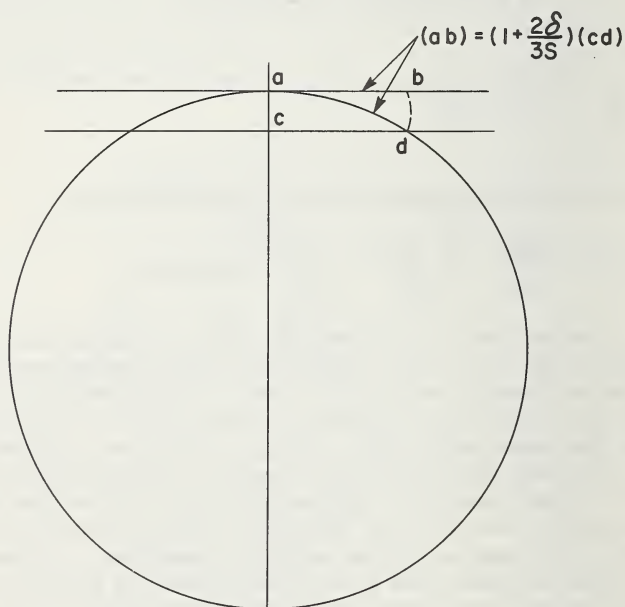


FIGURE 3.19. *Sphere in contact with flat plane.*

Actual contact patch radius will be between the values ab and cd , where d is the intersection point of sphere and plane and ab equals arc of ad .

Clearly if the sheet or surface were isotropic it would have to be made of a material having a high extensibility before fracture. This demands a low modulus, and such a structure would change dimension on inflation rather like a toy balloon. The alternative possibility of a material with a medium to high modulus would require a very high breaking strength and a very high yield point, and no such material has been found. It is for this reason that proposals for thin shell toroidal spring wheels of metal or plastic have all so far been abortive.

In order to get a rough idea of the deformation of a shell structure of double curvature made of high modulus filaments embedded in a matrix of low modulus material, consider the following case chosen for ease but reasonably accurate discussion. Figure 3.20 represents a two-ply sheet, made of one ply of filaments parallel to two parallel sides of the rhombus $ABCD$, and the other ply with filaments parallel to the other pair of sides. Imagine that this sheet of composite material undergoes a biaxial extension of the order of magnitude which would arise at the principal axes of a toroidal indenter stretching the originally flat sheet to the shape of the cap of double curvature discussed above. Consider two filaments AB and DC in one layer or ply, and two filaments BC and DA in the other ply, before stretch. If one assumes that the filaments are inextensible, then after extension the filaments move to $a'b'$ and $d'c'$ in one ply and $b''c''$ and $d''a''$ in the other ply. These movements are permitted by the low modulus matrix, which develops shears as indicated by the tilt of the lines $a'a''$, $b'b''$, $c'c''$, and $d'd''$ from their original $A'A''$, $B'B''$, $C'C''$, $D'D''$ as shown in figure 3.21. Within a ply there is shear and extension indicated by comparisons of $a'b'$ and $A'B'$ etc.

Change of cord length, assumed not to occur in this example, would of course exist in many practical cases. This would cause some modification of the strains in the matrix but in detail only.

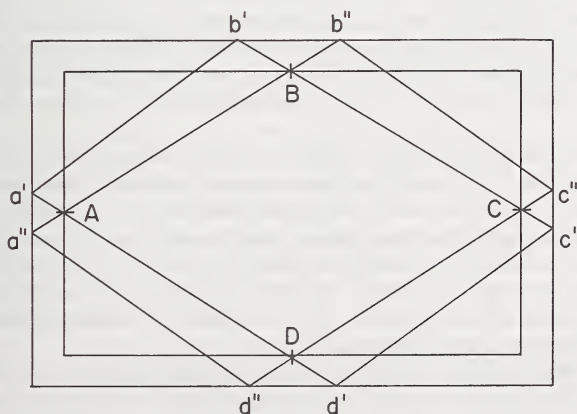


FIGURE 3.20. Two-ply high modulus filament embedded in low modulus matrix under biaxial extension.

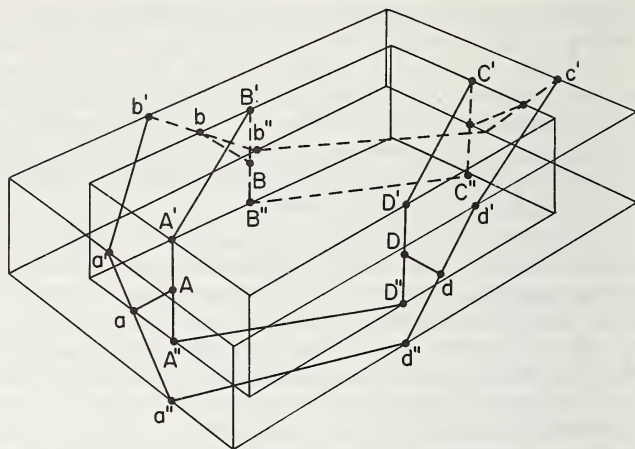


FIGURE 3.21. *Perspective view of figure 3.20 to show interply shears.*

As the local flattening of a surface of double curvature involves a process the reverse of the above, the problem is analogous but results in the initial tensions being reduced during the process instead of being increased. In some cases the cords will buckle in the process but because of their close juxtaposition within a layer, and because of the layered construction, the buckles are of a controlled character. The cords are elastically supported by the matrix in relation to the neighboring cords, and the wavelength of the buckles is determined by the consideration of a cord as an elastic beam on an elastic foundation.

This arbitrary example is artificial because it has been considered in the flat plane only, for ease of discussion and presentation. However, it does show how plies of high modulus cords or filaments embedded in a low modulus matrix can permit distortion in a structure which would not be possible if the structure were formed by an isotropic sheet of that material.

It is clear that in changing from a surface of double curvature to a plane surface the high modulus filaments must bend. They must also be flexible enough to be turned round the bead coils during the manufacturing process. Furthermore, during tire usage, conditions arise where flexibility or the ability to bend is vital. The most severe bending would probably be during accidental running of a tire in a deflated state. Reasons such as these require that the high modulus filaments must be flexible high modulus filaments.

Flexibility of the high modulus filaments is obtained by restricting the diameter of the filament or/and using a multiple fiber or multiple strand cord in which each separate strand of the high modulus material is sufficiently thin to keep the stresses below both the permanent set and the fatigue limit under any condition which might be met—even if the

occasion were infrequent. Typical cord cross sections are shown in chapter 1 of this book.

It is suggested here that a general requirement might be expressed in the following form. The high modulus filaments shall have, by the choice of strand or fiber diameter and construction or cabling, sufficient flexibility that they are not overstressed as judged by any appropriate criterion, including fatigue and permanent set, if bent as much as it is possible to bend the low modulus matrix of the size and character into which they are embedded. It follows that small tires with thin walls need the finest strand filaments in cabled cords, and that coarser strands may be permissible in the thicker walls of large tires.

3.4. Tire Construction Methods

The conflicting requirements of limited expansion of the structure during inflation, coupled with the need for internal shear movements within the sheet forming the surface or envelope when a tire structure of double curvature is flattened at the ground contact patch, necessitate the use of a multiplicity of relatively inextensible, but flexible filaments embedded in an easily distortable matrix. Accepting this, it can be seen that, in theory, there are a number of alternative ways of building a tire.

All methods of making a tire of these composite materials involve a building process followed by molding and vulcanization. The building process is the stage where the materials or components are placed in the required appropriate relative position one to the other, and will be discussed further below.

The molding process is needed for the compaction and consolidation of the various components, for example embedding the higher modulus filaments in the low modulus matrix to eliminate voids and to obtain the intimate contact necessary to secure adhesion between filaments and matrix, and also between layers of the matrix itself. The vulcanization process is required for changing the state of the rubber or rubber-like polymer used for the low modulus matrix, from the uncured plastic state necessary for the building and molding stages of the manufacturing processes to the elastic state essential for effective tire performance in the final product, and for the formation of the adhesive bonds between filaments and matrix and between all layers of matrix within the tire. The uncured plastic state of the rubber-like polymer has a feature of value during the building stage and also the molding stage, that of "self-tack" whereby two contacting surfaces adhere and, even if separated, readhere on recontact.

It should perhaps be mentioned at this point that although a fairly wide range of materials have been successfully used as the high modulus filaments e.g. cotton, rayon, nylon, polyester, glass, and steel, which range from organic, long chain polymeric to crystalline materials, the low modulus matrix has always been a long chain polymer of rubber or rubber-like characteristics. It is this material which requires vulcanization. Although many of the materials used in the filaments are affected

by the heat used in vulcanization, not all are, and in practically all cases the vulcanization stage is *not* required to bring the cord material into its required final physical state.

The molding process also fulfills at least one other function, namely the formation by molding of the tire tread pattern. In many of the more modern methods of building, the shaping of the tire from the assembled shape to the required final shape is carried out during the molding process.

The alternative ways of building a tire casing can be enumerated as follows:

A. The tire could be manufactured on a former or pattern substantially of the shape of the desired finished shape of the tire, as shown in figure 3.22a. Let this be denoted process *A*.

B. The tire could be made on a former of a shape other than that of the desired finished tire shape. The former could be a simple cylinder, as shown in figures 3.22b and 3.22c. In this case the change of shape can be effected as a separate process prior to the molding stage, called process *B1*, or during the molding stage, called process *B2*, using the same molding equipment in which the vulcanization is carried out.

C. Part of the tire could be manufactured on a former different from that of the final shape, and that part of the tire shaped to substantially that of the final tire shape, and then the remainder of the tire components could be added. Let this be called process *C*.

In each of the above cases the tire casing can be built in one of the following alternative ways, or some components built in one way and some in another.

- a. The tire casing could be assembled from sheets of high modulus filaments or cords embedded in a low modulus matrix, the sheets being produced by a separate previous process which ensures that the filaments are straight, parallel and equispaced, within the

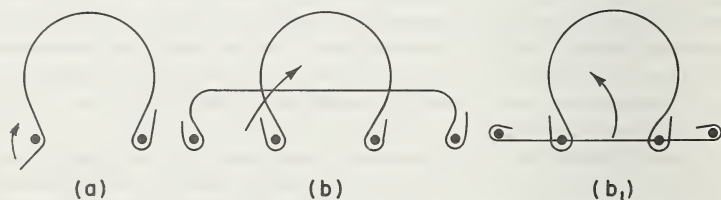


FIGURE 3.22. *Manufacturing processes I.*

- (a) Casing built on "core" former substantially the size and shape of the finished tire.
- (b) Casing built on a "low crown" former—a different shape from the finished tire, and distorted to the required shape in a subsequent process.
- (b₁) Casing built on a flat or cylindrical former and distorted to the required shape in a subsequent process.

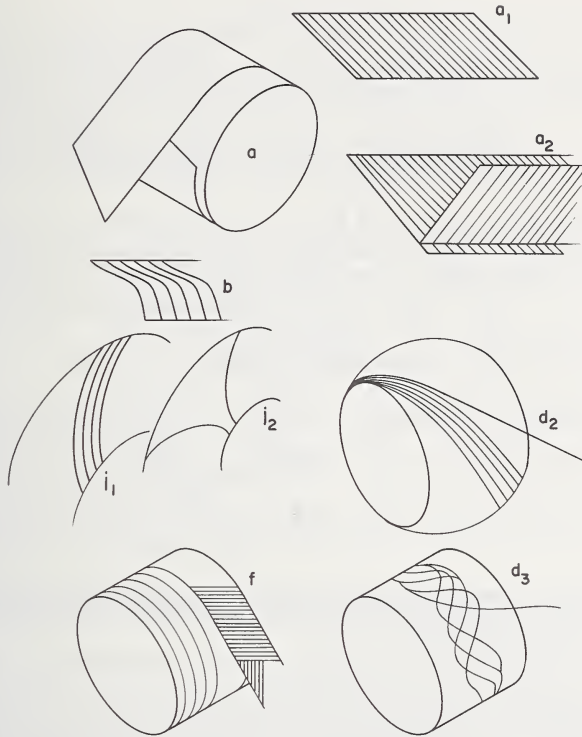


FIGURE 3.23. *Manufacturing processes II—tire casing building methods.*

- (a) Plies of material with multiple cords cut to dimensions and wrapped around a former.
 - a₁, single ply.
 - a₂, pocket or paired plies at opposite bias angles.
- (b) Plies with cranked or curved cord path.
- (c) No illustration (see text).
- (d or e) Single cord wound on former.
 - d₂, as a simple winding.
 - d₃, as a wave winding.
- (e) No illustration but as (d) using narrow strip of several cords.
- (f) Strip of material wound on former.
- (g) Peg winding—i₁ cords at one bias.
 - i₂, cords at cross bias.

rubber. These sheets can be laid on the building former shown in figure 3.23a either

- (1) individually, as shown in figure 3.23a₁,
- (2) in pairs having been previously put together so that their angles are complementary, as shown in figure 3.23a₂,
- (3) in pairs having been previously put together so that their angles are asymmetric,
- (4) in four or more layers having previously been assembled so that alternate layers are at complementary angles, or
- (5) in four or more layers having been previously assembled with their angles in some relationship other than alternately complementary.

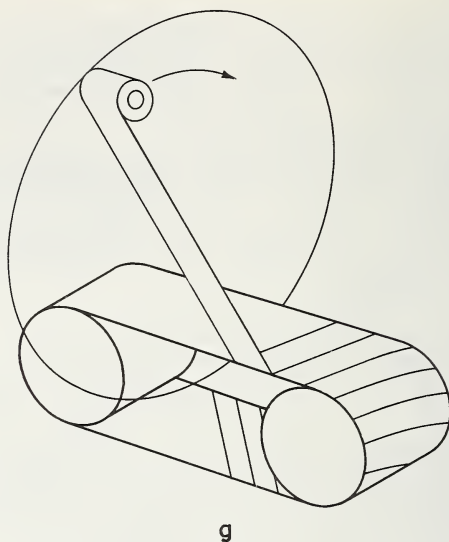


FIGURE 3.23. *Manufacturing processes II—tire casing building methods.*

(g) Band of pre-rubbered cords wound around and through the bead coils held apart.
 (h) Same, but for single cord.

- b. The rubbered multifilament sheets used for the assemblies (listed above in a.) could be distorted so that the cord paths were curved from the straight, as shown in figure 3.23b.
 - (1) Before assembling into pairs.
 - (2) After assembling into pairs.
- c. The rubbered multifilament sheets could be used as in a, but the curved effect or an asymmetric angle effect could be gotten by a relative rotation of one tire bead in relation to the other during building, shaping or molding.
- d. The cord or filament could be wound as a single rubbered cord on a former appropriate to building method A or B, p. 381;
 - (1) as a simple uniform winding.
 - (2) Great circle winding, with a slight advance of location at each turn, resulting in spaced winding, as in figure 3.23d₂, or
 - (3) controlled wave winding, as in figure 3.23d₃.

In all cases of d the cord can be rubbered at the building machine by passing it through an extruder die.
- e. A narrow band of pre-rubbered continuous cords can be wound on the former as a strip, with all of the possible variations listed in d above.

- f. A band of two or more layers of cords can be wound on the former as shown in figure 3.23f:
 - (1) with the constant angles differing at different places across the former.
 - (2) with differing numbers of layers at various places.
 - (3) with all the possible variations in d listed above.
- g. A band of pre-rubbered cords may be wound around and through the bead coils suitably held apart, the bobbin carrying the band of material passing through the bead coils during the winding process. This is shown in figure 3.23g.
- h. As in g but using a single cord rubbered at the building machine.
- i. A single cord wound from bead to bead, the cord being located by a series of pegs or slots:
 - (1) the cords all being parallel to one another in each layer as shown in figure 3.23i₁,
 - (2) the cord progressing forward at the opposite bias at each peg, as shown in figure 3.23i₂.
- j. As in i but using a narrow band of several cords.

The above classification seems to cover all possible ways of building a tire. All of these cases and combinations of cases seem to have been the subjects of patent applications. Many have been tried and used for some tire application or another at various times.

The vast majority of passenger car and truck tires were originally made using processes A and a2, but quite early in the history of the industry the process became B1 and a2, and quite soon afterwards B2 and a2. Today the vast majority of car tires, truck tires, earthmover and aero tires, and some belted cross bias casing tires are made this way. All production radial ply belted tires are made by processes C and a1, a2 or a3.

Most of the other methods have not gotten beyond the experimental stage, and practically all lack the flexibility of the current standard methods. One method which has become standard, that of g and B2 has been used extensively for the manufacture of cycle tires. It is restricted, by its character, to tires whose section width is much smaller than the bead diameter. The bobbin carrying the total material for the tire must be capable of passing through the bead coils while they are held apart and tensioned by either four drums or a system of arcuate guides, so that the portions of the bead coils between are straight and sufficiently tensioned so that the winding of the rubbered cord does not cause the beads to sag towards each other. There is another restriction of this method however, since the choice of bias angle is linked with the strip width being wound and the bead coil periphery. Furthermore, the bead coils must be sufficiently flexible for the passage around the roller system. The problems specific to this method have been mentioned as an example of the fact

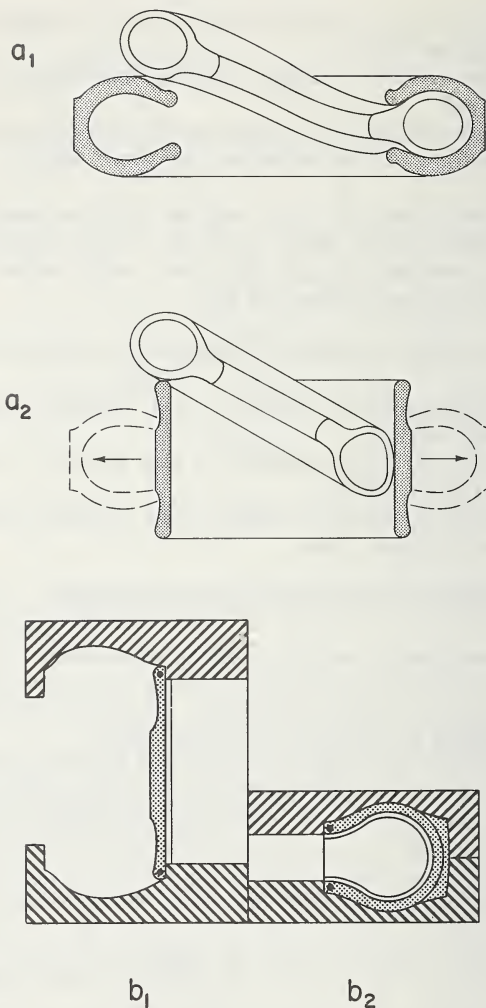


FIGURE 3.24. *Manufacturing processes III — Molding and vulcanization.*

(a) Shaping and fitting curing bag on the bladder as separate operation.

(b) Shaping as part of the diaphragm molding and vulcanization process.

that most of the alternative methods set out above have restrictive characteristics peculiar to each one.

The shaping and molding stages are illustrated in figure 3.24. There are two main alternatives. The curing bag or bladder is inserted into the already shaped tire, as in figure 3.24a₁, or into the unshaped tire as in figure 3.24a₂, during shaping by a machine process. Afterwards the tire is vulcanized in a mold in a press.

The more modern process is one in which the unshaped tire is introduced into a special press in which a cylindrical diaphragm shapes the tire as the press, carrying the two half molds, closes as illustrated in figures 3.24b₁ and 3.24b₂. The inflated diaphragm consolidates the tire during the molding and vulcanization process in the heated mold.

3.5. Cord Path—Practical Factors Determining Selection

Although in theory any cord path is possible in any molded shape there are several factors which restrict the range of practicable cord paths.

At the outset a choice must be made as to whether the cords are to be coated with rubber (I) collectively, that is in large numbers as a sheet of material, or (II) individually, or (III) in a group relatively few in number to produce a band or tape of rubbered cord.

In the first case (I), sheets of several feet in width and hundreds of yards in length, comprising a large number, say one or two thousand, cords across the width are produced in a continuous calendering process separate from the tire building. Sheets, called plies, of appropriate dimensions are bias cut from the calendered sheet so as to give the required angle of cord direction to the cut edge. This is the most common method and is a very flexible process, since a wide variety of ply dimensions can be produced as required. The only real limitation is that the initial rubbering process must be made with the cord spacing at its required amount, and the correct thickness of rubber applied.

In the other two cases (II) and (III), the cord would be rubbered as it is wound on a former of appropriate shape at the tire building machine.

The factors which control the speed of covering the high modulus cords with low modulus rubber-like compound are the temperature and temperature-time cycle and the vulcanization and scorch characteristics of the rubber-like material, along with the characteristics of the bonding process of rubber to cord. These place an upper limit to the speed at which the cord can pass through the rubbering stage. Clearly, without going into secondary detail consequent on the differences in the various processes involved, rubbering a thousand cords simultaneously is more expeditious than rubbering one or a score of cords at once. It is for this reason that the processes using calendered sheet material dominate in commercial tire production.

Processes involving curved cords, or other paths than straight, in the initial flat sheet even if produced initially straight and subsequently cranked in a special process, raise the problem that limitations on the closeness of spacing in the low angle cord region demands relatively wide spacing in the high angle cord region. The geometric necessity for this is clearly seen in figure 3.25.

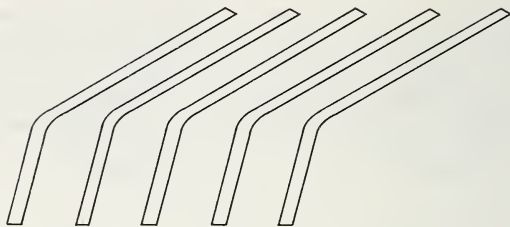


FIGURE 3.25. *Cranked cord limitation on cord spacing.*

The number of cord ends per inch in the high angle region is limited by the limitation of closeness of cord spacing in the low angle region.

3.6. Calculation of Cord Length

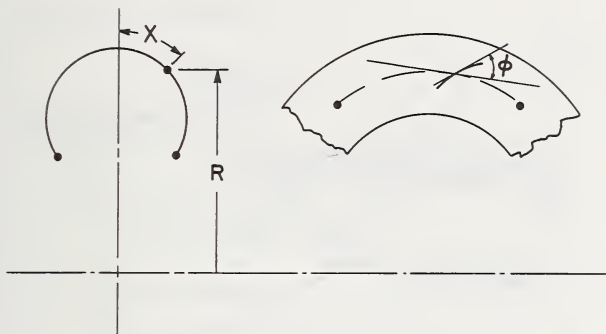
The integrals for finding the length of a line drawn on a solid of revolution are known explicitly only in very special cases, such as the constant angle helix on a cylinder, or a great circle on the surface of a sphere.

In the case of a tire, even if the tire cross section were circular, which it never is, the integration does not lead to a solution in a closed form. In the general case of a noncircular cross section the integral cannot be written explicitly, let alone evaluated and its solution stated.

On the other hand, if the path of a cord is traversed step by step, and the length and direction of each of the steps is recorded, it is possible, provided the cross-sectional shape of the tire is known, in numerical, graphical or mathematical terms to resolve the progress along the path into any definable coordinate system. This can be done whatever the cord path and whatever the tire cross-sectional shape.

This resolution into a known coordinate system is analogous to navigation at sea, with the difference that the map is not a plane, or a sphere, or generalized three-dimensional space. It is the surface of the solid of revolution of a cross section defined by the tire shape specific to the case in hand. Whatever the path or whatever the cross section, the progress in the desired coordinate system is recorded by resolution of the known step in the known direction, followed by simple summation in each coordinate. Integrals expressed as mathematical functions do not arise. In effect, the simple summations of the coordinates correspond to, and replace the need for, the integration along the path itself.

There are two simple relations between R , the radius, and $\cos \phi$, both as defined in figure 3.26, which hold over all possible cord paths in a tire. For this reason a graph of R vs. $\cos \phi$ is an important diagram. Note here that ϕ is defined as the angle between the cord tangent and a parallel on the tire surface, while R is the radius to the axis of rotational symmetry. The chart obtained by plotting R versus $\cos \phi$, or a formula relating the two quantities, or a numerical tabulation of pairs of values, is the full description of a cord path or as appropriate, of the movement of a point on the cord during processing. Pantographing movements and geodetic movements are linear and hyperbolic relations

FIGURE 3.26. Definitions of radius R and cord angle ϕ .

respectively on this chart. On the other hand, the geometry of the tire surface is completely described in terms of R versus X , where X is the distance along the meridian, that is the distance along the surface measured from the tire crown in the plane of a cross section of the tire as shown also in figure 3.26.

Given the cord path by means of R versus $\cos \phi$ on a former or mold of known R vs. X , then if the tire is shaped by a process involving movements expressed in terms of an appropriate transformation of R vs. $\cos \phi$, it is immediately possible to determine the R vs. $\cos \phi$ of the cord path in the finished tire.

It is also known that the R vs. $\cos \phi$ chart can be used to diagnose the character of the cord path in a tire, or to elucidate the character of the processes occurring during the shaping and molding stages of tire manufacture.

Consider any surface of revolution on which any cord path is drawn. Consider a tire made of two layers, one layer comprising a large number of cords of the same cord path and these cords being equispaced and encompassing the whole surface of this layer, and the second layer of the same system of cords but of opposite hand. Furthermore, consider that the cords in these two layers are pin-jointed one to the other at their crossing points. It has been shown in reference [1]² that the shape of this network can be changed, and provided that the surface is maintained to be a surface of revolution around the original axis, the trellising or pantographing of the cord structure will ensure that all times

$$\frac{\cos \phi}{R} = C_1$$

as shown in figure 3.27, where C_1 is a constant.

If the solid of revolution is a cylinder and if the helix angle is constant, R and ϕ are the same at all points on the path, so that one point on the R vs. $\cos \phi$ graph represents the whole helical path. This corre-

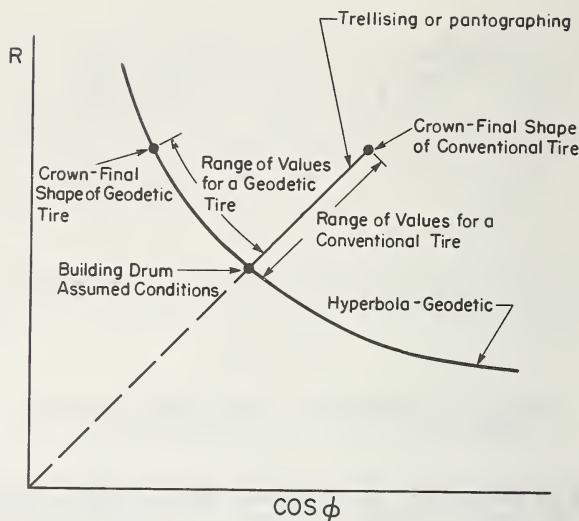


FIGURE 3.27. R - $\cos \phi$ chart.
Plots for conventional and geodetic paths.

sponds to the path on a cylindrical building drum. If the tire casing is shaped up by pantographing without slippage or extension of the cord then the cord path will be described by a portion of the straight line through this initial point and the origin, as illustrated also in figure 3.27.

It follows from a study of geodesics on any surface of revolution that the relation between R and $\cos \phi$ for points on such a path, which always follows the shortest route between any two points on the surface, is

$$R \cos \phi = C_2$$

where C_2 is a constant.

The fact that both of these relations may be displayed simultaneously on the R vs. $\cos \phi$ chart makes such a chart important. The plot on the R vs. $\cos \phi$ chart is independent of the cross-sectional shape, since a curve obtained by trellissing or pantographing always lies along a line through the origin, while a geodesic path always appears as a hyperbola asymptotic to the coordinates of the chart. This is shown in figure 3.27. This perhaps is made clearer if $\log R$ is plotted against $\log \cos \phi$, as in figure 3.28. Here, the two lines are straight at 45° to the coordinates, and are orthogonal to one another.

If in the pantographing system the cords extend, then the R vs. $\cos \phi$ values which are obtained lie on a new straight line through the origin with a slope of $(1 + \text{cord strain})$ times the slope of the line describing the original unstretched cord path, so that $R = R(1 + \epsilon)$ at a given value of $\cos \phi$. This is shown in figure 3.29.

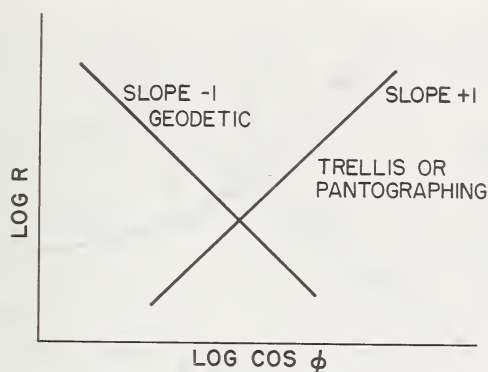


FIGURE 3.28. *Log R-log cos ϕ chart.*

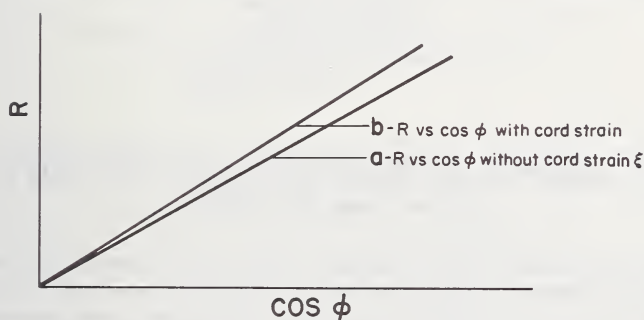


FIGURE 3.29. *R-cos ϕ . Effect of cord stretch.*

If the cord length changes in the ratio $(1 + \epsilon)$ the R-cos ϕ line changes from a to b where the slope of b is $(1 + \epsilon)$ times a.

The above discussion relates to the characteristics of an actual path of a cord on a surface of revolution. The presentation of information on a set of coordinates of R and $\cos \phi$ has another usage, that of depicting the changes or movement during shaping of the tire casing, or other manufacturing processes. Movement of the point on the R vs. $\cos \phi$ graph, representing a specific point on the actual tire cord, can be examined if the following facts are noted. As the cord lattice pantographs, the point on the R vs. $\cos \phi$ chart moves along a straight line through the origin, as illustrated in figure 3.30. As a cord stretches, the point on the chart moves along the hyperbola passing through the point, as in figure 3.30b. If slippage occurs the angle remains constant but the radius R changes. This results in a vertical displacement of the point, as in figure 3.30c. For further discussion of this concept see reference [1].²

² Figures in brackets indicate literature references at the end of this chapter.

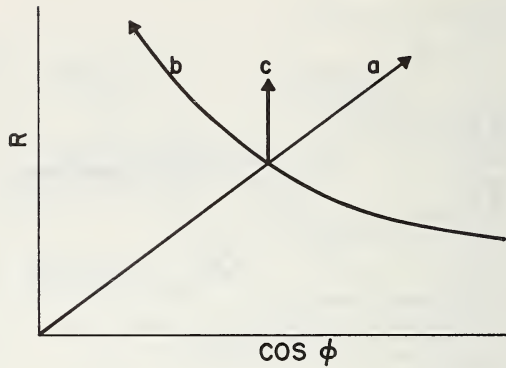


FIGURE 3.30. *Laws of change of $R \cdot \cos \phi$ at a point of the lattice.*

- (a) During pantographing.
- (b) During cord stretch.
- (c) During ply slippage.

3.7. Analysis of Manufacturing Methods by R vs. $\cos \phi$ Charts

The fact that the R vs. $\cos \phi$ presentation of changes of cord path enables the character of the changes to be understood, and the fact that the R vs. $\cos \phi$ representation of the actual cord path together with the R vs. X diagram for the surface of revolution on which the cord path lies completely defines the cord path in space, enables a system of cord path dimensions, and changes under manufacturing conditions to be set out.

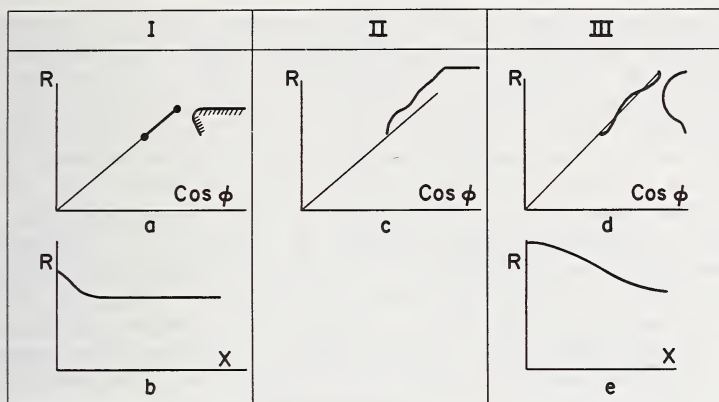
Consider three sets of data expressed in the form of five graphs or tabulations, as shown in figure 3.31. The graphical form is easiest to understand, although the numerical form enables the required precision to be met.

The curves of figure 3.31 labeled I show the cord path characteristics or R vs. $\cos \phi$ information, curve a , on the tire building former, which is a surface of revolution defined by the R vs. X statement determined by the generator of the surface, curve b .

The curves labeled II show the changes due to trellissing or pantographing, changes in cord extension, and any slippage of the plies at the trellissing pivot points, during manufacture, curve c .

The curves labeled III show the final cord path characteristic, or R vs. $\cos \phi$, curve d , in the finished tire casing of shape defined by its R vs. X information, shown in curve e .

Given any two sets of information out of the three, I, II, III, the other can be found explicitly, or, given any four of the five items of information (a), (b), (c), (d), (e), the fifth can be found exactly.

FIGURE 3.31. Representation of R - $\cos \phi$ method.

- I Original plied material on former.
 II Shaping process.
 III Final tire cord path.

It is possible that a bad choice of the given data will result in the remaining calculations taking on an impractical form. This is not a limitation or fault of the method, but rather the reverse—it shows the limitations of what can be done in the process of manufacture.

The calculations do not involve difficult mathematical functions, incomplete integrals or mathematical singularities, as would a method in which the length of a path is determined analytically from the coordinates. This method is, as mentioned earlier, one of step by step resolution of the cord path into the coordinates of the surface, analogous to navigation.

The details of the application of the method outlined here, including the choice of the incremental steps along the path of the cord so as to avoid systematic cumulative errors, along with examples of applications, are given in reference [1]. This reference also gives information on the R vs. $\cos \phi$ characteristics of paths other than the pantographing and geodetic cases.

In addition to the above uses, the R vs. $\cos \phi$ method of presenting information can be used as a diagnostic tool to investigate why a given tire does not conform to the expected cord path. The departures from the expected path can be interpreted in the light of the observed departures of the R vs. $\cos \phi$ from the normal characteristic. Cord crowding due to insufficient spacing in the initial material, cord extension, tight cords, and cord or ply slippage each have a specific effect on the chart.

It is a general truth that the most likely change during the shaping process is pantographing, since departures from pantographing and uniform stretch are caused by local effects, such as the tire contacting the mold at one region before another and the subsequent movement of parts of the casing being restricted by this contact with the mold.

The fact that the high modulus cords are embedded in a low modulus matrix which adheres to them is the reason why pantographing, corresponding to $\cos \phi/R=C_1$, occurs most readily. The low modulus matrix provides a low resistance to the shearing movements involved in pantographing, while the adhesion between the high modulus filaments or cords and the low modulus matrix or rubber resists slippage of one ply across another, and ensures pin-jointing or pivoting at filament intersection points between two adjacent layers of opposite bias.

Since a cylindrical former belongs to the group of axisymmetric surfaces which are developable, so that they can be made from a flat surface without internal distortions in the plane, then plies laid together on the flat wrap round the cylinder without pantographing. If the form is of any shape other than a cylinder, including those regions of a so-called flat (cylindrical) former which depart from a true geometrical cylinder, pantographing will occur appropriately.

3.8. Mechanism of Load Carrying—Infinitely Flexible Membrane

To understand the fundamentals of the mechanism by which a pressure inflated structure carries a load, consider cases of infinitely thin and flexible membranes. The flexibility is to be such that the forces set up by bending of the film are so low that they can be ignored. Thin soap films are often quoted as examples of such membranes.

Consider a tube of these characteristics, held in friction-free contact between two parallel flat plates whose distance apart is such as to compress the tube as in figure 3.32. At any point in the wall of the tube not in contact with the plates, an element of the surface is indistinguishable from the surface of a complete tube of the same material and characteristics free of contact with any plates, but of diameter $2r$, the separation distance of the two plates in the first case. It follows that the tension in the free wall of the tube held compressed between the two plates is $t=pr$, from elementary equilibrium. Since this holds right up to the actual point of contact with a plate, it follows that the free wall is truly semi-circular of constant radius of curvature r , and it meets the plates tangentially at the four contacting points. The total reaction on plane AB is $p \cdot (AB)$, and the tension in the free walls at A and B is

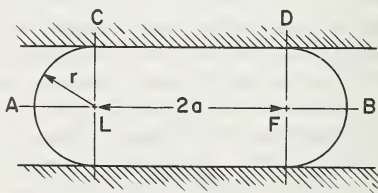


FIGURE 3.32. Flexible cylindrical tube compressed between two parallel flat plates.

each $t = pr$, and also $AB = 2r + 2a$ where $2a$ is the length CD of the film on the plate. Now, from equilibrium arguments, the total reaction on CD = total reaction on AB minus the resultant, in the direction normal to CD , of the pressures on the curved walls AC and DB . This leads to

$$p \cdot (CD) = 2p(a + r) - 2pr = 2pa$$

This is exactly what is to be expected when it is noted that the gas pressure acts in a direction normal to the plate CD , and to the flexible membrane in contact with the plate. Furthermore, as this surface of the tube is parallel to the plate CD , the tension in that part of the tube does not matter since it has no component normal to the plate. In the case just discussed, the tension in the wall just as it meets the plate tangentially is $t = pr$, and this must be resisted by the tension in the film across the plate which is in friction-free contact with the plate, so that the tension in the film or membrane in contact with the loading plate is $t = pr$. If the friction between the loading plate and tube were not zero, then the tension in the membrane across the plate would be modified according to the friction laws pertinent to the contacting surfaces, and possibly the manner of approach of the surfaces, as well as the elastic moduli of the tube wall and platen. But in any event this would not alter the load carried normal to the plate.

The main point to be noted is that as compared with the free tube, the use of the tube to support load on the parallel plates reduces the tension in the free walls of the tube, and in the case discussed the load carried is precisely equal to the gas pressure times the contact area between tube and plate.

If the wall of the tube could not be assumed infinitely flexible, then the bending stiffness and/or wall shear rigidity would cause the load to be supported by the platen to be greater than the pressure times the actual contact area. The stresses in the wall would be modified near the contact region, locally the wall curvature might vary from the semi-circular arc, and the tension in the membrane across the contact might be different. At this moment these effects are not relevant to the matter directly under discussion but are pertinent later.

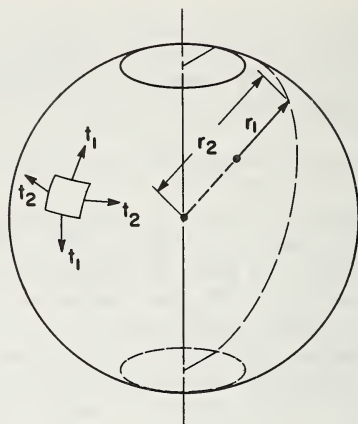
It will be noted that in the above case, if the material is inextensible as well as infinitely flexible, the overall periphery of the tube remains constant so that $2\pi r + 4a = 2\pi R$. As the load carried is $2ap = L$, it can be deduced that the plates approach towards each other by an amount

$$x = \frac{2L}{\pi p}$$

or put another way, at a deflection x the load carried is

$$L = 2ap = \frac{p\pi x}{2},$$

where L is the load per unit length of the tube.

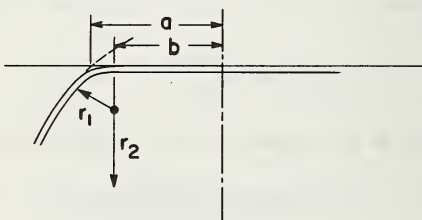
FIGURE 3.33. *Sketch of spherical element and nomenclature.*

Now consider the case of a complete spherical membrane or balloon, flexible yet inextensible, compressed between two parallel flat plates. The principal radii of curvature of the surface are r_1 = radius of curvature of the cross section in a plane radial to the axis of symmetry of the surface, and r_2 , the distance from the surface to the point where the radius r_1 extended meets the axis of symmetry of the surface, as in figure 3.33.

As the surface of that part of the balloon or membrane in contact with a plate is flat, r_2 at a point immediately adjacent to the edge of the contact patch is infinite and we have from the equation of normal equilibrium (see fig. 3.34).

$$p = \frac{t_1}{r_1} + \frac{t_2}{r_2} = \frac{t_1}{r_1} + \frac{t_2}{\infty} = \frac{t_1}{r_1}.$$

Since p is constant throughout the interior not in contact with the wall, including the region of the equator between the two plates where the

FIGURE 3.34. *Membrane in contact with plate.*

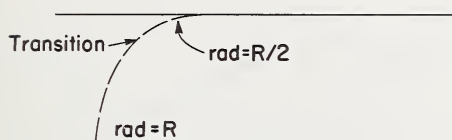


FIGURE 3.35. Transition of membrane surface of edge of contact with plate.

membrane is nearly spherical and has a tension t , approximately the same in both t_1 and t_2 directions, then

$$p = \frac{t_1}{r_1} = \frac{2t}{R}$$

where R is the radius of curvature of the spherical wall. Now $t_1 = t$ because, at any point on the curve representing the cross section in the radial plane (fig. 3.34) nothing contacts the membrane except gas inflation or the plate, and so just at the point where the membrane leaves the plate, $t_1 = t$ and so $r_1 = R/2$, as in figure 3.35.

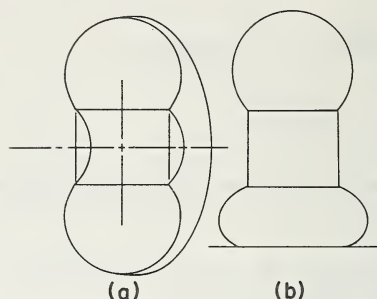
Therefore the radius of curvature of the cross section at the point in the membrane where it touches the plate is $R/2$ and the plate is tangential to the membrane surface arc at this point. The surface follows a transition curve from this point to the main region of the sphere, as in figure 3.35. Because of these facts the radius b of the actual contact is less than a , the radius of the intersection of the sphere and plane in figure 3.34.

As stated earlier, the load on the plate is equal to the product of the internal gas pressure and the actual contact area of the membrane on the plate. The only other loading which could come on to the plate is a shear loading within the thickness of the membrane around the perimeter of the contact patch, and this could only arise as a consequence of bending stresses in the membrane. Because of the initial assumption of infinite flexibility, these stresses cannot be present in the problem as discussed.

It also follows that the two contact patches are equal in area and that their midpoints are on the same normal to the flat plates.

Now consider a toroidal or tire-like structure of the same material as the previous balloon membrane but with a rigid tubular rim for the central zone or bore of the toroid, as in figure 3.36a. Assume that the junction between the thin flexible membrane and the rigid tubular rim or base has zero bending rigidity.

Inflation of the structure puts tensions in the membrane and it takes a shape as determined equilibrium and compatibility conditions. The membrane tensions are resisted by reactions at the edge of the tubular rim, and for our present purpose these can be discussed in terms of two components viz, radially outward tension and tension in an axial direction (that is paralleled to the axis of rotational symmetry or rotation of surface generators) at each point around the edge of the rim.

FIGURE 3.36. *Toroidal membrane on cylindrical rim.*

If a flat plate is pressed against the membrane while the structure is supported by the rim a reaction will develop between membrane and plate in the manner already discussed for the sphere and the cylinder, as in figure 3.36b. By the same arguments the load will be equal to the product of the actual contact area and the inflation pressure. The contact area will be approximately but not exactly elliptical, but its geometrical shape is of importance only for the discussion of the point about to be made.

The question now arises, how does the reaction develop at the rim? The air pressure is uniform and the rim base width is constant, and it follows that the resultant of the air pressure reactions on the rim is zero even when the plate is pressed against the membrane.

Consideration of the structure shows that the only possible way in which the reaction can develop at the rim is by the changes in magnitude and direction of the membrane stresses at their points of attachment to the rim, in the region of the membrane near the point where the plate is pressed against it.

As can be seen from figure 3.37 the curvature of the wall of the membrane increases in the region between the loading plate and the adjacent rim. Hence, because of the increased curvature the membrane stresses in this region are lower than elsewhere in the membrane walls, since $t = p \cdot r$. The deflection also causes the membrane to distort locally, increasing the angle between the direction of the wall and a line normal to the plate from the rim; this is true whatever the cross-sectional shape, shown in figure 3.38. This increase of angle reduces algebraically the cosine of the angle between the wall and the line of action of the applied load on the plate. The net effect of the reduced tension and reduced component at the deflected region is to develop the required reaction. The rim, in effect, hangs in the tensions of the undeflected walls as shown in figure 3.39. The radially outward components of the wall tensions are greater in the undeflected regions than in the deflected region. The system of load transmission is analogous to that of a cycle wheel where the hub hangs by the steel wire spokes from the top of the rim, which is loaded at the bottom as illustrated in figure 3.40.

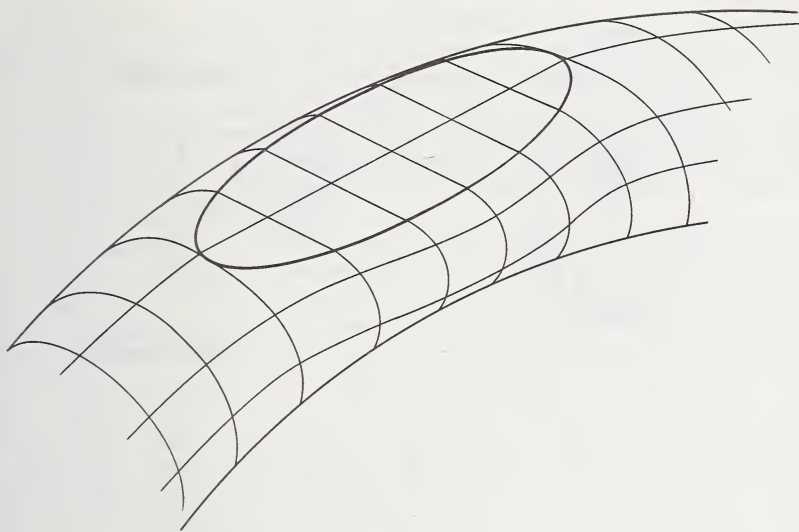


FIGURE 3.37. *Perspective sketch of toroidal shell contact.*

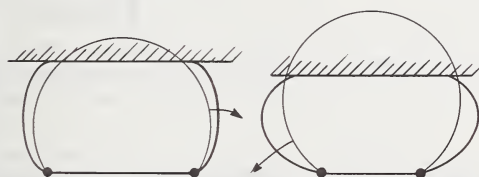


FIGURE 3.38. *Cross sections of figure 3.37 showing deflections of sidewalls which reduce the tension component radially outward at the inner cylinder edge.*

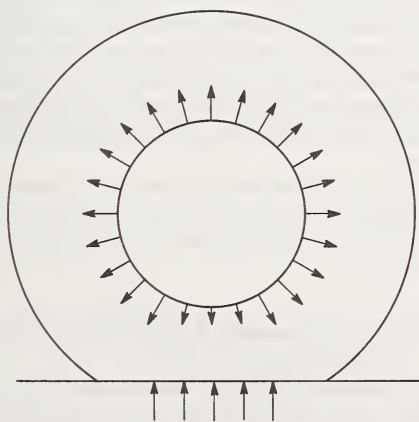


FIGURE 3.39. *Polar plot of radially outward component of wall tension of membrane toroid on inner cylinder.*

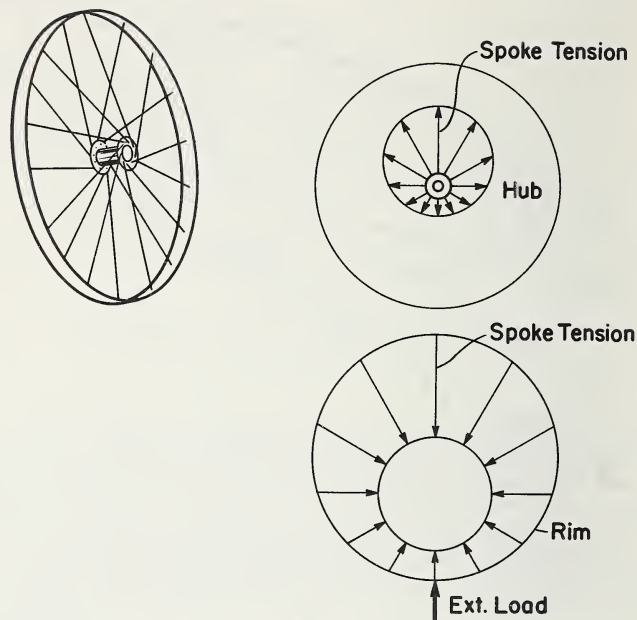


FIGURE 3.40. Load on hub of cycle wheel is carried by change of tension in spokes.

The above analysis assumes that the membrane structure is so flexible that the load which would be carried by it when uninflated is trivial.

If, as is usually the case, the structure had some bending stiffness, this would contribute some load support, and to do this it would need to develop bending stresses in the membrane, particularly around the edge of the contact patch where it contacts the loading platen. Bending stresses may also, but not necessarily, develop at the rim edge, where the presence of a flange on the rim would, of course, set up bending moments depending on its shape and the bending stiffness of the membrane at that region.

The objective of this discussion of some apparently academic cases is to get principles clear, because the actual tire case involves them and some further complications, particularly in the bead region because of the steel bead coils.

3.9. Mechanism of Load Carrying—Tire Structure

In an undeflected tire the cords are tensioned by the excess pressure of the inflating gas over the external or atmospheric pressure. The tire casing takes up its equilibrium shape, which is determined primarily by the cord paths, perhaps modified somewhat in local regions

by the presence of extra rubber, ply turn-ups, flippers, filler, etc. For clarity and ease of discussion we will ignore these features and their effects and start from the simple theoretical equilibrium shape.

As the tire is pressed against a flat roadway the tread rubber is compressed and at the same time the tire casing locally loses its axial symmetry and takes on a substantially flattened contact patch. If there were no tread rubber on the tire the casing would be flat over the area actually contacting the ground.

Let us continue our examination of the problem assuming that, for the present, there is no tread rubber. The cords in the area of the casing in actual contact with the ground will also lie in a flat plane parallel to the ground plane and hence, viewed along any line parallel to the ground plane, the line of the cord is straight. It follows that the tension in the cord bears no relation to the internal inflating gas pressure, in this particular region of the tire. To make this point emphatically clear it will be noted that the basic law determining the relation between tension in the casing cords and the internal gas pressure which it resists is based on the simple laws of statical force resolution, and in such cases a path of infinite radius of curvature results in zero resultant force opposing the gas pressure. The tension in the cords across the flat part on the contact patch is therefore determined primarily by the cord tension transmitted from the adjacent free wall of the tire, modified by the effects of the transition curvature around the perimeter of the flat contact patch. It also follows that the contact pressure between the tire casing and the ground will be equal to the inflation pressure, modified around the edges of the contact patch by the extra pressures set up by the bending stresses within the transition zone, as shown in figure 3.41.

In the case of practical tire designs the presence of tread rubber of differing thickness, of tread pattern design, and such factors as the bending stiffness caused by the multiple layers of cord cause the actual tire contact pressure to be locally greater than the inflation pressure, and in fact to differ in different parts of the contact patch. The contact pressure at the sides of the contact patch, under the shoulders of the tire tread, is often higher than the general contact pressure because of the reaction necessary to develop the bending stresses in the transition zone around the contact area. This is most marked if the shoulders of the tire tread are thicker than the tread at the crown of the tire.

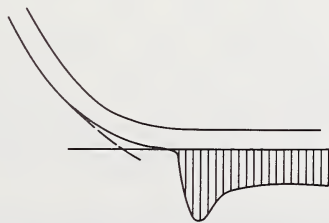


FIGURE 3.41. *Effect of casing bending stiffness on contact pressure.*

For these reasons the actual load carried by the tire is higher than the product of the overall contact area and inflation pressure. The extra reaction is carried by the tire acting as a structure.

The load carried by these two processes seems to be linearly additive. The load-deflection data of figure 3.42 can be analyzed by redrawing the various load-deflection curves for the range of inflation pressures as a lattice plot, as in figure 3.43. In this plot the load-deflection curve for a given pressure is started from a zero determined by the value of the inflation pressure, the zeros being located along the abscissa on a linear pressure scale.

Points on each curve for a given combination of load and deflection are taken from figure 3.42 and are joined to produce a line of constant deflection. This process produces a family of constant deflection curves

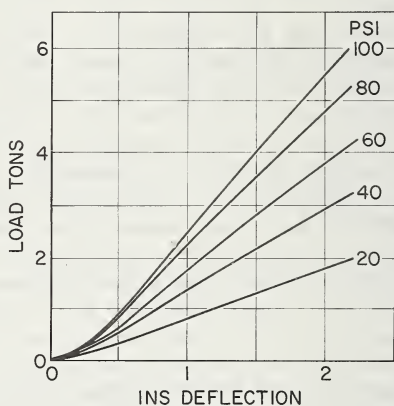


FIGURE 3.42. 11.00 x 20 tire deflection data over a range of pressures.

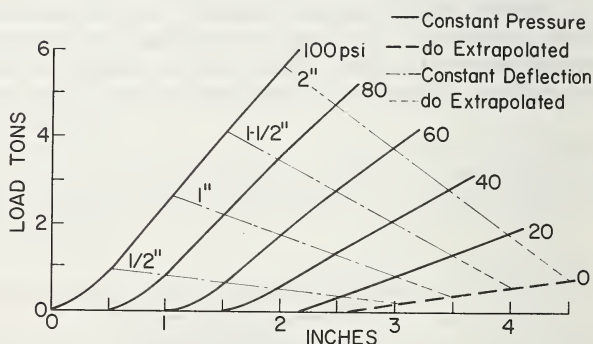


FIGURE 3.43. Lattice plot of 11.00 x 20 tire data of figure 3.42 showing both load-deflection curves at various pressures and also load-pressure curves at various deflections, thus separating pneumatic load and direct structural load.

laid across the original family of constant pressure curves. For any combination of pressure and deflection, the load developed can be read off. Interpolation at intermediate values is easy.

The constant deflection lines can be extrapolated to produce a curve for zero inflation pressure, shown as a dashed line in figure 3.43. The load at any specified pressure and deflection is seen to be the linear sum of the part dependent on the inflation pressure and the part due to the structural stiffness, or the stiffness at zero inflation pressure. It should be noted that the slope of a constant deflection line, shown chain dotted, is an effective area and is of the order of the contact area, as would be expected from the discussion above.

The stiffness of the structure can be expressed as an equivalent effective pressure, the value of which is determined by extrapolation of a constant deflection line through the line for zero inflation pressure. The horizontal intercept from the foot of the ordinate of the point where the given deflection line cuts the zero inflation line, to where the given deflection line cuts the zero load base line, determines an effective inflation pressure equivalent to the stiffness of the structure as shown in figure 3.44. Construction of curves of this type is described in references [2-4].

So far, the development of the load at and in the immediate vicinity of the tire-ground contact has been discussed. The load must be transmitted to the wheel and this involves not only the transmission of forces between bead and rim but also the transmission through the structure. The area of the wheel rim base acted upon by the air pressure is axially symmetrical and is a cylinder of constant length corresponding to the rim width, so the uniform inflation pressure cannot produce a resultant force on the rim.

To postulate how the force set up by the inflation pressure acting through the flattened contact region can produce stresses in the structure having a resultant equal to the load carried, consider two mechanisms of force transmission acting in parallel.

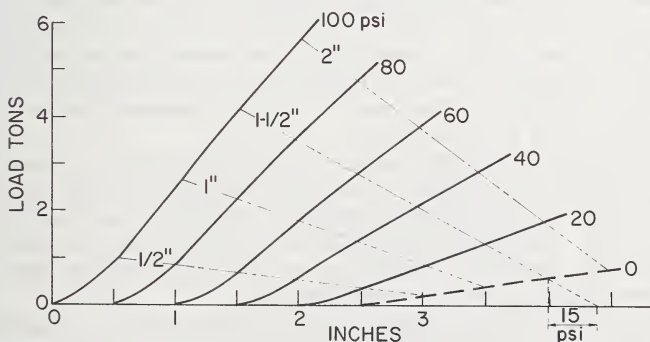


FIGURE 3.44. Line of constant deflection extrapolated to estimate structural stiffness as an effective inflation pressure.

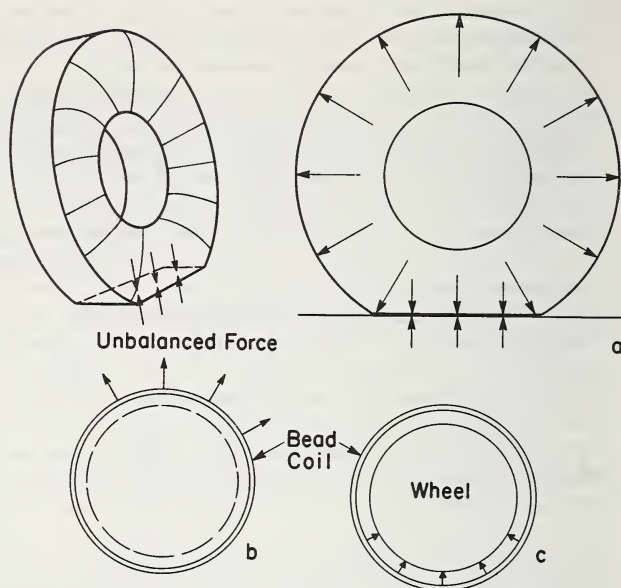


FIGURE 3.45. Load transfer from ground to wheel by effects of inflation.

First of all, consider a band approximately the width of that part of the tire tread and casing in contact with the ground, and with the same properties and construction as that region, extending around the whole periphery of the tire. This is shown in figure 3.45. At all points the inflation pressure acts on this band, and, at all places except that part in contact with ground, it is curved and so the tensions set up by inflation pressure resist and equilibrate the inflation pressure. In that portion in contact with the ground the inflation pressure forces are transmitted by compression through the band without producing a resultant reaction on the band or ring. The net result is that the absence of forces on this part of the band leaves the forces due to inflation pressure on the top sector of the band unresisted by an opposite force on the bottom sector, while at other parts of the tire outward forces have zero resultant, as shown in figure 3.45a.

The resultant upward force on the upper half of the ring, being greater than the resultant downward one on the lower half, causes the sidewall tensions in the upper half to be greater than the lower half, as shown in figure 3.45b, and this force pulls the bead coil against the base of the wheel rim above the contact area, thus transmitting the upward force to the wheel, as shown in figure 3.45c.

The other mechanism of force transmission from the ground to the wheel is analogous to that discussed earlier for the cases of a cylinder and a sphere, where the deflection of the walls at the contact region lowers tension forces in the walls in that region, and here, because the

bead coil has a high modulus, it bears on the base of the rim via the ply material around it with a force just sufficient to make up the total load, as shown in figure 3.45.

Both mechanisms lead to the same kind of transmission of force from tire to rim—the wheel rim hangs in the bead coils, which in turn hang in the tensioned casing cords which have lower tension in the contact region than elsewhere.

In addition to the load carried by a combination of these two mechanisms, some load is carried by the structure of the tire in the region of the contact, as would be expected if it were a solid tire. This load is carried by the structure of cords and rubber from the contact patch to the rim as a compression in the wall held stable by the inflation pressure and curvature, but its contribution is small. The structural load may also be transmitted via the bead ring system already discussed as a mechanism for the inflation load.

The true stress pattern in the tire structure is the sum of these several effects. An analysis of the problem will require the application of numerical methods, possibly based on strain energy methods, although finite element methods seem to be the most likely method of obtaining an estimate of the total structural stiffness. Two points will be made, however. The true estimate of structural stiffness will require the development of true finite displacement analysis—the analysis of lattices with substantial deformations so that the compatibility of the frame-

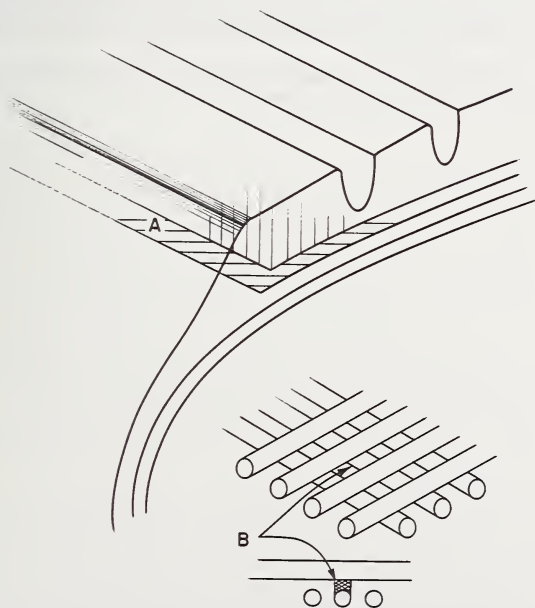


FIGURE 3.46. *Points of high stress in breaker and other regions.*

work is not violated, even where the framework is distorted substantially from its original state of axial symmetry. The second point is that even when satisfactory structural stiffness and load carrying capacity analyses have been established, the use of finite element models for stress estimation will be difficult and open to serious doubts because of the assumption of uniform stress in each element, basic to the method. One cannot estimate the peak stresses at the ends of high modulus elements, and these are the ones which determine failure starting points and fatigue life. The complexity of the problems to be faced are illustrated in figure 3.46. The stress is difficult to obtain at points such as *A*, the free end of a cord in a region where the stress in the low modulus matrix is changing rapidly, and *B*, the closest points on the surfaces of nearby crossing cords. Element sizes will need to be small to cope with this, and this may make the problem too difficult to handle.

Small changes in relative proportions and dimensions will have a large effect on the stresses at the cord ends. When it is noted that analyses by finite element methods of stresses at the ends of even single embedded wires in tension only involve a considerable number of elements, the truth of the statement earlier is clear. Practical size computations may be inadequate to estimate the important stresses but adequate to obtain overall structural stiffness.

References

- [1] Gough, V. E., Cord path in tyres, *Trans. I. R. I.* **40** (1), T20 (1964).
- [2] Gough, V. E., Tyre to ground contact stresses, *Wear* **2**, 107-126 (Nov. 1958).
- [3] Cooper, D. H., Radial stiffness of the pneumatic tyre, *Trans. I. R. I.* **40** (1), T58 (1964).
- [4] Gough, V. E., Tyres and air suspensions, *Advances in Automobile Engineering*, Tidbury, ed., p. 59 (Pergamon Press, 1963).

CHAPTER 4

Tire Stress and Deformation

Joseph D. Walter ¹

	Page
4.1. Introduction.....	406
4.2. Analytical techniques.....	407
4.2.1. Solutions for inflation loads.....	407
Inflation cord tension.....	418
Inflation bead tension.....	419
Cord-rubber interface shear stress.....	419
4.2.2. Solutions for centrifugal loads.....	421
4.2.3. Methods for analyzing the tire in service.....	426
4.3. Experimental techniques.....	430
4.4. Principal notation.....	439
References.....	440

¹ Central Research Laboratories, The Firestone Tire & Rubber Company, Akron, Ohio 44317.

4.1. Introduction

The conventional automobile tire possesses three distinct structural components: the rubber matrix which contains the air and provides abrasion resistance and road grip; the cords (textile, steel, or glass) which provide tensile reinforcement for the rubber and carry most of the load applied to the tire in service; and the steel beads which circumferentially connect the tire to the wheel of a car. These three components, with air under pressure, form a thin-walled composite toroidal shell which is both highly flexible and relatively inextensible. The purpose of this chapter is to discuss those methods of stress analysis which are applicable for the calculation or measurement of the stresses and strains developed in the three structural components of the present-day automobile tire.

Stress analysis is that branch of mechanics which is concerned with the quantitative determination of internal stresses and strains produced in a body as the result of external loads and deformation. Its methods are both theoretical and experimental. The complete stress analysis of the tire should establish the magnitude and direction as well as the type of stress at all points in the tire under each loading condition of interest. This information defines the so-called state of stress. Such knowledge, when combined with the material properties of the rubber, cord, and steel can be used to predict or explain the behavior of the tire in service.

The material properties of the three structural components of the tire are widely different. For example, the Young's moduli obtained at room temperature from statically conducted tests are approximately: 300–3000 psi for the rubber, 100,000–800,000 psi for the textile cords, and 30,000,000 psi for the steel bead wire. In addition, the final geometries into which these components can be combined are diverse. Presently, there are three distinct cord arrangements in automobile tire construction: bias, belted-bias, and radial. These material and geometric factors, coupled with the fact that the tire as a whole is an anisotropic body subjected to finite deformations which are rate and temperature dependent, have made the theoretical and experimental stress analysis of the tire more difficult than that associated with the majority of engineering structures.

It is not the purpose of this chapter to compile a bibliography containing every publication related to the subject of the stress analysis of pneumatic tires. Rather, the intent is to discuss the important topics and to present them in a logical order. The references to the literature are mainly directed to elucidating the textual material. However, every attempt has been made to settle questions of priority.

4.2. Analytical Techniques

4.2.1. Solutions for Inflation Loads

The simplest stress analysis problem to consider from a theoretical standpoint is the calculation of the shape taken by and the stresses developed in an inflated but otherwise unloaded bias tire. The first rigorous solution to this problem was obtained by Purdy [1]² in the United States in 1928.³ However, it was not until 1956, when Hofferberth [3] published his results in Germany, that such work became readily accessible to all tire engineers. Biderman's investigations [4] treating the same subject appeared in 1957 in the Soviet Union. In the remainder of this chapter it is convenient to refer to the solution of the inflated tire shape equation independently obtained by these three investigators as the PHB solution. The importance of this shape equation is due to the fact that once the geometry of the tire is accurately known, the stresses developed in it can be calculated.

Before developing the analytical details for this particular problem, it should be noted that some investigators have found it convenient to *a priori* assume that the inflated tire cross section can be adequately represented from bead to bead in the meridian plane by a portion of an ellipse since the PHB solution deviates only slightly from such a shape. While this assumption is valid for estimating such quantities as the surface area of a tire and the volume enclosed by a tire, it can easily lead to large errors in stress analysis since these stress calculations are very sensitive to small changes in geometry. However, since the basic equations employed in the PHB analysis are the same as those used when the shape is *a priori* assumed, it is useful to present the details of this latter, though less exact, approach before discussing the PHB solution.

A portion of a pressurized but otherwise unloaded toroidal shell is shown in figure 4.1. The axial coordinate z is an axis of revolution. Because of the very small bending stiffness of the tire walls, and the rotational symmetry of both the applied load and shell geometry, in-plane internal reactions develop which are constant through the shell thickness. These internal reactions, denoted by N_ϕ and N_θ , are usually called membrane stress resultants, and they act in the meridional and circumferential directions, respectively. Physically, the stress resultants represent forces per unit length.

The applied load (inflation pressure p) is just balanced by the internal reactions N_ϕ and N_θ —that is, force equilibrium exists—so that summing forces normal to the shell surface leads to the well known equilibrium equation

$$\frac{N_\phi}{r_\phi} + \frac{N_\theta}{r_\theta} = p \quad (4.1)$$

² Figures in brackets indicate literature references at the end of this chapter.

³ Purdy's original report is contained, in many places word for word, in Chapters I and II of his 1963 monograph [2].

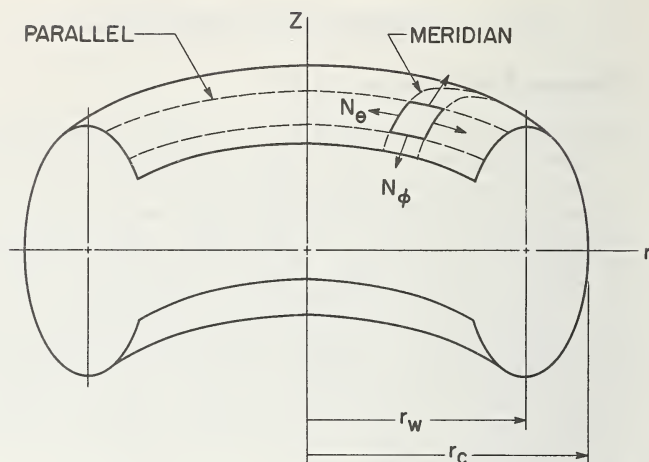


FIGURE 4.1. Portion of a pressurized toroidal shell.

where r_ϕ and r_θ are principal radii of curvature for the doubly curved toroidal surface. Both the stress resultants and the radii of curvature are functions of the radial distance r .

A second equation of equilibrium can be obtained from figure 4.1 by summing forces along the axis of revolution to obtain:

$$N_\phi = \frac{pr_\theta(r^2 - r_w^2)}{2r^2}. \quad (4.2)$$

Equations (4.1) and (4.2) are two equations for the two unknown stress resultants and they can be immediately solved when the meridional geometry of the toroidal shell is given. For example, in the case of an elliptic meridian, as in figure 4.2, it is known that

$$r_\phi = \frac{[b^4 + (a^2 - b^2)(r - r_w)^2]^{3/2}}{ab^4},$$

$$r_\theta = \frac{r[b^4 + (a^2 - b^2)(r - r_w)^2]^{1/2}}{a(r - r_w)}.$$

Thus, the stress resultants are found from eqs (4.1) and (4.2) by eliminating r_ϕ and r_θ to obtain

$$N_\phi = \frac{p(r + r_w)[b^4 + (a^2 - b^2)(r - r_w)^2]^{1/2}}{2ar},$$

$$N_\theta = \frac{p[2r(a^2 - b^2)(r - r_w) + b^4]}{2a[b^4 + (a^2 - b^2)(r - r_w)^2]^{1/2}}.$$

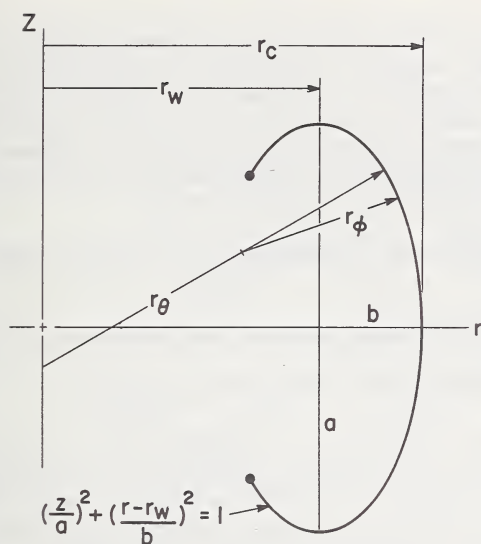


FIGURE 4.2. Cross section geometry of a toroid with an elliptic meridian.

Lorenz [5] obtained these equations for the stress resultants developed in a pressurized toroidal shell of elliptic cross section in 1910. Since then, several investigators [6-9] have employed these relations in their analyses of pneumatic tires. While the value of N_ϕ given above deviates only slightly from the value obtained from the PHB solution, the value of N_θ deviates considerably. In fact, inspection of the above results indicates that N_θ can be negative in some regions of the shell, depending on the eccentricity of the ellipse. This condition is difficult, if not impossible, to realize in a symmetrically loaded fabric structure such as an inflated tire.

Also note that eq (4.2) defining the meridional stress resultant N_ϕ for a toroid with an arbitrary meridian, is indeterminate at the radial location $r=r_w$ where the circumferential radius of curvature r_θ is undefined. This indeterminacy has the form 0/0. However, by recognizing that any equation for r_θ applicable to a toroidal shell always contains the quantity $(r-r_w)^{-1}$ and by employing appropriate limiting processes, the indeterminacy is removed regardless of meridional geometry and it presents no problems in membrane stress analysis—i.e., N_ϕ , as well as N_θ , is everywhere finite and continuous. Other arguments can be used to show that N_ϕ is always tensile and always has the same value at the radial position $r=r_c$ for any pressurized toroidal shell. It has been known for some time that the displacement analysis for this particular problem presents analytical difficulties at $r=r_w$ whenever the usual relations are employed to connect strains and displacements for shells of revolution [10]. In particular, the displacement in the z direction is singular at $r=r_w$ in the linear membrane theory of toroidal shells. This anomalous behavior can only be explained by resorting to a non-

linear membrane theory [11-14]⁴ or a linear bending theory [15-17]⁴ either of which involves considerable mathematical complexity. It should be emphasized, though, that these analytical difficulties in the displacement analysis do not keep us from predicting reasonably accurate membrane stresses and cord forces in inflated tires.

For actual tire structures, relations must be employed in addition to eqs (4.1) and (4.2) to account for the following:

- a. The load carrying capability of the cord and rubber components of the tire.
- b. The path of the cords from the bead to the crown in the tire.
- c. The unknown geometry of the tire cross section.

The first matter (a) needs to be discussed in some detail since at the present time there is no easy way to rigorously account for the combined load carrying capability of the cord and rubber. In the PHB analysis of tires the rubber is treated as a nonstructural liner whose only purpose is to contain the air and transmit load to the cords, i.e., its presence is entirely neglected. This engineering approximation, which greatly simplifies analysis, is more nearly realized at high than low inflation pressures. At very low pressures—below those used in service—the rubber is just as effective as the cord in supporting load and the approximation is not valid. For mathematical simplicity, then, it is assumed that the pressure is great enough to stabilize the tire shape and this shape is unchanged as the pressure is further increased, and the cords carry all of the applied load so that the surface to which all tire dimensions are referred is the surface midway between the plies. We consider a typical cord network element which is bounded by two adjacent meridians and two adjacent parallel circles as in figure 4.3. Note that the cord angle β is the angle between a meridian and a cord.⁵ Using figure 4.4, the resolution of forces in the meridional and circumferential directions, respectively, requires that

$$N_{\varphi} = nT \cos^2 \beta,$$

$$N_{\theta} = nT \sin^2 \beta,$$

where n is the product of the (even) number of plies in the bias tire multiplied by the number of cords crossing a line of unit length perpendicular to the cords, and T is the tension in an individual cord. These equations can be combined to yield either

$$N_{\varphi} + N_{\theta} = nT,$$

⁴ These cited references are only a few of many studies treating this subject.

⁵ Another common convention is to define the cord angle as the angle between a circumferential line and a cord, i.e., $\frac{1}{2}\pi - \beta$.

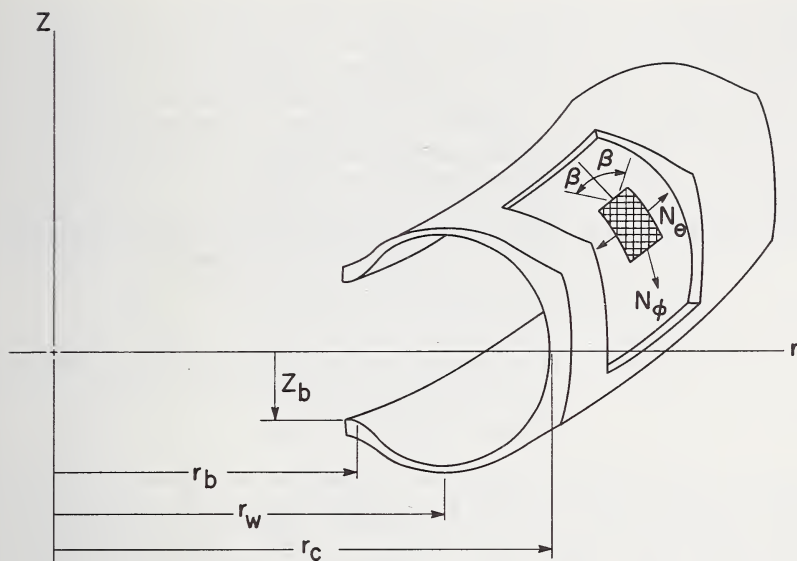


FIGURE 4.3. Typical geometry of a pressurized bias tire.

which is the basis of a failure law for filamentary composite materials under plane stress conditions [18], or

$$\frac{N_{\theta}}{N_{\phi}} = \tan^2 \beta, \quad (4.3)$$

which is the basis of the so-called netting analysis of composite materials. This netting concept is often referred to as a condition of balanced design [19] or equilibrium design [7]. Equation (4.3) is a special case of a more general relation first derived by Haas [20] in 1912 and, like eqs (4.1) and (4.2), it is based only on equilibrium considerations. Thus, we have three equations for the two unknown stress resultants, and these three equations can be simultaneously satisfied only if the tire (or any other fabric structure) is in its "equilibrium configuration." The concept of the equilibrium configuration is sufficiently important in the stress analysis of pneumatic tires to justify further consideration. A simple demonstration of this concept is afforded in the case of a pressurized cord-rubber cylinder as in figure 4.5. Equations (4.1) and (4.2) give with $r_{\theta} = r_c = r = R$, $r_{\phi} = \infty$, $r_w = 0$,

$$N_{\theta} = pR$$

$$N_{\phi} = \frac{1}{2}pR$$

so that eq (4.3) produces

$$\tan^2 \beta = 2 \quad \text{or } \beta = \pm 54.7^{\circ}.$$

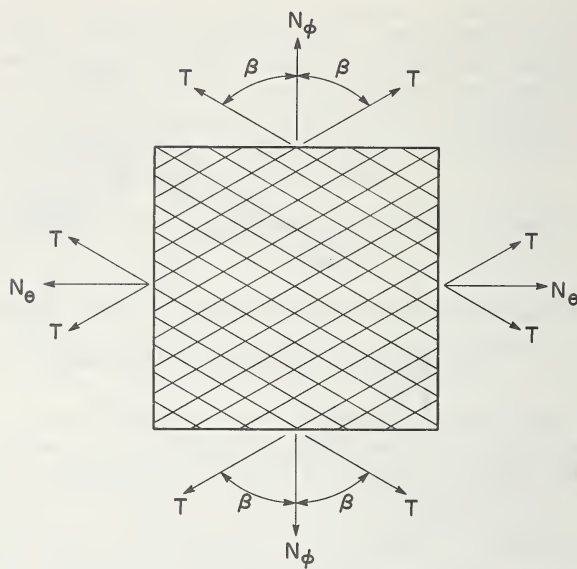


FIGURE 4.4. *Planar cord network element from a bias tire.*

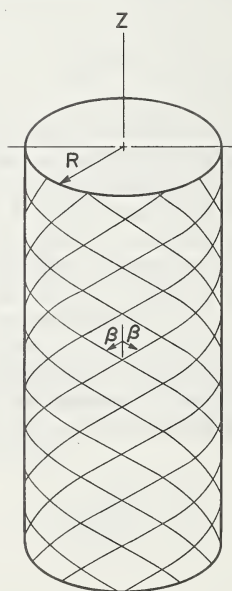


FIGURE 4.5. *Pressurized cord-rubber cylinder with cords at equilibrium angle ($= 54.7^\circ$).*

The implication of this result is: only if the cylinder is constructed with a helical cord path at $\pm 54.7^\circ$ with the longitudinal (z) axis will it retain its cylindrical shape when pressurized. If the cord angle β is less than or greater than this ideal angle, pressurization causes the cords to tend to seek their preferred or equilibrium orientation, but the rubber, since it has some strength, restricts this action. Thus, when $\beta \neq \pm 54.7^\circ$, the shape of the structure changes with pressurization and it is no longer cylindrical. As an extreme case, consider an initially uninflated cylinder containing cords parallel to its axis ($\beta = 0^\circ$) as shown in figure 4.6. After inflating, the resolution of forces gives

$$N_\theta = nT \sin^2 \beta = 0 \quad (a)$$

while the membrane theory of shells gives

$$N_\theta = pR \quad (b)$$

Since these membrane forces are determinate, eq (b) must be satisfied. From eq (a) no N_θ is generated by cord loads T , hence N_θ must come from stresses in the rubber, which is ill-suited for such stressing since it results in excessive deformation. For this reason such designs are generally avoided. When the cylinder of figure 4.6 is gripped at each end and inflated, it will exhibit large radial strains, associated with N_θ acting on the rubber matrix alone, at all regions of the cylinder except at the ends where it is restrained by grips. Under similar loading, a cylinder with a 54.7° cord path would exhibit little dimensional change.

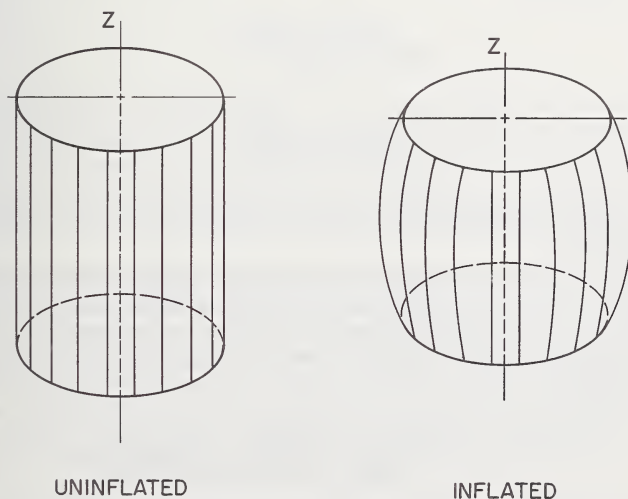


FIGURE 4.6. Cord-rubber cylinder with longitudinal cords ($=0^\circ$) before and after inflation.

The concept of the equilibrium configuration has been extensively used in the design and manufacture of fabric hose [21] and filament wound rocket motor cases [22]. These same ideas, of course, are valid for the more complicated geometry of tires, and Midgley [23] was aware of the implications of this concept as long ago as 1920. He recommended, without specifying the mathematics, that tires with cords having large values of β should be cured in a low oval mold while tires with cords having small values of β should be cured in a high oval mold. Tires produced in this fashion, i.e., close to their equilibrium configuration, would not tend to change their shape in service and would be free of unnecessarily imposed inflation stresses in the rubber matrix.

The second matter (b) is most easily disposed of by noting that a reasonable approximation to the cord path in tires of conventional construction⁶ is given by the so-called trellising or pantographing law [24] which relates the local cord angle β with its radial location r in the finished tire

$$\frac{r}{\sin \beta} = \frac{r_c}{\sin \beta_c} = \text{constant} \quad (4.4)$$

where the subscript c denotes a quantity evaluated at the crown ($r = r_c$) of the tire. Modifications of this equation, as well as some nonconventional cord paths, will be referred to later. As a consequence of prescribing the cord path through eq (4.4) and of employing the netting concept of eq (4.3), the meridional or cross-sectional shape of the tire is not arbitrary. Similarly, if the meridian curve were to be specified, there is no freedom as to the choice of the cord path [19].

The third matter (c) is taken care of by expressing the principal radii of curvature for a toroid in their differential form in rectangular cartesian coordinates [25], i.e.,

$$r_\varphi = \frac{[1 + (z')^2]^{3/2}}{z''}, \quad (4.5)$$

$$r_\theta = \frac{r[1 + (z')^2]^{1/2}}{z'}, \quad (4.6)$$

where z' and z'' denote the first and second derivatives of z with respect to r , respectively.

Equations (4.1-4.6) are the basic relations needed for the determination of the equilibrium contour of the bias tire. Eliminating all variables that depend on the radial distance r (N_φ , N_θ , r_φ , r_θ , and β), and combining the results leads to a second order nonlinear differential equation involving z'' and z' .

$$z'' + z'[1 + (z')^2] \left\{ \frac{r \sin^2 \beta_c}{r_c^2 - r^2 \sin^2 \beta_c} - \frac{2r}{r^2 - r_w^2} \right\} = 0.$$

⁶ Conventional construction means that the cords in each ply alternately form right and left handed helices on a cylindrical building drum before the tire is expanded into its final toroidal shape.

By the usual methods of ordinary differential equations [26], this relation can be reduced to a first order equation which, in turn, can be expressed as the indefinite hyperelliptic integral

$$z = \mp \int_r^{r_c} \frac{(r^2 - r_w^2) (r_c^2 - r^2 \sin^2 \beta_c)^{1/2} dr}{[(r_c^2 - r_w^2)^2 r_c^2 \cos^2 \beta_c - (r^2 - r_w^2)^2 (r_c^2 - r^2 \sin^2 \beta_c)]^{1/2}} \quad (4.7)$$

Equation (4.7) defines the equilibrium contour, $z = z(r)$, of the conventional bias tire and is equivalent to the results obtained independently by Purdy, Hofferberth, and Biderman, i.e., the PHB solution, except that Hofferberth included an average but unknown cord elongation in his equation. It cannot be integrated in closed form except for the special case of radially disposed cords [27], or $\beta_c = 0^\circ$. Its solution, then, generally requires the methods of either numerical or graphical integration. This integration is easily effected for given values of the parameters r_c , r_w , and β_c even though eq (4.7) is singular at the crown $r = r_c$. Purdy [2] has plotted typical equilibrium contours for different values of r_c , r_w , and β_c using graphical techniques. These graphical methods of integrating the tire contour integral are discussed in detail by Biderman [4, 28] and Day and Gehman [27]⁷. Ellis and Frank [29] have shown how these same calculations can be carried out on an analog computer. Biderman has developed an extensive set of nomograms based on graphical [4, 28] and numerical [30] procedures which permit one to calculate the equilibrium dimensions of an inflated tire knowing three quantities: the coordinates (z_b, r_b) which locate the so-called rim point on the inside tire surface, shown in figure 4.3 and which are used in eq (4.7) making it a definite integral; the length of the cord from bead to crown, L , which is given by

$$L = \int_s \frac{ds}{\cos \beta},$$

where the element of arc length, ds , is expressible in terms of eq (4.7); and the crown angle β_c . In effect, the first two items provide two equations for the determination of the two unknowns r_c and r_w which are then used with β_c in the calculation of the Biderman nomograms. Similar nomograms have been machine plotted by high speed digital computers [31].

The importance of having a relationship like eq (4.7) is that it allows tire engineers to carry out parameter studies without actually building tires. For example, it is easy to show that if the cord length and rim dimensions are held constant and only the crown angle is allowed to vary, low values of β_c lead to tires with tall, narrow equilibrium cross sections while high values of β_c lead to tires with low, wide equilibrium cross sections. The study of these equilibrium contours is of great importance as a guide to good mold design.

⁷ The tire contour integral given by Day and Gehman [27] contains a typographical error; specifically, an unneeded r appears in the denominator of their eq (4.13).

The lowest inflation pressure at which the assumptions inherent in this analysis are valid can be determined for a given tire by plotting a typical dimension, such as section width, as a function of pressure and then noting the pressure at which this dimension remains (relatively) unchanged as the pressure is increased. Biderman [4, 28] has done this for a 9.00-20 truck tire and has shown that the section width for this tire no longer changes, for all practical purposes, at an inflation pressure well below that recommended for use in service. In fact, if there is a significant change in a tire dimension during the early stages of inflation, this is an indication that the molded contour of the tire is different from its equilibrium contour.

Several refinements can be added to the basic analysis presented here for calculating the equilibrium configuration of a bias tire. The conventional cord path relation, eq (4.4), can be modified to include the effect of cord extensibility [3, 4, 32, 33] which means that the tire contour integral given by eq (4.7) will then include directly the material properties of the cord and indirectly the magnitude of the internal pressure. These factors, cord properties and internal pressure, always influence tire shape to some extent and in some cases, such as a nylon tire operating near its bursting pressure, cannot be neglected. A further modification of the preceding analysis is to completely replace eq (4.4) by another cord path of interest. For example, a geodesic path is defined by the theorem of Clairaut [34] as

$$r \sin \beta = r_c \sin \beta_c = \text{constant},$$

and has the remarkable properties that the distance between any two points on a cord is minimum and the tension at all points along a cord is constant. Many other types of nonconventional cord paths possessing some unusual or desirable properties when compared to the conventional cord path, eq (4.4), have been discussed by Purdy [2], Day and Gehman [27], and others [35-37]. In all cases, modifying the theory to include either the cord elongation or a nonconventional cord path leads to a singular hyperelliptic integral similar to eq (4.7) which, in general, does not possess a closed form solution.

Since an accurate prediction of meridional geometry is a prerequisite for calculating tire stresses, the validity of eq (4.7) can be demonstrated on an existing tire by determining the parameters r_c , r_w , and β_c by measurements and then using these value to plot the equilibrium contour, $z=z(r)$. The comparison between a theoretically predicted and an experimentally measured contour is shown in figure 4.7 for an 8.25-14 two-ply polyester tire [38]. These calculations were carried out numerically using a digital computer, which is a quicker and more accurate method than using graphical integration. Lauterbach [39], Mikell [40] and Lauterbach and Ames [41] have plotted comparable results for an 8.00-15 four-ply nylon tire using numerical integration techniques. In general, the agreement between theory and experiment is good. Deviations between the predicted and measured coordinates are largest in the bead region where the theory consistently predicts smaller axial

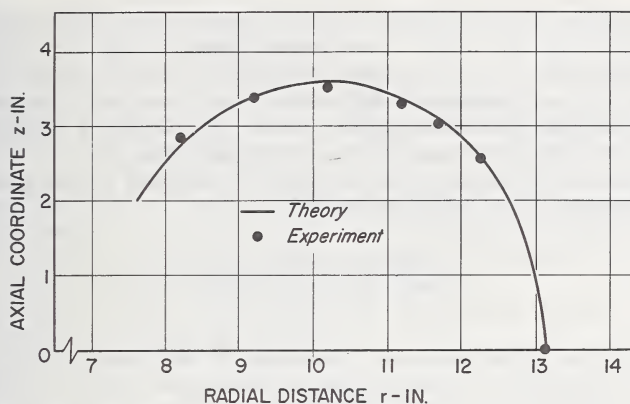


FIGURE 4.7. The equilibrium contour for an 8.25-14 two-ply polyester tire theoretically predicted by eq (4.7) and experimentally measured ($r_c = 13.12$ in., $r_w = 10.14$ in., $\beta_c = 55^\circ$) [38].

dimensions (z) than those observed. These deviations are expected near the bead since membrane theory is known to be inadequate [42] near shell boundaries, i.e., at the point of attachment of the tire to the rim and in areas where large changes in rigidity occur, i.e., at the location of the steel bead and the ply turn-ups.

Equation (4.7) can be used directly, without integration, to calculate the stress resultants using eqs (4.1) and (4.2):

$$N_\varphi = \frac{pr_c(r_c^2 - r_w^2) \cos \beta_c}{2r(r_c^2 - r^2 \sin^2 \beta_c)^{1/2}},$$

$$N_\theta = \frac{prr_c(r_c^2 - r_w^2) \cos \beta_c \sin^2 \beta_c}{2(r_c^2 - r^2 \sin^2 \beta_c)^{3/2}},$$

and the principal radii of curvature using eqs (4.5) and (4.6):

$$r_\varphi = \frac{r_c(r_c^2 - r_w^2)(r_c^2 - r^2 \sin^2 \beta_c)^{1/2} \cos \beta_c}{2r(r_c^2 - r^2 \sin^2 \beta_c) - r(r^2 - r_w^2) \sin^2 \beta_c},$$

$$r_\theta = \frac{rr_c(r_c^2 - r_w^2) \cos \beta_c}{(r^2 - r_w^2)(r_c^2 - r^2 \sin^2 \beta_c)^{1/2}}.$$

From the preceding analytical developments, it is possible to calculate the cord tension, the bead tension, and the cord-rubber interface shear stress developed in an inflated but otherwise unloaded bias tire. By themselves, these inflation forces and/or stresses are not responsible for the failure of any of the tire components (cord, rubber, steel) in service; rather, they are important because all loads that a tire receives in operation are superimposed on these initially developed inflation forces

and/or stresses. The derivations of the formulas for cord tension, bead tension, and interface shear stress are all based on the tire contour integral, eq (4.7). However, the lengthy manipulative details involved in each derivation are not presented here since they are well documented in readily accessible literature; rather, we list the pertinent equations, give an example of their use, and discuss their limitations.

Inflation Cord Tension: The tension T developed in the cords of an inflated bias tire is given by the formula

$$T = \frac{p\pi r_c^2(r_c^2 - r_w^2) \cos \beta_c}{N(r_c^2 - r^2 \sin^2 \beta_c)}. \quad (4.8)$$

For a given tire, cord tension is minimum at the bead where the radial distance r is minimum and is maximum at the crown where r is maximum. Equation (4.8) does not involve the modulus of the tire cord because of the inextensibility assumption used in the derivation of the tire contour integral. For the special case of radially disposed cords, $\beta_c = 0^\circ$, which is also a geodesic path, cord tension becomes

$$T = \frac{p\pi(r_c^2 - r_w^2)}{N}.$$

Equations equivalent to the above were first derived by Purdy [2]; many investigators have subsequently discussed such cord load formulas [4, 27, 28, 41]. A typical result obtained for the cord tension distribution, $T = T(r)$, for an 8.25-14 two-ply polyester tire at 24 psi inflation pressure is shown in figure 4.8 [38]. The equilibrium contour $z = z(r)$ for this tire is shown in figure 4.7. For comparison with the theoretical predictions, experimentally measured cord forces are also shown. These measure-

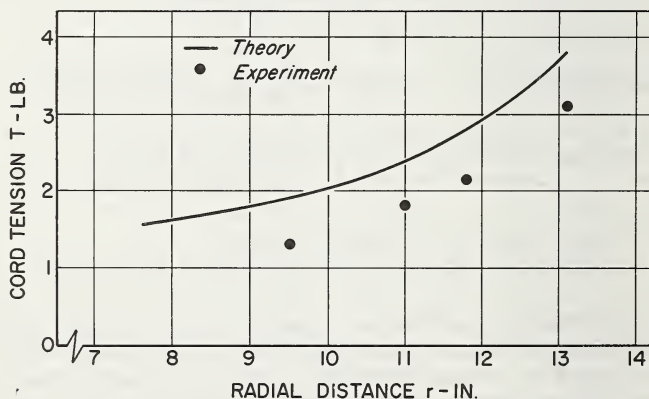


FIGURE 4.8. The cord tension distribution in an 8.25-14 two-ply polyester tire theoretically predicted by eq (4.8) and experimentally measured ($r_c = 13.12$ in., $r_w = 10.14$ in., $\beta_c = 55^\circ$, $p = 24$ psi, $N = 2350$) [38].

ments were made using miniature force transducers described later in this chapter and shown in figure 4.16.

Lauterbach and Ames [41] plotted the cord tension distribution in an 8.00-15 four-ply nylon tire at 24 psi inflation pressure and compared their predictions with the experimental measurements of Weickert [43]. These studies show that the maximum inflation cord load developed in typical automobile tires at rated pressure is approximately 10 percent of the cord breaking strength as determined from a room temperature, slow speed tension test of the greige cord. This large strength reserve is needed in order to provide adequate fatigue resistance and impact strength to the tire under service conditions [44].

Inflation Bead Tension: The tension B developed in each bead of an inflated bias tire is given by the formula

$$B = \frac{p(r_c^2 - r_w^2) \cos \beta_c}{2 \cos \beta_b} \quad (4.9)$$

where β_b is the cord angle at the "rim point" as illustrated in figure 4.3 and is nominally equal to the angle of the cord on the building drum (bias angle). For the special case of radially disposed cords, $\beta_c = \beta_b = 0^\circ$

$$B = \frac{p(r_c^2 - r_w^2)}{2}$$

which indicates that larger inflation bead forces occur in radial tires with cords normal to bead than in bias tires with cords inclined to bead. If the cords are disposed tangentially to the bead, no tension develops there as the tire is inflated. Equation (4.9) is the form recommended by Biderman [4]. The formula derived by Purdy [2] and discussed by Day and Gehman [27] is difficult to use since it involves differences of nearly equal large numbers. As has been previously discussed, the equilibrium contour of the inflated tire is not predicted accurately in the bead region. Equation (4.9), then, should be used with some caution since it is based on the tire geometry. Bead tension is plotted as a function of inflation pressure in figure 4.9 for an 8.25-14 two-ply polyester tire. The equilibrium contour and the cord tension distribution for this tire are shown in figures 4.7 and 4.8, respectively. Pugin [45] has shown that eq (4.9) is in error on the high side, that is, the actual bead forces in this tire due to inflation pressure are less than those predicted and shown in figure 4.9. Irodov [58] has attributed these differences to friction forces existing between the bead and rim which are neglected in eq (4.9).

Cord-Rubber Interface Shear Stress: When a filamentary composite structure such as a tire is loaded in some arbitrary fashion, the relatively weak matrix transfers most of the load to the stronger reinforcements. The mechanism available for this load transfer is interface shear stress which is generated over the contact surface existing between the cord and rubber. The bonding agent or adhesive that connects the cord to the rubber is not usually thought of as a structural component of the tire, but if this bond ruptures the tire will quickly fail in service due to

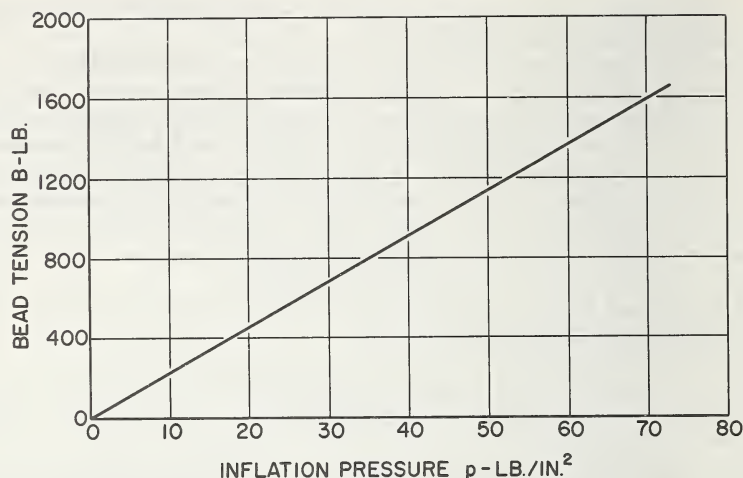


FIGURE 4.9. Bead tension as a function of inflation pressure using eq (4.9) for an 8.25-14 two-ply polyester tire ($r_c = 13.12$ in., $r_w = 10.14$ in., $\beta_c = 55^\circ$, $\beta_b = 28\frac{1}{2}^\circ$).

the relative movement of cord and rubber. In an inflated bias tire, the shear stress τ developed at the cord-rubber interface in the direction of the cords is given by the formula

$$\tau = \frac{pr_c \sin^2 \beta_c [(r_c^2 - r_w^2)^2 r_c^2 \cos^2 \beta_c - (r^2 - r_w^2)^2 (r_c^2 - r^2 \sin^2 \beta_c)]^{1/2}}{(r_c^2 - r^2 \sin^2 \beta_c)^2} \quad (4.10)$$

Equation (4.10) involves the rate of change of cord tension with cord length; thus, for radially disposed cords ($\beta_c = 0^\circ$), the cord-rubber interface shear stress vanishes since the cord tension is everywhere constant between the bead and the crown of the tire. The preceding expression differs from the equivalent result first obtained by Purdy [2] and discussed by Day and Gehman [27] by a factor $\sin \beta$ since in these two studies τ was interpreted as a shear stress existing circumferentially between the plies rather than being developed in the cord direction between cord and rubber. In any case, the values of the interface shear stress calculated from eq (4.10) at inflation pressures used in service are well below the rupture shear stress values generated in a cord-rubber pull-out test [46], just as the cord tension developed at normal inflation pressures is well below the breaking strength of the cords. A typical distribution of the shear stress $\tau = \tau(r)$ is given in figure 4.10 for an 8.25-14 two-ply polyester tire at 24 psi inflation pressure. The equilibrium contour, the cord tension, and the bead forces associated with this tire are shown in figures 4.7, 4.8, and 4.9 respectively. Note that τ vanishes at the crown and is maximum at the shoulder, a result that holds true for all bias tires.

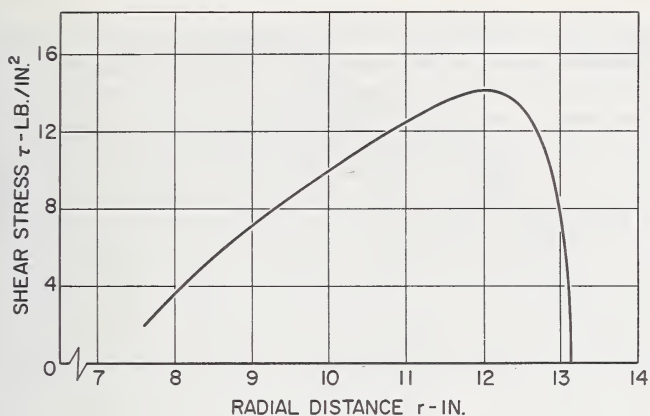


FIGURE 4.10. *The shear stress distribution in an 8.25-14 two-ply polyester tire according to eq (4.10) ($r_c = 13.12$ in., $r_w = 10.14$ in., $\beta_c = 55^\circ$, $p = 24$ psi).*

At the present time there is no generally accepted theory for accommodating a “belt” into the equations which govern the inflated equilibrium contour of tires. Consequently there is no way to predict the stresses developed at all locations in such tires. The circumferential constraint imposed by a belt causes a change in tire dimensions to occur compared to comparably constructed nonbelted tires. All of the published work in this area has dealt exclusively with the radial belted or, simply, radial tire. No definitive studies of a theoretical nature have been published for the belted-bias tire. Slyudikov [47] has made measurements of various radial tire dimensions as a function of belt properties and has shown that no simple linear relationships exist between the parameters. A formula used by Biderman, et al. [48], to predict the forces in the belt of an inflated radial tire gives values that are two to three times the values measured experimentally. Frank [49, 50] has made what is perhaps the most comprehensive study to date of the problem of predicting the equilibrium contour of the radial tire. This work includes as a special case the nonbelted bias tire. Böhm’s method [51] for analyzing the radial tire possesses an acceptable degree of rigor and is much simpler to apply than the method of Frank. It includes an empirically determined “girdling” or “belting” function. When this function is zero, the contour integral for the conventional bias tire is obtained. Without the belt, the equilibrium geometry of the tire with radially disposed cords is easily determined [27, 52]. Belted tires are also the subject of a separate chapter in a Russian monograph [53] of 1963.

4.2.2. Solutions for Centrifugal Loads

Any tire subjected to loads that are distributed in a rotationally symmetric fashion can be analyzed using the techniques given in the preceding paragraphs for the inflation problem. Such loads primarily produce a membrane response in the tire with negligible bending effects. Because

of symmetry, the meridional or cross-sectional geometry of the tire is identical at all circumferential locations and only ordinary, rather than partial, differential equations need to be employed to effect a solution suitable for stress analysis. Cord load formulas for axisymmetrically loaded tires are characterized by the absence of ply-to-ply variations in cord tension at a given location in the tire. Of course, for tires under actual operating conditions where the applied forces and moments lack rotational symmetry, deflection at the contact zone and ply-to-ply effects in the tire are important features which cannot be taken into account using this restricted theory. The most important case amenable to solution in the category of axisymmetrically loaded tires, other than the inflation problem, is the combination of internal pressure and centrifugal force. However, a tire inflated inside a constraining cylinder, i.e., a uniformly deflected tire, can be studied within the framework of this theory [54, 55]. Even the tire in a mold during vulcanization is loaded thermally and mechanically in an axisymmetric fashion. Neither of these last mentioned problems have received as much attention as the inflated, rotating tire.

The first analytical study of the bias tire subjected to both inflation and centrifugal loading was made by Bukhin [56] in 1960 who used a Ritz energy method to find the dynamic equilibrium contour. Bukhin discovered that at high angular velocities, the location at which maximum cord tension occurs in the tire can be displaced from the crown toward the bead. Wutzler [57] studied the same problem by working directly with the differential equations of the membrane theory of shells. For the rotating tire Wutzler concluded that bending as well as membrane effects can be important at low inflation pressures. Walter [38] developed equations for the dynamic equilibrium contour and the cord forces which reduce to the corresponding formulas of the PHB solution in the static case. These studies show that while the static equilibrium contour of the inflated tire is independent of pressure, the dynamic equilibrium contour of the inflated, rotating tire depends both on pressure and angular velocity.

The effect of a centrifugal load on an inflated, rotating tire can be investigated using the same techniques as employed in the analysis of the tire loaded solely by inflation pressure, except that eq (4.1) must be replaced by the more general equilibrium equation

$$\frac{N_\varphi}{r_\varphi} + \frac{N_\theta}{r_\theta} = p + \frac{mr^2\omega^2}{r_\theta} \quad (4.1')$$

where m is the mass per unit area of cord and rubber in the tire which is a function of position, and ω is the angular velocity of the tire. Equations (4.2)–(4.6) given earlier remain unchanged. Again, numerical or graphical techniques must be employed to integrate the resulting contour integral. Typical curves obtained by Walter [38] for the dynamic equilibrium contour $z = z(r)$ and the cord tension distribution $T = T(r)$

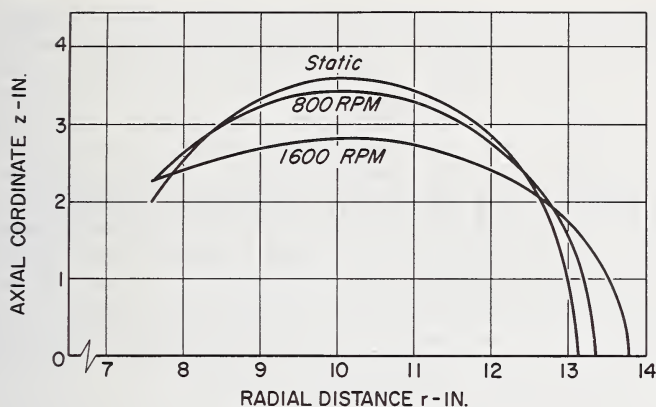


FIGURE 4.11. Theoretically predicted equilibrium contours for an 8.25-14 two-ply polyester tire at 24 psi inflation pressure and various angular velocities [38].

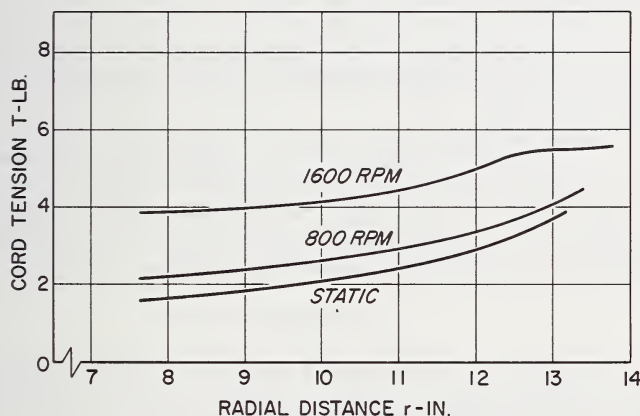


FIGURE 4.12. Theoretically predicted cord tension distributions for an 8.25-14 two-ply polyester tire at 24 psi inflation pressure and various angular velocities [38].

are shown in figures 4.11 and 4.12, respectively, for an 8.25-14 two-ply polyester tire at 24 psi inflation pressure and angular velocities up to 1600 rpm (about 120 mph). Figure 4.11 shows that as the angular velocity is increased, the tire diameter increases, while the section width and sidewall curvature decrease. Figure 4.12 shows that centrifugal effects can produce a twofold increase in cord tension compared to the static results. Up to 800 rpm, the change in tire shape and the increase in cord tension are negligible. Other features of this particular tire have been previously given in figures 4.7-4.10.

Formulas for the bead tension and cord-rubber interface shear stress can be developed for the case of centrifugal loading just as they have been for the inflation problem. Bukhin [56] has plotted the tensile force in the bead ring of a 7.50-16 tire as a function of speed up to 250 km/hr. Wutzler [57] has plotted the cord strain developed in a 5.20-14 tire up to speeds of 175 km/hr. by assuming that the tire cord obeys Hooke's law. An equation for the cord-rubber interface shear stress for a centrifugally loaded tire has not yet been published in the literature.

The study of the inflated and rotating but otherwise unloaded tire is related to the investigation of traveling waves in tires, even though this latter problem involves rolling at high speed on a road or drum, which is a condition of nonsymmetric loading. However, since eq (4.1') given previously can be used to qualitatively explain this phenomenon (even though in the strictest sense it is not applicable to nonsymmetric loads), it is appropriate to discuss this topic now.

Traveling waves⁸ first appear at a certain critical rolling velocity, V_{cr} , and are produced in that portion of the tire which has just left contact with the road or drum. Below this critical velocity no waves are present. The length and amplitude of the waves, as well as the rolling resistance and temperature of the tire, increase drastically as the velocity is increased above the critical value. This destructive process quickly produces tire failure. This failure is due to both stress and temperature extremes resulting from the severe mechanical and thermal loads acting on the tire.

The first meaningful theoretical study of the traveling wave problem was made by Turner [59] in 1954. He modeled the tire as a flat flexible membrane, infinitely long in the circumferential direction and bounded by rigid steel beads on each side. When this model is subjected to external excitation, a displacement perpendicular to the membrane is propagated as a transverse wave with a velocity c given by

$$c = (N_{\theta}/m)^{1/2}$$

which is recognized as the classical result for the speed of a transverse pulse moving along a stretched string. Turner emphasized that traveling waves are not a resonant vibration phenomenon (as are standing waves with their attendant nodes and antinodes), meaning that one cannot drive through the critical condition merely by increasing speed so that the tire again runs smoothly. As a consequence, every portion of rubber on the same circumferential line undergoes identical transverse motion when the tire rotates at a velocity greater than or equal to the critical value ($c \geq V_{cr}$).

To find the critical velocity for a bias tire, solve eqs (4.1') and (4.3) for the circumferential stress resultant to obtain

$$N_{\theta} = \frac{pr_{\theta} + mr^2\omega^2}{1 + r_{\theta}/(r_{\varphi} \tan^2 \beta)}.$$

⁸ Traveling waves, traction waves, and rippling are used synonymously in the tire mechanics literature. Many times, traveling waves have been incorrectly referred to as standing or stationary waves.

Using Turner's value for the speed of transverse wave propagation $c = (N_\theta/m)^{1/2}$ with the above equation and letting $V_{cr} = c = r\omega$, one finds

$$V_{cr} = \tan \beta (pr_\phi/m)^{1/2} \quad (4.11)$$

which is a result that is in qualitative agreement with experimental findings. For example, in 1951, Gardner and Worswick [60] in an extensive testing program showed that the critical velocity of a tire could be increased—and therefore its endurance at high speed could be increased—by increasing the inflation pressure p , decreasing the tire mass m , increasing the meridional radius of curvature r_ϕ , or increasing the angle β between a cord and a meridian. Thus, eq (4.11) expresses the real nature of the traveling wave phenomenon even though it does not take into account the effect that the forces in the contact zone have on the stress resultants. However, the usefulness of this relation strongly depends on the values of the parameters employed since β , r_ϕ , and m are a function of position, and, additionally, β and r_ϕ change with velocity while p increases above its initial value due to heat build-up.

As an illustration of the use of eq (4.11) for calculating critical tire velocity and the onset of traveling waves, consider the 8.25-14 two-ply polyester tire treated in figures 4.7-4.12. For simplicity we use the static tire dimensions at 24 psi inflation pressure and evaluate all functions of position at the crown ($r=r_c$). From the relationship for the meridional radius of curvature given earlier in this chapter with the dimensions and parameters given by Walter [38], we have

$$r_{\phi c} = 4.46 \text{ in.}$$

$$m_c = 71 \times 10^{-6} \text{ lb.-sec.}^2/\text{in.}^3$$

$$\beta_c = 55^\circ.$$

Thus, eq (4.11) gives

$$V_{cr} = 1750 \text{ ips (= 99.5 mph).}$$

This predicted critical velocity is below that visually observed in drum testing, but considering the simplicity of the calculation, it does provide a reasonable first approximation to the true experimental value.

Refinements in Turner's original work have been made primarily by investigators in Japan and the Soviet Union. These more advanced studies are general enough so that one can calculate, in addition to the critical velocity, the length and amplitude of the traveling waves as the speed of the tire is increased above the critical value. To date, the best agreement between theory and experiment can be found in a paper published in 1968 by Akasaka and Yamagishi [9]. They obtained critical velocities and wave lengths at various inflation pressures for 5.60-13 and 7.00-13 bias tires. Ames [61] has made an appraisal of world literature on the traveling wave phenomenon for both bias and radial

constructions. Frank and Hofferberth [50] have briefly discussed this problem and the related problem of tire vibration in their review article on tire mechanics.

4.2.3. Methods for Analyzing the Tire in Service

At the present time, no investigations have been published that adequately treat the theoretical determination of either stress or strain in the cord, rubber, and steel components of a tire under service conditions. Thus, most of our knowledge of problems in this category has been obtained through the use of experimental methods which are discussed in detail later in this chapter. In this section, then, we point out why there is a scarcity of literature on this subject and discuss those few attempts that have been made to cope with the problem.

Recall that the tire shape, the stress resultants and the cord forces can be reasonably predicted in axisymmetrically loaded tires using only the equilibrium equations of the membrane theory of shells. The strain-displacement equations for a toroid and the stress-strain relations for an anisotropic body were not employed in the study. However, these are the factors that must be included in any stress analysis of the tire in operation but they are also the ones that are most difficult to analytically incorporate into the theory. These strain-displacement and stress-strain laws cannot be neglected without causing appreciable error in those regions where bending effects might be important, such as in the bead region, near the belt edges, or in the contact zone of a rolling tire. Incorporating these factors into shell theory, as it is known today, proves to be the major difficulty hindering the rational development of the theoretical stress analysis of the tire under service loading conditions.

An extensive body of literature exists treating the structural mechanics of thin shells [10, 42]. However, most of this literature was written for analyzing the stresses occurring in conventional rigid structures made from steel or concrete. As a consequence the theory is formed around the concept that the shell geometry remains essentially fixed during the loading process. While this is a valid assumption for the kinds of structures just mentioned, it is not valid for pneumatic tires since their geometry undergoes substantial changes during loading. Some measure geometry undergoes substantial changes during loading. Some measure of the magnitude of the displacements involved in statically deflecting a 10.00-20 radial ply truck tire is given by Frank and Hofferberth [50]. In the inflated but otherwise unloaded condition the meridional radius of curvature r_ϕ varies between 100 and 200 mm. depending on location. The total thickness of the tire at the crown is 32 mm. of which 13 mm. is tread thickness; the sidewall thickness is 11 mm. At rated load the deflection at the crown is 36 mm. and the section width increases by 15 mm. It is apparent that these displacements are appreciable compared to the tire thickness and the initial values of the meridional radius of curvature. Thus, if conventional shell theory is to be applicable to the deflected tire problem, it can only be used as an approximation for those

cases where the loading is such that relatively small displacements are produced.

It should also be noted that in shell structures made from isotropic materials, a sound experimental basis exists for the Kirchhoff assumption which states that a perpendicular edge of the undeformed shell element remains perpendicular to the shell surface in the deformed state, i.e., plane sections remain plane. This assumption is usually associated with the requirement that the thickness of the shell be small compared to the principal radii of curvature. For the cord-rubber materials used in tire construction, there is at the present time no experimental evidence that the Kirchhoff assumption is justified. In fact, some evidence exists for glass reinforced plastic structures that plane sections do not remain plane under load [62]. This means that until further information is available, it is not possible to definitely relate bending strains to displacements, which is a crucial step in the analysis of any structure, without danger of error. Thus, the adaptation of conventional shell theory may represent yet a further approximation to the real situation existing in loaded tires.

A further difficulty peculiar to pneumatic tires is associated with their toroidal geometry. It has been mentioned earlier in this chapter that a singularity occurs in the displacement at the sidewall, using linear membrane theory, which can only be removed at the expense of considerable mathematical complexity [11-17]. Thus, even a small deformation analysis of the tire treated as a toroidal shell will involve this complication.

Up to this point we have only discussed geometric factors which cause difficulties in the stress analysis of the tire in operation. These factors appear as nonlinearities in the strain-displacement equations, with the requirement that the equilibrium equations be written for an element of the tire in the deformed state. There will also be complications in the stress-strain relations because of the anisotropy of the cord-rubber structure. Even if one assumes that stress and strain are linearly related through an orthotropic law, the behavior of typical materials used in tire construction is different in tension than in compression [63]. Also, it would be desirable to reflect rate and temperature effects in the stress-strain law by using a viscoelastic constitutive relation. Thus, in addition to geometric nonlinearities in the shell equations, an accurate formulation of the problem will also contain complex stress-strain relations if the theory is to be applicable to tires. The usual procedure in structural mechanics is to combine the equilibrium equations, the strain-displacement equations, and the stress-strain relations to obtain a differential equation or system of such equations whose solution is obtained subject to certain boundary conditions. Frank and Hofferberth [50] note that this approach, when applied to anisotropic toroidal shells, has never met with success in the field of tire mechanics.

Ames and Lauterbach [64] have circumvented all of the difficulties just mentioned by assuming that a deflected tire can be adequately described by a membrane state of stress. They avoided the formidable problem of predicting the deflected tire contour at a given load by meas-

uring the loaded tire shape directly. Reasonable analytical approximations were made for the pressure distribution in the contact zone, based on experimental measurements. Then they solved the differential equations applicable to shells of revolution on an analog computer to predict the stress resultants and the cord forces in a four-ply nylon tire. Since a deflected tire is not a surface of revolution, a more sound approach would have been to use the differential equations applicable to shells of arbitrary shape subjected to the same loads (inflation pressure and static deflection). Also, their calculated cord tensions did not show ply-to-ply cord force variations which, from experimental measurements [65], are known to be appreciable for this problem.

Gregory, et al. [66], have found an approximate solution for a tire loaded by internal pressure and subjected to a normal load over a small portion of its outer surface on the basis of differential equations set up by Biderman for a cord-rubber cylinder. Equations in closed form were obtained for the tire deflection, the pressure in the contact zone, and the tension in the cords in terms of inflation pressure and normal load. It was shown analytically that the maximum cord load occurs at the crown of the tire in the center of the footprint; this conclusion is not in agreement with experimental cord force measurements [65].

In those cases where the primary interest is in the tire displacement rather than the stresses, using energy methods to obtain solutions can be more successful than attempting to directly solve the differential equations governing the displacements. To use the energy principles, approximate functions are assumed for the displacement patterns which satisfy either the boundary conditions or the differential equations. These functions are then quantitatively determined by using techniques such as those of Ritz, Galerkin, or Trefftz [67]. One of the difficulties with the energy methods is that stresses are usually not calculated as accurately as displacements since the stresses depend on the derivatives of the displacements. This means that if the energy function for a pneumatic tire can be written, this principle can be used to determine the displacement characteristics of the tire under the action of external loads, and from these displacement characteristics, the stresses may be calculated. Frank and Hofferberth [50] give an outline of this procedure for the case of small displacements for shells of revolution. These authors are also of the opinion that if answers to problems associated with the tire in service are ever to be obtained in a closed mathematical form useful for further applications, it will only be through the use of the energy methods. Knowles and Reissner [70] have obtained an energy expression for thin elastic shells using rigorous geometrical relations. Their energy function contains certain terms not normally used in shell theory and, as a consequence, it should be more accurate for those cases where displacements are highly sensitive to local factors, as in a tire rolling under load. Clark, et al. [68], have attempted to apply the energy expression of Knowles and Reissner to the statically deflected tire problem but their solution is valid, at most, only for small displacements. The contributions of investigators in the Soviet Union who have used these methods have been reviewed by Biderman and Bukhin [69].

At the present time, these energy principles have only been successfully applied to axisymmetrically loaded tire problems, and these are the problems that are more easily solved using less involved techniques such as the direct solution of differential equations. However, energy methods do have the advantage of allowing computation of tire shape as a function of inflation pressure, which cannot be accounted for in eq (4.7).

The shell equations governing the problem of the tire rolling under load will be exceedingly complex, and based on the preceding comments there is some doubt as to whether such equations can be accurately formulated and solved. For this reason, it appears that direct numerical procedures based on more elementary principles might meet with greater success in attacking this problem. Among the more promising of these techniques is the finite element method [71] in which a continuous structure such as a tire is replaced by a finite number of elements interconnected at a finite number of nodal points.⁹ This type of idealization is inherent in the conventional analysis of frames and trusses. Loads acting on the tire would be replaced by statically equivalent concentrated forces acting at the nodal points of the finite element system. Displacements are related to loads using matrix equations in such a way that large numbers of elements are joined together. Digital computers capable of solving thousands of algebraic equations simultaneously are required to implement the finite element method effectively. While no definitive results have yet been published in the field of tire mechanics, the related problem of the elastic contact of a hollow sphere with a flat plate has been solved using this method [72].

A further aid in the study of axisymmetrically loaded tires is the ease with which the applied loads can be mathematically represented for the problems of practical importance, such as inflation pressure and centrifugal force. These loads are smoothly distributed over the tire and cause no abrupt changes in the toroidal geometry. For the tire in service, one has to consider radial, lateral, and circumferential forces and moments distributed over the tire which, besides being difficult to represent mathematically, cause significant changes in the geometry of a rolling tire, especially in the contact zone. In fact, at the present time there are no known methods available for predicting the displacements which occur at all points in a loaded tire. Analytical investigations have been mainly concerned with predicting tire deflections at one point—such as the crown—as a function of load [73]. From the previous discussion of the inflated but otherwise unloaded tire, we know that an accurate description of the entire geometry of the tire is needed in order to calculate the stresses. Additionally, most of our knowledge of the performance characteristics of tires has been experimentally obtained in a form suitable for chassis engineers concerned with suspension design who treat the tire as a “spring” which connects the vehicle to the road [74]. Thus, while it is experimentally straightforward and useful to measure such quantities as the lateral force on a tire in a cornering

⁹ The finite element method is also referred to as the extended Ritz method.

maneuver, tire engineers need to know for stress calculations the actual distribution of this lateral force and not the integrated result of this distribution at the wheel axle. This force distribution, either experimentally measured or theoretically predicted, would then be used as one of the inputs into the equations which govern the stress state of the loaded tire.

In order to study the tire in operation, stress analysts at the present time will have to be satisfied with investigating either highly idealized mathematical models of the whole tire or isolated components of part of the tire. For example, analytical investigations of anisotropic cylinders have established the fact that the plies should be layered in an order different from that usually employed in tire building [75]. That is, to have a symmetrical four-ply construction, the cords should be oriented in the order $\pm\beta, \mp\beta^{10}$ rather than the usual $\pm\beta, \pm\beta$. If these concepts hold true for toroidal shells, such ply arrangements would inhibit coupling between bending and membrane effects in the cord reinforced tire structure. Interestingly, these studies show that all two-ply structures are unsymmetrical. The stabilizer plies of belted tires and the beads of all tires are examples of components that can be reasonably studied independently of the rest of the tire structure. Thus, for radial tires, the behavior of a steel belt in a cornering maneuver [77] and the shear stress distribution between the carcass and the belt [78] have been studied using the classical equations of infinitesimal elasticity.

4.3. Experimental Techniques

Since theoretical methods are not sufficiently developed to allow tire engineers to predict the stresses generated in the cord, rubber, and steel components of a tire under service conditions, a great deal of effort has been expended developing experimental procedures for this purpose. These stress and strain measurements are important since they may suggest changes in tire design which will make more efficient use of construction materials and/or improve performance, especially with regard to tire cord fatigue phenomena. Additionally, experimental data can be used to validate analytical predictions in those cases where theory exists. Finally, experiments are often valuable in that they provide guidance in the development of an accurate mathematical model governing the tire loaded in some particular manner, i.e., experiments are useful in formulating theories.

In experimental mechanics, there are two broad classifications of methods for making strain measurements in stressed bodies, whether such bodies be tires or other load bearing structures. These two methods are commonly referred to as "point" and "whole-field" techniques [79].

In point methods, a strain gage (which could be a mechanical, optical, or electrical device) is used to measure the average strain in a particular direction over some given (usually small) gage length. It is apparent that

¹⁰ Woods [76] refers to this cord lay-up pattern as "paired" ply construction.

in many studies, large numbers of strain gages must be used to map a region of interest since such devices function only at a point.

Whole field methods yield data at many points simultaneously. They are ideally suited for locating regions where large strain gradients or stress concentrations exist. In the experimental stress analyses of tires, whole field methods have not been as commonly used as point methods.

The two earliest published articles covering the subject of tire stress analysis, Schippel's work [6] of 1923 and Hencky's work [80] of 1935, make no mention of experimental techniques for measuring strains in tires. In the period 1959-1962, three survey articles appeared which discussed many of the experimental methods known at that time [81-83]. Especially interesting is the work of Kern [81] and of Barson and Gough [83] who point out the limitations of several of the techniques especially developed for use with tires.

Methods for measuring strain which are applicable to pneumatic tires are not particularly different, in principle, from those methods developed in other areas of experimental stress analysis [84]. However, it has been necessary to design special transducing systems for tire engineering, since service strains occur in cord and rubber which are at least an order of magnitude greater than those which occur in the usual structural materials. In addition, the low elastic modulus of cord and rubber, compared to metals, causes many conventional strain measuring instruments to locally stiffen the area being measured due to their inherent mechanical rigidity. This stiffening causes extremely large measurement errors. For this reason special transducers with low mechanical impedance have been devised to be elastically compatible with cord and/or rubber.

Before discussing the more recent of these specialized techniques, we note that some relatively simple point methods of strain measurement have been used in the past. One of the easiest, but not very accurate or rapid methods for making strain measurements on tirecord is to remove rubber locally from the tire in the region of interest so that bare cord is exposed. By putting "bench marks" on the cord, strains can be calculated from the measured increase or decrease of the distance between bench marks due to an applied load. Furnas [85] is known to have used this method in 1933 to measure outer ply cord strains in the sidewall of an inflated and statically deflated tire using bench marks one inch apart. Loughborough, et al. [86], employed this same technique in 1950 to measure outer ply cord strains in the sidewall region of tires of various sizes. Both studies established the fact that in inflated and deflected bias tires, cords in the contact zone have their initially imposed inflation tension reduced all along their length.

An ingenious scheme was employed by Buckwalter [87] in 1932 to determine the strains in the innermost ply of an inflated and deflected tire. Buckwalter fastened small knots along the cords at equal intervals (0.4 in. bench marks) to form a repeated diamond pattern completely covering a section of the tire about 18 inches long. He then inserted an inner tube provided with an uncured section which had been swelled with carbon bisulfide and filled the uncured section with portland

cement. The tire was then inflated, the uncured section took the impression of the knots and was cured by the heat of setting of the cement. This operation was then repeated with the tire inflated and deflected. The rubber covered cement casts obtained from this procedure provided accurate maps of the diamond pattern of knots and made possible fairly precise measurements of the cord length changes which took place due to the deflection of the inflated tire. Buckwalter was mainly interested in relating his strain measurements to tirecord fatigue phenomena and showed that cords are weakest along their length at the location where maximum compression occurs.

Lauterbach and Ames [41] measured the cord strain arising from the vulcanization and expansion process in an uninflated tire by laying one inch strips of self-adhesive tape on the inside of the cured tire from bead to bead. The tape, when pulled away from the tire, had imprinted on it a replica of the first ply cord network. This replica, in conjunction with a mold drawing, permitted cord length changes arising from cure and expansion to be calculated. For a four-ply nylon tire, it was established that cord elongation occurs in the crown region and cord compression occurs in the bead region. Of course, the sign and magnitude of such cord strains will be greatly influenced by the parameters of the tire on the building drum relative to the mold geometry, as well as by the thermal shrinkage characteristics of the cord at the tire curing temperature.

Several special transducers have been successfully developed and extensively used by many European investigators for measuring surface rubber strains in tires. Biderman, et al. [88], reported data in 1957 obtained from a transducer which is a modification of the well-known clip gage used for measuring the Poisson contraction during the tensile testing of metallic specimens [89]. It is constructed by bonding electric resistance strain gages to the upper and lower sides of a piece of channel shaped spring steel. Legs with pins extend from the backbone of the gage and small pieces of vulcanized rubber are pushed on these pins, so that a definite spacing from the tire surface is achieved (see fig. 4.13). This device has good temperature compensation characteristics and because of the mechanical attenuation of the signal it can

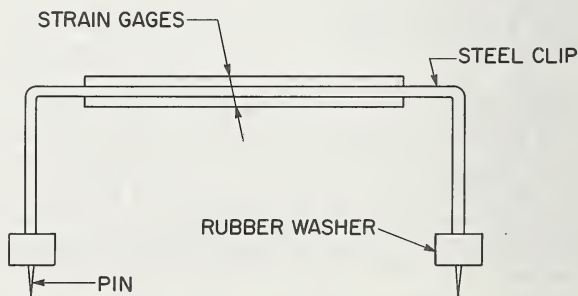


FIGURE 4.13. Clip gage for measuring large deformations [88].

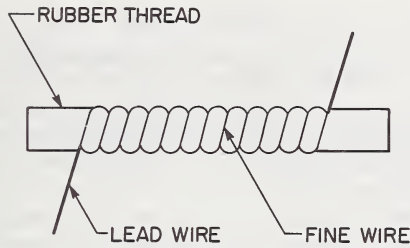


FIGURE 4.14. *Rubber wire transducer for measuring large deformations [94].*

measure strain magnitudes of 20–30 percent, or larger, depending on the length of the legs. Kern [81, 90–92] has used this transducer, as well as other types, to obtain strain measurements radially, circumferentially, and in the cord direction on the inside and outside rubber surface of automobile tires. He was the first investigator to study the effect of camber and cornering on tire strains and to map the principal strain trajectories in the contact zone of a deflected tire. Pugin [93] has used this clip gage to study the effect of crown angle on the sidewall deformation of bias tires rolling under load.

Another special transducer developed for measuring rubber strains was first described by Biderman and Pugin [119] in 1958 and later by Biderman [94] in 1959 and is shown in figure 4.14. It consists of a prestressed rubber thread with a diameter of 1.5 mm. onto which a coil of fine constantan wire has been wound with a small helical pitch. Compression or elongation of the rubber thread brings about an increase or decrease in the stress in the wire due to an increase or decrease in the diameter of the thread. This stressing changes the electrical resistance of the wire. Prestress of the rubber thread is necessary in order that the wire remain under mechanical load when the thread is extended to its maximum elongation. In order to make compressive measurements, the thread must be supported over its entire length on some sort of base to avoid buckling. For best results the rubber thread should have a low stiffness and small hysteresis. Calibration and temperature compensation of this gage are difficult. Pugin [82], however, recommends this transducer for measuring deformations under dynamic conditions in preference to the clip gage previously described. Such rubber-wire gages have been used to measure the circumferential and radial inflation strains in the proximity of artificial cuts introduced into the sidewall of agricultural tires [95] and to measure the sidewall strains developed in radial tires rolling on a drum [96].

Two published studies have dealt with the determination of internal cord and rubber strains in statically loaded tires using X-ray photography. Loughborough, et al. [86], used fine steel wires wrapped tightly around the cords as markers. Two markers were put on the same cord about one-half inch apart and the change in length between markers due to

inflation and deflection loads gave the strain. Weickert [43] treated one strand of a twisted cord with a metal salt and used the metal-shadowed cord as the marker. He also used one-sixteenth inch diameter steel balls as markers to detect carcass rubber strains between the second and third ply of a four-ply nylon tire. X-ray photography can also be used to measure the change in crown angle in the contact zone due to tire deflection using metal-shadowed cord [97].

Liquid metal gages have been developed to measure the large strains which occur in rubber. These devices consist of a small rubber tube or a cylindrical cavity in a rubber block filled with mercury. Their principle of operation is similar to the bonded electric resistance strain gage, i.e., a change in resistance due to change in geometry is a measure of strain. Hurry and Woolley [98] first described this type of strain gage in 1953 but presented no data from actual tire testing. Gregory, et al. [66], measured inflation strains and some dynamic strains at various locations on the inside and outside surface of an aircraft tire using mercury filled capillaries as the sensing elements. Similar devices have been developed to measure strains in human tissue [99].

Strains in the metallic bead rings of tires have been measured by Alekseev [100] and Pugin [101] using resistance wire strain gages. For these measurements a solid steel bead of appropriate diameter replaced the many strands of small diameter bead wire normally used in tire construction. Bead tension measurements were reported for various tire loadings (inflation, rotation, and rolling under load). Resistance foil strain gages have been applied to one wire in the bead bundle of an aircraft tire following the removal of a small portion of rubber and cord [66]. Strains due to wheel mounting, bead seating, inflation, and static vertical load are discussed. In statically loaded truck tires with steel cords, Forster [102] used resistance wire strain gages to measure the average strain across four adjacent outer ply cords at various locations between the bead and the shoulder.

Kern [103], using a method not described, compared the meridional and circumferential strain magnitudes developed on the inner carcass surface of a tire as a result of loading on a plane and a drum, and showed that larger strains are produced when a tire is deflected against the curved surface. Biderman [28, 104] has shown that for a 7.50-16 tire the meridional surface rubber strain pattern 50 mm. from the crown is considerably different in shape at 150 km/hr. than at 50 or 100 km/hr. The unusual high speed deformation pattern occurred because the tire was operating above its critical velocity with traveling waves present. Miniature force transducers using resistance foil strain gages have been developed by Clark and Dodge [105], Walter [106], and Patterson [107] which permit the direct measurement of the cord loads in a tire under operating conditions. These devices are placed in series with the cord and are embedded in the tire during building. In service, they provide a reproducible and easily monitored electrical signal which is an accurate analog of tirecord load. These transducers are much smaller than either the clip gage, the rubber-wire gage, or the liquid metal gages previously discussed.

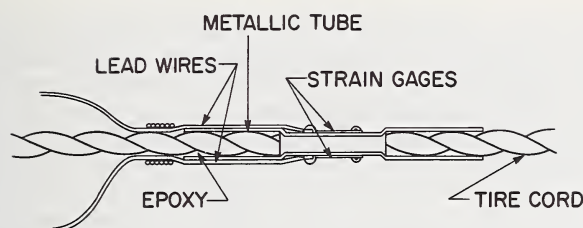


FIGURE 4.15. Cord force transducer used by Clark and Dodge [105, 108].

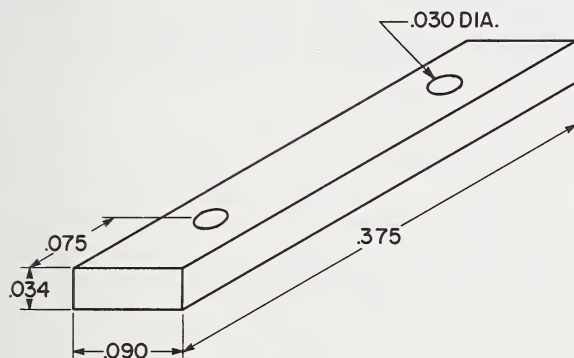


FIGURE 4.16. Cord force transducer used by Walter and Hall [65] (lead wires and strain gages not shown; dimensions in inches).

The force transducer used by Clark and Dodge is shown in figure 4.15; it is a 0.375 inch long thin walled beryllium-copper tube with tirecord bonded at each end. Extensive cord force measurements made at the crown, shoulder, and sidewall in the innermost ply of two- and four-ply nylon tires at different loads and pressures have been reported using this device [108].

The basic geometry of one of two types of load transducers used by Walter and Hall [65] is shown in figure 4.16; it is a 0.375 inch long aluminum alloy billet of rectangular cross section which averages force between two adjacent cords in a tire. This kind of transducer was used to measure cord forces in all plies of bias and belted bias tires in straight ahead rolling and cornering; the effect on the cord force pattern of wheel load, inflation pressure, obstacle impact, tire speed, rim width, and tire-road interface was also studied. Significant ply-to-ply cord force variations were detected, and the cord force patterns observed in the first ply as the transducer passed through the footprint were nearly a mirror image of those observed in the second ply at the same location. The cord tension developed at various locations in an inflated and rotating, but otherwise unloaded, two-ply polyester tire was measured with this device up to angular velocities of 1600 rpm—about 120 mph [38]. Patterson [107] used a force transducer 0.460 inch long of relatively complex geometry to measure the cord loads which occur during

shaping, cure, and postinflation of a 7.50-14 two-ply tire as shown in figure 4.17. These are the only published data treating this subject.

Some measure of the usefulness of these miniature force transducers is afforded in the investigation of cord loads in the ply turn-up region, i.e., near the bead. In this area, changes in tire stiffness and the closeness of the rim render theoretical stress analysis difficult if not impossible. Even surface rubber strains on the inside of the tire would be difficult to obtain in this otherwise inaccessible region. In the turn-up area, design variations exist among manufacturers because, for tires with two body plies, three different methods exist for wrapping fabric around the beads: a 2-0 tie-in with a step-in construction, a 2-0 tie-in with a step-out construction, and a 1-1 tie-in with a bead reinforce construction. These different constructions are shown in figure 4.18. Cord force data [109]

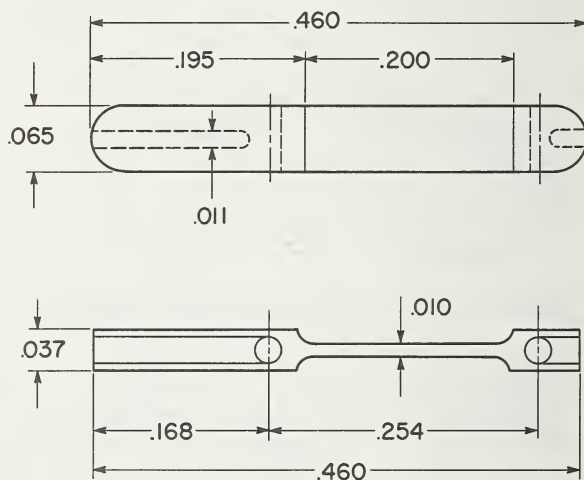


FIGURE 4.17. Cord force transducer used by Patterson [107] (lead wires and strain gages not shown; dimensions in inches).

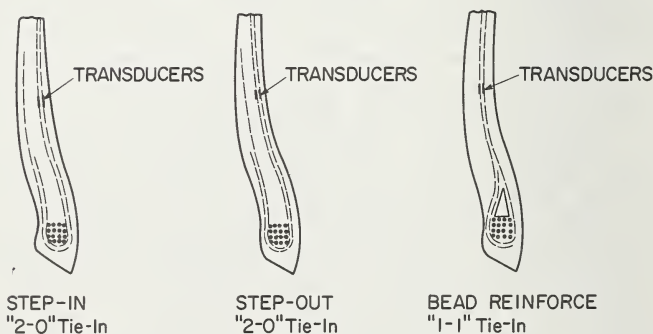


FIGURE 4.18. The three constructions for wrapping fabric around the bead of two-ply tires.

obtained in the middle of the step and at the edge of the reinforce are shown in figure 4.19 for otherwise identically constructed G78-15 belted bias tires with two polyester body plies and two fiberglass belts at rated load (1380 lb.) and pressure (24 psi) in straight ahead rolling at low speed (2 mph). In each case, the magnitude of the initially imposed inflation tension and the peak-to-peak cord force values are consistent with the type of turn-up design.

All of the experimental techniques discussed so far have been point methods. We conclude this chapter with a discussion of whole field methods, i.e., techniques which simultaneously give the stress, strain, or displacement field over some region of interest. There are four methods of whole field stress analysis that have been used or are potentially useful for measuring strains on the surface of a tire: surface grids, photoelasticity, moire, and holography. The biggest problem concerning the efficient use of these whole field methods is the difficulty in quantitatively interpreting data which occur simultaneously over a doubly-curved surface. This difficulty no doubt accounts for the scarcity of literature on this subject which is applicable to tires.

Strains are measured with surface grids by placing reference lines on, say, the sidewall of a tire, measuring the distance between lines before and after loading, and computing the strain as the change in length divided by the original length [110]. If the reference lines are in the form of a continuous rectangular grid pattern, sufficient information becomes available to determine the principal strain magnitudes and directions at every point. That is, the strain can be measured in

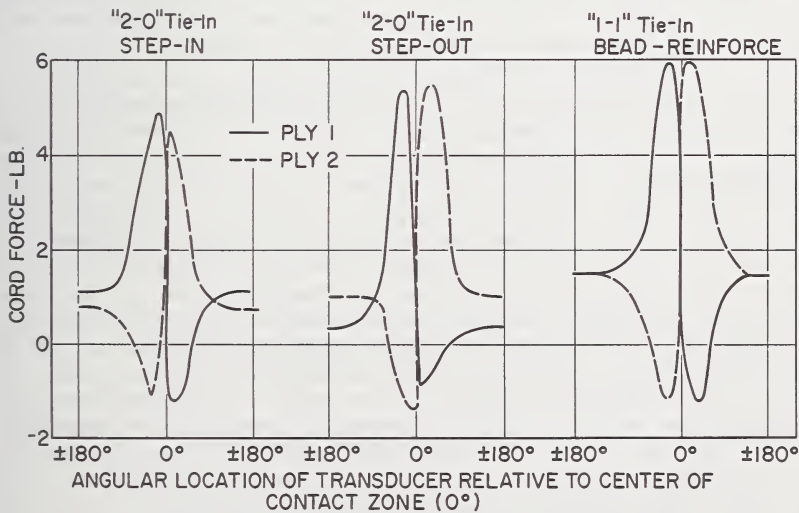


FIGURE 4.19. Cord forces measured at rated load and pressure in each ply in the turn-up region for G78-15 belted-bias tires [109] (see fig. 4.18 for transducer locations).

three directions by noting the change in length of the sides of the rectangular grid and the change in length of a diagonal; then the principal strains can be calculated from the usual rosette equation for strain at a point. In principle, this method is just a two dimensional extension of the technique used by Furnas [85] and Loughborough, et al. [86], to measure one dimensional cord strain. Barson and Gough [83] state that a grid method was their most successful technique for determining surface strains on tires. The grids were drawn on the rubber using white poster paint and were transferred to a flat glass surface for measurement using transparent self-adhesive tape. They report data obtained from statically deflected 5.20-13 four-ply tires.

Strains are measured photoelastically by detecting changes in the index of refraction of light passing through a birefringent material. The principle is based on the fact that polarized light, passing through a transparent medium under stress, will split into two polarized beams which travel in the planes of the principal strains. These beams have different velocities, and the resulting retardation is a measure of strain in the body. A photoelastic model is analyzed by use of an optical apparatus called a polariscope. With this device it is possible to determine the differences in the two principal strains from the isochromatics and the directions of the principal strains from the isoclinics. The specialized techniques of photoelasticity and the solutions to many plane two dimensional problems of the theory of elasticity are discussed in the treatise of Frocht [111]. Angioletti, et al. [112], have studied rubber birefringence and have analyzed the stresses in various rubber products photoelastically. Oppel [114] investigated the strains in the tread rubber of tires using this method. Recently, low modulus photoelastic coatings and adhesives which eliminate the need for models have been developed. These are suitable for use in the sidewall region [113] though no data obtained from tires have been reported in the literature.

The word "moire" is a French word that describes a silk screen effect and which is now used to denote an optical phenomenon which can be employed for surface strain measurement. The moire fringe method of experimental stress analysis is used to measure the relative displacements on a specimen by the mechanical interference of closely spaced lines. This technique has been reviewed by Theocaris [115] and is also referred to as mechanical interferometry or the photoscreen method. To use this technique a grid must be applied to the area of interest and a fringe pattern produced by straining must be measured. The fringes represent contours of equal displacement, and strains are calculated from the measured displacements through the use of the strain-displacement equations. The resulting measurement does not depend on a change in resistance (as with an electrical resistance strain gage) or index of refraction (as with photoelasticity). Thus, many of the problems inherent in the usual transducing systems (cement creep, stability, zero drift, etc.) can be avoided. Potter [116] has used the moire fringe method to measure strains in the range 1-10 percent in a pressurized neoprene rubber cylinder using two orthogonal sets of parallel lines with a spacing of 200 lines per inch. He discussed the

application of this technique to tires using long, thin grids with the long axis of the grid placed radially on the tire sidewall.

A technique that has a great deal in common with moire is the method of holographic interferometry based on wavefront reconstruction [117]. Wavefront reconstruction is a method for recording specific data about a three dimensional object in a medium such as photographic film, and then reconstructing a three-dimensional image of the object from this recording. Holographic fringes, like the moire fringes, result when load is applied to a body, and they also represent a locus of points of constant displacement. Its advantages compared to other whole-field methods are increased sensitivity (displacements as small as 10 micro-inches can be measured) and elimination of the need for mechanical attachments of any sort to the tire. At the present time holography is much more expensive than the other methods of experimental stress analysis partly because it requires a coherent light source such as a laser. This technique may have more potential as a nondestructive testing tool than as a quantitative analysis device since non-uniformities in the surface fringe patterns can be qualitatively interpreted as regions of internal stress concentration in the tire [118].

Recent developments in the entire field of experimental stress analysis are discussed in current issues and volumes of such publications as *Experimental Mechanics* and *Proceedings of the Society for Experimental Stress Analysis*.

4.4. Principal Notation

B = bead tension.

c = wave velocity.

m = tire mass per unit surface area.

n = number of plies in tire multiplied by the number of cords per unit length in a direction perpendicular to the cords.

N = total number of cords in tire.

N_ϕ = meridional stress resultant or force per unit of circumferential length.

N_θ = circumferential stress resultant or force per unit of meridional length.

p = inflation pressure.

r = radial coordinate (distance from axis of revolution to an arbitrary point on shell meridian).

r_b = radial distance from axis of revolution to "rim point" (see fig. 3).

r_c = radial distance from axis of revolution to crown.

r_w = radial distance from axis of revolution to widest part of shell meridian.

r_ϕ = meridional radius of curvature.

r_θ = circumferential radius of curvature.

T = cord tension.

V_{cr} = critical rolling velocity of tire.

z = axial coordinate (half-width at an arbitrary point on shell meridian).

z_b = axial distance to "rim point" (see fig. 3).

- z' = first derivative of z with respect to r .
 z'' = second derivative of z with respect to r .
 β = angle between the cord and a meridian plane at an arbitrary point on the tire.
 β_b = angle between the cord and a meridian plane at $r=r_b$ (equal to drum bias angle).
 β_c = angle between the cord and a meridian plane at the crown.
 τ = shear stress at cord-rubber interface.
 ω = angular velocity.

References

- [1] Purdy, J. F., Goodyear Tire & Rubber Co. Research Report, 1928 (unpublished).
- [2] Purdy, J. F., Mathematics Underlying the Design of Pneumatic Tires (Edwards Brothers, Ann Arbor, Michigan, 1963).
- [3] Hofferberth, W., Zur Festigkeit des Luftreifens, *Kautschuk und Gummi* **9**, WT225-WT231 (1956).
- [4] Biderman, V. L., Calculation of the Profile and Stresses in Elements of Pneumatic Tires Under Inflation Pressure (Russian), Transactions Tire Research Institute (NIISHP) **3**, pp. 16-51 (State Scientific and Technical Publishing House, Moscow, 1957).
- [5] Lorenz, H., Theorie der Rohrenfederanometer, *Zeitschrift des Vereines Deutscher Ingenieure* **54**, 1865-1867 (1910).
- [6] Schippel, H. F., Fabric stresses in pneumatic tires, *Industrial and Engineering Chemistry* **15**, 1121-1131 (1923).
- [7] Hofferberth, W., Zur Statik des Luftreifens, *Kautschuk und Gummi* **8**, WT124-WT130 (1955).
- [8] Zorowski, C. F. and Dunn, S. E., Measurement and Prediction of Cord Strains and Loading in Inflated Pneumatic Tires, Contract ERD-242 with Chemstrand Research, North Carolina State University, Raleigh, N.C. 27607.
- [9] Akasaka, T. and Yamagishi, K., On the standing waves in the shell wall of running tyre, *Transactions Japan Society for Aeronautical and Space Sciences* **11**, 12-22 (1968).
- [10] Flugge, W., *Stresses in Shells*, pp. 99-100 (Springer, Berlin, 1960).
- [11] Jordan, P. F., Stresses and deformations of the thin-walled pressurized torus, *Journal of the Aerospace Sciences* **29**, 213-225 (1962).
- [12] Sanders, J. L. and Liepens, A. A., Toroidal membrane under internal pressure, *AIAA Journal* **1**, 2105-2110 (1963).
- [13] Reissner, E., On stresses and deformations in toroidal shells of circular cross section which are acted upon by uniform normal pressure, *Quarterly of Applied Mathematics* **21**, 177-187 (1963).
- [14] Rossettos, J. N. and Sanders, J. L., Toroidal Shells Under Internal Pressure in the Transition Range, Contract Nonr 1866 (02) with Office of Naval Research, Harvard University, 1964, (AD603692 from Clearinghouse, Springfield, Va. 22151).
- [15] Clark, R. A., On the theory of thin elastic toroidal shells, *Journal of Mathematics and Physics* **29**, 146-178 (1950).
- [16] Clark, R. A., Gilroy, T. I. and Reissner, E., Stresses and deformations of toroidal shells of elliptical cross section, *Journal of Applied Mechanics* **21**, 37-48 (1952).
- [17] Tsui, E. Y. W. and Massard, J. M., Bending behavior of toroidal shells, *Journal of the Engineering Mechanics Division, ASCE* **94**, 439-464 (1968).
- [18] Gerard, G. and Lakshmikantham, C., Structural Design Synthesis Approach to Filamentary Composites, NASA CR-964 (1967).
- [19] Hartung, R. F., Planar-wound filamentary pressure vessels, *AIAA Journal* **1**, 2842-2844 (1963).
- [20] Haas, R., The Stretching of the Fabric and the Deformation of the Envelope in Nonrigid Balloons, NACA Third Annual Report, Report No. 16, 1917, pp. 149-250 (original publication in German, Berlin, Siemens-Schuckert Report, 1912).
- [21] Harkleroad, W. I., Basic principles of hose design, *Rubber Chemistry and Technology* **42**, 666-674 (1969); *Rubber World* **159** (2), 42-45 (1968).

- [22] Faupel, J. H., *Engineering Design*, pp. 312-317 (Wiley, New York, 1964).
- [23] Midgley, T., *Tire Construction*, U.S. Patent 1,802,088 (filed Oct. 7, 1920).
- [24] Gough, V. E., Cord path in tyres, *Transactions Institution of the Rubber Industry* **40**, T20-T57 (1964).
- [25] Eisenhart, L. P., *A Treatise on the Differential Geometry of Curves and Surfaces*, p. 120 (Dover, New York, 1960).
- [26] Ince, E. L., *Ordinary Differential Equations*, p. 43 (Dover, New York, 1956).
- [27] Day, R. B. and Gehman, S. D., Theory for the meridian section of inflated cord tires, *Rubber Chemistry and Technology* **36**, 11-27 (1963).
- [28] Biderman, V. L., et al., *Basic Theory of Pneumatic Tires* (Russian), *Automobile Tires (Construction, Design, Testing, and Usage)*, pp. 46-171 (State Scientific and Technical Publishing House, Moscow, 1963).
- [29] Ellis, J. R. and Frank, F., *The Equilibrium Shapes of Tyres*, College of Aeronautics, Cranfield, A.S.A.E. Report No. 1 (1966).
- [30] Biderman, V. L., Bukhin, B. L. and Nikolaev, I. K., Calculation of the equilibrium configuration of a rubber-cord envelope of revolution on a computer, *Soviet Rubber Technology* **25** (5), 27-29 (1966).
- [31] Schaffers, W. J., *Engineering Analysis of Bias Carcass Tires*, E. I. Du Pont de Nemours & Co. Research Report, 1965 (unpublished).
- [32] Bukhin, B. L., Calculation of the equilibrium configuration of a pneumatic tyre taking into account the elongation of the cord strands, *Soviet Rubber Technology* **22** (10), 38-41 (1963).
- [33] Ames, W. F., Stresses in cylindrically symmetric membranes reinforced with extensible cords, *Journal of the Franklin Institute* **272**, 185-190 (1961).
- [34] Struik, D. J., *Differential Geometry*, p. 134 (Addison-Wesley, Reading, 1961).
- [35] Walston, W. H. and Ames, W. F., Design and analysis of inflated membranes reinforced with extensible cords, *Textile Research Journal* **35**, 1078-1098 (1965); Walston, W. H., Ph.D. Thesis, University of Delaware (1964).
- [36] Mavrigian, G., Evaluation of the tire contour integral by elliptic integrals, *Rubber Chemistry and Technology* **40**, 961-967 (1967).
- [37] Bukhin, B. L., Levin, Y. S. and Uporina, L. A., Theoretical study of the forces in the carcass and of the shape of tyres wound from a single cord, *Soviet Rubber Technology* **25** (1), 28-32 (1966).
- [38] Walter, J. D., Centrifugal effects in inflated, rotating bias ply tires, *Textile Research Journal*, **40**, 1-7 (1970).
- [39] Lauterbach, H. G., Fundamental tire studies, *Du Pont Tire Yarn Technical Review*, 35-50 (May 7, 1959).
- [40] Mikell, W. G., Flat spotting and fundamental tire studies, *Du Pont Tire Yarn Technical Review*, 37-50 (May 1, 1958).
- [41] Lauterbach, H. G. and Ames, W. F., Cord stresses in inflated tires, *Textile Research Journal* **29**, 890-900 (1959).
- [42] Gol'denveizer, A. L., *Theory of Elastic Thin Shells*, pp. 474-483 (Pergamon, New York, 1961). (Original publication in Russian, Moscow, Gostekhteorizdat, 1953).
- [43] Weickert, B., Methods for measuring static strains in automobile tires, *Textile Research Journal* **32**, 705-710 (1962).
- [44] Desidlei, L. V., Khrapunov, L. G. and Rekitar, M. I., Carcass strength and its effect on tyre life, *Soviet Rubber Technology* **21** (6), 22-24 (1962).
- [45] Pugin, V. A., Stresses in the bead rings of tyres, *Soviet Rubber Technology* **21** (10), 8-12 (1962).
- [46] Wood, J. O., Pull-through adhesion test, *Transactions Institution of the Rubber Industry* **32**, 1-18 (1956).
- [47] Slyudikov, L. D., Cross-sectional profile of tyres having transverse carcass cords, *Soviet Rubber Technology* **21** (8), 24-28 (1962); Gummi, Asbest, Kunststoffe **16**, 620-623 (1963).
- [48] Biderman, V. L., Bukhin, B. L., Pugin, V. A. and Levkovskaya, E. Y., Calculation of initial forces in cords of the breaker strip of radial tyres, *Soviet Rubber Technology* **24** (3), 29-30 (1965).
- [49] Frank, F., Theorie und Berechnung der Statischen Kräfte und der Querschnittsform von Kreuzlagen-und Gurtelreifen, Paper presented at the Rubber Conference of the DKG, Berlin, 1968.

- [50] Frank, F. and Hofferberth, W., Mechanics of the pneumatic tire, *Rubber Chemistry and Technology* **40**, 271-322 (1967).
- [51] Böhm, F., Zur Statik und Dynamik des Gurtelreifens, *Automobiltechnische Zeitschrift* **69**, 255-261 (1967).
- [52] Biderman, V. L., Tyres with transverse carcass cords, *Soviet Rubber Technology* **19** (7), 10-12 (1960).
- [53] Biderman, V. L., et al., Radial Cord Tires (Russian), *Automobile Tires (Construction, Design, Testing and Usage)*, pp. 238-253 (State Scientific and Technical Publishing House, Moscow, 1963).
- [54] Rivlin, R. S., The deformation of a membrane formed by inextensible cords, *Archive for Rational Mechanics and Analysis* **2**, 447-476 (1959).
- [55] Gehman, S. D., Calculated deflected contours and load-deflection curves for tires, *Rubber Chemistry and Technology* **41**, 977-987 (1968).
- [56] Bukhin, B. L., Calculation of Stress and Deformation Appearing in Pneumatic Tires on Rotation (Russian), *Raschet na Prochnost* No. 6, pp. 56-65 (Moscow, 1960).
- [57] Wutzler, G., Die Deformation des Luftreifens unter Rotationssymmetrischer Belastung, *Plaste und Kautschuk* **14**, 679-683 (1967).
- [58] Irodov, V. A., Strength calculations on the bead rings of pneumatic tyres, *Soviet Rubber Technology* **20** (2), 17-18 (1961).
- [59] Turner, D. M., Wave Phenomena in Tyres at High Speed, *Proceedings Third Rubber Technology Conference* (London), pp. 735-748 (Heffer, Cambridge, 1954).
- [60] Gardner, E. R. and Worswick, T., Behavior of Tyres at High Speed, *Transactions Institution of the Rubber Industry* **27**, 127-146 (1951).
- [61] Ames, W. F., Wave Phenomena in Tires, Contract CST-435 with National Bureau of Standards, University of Iowa; Rep. No. 1-Dec. 31, 1967; Rep. No. 2-July 15, 1968; Rep. No. 3-Oct. 15, 1968.
- [62] Tarnopol'skii, Y. M. and Roze, A. V., Distortion of cross sections during deformation of oriented glass-reinforced plastics, *Polymer Mechanics* **1**, 69-73 (1965).
- [63] Clark, S. K., A review of cord-rubber elastic characteristics, *Rubber Chemistry and Technology* **37**, 1365-1390 (1964).
- [64] Ames, W. F. and Lauterbach, H. G., Stresses in Deflected Tires, *Proceeding International Rubber Conference* (Washington), pp. 50-56 (American Chemical Society, 1959).
- [65] Walter, J. D. and Hall, G. L., Cord load characteristics in bias and belted-bias tires, *SAE Paper No. 690522* (1969).
- [66] Gregory, R. K., Rastrelli, L. U. and Minor, J. E., Tire Structural Design Improvement, Contract AF33(657)-12861 with Air Force Systems Command, Southwest Research Institute, 1968 (ASD-TR-68-12).
- [67] Collatz, L., *The Numerical Treatment of Differential Equations*, (Springer, Berlin, 1959).
- [68] Clark, S. K., Tielking, J. T., Robbins, H. R. and Schreyer, H., Analysis of a pneumatic tire under load, University of Michigan ORA Report 02957-17-T (1963).
- [69] Biderman, V. L. and Bukhin, B. L., Methods of calculating stresses and deformations in the components of pneumatic tyres, *Soviet Rubber Technology* **20** (3), 15-19 (1961).
- [70] Knowles, J. K. and Reissner, E., On stress-strain relations and strain energy expressions in the theory of thin elastic shells, *Journal of Applied Mechanics* **27**, 104-106, (1960).
- [71] Zienkiewicz, O. C. and Cheung, Y. K., *The Finite Element Method in Structural and Continuum Mechanics*, (McGraw-Hill, London, 1967).
- [72] Rumbarger, J. H. and Herrick, R. C., Analysis of the Elastic Contact of a Hollow Ball with a Flat Plate, Contract F33(615)-68-C-1203 with U.S. Air Force, Franklin Institute Research Laboratories, 1968 (AFFDL-TR-68-123); also published as ASME Paper No. 69-LubS-5, 1969.
- [73] Rotta, J., Zur Statik des Luftreifens, *Ingenieur-Archiv* **17**, 129-141 (1949).
- [74] Nordeen, D. L. and Cortese, A. D., Force and moment characteristics of rolling tires, *SAE Paper No. 713A*, (1963).
- [75] Whitney, J. M. and Halpin, J. C., Analysis of laminated anisotropic tubes under combined loading, *Journal of Composite Materials* **2**, 360-367 (1968).
- [76] Woods, E. C., *Pneumatic Tyre Design*, p. 45 (Heffer, Cambridge, 1952).

- [77] Longmore, D. K. and Goodall, J. R., Elastic Behavior of Radial Tyre Breakers, Proceedings International Rubber Conference (Brighton), pp. 389-404 (Universities Press, Belfast, 1967).
- [78] Böhm, F., Mechanics of the belted tire, University of Michigan ORA Translation No. 5, (1967); Ingenieur-Archiv **35**, (1966).
- [79] Dove, R. C. and Adams, P. H., Experimental Stress Analysis and Motion Measurement, p. 18 (Merrill, Columbus, Ohio, 1964).
- [80] Hencky, H., Stresses in rubber tires, Mechanical Engineering **57**, 149-153 (1935).
- [81] Kern, W. F., Strain measurements on tires by means of strain gauges, Revue Generale du Caoutchouc **36**, 1347-1365 (1959); Kautschuk und Gummi **13**, WT59-WT68 (1960).
- [82] Pugin, V. A., Electrical strain gages for measuring large deformations, Soviet Rubber Technology **19** (1), 23-26 (1960).
- [83] Barson, C. W. and Gough, V. E., Measurement of strain of materials of large extensibility, British Journal of Applied Physics **13**, 168-170 (1962).
- [84] Hetenyi, M. (ed.), Handbook of Experimental Stress Analysis. (Wiley, New York, 1950).
- [85] Furnas, A. R., Firestone Tire & Rubber Co. Research Report, (1933) (unpublished).
- [86] Loughborough, D. L., Davies, J. M. and Monfore, G. E., The measurements of strains in tires, Canadian Journal of Research **28** (F), 490-501 (1950); Revue Generale du Caoutchouc **29**, 712-716 (1952).
- [87] Buckwalter, H. M., United States Rubber Co. Research Report, (1932) (unpublished); ASTM Committee D-13 Meeting, Providence, Rhode Island, (1933).
- [88] Biderman, V. L., Drozhzhin, P. K., Pugin, V. A. and Shchaveleva, V. F., Experimental Investigation of Deformations in Elements of Pneumatic Tires (Russian), Transactions Tire Research Institute (NIIShP) **3**, pp. 5-15 (State Scientific and Technical Publishing House, Moscow, 1957).
- [89] Perry, C. C. and Lissner, H. R., The Strain Gage Primer, p. 275 (McGraw-Hill, New York, 1962).
- [90] Kern, W. F., Über die Cordbeanspruchung in Reifen, Faserforschung und Textiltechnik **11**, 401-408 (1960).
- [91] Kern, W. F., Über Verformungsmessungen an Kraftfahrzeugreifen mittels spezieller Dehnungsgeber, Automobiltechnische Zeitschrift **63**, 33-41 (1961).
- [92] Kern, W. F., Hafner, K. and Nippold, H., Über die Auswertung von Verformungsmessungen an Reifen, Kautschuk und Gummi Kunststoffe **16**, 619-627 (1963).
- [93] Pugin, V. A., Effect of the angle of the cord on its deformation in the area of the tyre wall, Soviet Rubber Technology **22** (3), 21-24 (1963).
- [94] Biderman, V. L., Deformation of tyre elements during rolling, Revue Generale du Caoutchouc **36**, 1366-1371 (1959).
- [95] Dzhafarov, I. D., Deformation in the damage zone of a tyre, Soviet Rubber Technology **26** (3), 38-39 (1967).
- [96] Biderman, V. L., Pugin, V. A. and Fil'ko, G. S., Deformation and stresses in the cover rubber of the sidewall of a radial tyre, Soviet Rubber Technology **24** (7), 18-20 (1965).
- [97] Hinden, H. B., The unique characteristics of the radial wire tire, SAE Paper No. 278A, (1961).
- [98] Hurry, J. A. and Woolley, R. P., A new high range strain gage, Rubber Age **73**, 799-800 (1953).
- [99] Gibbons, G. E., Strandness, D. E. and Bell, J. W., Improvements in design of the mercury strain gauge plethysmograph, Surgery, Gynecology, & Obstetrics **115**, 679-682 (1963).
- [100] Alekseev, P. I., Stressing of the bead rings of a tyre under various conditions of deformation, Soviet Rubber Technology **19** (2), 18-22 (1960).
- [101] Pugin, V. A., Stresses in the bead rings of tyres, Soviet Rubber Technology **21** (10), 8-12 (1962).
- [102] Forster, M. J., Firestone Tire & Rubber Co. Research Report, (1952) (unpublished).
- [103] Kern, W. F., Observations on the relation between laboratory and test stand measurements of tire treads and their behavior on the road, Rubber Chemistry and Technology **29**, 806-828 (1956).
- [104] Biderman, V. L., Critical Speed of a Rotating Pneumatic Tire—Basic Experimental Data (Russian), Raschet na Prochnost No. 7, Part 3, pp. 324-349 (Moscow, 1961).

- [105] Clark, S. K. and Dodge, R. N., Development of a textile cord load transducer, ORA Report 01193-1-T, (University of Michigan, 1968).
- [106] Walter, J. D., A Tirecord Tension Transducer, *Textile Research Journal* **39**, 191-196 (1969).
- [107] Patterson, R. G., The Measurement of Cord Tensions in Tires, *Rubber Chemistry and Technology* **42**, 812-822 (1969).
- [108] Clark, S. K. and Dodge, R. N., A Load Transducer for Tire Cord, SAE Paper No. 690521, (1969).
- [109] Walter, J. D., Firestone Tire & Rubber Co. Research Report, (1969) (unpublished).
- [110] Parks, V. J., The Grid Method, *Experimental Mechanics* **9** (7), 27N-33N (1969).
- [111] Frocht, M. M., Photoelasticity. (Wiley, New York, 1941 (Vol. I), 1948 (Vol. II)).
- [112] Angioletti, A., Eccher, S., Polvara, O. and Zerbini, V., Rubber birefringence and photoelasticity, *Rubber Chemistry and Technology* **38**, 1115-1163 (1965).
- [113] Anonymous, Modern photoelastic stress analysis, Bulletin B-1200-1, (Photolastic Inc., Malvern, Pennsylvania).
- [114] Oppel, G., Konstruktionsprüfung von Gummifederungen für Motorfahrzeuge mit dem Einfreiverfahren und mit Spannungsoptik, *Automobiltechnische Zeitschrift* **51**, 77-84 (1949).
- [115] Theocaris, P. S., Moire Fringes: A Powerful Measuring Device, *Applied Mechanics Reviews* **15**, 333-339 (1962).
- [116] Potter, J. M., Measurement of Strain on Curved Surfaces Using the Moire Method, M. S. Thesis, University of Illinois, (1968).
- [117] Haines, K. A. and Hildebrand, B. P., Surface-Deformation Measurement Using the Wavefront Reconstruction Technique, *Applied Optics* **5**, 595-602 (1966).
- [118] Grant, R. M. and Brown, G. M., Holographic Nondestructive Testing (HNDDT) in the Automotive Industry, SAE Paper No. 690051, (1969).
- [119] Biderman, V. L. and Pugin, V. A., Wire Strain Gauge for Measurements of Large Deformations (Russian), *Zavodskaya Laboratoriya* **24** (7), 874-875 (1958).

CHAPTER 5

The Contact Between Tire and Roadway

Samuel K. Clark ¹

	Page
5.1. Introduction.....	446
5.2. Contact area.....	447
5.2.1. Experimental measurements.....	447
5.2.2. Theory.....	454
5.3. Slip between tire and roadway.....	463
5.4. Contact pressures.....	471
References.....	498

¹ Department of Engineering Mechanics, University of Michigan, Ann Arbor, Michigan 48104.

5.1. Introduction

The purpose of this chapter is to examine both the experimental data and the appropriate mathematical models for three characteristics of a rolling elastic tire. These characteristics are:

- a. The area of contact between the tire and road.
- b. The slip or relative motion between the tire and road.
- c. Normal and tangential contact stresses between tire and road.

Since the forces needed for vehicle support, guidance and maneuvers all arise in the tire contact area, study of these characteristics and application of the resulting theory should improve both the mechanical properties of tires and the control of vehicles. These characteristics are all influenced by the operating parameters of a tire, such as its inflation pressure, its rolling velocity, its path of rolling relative to its midplane, its load as well as its size and shape. For this reason it is quite difficult to give a complete definitive description of all possible interacting factors, and for the most part it will be necessary to rely on rather insufficient experimental evidence which merely indicates trends and magnitudes, as well as some relatively simple theoretical ideas which from time to time may prove helpful in explaining the general characteristics of observed phenomena.

In addition to the influences which are listed above, it is obviously true that the characteristics of contact between a tire and roadway depend as well on the particular type of roadway surface to be studied, as well as on any possible contaminants between the tire and roadway. For the most part one is interested in the influence of water in relatively small depths, and its effect can be marked on contact processes, particularly at high velocities. Roadway surfaces usually are constructed to be relatively smooth compared to tire tread patterns, and there is little if any information available in the literature on the influence of road roughness on contact characteristics.

The quantities of interest here are shown in the sketch of figure 5.1.

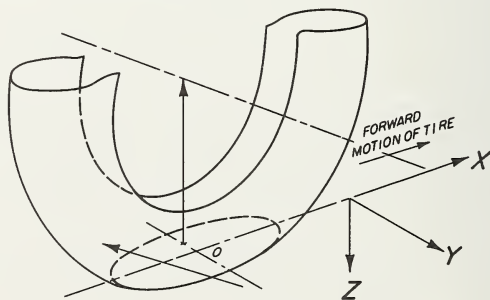


FIGURE 5.1. *Total reaction from ground to tire expressed as the combined effect of two forces, one normal and one tangential to the ground plane.*

5.2. Contact Area

5.2.1. Experimental Measurements

The shape of the contact area between the tire and roadway depends on the tire cross section shape and structure. For example, the contact area between an aircraft tire and a flat surface usually appears to be nearly elliptical in shape. This is illustrated in figure 5.2. This is generally the kind of shape associated with a tire which has little if any external tread or shoulder region, but is primarily a toroidal carcass with small additional tread rubber.

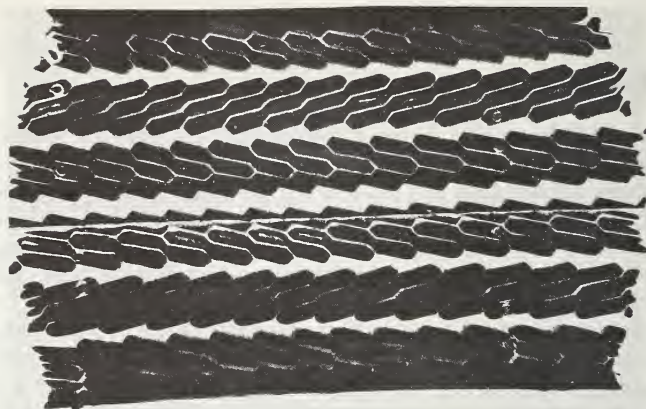
For an automotive tire a somewhat different set of relationships exists due to the fact that the usual construction involves the use of a relatively heavy tread, particularly in the shoulder region. In this case any significant contact spreads over the entire width of the tire between shoulders so that the contact area tends to have essentially straight parallel sides, and the width of this contact area is nominally independent of tire deflection. A typical contact area is shown in figure 5.3.

AIRCRAFT TIRE
32 x 8.8
8 PLY-RATING

86 psi
6000 lb. Vert. Load
1-3/4" Vert. Defl.



FIGURE 5.2. *Contact patch of a typical aircraft tire.*



8:00 x 14 Automotive Tire
 Four ply Rayon Bias Ply Construction
 24 psi inflation 1.25" Deflection
 1350 lbs load

FIGURE 5.3. Typical contact area for an automotive tire.

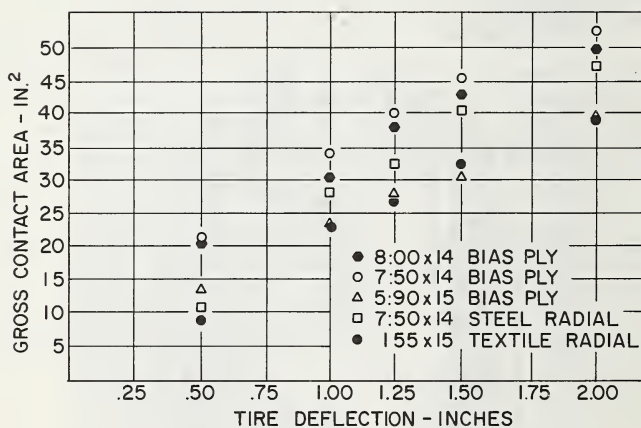


FIGURE 5.4. Gross contact area vs. tire deflection.

Data relating gross contact area to tire deflection is shown in figure 5.4 for a typical set of automotive tires of different size and manufacture. It is seen from this that the relationship between tire deflection and gross contact area is nearly linear, accounting for some experimental scatter in the data. Similar results have been reported by Hadekel [1]² previously.

² Figures in brackets indicate literature references at the end of this chapter.

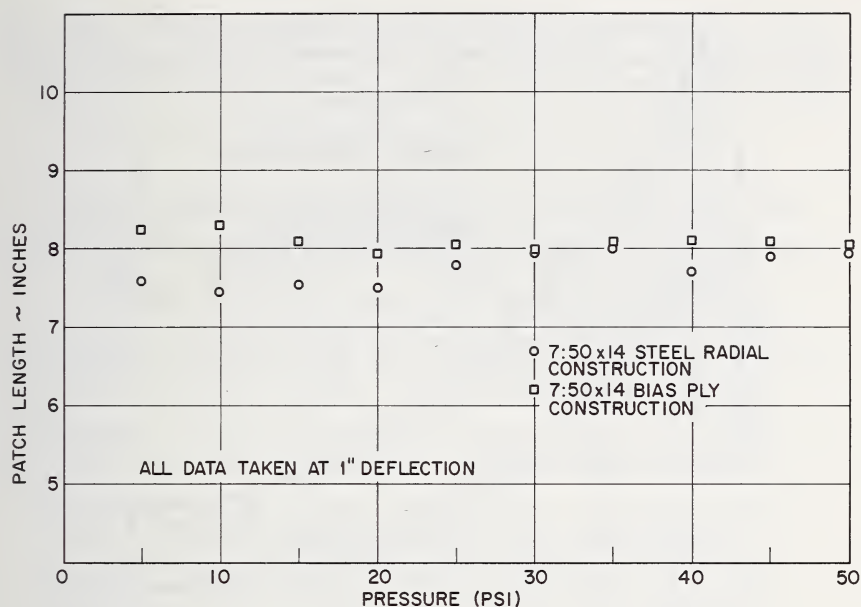


FIGURE 5.5. Plot of contact patch length vs. pressure for two automotive tires at fixed deflection.

Experimental evidence indicates that tire deflection is the most important variable governing the area of contact between the tire and roadway. If inflation pressure and load are simultaneously varied so as to maintain constant tire deflection, the contact area of the tire will remain effectively constant. This conclusion was previously reached by Michael [2] on the basis of aircraft tire data, but is also shown here in figure 5.5 from unpublished data [3]. This tends to lend credibility to the inextensible membrane or shell bending models for contact phenomena.

There is not too much evidence available in the literature concerning the role of curved surfaces in forming contact areas with pneumatic tires. For example, the contact of a pneumatic tire with a cylindrical surface is of considerable interest due to the large amount of indoor tire testing carried out on cylindrical steel roadwheels. Some preliminary data is available on this effect from the work of Dodge [3] and this is shown in figure 5.6, where the variations of contact patch length with surface radius are shown for two different automotive tires.

The contact area of a slowly rolling tire may be slightly different from that of a standing tire, but it is not clear that such differences would be large. In some cases carcass deformation would be slightly different in standing as opposed to pure rolling due to the presence of friction between the roadway and the wheel. Experimental data on this point has

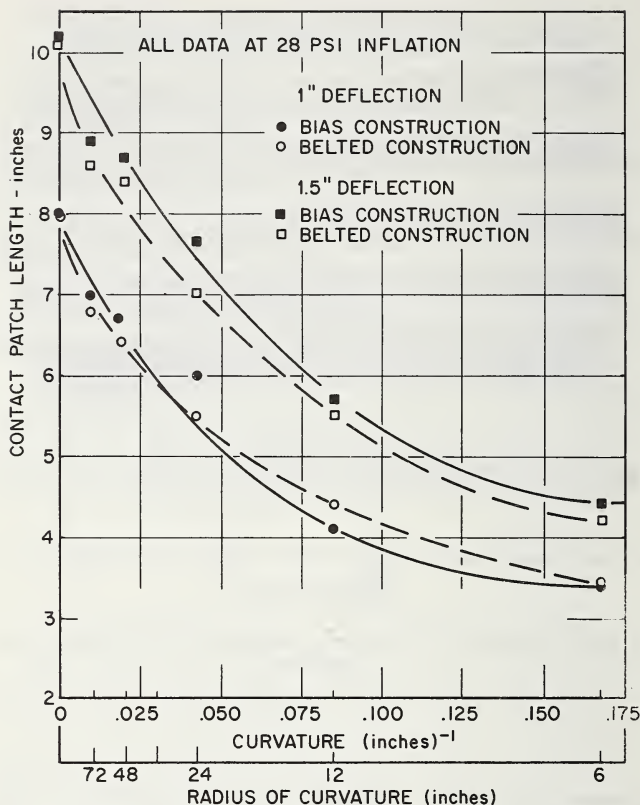


FIGURE 5.6. Plot of contact patch length vs. roadwheel curvature for two different tires and two different deflections.

been obtained by the U.S. Army Engineer Waterways Experiment Station [4] for a single truck tire. This data is summarized in table 5.1.

There is only limited data available on the influence of velocity on the area and shape of the contact region between a tire and roadway. Seitz [5] gives footprint data taken on a roadwheel. In figure 5.7 is shown the contact area for a textile belted tire at various speeds at constant load, while similar data for a steel belted tire and a bias-ply tire is shown in figures 5.8 and 5.9 respectively. Figure 5.10 shows contact areas as a function of tread radius, while figure 5.11 shows the bias-ply tire contact area again as a function of velocity. Figure 5.12 gives a similar presentation for a belted tire whose contact area is a function of velocity. These measurements were made on a cylindrical roadwheel, but still give a valuable indication of the general influence of velocity on contact area. While

the trends are not completely clear, it appears that increasing velocity of travel generally tends to increase the contact area slightly, all data being taken at constant load. It is known that increasing velocity may

TABLE 5.1. *Static and rolling contact patch areas and dimensions (slow rolling conditions)*

Test condition	Inflation	Load	Deflection		Contact area		
	psi	pounds	inches	%	length	width	area
Stationary	60	4500	1.56	17.3	11.4	6.4	67
Rolling	60	4500	1.56	17.3	11.4	6.6	67
Stationary	60	3000	1.12	12.5	9.9	6.0	52
Rolling	60	3000	1.12	12.5	10.2	6.0	58
Stationary	60	1500	0.50	5.5	7.7	4.6	29
Rolling	60	1500	.50	5.5	7.8	4.8	31
Stationary	30	4500	2.22	24.6	16.0	8.2	125
Rolling	30	4500	2.22	24.6	15.8	8.5	115
Stationary	30	3000	1.75	19.4	12.4	7.4	83
Rolling	30	3000	1.75	19.4	12.4	7.1	81
Stationary	30	1500	0.88	9.7	9.9	5.6	47
Rolling	30	1500	.88	9.7	9.2	5.3	43
Stationary	15	4500	5.00	55.4	20.0	9.3	188
Rolling	15	4500	5.00	55.4	20.2	10.5	161
Stationary	15	3000	2.75	30.4	16.1	8.2	130
Rolling	15	3000	2.75	30.4	15.5	8.2	115
Stationary	15	1500	1.31	13.1	10.5	6.6	63
Rolling	15	1500	1.31	13.1	11.0	6.2	63

cause the center of normal pressure to move slightly forward in the contact area, since the power loss characteristics of the rolling tire may result from such a forward shift. This apparently is not accompanied by a geometric shift of the actual contact area, according to the data of Seitz.

Finally, some photographic information is available on the nature of an actual contact patch under rather slow cornering conditions. This was obtained by photographing through a glass plate as the tire is run over the plate. A still picture from such a movie is given in figure 5.13, showing typical cornering distortion of the contact patch.

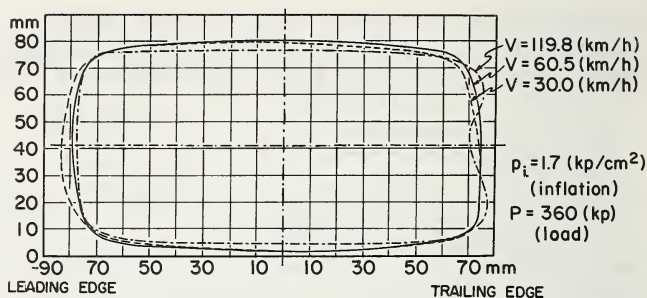


FIGURE 5.7. Contact area for a textile belted tire at various speeds, taken at constant load.

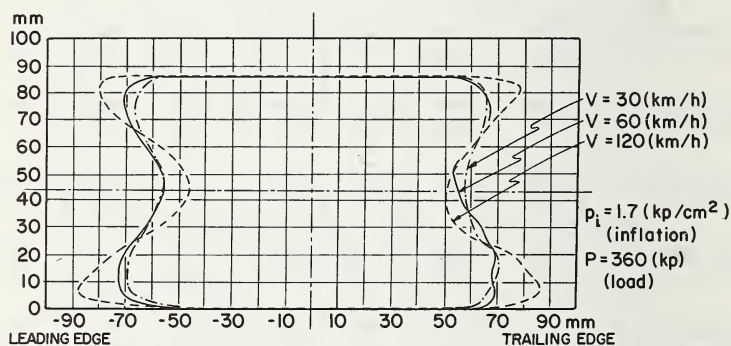


FIGURE 5.8 Contact area for a steel belted tire at various speeds, at constant load.

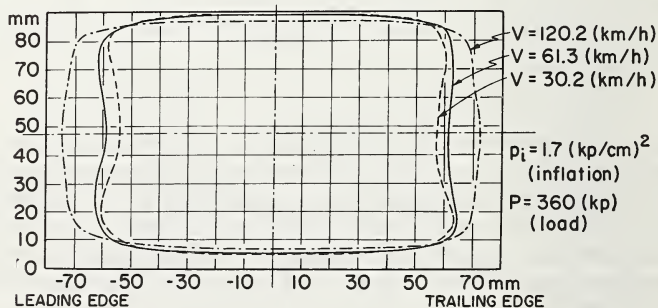


FIGURE 5.9. Contact area for a bias ply tire, with 37° crown cord angle, at various speeds, at constant load.

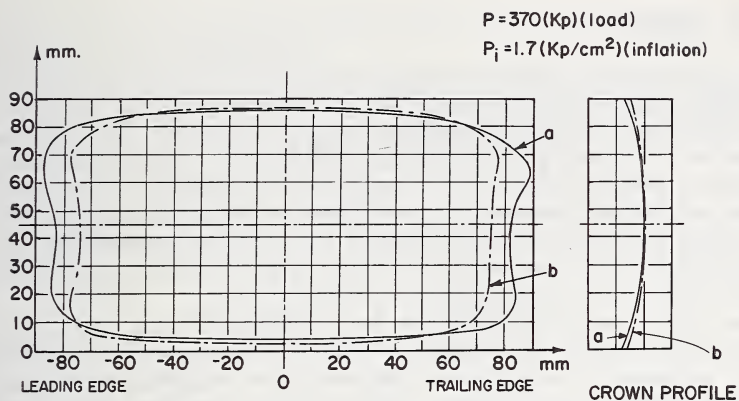


FIGURE 5.10. Contact areas for a bias ply tire with 37° crown cord angle as a function of tread radius, taken statically at equal loads.

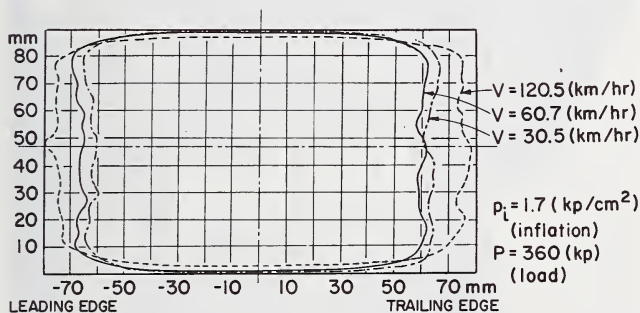


FIGURE 5.11. Contact area of a normal tire as a function of velocity, at constant load.

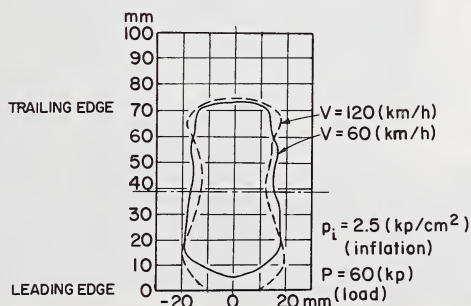


FIGURE 5.12. Contact area of a steel belted tire at high inflation pressure and extremely light load, at constant vertical load.

5.2.2. Theory

No single unified theory exists for describing the area of contact of a tire with a rigid roadway or test wheel. Most of the reasons for this lie in the complexity of the tire construction, since from the point of view of mathematical modeling of the tire its shell-like structure and rather soft serrated tread are difficult to represent analytically. Nevertheless, several specialized theories are available for approximately describing the dimensions of the contact area of the tire with a roadway or test wheel, and these are useful in explaining some of the phenomena which are observed.

One type of problem which has been studied in some detail is that involving the contact of isotropic solid elastic bodies with geometrically simple surfaces. This solution obviously has application in various kinds of bearings and friction drive devices. For the case of small deformations of solid bodies in contact with one another, the contact

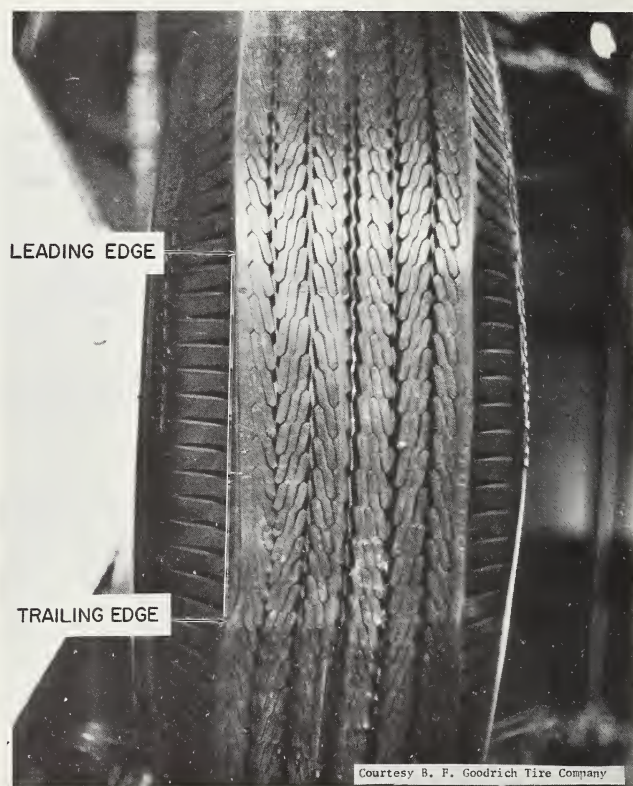


FIGURE 5.13. *Photograph of contact patch of a loaded tire. (Courtesy B. F. Goodrich Company.)*

areas have been expressed in particularly useful form by Whittemore and Petrenko [7], who conclude that

- Contact area between an infinitely rigid plane and an elastic body of double curvature, with principal radii of curvature R_c and R_t , as shown in figure 5.14, is an ellipse.
- Upon experiencing a deflection δ against a rigid plane, as shown in figure 5.15, the semi-major and semi-minor axis of the contact ellipse are given by

$$c = \left[\frac{\alpha \Delta^{1/3}}{\lambda^{1/2}} \right] \delta^{1/2} \quad d = \left[\frac{\beta \Delta^{1/3}}{\lambda^{1/2}} \right] \delta^{1/2} \quad (5.1)$$

where Δ is given by

$$\Delta = \frac{4}{\frac{1}{R_t} + \frac{1}{R_c}} \quad (5.2)$$

TABLE 5.2.

θ	0°	10°	20°	30°	35°	40°	45°	50°	55°
α	∞	6.612	3.778	2.731	2.397	2.136	1.926	1.754	1.611
β	0	0.319	0.408	0.493	0.530	0.567	0.604	0.641	0.678
λ851	1.220	1.453	1.550	1.637	1.709	1.772	1.828

θ	60°	65°	70°	75°	80°	85°	90°
α	1.486	1.378	1.284	1.202	1.128	1.061	1.00
β	0.717	0.759	0.802	0.846	0.893	0.944	1.00
λ	1.875	1.912	1.944	1.967	1.985	1.996	2.00

and α , β and λ must be taken from table 5.2 in terms of the angle θ , this angle being defined by

$$\cos \theta = \frac{\left(\frac{1}{R_t} - \frac{1}{R_c} \right)}{\left(\frac{1}{R_t} + \frac{1}{R_c} \right)}. \quad (5.3)$$

From these results it is seen that the isotropic contact theory, often known as the Hertz contact theory, predicts linear dimensions which are dependent upon the deflection to the exponent 0.5. Since the contact area is an ellipse, it becomes linearly proportional to deflection in the form

$$A = \pi dc = \delta \left[\frac{\alpha \beta \Delta^{2/3}}{\lambda} \right] \quad (5.4)$$

where the factor in parentheses is a function of the relative values of tire radius R_c and tread radius R_t .

While this type of solution certainly does not represent an automobile tire completely, it is interesting to note that another situation does exist in practice where the contact area can also be shown to be linearly dependent on deflection by quite a different form of analysis. This occurs in an aircraft tire where the tread is relatively thin compared to automotive tires. Here the cross section of the tire is close to being circular, with a radius of curvature approximately equal to half of the section width w . In this case, it has been demonstrated by many experiments that the contact area between tire and roadway is also approximately an ellipse. Here it is common to treat the tire as a carcass of zero bending rigidity, and of membrane characteristics such that it can map itself onto the flat roadway by appropriate membrane compression of the carcass. A side view of this assumed tire geometry is shown in figure 5.16,

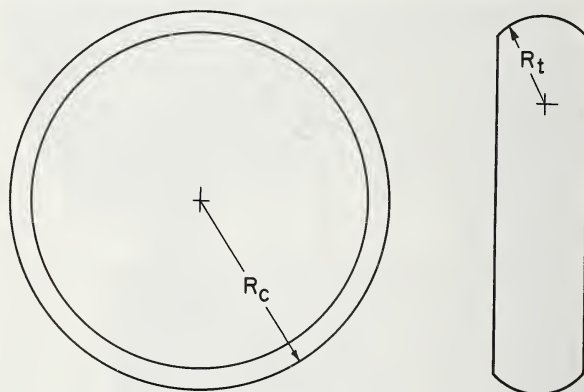


FIGURE 5.14. Radii of curvature R_c and R_t of tire tread surface.

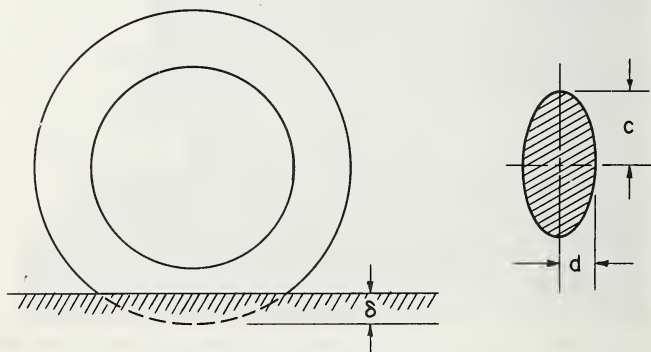


FIGURE 5.15. Idealized contact geometry between a torus and a plane.

where the tire with original running band AOB is presumed to map itself onto the plane CC by assuming the shape $AO'B$. The geometry of this deformation is such that the right triangle $DO'E$ is governed by the relation

$$R_c^2 = (R_c - \delta)^2 + \left(\frac{l}{2}\right)^2. \quad (5.5)$$

where it is assumed that the original and final tire shape is the same outside of the contact area. From this one may obtain the contact length

$$\frac{l}{2} = \delta^{1/2} (D_c - \delta)^{1/2}. \quad (5.6)$$

If one considers the section of the tire at right angles to that shown in figure 5.16, as illustrated in figure 5.17, then it is seen that an analogous

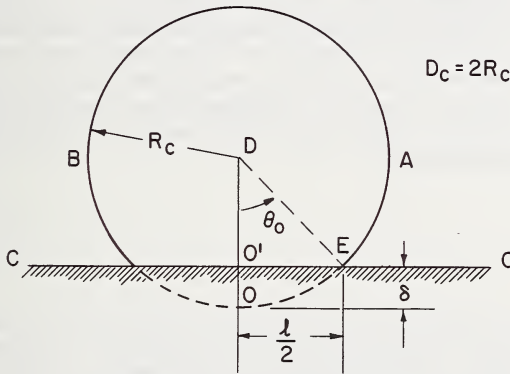


FIGURE 5.16. *Tire contact symbols.*

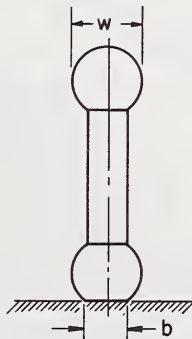


FIGURE 5.17. *Cross section view of a tire in contact.*

geometry governs the mapping of the tire in this cross-sectional dimension. Using the same type of analysis as previously, the width of the contact ellipse b is given by the expression

$$\frac{b}{2} = \delta^{1/2} (w - \delta)^{1/2}. \quad (5.7)$$

Since the contact area is elliptical in shape, its value is given by

$$\begin{aligned} A &= \pi \frac{l}{2} \frac{b}{2} = \pi \delta \sqrt{(w - \delta)(D_c - \delta)} \\ &\approx \pi \delta \sqrt{D_c w} \end{aligned} \quad (5.8)$$

Thus, for an aircraft tire, one might also anticipate a linear, or nearly linear, relationship of area with deflection if the membrane carcass theory is valid. Experiments with aircraft tires on this point have been conducted by Michael [2] as quoted by Hadekel [1]. This data appears to be extremely linear up to quite large deflections, and to be essentially independent of inflation pressure, so that there appears to be some physical basis for acceptance of the membrane theory for aircraft tires. Very similar relations have been obtained from the data of Smiley and Horne [6], with slight modification in the numerical constants associated with the linear relationship.

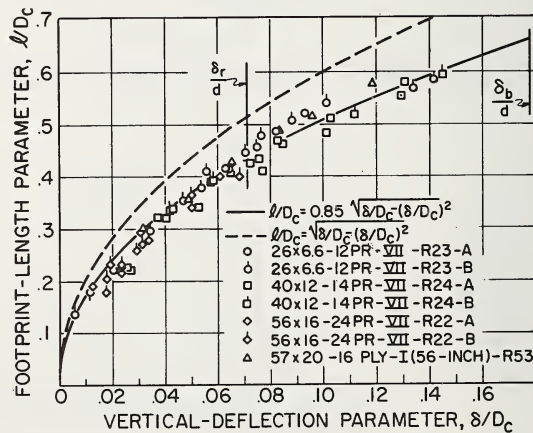


FIGURE 5.18. Variation of footprint-length parameter with vertical deflection parameter for several types I and VII tires (aircraft).

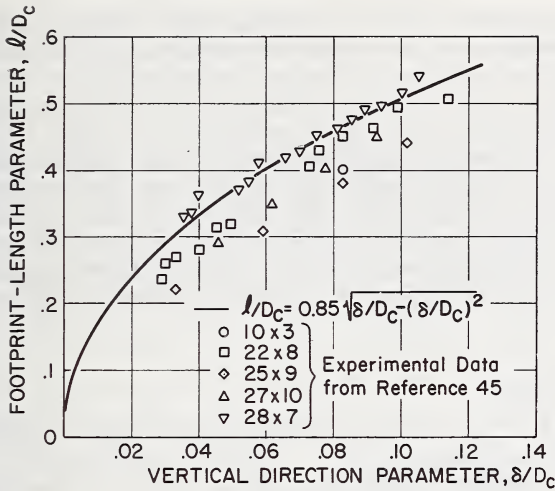


FIGURE 5.19. Variation of footprint-length parameter with vertical deflection parameter for several German aircraft tires.

For an automotive tire the presence of the shoulder region causes the contact area to be close to a rectangle whose length varies with deflection of the tire. Two different methods have been proposed for calculation of the contact patch length. The simpler one, which is useful mainly for static or slow rolling considerations, utilizes an experimentally determined fraction of the geometric contact length given by eq (5.6). Experimental data is given by Smiley and Horne [6] for this using aircraft tires in figures 5.18 and 5.19, along with a curve showing the best fit obtained by using a fraction of the geometric intersection length, in this case 85 percent of it.

A more complicated theory has been proposed by Böhm [8], Fiala [9], and Clark [10] which attempts to take into account the dynamic characteristics of the contact patch. This model visualizes the running band of the tire as consisting of a circular shell on an elastic foundation, the elastic foundation representing the effect of sidewall support. In reference [10] mathematical techniques are given for transforming these shell equations into moving coordinates so that the shell may be visualized as moving down a flat plane at some rolling velocity V_0 . In both cases, it is possible to calculate the length of contact patch by solution of the governing differential equation.

On the assumption that the running band undergoes pure bending and is inextensible, one may solve the equations governing displacement of the cylindrical shell on an elastic foundation for the specific case of contact with a rigid frictionless plane, provided that one assumes that the initial geometry of the shell continues to be valid. Under this assumption, it is possible to assign values to the bending stiffness of the running band of the tire, and to the elastic support given to the running band by the pressurized sidewalls. This allows direct numerical calculation of the contact patch length as a function of vertical tire deflection. Such a typical calculation is given in figure 5.20, compared with experiments taken from a tire used as a model to obtain the stiffness and elastic

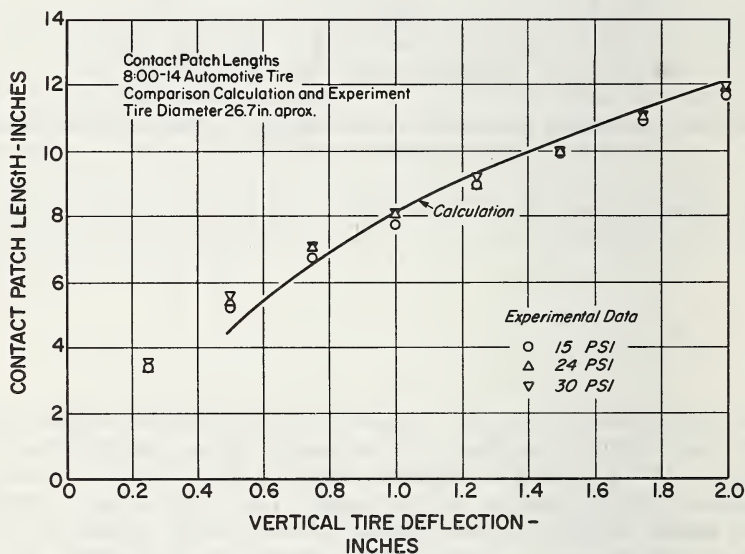


FIGURE 5.20. Plot of contact patch length vs. vertical tire deflection.

spring support data. Dodge [11] has compared the results of calculations and experimental tire contact patch length for seven different automotive tires, five bias ply and two radial. These comparisons are given in figure 5.21.

The foregoing discussion has concerned itself with gross contact area. The presence of grooves and kerfs, designed to channel or wipe water, will substantially reduce this gross contact area so that the net contact area is considerably less. The exact value of this must be determined for each individual tread pattern. A representative set of different automotive tires yields data as shown in table 5.3.

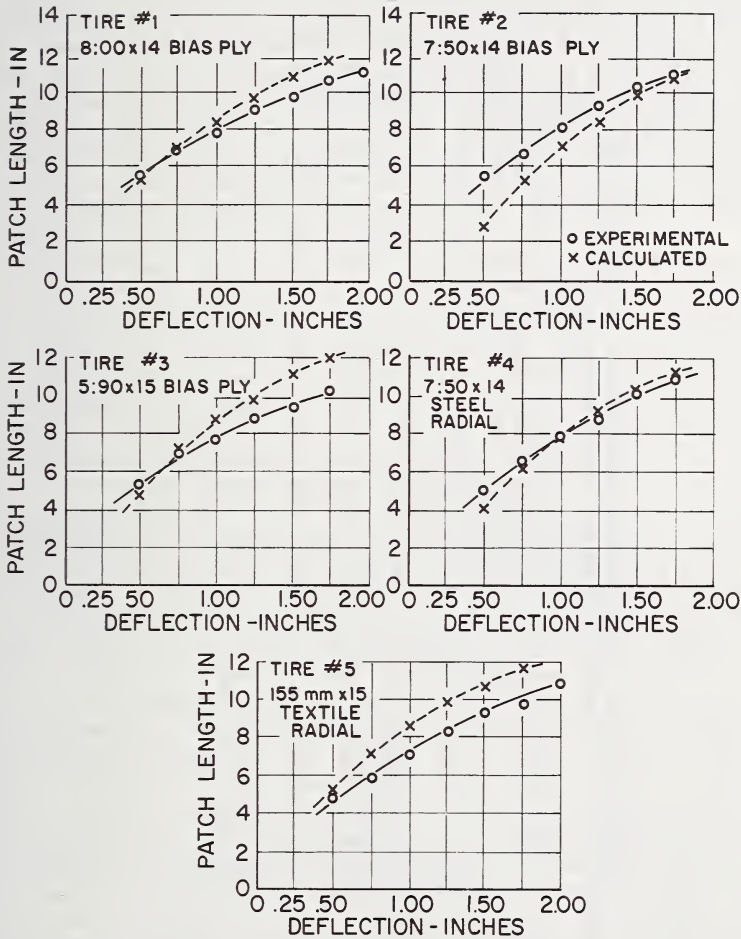


FIGURE 5.21. Contact patch length-deflection characteristics for five automotive tires.

TABLE 5.3. *Ratio of net footprint area to gross footprint area for several tires*

Tire	Tread pattern	1.0" Deflection			1.5" Deflection			2.0" Deflection		
		Net* area	Gross* area	N.A. G.A.	Net* area	Gross* area	N.A. G.A.	Net* area	Gross* area	N.A. G.A.
7:50 × 14 bias.....	Groove and kerf..	28.2	34.3	0.84	37.7	45.6	0.83	45.6	52.4	0.87
8:00 × 14 bias.....	Groove and kerf..	26.4	31.6	.84	33.6	43.2	.78	38.4	49.2	.78
5:90 × 15 bias.....	Groove and kerf..	19.5	23.3	.84	25.3	30.6	.83	35.6	39.6	.90
7:50 × 14 steel radial.	Groove and kerf..	22.5	28.0	.81	34.6	40.2	.86	38.5	47.0	.82
155 × 15 radial.....	Groove and kerf..	18.5	22.9	.81	23.8	32.5	.73	32.6	39.1	.83

*Dimensions : in.².

5.3. Slip Between Tire and Roadway

In all of the discussion which has been given here, nothing has been said of the role of slip in the contact patch. Since this becomes important for purposes of describing the yawed rolling tire, as well as in braking and accelerating a vehicle, it is necessary to discuss this question briefly.

The term "developable surface" is generally used to denote a curved surface which can be formed by simple folding or bending of a flat sheet, without extension or compression of this sheet. A cylinder is an example of a developable surface, as is a cone. The concept of a developable surface is important since it represents a kind of surface which may be placed in finite area contact with a flat plane by simple bending processes without stretching, tearing or compressing the sheet. Both the cylinder and cone exhibit this kind of behavior.

A surface which is not developable can only be formed from a flat sheet by means of stretching or contracting the sheet in its plane. A toroid, which is generally the shape of most tires, is not developable. Thus, when a tire is brought into contact with a flat roadway such a geometric process can only take place by both simultaneous bending and compressing of the tire surface. This means that tread elements in contact with the roadway will generally undergo a small deformation in the plane of the carcass as such tread elements pass through the contact patch of the rolling tire and exit out the trailing edge. This process takes place in every tire. It is possible to minimize the membrane stretching and contraction by making the carcass structure of the tire as rigid as possible. This is generally the principal behind the radial or belted tire constructions. It is also possible to minimize such membrane distortions by use of extremely stiff materials for the tire carcass, such as steel wire or glass. Since the membrane deformations actually take place in the carcass of the tire, it should be possible to prevent motion of the tread on the contact surface by choice of an appropriately soft tread compound. Unfortunately this normally counteracts attempts to secure a long wearing tread material, so that it is usually not possible to make the shear stiffness of the tread itself low enough to prevent all motion. This description just given applies primarily to straight line motion of the tire, and describes what might be thought of as secondary slip between tread and roadway, that is to say, slip whose magnitude is of the order of a few thousandths of an inch while a particle on the surface of the tire moves through the contact patch. The direction of such secondary slip may be partly longitudinal and partly transverse, depending on tire construction and local friction conditions.

Over and above secondary slip exists a phenomena which might be classified as primary slip. This normally takes place independent of the nondevelopable nature of the toroidal tire, and can be thought of as a function of such parameters as steer angle, braking torque, and driving torque acting on the tire. The most common of these phenomena is that of steer angle. Here, the contact area of the tire with the roadway is first of all distorted due to the presence of the steering effort, and finally is separated into two regions due to this steering effort. The first region is

one of essentially static contact between the tire and the road surface, but nevertheless a region in which secondary slip may exist. The second region, adjoining the first, is the region of primary slip where the tangential surface stresses necessary to maintain geometric distortion of the tread surface exceed the local frictional stresses available, so that the tire surface exists in part in a state of slipping in a gross sense. The order of magnitude of such primary slip might be in the neighborhood of 0.1 inches or more.

It is difficult to measure the contact areas under such conditions of yawed rolling, but these have been observed on model tires through a glass plate by Saito [12]. Drawings are given in figure 5.22 showing the growth of the primary slip area with increasing steer angle.

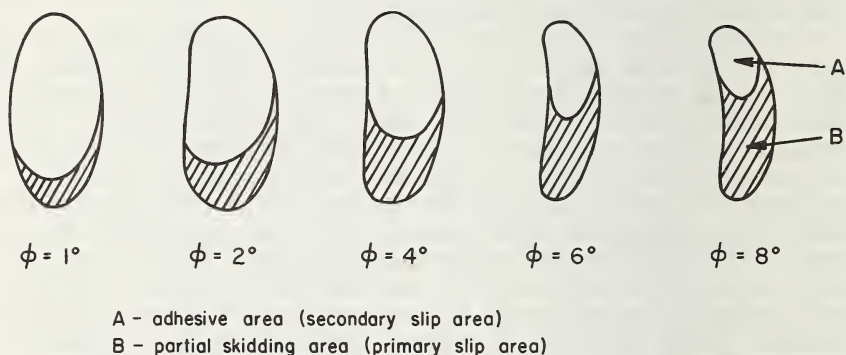


FIGURE 5.22. Slip areas as a function of steer angle ϕ as determined by visual observation.

It should be noted in figure 5.22 that the primary slip is confined to the rear of the contact patch in all cases. Effective stationary contact between tire and roadway, marred only by secondary slip, occurs always at the leading edge of the contact patch as the tire rolls.

In regard to straight line motion of the tire under braking or tractive effort, there is probably always a certain amount of primary slip when the wheel is in this condition, but the magnitude of this slip is variable. The size of the zones of slip may also change, depending on the magnitude and direction of the applied wheel torque. At the point where a driven wheel comes into contact with the road and also at the point where it leaves the road, the tire surface attempts to slip in the direction in which the wheel is turning, while at the center of the contact area there is a region where the tendency is to slip in the opposite direction. Novopol'skii and Nepomnyashchii [13], present diagrams showing the change in the positions of tread elements along the contact length of a tire relative to

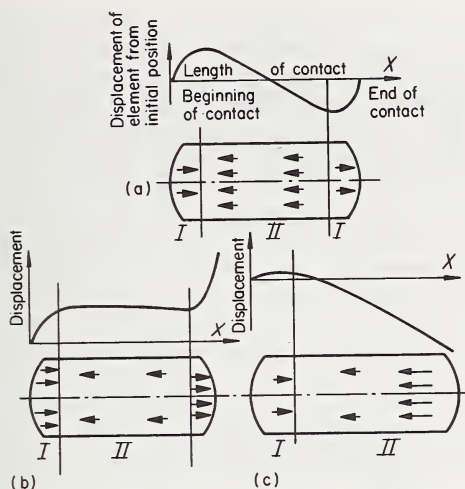


FIGURE 5.23. *Displacement of tread elements along contact length of tire: (a) free rolling, (b) driving, (c) braked.*

Zone I Longitudinal tangential stress acting from tire to roadway in direction of motion.
 Zone II Longitudinal tangential stress acting from tire to roadway opposite to direction of motion.

the positions which they occupied at the instant of entering contact. This is shown in figure 5.23. The slipping of a driving or braking wheel is also determined by the magnitude of the tangential forces acting in the plane of contact. Figure 5.23 also shows displacement curves for the tread of a driving wheel and for the tread of a braked wheel. Note that in both of these latter cases the tendency for primary slip is confined to the rear of the contact patch, just as in yawed rolling shown in figure 5.22.

This type of behavior is exemplified by measurements taken on an automotive tire and presented in reference [13]. This data is given in figure 5.24 where it is shown that the slip measured at the surface of a tread element is essentially in accord with what one would expect from the idealized representation of figure 5.23.

In these cases the differentiation between primary and secondary slip regions is not particularly clear. For example, the first plot of figure 5.24 shows a freely rolling wheel without applied torque. Here, essentially all of the tire is at a slip level low enough so as to be classed as secondary slip. On the other hand, the last plot of figure 5.24 shows the slip of a braked wheel in which slip values are large enough so that they might be

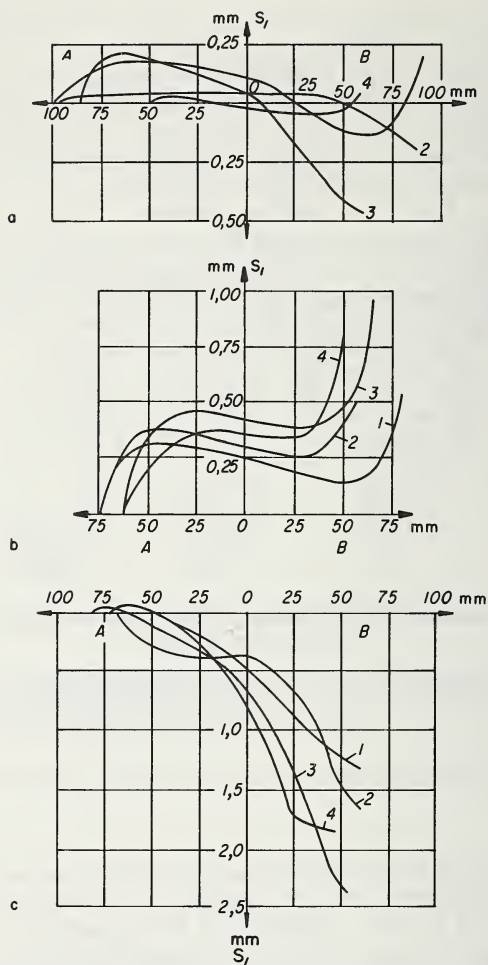


FIGURE 5.24. Longitudinal slipping in the contact zone of a 6.00-16 tire.

(a) driven wheel-zero torque, (b) driving wheel-torque = 25 Kgf · m., (c) braked wheel-torque = -25 Kgf · m.

Contact length measured along the abscissa, with A the point of first contact and B the point of last contact. Ordinate is longitudinal displacement of a tread element from its initial position. Downward is in the direction of turning of the wheel.

Curve 1, middle of tread; Curve 2, 17 mm. from tread centerline; Curve 3, 34 mm. from tread centerline; Curve 4, 51 mm. from the tread centerline, i.e., edge of tread.

thought of as primary slip toward the end of the contact region. It is clear, of course, that in the case of steering under fairly large steer angles the slip at the rear of the contact patch might be primary slip, of the order of centimeters, while under complete locked wheel skidding the slip values would be very large, and the entire contact patch would be in a state of primary slip.

One comment should be made concerning the measurements of slip commonly available in the literature. They are obtained in almost all cases by rolling the tire over a plate which has protruding from its smooth surface a small pin of low mechanical impedance. The pin contacts the tread as the tread element moves into contact with the roadway, and from that point onward registers a signal proportional to slip as the tread element moves through the contact patch. Thus all measurements are made with respect to the leading edge of the contact patch, which serves as a zero reference. The data previously quoted have pertained to slip in the longitudinal direction, i.e., slip in the direction of travel of the rolling wheel. Biderman, Volodina, and Pugin [14] have used similar techniques to measure deformation of the tire carcass. While this is not the same as the slip between tread elements and the roadway, it nevertheless takes on the same character. Transverse slip, at right angles to the direction of travel of the wheel, also takes place in the contact patch. Its nature may be inferred from figure 5.25, which gives data on meridional displacement of the tire carcass itself as the tire rolls through the contact area.

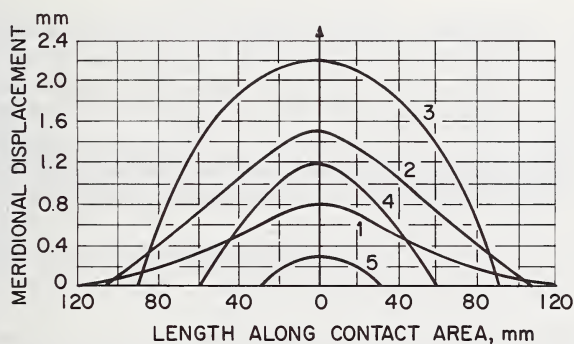


FIGURE 5.25. *Meridional displacement of carcass.*

Distance from crown: 1-10mm; 2-20mm; 3-40mm; 4-50mm; 5-55mm. Straight line slow rolling. 6.00-16 tire, longitudinal ribs 2mm high.

It is clear that the question of slip during the rolling process is intimately connected with the normal pressure distribution which exists in the contact area. The normal pressure distribution does not suddenly rise at the edge of the contact area from zero to a finite value, but rather increases, however gradually or suddenly, at a finite rate. This means that inevitably there will be a narrow ring or boundary layer around the edge of the contact patch on which the normal pressure distribution is very small, so that consequently the available adhesion limits are very small. At these regions it would be natural to expect that at least secondary slip would occur simply due to the fact that horizontal friction forces are unable to further restrain elastic displacement of the rolling tire. The experiments of Mindlin [39] tend to substantiate this.

An analogy to this has been given by Reynolds, and is quoted by Hadekel [1]. Imagine a belt on a pulley, transmitting a definite power, and therefore having a difference in tension between entry and exit, and hence also a difference of strain between these points. A given element of the belt undergoes some change in length from entry to exit, which is possible only if there is relative sliding. Reynolds concluded that there must be some sliding near the edges of the contact region, even in the absence of horizontal forces other than rolling resistance.

The question of slip in a rolling tire has been studied by Novopol'skii and Tret'yakov [15] who conclude:

- a. When a tire rolls, the slip areas are where contact begins and ends.
- b. Torque greatly increases both the area of the slip and the amount of slip where contact ends. There is only an insignificant change in the amount of slip where contact begins.
- c. Both the carcass design and the type of tread pattern have a real effect on the slip but the part played by the carcass design is of greater importance.

One of the commonest cases in which an external influence changes the slip picture dramatically occurs when the tire runs on a wet roadway. This problem has been studied in some detail for aircraft tires by Horne et al. [16], due to its importance for the landing of aircraft on wet runways. It is also of some importance in automotive tires, since the presence of water can materially decrease the region in which secondary slip, or effective tire contact, is present. As long as at least some of the tire is in effective contact with the roadway, then lateral and guiding forces are available for maneuvering the vehicle. As soon as such effective contact is lost then these forces are also lost and complete overall skid may result.

It is generally realized that as speed increases, the removal of water in the contact area becomes progressively more difficult. The volume of water to be removed per unit time, and the inertia and viscosity forces necessary to do this, all increase. Below the so-called hydroplaning speed, defined as that speed at which all effective contact is lost, the ground contact area may be idealized into three zones. These are shown in figure 5.26, taken from Kelley and Allbert [17]. The effective length of zones *A* and *B* in figure 5.26 progressively increase with vehicle velocity, thus reducing the size of the contact zone *C* until, at hydroplaning velocity, the entire contact area is water borne. Two phenomena are mainly responsible for this progressive penetration of the water layer into the contact zone.

- (1) Hydrodynamic pressure due to the impact of the tire on the water layer. This impact on the stationary water film results in a hydrodynamic wedge which forms between the inclined tire tread surface and the ground, immediately ahead of the contact zone. Hydrodynamic pressures which result from the change in mo-

mentum of the surface water produce an upward thrust on the tire tread just forward of the contact area. The magnitude of this thrust depends mainly on the depth of the water layer, the tread width and the forward velocity of the tire. The hydroplaning speed has been approximated by Horne as

$$V_p = 10.35[P]^{1/2}$$

where V_p is the minimum hydroplaning speed in miles per hour and P the tire inflation pressure in psi.

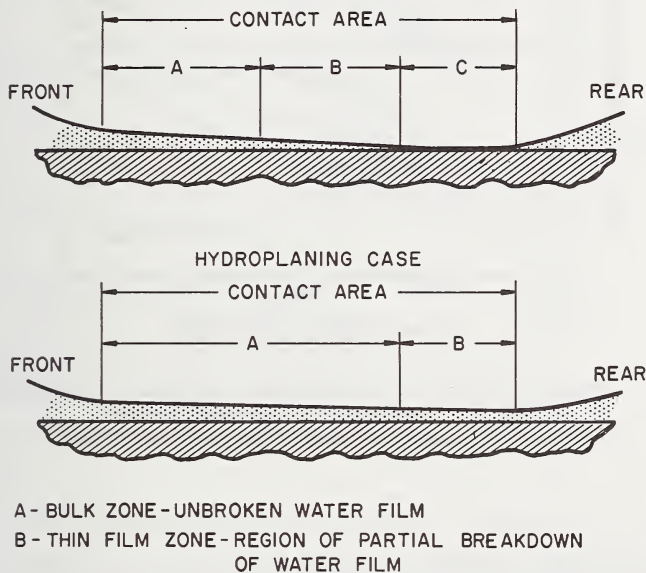


FIGURE 5.26. *The three-zone concept of contact area under wet conditions.*

A, unbroken water film; B, thin film zone, partial breakdown of water film; C, contact zone.

- (2) A squeeze film in the vicinity of zones A and B. As shown in figure 5.26, the thickness of the water film decreases progressively towards the rear. Considered independently of the "water wedge", the size of zones A and B depends on the relation between the times taken by each element of the tread entering the contact area to squeeze through the film and to travel the full length of contact. For a particular tread element the time to squeeze through the film depends on the dimensions of the tread element, the thickness and viscosity of the water film and the surface texture. This time is independent of speed. The second time, that necessary to travel the length of contact, varies inversely with speed. It is thus possible that at some speed the time necessary to penetrate the water film will exceed the time in which the tread element is in the water film, so that an unbroken water film will exist through the entire contact area.

The combined effects of the water wedge and viscous lubrication may result in minimum hydroplaning speeds considerably lower than that given in the previous equation.

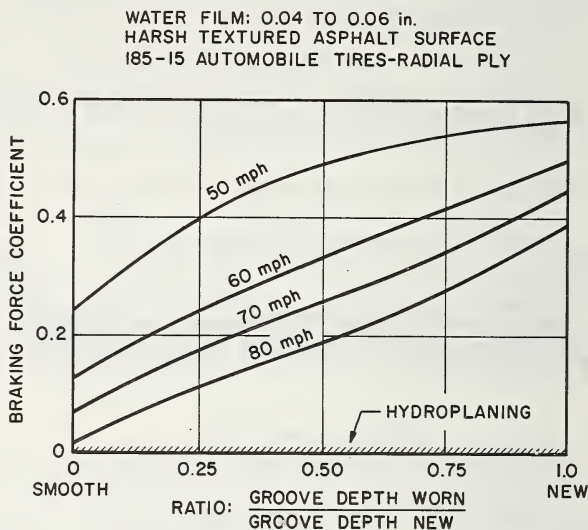


FIGURE 5.27. *Effect of tread pattern groove depth on braking grip, under flooded road conditions. Wear maximizes hydroplaning tendencies.*

Figure 5.27 shows the effect of tread groove depth on braking characteristics under flooded road conditions. On smooth surfaces, under wet conditions, tread pattern designs showing the least loss in braking force coefficient, and the highest hydroplaning speeds, have three main features:

- (1) Wide, preferably straight and unobstructed grooves or channels to facilitate removal of water trapped in the wedge immediately ahead of the contact areas.
- (2) Narrow ribs or block elements which, by effectively reducing flow distances, shorten the time required to squeeze thin water films from between the tire and the smooth surface.
- (3) Slots or knife-cuts in the surfaces of the main rib which act as low pressure reservoirs and also effectively shorten the flow distances.

These three design characteristics refer mainly to high speed conditions. They conflict somewhat with both low speed wet holding performance and with other tire requirements such as pattern stability and durability.

TABLE 5.4. *Factors influencing effective braking friction between tire and wet road (100 mph maximum)*

Factors	Level of variability due to factor considered
Tire factors	
1. Tread pattern design. Scale of effect recorded during assessment of practical tire pattern designs.	Up to 4:1
2. Tread materials. Maximum effect due to tread material changes within range of materials currently available	Up to 1.5:1
3. Patterned tire. Smooth tire	Up to 8:1
Road factors	
1. Road surface characteristics. Scale of effect recorded during assessments of practical tire pattern designs	Up to 5:1
2. Water depth. Effect of variation in depth of water film covering a road surface in the range 0.05–0.20 in.	Up to 3:1
Vehicle factors	
1. Speed. Reduction in braking force coefficient due to an increase in speed from 30 to 80 mph (patterned tires only)	Up to 10:1
2. Braking system. Perfect nonlocking system versus locked wheel braking	Up to 3:1

Note: Cases of braking force coefficients below a value of 0.1 have been excluded.

Kelley and Allbert have attempted to assess the variability inherent in the various factors affecting braking friction between a tire and the wet road. These are given in table 5.4. From the results of this table, it is seen that the most important characteristics in regard to total braking force lie in the patterned versus smooth tire, and in the speed at which the braking force is measured. The pattern remains the main design variable which can be controlled by the tire designer, so that it would be anticipated that significant wet road improvement could be obtained by use of proper tread patterns which are capable of channeling water away from the contact region at maximum flow rates.

5.4. Contact Pressures

At the interface between the tire and the roadway an element of tire surface area is acted upon by a force vector which can be expressed as two components, one perpendicular to the contact surface, called the normal component, and one tangential to the contact surface. This is

shown in figure 5.1. This latter component may be further decomposed into two components, each lying in the contact plane, but one parallel to the central plane of the tire and the other perpendicular to it. These components in the contact plane are commonly called the shear components. With equal validity they could be expressed as components parallel and perpendicular to the direction of travel of the wheel. Either decomposition would be useful for describing the shear effects.

In this section attention is directed first to the normal pressure distribution components caused by contact of the tire with some other surface. As a basic primary concept, one might state that

$$p = p_0 + f \text{ (Tire structural characteristics, tire driving or braking torque, tire side forces, tire velocity, etc.)} \quad (5.9)$$

where p is the vertical pressure component at any point, p_0 is the inflation pressure of the tire and f is some general functional relationship which insofar as is now known is extremely complicated, and can best be described in a qualitative sense.

In eq (5.9), we postulate that the net pressure distribution at any point depends primarily upon the inflation pressure, and there is considerable experimental evidence to indicate that this is indeed true. Such a conclusion was used by Hadekel [1] as the basis for one of his estimates of the net contact pressure of a tire. On the other hand, subsequent studies have shown that the characteristics determining the function f also play an important part in defining the detailed tire pressure distribution. In general, these characteristics may be thought of as being divisible into two major parts:

- a. Tire structural characteristics.
- b. Tire operating variables.

Of these two types of influences, the use of theory is most beneficial in discussing the role of structural parameters in modifying the basic inflation pressure distribution. Some of the most important aspects of the various simple theories will be reviewed here.

In the first instance, consider the contact against a flat surface of an inflated membrane with vanishing bending stiffness. No matter what the tension in the membrane, the fact that it is in geometric contact with the flat surface means that the contact pressure distribution is exactly equal to the inflation pressure inside the membrane, and it is this line of reasoning which allows one to postulate that the primary component of tire vertical contact pressures is the inflation pressure. On the other hand, if the tire is in contact with a cylindrical road wheel then this statement is no longer true, since the cover tension now plays some role in defining the net contact pressure. This is expressed analytically as

$$p = p_0 + \frac{N}{R} \quad (5.10)$$

where N represents the shell membrane force per unit length while R represents the radius of the road wheel contacting the tire. From this it

may be seen that the road wheel test may generally be expected to exhibit slightly higher average contact pressures than actually exist on the highway.

It is of interest to attempt to classify the various structural parameters of the tire which affect the vertical contact pressure, in order to obtain some idea of the influence of these parameters.

First of all, the tire is basically a structural shell. To an even greater approximation, one may roughly consider a tire to be represented by an elastic running band elastically supported by the tire side walls. This type of model is particularly applicable to a radial tire, although it also can be used to express the characteristics of a bias ply tire. Using such a model, attention may be primarily directed to the fore-and-aft variation of the pressure distribution, since effects of right angles to this will be very similar. This will allow description of the pressure distribution as a function of only one dimension, namely that measured down the length of the contact patch, which will considerably simplify the discussion which follows.

The tire structural components of most importance in describing the effect of the tire carcass upon normal contact pressures are:

- a. Elastic support of the tread by the sidewall.
- b. Bending of the tread.
- c. Shear deformation of the tread.
- d. "Snap through" buckling of the tread, defined as the tendency of the tread to seek a *deformed* equilibrium position due to membrane compression.
- e. Normal compliance or stiffness of the tread.

The role of these various components has been discussed from the theoretical point of view by Clark [37] who also performed model experiments designed to illustrate some of these effects. If the tire is thought of as a running band supported by an elastic foundation, then deformation of the elastic foundation requires a pressure distribution which should be very close to being proportional to the amount of radial deformation undergone by the tire. The interference of the tire running against a flat plane is known from the geometry, and the form of pressure distribution associated with deformation of the side wall may be expressed as

$$p_a = k \left(1 - \frac{\cos \theta_0}{\cos \theta} \right) \quad (5.11)$$

where p_a represents the contact pressure needed to deform the elastic sidewall, k is the sidewall foundation stiffness in units of pressure, while θ_0 represents the angle of geometric interference as shown in figure 5.16. This type of pressure distribution is illustrated in figure 5.28,

while in figure 5.29 an actual pressure recording down the length of the contact patch is given by a model wheel made with an isotropic annular band. This is a nearly pure elastic foundation and exhibits a pressure distribution similar to that predicted by eq (5.11).

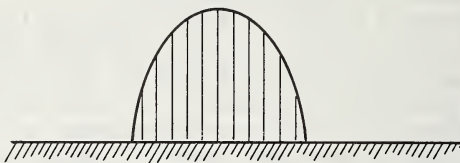


FIGURE 5.28. *Idealized elliptic pressure distribution.*

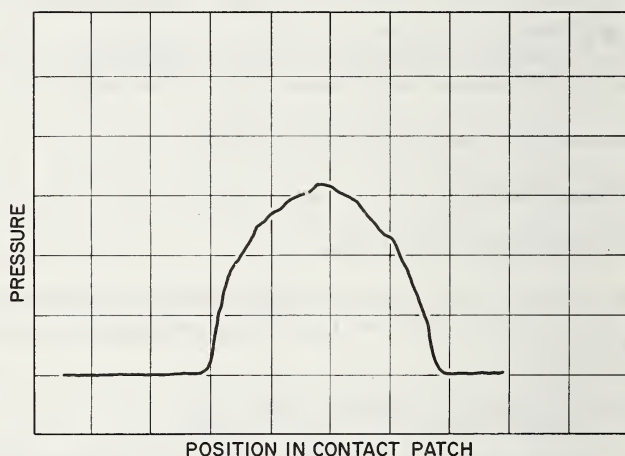


FIGURE 5.29. *Measured pressure distribution of a silicone rubber ring with rigid hub.*

The bending of the running band itself represents an interesting form of pressure distribution, since in considering the deformation of a circular band in contact with a flat plane, a finite bending moment is required to change the original curvature $1/r$ of the running band to a zero curvature, which it must have when it conforms with the plane. In addition, this change in curvature, and hence the bending moment, must be constant within the region of contact. The only pressure distribution satisfying these equilibrium and bending moment requirements is made up of a pair of concentrated forces, located at each end of the contact patch. This is illustrated in figure 5.30 schematically, while figure 5.31 shows an actual pressure distribution recording taken from a model test, in which a running band free of elastic support is rolled over a pressure transducer buried in a steel plate.



FIGURE 5.30. Idealized pressure distribution for a circular ring.

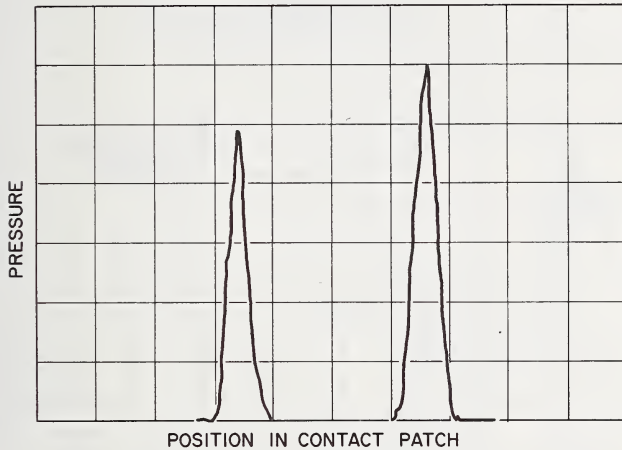


FIGURE 5.31. Measured pressure distribution for a circular metal band on a flat plane.

The case of pure bending of the running band is an idealization. In any real situation some transverse shear deformation of the running band must be present. The problem of the curved ring in contact with the flat plane, utilizing both bending and shear deformation of the material, has been studied by both Robbins [18] and Akasaka [19]. Both of these authors conclude that the role of transverse shear deformation is to change the idealized concentrated force distribution into a continuous one. The form of this pressure distribution is illustrated in figure 5.32, in a schematic sense, while a pressure recording taken from a worn automotive tire is given in figure 5.33.

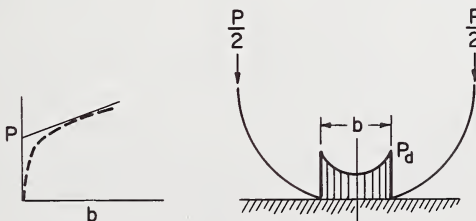


FIGURE 5.32. Theoretical pressure distribution for a circular ring, with shear deformation, in contact with a rigid plane.

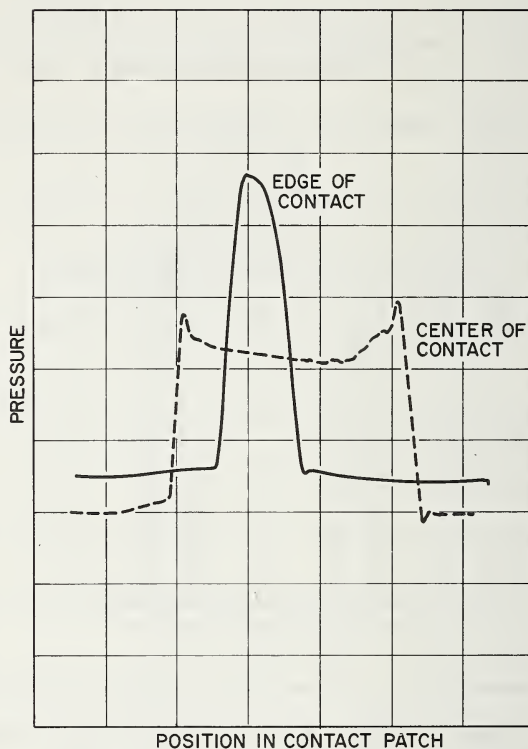


FIGURE 5.33. *Measured vertical contact pressure on a 7.50-14 automotive tire with worn tread.*

Buckling of the tread, or “running band” usually would occur at somewhat larger deflections. This phenomena has been studied extensively from the point of view of structural shell theory, although often using concentrated forces or uniform pressure loadings in order to obtain stability criteria. Experimental evidence gives a good idea of what happens here, although it is clear from the nature of the phenomena itself. Imagine an internally inflated membrane subjected only to inflation and buckling effects. The pressure distributions for small and large deflections respectively are shown in figure 5.34. Due to buckling, the pressure is decreased markedly in the center of the contact region, as would be expected. Unfortunately the form of decrease of the contact pressure near the center of the contact area is similar to that predicted by shear deformation, and it is difficult to distinguish between the two causes of smaller contact pressure near the center. Such a phenomena may also be observed on model tests by increasing the deflection substantially, as is shown in figure 5.35.

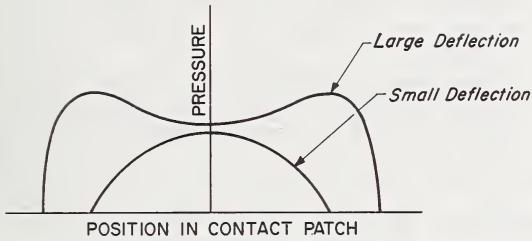


FIGURE 5.34. Idealized pressure distributions due to buckling.

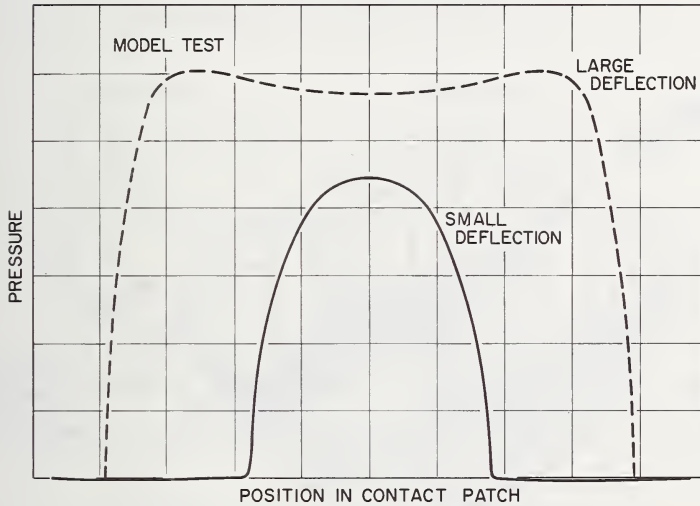


FIGURE 5.35. Measured pressure distribution on tire model at small and large deflections.

The role of normal compliance, or stiffness of the tread, is not well understood in forming the total pressure distribution pattern, since few pertinent theoretical studies involving shell theory interacting with normal stiffness exist. The general role of normal compliance can be seen by referring to the well-known cylinder contact solutions of Hertz [20] for an isotropic body. This approximates the type of contact pressure obtained when a low normal stiffness exists, since most of the deformation due to contact is confined to a relatively thin surface lamina. The Hertz solution for a cylinder in contact gives a semi-elliptical pressure distribution as shown in figure 5.28. Unfortunately, it is nearly identical in shape to the pressure distribution required to deform the elastic foundation for the tread, and it is difficult to distinguish between them. However, figure 5.35 shows a recording of the pressure distribution of a model having a relatively soft isotropic outer band simulating the tread of the tire. This illustrates the general role of normal compliance, and illustrates further

that pressure distributions such as shown in figures 5.33 or 5.34 do not rise abruptly, but rather exhibit some sort of gradual build up of pressure from the edge of contact.

Many of the phenomena just discussed can be observed clearly on pressure distribution recordings taken from various kinds of pneumatic tires. Some of this data has been reviewed briefly by Hadekel, with particular emphasis on the early work by Kraft [21], and by Markwick and Starks [22] who dealt with automotive tires. More recently, much more detailed measurements on truck tires have been reported by Bode [23], who reports data such as shown in figures 5.36–5.40.

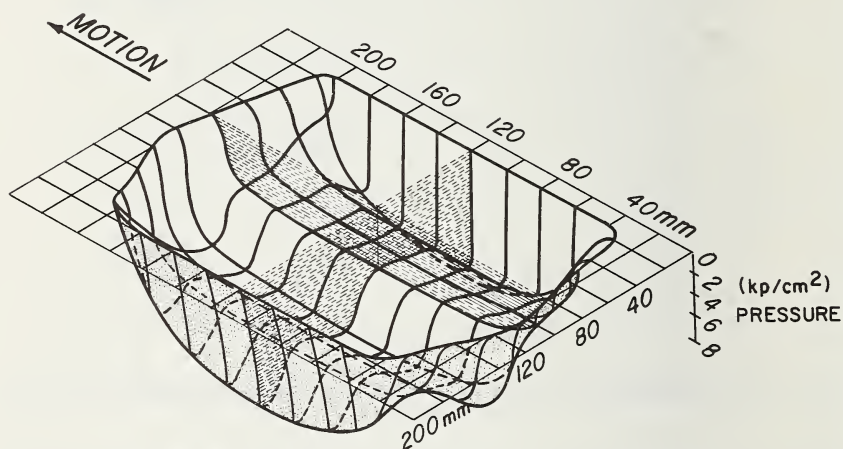


FIGURE 5.36. Pressure distribution under a tire with no tread pattern, i.e., smooth surface. Static load 3740 Kp., inflation 6.5 atm gage, velocity 18.3 Km/hr.

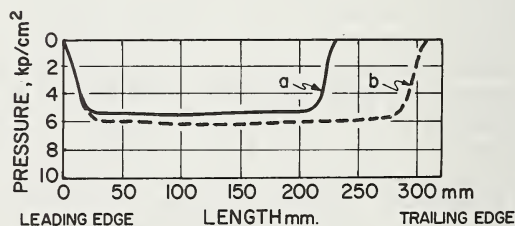


FIGURE 5.37. Pressure distribution down the length of a tire with no tread pattern, at constant 15 Km/hr velocity, for two loads: (a) static load 1680 Kp., inflation 6.5 atm; (b) static load 3740 Kp., inflation 6.5 atm.

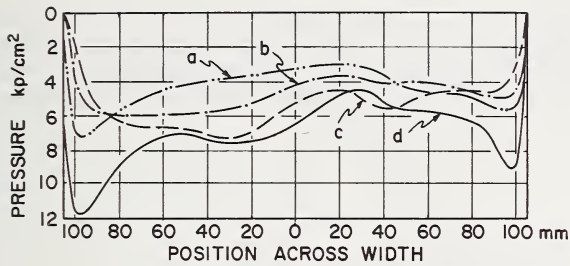


FIGURE 5.38. *Influence of load and internal pressure on contact pressure distribution under a tire with no tread pattern.*

Constant velocity 15 Km/hr measured across the tire width. (a) Load 1680 Kp, inflation 3.5 atm; (b) load 1680 Kp, inflation 5.0 atm; (c) load 1680 Kp, inflation 6.5 atm; (d) load 3740 Kp, inflation 6.5 atm.

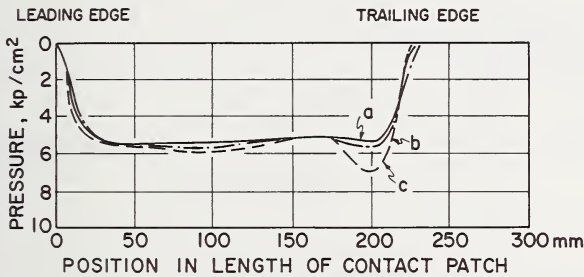


FIGURE 5.39. *Influence of the tractive force on pressure distribution under a smooth tire, taken down the length of the tire.*

Load 1680 Kp; inflation 6.5 atm. (a) 0.6 m/s^2 acceleration $V = 10.2 \text{ Km/hr}$; (b) 1.6 m/s^2 acceleration $V = 8.4 \text{ Km/hr}$; (c) 4.1 m/s^2 acceleration $V = 3.9 \text{ Km/hr}$.

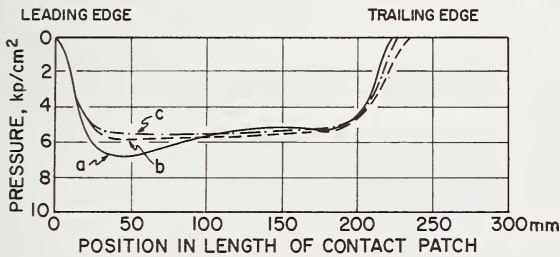
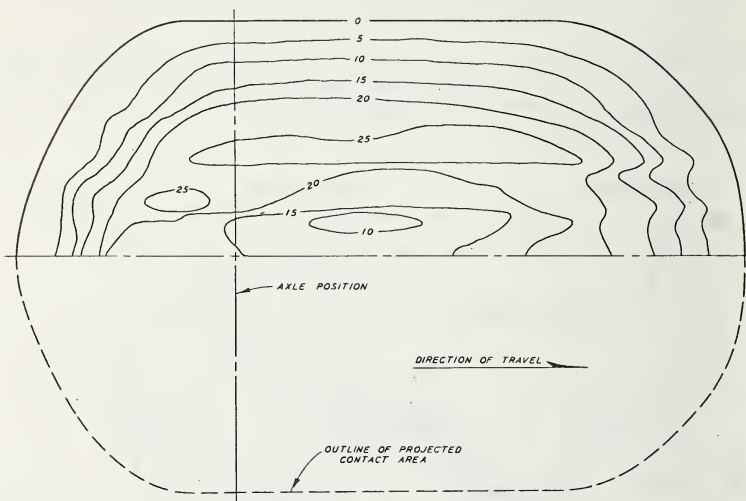


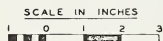
FIGURE 5.40. *Influence of the braking force on pressure distribution under a smooth tire, taken down the length of the tire.*

Load 1680 Kp; inflation 6.5 atm. (a) -4.1 m/s^2 deceleration $V = 10.0 \text{ Km/hr}$; (b) -2.7 m/s^2 deceleration $V = 35.7 \text{ Km/hr}$; (c) -2.0 m/s^2 deceleration $V = 14.5 \text{ Km/hr}$.

A very complete set of data on normal stresses taken in various soils has been reported by Green [24]. A typical pressure contour plot of a tire in sand is shown in figure 5.41, while the total soil pressure distribution is given more accurately by figures 5.42-5.44. A further compar-



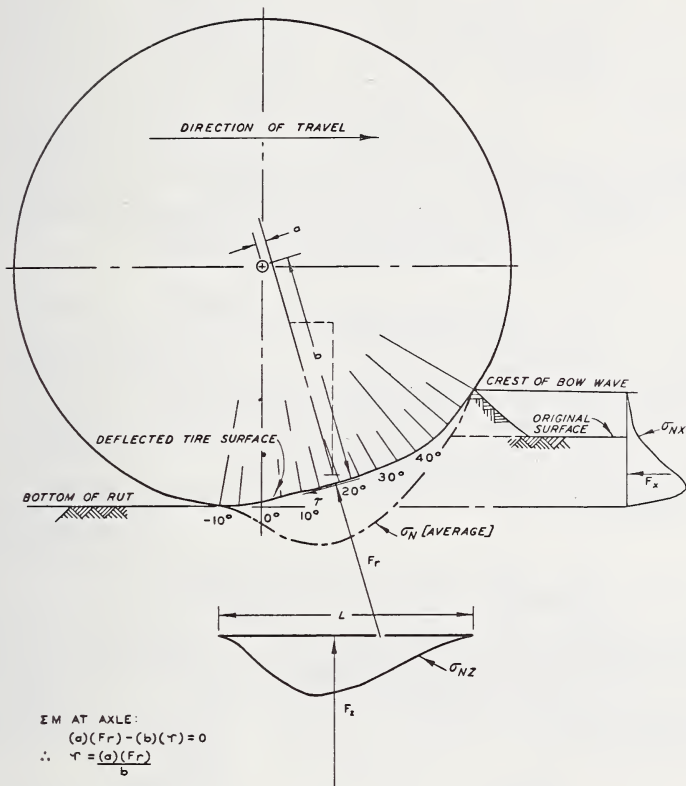
NOTE: CONTOURS ARE STRESSES IN PSI.



DISTRIBUTION OF NORMAL STRESSES PROJECTED ON HORIZONTAL PLANE

TOWED WHEEL IN SAND
11.00-20, 12-PR SMOOTH TIRE
3000-LB LOAD 15-PSI INFL PRESS.
0- TO 6-IN. CONE INDEX = 30

FIGURE 5.41. *Distribution of normal stresses under a towed tire in sand.*



ASSUMPTIONS:
 $\sigma_N = \sigma_{NX} = \sigma_{NY} = \sigma_{NZ}$
 AXLE FRICTION NEGLIGIBLE

NORMAL AND TANGENTIAL FORCES ON A TOWED PNEUMATIC TIRE IN SOFT SOILS

FIGURE 5.42. Stresses in a towed wheel in soft soil.

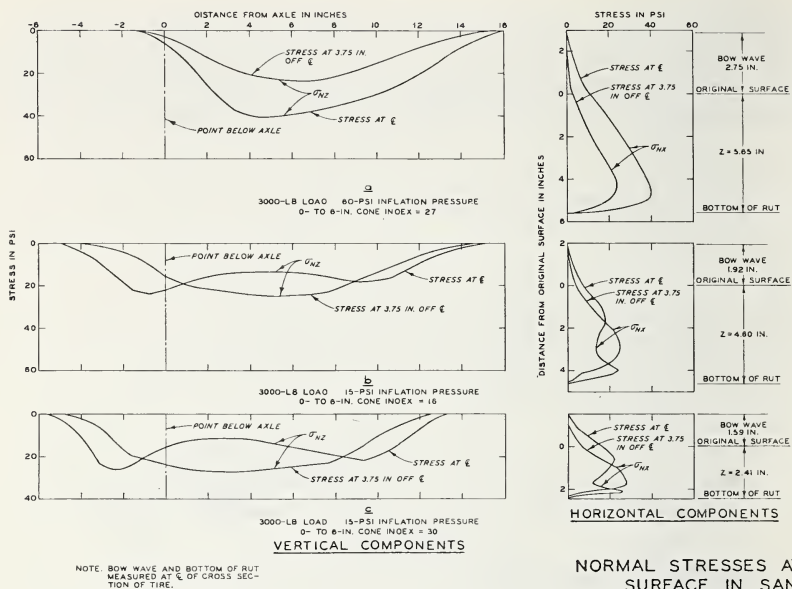


FIGURE 5.43. Normal stresses at tire surface in sand.

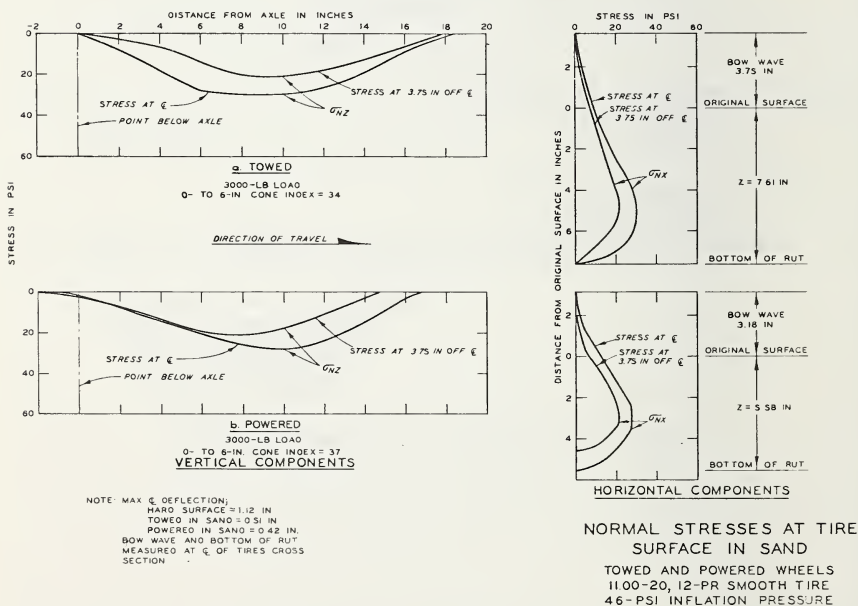
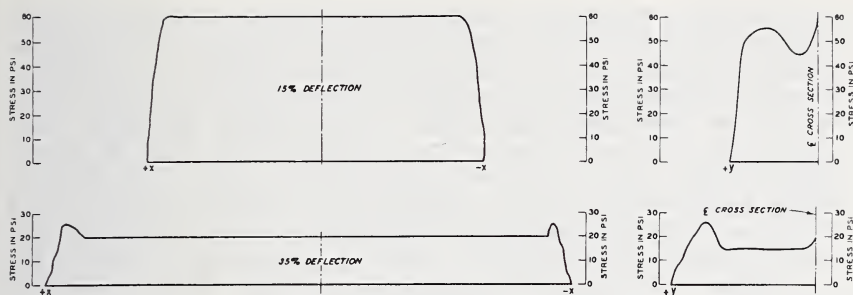
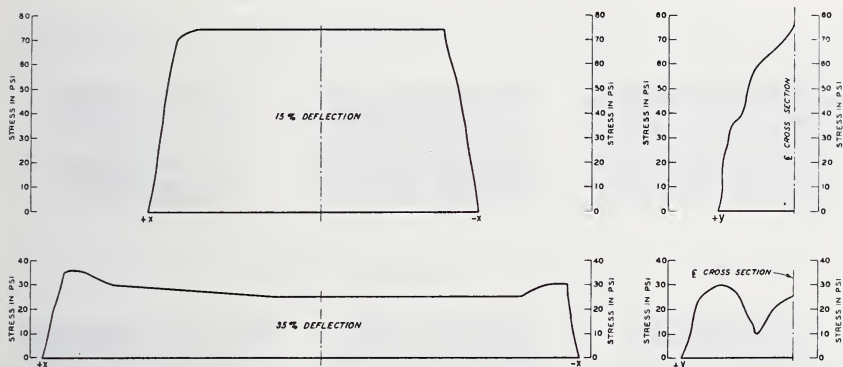


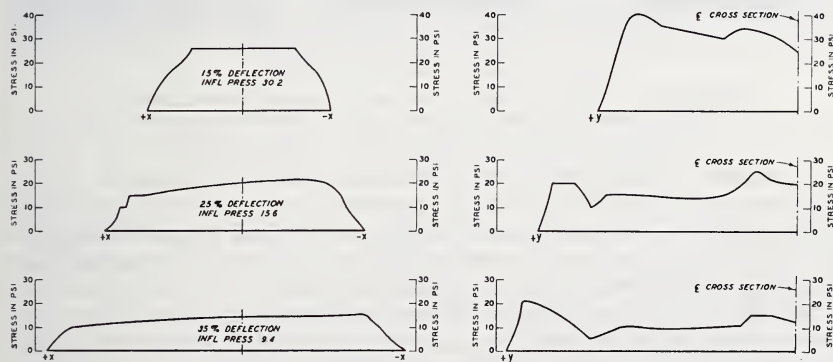
FIGURE 5.44. Normal stresses at tire surface in sand.



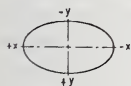
a. 6.00-16, 4-PR (STD CONST) SMOOTH TIRE



b. 6.00-16, 4-PR (RADIAL PLY) SMOOTH TIRE



c. 16.00-15, 2-PR SMOOTH TIRE



DIRECTION OF TRAVEL

HORIZONTAL SCALE
IN INCHES
0 1 2

FIGURE 5.45. Vertical stresses along principal axes of contact ellipse of three tires of dissimilar construction under constant 890 lb. load but with different inflation pressures.

tive study between various types of tires has been reported by Freitag and Green [25] which is in part summarized in figure 5.45 where pressure distributions taken both along the length and width of three common types of automotive tires are presented. These tires were tested in contact with an essentially rigid surface. They illustrate the rather interesting point that the presence of a four-ply structure with its greater bending rigidity tends to emphasize the pressure spikes located at forward and leading edges of the contact patch, as might be expected from the simple theoretical discussion of the bending of a curved ring, as previously outlined and illustrated in figures 5.31 and 5.33. A similar but less detailed study has been presented by Hofelt [26] as shown in figure 5.46.

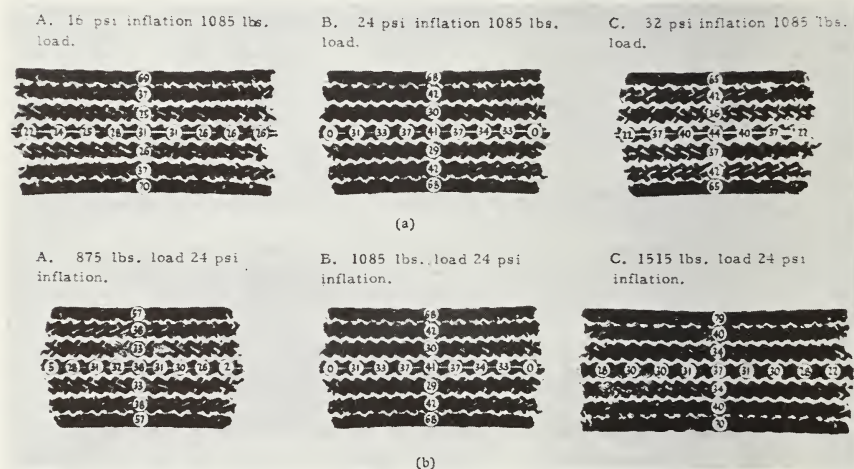


FIGURE 5.46. *Effect of inflation and load on normal contact pressure.*
(a) Effect of inflation at constant load, (b) effect of load at constant inflation pressure.

A number of theoretical investigations and mathematical models have been proposed for explaining or calculating contact pressure distributions between various types of bodies and a rigid plane. Hofferberth and Frank [27] mention the work of Martin [28] as well as that of Vlasov [29]. In the latter case a variational method is suggested for the treatment of two-dimensional contact problems involving plates and shells, while in the former case symmetric two-sided flattening of cylindrical and spherical shells has been considered. Basically, the problem usually reduces to the matching of two equations, one equation describing the free surface of that portion of the plate or shell not in contact with the rigid plane, under known external loads but with unknown deformations. The second region describes the area of the plate or shell in contact with the rigid plane, and this defining equation usually is written in terms of known deformations but unknown load distribution. Continuity of displacement must take place and hence the two sets of equations

must be matched, usually at the unknown boundary of contact. This introduces an additional degree of freedom into the system, and often makes such a matching process amenable only to trial and error solution. Böhm [30] has extended Martin's theory and developed it for the one-sided flattening of the toroidal shell with circular cross section, but without numerical results. Martin found theoretically that the contact pressure distribution is rectangular under a flattened cylinder, with a value smaller than that of the inflation pressure providing the cylinder has bending stiffness. Equilibrium is maintained by a pair of concentrated bending moments which act at the forward and leading edges of the contact patch, these bending moments arising due to the fact that it is not possible to match bending moment and shear at the junction of the contact region with the free surface. On the other hand, the inclusion of shear deformation by Akasaka and Robbins leads to theoretical pressures as shown in figure 5.47.

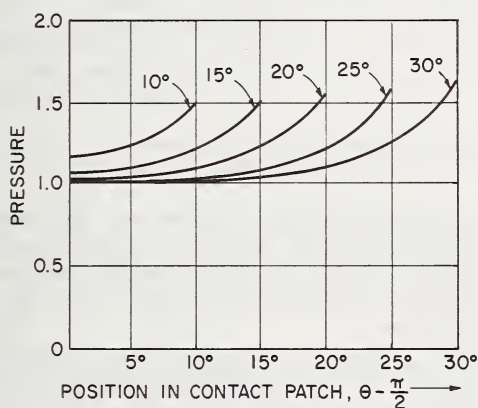


FIGURE 5.47. *Calculated pressure distributions under a flattened cylindrical shell, under internal pressure p , with different degrees of flattening.*

The angles given are characteristic for half of the flattened, originally cylindrical portion of the arc.

A great deal of interest has been shown in the role of velocity in modifying the contact pressure distributions just discussed. A number of investigations have examined this, including the previously discussed work of Bode as well as the work of Zakaharov and Novopol'skii [31]. In general, the results seem to show that increasing speed causes an increasing vertical contact pressure at the forward end of the contact patch and a decreasing value at the rear portion of the contact patch. This is schematically illustrated in figure 5.48, and has been experimentally confirmed by Zakaharov and Novopol'skii [31]. Attempts have been made by Clark [10] to utilize a relatively simple shell and elastic foundation theory to predict dynamic contact pressures, but due to the inability of such a simplified model to accurately provide for continuity of shear and bending moment through the edge of the contact patch, the

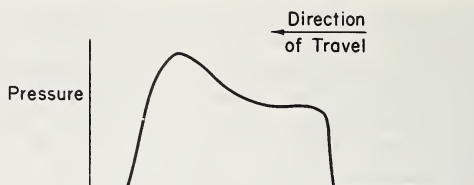


FIGURE 5.48. *Idealized pressure distribution as influenced by speed of travel.*

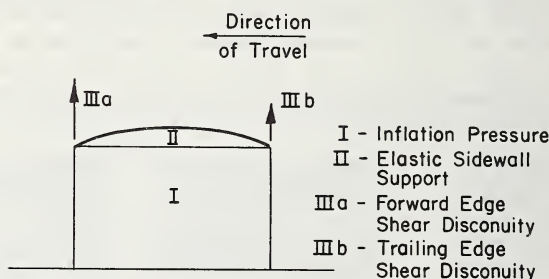


FIGURE 5.49. *Calculated dynamic pressure distribution from simple elastic shell tire model, without shear deformation.*

corresponding dynamic pressure distributions are predicted in the form shown in figure 5.49. It is clear that shear deformation must be added to such a theory before realistic contact pressure distributions will be available. However, the general trends of such dynamic pressure distributions are apparent.

The necessity for including shear deformation effects, and for discarding the restrictions of the Kirchhoff bending hypothesis, were also discussed by Essenburg and Gulati [32] who studied the axisymmetric contact of plates. They concluded that only by such a relaxation of conventional bending theory could the contact problem be successfully approached.

All measurements on automotive tires show a relatively high normal contact pressure region in the shoulder area of the tire tread, due to the heavy tread shoulder conventionally used on such tires. This means that generally one finds higher pressures at the shoulder than at the center of contact. This has been illustrated in the experimental data given, but bears repeating.

Vermeulen and Johnson [33] have discussed the contact of nonspherical elastic bodies transmitting tangential forces, and have by such an effort given at least a beginning to a formal theory for tractive forces in combination with the contact problem. Vermeulen and Johnson presume that the presence of tangential forces does not, to a first approximation, change or alter the normal pressure distribution. Their discussion further presumes that the contact surface of two rolling bodies transmitting a tangential force is divided unsymmetrically into a region of

slip and a region of no slip. The no-slip region is adjacent to the leading edge of the contact boundary, independent of the direction of the torque. Elliptical contact regions are assumed, and it is also assumed that regions of no slip are located adjacent to the contact ellipse at the leading edge.

The tangential component of the contact stress between a tire and roadway has been studied rather extensively due to its close association with the processes of tire wear and skid. Hadekel [1] quotes from the early work of Martin [28], Markwick and Starks [22] and Kraft [21]. Most of these early measurements were made with mechanical dynamometer systems imbedded in a flat plate, which allowed a rolling tire to actuate a recording system and to measure the resulting tangential surface stress in terms of its components in the direction of travel and at right angles to the direction of travel. In particular, Martin has idealized these measurements into two vector components, each of which must be doubly symmetric about the centerline of the contact area for a stationary tire without side or longitudinal force acting on it. This is illustrated in figure 5.50. These components combine in such a way as to form shear stress resultants which are roughly directed toward the center of the contact zone.

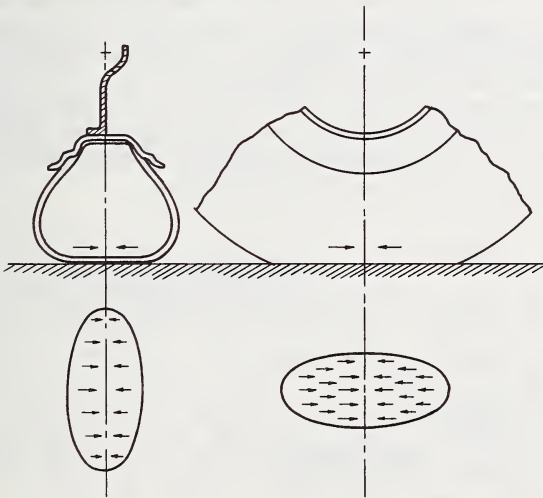


FIGURE 5.50. *Shear stress distribution in the contact patch of an aircraft tire.*

The distribution of tangential forces as given in figure 5.50 is idealized, since there the tire is presumed to have been loaded statically and not rolled into position. In this case it is clear that the deformation of the nondevelopable tire surface, so as to cause contact with the flat roadway, will almost surely result in both bending and membrane deformations of the tire carcass with consequent symmetric strain distribution. The friction coefficient between the tread and roadway prevents the free con-

traction or expansion of the tread surface, so that local shear stresses are set up in the tread elements between the essentially rigid roadway and the deforming or straining tire carcass. It is these shear stresses which on the road surface become the tangential force components during straight line rolling, and at the same time serve to bring the elastic tire carcass into the state of compatibility of deformation with the entire roadway and tire structure system. Were it not for the coefficient of friction between the tread surface and roadway, the tire carcass would freely deform and there would be no tangential stress distribution. Were it not for the elastic characteristics of the tire tread elements and the tire carcass, there would be complete slip throughout the contact region as deformation took place. In truth, the actual phenomena lies somewhere between these two conditions. Under conditions of static deformation of the tire against a roadway, with appreciable friction coefficient, most of the contact surface is relatively free of slip, while in cases of heavy braking or yawed rolling, substantial amounts of primary slip are observed.

Detailed experiments on the friction of rubber indicate that, potentially, friction coefficients are available which exceed those normally observed in a typical pneumatic tire in contact with a roadway. It is felt that the cause of this probably lies in the fact that small amounts of slip (secondary slip) exist almost entirely throughout the contact patch for most practical cases of tire rolling, so that in effect the measurement is of the coefficient of friction of rubber in a state of secondary slip, and not in a state of maximum friction coefficient.

The apparent symmetry of the static shear stress distribution is shown in detail by some of the early experimental results of Martin, given in figure 5.51, for the shear stress component perpendicular to the mid-plane of the wheel, i.e., in the lateral direction.

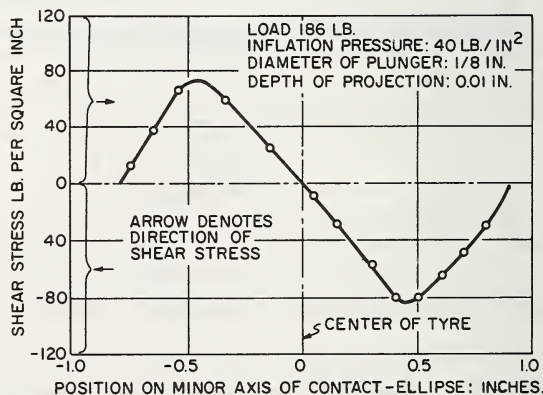


FIGURE 5.51. *Shear stress distribution across the width of an aircraft tire.*

The exact distribution of the lateral component of the tangential contact stress is not well understood even for a stationary tire. The work of

Biderman, Volodina and Pugin [14] seems to indicate that for a standing or slow rolling tire the lateral (sideward) component of the tangential contact stress starts from zero at the forward edge of the contact area, reaches a maximum some distance away from this point and then decreases to zero at the trailing edge of the contact area. This is inferred from meridional displacements of the carcass, but is in complete accord with figure 5.51.

Novopol'skii and Nepomnyashchii [13] have studied the longitudinal component of the tangential stress vector in some detail, and have proposed two causes for this stress component in a rolling tire without steer angle. These are:

a. Deformation of the carcass with respect to the contact plane, giving rise to a shear stress approximated by the expression

$$\tau = k \left[\frac{\theta}{\theta_0} \sin 2\theta_0 - \sin 2\theta \right] \quad (5.12)$$

where τ = longitudinal shear stress

k = carcass stiffness constant

and the other symbols are defined in figure 5.16.

b. A uniformly distributed shear stress caused by tire rolling losses, which for commercial automotive tires is a negligible factor compared to carcass deformation.

The form of the shear stress variation down the length of the contact patch predicted by eq (5.12) is given in figure 5.52.

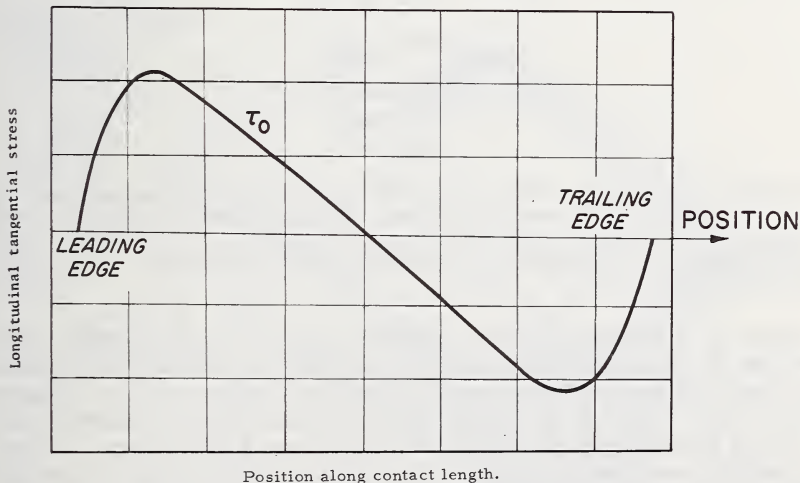


FIGURE 5.52. Distribution of longitudinal tangential stresses along the contact length between a tire and the road while the wheel is in motion.

The action of a driving torque changes the magnitude and distribution of the tangential forces over the plane of contact. No equation has yet been found to connect the tangential force and the torque, but a qualitative picture can be drawn by considering the rotation of an elastic wheel.

Figure 5.53 shows the rotation of a wheel transmitting torque M_t . As a result of the torque transmitted through the wheel, two sets of forces act upon it—the reaction of the wheel axis P_k , and equal to it in the opposite direction the reaction of the road acting in the plane of contact. As a first approximation it may be assumed that the reaction of the road P_k is evenly distributed over the area of contact. The component of tangential stress from the reaction P_k is denoted as τ_p (see fig. 5.53).

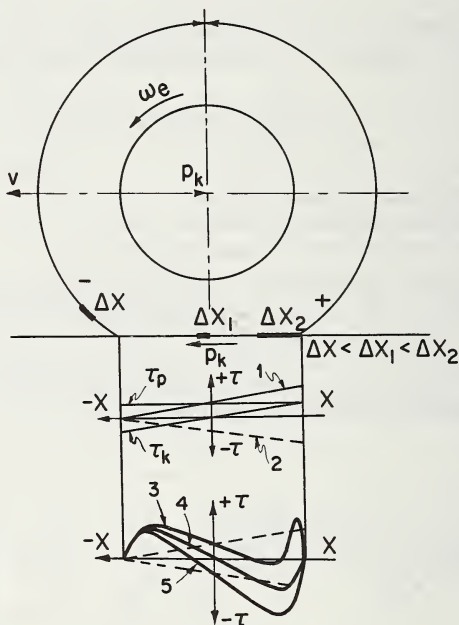


FIGURE 5.53. Rotation of a driving wheel (the distribution of longitudinal tangential stresses in the contact zone of driven, driving, and braked wheels).

(1) total component of the longitudinal tangential stress τ_m due to the driving torque; (2) component τ_m due to the braking torque; (3) distribution of longitudinal tangential stress along the contact length of a driving wheel; (4) ditto, for t_0 of a free wheel; (5) ditto for a braked wheel.

There is a certain amount of adhesion over the area of contact, and because the tire possesses tangential elasticity the torque will compress the tread elements in the zone immediately before contact (denoted by the sign $-$) and at the same time will stretch those elements in the area just after contact has been released (denoted by the sign $+$). Thus, an initially compressed element, Δx , of the tread, is released from this compression as it passes through the contact area, reverting to its normal state Δx_1 , then it undergoes stretching and emerges from contact in a stretched state Δx_2 .

Since the elements, as they pass into the contact area, are in direct contact with the road, any change in their dimensions is prevented by the force with which each element grips the road surface, and tangential stresses τ_k arise in the plane of contact. As a first approximation it is assumed that the stress τ_k changes linearly along the length of the contact zone, at the center of contact $\tau_k = 0$ (see fig. 5.53). Thus tangential stress τ_m , which is the sum of τ_k and τ_c is also linear and is represented by straight line 1 in figure 5.53.

When the wheel is braked the situation is reversed, i.e., immediately before contact the tread elements are stretched, and they contract at the point at which contact is released. In this case it is line 2 (fig. 5.53) which represents the tangential stress τ_m .

Thus, the magnitude and direction of the longitudinal tangential stresses, τ , acting in the plane of contact of a driving or braked wheel are determined by the sum of the stresses created in the rolling of a free wheel, τ_0 , and the additional stresses τ_m created by the application of a torque. The lines representing the resultant tangential stresses along the length of the contact zone of a driving or braked wheel are shown at the bottom of figure 5.53. The precise way in which these stresses are distributed over the contact area depends on the design of the tire, the radial load, the internal air pressure, and the adhesion to the road. These tangential stresses can cause local slipping of the tread elements on the road. It is clear that radial, bias and other tire constructions would exhibit different detailed shear stress distributions, even for the same tractive force.

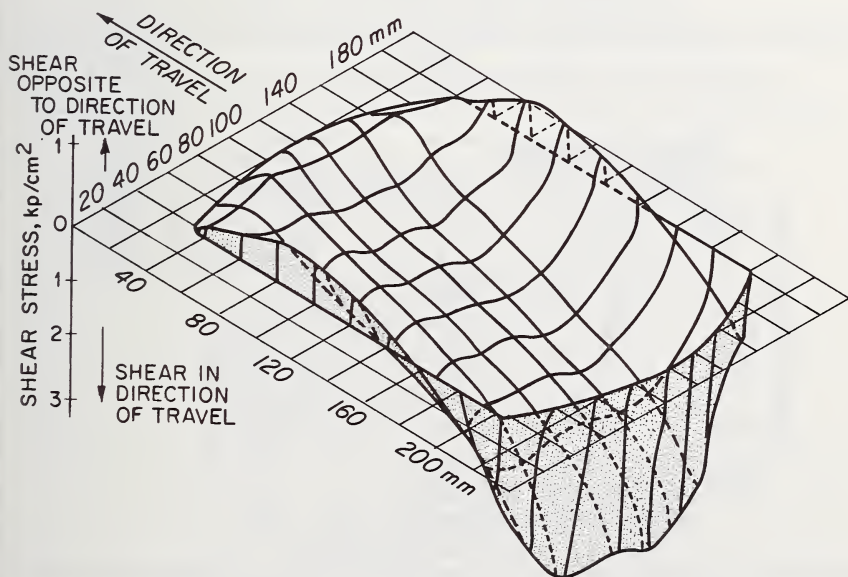


FIGURE 5.54. Distribution of shear stress in the running direction of a smooth, braked tire.

Extensive experimental work on the longitudinal component of the contact shear stress has recently been published by Bode [23]. Here, an effort is made to assess the role of traction and braking in forming the longitudinal component of tangential contact stress. Figure 5.54 shows a three-dimensional plot of such a stress component over the entire contact area, while figures 5.55 and 5.56 from Bode show that the influence of either braking or tractive forces is to throw the major part of the longitudinal component of tangential stress to the rear of the contact patch, as one might anticipate. The direction of this component of the tangential stress is dependent on the presence of tractive or braking forces. Even

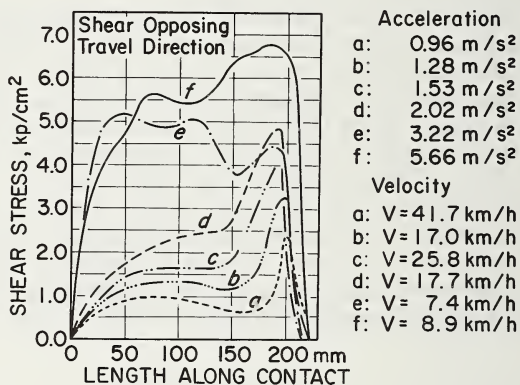


FIGURE 5.55. Distribution of shear in the running direction of a smooth tire under tractive force.

Static load 1590 Kp., inflation 6.5 atm.

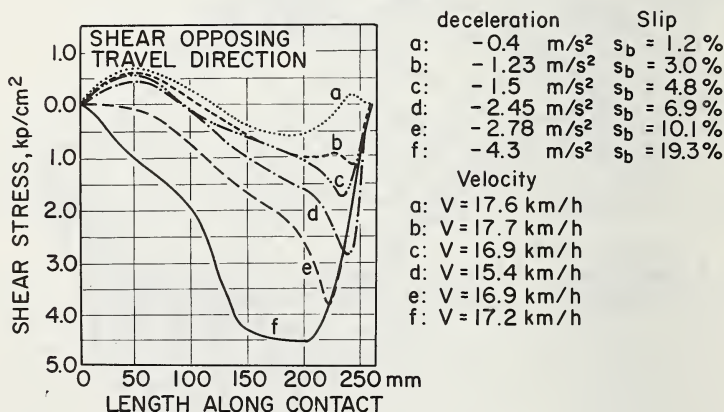


FIGURE 5.56. Distribution of shear in the running direction of a smooth tire under braking force.

Static load 2610 Kp., inflation 6.5 atm.

moderate values of such forces are sufficient to completely change the distribution of tangential stress, again as might be expected.

It is possible to separate out the effects of traction on shear from the normal tire deformation effects on shear. This is done in figure 5.57, where the heavy lines show the net shear distribution taken in the longitudinal direction down the length of the contact patch, and caused directly by the tractive effort. This is obtained by subtraction from the data of figure 5.55, while a similar construction can be performed for the effects of braking on shear. This is shown in figure 5.58, again taken from Bode. From this it is seen that the effects of traction and braking are essentially mirror images of one another insofar as they influence the

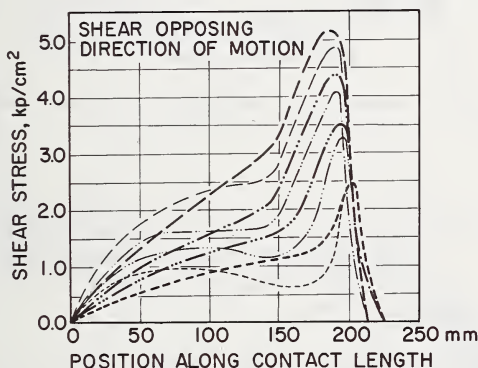


FIGURE 5.57. *Distribution of shear along the length in running direction.*

Super-position of shear due to deformation and acceleration. Heavy lines are shear stresses due to acceleration alone.

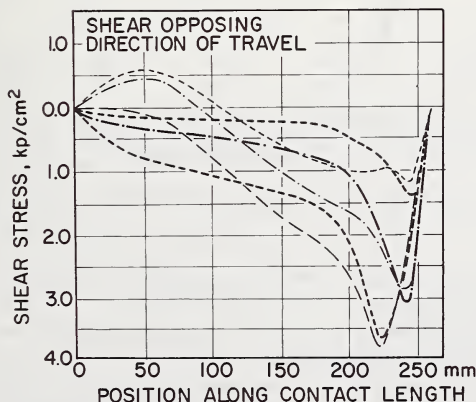


FIGURE 5.58. *Distribution of shear along the length in running direction.*

Super-position of shear due to deformation and braking, from figure 5.56. Heavy lines are due to braking alone.

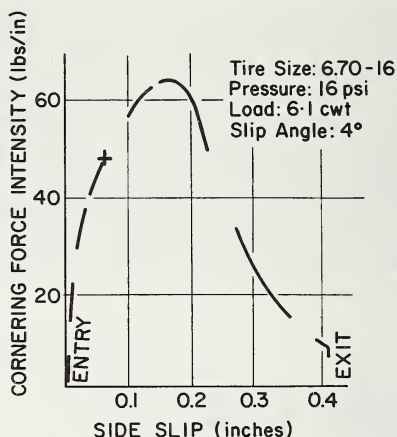


FIGURE 5.59. Cornering force intensity vs. tread lateral distortion.

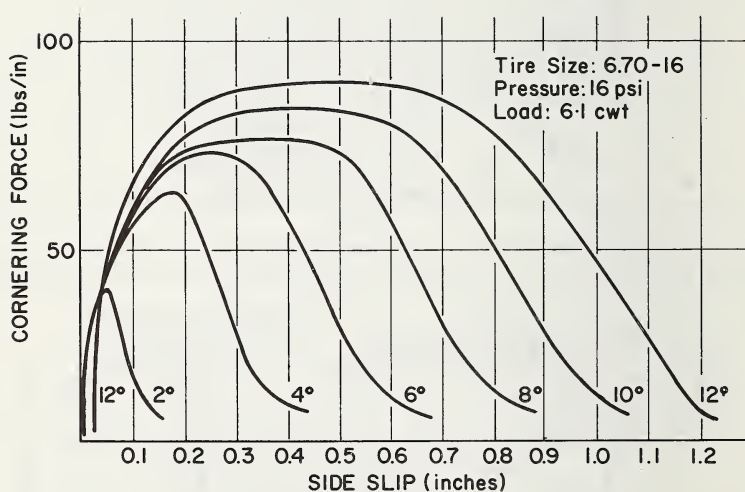


FIGURE 5.60. Cornering force intensity vs. tread lateral distortion at slip angles up to 12°.

magnitude and distribution of the longitudinal component of tangential force in the contact area.

The experimental data given by Bode agrees with the measurements of Novopol'skii and Nepomnyashchii.

The lateral component of the tangential stress, at right angles to the direction of tire travel, has been extensively investigated by Gough [34], [35] and by Cooper [36] for the case of yawed rolling, where the lateral tangential forces are much larger than exist for straight-line rolling. In

the case of yawed rolling, one may think of the tangential stress distribution as first associated with forcing the elastic nondevelopable pneumatic tire against a flat roadway, followed by the addition of effects due either to yawed rolling, braking or acceleration. Viewed in this way, one might postulate that the yawed rolling, braking or acceleration effects are clearly dominant. Figure 5.59, taken from Cooper, shows the distribution of cornering force intensity as a function of tread lateral distortion at the center of a yawed tire. Cornering force intensity is obtained by integrating the lateral component of tangential stress across the width of the

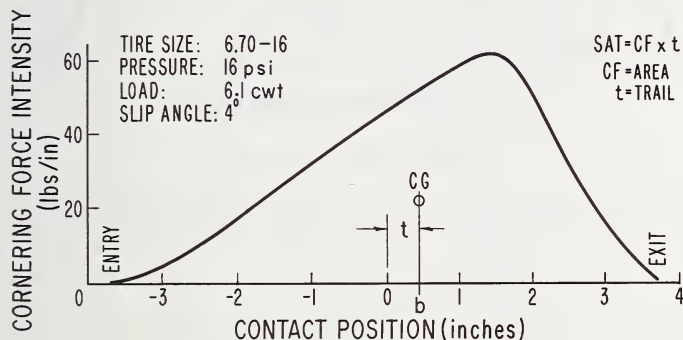


FIGURE 5.61. Cornering force intensity along the contact spot.

tire contact patch. A more complete set of such curves is shown in figure 5.60 from the same source. Figure 5.61 shows the cornering force intensity plotted against position in the contact patch, giving a much clearer picture of the asymmetric nature of this force component due to yawing. In figure 5.61, the centroid of the area under the cornering force intensity curve lies behind the geometric center of the contact area, here denoted by 0, which gives the self-aligning torque to the tire. The distance t in figure 5.61 is called the pneumatic trail. A more complete set of curves of cornering force intensity as a function of position in the contact patch are given for various yaw angles in figure 5.62. Finally, the results of such measurements may be combined into a single plot such as shown in figure 5.63.

Due to the method of making these measurements, it is not possible to determine the exact distribution of the lateral (sideward) component of

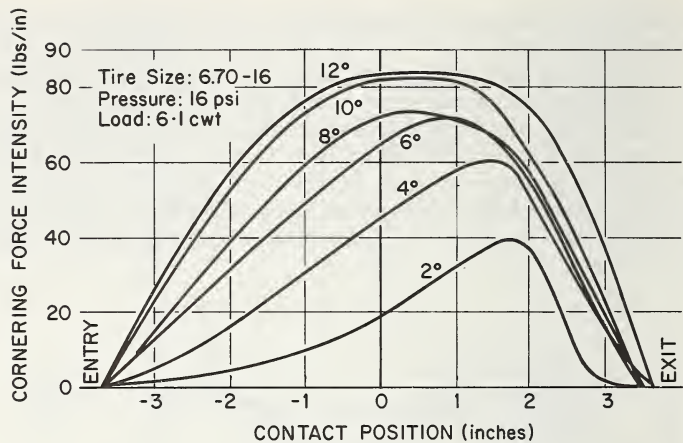


FIGURE 5.62. Cornering force intensity at slip angles up to 12°.

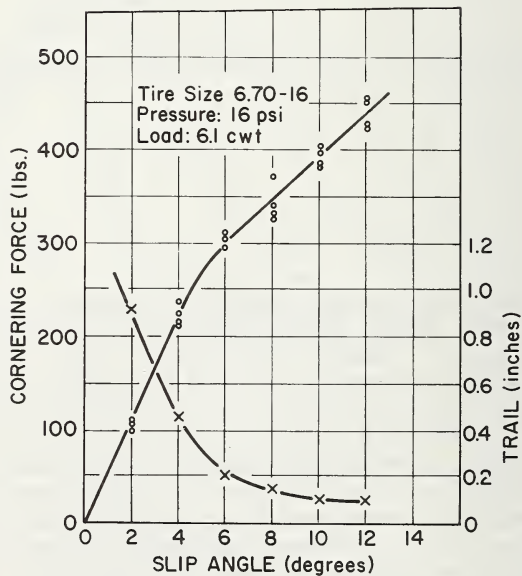


FIGURE 5.63. Cornering force and trail at slip angles up to 12°.

tangential contact stress across the width of the contact area. Only the integrated value is given.

In figure 5.63 it is seen that the pneumatic trail decreases substantially as the steer angle increases. This is related to the shape of the cornering force intensity curve with increasing steer angle, since the

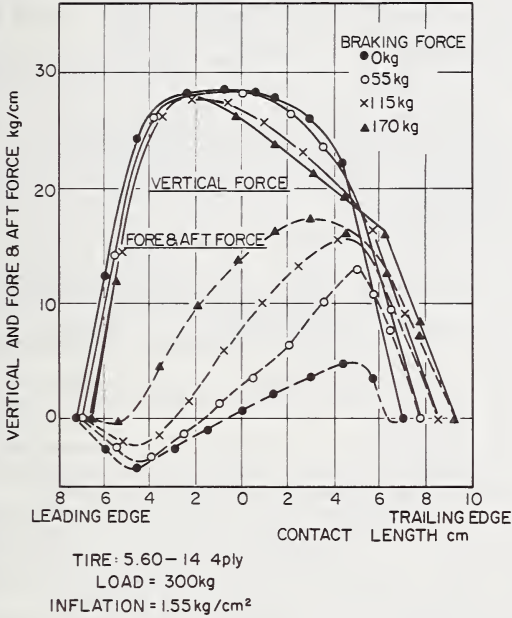


FIGURE 5.64. Vertical force and braking force distributions.

greater slip in the contact patch results in a more symmetric cornering force distribution.

The interaction of vertical pressure distribution with braking and yaw has been studied experimentally by Iritani and Baba [37]. They show that there is little change in vertical pressure due to yaw, but a measurable amount due to braking. This latter effect is shown in figure 5.64.

References

- [1] Hadekel, R., The Mechanical Characteristics of Pneumatic Tyres, S. and T. Memo No. 10/52 (British Ministry of Supply, TPA 3/T1B, 1952).
- [2] Michael, F., Zur Frage der Abmessungen von Luftreifen für Flugzeuglaufräder (The Problem of Tire Sizes for Aircraft Wheels), Jahrbuch 1932 der D.V.L., **3**, p. 17. Available in English translation as NACA TM 689 (1932).
- [3] Dodge, R. N. (Unpublished data).
- [4] Stresses Under Moving Vehicles, Report 4 (U.S. Army Engineer Waterways Experimental Station Technical Report No. 3-545, July 1964).
- [5] Seitz, Norbert, Die Kräfte in der Bodenberührungsfläche schnell rollender Reifen, Fortschritt-Berichte, VDI-Zeitschrift **12** (19), 46 (1968).
- [6] Smiley, R. S., and Horne, W. B., Mechanical Properties of Pneumatic Tires with Special Reference to Modern Aircraft Tires, NACA Technical Note 4110 (Jan. 1958).
- [7] Whittemore, H. L., and Petrenko, S. N., Friction and Carrying Capacity of Ball and Roller Bearings, Nat. Bur. Stand. (U.S.), Tech. Note 201 (1921).
- [8] Böhm, F., Mechanik des Gürtelreifens, Ingenieur-Archiv **25**, 82 (1966).
- [9] Fiala, E., and Willumeit, H.-P., Radiale Schwingungen von Gürtel-Radialreifen, A. T. Z. **68** (2), 33 (Feb. 1966).
- [10] Clark, S. K., The rolling tire under load, SAE Paper No. 650493 (SAE Midyear Meeting, Chicago, Ill., May 17-21, 1965).
- [11] Dodge, R. N., Prediction of pneumatic tire characteristics from a cylindrical shell model, Report 02957-25-T, (Office of Research Administration, The University of Michigan, Ann Arbor, Mich., March 1966).
- [12] Saito, Y., A study of dynamic steering properties of pneumatic tires, Proc. 10th FISITA Congress, Tokyo, 1964.
- [13] Novopol'skii, V. I., and Nepomnyashchii, E. F., The interaction of a motor vehicle tyre tread with the road surface. Abrasion of Rubber, D. I. James, ed., (Palmerton Publishing Co., New York).
- [14] Biderman, V. L., Volodina, T. N., and Pugin, V. A., Determining the relationship between the deformation of a tyre carcass and the displacement of the carcass relative to the road, Sov. Rubber Tech. **25** (7), 37 (July 1966).
- [15] Novopol'skii, V. I., and Tret'yakov, O. B., Slip of the elements of the tread pattern in the contact area of tires, Sov. Rubber Tech. **22** (11), 25 (Nov. 1963).
- [16] Horne, W. B., Yager, T. J., and Taylor, G. R., Recent research on ways to improve tire traction on water, slush, or ice. Paper presented at AIAA Aircraft Design and Technology Meeting, Los Angeles, Calif., Nov. 15-18, 1965.
- [17] Kelley, J. D., and Allbert, B. J., Tread design of tire affects wet traction most, SAE Journal **76** (9), 58 (Sept. 1968).
- [18] Robbins, D. H., The contact of certain elastic shells with rigid flat surfaces, Report 05608-7-T, (Office of Research Administration, The University of Michigan, Ann Arbor, Mich., Sept. 1965).
- [19] Akasaka, T., On the bending of a tire, Series B-9, Report No. 19, Chuo University, Tokyo, Japan.
- [20] Hertz, H. J., reine angew. Math. **92**, 156 (1886). See also Timoshenko, S. P., and Goodier, J. N., Theory of Elasticity (McGraw-Hill Book Co., New York, 1956).
- [21] Kraft, P., Force distribution in the contact surface between tire and runway, NACA TM 1365 (Aug. 1954).
- [22] Markwick, A. H. D., and Starks, H. J. H., Stresses between tire and road, J. Inst. Civil Engineers **16**, 309 (1941).
- [23] Bode, G., Kräfte und Bewegungen unter rollenden Lastwagenreifen, A. T. Z. **64** (10), 300-306 (1962).
- [24] Green, A. J., Normal stresses at the tire-soil interface in yielding soils (U.S. Army Waterways Experiment Station Report, Vicksburg, Miss.).
- [25] Freitag, D. R., and Green, A. J., Distribution of stresses on an unyielding surface beneath a pneumatic tire (U.S. Army Waterways Experiment Station Report, Vicksburg, Miss.).
- [26] Hofelt, C., Factors that influence skid resistance, Part V: Effect of speed, load distribution, and inflation, Proc. First International Skid Prevention Conference, Charlottesville, Va., Aug. 1959.

- [27] Frank, F., and Hofferberth, W., Mechanics of the pneumatic tire, *Rubber Chem. Tech.* **40** (1), 271 (Feb. 1967).
- [28] Martin, F., Theoretische Untersuchungen zur Frage des Spannungszustandes in Luftreifen bei Abplattung, *Jahrbuch der deutschen Luftfahrtforschung*, Teil I, 470 (1939).
- [29] Vlassov, V. Z., *Izvest. Akad. Tekh. Nauk*, No. 6, 819 (1949).
- [30] Böhm, F., *Zur Mechanik des Luftreifens*, Habilitationsschrift th., Stuttgart, 1965.
- [31] Zakaharov, S. P., and Novopol'skii, Distribution of specific pressure of a tire on the road at high velocities (in Russian), *Trudy Nauchno-Issledovatel'skogo Instituta Shinnoi Pronyschlennosti*, Sbornik 3, *Methody Rascheta i Ispytaniya Avtomobil'nykh Shin*: U.S.S.R. Nauchno, Moscow: 1957, p. 139-53; *Rubber Abs.* **36**, 439 (Sept. 1958).
- [32] Essenburg, F., and Gulati, S. T., On the contact of two axisymmetric plates, *J. Appl. Mech.* **33** (2), 341 (June 1966).
- [33] Vermeulen, P. J., and Johnson, K. L., Contact of nonspherical elastic bodies transmitting tangential forces, *J. Appl. Mech.* **31** (2), 338 (June 1964).
- [34] Gough, V. E., Tyre to ground contact stresses, *Wear* **2**, 107 (1958/59).
- [35] Gough, V. E., Practical tyre research, *SAE Trans.* **64**, 310 (1956).
- [36] Cooper, D. H., Distribution of side force and side slip in the contact area of the pneumatic tire, *Kautschuk und Gummi* **11** (10), WT 273-277 (Oct. 1958).
- [37] Clark, S. K., Untersuchung der Verteilung des Auflagerdruckes in Luftreifen (An analysis of contact pressure distributions for pneumatic tires), *Kautschuk und Gummi Kunststoffe* **8**, 433 (1969).
- [38] Iritani, S., and Baba, T., Forces on the contact patch of the tyre, Paper No. 3.1, Tenth International FISITA Congress, Tokyo, Japan, 1964.
- [39] Mindlin, R. D., *Mechanics of Granular Media*, Proc. Second U.S. Nat. Cong. Appl. Mech. (1954). Published by A.S.M.E., New York.



CHAPTER 6

Skid Resistance and Directional Control

A. Schallamach ¹

	Page
6.1. Introduction.....	502
6.2. Theory.....	502
6.3. Cornering and side force.....	508
6.4. Braking and circumferential slip.....	515
6.5. The speed dependence of rubber friction.....	518
6.6. Hydrodynamic effects on wet roads.....	520
6.7. The velocity dependence of the braking coefficient on wet roads.....	523
6.8. The effect of tread pattern and carcass construction on tire friction.....	526
6.9. Tread compound effects on wet friction.....	531
6.10. Aquaplaning (hydroplaning).....	534
6.11. Winter tires.....	539
References.....	544

¹ The Natural Rubber Producers' Research Association, Welwyn Garden City, Hertfordshire, England.

6.1. Introduction

Speed and direction of a self-propelled vehicle are primarily controlled by the forces between tires and road. These forces have an upper limit set by the available coefficient of friction; once the ratio between horizontal traction and normal pressure exceeds this limit anywhere in the contact area, local sliding occurs. It is important to remember that sliding friction has no preferred direction; effective control is therefore lost when sliding extends over the whole contact area. This happens, for example, when the wheels are locked; then the mass center of the vehicle slides to a stop in the direction in which it was last traveling when the wheels were locked. It would appear at first sight that such a contingency arises whenever the circumferential velocity of the wheels relative to the vehicle differs in direction or magnitude from the traveling velocity, because the whole contact area should be expected to slide under these circumstances. This reasoning is, however, valid only for the extreme case of an infinitely stiff wheel rolling on an infinitely stiff track. Possibly the most valuable property of an elastic wheel like the pneumatic tire is that it can travel at an angle to its plane and/or with a velocity differing from its circumferential velocity without involving the whole contact area in sliding motion.

Another Chapter [1]² describes how horizontal forces acting on the wheel axle produce tractions and consequent strains in and near the contact area. These strains lead to differences between traveling and circumferential velocities, but can at the same time ensure adhesion between tire and road over at least part of the contact area (normally the front part) and thus allow control to be maintained.

6.2. Theory

In order to facilitate further discussion, the relevant facts on the connection between the forces applied to a wheel and changes in its velocity shall be briefly reviewed, and equations derived which allow a semiquantitative assessment of the functional relations. Aerodynamic forces and rolling resistance will be neglected.

The treatment is made easier by introducing the concept of slip, s , which is a vectorial kinematic quantity defined by eq (6.1)

$$s = (\mathbf{v} - \mathbf{V})/|\mathbf{v}| \quad (6.1)$$

where \mathbf{v} is the velocity of the road relative to the wheel axle, and \mathbf{V} is the circumferential velocity of the wheel in the plane of the contact area,

² Figures in brackets indicate the literature references at the end of this chapter.

also measured relative to the axle of the wheel. When the wheel rolls in a direction making the angle θ with its plane (side slip),

$$s = \sin \theta. \quad (6.2)$$

Pure circumferential slip is given by eq (6.3)

$$s = 1 - V/v. \quad (6.3)$$

When braking ($v > V$), s is positive with the maximum value of unity for a locked wheel. During acceleration ($v < V$), s is negative and becomes negative infinity when the stationary wheel spins. Circumferential slip has a simple physical meaning. During braking, kinetic energy is consumed in brakes, tires and road; even when the road is not appreciably deformed, it takes up a great part of the braking energy as heat. The slip s is the proportion of energy lost in tire and road and clearly cannot exceed 100 percent.³ Similarly, part of the engine power is lost in the tires during acceleration; s is the ratio between losses in the tires and road, and gain in kinetic energy of the vehicle. Hence its negative sign and its infinite upper limit.

The strains set up in the contact area of a slipping wheel are illustrated by the model experiment of figure 6.1 which shows the contact area of a small, solid wheel on a transparent track. All cases have in common that a circumferential element of the wheel on entering the contact area adheres to the track at first. As the element moves further into the contact area, the imposed slip produces a deflection which increases linearly with increasing distance from the front edge. This is most clearly seen for side slip, figure 6.1b, where the deflection is normal to the plane of the wheel and increases at a rate equal to $\tan \theta$. The accompanying surface stress increases in the same sense until the local value of limiting frictional stress is reached and the element begins to slide back toward its undeformed position.

A braking force, figure 6.1c, lengthens an element in the circumferential direction before entering the contact area, and the element adheres at first to the track in this state of strain; the deflection of the wheel increases linearly with increasing distance from the front edge at the rate $(v - V)/V = s/(1 - s)$. As with side slip, sliding starts (towards the front of the contact) when the ensuing stresses reach the local frictional stress limit. A driving torque, figure 6.1d, produces contraction of an element before entering the contact region; traction and deflections have the opposite sign to those for a braked wheel, and an element finally slides out of the contact area.

An exact calculation of the forces on a slipping wheel presents considerable difficulties for tires because of their complex structure, but useful expressions can be derived for a simple model which replaces the tire by a toothed wheel, it being assumed that the teeth can deform inde-

³ Positive slips greater than 100 percent can, in principle, be achieved by making the rotation of the wheel oppose the direction of motion.

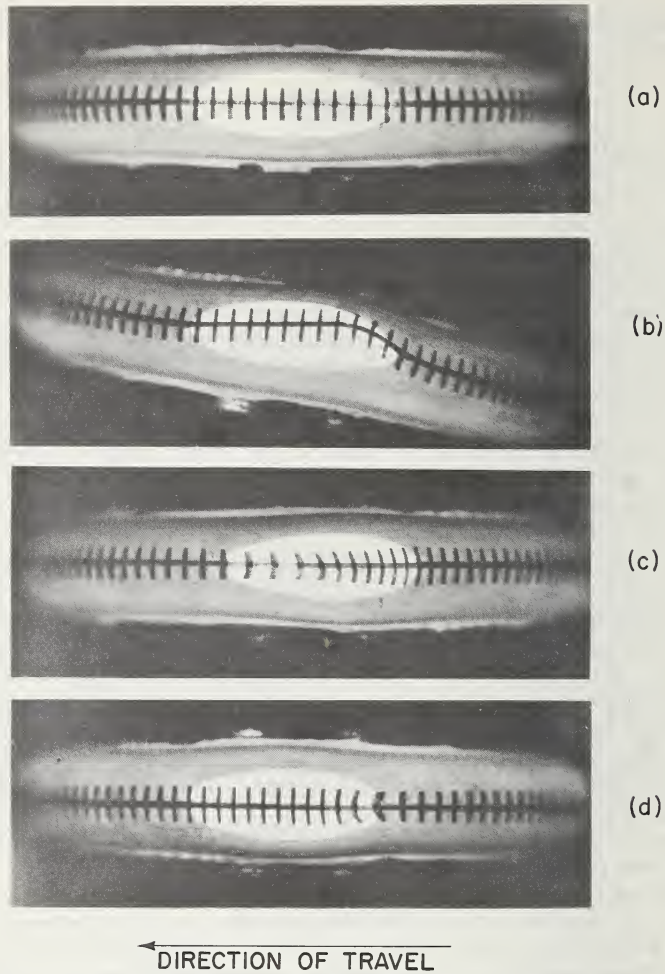


FIGURE 6.1. *Model experiment to illustrate the conditions in the contact area of slipping wheels.*

(a) Free rolling; (b) side slip (crab walk); (c) braking; (d) accelerating. Traveling direction from right to left. From Schallamach, ref. [2].

pendently of each other and obey Hooke's law in their stress-strain relationships [3]. The coefficient of friction must enter the calculations. The discussion in chapter 1.2 [4] has emphasized the dependence of rubber friction on load, temperature and sliding speed, all of which vary in the different parts of the contact. A constant coefficient of friction can nevertheless be assumed in a first theoretical attempt without grossly violating physical reality; some justification for this approximation will be given later in this chapter.

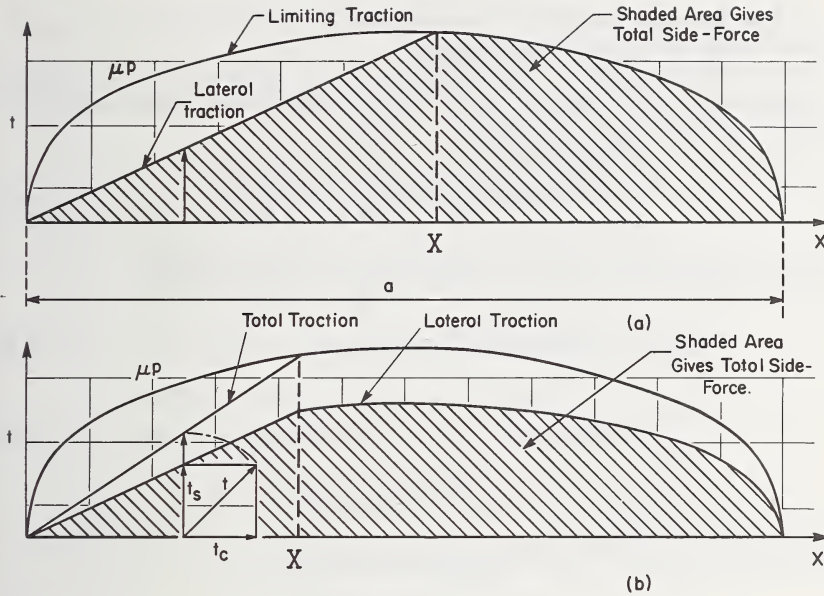


FIGURE 6.2. (a) Horizontal traction in the contact area of a wheel with side slip; (b) traction resulting from simultaneous side and circumferential slips.

μp is the limiting friction; the shaded area gives the side force in both cases.

The tangential force t_s per unit length of contact developed when the model rolls with side slip is shown in figure 6.2a. Because of the postulated validity of Hooke's law, the traction increases initially at a rate proportional to the stiffness k_s of the wheel,

$$t_s = k_s x \tan \theta \quad (6.4)$$

where x is the coordinate of the surface element relative to the undistorted wheel. The limiting tangential traction μp is indicated by the semi-oval curve; μ is the coefficient of friction and p , the assumed normal force distribution per unit of length. When $t_s = \mu p$ at the point $x = X$, sliding begins, and t_s in the rest of the contact is given by

$$t_s = \mu p \quad (6.5)$$

The shaded area represents the sideforce due to the slip $\sin \theta$.

A diagram similar to figure 6.2a would depict the force distribution t_c due to circumferential slip, with eq (6.4) being replaced by eq (6.6)

$$t_c = k_c x s / (1 - s). \quad (6.6)$$

The stiffness k_c is considerably greater than k_s .

Sideforce S , braking force B and driving force A are therefore formally given by the same type of expression.

If the normal pressure distribution is taken to be elliptical along the contact area, and constant across it, the calculation yields eq (6.7) in which F stands for S , B or A :

$$F = (\mu L / \pi) \left(\sin^{-1} \frac{2c}{1+c^2} + \frac{2c}{1+c^2} \right) \quad (6.7)$$

L is the normal load, and c is defined by eqs (6.8) and (6.9):

$$c = \frac{\pi}{8} (k_s a^2 / \mu L) \tan \theta \quad \text{for side slip,} \quad (6.8)$$

$$c = \frac{\pi}{8} (k_c a^2 / \mu L) s / (1-s) \quad \text{for circumferential slip,} \quad (6.9)$$

a = length of the contact.

It is easily seen that eq (6.7) reduces at low slip to

$$S_{\text{small slip}} = \frac{1}{2} k_s a^2 \theta, \quad (6.10)$$

$$B_{\text{small slip}} = A_{\text{small slip}} = \frac{1}{2} k_c a^2 s. \quad (6.11)$$

The coefficient of friction has disappeared from (6.10) and (6.11) because the contribution from the sliding region in the contact area becomes negligible and only the wheel stiffness matters. The linear relation between force and slip reflects Hooke's law. At large slip and/or a low coefficient of friction F tends asymptotically to the value μL .

Figure 6.3 shows the theoretical dependence of $F/\mu L$ on c . It is instructive to compare the two components making up the force F , i.e., the contributions from the adhesion and sliding regions which have also been plotted in figure 6.3, based on the elliptical normal pressure distribution used to generate eq (6.7). The adhesion component, which dominates F at low values of c , reaches a maximum at $c = 1/\sqrt{3}$, and is outweighed by the sliding component when c exceeds about 0.82. What must be borne in mind is that the great contribution made to F by the sliding region of the contact at large values of c is directionally controlled only by the remaining adhesion in the front part of the contact patch, because of the already mentioned direction-insensitive nature of sliding friction.

Tires have at times to sustain lateral and longitudinal slip simultaneously, and the forces resulting from such a condition differ from those for one kind of slip only. Figure 6.2b illustrates the reason for this effect by showing the influence of circumferential slip on the side force. Circumferential tractions t_c act then jointly with side tractions t_s in the contact area, giving the total force per unit length t in the form

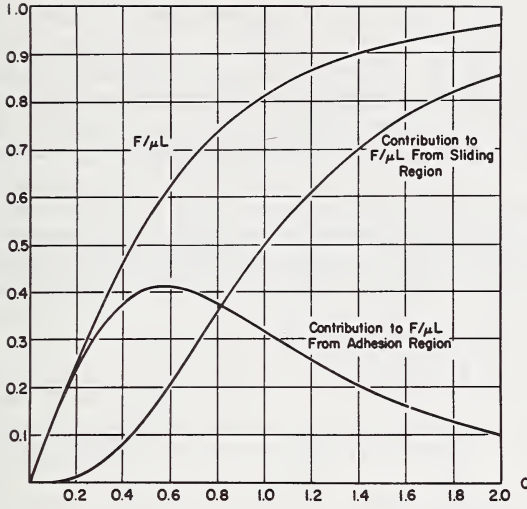


FIGURE 6.3. Force F on a slipping wheel as function of the variable c according to eq (6.7), and its two components.

$$t = (t_s^2 + t_c^2)^{1/2} \quad (6.12)$$

and sliding sets in when this combined force equals μp . The point X is therefore shifted forward as compared with the case of only one of these tractions acting. Furthermore, the frictional force in the sliding region is now taken up by both the lateral and longitudinal stiffness of the tire so that only part of the sliding friction is available for the side force. The shaded area giving the side force is much smaller than the corresponding area in figure 6.2a for side slip only. These considerations apply to braking and driving forces which reduce the side force equally. Theory gives the following equation for the side force S as function of simultaneous side slip $\sin \theta$ and circumferential slip s :

$$S = \frac{\mu L}{\pi} \frac{k_s \sin \theta}{(k_s^2 \sin^2 \theta + k_c^2 s^2)^{1/2}} \left[\sin^{-1} \frac{2c}{1+c^2} + \frac{2c}{1+c^2} \right] \quad (6.13)$$

where

$$s = \cos \theta - V/v$$

and

$$c = \frac{\pi}{8} \frac{(k_s^2 \sin^2 \theta + k_c^2 s^2)^{1/2}}{\cos \theta - s} \left(\frac{a^2}{\mu L} \right)$$

The ratio between side force and either braking or accelerating force is

$$S/B = S/A = (k_s \sin \theta)/(k_c s) \quad (6.14)$$

The relevance of these considerations to the control of a vehicle is to be discussed now.

6.3. Cornering and Side Force

The sketch in figure 6.4 shows a highly idealized vehicle with equal front and rear weight distribution traversing a circular curve. It has been assumed when drawing this picture that the car is conventionally rear-driven, and that its mass center coincides with the geometrical center.

The vehicle has to counter the centrifugal force, marked as the vector C , with its components C_n and C_p . To balance the centrifugal force, the wheels have to make the slip angles θ_f and θ_r with the instantaneous velocity v in order to develop the side forces S_r and S_f at right angles to their

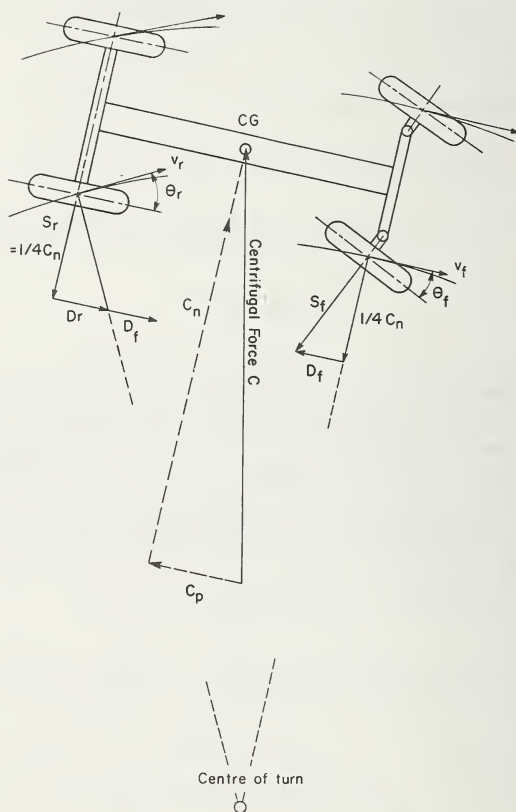


FIGURE 6.4. *Equilibrium of forces on a rear-driven vehicle describing a circular curve in the stationary state.*⁴

Rolling resistance, wind resistance, weight transfer and self-aligning torque have been neglected.

⁴ Continental spellings of such words as centre, tyre, behaviour, etc. have been changed in the text and figure captions to the Americanized forms. It was not feasible, however, to change them within the figures themselves, where they have been left as originally submitted.

planes. The sum of these cannot by itself equilibrate C ; an additional force has to be supplied in the direction of the chassis in order to offset the drag forces D_f and D_r of the slipping tires. This force is the source of the energy loss incurred when negotiating the bend and is, incidentally, a measure of the wear accompanying cornering. It is, of course, delivered by the engine. The front wheels, being free to rotate, cannot take up a circumferential force, and their contact area has only to cope with the side force. The driving force D for both front and rear wheels has therefore to be produced by the rear wheels, bringing about circumferential slip in addition to side slip. If front and rear wheels carry the same load and are inflated to the same pressure, the rear wheels need then a larger slip angle than the front wheels to produce a given side force, for reasons discussed at the end of the preceding section. When specifying different inflation pressures for front and rear tires, the car manufacturer may take this effect into account and also consider the weight distribution. In any case, the cornering maneuver is governed by the relation between side force and slip angle, and by the influence of circumferential slip on this relation.

The full lines in figure 6.5a give experimental data on the slip angle dependence of the side force under various road conditions and clearly demonstrate the effect of the coefficient of friction on magnitude and de-

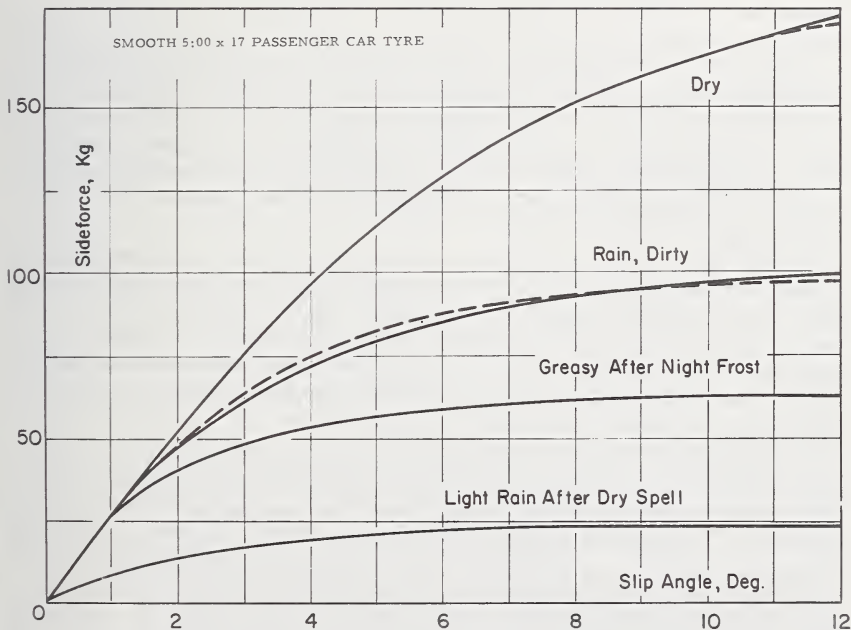


FIGURE 6.5a. Full lines, slip dependence of the side force of a smooth 5.00-17 tire on asphalt under different weather conditions; load, 307 kg.

The dotted lines are theoretical curves. From Förster, ref. [5].

tailed shape of the side force curves. Figure 6.5a refers to a smooth tire, and the influence of moisture on the road is greater here than for patterned tires but this does not detract from the general validity of the observed changes.

The upper three curves have the same initial slope, and the side force at small slip is independent of the condition of the road. This is the region where the lateral stiffness of the tire dominates the side force. The lowest curve in figure 6.5a appears to be an exception to this rule, but its initial slope is difficult to determine from the published figure. This curve is of interest, though, because it shows the extremely low friction coefficient (about 0.075) possible on a wet road after dryness and is often experienced in practice as a driving hazard. The most probable reason for this effect is the formation of a thin layer of viscous mud on the road which leads to hydrodynamic effects dealt with in a later section.

All curves are similar to the theoretical F vs. c curve in figure 6.3; the measure of quantitative agreement is shown by the dotted curves in figure 6.5a which have been calculated by means of eq (6.7). This required a knowledge of the quantity $k_s a^2$ appearing in the expression for c , eq (6.8). As this chapter is not concerned with the derivation of tire parameters from tire construction, the various factors in eqs (6.7) and (6.8) were obtained by superimposing a doubly-logarithmic plot of the experimental curve on a corresponding plot of the theoretical curve. The horizontal displacement to effect coincidence gives $(\pi/8)k_s a^2/\mu L$, and the vertical displacement gives μL so that all factors, including $k_s a^2$ are found. The resulting theoretical side force curve for the dry road is practically indistinguishable from the experimental curve at slip angles up to 10° . The second theoretical curve in figure 6.5a (rain, dirty) was calculated with the same value of $k_s a^2$, and a coefficient of friction giving best overall fit. The semiquantitative agreement between theory and experiment shown in figure 6.5a indicates that the theory can form the basis for further reasoning.

Beyond the region of small slip in which the side force is determined by the stiffness of the tire, the curves break away from the initially linear side force vs. slip relation and approach their limiting values at slip angles which become progressively smaller as friction decreases. Apart from the obvious restriction on speed and turning radius imposed by low friction, operating at side forces near the limit μL can become difficult, because of the following reason.

The diagram in figure 6.4 of the forces balanced by the tires of a cornering vehicle shows that the normal component of the centrifugal force acting on a front wheel, $\frac{1}{4}C_n$, must equal the component $S_f \cos \theta_f$ of the side force. As the two factors of this product vary with θ_f in opposite senses, its value has a maximum at a certain critical slip angle θ_c . The conditions are best visualized by a polar plot of side force vs slip angle, figure 6.5b; the ordinate gives immediately $S \cos \theta$. The two curves in figure 6.5b have been drawn for a tire with a stiffness $k_s a^2/L$ of 11.32 and coefficients of friction of 0.91 and 0.25. The angle θ_c for maximum $(S/L) \cos \theta$ can be calculated from the theoretical expression for the

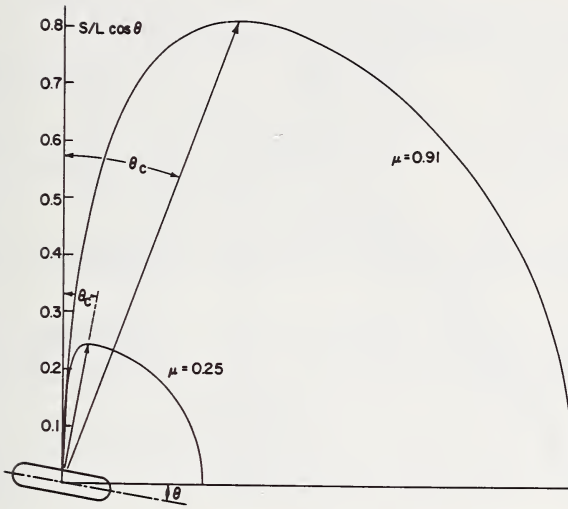


FIGURE 6.5b. Polar diagram of side force vs. slip angle for a passenger car tire.

At large slip angles, the curves are circles centered in the origin.

side force given by eq (6.7), and is found to be about 21° for $\mu = 0.91$, but only about 10° for $\mu = 0.25$ and 7.5° for $\mu = 0.15$.

The practical aspect of these findings is not only that the effective cornering force $S \cos \theta$ becomes independent of slip near the critical slip angle θ_c but that at angles exceeding θ_c the turning radius at constant velocity *increases* with increasing slip angle. This reversal in the usual response of turning radius to changes in slip angle is likely to occur on slippery or icy roads and, of course, severely impairs handling of the vehicle.

The complications which arise from braking in a curve come from the reduction in side force by longitudinal slip, as explained in figure 6.2b. Figure 6.6 gives experimental examples of this effect; more comprehensive data for cross ply and radial tires on various wet surfaces have recently been given by Holmes and Stone [47]. Apart from lowering the limiting side force, braking forces bring forward the departure from the initial linear dependence of side force on slip to smaller slip angles. Equations (6.13) and (6.14), though agreeing qualitatively with these findings, predict smaller effects than found experimentally. The probably reason is that theory assumed mutual independent of stresses due to simultaneous lateral and longitudinal slip.

The consequences of braking in a curve are shown schematically in figure 6.7. The left hand side shows a tire moving along the circular curve of radius R under equilibrium conditions, the centrifugal force C and driving force D being balanced by the side force S . A braking force B (right hand side of fig. 6.7) reduces the side force at the existing slip angle to S' . The resultant of B and S' has a smaller radial component

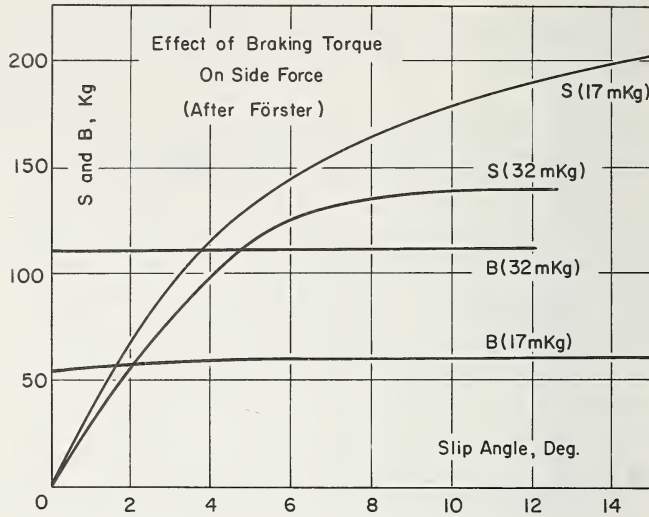


FIGURE 6.6. Effect of braking torques (given in brackets) on the side force of a 4.75-17 tire at 30 km/hr. on dry asphalt; load 305 kg.

From Förster, ref. [5].

than the original force S . Only the centrifugal force C' can be balanced, and the radius of the turn is increased to R' .

A subject closely connected with side force characteristics of tires is oversteer and understeer. Figure 6.8 shows diagrammatically a car travelling straight in the direction v and suddenly hit by a disturbing force F normal to v . The response of the vehicle to this force is shown for the case that the rear wheels have a lower side force coefficient and hence drift off at a greater slip angle than the front wheels; after a short instant, the vehicle moves from position 1 into position 2. It is immediately seen that it moves on an arc with the center of curvature on the right hand side of the drawing. A centrifugal force is thus engendered in the same direction as F and reinforces its effect. A self-deteriorating state is brought about which can make control difficult, particularly at high speeds.

The response of a vehicle to a disturbing force sketched in figure 6.8 is a simple case of oversteer. The SAE (J 670 a) defines oversteer more generally in terms of the change in turning radius on changing the steering angle. The example given here is covered by the SAE definition as limiting case when the turning radius changes without change in steering angle. Understeer is the response of a vehicle to a disturbing force opposite to that in figure 6.8.

Extreme oversteer occurs when the rear wheels are locked and have lost all directional function. If the car happens to make a small angle with the travelling direction, *side force* on front wheels and *frictional force* on rear wheels leave a couple around the mass center which increases the

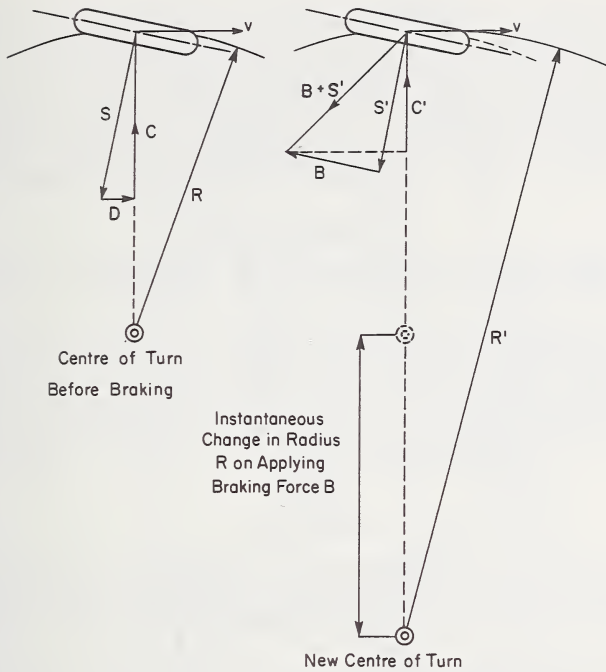


FIGURE 6.7. *Effect of an instantaneously applied braking force on the turning radius of a cornering tire (schematic).*

angle. This unstable state can, with inertia effects, make the car turn front to rear, which is a stable condition. Tires for skid tests are therefore often mounted on the front wheels, and only these are braked.

This discussion of cornering and side force characteristics will be concluded with a short description of a related phenomenon which can affect handling of vehicles at large slip. The resultant of the side force distribution along the tire-road contact area does not pass through its center (compare fig. 6.2a) but is displaced to the rear by a distance called the pneumatic trail. Side force multiplied by pneumatic trail gives a couple tending to reduce the slip angle. This so-called self-aligning torque is felt at the steering wheel as a measure of the cornering effort. The self-aligning torque T for our model wheel is given by eq (6.15)

$$T = \frac{2}{3} \frac{\mu a L}{\pi} \frac{c}{(1 + c^2)^2} \quad (6.15)$$

where c is defined by eq (6.8). Following Gough's suggestion [6], the side force has been plotted in figure 6.9 as function of T , both quantities being expressed in dimensionless form. The graph reproduces the essential features of experimental curves, in particular the maximum of T .

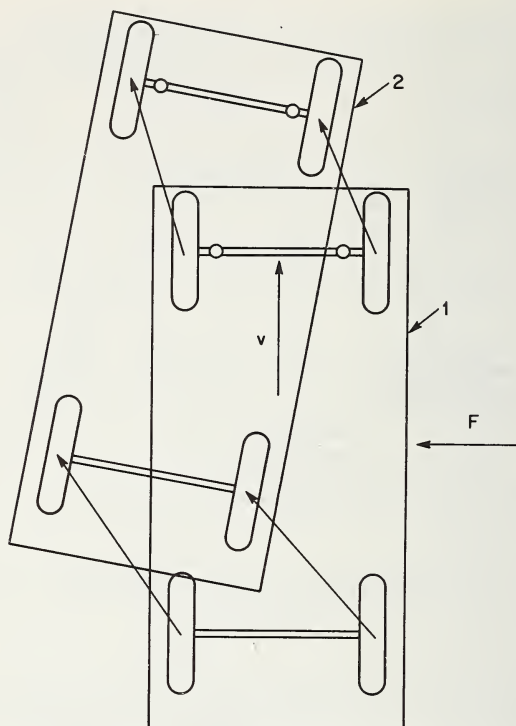


FIGURE 6.8. Response of a vehicle with oversteer characteristics to a disturbing force F .

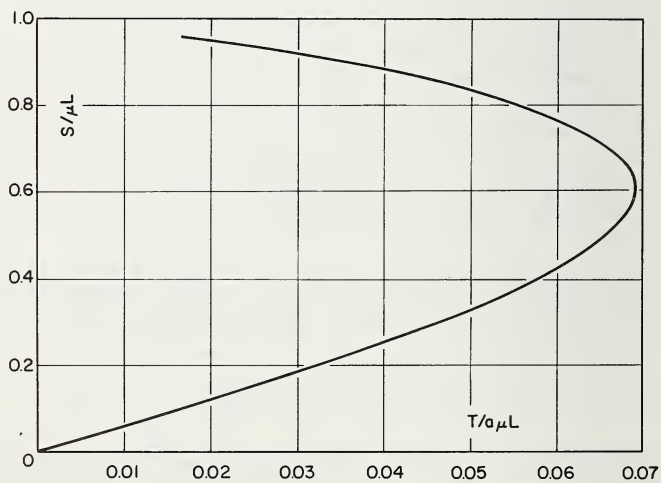


FIGURE 6.9. Theoretical relation between side force and self-aligning torque according to eq (6.15).

The self-aligning torque helps in the handling of the vehicle because the associated restoring couple on the steering wheel feeds back to the experienced driver information on the side force; in particular, the change in self-aligning torque with changing steering angle allows him to judge the approach to limiting conditions [22]. According to experience, the self-aligning torque should be at its maximum when the side force has reached a value of 0.65 to 0.75 μL [25].

6.4. Braking and Circumferential Slip

When a braking force acts on the wheels and slip develops, the vehicle covers a longer distance per unit time than corresponds to its rolling radius and angular velocity; the opposite effect occurs with a driven wheel. The slip is derived from the ratio between the angular velocity of the slipping wheel, ω , and that of an otherwise identical, but freely rolling wheel, ω_0 , thus

$$s = 1 - \omega/\omega_0 \quad (6.16)$$

which expression comes directly from eq (6.3). In contrast to the slip dependence of the side force, the slip dependence of the braking force is, of course, of practical importance up to the maximum value of 100 percent.

Experimental work has been concentrated on braking performance on wet roads because a great proportion of accidents can be attributed to insufficient braking force under such conditions. Figure 6.10 shows typical curves obtained with patterned and smooth tires on two different wet road surfaces. All curves have a maximum at a slip between 10 percent and 20 percent, followed by a gradual decrease of the braking force; a more sudden drop precedes locking of the wheels. Figure 6.10 exhibits two other significant features. A smooth tire has a lower braking force than a patterned tire but the difference vanishes at small slip; the effect of the road surface on the braking force can be great and outweigh differences between patterned and smooth tires but this difference, too, disappears at small slip.

The common initial slope of all four curves in figure 6.10 agrees with elementary theory if it is assumed that the stiffnesses of patterned and smooth tires do not greatly differ; the subsequent shape of the curves does not conform to theory which predicts an asymptotic approach to a maximum. Attempts at fitting theoretical curves to the data for patterned tires are shown in the graph. To do this, the tire stiffness was estimated from the initial slope, which gave $k_c a^2/L = 45$; this value is between four and five times greater than the corresponding parameter for side slip, $k_s a^2/L$. The coefficients of friction were chosen to give best agreement with the experimental curves at moderate slip.

The great difference between the longitudinal and lateral stiffnesses of tires leads to an important quantitative difference between the slip dependence of the braking and side forces. It is easily seen from eqs

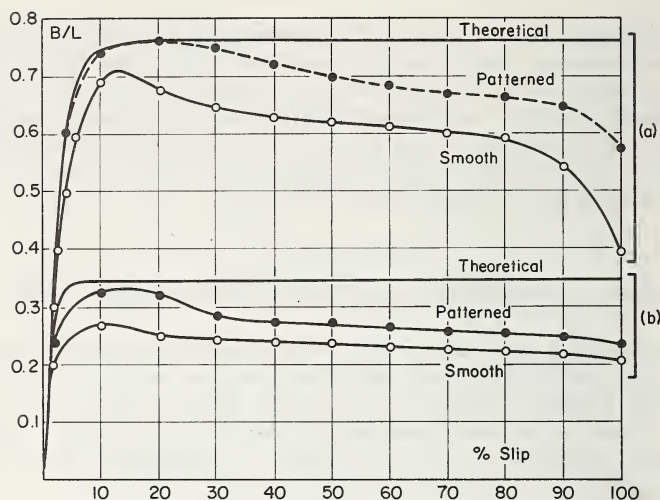


FIGURE 6.10. Slip dependence of the braking force coefficients B/L of 5.00-16 tires on (a) wet fine textured asphalt and (b) on wet polished gravel carpet, from Giles [7], and theoretical curves.

B is braking force, L is normal load.

(6.7) and (6.9), and from a comparison between figures 6.5 and 6.10, that the limit μL of the braking force B is approached at much lower absolute values of the slip than the side force. When braking to a stop, the braking force is therefore almost entirely determined by the available friction between tire and road, and the assumption of a constant coefficient of friction will be shown to become untenable under such conditions. This subject is treated in more detail in the next section but certain conclusions drawn from tire mechanics have a bearing on the problem.

As the braking force increases rapidly with increasing slip, so does the contribution to the total kinetic energy loss made by the tires, which is given by the product Bs and increases initially as the square of B . The consequence of this energy dissipation is, of course, a frictional temperature rise in the contact area; there is no principal difference in this respect between braking and cornering but the energy losses when cornering at a comparable slip $\sin \theta$ are given by $S \sin \theta$ and are considerably smaller because the side force is so much lower than the braking force.

Another difference between braking and cornering is the slip dependence of the time a tire surface element spends in the contact area. When the wheels are locked ($s=100$ percent), the element produces frictional energy continuously and suffers a temperature rise, the stationary value of which is determined by the cooling effect of the road surface and the heat transfer from the free parts of the tire surface via conduction through the tire. If, however, the wheel is still rotating, its dwelling time in the contact area is finite, and the frictional temperature rise is limited by the amount of sliding that has taken place during

this period, the length of which is $a/V = a/v(1-s)$, where a is the contact patch length.

Frictional temperature rise is the most likely reason for maxima in the braking force vs. slip curves observed on dry roads because the friction coefficient of current tread compounds decreases with increasing temperature at sliding velocities in the range of travelling speeds. On wet roads, hydrodynamic effects appear to be the predominant cause of the maxima; the removal of water from the contact area becomes increasingly difficult as slip increases and a slip velocity develops (see sec. 6.6).

When the brakes of a vehicle are suddenly applied, as in an emergency stop or during typical braking trials, the slip increases from zero to 100 percent within a short interval, and the time dependence of the braking force follows curves similar to those in figure 6.10. The example given in figure 6.11 reproduces the main features of the curves in figure 6.10, the most prominent of which is again the maximum of the braking force; it is known from braking experiments with simultaneous recording of the slip that the wheels lock after the maximum has been passed (compare fig. 23 in ref. [21]). The results of braking tests are usually obtained in the form of records like figure 6.11, and the braking performance of tires is specified by the two numerical values indicated in that graph: the peak friction coefficient μ_p , and the sliding coefficient μ_s which gives the constant braking force with locked wheels.

An advice often given for braking on slippery roads is to "pump" the brakes, i.e., to apply and release them in quick succession. The main advantage of this technique is maintenance of directional control by preventing the wheels from locking; it is also seen to afford the possibility, if used with skill, to operate in a slip region of higher braking force than with locked wheels. Aircraft are frequently equipped with braking systems which automatically prevent locking of the wheels.

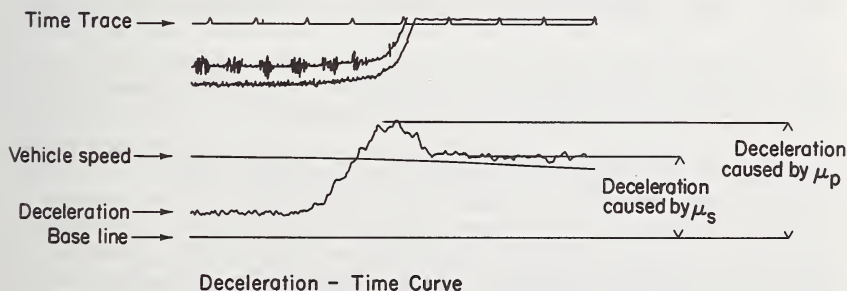


FIGURE 6.11. Time record of speed and deceleration during application of the brakes on a 6.40-15 tire.

From Grosch and Maycock [8].

The dependence of the coefficients μ_p and μ_s on relevant parameters such as driving speed, road condition and properties of the tread are to be discussed now in the framework of existing knowledge of rubber friction and hydrodynamic effects in the contact area on wet roads. Confining the discussion to the two braking coefficients does not necessarily restrict the generality of the findings. The limiting values of the side force appear to be determined by the same factors as the braking force. Figure 6.12 shows that, at least at moderate velocities, the relation between μ_s and the side force at large slip is very nearly linear.

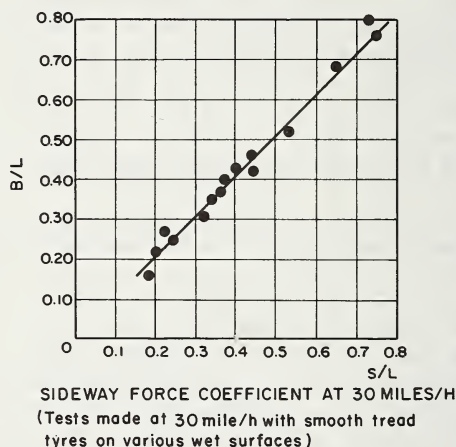


FIGURE 6.12. Relation between braking coefficient B/L and side force coefficient S/L of smooth tires on various wet roads at low speed.

From "Road Safety", p. 518, ref. [9].

6.5. The Speed Dependence of Rubber Friction

An earlier section of this book has shown that rubber friction, whatever its detailed mechanism, is essentially a viscoelastic phenomenon, and that its velocity dependence is interrelated with its temperature dependence through the rate-temperature equivalence principle characteristic of all viscoelastic processes. This principle states that a change in temperature from the so-called Standard Reference Temperature T_s (a material constant) to the temperature T is equivalent to a change in velocity—or rate in general—by a factor a_T which is given by the Williams-Landel-Ferry (WLF) equation. The validity of the WLF equation has been amply verified for dry friction. Recent laboratory work has revealed a similar principal for lubricated rubber friction, but a change in temperature is then equivalent to a change in velocity by a factor $(\eta_T/\eta_0) \cdot a_T$, where η_T and η_0 are the viscosities of the lubricant at the

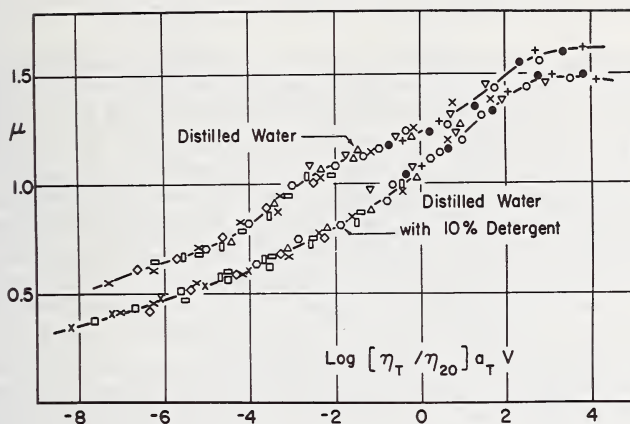


FIGURE 6.13. Mastercurves for lubricated friction of unfilled acrylonitrile-butadiene rubber on a grindstone.

Reference temperature, 20° C. From Grosch [10].

experimental temperature and at the reference temperature [10]. Figure 6.13 gives two "master-curves" for unfilled acrylonitrile-butadiene rubber sliding on a grindstone lubricated with distilled water, and with water containing detergent. With distilled water, the curve is very similar to results on dry, rough tracks [11], though friction is generally lower. The detergent removes the hump on the low velocity side of the incipient maximum and further reduces the friction level. The hump has, in the case of dry friction, been attributed to molecular adhesion, and the maximum to mechanical energy losses. If these explanations hold here, then it appears from figure 6.13 that pure water in the interface allows a certain amount of molecular adhesion to be retained, and that adhesion is eliminated only by the detergent.

The velocity dependence of rubber friction is complicated in practice by frictional temperature rise at any but the lowest sliding velocities; the experimental velocities in figure 6.13 did not exceed 10 cm/sec. Once a relation between temperature and velocity dependence is established, this problem can be dealt with at least qualitatively. It is easily derived that the total velocity coefficient of friction, $d\mu/dv$, is given by eq (6.17)

$$\frac{d\mu}{dv} = \left(\frac{\partial \mu}{\partial v} \right)_T \left[1 + v \frac{d \log (a_T \eta_T / \eta_0)}{dT} \frac{dT}{dv} \right] \quad (6.17)$$

where v is the sliding velocity and dT/dv the frictional temperature rise. As both the factors a_T and η_T/η_0 decrease with increasing temperature, the frictional temperature rise is seen to reduce the actual velocity coefficient of friction from the value it would have at constant temperature. This argument supports the assumption made earlier that a velocity-independent coefficient of friction is a reasonable first approach to the

conditions in the contact area of tires at moderate slips on dry and wet roads.

When braking, the slip and therefore the sliding velocity increase rapidly to a value not much below the original traveling velocity. (At 30 mph, the velocity has dropped by perhaps 10 percent when the wheels lock.) The frictional temperature rise is exacerbated by the simultaneous reduction in the angular velocity of the wheels, as described at the end of the last section. The expression between square brackets in eq (6.17) eventually becomes negative, and the observed velocity coefficient of friction has then the opposite sign to that at constant temperature. As $(\partial\mu/\partial v)_T$ of common tread compounds under operating conditions is positive, a decrease in friction during braking is to be expected in spite of the increase in sliding velocity. These considerations are necessarily qualitative because the frictional temperature rise in the contact area of a tire is difficult to estimate. Although the shape of experimental braking deceleration vs. time curves is consistent with this explanation, it is clear from the data in figure 6.10 that the temperature dependence of rubber friction plays only a contributory role in wet skid resistance.

6.6. Hydrodynamic Effects on Wet Roads

Effective friction under wet conditions is obviously conditional upon some form of contact between tire and road but it is difficult to define what constitutes a frictionally effective contact. Some of the current controversy about the elementary mechanism of wet skid resistance revolves about this question but there can be no doubt about the necessity of removing water from the contact area as far as possible.

When two bodies are brought together in a liquid medium, the liquid resists their approach by hydrostatic pressures which originate from the viscosity of the liquid flowing out of the gap between them and, at high velocity, from the inertial forces necessary to accelerate the liquid.

Figure 6.14a represents schematically part of a tire surface about to contact a flat-ended road asperity at the speed dh/dt through intervening water. Neglecting inertia effects, the force P required to bring these two bodies together when their surfaces are approximately parallel is

$$-P = \text{constant} \times \eta (D^4/h^3) dh/dt \quad (6.18)$$

where D is a length characterizing the lateral dimension of the asperity. (For a review of the subject and derivation of eq (6.18), see ref. [12].) P increases rapidly with increasing size of the asperity and with decreasing distance of the bodies; it is impossible in theory to remove all the liquid between them. The pressure distribution across the gap is of particular importance. It has a peak and is, in the simple case of a cylindrical asperity, parabolic with a maximum twice the average value. In consequence, the tire surface is indented, and liquid can be trapped between tire and asperity.

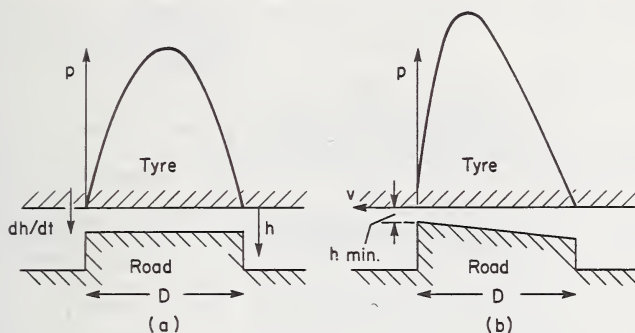


FIGURE 6.14. (a) Pressure distribution in the gap between two bodies approaching each other vertically in a liquid medium at the velocity dh/dt ; (b) Pressure distribution in the gap between an infinite plane and an inclined plane of limited extension moving relative to each other with the velocity v .

An instructive laboratory result is quoted in figure 6.15a [13]. A soft rubber hemisphere of 2.3 cm. radius was put on glass plate covered with a viscous liquid ($\eta=10$ stokes) under a load of 10g. The profile of the rubber surface in the contact region after 5 sec. and 5 min., as determined interferometrically, demonstrates the trapped liquid bell and its persistence.

Squeeze films are drastically reduced in thickness by making the lateral dimensions of the contacting bodies small, since these enter eq (6.18) to the fourth power. This remedy as applied to tires is, of course, to subdivide the tread into a tread pattern. The topology of a skid resistance road surface must fulfill two requirements: an open macrotexture to facilitate gross drainage, and microharshness of the asperities to produce subdivision of the surface into sharp points which can penetrate the remaining water film because of the large pressures at the contact points [12]. With this in mind, it is useful broadly to

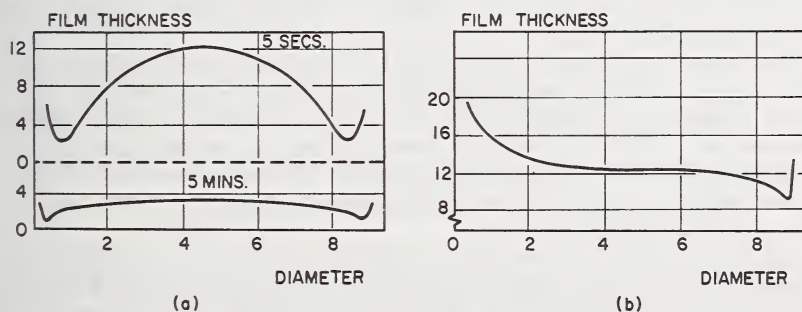


FIGURE 6.15. (a) Profile of the surface of a rubber sphere in contact with a flat surface covered with a viscous liquid. (b) Profile of the same rubber sphere sliding toward the left.

Scales: abscissa, 3.5 divs = 1 mm; ordinate, 1 div = 2000 Angstrom units. From Roberts and Tabor [13].




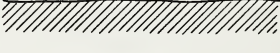
SURFACE		SCALE OF TEXTURE	
		MACRO (LARGE)	MICRO (FINE)
A		ROUGH	HARSH
B		ROUGH	POLISHED
C		SMOOTH	HARSH
D		SMOOTH	POLISHED

FIGURE 6.16. *Classification of road surfaces.*

From Sabey [14].

classify road surfaces into the four prototypes shown in figure 6.16, due to Sabey [14]. This classification, first suggested by Allbert and Walker [22], is paralleled by the four basic surfaces proposed by Percarpio and Bevilacqua [15] for the laboratory assessment of the skid resistance of tread compounds, using the Portable Skid Tester developed by the British Road Research Laboratory [16].

A second manifestation of visco dynamic effects occurs when two bodies slide over each other and their surfaces make an angle as sketched in figure 6.14b. The same quantity of water intercepted per unit time at the wide side of the gap must also leave it at the narrow end and hence acquire velocity during its passage through the gap. Even if inertial effects are neglected again, the viscosity of the liquid requires, to maintain motion, a hydrostatic pressure the distribution of which is shown in figure 6.14b for the conditions sketched there. For the basic theory see reference [17].

The important aspect of the effect is that it is not contingent on a deliberately provided wedge-shaped gap. Experience shows that a liquid wedge can automatically form even in nominal point contacts because the hydrostatic pressure developed in the wedge is great enough to produce sufficient elastic deformation of the contacting bodies to accommodate it [18]. This is, in fact, the basis of hydrodynamic lubrication of machine parts.

A good example of how little is needed to create these conditions is given in the paper by Roberts and Tabor [13]. Figure 6.15b shows the center profile of their rubber sphere when sliding over plate glass at 0.1 cm/sec., and exhibits the liquid wedge in the interface; the coefficient of friction was only 0.04.

The theoretical treatment of hydrodynamic lubrication needs numerical methods for its evaluation. Elementary theory predicts that the min-

imum thickness of the liquid wedge, h_{\min} (see fig. 6.14b), under a load P should be given by an equation of the type

$$h_{\min} = \text{const.} \times D^{3/2} (\eta v / P)^{1/2} \quad (19)$$

From this, it is easily deduced that the "frictional force" is proportional to $(\eta v)^{1/2}$, as has been confirmed by Cohen and Tabor [19] when sliding a steel ball over lubricated rubber at sufficiently high speed.

Moore [20] has theoretically investigated the case of a 2-dimensional rounded asperity sliding over rubber lubricated with water, and has found very low values for the expected coefficient of friction (about 0.01). He comes to the conclusion that the much higher values of commonly observed skid resistances must be due to microroughness of the road asperities penetrating the water film. It will be seen, therefore, that both the reduction of squeeze films and the prevention of hydrodynamic lubrication require harshness of the road cover of the kind indicated by surfaces A and C in figure 6.16.

The effect of squeeze films and hydrodynamic lift on the whole contact area of a tire rolling on a wet road can be assessed now. In the absence of slip, a squeeze film is maintained under the rolling tire with an overall thickness which decreases towards the rear of the contact because sinkage increases with time of contact. The film will, in general, be pierced by sharp points on the road. When the brakes are applied, or a curve is entered, and a slip velocity Δv develops, a hydrodynamic lift comes into operation and the film increases in thickness according to eq (6.19), as $(\eta \Delta v)^{1/2}$. It is as if water were pumped into the contact area. The water wedge intervening between tire and road is extended toward the rear of the footprint. The number of individual contacts between tire and road asperities, which are naturally distributed in height, is reduced but remains more concentrated at the rear than near the front part of the footprint. The consequent loss in braking or cornering force increases therefore with the slip and the traveling velocity.

Squeeze film thickness and hydrodynamic lift increase also with the viscosity, as seen from eqs (6.18) and (6.19). This explains the severe loss in friction on muddy roads even at moderate velocities, as exemplified by the lowest curve in figure 6.5a.

The effect of inertial forces arising in the water film at high speeds will be discussed separately in connection with hydroplaning.

6.7. The Velocity Dependence of the Braking Coefficient on Wet Roads

The braking performance of tires is generally judged by the deceleration of the vehicle on which they are mounted when the wheels are braked for a short time at various initial speeds. The test tires are usually fitted to the front wheels, and only they are braked in order to maintain directional control, as discussed in section 6.3 in connection with oversteer. The braking system is often modified by an adjustable needle valve in the brake fluid line to give an approximately constant interval between appli-

cation of the brakes and locking of the wheels. The deceleration is recorded to give curves similar to that shown in figure 6.11 from which the braking coefficients μ_p and μ_s are determined by dividing the braking force by the load carried on the front wheels. Allowance is made for the load transfer during braking because the deceleration force acts on the vehicle at the height of the center of gravity.

Maycock [21] has carried out skid measurements on various wet road surfaces, using for his experiments smooth tires, tires with seven straight ribs and similar seven-ribbed commercial tires with sipes. From his data, we reproduce in figures 6.17 and 6.18 the results obtained with oil-extended SBR treads on the following four road surfaces:

- Quartzite, a rough, harsh surface resembling prototype *A* in figure 6.16.
- Round gravel, like surface *B* in figure 6.16.
- Fine, cold asphalt, approximating surface *C*.
- Polished concrete, with a texture intermediate between *C* and *D*.

All surfaces were kept wet by spray-bars; the open structure of quartzite and gravel afforded much better drainage than the other two surfaces. The speed dependence of the braking coefficients was sensibly linear in the experimental range, with the exception of smooth tires on the badly drained surfaces for which the curves were convex

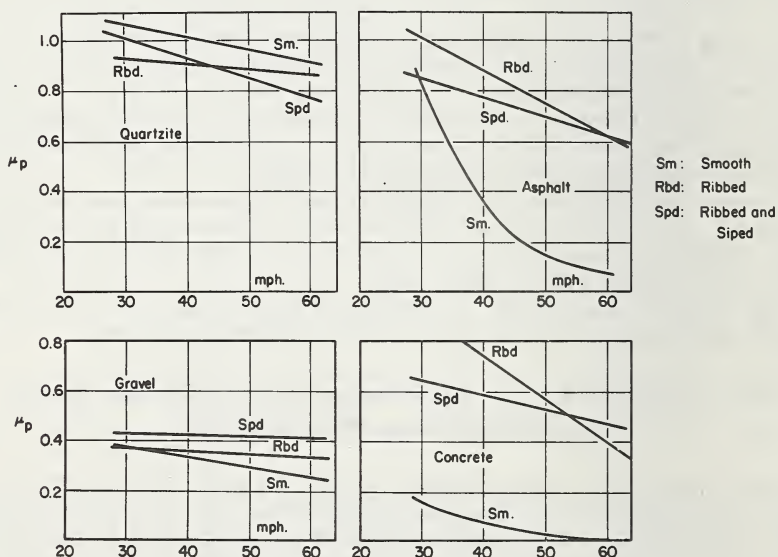


FIGURE 6.17. Velocity dependence of the peak braking coefficient of oil-extended SBR tires on various wet roads.

From Maycock [21].

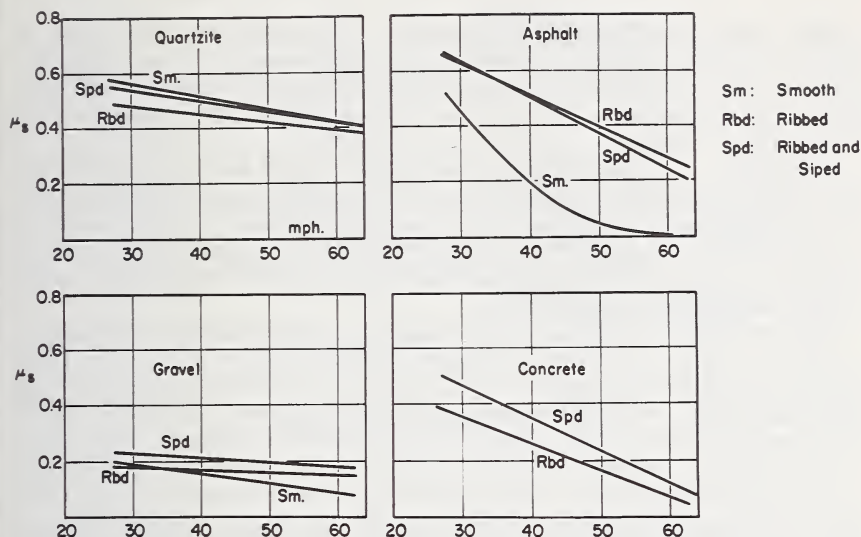


FIGURE 6.18. Velocity dependence of the sliding braking coefficient of oil-extended SBR tires on various wet roads.

From Maycock [21].

to the speed axis. (The linear braking coefficient-velocity relations in these and later figures must not be extrapolated to higher velocities.) The sliding coefficient of smooth tires on concrete was less than 0.05 and has been omitted from figure 6.18.

The graphs in figures 6.17 and 6.18 forcibly demonstrate the interaction between tire surface and road surface in determining the available friction. Considering the ribbed and commercial siped tires together as patterned tires, and comparing their performance with that of smooth tires, it is immediately seen that the difference in braking coefficient is most marked on the asphalt and concrete surfaces. The tread pattern raises the level of friction and, what is more important, reduces its speed dependence which, however, is still pronounced. In contrast, there is little pattern effect on quartzite, a high level of friction being maintained over the whole speed range. Round gravel, though obviously an unsuitable road surface, again produces only a small speed effect.

The advantages of a tread pattern over a smooth tire are pronounced on badly drained surfaces where the configuration of the tire surface must be relied upon for the removal of water from the contact area. Sabey [14] has generalized this conclusion by stating that the effectiveness of a tread pattern is best assessed on slippery surfaces with bad drainage.

The existence of a peak braking coefficient is understandable from section 6.5 and, more particularly, section 6.6; a cause contributing to the effect is most probably that water is periodically cleared from the tread of a rotating tire. The substantial difference between peak and

sliding coefficients evident from figures 6.17 and 6.18 shows that at least a vestige of vehicle control can be maintained even on a slippery road as long as the wheels keep turning. The peak coefficient appears also to be relevant for another aspect of road safety, the cornering ability of tires on wet roads.

Cornering, or "road-holding" tests, are carried out by determining the maximum velocity at which the test car can describe a circular curve of given radius. Considering that the wheels always rotate during a road-holding test, the influence of hydrodynamic effects on the results should be more nearly related to that under peak friction than under sliding conditions in braking tests.

Meades [28] has compared the braking coefficients of a commercial radial tire on a wet slippery surface (brushed concrete) at speeds between 30 and 85 mph with what he calls the maximum cornering force but what seems to be the maximum centrifugal force attainable on circular tracks. The results strongly suggest that the maximum supportable centrifugal force is indeed similar in magnitude and velocity dependence to the peak braking force when hydrodynamic effects play an important role in determining friction at high speeds; the linear relation between side force and braking force during sliding in figure 6.12 was found at a relatively low speed.

6.8. The Effect of Tread Pattern and Carcass Construction on Tire Friction

Most production tread patterns are based on circumferential ribs separated by grooves which must be wide enough to accommodate the displaced water without developing a hydrostatic pressure. The rib width should be as small as practicable, according to eqs 6.18 and 6.19, and preferably straight so as not to impede the flow of water [22]. Figure 6.19 gives results obtained by Allbert and Walker [22] with radial tires having respectively four, five, and six grooves of equal width. These tests carried out on a smooth road show the improvement in friction at high speed effected by increasing the number of ribs. Similar experiments by Maycock [23] indicate that a further increase in the number of ribs up to 13 produces no significant advantage in braking performance, but Allbert and Walker [22] found the maximum cornering force on an indoor rig to increase continuously with the number of ribs; the cornering coefficients were very low, though, not exceeding 0.2 at 30 mph. Maycock also investigated the effect of groove width on the skid resistance of tires with five ribs of equal width (0.5 in.); the brake coefficient reached an asymptotic maximum for a ratio of groove width to rib width of about 0.4.

The ribs of commercially produced tires are generally zig-zag shaped. Kelley [24] points out that the obstruction of free flow of water along the grooves of such tires is compensated by the wiping action of the rib edges making an angle with the direction of motion. Experimenting with vari-

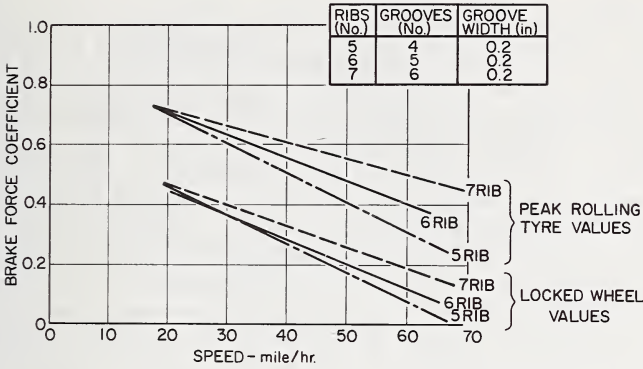


FIGURE 6.19. Effect of number of ribs on the braking coefficient of tires on wet, smooth mastic asphalt; 185×15 radial tires.

From Allbert and Walker [22].

ous patterns, he found that stopping traction could be optimized for certain rib shapes to give friction values slightly higher than those of straight-ribbed tires. Kelley's findings on the effect of rib number on braking are in broad agreement with those of the previously cited authors, but the cornering power decreased slightly with increased number of ribs; comparison between his braking and cornering results are difficult because the cornering experiments were carried out on a considerably rougher road.

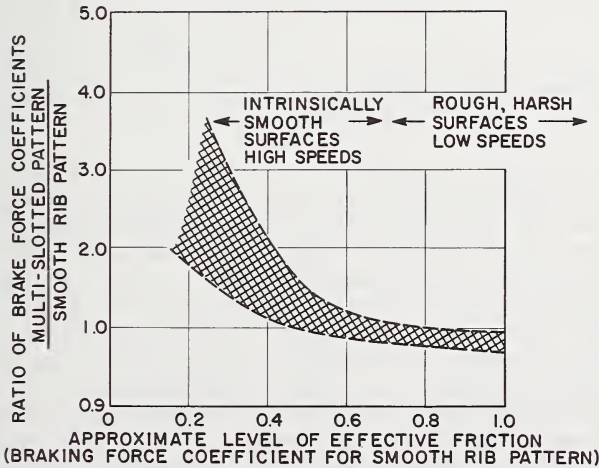


FIGURE 6.20. Effect of sipes on the braking coefficient of tires on seven wet road surfaces at speeds up to 70 mph.

From Allbert and Walker [22].

The influence of sipes on the braking coefficient is not too clear from the data in figures 6.17 and 6.18 but a more detailed analysis of all results shows them to be most effective on badly drained and hence slippery surfaces, and that the advantage increases with increasing speed. Allbert and Walker [22] diagrammatically represent the achievable improvement in braking force derived from sipes by the graph in figure 6.20. Kelley [24] has given data for the stopping traction (at an unspecified speed) of two differently siped, and an unsiped tread with five zig-zag ribs. Predominantly diagonal sipes in a five-ribbed tire improved braking on a low-friction surface by some 80 percent as compared with the plain-ribbed tire. A rather different tread pattern with only three ribs, the center rib being very broad and having transverse siping, raised the braking coefficient by some 220 percent. On a rough road, the differences were very small, and the cornering power on a surface of intermediate roughness was slightly reduced by siping.

Sipes obviously influence tire friction by further subdividing the tread surface and consequently reducing squeeze film thickness and hydrodynamic lift. In addition, the great number of edges introduced by siping provides multiple wiping [25] similar to the action of zig-zag shaped ribs.

Any tread pattern can function satisfactorily on a wet road only as long as grooves and sipes constitute a water reservoir of sufficient capacity, and its effectiveness decreases therefore with increasing wear of the tread. The curves in figure 6.21, due to Sabey [26], show the decline in sliding friction with decreasing tread depth which is, expectedly, more pronounced on smooth, i.e., badly drained, than on rough roads.

The equations developed in section 6.2 for the ground forces in the contact area of slipping tires have shown the importance of the stiffness factors k_s and k_c in determining these forces at low and moderate slip. Tire stiffness is dominated by the carcass construction of which two types are in current use, the conventional cross-ply and the radial, or belted, carcass. Radial carcasses have a number of variants but their distinguishing feature is a relatively stiff breaker belt under the tread, and a carcass proper with practically radial cords or wires from which the construction derives its name. The breaker belt gives the tire great lateral and longitudinal stiffness so that the necessary ground forces are obtained at lower slips than with cross-ply tires. It has been stated by Gough et al. [27], however, that very stiff belts have the disadvantage of producing a peak in the cornering force vs. slip angle curve, and the transition from the region where the cornering force originates mostly from adhesion in the front part of the contact to the region where frictional sliding contributes most of the side force can become too abrupt for satisfactory control; less stiff belts are therefore preferable.

The braking coefficients of treads with identical tread patterns on cross-ply and radial carcasses differ only little from each other. According to data given by Allbert and Walker [22], the peak coefficient at higher speeds is somewhat greater, and the sliding coefficient lower on the radial carcass. Kelley [24], comparing various tread patterns on both radial and conventional carcasses, found only a marginal advantage of radial tires in stopping power and cornering traction.

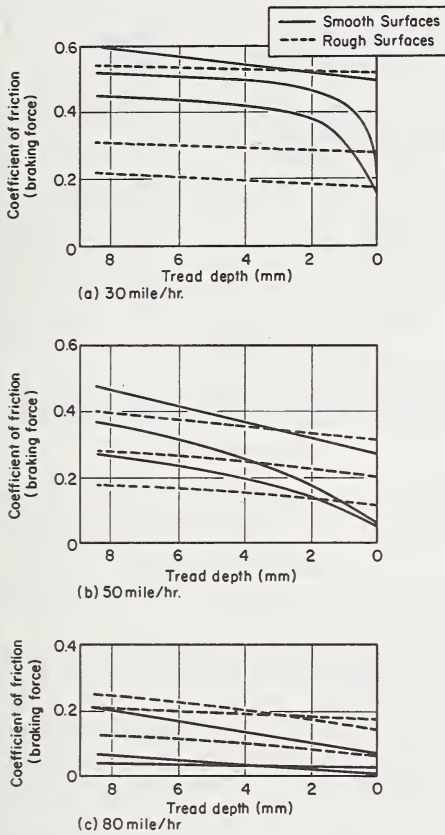


FIGURE 6.21. *Effect of tread depth on wet road skidding resistance at different speeds.*

From Sabey [26].

Meades [28] has measured the braking coefficients of five commercial tires each with radial and conventional construction. The mean curves drawn through the experimental points for these two types of tire on two different surfaces are shown in figure 6.22 and indicate that radial tires have, on the whole, higher and less speed-dependent braking coefficients than cross-ply tires on badly drained surfaces where hydrodynamic effects matter. The same author has extended the experimental velocity range on another surface, brushed concrete, to 120 mph; the sliding values of the braking coefficients are reproduced in figure 6.23 and show the coefficients for radial and cross-ply tires to become equal at speeds over 90 mph. This graph is noteworthy for showing the level of stopping power at very high driving speeds, and the breakdown of the linear braking coefficient-velocity dependence valid at lower speeds. It is of some interest to estimate the stopping distance from 100 mph,

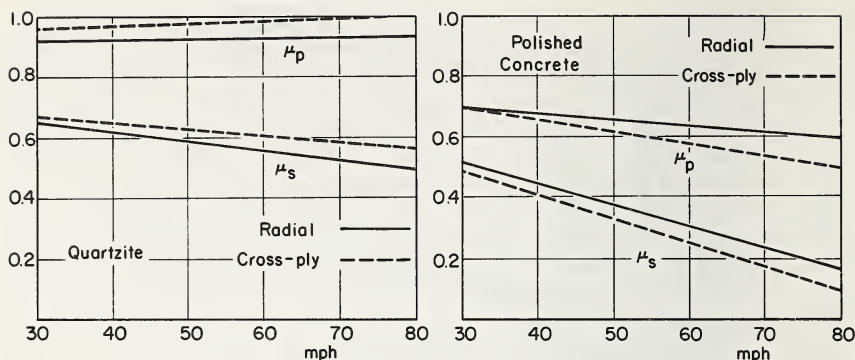


FIGURE 6.22. Average velocity dependence of the braking coefficients of commercial cross-ply and radial tires on two wet road surfaces.

From Meades [28].

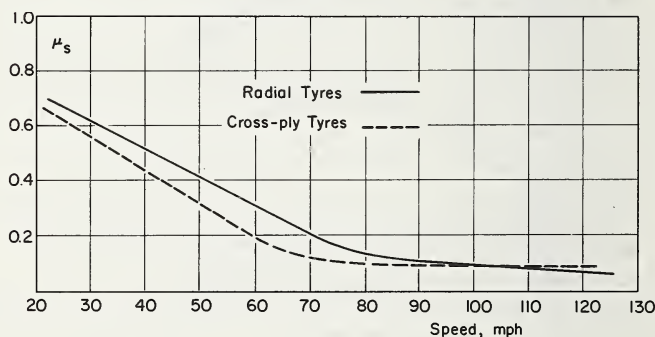


FIGURE 6.23. Average velocity dependence of the sliding coefficient of four radial and five cross-ply commercial tires, all with synthetic treads, on wet brushed concrete.

From Meades [28].

assuming that the velocity dependence of friction followed the curves in figure 6.23 during deceleration. The result is 577 meters for radial, and 734 meters for cross-ply tires.

Allbert and Walker [22] make the general observation that radial carcasses allow more complex tread patterns and a wider range of tread materials to be used and thus make it possible to achieve higher braking coefficients than is practicable with cross-ply tires. The data in figure 6.24 presumably represent the optimum braking coefficients attainable on a smooth road with either carcass construction. From the sizeable improvement in the peak coefficient at high speeds, one would expect a similar improvement in cornering power to be effected by radial carcass construction, according to the reasoning outlined at the end of the last section.

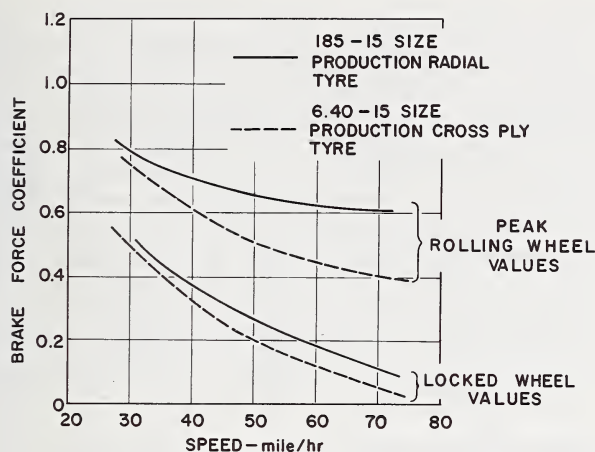


FIGURE 6.24. *Velocity dependence of the braking coefficients of production radial and cross-ply tires on wet, smooth mastic asphalt.*

From Allbert and Walker [22].

6.9. Tread Compound Effects on Wet Friction

The hardness of practical treads varies over a small range, and closer consideration suggests that soft treads may have an advantage over harder ones on some rough roads because of their greater ability to wrap themselves around asperities and thus to produce a larger contact area. Two natural rubber treads investigated by Grosch and Maycock [8] differed in hardness by 6 IRHD units because of different levels in filler loading. Both sliding and peak coefficients of friction of the softer tread were some 13 percent higher on gravel but 5 percent lower on asphalt and concrete; the two compounds differed little on quartzite.

The two most common tread rubbers are natural rubber (NR) and styrene-butadiene copolymer (SBR). NR, formerly the only commercially available rubber, is now generally reserved for the treads of heavy tires, and passenger treads are, as a rule, made from SBR. Both rubbers are often blended with butadiene rubber (BR); SBR, or its blends with BR, are nearly always extended with a heavy oil.

Figure 6.25 compares the braking coefficient of passenger tires with treads of NR and oil-extended high-styrene SBR (OE H-SBR) [21]. The peak values of OE H-SBR are consistently higher than those of NR, the improvement amounting to about 27 percent on all surfaces and over the whole velocity range. The relation between the sliding coefficients of the two rubbers is more complicated because they depend less on speed for NR than for OE H-SBR; the two compounds reverse ranking on the badly drained surfaces at moderately high velocities.

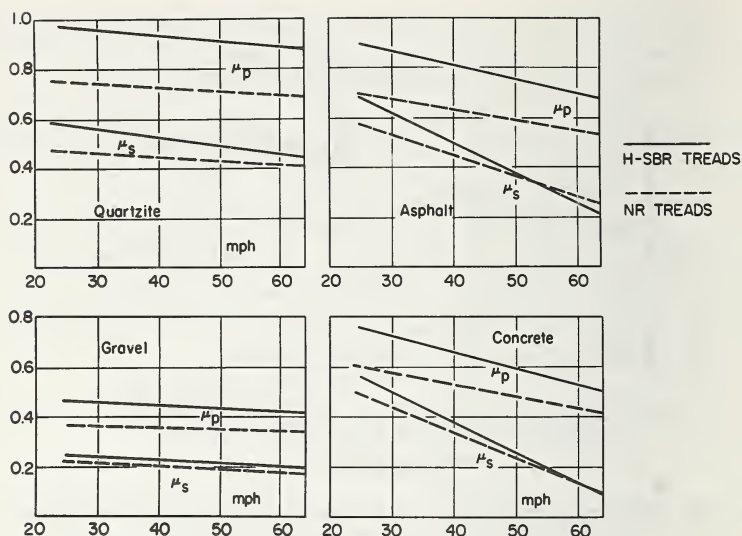


FIGURE 6.25. Velocity dependence of the braking coefficients of tires with treads of oil-extended high-styrene SBR and of NR on four different wet road surfaces.

From Maycock [21].

The superiority in skid resistance of SBR-based treads over NR observed under many conditions has been attributed to the higher internal viscosity, or hysteresis, of SBR but authors differ in their interpretation of these findings, as will be detailed later. The difference in hysteresis between the compounds in figure 6.25 is accentuated by the SBR being oil-extended and having a higher filler-level than the NR (60 pph of super-abrasion furnace black as against 48 pph of high-abrasion furnace black.)

A simple measure of hysteresis is derived from the resilience, i.e., the fraction of kinetic energy recoverable after impact on some pendulum device. If ρ is the resilience, $(1 - \rho)$ gives the hysteresis loss; at 20° C, the losses in the OE H-SBR tread are about 50 percent higher than in the NR tread as determined from their resiliences. A difficulty arises here from the fact that hysteresis, a viscoelastic property, depends on rate and temperature. Apart from uncertainty about the local temperature during sliding, the fundamental deformation period of the process depends on sliding speed and average distance between the road asperities; this time may be short compared with the impact time of a technological resiliometer. Sabey and Lupton [29], comparing skid ratings on the Portable Skid Tester [16] with resiliences, found correlation between the two quantities to be most significant when the resiliences were determined at temperatures some 40° C lower than the skid values. Lowering the temperature has, of course, the same effect as shortening the impact time, according to the rate-temperature equivalence principle.

The influence of hysteresis on wet skid resistance has been more strictly confirmed by results with one rubber compounded to different levels of hysteresis. The graphs in figure 6.26 refer to oil-extended NR (OENR) and ordinary NR treads, both filled with 50 pph of high-abrasion furnace black. The hysteresis loss at 20° C of the OENR was about 50 percent higher than that of the NR. Figure 6.26 bears a strong resemblance to figure 6.25 although the tread patterns were different in the two sets of experiments; an intrinsically resilient rubber like NR is seen to give wet skid resistances of the same order as a synthetic rubber when compounded for low resilience. A feature shared by figures 6.25 and 6.26 is the more uniform increase in the peak than in the slide coefficient of braking when the hysteresis of the tread is increased. From what has been said before, hysteresis of the tread may therefore be expected to improve cornering power over a larger velocity range than it will improve stopping ability.

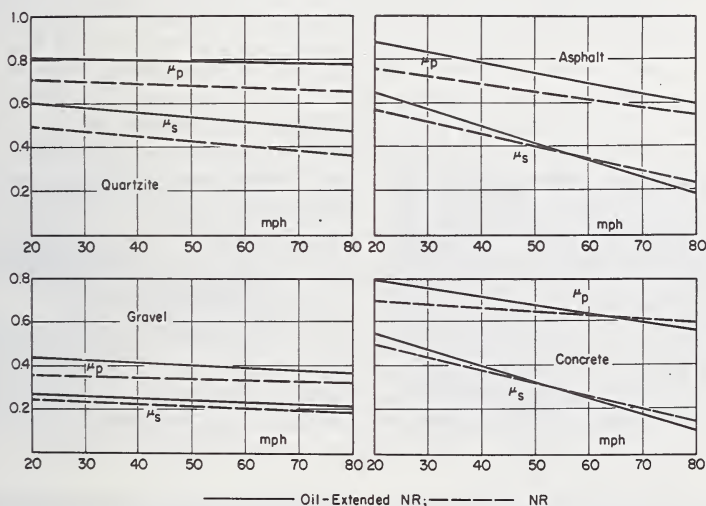


FIGURE 6.26. Velocity dependence of the braking coefficients of tires with treads of NR and oil-extended NR on four different wet road surfaces.

From Grosch and Maycock [8].

A consistent theory of the influence of hysteresis on *lubricated* rubber friction has been put forward by Tabor [30, 31]. He attributes the frictional force solely to mechanical energy losses which occur in the tread surface when road asperities pass over it. The coefficients of friction found in the laboratory on well lubricated rubber are low; they increase with the load but it needs about 2 kg. on a steel ball of $\frac{1}{8}$ in. diameter to reach a value of only 0.25 [30]. While the theory is certainly true for near ideally lubricated friction, rubber sliding on a wet road meets this condition only at speeds sufficiently high to produce a water film which pre-

vents direct contact between tread and road asperities. The Tabor mechanism will then contribute to the frictional force, and quite probably helps to maintain the low but finite friction at high speeds in figure 6.23.

Doubt has also been thrown on the validity of the mechanical energy theory at moderate speeds by experiments with tires having a thin veneer of resilient rubber on a tread of low resilience, and vice versa [32]. Service tests gave skid results representative of the surface veneer even when only 0.2 mm. thick. The mechanical energy losses thought to determine wet friction involve, however, a deeper layer so that the hysteresis of the underlying material should have shown up in the results.

The account given by Bulgin, Hubbard and Walters [33] for hysteresis effects on wet friction starts with an observation on dry friction. The speed and temperature dependence of the friction of different polymers are similar, with the curves shifted along the velocity or temperature axis according to their glass transition temperature (butyl rubber is an exception) [4, 11]. Maximum friction is reached for a combination of speed and temperature which depends on the glass transition temperature, and can be estimated from an empirical equation relating temperature of maximum friction to glass transition temperature and logarithm of the sliding velocity. Experimenting with treads having various glass transition temperatures, friction on wet and dry roads has been found to increase with increasing glass transition temperature up to values of -20°C , the operating conditions in the contact area apparently giving then maximum friction. As treads with high glass transition temperatures become unduly stiff in cold weather (see also sec. 6.11), the best practical compromise is, according to Bulgin and co-workers, treads with glass transition temperatures between -30°C and -40°C . It has not been established yet whether the improvement in wet skid resistance brought about by oil-extension falls under this empirical rule.

The similarity between the temperature dependence of dry and wet friction leads then to the conclusion that tire friction on wet roads originates from dry patches in the rear of the contact area where water has been effectively squeezed out or wiped away (sec. 6.6). The influence of hysteresis on wet friction follows from work on the viscoelastic nature of dry rubber friction [4, 11].

6.10. Aquaplaning (hydroplaning)

When water is displaced from the contact area at high speeds, inertia effects can no longer be neglected. The pressure in a liquid of density γ accelerated from rest to the velocity v (or stopped from the velocity v), p_d , is

$$p_d = \frac{1}{2} \gamma v^2 \quad (6.20)$$

and should be contrasted with the linear speed dependence of pressures arising from viscous effects. Moore [12] quotes eq (6.21) for the force exercised by squeeze films when inertia is taken into consideration:

$$P = -\text{const.} \times \left(\eta \frac{D^4}{h^3} \right) \frac{dh}{dt} \left\{ 1 - 0.1 \left(\frac{\gamma}{\eta} \right) \left[\frac{8}{7} h \frac{dh}{dt} - h^2 \frac{d^2h}{dt^2} / \frac{dh}{dt} \right] \right\} \quad (6.21)$$

which shows that the lateral size D of the approaching bodies affect the force in the same way as in the absence of inertia effects. Previous remarks about the bearing of tread patterns and road surface topology on wet tire friction need therefore not be modified but hydrodynamic lifts become greater.

The photographs in figure 6.27 show the contact area of an aircraft tire passing over a flooded glass truck at different speeds [34]. As the speed increases, the water wedge under the front part of the contact is extended backward until only a small patch adheres to, or is at least in the proximity of the track. Eventually, the tire is only supported by water, with almost complete loss of control. This condition is called hydroplaning or aquaplaning. Horne and Joyner [34] give the empirical equation (6.22) for the velocity v_p at which hydroplaning begins:

$$v_p(\text{mph}) = 10.35 \sqrt{p_i(\text{psi})} \quad (6.22)$$

20×4.4 AIRCRAFT TIRE FOOTPRINTS

VERT. LOAD=500LB; $p=30\text{LB/SQ IN.}$; WATER DEPTH=0.5 IN.

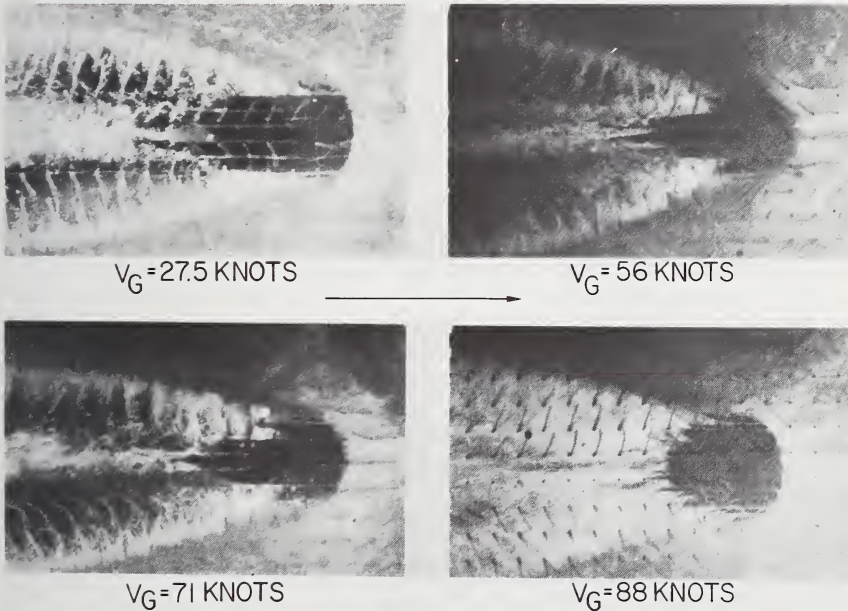


FIGURE 6.27. Contact area on flooded glass of a 20×4.4 aircraft tire under 500 lb. load at various speeds (1 knot=1.15 mph; water depth, 0.5 in.).

From Horne and Joyner [34].

(p_i = inflation pressure) but the authors stress that this equation holds only for smooth or close-patterned tires, and for ribbed tires when the water depth exceeds the groove depth. The velocity at which the smooth tire in figure 6.18 loses discernible friction on wet asphalt very nearly agrees with eq (6.22). Allbert [35] has shown, however, that the minimum hydroplaning speed of a radial tire on an indoor drum increases with increasing inflation pressure only as long as the tire deflection is kept constant; at constant load, hydroplaning speed decreases with increasing inflation pressure.

Although comparison between eqs (6.20) and (6.22) indicates that hydroplaning can originate from the inertia of the water film, it must not be forgotten that similar effects may occur at much lower speeds. The danger of a viscous medium on the road has already been mentioned; Allbert [35] cites instances of hydroplaning of worn truck tires on certain road surfaces at half the velocity predicted by eq (6.22).

The more complex conditions leading to hydroplaning of patterned tires are illustrated in figure 6.28 which gives the speed dependence of the water pressure under the center groove and adjacent rib of an aircraft tire rolling over a flooded track. The groove pressure follows closely the hydrodynamic pressure p_d of eq (6.20). The pressure under the rib rises much faster than p_d at low speeds and then begins to level out; rib and groove pressure become equal when hydroplaning sets in. Below this critical velocity, water can flow from under the rib into the groove because of the higher rib pressure; at greater speeds, water can no longer safely escape. Horne and Joyner remark that the velocity dependence of the rib pressure cannot be explained by inertia effects and ascribe it to viscous effects. Equation (6.21) suggests why this could be so. The inertia term in eq (6.21) vanishes for thin squeeze films (small h), and the water film under the rib will certainly be thinner than the water depth in the grooves.

A spectacular feature of hydroplaning is that tires stop rotating even though the vehicle moves at considerable speed; rolling resistance and bearing friction outweigh the drag forces in the water layer. In consequence, a catastrophic loss of side force occurs which is quite as serious as the loss in braking power. This "spin down" and accompanying decrease in cornering force as observed on an indoor rig is shown in figure 6.29. The speed dependence of the cornering force of patterned and smooth tires on two different concrete tracks given in figure 6.30 follows the same trend as the corresponding curve in figure 6.29, and shows directly the importance of tread pattern and road surface topology on cornering power on wet roads. It also demonstrates how road-holding ability of a patterned tire can disappear in deep water at a relatively low speed.

Boness [36] has theoretically investigated how the thickness of the water film under a smooth tire depends on the water depth when only inertial forces are considered. He finds that for a tire of radius R , contact length a , and water depth H

$$h_{\min} = 0.25 (a/R)^{0.66} (p_d/E)^{1.1} (H/R)^{0.625} \quad (6.23)$$

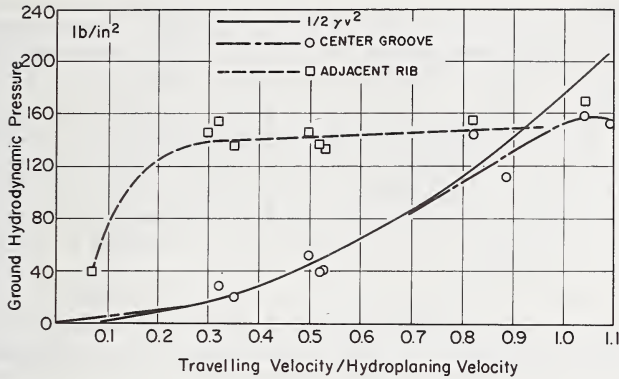


FIGURE 6.28. Speed dependence of water pressure under rib and groove of a 32×8.8 aircraft tire; water depth, 1 in.

From Horne and Joyner [34].

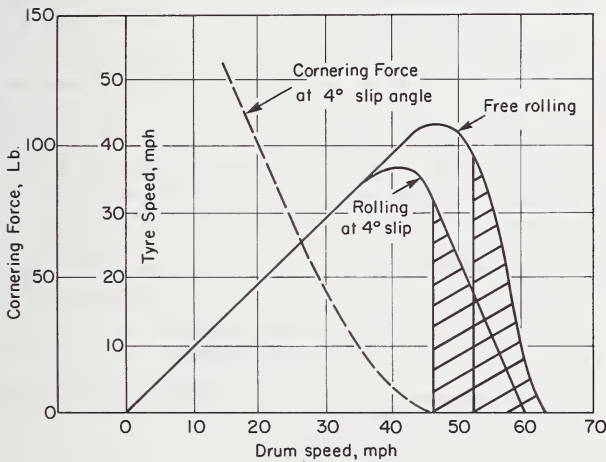


FIGURE 6.29. Spin down at zero and 4° slip angle, and cornering force at 4° slip on a wet drum rig.

In the shaded region, tire will not spin up again if braked to a stand still. From Allbert [35].

where E measures the stiffness of the tire, and p_d is given by eq (6.20). Equation (6.23) agrees well with experimental results for h_{\min} obtained by Gray [37] with an aircraft tire at 100 mph; it is difficult to see, though, why smooth tires begin to hydroplane, according to figure 6.30, at about the same speed in different depths of water.

Whether high-speed braking coefficients of the order of 0.1 (fig. 6.23) and similar values given by Horne and Joyner [34] for patterned tires indicate full hydroplaning, or still contain elements of friction proper

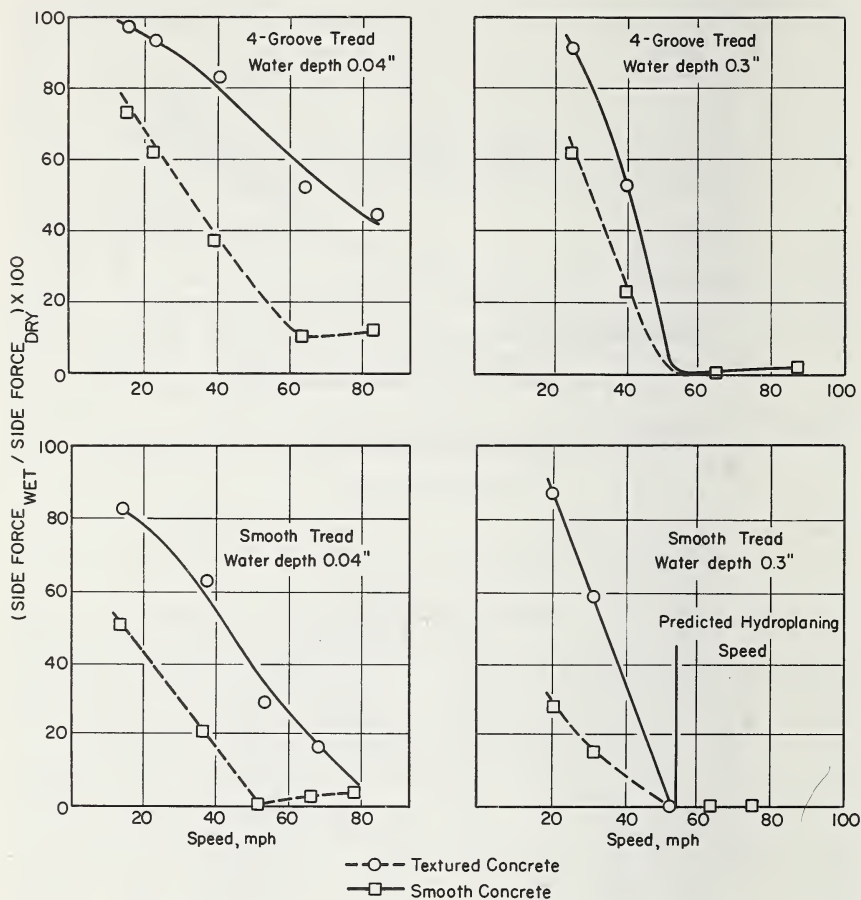


FIGURE 6.30. Speed dependence of cornering force of smooth and patterned passenger tires on two different wet tracks.

From Horne and Joyner [34].

is a moot point. The length of the stopping distances given earlier are serious by any reckoning. Nevertheless, given a well-patterned tire and a good road surface, hydroplaning is hardly a problem at speeds to which road traffic is limited but it constitutes a hazard for aircraft landing at high speed on wet runways. According to one U.S. Airline, quoted by Horne et al. [38], loss of control due to this cause occurs every 500th wet landing.

An effect sometimes accompanying hydroplaning is "reversion", i.e., damage to the tread with all the appearances of local overheating. In one form, the tire surface has a scar roughly of the size of the contact patch which is obviously due to frictional heating [38]. Surprisingly this damage

has not been noticed after dry landings; the brakes are probably not fully applied in that case so that the frictional heat is distributed over the whole tread surface and, furthermore, damaged rubber is removed by abrasion. The wheels will easily lock on a wet runway. Another type of reversion is degradation of rubber just under the tread surface, sometimes leaving a top skin of apparently undamaged rubber which can easily be peeled off [39]. This damage must be due to energy losses below the surface when the tread slides over asperities (compare the wet friction mechanism envisaged by Tabor, sec. 6.9). The energy density has a maximum at a depth of about a quarter of the diameter of the contact area [40].

Reversion has been observed on car and truck tires. Allbert [35] states that for reversion to occur, the inflation pressure must be greater than 50 psi, the wheels must be locked and start to slide at no less than 60 mph, and the water must be shallow with a depth of about 1 mm.

6.11. Winter Tires

The heavily profiled treads of winter tires are designed to provide grip on snow, and to facilitate clearance of the pattern when free of the road. The Swiss Automobile Club have tested, in cooperation with the Technicum at Biel, traction and braking on hard snow and ice of 14 European brands of winter tires, two radial tires, and a new and a worn ordinary cross-ply tire [41]. Two of the winter tires had ice studs, and one tire was furnished with snow chains. The shaded areas in figure 6.31 give the range of driving and braking force coefficients at 10 km/hr. of the various winter tires at different slips; values for the radial tires fall within the same region. The spread of the driving force coefficients at large slips is surprising; the appearance of the different tread patterns gives no immediate clue to the reason for the spread.

Braking force coefficients on ice remained practically constant at slips greater than 15 percent, and ranged between 0.1 and 0.2 for all nonstudded tires. The studded tires gave higher values but only one of them was markedly superior on ice.

The effect of studs has been studied in more detail by Bird and co-workers [42] with special reference to its temperature dependence. The curves in figure 6.32 give friction coefficients derived from the authors' calculated stopping distances from an initial velocity of 20 mph. Studs are seen to improve friction most at temperatures from 0° C to -10° C, their effectiveness tending to disappear at -20° C. An increase in the number of studs was most effective if they were inserted in new rows. An arrangement of 260 studs in eight rows, with 52 studs in the outer rows and 26 each in the inner ones, raised the coefficient of friction on ice at about -5° C by 150 percent at a sliding speed of 37.3 mph, and by 90 percent at 12.4 mph. Sapp [43], who gives no details of the stud arrangement apart from stating that the outer rows are most effective, found an almost linear increase in skid rating with the total number of studs on front and rear tires. As one would anticipate, the advantage derived from studs was less on snow than on ice.

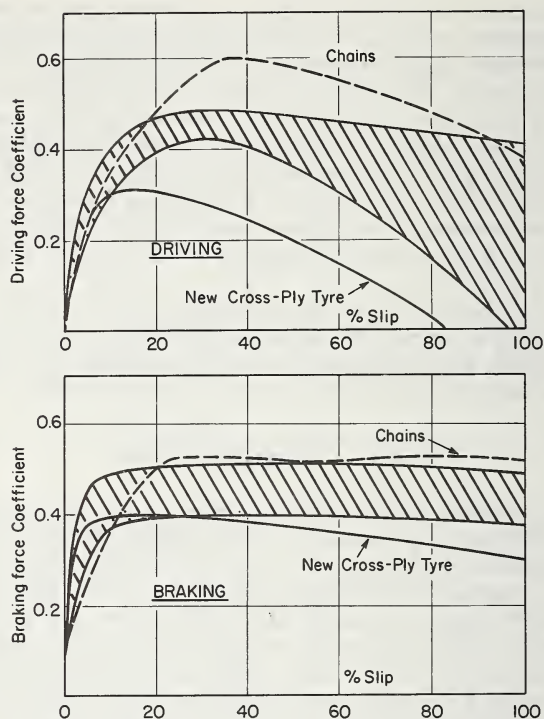


FIGURE 6.31. Slip dependence of driving and braking force coefficients on hard snow at 10 km/hr.

From Swiss Automobile Club [41].

The drawback of studs is that they loose grip when their points wear round, and they damage the road surface. Sapp gives data for the reduction in the friction on ice of studded tires with continued service. In a test in which only the rear tires were studded, the improvement in traction over non-studded tires fell from an initial 83 percent to 9 percent after 10,000 miles; the improvement in braking power was reduced from 34 percent to 14 percent.

Another observation of the same author is that studs increased the cornering ability of cars only when both front and rear tires were studded. Although this result could almost be deduced from first principles, it was worth practical demonstration.

An interesting point brought out by figure 6.32 in the increase in friction with decreasing temperature. This is an important effect characteristics of rubber friction on ice over a considerable temperature range. Laboratory results obtained with the Portable Skid Tester [16] for an NR and an SBR tread compound on a wet and, below 0° C, ice-covered track are reproduced in figure 6.33 (the Skid Tester reading is roughly equal to 100 times the friction coefficient). On lowering the

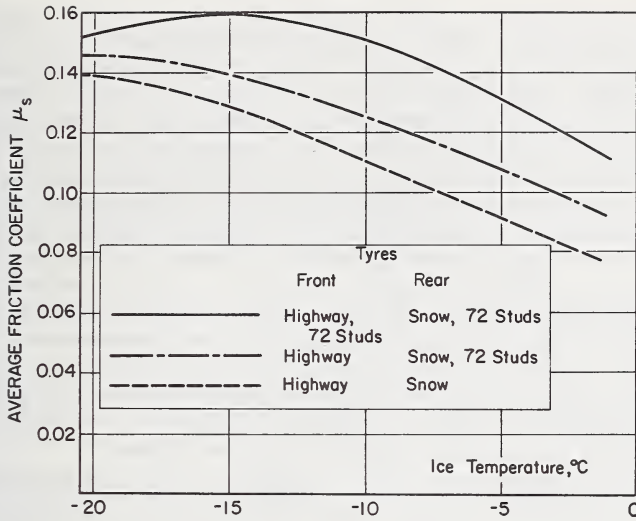


FIGURE 6.32. Temperature dependence of sliding friction on ice of various combinations of studded and non-studded tires.

From data given by Rosenthal et al. [42].

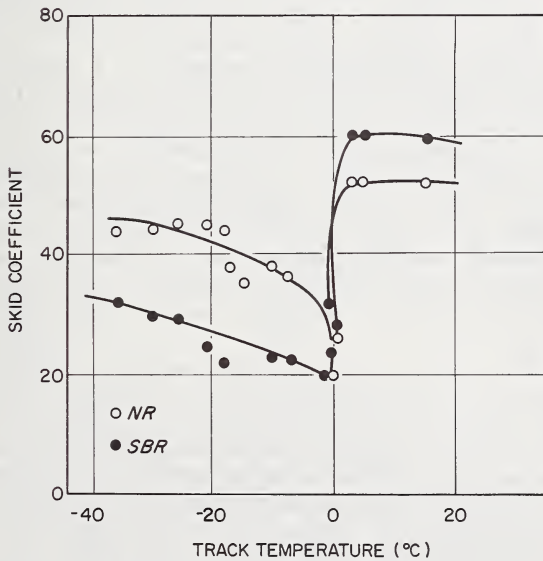


FIGURE 6.33. Temperature dependence of the skid resistance of a NR and a SBR tread rubber on a wet or icy track; Portable Skid Tester.

From Grosch [44].

temperature, friction of both compounds drops to a low value at 0° C and then rises again, but NR produces now greater friction than SBR, in contrast to their ranking on the wet track. Service tests with tires have given similar results [32]. The low friction at 0° C is, no doubt, due to melting ice forming a well lubricated, smooth track; the temperature dependence of friction below 0° C is more difficult to understand.

If ice is taken to be a smooth, *dry* track, and the frictional behavior of the two compounds is estimated from the existing laboratory evidence on dry friction [4, 11], NR should have a higher coefficient of friction on ice than SBR at the speeds involved here (about 300 cm/sec.), but the temperature coefficient of friction should be positive for both rubbers. This results from the fact that the temperatures in question lie on the left-hand side of the peak in the friction vs. temperature curve for 300 cm/sec., and from the difference between the glass transition temperatures of the two rubbers. While the higher friction of NR on ice can be explained in this way, the negative temperature coefficients of friction in figures 6.32 and 6.33 suggest extraneous effects.

Bowden and Tabor [45] report a similar increase with decreasing temperature in the friction of skis and attribute it to ice or snow being melted in the contact area by frictional heat. The estimated thickness of ice melted under the test piece of the Skid Tester is between 2 and 4×10^{-5} cm. if uniformly distributed over the nominal contact. The true contact area may easily be smaller by an order of magnitude, and thus be covered by sufficient instantaneously melted ice to provide partial hydrodynamic lubrication which will become more difficult, though, with decreasing temperature. This mechanism qualitatively predicts, therefore, a negative coefficient of friction on ice.

French and Patton [32] have drawn attention to a negative correlation between hardness and tire friction on ice (in contrast to friction on wet roads) and say that treads with a hardness above 85 become practically useless. They could also demonstrate the effect by running tires for a short distance before the test to increase their internal temperature and thus reduce their hardness. This procedure led to increased hill climbing ability. The effect, which is most probably connected with an increase in true contact area on lowering the hardness, would be expected to work for the advantage of NR tires; NR hardens less than SBR at low temperatures because of its lower glass-transition temperature.

Whatever its explanation, treads based mainly on NR have markedly higher friction on ice and snow than treads of similar SBR compounds. Table 6.1 gives results of trials carried out with studded and unstudded tires in Sweden [44]. All treads were oil-extended and blended with BR in various proportions. It is interesting to note that the braking coefficients of the non-studded NR tires exceeded those of the studded SBR tires; this finding was qualitatively confirmed by hill climbing tests.

Sapp [43] points out the difficulties encountered when evaluating winter tires, and the results in table 6.1 may not be reproduced exactly under all winter conditions. However, more recent trials on ice, also in Sweden, showed NR and OENR tires to be about 17 percent better in

skid resistance than commercial synthetic winter tires [46]. It was not possible to distinguish with statistical significance between the ratings of NR and OENR but cornering tests discriminated more sharply between the treads. The results, obtained on ice, are given in table 6.2 in which the cornering power ratings are expressed in terms of the maximum velocity achievable on a circular path of 31 m. diameter, and in terms of the maximum radial acceleration. The NR tread is seen to have a substantial advantage in road-holding over the commercial tire; OENR, though worse than NR, still offers a useful safety margin over the synthetic tread.

Only a tentative explanation can be advanced for the greater difference between the tread compounds in cornering power than in skid resistance; it is based on the discussion of cornering on wet roads at the end of section 6.7. If melt-water is produced in the contact area, its removal is easier when the tire rotates than when it slides. If, furthermore, the true friction of NR on ice is greater than that of SBR (the main constituent of synthetic winter tires), and this is suggested by work on dry friction, then it can come into effect to a greater extent under a slipping than under a sliding tire.

TABLE 6.1. *Mean braking coefficients on road ice at 10 mph and temperatures between -6° and -2° C*
(From Grosch, [44])

Ratio base polymer/BR	Not-studded		Studded	
	OENR	OESBR	OENR	OESBR
100/0	0.279	0.213	0.288	0.257
80/20	.271	.196	.293	.255
60/40	.221	.194	.229	.217
Skid rating OENR vs. OESBR (%)				
100/0	131		112	
80/20	138		115	
60/40	114		106	

TABLE 6.2. *Relative cornering power on ice*
(From Grosch et al. [46])

Tread	Velocity rating	Friction rating
NR	125	157
OENR	115	131
Commercial	100	100

References

- [1] Chapter 7 of this book.
- [2] Schallamach, A., *Rubber Chem. Tech.* **33**, 857 (1960).
- [3] Schallamach, A., and Turner, D. M., *Wear* **3**, 1 (1960).
- [4] Ludema, K. C., Friction of rubber, Chapter 1.2 of this book.
- [5] Förster, B., *Deutsch. Kraftf. Forsch., Zwischenbericht* 22 (1938).
- [6] Gough, V. E., *Auto. Engr.* **44**, 137 (1954).
- [7] Giles, C. G., *High. Res. Rec.* **46**, 43 (1964).
- [8] Grosch, K. A., and Maycock, G., *Trans. I. R. I.* **42**, T 280 (1966).
- [9] Research on Road Safety (H. M. Stationary Office, London, 1963).
- [10] Grosch, K. A. (Private communication).
- [11] Grosch, K. A., *Proc. Roy. Soc. A* **274**, 21 (1963).
- [12] Moore, D. F., *Wear* **8**, 245 (1965).
- [13] Roberts, A. D., and Tabor, D., *Wear* **11**, 163 (1968).
- [14] Sabey, B. E., Road Tar (in course of publication).
- [15] Percarpio, E. P., and Bevilacqua, E. M., *Rubber Chem. Tech.* **41**, 854 (1968).
- [16] Giles, C. G., Sabey, B. E., and Cardew, K. H. F., *ASTM Spec. Tech. Publ. No. 326*, Philadelphia, Pa. (1962).
- [17] Mitchell, A. G. M., *Viscosity and Lubrication, The Mechanical Properties of Fluids*, second edition (Blackie and Son Ltd., 1944).
- [18] Archard, J. F., and Kirk, M. T., Paper 15, *Proc. IME, (Lubrication and Wear Group Convention, Eastbourne)* (1963).
- [19] Cohen, S. C., and Tabor, D., *Proc. Roy. Soc. A* **291**, 186 (1966).
- [20] Moore, D. F., *Int. J. Mech. Sci.* **9**, 797 (1967).
- [21] Maycock, G., *Proc. IME* **180**, 122 (1965-66).
- [22] Allbert, B. J., and Walker, J. C., *Proc. IME* **180**, 105 (1965-66).
- [23] Maycock, G., Report LR 122, Road Research Laboratory, Crowthorne, Berks, England (1967).
- [24] Kelly, J. D., SAE Paper No. 680138, (Auto. Engr. Cong., Detroit, Mich., 1968).
- [25] Gough, V. E., and French, T., *Pro. First Inter. Skid Prevention Conf., Charlottesville, Va., Part I*, p. 189 (1959).
- [26] Sabey, B. E., Road Tar (in course of publication).
- [27] Gough, V. E., Jones, F. B., and Udall, W. S., SAE Paper No. 990A (Inter. Auto. Engr. Cong., Detroit, Mich., 1965).
- [28] Meades, J. K., Report LR 73, Road Research Laboratory, Crowthorne, Berks, England (1967).
- [29] Sabey, B. E., and Lupton, G. N., *Rubber Chem. Tech.* **37**, 878 (1964).
- [30] Tabor, D., *Engineering* **186**, 838 (1958).
- [31] Greenwood, J. A., and Tabor, D., *Proc. Phys. Soc.* **71**, 989 (1958).
- [32] French, T., and Patton, R. G., *Fourth Rubber Tech. Conf., London, 1962*, p. 196 (I. R. I., London, 1963).
- [33] Bulgin, D., Hubbard, G. D., and Walter, M. H., *Fourth Rubber Tech. Conf., London, 1962*, p. 173 (I. R. I., London, 1963).
- [34] Bulgin, D., *Kaut. Gummi Kunstst.* **20**, 601 (1967).
- [35] Horne, W. B., and Joyner, U. T., SAE Paper No. 650145, (Inter. Auto. Engr. Cong., Detroit, Mich., 1965).
- [36] Allbert, B. J., SAE Paper No. 680140 (Auto. Engr. Cong., Detroit, Mich., 1968).
- [37] Boness, R. J., *Auto. Engr.* **58**, 260 (1968).
- [38] Gray, W. E., *J. Roy. Aero. Soc.* **67**, 302 (1963).
- [39] Horne, W. B., Yager, T. J., and Taylor, G. R., *De Ingenieur* **78**, L39 (1966).
- [40] Gough, V. E., Hardman, J. H., and MacLaren, J. R., *Trans. I. R. I.* **32**, 27 (1956).
- [41] Timoshenko, S. P., *Theory of Elasticity*, first edition, p. 344 (McGraw-Hill, 1934).
- [42] Automobil Club der Schweiz, Berne, Winterreifen Prüfung, (1962).
- [43] Rosenthal, P., Haselton, F. R., Bird, K. D., and Joseph, P. J., CAL Report No. YM-2360-K-1 (Cornell Aeronautical Laboratory, Inc., 1967).
- [44] Sapp, T., SAE Paper No. 680139 (Auto. Engr. Cong., Detroit, Mich., 1968).
- [45] Grosch, K. A., *Rubber Age* **99** (10), 63 (1967).
- [46] Bowden, F. P., and Tabor, D., *The Friction and Lubrication of Solids*, p. 66 (Oxford: Clarendon Press, 1950).
- [47] Grosch, K. A., Schallamach, A., Southern, E., and Swift, McL. P., *Intern Rubber Conf., Moscow* (1969).
- [48] Holmes, K. E., and Stone, R. D., *Proc. IME* **183**, 3H-35 (1968-69).

CHAPTER 7

The Tire as a Vehicle Component

H. C. A. van Eldik Thieme¹ and H. B. Pacejka¹

	Page
7.1. Introduction.....	548
7.1.1. Nomenclature.....	549
7.1.2. List of symbols.....	550
7.2. Straight line rolling experiments (H. C. A. van Eldik Thieme)..<	553
7.2.1. Introduction to total force and moment measurements...	553
Historical.....	553
Laboratory tests.....	553
Towed trailer road tests.....	556
Six-component tire testers.....	559
Road platform tire tester.....	565
7.2.2. Load-deflection relationships.....	567
Vertical load-deflection relationships.....	568
Horizontal load-deflection relationships.....	574
Actual vertical dynamic tire forces.....	579
7.2.3. Effective rolling radius.....	584
Introduction.....	584
Methods of measuring effective radius.....	587
Parameters affecting the effective radius.....	588
7.2.4. Rolling resistance.....	591
Introduction.....	591
Methods of measuring rolling resistance.....	592
Tire conditioning.....	595
Parameters affecting the power loss.....	596
Cornering.....	600
Braking and traction.....	601
Temperature measurements.....	602
7.2.5. Braking and traction.....	603
Braking.....	603
Traction.....	613
7.2.6. Tire nonuniformities.....	616
Introduction.....	616
The tire manufacturing process.....	617

¹ Delft University of Technology, Delft, The Netherlands.

	Page
Treads.....	618
Cord angle and ply fabric.....	619
Building and curing.....	620
Stability of materials.....	620
Wheel uniformity.....	621
Effect of tire nonuniformity on vehicles.....	621
Tire uniformity grading machines.....	624
References.....	628
7.3. Cornering and camber experiments (H. C. A. van Eldik Thieme).....	631
7.3.1. Introduction.....	631
Nonsteered vehicles.....	631
Steered vehicles.....	636
7.3.2. Cornering experiments.....	639
Photography of contact area deformations.....	639
Movable platform measurements with the Gough apparatus..	640
Road and drum test measurements.....	649
7.3.3. Camber and cornering.....	663
Camber.....	663
Combination of camber and cornering.....	664
Actual slip and camber angle measurements.....	665
7.3.4. The influence of braking and traction on cornering.....	669
Dry surface measurements.....	669
Wet surface measurements.....	670
7.3.5. Difficulties in measuring forces and moments.....	675
General observations.....	675
The nature of the track surface.....	676
Conditioning of the tire.....	685
Trailer road tests versus drum tests.....	686
Trailer road tests versus vehicle tests on the road.....	689
Tire characteristic variations due to manufacturing fluctuations.....	690
References.....	691
7.4. Tire in-plane dynamics (H. B. Pacejka).....	695
7.4.1. Low frequency properties.....	695
Normal force-deflection characteristics.....	695
Enveloping properties (obstacles).....	702
Longitudinal slip.....	711
Theory of the longitudinal force response to road wavyness, tire nonuniformity, and vertical and longitudinal axle motions.....	716
7.4.2. High frequency properties.....	726
Vertical and longitudinal vibration transmission.....	726
Tread band free vibrations.....	733
Standing waves.....	743
References.....	754
7.5. Yaw and camber analysis (H. B. Pacejka).....	757
7.5.1. Steady state motion.....	763
Side slip.....	763

	Page
Camber and turning.....	782
Influence of braking and traction forces.....	788
Approximate mathematical representation of combined effects.....	799
7.5.2. Nonsteady state motions.....	803
Horizontal motions (transient and shimmy).....	804
Effect of a time-varying load.....	820
References.....	837

7.1. Introduction

The combination of road, tire, vehicle, and driver forms one entity. The mechanical characteristics of the tire in contact with the road must combine with the mechanics of the vehicle to help in producing operational characteristics of the tire-vehicle system which are satisfactory to the driver.

"The complexity of the structure and behavior of the tire are such that no complete and satisfactory theory has yet been propounded. The characteristics of the tire still present a challenge to the natural philosopher to devise a theory which shall coordinate the vast mass of empirical data and give some guidance to the manufacturer and user. This is an inviting field for the application of mathematics to the physical world."

In this way Temple formulated the situation of more than one decade ago (Endeavour, October 1956). Since then, in numerous institutes and laboratories, the work of the earlier investigators has been continued. Considerable progress in the development of tire mechanics during the last decade has led to a better understanding of tire behavior. Owing to the infinite complexity of the pneumatic tire and its interaction with the road it does not appear at present, despite the progress made, that Temple's view will be altered in the foreseeable future. Thanks to new and more refined experimental techniques becoming increasingly available, and to the introduction of the electronic computer, the goal of formulating more realistic mathematical models based on better insight and leading to more reliable prediction of tire performance may be achieved.

The authors of this chapter do not claim to have supplied a picture of tire behavior which covers all knowledge achieved hitherto. A selection of studies has been made in order to provide the engineer and the student with background material necessary for the investigation and the understanding of tire and vehicle functional performance.

From the point of view of the engineer and the applied mathematician the mechanical behavior of the tire must be systematically investigated in terms of its reaction to various kinds of input related to vehicle motions and road parameters.

With reference to the role of a tire it is convenient to distinguish between symmetric and anti-symmetric modes of performance. First, the tire supports the vertical axle load and transmits longitudinal braking or driving forces. Second, the tire is called upon to supply the lateral cornering and camber forces which are necessary for the directional control of the vehicle.

The major portion of this chapter, consisting of an experimental and an analytical part, has been subdivided according to these categories. The experimental part (secs. 7.2 and 7.3) has been generally restricted to steady-state or slowly varying motions, whereas the analytical part (secs. 7.4 and 7.5) treats also high-frequency and nonsteady state behavior of the tire. Experimental results have also been added.

Many of the investigations discussed in this chapter have been carried out at the Vehicle Research Laboratory of the University of Technology, Delft, Holland. The authors wish to express their appreciation to the members of the staff of this laboratory: G. J. van der Burgt²; A. P. C. van Heesewijk³ and his design office; E. G. J. M. de Vries and his electronic measuring department; P. Buis³, D. A. Timan and J. H. M. Rooney for their numerous tire experiments, as well as to H. M. Snijders and P. J. Jillesma for their assistance in manufacturing various instruments and apparatus.

7.1.1. Nomenclature

For both the experimental and theoretical investigations of tire behavior described in this chapter, we have attempted to use a uniform system of notation. As a rule, the meaning of symbols has been explained in the text. For this reason, only a list of the most important symbols will be given below. The choice of symbols has been inspired by the list which has been proposed by a SAE committee in 1965 (cf. ref. [3])⁴ indicated at the end of sec. 7.3). A number of changes and additions appeared to be necessary in order to obtain a more or less systematic and usable system of symbols adjusted to the specific subjects of this chapter.

Constant quantities describing construction, configuration and properties of the real tire or of the theoretical model are defined in such a way that they become positive. In most cases, the positive sense of variable quantities are chosen in accordance with the (C, x, y, z) system of axes shown in figure 7.1.1. The origin C , defined as contact center, is the point of intersection of the road-plane, the wheel center-plane and the plane which is situated normal to the road-plane and which passes the wheel axis. The x -axis points forward and forms the intersection of the wheel center-plane and road-plane. The z -axis points downward and is directed perpendicular to the road-plane. Consequently, the y -axis is the perpendicular projection of the wheel axis onto the road. In the same figure 7.1.1, the positive directions of forces and moments acting from road to tire have been indicated, as well as the positive senses of the variables which describe the deviations of the position and the motion of the wheel center-plane with respect to the rectilinear steady state motion of the wheel center-plane, which in that case coincides with the (\bar{x}, \bar{z}) plane of the coordinate system $(0, \bar{x}, \bar{y}, \bar{z})$ fixed to the road with the \bar{z} -axis directed vertically. As in figure 7.1.1, the road-plane has in most cases been considered as a smooth horizontal surface.

In some cases an alternative definition of positive sense has been felt to be preferable. In order to work with positive quantities, the tire normal load has been defined as $F_N (= W) = -F_z$. Similarly, the quantity $F_r = -F_x$ has been introduced, denoting the rolling resistance force

² For his help and valuable suggestions.

³ Has left the Laboratory of Vehicle Research.

⁴ Figures in brackets indicate literature references at the end of this section.

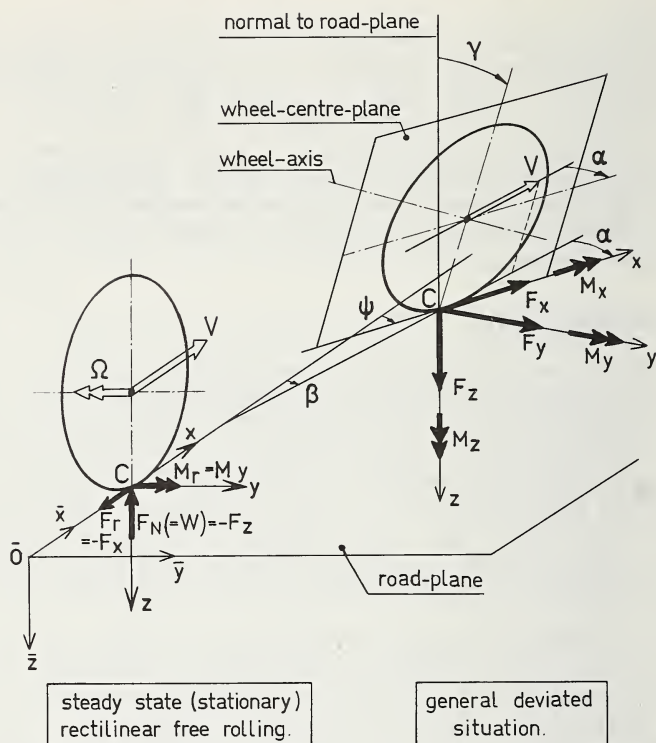


FIGURE 7.1.1. *Nomenclature and coordinate system for a wheel on a plane surface.*

during free rolling, i.e., at constant forward velocity and without traction or braking torques. Also, the sense of the speed of rotation Ω of the forward rolling wheel has been defined as positive. Sometimes, the absolute values of the longitudinal force F_x have been considered. They are designated as the braking force $F_B (= -F_x)$ and the traction force $F_T (= F_x)$.

The lateral force acting from road to tire, F_y , has been provided with an additional subscript α or γ in cases when it has been felt necessary to express whether side slip or camber causes the lateral force.

7.1.2. List of symbols

L , F and T denote length, force and time units respectively.

RAD denotes radians.

a half length of contact area (L)

b half width of contact area (L)

$c_{t, c, r}$ foundation stiffness per unit length in tangential (t), lateral (c) and radial direction (r) respectively (F/L^2)

$c_{p, x, y}$ stiffness of tread rubber per unit area in longitudinal (x) and lateral direction (y) respectively (F/L^3)

c_s	tensile tread band (carcass) stiffness per unit length (F)
$C_{cx, y}$	carcass stiffness in contact region in x and y directions respectively (F/L)
$C_{F\alpha}$	($=\partial F_y/\partial\alpha$ at $\alpha=0$) cornering stiffness (cornering rate) (F/RAD)
$C_{F\gamma}$	($=\partial F_y/\partial\gamma$ at $\gamma=\alpha=0$) camber rate (cf. eq (7.5.61)) (F)
$C_{M\alpha}$	($=-\partial M_z/\partial\alpha$ at $\alpha=0$) cornering stiffness (aligning rate) (FL/RAD)
C_r	($=\partial M_r/\partial f$ at $\delta=\delta_0$) rolling resistance coefficient (F)
C_x	($=-\partial F_x/\partial x_a$ or $\partial F_x/\partial r_l\chi$ at $F_x=0$) longitudinal or tangential stiffness in contact region of non-rolling tire (F/L)
C_y	($=-\partial F_y/\partial y_a$ at $F_y=0$) lateral tire stiffness in contact region of non-rolling tire (F/L)
C_z	($=\partial W/\partial f=\partial W/\partial z_a$ at $\delta=\delta_0$ or $z_a=0$) normal tire stiffness (F/L)
C_κ	($=\partial F_x/\partial\kappa$ at $\kappa=0$) longitudinal slip stiffness (F)
C_ψ	($=-\partial M_z/\partial\psi$ at $M_z=0$) torsional stiffness about vertical axis of non-rolling tire (FL/RAD)
EI	flexural rigidity of tread band (FL^2)
$F_{B, T}$	braking and traction force respectively (F)
F_N	($=W=-F_z$) tire normal load (F)
$F_{x, y, z}$	longitudinal, cornering (= lateral) and normal force acting from road to tire (cf. fig. 7.1.1) (F)
$G(x, \xi)$	Green's function
I_χ	polar moment of inertia of wheel about wheel axle (FLT^2)
l	wavelength of standing wave (L); half of projected contact length (cf. fig. 7.5.1 of sec. 7.5)
M_r	($=M_y$) rolling resistance moment (cf. fig. 7.1.1.) (FL)
$M_{x, y, z}$	moment acting from road to tire (cf. fig. 7.1.1), M_z = aligning torque (FL)
n	frequency of motion (Hz)
$p_{x, y, z}$	contact force per unit area acting upon tire in negative x , y and z direction respectively (F/L^2)
p_i	inflation pressure (F/L^2)
$q_{x, y, z}$	contact force per unit length acting upon tire in negative x , y and z direction respectively (F/L)
r	(or R) tire radius (L)
r_e	(or R_e) effective radius of rolling (L)
r_l	(or R_l) loaded tire radius = wheel center height (L)
R	radius of curvature (L)
s	distance travelled (L); mode number
S	tension force in tread band (F)
t	time; pneumatic trail ($=-M_z/F_y$) (L)
u	tangential (longitudinal) deflection (L)
v	lateral deflection (L)
$v_{c, p}$	lateral deflection of carcass and tread rubber respectively (L)
V	($=ds/dt$) speed of travel (L/T)
$V_{c, r, s}$	creep (slip), rolling and sliding velocity respectively (L/T)

w	radial deflection (positive outwards) (L)
W	($= -F_z$) tire normal load (F)
X	longitudinal horizontal force acting upon tire (F)
x, y, z	coordinates with respect to moving system (fig. 7.5.1)
$\bar{x}, \bar{y}, \bar{z}$	coordinates of contact center C with respect to system fixed in space
x_a, y_a, z_a	variation of wheel center position with respect to steady state motion
$\bar{x}_c, \bar{y}_c, \bar{z}_c$	coordinates of contact point with respect to system fixed in space
α	slip angle (cf. fig. 7.1.1); crown angle
β	($= \arctan d\bar{y}/ds$) path angle (cf. fig. 7.1.1)
γ	camber angle of wheel center plane (cf. fig. 7.1.1)
δ	normal tire deflection (positive toward the center) (L)
λ	wavelength of motion (L)
κ	longitudinal slip value (cf. eqs (7.4.27, 7.5.64)
$\kappa_{B, T}$	percentage of brake and traction slip respectively
μ	coefficient of friction
ϕ	($= d\psi/ds$) spin = yaw rate (RAD/L)
ψ	yaw angle (cf. fig. 7.1.1)
χ	deviation from steady state angle of rotation Ωt (cf. fig. 7.4.13)
ρ	mass density of tire tread band (FT^2/L^2)
σ	relaxation length for tire model without tread rubber (L)
σ^*	relaxation length for tire model with tread rubber (L)
ω	frequency of motion (RAD/T)
ω_s	reduced, spatial or path frequency (RAD/L)
Ω	speed of rotation of wheel (RAD/T)

7.2. Straight Line Rolling Experiments

H. C. A. van Eldik Thieme

In this section part 7.2.1 is devoted to a description of the equipment used to measure forces and moments required for the investigations as treated in sections 7.2 and 7.3.

7.2.1. Introduction to Total Force and Moment Measurements

Historical

A variety of measuring devices have been designed to determine the forces and moments that arise in the tire contact area. Although initially the interest was in load-deflection relationships in a radial direction, later research emphasized the rolling resistance and the nonskid qualities of tires (braking force coefficient). The need to evaluate the cornering force coefficient and the slip angle was discussed as early as 1930 by Bradley and Allan. The research in this area is well summarized in the master reference list given in the papers by Milliken [1],¹ Gough [2], and Kollmann [3].

Laboratory Tests

The majority of tests conducted to measure tire characteristics have been run in laboratories, where the tire rolls on a large drum. However, internal drum tire test machines are also available [3-5].

These indoor tests are useful for comparing the characteristics of different tires, but do not give exact information on the tire behavior on flat roads because significant differences in the tire behavior are induced by the curvature of the drum. Kollmann [3] and Krempel [4] have discussed the effect of the radius of curvature of external and internal drums (fig. 7.2.1). They report that the advantage of an internal drum lies mainly in the fact that it can be covered with any surface, including an exactly defined thickness of water.

To eliminate the effects caused by the curvature of the drum, a flat rotating disc has been used [3], but due to the finite width of the tire tread the velocity of the inner and outer tire tread edge will be different, causing slip in the contact area (fig. 7.2.2).

Another method of reproducing the traveling ground is the belt-type tire tester, as shown in figure 7.2.3, consisting of an endless steel band or conveyor belt running on two drums. The flexible belt is supported in the

¹ Figures in brackets indicate the literature references at the end of this section.

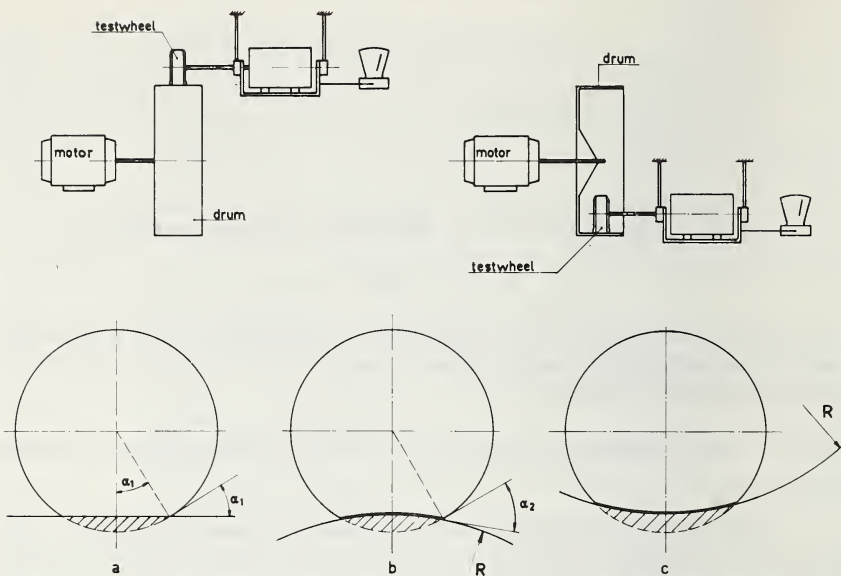


FIGURE 7.2.1. Schematic representation of test tires on external and internal drums.

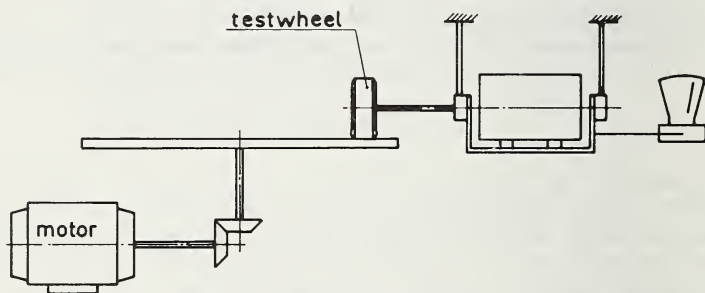
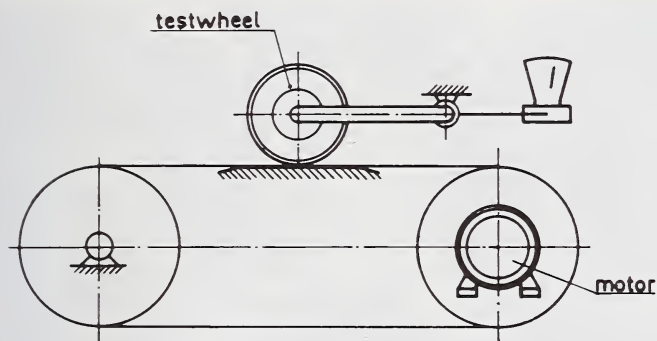
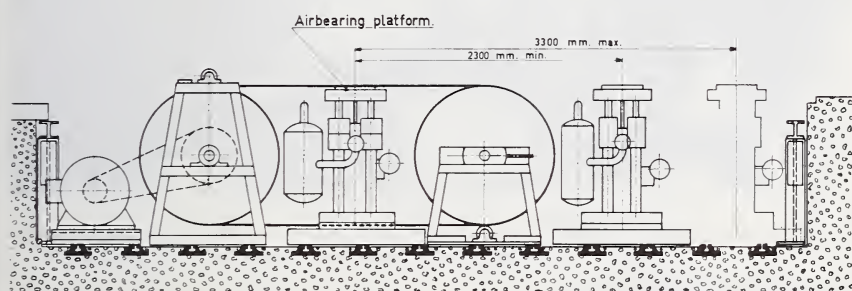


FIGURE 7.2.2. Test wheel on flat rotating disc.

tire contact area by an extremely stiff and thin air bearing, in order to minimize the air gap variation due to the required variable vertical loading of the test tire. A drawback of such an air bearing is the large air consumption [6-7].

These belt testers are sometimes equipped with an electro-hydraulic vibrator in order to induce a variable load via the air bearing platform to the running belt (fig. 7.2.4). The static tire load in such cases is carried by a special device mounted to the foundation block. Through the use of such a shaker system, it is possible to excite in the laboratory the various modes of vibration of an automobile, including the inputs due to tire nonuniformities [8-9].

Another indoor test is the method using a movable platform, as illustrated in figure 7.2.5.

FIGURE 7.2.3. *Endless belt tire tester.*FIGURE 7.2.4. *Belt tire tester equipped with an electro hydraulic vibrator to simulate road excited vibrations.*

The necessity to measure in a laboratory all forces and moments acting on a tire, without excessive wear which would change the tire characteristics, dictated the design of various movable table machines [10–14]. These flat surface machines have the limitation of low speed, but afford the easy control of test variables that can be only achieved in a laboratory. Most tables provide for the possibility of bonding various surface materials, and others provide for a glass section for observing and photographing tire deformations. Often the road surface can be wet, dry or iced at a controlled temperature for additional frictional studies [15]. Most machines measure the forces and moments of a loaded, steered, cambered or torqued tire. The results are often shown in the form of a carpet plot [12], because this technique allows one variable to be plotted as a function of two variables, so that accurate interpolation with respect to both independent variables is possible.

The Delft movable platform machine as shown in figure 7.2.5 is equipped with an air spring device, in order to maintain a constant normal tire load, as required for tests as described in section 7.3.2 (fig. 7.3.21).

The same machine can also maintain constant center height. The machine is equipped with a slide mechanism and a turntable, both with graduated scales [14].

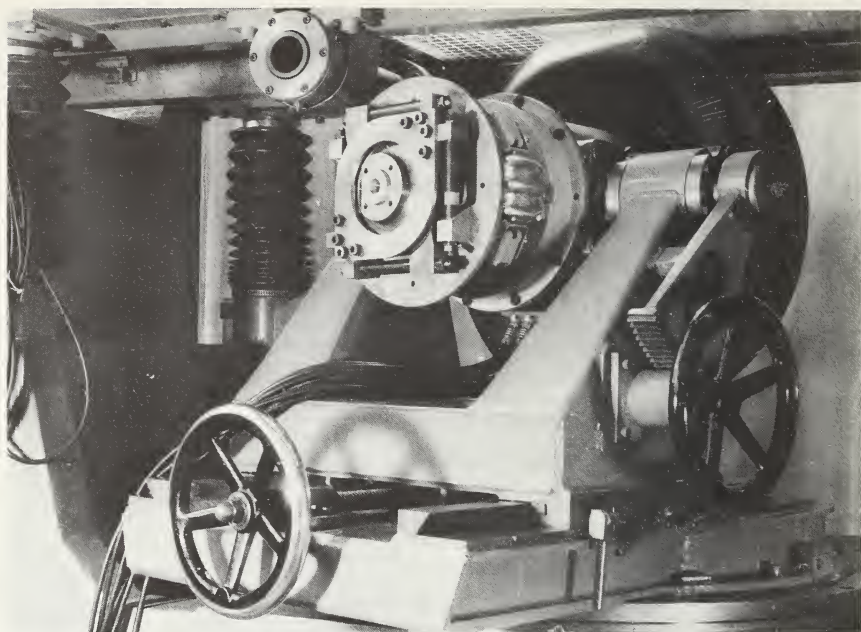


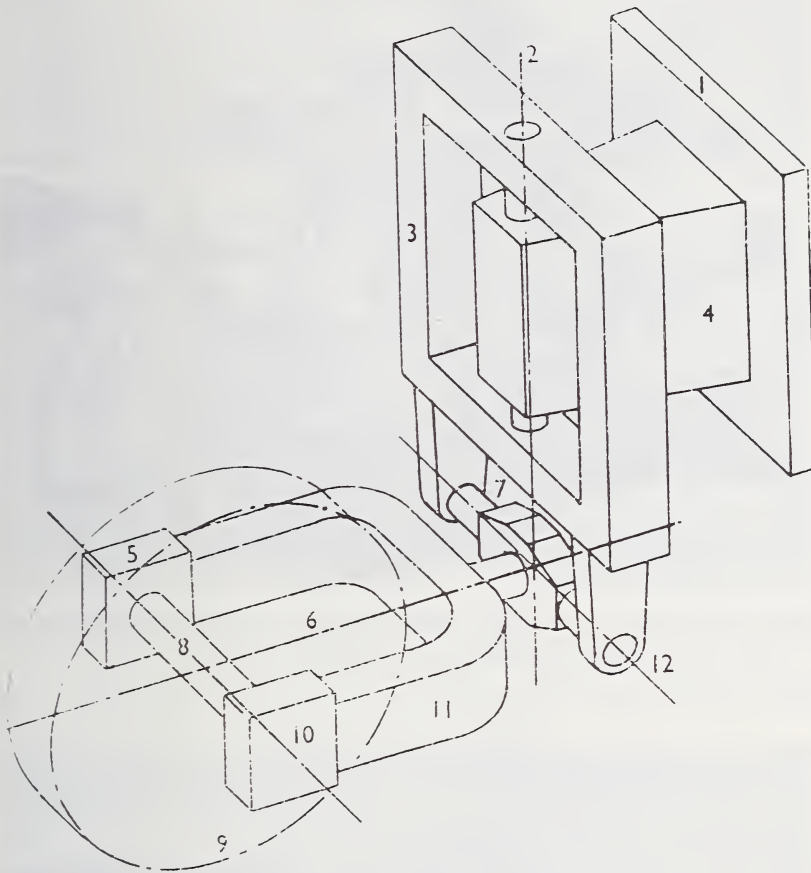
FIGURE 7.2.5. *Movable platform machine with glass section to observe tire deformation.*

Towed Trailer Road Tests

The testing methods described above do not represent actual operating conditions, and therefore devices were developed for measuring tire characteristics on road surfaces. The Air Force-Cornell tire tester [1] is well known, consisting of a single-wheeled trailer towed behind a truck (fig. 7.2.6). The axle carrying the test tire is supported at its ends by units which measure five forces, provision being made to include an instrumented linkage for measuring the brake torque. The load cells are mounted on the free ends of an U-shaped frame whose normal position is in a horizontal plane. The mechanism permits the test tire to be steered and cambered 30 degrees and vertically loaded with a variable force up to 3,000 lbs.

Because the true slip angle applied to the tire consists of the steering angle (tire relative to truck) minus the truck slip angle (truck relative to direction of motion at test wheel), a fifth wheel unit was added to measure the truck slip angle (fig. 7.2.7).

Another tire tester developed at the Delft Vehicle Research Laboratory avoided the difficulty in measuring the slip angle by using two test wheels in a trailer; the tire of the second wheel running at an equal but opposed slip angle to the measuring wheel [10]. In this way the lateral forces induced by both wheels are now in equilibrium, resulting in zero slip angle for the test trailer. Of course the motion of the trailer without test tires must have zero slip angle, if accurately aligned and



Mechanical Components

- | | |
|--------------------------------|----------------------|
| 1. Bed-plate (fixed to truck). | 7. Trunnion. |
| 2. Steering axis. | 8. Axle. |
| 3. Hinge frame. | 9. Test tyre. |
| 4. Hinge box. | 10. Right load cell. |
| 5. Left load cell | 11. Wheel frame. |
| 6. Camber adjustment axis. | 12. Pitch axis. |

FIGURE 7.2.6. *Schematic representation of Cornell tire tester.*

fitted with tires having acceptable tire nonuniformity. A special air-sprung trailer (fig. 7.2.8) with a comfortable cabin for mounting auxiliary equipment was developed, including a six-component tire tester. In



FIGURE 7.2.7. *Single wheeled trailer behind a truck for measuring tire characteristics.*
A fifth wheel is also shown for accurate slip angle measurements.



FIGURE 7.2.8. *Towed trailer road tests with a six-component tire tester.*
The test wheel is mounted in the airsprung trailer.

this trailer the tire load on the test wheel is kept constant by means of an air spring, so that vertical movements of the trailer cannot influence the measuring results. The steering system for varying the slip angle employs an extensive hydraulic regulating apparatus, in order to rapidly adjust the various slip angles desired under constant vertical tire loads. The camber of the tire tester can also be adjusted. A water tank for spraying the road has been placed in the truck towing the trailer.

Six-component Tire Testers

The paper in 1956 by Close and Muzzey [1] described one of the most modern means of measuring tire characteristics, since it was the first complete machine to measure tire parameters on flat road surfaces at different speeds and loads. Most available tire testing equipment was capable of measuring the steady state characteristics of the tire, but for steering system stability problems the time or distance behavior of the tire must be known.

The obvious advantage of a six-component tire tester is not only its ability to measure tire characteristics on flat roads, but also its utility as a precision laboratory test machine on a drum.

In this way it is possible to compare test results obtained from road and drum tests with the same tire.

The interpretation of forces acting in the tire road contact area has been discussed by Fonda, Close and Muzzey [1].

In the contact area of a cambered tire there is a distribution of forces normal to the road plane and a distribution of shearing forces in the road plane. These forces can be resolved into three forces and moments acting on the tire at the so called center of tire contact C .

Figure 7.2.9 shows a cambered wheel in contact with the ground, and an enlarged view shows the forces at a point x, y in the area A .

The equations are given by:

$$\begin{aligned} F_x &= \int_A dF_x & M_x &= \int_A y \cdot dF_z \\ F_y &= \int_A dF_y & M_y &= \int_A -x \cdot dF_z \\ F_z &= \int_A dF_z & M_z &= \int_A (x \cdot dF_y - y \cdot dF_x) \end{aligned}$$

The vector of the pressure in the positive direction exerted by the tire upon the road is denoted p_x, p_y, p_z . Thus p_x is the force per unit area, and $p_x \cdot dA = -dF_x$, $p_y \cdot dA = -dF_y$, $p_z \cdot dA = -dF_z$ and therefore

$$M_z = \int_A (p_x \cdot y - p_y \cdot x) dA, F_x = - \int_A p_x dA, F_y = - \int_A p_y dA \quad [40].$$

The choice of the location of the origin C_w of an additional set of axis $x^*y^*z^*$ through the center of the wheel reduces misinterpretation.

Figure 7.2.10 shows the new axis, and after transformation we obtain:

$$F_x^* = F_x \quad M_x^* = M_x - F_y R \cos \gamma - F_z R \sin \gamma$$

$$F_y^* = F_y \quad M_y^* = M_y + F_x R \cos \gamma$$

$$F_z^* = F_z \quad M_z^* = M_z + F_x R \sin \gamma$$

Because the load cells make their measurements with respect to the wheel axis, a third set of axis is shown in figure 7.2.11, and, after transformation, the equations read:

$$F_x^* = F_{xw}$$

$$M_x^* = M_{xw}$$

$$F_y^* = F_{yw} \cos \gamma - F_{zw} \sin \gamma$$

$$M_y^* = M_{yw} \cos \gamma - M_{zw} \sin \gamma$$

$$F_z^* = F_{zw} \cos \gamma + F_{yw} \sin \gamma$$

$$M_z^* = M_{zw} \cos \gamma + M_{yw} \sin \gamma$$

Figure 7.2.12 finally illustrates the relationship of wheel axis forces and moments to load cell forces for the Cornell tire tester. The load cell readings can be used to compute the externally applied forces and moments for the coordinate axes shown.

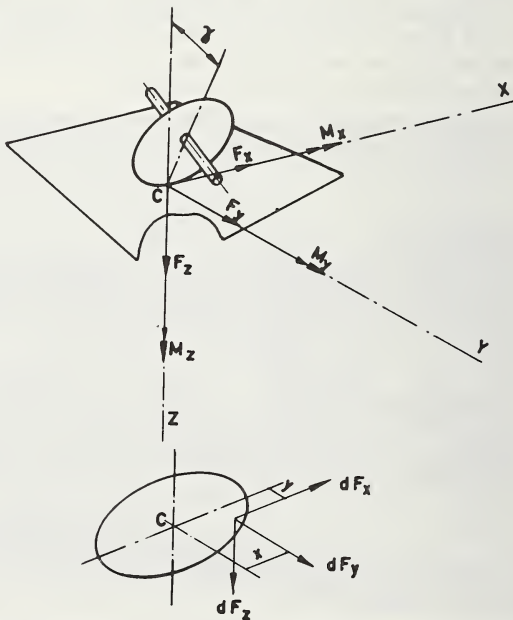


FIGURE 7.2.9. Forces and moments of a cambered wheel with enlarged view of the contact area.

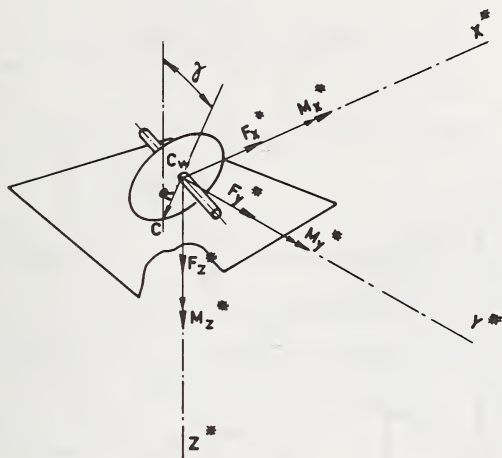


FIGURE 7.2.10. Transformation of forces and moments from contact center C of figure 7.2.9 to center of the wheel C_W .

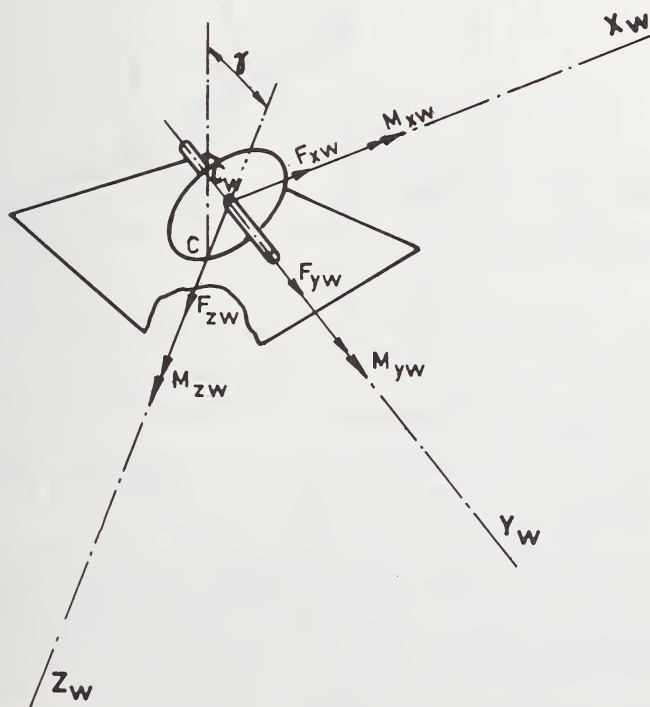


FIGURE 7.2.11. The load cells make their measurements with respect to the wheel axis requiring the transformation of forces and moments to a third set of axes (X_W, Y_W, Z_W) .

$$F_{xw} = f_{xl} + f_{xr} \quad M_{xw} = bf_{zr} - af_{zl}$$

$$F_{yw} = f_y \quad M_{yw} = m_y$$

$$F_{zw} = f_{zl} + f_{zr} \quad M_{zw} = af_{xl} - bf_{xr}$$

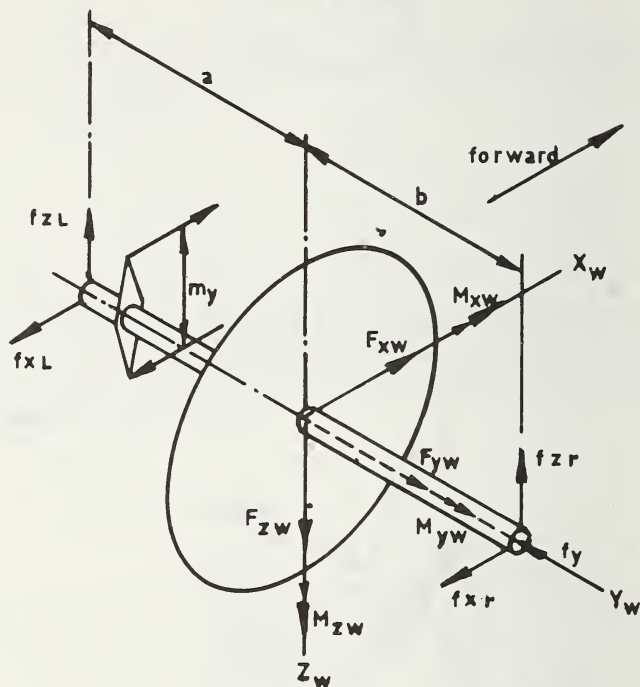


FIGURE 7.2.12. Relationship of wheel axis forces and moments to load cell forces for the Cornell tire tester.

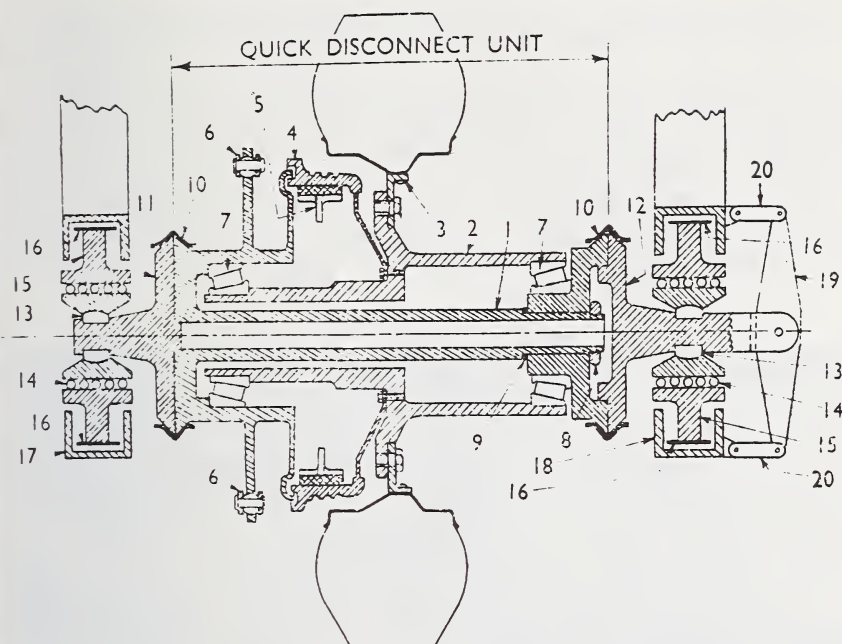
In figure 7.2.13, the axle arrangement for the tire tester is shown for the Cornell tire tester.

To provide for easier changing of the tire to be tested, a somewhat different design was chosen for the Delft tire tester built in 1959. After some modifications it proved to be successful [14].

Using the same notations and symbols as figure 7.2.12, the reader will observe the different design approach in figure 7.2.14. The considerable advantage obtained with this new design is the possibility of mounting the tire at a free end of the measuring axle as shown in figure 7.2.15.

Referring again to figure 7.2.14 it is observed that in this Delft tire tester the axle and axle bearing box are connected to the frame with the measuring devices P , Q , R and a flexible coupling S .

To calibrate the tire tester a special very stiff test rig was built (fig. 7.2.16) having three absolute perpendicular axis, the tire tester being



Axle Arrangement, Plan View

- | | |
|-------------------------------|----------------------------------|
| 1. Axle, non-rotating. | 11. Stub axle, left hand. |
| 2. Hub. | 12. Stub axle, right hand. |
| 3. Wheel and test tyre. | 13. Spherical bearings. |
| 4. Brake drum. | 14. Linear ball bushings. |
| 5. Brake shoe. | 15. Spiders. |
| 6. Brake torque links. | 16. Flexures. |
| 7. Taper roller bearings. | 17. Load-cell frame, left hand. |
| 8. Nut, bearing adjustment. | 18. Load-cell frame, right hand. |
| 9. Shims, bearing adjustment. | 19. Side force beam. |
| 10. V-band couplings. | 20. Links. |

FIGURE 7.2.13. Axle arrangement for the Cornell tire tester.

accurately fixed to an extremely stiff bed plate. With the aid of three dead weight controlled dynamometers several combinations of forces and moments can be induced on the tire tester, giving the required output corrections. With the test rig it is also possible to prove that, for instance, a static force in the *X*-direction will not influence the output of strain gage bridges in other directions.

Not only static calibration is required, but also assessment of the dynamic behavior of the measuring unit is necessary, in order to define its limitations.

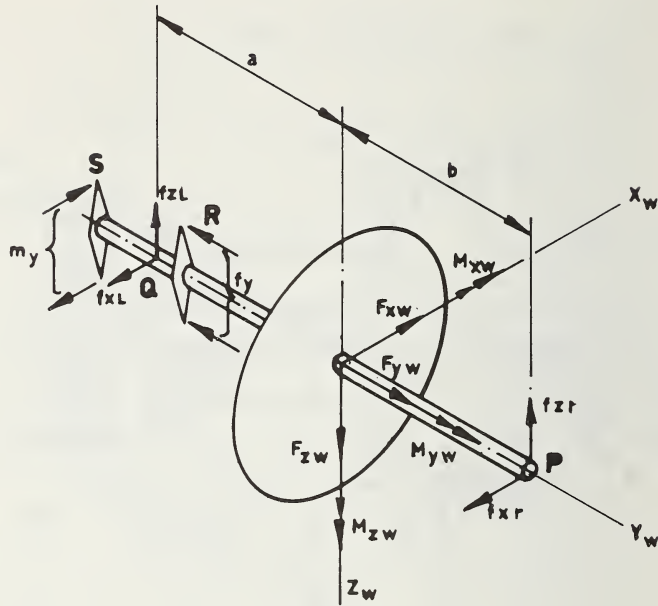


FIGURE 7.2.14. Relationship of wheel axis forces and moments for the Delft tire tester.

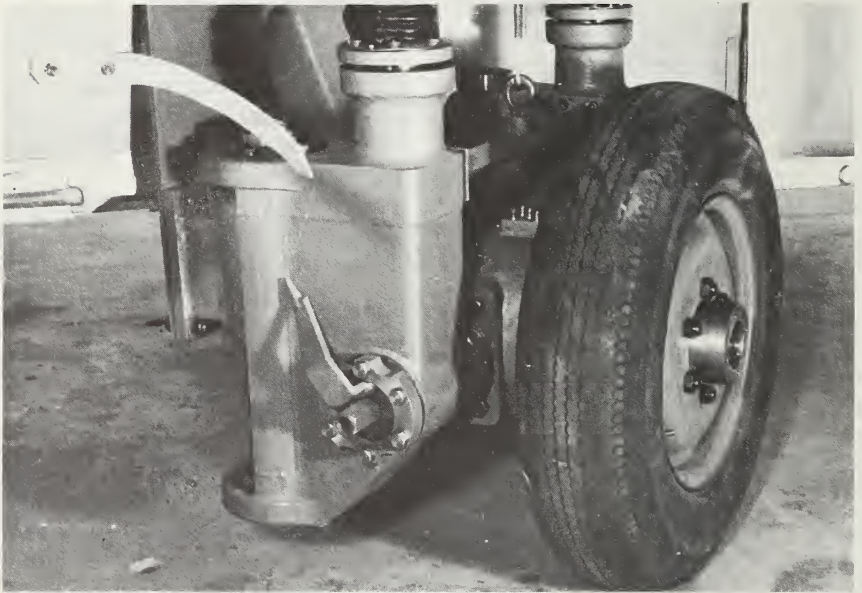


FIGURE 7.2.15. The possibility of mounting the tire at a free end of the measuring axle is shown.

The camber of the tire tester can be adjusted.

Considering the automobile as a two degrees of freedom system, we observe a low body frequency (0.8–2 Hz) and the high axle frequency (10–16 Hz).

Influence of any of these vibrations on actual force variations of the tire requires a tire tester with reasonably high limiting frequencies. After mounting the tire tester in a rigid structure, excitation was impressed with an excitor in all three mutually perpendicular directions. Experiments were made with a loaded tire as well as with wheel and tire removed, the first resonant peak being observed 55 Hz, and flat response curves were obtained up to 30 Hz, deviations beginning at 35 Hz. An

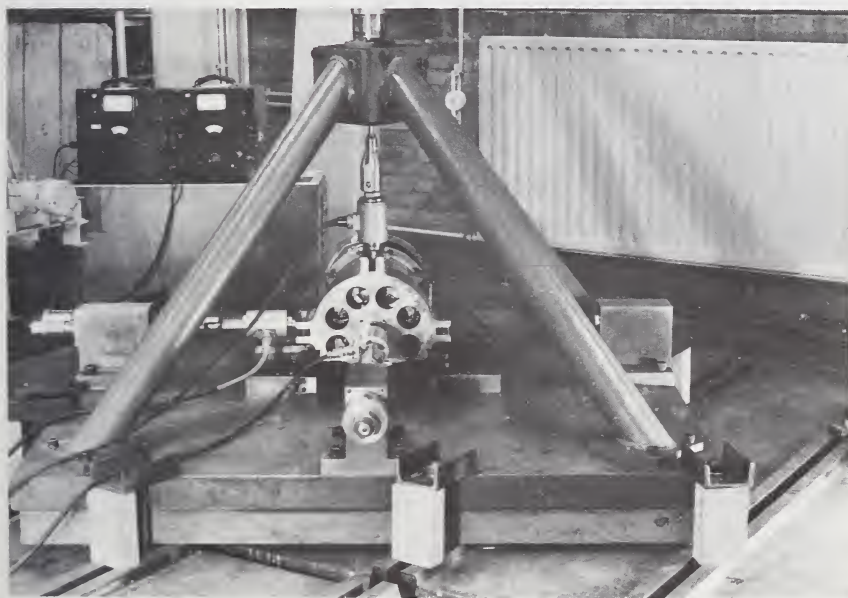


FIGURE 7.2.16. Test rig having three perpendicular axis to calibrate the Delft tire tester.

approximate method was employed to calculate the resonant frequencies of the complex system, and yielded a frequency spectrum close to that determined experimentally. Filters with suitable cut off frequencies were available to eliminate disturbing resonant frequencies [17].

Road Platform Tire Tester

An apparatus for measuring the total forces exerted on a road surface by the wheels of a moving vehicle can be of considerable interest, because it gives information about load transfer, cornering and traction or braking forces of a vehicle passing over the measuring platform [14].



FIGURE 7.2.17. Road platform tire tester having the possibility of measuring three perpendicular forces of a tire moving over the platform.

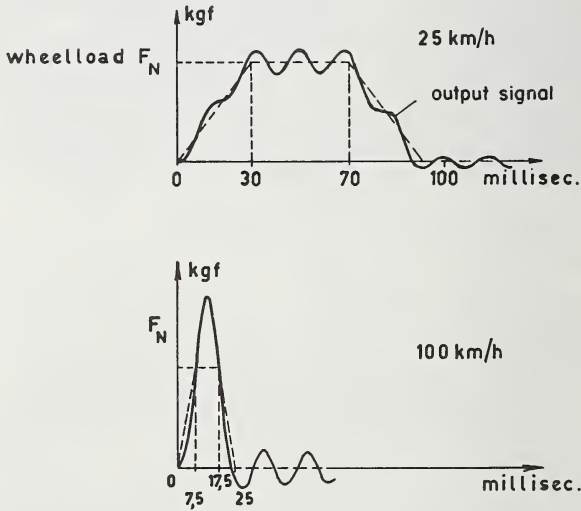


FIGURE 7.2.18. Response curves of the road platform tire tester for vertical tire load at two speeds.

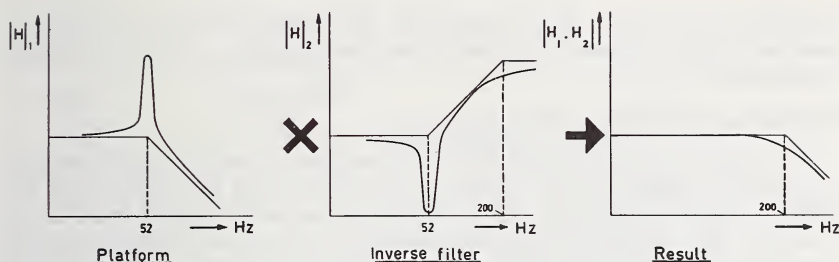


FIGURE 7.2.19. Illustration of results obtained with the road platform tire tester by adding a filter with an inverse transfer function.

A photograph of such a platform with a steel surface table is shown in figure 7.2.17. There is the possibility of bonding various surface materials to the table. The platform is supported by strain gaged bars operating in bending, the strain gages being bonded to the bars in such a way that only shear and vertical forces are measured [18–19].

An approach such as this is satisfactory when measuring total tire forces at low car speeds, because the output signal obtained is not strongly influenced by the excitation of the lowest natural frequency of the platform at about 50 Hz. Figure 7.2.18 shows in dashed lines the supposed trapezoidal load of a tire moving onto, over and off the platform, as well as the output signal obtained at speeds of 25 km/hr.. What happens when the tire passes over such a platform at 100 km/hr. is also illustrated; it is seen that it is impossible to find the trapezoid from the output signal obtained. However, using a filter with an inverse transfer function of the measuring platform [20–21], satisfactory results could be obtained as shown in figure 7.2.19. This example may illustrate that a platform originally intended to calibrate a mobile tire tester on the proving ground, with certain limitations, could also be used as a tire tester.

A better approach is of course to raise the stiffness of the measuring system by replacing the bending elements supporting the table by bars in compression or tension. The same output of the strain gage bridges will be obtained with much lighter bars, having the advantage that the lowest natural frequency will be raised by, for instance, a factor of six. The complicated inverse filter measuring system may be omitted [22].

Besides the possibility of measuring three perpendicular forces F_x , F_y , F_z of a tire moving over a road platform, the position and path of the test wheel with respect to the platform axes have to be known, as will be treated in the sections 7.3.3 and 7.3.5.

7.2.2. Load-Deflection Relationships

In this section the vertical load deflection characteristics will be treated. In addition, some attention will be paid to the longitudinal (tangential) behavior, and to a lesser extent the lateral and torsional char-

acteristics of the tire will be discussed. The latter two types of deformation are directly related to cornering and yaw response of the tire treated in sections 7.3 and 7.5.

Vertical Load-Deflection Relationships

The lowest natural frequency of the vertical vibrations of an automobile is determined mainly by the sprung mass and the stiffness of the wheel suspension springs. This frequency normally ranges from about 1 to 3 Hz. The second resonant frequency is determined by the unsprung mass and the radial tire stiffness. It usually lies in between 8 and 20 Hz. The radial tire flexibility influences the vehicle vertical motion and the time variation of the vertical tire load. The former aspect is important for ride quality, whereas the second aspect indirectly influences the directional stability of the vehicle. Besides, tire flexibility plays an important role in the life of vehicle components and road surface.

When a standing tire (nonrolling, $V=0$) is loaded vertically and afterwards unloaded, a loop in the load-deflection curve is observed, which is due to hysteresis and friction losses [14]. Investigation with a tire rolling on the inner surface of a rotating drum of 3.8 m. diameter [5], shows that the loop area decreases with increasing rolling speed as in figure 7.2.20. It has been generally accepted that the damping produced by the rolling tire is very small, and can be neglected in studies dealing with vertical axle motions of relatively low frequencies. Results obtained with the

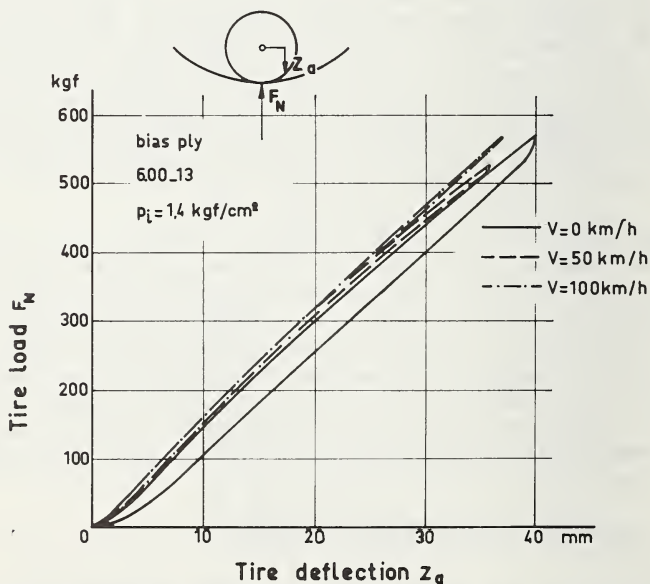


FIGURE 7.2.20. Vertical load deflection relationships at various speeds for a bias-ply tire, obtained on an internal drum machine.

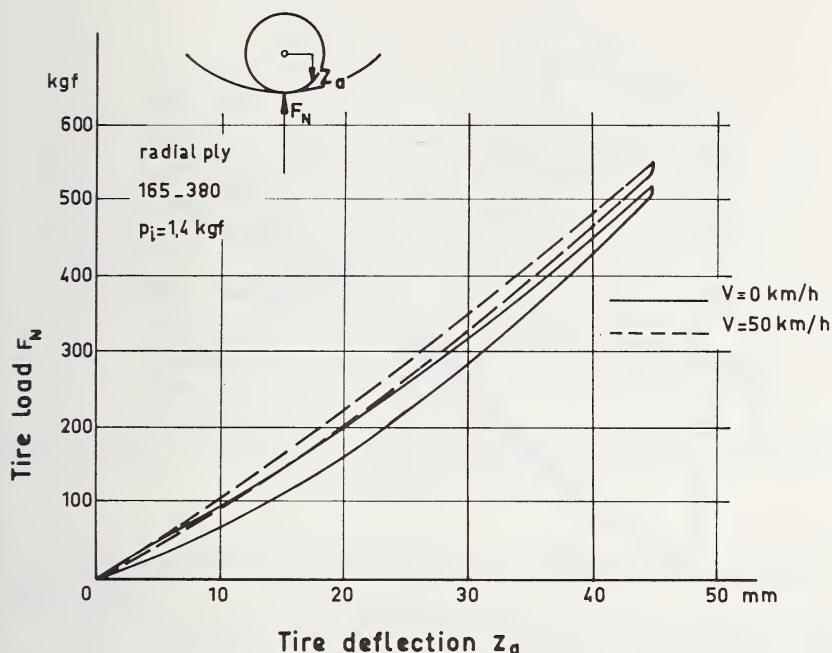


FIGURE 7.2.21. Vertical load deflection relationships at two speeds for a radial ply tire obtained on an internal drum machine.

Delft tire tester are in conformity with the above statement [10]. The curves of figure 7.2.20 furthermore indicate that for the bias ply tire under consideration an increase of the vertical stiffness occurs with increasing speed. The behavior of a radial ply tire shows a similar trend and has been illustrated in figure 7.2.21. The shape of the curves, however, are different [5]. Typical for bias ply tires is the double curved shape. The radial ply belted tire usually shows a progressive load-deflection curve as represented in figures 7.2.22-23. These results were obtained with the Delft tire tester on a drum of 2.5 m. diameter [23-24].

The inflation pressure p_i has a marked effect on the radial stiffness. For a nonrolling bias ply tire the curves shown in figure 7.2.24 have been obtained [5]. Similar results are shown for a 165-13 tire rolling at 5 km/hr. on a steel drum of 2.5 m. diameter [24].

The tire stiffness is composed of a more or less constant part originating from the structural rigidity of the tire, and of a part dependent on the air pressure p_i [25-26]. Under rated conditions, the latter part is predominant. It has been found that the structural rigidity of the aircraft tires may supply 3 to 8 percent of the total stiffness, whereas for automobile tires this percentage may amount to about 15 percent [26-28]. These relatively low percentages explain the considerable influence which the

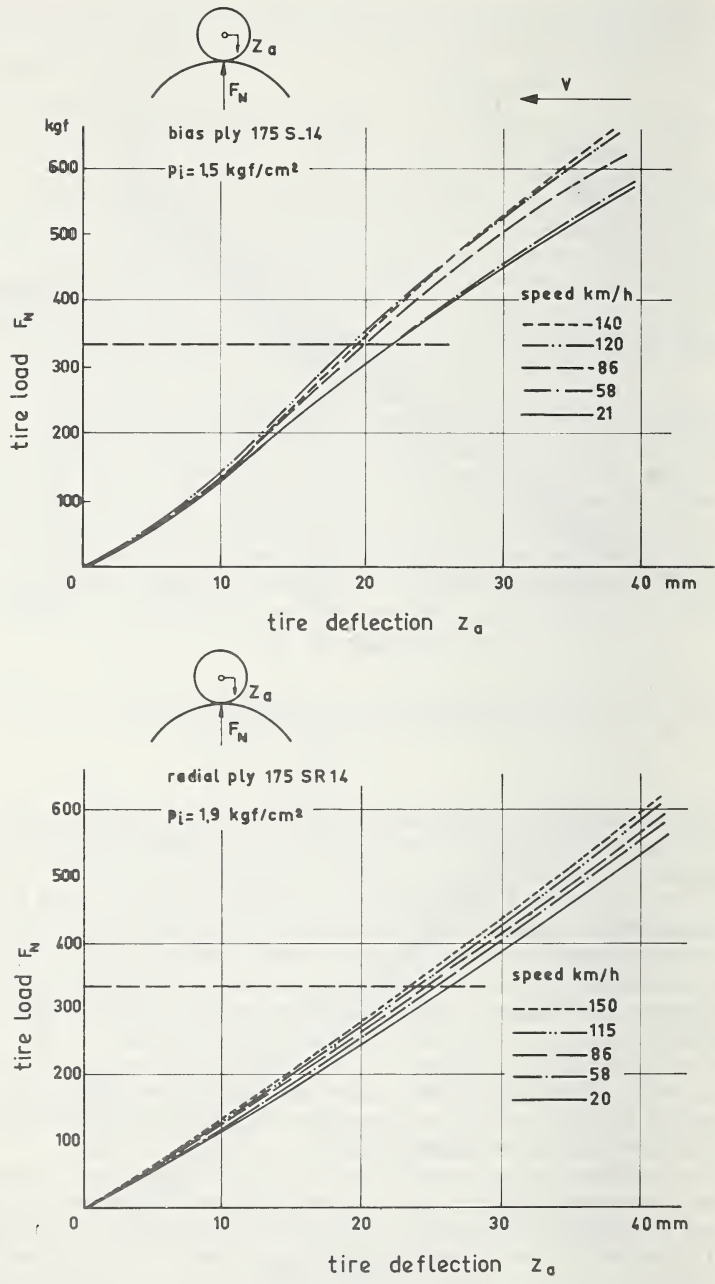


FIGURE 7.2.22. Vertical load deflection relationships at various speeds obtained on an external drum machine for a bias ply and radial ply tire.

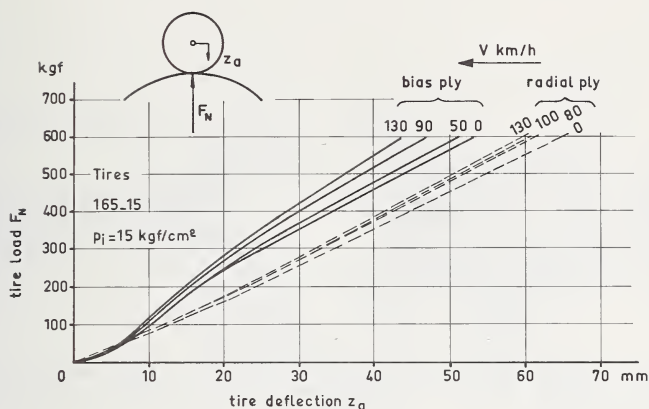


FIGURE 7.2.23. Demonstration of the difference in behavior of a radial ply and bias ply tire at various speeds.

inflation pressure has upon the radial tire stiffness, as indicated in figure 7.2.24.

According to measurements of Henker [5] the radial stiffness of the tire under consideration becomes approximately 20 percent lower when the tire rolls upon an external drum surface, as compared with an internal drum surface of the same diameter. This means that when the tire rolls over a flat surface, the stiffness is expected to become approximately 10 percent lower than values obtainable from the internal drum machine.

It has been often observed that characteristics for both radial and bias ply tires can be approximated very well by straight lines passing through the origin. Only for relatively low values of vertical load does a noticeable deviation from linearity take place. The slope of these straight lines determines the vertical stiffness of the tire, which consequently is assumed to be independent of load in the practical range of interest. Figure 7.2.25 presents the results obtained for the spring stiffness of the tire as a function of speed for a number of values of inflation pressure [29]. It may be noted that according to these experiments, the stiffness of the bias ply tire is very sensitive to the speed of travel. Similar results were obtained with the Delft tire tester as shown in figure 7.2.26. Due to the increase in observed radial stiffness an increase in loaded tire radius (wheel center height) will occur. This increase with speed will become even larger due to the phenomenon of tire growth. Figure 7.2.27 shows the increase of the free tire radius R due to tire growth, and the increase of the loaded radius R_l due to both tire growth and stiffening of the tire [29].

An alternative method for the assessment of the radial stiffness consists in determining the resonant frequency of a single mass spring system with known inertia and spring stiffness of applied load, in series with the resilient tire rolling on a drum or belt [30]. A schematic of this

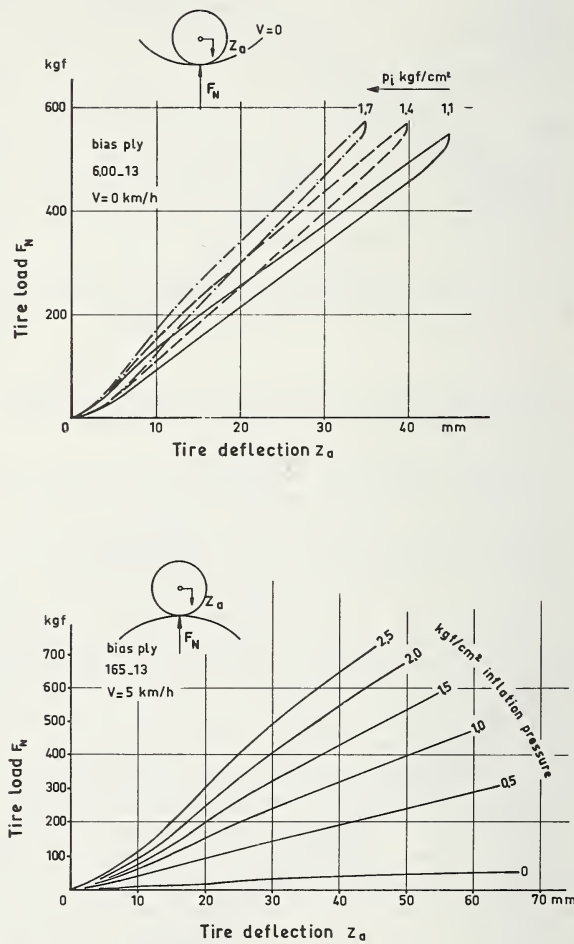


FIGURE 7.2.24. Variation of vertical load deflection relationships as a function of the inflation pressure p_i .

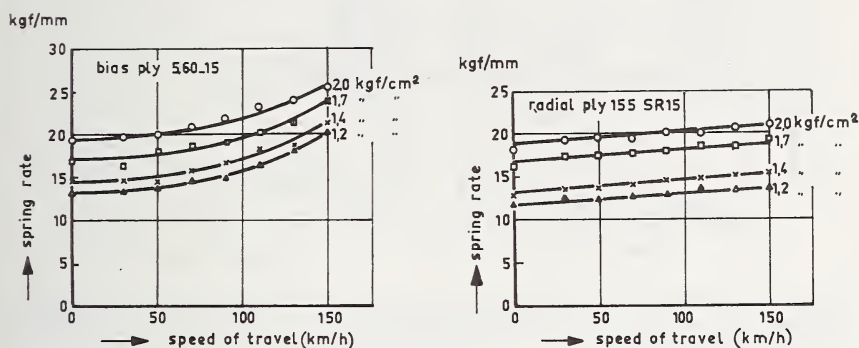


FIGURE 7.2.25. The vertical stiffness or spring rate as a function of speed at various inflation pressures for a bias ply and radial ply tire.

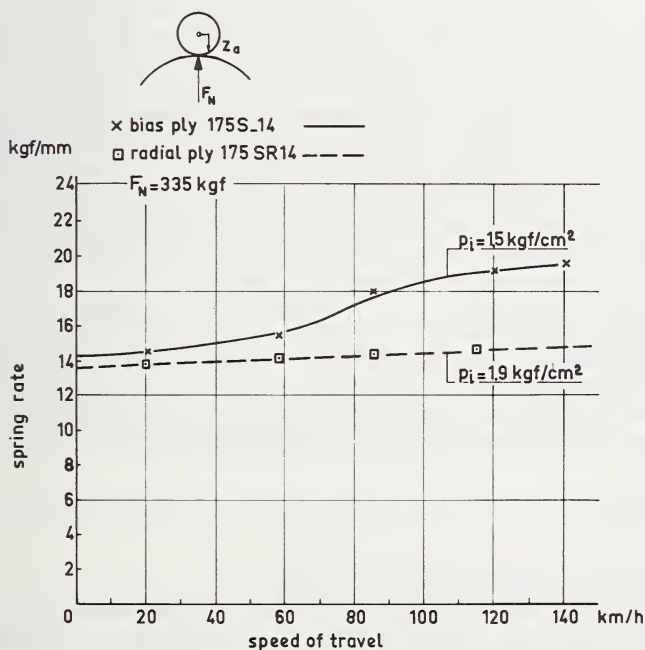


FIGURE 7.2.26. The spring rate as a function of speed, demonstrating the difference in behavior of a bias ply and a radial ply tire.

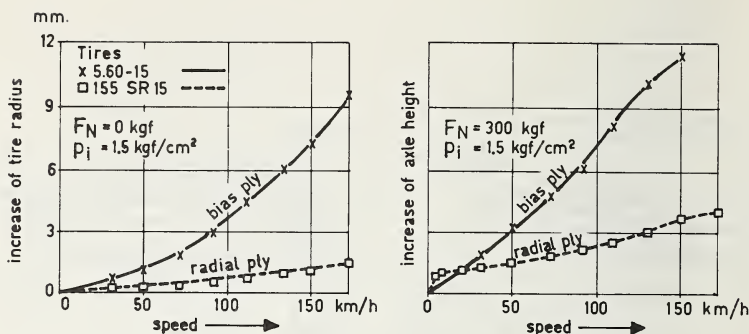


FIGURE 7.2.27. The increase of the free tire radius at $F_N = 0$ kgf as a function of speed, and the increase of the loaded radius at $F_N = 300$ kgf as a function of speed for a bias ply and a radial ply tire.

drum type machine has been shown in figure 7.2.28 operating in the frequency range of 10–15 Hz. The value of the spring rate obtained by this method is called the dynamic tire stiffness, and it is shown that the dynamic stiffness decreases sharply as soon as the tire is rolling. Beyond a speed of about 20 km/hr. the influence of speed becomes less important, as demonstrated in figure 7.2.28. These findings are in contrast to the results as shown in figure 7.2.25 and figure 7.2.26, obtained from the slopes of the load deflection curves at different speeds of rolling. For amplitudes within the range investigated, up to 10 mm., the stiffness of the rolling tire remains nearly constant, whereas a nonrolling tire shows a non linear decrease of the stiffness with amplitude [31].

For further information on tire spring rate the reader is referred to the literature. The influence of preload, inflation pressure, rim width, and cord angle has been discussed in reference [31], the influence of, among other things, speed and drum curvature in references [5.32] and of tire size in references [33–34]. In section 7.2.1 of this chapter the tire loading process and the enveloping properties of the tire have been analyzed.

Horizontal Load-Deflection Relationships

The literature on the horizontal elastic characteristics of the non-rolling tire is scarce. Some of our own unpublished investigations will be discussed below.

The same tires as in figure 7.2.23 and figure 7.2.26, have been examined under rated conditions, and are of the radial and of the conventional bias type.

The tire is now loaded upon a flat cast iron plate, in contrast to the tests described previously. The normal load has been kept constant during

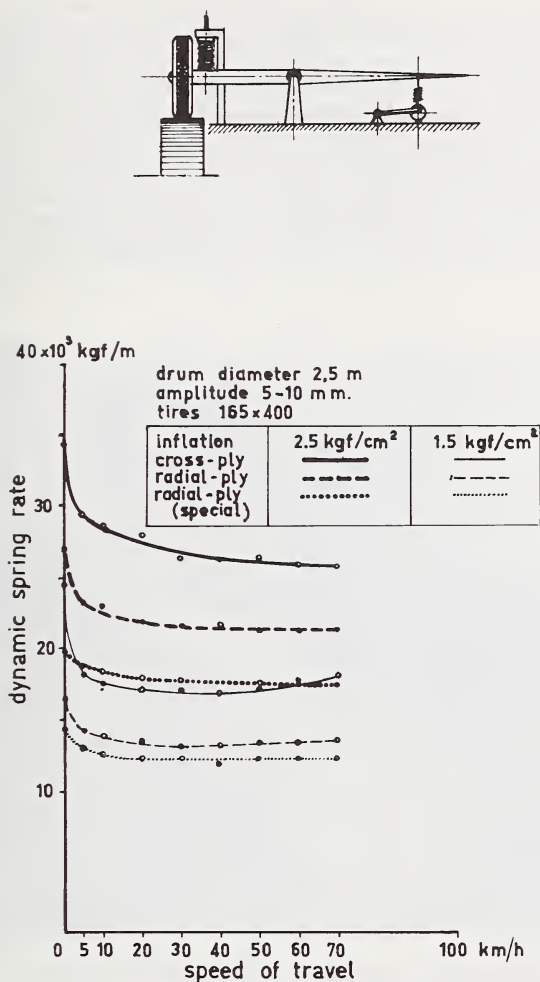


FIGURE 7.2.28. The decrease of the vertical dynamic spring rate as a function of speed.

each test. The measured vertical stiffness of the nonrolling tire amounts to approximately $C_z = 17$ and 20 kgf/mm , respectively. Except for the longitudinal stiffness characteristics, all force and moment measurements have been executed with the six-component measuring hub.

The longitudinal stiffness C_x of a tire is important for the study of longitudinal isolation of disturbances caused by road irregularities. The longitudinal stiffness may be determined in two ways which do not

necessarily give the same results. With the first method, the wheel is fixed in space and the surface upon which the tire is loaded is displaced in the longitudinal direction as shown in figure 7.2.29. With the second method the surface and the wheel axle remain fixed, while the wheel is rotated by a torque about the wheel axis. The resulting tire deformations are different in these two cases. The results obtained with the second method are presented in figure 7.2.30. The deformation rate of all tests was low. The rotation of the wheel has been increased until complete sliding takes place. The longitudinal (tangential) stiffness of the radial ply belted tire appears to be much lower than the stiffness of the bias

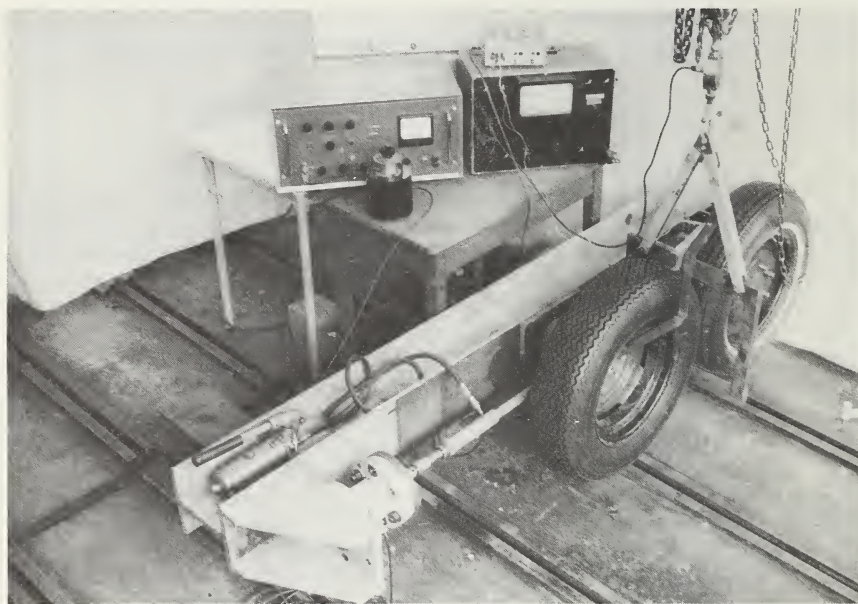


FIGURE 7.2.29. *Measurement of the longitudinal stiffness.*

The left wheel fixed in space is loaded with an identical tire. The force required to displace the steelplate is measured with a dynamometer.

ply tire. At zero longitudinal displacement of the wheel at road level, we obtain for the stiffness approximately $C_x = 27$ and 45 kgf/mm. respectively [35].

The lateral stiffness C_y of a nonrolling tire is important for the relaxation properties of the rolling tire. In combination with the cornering stiffness $C_{F\alpha}$, to be discussed later, the so-called relaxation length can be determined (eq 7.5.51)). The lateral compliance may furthermore give rise to a lateral and yaw vibration of the vehicle with respect to the lower tread portions of the tires.

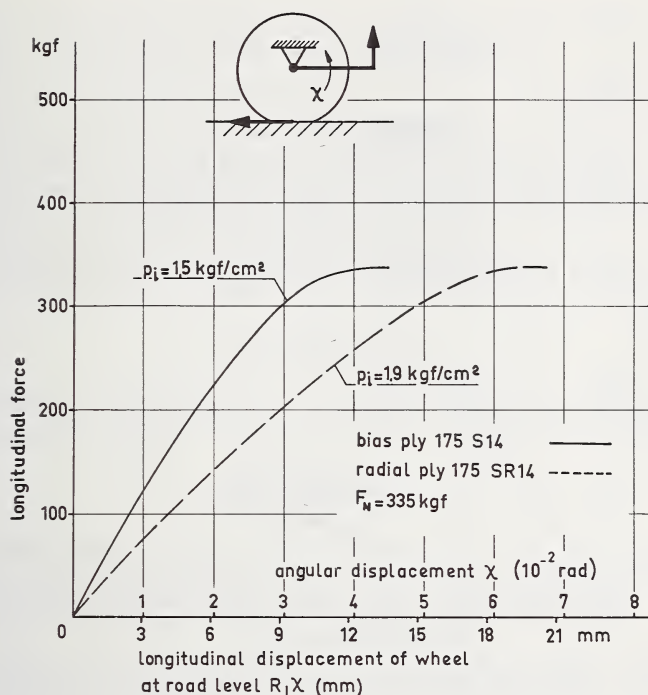


FIGURE 7.2.30. The tangential stiffness of the radial ply tire is much lower than the bias ply tire.

For the same radial and bias ply tires figure 7.2.31 shows the measured lateral force-displacement characteristics. The flat cast iron plate on which the tire is loaded has been moved sideways, until complete sliding takes place. Again the radial ply tire shows a lower stiffness than the bias ply tire. We obtain at zero displacement approximately $C_y = 9$ and 12 kgf/mm , respectively.

Similar results were obtained by another method as reported by the author [10].

The torsional stiffness C_ψ of a nonrolling tire about its vertical axis can be used in combination with the self-aligning torque rate $C_{M\alpha}$ for the determination of the longitudinal tread stiffness parameter κ^* (eq (7.5.120)). The torsional stiffness may furthermore be of value for the assessment of the steering wheel torque required at zero or nearly zero forward speed (parking).

The characteristics obtained are presented in figure 7.2.32. The turning of the wheel about the vertical axis has been continued until full sliding with respect to the flat cast iron plate occurs. Similar to the tests discussed above, the radial tire appears to be more compliant also in this respect. We find at zero angle of rotation approximately $C_\psi = 250$ and 290 kgf/m/rad respectively [35].

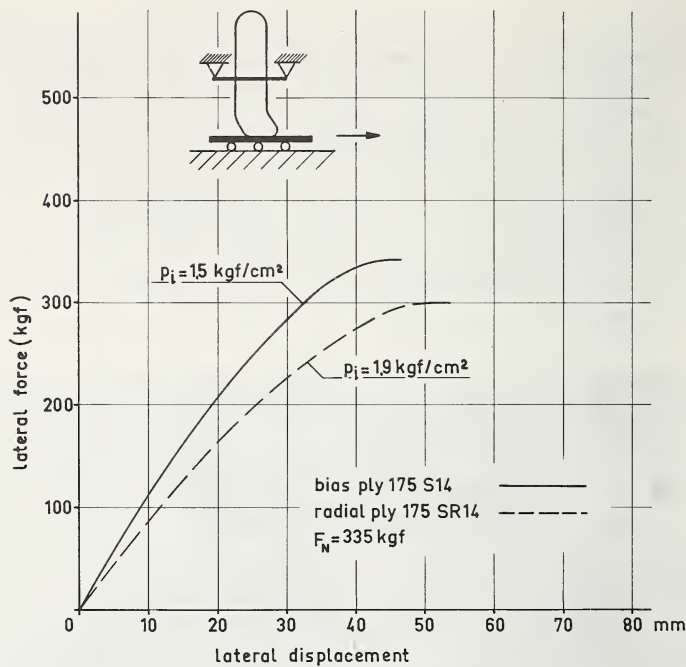


FIGURE 7.2.31. The lateral stiffness of the radial ply tire is much lower than the bias ply tire

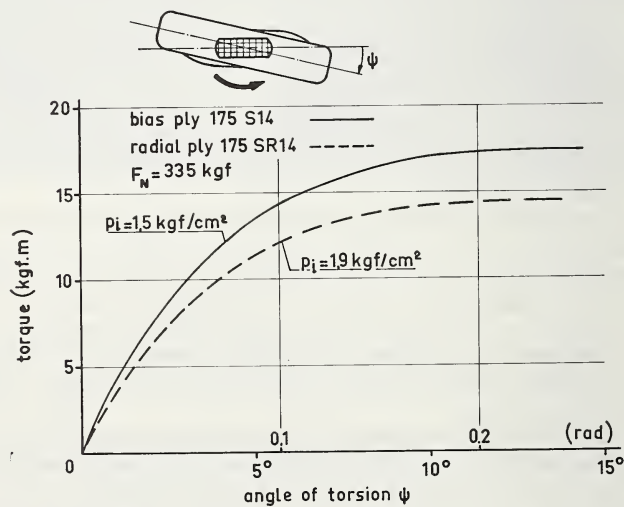


FIGURE 7.2.32. Comparison of bias ply and radial ply tires in their torsional stiffness behavior

In the past similar tests have been executed on the movable platform machine, as illustrated in figure 7.2.5 of section 7.2.1.

Actual Vertical Dynamic Tire Forces

The measurement of dynamic tire force has been required for various purposes, such as car handling, optimizing shock absorber settings, studies of what is decisive in respect to dynamic stress imposed upon the wheel or road when passing over wavy short unevennesses, analysis of enveloping forces of tires passing obstacles, etc.

The dynamic tire force F_z consists of a constant part F_{z0} and a variable part \bar{F}_z . Consequently, we have:

$$F_z = F_{z0} + \bar{F}_z$$

Considering a very simple two mass system such as shown in figure 7.2.33, it seems very easy to find the tire force variations \bar{F}_z from:

$$\bar{F}_z = m_b \ddot{z}_b + m_a \ddot{z}_a$$

The measurement of the accelerations of only the car body and the axle are required. But with such a simplification it is very difficult to calculate the reduced masses involved accurately enough [36-37]. Even with a supposedly rigid car body the actual vibrations are much more complicated, due to rolling, pitching, bouncing, etc. Acceleration measurements usually fail to give results accurate enough to yield useful data on actual tire forces.

To measure the dynamic tire force \bar{F}_z during road tests, the tire is considered to have no damping. We obtain \bar{F}_z by measuring the tire deflection through the variable distance between axle center line and the ground, and by assuming a known value of the radial stiffness C_z . It follows from figure 7.2.33 that:

$$\bar{F}_z = C_z(z_c - z_a)$$

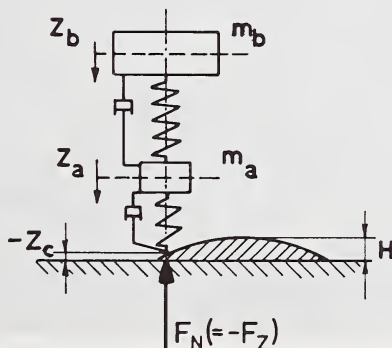


FIGURE 7.2.33. Model of two mass spring system passing over an uneven road surface.

The radial tire stiffness C_z may be obtained as a function of speed from laboratory drum tests. This test method can be refined by using an electrohydraulic vibrator to shake the rolling tire at different amplitudes and frequencies [23–31].

In other cases the frequency sensitivity is obtained by mounting the test wheel in a stiff frame with an actuator plate moving the footprint up and down. But it should be noted that results in this case are obtained with a nonrolling tire, and the influence of the deformation of the cross section of a rolling tire due to centrifugal forces cannot be taken into account. It will be very difficult to correct for an “effective” tire mass in this case. Having discussed the radial tire stiffness, we observe several methods of measuring the tire deflection.

The Mühlfeld antenna system [38] measures the variable capacity of a moving condensor plate above the ground, and requires a plate area of about 25×25 cm. As a consequence, dynamic tire loads due to road unevenness of half wavelength less than 25 cm. cannot be accurately measured. There is thus some uncertainty of the value of the dynamic tire stiffness when passing over a short obstacle.

Another system introduced by von Bomhard [39, 90] measures the variation of the width of a cross section of the tire. Later modifications having sensing devices with a roller assembly measure the position of a point on the left and right hand side of the tire wall as in figure 7.2.34.

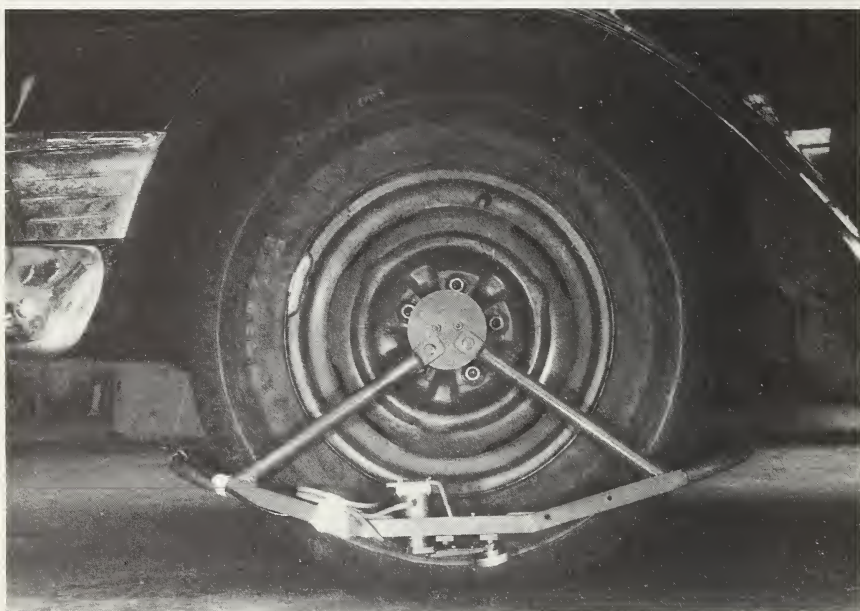


FIGURE 7.2.34. *Method of obtaining the vertical dynamic tire force by measuring the variation of the width of a cross section of the tire.*

The buffing ribs of the side walls in contact with the rollers have to be ground to correct for the lateral tire nonuniformity. The normal procedure of averaging left and right hand displacements of the tire wall as a measure of the vertical load gives erroneous results when rolling under a slip angle. It is seen from figure 7.2.35 that the lateral and radial displacements of a point on the tire wall are very much dependent on the value of the slip angle [40]. The method of making these measurements is illustrated in figure 7.2.36. As can be seen from the photograph, a point

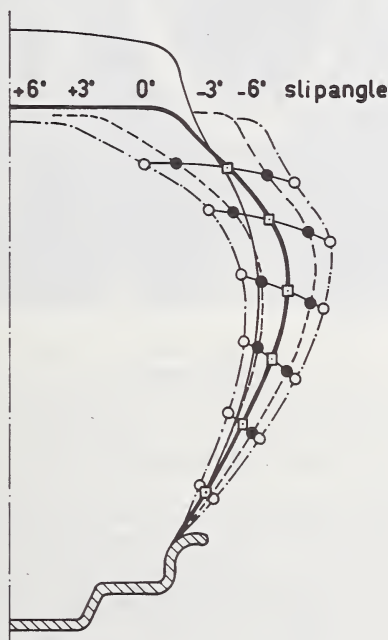


FIGURE 7.2.35. Influence of the slip angle on the lateral and radial displacements of a point on the tire wall.

on the tire wall is contacted by two spring loaded wires, which are perpendicular to each other, the wires being attached to potentiometers. This method, shown in figure 7.2.34, can only be used in straight line rolling on relatively smooth roads when no lateral forces are present, and corrections have to be made for the speed dependent character of the tire width.

The radial and lateral displacement of a point on the tire wall is also very much dependent on the position in degrees from the contact

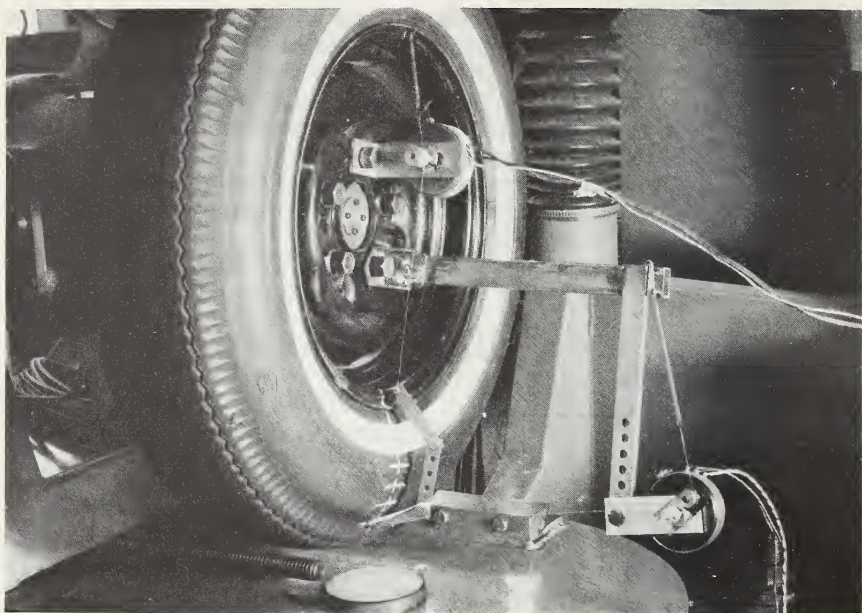


FIGURE 7.2.36. *Method of measuring the lateral and radial displacements of a point on the tire wall.*

center (fig. 7.2.37) due to the buckling effect in the center of the contact zone [40].

Attempts have been made to measure the tire deflection at a point in the wheel center plane at the inner liner of the tread when passing through the contact zone (fig. 7.2.38). A spring loaded flexible cable was bonded to a piece of canvass attached to the inner liner of the tire, while the other end of the cable was connected to a potentiometer mounted in the wheel rim of a tubeless tire. The restraining spring was relatively stiff in order to give a frequency response compatible with the large accelerations of the tread when passing through the contact zone, resulting in a low life of the potentiometer bearing. A photocell device was used to trigger the instant of passing through the center of the contact zone. Because the potentiometer reading had to be corrected for the speed dependent character of the tire tread deflection, and on rough roads the slider vibrated upon the potentiometer windings, this method appeared to be too complicated and unreliable.

Various other sensing devices have been proposed to measure the tire deflection of a point in the wheel center plane at the inner liner of the tread when passing through the contact zone. Such devices are based on the measurement of the variation of the resistance [40-42], capacitance or inductance, on photocell counter devices for light beam pulses, on the detection of the variation of the radioactivity of an emitter

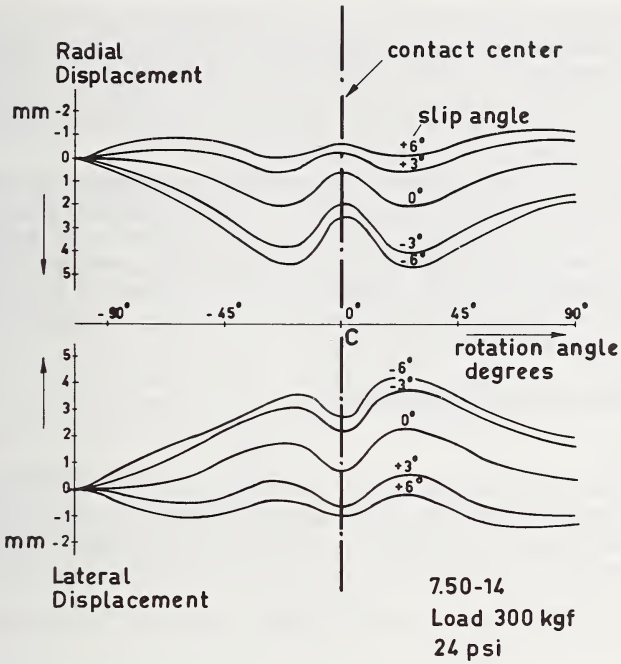


FIGURE 7.2.37. Variation of the lateral and radial displacements of a point on the tire wall as a function of the wheel rotation through the contact center.

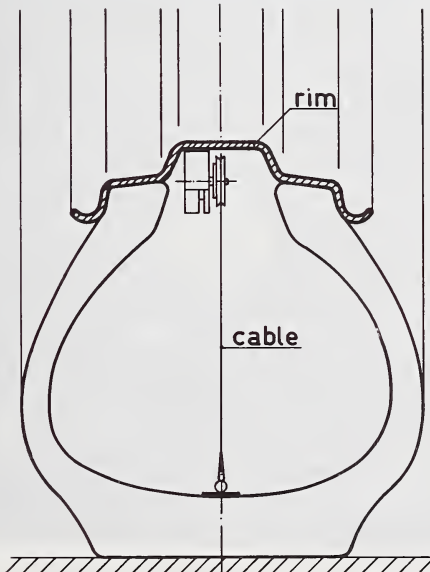


FIGURE 7.2.38. Measurement of the radial tire deflection with a spring loaded cable connected to a potentiometer.

plate mounted in the tread, etc., but all methods apparently are without success under conditions of a combination of traction and cornering [40].

Another method used the measurement of the variation of the signal from a strain-gaged symmetrical rim, but due to the momentary position of the strain gage bridge the load variations cannot be accurately measured when passing over an obstacle [43-44].

The method of measuring inflation pressure changes has also been reported for a tire rolling over a cleat on a test wheel [45]. The very small change in inflation pressure of the tire was detected with a differential manometer mounted outside the test tire, and this pressure change can be related to the process of envelopment of the obstacle. A similar method was adopted with a sensing device mounted at the rim inside a tubeless tire.

7.2.3. Effective Rolling Radius

Introduction

An analysis of the deformations of a rolling tire shows that the effective rolling radius R_e is the ratio of the linear velocity V of the wheel center in the X -direction to the angular velocity Ω of the wheel:

$$R_e = \frac{V}{\Omega}$$

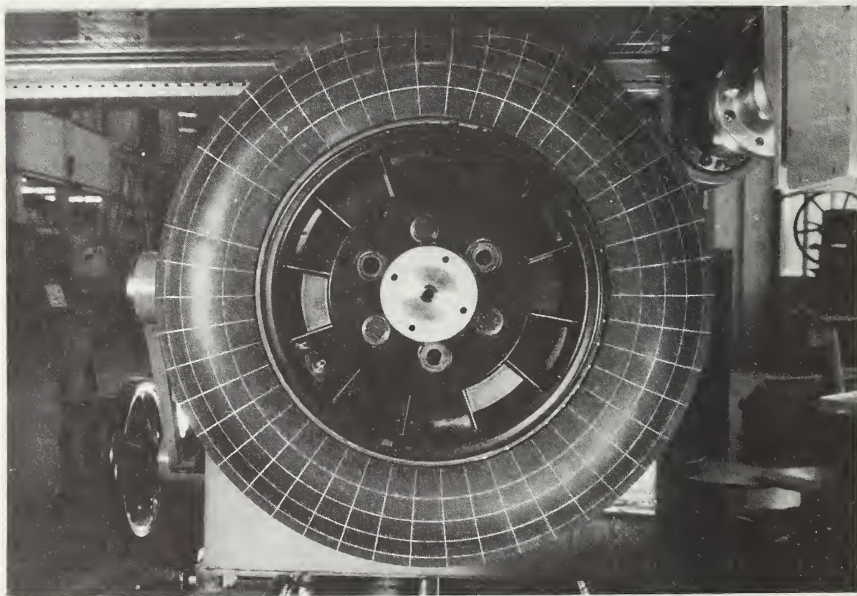


FIGURE 7.2.39. Measurement of free radius R , loaded radius R_l and effective radius R_e on the movable platform machine.

The effective rolling radius is often erroneously assumed to be equal the center height h or so called loaded radius R_l , being the distance from the center of tire contact to the wheel center. When R is the undeflected free tire radius, it will be shown that:

$$R_l < R_e < R$$

that is, the rolling tire travels farther per revolution than determined by using its center height as rolling radius, but less than described by the free tire radius.

A rolling wheel may be considered as a wheel rolling along the stationary ground, or the center of the wheel may be taken as fixed, so that the ground moves relative to it. Both cases will lead to correct results and the latter case is represented in the flat platform machine.

Consider figure 7.2.39, which represents a tire on a flat platform machine with a number of equally spaced radii, drawn on the surface of the undeflected free tire, dividing the circumference into n equal elements, each with length $l = \frac{2\pi R}{n}$.

It is observed from the photograph that tread elements in the zone immediately before contact are compressed, as well as elements in the area just after contact has been lost (fig. 7.2.40). Due to compression the tread elements in the contact zone are shorter, and therefore in $\frac{1}{n}$ of a

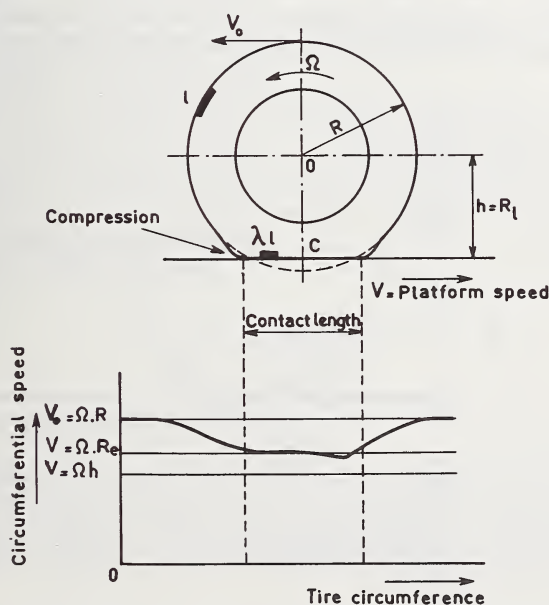


FIGURE 7.2.40. Circumferential speed of a tread element when passing through the contact zone.

revolution of the wheel, the platform moves a distance λl , which is less than length $l = \frac{2\pi R}{n}$. This is the same as saying that when the platform moves a distance $2\pi R$, the wheel will turn more than one revolution.

From tests with a nominal loaded tire under straight line rolling conditions we also observe very little longitudinal slip in the contact area (resulting in almost no wear), so that the compressed tread elements will travel with the platform speed V .

When the circumferential speed of the undeflected upper part of the tire is called V_o , we find [24]

$$n = \frac{V_o}{l} = \frac{V}{\lambda l} \quad V = \lambda V_o$$

$$\left. \begin{array}{l} V_o = \Omega R \\ V = \Omega R_e \end{array} \right\} \quad R_e = \lambda R$$

$$R_l < R_e < R$$

This was demonstrated experimentally by several authors [46–47] and is in accordance with the situation shown in figure 7.2.41, where the wheel center O is maintained fixed and the platform, in position 1, moves to the right over the distance X . Then the point of the tire surface ini-

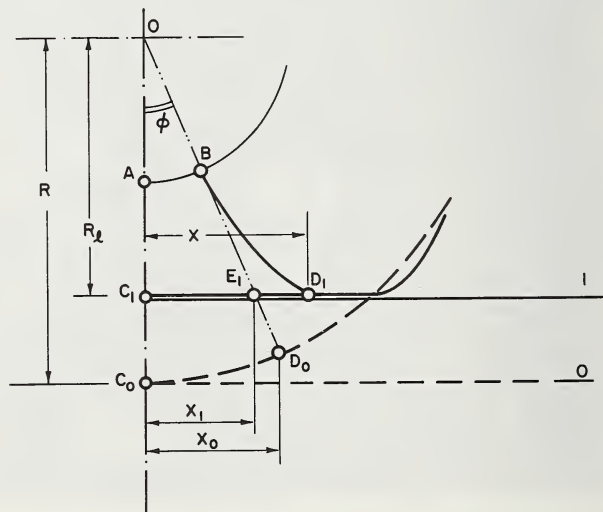


FIGURE 7.2.41. Deformation of a tire on a movable platform when a radial load is applied.

tially at C_1 moves to D_1 . Simultaneously, the point of the tire at the rim of the wheel A moves to B . The wheel thus rotates over the angle $AOB = \varphi$. The distance between the center of the wheel and the platform in the position 0 (no load) and position 1 (loaded) is $OC_0 = R$ and $OC_1 = R_l$ respectively [47]

$$C_1 D_1 = X = R_e \cdot \varphi$$

$$C_1 E_1 = X_1 = R_l \operatorname{tg} \varphi$$

$$X_0 = R \sin \varphi$$

whence $\frac{R_e}{R_l} = \frac{X}{X_1} \cdot \frac{\operatorname{tg} \varphi}{\varphi}$ and $\frac{R_e}{R} = \frac{X}{X_0} \cdot \frac{\sin \varphi}{\varphi}$

For φ not too large, $\operatorname{tg} \varphi / \varphi$ is slightly larger and $\sin \varphi / \varphi$ is slightly smaller than unity.

Instead of an effective rolling radius, an effective deflection $\delta_{\text{eff}} = R - R_e$ can be introduced, which differs from the actual deflection $\delta = R - R_l$.

Methods of Measuring Effective Radius

A. Movable platform (fig. 7.2.39)

Flat surface machines have the limitation of low speed, but good control of variables can be achieved.

The radial load is applied and measured by means of a load cell, the free radius R and loaded radius R_l are measured with a scale.

When the platform is moved over a measurable distance X , the corresponding angle of rotation φ of the wheel is determined by means of a scale and pointer or other suitable instrument attached to the supporting structure and wheel rim respectively.

The effective rolling radius is:

$$R_e = 180 \frac{X}{\pi \varphi}$$

when φ is measured in degrees.

B. Drum tests

After conditioning the test tire at the required load, inflation pressure and speed, the effective radius is determined by the ratio of the circumferential drum speed V and the angular velocity Ω of the test tire,

$$R_e = \frac{V}{\Omega}$$

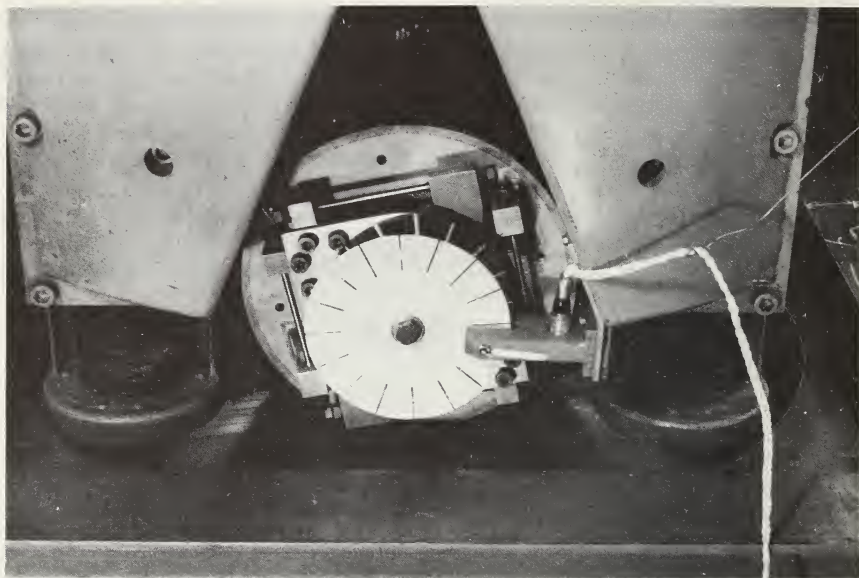


FIGURE 7.2.42. *Photocell counting device for measurement of angular velocity.*

The angular velocity is accurately measured with a photocell counting device as in figure 7.2.42, which may be equipped with continuous recording for the angular velocity [10, 24].

The variation in the effective rolling radius per wheel revolution due to tire nonuniformities can also be measured with drum tests (sec. 7.2.6). Nonuniformities produce angular wheel accelerations that result in tangential force variations as measured with a tire tester or uniformity machine.

The free radius R of the tire can be measured at a given speed through skimming contact with the drum, by measuring the distance between wheel center and the surface of the rotating drum. (See also tire uniformity machine, sec. 7.2.6 (fig. 7.2.81)).

C. Road tests

Road tests have been reported [48] by driving an automobile at walking speed over a measured distance and counting the number of revolutions of the free rolling front wheel. Tests were run with several tires at various inflation pressures.

Parameters Affecting the Effective Radius

A. Carcass construction

Factors influencing the deformations of the rolling tire, such as carcass construction, tread thickness, number of plies, cord type and

cord angle, rubber compound, etc., will also influence the effective radius.

Experimental results, obtained with the Delft tire tester mounted in a rig with loading device above a drum 2.5 m. in diameter, show the difference in behavior of a conventional bias compared with a radial-belted tire.

Using $R_e = \lambda R$, the conventional bias tire shows a value of $\lambda = 0.96$ and $h = R_l = 0.94R$.

For the radial ply construction with an inextensible belt, having less compression of the tread elements when passing through the contact zone, values of $\lambda = 0.98$ were obtained. The radial deflection of this tire is more than in the former case, giving a value of $R_l = 0.92$ [24].

B. Effect of tire load and inflation pressure

An increase in load at constant pressure results in a larger deflection of the tire. Due to an increase of the compression of the tread, a decrease of the effective radius is observed shown in figure 7.2.43.

A decrease of inflation pressure has the same effect as an increase of tire load.

C. Effect of speed

The effect of speed is shown in figure 7.2.43 for a conventional bias tire, as measured on a drum of 2.5 m. in diameter. Due to larger centrifugal forces at higher speeds the tire will grow, resulting in an increase of effective radius R_e , increase of loaded radius R_l and an increase of free radius R . This effect will be almost negligible for the radial belted tire, due to its inextensible belt as shown in figure 7.2.44.

Other measurements obtained from an internal drum of 3.8 m. in diameter on a conventional bias tire 5.60-15 and a radial belted tire 155 SR 15 also show the difference in behavior of these tires [29].

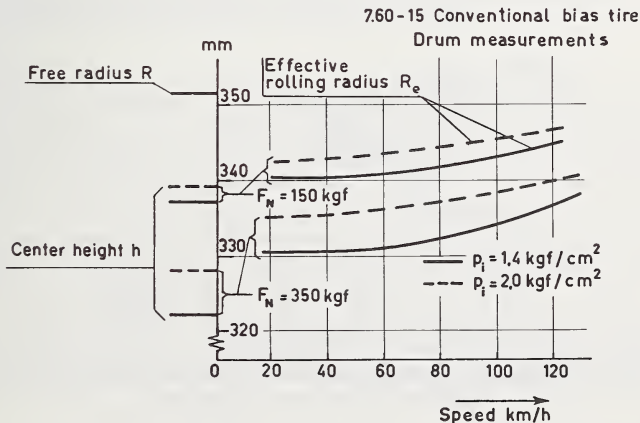


FIGURE 7.2.43. Effect of tire load and inflation pressure on the effective radius as a function of speed.

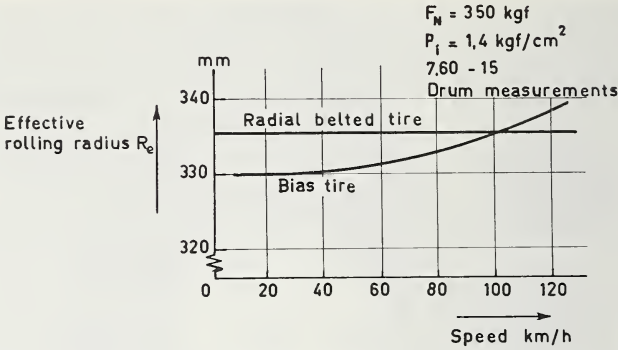


FIGURE 7.2.44. Variation of the effective radius as a function of speed for a bias and radial belted tire.

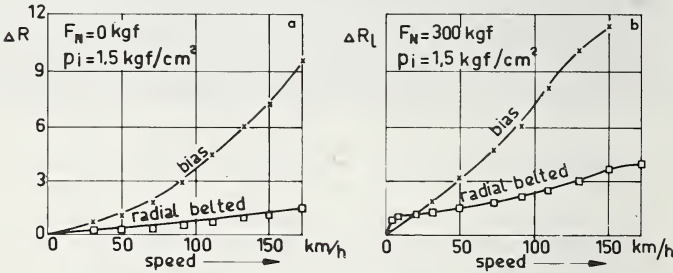


FIGURE 7.2.45. (a) The increase ΔR of the free radius R as a function of speed under zero load condition for a bias and radial belted tire.
(b) The increase ΔR_L of the loaded radius R_L as a function of speed for a bias and radial belted tire.

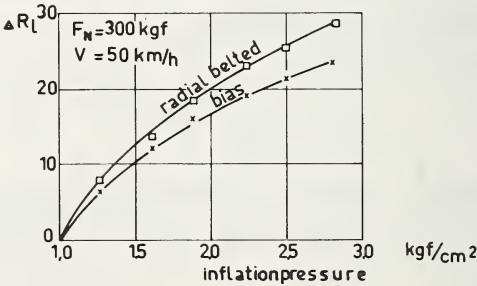


FIGURE 7.2.46. The influence of the inflation pressure on the increase ΔR_L of the loaded radius for a bias and radial belted tire.

The influence of increase of inflation pressure from 1.0–3.0 kgf/cm.² on the unloaded radius R was negligible (1 mm.). The increase of the free radius ΔR with speed for both tires under zero load conditions is shown in figure 7.2.45a while the increase $\Delta R = \Delta h$ of the loaded radius R_l at a load of 300 kgf. is illustrated in figure 7.2.45b. The influence of inflation pressure at constant load of 300 kgf. and constant speed of 50 km/hr. is illustrated in figure 7.2.46, showing the largest increase ΔR_l in loaded radius for the radial belted tire.

The influence of different speeds and loads for the conventional bias tire is shown in figure 7.2.47. The decrease ΔR_l at “zero” speed was actually measured at approximately 2 km/hr.

D. Effect of braking and traction

The effect of tangential loading on the effective radius through braking or traction forces will be discussed in section 7.2.5.

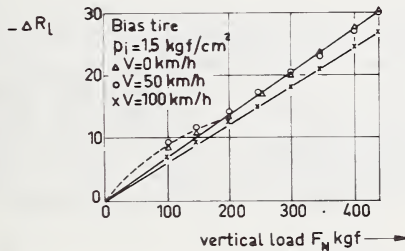


FIGURE 7.2.47. The influence of the variation of the vertical load and speed on the decrease ΔR_l of the loaded radius for a bias tire.

7.2.4. Rolling Resistance

Introduction

The rolling resistance of a free rolling tire is mainly caused by the internal friction in the rubber and cord, while the slip in the contact zone and the windage losses at moderate speeds are of less importance. Slippage of tread surface on the road is about 5–10 percent of the total losses, while the drag due to air friction represents 1–3 percent of the total loss. Other factors influencing the rolling resistance are bad road conditions, involving large tire deflections, the presence of snow or the deformation of soft soil.

At constant speed, a free rolling wheel requires a horizontal force F_r in the wheel center to overcome the rolling resistance. The balance of moments around the wheel center is shown in figure 7.2.48

$$F_r \cdot h = F_N \cdot f_r$$

where F_N = load carried by the wheel h = axle height above the ground.

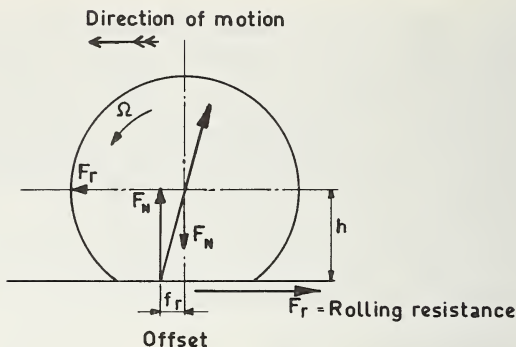


FIGURE 7.2.48. Rolling resistance of a free rolling tire.

The rolling resistance force F_r is the resultant of the longitudinal tangential stresses in the contact patch, while the resultant F_N of the normal force distribution has an offset, ahead of the contact center as in figure 7.2.49. The rolling resistance is commonly expressed per unit of load of the tire, thus lb./1000 lb. or kgf./1000 kgf. The unit of load varies in some cases, such as earthmover tires, where it is defined as the resistance per ton of load or for bicycle tires where it is given in lb./100 lb. or kgf./100 kgf. The coefficient of rolling resistance f_r is defined as

$$f_r = \frac{F_r}{F_N} \text{ or, expressed as a percentage, } f_r = \frac{F_r}{F_N} \times 100\%.$$

The rolling resistance of a tire is dependent on the load, inflation pressure, temperature, road conditions and speed. The level of the rolling resistance ranges from 10 to 25 kgf./1000 kgf. for passenger sizes, whereas for commercial sizes these values vary from 5 to 15 kgf./1000 kgf. The power loss or power consumption is defined as the horsepower used by the rolling tire at the indicated speed and under the stated conditions of load and inflation.

Methods of Measuring Rolling Resistance

A. On the road

Several methods are used to measure the rolling resistance on the road under exact working conditions [49].

- a. Towing a vehicle at constant speed.
- b. Allowing a vehicle to coast and measure the rate of deceleration.
- c. Measurement of the torque in the drive shaft of the vehicle required to maintain its speed.

It has been found extremely difficult to find the rolling resistance accurately from these tests, because it is not easy to separate other friction from the measured results.

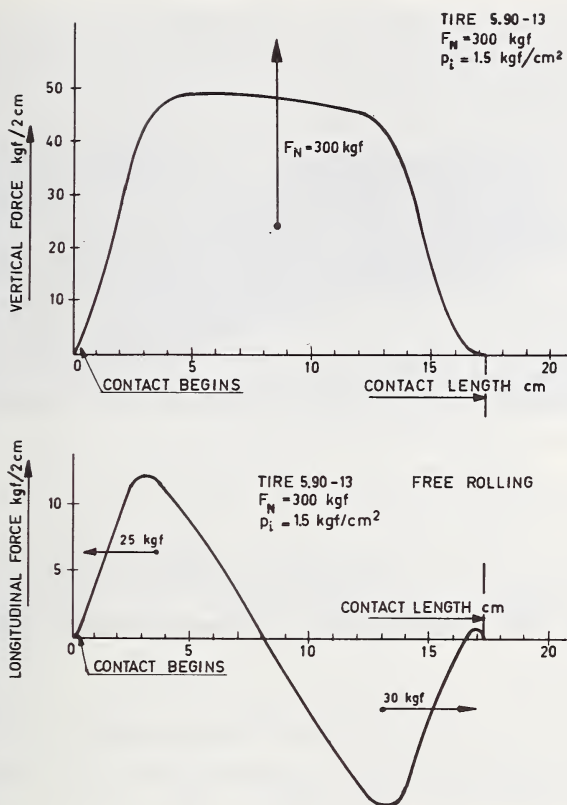


FIGURE 7.2.49. The vertical force and longitudinal force distribution over the contact length of a free rolling tire.

The principal method of towing a trailer has been refined by towing a shrouded passenger car over a range of speeds, and measurement of the forces between the shroud and the enclosed vehicle (fig. 7.2.50a, b). This approach, due to the Motor Industries Research Association of Great Britain, involved the isolation of a complete car from aerodynamic forces by a plywood enclosure mounted on a two-wheeled light weight trailer with sheet rubber skirting attached to the bottom of all the sides.

A similar arrangement is the towing of a shrouded single wheeled trailer at constant speed, and measuring the towing force by means of a dynamometer.

Because the horizontal force to be measured is only about 1 percent of the vertical load on the trailer, the determination of differences due to load changes, air pressure, or tire construction characteristics calls for an extremely high accuracy of measurement and carefully controlled conditions of operation [50].

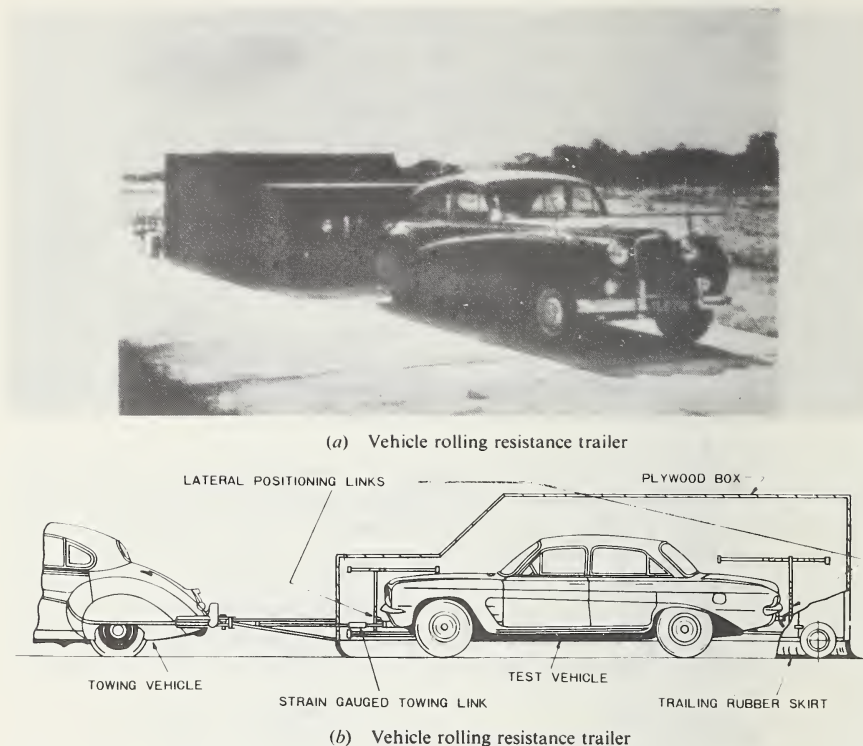


FIGURE 7.2.50. *Method of measuring the rolling resistance by towing a shrouded passenger car.*

Difficulty has been experienced in obtaining a constant pull at constant speed, because of the inertia of the trailer, but results are also dependent on the gradient of the test road surface, the friction of the wheel bearings, climatic conditions, etc. It is almost impossible to control the tire temperature. In view of all these difficulties, it is generally accepted that indoor machine tests give more reliable comparative values between different tires or operating conditions.

B. Indoor Machine Tests

Practically all methods measure the rolling resistance by loading the tire against a smooth-faced steel drum, and by accepting that significant differences in tire behavior are induced by the curvature of the drum so that the values obtained are not those which would be obtained under actual road conditions. The obvious advantages are that it is comparatively simple to maintain control over the variables speed, load, inflation pressure and temperature.

Four methods are used to determine the rolling resistance under free rolling conditions:

- a. In the *inertia method* the tire is loaded against a drum of known moment of inertia and the horsepower consumption of the tire is found from the rate of deceleration of the drum through the chosen speed or range of speed. The test is repeated with the tire in skimming contact under zero load and the drum slows under bearing friction and the windage of the drum and tire. From both speed-time curves the rolling resistance is determined. This simple method has the disadvantage that it is impossible to determine the rolling resistance under stationary conditions at a given speed, and only limited control of temperature is possible [49-51].
- b. In the *torque-shaft method* the torque M can be determined on the shaft in the drive to the drum by measuring the twist of a torsion shaft. The twist is measured both with the tire in skimming contact and with the tire loaded against the drum. The difference between the torques is used to determine the rolling resistance or the coefficient of rolling resistance f_r , and can usually be measured with an accuracy of 0.5-1.0 percent [52].
- c. In the *motor torque reaction method* the motor driving the drum is trunnion mounted in order to measure the torque reaction in the stator by a rigidly attached moment arm which engages with a spring balance or a load cell [51]. The measuring technique is the same as in test (b), and in both methods constant speed is very important to avoid errors due to acceleration and deceleration of high inertia test drums.
- d. The tire to be tested with the *six-component tire tester* is mounted in a rig with a loading device above the drum (fig. 7.2.51). This method calls for an extremely high accuracy in placing the center of the tire in a vertical direction above the centerline of the drum. It is convenient to average results obtained from tests with clockwise and counterclockwise rotations of the drum.

Tire Conditioning

Since the rolling resistance of a new tire decreases during the first hours of running, the tires are preconditioned by running them 2-15 hours at about 50 km/hr. under 80-100 percent of their maximum scheduled load and inflation pressure. The tire will deform from its cured state to an equilibrium condition by adjusting its localized stresses internally. A distance of 150-300 km. is, however, often considered sufficient as a break-in period to bring the tire down to its ambient level of power loss [53].

After preconditioning, the load, speed, and inflation pressure are adjusted to the desired values for test, and the tire is run until the temperature of the air contained within the tire remains constant for at least 10 minutes. Readings of rolling resistance and the temperatures of the contained air and the ambient air are recorded. Immediately after readings are taken, the tire is lifted from the drum and stopped. Then the tire temperature is measured by a thermocouple needle at about four pre-selected points in the shoulder and in the tread.

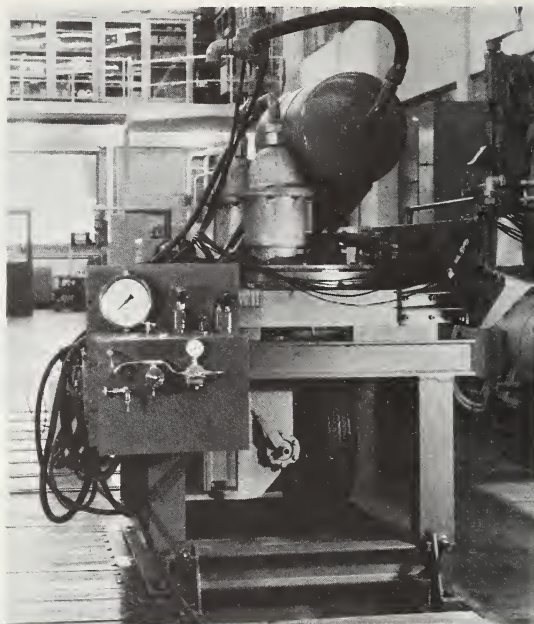


FIGURE 7.2.51. *Mounting of the six-component Delft tire tester in a rig with an air-spring loading device above the drum.*

The sequence of measuring the various combinations of load, speed, and inflation are varied in accordance with a statistical design, in order to eliminate systematic bias [54].

Parameters Affecting the Power Loss

The most important factor influencing the power consumption in the rolling tire is the hysteresis of the materials, representing 90–95 percent of the total power loss. Decrease of the deformation of the tire during rotation through the contact zone and decrease of vibrations after deformation will help to minimize the power loss, as well as optimizing the tire structure and rubber compound to lower hysteresis loss [53].

A. Effect of tire load, radial deformation and inflation pressure.

An increase in load at constant pressure and speed results in larger tire deflection and consequent increase in rolling resistance as illustrated in figure 7.2.52.

An increase in inflation pressure at constant load and speed results in less tire deflection, lower hysteresis loss and consequently, less rolling resistance [55]. It also may reduce the amount of scrub because it reduces the size of the contact area.

B. Effect of speed.

The effect of speed is shown in figure 7.2.53 with constant load and con-

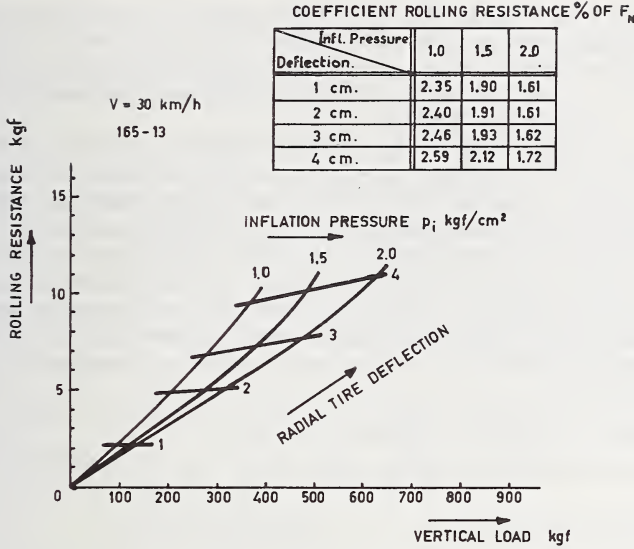


FIGURE 7.2.52. Effect of vertical tire load and inflation pressure on the rolling resistance.

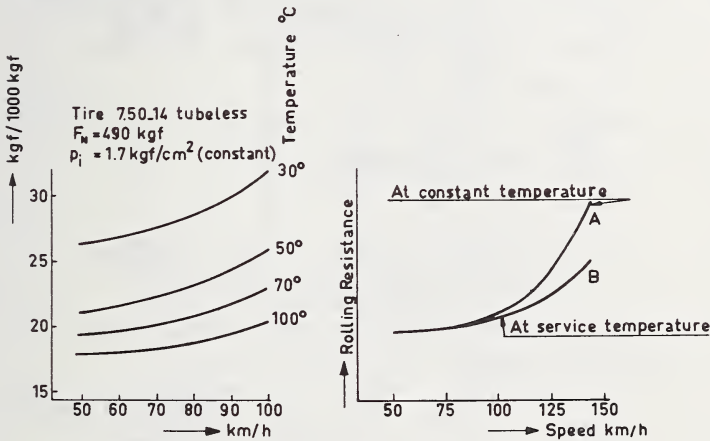


FIGURE 7.2.53. Effect of speed on the rolling resistance.

stant inflation pressure [51]. The data are plotted in the form of rolling resistance against speed as curves of constant temperature. At higher speeds a progressive increase is observed as indicated in the lower figure. At constant temperature curve *A* indicates the behavior, while curve *B* shows the effect of the higher "service" temperatures. Because the inflation pressure was kept constant during these tests, there is an additional stabilizing effect tending to further reduce the increase of

rolling resistance with speed, as a result of the rise in inflation pressure as the tire gets hotter. There is another “fortunate” effect in that the hysteresis loss decreases as the temperature increases. Also, slippage losses in the contact area are reduced at higher tread temperature due to a lower coefficient of friction.

When starting at room temperature conditions, the rate at which the temperature of a passenger tire rises and the rolling resistance diminishes is shown in figure 7.2.54. Both level off to constant values. The curves represent constant load, speed and inflation pressure.

The equilibrium temperature as measured with a thermocouple needle in the shoulder after a run of 30 minutes is shown in the form of temperature against speed in figure 7.2.55. On flat roads these temperatures will be lower due to less deformation. The temperature of the contained air is about 25–30°C lower than the shoulder temperature at equilibrium conditions.

C. The effect of rubber compound and cord.

The hysteresis losses within rubber and cord are well known. It fol-

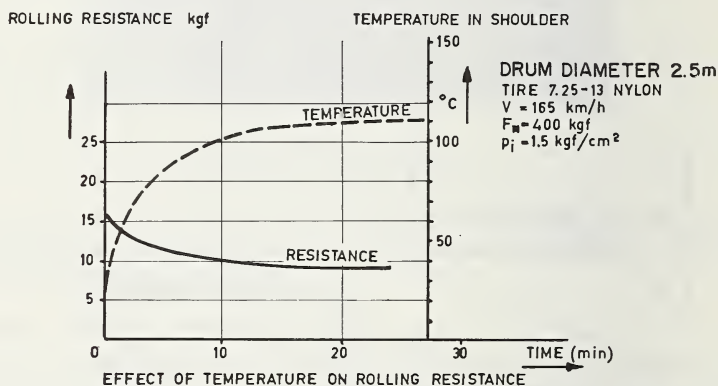


FIGURE 7.2.54. Effect of temperature on rolling resistance.

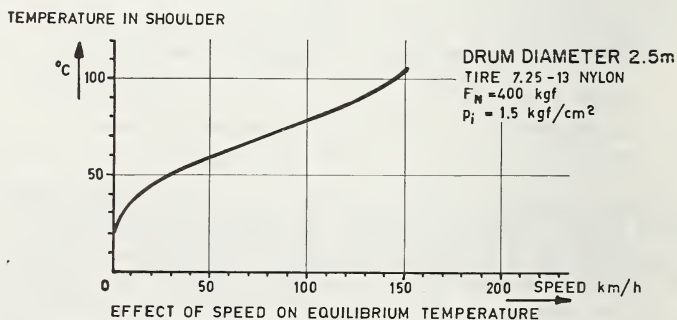


FIGURE 7.2.55. Effect of speed on equilibrium temperature in shoulder.

lows that the higher the hysteresis losses the higher the rolling resistance. This subject has been treated in chapter 1. Readers are also referred to details given about energy losses due to tread, side wall, ply rubber and cord in the literature [53, 55, 56].

D. The effect of carcass construction.

To show the influence of the carcass construction and tread thickness, the difference in behavior of a conventional bias and a radial belted tire is shown in figure 7.2.56. As can be seen, the radial ply construction, having an inextensible belt, shows an advantage when new. To study the effect of the tread, the tires were buffed to the bottom of the tread and rerun for rolling resistance [53], showing a significant change in behavior. The rolling resistance of the conventional bias tire reduces to almost half with a decrease in rolling losses in the high speed range. The radial-belted tire, although showing a loss in power consumption at the lower speeds, showed an increase in rolling resistance at the higher speeds.

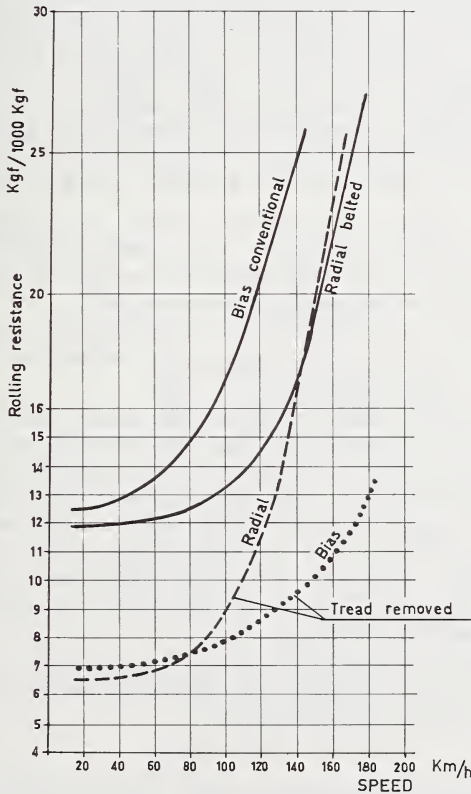


FIGURE 7.2.56. Effect of tread wear on the rolling resistance—speed relationship for a bias and radial belted tire.

In the bias construction, the inertia losses are associated with the vibration or standing wave of the tread and its associated mass. When the tread is removed, the weight reduction reduces the resulting inertial losses.

In the radial belted tire the rigidity of the belt prevents the standing wave in the tread area of the tire, and the deformation is associated basically with the flexural stiffness of the carcass side wall.

Due to the loss of the tread mass the added tension component in the sidewall is lost with the reduction of the tread-imposed centrifugal force. In radial belted tires the wave formation is associated mainly with the flexural rigidity of the carcass side wall, and the amount of tread has a much smaller influence on the critical speed. Radial ply tires as high speed tires therefore require a special approach because of their lower critical speed [57].

Changes in the design parameters, such as the angle of the cords at the crown, the number of plies in the carcass and the rim width affect the deformation of the tire and consequently the rolling resistance. Truck tires appear to have lower rolling resistance values (5–6 kgf./1000 kgf.) than passenger car tires, because of other tread rubber compounds, higher inflation pressure and radial stiffness [54].

Lower cord angle increases the radial stiffness of the tire and consequently decreases the deformation at a given load and inflation. Because the circumferential stiffness is also increased due to a lower cord angle the inertia losses are also decreased at high speed [53, 58].

Changing from four-ply to two-ply design gives a reduction in the hysteresis losses which is related to the mass of the tire and to an increase in the deformation. The combined effect of these two factors leads to a decrease in the rolling resistance [58].

The effect of the rim width is that mounting of a conventional bias tire on a wider rim gives a decreasing tire deflection, and therefore a reduction of the rolling resistance [51, 58].

The height-to-width ratio, known as the aspect ratio of the tire, has recently received much attention. The trend towards lower aspect ratios will continue, and low ratios of about 0.70 are already installed on cars, compared with 0.84–0.95 for bias tires of several years ago [59].

Lowering the aspect ratio is advantageous with respect to rolling resistance because the radial stiffness is increased and the tread is flatter, which also decreases the deformation and consequently the hysteresis loss. Due to an increase in circumferential stiffness the inertia losses at high speed are reduced [53].

At low speed the section height effect is greater for the bias tire than the radial belted, but the high speed performance shows significant improvements for the radial belted tire.

Cornering

As the slip angle increases the rolling resistance increases due to a component of the cornering force F_y in the direction of motion, and also due to a slight increase of F_r as shown in figure 7.2.57.

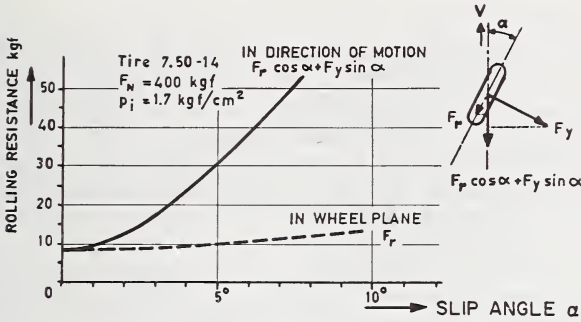


FIGURE 7.2.57. Effect of slip angle on rolling resistance.

Braking and Traction

The effects of braking and traction are shown in figure 7.2.58, where the rolling resistance values are plotted against braking and traction coefficients. These coefficients have been defined as the tangential braking or traction force $F_{B,T}$ divided by the radial tire load F_N . Due to an increase in tractive or braking effort an increase in longitudinal slip is observed, resulting in a higher rolling resistance [51, 60].

The rolling losses under braking and traction conditions are equal to:

$$F_B V - M_B \Omega \text{ and } M_T \Omega - F_T V$$

respectively, where

$$F_B = -F_x = \text{braking force}$$

$$F_T = +F_x = \text{traction force}$$

$$M_B = \text{braking torque}$$

$$M_T = \text{traction torque}$$

$$\Omega = \text{angular velocity}$$

$$V = \text{speed.}$$

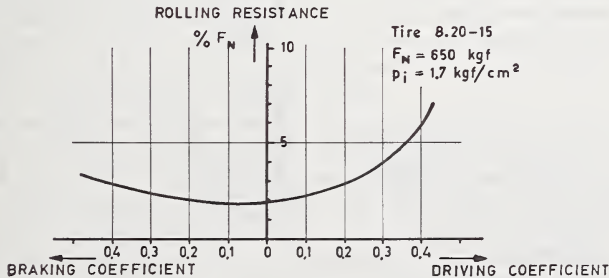


FIGURE 7.2.58. Effect of braking and traction on rolling resistance.

Temperature Measurements

Because tire temperatures are related to power and affect the service life of tires, the measurement of the tire temperatures is considered as a reliable indicator of the energy put into it and the durability of the tire.

Due to deformation and hysteresis, heat is generated within the tire. Studying the heat build-up has always been an important factor in assessing the durability of the tire. This is because severe testing is often associated with tread separations from the cord body resulting from thermal degradation and high centrifugal force.

Operating temperatures have been measured while the tire is running by means of thermocouples vulcanized or inserted into the tread or plies, but the life of these thermocouples is short because of fatigue breakage under load.

More frequently, measurements have been made by inserting thermocouple needles under the tread or in the plies after stopping the tire. Measurements of the temperature of the air in a tire are also made, as well as determining the tire surface temperature.

Figure 7.2.59 shows typical values of tire temperatures taken on an indoor test wheel as a function of speed, and with various test conditions. It appears that many normal passenger car tires operate in the vicinity of 100°C at normal conditions, measured in the air cavity [62].

Several authors report the measurement of tire surface temperatures using a contact thermometer or thermistor to relate the average skin or groove temperature to heat loss or the relative wear rating of tread compounds [61, 56].

Other methods were developed for determining the temperature of the air in a tire [63].

The difficulties encountered using thermocouple needle measurements are also reported in the literature [56, 64, 65].

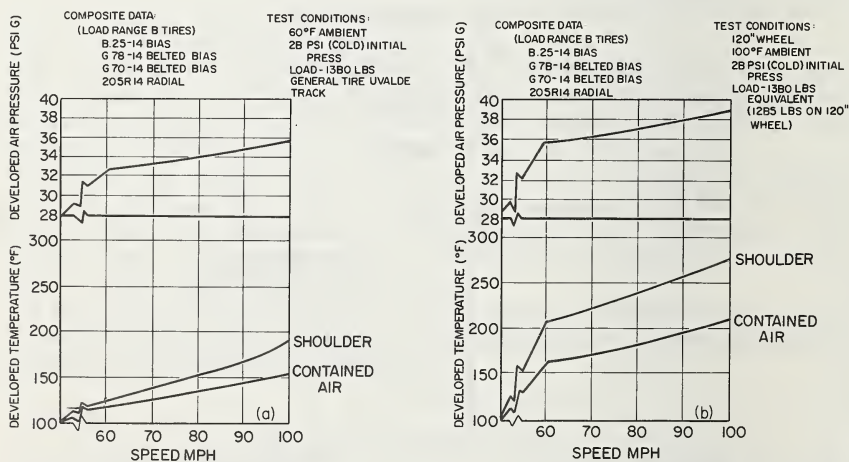


FIGURE 7.2.59. (a and b) Equilibrium pressure and temperature rise as functions of tire load and speed.

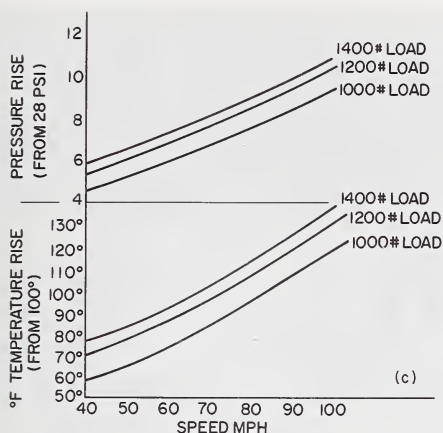


FIGURE 7.2.59. (c) *Equilibrium pressure and temperature rise as functions of tire load and speed.*

Refinements in measuring techniques made it possible to measure internal tire shoulder temperatures under road testing conditions of high loading and speeds, to study durability and reliability of the tire [65, 66]. In endurance testing on indoor machines it has often been found advantageous to trace the hot spots before severe tread separation occurs. The use of lead-sulphide photo-conductive cells for high speed pyrometry has been reported [67, 68, 69].

7.2.5. Braking and Traction

Braking

A. Deformations

The difference in deformations between a free rolling and a braked tire has already been discussed in chapter 6. However, to facilitate the understanding of the following paragraph, another illustration of tire deformations shall be given [24].

To show this difference in behavior, a photograph was first taken of a freely rolling tire and afterwards, using the same negative, a second photo on top of the first one has been made of a braked tire. Triggering of the camera has occurred at exactly the same position as in the free rolling case. This is shown in figure 7.2.60.

By measuring the distance between the radii which were originally equally spaced on the surface of the undeflected tire, the deformations of tread and sidewalls can be determined for various braking conditions.

Figure 7.2.61 shows some results thus obtained on the movable platform machine, and it is seen when a braking force is applied that the tread elements before contact are stretched. The alterations of the deformation are also clearly shown on a photo of the contact area of a braking tire in figure 7.2.62.

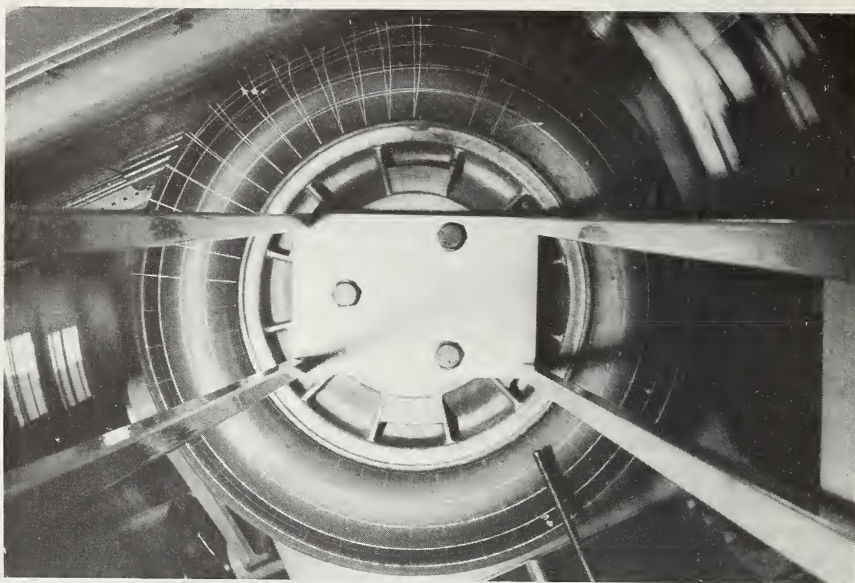


FIGURE 7.2.60. *The difference in deformation between a free rolling and a braked tire.*

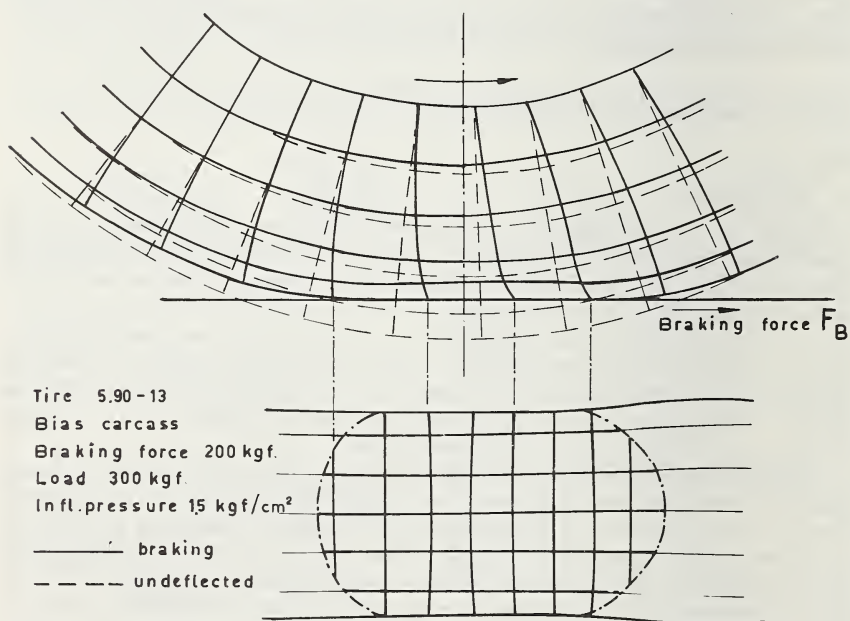


FIGURE 7.2.61. *Deformations due to braking.*

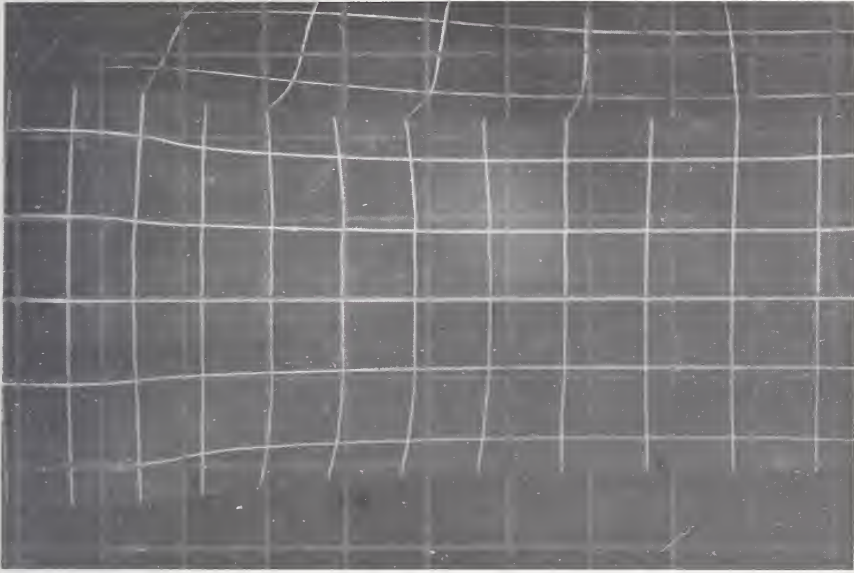


FIGURE 7.2.62. *Photo through glass plate of contact area of braking tire.*

B. Force distributions

a. Longitudinal force distribution.

The movable platform machine is also equipped with an apparatus incorporating three measuring bars 2 cm. long and 20 cm. wide for measuring the distribution of the vertical, longitudinal, and lateral forces [14, 24].

With this modified "Gough" apparatus shown in figure 7.2.63, the distribution of the longitudinal shear forces in the contact area is determined. The distribution of the forces created by a free rolling tire is represented by line 1 in figure 7.2.64, and the additional shear force created by the braking torque is represented by line 2. The resultant shear force distribution along the length of contact is therefore represented by line 3, as measured with the longitudinal force bar of the Gough apparatus. The precise form of this curve depends very much on the magnitude of the braking force for a given radial load, inflation pressure, coefficient of friction, etc. as described in chapter 5, figure 5.52. The reason for such a force distribution becomes clear by looking again at figure 7.2.61. An extended tread element adheres to the platform on first entering the contact zone (ch. 6, fig. 6.1c). As it moves further into the contact area, it produces a deflection which increases linearly with increasing distance (causing an increasing longitudinal force) until the local value of limiting frictional force is reached and the tread element begins to slide back, thus reducing again the longitudinal force as shown by line 3 in figure 7.2.64.

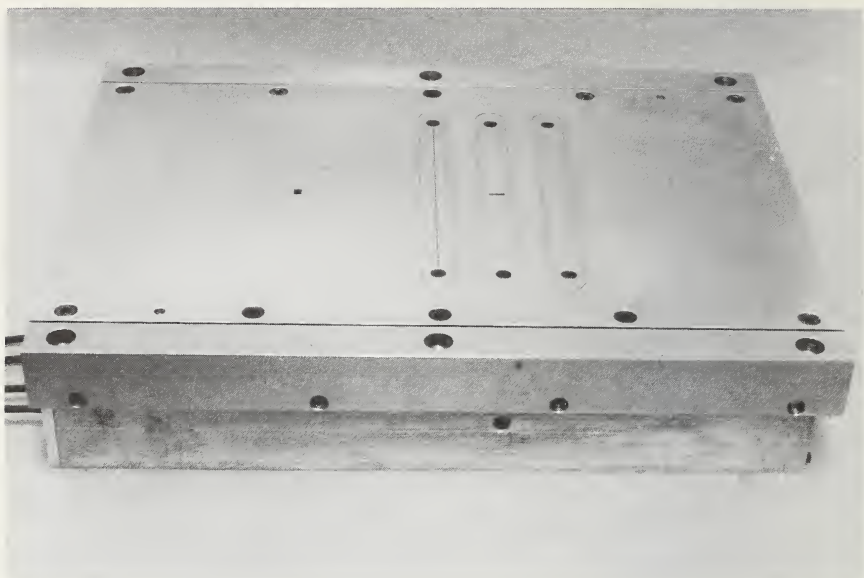


FIGURE 7.2.63. *Modified Gough apparatus incorporating three bars measuring the lateral, longitudinal and vertical partial forces.*

The total longitudinal force F_B may be obtained using the six-component tire tester, also mounted in the Delft movable platform machine of figure 7.2.5. The result obtained can be compared with the value obtained from the longitudinal force measuring bar, by integrating the longitudinal force function as the tire travels over it.

b. Vertical force distribution.

The vertical force distribution is measured by a second bar of the Gough apparatus. The difference in behavior of a free rolling and braked tire is shown in figure 7.2.65. The total vertical force F_N may be obtained either by integrating the vertical force function, or by using the tire tester, the latter method being preferable. The offset of F_N before the contact center may also be obtained. As already discussed in section 7.2.4, the coefficient of rolling resistance f_r is higher than in the free rolling case, mainly due to a rise in slip-induced rolling resistance. The balance of moments around the wheel center O reads (fig. 7.2.64):

$$F_B \cdot h = M_B + F_N f_r$$

Due to the braking torque, it is observed that the distance h is smaller than in the free rolling case [24].

c. Longitudinal sliding

Attempts have been made to measure the longitudinal sliding with a small cam wheel mounted in the longitudinal force bar of the Gough ap-

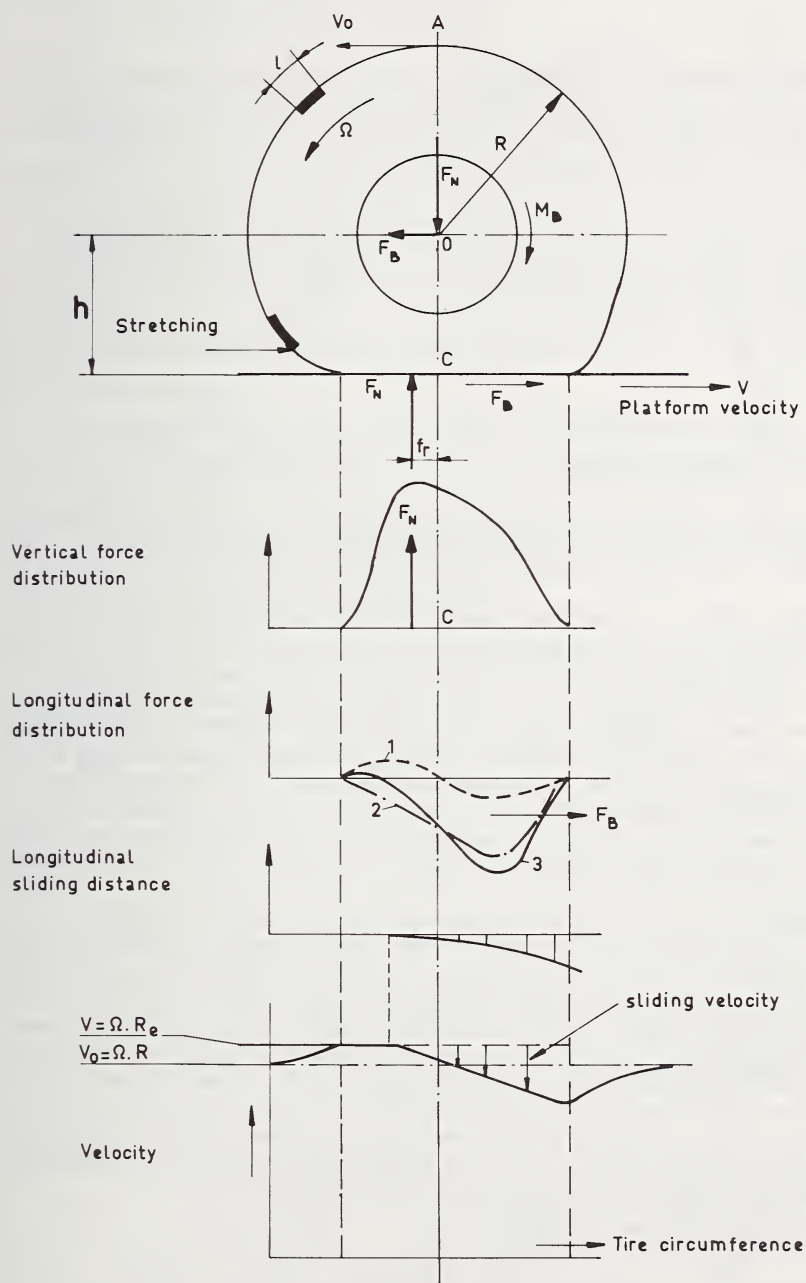


FIGURE 7.2.64. Distribution of forces, longitudinal sliding distance and sliding velocity, over the contact length of a braked tire.

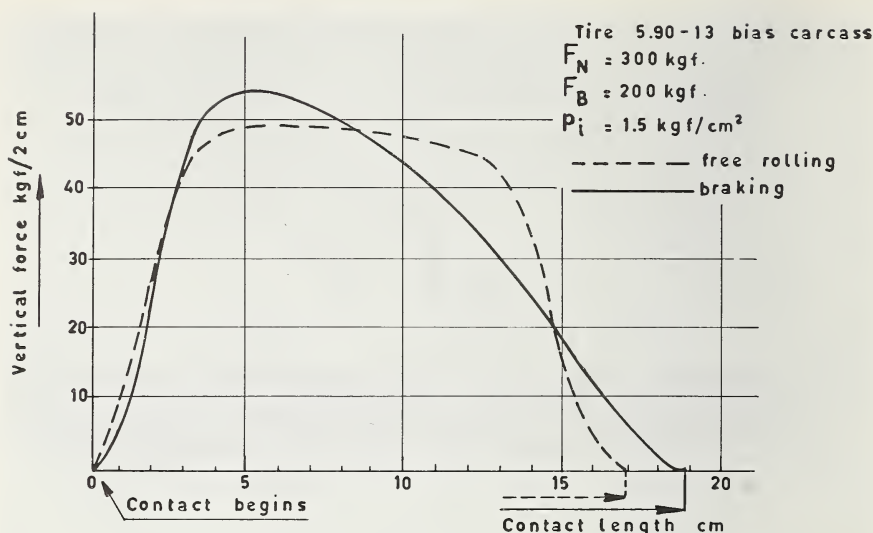


FIGURE 7.2.65. Comparison of vertical force distributions over the contact length of a free rolling and braking tire.

paratus. The cam wheel can rotate, but does not measure the longitudinal sliding of one single tread element because due to the sliding motion the neighboring tread element subsequently comes into contact with the cam wheel. The total longitudinal sliding distance is measured with a potentiometer coupled to the cam wheel shown in figure 7.2.63. It is the sum of the longitudinal sliding of all different tread elements along a line parallel to the direction of travel of the platform. These measurements of sliding in the contact patch were not accurate enough. Photography of the contact area of the tire, marked with a grid, during motion of the glass surface of the platform machine, appeared to give better results (fig. 7.2.62).

Due to stretching of the tread elements before contact the circumferential velocity will increase, and on the assumption of no sliding in the front part of the contact zone for a moderate braking force, the tread elements coming into contact with the platform will start to travel with the platform speed V . The longitudinal shear force which increases towards the rear of the contact zone, in combination with the decreasing vertical force, will cause rearwards sliding of the tread elements in the rear part. The resulting longitudinal sliding distance and sliding velocity curves, taken over the contact length, are shown in figure 7.2.64. Increasing braking force at constant vertical load will result in increasing sliding over the contact length as in figure 7.2.66.

The slip ratio may be defined to be:

$$\kappa_B = \frac{\Omega_o - \Omega_B}{\Omega_o}$$

where Ω_o = angular velocity at free rolling

Ω_B = angular velocity at braking

Both values can be measured at constant forward speed of the platform or at constant drum speed [sec. 7.2.3, fig. 7.2.42]. As the braking force F_B increases so does the percent slip. The resulting braking force coefficient $\frac{F_B}{F_N}$ is shown in figure 7.2.66 for constant speed as measured on a dry steel drum of 2.5 m. in diameter.

The difference in behavior of a radial ply and bias ply tire is clearly demonstrated in figure 7.2.67 at a constant speed of 40 km/hr. [70]. It is seen that the position of the peak coefficient μ_{lp} is often very difficult to determine since the curves are sometimes rather flat. Similar results are also often obtained on wet surfaces [71].

D. Effective radius

Returning to figures 7.2.61 and 7.2.62, the stretch of the tread elements just before contact, as measured from the photograph, appears to be approximately 10 percent. Assuming again no sliding in the front part of the contact zone, the same reasoning as in the free rolling case (sec. 7.2.3) results in: $V = 1.1V_o$, that is $R_e = 1.1R$, showing an increase in effective radius compared with the free rolling condition ($R_e = 0.96R$) and a decrease in angular velocity Ω [70].

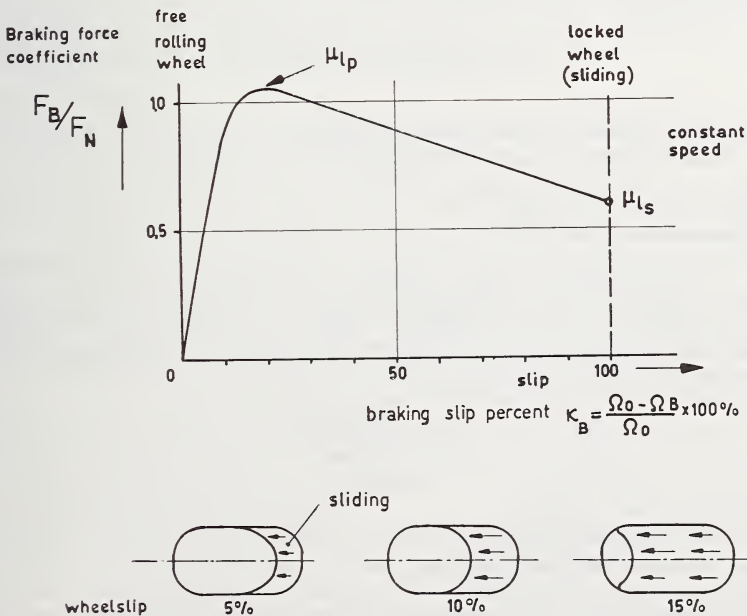


FIGURE 7.2.66. The relation between braking force coefficient and braking percent slip.

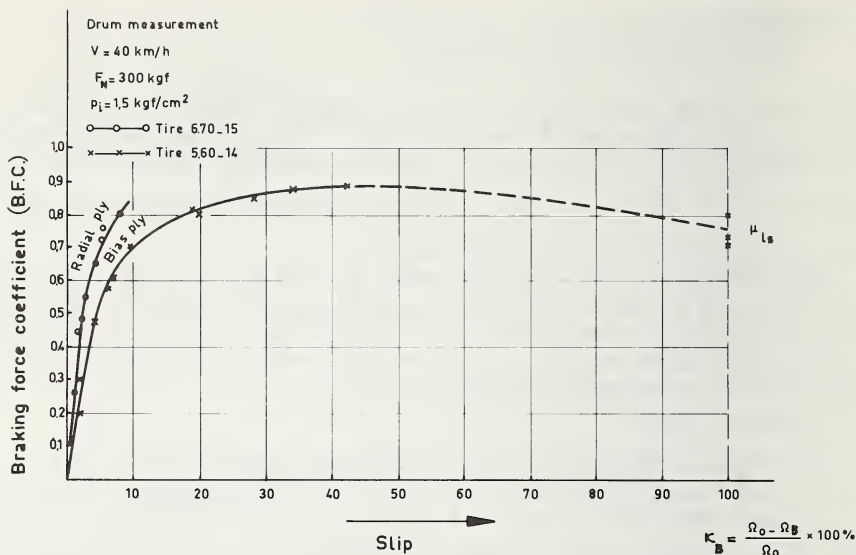


FIGURE 7.2.67. Comparison of the braking force coefficient-braking slip relationships of a radial ply and bias ply tire at constant drum speed.

The slip ratio may be defined to be:

$$\kappa_B = \frac{\Omega_0 - \Omega_B}{\Omega_0} = \frac{R_{eB} - R_{eo}}{R_{eB}}$$

where R_{eo} = effective radius at free rolling

R_{eB} = effective radius at braking

E. Wet road measurements

a. Distance method [72].

The locked wheel “sliding” friction coefficient is determined during the speed interval under investigation.

The calculation of this friction value, sometimes called “braking coefficient” is based on the accurate measurement of the skid distance s and the speed V . It follows that:

$$\mu_{ls} = \frac{V_1^2 - V_2^2}{2gs}$$

where V_1 = initial velocity

V_2 = final velocity

g = gravitational constant.

Due to the erroneous assumption in the above formula of a constant deceleration over the speed interval (μ being speed dependent) it is

rather difficult to compare results obtained with different tires on various road surfaces. Because standard vehicles are used, a large number of tests are required to arrive at an acceptable accuracy of the averaged μ_{is} values. This is usually done at speed increments of about 10 km/hr. in the required speed range of the test vehicle.

b. Deceleration method.

As discussed in chapter 6, the braking performance of tires can also be measured by the deceleration of the vehicle. In this method only the front wheels of the test vehicle are braked in order to maintain directional stability of the vehicle at all speeds [73].

Both the peak value of the braking force coefficient μ_{lp} , and the locked wheel slide value μ_{ls} are determined from the film record of deceleration (ch. 6, fig. 6.11).

Because these tests can be executed on a relatively short test surface, having a more or less constant frictional character and uniform water depth, comparison of tire data thus obtained is usually preferred over the stopping distance method. The distance method with its long skid distances has a poorer accuracy especially in the higher speed range [72].

It has often been observed with the deceleration method that radial ply tires gave higher peak braking force coefficients μ_{lp} on all surfaces than do bias ply tires. The differences between these peak coefficients were almost independent of speed and were least on coarse-textured surfaces, and greatest on fine-textured surfaces, ranging from almost zero to about 0.1. The radial ply tires gave higher locked braking force coefficients μ_{ls} on the fine textured surfaces but lower coefficients on the coarse textured surfaces than did the bias ply tires [73].

c. Force method.

Numerous braking force tests with different tire constructions and tread rubber compounds have been executed on a variety of dry and wet road surfaces and are reported in the literature.

The advantages of the towed trailer road tests are that the towing truck can maintain constant speed at the desired level, uniform wetting immediately ahead of the tires is obtained, and a large variation in tire loading is possible without any load transfer effects (fig. 7.2.8).

During these road tests it appears very difficult to obtain braking force coefficient values in the range between the peak braking force coefficient μ_{lp} and the locked braking force coefficient μ_{ls} ($\kappa_B = 100$ percent), because of almost immediately locking of the wheel after μ_{lp} has been reached. For this reason, usually only μ_{lp} and μ_{ls} are determined to compare tread designs, rubber compounds, tire constructions etc. The numerous results obtained are very similar to data published in the literature [73] and discussed in chapter 6.

Another method to determine the braking force coefficient has been published by the Road Research Laboratory [71]. Force measurements are made on a fifth wheel mounted in a test vehicle. The angular velocity of this test wheel can be held at any desired value, independent of the vehicle speed.

At the beginning of a series of tests a record of wheel rotation is obtained with the free rolling tire in order to obtain its rolling radius R_{eo} for evaluation of the braking slip.

$$\kappa_B = \frac{R_{eB} - R_{eo}}{R_{eB}}$$

Typical curves of braking force coefficient against braking slip κ_B are shown in figure 7.2.68 for a bias ply tire on three out of five of the test surfaces from table 7.2.1.

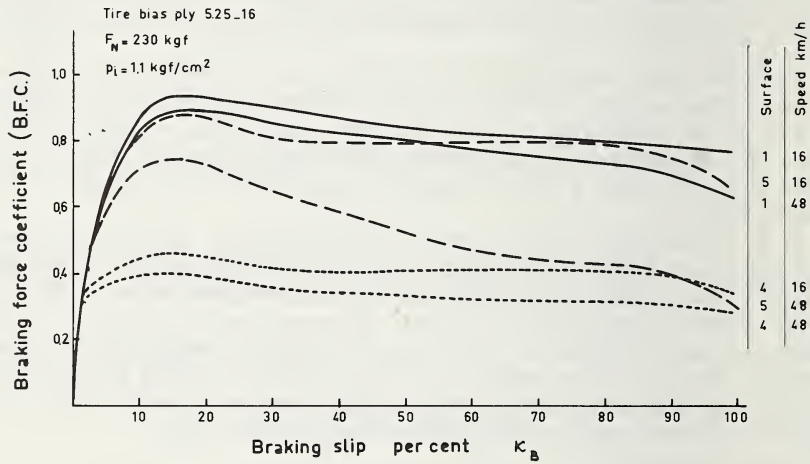


FIGURE 7.2.68. Typical curves of braking force coefficient against braking percent slip for a bias ply tire on three road surfaces at two speeds.

Surface 1 (rough, harsh), surface 4 (rough, polished), surface 5 (smooth, polished).

TABLE 7.2.1.

No.	Description	Texture
1	9.5 mm. quartzite macadam carpet	Rough, harsh
2	Fine cold asphalt	Smooth, harsh
3	9.5 mm. mixed aggregate macadam carpet	Rough
4	9.5 mm. Bridport macadam carpet	Rough, polished
5	Mastic asphalt	Smooth, polished

The curves show in general a rapid initial rise, and then become gradually less steep as they approach a peak at approach 7–25 percent slip. Beyond the peak there may be a slowly falling region and finally a more rapid fall from 80 or 90 percent to the locked wheel values at 100 percent slip.

The rough and harsh surface No. 1 is capable of giving a high coefficient. The harsh microtexture has the largest effect on the coefficient in comparison with the other surface No. 4. It has been shown that tires of radial ply construction have a more rapid initial rise of the braking force coefficient curve than bias ply tires. On harsh surfaces the radial ply tires gave higher peak coefficients but on polished macadam surfaces lower values were observed. The same was true but less obvious for the locked wheel case [71].

Curves of pure braking force coefficient against braking slip give valuable data for development of anti-skid braking systems. These systems are of particular value when braking and cornering forces act simultaneously [71, 74].

Traction

A. General observations

Having discussed the behavior of a braking tire at length in the previous section, a short description of the action of a driving torque M_T will be sufficient because the situation is analogous.

When a tractive force F_T is applied, the tread elements ahead of contact are compressed. The resultant shear force distribution along the length of contact, as measured with the longitudinal force bar of the Gough apparatus, is shown in figure 7.2.69. As discussed (ch. 5, fig. 5.53), the form of this curve depends on the magnitude of the tractive force. The resultant shear force distribution (line 3) can be seen as the sum of the force distribution of a freely rolling tire (line 1) and the additional shear force created by the tractive force (line 2).

A compressed tread element adheres to the moving platform when first entering the contact zone. As it moves further the increasing deflection of the tread element produces a linearly increasing longitudinal force. Beginning in the rear part of the contact zone, forward sliding of the tread element will be observed [24]. The resulting longitudinal sliding distance and sliding velocity are also shown in figure 7.2.69.

The slip ratio may be defined to be:

$$\kappa_T = \frac{\Omega_T - \Omega_o}{\Omega_T} = \frac{R_{eo} - R_{eT}}{R_{eo}}$$

where Ω_o = angular velocity at free rolling

Ω_T = angular velocity with traction

As the tractive force F_T increases, so does the percent slip, and the resulting traction force coefficient $\frac{F_T}{F_N}$ as a function of percent slip may be plotted, giving a curve similar to that obtained for the braking force coefficient.

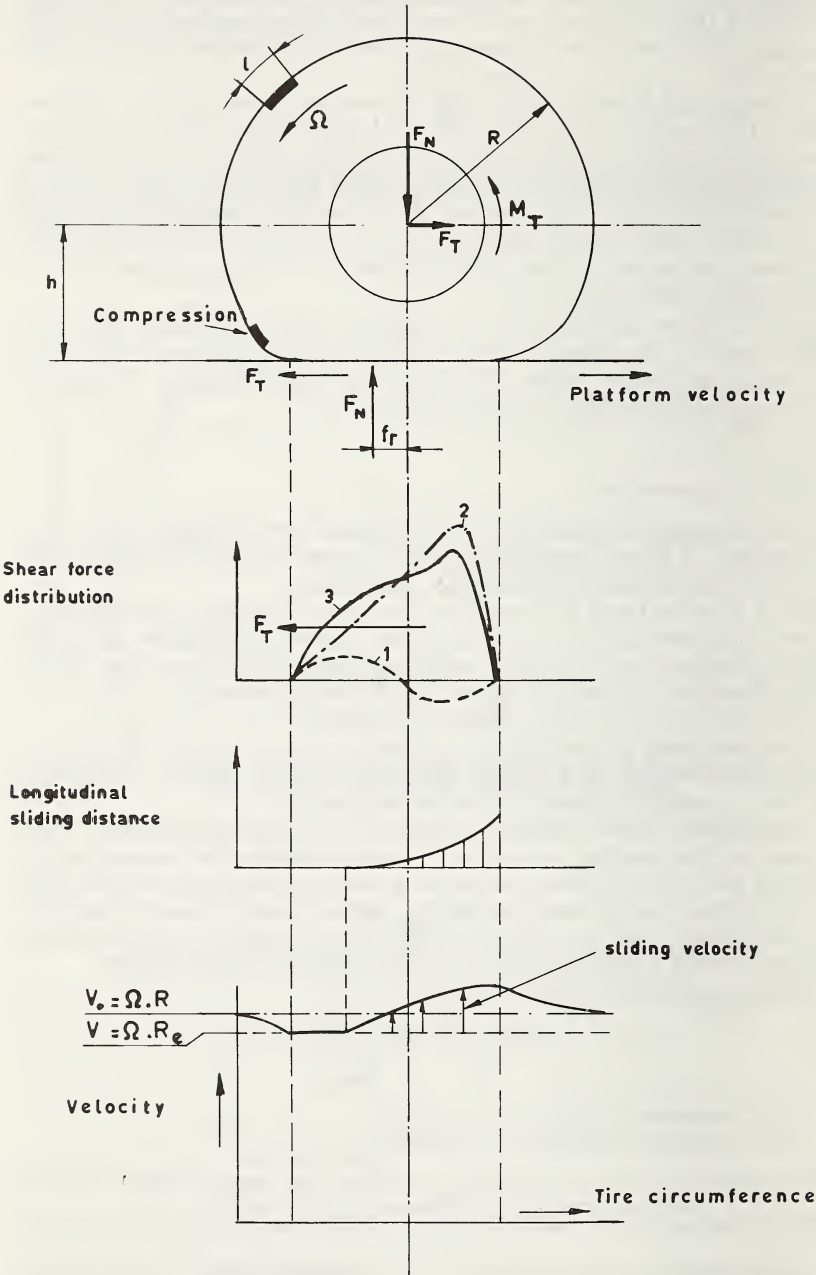


FIGURE 7.2.69. Distribution of forces, sliding distance and sliding velocity over the contact length of a tire under the action of a driving torque M_T .

The decrease in effective radius R_{eT} compared with the free rolling case may be obtained by measuring Ω_T and Ω_o at constant platform speed or drum speed.

B. Wet road measurements

a. Break-away method.

A light truck fitted with the test tire is attached to a large dynamometer truck. The dynamometer truck is used for braking and maintains a low constant forward speed of about 5 km/hr. to ensure rolling of the test tire. By measuring the maximum tractive draw-bar force developed by the tire in the low slip range of less than 15 percent, the test determines the maximum force available to accelerate a vehicle, as the torque is gradually increased until the tire slides completely [72].

b. Dynamic slip method.

This is a continuation of the break-away test, because dynamic testing is conducted at 75 to 200 percent slip.

Traction ratings for both break-away and dynamic tests are given as a ratio of tractive force to tire load. Typical recordings are shown in figure 7.2.70 [72].

c. Maximum acceleration method.

The tire comparisons are based on the speed at wheel spin in the speed range 40 to 100 km/hr. using a passenger car. The procedure is to drive the car on the test surface at constant speed, then accelerate by means of a full throttle down shift, or limiting the throttle position in order to reduce the maximum available torque to a level compatible with the test conditions of surface and tires.

The driving force vs. speed curves of the different gear ranges for the test car are usually first obtained on a drum dynamometer or derived

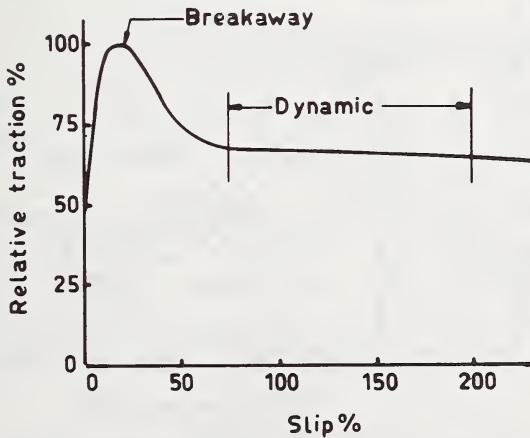


FIGURE 7.2.70. Relation between relative traction force percent and traction percent slip.

from engine torque curves. The theoretical point of slip is shown in figure 7.2.71 at the intersection of the maximum available driving force and the tractive coefficient curves for two different tires on the same test surface. The speed at the point of wheel spin indicates relative tire traction. Tire comparisons are based on the maximum speed attained before wheel spin, or the least time required to travel a given distance. For the latter test, slip may occur throughout the test distance [72].

Several other methods are used to measure the tire resistance to wheel spin under conditions of acceleration and with the vehicle travelling straight ahead. Among these the single tire test technique is reported [72, 75].

C. Factors affecting traction on wet roads.

The tire variables affecting passenger tire traction on wet road surfaces include: tread design, tread compound and tire construction (ch. 6).

The tread design variables are bladed tread pattern versus plain design, groove pattern, tread width, tread radius and center shoulder effect.

The tire construction variables such as crown angle, tread reinforcement, and radial construction versus bias construction have a smaller effect on the wet tractive effort than the tread design variables.

Tread compounding is another complicated subject. For further information the reader is referred to the literature [59, 76].

7.2.6. Tire Nonuniformities

Introduction

As road surfaces became smoother their contribution to vibration de-

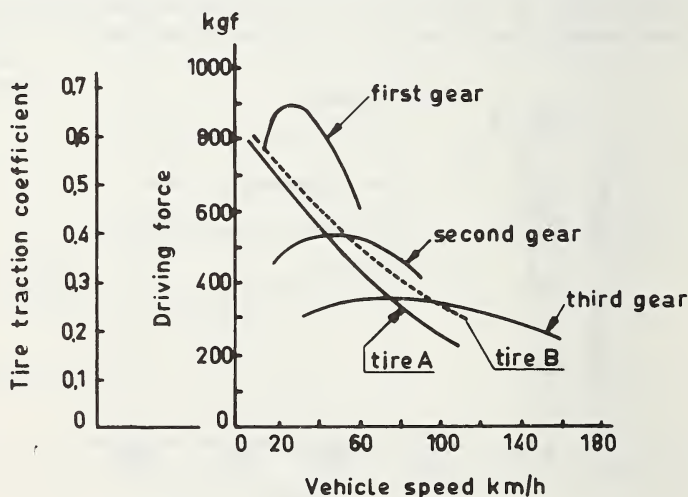


FIGURE 7.2.71. Illustration of maximum acceleration method giving the relationship of tire traction to driving force.

creased and increased attention has been focused on the tire-excited vibrations introduced by the nonuniform properties of the tire.

It is impossible to manufacture perfectly uniform tires because each item has its own manufacturing tolerances. Only the rigid control of all processes throughout the manufacture of materials and components for tire building can minimize the unavoidable imperfections affecting uniformity.

Lack of uniformity around the tire will produce variations in forces applied by the tire to the vehicle, and repeat its influence with each revolution of the tire. The resulting periodic vehicle vibrations are speed dependent and often very annoying to the driver and passenger. Parts of the vehicle vibrate and radiate energy as sound heard by the passenger, and vibrations of the steering wheel, floor and seats are felt directly by the driver and passenger [77].

The transmission of vibrations by the tire caused by road irregularities, or by the natural frequencies inherent in the tire structure, are not considered in this section, since these characteristics are not dependent on the degree of nonuniformity. But it should be observed that chassis tuning capable of attenuating all tire vibrations resulting from various road irregularities is extremely difficult, even more so because the various related vibratory systems should also avoid natural frequencies that might synchronize with natural tire frequencies.

The Tire Manufacturing Process

A passenger car tire may be composed of approximately 100 separate ingredients. To insure quality and uniformity among these materials, all have their own physical and chemical test qualifications. Tires are made of four basic materials as shown in figure 7.2.72, illustrating the many steps in the manufacturing process that should receive inspection and evaluation to insure conformity to the standards of quality and uniformity [78].

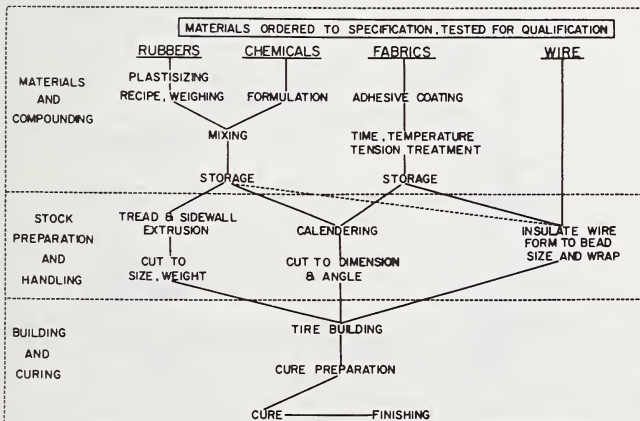


FIGURE 7.2.72. Representation of the many steps in the tire manufacturing process.

The phase of the stock preparation, being the fabrication of the rubber compounds, fabrics, and wire into basic components of the tire, is very critical of weight and dimensional tolerances.

Treads

The tread length, weight, and gage must be carefully controlled to insure uniform distribution of tread in the finished tire. Treads are generally applied to the building drum in such a way that one end butts the other end, tending to concentrate any variation in length at the tread splice. Exceeding the specified tolerances will result in an unacceptable nonuniformity. Figure 7.2.73, obtained from special uniformity machines, shows the effect of short tread length, but of course excessive length due to stretching the tread during application on the building drum will also affect the radial force, radial run out and tread shoulder thickness [78]. A thick tread joint causes unbalance, and this has long been known as a very important source of nonuniformity because the unbalanced force is proportional to the square of the velocity. Balance can be compensated for, either statically or dynamically. But a thick tread joint is also less flexible than the rest of the tread and this difference in stiffness cannot be corrected for or compensated by adding suitable balance weights to the wheel. The forces necessary to accelerate the tire tread in the contact area may change appreciably with a nonuniform mass distribution. The variation in inertial forces will also cause fluctuations of the effective rolling radius. The effective rolling radius variations can be obtained by measuring both wheel and drum angular velocities on uniformity machines. Rolling radius variations produce angular accelerations that result in tangential force variations proportional to forward speed. Heavy tread splices will also show fluctuations in the rolling resistance [79].

Poor tread centering on a portion of the tire will result in fluctuations of the lateral force and shoulder gage thickness variation curves [78].

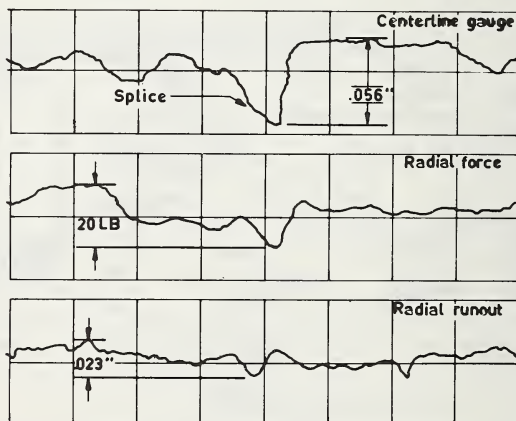


FIGURE 7.2.73. *The influence of non uniform distribution of tread on the radial force and radial runout.*

Cord Angle and Ply Fabric

The transformation from the cylindrical building drum shape into the toroidal configuration within the tire mold is shown in figure 7.2.74 with corresponding dimensional changes.

Any irregularities in the ply fabric are magnified due to the pantographing of the cords during the shaping of the flat ply stock into the final tire. Since a one degree variation in bias angle can result in 2-3 degrees variation in the cured tire, it will be evident that angle variation within a tire can have significant effects on the dimensions as well as the related forces. Figure 7.2.75 shows the effect of angle change on tire shape for several tires which have common contour lengths from bead to bead [78]. Since the cord angle determines the ratio of height to width of the tire carcass, the measurement of the width variation at the tire walls can give an indication of the cord angle variation in the tire.

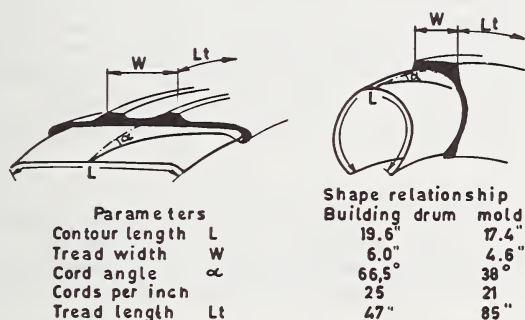


FIGURE 7.2.74. Transformation from the cylindrical building drum shape into the tire mold for a bias ply tire.

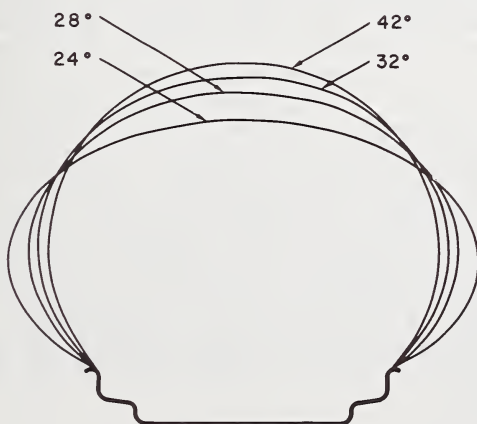


FIGURE 7.2.75. The effect of centerline angle change on tire shape.

Building and Curing

When the tire builder cuts the ply fabric too short, causing an open ply splice, the effect can be an intolerable lateral and radial runout (fig. 7.2.76). Also, bulky ply stock splices or wrinkled and wavy plies should be avoided. Another cause of nonuniformity resulting in eccentric beads may be due to improper alignment in the tire building machine.

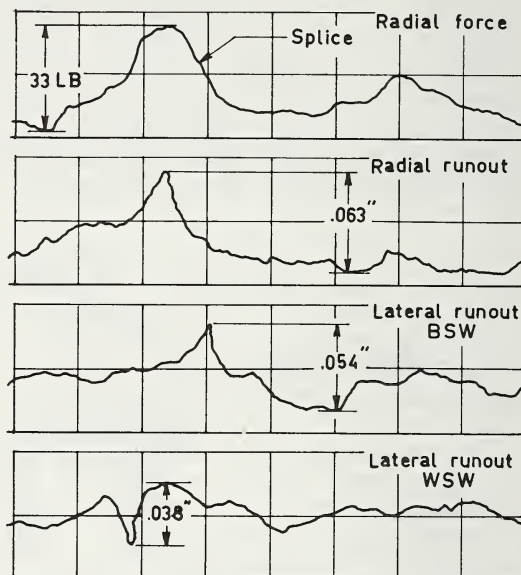


FIGURE 7.2.76. *The effect of an open ply splice on lateral and radial runout.*

A correctly specified drum width is important, since too wide a drum results in irregular and loose cords, while too narrow a drum results in pulled or slipped cords in the cured tire [78]. The development of the radial belted tire has progressed rapidly, but their adoption as original equipment has been slow. This may be due to large investments in bias conventional tire building equipment, but also to the difficulties encountered in mass production of this type of tire to the required degree of uniformity. The radial ply tire has two or three layers of cord at an angle of 88–90 degrees to the crown and about three to six layers of cords forming a circumferential belt. Although many possibilities exist, the belt cords lie generally at an angle of 12–20 degrees to the crown centerline. Accurate building and centering of the belt have received concentrated effort in the area of precision assembly to minimize irregularities affecting uniformity. Precision building and special handling techniques are also required for bias-belted tires or tires with asymmetric carcasses.

Stability of Materials

Analyzing the influence of moisture on various cords (rayon, polyester,

nylon), it was found that in the region of cord tension due to inflation pressure within the tire, a large variation of cord elongation was observed for different relative humidity conditions. The uniformity of a tire may be adversely affected if the moisture content varies within a tire or during a production run of tires. Polyester cords have excellent characteristics in this respect [78].

A localized difference in cord modulus in a ply will cause the tire to bulge slightly in the vicinity of the more extensible cords, affecting the radial force [79].

Another class of tire nonuniformity is the temperature induced or so called heat-induced nonuniformity, found to exist in tires made with thermoelastic cords such as nylon and polyester.

It was observed that uneven cooling of the tire during the conventional postcure inflation process caused temperature differences across the tire. Due to the temperature sensitivity of thermoelastic cords, these temperature differences caused cord shrinkage, resulting in temperature induced nonuniformities. Temperature measurements of tires on the postcure inflators revealed differences of about 15° C around the circumference, with the hotter part commonly opposite the cooler part. To obtain uniform temperatures across the tire a special tie cooling apparatus was developed [80].

Wheel Uniformity

Car wheels are subject to manufacturing fluctuations and contain some degree of nonuniformity. The maximum radial and lateral runout at the beads should not exceed approximately 1.5 mm. (D.I.N. 7817). Accurate wheel centering contributes greatly to a good degree of uniformity.

Tire uniformity measurements are made either on precision rims or car wheels.

Figure 7.2.77 shows car wheel radial and lateral runouts as measured on the beads, together with the corresponding free tire runouts as measured on the side walls of a preconditioned tire. Lateral runout spectra of wheel and tire sometimes show a good correlation.

Effect of Tire Nonuniformities on Vehicles

The tire-excited vehicle vibrations introduced by the nonuniform properties of the tire are felt as vibrations of the parts of the car in contact with the passenger, and heard as sound in the passenger compartment. The automobile plays a significant part in the transmission of shake, thump and roughness, as shown by the results of running the same set of tires on different cars. It appears that no car is insensitive to tire force variations, but some are more sensitive than other cars. Shake problems can come from radial or lateral force variations and depend primarily on the amplitudes of the first and second harmonics of the force variation [81]. Since the force variations repeat themselves with each revolution of the tire, they constitute a periodic forcing input to the various vibrating systems of the vehicle. It is a relatively simple matter with today's computer capability to analyze the quantity of each harmonically

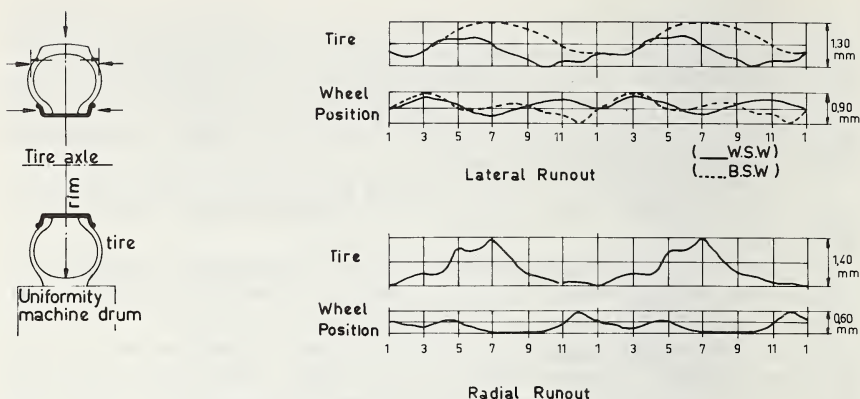


FIGURE 7.2.77. Car wheel radial and lateral runout together with the corresponding free tire runouts.

related sine wave which makes up the complex curve. The periodicity allows a representation of the force variations by a series of sine waves, each at a frequency equal to an integral multiple of the wheel frequency. Each sine wave component is called a harmonic of the wheel frequency, and when all harmonics are summed with their proper phase relationships, the original variation is reconstructed [81]. This so-called Fourier analysis of a runout curve is shown in figure 7.2.78.

The amplitudes A_n of the harmonics are the magnitudes of the Fourier coefficients of the periodic waveform expressed in the form:

$$F(t) = A_0 + \sum_{n=1}^N A_n \sin(2\pi n f + \varphi_n)$$

with f = frequency and φ_n = phase angle.

With the aid of a mathematical shake model embodying beam effects, it is possible to compute the response of the structure of a car to measured tire radial force variations. It was observed that the amplitude of the first harmonic of tire radial force variation is an important parameter in vehicle beaming shake. This is a mode of vibration of the entire sprung mass involving predominantly bending deformation of the entire structure [82].

Sometimes subjective ride ratings are used to demonstrate improvements in shake. For instance, tires having a certain level of nonuniformity are reduced to a lower value by removing a very small amount of rubber from certain regions of the shoulder ribs with special alteration machines (fig. 7.2.79). These machines reduce the radial force variation and provide uniformity improvements on an automated basis. The alteration results in a demonstrable improvement in tire shake, but has no consistent effect upon tire roughness [83].

The usual manner of demonstration is to select tire-wheel combinations of known uniformity and evaluate the systems for shake and roughness on the given car. The tire-wheel combinations are then altered to better

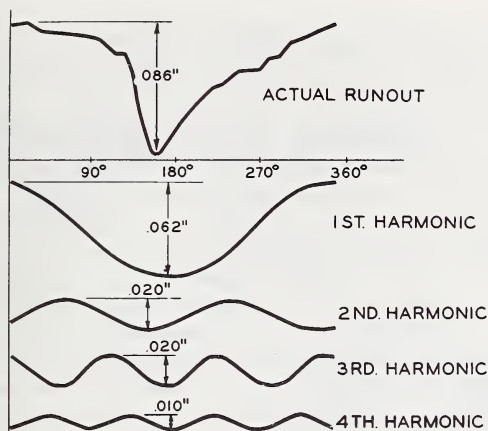


FIGURE 7.2.78. Fourier analysis of a runout curve.

uniformity levels, and the tests repeated. If tires are reduced to radial force variations of 15 lbs. or less, tire shakes will usually be rated better [83].

Subjective ride rating requires careful selection and thorough training of the personnel involved in rating the vibration characteristics [84-86]. These subjective ratings, on the basis of studies of human tolerance to

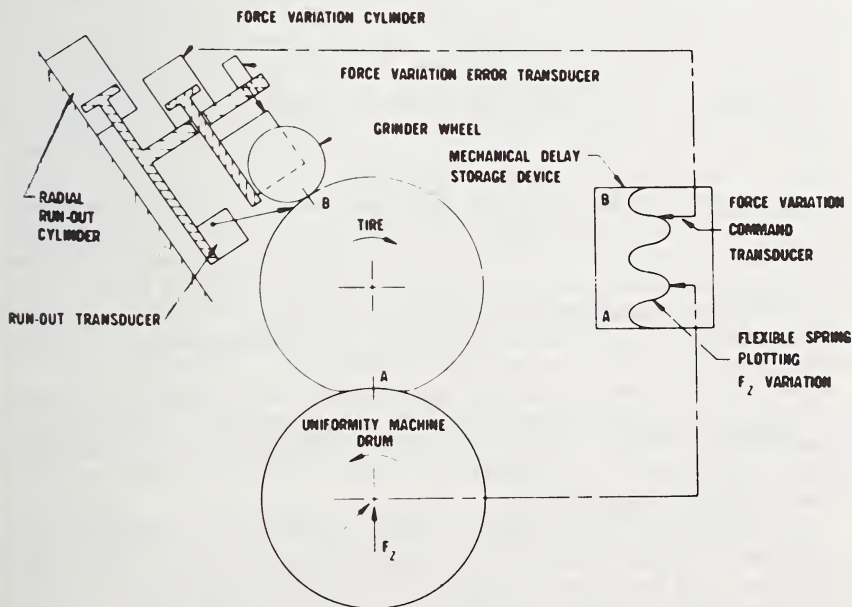


FIGURE 7.2.79. Automatic reduction of radial force variation by removing a small amount of rubber.

vibration, can be used to establish acceptable tire nonuniformity tolerances as measured on tire uniformity grading machines.

Tire thump is a low pitched noise and is thought to be related to the 4th through 9th harmonic of tire rotation. Thump sound intensity is determined by the loudness of amplitude of modulation of the sound pressure wave, and the sharpness of the increases and decreases of the modulation envelope of the sound pressure wave [77].

Roughness intensity is also dependent on the modulation envelope, but this envelope appears different at high and low speeds. There is an indication that of the harmonics present, the 4th through 15th are of consequence to roughness [77]. Another type of vibration observed is waddle, which is combination of nosing and rolling motion of the vehicle. This motion is very sensitive to tire nonuniformities. Because the lateral and radial forces vary with each wheel revolution, and the effective rolling radii of left- and right-hand wheels are not exactly the same, the resulting motions may be in phase or in opposite phase. The effect may be felt through the steering wheel and experienced on flat roads as low frequency oscillatory forward motion combined with slight rolling motion. This low frequency nosing action of the vehicle can, for instance, be recorded with a drift angle meter attached to a front wheel, as described in section 7.3.3 figure 7.3.43.

Tire Uniformity Grading Machines

Numerous tire uniformity machines are described by various authors and many machines are in use. Figure 7.2.80 is a schematic of a tire uniformity machine [83]. The test tire is mounted on a precision rim with provision for rapid tire inflation. The tire is loaded against a drum of the largest size that is practical, since the roll size affects the force variations [82]. The tire is run at zero camber and zero slip angle at speeds less than 60 rpm. This low speed of 60 rpm or 1 rps has been chosen so that the amplitude of the tenth harmonic of the force variations can be reliably measured. This requires the minimum machine and tire resonant frequencies to be at least four times the frequency of the tenth harmonic, or 40 times the rotational frequency. Since the lowest tire resonance occurs at approximately 40 c.p.s., it is necessary to restrict the maximum wheel speed to 1 rps [82].

Reproducible results for both forward and reverse rotations are only obtained when the tires are properly conditioned.

The resulting force variations are recorded at the specified inflation and load, with a fixed distance between the tire and drum axle. This constant height method is employed since a constant load will cause axle height variations for nonuniform tires with resulting inertial and frictional errors in load application.

Some machines can measure radial, lateral and tangential force variations in tires, as well as free radial runout variations, free width variations, and the crown thickness. Free radial runout variations, are measured either on the centerline or on both shoulder ribs. The free measurements can be executed when force variations are measured, the displacement transducers being located a sufficient angular distance

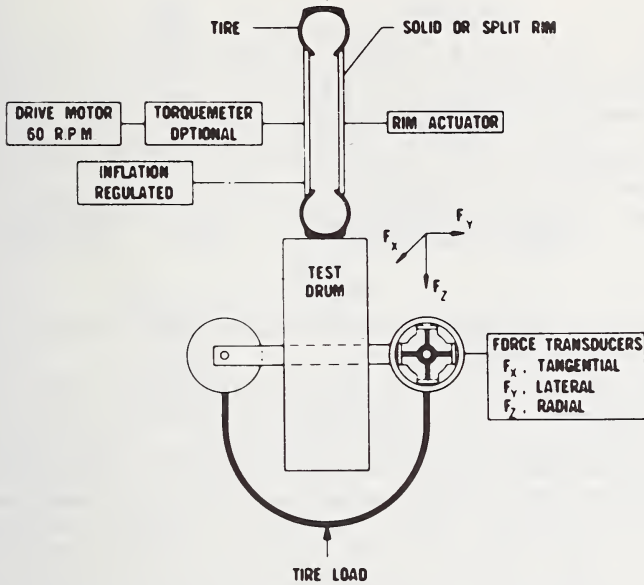


FIGURE 7.2.80. Scheme of a tire uniformity machine.

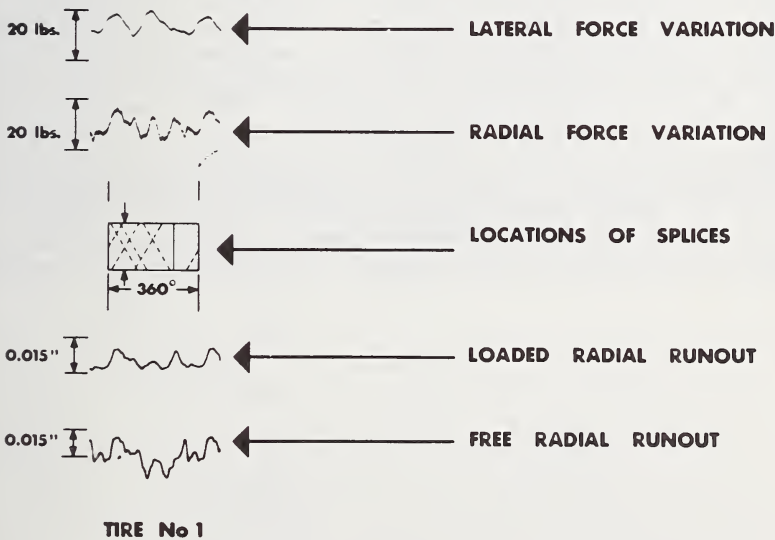


FIGURE 7.2.81. The relation between the location of splices and the corresponding uniformity measurements.

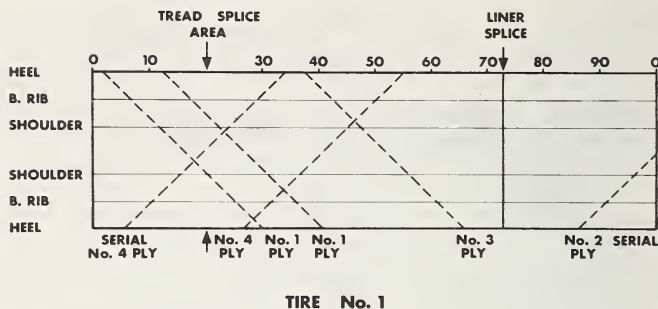


FIGURE 7.2.82. Chart showing the location of all ply splices and the liner splice.

from the footprint area to avoid distortions from loading [83]. However, the measurement of free radial runout is sometimes made on special machines with a preconditioned unloaded tire. A displacement transducer fixed in space contacts the crown of a slowly rotating tire.

To illustrate some results obtained from uniformity grading machines, figure 7.2.81 shows the effect of splices on uniformity measurements. After the measurements the tires were cut circumferentially in three places: the crown and the two buffing ribs on the sides of the tire. The location of all ply-splices and the liner splice were determined and noted on a chart. A typical chart is shown in figure 7.2.82, and a replica of this chart is shown with the corresponding uniformity measurements of figure 7.2.81. The measurements are "phased" so that all start from a common reference point on the tire, and the splice locations were determined according to the same reference point. We see that radial force variations occur at the liner splice and near the intersection of ply splices, where such intersections occur near the crown. The lateral force, loaded radius, and the free radius also show variation near the liner splice [88].

Another way to show that an automobile must be sensitive to uniformity fluctuations is the Gough-plot of cornering force versus self-aligning torque. It shows in a single plot the cornering force and the self-aligning torque generated at any position around the tire when the tire is rolled in clockwise and counterclockwise directions. Figure 7.2.83 shows the characteristic data for a poorly constructed steel belt tire manufactured during the early stages of development of this tire [89].

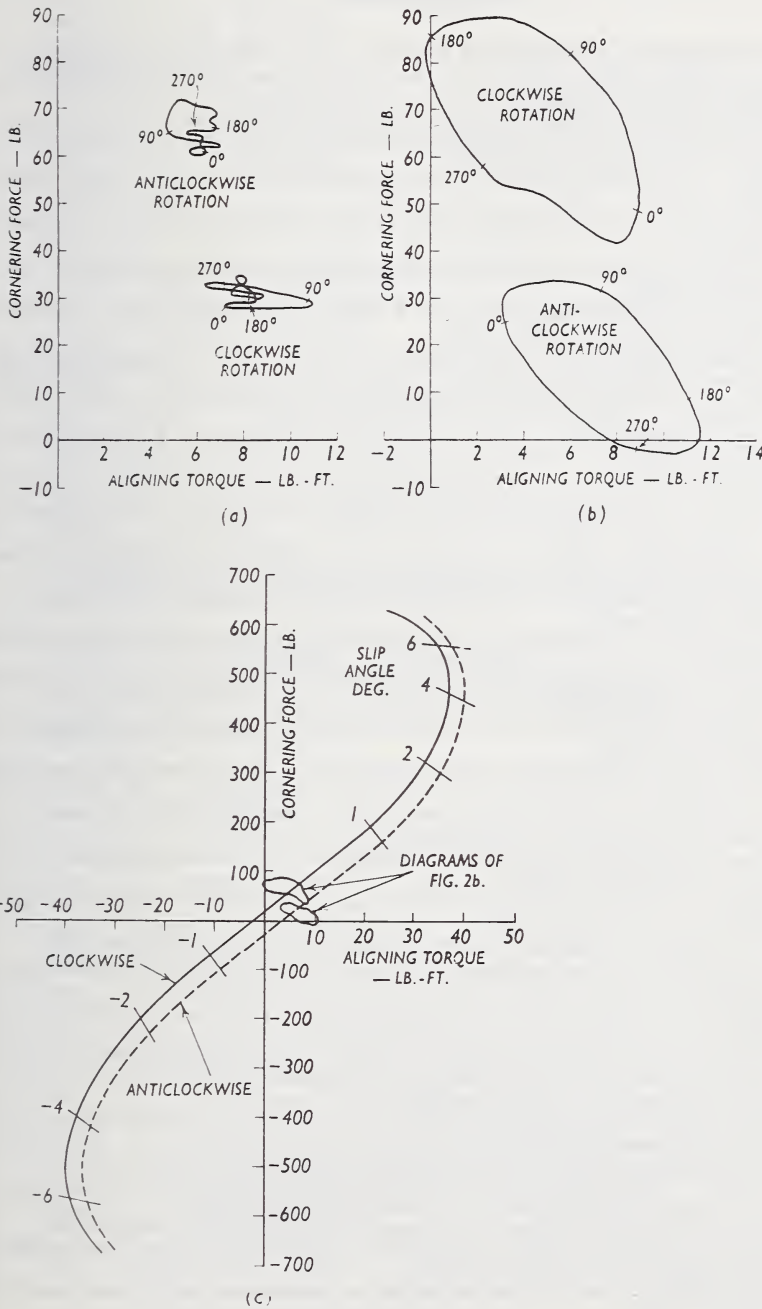


FIGURE 7.2.83. Gough plot of cornering force versus aligning torque fluctuations for a poorly constructed radial belt tire.

References

This bibliography refers frequently to V.R.L.D. reports made by the Vehicle Research Laboratory at Delft. These reports are in the Dutch language and can be obtained in microfilm or blueprint on payment.

- [1] Milliken, W. F., and Whitcomb, D. W., Close, W., and Muzzey, C. L. e.a., Symposium on research in automobile stability and control and tire performance, IME, Auto. Div., p. 107; SAE Trans., 344 (1956).
- [2] Gough, V. E., and Roberts, G. B., Dunlop cornering force machine, Trans. I.R.I. 33(5), (1957).
- [3] Kollmann, K., New testing machine for the study of tires, Revue Gén. du Caoutchouc (10) (1959).
- [4] Krempel, G., Experim. Beitrag zu Untersuchungen an Kraftfahrzeugreifen, Diss. Karlsruhe (1965).
- [5] Henker, E., Dyn. Kennlinien von P. K. W.-Reifen, Wissenschaftl.-Techn. Veröffentlichungen Automobielen H3 (1968).
- [6] Bruinsma, F., Design and measurements of an airbearing for a running belt with an electro-hydraulic vibrator system, V.R.L.D. Report No. 472^{a, b, c} (Sept. 1968).
- [7] Groels, G. K., Measurements and improvements on an airbearing, V.R.L.D. Report No. M080 (Aug. 1969).
- [8] Elsinga, H., Design of an endless steel band road simulator, V.R.L.D. Report No. 511 (March 1969).
- [9] Spaink, G. N., Friction and drainage measurements on abrasion paper of different qualities, V.R.L.D. Report No. 391 (April 1967) (Translated by Cornell Aeronautical Laboratory, Inc., Buffalo).
- [10] Van Eldik Thieme, H. C. A., Experimental and theoretical research on mass spring systems, FISITA 1960 (Elsevier Publishing Company, Amsterdam) p. 386.
- [11] Gough, V. E., and Whitehall, S. G., Universal tire test machine, FISITA 1962 (Inst. Mech. Eng., London).
- [12] Nordeen, D. L., and Cortese, A. D., Force and moment characteristics of rolling tires, SAE Paper No. 713A (June 1963); SAE Trans., 325 (1964).
- [13] Nothstine, J. R., and Beauvais, F. N., Laboratory determination of tire forces, SAE Paper No. 713B (1963).
- [14] Van Eldik Thieme, H. C. A., The measurement of tire characteristics, De Ingenieur, No. 28 and 30 (1964).
- [15] Ginn, J. L., and Marlowe, R. L., Road contact forces of truck tires, SAE Paper No. 670793 (1967).
- [16] Heesewijk, A. P. C. van, and Groeneweg, H. H., Description of six component tire tester, V.R.L.D. Report No. P055 (Aug. 1967).
- [17] Savkoor, A. R., Dynamic behaviour of an orthogonal tyre force measuring unit, V.R.L.D. Report No. P029 (July 1963).
- [18] Edema, L., Measuring platform, V.R.L.D. Report No. P017 (Nov. 1961); P017^a (Jan. 1962).
- [19] Van der Zee, P., Calibration of platform, V.R.L.D. Report No. 323 (Sept. 1964).
- [20] Van Donkelaar, H., Dynamic response of platform, V.R.L.D. Report No. 358 (Sept. 1965).
- [21] Yspeert, A. J., Inverse filter for measuring platform, V.R.L.D. Report No. 377 and 377^A.
- [22] Voermans, J. J., Results of pulsator excitations of measuring platform, V.R.L.D. Report No. 422 (Feb. 1968); Design of new measuring platform for truck tires, V.R.L.D. Report No. 150 (March 1968).
- [23] Bakker, C. C., Normal force and longitudinal force response to vertical axle motions, V.R.L.D. Report No. 486 (Nov. 1968).
- [24] Buis, P., Pneumatic tires, V.R.L.D. Report No. P084 (1967).
- [25] Koolhof, F. J. W., Polman, J., and Olland, R. C., Static and dynamic testing of pneumatic tires, V.R.L.D. Reports No. A032, P004-P005 (1958/59).
- [26] Cooper, D. H., Radial stiffness of the pneumatic tire, Trans. I.R.I. 40, 58 (1965).
- [27] Weber, G., Theorie des Reifens mit ihrer Auswirkung auf die Praxis bei hohen Beanspruchungen, A.T.Z. 56(12), 325 (1956).
- [28] Stulen, J. H. B., Comparison of road and drum measurements, V.R.L.D. Report No. 326 (Nov. 1964).

- [29] Gengenbach, W., and Weber, R., Messung der Einfederung von Diagonal-und gürtelreifen, A.T.Z. **71**, 196 (1969).
- [30] Chiesa, A., and Tangorra, G., The dynamic stiffness of tyres, *Revue Gén. du Caoutchouc* **36**(10), 1321 (1959).
- [31] Rasmussen, R. E., and Cortese, A. D., Dynamic spring rate performance of rolling tires, SAE Paper No. 680408 (1968).
- [32] Krempel, G., Experimenteller Beitrag zu Untersuchungen an Fahrzeugreifen, Diss. (1965); A.T.Z., 1 and 262 (1967).
- [33] Davisson, J. A., Design and application of commercial type tyres, SAE Paper No. SP-344 (1969).
- [34] Strigle, C. E., Wide base tires—a new concept for light trucks, SAE Paper No. 680083 (Jan. 1968).
- [35] Timan, D. A., and Rooney, J. H. M., Static load deflection relationships of several tires, V.R.L.D. Report No. P108 (Jan. 1969).
- [36] Essers, E., and Kotitschke, J., Ueber die dynamischen Radlasten von Lastkraftwagen, Techn. Hochschule Aachen (1957).
- [37] Vegter, T., Measurements of dynamic wheel loads, V.R.L.D. Reports 214 (1959) and U020 (1960).
- [38] Mühlfeld, A., Ein hochfrequenztechnisches Verfahrens für Reifen und Schwingungsmessung, Diss. T. H. Braunschweig (1949); A.T.Z., 147 (1953).
- [39] Bomhard, F. J. von, Verfahren zur Messung der dynamischen Radlast beim Kraftwagen, Diss. T. H. München (1956); Deutsche Kraftfahrtforschung **131** (1959).
- [40] Burgman, E. F. M., Dynamic tire deflection measurements, V.R.L.D. Report No. 390 (1967).
- [41] Knight, S. J., and Green, A. J., Deflection of a moving tire on firm to soft surfaces, SAE Trans. **5**, 116 (1962).
- [42] Gengenbach, W., and Weber, R., Neues Verfahren zur gleichzeitigen Bestimmung der Einfederung und der Verformung eines Reifens in Umfangsrichtung während des Betriebes, *Automobil Industrie* **3**, 93 (1969).
- [43] Svenson, O., Untersuchung dynamische Kräfte zwischen Rad und Fahrbahn, deutsche Kraftfahrtforschung **130** (1959).
- [44] Senger, G., Ueber dynamische Radlasten beim Ueberrollen kurzweiliger Unebenheiten durch schwere luftreifen, Deutsche Kraftfahrtforschung **187** (1967).
- [45] Lippmann, S. A., Nanny, J. D., Analysis of the enveloping forces of passenger tires, SAE Paper No. 670174 (Jan. 1967).
- [46] Missel, H., Research on tire behaviour on a flat road, Diss. Techn. Univ. Delft (1932).
- [47] Floor, W. K. G., The effective rolling radius of pneumatic tyred wheels, Nat. Aeron. Res. Inst. Report 428 (1954).
- [48] Vickers, H. H., and Robison, S. B., Measurement of tread motions and application to tire performance, Proc. Int. Rubber Conf., 1959.
- [49] Evans, R. D., Factors affecting the power consumption of pneumatic tyres, Proc. Second Rubber Tech. Conf., London, 1948, p. 438.
- [50] Fogg, A., Measurement of aerodynamic drag and rolling resistance of vehicles, FISITA Congress, 1964 (Soc. Auto. Eng. of Japan, Tokyo).
- [51] Roberts, G. B., Power wastage in tires, Proc. Int. Rubber Conf., Nov. 1959.
- [52] Frolov, L. B., and Khromov, M. K., Determination of the rolling resistance of tyres by an electric torque meter, Sov. Rubber Tech. (9) (1965).
- [53] Curtiss, W. W., Low power loss tires, SAE Paper No. 690108 (Jan. 13–17, 1969).
- [54] Stiehler, R. D., and Steel, M. N., Power loss and operating temperature of tires, Proc. Int. Rubber Conf., Washington, Nov. 1959, p. 73.
- [55] Collins, J. M., The relevance of elastic and loss moduli of tyre components to tyre energy losses, Paper to Div. Rubber Chemistry, Am. Chem. Soc. (1964).
- [56] Kainradl, P., Kaufmann, G., and Schmidt, F., Zusammenhang der Erwärmung von L.K.W. Reifen mit den visco-elastischen Eigenschaften der verwendeten Gummiqualitäten, *Kautschuk und Gummi-Kunststoffe* (1), 27–36 (1966).
- [57] Yurkovski, B., Effect of design parameters on the rolling resistance of tyres, Sov. Rubber Tech. (11), 32–54 (1966).
- [58] Khromov, M. K., and Bruev, E. V., Rolling losses of radial ply tires in a wide speed range, Sov. Rubber Tech. (1965).
- [59] Anonymous, Tyres, a review of current constructions, developments, performance, *Automobile Engineer*, 274–288 (July 1969).

- [60] Paish, M. G., Effects of tractive effort on rolling resistance and slip of pneumatic tyres, Motor Industry Research Association M.I.R.A. Report 1965/16.
- [61] Grosch, K. A., The effect of tyre surface temperature on the wear rating of tread compounds, J. I.R.I. 1(1) (Jan. 1967).
- [62] Spelman, R. H., Determination of passenger tire performance levels—high speed, SAE Paper No. 690508 (Chicago, Illinois, May 1969).
- [63] Richey, G. G., Hobbs, R. H., and Stiehler, R. D., Temperature studies of the air in a truck tire, Rubber Age **79**, 273–276 (1956).
- [64] Horning, V. J., The temperature measurement at the Government Tire Test Fleet, Rubber Age **74**, 395–396 (1953).
- [65] Coddington, D. M., Marsh, W. D., and Hodges, H. C., New approach to tire durability testing, Rubber Chem. Tech. **38**(4), 741–756 (1965).
- [66] Ludwig, G., Rhodes, D., and Simson, B., Thermistor takes temperature of running tire, Nat. Bur. Stand. (U.S.), Tech. News Bull. **52**(6), 119–120 (1968).
- [67] Parker, R. C., and Marshall, P. R., The measurement of the temperature of sliding surfaces, Proc. IME **148**, 209 (1948).
- [68] Minkes, S., Surface temperature measurements by an infrared radiation method with indium-antimonide cells, V.R.L.D. Report No. 538^{a, b, c} (1969).
- [69] Hoogen, E. v.d., Possibilities to trace hot spots in the tread of tires. V.R.L.D. Report P012 (1960).
- [70] Buis, P., Braking measurements on pneumatic tires, V.R.L.D. Report No. 313 (1963).
- [71] Holmes, K. E., and Stone, R. D., Tyre forces as functions of cornering and braking slip on wet road surfaces, R.R.L. Report LR254 (Road Research Laboratory, 1969).
- [72] Davisson, J. A., Basic test methods for evaluating tire traction, SAE Paper No. 680136 (Jan. 1968).
- [73] Meades, J. K., The effect of tyre construction on braking force coefficient, R.R.L. Report LR224 (Road Research Laboratory, 1969).
- [74] Hörz, E., Die Einfluss von Bremskraftreglern auf die Brems- und Führungskraft eines gummbereiften Fahrzeugs, Deutsche Kraftfahrtforschung **195** (1968).
- [75] Bajer, J. J., Proposal for a procedure for evaluating wet skid resistance of a road-tire-vehicle, SAE Paper No. 690526 (May 1969).
- [76] Kelley, J. D., Factors affecting passenger car tire traction on the wet road, SAE Paper No. 680138 (Jan. 1968).
- [77] Radt, H. S., The mechanism of tire thump and roughness, SAE Paper No. 322C (1961).
- [78] Davisson, J. A., Factors of tire design and manufacture affecting uniformity, SAE Paper No. 650521 (1965).
- [79] Lippmann, S. A., The forces and torques associated with roughness in tires, SAE Paper No. 322D (1961).
- [80] Cimprich, F. J., Elimination of temperature induced non-uniformity in tires by air-ring control, SAE Paper No. 690075 (1969).
- [81] Morrish, L. M., and Haist, R. R., The effect of loaded radial runout on the roughness and shake, SAE Paper No. 322E (1961).
- [82] Nordeen, D. L., and Rasmussen, R. E., Factors influencing the measurement of tire uniformity, SAE Paper No. 650734 (1965).
- [83] Hofelt, C., Uniformity control of cured tires, SAE Paper No. 690076 (1969).
- [84] Van Eldik Thieme, H. C. A., Passenger riding comfort criteria and methods of analysing ride and vibration data, SAE Paper No. 295A (1961).
- [85] Hofkamp, H. J., Perception of shocks in vehicles, V.R.L.D. Report No. V119 (1969).
- [86] I.S.O. Committee, Mechanical vibration and shock, I.S.O./T.C.—108–100E (June 1969).
- [87] Bajer, J., The control of tire nonuniformity and a passenger car from manufacturer's point of view, SAE Paper No. 667B (1963).
- [88] Hofelt, C., Tarpinian, H. R., and Draves, C. Z., Measuring tire uniformity, SAE Paper No. 65022 (1965).
- [89] Gough, V. E., Barson, C. W., Gough, W. S., and Bennett, W. D., Tyre uniformity grading machine, SAE Paper No. 322A (1961).
- [90] Slager, K. M., Dynamic tire deflection measurements, V.R.L.D. Report No. 318 (1964).

7.3. Cornering and Camber Experiments

H. C. A. van Eldik Thieme

7.3.1. Introduction

When an externally applied side force F acts at the centerline of a nonrolling wheel, the lateral frictional forces exerted by the road surface on the tire will cause a lateral tire deformation as shown in figure 7.3.1. The top part T of the tire, not in contact with the road, is seen to be almost undeformed. Usually we are not so much interested in the deformation of a standing tire as we are in the phenomena of the rolling tire. Therefore consider a side force acting on a rolling wheel. The undeformed top part T of the tire rolls gradually into the deformed condition by coming into contact with the road surface [1].¹

A top view of the lateral deformation is given in figure 7.3.1b, assuming that these lateral tire deformations have attained steady state. At the instant of contact with the road, we observe that the peripheral carcass line already has a lateral deflection $A'A$. Passing through the contact zone, the lateral carcass deflection increases until point E is reached, after which side slip of the line reduces the lateral deflection. Due to some extra lateral tread rubber deformation EB , the tread elements first coming in contact with the road adhere to the road surface over the distance AB . The equatorial line running along the middle of the tread surface shows the lateral deformation of the tire tread, as represented by line ABD , where all deformations are exaggerated for clarity (fig. 7.3.1c).

The direction of travel of the wheel is indicated by line AB , making an angle with the plane of the wheel. The angle is called the slip angle. The resultant lateral tire force F_y acts a distance t behind the geometric center C of the contact area, causing the tire to generate a self-aligning torque M_z . The distance t is called pneumatic trail. The diagram shown in figure 7.3.1d is a schematic representation of figure 7.3.1b. A slip angle α is formed between the direction of travel of the center of tire contact C and the x -axis situated in the wheel plane.

Side forces may be due to centrifugal action when cornering, road unevenness, small movements of the wheels for directional control, wind forces, and the lateral component of the weight on a cambered road surface. For illustration, some typical cases of automobile response to side forces will be discussed below.

Nonsteered Vehicles

Consider the simplified case of a vehicle having constant forward speed, with a driver holding the steering wheel in a fixed straight ahead

¹ Figures in brackets indicate the literature references at the end of this section.

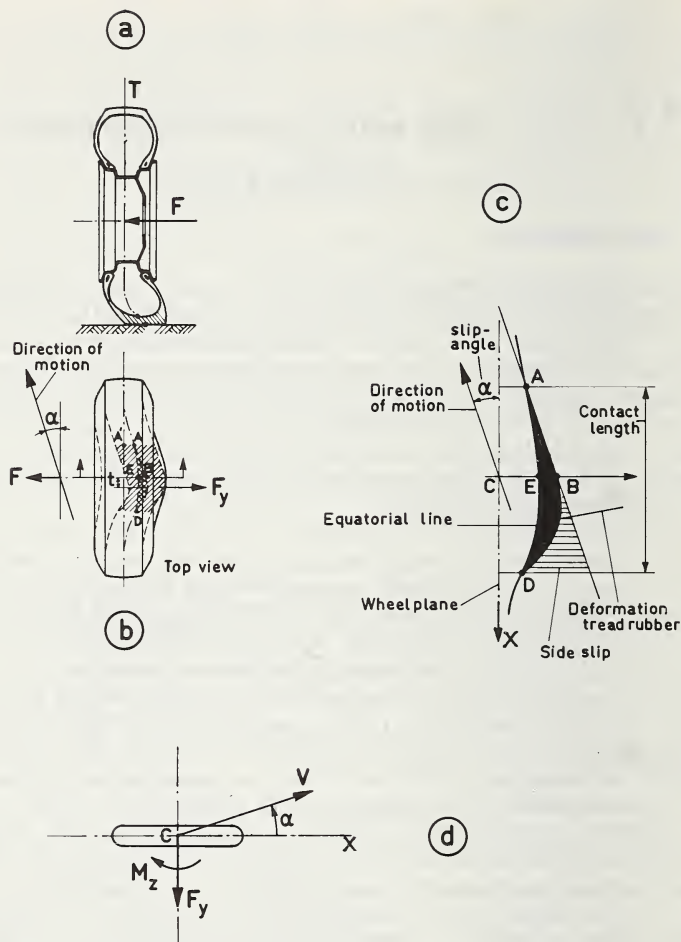


FIGURE 7.3.1. An externally applied side force causes a lateral tire deformation.

The slip angle α of the direction of motion with the plane of the wheel is shown together with the resultant lateral tire force F_y and the self-aligning torque M_z .

position. The vehicle is allowed to change its direction of motion under the action of lateral forces. This condition has been represented in figure 7.3.2.

The externally applied lateral force must be in equilibrium with the lateral forces F_y acting on the tires by the road. These forces result in slip angles α_f and α_r of the front and rear wheels. The relation between lateral force and slip angle is governed by the tire characteristic. We first consider the particular case in which, at equal front and rear slip angle ($\alpha_f = \alpha_r$), the resultant lateral tire force acts in the center of gravity C_G . When the external lateral force is also applied at the C_G

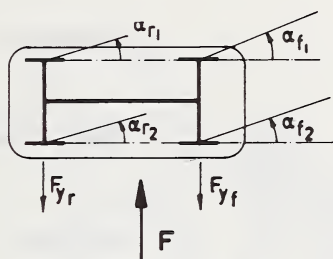


FIGURE 7.3.2. The effect of an externally applied lateral force on the front and rear wheel slip angles.

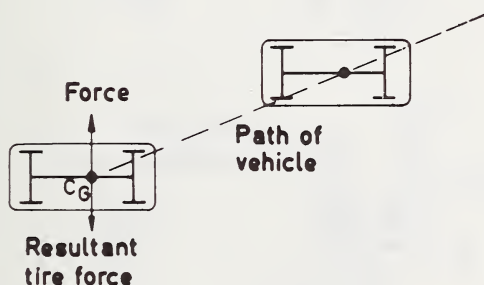


FIGURE 7.3.3. Path of the vehicle at equal front and rear slip angles (neutral steer).

(for instance on a cambered road), the vehicle drifts sideways along a linear path, with an angle between its longitudinal vehicle axis and the direction of motion. When this translatory motion (without yaw velocity) takes place as shown in figure 7.3.3, the automobile is said to have a neutral steer character. A concept often employed is the neutral steer-point, or the neutral steer-line in the X - Z plane, upon which an externally applied lateral force will not produce a yaw velocity. In the particular case of neutral steer considered above, the neutral steer-point coincides with the center of gravity.

In figure 7.3.4 the response in case of understeer and oversteer has also been shown. In these cases the neutral steer-point is located behind and in front of the center of gravity, respectively. For an external lateral force acting at the center of gravity we have with an understeer vehicle $\alpha_f > \alpha_r$ and with an oversteer vehicle $\alpha_f < \alpha_r$.

As discussed before, the externally applied lateral force may also be due to side winds. The resultant side wind force F_w is supposed to act at the so-called "center of pressure" C_p , and this point may be located in front of the center of gravity C_G . The location of C_p depends on the

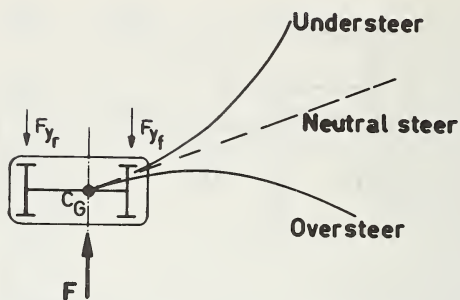


FIGURE 7.3.4. Illustration of understeer, neutral steer and oversteer.

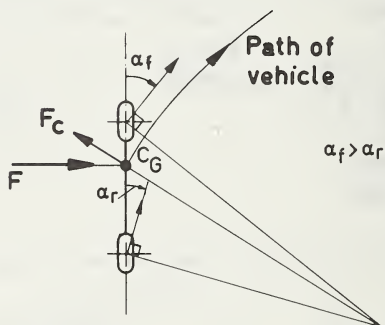


FIGURE 7.3.5. Path of the vehicle when $\alpha_f > \alpha_r$.

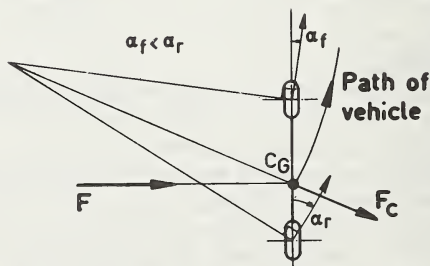


FIGURE 7.3.6. Path of the vehicle when $\alpha_f < \alpha_r$.

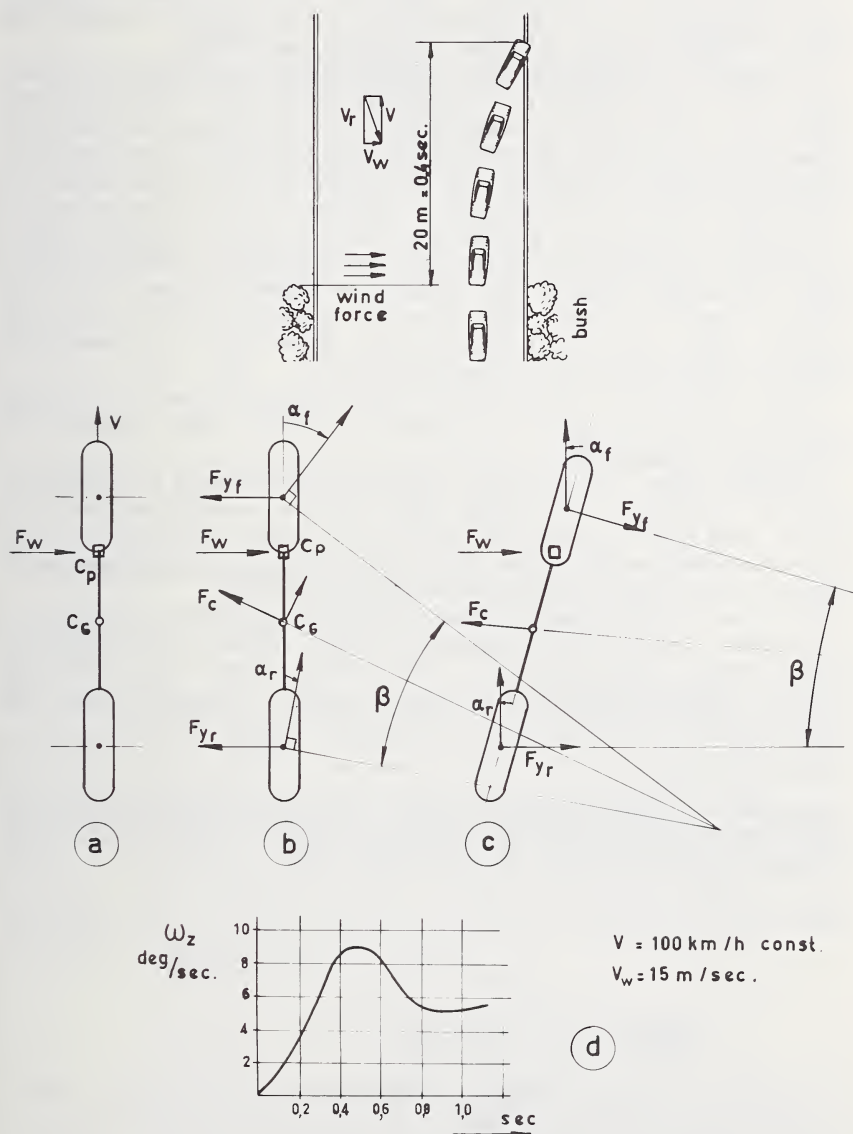


FIGURE 7.3.7. Path of the vehicle with the resultant side wind force F_w acting in the center of pressure C_p .

aerodynamic styling of the vehicle, on the forward vehicle speed, and on the magnitude and direction of the wind velocity.

It is clear that depending upon vehicle inertia, tire characteristics and magnitude and point of application of the external lateral forces, the slip angles of the front and rear wheels may differ considerably.

A simplified explanation may be given using an idealized model, where the center of gravity of the vehicle is assumed to lie in the road surface. It is furthermore assumed that at front and rear, the left and right wheels have equal slip angles, which means that the wheels may be imagined as being compressed together along the axle center lines, and consequently that the automobile is replaced by a two-wheeled model.

Consider a side force applied at the center of gravity when the vehicle is moving forward along a straight path. Assume the front wheel to exhibit larger slip angles than the rear wheels, as shown in figure 7.3.5. This tends to turn the vehicle away from the applied lateral force F . The rotation about the instantaneous center gives rise to a centrifugal force F_C which opposes the applied side force F .

If the side force F produces slip angles $\alpha_f < \alpha_r$, then the resulting centrifugal force F_C tends to help the side force F . This condition has been shown in figure 7.3.6.

Consider again a nonsteering vehicle moving forward at a constant speed of 100 km/hr. in a straight path, but now suddenly subjected to a side wind with a lateral velocity $V_w = 15$ m/sec. resulting in a side force F_w acting at the center of pressure C_P (fig. 7.3.7a). It may be of interest to show some experimental results obtained [2].

It is observed that after a sudden wind force application the transient motion may develop in a complicated manner. Figure 7.3.7 illustrates such a behavior, where first (fig. 7.3.7b) both tire forces oppose the wind force F_w and afterwards the tire forces appear to change in sign. The variation of the yaw velocity observed is also shown (fig. 7.3.7d).

Steered Vehicles

Consider a vehicle running through a curve with a transverse slope of the road surface. The forces acting on the simplified vehicle with rigid suspension system are shown in figure 7.3.8.

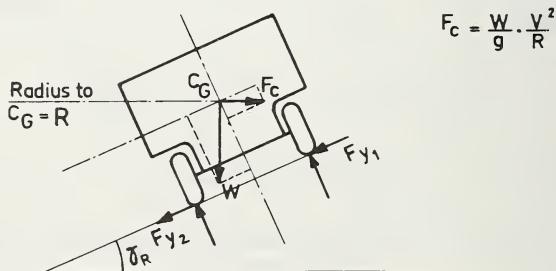


FIGURE 7.3.8. Forces acting on a vehicle running through a banked curve.

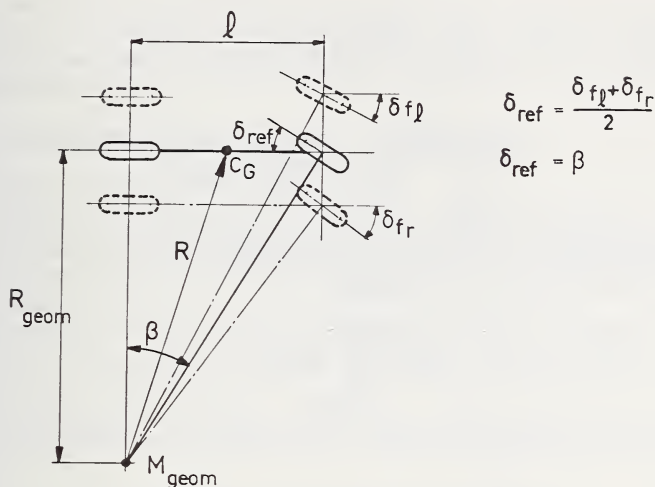


FIGURE 7.3.9. The reference steer angle δ_{ref} and the geometric radius of turn R_{geom} .

The equation of forces in the direction of the slope reads:

$$F_{y_1} + F_{y_2} = \frac{W}{g} \cdot \frac{V^2}{R} \cos \gamma_R - W \sin \gamma_R$$

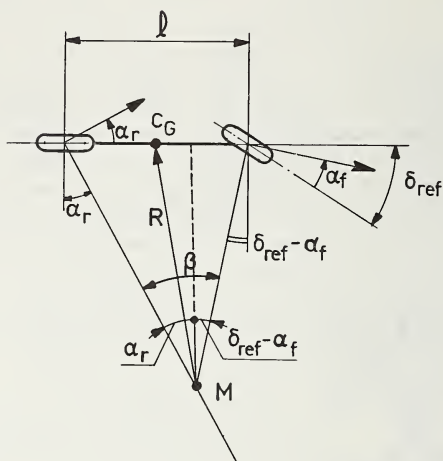
When the component of the inertial force F_C is in equilibrium with the component of the weight (equilibrium speed), there are no lateral tire forces F_y required in the road surface and consequently the slip angles of the wheels are zero.

A similar condition arises when going through a flat curve with a vehicle speed approaching zero (fig. 7.3.9). In this simplified case of a vehicle having an ideal Ackermann steer geometry, the wheel base angle β is equal to the reference steer angle δ_{ref} . For $R \gg l$, where l is the wheelbase, the geometric radius of turn $R_{geom} = l/\beta$ may be taken equal to R . For $V \rightarrow 0$ we consequently have:

$$R = R_{geom} = \frac{l}{\delta_{ref}}$$

The idealized two-wheeled model also shown in figure 7.3.9 can be used effectively to interpret experimental tire data for application to a vehicle traveling at a speed V . The steer angle δ required to keep a vehicle on a constant radius path in a so-called steady state turn is a function of the front and rear slip angles.

Assuming that all angles and traction forces are small, the equation for the required steer angle follows from figure 7.3.10

FIGURE 7.3.10. *Idealized two wheeled model.*

$$\beta = \frac{l}{R} = \delta_{ref} - \alpha_r + \alpha_r$$

$$R = \frac{l}{\delta_{ref} - (\alpha_f - \alpha_r)}$$

Consequently when:

$$\alpha_f = \alpha_r \quad \text{then } R = R_{geom} \text{ (neutral steer)}$$

$$(\alpha_f - \alpha_r) > 0 \text{ then } R > R_{geom} \text{ (understeer)}$$

$$(\alpha_r - \alpha_f) < 0 \text{ then } R < R_{geom} \text{ (oversteer)}$$

This simplified analysis of vehicle behavior illustrates the definition of understeer and oversteer in the linear representation.

To obtain a better understanding of the behavior of vehicles at low and high lateral accelerations, including the influence of suspension system, it is necessary to consider a number of other important quantities such as moments of inertia, lateral and longitudinal load transfer, steering system elasticity, roll steer and roll camber, self-aligning torques at the front and rear wheels, etc.

It is obvious that the study of directional vehicle control is very complicated, and beyond the scope of this book. The reader is referred to the literature for a more detailed treatment of the subject of vehicles having steered front wheels [3-6]. Readers are also referred to the reference list of section 7.5 [29-43].

It is hoped that the simplified introduction given above has shown the importance of obtaining experimental tire data, such as slip angle, cornering force and self-aligning torque relations, to be treated in the following subsections.

7.3.2. Cornering Experiments

Photography of Contact Area Deformations

The difference in deformation between a vertically loaded free rolling tire ($\alpha=0$) and a cornering tire can be illustrated by photographing the contact area of tires through a glass plate with grids during slow motion [5] (fig. 7.3.65).

Measurements of the resulting deformations can be carried out in the same way as previously discussed in section 7.2.5 for the case of a braking tire.

First a photograph is taken of the free rolling tire ($\alpha=0$). Then a second photograph can be taken of a standing laterally undeformed tire,

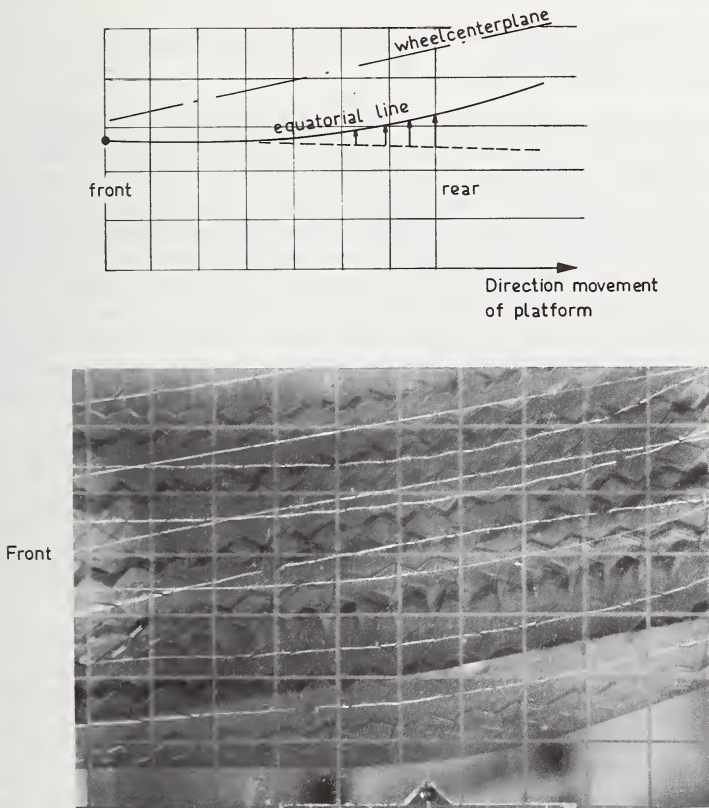


FIGURE 7.3.11. Cornering experiment showing deformation of equatorial line.

set of a predetermined angle to the direction of motion of the movable platform, representing static condition.

Afterwards, using the same negative, a third photograph is made on top of the second one, but now with the tire rolled in the laterally deformed steady state cornering condition (fig. 7.3.11). The difficulty with this method is the experience necessary to synchronize the photographs, but it is also very time consuming to analyze the photographic data to define the form of the equatorial line.

A glass plate device to study tire deformations is also used at several proving grounds by driving a vehicle straight onto the glass plate with the front wheels toed-in to a predetermined steer angle. Due to steering system flexibility it is difficult to measure the exact slip angles, and it seems desirable to use a slip angle measuring device as described in section 7.3.3, figures 7.3.43-44.

The photographic technique is either to attach the camera onto the vehicle and photograph through the glass plate, looking at the contact patch in a mirror, or to photograph from beneath as tires pass over the glass surface [7].

Movable Platform Measurements with the Gough Apparatus

A. Lateral deformations

The deformation due to the lateral flexibility of a tire rolling at a slip angle may also be obtained with a flat surface modified version of the original Gough apparatus [6] mounted in the flat platform machine [5] (fig. 7.3.65). The platform travels at a constant speed of about 0.05 m/sec.

When the platform has travelled such a distance that the lateral tire deformations are assumed to have reached steady state condition, the tire is allowed to roll over the Gough apparatus [10]. The original version of this apparatus, mounted behind the moving glass plate, had a steel upper surface. In order to avoid a difference in coefficients of friction on steel and glass, both surfaces are now covered with a sheet of transparent perspex. As discussed [5], the Gough apparatus has three measuring bars.

The bar measuring the lateral force distribution is equipped with a steel fork which can move in a narrow slot, situated on the lateral centerline of this transverse bar of the Gough apparatus. Lateral sliding of the tread element penetrated by the steel fork, with respect to the platform (fig. 7.3.12), is recorded using a potentiometer coupled to the steel fork [10]. We speak of sliding because a relative motion of a tread element with respect to the road surface is observed.

Because the test tire is mounted on a structure with a turntable having a transverse slide, the mechanism allows for a lateral movement of the wheel center plane with respect to the platform. The initial lateral deformation $A'A$ of the tire where contact begins (fig. 7.3.1b) can now be taken into account by a suitable transverse movement CM of the slide, so that the steel fork penetrates the tire tread surface exactly at point A of the equatorial line as marked on the tread (fig. 7.3.13). This is done by observation in the longitudinal direction of the platform at the position of the steel fork with respect to the equatorial line.

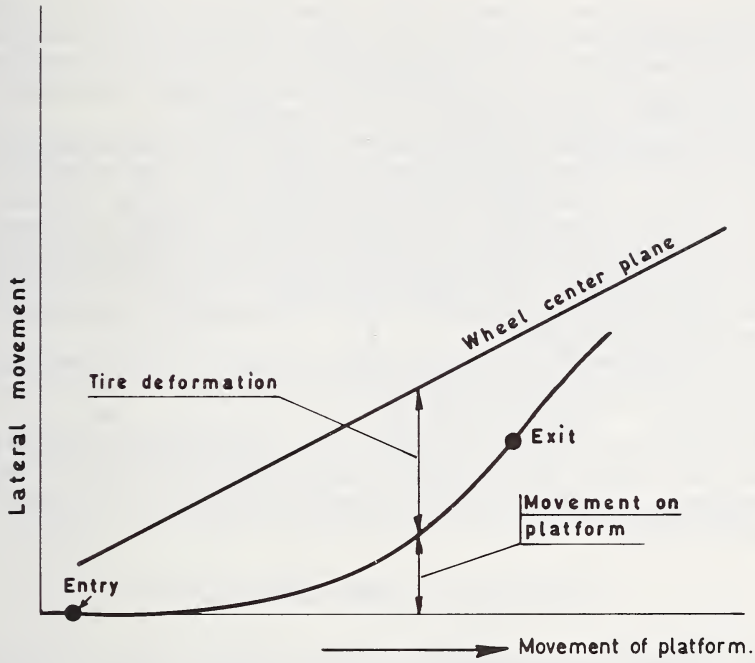


FIGURE 7.3.12. Movable platform measurements showing lateral tire deformation and sliding of a tread element with respect to the platform.

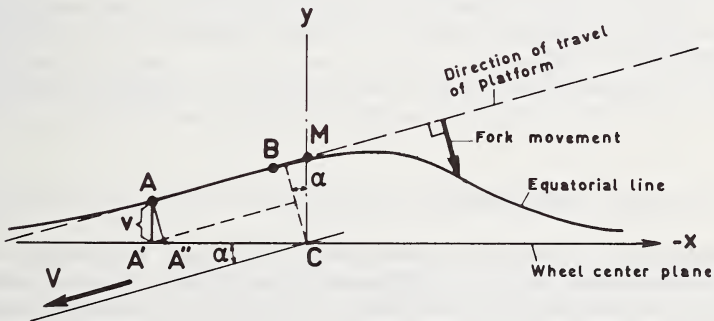


FIGURE 7.3.13. Geometry of lateral slip and deformation of the equatorial line within the contact zone.

At low slip angles we observe that a tread element coming into contact with the slowly moving platform first adheres almost fully to the surface, so that the assumption of no lateral sliding is reasonable ($V_{sx} = V_{sy} = 0$) and the original undeformed equator line travels parallel to the direction of motion. The steel fork does not move laterally.

As the tread element moves further in the contact zone, it produces a deflection v with respect to the wheel plane which, depending on the lateral carcass stiffness C_c and the rubber tread element stiffness C_p [27], increases linearly with increasing distance, causing an increasing lateral force until the local limiting frictional force is reached. The tread element then begins to slide towards the wheel center plane. This lateral sliding of the tread element with respect to the platform is measured with the movable steel fork.

We are interested in the displacements u and v of a tread element with respect to its position in the undeformed situation in the X and Y direction respectively.

The initial lateral displacement v of the tread element A , which first comes into contact with the platform (fig. 7.3.13) can be found to within a small error, using the assumption that $A'A'' = 0$. Hence, as represented in figure 7.3.13,

$$v = CM \cos \alpha - (AM - CM \sin \alpha) \tan \alpha.$$

The vertical force measuring bar gives a reference signal on a record indicating the moment that contact begins with the platform. This is point A on the equator line, M being the center of the turntable supporting the test tire, and is indicated by a microswitch signal received from the moving platform, so that the distance AM is known.

The distance CM is read from a scale attached to the support of the lateral slide mechanism, and the rotation angle α of the turntable is also read from a scale.

By transformation of the fork measurements, as indicated, the lateral deformation v can now be calculated.

B. Longitudinal deformation

As already discussed in section 7.2 (see [5] of sec. 7.2 and fig. 7.3.63), the measurement of the longitudinal deformations with a camwheel mounted in the longitudinal force bar is a very time consuming procedure because several runs are necessary to obtain a reasonable accuracy. Due to the lateral sliding, other neighboring tread elements will come into contact with the circumference of the camwheel. However, the track of one individual tread element of the equatorial line over the surface can be constructed approximately because the lateral movement of one tread element, as measured with the fork, is known.

By repeating the longitudinal deformation measurements several times, by giving the slide a lateral movement of 5 mm. or less after each run,

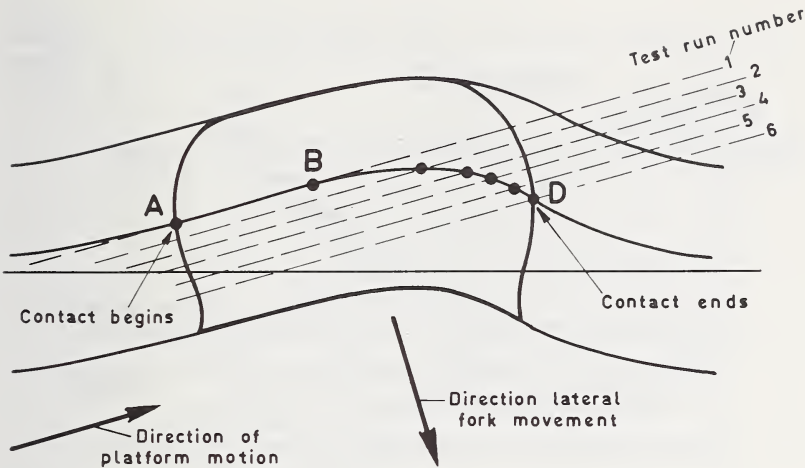


FIGURE 7.3.14. Longitudinal deformation measurements in the contact zone.

the real longitudinal slip line of one tread element can be reconstructed [9]. As can be seen in figure 7.3.14, several lines are drawn parallel to the direction of travel of the platform. The different points of intersection of these lines with the deformed equator line give an indication of the position along the contact length of the original tread element. The real longitudinal slip line, is now reconstructed with parts of the individual longitudinal slip lines belonging to the points of intersection with the lateral slip line as shown in figure 7.3.15.

C. Combination of lateral and longitudinal deformation

The lateral and longitudinal movement of a tread element of the equatorial line can now be calculated and figure 7.3.16 shows the paths of a tread element, parallel and perpendicular to the direction of motion, for different slip angles α [24]. From these results it is seen that without braking or driving forces longitudinal sliding occurs, and that the lateral sliding at the end of the contact zone is almost perpendicular to the direction of motion.

At increasing slip angles the deformation of the contact zone will increase, resulting in increasing lateral forces. It is seen that at larger slip angles the adhesive zone decreases, resulting in an increasing sliding zone at the rear of the contact area (fig. 7.3.17).

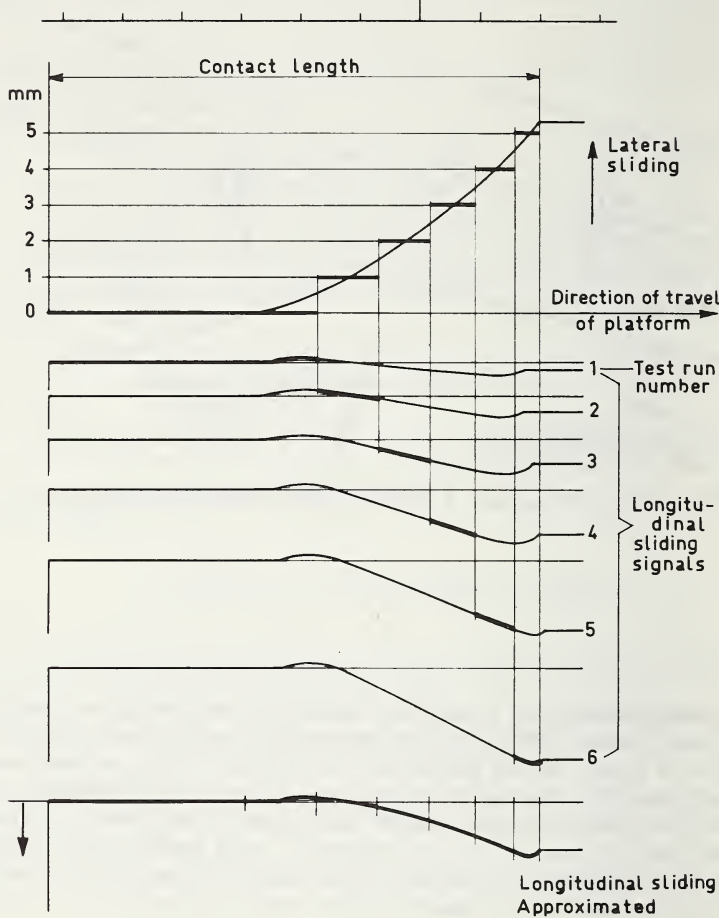


FIGURE 7.3.15. *Reconstruction of the longitudinal slip line of a tread element moving through the contact zone.*

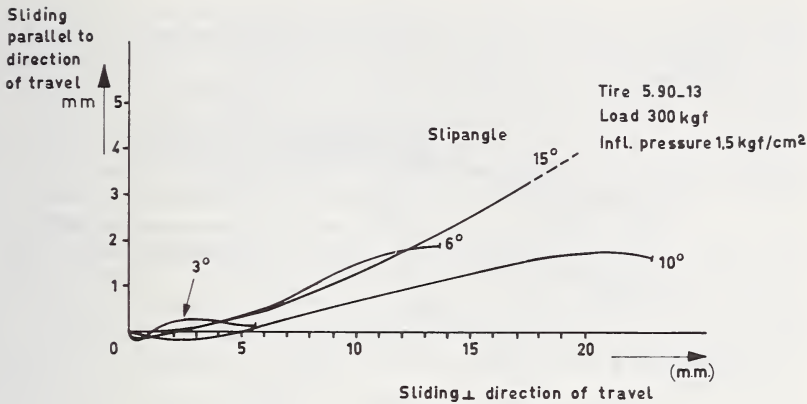


FIGURE 7.3.16. Paths of a tread element for different slip angles α .



FIGURE 7.3.17. The sliding zone at the rear of the contact area.

D. Sliding velocity

As can be seen from the lateral deformation curve of the equatorial line, a tread element gradually rolls into its deformed situation. We observe at the leading edge A where contact begins a lateral deflection v with respect to the undeformed situation (fig. 7.3.18).

Assuming adhesion over the distance AB , the drifting tire shows an equator line which is straight and parallel to the vector V , hence $\partial v / \partial x = \alpha = \text{constant}$. Because no lateral sliding occurs in this region, the lateral sliding velocity $V_{sy} = 0$. Consequently, the value of the deformation velocity V_d of the tread element will be equal to the lateral component $V \sin \alpha$ of the forward velocity V , so that we can write:

$$V_{sy} = -V \sin \alpha + V_d = 0$$

Travelling further in the contact zone over the distance BH , we observe a decrease of $\partial v / \partial x$ until point H , where we obtain the value $\partial v / \partial x = 0$ and $V_{sy} = -V \sin \alpha$.

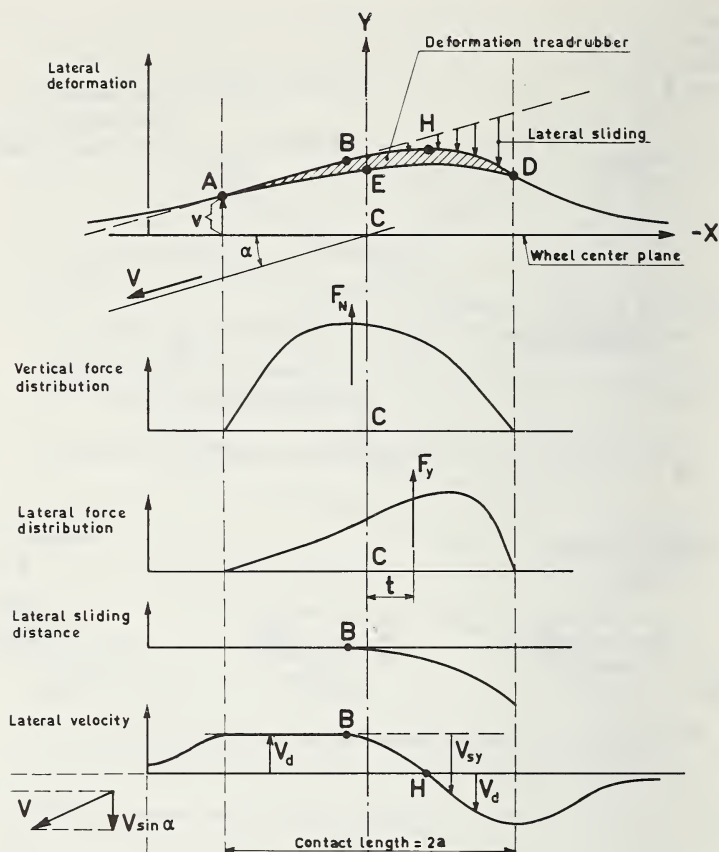


FIGURE 7.3.18. *Distribution of forces, lateral sliding distance and lateral velocity over the contact length.*

Due to the change in slope beyond H of the lateral deformation curve of the equatorial line, the lateral deformation velocity V_d now changes in sign resulting in further increase of the sliding velocity V_{sy} beyond point H .

Having reached the rear end of the contact zone at point D , the tread element of the equatorial line gradually returns to the wheel center plane as indicated in the figure [24].

E. Lateral force distribution

In discussing the lateral deformation of the tire, we observed for moderate slip angles α that a tread element on entering the contact zone

at first adheres to the platform. As the tread element moves further in the contact zone, it produces a deflection which increases linearly with increasing distance, causing an increasing lateral force. Dependent on the vertical force distribution, which gradually drops to zero at the rear of the contact zone, the local limiting friction is reached, and the tread element begins to slide back towards the wheel center plane, thus reducing the lateral force, as shown in figure 7.3.18. Note that the peak value of lateral force distribution is not reached until after sliding has started.

When the tire travels over the lateral force measuring bar of the Gough apparatus, we obtain the lateral force function. The resultant lateral force F_y may be obtained by integrating the recorded force function, and can be compared with the total lateral force F_y , as measured with the six-component tire tester, also mounted in the movable platform machine.

For moderate slip angles α , as shown in figure 7.3.19, the resultant lateral force F_y acts at a distance t behind the contact center C . The distance t is known as the pneumatic trail.

Neglecting the longitudinal force distribution in the contact area, we find, in this simplified case of purely lateral slip, a value for the moment about a vertical axis $M_z = -F_y \cdot t$.

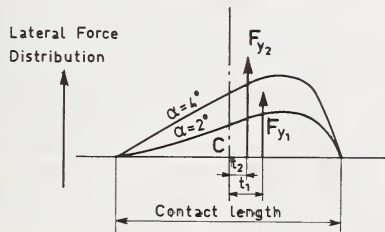


FIGURE 7.3.19. The resultant lateral force F_y acts a distance t behind the contact center C (pneumatic trail).

In reality the longitudinal forces in the contact area influence the moment about the contact center C (fig. 7.5.40b), resulting in a total cornering moment M_z known as the self-aligning torque. The force F_y is usually called the cornering force. A more complete set of curves of the lateral or cornering force distribution over the contact area, obtained with the Gough apparatus, are given for various slip angles in Chapter 5 (fig. 5.58). The result of the cornering force-slip angle relation is shown in Chapter 5 (fig. 5.59), also indicating the pneumatic trail.

Bars for measuring the lateral force distribution have also been built into a drum of 3 m. in diameter, and the results obtained are similar to those just discussed [10].

F. Tread wear resistance

A nondestructive estimate of resistance to tread wear [11] of various tire constructions is very important to the tire manufacturer, because tread wear tests on the road require a large number of tires and are usually quite time consuming.

Although laboratory studies of movement of tread block elements on a glass plate add to the knowledge of wear, they fail to solve problems of varying rates of average wear.

The original Gough apparatus [8] made it possible to give an estimate of work done by the lateral frictional forces during passage through the contact patch when cornering.

The force as measured with the lateral force measuring bar is recorded against the lateral movement of the central rib of the tread. The resulting diagram gives, by measuring the area under the curve, the work done by the lateral force when cornering. The tests are made at a range of slip angles. From results obtained, it is found that the work done plotted against the cornering force coefficient F_y/F_N are straight lines for different loads when shown on log-log paper.

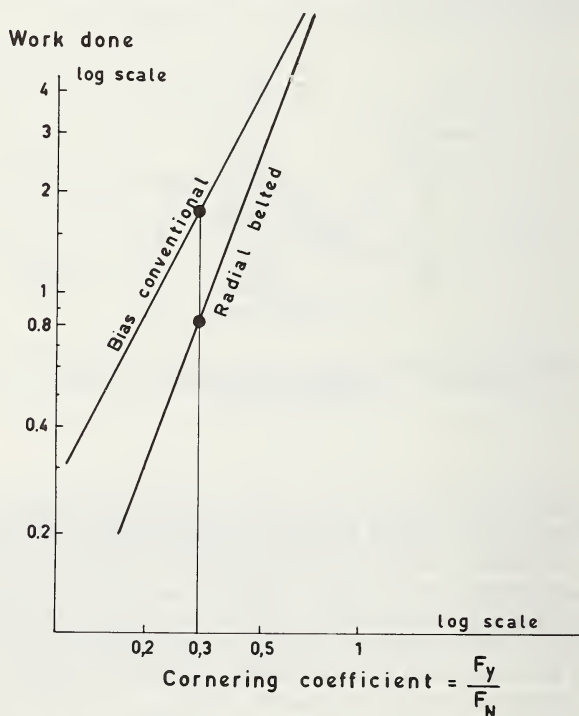


FIGURE 7.3.20. Estimate of work done by the lateral frictional forces during passage through the contact zone when cornering.

Tread wear measurements obtained from road tests, made with vehicles driven continuously around a constant radius at constant speed, showed similar straight lines when tread wear was plotted against the cornering coefficient on log-log paper. Neglecting longitudinal slipping, it follows that work done by the lateral forces is strongly related to tread wear. The fact that the slope of the lines on the log (work done) versus log (cornering coefficient) is influenced by the tire construction (fig. 7.3.20), means that some decision must be made as to what cornering coefficient should be chosen for the basis of comparison of work done. The choice was a cornering coefficient of 0.3, which corresponds to a vehicle executing a lateral acceleration of 0.3 g. [11].

The average value of 0.3 g. has also been obtained from statistical acceleration studies with 9 different makes of cars and 6 drivers, where the lateral component of the gravitational force [12] due to the roll angle has also been taken into account.

The figure indicates that the work done, and consequently the wear rate of a conventional bias tire is higher than a radial belted tire under similar conditions.

Road and Drum Test Measurements

A. General observations

Although thousands of road and drum tests have been made it is felt to be outside the scope of this chapter to discuss the influence of parameters such as type of cord, cord angles, number of plies, rim width, aspect ratio, stiffening of sidewalls and reinforcement of beads, bias, bias belted, radial belted, or combinations of radial bias tires, etc. Due to its frictional character, the cornering force curve is also dependent on the texture of the road surface, the rubber compound and curing, the temperature and the speed of sliding in the contact patch. It will be obvious that the data mentioned above are not always available, and therefore parameters which can be influenced by the vehicle engineer will be discussed, such as slip angle, normal load, inflation pressure and speed.

As indicated, tire cornering force and self-aligning torque data depend on so many factors that a general discussion is very difficult.

However, some attention will be given in this section to the influence of tire construction, tread pattern and tread resilience. For further information the reader is referred to chapter 6 and its literature references.

Further it should be noted that in order to obtain reproducible results, a standard test procedure which conditions the tire is required.

The data presented here for F_y and M_z are obtained under steady state rolling conditions. When a tire is made to roll at a slip angle α , it gradually rolls into its deformed shape as in figure 7.3.1, thereby developing an increasing lateral force with increasing distance travelled. After a distance of about 4–5 times the contact length the lateral deformations nearly attain their steady state values, and the lateral force F_y will remain constant (fig. 7.3.21).

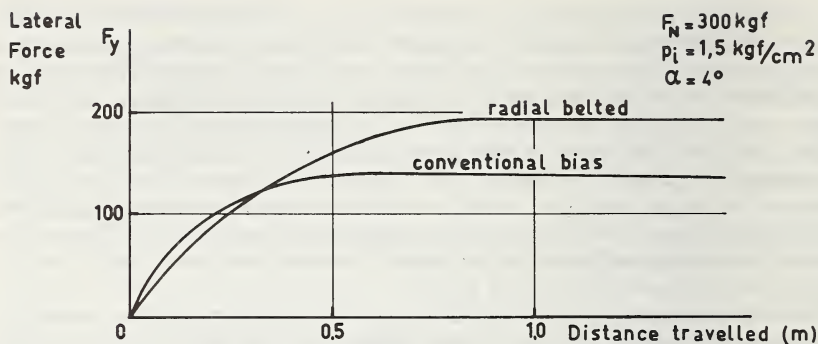


FIGURE 7.3.21. A tire made to roll at a constant slip angle α develops an increasing lateral force with increasing distance travelled and attains the steady state value.

B. Effect of slip angle α

a. Dry roads.

The influence of the slip angle α on the lateral force F_y for constant normal load F_N and constant inflation pressure p_i is shown in figure 7.3.22 for a conventional bias tire and a radial belted tire.

For small values of the slip angle of approximately 1–2 degrees, the lateral force function $F_y(\alpha)$ is usually considered to be linear.

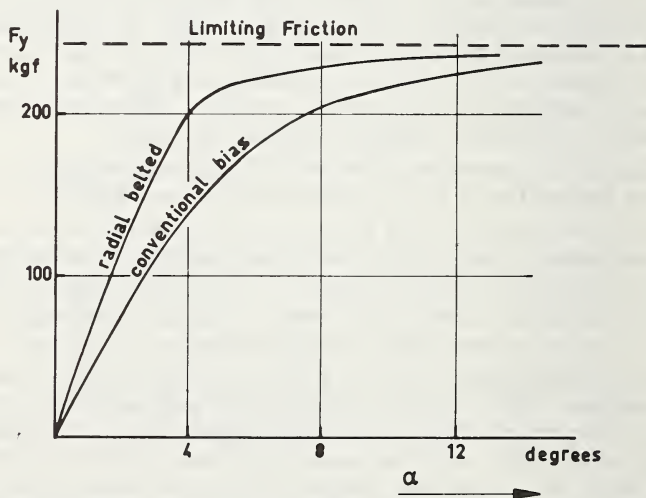


FIGURE 7.3.22. Lateral force versus slip angle.

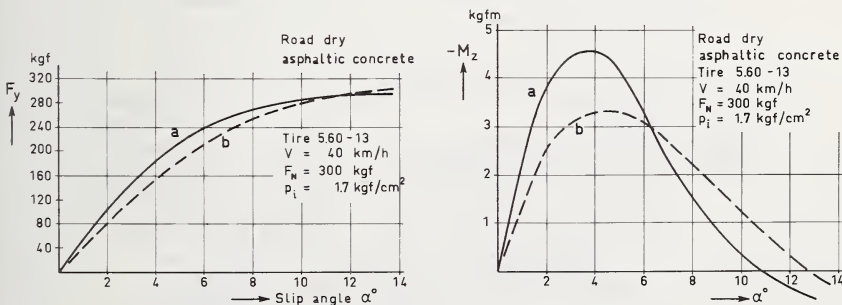
The slope of the curve indicates the so-called cornering force stiffness $C_{F\alpha} = (\partial F_y / \partial \alpha)_{\alpha=0}$. This value is very much dependent on the tire construction due to different values of the lateral carcass stiffness c_c and tread rubber stiffness c_p (fig. 7.5.33). Because it may be observed that at the larger slip angles the lateral force F_y increases, but the adhesive zone decreases, resulting in an increased sliding to the rear of the contact zone (fig. 7.3.17), the shape of the $F_y(\alpha)$ relation may be understandable.

Although the laterally stiffer tire reduces tread motion in the contact patch, and thus gives less wear, the variation in lateral force shown in figure 7.3.22 may be too sudden for the capabilities of most drivers, especially on wet roads. Some compromise has to be made, and the tire designer can influence the shape of these curves considerably by increasing or decreasing the cornering force stiffness, as shown in figure 7.3.23. It should be observed that the recorded $F_y(\alpha)$ curves, as shown in the figure, very often do not pass through the origin. It is a common practice to shift all curves horizontally so as to pass through the origin, in order to compare results, thereby neglecting the well known existence of cornering forces at zero slip angle.

The same shifting applies for the self-aligning torque curves shown in the following figures.

As shown in figure 7.3.19, the resultant lateral force F_y acts at a distance t behind the contact center, partly explaining the value of the cornering moment M_z . At increasing slip angle α the lateral force F_y increases, resulting in an increasing moment M_z . The slope of the $M_z(\alpha)$ curve, as illustrated in figure 7.3.23, indicates the cornering moment stiffness $C_{M\alpha} = -(\partial M_z / \partial \alpha)_{\alpha=0}$.

Due to the decrease of the pneumatic trail t with increasing slip angle, the moment M_z reaches a maximum, and then drops to lower values.



Tires a and b are of different construction

FIGURE 7.3.23. Effect of tire construction on lateral force and self aligning torque versus slip angle.

The moment $M_z = \int_A (p_x \cdot y - p_y \cdot x) dA$ is influenced by the longitudinal and lateral force distributions, which are asymmetrical in shape over the contact area A (fig. 7.5.40b).

We observe that the rolling resistance force is now acting out of the wheel plane due to the lateral tire deformation. The local forces developed are also dependent on the longitudinal and lateral carcass and tread stiffnesses. Dependent on the vertical force distribution in the contact area, the local limiting frictional force may be reached and sliding occurs when $\sqrt{p_x^2 + p_y^2} = \mu p_z$. But as observed in section 7.3.5 (fig. 7.3.52), the coefficient of friction μ , depending very much on the speed of sliding, reaches a maximum at a certain sliding velocity and then drops to lower values. In the rear zone of the contact area the lateral sliding velocity V_{sy} increases (fig. 7.3.18), which may result in a decrease of the coefficient of friction.

Combining all these effects, the shape of the $M_z(\alpha)$ curve may now be explained, and also the fact that a positive self-aligning torque M_z can be obtained at high slip angles α .

To indicate what happens when a dry road becomes wet, the $F_y(\alpha)$ and $M_z(\alpha)$ relations are shown for both conditions for another tire (fig. 7.3.24).

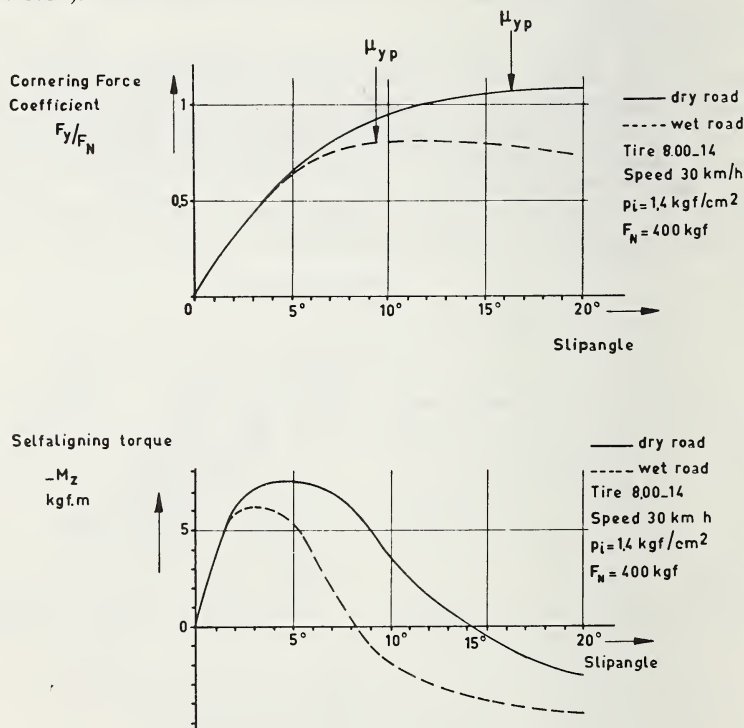


FIGURE 7.3.24. Effect of road condition on the cornering force coefficient and self aligning torque-slip angle relationships.

b. Wet roads.

The difference in behavior on dry and wet roads may be best illustrated under extreme conditions, such as on a wet smooth polished asphalt test track. This road, as measured with the drainage meter (sec. 7.3.5, fig. 7.3.55) showed zero drainage, and a low skid resistance value of about 25, as measured with the Portable Skid Resistance Meter (sec. 7.3.5, fig. 7.3.57), indicating the dangerous situation of no micro- and no macro-roughness. The wetted road temperature was about 18° C. The test results were obtained with the towed trailer (see ref. [1] of sec. 7.2, also fig. 7.2.8) by increasing the slip angle α very slowly, under constant vertical load F_N and at a constant speed of 40 km/hr.

It is observed on wet roads that the lateral force F_y increases with increasing angle α (fig. 7.3.25), but drops at larger slip angles. Returning to lower slip angles, it is seen that the lateral force F_y cannot recover its initially higher values as shown by the closed loops at the indicated speed of 40 km/hr. At a slightly lower speed (30 km/hr.), this loop has not been observed in testing tire "a" (fig. 7.3.26). The variation in lateral force for tire "b" is less than for tire "a," indicating a slight preference for tire "b" under these conditions. The self-aligning torque values M_z for tires "a" and "b" are also different as shown in figure 7.3.27. The footprint area of both tires has at equal loading conditions the same value, but the value of the contact length of tire "a" is about 15 percent higher. This may explain the higher maximum value of the self-aligning torque of tire "a" compared with the lower value of tire "b."

The tread pattern, tread resilience, and tread hardness, obviously play a significant role. Difference in skidding performance may be largely attributed to these differences in tread pattern design and resilience. The center rib of tire "a" has, contrary to tire "b," no sipes or kerfs.

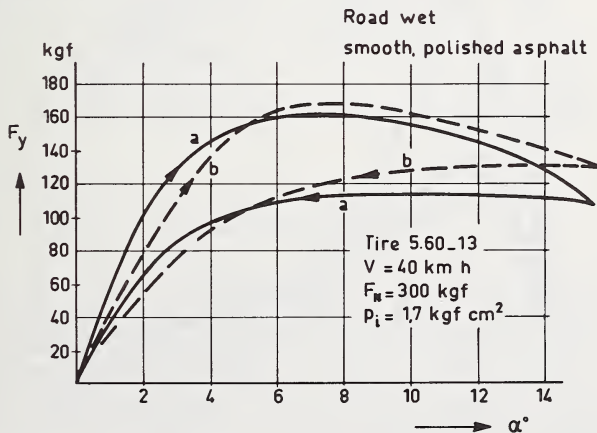


FIGURE 7.3.25. The effect of tire construction on the cornering force-slip angle relationships.

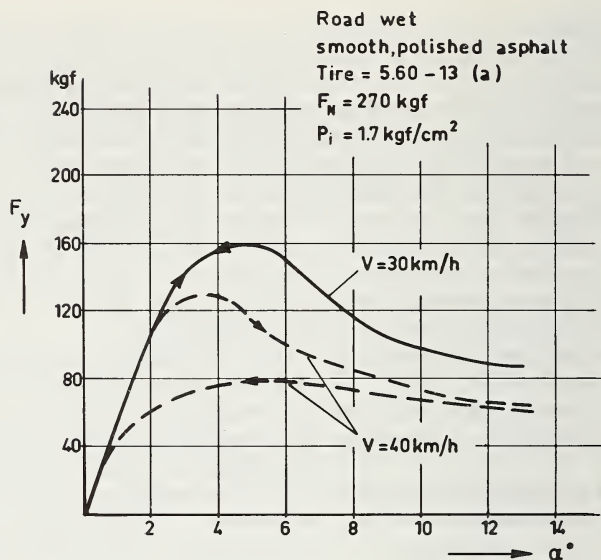


FIGURE 7.3.26. The effect of speed on the cornering force-slip angle relationships.

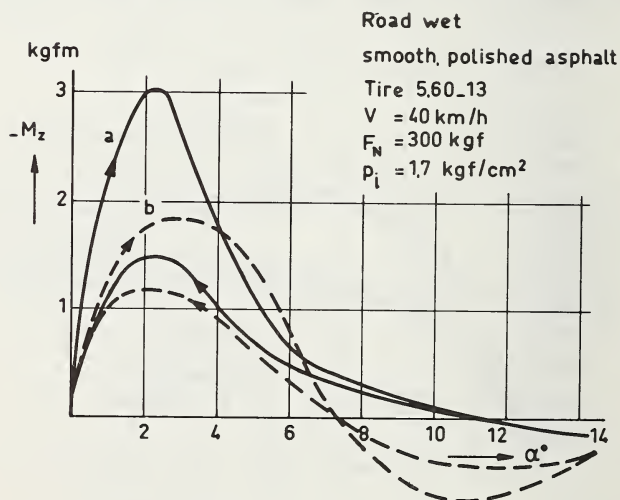


FIGURE 7.3.27. The effect of tire construction on the self-aligning torque-slip angle relationships.

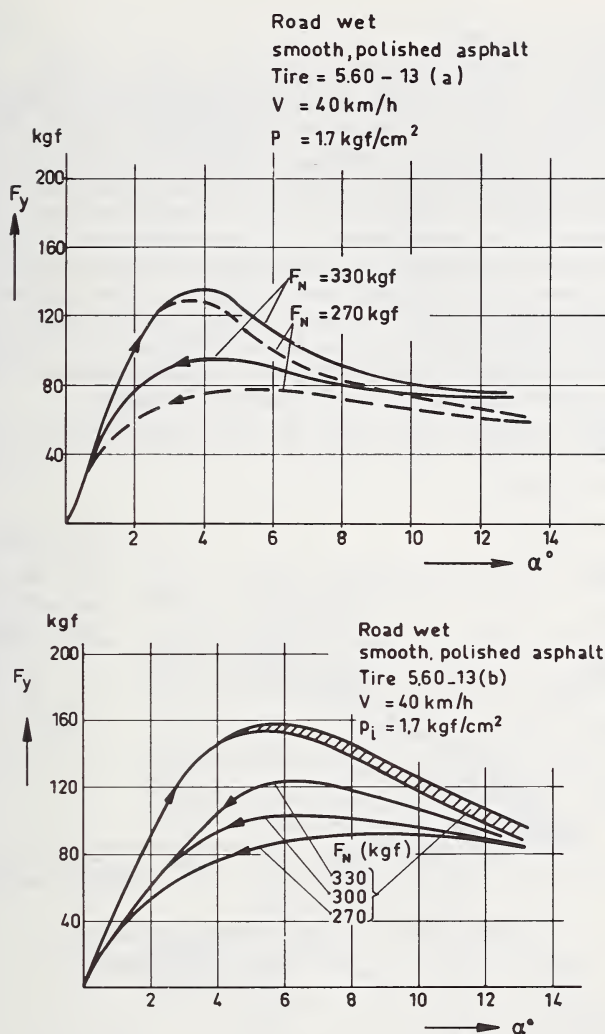


FIGURE 7.3.28. The effect of normal load on the cornering force-slip angle relationships shown for tire a and tire b.

Both tires have four drainage grooves, but the width of the drainage grooves of tire "a" are smaller than those of tire "b," and the outer ribs of tire "b" have more sipes. Tire "b" has a lower tread rubber resilience than tire "a," and the tread rubber hardness of tire "b," with a value of 61, is higher than tire "a," the latter having a hardness of 56.

To judge which tire is better from this test along may be very difficult because the normal load (fig. 7.3.28a, b) also plays an important role when cornering, due to weight transfer. Therefore we shall now discuss the lateral force and self-aligning torque relations versus the normal load.

C. Effect of normal load

The influence of the normal load $W = F_N$ on the cornering force F_y is shown in figure 7.3.29. In discussing the vertical load-deflection curves (sec. 7.2.4, fig. 7.2.49), we observed an increasing contact length with increasing load at constant inflation pressure, resulting in almost no increase of the vertical contact pressure p_z (ch. 5, fig. 5.32). The cornering force often shows at each slip angle a certain maximum value. The observed drop of the lateral force F_y at increasing load F_N and at larger slip angles may be explained by the influence of the increasing longitudinal forces and the decreasing lateral stiffness. The longitudinal force distribution shows increasing forces with increasing load (fig. 7.2.49) and therefore influences the lateral force F_y obtainable. Combining this effect and the decrease in lateral stiffness with decrease in normal load, the shapes of the lateral force curves may be explained.

Due to the nonlinear shape of the F_y - F_N curve (fig. 7.3.30), load transfer from one wheel to another has an effect upon the values of the

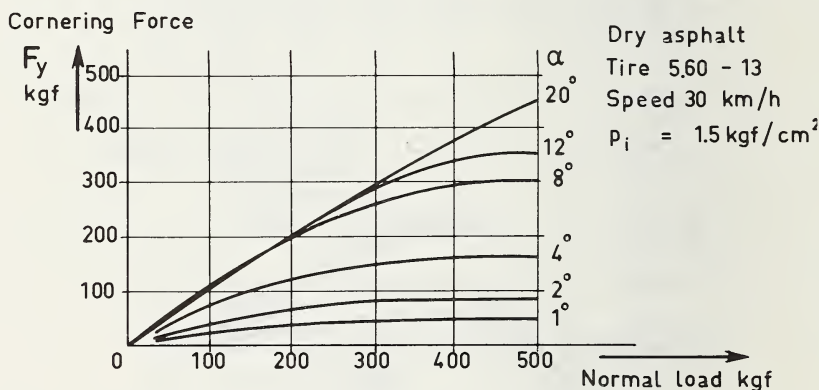


FIGURE 7.3.29. Cornering force versus normal load.

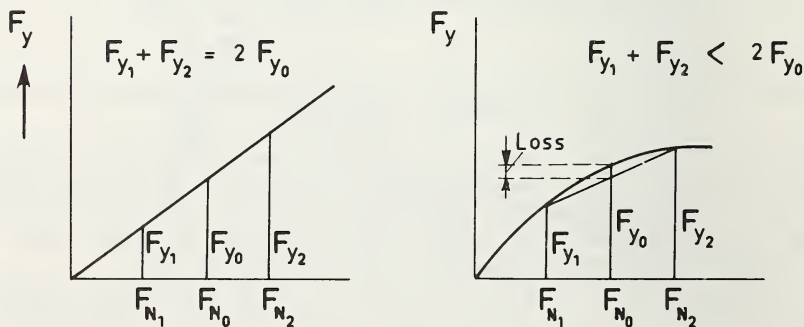


FIGURE 7.3.30. The loss in lateral force F_y due to load transfer.

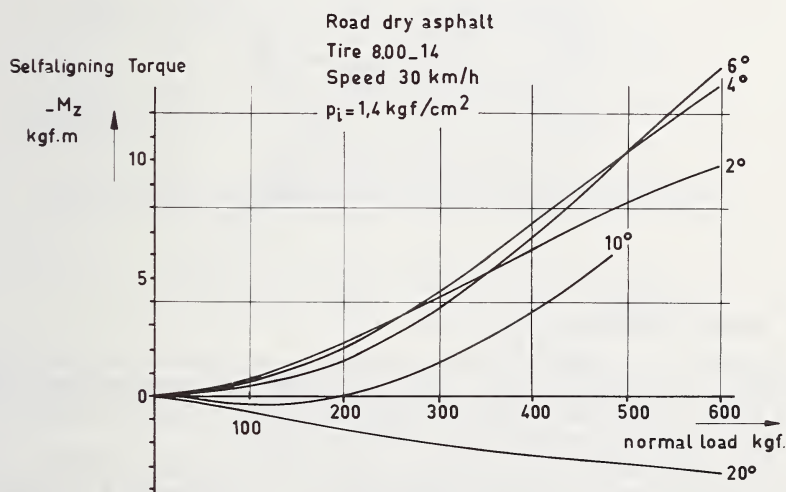
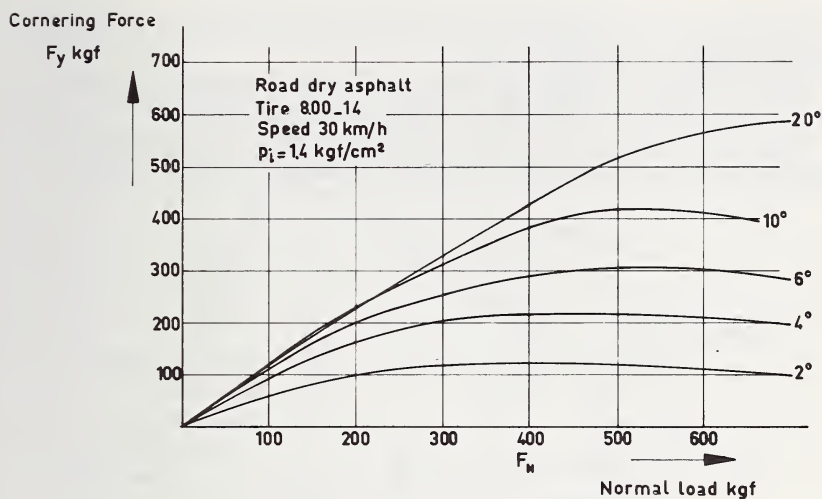


FIGURE 7.3.31. Cornering force and self aligning torque versus normal load.

slip angles required for the generation of the total side force which balances the centrifugal force F_c when cornering.

If the $F_y - F_N$ curve were linear no loss in lateral force F_y would be observed at constant slip angle. Because the weight of the car remains the same when cornering, load transfer results in increase of the required slip angles α to balance the centrifugal force F_c . A similar effect is observed when driving on bad, uneven roads with large variations in the

normal load, also causing a loss in cornering force due to the nonlinear shape of the curve (cf., sec. 7.5.2).

The self-aligning torque M_z increases with increasing normal load due to the increasing contact length, as shown in fig. 7.3.31 [15].

The Gough plot of the F_y - M_z relation for different slip angles at constant normal load and inflation pressure is shown in figure 7.3.32.

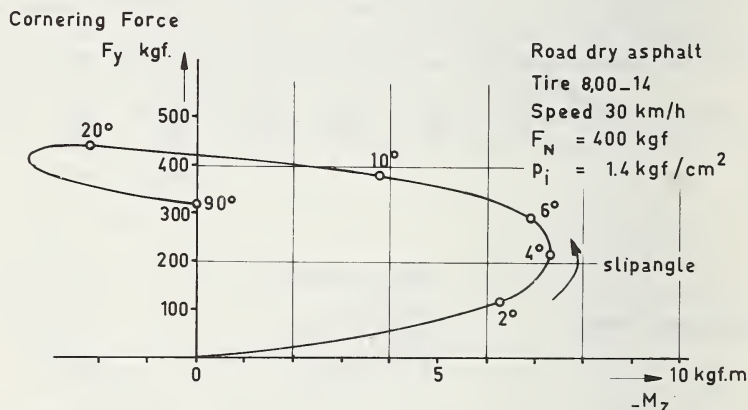


FIGURE 7.3.32. Gough plot of cornering force versus self-aligning torque.

D. Effect of inflation pressure p_i

Increase of inflation pressure results in an increase of the lateral stiffness, as observed from static load-deflection measurements (sec. 7.2.2, fig. 7.2.32) and therefore the lateral force F_y tends to increase at constant normal load and constant slip angle [16].

The self-aligning torque M_z decreases with increasing inflation pressure p_i because the contact length decreases, resulting in a decrease of the pneumatic trail t .

Results obtained from measurements with a drum of 4.0 m. in diameter [17] are illustrated in figure 7.3.33.

E. Effect of velocity

The influence of speed on the lateral force F_y is considered to be rather unimportant on dry roads. The effect of increased speed may be a slight increase in lateral force. The added tension component in the carcass due to the centrifugal force tends to increase the tire stiffness, but the contact length decreases.

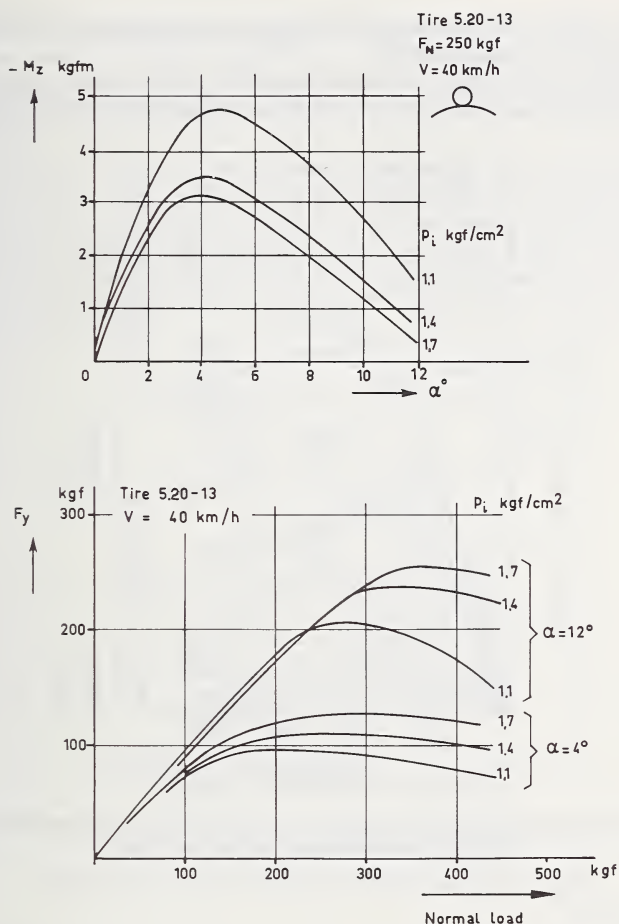


FIGURE 7.3.33. The effect of inflation pressure p_i on self aligning torque and cornering force.

On wet roads, however, the decrease in lateral force F_y may be considerable at higher slip angles [14]. The tread pattern and state of the road surface are extremely important parameters determining the directional stability. Although the speed dependence of the cornering force of patterned and smooth tires has been shown in chapter 6, figure 6.30, it may be of interest to show some cornering force coefficient (C.F.C.)—slip angle relations in figure 7.3.34 as obtained on different wetted road surfaces with patterned and smooth bias ply tires, the depth of water being of the order of 0.5–0.75 mm.

The patterned tire was size 5.25-16 and had a Lupke pendulum resilience value of 31 at 20° C, compared with a smooth 5.00-16 tire having a

resilience value of 55. The hardness values were approximately the same, namely 62 and 63, respectively.

The details of the test surfaces are given in the table below, and the numbers of the test surfaces are the same as in figure 7.3.34 [14].

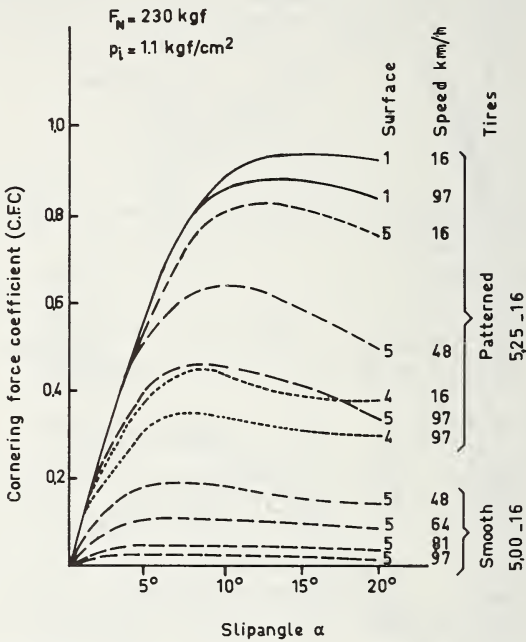


FIGURE 7.3.34. *The effect of velocity and tread pattern on the cornering force coefficient-slip angle relationships on various wet roads.*

Surface 1 (rough, harsh), surface 4 (rough, polished), surface 5 (smooth, polished).

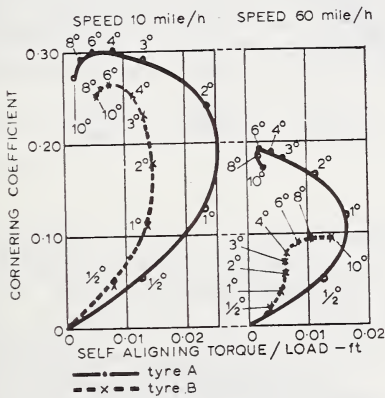
Detail of Test Surfaces

No.	Description	Texture
1	9.5 mm quartzite macadam surface	rough, harsh
4	9.5 mm Bridport macadam surface	rough, polished
5	mastic asphalt	smooth, polished

The influence of speed and surface is clearly illustrated, and it is shown that the initial part of the curve is nearly linear and independent of the surface, except at the higher speeds. The patterned tire gives

greater C.F.C. values than the smooth. In general, tires of low tread resilience give greater values than those of high resilience tread rubber. Therefore the smooth tire, having a high resilience tread rubber gives extremely low C.F.C. values on the smooth polished mastic asphalt surface No. 5.

In the extreme case of aquaplaning conditions, the cornering forces fall to such a low value that a vehicle may be directed from its straight path by the influence of a sidewind or a cambered road. The feel at the steering wheel should give sufficient early warning, but in certain cases the self-aligning torque—cornering force relations can have a distorted shape (fig. 7.3.35), suggesting that the steering feel may not always be a reliable indicator [18].



A Satisfactory tread pattern.

B Unsatisfactory tread pattern characteristics.

FIGURE 7.3.35. The effect of speed on the cornering force-self aligning torque relationships on a wet road.

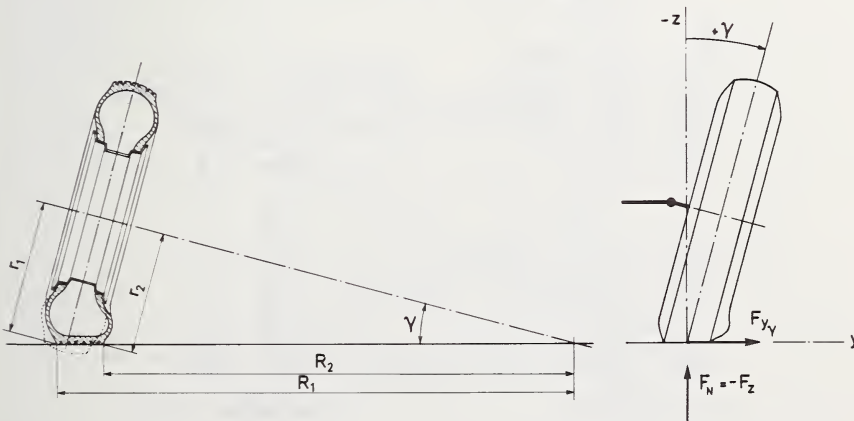


FIGURE 7.3.36. The camber angle γ produces a lateral tire deformation resulting in a camber force $F_{y\gamma}$.

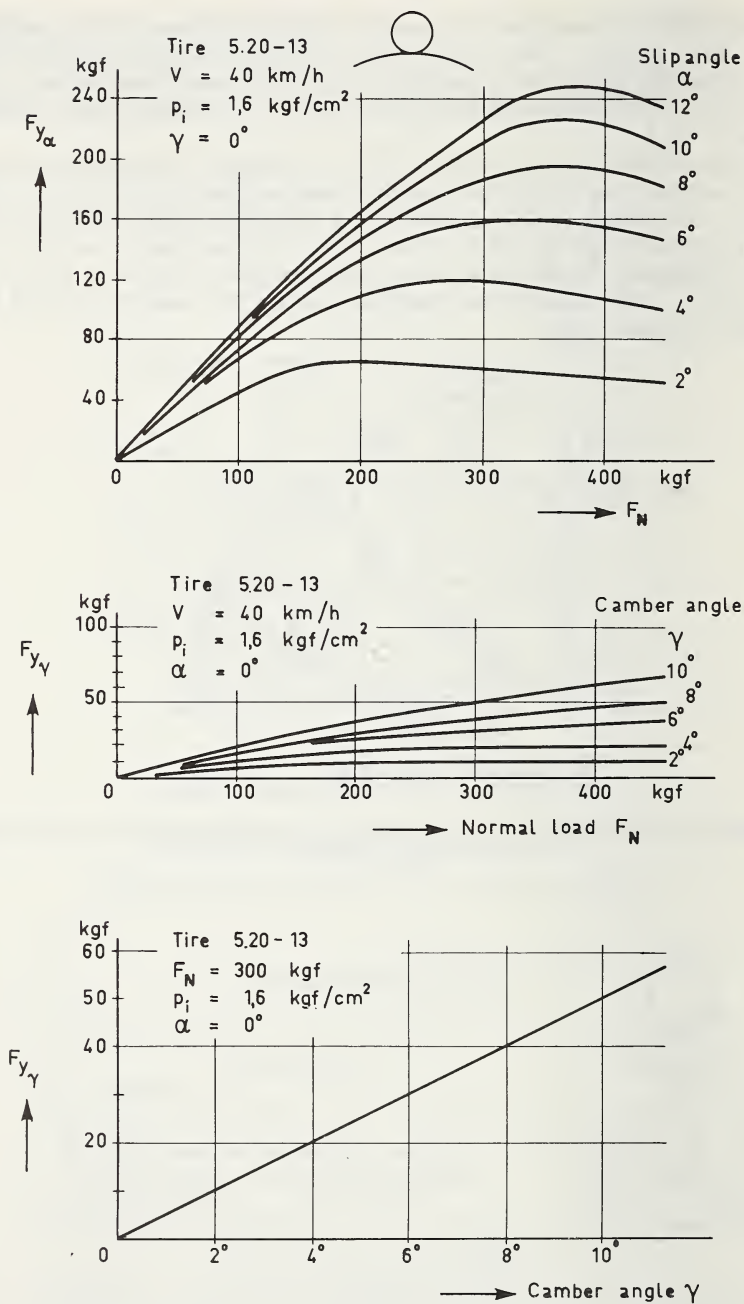


FIGURE 7.3.37. Comparison of cornering force and camber force values.

7.3.3. Camber and Cornering

Camber

The inclination of the wheel plane to the vertical indicates the camber angle γ and is called positive when the wheel leans outward at the top and negative when it leans inward (fig. 7.3.36).

The undeformed top part of the tire rolls gradually into the deformed condition by coming in contact with the road surface, as illustrated in the figure. A lateral tire deflection is observed, resulting in a camber force $F_{y\phi}$.

As demonstrated in figure 7.3.37 the lateral force $F_{y\gamma}$ developed by a camber angle γ is much smaller than the lateral force $F_{y\alpha}$ developed by an equal slip angle α . The results shown are measured on a drum of 4.0 m. in diameter [17]. Similar relations obtained on a drum of 2.5 m. in diameter are shown for another tire (fig. 7.3.38).

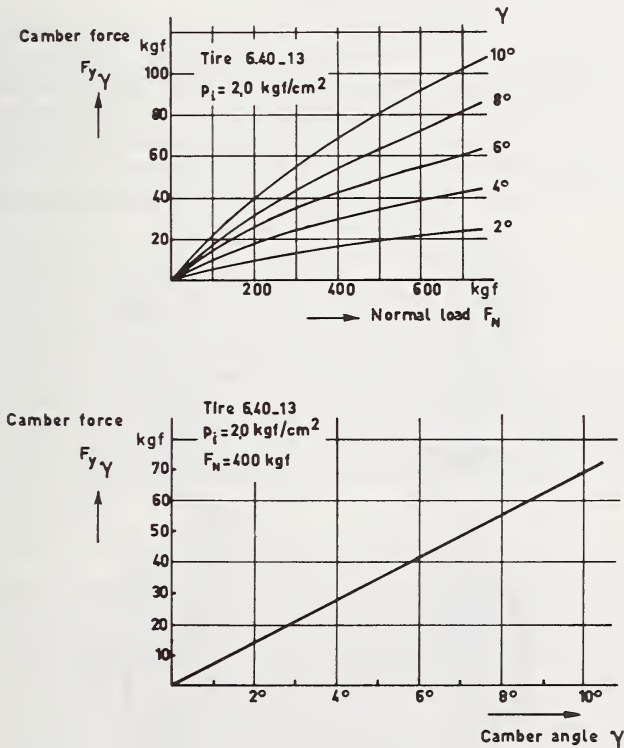


FIGURE 7.3.38. Camber force versus normal load and camber angle.

For this conventional bias tire the camber force developed can be approximately related to the normal load by:

$$F_y = F_N \tan \gamma = C_{F\gamma} \cdot \gamma$$

with a constant camber force stiffness $C_{F\gamma}$, because of the linear character of the lateral force – camber angle relation.

Radial ply tires show less camber force. The resultant lateral camber force is said to act a certain distance ahead of the contact center, and this distance is called the pneumatic lead, resulting in a camber moment $M_{z\gamma}$. The camber moment is usually small and may be neglected. The explanation of the camber moment is given by considering the rolling tire to consist of two narrow tires, mounted rigidly a distance $2b$ apart on a spindle. As can be seen in figure 7.3.36, the rolling radius $r_1 > r_2$. Because the distances travelled are equal, but the rolling radii are different, an antisymmetric longitudinal slip must occur, producing two equal longitudinal forces $F_{x\gamma}$, which act in opposite directions, resulting in a moment $M_z = 2F_{x\gamma} \cdot b$. (See also fig. 7.5.21).

Combination of Camber and Cornering

The combination of lateral forces due to a slip angle α and a camber angle γ is shown in figure 7.3.39, and according to the sign convention it is shown that for positive values of α and γ the lateral forces $F_{y\alpha}$ and $F_{y\gamma}$ act in the same directions. The influence of the camber angle γ on the total lateral force F_y decreases with increasing slip angle α , due to sliding in the contact area. This is best illustrated (fig. 7.3.40) at low normal load, for the case where $F_{y\alpha}$ and $F_{y\gamma}$ both act in the same direction.

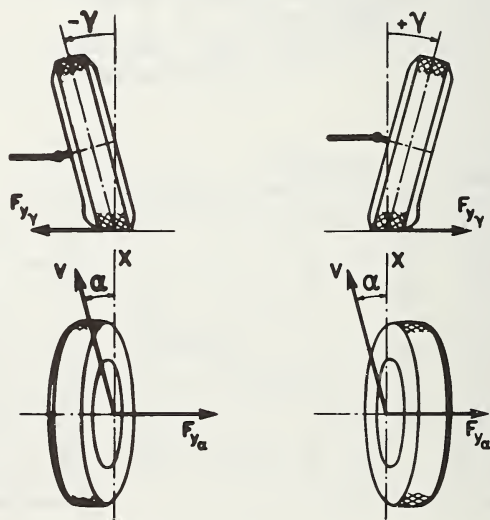


FIGURE 7.3.39. *The combination of lateral forces due to camber and cornering.*

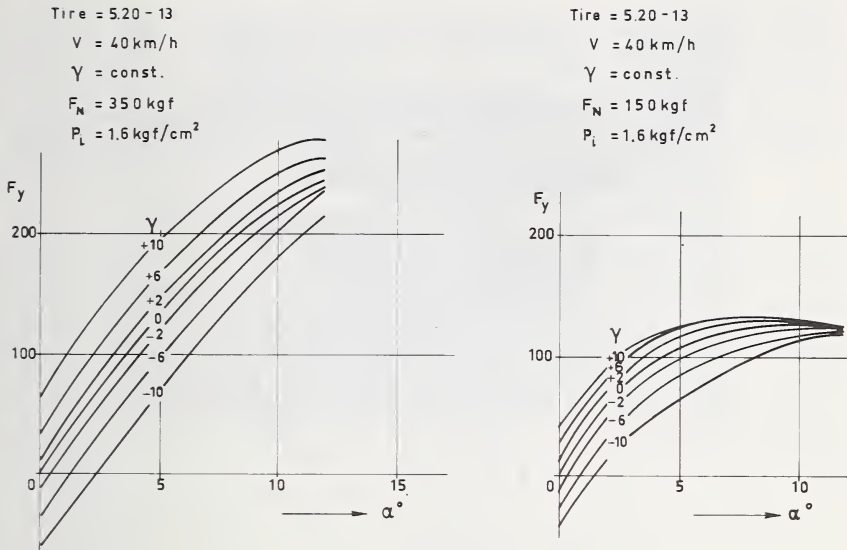


FIGURE 7.3.40. The effect of normal load on the total lateral force F_y due to camber and cornering.

A positive camber angle γ develops a camber force at zero slip angle, which can be counteracted by giving the wheels toe-in.

Static toe-in of a pair of wheels is the difference in the transverse distance between the wheel planes taken, respectively, at the extreme rear and front points of the tire treads. When the distance at the rear is greater the wheels are said to be "toed-in" [3].

Camber angle variations due to change in wheel track of independent suspension linkages result in lateral sliding or "scrub" over the road surface. The scrubbing action can result in unacceptable tire wear.

The camber angle variation with respect to time causes the wheel to be subjected to a gyroscopic moment $M_z = I_X \cdot \Omega \cdot \dot{\gamma}$, where I_X is the polar moment of inertia.

Actual Slip and Camber Angle Measurements

A well known method of obtaining slip angles is by using a vehicle with two symmetrically toed-in front wheels. However, elastic deformations due to braking forces can influence the slip angles introduced into the system. Because the tire forces of a vehicle under steady-state cornering conditions are also of interest, another method is required to measure the slip and camber angle of the test wheel.

Assuming zero camber angle γ , the unknown slip angle α can be found by tracing the path of two spring loaded ballpoint pens, situated a fixed distance l apart on a subframe of the axlestub [19]. The pens will

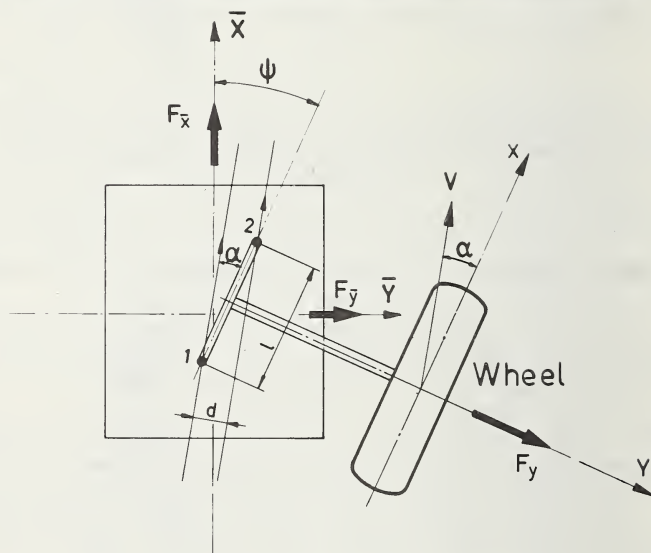


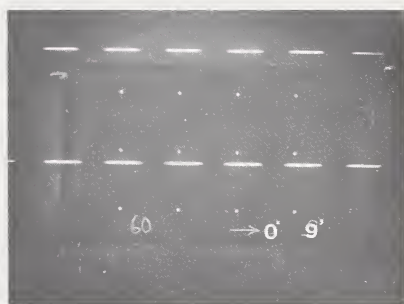
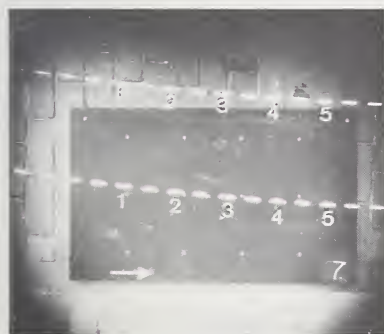
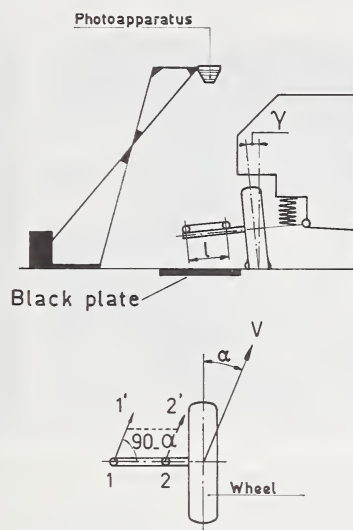
FIGURE 7.3.41. Slip angle measuring apparatus mounted on a wheel passing over the road platform tire tester.

trace two lines separated by a distance d , depending on the slip angle α introduced as in figure 7.3.41. It follows that $\sin \alpha = d/l$. If the direction of travel coincides with the \bar{x} -axis of the platform ($\Psi = \alpha$), the cornering force F_y is obtained from the road platform tire tester (sec. 7.2.1):

$$F_y = -F_{\bar{x}} \sin \alpha + F_{\bar{y}} \cos \alpha$$

where $F_{\bar{x}}$ and $F_{\bar{y}}$ indicate the forces on the tire.

A better method is using two electronic flashlamps triggered about 100 times per second with a short duration of the flash to ensure reasonable clear photographs at different vehicle speeds. The flashlamps are placed on a distance l on the axle stub in holders showing a small rectangular slot, giving dashed lines on a photograph. The photo apparatus is placed in a structure well above the road (figs. 7.3.42a, b and 7.3.61).



Dash No	1	2	3	4	5
$\text{tg } \alpha_1$	0.1785	0.1475	0.1183	0.0948	0.0837
$\text{tg } \alpha_2$	0.1538	0.1418	0.0964	0.0816	0.0805
α_1	$10^\circ 7'$	$8^\circ 24'$	$6^\circ 45'$	$5^\circ 25'$	$4^\circ 47'$
α_2	$8^\circ 45'$	$8^\circ 40'$	$5^\circ 30'$	$4^\circ 40'$	$4^\circ 36'$

FIGURE 7.3.42. Photographic slip angle measuring technique using two electronic flash lamps placed on the axle stub.

A small inclination of the axle stub arm due to cambering will hardly influence the accuracy of the slip angle measurements. But obtaining the slip angles from the dashed lines on the photograph is time consuming work. Therefore this method has been used to control a special slip and camber angle measuring device (S.C. meter) as shown in figure 7.3.43. The idea for such a device originated in 1964 with the Motor Industry Research Association (M.I.R.A.) in England.

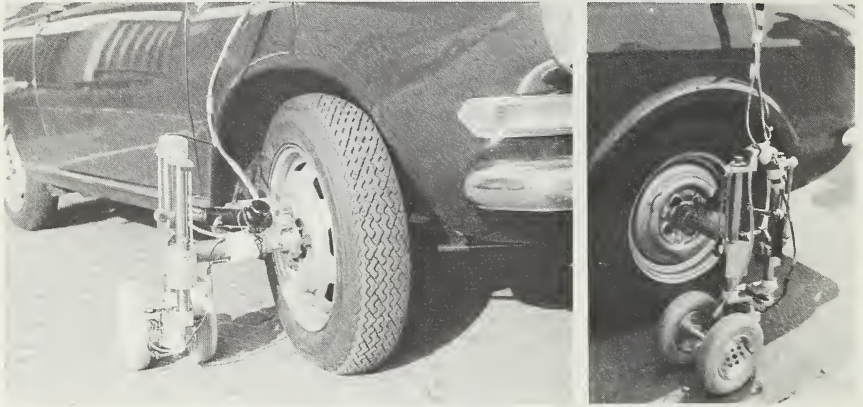


FIGURE 7.3.43. *Slip and camber angle measuring device.*

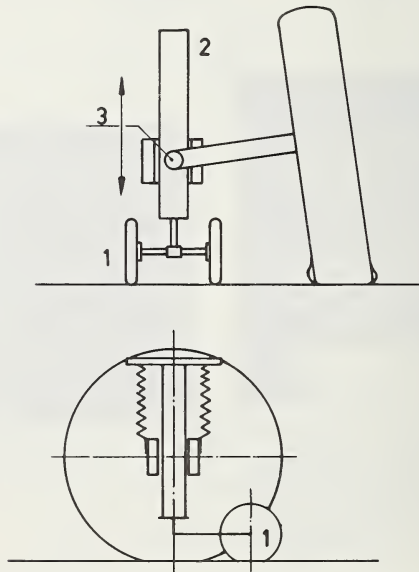


FIGURE 7.3.44. *Principle of the slip and camber measurements.*

The principle of the slip angle measurement is that a free trailing axle (1), gives the required direction of motion of the front wheel of a motorcar (fig. 7.3.44). Because two small spring-loaded trailing wheels are used, the tubes (2) of the supporting frame are always perpendicular to the road surface. The joint (3) between axle stub and frame allows the measurement of the camber angle. The joint (3) is situated in the vertical center line of the tubes (2).

The slip angle measurements, however, require correction charts as a function of the lateral acceleration [19, 20].

The result is that the S.C. meter can be used on smooth and slippery or even on bumpy roads as a tool to measure with reasonable accuracy the required angles under cornering conditions.

Of course, this device can also be used without the road platform (fig. 7.3.43). As an example, this device gives information about car "waddle" when driving at low speeds on straight flat roads, due to tire nonuniformity. The slip angle varies in such a case from 0.1–0.0 degree (sec. 7.2.6).

7.3.4. The Influence of Braking and Traction on Cornering

Dry Surface Measurements

The combination of a longitudinal force F_x and lateral force F_y , gives a resultant horizontal force K as shown in figure 7.3.45 for the case of a braking tire.

The difference in behavior of a bias ply and radial ply tire is illustrated. As can be expected, the lateral and longitudinal carcass and tread rubber stiffnesses will greatly influence the results obtained.

The radial ply tire produces a more or less symmetrical shaped curve for braking and traction. The bias ply tire produces a more pronounced slope in the curve, as shown in dashed lines.

The bias ply curve illustrates the effect that braking gives a higher obtainable lateral force F_y than traction, for a given value of the longitudinal force F_x , at constant vertical load and constant inflation pressure.

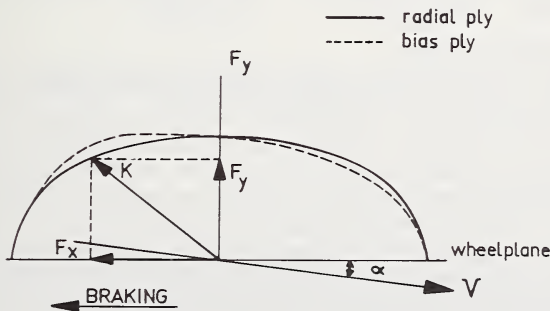


FIGURE 7.3.45. The influence of braking and traction forces on the lateral force for a radial ply and bias ply tire.

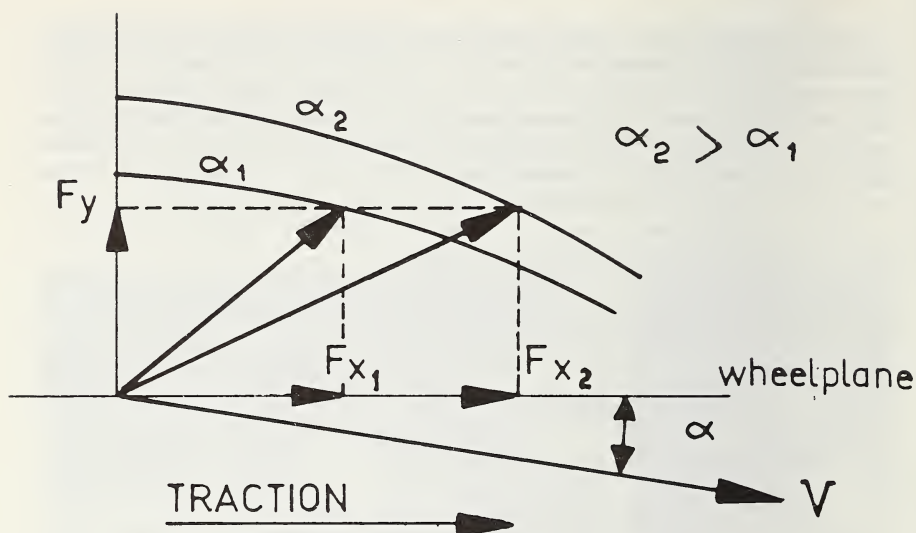


FIGURE 7.3.46. *The effect of traction forces on the lateral force.*

The fact that larger traction forces often require larger slip angles α to obtain the same lateral force F_y is illustrated in figure 7.3.46, thus influencing the over- or under-steer character of a vehicle.

Measurements taken on a dry steel drum of 4 m. in diameter are shown in figure 7.3.47a, b for a number of slip angles [17].

The effect of braking and traction forces on cornering force F_y and self-aligning torque M_z is illustrated in figure 7.3.48 for two different loads at a constant speed of 40 km/hr. and constant inflation pressure of 1.4 kgf/cm.² [17].

Wet Surface Measurements

Numerous tests have been carried out since 1960 with the Delft tire test trailer (fig. 7.2.8), but results have not been published in the literature. The results obtained on different wet road surfaces with various tires, however, are similar to those reported by the British Road Research Laboratory [14], and because these results are readily available, they will be discussed. The force measurements are made on a fifth wheel which can be set at a slip angle in the range of 0–20°, and whose angular velocity can be held at any desired value, independent of the vehicle speed, by means of a hydraulic transmission driven from the normal vehicle drive [21].

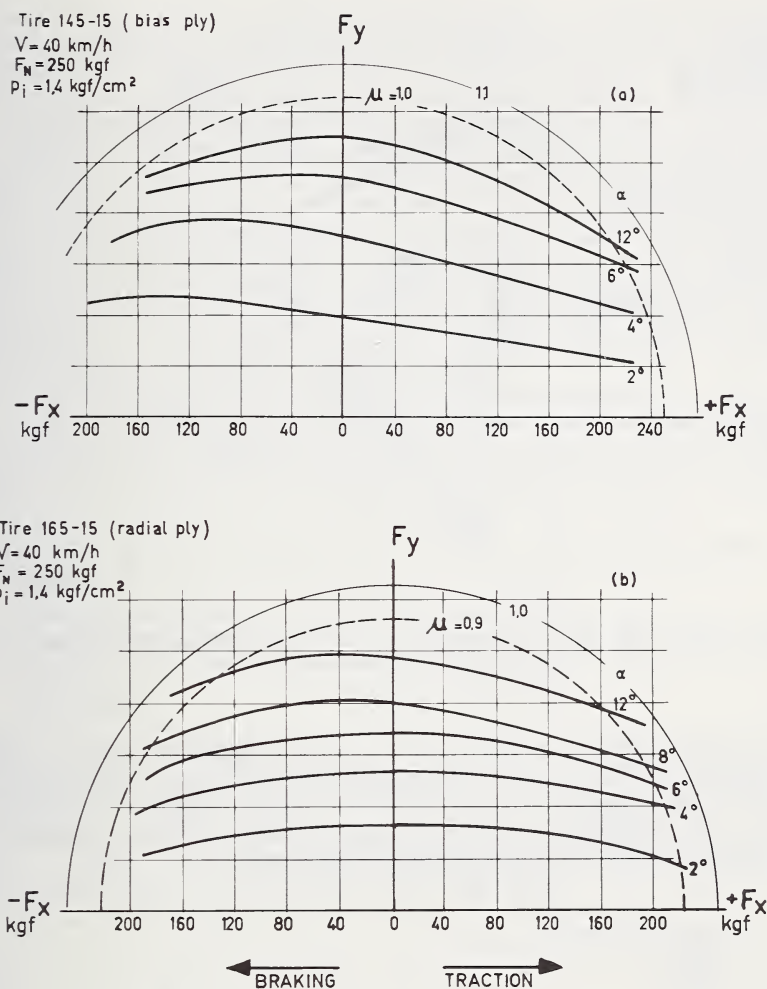


FIGURE 7.3.47. Lateral force-longitudinal force relationships at constant slip angles for a bias ply and radial ply tire.

In the following the results obtained with only one tire will be discussed. For further information the reader is referred to the literature, where detailed information is given on the test procedure and the evaluation of results, with further details of 10 test tires and 5 test surfaces [14].

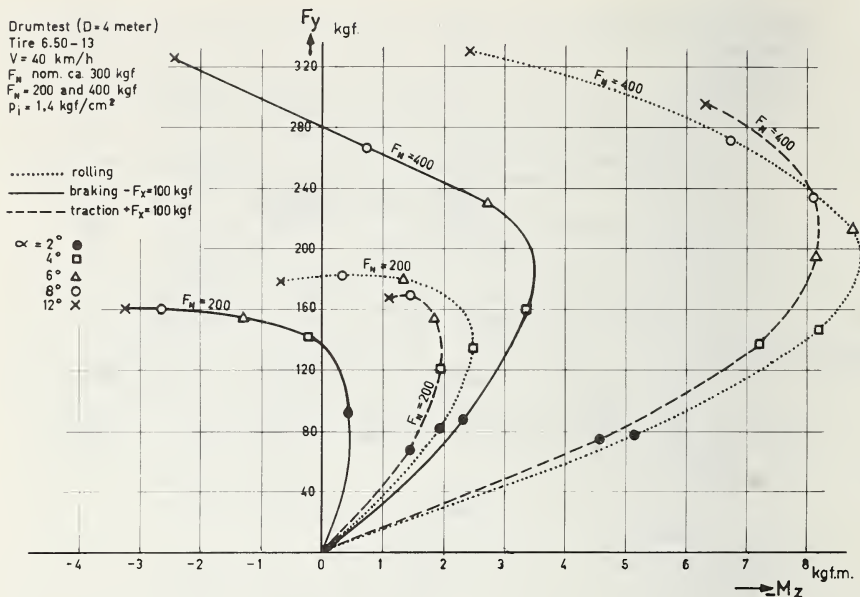


FIGURE 7.3.48. The effect of longitudinal forces on the cornering force-self aligning torque relationships given for two normal loads.

The effect of the combined action of a longitudinal force F_x and a lateral force F_y on a wet surface is illustrated in figure 7.3.49 for a patterned radial ply tire, with steel reinforcing belt. The test surface was a 9.5 mm. Bridport macadam, having a rough, polished texture. The depth of water was in the order of 0.5-0.75 mm.

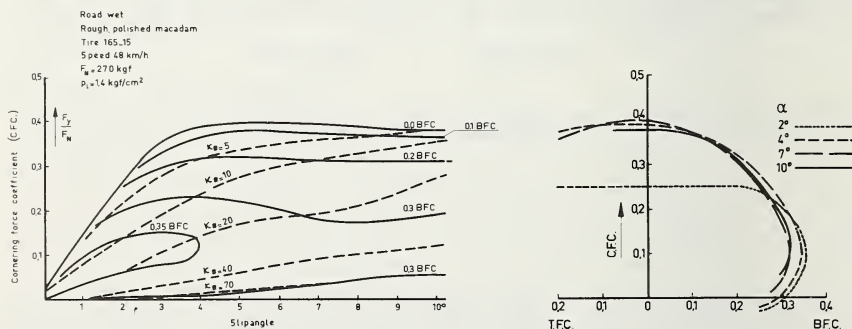


FIGURE 7.3.49. The effect of the combined action of a longitudinal force and a lateral force on a wet surface is shown for constant braking force coefficients (BFC) and constant braking percent slip κ_B .

A small braking force, generating little slip, does not affect the cornering force stiffness very much, but reduces the maximum cornering force coefficient (C.F.C.) and the slip angle at which the peak is observed. It is shown that at increasing braking force coefficient B.F.C., the C.F.C. curve breaks away and reaches a lower maximum than before. At B.F.C. values greater than the locked wheel value, the curves become closed loops, as shown for a value of 0.35 B.F.C., illustrating the effect that a large braking force cannot be satisfied at slip angles greater than a certain amount [14]. The 0.3 B.F.C. curves do not appear as loops, because they extend outside the slip angle range covered by the figure.

The dashed lines, indicating constant braking slip κ_B , are quite different from those of constant B.F.C. If a definite braking slip is imposed, the C.F.C. slip angle curve has a smaller initial slope, a lower peak, and attains the peak at larger slip angles.

The effect of percent braking slip κ_B on the cornering force coefficient C.F.C. at a given slip angle is shown in figure 7.3.50 for three different vertical loads. The well known fact that the cornering force falls off very rapidly with braking slip is clearly demonstrated on this type of road surface.

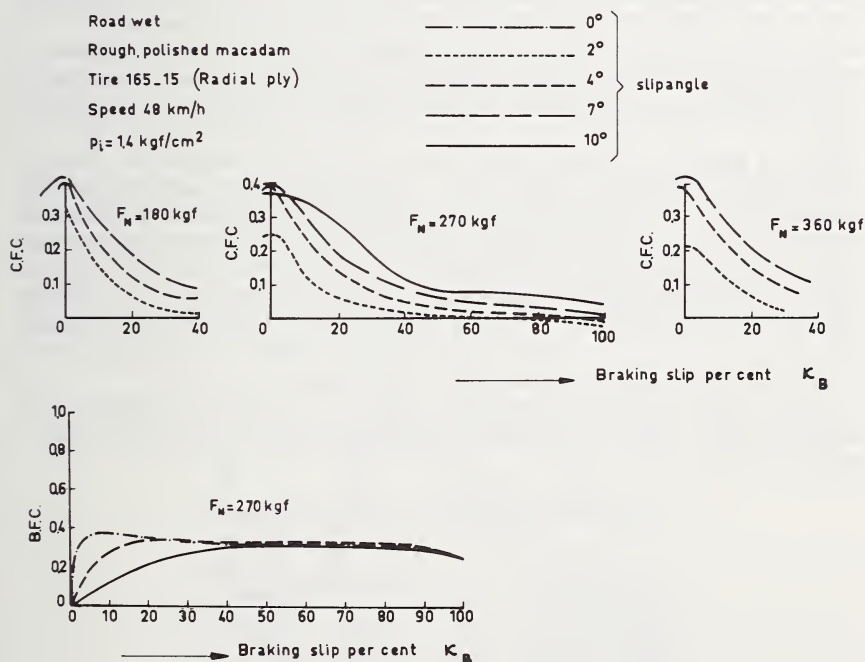


FIGURE 7.3.50. The effect of braking percent slip κ_B on the cornering force coefficient CFC at a given slip angle for three vertical loads.

The braking force coefficient (BFC) versus braking percent slip κ_B is also shown.

The effect of brake slip on the braking force coefficient B.F.C., is also shown in the figure for slip angles of 0, 4 and 10 degrees. These effects are important when considering anti-locking devices.

The effect of traction, as observed with a special test vehicle, has also been reported [14], but discussion of results obtained will be omitted.

However, because cornering traction methods, using conventional vehicles, may be of interest from the standpoint of vehicle safety and control, a short description will be given.

Conventional vehicle tests

Because under maximum braking or driving conditions, the available lateral force component is almost zero, there will be no force available for the vehicle control. In cornering traction tests utilizing standard vehicles, all tires on the vehicle are subjected simultaneously to their individual complex conditions of load, inclination, torque, slip angle, speed, etc. [22].

The nontethered cornering traction test is based on the combined effects of all tires on the vehicle and their ability to generate sufficient forces to overcome the centrifugal effects on the vehicle.

For this test a car is driven in a circle at increasing speeds until break-away occurs. The driver follows a procedure of increasing the speed in 0.5–1 km/hr. increments on alternate laps until a clearly distinguishable level of the vehicle control is lost or rear breakaway is detected.

The maximum speed attained is usually the basis for tire comparison. The momentary road surface condition, water depth, wind temperatures of road and tire, etc. play an important role in the maximum attainable speed.

Out of many procedures one test is to drive the vehicle in third or fourth gear on the test surface at a predetermined speed while trying to follow a curved path. Arriving at the curve, the vehicle is accelerated by means of a full throttle down shift. The driver follows again a procedure of increasing the speed in 1 or 2 km/hr. increments on successive laps, until at the so-called trace speed a distinguishable level of vehicle control loss at the end of the curve is observed. The speed just before this loss of control is called "just holding." When skidding already occurs at certain point, we speak of moderate slip.

Results obtained with a standard vehicle, on a smooth polished wet asphalt surface, gave for the tires *a* and *b* of figures 7.3.25–28 the following speeds in km/hr.:

	Tire <i>a</i>	Tire <i>b</i>
Just holding.....	37.5	40.9
Trace.....	37.5	42.8
Moderate slip.....	40.9	45

The large difference in cornering characteristics of tires *a* and *b* on the same test surface have been discussed previously (figs. 7.3.25–28).

The combined effects of accelerating or braking while cornering are also considered in the so-called slalom test, where the car is driven alternately around a series of equally spaced markers positioned on the test surface.

Although a variety of test methods have been devised, all methods are subject to many factors which may adversely affect the repeatability and accuracy of data. Even when A.S.T.M. E-17 control tires are used for establishing the friction coefficient rating of the test surface, this practice does not provide the basis for the comparison of test data among different tests. A program to determine the tractive performance level for all modes of operation requires a large number of tests, and to reduce variations the individual tests have to be repeated several times in order to average the data obtained [22].

7.3.5. Difficulties in Measuring Forces and Moments

General Observations

The forces and moments acting between tire and road depend on the distribution of the local normal pressure and the local tangential stresses in the contact patch. The tangential stress occurring at a point x, y in the area A (fig. 7.2.9) is determined by the local normal pressure and the local friction coefficient between tread and road surfaces. The normal pressure is dependent upon the construction of the tire and the design of the tread pattern for a given load and inflation pressure. The coefficient of friction of a rubber compound against a clean dry road surface varies with the speed of sliding and the temperature. Under isothermal conditions, the coefficient of friction tends to a constant value at very low sliding speeds, approaching static conditions. As the speed of sliding increases, the coefficient of friction rises and attains a maximum value at a certain speed (fig. 7.3.51). The friction coefficient at constant speed varies with the test temperature, as shown for a butadiene rubber compound on a glass surface (fig. 7.3.52). In the contact patch of a rolling tire, the temperature rises at higher speeds and the resulting friction is

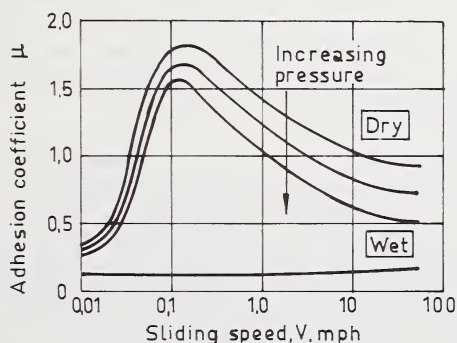


FIGURE 7.3.51. *The effect of sliding speed on the adhesion coefficient.*

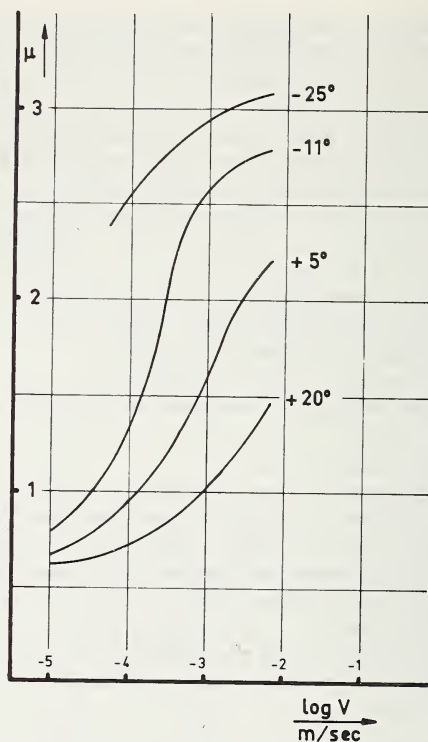


FIGURE 7.3.52. The effect of temperature on the coefficient of friction at constant speed for a butadiene rubber on glass.

determined by the combined effect of speed and temperature. The nature of the track surface, the rubber compound, the temperature and the speed of sliding influence the local coefficient of friction in the contact patch. The highest coefficients of friction are obtained on clean dry surfaces, but contamination and/or water cause a decline in the forces developed.

The Nature of the Track Surface

In order to evaluate tire characteristics obtained from road tests, the magnitude of the road surface influence should be assessed. When comparing tire test data it seems advisable to include in the program test results obtained with a special standardized reference tire as a yardstick for the frictional rating of the road surfaces. If possible the road surface characteristics should be obtained separately, in the form of a description of the macro- and microroughness of the test surface (fig. 7.3.53). Because the friction of rubber is temperature dependent, the surface temperature plays an important role and should be given in test reports.

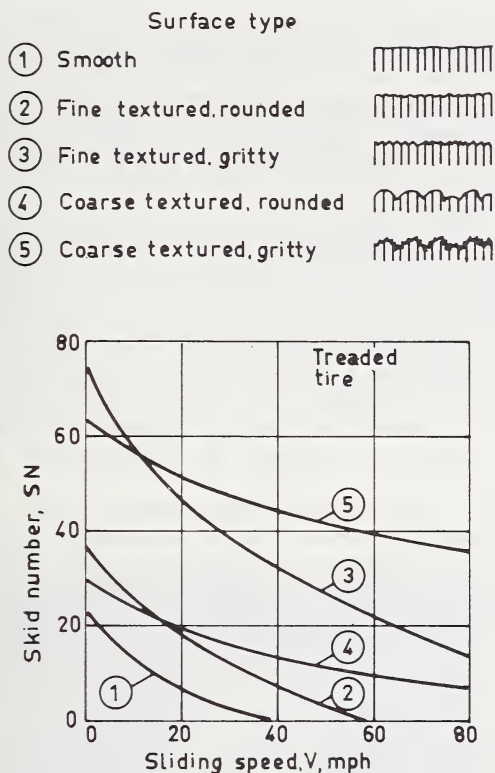


FIGURE 7.3.53. *The effect of the surface condition on the skid resistance.*

(Skid number SN is the ratio of skid resistance to wheel load times 100.)

Macro texture

The effective friction on wet roads is controlled by the removal of the fluid film throughout the contact patch of the tire. The road surface drainage via macro texture (1–10 mm.) is thought to have an influence upon the fluid displacement.

A photograph of the surface texture should be made available, indicating if required the size of coated chippings or quartzite macadam.

Stereo photography to determine the mean void width has been used, giving a good picture of the form of the texture [26]. In other cases, profile traces are obtained with an electromechanical roughness meter.

Stereo photographs have been taken to record the surface profile, from which the “profile ratio” was evaluated. The profile ratio is defined as the ratio of the length of the surface profile along a line to the length of the base line. This method used to assess the profile bears some relation

to texture depth and takes into account the shape of the profile. Analysis has indicated that the top 40 to 50 thousandths of an inch (1–1.25 mm.) is the most significant part of the profile in determining the decrease in braking force coefficient with speed. It has been suggested that the decrease in coefficient of friction μ_{ts} ($\kappa_B=100\%$) from 50 km/hr. to 125 km/hr. should not be greater than one quarter, with a minimum value of $\mu_{ts}=0.3$, as measured with the small trailer apparatus of the Road Research Laboratory [27].

In the sand patch method a known amount ϕ of fine dry sand or powder is applied to the surface and is distributed in such a way that the sand just fills the depressions and hollows in the area A covered. The drainage property is considered proportional to the ratio ϕ/A . This method gives no information concerning the separation and shape of the texture height and the effectiveness of the surface drainage channels. We are interested in the channelling system and not in the hollows. We also want to take into account the draping behavior of tread rubber over the individual asperities reducing the effectiveness of the surface drainage channels.

With a drainage meter according to a design by Moore [28] the water removing properties of a surface can be determined. A transparent bottomless cylinder is provided on its underside with a rubber ring upon which the meter is placed on the surface to be investigated. The drainage meter is loaded with the desired number of load rings so that the rubber ring will drape itself over the asperities much as a tread element does.

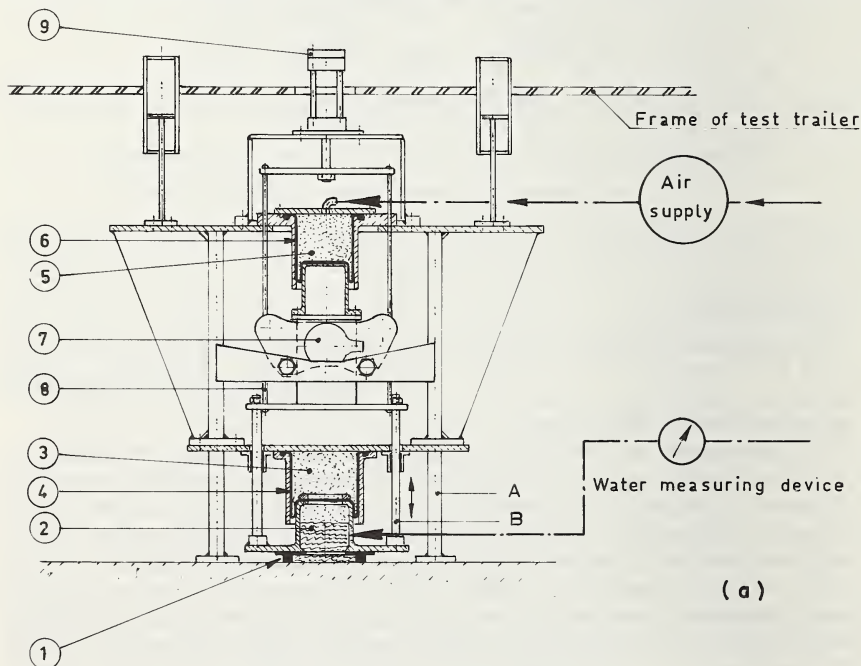


FIGURE 7.3.54a. Road drainage meter.

The time required for the water level to fall from the top mark to the bottom mark was originally measured and characterized the drainage potential of the surface.

Figure 7.3.54*a, b* shows the Delft drainage meter with an electromagnetic operated valve to fill the outflow meter accurately to the desired level. In order to measure the drainage on coarse roads it appeared necessary to compensate for stones or road unevennesses under the rubber ring by placing foam rubber between the cylinder and the rubber ring. The real measuring time was reduced to 10 seconds [29]. In view of the large number of tests, the measurement results are automatically printed with a digital recorder. Other data, such as water temperature and number of load rings, are fed into a special computer program giving the drainage number, defining the degree of drainage of the macro texture of the road surface in question [30]. The criterion for the drainage capacity of a road surface is expressed in the formula:

$$W = \gamma^n \cdot H_{eq \ 1.5}$$

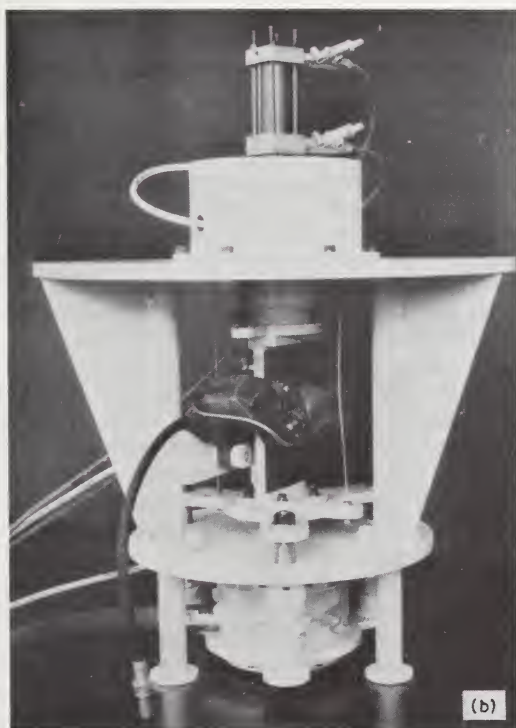


FIGURE 7.3.54*b*. Road drainage meter.

The factor γ indicates the influence of an increasing tire contact pressure (number of load rings) on the drainage capacity of the road.

$$\gamma = \frac{H_{eq\ 0.5} - H_{eq\ 1.5}}{H_{eq\ 1.0}}$$

The equivalent height $H_{eq\ 1.5}$ is the distance of the underside of the rubber ring of the cylinder to a supposed flat plate, giving the same time of water flow as obtained from measurements on a road surface with a contact pressure of 1.5 kgf/cm.². The results obtained from a large variety of road surfaces showed an extremely good correlation (0.98) for $W = \sqrt{\gamma \cdot H_{eq\ 1.5}}$ with results obtained by the Netherlands Road Research Laboratory from the sand patch method, giving the texture depth (TD) in mm.

$$TD = 10 \frac{4\phi}{\pi D^2}$$

ϕ = volume of sand in cm³.

D = diameter of the area A covered with sand in cm.

The results of an experimental program to establish a correlation between drainage meter and skid resistance on different wet road surfaces are shown in table 7.3.1.

The high drainage number H_{eq} obtained on harsh and rough asphalt with quartzite surface, indicates an excellent drainage capability. The smooth polished asphalt shows the dangerous condition of no drainage, having a zero value of the drainage number. The braking force coefficient μ_{xs} for $\kappa = 100$ percent, also indicates lower values on the smooth asphalt as compared with the asphalt and quartzite surface. The portable skid resistance values (SRT) are also shown in the table.

A new drainage meter measures the drainage as the total water flow during 10 seconds at different water pressures (0.4–7 kgf/cm.²).

The drainage meter is shown in figure 7.3.54*b*. After lowering frame A from the test trailer of figure 7.2.8 to the road surface, the contact pressure between rubber ring and road can be varied with the air pressure in chamber 5 of part B . This part B is then fixed in its position with the aid of a disk brake (7). The water pressure in chamber 2 is variable between 0.4 and 7 kgf/cm.².

Results obtained with this drainage meter are shown in figure 7.3.54*c* for two different road surfaces. There is a strong indication, that for contact pressures in the range of truck tires (6–7 kgf/cm.²) no drainage exists on the concrete road, whereas for the average passenger car tire pressure of 1.5 kgf/cm.² a reasonable drainage is still available.

This influence of the tire contact pressure has also been observed on towed truck trailer road tests, using the force method and giving the locked braking force coefficient μ_{ls} (fig. 7.3.55*b*).

TABLE 7.3.1. *Results of Road Measurements*

Road surface description	Texture		Coefficient of friction ($V = 50$ km/h)		SRT value	Drainage number H_{eq} (mm)		
	macro	micro	μ_{xp}	μ_{xs}		$p_i = 0.5$	$p_i = 1$	$p_i = 1.5$ kgf/cm ²
Asphalt.....	rough	harsh	0.78	0.53	82	0.640	0.389	0.303
Asphalt and quartzite.....	rough	harsh	0.85	0.61	79	0.867	0.599	0.382
Asphalt.....	smooth	polished	0.85	0.51	67	0.295	0.137	0
Concrete.....	smooth	harsh	0.83	0.53	69	0.137	0.102	0.076
Mixed aggregate.....	rough	polished	0.93	0.60	65	0.415	0.267	0.203

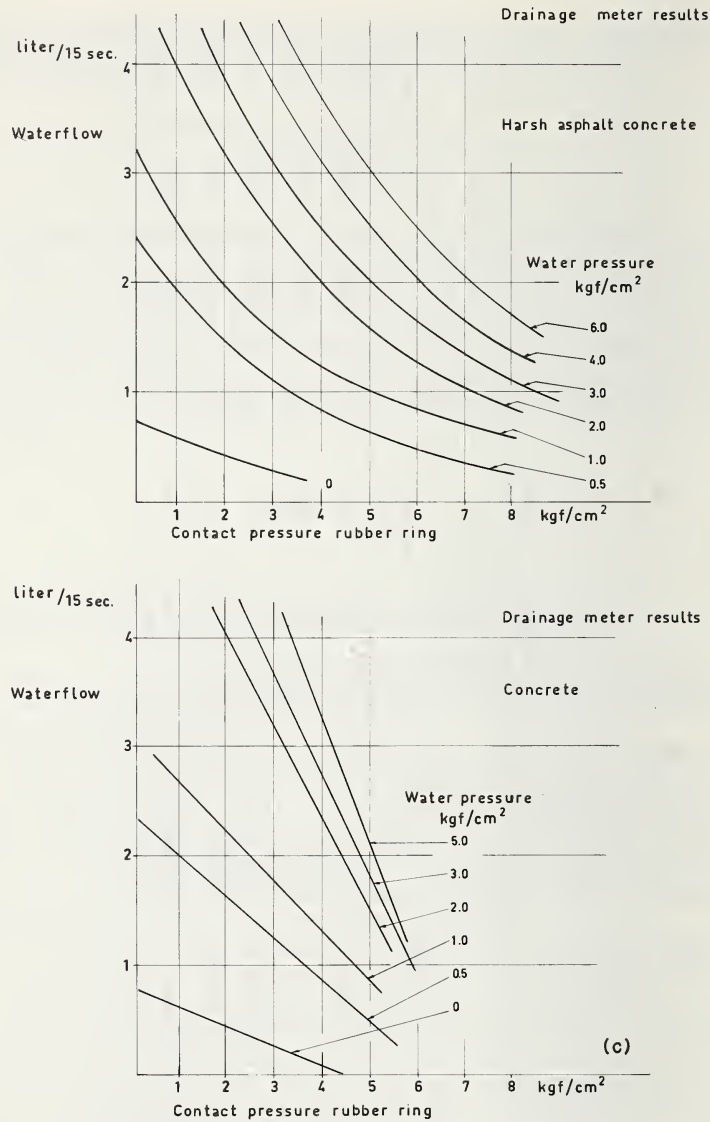


FIGURE 7.3.54c. Road drainage meter results.

Micro texture

Small sharp points in the road surface can penetrate a thin fluid film, but can also penetrate into the rubber tread surface of the tire. Because the surfaces have thin films of oxide layer and water, they are far from chemically clean and therefore it is not entirely a water film penetration. A microroughness of 0.05–0.1 mm. on top of the macro texture produces a high resistance to slip. The adhesive friction process consists of the formation of adhesive bonds at the real area of contact, at the tips of the hard asperities, and is caused by the normal load. The elastically stored energy in shear, due to the tangential force, will try to overcome the surface energy of the hard solid so as to free adhesive bonds [24]. Only the rubber molecules forming the real area of contact may be considered near enough to the field of forces of the hard solid and the deformation is therefore concentrated in a very thin layer below the surface. Under the action of the tangential force the adhesive bonds break and a fresh cycle then begins with formation of new bonds elsewhere on the surface.

In extreme cases, the stresses at the tips will be large enough to rupture the rubber, causing abrasion, as has been proved in sliding on dry quartzite [32]. The measurement and classification of the road surface microroughness with a mechanical roughness meter is a difficult subject because the microroughness is superimposed on the texture.

The small-scale macroscopic roughness is sometimes measured with a foil-piercing technique. In this technique a piece of aluminum foil placed on the road surface is given an impact by a rubber tipped rod released from a predetermined height [33]. The sharper tipped particles pierce the foil and the number of piercings per square centimeter are counted.

Another more reliable method using replicas has been developed by the Dutch State Road Building Laboratory. A cast of the surface is made with synthetic resin of silicon rubber. The cast is sectioned and the section surface is projected on photographic paper. With a special optical system the profile can then be measured and evaluated [25].

Skid testers

The British Portable Skid Resistance Tester is a pendulum device which measures the friction resistance of a wetted surface to the passage of a rubber slider. Upon release from a horizontal position the pendulum and pointer swing through an arc, the pendulum returns but the pointer stays at the farthest point of the arc (fig. 7.3.55a), and the number read from the scale gives the skid resistance value (S.R.T.). This instrument gives as a first approximation a reasonable indication of the microroughness, but cannot measure the drainage properties of the road surface. It is a low speed tester (2.8 m/sec.) and cannot sense the friction level at higher speeds. As a result, this tester rated the two surfaces number 3 and 5 of figure 7.3.53 as very similar [23], even though the friction levels of these surfaces were quite different at sliding speeds of 40 mph. The skid number SN is defined as the ratio of skid resistance to wheel load times 100. A skid number of 50 implies that the locked tire generates a skid resistance of 50 percent of the wheel load [23].

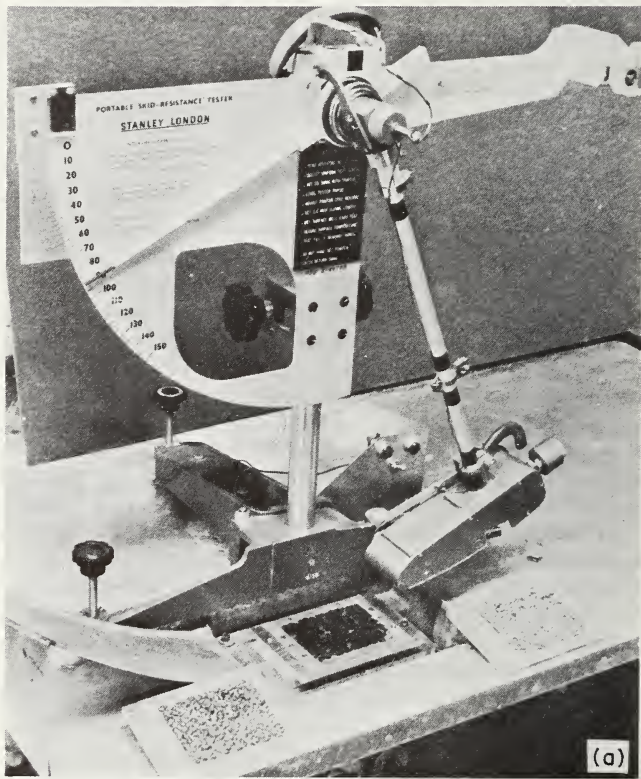


FIGURE 7.3.55a. *The British portable skid resistance tester.*

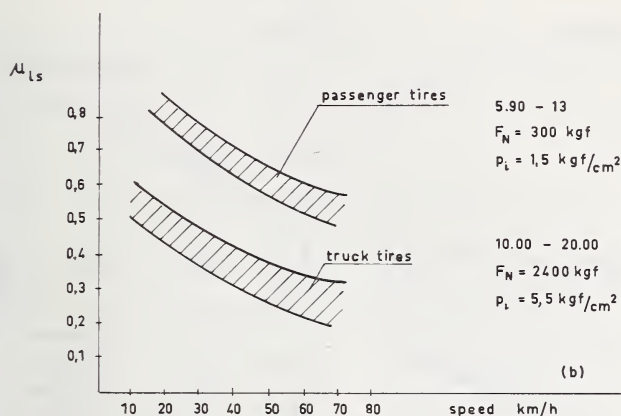


FIGURE 7.3.55b. Friction coefficient vs. speed for two types of vehicle tires.

The shortcoming of all low-speed portable testers, their inability to sense the drainage properties of a surface and its friction level at higher speeds, initiated the study and design of several Delft skid testers [34, 35].

In wet countries with mixed traffic, it is vital to safety that there is no dangerous discrepancy in stopping ability of trucks and busses with respect to passenger cars. Since most truck and bus tires operate at high inflation pressures, when compared with passenger tires, it is interesting to evaluate truck tire tests versus passenger car tire tests on surfaces having various macro- and microroughnesses.

With the Delft tire skid trailer [36, 37] an experimental program has been initiated to study the behavior of truck tires having differences in tread design, compound and construction on a variety of road surfaces.

Towed trailer road tests results obtained from passenger car tires and truck tires are indicated in figure 7.3.55b. The large difference in the locked braking force coefficient μ_{ls} for the average passenger car tire and truck tire is clearly demonstrated.

Conditioning of the Tire

Due to surface conditions of both tire and road, and the temperature dependent character of the friction, a precise description of the test conditions is absolutely necessary to compare test results of different tires.

The initial wear of the top layer of the tread rubber of a new tire, and the warming-up effect during rolling and slipping, produce large variations in the cornering force as shown in figure 7.3.56. These are typical cornering forceslip angle relations as a function of the number of tests on a 6.40-13 bias angle tire with a natural tread rubber compound under

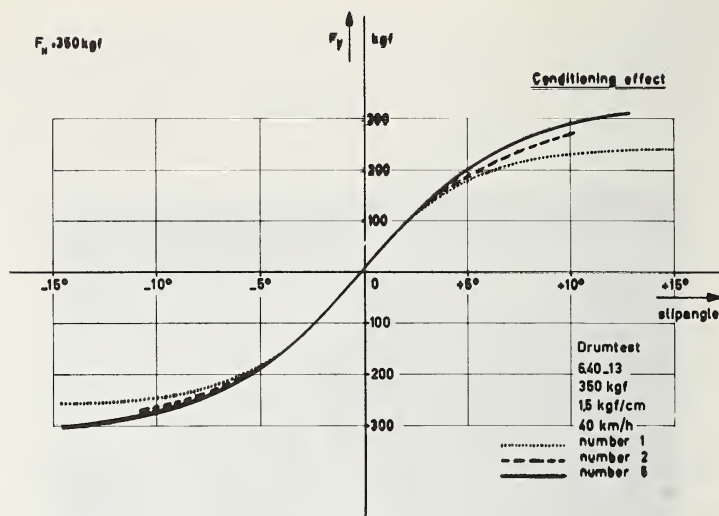


FIGURE 7.3.56. The conditioning of the tire.

a constant normal load of 350 kgf. and a constant inflation pressure of 1.50 kgf/cm². In test number one, the new cold tire was pressed against a drum of 250 cm. in diameter, rotating at a constant speed of 40 km/hr. and having a smooth steel surface. In order to prevent unsymmetrical wear of the tread, the slip angle was varied in 30 seconds between +15° and -15°. The cornering force versus slip angle was registered as record number 1. After this first test the loaded tire was cycled 10 times between +10° and -10°. Now, with a cycle time of 3 seconds, record number 2 was obtained after 30 seconds [38].

The same 10 cycles were repeated, giving test number 3, and so on, but in all tests the normal load and the inflation pressure were kept constant. When after a number of tests reproducible results were obtained, with a more or less equilibrium temperature of the tire, say after six tests, the average value of the cornering force for the sixth to tenth test was considered to be representative for the test tire in question, as in figure 7.3.57. From the above description it follows that to obtain comparable results for both laboratory drum tests or road tests, it is necessary to "run in" test tires and to control the temperatures. A common procedure, before drum test, road trailer tests, or vehicle tests are executed, is that all tires are run for break-in for a distance of about 300 km, at a speed of 80 km/hr. and with no hard cornering maneuvers.

Trailer Road Tests Versus Drum Tests

Due to significant differences induced by the curvature of the drum, the cornering force coefficient and self-aligning moment coefficient

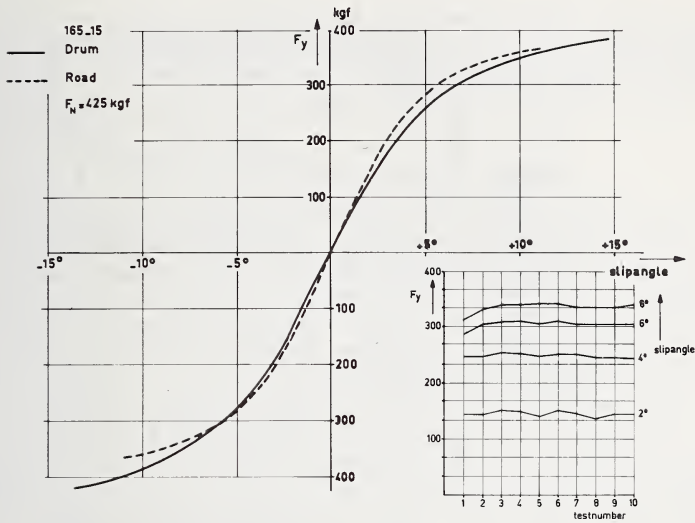


FIGURE 7.3.57. The differences in cornering force-slip angle relationships of drum and road tests.

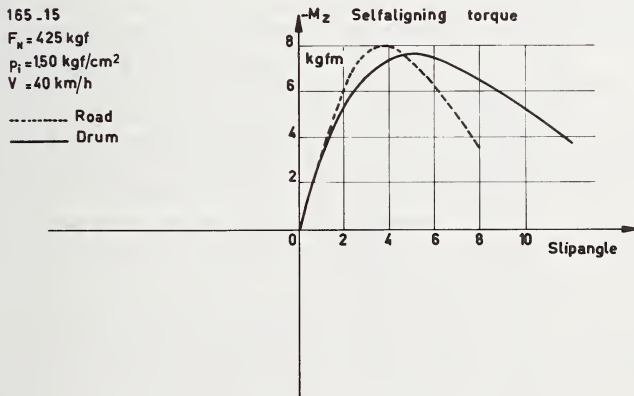


FIGURE 7.3.58. Illustration of the self aligning torque-slip angle relationships obtained on drum and road tests.

obtained from drum tests can be about (10–20%) lower than the values resulting from flat dry concrete road tests. To illustrate these differences in characteristics, the solid lines drawn in figure 7.3.57 show drum test results, whereas the dashed lines give road test results obtained with the same “run in” 165–15 tire. The self-aligning torque has been shown in figure 7.3.58.

TABLE 7.3.2.

Test tire number	Tire size	Cornering force kgf						Self aligning torque kgfm					
		$F_y (\alpha = 2^\circ)$			$F_y (\alpha = 10^\circ)$			$-M_z (\alpha = 2^\circ)$			$-M_z$ (maximum)		
		Drum	Road	Difference %	Drum	Road	Difference %	Drum	Road	Difference %	Drum	Road	Difference %
1	165-13	106	128	-17	318	336	-5	4.8	5.8	-17	6.6	6.7	-1.5
2	165-13	98	112	-20	293	305	-4	3.4	4.3	-21	5.4	5.6	-3
3	165-SR 13	71	97	-27	246	274	-10	2.8	3.6	-22	5.9	9.7	+3
4	165-SR 13	80	88	-9	256	274	-7	3.3	3.7	-11	5.7	6.1	-6
5	165-SR 14	69	87	-21	252	274	-8	3.4	4.0	-15	7.5	7.1	+6
6	165-SR 14	68	87	-22	250	270	-7	3.4	4.3	-20	8.4	7.5	+12
7	165-15	128	144	-11	366	358	+2	5.3	6.4	-17	7.7	8.1	-5
8	165-15	78	93	-16	313	330	-5	4.7	5.2	-10	6.7	6.6	+1.5
9	185-HR 14	93	114	-18	310	330	-6	4.8	5.7	-17	9.8	9.0	+10
10	185-HR 14	95	116	-18	309	339	-9	4.9	6.2	-21	8.8	9.0	-2

To compare results of normal and experimental tires tested according to the program described above under nominal constant load conditions, and constant inflation pressure of 1.50 kgf/cm^2 at a speed of 40 km/hr. , table 7.3.2 gives some results. The influence of the tire architecture is clearly shown.

Trailer Road Tests Versus Vehicle Tests on the Road

Having discussed drum tests versus tire trailer tests, it may be of interest to establish whether tire characteristics obtained from towed trailer tests correlate with conventional vehicle tests on the road. The problem encountered in the construction of a tire and the construction of the vehicle suspension is, what are the actual operating conditions. It is therefore essential to establish whether certain trailer and laboratory tests are realistic or not. The tire characteristics obtained from the trailer tests as shown in figures 7.3.25–28 already account for road surface irregularities, but it still remains a problem to decide which tire out of a number of test tires is the best from the standpoint of safety and vehicle handling properties. The essence of the problem for the tire engineer is to know, what is the best compromise in tire construction regarding tread, carcass stiffness, tread compound, etc., in order to meet as far as possible the conditions given by the vehicle suspension engineer.

Vehicle response tests determine vehicle handling properties by measurement of vehicle handling behavior in steady state cornering and transient maneuvers, and by measurement of control modulation [39]. The effect of the driver on vehicle behavior has been practically eliminated in these tests.

To correlate trailer test results with vehicle response tests for a given set of tires, it is necessary to determine the actual conditions encountered on different road surfaces. Therefore, measurements of vehicle response tests should include the measurements of the tire forces on all wheels, as well as the measurements of the path of the center of gravity of the vehicle and the path of its individual wheels.

The measurement of the individual tire forces can be conducted with the aid of the three-component road platform tester, as described in section 7.2.1 and shown in figure 7.2.17. The procedure of measuring the actual tire forces with a road platform having the same surface as the test track may be preferred over the method of using force transducers built into each individual axle. It avoids the necessity of designing another axle force measuring device for each vehicle type.

Two road platforms already provide much information, but if required four of these platforms could be used. At present the author has only conducted experiments with one road platform, and load transfer could be clearly demonstrated.

The measurement of the actual slip and camber angles when passing over the road platform can be carried out with the S.C. meter as described in section 7.3.3 and shown in figure 7.3.43.

The path over the platform can be found by using the method of mounting flashlights on the axle stub as shown in figure 7.3.42 and placing a photo apparatus in a steel structure well above the road. The dashed

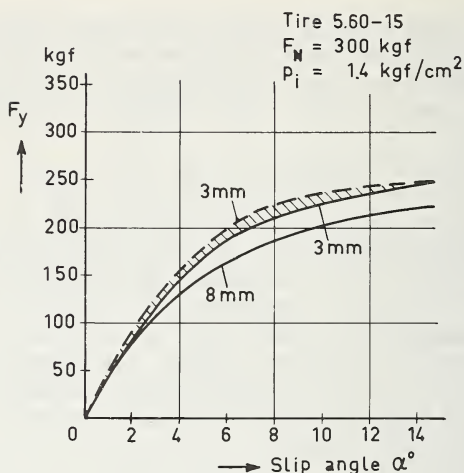


FIGURE 7.3.59. The effect of tread depth and manufacturing fluctuation on the tire characteristics.

lines obtained on the photograph indicate the path over the road platform.

The path of the center of gravity of the vehicle can be traced by filming or photographing from a high tower made of a steel structure, placing flashlamps on the front and rear ends of the test vehicle.

Of course, if required, the well known techniques of using accurate accelerometers and gyros can be added to the instrumentation, but corrections for vehicle pitch and yaw motions have to be made.

The disadvantage of the combination of these methods is the complexity of the total instrumentation system. However, it is for obvious reasons of great importance to relate trailer test data to those obtained from vehicle performance.

Tire Characteristic Variations Due to Manufacturing Fluctuations

Tires of the same manufacturer and having successive serial numbers should have the same cornering characteristics. Due to problems of tire processing and variation in tire components, substantial differences in tire characteristics are often observed. To prove this, two tires 5.60-15, both having 3 mm. tread depth, were compared at a speed of 0.2 m/sec. on a platform tire tester having a concrete surface [16]. Up to two degrees slip angle the results obtained were similar, but above two degrees slip angle it is seen that large variations can occur as in figure 7.3.59. The influence of the tread depth is also shown, and the well known phenomena is observed that with 8 mm. tread depth, that is, with less wear, a lower cornering force is observed on a dry concrete road.

Comparison of two tires of the same European manufacturer, but according to serial numbers traced to come from different factories,

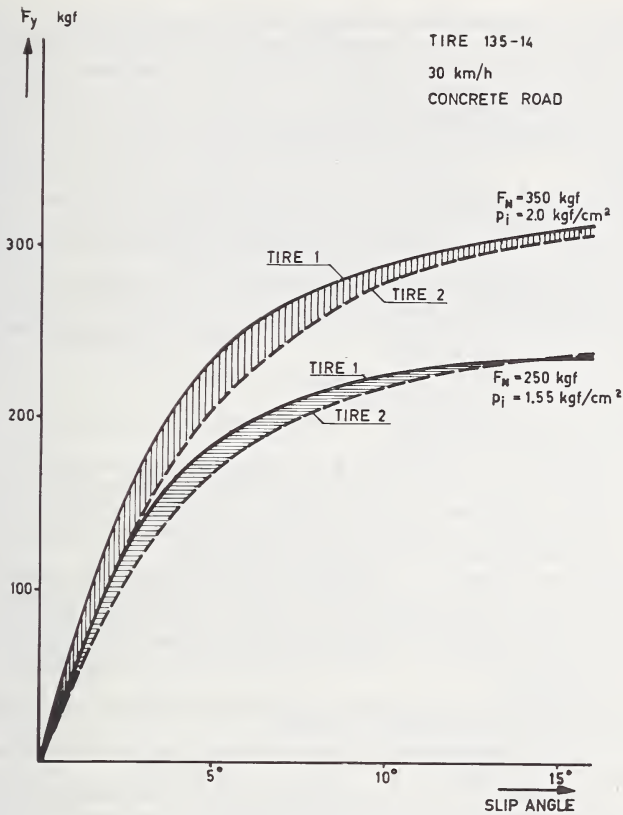


FIGURE 7.3.60. Variation in tire characteristics due to manufacturing fluctuation.

gave still greater differences in cornering characteristics as shown in figure 7.3.60. Such a variation in tire manufacturing is difficult for the car manufacturer, because both tires of figure 7.3.60 could be mounted on the same car. It appears desirable that car manufacturers specify allowable force variations.

References

This bibliography refers frequently to V.R.L.D. reports made by the Vehicle Research Laboratory at Delft. These reports are in the Dutch language and can be obtained in microfilm or blueprint on payment.

- [1] Freudenstein, G., Luftreifen bei Schräg- und Kurvenlauf, Deutsche Kraftfahrtforschung **152** (1961).

- [2] Grotewohl, A., *Seitenwinduntersuchungen an Personenwagen*, A.T.Z., 11/12 (1967).
- [3] Vehicle Dynamics Terminology, Handbook Supplement, SAE J 670a (1965).
- [4] Nordeen, D. L., Analysis of tire lateral forces and interpretation of experimental tire data, SAE Paper No. 670173 (1967).
- [5] Bundorf, R. T., The influence of vehicle design parameters on characteristic speed and understeer, SAE Paper No. 670078 (1967).
- [6] Bergman, W., The basic nature of vehicle understeer-oversteer, SAE Paper No. 957B (1965).
- [7] Sabey, B. E., and Lupton, G. N., Photography of the real contact area of tires during motion, Road Research Laboratory Report LR64 (1967).
- [8] Gough, V. E., Practical tire research, SAE Trans. **64** (1956); Tire to ground stresses, *Wear* **2**(2) (Nov. 1958).
- [9] Rooney, J. H. M., Measurements of the longitudinal deformation of a tread element, V.R.L.D. Report No. P090 (1967).
- [10] Iritani, S., and Baber, T., Forces on the contact patch of the tire, Paper B6, Proc. 10th FISITA Congress, Tokyo, 1964.
- [11] Gough, V. E., Nondestructive estimation of resistance of tire construction of tread wear, SAE Paper No. 667A (1963).
- [12] Corp, H. A. van, Determination of lateral accelerations acceptable by motorists, V.R.L.D. Report No. 369 (1966).
- [13] Dijks, A., Timan, D. A., and Ruyter, T. J., Trailer road tests versus vehicle tests on a smooth polished road surface, V.R.L.D. Report No. P119 (June 1969).
- [14] Holmes, K. E., and Stone, R. D., Tyre forces as functions of cornering and braking slip on wet road surfaces, Road Research Laboratory Report LR254 (1969).
- [15] Buis, P., Pneumatic tires, V.R.L.D. Report No. 084 (1967).
- [16] Koeszler, P., and Senger, G., Vergleichende Untersuchungen der Seitenführungseigenschaften von Personenwagen Reifen, *Deutsche Kraftfahrtforschung* **172** (1964).
- [17] Henker, E., Dynamische kennlinien von P.K.W. reifen (V.E.B. Druckerei, D.D.R.); Wissenschaftlich-technische Veröffentlichungen aus dem Automobilbau. **H3** (1968).
- [18] Allbert, B. J., and Walker, J. C., Tyre to wet road friction at high speeds, *Proc. IME* **180**, 105 (1965/66).
- [19] Koning, C. J. de, Design considerations of a device for measuring the camber- and slip angle, V.R.L.D. Reports No. 398^{a, b, c} (1967).
- [20] Lems, F. L., The measurement of camber and slip angles of motorcars, V.R.L.D. Reports No. 464^{a, b} (1968).
- [21] Giles, C. G., Lander, F. T. W., and Holmes, K. E., A test vehicle for studying the skid resisting properties of tyres and road surfaces under controlled cornering and braking, Road Research Laboratory Report LR99.
- [22] Davisson, J. A., Basic test methods for evaluating tire traction, SAE Paper No. 680136 (Jan. 1968).
- [23] Kummer, H. W., and Meyer, W. E., Tentative skid-resistance requirements for main rural highways, Nat. Corp. Highway Res. Program Report 37 (Highway Research Board, Washington, D.C. 20418).
- [24] Savkoor, A. E., The isothermal friction of rubber compounds on nominally smooth hard tracks, V.R.L.D. Report No. PO93 (1968).
- [25] Spaink, G. N., Friction and drainage measurements on abrasion paper of different qualities, V.R.L.D. Report No. 391 (Apr. 1967) (Translated by Cornell Aeronautical Laboratory, Inc., Buffalo).
- [26] Schulze, K. H., and Beckmann, L., Friction properties of pavements at different speeds, A.S.T.M. Spec. Tech. Publ. No. 326 (1962).
- [27] Sabey, B. E., Wet road skidding resistance at high speeds on a variety of surfaces on A 1, Road Research Laboratory Report LR131 (1968).
- [28a] Moore, D. F., Drainage criteria for runway surface roughness, Cornell Aeronautical Laboratory, Buffalo, J. Roy. Aero. Soc. (London) **69**(653) (1965).
- [28b] Moore, D. F., A history of research on surface texture effects, *Wear* **13**, 381-412 (1969).
- [29] Edelman, A., Measurements with a refined drainage meter, V.R.L.D. Report No. 473 (Sept. 1968).
- [30] Ernst, H. C., Correlation of results of measurements of coefficients of friction obtained with a road trailer tire tester, a skid resistance tester (S.R.T.) and a modified Dr. Moore drainage meter, V.R.L.D. Report No. 497I (June 1969).

- [31] Ernst, H. C., Development of a Delft high pressure drainage meter, V.R.L.D. Report No. 497^{II} (Aug. 1969).
- [32] Grosch, K. A., and Maycock, G., Influence of test conditions on wet skid resistance of of tyre tread compounds, Trans. I.R.I. **42**(6)(1966).
- [33] Gillespie, T. D., Pavement surface characteristics and their correlation with skid resistance, Penn. Dept. Highways Program Report No. 12 (1965).
- [34] Gerritsen, R. R. V., Description of portable pavement friction testers. Design of a pendulum tester, V.R.L.D. Reports No. 392-395 (1967).
- [35] Koelewijn, A. C., Pavement friction testers, V.R.L.D. Report No. 516 (1969).
- [36] Paar, H. G., Skid trailer for testing truck tires, V.R.L.D. Report No. 376 (Nov. 1966).
- [37] Schrier, J., and Groeneweg, H. H., Design and calculation of a skid trailer for testing truck tires, V.R.L.D. Report No. M077 (May 1968).
- [38] Timan, D. A., and Ruyter, T., Cornering force and self-aligning torque measurements on a drum and dry road with the tire tester, V.R.L.D. Report No. P100 (Oct. 1968).
- [39] Bergman, W., Considerations in determining vehicle handling requirements, SAE Paper No. 690234 (Jan. 1969).



7.4. Tire In-Plane Dynamics

H. B. Pacejka

In this part the symmetric behavior of tires will be discussed. Section 7.4.1 is devoted to relatively low-frequency phenomena with inertia effects of the tire neglected. Attention will be paid to the normal and longitudinal problem. Section 7.4.2 treats the high-frequency vibrational behavior of tires, again mainly restricted to symmetric or in-plane aspects.

The frequency below which tire inertia effects may be neglected must lie well below the lowest natural frequency of the tire. Distinction may be drawn here between radial and longitudinal motions and between different types of tire construction. However, it is estimated that in general the low frequency range can be extended up to about 20 Hz. It may be noted that for lateral tire movements this limit must be reduced (cf. sec. 7.5.3 on gyroscopic effects).

7.4.1. Low Frequency Properties

Normal Force-Deflection Characteristics

It has been generally accepted that pneumatic tires transmit their normal load mainly by the formation of a finite flat contact area, A , which enables the internal air pressure, p_i , to remain in equilibrium with the external vertical contact pressure, p_z . We would therefore expect the normal load, W , to be approximately equal to the inflation pressure multiplied by the contact area. This would indeed apply for a thin envelope or membrane. However, the tire tread-band in particular cannot be considered to be thin. Automobile tires often show nearly rectangular foot prints. This is due to the nearly flat profile of the undeflected tire cross section. The effective area, defined as $A_e = W/p_i$, then becomes less than the gross foot print area A . This is because the contour of the presumably thin side wall cross section does not show a horizontal tangent at the point where the contact area begins. The tension force in the side wall, caused by the air pressure, has an upward component which reduces the resulting pneumatic force. Later on in this paragraph an analysis of this phenomenon will be given. Use will be made of a tire model showing thin flexible side walls and a rigid tread-band cross section. In this analysis the internal pressure p_i has been kept constant. For automobile tires this is an acceptable assumption. The effect of pressure rise may not be negligible for aircraft tires because of their relatively large deflections [1].¹

¹ Figures in brackets indicate the literature references at the end of this section.

In the absence of internal air pressure the tire model proposed is not capable of transmitting a radial force if one neglects the flexural rigidity of the tread-band. Consequently, the vertical stiffness of the tire model is of a completely pneumatic nature. In reality, however, this is not entirely so. Experiments of various investigators [1, 2, 13] indicate that the rigidity of the cover (side walls and tread-band) causes a noticeable contribution to the force transmission. According to these references, under rated inflation pressure conditions the carcass carries about 15 percent of the vertical load for cross ply automobile tires and 3 percent to 8 percent in case of aircraft tires. As a result of this cover rigidity the effective area A_e increases and may even exceed the gross foot print area A .

The above observations hold for standing or nonrotating tires pressed against a flat surface. On curved surfaces the tension force in the tread-band will take part in the force transmission. In addition, we observe that with given radial deflection at the contact center, the contact length changes with curvature of both tire and surface. It is therefore to be expected that experiments indicate a dependence of normal tire stiffness upon road surface curvature. Both Marquard [3] and Chiesa [4] found a decrease in stiffness with decreasing radius of curvature of the surface. Marquard has shown that the influence of surface curvature can be roughly approximated with the following equation:

$$\frac{C_{z, \text{curved}}}{C_{z, \text{flat}}} = \left(\frac{R}{R + r} \right)^{1/3} \quad (7.4.1)$$

In this equation, which originates from the Herzian theory of two parallel cylinders pressed against each other, C_z denotes the normal tire stiffness expressed as tire force per unit deflection, R the radius of the contact surface and r the tire radius. Marquard found the formula to follow the experimental trend for ratios as small as $R/r = 0.25$. When traversing obstacles with radii of curvature much smaller than the tire contact length, the tire clearly demonstrates its more than zero-dimensional nature. A subsequent section treats the enveloping properties of tires. The remainder of this section will be confined to the contact with flat surfaces.

Until now, the tire has been considered as nonrotating. Once the tire rolls, fresh elements of cover are continuously entering the deformation region. There is no *a priori* reason to believe that deformation of a rolling tire follows the same rules which hold for a standing tire. Hysteresis, which has been found to damp the vertical motion of the axle with a nonrotating wheel, appears to be practically absent with a rotating tire once the rate of rolling becomes high as compared to the rate of deflection. Instead, hysteresis produces rolling resistance. In addition, it appears that vertical tire stiffness is affected by the rolling process. Rasmussen and Cortese [5] determined the effective tire stiffness by means of resonant tests. They show that the effective normal stiffness of

a rolling tire is virtually independent of hub amplitude whereas the effective stiffness of a nonrolling tire varies with amplitude in a non-linear fashion. At small amplitude the standing tire shows considerably larger values for the stiffness than the rolling tire (50% higher at 1.5 mm. amplitude for a 6.50-14 tire). For increasing amplitudes the stiffness of the standing tire decays gradually and tends to the constant value of the rolling tire (15% higher at 10 mm.). Chiesa and Tangorra [4] found with their resonance tests that this level of stiffness is not very much affected by the speed of rolling once the speed has exceeded a value of about 20 km/hr. (cf. fig. 7.3.32). The above observations are of particular importance for the execution of laboratory ride simulator tests (cf. Betz [6]).

At high rolling speeds the dynamic aspect, which among other things is responsible for the formation of standing waves (sec. 7.4.2), must be taken into account. Dodge [7] made an attempt to attack this problem. With the aid of equations describing the dynamics of a rotating shell, corresponding to eqs (7.4.90-91), the radial stiffness of the shell subjected to a radial point load has been determined. The results are complicated and difficult to interpret and are not directly applicable to the tire pressed upon a flat surface. An extension of the analysis is needed where the following additional parameters are introduced: finite contact length, internal pressure, tension force in tread-band and tangential stiffness of tread-band with respect to the wheel rim. Another theory related to the work of Dodge has been proposed by Clark [43]. In this study the contact length has been considered as finite.

Before going into details of the static loading process, we consider the following simple but interesting observation. For small normal tire deflections the contact length varies approximately as the square root of the deflection. Consequently, for a foot print of constant shape the contact area varies as the deflection. This means that, with the assumption that the normal load equals internal pressure multiplied by a fixed percentage of the contact area, the force-deflection curve is linear for small values of the deflection.

For a more sophisticated analysis of the normal force-deflection problem we make use of the membrane concept employed by Rotta [8] and Senger [9] among others for the analysis of the elastic properties of a tire segment, and by Pacejka [10] for the investigation of air springs. Senger used the model described earlier, consisting of flexible side walls and a tread-band with rigid cross section. Senger replaced the circular band by a linear elastically-supported beam under tension. The beam is transversely deflected by the application of a normal force distributed over a finite length. The longitudinal tension force influences the resulting transverse stiffness due to the curvature caused by the application of the normal forces. In the writers opinion the transformation to a linear beam is not valid for analyses of radial deformations. In reality, the contact area is not curved when pressed on a flat road. Therefore the tension force, if present in this area, cannot influence the force distribution in the contact area. Flexural rigidity of tread band and side walls produce additional normal forces but will be neglected henceforth.

Theoretical load-deflection relationship.

For the determination of the vertical force acting on a deflected tire we divide the tire into a large number of thin segments, and imagine this force to be composed of the elementary radial forces acting on these segments. For the calculation of the elementary forces we need to know the load-deflection characteristic of one segment. This characteristic will be designated as the radial foundation characteristic.

We consider the model of the tire cross section shown in figure 7.4.1. The side wall is assumed to behave as an inextensible membrane. For the segment having a nearly uniform thickness, the membrane assumes a circular shape under the action of the internal air pressure p_i . The stresses in the membrane would not change if the membrane were extended according to the dashed line shown in the figure. Evidently, the external vertical force acting on the segment of unit thickness equals

$$q_z = \int_{-b}^b p_z dy = 2p_i b_e \quad (7.4.2)$$

with $2b_e$ denoting the effective width indicated in figure 7.4.1. With tire parameters l and h_{so} introduced in the figure, we obtain the following equations for b_e and the radial deflection $-w$ in terms of the parameter ϕ_s

$$h_{so} + w = l \frac{\sin \phi_s}{\phi_s}, \quad (7.4.3)$$

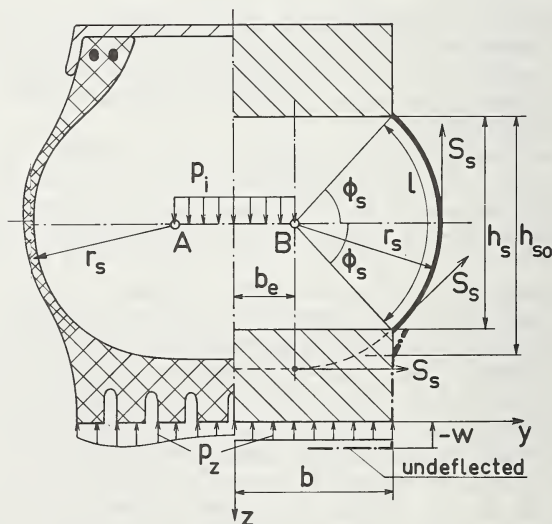


FIGURE 7.4.1. Real and model representation of tire cross-section.

$$2(b - b_e) = l \frac{\cos \phi_s}{\phi_s}. \quad (7.4.4)$$

The arc length l is assumed to be a given constant. At zero deflection, i.e., $w=0$, the effective side wall height is h_{so} . Due to the tensile rigidity of the tread band, the effective width b_e does not, in general, vanish in the undeflected case. The resulting radial force produces the hoop tension force which is present in the undeflected portion of the tire tread band.

These observations indicate that this characteristic will in general not pass through the origin ($q_z=0, w=0$). The foundation characteristic can be calculated from the equations above. For a segment with relative dimensions $l=1.75 b$, $h_{so}=1.6 b$, the dimensionless foundation characteristic is presented in figure 7.4.2. From the equations (7.4.3-4) the stiffness of a segment in the radial direction (radial foundation stiffness per unit length) can be derived. We obtain:

$$c_r = -2p_i \left(\frac{db_e}{dw} \right) = p_i \left(\frac{\cos \phi_s + \phi_s \sin \phi_s}{\sin \phi_s - \phi_s \cos \phi_s} \right). \quad (7.4.5)$$

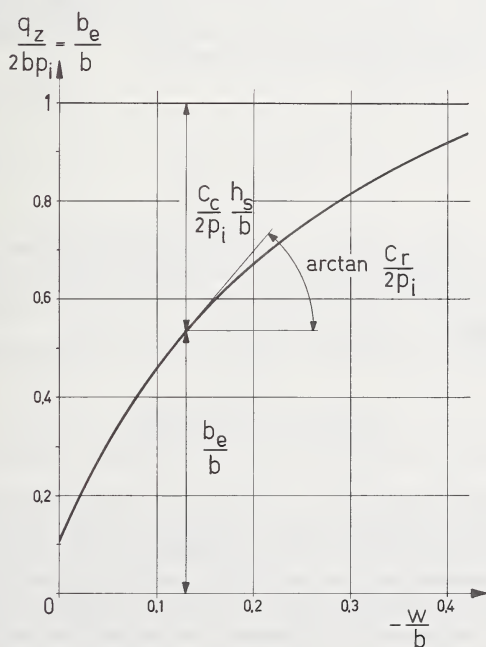


FIGURE 7.4.2. Radial foundation characteristics with radial stiffness, c_r , and lateral stiffness, c_e , of tire segment of unit thickness shown in figure 7.4.1.

Together with eq (7.4.3) c_r can be calculated as a function of w .

In addition, we derive the lateral stiffness c_c of the tire segment. With a small lateral displacement v of the tread band in lateral direction y , point A (fig. 7.4.1) moves upward and point B downward a distance $(b - b_e)v/h_s$. The total lateral force acting on a segment of unit thickness becomes $2p_i(b - b_e)v/h_s$. Hence, the lateral stiffness of the segment (lateral foundation stiffness per unit length) reads:

$$c_c = 2p_i \left(\frac{b - b_e}{h_s} \right) = \frac{1}{h_s} (2p_i b - q_z). \quad (7.4.6)$$

The lateral stiffness in an appropriate dimensionless form appears to bear a simple relationship to the dimensionless radial foundation stiffness, as shown in figure 7.4.2. From this figure it can be observed that both the radial and lateral stiffness decrease with increased deflection ($-w$). The lateral stiffness even becomes negative for $b_e > b$. The lateral stiffness is of particular importance in the analysis of the cornering behavior of tires, to be dealt with in part 7.5. Rotta [8] and Clark [11] employed alternative models for the determination of the lateral foundation stiffness.

We shall continue now with the normal loading problem and determine the load-deflection curve of the tire from the foundation characteristic of figure 7.4.2. The radial deflection $-w$ varies along the contact line. The contact length depends on the normal tire deflections, δ , and the tire radius r . We use the approximate equations

$$a^2 = 2r\delta \quad (7.4.7)$$

and

$$-w = \delta - \frac{x^2}{2r} \quad (7.4.8)$$

where x denotes the coordinate in the longitudinal direction. In figure 7.4.3 a comparison is made between calculated values of contact length and experimental data from Senger [9]. Note that at large deflections the calculated values are somewhat high.

The dimensionless normal load expressed in the integral form

$$\frac{W}{4b^2 p_i} = \int_0^{a/b} \frac{b_e}{b} d\left(\frac{x}{b}\right) \quad (7.4.9)$$

can be calculated, in principle, with the aid of the foregoing equations. In the actual calculation the radial foundation characteristic of figure 7.4.2 has been approximated by a quadratic function of w/b , coinciding with the original curve in $-w/b = 0, 0.2$, and 0.4 . The final result for a tire with $r = 5.4 b$ has been shown in figure 7.4.4 in comparison with measured data deduced from Senger's experimental results. Perhaps owing to deviations between calculated and measured values of contact length (fig. 7.4.3), the agreement is better than expected. As has been mentioned before, around 15 percent of the normal force transmission

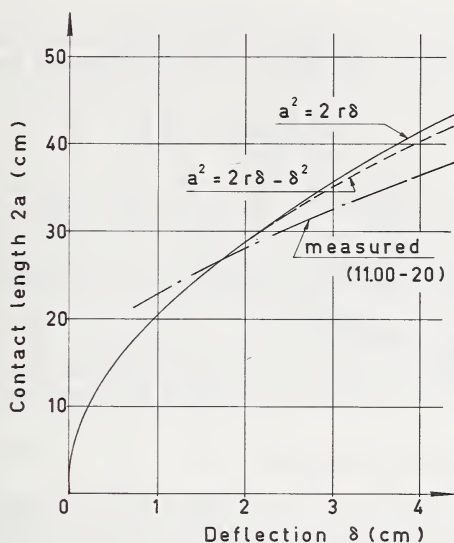


FIGURE 7.4.3. Experimental and calculated values of contact length [9].

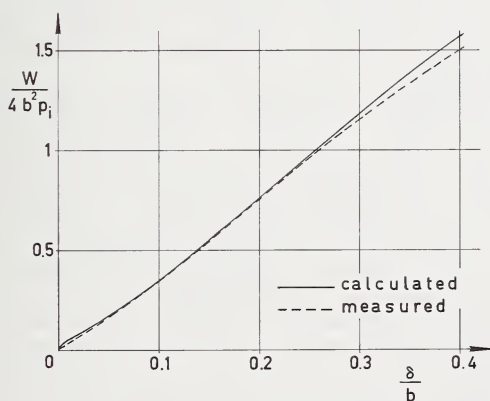


FIGURE 7.4.4. Calculated nondimensional load deflection curve compared with experimental results of Senger [9] for a 11.00-20 cross-ply truck tire ($p_i = 4-7$ bar).

is attributable to carcass rigidity. The shape of the measured and calculated curves is representative for cross-ply tires. It suggests that for most purposes a linear load-deflection relationship can be used with sufficient accuracy. Vibration tests of Rasmussen and Cortese [5] and of Betz [6] with rolling tires substantiate this result.

Tiemann [12] found great similarity between reduced load-deflection curves for a great variety of automobile and truck tires. Here, distinction must be made between bias-ply and radial tires. For each of these cate-

gories of tires it turns out that the dimensionless-load versus dimensionless deflection can be reasonably well represented by a single curve

$$\frac{W}{p_i B \sqrt{2rH}} = F\left(\frac{\delta}{H}\right) \quad (7.4.10)$$

where B is section width, H is section height and r is rim radius. For bias-ply tires the doubly-curved form of figure 7.4.4 applies, whereas radial tires show a continuously concave characteristic. For aircraft tires Smiley and Horne [13] propose a similar equation. To account for the influence of cover rigidity they replaced p_i by $p_i + 0.08 p_r$, with p_r denoting the rated inflation pressure. Since the measured curves are so similar to those given by eq (7.4.10), it seems possible that vertical load-deflection curves could be calculated for each type of tire construction.

Enveloping Properties (Obstacles)

An important property of a pneumatic tire is its ability to cushion a vehicle against short road irregularities. A rigid wheel passing over an obstacle would acquire a sudden vertical velocity which involves extremely large vertical accelerations. Experiments never show such large accelerations so that obviously the elastic enveloping properties enable the pneumatic tire to partially "swallow" the obstacle while rolling over it. The resulting vertical displacement of the axle is small relative to the height of the obstacle.

Most of the published information on this subject concerns experimental data relating tire parameters to the response of tire forces or wheel axle motions as the tire slowly rolls over an obstacle. A number of investigators have examined the response of the vertical and longitudinal tire forces to a short prismatic obstacle extending over the whole tire width, and possessing a rectangular, trapezoidal, sinusoidal or cylindrical cross section. In these tests the axle height above the road plane has been kept constant. As an illustration we present in figure 7.4.5 (from Gough [14]) the response of a bias-ply and a radial tire. It is seen that in the variation of the vertical load $W = -F_z$ between two maxima, a minimum arises when the wheel axle is located directly above the center of the obstacle. In this particular situation the minimum becomes even lower than the initial normal load $-F_{z0}$ occurring on a flat surface. Extensive tests of Julien [15] show that the shape of the curves vary both with size and shape of the obstacle and with the vertical deflection of the tire. It appears that the minimum in vertical force variation only arises when the static tire deflection is sufficiently large and the obstacle size sufficiently small. The longitudinal force invariably shows one maximum and one minimum. These extreme values are virtually independent of initial tire deflection [15].

From experiments conducted by Lippmann and his associates [16, 17] it appears that with fixed axle height the vertical and longitudinal peak forces vary nearly proportionally with internal pressure. For ordinary inflation pressures the major part of the forces arise from internal

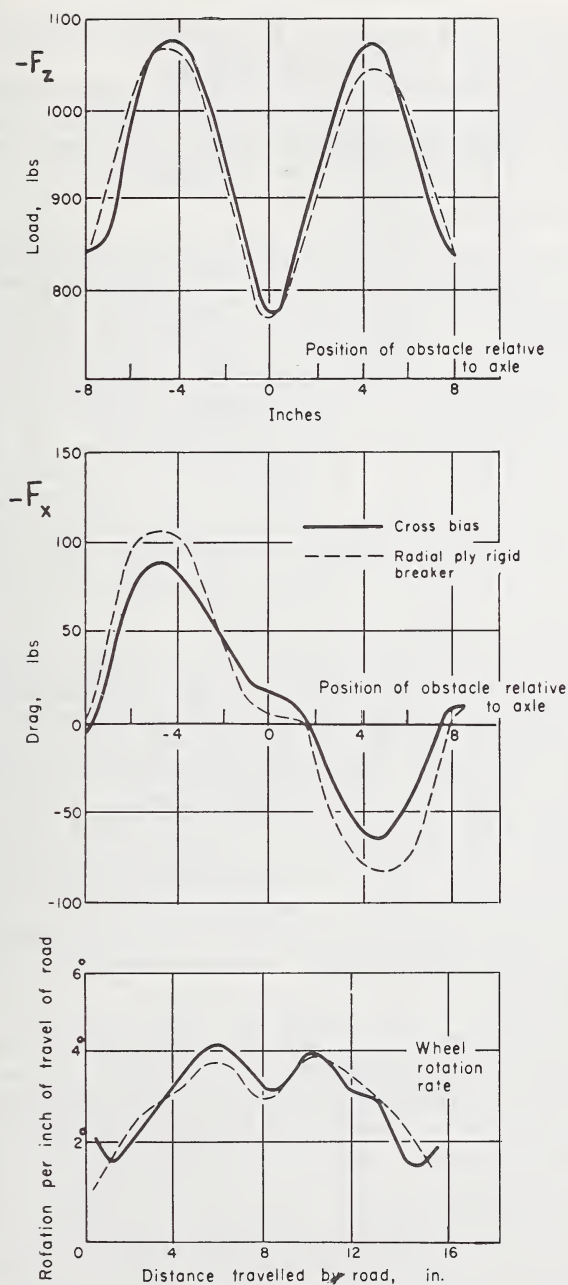


FIGURE 7.4.5. Variation of normal load and drag force as well as angular speed of wheel rim as a function of obstacle position with respect to wheel axle [14].

pressure. This leads Lippmann to the conclusion that the core of the process tests on some pneumatic mechanism.

Figure 7.4.5 furthermore shows the wheel rotation per unit of travel on the road. The angular acceleration of the wheel caused by obstacles will generate additional longitudinal forces which may become quite considerable in magnitude, particularly at high speed.

Theory of enveloping capabilities.

An adequate theory explaining these measured force variations has not been found in the existing literature. The following relatively simple theory may furnish some insight into the problem. We employ a tire model consisting of a large number of radially directed springs. The influence of tread band tension and bending stiffness will be neglected. It has been pointed out in section 7.4.1 that the spring forces are mainly due to pneumatic action. It is assumed furthermore that these forces are directed perpendicular to the tire peripheral line. For the sake of simplicity the shape of the peripheral line is considered to remain circular outside the contact zone, which extends from the leading to the trailing contact points. When, in addition, the stiffness of the springs is constant i.e., linear foundation characteristic, the vertical force which acts on the tire can be obtained approximately by multiplying the overlapping area of the tire circumscribed circle and the road profile by the foundation stiffness per unit length of circumference. According to the behavior of such a tire model, the vertical force increases when a short obstacle is encountered. The force remains constant as long as the obstacle contour lies completely inside the circumscribed circle. The experimental evidence of the occurrence of a minimum force cannot be explained with this simple model unless a nonlinear softening foundation characteristic is assumed. As has been indicated in section 7.4.1, such a spring characteristic of a tire element will indeed exist (fig. 7.4.2). During the time in which the obstacle is completely swallowed by the tire, it is obvious that the vertical force becomes a maximum when the obstacle is in the foremost and rearmost positions since the slope of the load-deflection curve is then greatest. In the center position a minimum is expected as the obstacle now deforms the tire in the range of lowest stiffness.

Experiments indicate that under particular conditions a minimum vertical force can arise which is even lower than the initial force without an obstacle. Since the force-deflection characteristic of a tire element is not expected to be particularly nonlinear in the practical range of deflection, some other mechanism must be responsible for this phenomenon.

It is believed that a second possibly important effect on enveloping an obstacle is the shrinkage of the circumference of the circumscribed circle of the tread band, which is assumed inextensible in the ensuing analysis. This circumference must become shorter in order to supply length in the contact zone where the obstacle is partially surrounded by the tread band. In figure 7.4.6 two circumscribed circles are shown. The larger circle shows the tire pressed against a flat surface. Its size reduces to the smaller circle when the obstacle is in the contact center.

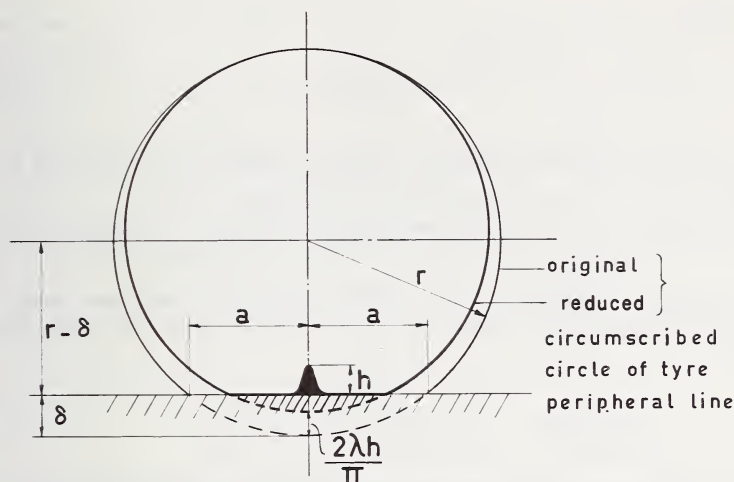


FIGURE 7.4.6. Tire peripheral line with and without the intrusion of an obstacle.

It has been assumed that the tread band deformations caused by the intrusion of the obstacle vanish at the top of the tire. Consequently both circles touch each other in this point. The difference in length of the two circumferences equals the difference between obstacle contour length and its base length. The relatively small variation of the difference between arc length and chord length (contact length) of the circles in these two cases has been neglected. The possibility of partial loss of contact has been disregarded, an assumption which is admissible only in case of relatively smooth obstacles.

The reduction of the circumference of the circumscribed circle has been designated as $2\lambda h$, in which h denotes the obstacle height and λ a nondimensional form parameter of the obstacle. For a rectangular obstacle shape, $\lambda = 1$. The value of λ decreases when the shape becomes trapezoidal. The decrease in diameter of the circumscribed circle becomes $2\lambda h/\pi$. For small values of h the area of the section with chord length $2a$ and width $2\lambda h/\pi$ is approximately $4\lambda ha/\pi$. With c_r denoting the radial (vertical) stiffness of the foundation per unit area, F_{z0} the initial vertical load and A the area of the obstacle cross section, we obtain for the vertical load acting on the tire when the obstacle has arrived directly below the wheel axle:

$$-F_z = -F_{z0} + c_r \left(A - \frac{4\lambda ha}{\pi} \right). \quad (7.4.11)$$

It is seen that from this formula a decrease in vertical force can indeed occur even using linear foundation characteristics. The condition at

which this occurs is:

$$A < \frac{4\lambda ha}{\pi}. \quad (7.4.12)$$

It is of importance to introduce another form factor σ defined by the relation:

$$A = \sigma h^2. \quad (7.4.13)$$

For a square cross section $\sigma = 1$. When the length becomes larger than the height σ increases. The condition (7.4.12) reads in dimensionless form:

$$\frac{h}{a} < \frac{4}{\pi} \cdot \frac{\lambda}{\sigma}. \quad (7.4.14)$$

Julien [15] has carried out experiments with an obstacle of square cross section. We wish to compare his experimental results with our theory. For this purpose we adopt a trapezoidal obstacle to the shape of which the real tire deforms reasonably closely when it rolls over a square obstacle. The symmetric trapezoid chosen has a height h , a base line $3h$ and a top line h . The area becomes $A = 2h^2$ so that $\sigma = 2$ and the parameter $\lambda = \sqrt{2} - 1 = 0.414$. The condition (7.4.14) then becomes $h/a < 0.263$. From the results of Julien's experiments with a 5.0-15 tire it can be deduced that the minimum vertical force becomes less than the initial load at the same axle height when the ratio obstacle height to half contact length, h/a , becomes less than the values shown in the table below, valid for three values of initial tire deflection δ .

The agreement with the theoretical value 0.263 is very good considering the simplicity of the model employed and its great sensitivity to the shape of the obstacle, i.e., the shape of the actual tire deformation. It may be noted that the critical ratio h/a increases with increasing initial deflection δ . This can be explained by the softening character of the nonlinear foundation characteristic. This nonlinearity will in general raise the critical value of h/a .

TABLE 7.4.1. Critical values of h/a

h (cm.)	δ (cm.)	a (cm.)	$\frac{h}{a}$
2	1.7	9.8	0.205
3	2.1	11.2	.267
4	2.6	12.4	.322

Using this theoretical tire model, the variation of the vertical and longitudinal force has been calculated for a trapezoidal obstacle moving from the leading edge to the center of the contact area. The results are

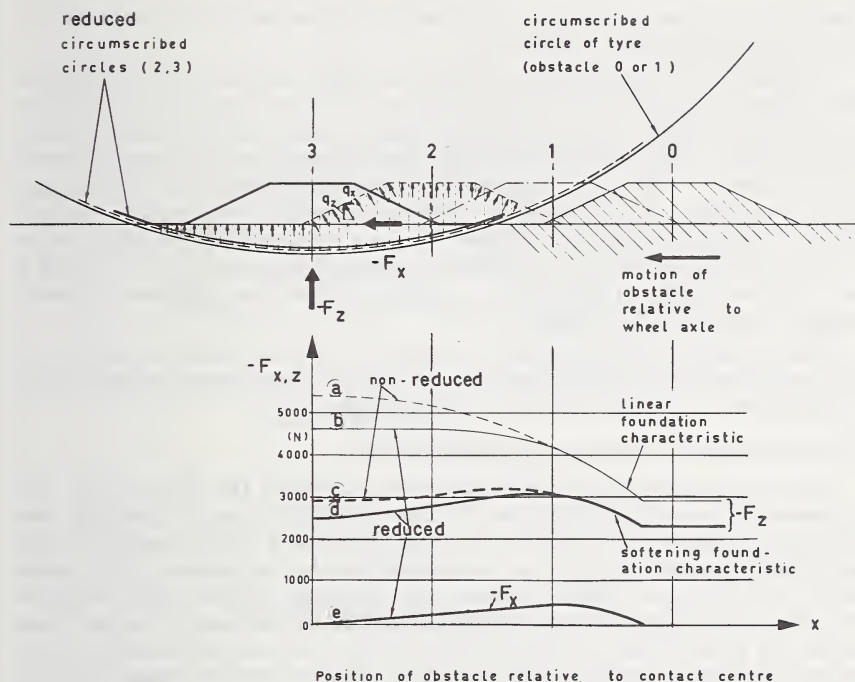


FIGURE 7.4.7. Calculated variation of vertical and longitudinal force as a function of position of obstacle relative to contact center.

shown in figure 7.4.7. The influence of foundation nonlinearity and of shrinkage of the tread-band are clearly demonstrated. The calculations have been carried out for a tire with a cross section proportional to that of the tire model used in section 7.4.1, of which the dimensionless foundation characteristic has been shown in figure 7.4.2. The tire model parameters are: $r=27$ cm., $\delta=1.5$ cm., $a \approx 9$ cm., $b=5$ cm., $l=8.25$ cm., $h_{so}=8$ cm., $p_i=2$ atm. The trapezoidal obstacle has the dimensions: height $h=2$ cm., base line $=12$ cm., top line $=4$ cm. This shape has been chosen for simplifying the calculations during the first stage of contact. As the sloping side of the obstacle touches the peripheral line at the instant of first contact, there will be practically no change in length of the circumscribed circle during the first stage up to position 1. From this position on, reduction of the circumference will take place. The dotted arc indicates the reduced circumference for the intermediate position 2. The circumference is minimum as soon as the obstacle lies completely inside the circle.

For position 2 the pressure distribution along the contact line has been shown. The vertical components q_z are found with the aid of the stiffness shown in figure 7.4.2. The integral of these components form the vertical

load $-F_z$. In the same way, the integral of the horizontal components q_x form the drag force $-F_x$.

In figure 7.4.7 the calculated force variations are shown. The vertical force has been calculated for four different combinations of the following assumptions: linear ($c_r = 160 \text{ N/cm}^2$) and nonlinear foundation characteristic (fig. 7.4.2) and reduced and original circumferential length (curves a , b , c , and d). Curve b , computed using the linear theory but with length reduction taken into account, is close to exhibiting a minimum. According to condition (7.4.14) a minimum of curve b lower than the initial value $-F_{z0}$ would arise when the obstacle is reduced in size so that $h < 0.076 \times a = 0.68 \text{ cm}$. This critical value increases when the nonlinear characteristic is taken into account.

The variation of longitudinal force does not show great sensitivity to the model employed. Only curve e has been shown corresponding to the combination of length reduction and nonlinearity.

The development of a linear response theory.

One of the most important questions concerns the linearity of tire response to road irregularities. A linear behavior would simplify the analytical treatment considerably. The tire has a finite contact length and consequently is subjected to a large number of inputs at the same time. The contact length varies with obstacle height, and negative reaction forces cannot be transmitted so that partial loss of contact can occur. In spite of these difficulties, which do not benefit linearity, Lippmann and his associates [16, 17] have experimentally shown that an almost linear relationship exists between tire force variation and obstacle height. Tests have been carried out with constant axle height and for the elementary step shape obstacle. Even the measured force variation of a tire traversing a series of composite cleats (combinations of blocks with rectangular cross sections and extending over the full tread width) could reasonably well be derived by linear combinations of the response to a unit step in elevation of the road surface. A more refined combination of these responses, where a distinction has been drawn between positive and negative steps, gave very good correspondence to the measured total force variation. The applicability of this more refined method is limited since linearity has been lost; for mathematical details we refer to the original papers [16, 17]. The linear mathematical representation of the tire force response to road irregularities, based on the principle of superposition enunciated in the forementioned papers, will be discussed hereafter. It has been stated that the assumption of linearity leads to sufficient accuracy in most practical cases.

In figure 7.4.8 the positive directions are given for road coordinates (\bar{x}_c , \bar{z}_c), wheel axle position or distance traveled ($s = \bar{x}$), and reaction forces (normal load $-F_z$ and drag force $-F_x$). Figure 7.4.9 shows the force responses to positive and negative unit steps in road elevation. The curves correspond in character to data given in [17]. Note that the curves differ slightly for positive and negative steps. The average of the absolute changes in force may be taken as the characteristic response to a unit (upward) step. This function has been designated as $\psi_x(\xi)$ for

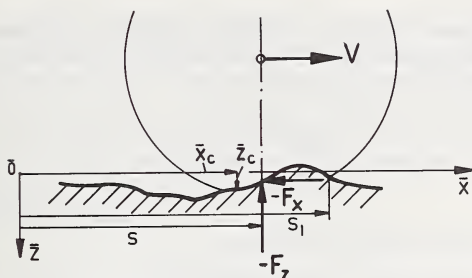


FIGURE 7.4.8. Positive directions of coordinates and forces.

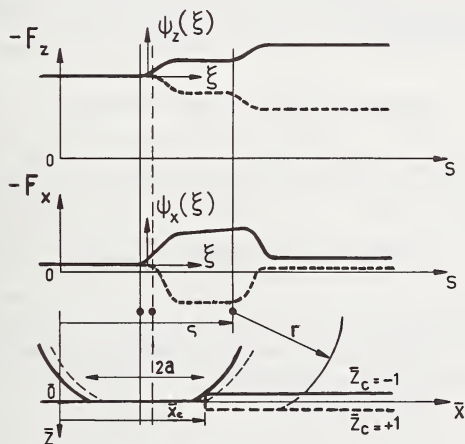


FIGURE 7.4.9. Experimental force response to positive and negative steps in road elevation.

the longitudinal force response and as $\psi_z(\xi)$ for the vertical force response. The newly introduced coordinate ξ denotes the distance traveled by the wheel axle from the instant of first contact with the step irregularity.

We now decompose the road contour, $\bar{z}_c(\bar{x}_c)$, into an infinite series of small positive and negative steps and use the principle of superposition in order to obtain the total response. Expressed in the form of the superposition integral of Duhamel, we obtain for the variation of the tire forces as a function of the distance traveled by the foremost contact point $s_1 = s + a$ with a denoting the assumedly constant half contact length:

$$F_{x,z}(s_1) = F_{x,z_0} + \int_a^{s_1} \frac{d\bar{z}_c(\bar{x}_c)}{d\bar{x}_c} \psi_{x,z}(s_1 - \bar{x}_c) d\bar{x}_c \quad (7.4.15)$$

At the starting position ($s_1 = a$) the forces have the value F_{x,z_0} . This general integral approach of expressing the response may be written in

the form of the more widely applicable frequency response of tire forces to road irregularities. Following Lippmann's analysis we first rewrite the above equation. With the conditions

$$\bar{z}_c = 0 \text{ for } \bar{x}_c < a$$

$$\psi_{x,z} = 0 \text{ for } \bar{x}_c > s_1$$

this equation may be written as follows

$$F_{x,z}(s_1) = F_{x,z0} + \int_{-\infty}^{\infty} \frac{d\bar{z}_c(\bar{x}_c)}{d\bar{x}_c} \psi_{x,z}(s_1 - \bar{x}_c) d\bar{x}_c. \quad (7.4.16)$$

The contour of the road may be expressed as a Fourier integral over the spatial frequency ω_s :

$$\bar{z}_c(\bar{x}_c) = \frac{1}{2\pi} \int_{-\infty}^{\infty} D(\omega_s) e^{i\omega_s \bar{x}_c} d\omega_s. \quad (7.4.17)$$

The Fourier transform becomes now with the above version of the Fourier integral:

$$D(\omega_s) = \int_{-\infty}^{\infty} \bar{z}_c(\bar{x}_c) e^{-i\omega_s \bar{x}_c} d\bar{x}_c. \quad (7.4.18)$$

The quantity $D(\omega_s)d\omega_s/2\pi$ is the contribution of those harmonic components of the road contour whose spatial frequencies are included in the interval between ω_s and $\omega_s + d\omega_s$.

Differentiation of (7.4.17) yields

$$\frac{d\bar{z}_c(\bar{x}_c)}{d\bar{x}_c} = \frac{1}{2\pi} \int_{-\infty}^{\infty} i\omega_s D(\omega_s) e^{i\omega_s \bar{x}_c} d\omega_s. \quad (7.4.19)$$

Substitution of this expression into (7.4.16) yields with $\xi = s_1 - \bar{x}_c$:

$$F_{x,z}(s_1) - F_{x,z0} = \frac{1}{2\pi} \int_{-\infty}^{\infty} i\omega_s D(\omega_s) e^{i\omega_s s_1} \left[\int_{-\infty}^{\infty} e^{-i\omega_s \xi} \psi_{x,z}(\xi) d\xi \right] d\omega_s. \quad (7.4.20)$$

The quantity in brackets is the Fourier transform of $\psi_{x,z}(\xi)$ describing the spectral content of the tire force response to a unit step variation of the road level. This function is designated as $C_{x,z}(\omega_s)$. Hence eq. (7.4.20) becomes:

$$F'_{x,z}(s_1) - F_{x,z0} = \frac{1}{2\pi} \int_{-\infty}^{\infty} i\omega_s D(\omega_s) C_{x,z}(\omega_s) e^{i\omega_s s_1} d\omega_s. \quad (7.4.21)$$

Instead of measuring the response to a step, it may be more practical to take a bump of short duration as the input. Such a bump may consist

of an upward step followed after a delay by a downward step of equal height. The cross section of the unit bump has an area equal to unity and a length tending to zero. The response to such a function simply equals the distance derivative of $\psi_{x,z}(\xi)$. The Fourier transform of the response to a unit bump represents the frequency response function of the tire force to road irregularities. This function, designated as $H_{x,z}(\omega_s)$, consequently equals $i\omega_s C_{x,z}(\omega_s)$.

We finally obtain for (7.4.21):

$$F_{x,z}(s_1) - F_{x,z0} = \frac{1}{2\pi} \int_{-\infty}^{\infty} D(\omega_s) H_{x,z}(\omega_s) e^{i\omega_s s_1} d\omega_s. \quad (7.4.22)$$

In practice $H_{x,z}(\omega_s)$ may be obtained by taking the Fourier transform of the response to a bump which is short with respect to the shortest wavelength of interest and dividing the result by the area of the bump cross section.

Lippmann and Nanny [17] conducted a harmonic analysis of the response of vertical and longitudinal forces to a cleat by feeding the recorded signals into a tuneable resonator (tire 8.15-15 two-ply, $p_i=2$ atm., deflection 2.54 cm.; cleat 1.27 cm. long, 0.63 cm. high; speed ≈ 1 m/sec.). The amplitude spectra exhibit two broad maxima. For the vertical force response their maxima occur at the 2.4th and 14th order of the tire revolution, and for the longitudinal response at the 8th and 21st order. These figures correspond for the tire under consideration to the following frequencies per unit of speed, reciprocal value of wavelength expressed as (cycles/sec/meters/sec.): vertical 1.1 and 6.3 c/m., longitudinal 3.6 and 9.4 c/m. At shorter wavelengths (higher frequencies) the amplitude decays to low values.

In the theories and experiments mentioned above the motions are assumed to develop slowly so that inertia forces can be neglected. The traversing of obstacles at higher velocities involves high frequency vibrations and dynamic forces in the tire tread band, the nature of which will be dealt with in section 7.4.2.

In the literature, tests are described which have been carried out at higher speeds. In these tests the wheel axle has been free to move in its suspension. Care must be taken in the interpretation of the results as they do not solely refer to the response of the tire. We may mention here the work of Barson [18] and Guslitzer [19] who measured the motion of vehicle components when passing over an obstacle. In the latter reference attention has also been given to failure of tires due to obstacles. The forces acting from the tire to the ground when rolling over an obstacle have been measured by Hey [20] for a relatively long single sinusoidal obstacle and by Senger [9] for a relatively short semicylindrical obstacle. The velocities in these latter two tests did not exceed 50 km/hr.

Longitudinal Slip

A tire which rolls freely at constant speed of travel, i.e., not subjected to driving or braking torques, requires a thrust in the longitudinal direction acting on the wheel axle in order to overcome the rolling resistance.

As has been shown in figure 7.2.56 the rolling resistance depends on the normal load. For steady state motion the thrust P is in equilibrium with the drag force F_r and the rolling resistance moment $M_r = r_l F_r$, where r_l denotes the axle height above the road surface. At constant speed we may employ the linear relationship

$$M_r (= r_l F_r) = D_r W = C_r \delta \quad (7.4.23)$$

with $W (= -F_z)$ denoting the normal load and δ the normal tire deflection. The coefficients of rolling resistance D_r and C_r are, at least in the low speed range, not influenced much by the speed V (cf. figs. 7.2.57, 7.2.60).

At free rolling the angular velocity Ω and the speed V are related through the effective radius of rolling r_e

$$V = \Omega r_e \quad (7.4.24)$$

It has been found experimentally that

$$r_l < r_e < r \quad (7.4.25)$$

According to Whitbread (cf. [1, 13 or 21]) the following approximate relation exists

$$r_e = r - \frac{1}{3} \delta \quad (7.4.26)$$

This expression has been found by considering the compression of the tread band in the contact area due to the normal deflection of the tire. Tests with aircraft tires roughly confirm this formula [13]. For a tire with an inextensible thin tread band and a worn-off tread pattern, so that creep of the tread band with respect to the road does not take place, the effective radius tends to the free radius r . Figure 7.2.48 provides more information about the variation of rolling radius with speed for different tire constructions.

We define now the longitudinal or tangential creep or slip velocity V_{cx} as the tangential speed of a point C' fixed to the wheel rim and situated at road level (fig. 7.4.10). At the instant considered point C' coincides with the contact center C , which, according to its definition, is located on a line normal to the road surface and passing through the wheel axle. Consequently, for a horizontal road surface, C' lies directly below the wheel axle.

The longitudinal slip value relates the slip velocity to the speed of travel.

$$\kappa = -V_{cx}/V = -\frac{V - r_l \Omega}{V}. \quad (7.4.27)$$

In section 7.5.1 a slightly different definition for the longitudinal slip value has been adopted, viz $\kappa = -V_{cx}/r_l \Omega$. Their values are nearly the same at moderate longitudinal slip.

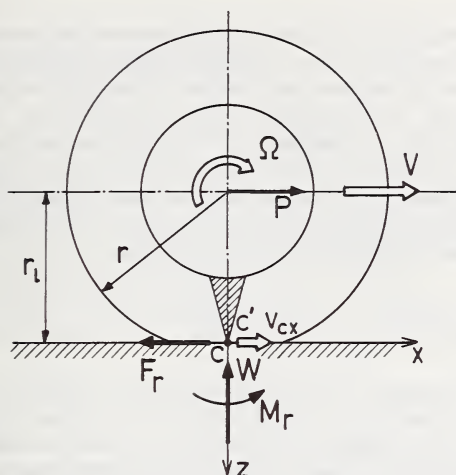


FIGURE 7.4.10. Rolling resistance and longitudinal slip.

Assuming that relation (7.4.26) exists, the longitudinal slip speed becomes at free rolling

$$V_{cx} = \frac{2}{3} \delta \Omega \quad (7.4.28)$$

or, expressed in more general terms,

$$V_{cx} = \eta \delta \Omega \quad (7.4.29)$$

from which we obtain the longitudinal slip value at free rolling:

$$\kappa = -\eta \frac{\delta}{r_e} \approx -\eta \frac{\delta}{r} \quad (7.4.30)$$

The value of η is approximately $\frac{2}{3}$ for bias ply tires and tends to unity in case of an inextensible tread band with little tread rubber.

When applying additional driving or braking torques the slip value changes in a manner analogous to that of the tire cornering characteristic relating lateral force to slip angle. Figure 7.4.11 gives an example of measured longitudinal slip characteristics, taken from Hörz [22].

Longitudinal slip is based on the following mechanisms. The first stems from the inextensible band theory, which states that since the same quantity of material passes at the top and at the bottom of the tire per unit time, longitudinal slip must occur at the road level. Secondly, we have the influence of compressibility or extensibility of the tread band. Compression in the contact area due to vertical deflection of the tire diminishes the slip due to the first mechanism. Also under the action of tangential force, the density in the neighborhood of the contact area

may change. As a result of this, the tangential velocity at the top and the bottom do not necessarily have to be the same. Third, one may include the influence of tread rubber longitudinal elasticity, which enables the tread band to move with respect to the road without sliding. Finally, we have the possibility of partial or total sliding in the contact area.

The first effect merely depends on geometry and does not involve resultant longitudinal forces. The second and third effects give rise to pure deformation slip characterized by the longitudinal or tangential creep, or slip stiffness C_κ defined by the relation

$$C_\kappa = \frac{\partial F_x}{\partial \kappa} \quad (7.4.31)$$

Since the tensile rigidity of the tread band is relatively large, the deformation slip is expected to be mainly due to tread rubber elasticity. The longitudinal slip stiffness C_κ can then be expressed in terms of longitudinal tread profile rubber stiffness per unit area c_{px} , half contact length a and half contact width b of the assumed rectangular contact area:

$$C_\kappa = 4a^2bc_{px} \quad (7.4.32)$$

This expression suggests that C_κ varies approximately as the square of the contact length. With the assumption that the contact length varies

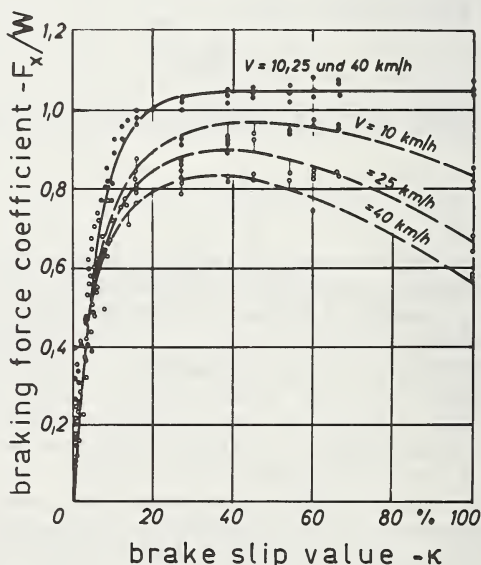


FIGURE 7.4.11. Example of measured longitudinal slip characteristics [22].

quadratically with the normal deflection δ , we obtain for a linear tire load-deflection characteristic $W = C_z \delta$:

$$C_\kappa = \frac{\delta}{\delta_o} C_{\kappa o} = \frac{W}{W_o} C_{\kappa o} \quad (7.4.33)$$

with index o denoting the original situation. From test data [13, 21, 22, 23] it can be deduced that the value of C_κ ranges from 5 to 15 times the vertical load W . This indicates that C_κ is of the same order of magnitude as the cornering force stiffness $C_{F\alpha}$ (sec. 7.5.1).

For small deviations from the steady state conditions the longitudinal force-slip characteristic may be linearized and written in the form

$$F_x = F_{xo} + \bar{F}_x \quad (7.4.34)$$

where the index o indicates the original situation and the upper bar indicates the deviation from this situation. The variable part \bar{F}_x is a linear function of the variation of vertical deflection δ and of longitudinal slip value $\bar{\kappa}$. With $-F_{xo} = F_{ro}$ denoting the original rolling resistance force we obtain in general:

$$F_x = -F_{ro} + \frac{\partial F_x}{\partial \delta} \bar{\delta} + \frac{\partial F_x}{\partial \kappa} \bar{\kappa}. \quad (7.4.35)$$

The values of the partial derivatives should be determined experimentally. From eq (7.4.31) the value of $\partial F_x / \partial \kappa$ obviously equals $C_{\kappa o}$. With our knowledge of effective radii at free rolling we may derive $\partial F_x / \partial \delta$ theoretically. From figure 7.4.12 we deduce for the longitudinal force at

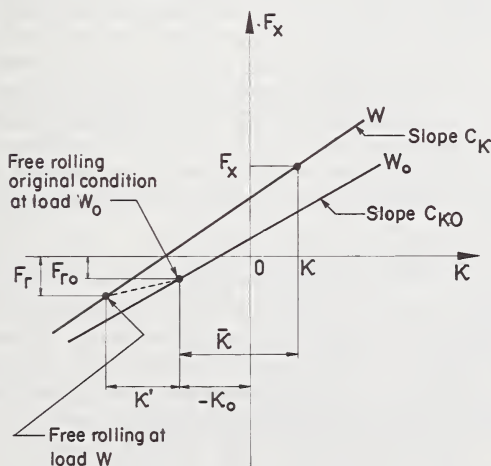


FIGURE 7.4.12. Longitudinal slip characteristics near the steady state conditions (subscript o).

$W = W_o + \bar{W}$ (or $\delta = \delta_o + \bar{\delta}$) and $\kappa = \kappa_o + \bar{\kappa}$:

$$F_x = -F_r + C_\kappa(\bar{\kappa} + \kappa') \quad (7.4.36)$$

The quantity κ' denotes the variation in longitudinal slip value of a freely rolling tire due to a variation in normal deflection $\bar{\delta}$. According to eq (7.4.30) the value of κ' reads:

$$\kappa' = \eta \frac{\bar{\delta}}{r_e} \quad (7.4.37)$$

The rolling resistance force F_r becomes according to eq (7.4.23):

$$F_r = \frac{1}{r_l} C_r \delta \quad (7.4.38)$$

We finally obtain for eq (7.4.36), linear in the variations $\bar{\kappa}$ and $\bar{\delta}$, and with δ neglected with respect to r :

$$F_x = -F_{ro} + C_{\kappa o} \bar{\kappa} + \frac{1}{r_o} (\eta C_{\kappa o} - C_r) \bar{\delta}. \quad (7.4.39)$$

Herewith, the coefficients of eq (7.4.35) have been determined. The equation above is of great value for the theoretical assessment of the longitudinal force response to road irregularities and tire nonuniformity. The next section is devoted to this problem.

At relatively large values of longitudinal slip linearity is lost. For the theoretical treatment of the behavior in the nonlinear range it is more straight forward to use the alternative definition of longitudinal slip value $\kappa = -V_{cx}/\Omega r_l$ which results in a complete analogy with the side slip phenomenon. For more information we refer to side slip theories enunciated in section 7.5.1. The latter part of this section treats the problem of the interaction of longitudinal and lateral slip. We furthermore refer to the early theories of Reynolds [24], Fromm [25], and Julien [26]. Experimental data are available in the publications of Yu Chen [21], Hörz [22], and a very extensive investigation of the behavior on wet roads by Holmes and Stone [23]. For aircraft tires we refer to Smiley and Horne [13].

Theory of the Longitudinal Force Response to Road Wavyness, Tire Nonuniformity and Vertical and Longitudinal Axle Motions

For the development of a theory of the longitudinal force response to in-plane variations of wheel axle position, road contour, tire radius and tire radial stiffness, a theoretical tire model is proposed, shown in figure 7.4.13, in which the following properties are represented:

1. radial tire elasticity with stiffness normal to road C_z ,
2. tangential carcass elasticity with stiffness tangential to the road C_{cx} ,
3. tangential slip of carcass with respect to the road with slip stiffness C_κ .

One effect of nonuniformity in mass distribution may be the variation in effective normal stiffness with speed of travel. By measuring the periodic tire radial stiffness variations as a function of rotational speed this effect will be included automatically. Also, the contribution of the mass nonuniformity to the change of radial runout with rotational speed should be recognized.

The mass of the lower portion of the tire is subjected to the action of tangential Coriolis forces which arise when the lower tread-band portion moves in a radial direction with respect to the wheel axle. Similarly, a variation in tread-band mass causes a resultant tangential Coriolis force even in the case of fixed axle height. In both cases the variation in angular momentum of the tire-wheel combination about the wheel axle gives rise to the fore and aft force variations.

The influence of these effects deserves closer investigation. It may be noted, however, that the whole phenomenon is restricted to a portion of the tire near the contact area. The tangential forces are in equilibrium with the inertial forces acting on the particles present in this portion. Therefore, the net force to be measured at the wheel axle is expected to be very small, if present at all.

A rough calculation may provide some quantitative insight. Consider a tire with radius $r = 0.3$ m., contact length $2a = 0.15$ m. and tread-band mass per unit length 1.5 kg/m. The mass which moves when deflecting the tire becomes approximately 0.25 kg. When the tire rolls over a flat surface at a constant speed $V = 30$ m/sec. and a constant angular speed $\Omega = 100$ rad/sec., and moves vertically with a frequency of 10 Hz and an amplitude of 0.005 m., the lower tread band portion will be subjected to a Coriolis force which has an amplitude equal to

$$2 \times 0.25 \times 2\pi \times 10 \times 0.005 \times 100 \approx 16 \text{ Newtons} = 3.57 \text{ lbs.}$$

The problem of the influence of a gradient in mass distribution may be illustrated with the following example. Consider the same tire in steady state motion but possessing a heavy spot of 0.05 kg. This tire element will be subjected to a Coriolis acceleration at the entrance of the contact area equal to $2a(V/r)^2$. The Coriolis force consequently becomes $0.15 \times 100^2 \times 0.05 = 75$ Newtons $= 16.8$ lbs. Theoretically, these forces are measurable at the contact surface and not at the wheel axle.

We shall now turn to the restricted problem where inertia effects in the lower region of the tire are not considered. For the tire model of figure 7.4.13 the equations of motion will be presented. Again, the symbols provided with index o denote the stationary or average value and the upper bar indicates the variable part. We restrict ourselves to small deviations from the rectilinear stationary motion, and can therefore linearize the mathematical representation.

The vehicle has a constant speed of travel V . The distance traveled becomes

$$s = Vt. \quad (7.4.40)$$

The contact center has a coordinate in \bar{x} -direction somewhat deviating from s .

We write

$$\bar{x}_c = s + \Delta x \quad (7.4.41)$$

where

$$\Delta x = x_a - r_l \frac{d\bar{z}_c}{d\bar{x}_c} \quad (7.4.42)$$

Taylor's formula yields for the slope at \bar{x}_c

$$\frac{d\bar{z}_c}{d\bar{x}_c} = \frac{d\bar{z}_c}{ds} + \frac{d^2\bar{z}_c}{ds^2} \Delta x + \dots \quad (7.4.43)$$

In the linear representation we may omit the terms with Δx . For the longitudinal force acting in the contact center we obtain

$$X_o = -F_{ro}, \quad (7.4.44)$$

$$\bar{X} = \bar{F}_x + W_o \frac{d\bar{z}_c}{ds}. \quad (7.4.45)$$

According to eq (7.4.39) the tangential force variation equals

$$\bar{F}_x = C_{\kappa o} \bar{\kappa} + \frac{1}{r_o} (\eta C_{\kappa o} - C_r) \bar{\delta}. \quad (7.4.46)$$

This equation, valid for steady state longitudinal slip, can be used with good approximation for nonstationary motions with wavelengths which are long relative to the contact length. The problem is analogous to that of the shimmy phenomenon treated in section 7.5.2.

The tangential slip value defined by eq (7.4.27) becomes

$$\kappa = \frac{-V_{cx}}{V + \dot{x}_a} \quad (7.4.47)$$

with the steady state value

$$\kappa_o = -\frac{V_{cxo}}{V} \approx -\eta \frac{\delta_o}{r} \quad (7.4.48)$$

and variable part

$$\bar{\kappa} = -\frac{\bar{V}_{cx}}{V} - \kappa_o \frac{\dot{x}_a}{V}. \quad (7.4.49)$$

The tangential slip speed reads

$$V_{cx} = V + \dot{x}_a - (\Omega + \dot{\chi} + \dot{\psi})r_l. \quad (7.4.50)$$

with

$$r_l = r - \delta = r_{l0} + \bar{r} - \bar{\delta}$$

we obtain for the variation of V_{cx}

$$\bar{V}_{cx} = \dot{x}_a - \Omega(\bar{r} - \bar{\delta}) - r_{l0}(\dot{\chi} + \dot{\psi}). \quad (7.4.51)$$

When neglecting δ with respect to r we obtain for eq (7.4.49)

$$\bar{\kappa} = -\frac{1}{V} \{ \dot{x}_a - \Omega(\bar{r} - \bar{\delta}) - r_o(\dot{\chi} + \dot{\psi}) \}. \quad (7.4.52)$$

The equation of constraint for $\bar{\delta}$ reads:

$$\bar{\delta} = -\bar{z}_c + z_a + \bar{r}. \quad (7.4.53)$$

For the variation of the tangential force we have the additional relation

$$\bar{F}_x = -C_{cx}r_o\psi. \quad (7.4.54)$$

The normal load

$$W = C_z\delta = (C_{z0} + \bar{C}_z)(\delta_o + \bar{\delta}). \quad (7.4.55)$$

Instead of using the variable stiffness \bar{C}_z we prefer to introduce the variable static deflection $\bar{\delta}_o$. This quantity can, in principle, be determined by measuring the variation of the axle height of a perfectly round tire which rolls under constant vertical load \bar{W}_o over a smooth flat surface. The following relation applies

$$\bar{\delta}_o = -\delta_o\bar{C}_z/C_{z0}. \quad (7.4.56)$$

Hence, the following relation holds for the variation in normal load

$$\bar{W} = C_{z0}(\bar{\delta} - \bar{\delta}_o). \quad (7.4.57)$$

According to relation (7.4.23) the variation in rolling resistance moment becomes

$$\bar{M}_r = D_r\bar{W} = C_r(\bar{\delta} - \bar{\delta}_o) \quad (7.4.58)$$

with C_r approximately given by

$$C_r = \frac{F_{ro}r_o}{\delta_o}. \quad (7.4.59)$$

The dynamic equilibrium about the wheel axle is governed by the differential equation

$$I_x \ddot{\chi} = -F_x r_l - M_r = F_{r0}(\bar{r} - \bar{\delta}) - r_o \bar{F}_x - \bar{M}_r. \quad (7.4.60)$$

For the eight unknown quantities \bar{X} , \bar{F}_x , \bar{M}_r , χ , ψ , $\bar{\delta}$, $\bar{\kappa}$ and s we have to our disposal the eight equations (7.4.40, 45, 46, 52, 53, 54, 58, 60). For the unknowns \bar{X} , χ and ψ we obtain by elimination of the remaining unknown quantities the following set of equations

$$\bar{X} = -C_{cx} r_o \psi + W_o \frac{1}{V} \dot{z}_c, \quad (7.4.61)$$

$$I_x \ddot{\chi} - C_{cx} r_o^2 \psi = (F_{r0} + C_r)(\bar{z}_c - z_a) - C_r(\bar{r} - \bar{\delta}_o), \quad (7.4.62)$$

$$r_o(\dot{\chi} + \dot{\psi}) + \frac{C_{cx}}{C_{\kappa o}} V r_o \psi = \left(1 - \eta + \frac{C_r}{C_{\kappa o}}\right) \frac{V}{r_o} (z_a - \bar{z}_c) - \left(\eta - \frac{C_r}{C_{\kappa o}}\right) \frac{V}{r_o} \bar{r} + \dot{x}_a. \quad (7.4.63)$$

These equations of motion can be used in the analysis of wheel suspension vibrations. We shall concern ourselves here with the derivation of the response functions of the longitudinal force to each of the input quantities. It should be recognized that some of these input quantities depend upon each other in a way which is a function of the suspension properties.

A final elimination of the variables χ and ψ and the introduction of the operator $p = d/dt$ yields the following expression for the response of the longitudinal force variations \bar{X} to the road irregularities \bar{z}_c , the radial runout \bar{r} , the variation in static deflection $\bar{\delta}_o$ and furthermore to the longitudinal and vertical axle motions x_a and z_a :

$$\begin{aligned} \bar{X} = & - \left[\left\{ I_x \left(1 - \eta + \frac{C_r}{C_{\kappa o}} \right) \frac{V}{r_o} p + r_o (F_{r0} + C_r) \right\} (z_a - \bar{z}_c) \right. \\ & + \left\{ I_x \left(\frac{C_r}{C_{\kappa o}} - \eta \right) \frac{V}{r_o} p + C_r r_o \right\} \bar{r} \\ & \left. - C_r r_o \bar{\delta}_o + I_x p^2 x_a \right] A^{-1} + \frac{W_o}{V} p \bar{z}_c \end{aligned} \quad (7.4.64)$$

in which

$$A = \frac{I_x}{C_{cx}} p^2 + \frac{I_x}{C_{\kappa o}} V p + r_o^2.$$

From this expression of combined responses the single absolute frequency response functions can be derived.

Frequency response to vertical axle motions.

After replacement of p by $i\omega$, with ω denoting the frequency of the motion, we find for the response to vertical axle motions the following amplitude ratio,

$$\left| \frac{\bar{X}}{z_a} \right| = \frac{F_{r0} + C_r}{r_o} \sqrt{\frac{1 + 4f_2^2 v^2}{(1 - v^2)^2 + 4f_1^2 v^2}}, \quad (7.4.65)$$

where have been introduced the nondimensional quantities

$$2f_1 = V \frac{\sqrt{C_{cx} I_X}}{r_o C_{\kappa 0}}, \quad (7.4.66)$$

$$2f_2 = 2f_1 \frac{(1 - \eta) C_{\kappa 0} + C_r}{F_{r0} + C_r}, \quad (7.4.67)$$

$$v^2 = \frac{\omega^2}{\omega_{\chi 0}^2} \quad (7.4.68)$$

with $\omega_{\chi 0}$ denoting the rotational natural frequency of the standing tire about the wheel axle

$$\omega_{\chi 0} = \sqrt{\frac{C_{cx} r_o^2}{I_X}}. \quad (7.4.69)$$

For illustration, some aspects of the response will be discussed for a tire-wheel combination with parameter values:

$$I_X = 0.6 \text{ kgm.}^2, \quad C_{cx} = 5 \times 10^5 \text{ N*/m.}, \quad r_o = 0.3 \text{ m.},$$

$$n_{\chi 0} = \omega_{\chi 0} / 2\pi = 43 \text{ Hz}, \quad \eta = 2/3, \quad C_{\kappa 0} = 40000 \text{ N}, \quad (7.4.70)$$

$$F_{r0} = 60 \text{ N}, \quad d_o = 0.02 \text{ m.}, \quad W_o = 4000 \text{ N}, \quad C_r = 900 \text{ N}.$$

The dimensionless parameters become, for this configuration,

$$f_1 = 0.023 \text{ } V \text{ and } f_2 = 0.342 \text{ } V.$$

For $\omega = 0$ we find

$$\left| \frac{\bar{X}}{z_a} \right|_{\omega=0} = \frac{F_{r0} + C_r}{r_o} = 3200 \text{ N/m.} \quad (7.4.71)$$

* N = Newton = .223 lbs. force.

For small $\omega (\ll \omega_{\chi_0})$ we may simplify to

$$\begin{aligned} \left| \frac{\bar{X}}{z_a} \right|_{\omega \rightarrow 0} &= \frac{F_{r_0} + C_r}{r_0} \{1 + (1 + 2f_2^2 - 2f_1^2)v^2\} \\ &= \frac{F_{r_0} + C_r}{r_0} \left[1 + \left(\frac{I_\chi}{C_{cx}r_0^2} + \frac{1}{2} \frac{V^2 I_\chi^2}{r_0^4 C_{\kappa_0}^2} \left\{ \left(\frac{(1-\eta)C_{\kappa_0} + C_r}{F_{r_0} + C_r} \right)^2 - 1 \right\} \right) \omega^2 \right] \\ &= 3200 \left\{ 1 + (1 + 0.233V^2) \frac{n^2}{1900} \right\}, \quad (7.4.72) \end{aligned}$$

where V denotes the speed of travel expressed in m/sec. and n denotes the frequency of the axle motion in Hz. It may be observed that the magnification of the zero frequency response (7.4.71) is in particular due to the large tangential slip stiffness C_{κ_0} and the moment of inertia I_χ . The effect of changing C_{cx} is noticeable only at very small values of speed V . The factor η defined by eq (7.4.29) can exert considerable influence. A value of η close to one is favorable, which can be explained by the fact that if $\eta = 1$ the variation of the effective radius at free rolling with deflection becomes very low and is in that case only due to the change in rolling resistance.

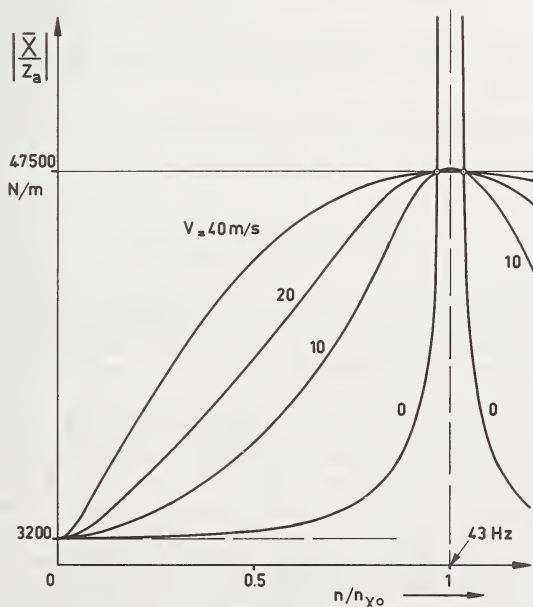


FIGURE 7.4.14. Frequency response curves for longitudinal force X with respect to vertical axle motions z_a , calculated for the tire-wheel parameter values (7.4.70).

At higher frequencies the amplitude ratio deviates from the approximation (7.4.72). In figure 7.4.14 response curves are drawn for several speeds of travel. Besides the point at zero frequency where the curves come together, two more invariant points appear to exist where the response is independent of V . Since these points show the same amplitude ratio and are located near the natural frequency n_{κ_0} , their height gives a good indication of the maximum amplitude ratio, which occurs near the natural frequency and is virtually independent of V . The curves show furthermore that for the higher range of speeds this maximum becomes very broad, which means that high amplitude ratios can be attained at relatively low frequencies.

From eq (7.4.65) we obtain for the amplitude ratio in the invariant points

$$\left| \frac{\bar{X}}{z_a} \right|_{\text{inv}} = \frac{F_{r_0} + C_r}{r_0} \frac{f_2^2}{f_1} = \frac{(1 - \eta)C_{\kappa_0} + C_r}{r_0} = 47500 \text{ N/m.} \quad (7.4.73)$$

or a magnification of about 15 times the zero frequency response. From the expression above it follows again that large C_{κ_0} and low η are unfavorable. The speed V and the parameters I_χ and C_{cx} do not influence the response in the higher frequency range, near the frequencies of the invariant points, given by

$$\omega_{\text{inv } 1,2}^2 = \omega_{\kappa_0}^2 \left(1 \pm \frac{f_1}{f_2} \right). \quad (7.4.74)$$

Obviously, the invariant points lie close to and on either side of the natural frequency.

Frequency response to longitudinal axle motions.

From eq (7.4.64) we find for the response to x_a :

$$\left| \frac{\bar{X}}{x_a} \right| = \frac{C_{cx}v^2}{\sqrt{(1-v^2)^2 + 4f_1^2v^2}}. \quad (7.4.75)$$

This is the well-known form for the acceleration response of a single mass-spring system excited by a force. The dimensionless coefficient of damping become for our system:

$$2f_1 = V \frac{\sqrt{C_{cx}I_\chi}}{r_0C_{\kappa_0}}. \quad (7.4.76)$$

Damping obviously increases with increasing speed V and decreases with increasing slip stiffness C_{κ_0} . Compared with the response to z_a , the speed V has an opposite effect whereas a variation of C_{κ_0} changes the response in the same direction. The effects of C_{cx} and I_χ are more difficult to evaluate since they influence the response also in other respects. At relatively low frequencies I_χ is the most important parameter. For the parameter values of (7.4.70) we find a dimensionless damping

coefficient $f_1 = 0.023 V$. Consequently, the damping becomes critical at a speed approximately equal to $V = 40$ m/sec.

Frequency response to variations in static deflection.

From the expression for the combined response (7.4.64) we obtain

$$\left| \frac{\bar{X}}{\delta_0} \right| = \frac{C_r/r_0}{\sqrt{(1-v^2)^2 + 4f_1^2 v^2}} \quad (7.4.77)$$

which corresponds to the displacement response of a single mass-spring system excited by a force. The response to variations in radial stiffness or static deflection as formulated above is very small. However, the indirect response with axle free to move vertically will be appreciable. The variations in radial stiffness induce vertical axle motions which involve a response of the longitudinal forces just discussed.

Frequency response to radial runout.

The absolute frequency response function to radial runout \bar{r} reads:

$$\left| \frac{\bar{X}}{\bar{r}} \right| = \frac{C_r}{r_0} \sqrt{\frac{1 + 4f_3^2 v^2}{(1-v^2)^2 + 4f_1^2 v^2}} \quad (7.4.78)$$

with the dimensionless parameters

$$2f_1 = V \frac{\sqrt{C_{cx} I_x}}{r_0 C_{\kappa 0}}, \quad (7.4.79)$$

$$2f_3 = 2f_1 \frac{-\eta C_{\kappa 0} + C_r}{F_{r0} + C_r}. \quad (7.4.80)$$

It may be noted that great similarity exists with the response to vertical axle motions (7.4.65). The characteristics are similar to those shown in figure 7.4.14. The level of the response, however, can become considerably higher in the higher speed range. This is due to the fact that in the dimensionless parameter f_3 the factor $1 - \eta$ has been replaced by $-\eta$. For tires with η tending to one (inextensible tread band and little tread rubber) which was favorable for the response to vertical axle motions, it turns out that their response to radial runout becomes worse. For the values used in (7.4.70) we obtain for the amplitude ratio at the invariant points

$$\left| \frac{\bar{X}}{\bar{r}} \right|_{\text{inv}} = \frac{C_r}{r_0} \frac{|f_3|}{f_1} = \frac{C_r}{r_0} \frac{|-\eta C_{\kappa 0} + C_r|}{F_{r0} + C_r} = 80500 \text{ N/m}. \quad (7.4.81)$$

or about 8 kgf. per mm. radial runout. The magnification with respect to the zero frequency response amounts approximately 27 times.

Frequency response to road irregularities.

According to eq (7.4.64) the response to road irregularities can be formed by adding an extra term to the negative of the response to vertical axle motions

$$\frac{\partial \bar{X}}{\partial \bar{z}_c} = -\frac{\partial \bar{X}}{\partial z_a} + W_o \frac{1}{V} p. \quad (7.4.82)$$

The solution for this combination of responses to variations in \bar{r}_l and in slope $d\bar{z}_c/ds$ is difficult, and is in fact impractical since no useful information can be obtained other than that which can be drawn immediately from (7.4.82). One might as well consider the slope $d\bar{z}_c/ds$ as an isolated input, the response to which must be regarded in combination with the response to axle height to roadway variations. The response to slope variations at constant axle distance from the road surface simply equals the average normal load W_o .

7.4.2. High Frequency Properties

In the high frequency range, well above 30 Hz, tires exhibit a number of natural frequencies in vertical (radial), longitudinal (tangential) and lateral direction and will consequently show continuously distributed vibrations of side walls and tread band.

Although the intensities of the high frequency vibrations of the unsprung masses are lower than those of the lower frequency resonances, research on this class of high frequency vibrations is valuable since they are lightly damped and in some cases are even amplified because of local resonances occurring in the vehicle. They also play a fundamental role in acoustical effects.

The high frequency vibration behavior of rolling tires is a very complicated matter and has been dealt with only briefly in the literature. In the following, important experimental and theoretical investigations on high frequency tire properties will be discussed.

Vertical and Longitudinal Vibration Transmission

In recent years the transmission of high frequency vibrations from contact patch to wheel hub has been experimentally investigated by Chiesa, Oberto and Tamburini [27, 28] and by the team of Gough and Barson [18, 29].

Chiesa and his group mainly reported on investigations with the nonrolling tire excited by a vertically vibrating platform on which the tire stands. Barson and Gough, in addition, executed experiments with tires which roll over a drum to which can be attached a great variety of artificial road irregularities, ranging from sinusoidal shapes to random surfaces. In the case of a sinusoidal profile a wide frequency range can be investigated by varying the drum speed. In their extensive investigation the longitudinal aspect of vibration transmission has been included.

Figures 7.4.15a, b (from [18]) respectively show the vertical transmission ratio (amplitude ratio) of hub relative to platform for the non-rolling tire and the r.m.s. value of the vertical hub acceleration for the tire rolling over a sinusoidal drum surface with wavelength 0.133 m. and

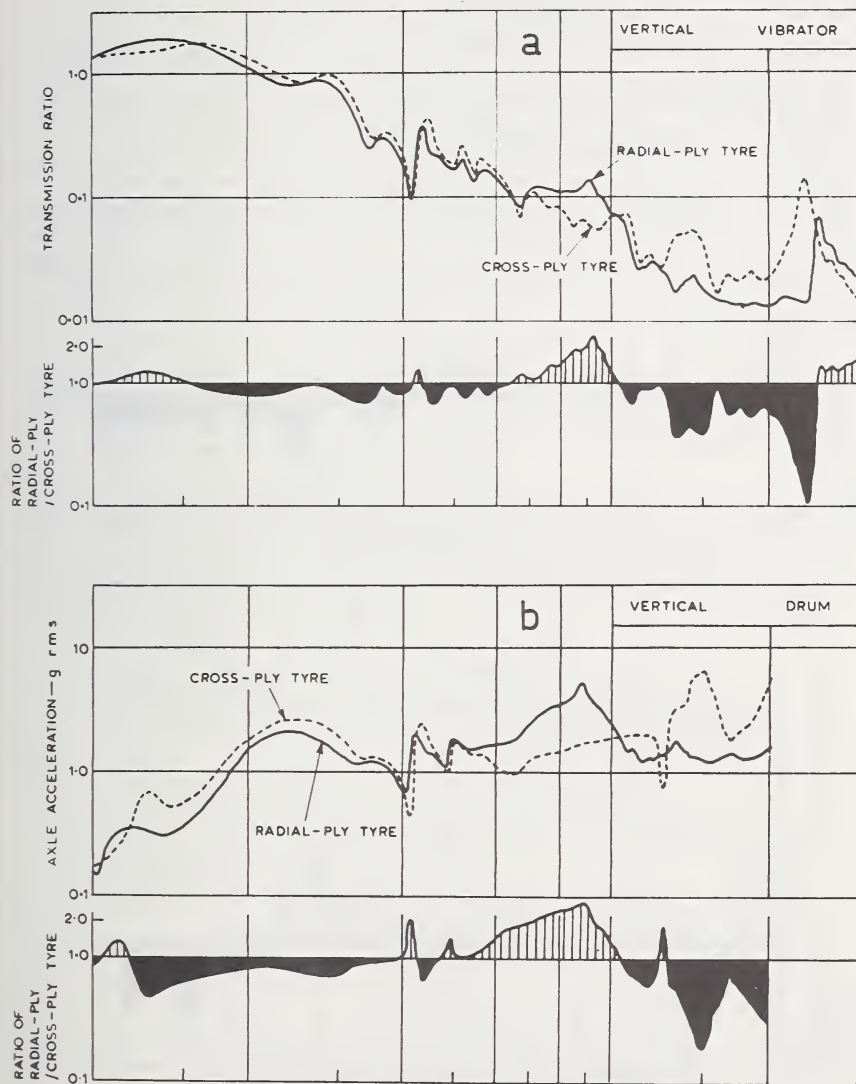


FIGURE 7.4.15. Comparison of cross-ply and radial-ply tires in their vertical vibrational behavior.

Test carried out on vertically vibrating platform (a) and on rotating drum (b) with sinusoidal surface (wavelength 0.133 m, amplitude 3 mm, speed 5–100 km/h) [18].

amplitude ≈ 3 mm. Both tests have been carried out with a laboratory strut-type wheel suspension showing vertical and longitudinal compliance, the latter resulting in a longitudinal natural frequency of about 11 Hz. In figures 7.4.16a, b the results of analogous tests for longitudinal

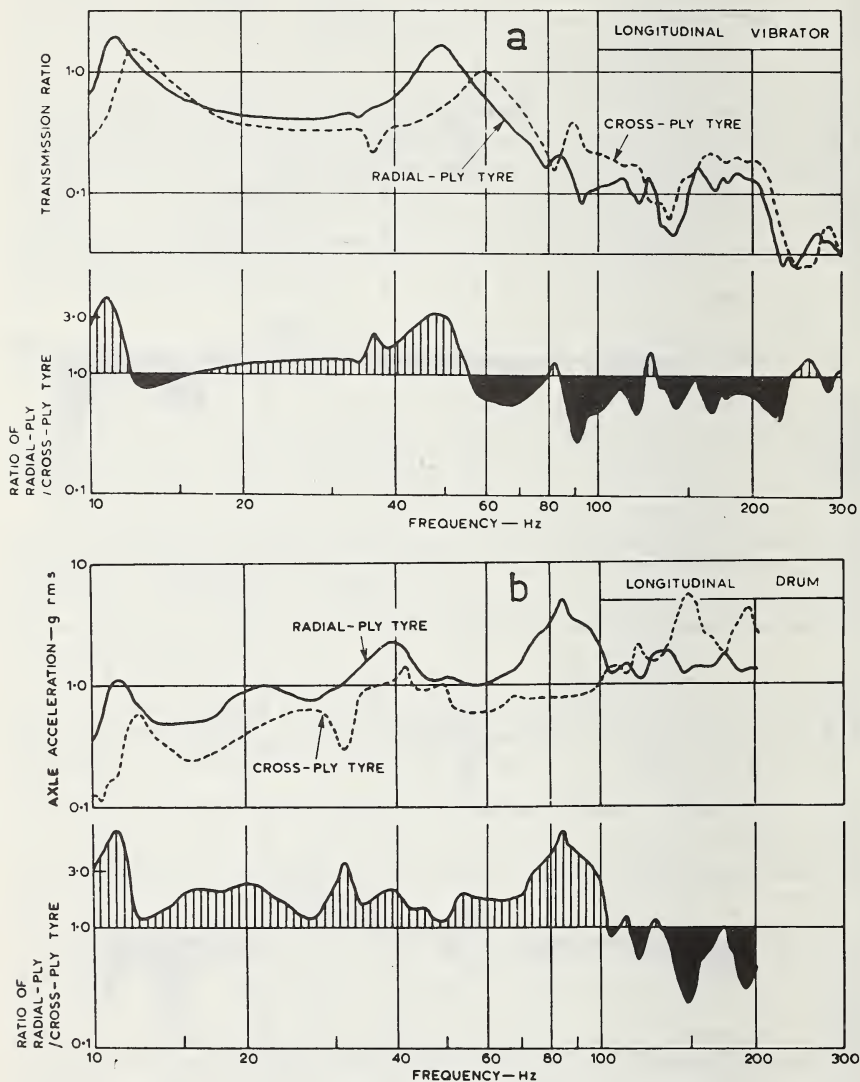


FIGURE 7.4.16. Comparison of cross-ply and radial-ply tyres in their longitudinal vibrational behavior.

Tests carried out on longitudinally vibrating platform (a) and on rotating drum (b) under same conditions of figure 7.4.15 (b) [18].

vibration transmission have been shown. In this case the vibrator platform is excited in the longitudinal direction, while for the drum test the same sinusoidal surface is used as in figure 7.4.15b.

These experiments have been carried out with radial and bias ply tires of the same dimensions. For clear comparison of the properties of these tires their response ratio has been shown in the lower diagrams. It may be noted that for the vertical transmission of vibrations qualitative similarity exists between results of both types of test, platform and drum. The same resonance frequencies (attributable to both tire and suspension) arise, and from both tests the advantage of radial ply tires appears above 100 Hz, the "road roar" range. Their disadvantage in the range of 60–100 Hz is also clear. In particular, for the longitudinal aspect of vibration transmission, the drum test appears to be essential. From this test (fig. 7.4.16b) it can be shown that the radial ply tire causes a much greater longitudinal response below 100 Hz than the cross ply tire.

The similarity of vertical response between rolling and standing tires led Chiesa to adopt the oscillating platform test for further detailed investigation of the vertical vibration transmission. In order to overcome the problem of the presence of resonances other than those attributable to the tire, the tire has been mounted on a massive heavy wheel of approximately the same weight as the load sustained by a single tire fitted to a car. This wheel was supported on the vibratory table by an air spring system of negligible stiffness.

In the experimental investigation described in [27] a comparison has been made between the vibrational behavior of radial and cross ply tires. The oscillating platform produces vertical hub oscillations via tread band and sidewall vibrations distributed along the tire circumference. The

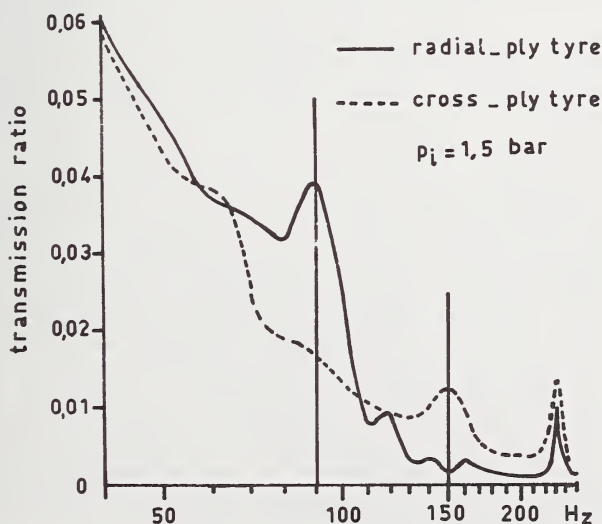


FIGURE 7.4.17. Amplitude ratio between hub of heavy wheel and vibrating platform [27].

question of whether a correlation exists between these distributed vibrations and the complex transfer function of platform motion to hub motion forms the major part of that research.

The amplitude ratio of the hub oscillation and the sinusoidal platform oscillation has been shown in figure 7.4.17 for both types of tire as a function of platform frequency. With the radial tire the system exhibits a very pronounced resonance at about 90 Hz, followed by a number of less important resonances. The cross ply tire, however, exhibits only one resonance near 150 Hz. In practice, this indicates that the radial tire has more potential for developing resonances in the vehicle than the cross ply tire. The tests have been carried out with an inflation pressure $p_i = 1.5$ bar, (1 bar \approx 1 atm.). At higher inflation pressures the resonances appear to shift to slightly higher frequencies and the amplitude ratios increase a little. This is true for all resonances except the peak occurring at about 230 Hz, being due to the resonance of the air column within the tube. This appears to vary only with tire size and type of gas used for inflating the tire. Experience shows that the whole picture of the transmission curve changes substantially when varying the tire size. When the type of tire construction remains the same, the only effect is that with larger sizes all resonance frequencies shift towards lower values. These results are of importance for the tuning between tire and vehicle.

For determining the correlation between transmission curves and tire vibrations, Chiesa and his co-workers found the shape of the deformed equatorial line by measuring the hub and tire tread band and sidewall motions by means of accelerometers. The instantaneous displacement of a point of the tread band is obtained by vectorial combination of the radial and tangential displacements deduced from the signals of micro-accelerometers placed between tube and tire. By connecting the positions of the points at several locations (azimuth angles) the instantaneous deformation line is obtained. These displacements occur relative to the stationary equatorial line, which is deformed due to the average vertical load. For purposes of this research it has been considered acceptable to take as a reference equatorial line a perfect circle. In figure 7.4.18 deformation patterns of a radial and a cross ply tire have been shown with respect to the circular reference line. The deformation patterns which are shown here for a series of excitation frequencies are obtained at that instant where the highest vertical resultant at the hub of the heavy wheel occurs. The phase delay angle ϕ_r of the hub vertical motion relative to the shake table motion has been indicated for each frequency. The vertical bold line segment indicates the amplitude of the platform motion.

At low frequencies the deformation is limited to the region near the contact area. By increasing the frequency the first mode of vibration is attained. At this natural frequency (radial ply \sim 90 Hz, bias ply \sim 150 Hz) the deformation patterns are similar (two nodes). It can be seen from the figure that with increasing frequency the number of wavelengths along the circumference increases. At a frequency of 190 Hz the radial ply tire already has seven wavelengths whereas the conventional bias ply tire shows only two wavelengths at this frequency.

From observations over one complete period of excitation it has been found that the wavy deformation as a whole does not vanish periodically.

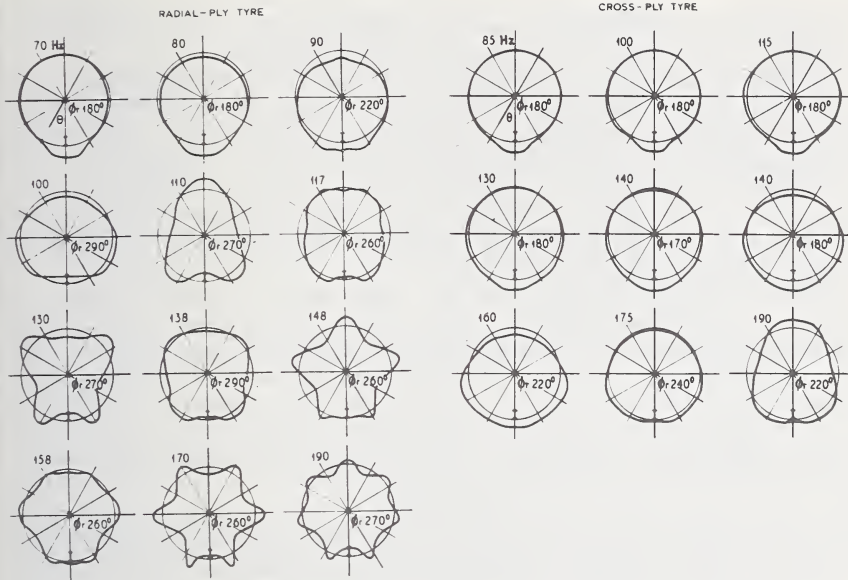


FIGURE 7.4.18. Deformation lines of radial and cross-ply tire for a series of frequencies taken at the instant of highest vertical resultant characterized by the phase delay angle ϕ_r relative to the platform motion.

The nodes appear to move a little along the circumference, which is peculiar to dissipative distributed vibrations. Moreover it appeared that the number of nodes may vary during one period.

Measurements of the lateral displacements of the sidewall indicate that a simple, generally valid relation with the radial tread displacements exists. It appears that these motions are always out of phase, i.e., when the one contracts the other expands. This is true except in the direct vicinity of the contact area where both motions are in phase.

For investigating the correlation between the deformation line of the tread band and the vertical force transmission, the following procedure was adopted. In increments of 10 degrees of azimuth angle the vertical component of the displacement of the points of the equatorial line have been determined, after which their algebraic sum has been calculated. This sum has been determined for a number of instances over one excitation period and it appears that the variation with time is approximately harmonic. In figure 7.4.19 the amplitude ratio and the phase relationship of this calculated sum with respect to the platform motion has been shown, together with the measured response of the hub motion. It appears that the agreement is very good between the calculated sum of the vertical deformation, which may be considered to be proportional to the force transmitted, and the experimental results of figure 7.4.17, after the latter are cleared of low-frequency components. As Chiesa states, the correlation which has been found to exist furnishes a broad

basis for the understanding of the high-frequency (vertical) behavior of tires, to add to the well known low-frequency phenomena.

Similar research can in principle be carried out for the investigation of longitudinal and lateral force transmission. It may provide some insight, but the practical application of the results obtained with a horizontally shaking platform will be difficult, since the motions of the lower part of the tread-band running on a road are not known due to longitudinal and lateral creep phenomena. Moreover, for longitudinal force transmission the slope of a wavy road surface plays an important role, as has been shown in the previous section 7.4.1.

The natural frequencies and the mode shapes of the motions in these two directions however, are no doubt of importance for general information and for purpose of tuning the tire-vehicle combination. The information shown in figure 7.4.20 has been taken from reference [18]. It shows several modes of the tire-suspension combination. The tire is of the radial ply type and the suspension is of the strut type having large longitudinal compliance. The resonances will change with mass, polar moment of inertia and longitudinal compliance of the tire. Probably the only peak which is due to tire natural vibrations is the one between 80 and 90 Hz, which corresponds to the mode found with the vertical excitation. The resonance occurring at about 50 Hz does not correspond to the natural frequency of the tire rotating as a whole with respect to the wheel fixed in space (cf. sec. 7.4.2, table 7.4.2: 45.5 Hz) but represents the natural rotational vibration of the wheel with a great part of the tire (about a point approximately midway between hub and upper rim) with respect to the contact patch. The peak at about 13 Hz will be due to the natural frequency of the system, mainly owing to the longitudinal compliance of the suspension.

The experiments discussed above are carried out on a tire mounted on a hub which must be capable of moving in order to obtain the overall transmissibility. The natural frequencies of the tire itself might be measured more accurately on a tire mounted on a rim which is fixed in space. The results of some of these investigations will be given in the subsequent paragraph as an illustration of the theory (cf. figs. 7.4.24-25).

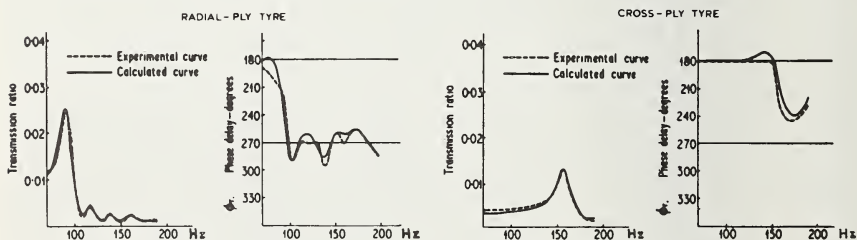
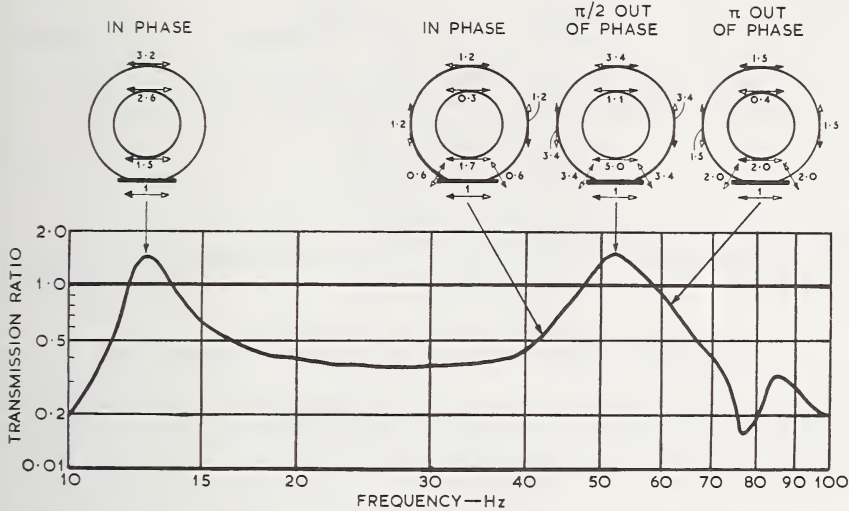


FIGURE 7.4.19. Amplitude ratio and phase delay of calculated sum of vertical deformations distributed along the circumference with respect to platform motion (adapted scale) compared with measured hub response of figure 7.4.17, after being cleared of the lower frequency components arising from the vibration of the system considered as a rigid mass-spring system.



The magnitude and sense of the vibration are shown by the numbers and by the shading of the arrows. The phase with respect to the input for all the stations on any one diagram is shown above the diagram. The unity transmission ratio line defines the magnitude of the input to the tyre. The transmission ratio curve itself refers to longitudinal vibrations at the axle.

FIGURE 7.4.20. Modes of vibration of the suspension-wheel-tire (radial-ply) combination for longitudinal excitation by a vibrating platform.

Tread-Band Free Vibrations

For the development of a theory for the plane vibrations of a tire one may consider a circular membrane under tension or a circular beam or a combination of these two. In the early literature we encounter a number of theories for the vibration of a two-dimensional elastically-supported circular beam or shell [30, 31]. More recent studies by Tielking [32] and Böhm [33] and a more simple theory by Fiala and Willumeit [34] lay specific emphasis on the vibration of a pneumatic tire. The complicated case of a torodial shell has been solved, after many simplifying assumptions, by Federhofer [35]. In the theory presented below we treat the vibrations of circular beam and make use of the method employed by Tielking, which is based on the principle of Hamilton. In an example we present the equations and results as given by Böhm, which also cover vibrations in the lateral direction.

Unlike Tielking, we introduce a tension force acting in the beam which may be due to the internal pressure and the rotational speed. We also account for the tangential stiffness between beam (tread-band) and wheel rim. In figure 7.4.21 the pneumatic tire model is shown. Damping is not considered.

The application of Hamilton's principle requires the determination of the potential and the kinetic energy of the model as well as the work done by internal pressure forces.

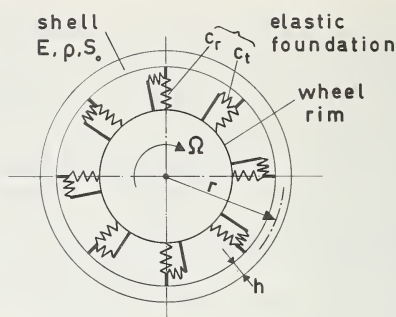


FIGURE 7.4.21. Cylindrical beam or shell model for a pneumatic tire.

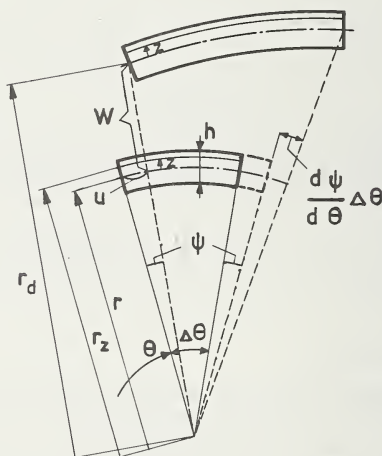


FIGURE 7.4.22. Displacement and deformation of tread band element.

The potential energy is composed of a part due to elastic deformations of the beam and a part due to radial and tangential displacements of the tread band with respect to the wheel rim. For the determination of these quantities we introduce the independent angular coordinate θ and the tire radius r , representing the position of a tread element at rest with respect to a coordinate system fixed to the wheel. Furthermore we introduce the dependent coordinates $u = r\psi$ and w , denoting the tangential and radial displacements, respectively, of the element with respect to the original position.

Figure 7.4.22 shows an element in the original position (possibly influenced by the centrifugal force) and in the deformed and deflected situation. The tangential strain at the original radius $r_z = r + z$ is influenced by the initial strain ϵ_0 (due to internal pressure and centrifugal force), by the additional "angular" strain $d\psi/d\theta$ and by the radial dis-

placement w and its derivatives. The strain becomes:

$$\epsilon_z = \epsilon_o + \left\{ 1 + \frac{w}{r_z} + \frac{1}{2} \left(\frac{dw}{r_z d\theta} \right)^2 - \frac{z}{r_z r} \left(1 - \frac{w}{r} \right) \frac{d^2 w}{d\theta^2} \right\} \left(1 + \frac{d\psi}{d\theta} \right) - 1$$

with

$$r_z = r + z.$$

The potential energy due to tread band deformations becomes, per unit width:

$$V_t = \frac{1}{2} E \int_h \int_{\theta=0}^{2\pi} r_z \epsilon_z^2 dh d\theta.$$

where the integration is over the tread band thickness h and in which E denotes the elastic modulus of the beam material. With the introduction of $u = r\psi$, $I = 1/6bh^3$ (moment of inertia) and $S_o = c_s \epsilon_o$ (tension force with c_s denoting the tensile rigidity) we obtain, with the assumption that ϵ_o and $(h/r)^2$ are negligible with respect to unity:

$$V_t = \frac{1}{2} \int_0^{2\pi} \left[\frac{EI}{r^3} \left(\frac{\partial^2 w}{\partial \theta^2} + w \right)^2 + \frac{S_o}{r} \left(\frac{\partial w}{\partial \theta} \right)^2 + \frac{c_s}{r} \left(\frac{\partial u}{\partial \theta} + w \right)^2 \right] d\theta. \quad (7.4.83)$$

in which only the second-order terms are shown.

The potential energy stored in the elastic foundation becomes, using c_r and c_t to denote the radial and tangential stiffness per unit length:

$$V_c = \frac{r}{2} \int_0^{2\pi} \left[c_r w^2 + c_t u^2 \right] d\theta. \quad (7.4.84)$$

The work done by the internal pressure p_i is:

$$W_p = 2bp_i \left(\frac{1}{2} \int_0^{2\pi} r_d^2 d\phi - \pi r^2 \right)$$

with

$$d\phi = d(\theta + \psi) = \left(1 + \frac{\partial \psi}{\partial \theta} \right) d\theta = \left(\frac{1}{r} \frac{\partial u}{\partial \theta} + 1 \right) d\theta$$

and

$$r_d = r + w.$$

When retaining only the second-order terms we obtain:

$$W_p = bp_i \int_0^{2\pi} \left(2w \frac{\partial u}{\partial \theta} + w^2 \right) d\theta. \quad (7.4.85)$$

For calculation of the kinetic energy we consider figure 7.4.23. The wheel rotates with an angular velocity Ω . In addition, a tread element has a velocity with respect to the wheel. The velocity vector of such

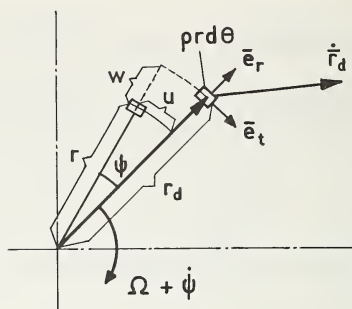


FIGURE 7.4.23. Position of an element and its velocity.

an element expressed in terms of the unit vectors in radial and tangential direction \bar{e}_r and \bar{e}_t becomes:

$$\begin{aligned}\dot{r}_d &= \dot{r}_d \bar{e}_r + (\Omega + \dot{\psi}) r_d \bar{e}_t \\ &= \dot{w} \bar{e}_r + (\Omega + \dot{\psi}) (r + w) \bar{e}_t.\end{aligned}$$

With the use of this expression we obtain the following formula for the kinetic energy of the shell per unit width with ρ denoting the mass per unit area:

$$\begin{aligned}T &= \frac{1}{2} \rho r \int_0^{2\pi} |\dot{r}_d|^2 d\theta \\ &= \frac{1}{2} \rho r \int_0^{2\pi} \{ \dot{w}^2 + (\Omega + \dot{\psi})^2 (r + w)^2 \} d\theta\end{aligned}$$

which becomes when retaining only second-order terms and with $u = r\psi$:

$$T = \frac{1}{2} \rho r \int_0^{2\pi} \{ \dot{w}^2 + \Omega^2 w^2 + \dot{u}^2 + 4\Omega w \dot{u} \} d\theta. \quad (7.4.86)$$

According to Hamilton's principle the time integral of the Lagrangian L must be minimized, so that:

$$L = T - V + W_p. \quad (7.4.87)$$

The Lagrangian density $\partial L / \partial \theta$ is easily formulated by combination of the above expressions. We obtain:

$$\begin{aligned}\frac{\partial L}{\partial \theta} &= \frac{1}{2} \rho r (\dot{w}^2 + \Omega^2 w^2 + \dot{u}^2 + 4\Omega w \dot{u}) - \frac{1}{2} \frac{EI}{r^3} \left(\frac{\partial^2 w}{\partial \theta^2} + w \right)^2 - \frac{1}{2} \frac{S_o}{r} \left(\frac{\partial w}{\partial \theta} \right)^2 \\ &\quad - \frac{1}{2} \frac{c_s}{r} \left(\frac{\partial u}{\partial \theta} + w \right)^2 - \frac{1}{2} r (c_r w^2 + c_t u^2) + b p_i \left(2w \frac{\partial u}{\partial \theta} + w^2 \right). \quad (7.4.88)\end{aligned}$$

The time integral of this quantity becomes stationary when the following Euler-Lagrange differential equations for the dependent variables w and u , which hold for our case of two independent variables θ and t , are satisfied [36]. With the abbreviations $(\cdot)' = \partial(\cdot)/\partial\theta$ and $(\cdot)\dot{ } = \partial(\cdot)/\partial t$ we obtain

$$\begin{aligned} -\frac{\partial L'}{\partial w} + \frac{\partial}{\partial t} \left(\frac{\partial L'}{\partial \dot{w}} \right) + \frac{\partial}{\partial \theta} \left(\frac{\partial L'}{\partial w'} \right) - \frac{\partial^2}{\partial \theta^2} \left(\frac{\partial L'}{\partial w''} \right) &= 0, \\ -\frac{\partial L'}{\partial u} + \frac{\partial}{\partial t} \left(\frac{\partial L'}{\partial \dot{u}} \right) + \frac{\partial}{\partial \theta} \left(\frac{\partial L'}{\partial u'} \right) &= 0. \end{aligned} \quad (7.4.89)$$

Application of these equations gives the following equations of motion for the cylindrical beam of unit width.

$$\begin{aligned} \rho(\ddot{w} - \Omega^2 w - 2\Omega \dot{u}) + \frac{EI}{r^4} (w^{IV} + 2w'' + w) - \frac{S_o}{r^2} w'' \\ + \left(\frac{c_s}{r^2} - \frac{2p_i b}{r} \right) (u' + w) + c_r w = 0, \end{aligned} \quad (7.4.90)$$

$$\rho(\ddot{u} + 2\Omega \dot{w}) + c_t u - \frac{c_s}{r^2} (u'' + w') + \frac{2p_i b}{r} w' = 0. \quad (7.4.91)$$

Working along similar lines Tielking obtained almost the same equations. However in the dynamic part of the second equation the additional term $-\rho\Omega^2 u$ appears in his theory, while Tielking did not consider S_o and c_t .

The remaining analysis will be simplified by using the concept of inextensibility of the cylindrical beam ($c_s \rightarrow \infty$). It is believed that this approximation is particularly good when the consideration is restricted to radial ply belted tires. Mathematically this may be accomplished by putting:

$$u' = -w. \quad (7.4.92)$$

We obtain by elimination of the terms with coefficient c_s in the equations (7.4.90) and (7.4.91):

$$\begin{aligned} \rho(\ddot{w}'' - \ddot{w} + 4\Omega \dot{w}' - \Omega^2 w'') + \frac{EI}{r^4} (w^{VI} + 2w^{IV} + w'') \\ - \frac{S_o}{r^2} w^{IV} + \left(\frac{2p_i b}{r} + c_r \right) w'' - c_t w = 0. \end{aligned} \quad (7.4.93)$$

In an analogous way Bryan [31] derived essentially the same equation. In his study of oscillatory motions it is assumed that the radial displacement w varies harmonically in the form:

$$w = A \sin(s\theta + \omega t). \quad (7.4.94)$$

Substitution in eq (7.4.93) yields

$$\rho(s^2\omega^2 - \omega^2 - 4\Omega s\omega + \Omega^2 s^2) + \frac{EI}{r^4}(-s^6 + 2s^4 - s^2) - \frac{S_0}{r^2}s^4 - \left(\frac{2p_i b}{r} + c_r\right)s^2 - c_t = 0 \quad (7.4.95)$$

with the definition

$$\bar{\omega}^2 = \left\{ \frac{4\Omega^2 s^2}{s^2 + 1} - \Omega^2 s^2 + \frac{EI}{\rho r^4} s^2 (s^2 - 1)^2 + \frac{S_0}{\rho r^2} s^4 + \frac{1}{\rho} \left(c_r + \frac{2p_i b}{r} \right) s^2 + \frac{1}{\rho} c_t \right\} / (s^2 + 1) \quad (7.4.96)$$

we obtain

$$\omega = \frac{2\Omega s}{s^2 + 1} \pm \bar{\omega}. \quad (7.4.97)$$

The possible solutions become herewith:

$$\begin{aligned} w_1 &= A_1 \sin \left(s\theta + \frac{2\Omega s}{s^2 + 1} t + \bar{\omega} t \right) \\ w_2 &= A_2 \sin \left(s\theta + \frac{2\Omega s}{s^2 + 1} t - \bar{\omega} t \right) \end{aligned} \quad (7.4.98)$$

In the particular case $A_1 = A_2 = A$ we obtain for the solution $w = w_1 + w_2$:

$$w = 2A \sin \left(s\theta + \frac{2\Omega s}{s^2 + 1} t \right) \cos \bar{\omega} t \quad (7.4.99)$$

in which $\bar{\omega}$ obviously represents the frequency of the vibration. The mode number s denotes the number of periods along the tire circumference. The number of nodes is twice as much. The position of a node

$$\theta_n = -\frac{2\Omega t}{s^2 + 1} + \frac{k\pi}{s} \quad (k = 1, 2, \dots) \quad (7.4.100)$$

changes with respect to the wheel with an angular speed Ω_t^* :

$$\Omega_t^* = \frac{-2}{s^2 + 1} \Omega. \quad (7.4.101)$$

For the observer stationary in space the nodes move with a different velocity, Ω^* , which obviously equals $\Omega_t^* + \Omega$:

$$\Omega^* = \frac{s^2 - 1}{s^2 + 1} \Omega. \quad (7.4.102)$$

For each number of periods s the frequency of the vibration may be calculated with the aid of equation (7.4.96). The frequencies depend on tire parameters and to a very small extent on the rotational speed Ω . The tension force S_0 may be a function of Ω (cf. sec. 7.4.2 on standing waves).

Böhm, who did not consider a rotating tire, calculated the values of these parameters from the tire construction, geometry and material properties. Böhm's equations differ in some respects from those derived above [90, 91]. Böhm's equations, for the derivation of which we refer to the original article [33], read:

$$\rho \ddot{w} + \frac{EI}{r^4} (w^{IV} + w'') + \frac{c_s}{r^2} (u' + w) - \frac{S_0}{r^2} (w'' + w) + c_r w = 0, \quad (7.4.103)$$

$$\rho \ddot{u} + \frac{EI}{r^4} (w''' + w') - \frac{c_s}{r^2} (u'' + w') + c_t u = 0. \quad (7.4.104)$$

With the assumed solutions

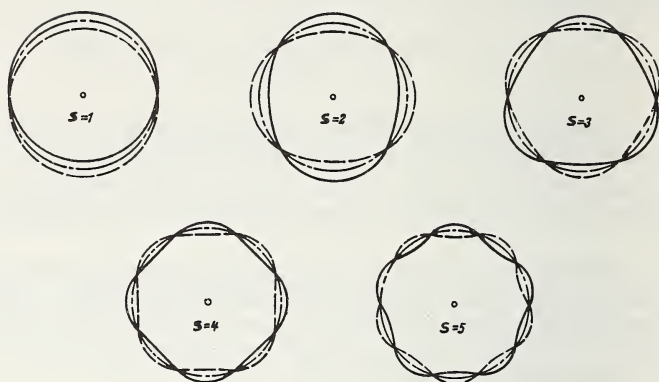
$$w = A \sin \omega t \sin s\theta, \quad u = B \sin \omega t \cos s\theta \quad (7.4.105)$$

inserted in these equations the natural frequencies can be obtained for the various mode numbers s . The calculations were carried out by Böhm for a 135-13 radial ply Michelin X tire with inflation pressure $p_i = 1.25$ bar. The following calculated values hold for the total width $2b (= 0.075$ m.): $\rho = 1.25$ kg/m., $EI = 0.7$ Nm.², $c_s = 59 \times 10^4$ N, $S_0 = 1920$ N, $c_r = 75 \times 10^4$ N/m.², $c_t = 12.8 \times 10^4$ N/m.², $r = 0.273$ m.

In table 7.4.2 both the calculated and measured frequencies $n = \omega/2\pi$ (Hz) are shown for mode numbers 0-5. For comparison we have added the results obtained with the equation earlier derived (7.4.96) for $\Omega = 0$, so that $\omega = \bar{\omega}$. For each mode number a second natural frequency exists which, according to the theory, is 4 to 8 times higher than the lower one shown in table 7.4.2. The frequency 45.5 Hz at mode number $s = 0$ corresponds to the mode shape showing pure tangential torsion of the tread band with respect to the wheel rim. The second frequency at $s = 0$, which occurs at 376 Hz exhibits purely uniform radial displacements of the tread band. The experiments were carried out by applying a radial excitation force so that the low frequency zero-mode natural frequency was not detected.

In figure 7.4.24 the theoretical and measured mode shapes are presented. The experimental frequency response characteristic for the radial displacement amplitude A , with respect to the radially applied

THEORY



EXPERIMENT

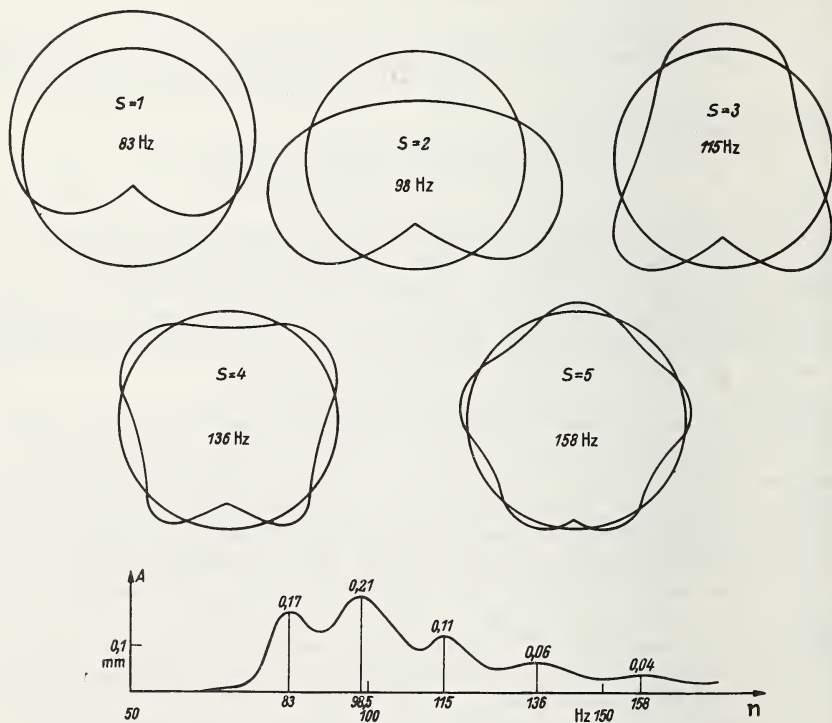


FIGURE 7.4.24. Theoretical and experimental mode shapes and measured frequency response characteristic of the radial tread band deflections with respect to a radial excitation force for a radial-ply Michelin X 135-13 tire with $p_i = 1.25$ bar (from Böhm [33]).

excitation force amplitude (constant) has also been indicated. The correspondence between theory and experiment is good enough for technical purposes. The differences between eqs (7.4.90–91) and (7.4.103–104) turn out to be of no importance in the range of mode numbers investigated. Also, it appears that the concept of inextensibility used in eq (7.4.93) is acceptable for this tire. From the calculations it appears that the influence of the bending stiffness EI starts at higher values of s . At $s=5$ the influence of EI on ω amounts approximately 2 percent. We shall see that in the study of standing waves with relatively small wave lengths the influence of the bending stiffness is appreciable.

TABLE 7.4.2. *Natural frequencies of symmetric (plane) tread band vibrations*

	$s=0$	$s=1$	$s=2$	$s=3$	$s=4$	$s=5$
Measured $n(\text{Hz})$		83	98.5	115	136	158
Calculated $n(\text{Hz})$ (eqs (7.4.103–104))..	45.5	83.7	105.5	119	134	150
Calculated $n(\text{Hz})$ (eq (7.4.96)).....	45.5	87	109	123	138	154

Lateral vibrations

For the same 135–15 Michelin X tire Böhm also studied the lateral vibrations. We shall restrict ourselves here to a short presentation of his theoretical and experimental results. For the derivation of the equations we refer to the original paper [33].

Again two degrees of freedom are considered for an element of the tire tread-band. The variables are: the lateral deflection v and the torsion angle β about a tangent to the peripheral line. These so-called anti-symmetric variables are not coupled with the symmetric variables u and w . With the assumed solution

$$v = A \sin \omega t \sin s\theta \quad \text{and} \quad \beta = B \sin \omega t \cos s\theta \quad (7.4.106)$$

the following eigenvalue determinant is obtained:

$$\begin{vmatrix} \frac{EI_z}{r^4} s^4 + \left\{ \frac{GI_p}{r^4} + \frac{S_o}{r^2} + \frac{c_t b^2}{r^2} \right\} s^2 & \left\{ \frac{GI_p}{r^3} + \frac{EI_z}{r^3} \right\} s^2 + p_i b^* \\ + c_c - \rho \omega^2 \left(1 + \frac{b^2}{3r^2} s^2 \right) & \\ \left\{ \frac{GI_p}{r^3} + \frac{EI_z}{r^3} \right\} s^2 & \frac{GI_p}{r^2} s^2 + \frac{EI_z}{r^2} + c_T - \rho \omega^2 \frac{4b^2 + t^2}{12} \end{vmatrix} = 0 \quad (7.4.107)$$

in which $S_o = 1920$ N (total tension force), $GI_p = 3.2$ Nm.² (torsional stiffness of tread band), $EI_z = 150$ Nm.² (bending stiffness of tread-band about

wheel radius), $c_t = 12.8 \times 10^4 \text{ N/m}^2$ (tangential foundation stiffness), $c_c = 10^5 \text{ N/m}^2$ (lateral foundation stiffness), $c_T = 1050 \text{ N.m/rad.m.}$ (torsional foundation stiffness), $p_i = 1.25 \times 10^5 \text{ N/m}^2$, $\rho = 1.56 \text{ kg/m}^3$, $r = 0.273 \text{ m}$, $2b = 0.075 \text{ m}$. (width of carcass breaker), $b^* = 0.056 \text{ m}$. (reduced width), $t = 0.003 \text{ m}$. (side wall thickness).

In table 7.4.3 the calculated and measured natural frequencies are presented for mode numbers $s = 0-4$. Figure 7.4.25 shows the measured mode shapes of the lateral deflection and in addition the frequency response characteristics of the lateral tread deflection with respect to an excitation force acting upon the tread-band in purely lateral direction.

TABLE 7.4.3. *Natural frequencies of anti-symmetric (lateral) tread band vibrations*

	$s = 0$	$s = 1$	$s = 2$	$s = 3$	$s = 4$
Measured $n(\text{Hz})$	39	44	76	114	149
Calculated $n(\text{Hz})$	40.0	42.7	64.2	110	162

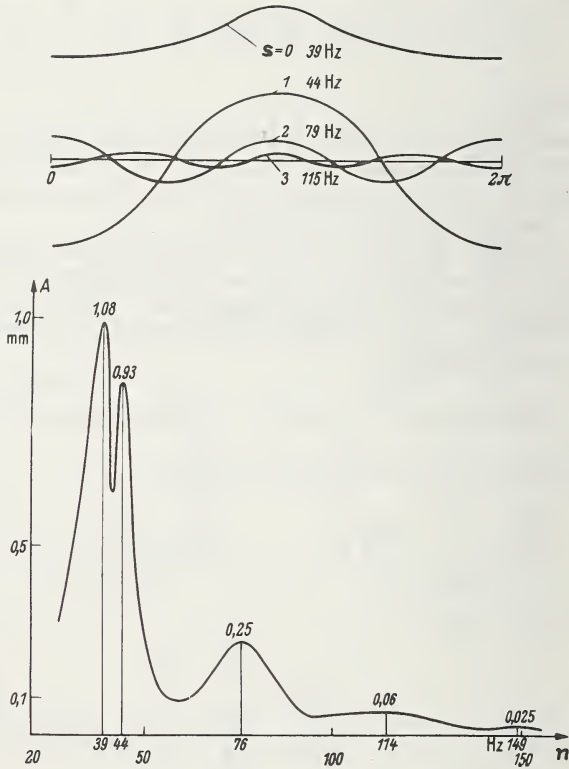


FIGURE 7.4.25. *Experimental mode shapes and measured frequency response characteristic of the lateral deflection of the tread band with respect to a lateral excitation force acting upon the tread band.*

Same tire as in figure 7.4.24 (from Böhmer [33]).

Böhm found the mechanical characteristics of the tire by working backwards from the measured spectra of natural frequencies, and found good agreement with the above values which were calculated from tire dimensions and material properties. Böhm states that the backward calculation of physical values is a powerful method, since the measured natural frequencies describe the system more precisely than do static deformation experiments.

Standing Waves

When rolling at high speed, waves are formed on a tire behind the area of contact with the road. The repeated deformation caused by the wave process results in a considerable heat buildup which reduces the strength of the tire and may lead to its ultimate destruction.

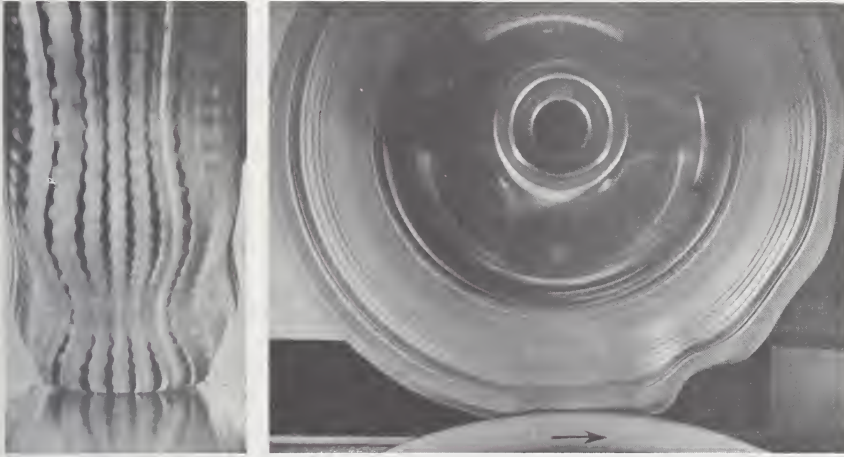


FIGURE 7.4.26. Standing wave formation at high speeds of travel (from B. Nylon S., Great Britain).

Because these waves present a stationary appearance to an observer they have been called standing waves. Figure 7.4.26 gives a very good illustration of such a stationary wave deformation. Gardner and Worswick [37] published considerable experimental information on this phenomenon. Turner also [38] provides interesting theoretical and experimental information on amongst other things the power consumption owing to standing waves. More recently Drozdov, et al. [39], Togo [40], Böhm [33] and Fiala [34] presented theories on standing waves. Ames [41] prepared a literature survey in which mention has been made of other Russian and Japanese work. Ames proposes the introduction of non-linear elements in the dynamics of the tread-band and side wall motion. Akasaka and Yamagishi [42] studied the standing waves in the shell wall of a running tire by considering the tire as a cord reinforced toroidal

membrane shell with elliptical cross section. The cords have been assumed to be inextensible, the flexural rigidity has been neglected, and tangential displacements have been neglected. Solutions have been obtained by means of Galerkin's method. In the theories to be presented below we shall restrict ourselves to shells of a circular cylindrical shape. Tangential displacements will also be neglected here.

Membrane theory

The equation of the transverse motion of a membrane stretched in longitudinal directions reads:

$$\rho \frac{\partial^2 w}{\partial t^2} = S \frac{\partial^2 w}{\partial x^2} \quad (7.4.108)$$

where ρ represents the mass per unit length, S the tension force, w the transverse displacement, x the longitudinal coordinate and t the time. After a disturbance a wave is formed which propagates with a velocity

$$V_p = \sqrt{\frac{S}{\rho}}. \quad (7.4.109)$$

It is expected that when a normal load is applied which travels with respect to the membrane with a speed equal to the above propagation velocity a critical situation occurs. Togo [40] has investigated this problem for an elastically supported membrane and found that for speeds in excess of this critical value a standing wave is formed behind the point of loading. In front of this point the displacement vanishes.

We shall examine the problem of a circular membrane or string under tension, radially supported by an elastic foundation which may show some viscous damping. The tension is supplied by the inflation pressure. This model tire rolls over a perfectly smooth horizontal surface and is loaded vertically. We introduce the quantities: r =tire radius, Ω =rotational speed; $V \simeq \Omega r$ =speed of travel; W =normal load; p_i =inflation pressure; c_r =radial stiffness of foundation per unit length; k_r =coefficient of radial damping per unit length; c_s =tensile carcass stiffness of unit length (=average elastic modulus times tread-band cross section); θ =angular coordinate with respect to an axes-system fixed to the wheel; w =outward displacement of rotating membrane due to W ; η =percentage of centrifugal force restored by radial forces; $1-\eta$ =percentage of centrifugal force restored by tangential tension forces; S_0 =tension force in nonrotating tire; $2b$ =effective tread-band width.

It is assumed that only radial displacements occur. In figure 7.4.27 forces acting on a membrane element of unit width are indicated. The following partial differential equation applies for the radial displacements $w(\theta, t)$ due to the load W in zones outside of the contact area.

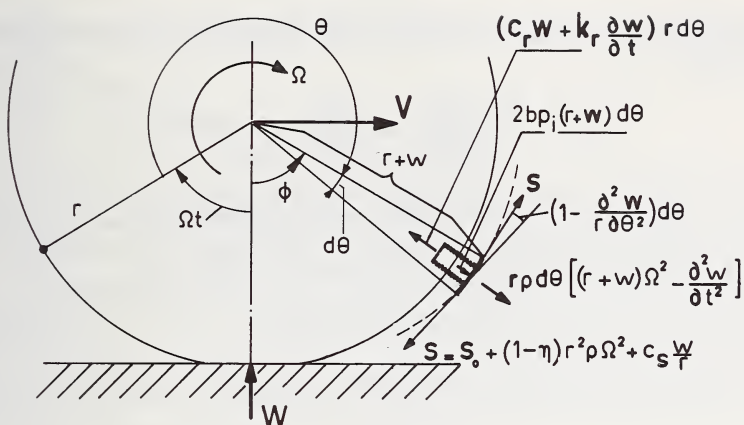


FIGURE 7.4.27. Forces acting on membrane element.

Consequently, the growth of tire radius due to centrifugal forces is not included in w .

$$\rho \frac{\partial^2 w}{\partial t^2} + k_r \frac{\partial w}{\partial t} - \left\{ \frac{S_0}{r^2} + (1-\eta)\rho\Omega^2 \right\} \frac{\partial^2 w}{\partial \theta^2} + (c' - \rho\Omega^2)w = 0, \quad (7.4.110)$$

where

$$c' = c_r + \frac{c_s}{r^2} - 2b \frac{p_i}{r}. \quad (7.4.111)$$

This equation corresponds to eq (7.4.90) for $u=0$ and $EI=0$ but with the additional tension force due to Ω^2 . The solution of this equation represents the tire deformation seen with respect to a rotating coordinate system. For the description of the standing wave phenomenon we shall adopt coordinates with respect to a system fixed in space. The angle ϕ is introduced indicating the position of a tread element with respect to the vertical through the wheel axis (cf. fig. 7.4.27),

$$\phi = 2\pi - \Omega t - \theta \quad (7.4.112)$$

Equation (7.4.110) then assumes the following form:

$$\rho \frac{\partial^2 w}{\partial t^2} + k_r \frac{\partial w}{\partial t} + \left(\eta\rho\Omega^2 - \frac{S_0}{r^2} \right) \frac{\partial^2 w}{\partial \phi^2} - k_r \Omega \frac{\partial w}{\partial \phi} - 2\rho\Omega \frac{\partial^2 w}{\partial t \partial \phi} + (c' - \rho\Omega^2)w = 0. \quad (7.4.113)$$

In case of stationary appearance of the radial deformations all deriva-

tives with respect to time vanish. We obtain the ordinary differential equation:

$$\left(\eta\rho\Omega^2 - \frac{S_0}{r^2}\right) \frac{d^2w}{d\phi^2} - k_r\Omega \frac{dw}{d\phi} + (c' - \rho\Omega^2)w = 0 \quad (7.4.114)$$

which could have been obtained immediately from (7.4.110) by putting $\partial/\partial t = -\Omega d/d\phi$ and $\partial/\partial \theta = -d/d\phi$, which transformations are valid in case of deformations being stationary with respect to a coordinate system fixed in space. The general solution of (7.4.114) reads:

$$w = C_1 e^{\lambda_1 \phi} + C_2 e^{\lambda_2 \phi} \quad (7.4.115)$$

in which the roots of the characteristic equation become:

$$\lambda_{1,2} = \frac{k_r\Omega \pm \sqrt{k_r^2\Omega^2 - 4\left(\eta\rho\Omega^2 - \frac{S_0}{r^2}\right)(c' - \rho\Omega^2)}}{2\left(\eta\rho\Omega^2 - \frac{S_0}{r^2}\right)} \quad (7.4.116)$$

Comparison with existing theories of Böhm [33], Fiala [34], and Togo [40], the latter two being reduced here to the case without bending stiffness of the tread-band, reveals that their results deviate from (7.4.116) in the following respects. Fiala and Togo neglect the effect of damping ($k_r=0$), Togo and Böhm assume that the centrifugal force does not influence the tension force S ($\eta=1$), Fiala assumes the opposite ($\eta=0$) and Togo neglects $\rho\Omega^2$ with respect to c' .

For small values of k_r the solution (7.4.116) may be written as:

$$\lambda_{1,2} = \frac{-k_r\Omega}{2\left(\frac{S_0}{r^2} - \eta\rho\Omega^2\right)} \pm \sqrt{\frac{c' - \rho\Omega^2}{\frac{S_0}{r^2} - \eta\rho\Omega^2}} \quad (7.4.117)$$

These roots become complex and consequently the solution (7.4.115) becomes oscillatory when Ω satisfies the following condition

$$\Omega_1 < \Omega < \Omega_2 \quad (7.4.118)$$

where Ω_1 and Ω_2 are critical values of rotational speed expressed by:

$$\Omega_1^2 = \frac{S_0}{\eta\rho r^2}, \quad \Omega_2^2 = \frac{c'}{\rho} \quad (7.4.119)$$

Before discussing the solutions in greater detail, we shall first examine the order of magnitude of Ω_1 and Ω_2 according to a number of known theories. For a 135-13 Michelin radial ply tire Böhm obtains by experimental means the following physical values: $S_0 = 1920$ N., $\rho = 1.56$ kg/m.,

$c_s = 59 \times 10^4$ N., $c_r = 75 \times 10^4$ N/m.², $2p_i b \approx 10^4$ N/m. ($p_i = 1.25$ bar),
 $r = 0.273$ m.

We obtain with $\eta = 1$:

$$\Omega_1 = 128s^{-1} \quad (V_1 = 126 \text{ km/hr}),$$

$$\Omega_2 = 2350s^{-1} \quad (V_2 = 2300 \text{ km/hr}).$$

For a Bridgestone 165-400 4 PR diagonal ply tire investigated by Togo (to be treated later on in greater detail) the following theoretical values can be derived $c'/2b = 5 \times 10^7$ N/m.³ (≈ 5 kgf/cm.³), $S_o/2r^2b = 136 \times 10^3$ N/m.³ (≈ 0.0136 kgf/cm.³), $\rho/2b = 21.8$ kg/m.² ($\approx 2.22 \times 10^{-6}$ kgf·s²/cm.³), $p_i = 13 \times 10^4$ N/m.² ($= 1.3$ bar), $r = 0.34$ m., which values result with $\eta = 1$ in.:

$$\Omega_1 = 78s^{-1} \quad (V_1 = 96 \text{ km/hr}),$$

$$\Omega_2 = 1500s^{-1} \quad (V_2 = 1830 \text{ km/hr}).$$

For a 165-400 radial ply tire we obtain, according to the formulation of Fiala [34], $c' = 35 \times 10^4$ N/m.², $\rho = 2.1$ kg/m., $r = 0.33$ m. With Fiala's assumption $\eta = 0$ the following results are obtained for $p_i = 1$ bar:

$$\Omega_1 \rightarrow \infty \quad (V_1 \rightarrow \infty),$$

$$\Omega_2 = 410s^{-1} \quad (V_2 = 480 \text{ km/hr}).$$

The three theories deviate considerably from each other. Apart from the differences in η we have noted, amongst other things, that Fiala took $c_s = 0$, which, in particular for a radial tire, is believed to be an unacceptable assumption. It causes the low value of Ω_2 obtained with Fiala's theory.

We continue now the discussion of the solution and write for (7.4.117), with the aid of (7.4.119):

$$\lambda_{1,2} = \frac{-k_r \Omega}{2\eta\rho(\Omega_1^2 - \Omega^2)} \pm \sqrt{\frac{1}{\eta} \frac{\Omega_2^2 - \Omega^2}{\Omega_1^2 - \Omega^2}}. \quad (7.4.120)$$

Two different classes of values will be considered. The first category refers to the theories of Togo and Böhm which hold for $\Omega_2 > \Omega_1$. We obtain for the speed ranges:

a. $\Omega < \Omega_1$: Real roots λ_1 and λ_2 . Assume k_r small enough so that for the Ω considered one positive (λ_1) and one negative root (λ_2) exist. With the requirements that for $|\phi| \rightarrow \infty$ the deflection w remains finite

the solutions (7.4.115) become for the regions outside of the contact area with length $2a$:

$$\left. \begin{aligned} \phi < -\frac{a}{r}: & \quad w = C_1 e^{\lambda_1 \phi}, \\ \phi > \frac{a}{r}: & \quad w = C_2 e^{\lambda_2 \phi}, \end{aligned} \right\} \quad (7.4.121)$$

indicating an almost symmetrical monotonically damped deflection. In the neighborhood of Ω_1 , the deflection at the rear must vanish due to the presence of k_r ($\lambda_2 < \lambda_1 < 0$, $C_1 = 0$).

b. $\Omega_1 < \Omega < \Omega_2$: Complex roots $\lambda_{1,2} = \alpha \pm i\beta$ with α and β real positive numbers. With the same conditions ($|\phi| \rightarrow \infty$, w finite) we obtain in this range of rotational speed:

$$\left. \begin{aligned} \phi < -\frac{a}{r}: & \quad w = C_1 e^{\alpha \phi} \sin(\beta \phi + \psi_1), \\ \phi > \frac{a}{r}: & \quad w = C_2 e^{\alpha \phi} \sin(\beta \phi + \psi_2) = 0, \quad (C_2 = 0). \end{aligned} \right\} \quad (7.4.122)$$

Consequently, in this speed range a standing wave will be formed behind the contact area. The wave damps out due to the presence of the radial damping coefficient k_r . In front of the contact area the solution would indicate an exponentially increasing deflection w which is in disagreement with boundary conditions, so that the constant of integration C_2 must vanish, resulting in a front portion of the tire tread-band of which the deflection w vanishes. Figure 7.4.26 shows a beautiful picture of the actual deformation when operating in excess of the critical speed.

The theoretical wave length of the standing wave varies with speed according to the following formula:

$$l = \frac{2\pi r}{\beta} = 2\pi r \sqrt{\eta \frac{\Omega^2 - \Omega_1^2}{\Omega_2^2 - \Omega^2}}. \quad (7.4.123)$$

Figure 7.4.28 gives a graphical representation of the variation of l with Ω . It should be noted that the wavelength increases with Ω from zero to infinity, at which Ω_2 has been reached.

c. $\Omega > \Omega_2$: This is a fictitious case as the tire will be destroyed long before this very high speed range is reached. The theory predicts two real roots for the stationary solution. A stationary situation, however, will never be reached since with the unloaded undisturbed tire, where derivatives with respect to θ vanish, according to eq (7.4.110) an unstable situation occurs. The last coefficient becomes negative in this speed range and the tire explodes.

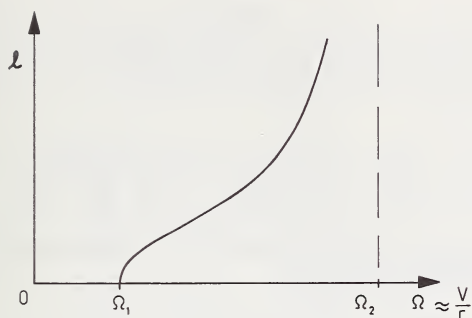


FIGURE 7.4.28. Wavelength l of the membrane type tire model as a function of speed V for the case that $\Omega_2 > \Omega_1$.

In the second category of values $\Omega_1 > \Omega_2$ which refers to the theory of Fiala, we distinguish:

a. $\Omega < \Omega_2 (< \Omega_1)$: Two real roots exist resulting again in a practically symmetric damped deflection on both sides of the contact area.

b. $\Omega_2 < \Omega < \Omega_1$: When a stationary deflection would have been attained, two complex roots $\lambda_{1,2} = -\alpha' \pm i\beta'$ arise with α' and β' representing positive real numbers. We find now a damped standing wave in front of the contact area (not recognized by Fiala) and vanishing deflections at the rear. The wavelength appears to decrease with increasing Ω until Ω_1 is attained, where the wavelength vanishes. This decrease corresponds to theoretical findings of Fiala who did not neglect the bending stiffness of the carcass tread band. This, however, does not influence the value of the critical rotational speed Ω_2 . Also when the bending stiffness is introduced, the tire is theoretically expected to explode in excess of Ω_2 so that Fiala's theory does not seem to have practical value. The third speed range, $\Omega > \Omega_1$, is of no interest to our analysis.

Influence of flexural rigidity.

The introduction of bending stiffness gives rise to additional terms in the equation of motion. Consideration of equation (7.4.90) with $u=0$, derived in the preceding section, shows the additions to be introduced. In case of deformations stationary with respect to an axes-system fixed in space, we may write $\partial/\partial\theta = -d/d\phi$. Equation (7.4.114) now becomes, when damping is omitted:

$$\frac{EI}{r^4} \frac{d^4 w}{d\phi^4} + \left(2 \frac{EI}{r^4} - \frac{S_0}{r^2} + \eta \rho \Omega^2 \right) \frac{d^2 w}{d\phi^2} + \left(c' + \frac{EI}{r^4} - \rho \Omega^2 \right) w = 0 \quad (7.4.124)$$

This equation differs in some respects ($EI (w'''' + w'')$ instead of $EI (w'''' + 2w'' + w)$) with respect to the equations of other authors

(Togo, Böhm, Drozdov, Fiala). We shall adopt the simplification introduced by Togo, viz omission of $\rho\Omega^2$ relatively to c' , and follow the line of his theory [40]. The following quantities are introduced for the sake of abbreviation:

$$\nu^2 = \frac{EI}{\eta\rho r^4}, \quad \Omega_1^2 = \frac{S_0}{\eta\rho r^2}, \quad \Omega_2^2 = \frac{c' + EI/r^4}{\eta\rho} \quad (7.4.125)$$

With Togo's simplification we obtain for the solutions $w = \exp(\lambda\phi)$ the following characteristic equation:

$$\nu^2\lambda^4 + (2\nu^2 - \Omega_1^2 + \Omega_2^2)\lambda^2 + \Omega_2^2 = 0 \quad (7.4.126)$$

with four roots determined by:

$$\lambda^2 = \frac{\Omega_1^2 - \Omega_2^2 - 2\nu^2 \pm \sqrt{(\Omega_1^2 - \Omega_2^2 - 2\nu^2)^2 - 4\nu^2\Omega_2^2}}{2\nu^2} \quad (7.4.127)$$

$$= \alpha \pm \sqrt{\alpha^2 - (\Omega_2/\nu)^2}.$$

The discriminant vanishes at two speeds Ω_L and Ω_U :

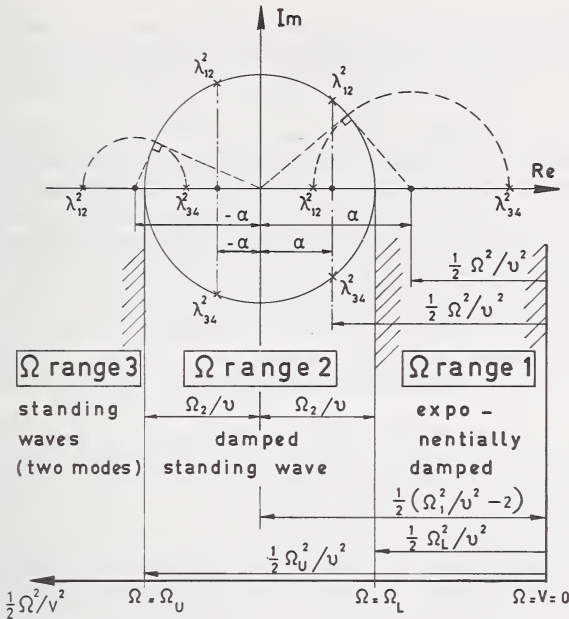
$$\begin{aligned} \Omega_L^2 &= \Omega_1^2 - 2\nu\Omega_2 - 2\nu^2, \\ \Omega_U^2 &= \Omega_1^2 + 2\nu\Omega_2 - 2\nu^2. \end{aligned} \quad (7.4.128)$$

These speeds represent the lower and upper critical rotational speeds for the stretched beam type of model, whereas Ω_1 is the critical rotational speed for the stretched string type model. The solution (7.4.42) may be divided into three speed ranges 1, 2 and 3 also indicated in figure 7.4.29:

1. $\Omega < \Omega_L$: Four real roots. The deflection curves are combinations of two damped exponential curves.
2. $\Omega_L < \Omega < \Omega_U$: Four complex roots. The deflection curves are of a damped oscillatory character.
3. $\Omega_U < \Omega$: Four imaginary roots. Standing waves are formed composed of two different modes.

As an effect of the bending stiffness, a range of rotational speed arises in which damped waves are formed in front of and behind the contact area. This speed range $\Omega_L < \Omega < \Omega_U$ is situated on both sides of the value $\sqrt{(\Omega^2 - \nu^2)}$, which represents the critical rotational speed arising when in eq (7.4.124) the fourth derivative is omitted.

Above the upper critical speed Ω_U the standing wave appears only behind the loading point. At $\Omega = \Omega_U$ the standing wave already has a

FIGURE 7.4.29. Solutions of λ^2 according to eq 7.4.27.

finite wavelength. Beyond this critical speed two wavelengths arise, one of which increases and the other decreases with increasing Ω , as may be deduced from figure 7.4.29. Turner [38] reported that such a combination of wavelengths indeed can occur in practice. It is expected, however, that in most cases the shorter waves are suppressed as a result of material damping.

Example of calculation of the critical speed and wavelength for a bias ply tire.

The following equation which corresponds to eq (7.4.124) seems to have been used by Drozdov and others [39] in their calculations:

$$C \frac{d^4 w}{d\xi^4} + \left(\frac{\bar{\rho} V^2}{p_i r_1} D - B \right) \frac{d^2 w}{d\xi^2} + \left(A - \frac{\bar{\rho} V^2}{p_i r_1} \right) w = 0. \quad (7.4.129)$$

The expressions for the parameters A , B , C and D used by Drozdov may be found in the original paper. The quantity r_1 denotes the radius of the tire cross section (half tire width) and $\xi = x/r_1$ represents the dimensionless tangential coordinate ($x = \phi r$).

Togo [40] adopted the same equations but used different expressions for A , B , C and D . We shall present here the theoretical and experi-

mental results of Togo for a bias ply Bridgestone tire with the following data (1 kgf. \approx 10 N): Tire 165 \times 400 4 Pr SAD; outer diameter $2r = 68$ cm.; tire width $2r_1 = 17$ cm.; inflation pressure $p_i = 1.3$ kgf/cm.², tire load 300 kgf.

The tire characteristic values to be used in the analysis are: crown angle = average cord angle measured from the wheel center plane $\alpha = 40^\circ$; number of cord plies $n = 4$; number of cords at tire crown per ply and per cm. width $i = 9$ cm.⁻¹; average thickness of tread band $h = h_1 + h_2 = 1.9$ cm.; distance from neutral ply to outer surface $h_1 = 1.7$ cm.; distance from neutral ply to inner surface $h_2 = 0.2$ cm.; elasticity modulus of rubber $E_R = 117$ kgf/cm.²; Poisson's ratio of rubber $\mu = 0.2$ (0.5 according to others); mass of tire per unit area $\bar{\rho} = 2.22 \times 10^{-6}$ kgf \cdot s²/cm.³; tensile elasticity modulus of a cord $E_C = 50$ kgf.; flexural rigidity of the ply layers per unit width $A_C = iE_C \sum_n y^2 \cos^4 \alpha = 7.75$

kgf \cdot cm. (y = distance of ply from neutral ply); flexural rigidity of rubber tread-band $A_R = \frac{1}{3} E_R (h_1^3 + h_2^3) / (1 - \mu^2) = 200$ kgf \cdot cm.; it has been assumed furthermore that the centrifugal force does not influence the tension S of this bias ply tire so that $\eta = 1$.

From Togo's analysis it can be deduced that the dimensionless parameters A , B , C and D of eq (7.4.129) are expressed as follows (the relations with parameters of eq (7.4.124) are given in between brackets):

$$\left. \begin{aligned} A & \left(= \frac{c' r^4 + EI}{2b p_i r_1 r^2} \right) = \frac{E_R h r^2 (1 + \tan^4 \alpha - 2\mu \tan^2 \alpha)}{p_i r_1^3 (1 - \mu^2)} \\ B & \left(= \frac{S_0 r^2 - 2EI}{2b p_i r_1^3} \right) = \left(\cot^2 \alpha - \frac{A_C + A_R}{p_i r_1^3} \right) \frac{r^2}{r_1^2} \\ C & \left(= \frac{EI r^2}{2b p_i r_1^5} \right) = \frac{A_C + A_R}{p_i} \cdot \frac{r^2}{r_1^5} \\ D & = \eta \frac{r^2}{r_1^2} \end{aligned} \right\} \quad (7.4.130)$$

Substitution of the solution $w = e^{i\beta\xi}$, β real, yields relations which hold in the speed range $\Omega > \Omega_U$ where standing waves are formed behind the contact area. The dimensionless reduced frequency β is inversely proportional to the wavelength l ,

$$\beta = \frac{2\pi r_1}{l}. \quad (7.4.131)$$

We obtain the equation:

$$C\beta^4 - \left(\frac{\bar{\rho} V^2}{p_i r_1} D - B \right) \beta^2 + \left(A - \frac{\bar{\rho} V^2}{p_i r_1} \right) = 0 \quad (7.4.132)$$

with the solution:

$$2C\beta^2 = \frac{\bar{\rho}V^2}{p_i r_1} D - B \pm \sqrt{\left(\frac{\bar{\rho}V^2}{p_i r_1} D - B\right)^2 - 4C\left(A - \frac{\bar{\rho}V^2}{p_i r_1}\right)}. \quad (7.4.133)$$

Again, two wavelengths occur theoretically. When the discriminant vanishes, the critical value of speed V_c is attained, above which sinusoidal solutions of w exist. At this point of transition the values of V , β and l will be provided with the index U . We derive:

$$V_c^2 = \frac{p_i r_1}{\bar{\rho} D} (B + 2C\beta_c^2) \quad (7.4.134)$$

$$\left(\approx \frac{p_i r_1}{\bar{\rho} D} (B + 2\sqrt{AC}) \right)$$

in which

$$\beta_c^2 = \left(\frac{2\pi r_1}{l_c}\right)^2 = -\frac{1}{D} + \sqrt{\frac{1}{D^2} - \frac{B}{CD} + \frac{A}{C}} \left(\approx \sqrt{\frac{A}{C}} \right). \quad (7.4.135)$$

Expression (7.4.135) is the same as the one used by Drozdov. With the tire data listed above we obtain: $V_c = 201$ km/hr. and $l_c = 16$ cm. With eqs (7.4.127–128) we find practically the same result for $V_c (= r\Omega_c)$ and l_c , the lower critical speed V_L becomes imaginary. For $V_1 = r\Omega_1$, which is the critical speed in case of the absence of bending stiffness, we obtain: $V_1 = 96$ km/hr. Considering equation (7.4.124) once again, it may be concluded that Togo's simplification ($\rho\Omega^2 \ll c'$) and the omission in the coefficients of w'' and w of El/r^4 (Böhm, Fiala, Togo, Drozdov) are permissible since their effects appear to be extremely small.

Togo has carried out a number of test runs on a steel drum using the tire described above. Wavelength and amplitude of the standing wave have been measured from photographs. Figure 7.4.30 shows the meas-

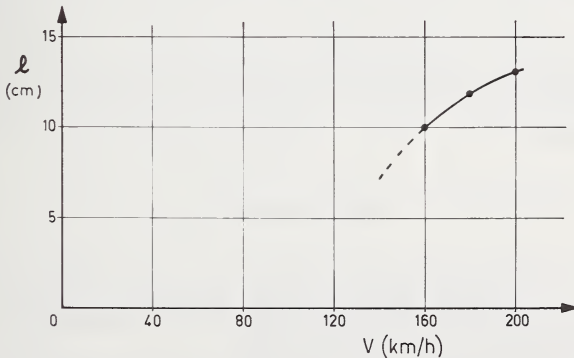


FIGURE 7.4.30. Experimentally obtained relation between wavelength l of standing wave and speed V for a Bridgestone cross-ply tire 165–400 ($p_i = 1.3$ bar) on a steel drum (Togo [40]).

ured relation of wavelength versus speed. At the speed 140 km/hr., Togo did not observe a wavy deformation but the endurance test was ended after four minutes due to ply separation.

Comparison with theoretical results suggests that the theory only provides an approximate insight into the problem. Drozdov reported similar discrepancies between theory and experiment. Attempts have been made to obtain a better agreement through the introduction of an effective (smaller) tread thickness for the calculation of the flexural rigidity. This may be supported by figure 7.4.26 (rear view) which clearly shows the manner in which the tread rubber deforms. If we assume that the effective thickness is half of the geometric thickness h , then the quantity $A_c + A_R$ becomes approximately one-eighth of its originally calculated value. The critical values become now: $V_c = 150$ km/hr. and $l_v = 9.5$ cm., which results are closer to the experimental values of figure 7.4.30.

From the analysis above and in particular from eq (7.4.134) with eq (7.4.130) it may be concluded that the critical speed is shifted to higher values when:

1. bending stiffness of tread EI is enlarged (n enlarged, α reduced),
2. tension force in tread S_0 is enlarged (p_i enlarged),
3. radial tire stiffness c_r is enlarged (shape cross section, sec. 7.4.1).
4. tensile tread-band rigidity c_s is enlarged (α reduced),
5. percentage of the centrifugal force restored by radial forces η is reduced (α reduced),
6. mass density ρ is reduced.

The influences of inflation pressure p_i , crown angle α and number of plies n are in accordance with experiments of Gardner and Worswick [37] (bias ply). Experiments of Curtiss show that unfavorable interaction between parameters may occur. From measured rolling resistance curves (cf. fig. 7.2.60) it is seen that radial and bias ply tires behave differently when the mass of the tread-band is reduced through removal of the tread. As expected, the bias ply tire then shows an increase in critical speed above which standing waves occur, causing a further progressive rise of the rolling resistance with speed. For the radial tire, however, it appears that the critical speed decreases, which, according to Curtiss, may be explained by the loss in carcass sidewall rigidity due to a reduction in tension in the sidewall caused by the decrease in tread-imposed centrifugal force.

References

- [1] Hadekel, R., The mechanical characteristics of pneumatic tires, S & T Memo, No. 10/52 (British Ministry of Supply, TPA 3/TIB, 1952).
- [2] Weber, G., Theorie des Reifens mit ihrer Auswirkung auf die Praxis bei hohen Beanspruchungen. A.T.Z. **56** (12), 325 (1954).
- [3] Marquard, E., Untersuchung über den Einfluss der Stossdämpfer auf die Zwischen Rad und Fahrbahn auftretenden senkrechten dynamischen Bodenkräfte, Deutsche Kraftfahrtforschung **104**, 32 (1957).
- [4] Chiesa, A., and Tangorra, G., The dynamic stiffness of tires, Revue Gên. du Caoutchouc **36**(10), 1321 (1959).

- [5] Rasmussen, R. E., and Cortese, A. D., Dynamic spring rate performance of rolling tires, SAE Paper No. 680408 (1968).
- [6] Betz, E. R., Studying structure dynamics with the cadillac road simulator, SAE Paper No. 660101 (1966).
- [7] Dodge, R. N., Dynamic stiffness of a pneumatic tire model, SAE Paper No. 650491 (1965).
- [8] Rotta, J., Zur Statik des Luftreifens, Ing. Archiv 1949, p. 129.
- [9] Senger, G., Ueber dynamische Radlasten beim Ueberrollen Kurzwelliger Unebenheiten durch schwere Luftreifen, Deutsche Kraftfahrtforschung **187** (1967).
- [10] Pacejka, H. B., Theoretische beschouwingen over het gedrag van luchtveren, De Ingenieur **72**(10), (maart 1960).
- [11] Clark, S. K., An analytical model for lateral stiffness of a pneumatic tire, Paper 3-01, FISITA, Barcelona, 1968.
- [12] Tiemann, R., Aehnlichkeitsbeziehungen im Federungsverhalten von Luftreifen, A.T.Z. **65**(4), 97 (1963).
- [13] Smiley, R. F., and Horne, W. B., Mechanical properties of pneumatic tires with special reference to modern aircraft tires, NASA Tech. Note 4110 (1958).
- [14] Gough, V. E., Tires and air suspension, Advances in Automobile Engineering, Tidbury, ed., (Pergamon Press, 1963).
- [15] Julien, M. M. A., and Paulsen, M. J., Méthode expérimentale de mesure et definition du pouvoir absorbant du pneumatique, J. de la S.I.A., janvier 1953, p. 33.
- [16] Lippmann, S. A., Piccin, W. A., and Baker, T. P., Enveloping characteristics of truck tires, SAE Trans. **74** (1966).
- [17] Lippmann, S. A., and Nanny, J. D., A quantitative analysis of the enveloping forces of passenger tires, SAE Paper No. 670174 (1967).
- [18] Barson, C. W., James, D. H., and Morcombe, A. W., Some aspects of tire and vehicle vibration testing, Proc. IME **182**, 3B, 32 (1967-68).
- [19] Guslitzer, R. L., On the interaction of a motor-vehicle tire with an obstacle, Translation 817, Rubber Res. Ass. British Rubber Manufacturers, 1957.
- [20] Hey, K. F., Untersuchungen von Längskräften zwischen Reifen und Fahrbahn beim Ueberfahren von Hindernissen, Diss. T. H. Braunschweig (1963).
- [21] Yu Chen, Studies of the interfacial phenomena during braking, Ford Motor Tech. Report A-788, 30 (1958).
- [22] Hörz, E., Der Einfluss von Bremskraftreglern auf die Brems- und Führungskraft eines gummiereiften Fahrzeugs, Deutsche Kraftfahrtforschung **195** (1968).
- [23] Holmes, K. E., and Stone, R. D., Tire forces as functions of cornering and braking slip on wet road surfaces, Proc. Symp. on Handling of Vehicles under Emergency Conditions, IME, Auto. Div. (1969).
- [24] Reynolds, O., On rolling friction, Phil. Trans. Roy. Soc. **166**, 155 (1876).
- [25] Fromm, H., Berechnung des Schlupfes beim Rollen deformierbarer Scheiben, ZAMM **7**, 27 (1927).
- [26] Julien, M., L'envirage et la tenue de route, S.I.A. (April 1937).
- [27] Chiesa, A., Obert, L., and Tamburini, L., High-frequency vibrations in tires under vertical perturbation and their transmission to the wheels, Auto. Engr., 520 (1964).
- [28] Chiesa, A., Vibrational performance differences between tires with cross-biased plies and radial plies, SAE Paper No. 990B (1965).
- [29] Barson, C. W., Gough, V. E., Hutchinson, J. C., and James, D. H., Tire and vehicle vibration, Proc. IME, Auto. Div., 1964-65, p. 213.
- [30] Strutt, J. W. (Lord Rayleigh), The Theory of Sound, Vol. 1, London, 1878, p. 332.
- [31] Bryan, J. W., On the beats in the vibrations of a revolving cylinder or bell, Proc. Cambr. Phil. Soc. **7**, 101 (1890).
- [32] Tielking, J. T., Plane vibration characteristics of a pneumatic tire model, SAE Paper No. 650492 (1965).
- [33] Böhm, F., Mechanik des Gürtelreifens, Ing. Archiv **35**, 82 (1966).
- [34] Fiala, E., and Willomeit, H. P., Radiale Schwingungen von Gürtel-Radialreifen, A.T.Z. **68** (2), 33 (1966).
- [35] Federhofer, K., Zur Schwingzahlberechnung des dünnwandigen Hohlenreifens, Ing. Archiv **10-11**, 125 (1939-1940).
- [36] Flügge, W., Handbook of Engineering Mechanics (McGraw-Hill, 1962), pp. 16-2, 24-6.
- [37] Gardner, E. R., and Worswick, T., Behaviour of tyres at high speed, Trans. I.R.I. **27**, 127 (1951).

- [38] Turner, D. M., Wave phenomena in tyres at high speed, Third Rubber Tech. Conf. London, Trans. I.R.I. (June 1954).
- [39] Drozdov, V. K., e.a., Formation of stationary waves on pneumatic tires at high rolling speeds, Sov. Rubber Tech. 19(12), 36 (1960).
- [40] Togo, K., Standing Wave on Pneumatic Tire at High Speed, Memoirs of the Defense Academy, Japan, Vol. IV, No. 1 (1964), p. 43.
- [41] Ames, W. F., Wave phenomena in tires, University of Iowa, Tech. Report 1 (1967).
- [42] Akasaka, T., and Yamagishi, K., On the standing waves in the shell wall of running tyre, Trans. Japan Soc. Aer. Space Sc. 11(18), 12 (1968).
- [43] Clark, S. K., The rolling tire under load, SAE Paper No. 650493 (1965).

7.5. Yaw and Camber Analysis

H. B. Pacejka

The so-called antisymmetric (cornering and camber) behavior of tires is of importance for the investigation of the maneuverability and stability of automobiles. In particular, the stationary (steady state) characteristics are employed in such investigations. However, the knowledge of nonsteady state tire properties is necessary for the investigation of transient motions or of parasitic motions such as shimmy.

The literature provides a vast amount of experimental data, which in particular covers the stationary cornering properties of tires. Cornering characteristics of automobile tires are published, amongst others, by Joy and Hartley [1],¹ Gauss and Wolff [2], Fonda [3], Freudenstein [4] (truck tires), Nordeen and Cortese [5], Henker [6], and Fonda and Radt [7]. With special reference to aircraft tires, Smiley and Horne [8] have presented a systematic survey of mechanical tire properties. Hadekel [9] (1952) and Smiley [10] (1956) gave critical outlines and extensions of existing theories for tire motions and wheel shimmy.

In the theory of tire mechanics relevant to the type of motion we are considering in this section, the road is assumed to be a smooth level boundary surface of an undeformable half space, while the tire is represented by some elastic model. The literature provides tire models of various degrees of complexity. For all these models the following fundamental observations are applicable.

When the tire moves over the road, horizontal deformations will generally occur over and above the deformation due to static vertical load. When the wheel moves in such a way that the contact points of an imaginary tire, which differs from the real tire only in that it does not show horizontal deformations, do not move with respect to the road, we speak of pure rolling. When all the contact points of that imaginary tire show the same relative velocity with respect to the road, we speak of longitudinal (fore and aft) slip or creep when this relative velocity and the rolling velocity have the same directions. We speak of lateral (side) slip or drift when the relative velocity is directed perpendicular to the rolling velocity. The angle between wheel center plane (direction of rolling) and the vector of the velocity of the wheel center is called the slip angle. When the wheel rotates about a vertical axis through the wheel center without showing longitudinal or lateral slip, we speak of pure spin. When the wheel plane is tilted with respect to the vertical plane, the tire is said to show a camber or inclination angle.

A real tire will show additional horizontal deformation. In the case of dry-frictional contact, the additional horizontal deformations may

¹ Figures in brackets indicate the literature references at the end of this section.

cally so that a finite contact area is present. The center C travels with a constant speed V over the $(\bar{x}, 0, \bar{y})$ plane. The traveled distance s equals

$$s = Vt \quad (7.5.1)$$

where t denotes the time. The tangent to the orbit of C makes an angle β with the fixed \bar{x} -axis. With respect to this tangent the x -axis is rotated with an angle α , defined as the slip angle. The angular deviation of the wheel plane with respect to the \bar{x} -axis (yaw angle) is denoted by

$$\psi = \beta + \alpha \quad (7.5.2)$$

For small values of β the following relation with \bar{y} , the lateral displacement of C , holds

$$\beta = \frac{d\bar{y}}{ds} \quad (7.5.3)$$

The horizontal displacements of a contact point with respect to its position in the horizontal undeformed situation with coordinates (x, y) are indicated by u and v in x - and y -direction respectively. The displacements are functions of x, y and the independent variable s or t .

The position in space of a material point of the rolling and slipping body in contact with the road (cf. fig. 7.5.1) is indicated by the vector

$$\bar{p} = \bar{s} + \bar{q}$$

where \bar{s} indicates the position of the contact center C in space and \bar{q} the position of the material point with respect to the moving system (x, C, y) ,

$$\bar{q} = (x + u)\bar{e}_x + (y + v)\bar{e}_y$$

with \bar{e}_x and \bar{e}_y representing the unit vectors. The vector of the sliding velocity of the material point relative to the road becomes ($\dot{x} = dx/dt$, etc.):

$$\bar{V}_s = \dot{p} = \dot{s} + \dot{q} = \bar{V} + (\dot{x} + \dot{u})\bar{e}_x + (\dot{y} + \dot{v})\bar{e}_y + \dot{\psi}\{(x + u)\bar{e}_y - (y + v)\bar{e}_x\}$$

in which \bar{V} denotes the vector of the speed of travel of the contact center C . We introduce furthermore:

$$\bar{V}_r = -(\dot{x}\bar{e}_x + \dot{y}\bar{e}_y)$$

denoting the vector of the rolling velocity and

$$\bar{V}_c = \bar{V} - \bar{V}_r$$

representing the vector of the slip or creep velocity of the body with respect to the road. We realize furthermore that

$$\dot{u} = \frac{du}{dt} = \frac{\partial u}{\partial x} \frac{dx}{dt} + \frac{\partial u}{\partial y} \frac{dy}{dt} + \frac{\partial u}{\partial t},$$

$$\dot{v} = \frac{dv}{dt} = \frac{\partial v}{\partial x} \frac{dx}{dt} + \frac{\partial v}{\partial y} \frac{dy}{dt} + \frac{\partial v}{\partial t}.$$

The sliding velocity becomes herewith in vectorial form:

$$\begin{aligned} \bar{V}_s = \bar{V}_c - \left\{ \frac{\partial u}{\partial x} V_{rx} + \frac{\partial u}{\partial y} V_{ry} - \frac{\partial u}{\partial t} + \frac{d\psi}{dt} (y+v) \right\} \bar{e}_x \\ - \left\{ \frac{\partial v}{\partial x} V_{rx} + \frac{\partial v}{\partial y} V_{ry} - \frac{\partial v}{\partial t} - \frac{d\psi}{dt} (x+u) \right\} \bar{e}_y. \end{aligned}$$

Henceforth we shall neglect the terms $v \cdot d\psi/dt$ and $u \cdot d\psi/dt$, as these are small of the second order.

The components in x - and y -direction of the sliding velocity V_s of a point of a rolling body in the contact area with respect to the road are in general:

$$V_{sx} = V_{cx} - y\omega_z - V_{rx} \frac{\partial u}{\partial x} - V_{ry} \frac{\partial u}{\partial y} + \frac{\partial u}{\partial t}, \quad (7.5.4)$$

$$V_{sy} = V_{cy} + x\omega_z - V_{rx} \frac{\partial v}{\partial x} - V_{ry} \frac{\partial v}{\partial y} + \frac{\partial v}{\partial t},$$

where (V_{cx}, V_{cy}) denotes the vector of the creep or slip velocity of the tire, which is the sliding velocity of the point C' of the horizontally undeformed imaginary tire, which coincides with the center C at the instant considered; (V_{rx}, V_{ry}) is the vector of the rolling velocity with which point C moves relative to C' . Moreover, ω_z denotes the angular velocity of the system (C, x, y, z) about the z -axis (yaw velocity):

$$\omega_z = \frac{d\psi}{dt} = \frac{d\beta}{dt} + \frac{d\alpha}{dt} \quad (7.5.5)$$

For better understanding, figure 7.5.1 illustrates the way in which V_{sy} arises for the case $V_{ry} = 0$. We will restrict ourselves to small values of lateral slip and assume $|\alpha| \ll 1$. For the system under consideration, i.e., the tire, where only rolling in the x -direction occurs, the following relations hold:

$$V_{rx} = V \text{ and } V_{ry} = 0, \quad (7.5.6)$$

when in addition the longitudinal creep velocity is taken equal to zero, which is approximately the case when no driving or braking forces are applied. We obtain for the creep or slip velocities:

$$V_{cx} = 0 \text{ and } V_{cy} = -V\alpha \quad (7.5.7)$$

We introduce the variable ϕ denoting the spin:

$$\phi = \frac{\omega_z}{V} = \frac{d\psi}{ds} \quad (7.5.8)$$

The latter part of this relation holds owing to eqs (7.5.1) and (7.5.5). We finally obtain the following expressions for the sliding velocities of a point with coordinates (x, y) :

$$\left. \begin{aligned} V_{sx}/V &= -\gamma\phi - \frac{\partial u}{\partial x} + \frac{\partial u}{\partial s} \\ V_{sy}/V &= -\alpha + x\phi - \frac{\partial v}{\partial x} + \frac{\partial v}{\partial s} \end{aligned} \right\} \quad (7.5.9)$$

When the vector of the pressure exerted in the positive direction by the tire upon the road is denoted by (p_x, p_y, p_z) , we obtain the following relations for the case with finite friction coefficient μ . In the adhesion region, defined as the area where no sliding occurs ($V_{sx} = V_{sy} = 0$), the relations

$$\left. \begin{aligned} \frac{\partial u}{\partial x} - \frac{\partial u}{\partial s} &= -\gamma\phi, & \frac{\partial v}{\partial x} - \frac{\partial v}{\partial s} &= -\alpha + x\phi, \\ \sqrt{p_x^2 + p_y^2} &< \mu p_z \end{aligned} \right\} \quad (7.5.10)$$

hold, and in a sliding region the relations (7.5.9). For the pressure we obtain in vectorial form:

$$(p_x, p_y) = \mu p_z (V_{sx}, V_{sy})/V_s \quad (7.5.11)$$

where

$$V_s = \sqrt{V_{sx}^2 + V_{sy}^2}, \quad (7.5.12)$$

the velocity components V_{sx}, V_{sy} being determined by (7.5.9).

For the case where only lateral slip occurs ($\phi = 0$), and, in addition, $p_x = V_{sx} = 0$ throughout the contact area (which may occur with simplified systems to be treated later on), the relations (7.5.9-11) reduce to:

$$\left. \begin{aligned} \frac{\partial v}{\partial x} - \frac{\partial v}{\partial s} &= -\alpha, \\ |p_y| &< \mu p_z \end{aligned} \right\} \quad \text{in an adhesion region,} \quad (7.5.13)$$

$$\left. \begin{aligned} \frac{\partial v}{\partial x} - \frac{\partial v}{\partial s} &= -\alpha - \frac{V_{sy}}{V}, \\ |p_y| &= \mu p_z \operatorname{sgn}^* V_{sy} \end{aligned} \right\} \quad \text{in a sliding region.} \quad (7.5.14)$$

*sgn signifies "sign of."

The equations above apply in general. Their solutions contain constants of integration which depend on the construction of the tire of which an approximate physical description may be given. In case of a steady state motion, the partial derivatives with respect to the distance traveled s become zero ($\partial v/\partial s = \partial u/\partial s = 0$).

Tire models.

Many theories are known which describe the qualitative or quantitative behavior of the steady state or nonsteady state drifting tire. The influence of camber has been studied only to a very limited extent. Due to the immense complexity of the tire structure most theories are restricted to a qualitative description of tire behavior. Particularly in case of the application of more advanced tire models, this qualitative picture can be adapted for quantitative use through fitting of the parameters. This can be done by means of full scale tire experiments, either static or semi-static [4, 11, 23] or with the rolling tire [13]. The first method leads to a greater insight into the problem, while the second achieves higher accuracy since in that case the cornering characteristics which are to be fitted are measured directly.

It should be pointed out that in order to avoid conceptual errors, which may arise due to the use of oversimplified models, the development of advanced tire models firmly based on actual tire geometry and material properties is of great importance. In this connection the work of Frank [11, 12] should be mentioned.

A fundamental difference in structure is apparent between the tire models employed in steady state and nonsteady state tire theories. In most steady state theories, a model is used consisting of an elastic structure (the carcass) provided with a great number of elastic tread elements (see fig. 7.5.2). The tread elements contact the road surface in the contact area, where a region of sliding may occur when the adhesion limit is locally exceeded. In most nonsteady state studies tread elements have been omitted and, in addition, adhesion has been considered complete in the entire contact area. The use of an elastic continuous structure representing the carcass is essential in nonsteady state tire theories.

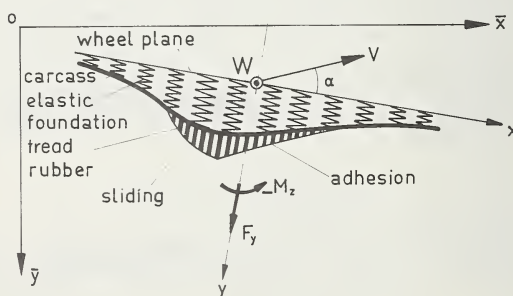


FIGURE 7.5.2. Top-view of tire model in steady state rolling with constant slip angle α .

7.5.1. Steady State Motion

Side Slip

Models of the carcass commonly encountered in the tire literature can either be of the beam type or of the stretched string type. The exact representation of the carcass by a beam instead of a stretched string is more difficult because of the fact that the differential equation for the shape of the deformed peripheral line of the carcass becomes of the fourth instead of the second order. For the study of steady state tire behavior, most authors therefore approximate the exact expressions for the lateral deformation of the beam.

As an extension of the model of Fromm and of Julien (cf. [9] for references) who did not consider carcass elasticity, Fiala [13] and Freudenstein [4] developed theories in which the carcass deformation has been approximated with a symmetric parabola determined only by the lateral force. Böhm [15] and Borgmann [16], the latter without tread elements, use asymmetric approximate shapes determined by both the lateral force and the aligning torque. Moreover, Böhm considers in his steady state side slip theory a two-dimensional contact area provided with a finite number of tread elements which due to the width of the tread, will also deform in longitudinal direction under lateral carcass deformation. As an additional complexity, Borgmann and Böhm both introduced a coefficient of friction which is a function of the sliding velocity.

Frank [11] has carried out a thorough comparative investigation of the various one-dimensional models. He employed a general fourth order differential equation with which stretched string, beam and stretched beam tire models can be examined. He obtained the exact solution of the stationary side slip problem with the aid of a special analog computer circuit. A correlation with Fourier components of the measured deformation of real tires revealed that the stretched string type of model is more suitable for the simulation of a bias ply tire, whereas the beam model is more appropriate for the radial ply tire. It appears, furthermore, that the use of a stretched string model requires a tension force which is of the order of 25000 N, whereas measurements of Hinton [14] indicate that the tension force amounts to about 2000 N. This implies that apparently the stiffness of the carcass (shear and bending) is responsible for the rest of the effective tension force.

In reference [23] Savkoor enunciates his theory for the development of a general mathematical model for the description of the lateral behavior of the tire. He uses results of experiments carried out with a tire which rolls slowly at a constant slip angle.

Figure 7.5.3 (taken from [12]) presents the calculated characteristics of several types of models. The parameters in cases *a*, *b* and *c* are chosen in such a way as to give a best fit to experimental data for the cornering force at small slip angles. Curves *d* show the result when carcass elasticity has been neglected and only the flexibility of the tread elements is taken into account (Fromm [9]). When the elastic constant of Fromm's model is chosen in a similar way, no difference between Fromm's and Fiala's results appear, since due to Fiala's approximations the coefficients

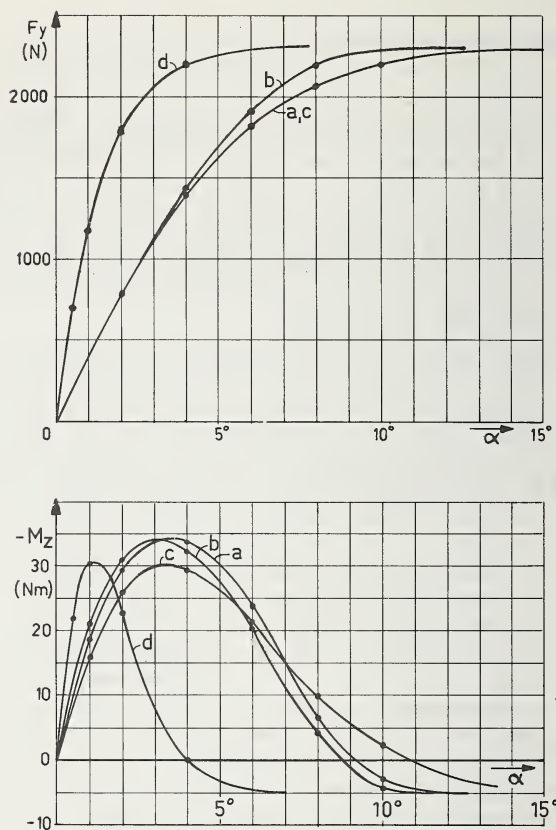


FIGURE 7.5.3. Comparison of calculated characteristics for the cornering force (F_y) and the aligning torque ($-M_z$) versus slip angle α (from Frank [12]).

Coefficient of friction μ constant. Vertical pressure distribution q_z slightly asymmetric. The curves stand for: a. stretched beam model, b. beam model, c. approximation of Fiala, d. model of Fromm (rigid carcass).

in the expressions for $F_y(\alpha)$ and $M_z(\alpha)$ are equal to those obtained directly by Fromm.

In the calculations for figure 7.5.3, Frank applied a vertical force distribution $q_z(x)$, found from measurements, lying between a parabolic and an elliptic shape. The positive aligning torque obtained at high values of α (fig. 7.5.3) arose due to a slightly asymmetric shape of $q_z(x)$ introduced in those calculations. The phenomenon that in practice the aligning torque indeed varies in this way is probably due to a combination of several effects. Apart from the cause just mentioned above, the rolling resistance force acting out of the wheel plane, due to the lateral deformation, may contribute. Another important factor causing the moment to become positive is the fact that the coefficient of friction is not a constant but depends on the sliding velocity, the latter

having its highest values in the real portion of the contact area. This factor may also cause the slight drop in the $F_y(\alpha)$ curves as has sometimes been found experimentally at high values of α . The influence of different but symmetric shapes for the vertical force distribution along the x -axis has been theoretically investigated by Borgmann [16]. He finds that, especially for tires exhibiting a low carcass stiffness, the influence of the pressure distribution is of importance and has, as may be expected, particular effect on the aligning torque at higher values of the slip angle. Many authors adopt the parabolic distribution for purpose of mathematical simplicity (Fiala [13], Freudenstein [4], Bergman [17], Pacejka [18]).

Figure 7.5.3 shows that, when the model parameters are chosen properly, the choice of the type of carcass model hardly influences the results. For illustration, we shall present now the theory of steady state side slip with the aid of the simple model of Fromm (cf. [9]), and the more advanced model of the stretched string type with and without tread elements (for details cf. Pacejka [19]). These two examples were chosen for reasons of their connection with theories to be presented later on concerning the influence of a driving or braking force and non-steady state tire behavior, respectively.

Tire model with elastic tread elements and rigid carcass (Fromm).

The model to be treated first is shown in figure 7.5.4. The steady state drifting tire shows a contact line which is straight and parallel to the velocity vector V in the adhesion region, and curved in the sliding region where the available side force becomes lower than the force which would be required for the tips of the tread elements to follow the straight line further. In the adhesion region the shape of the deformation is in accordance with the general equation (13). It is easy to prove that at the leading edge the deformation of the tread elements vanishes. Consequently the lateral deformation in the adhesion region reads, when the drift angle α is assumed to be relatively small so that we can

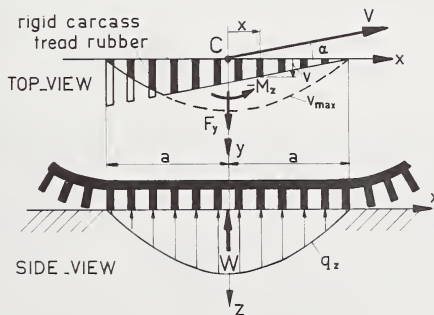


FIGURE 7.5.4. Simple model of drifting tire (Fromm).

write $\tan \alpha \approx \alpha$:

$$v = (a - x)\alpha \quad (7.5.15)$$

where a denotes half the contact length.

In case of vanishing sliding, which will occur for $\alpha \rightarrow 0$ or for $\mu \rightarrow \infty$, expression (7.5.15) holds for the entire region of contact. After the introduction of the total lateral stiffness c_p of all profile elements per unit length of the assumedly rectangular contact area, the following expressions for the cornering force F_y and the aligning torque $-M_z$ are obtained:

$$\left. \begin{aligned} F_y &= c_p \int_{-a}^a v dx = 2c_p a^2 \alpha \\ -M_z &= -c_p \int_{-a}^a v x dx = \frac{2}{3} c_p a^3 \alpha \end{aligned} \right\} \quad (7.5.16)$$

The cornering stiffnesses for the force and the moment consequently become respectively:

$$\left. \begin{aligned} C_{F\alpha} &= (\partial F_y / \partial \alpha)_{\alpha=0} = 2c_p a^2 \\ C_{M\alpha} &= -(\partial M_z / \partial \alpha)_{\alpha=0} = \frac{2}{3} c_p a^3 \end{aligned} \right\} \quad (7.5.17)$$

We will consider now the case of a finite value of μ and a pressure distribution which gradually drops to zero at both edges. For purpose of simplicity we assume a parabolic distribution of the vertical force per unit contact length as expressed by

$$q_z = \frac{3W}{4a} \left\{ 1 - \left(\frac{x}{a} \right)^2 \right\} \quad (7.5.18)$$

where W represents the vertical wheel load ($= -F_z$). The largest possible side force distribution consequently reads:

$$q_{y \max} = \mu q_z = \frac{3}{4} \mu W \left(\frac{a^2 - x^2}{a^3} \right) \quad (7.5.19)$$

In figure 7.5.4 the maximum possible lateral deformation $v_{\max} = q_{y \max} / c_p$ has been indicated. We introduce for the sake of abbreviation the following tire model parameter

$$\theta = \frac{2}{3} \left(\frac{c_p a^2}{\mu W} \right) \quad (7.5.20)$$

The distance from the leading edge to the point where the transition from the adhesion to the sliding region occurs equals $2a\lambda$ and is determined

by the nondimensional quantity λ , which bears the following relation to the slip angle α (assumed positive):

$$\lambda = 1 - \theta\alpha. \quad (7.5.21)$$

From this equation the angle α_{sl} can be calculated, at which total sliding starts ($\lambda = 0$):

$$\alpha_{sl} = 1/\theta. \quad (7.5.22)$$

The force F_y and the moment M_z can now be derived easily as a function of α . The results read:

$$\left. \begin{aligned} F_y &= \mu W(1 - \lambda^3) = \mu W \{ 3\theta\alpha - 3(\theta\alpha)^2 + (\theta\alpha)^3 \} \\ &\quad \text{for } \alpha < \alpha_{sl} \\ F_y &= \mu W \\ &\quad \text{for } \alpha_{sl} < \alpha < \frac{\pi}{2} \end{aligned} \right\} \quad (7.5.23)$$

$$\left. \begin{aligned} -M_z &= \mu W \lambda^3(1 - \lambda) = \mu W a \{ \theta\alpha - 3(\theta\alpha)^2 + 3(\theta\alpha)^3 - (\theta\alpha)^4 \} \\ &\quad \text{for } \alpha < \alpha_{sl} \\ M_z &= 0 \\ &\quad \text{for } \alpha_{sl} < \alpha < \frac{\pi}{2} \end{aligned} \right\} \quad (7.5.24)$$

These relationships are shown graphically in figure 7.5.5. They correspond with curves *c* or *d* in figure 7.5.3, but now for a symmetric parabolic pressure distribution. The pneumatic trail t , which indicates the distance behind the contact center C where the resultant lateral force acts, becomes at vanishing slip angles:

$$t_0 = - \left(\frac{M_z}{F_y} \right)_{\alpha \rightarrow 0} = \frac{C_{M\alpha}}{C_{F\alpha}} = \frac{1}{3} a \quad (7.5.25)$$

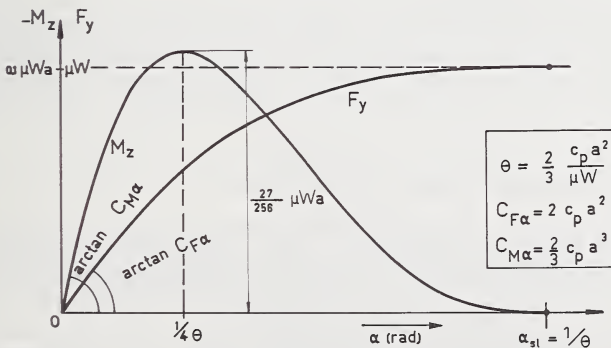


FIGURE 7.5.5 Cornering characteristics of the simple model with rigid carcass (Fromm).

This value is smaller than normally encountered. The introduction of an elastic carcass will, as we shall see, improve this quantitative aspect.

Another point in which the simple model deviates considerably from experimental results is the effect of a variation of the vertical wheel load W . With the assumption that a changes quadratically with W , it can easily be shown the F_y and M will vary proportionally with W and $W^{3/2}$ respectively. As will appear later in this respect also the introduction of an elastic carcass improves agreement with experiment.

It should be noted that Fiala, who obtained the same expressions (7.5.23–24) via approximation of his more complex relations derived from a model with both beam and tread rubber, succeeded in finding suitable values of his original model parameters (combinations of which govern the parameter comparable with our quantity θ) so that reasonable agreement with experimental curves are obtained including the variation with wheel load W . This latter relation $F_y(W)$ even appears to show a maximum, after which F_y drops with increasing W . An investigation is needed as to whether this drop is due to the approximation of a symmetric parabolic shape of carcass. It should be noted that with Fiala's model a drop of F_y versus W is accompanied by a region of negative lateral force distribution in the forward portion of the contact line. This force distribution does not appear to be possible for stretched string tire models. Another theory explaining this drop, which has been observed in many experiments (Gauss and Wolff [2]), makes use of the reduction of the lateral stiffness of the carcass as a function of vertical deflection, due to variations in geometry of the cross section of the tire in the contact region (cf. Rotta [20] for theory, Smiley and Horne [8] for experimental verification and Bergman [17] for application).

Curves obtained in the experiments of Freudenstein [4] for truck tires and Nordeen and Cortese [5] for passenger car tires do not show such a maximum in their ranges of measurement. As an illustration, some experimental results are shown in figures 7.5.6–8. In these figures different ways of plotting are shown, each of which have their specific advantages. The curves of figure 7.5.6 may be more suitable for use in the analysis of automobile motions. Both the functions $F_y(\alpha)$ and $F_y(W)$ are directly obtainable from this kind of carpet plot. For further information we refer to part 7.3 which contains an extensive collection of experimentally determined cornering force and aligning torque characteristics (figs. 7.3.22–35). In order to obtain a deeper insight into the problems related to side slip, we shall turn now to the treatment of a more advanced tire model.

Stretched string model with tread elements.

The analysis to be presented now has been taken in an abridged form from Pacejka [19]. We shall start with a more general analysis which will also cover the possibility of antisymmetric longitudinal deformations occurring in the shimmy motion to be dealt with in section 7.5.3. In figure 7.5.9 a top view of the model is shown in an arbitrary position. The carcass is represented by a number of elastically supported parallel strings under tension, which are connected by cross cords. The points

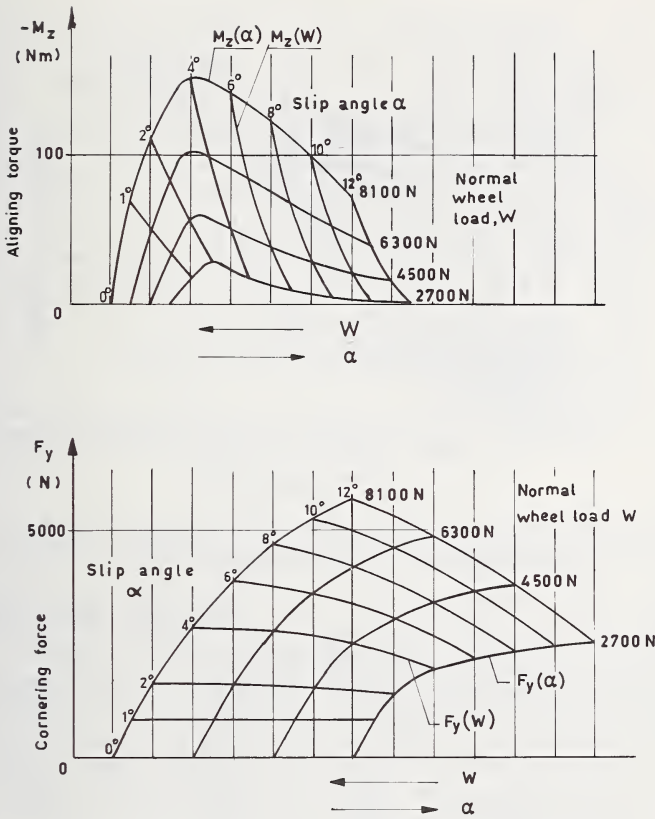


FIGURE 7.5.6. Carpet plots of cornering characteristics for 7.60-15 tire (presumably conventional cross-ply), $p_i \approx 2$ bar.

Dry flat road surface, low speed (from Nordeen and Cortese [5]).

of connection can move only laterally, and their mutual distance remains the same. When the strings are deformed laterally the rubber between the strings will be sheared. Through the continuous elastic support, axial forces distributed over the length of the band can be transmitted to the wheel plane. To this band under tension, several rows of an infinite number of elastic blocks are attached, representing tread elements. In contact area of length $2a$ and width $2b$ the ends of these elements are in contact with the road surface. The strings are assumed to be of infinite length.

The longitudinal deformation u is assumed to be proportional to the longitudinal component of the contact pressure. The following relation holds:

$$p_x = -c_{px}u, \quad (7.5.26)$$

where p_x is the force and c_{px} the longitudinal stiffness of the profile elements, both per unit area.

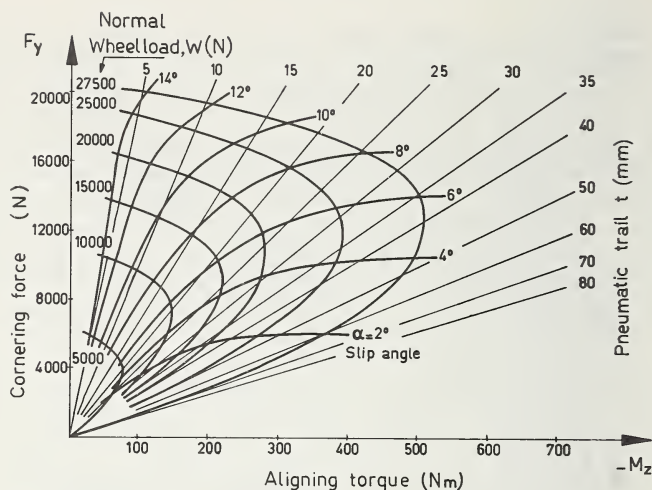


FIGURE 7.5.7. Gough-plot of truck cross-ply tire 9.00-20 eHD, $p_i = 5.5$ bar.

Dry road measurements, $V = 10$ Km/h (from Freudenstein, Ref. [4]).

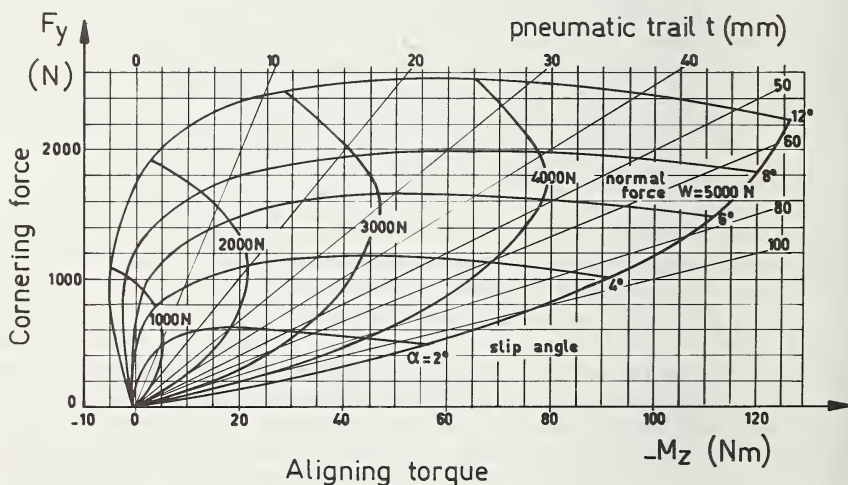


FIGURE 7.5.8. Gough-plot of 6.00-13 Dunlop tire, $p_i = 1.4$ bar, dry internal drum with inner diameter 3.8 m, speed $V = 40$ km/h (from Henker [6]).

The lateral deflection v is made up of the lateral deflection of the string (the carcass) v_c and the lateral deflection of the tread rubber v_p :

$$v = v_c + v_p. \quad (7.5.27)$$

We will consider only the case where v_p is constant along the width of

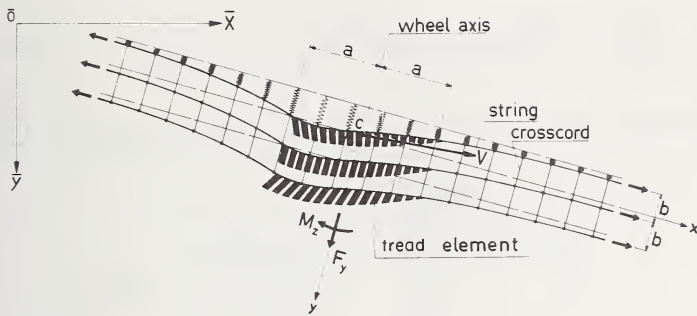


FIGURE 7.5.9. Top-view of tire model considered.

the contact area, as will occur in cases to be investigated. We assume v_p to vary proportionally with q_y as expressed by:

$$2bp_y = q_y = -c_p v_p \quad (7.5.28)$$

where q_y denotes the lateral force and c_p the lateral stiffness of the tread elements, both per unit length.

In order to obtain an expression for the deflection of the strings we must consider the equilibrium of an element of the tire model as shown in figure 7.5.10, where the longitudinal displacements u , resulting in a second-order effect, are neglected. In the lateral direction, the equilibrium of forces acting on the element of length dx and full tread width $2b$ results in the following equation:

$$\begin{aligned} -q_y dx - c_c v_c dx + D - D - \frac{\partial D}{\partial x} dx - S_1 \frac{\partial v_c}{\partial x} \\ + S_1 \left(\frac{\partial v_c}{\partial x} + \frac{\partial^2 v_c}{\partial x^2} dx \right) = 0, \end{aligned} \quad (7.5.29)$$

where c_c denotes the carcass stiffness ("pneumatic stiffness") per unit length (cf. eq (7.4.6), fig. 7.4.2), S_1 the longitudinal component of the total tension force in the strings and D the shear force in the cross section of the tread-band. The shear force is assumed to be a linear function of the shear angle, according to the formula:

$$D = -S_2 \frac{\partial v_c}{\partial x}. \quad (7.5.30)$$

With the introduction of the constant $S = S_1 + S_2$ we deduce from eq (7.5.29):

$$q_y = S \frac{\partial^2 v_c}{\partial x^2} - c_c v_c. \quad (7.5.31)$$

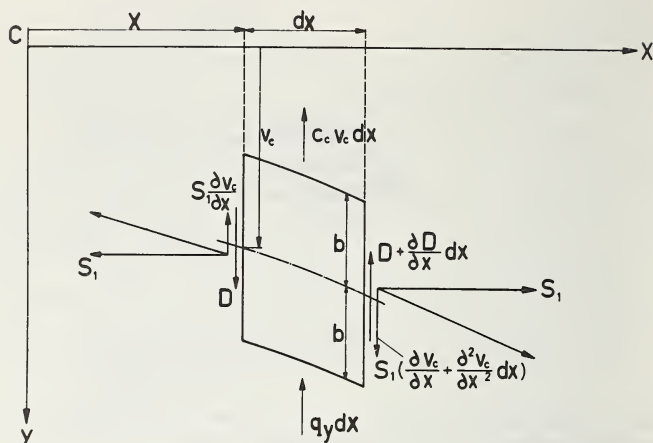


FIGURE 7.5.10. Equilibrium of deflected tire element.

In the part of the tire not making contact with the road the contact pressure vanishes so that:

$$S \frac{\partial^2 v_c}{\partial x^2} - c_c v_c = 0 \quad \text{for } |x| > a. \quad (7.5.32)$$

For that part making contact with the road we obtain, with eqs (7.5.27–28, 7.5.31)

$$S \frac{\partial^2 v_c}{\partial x^2} - c_c v_c = -c_p (v - v_c) \quad \text{for } |x| < a \quad (7.5.33)$$

We introduce the tire constants:

$$\sigma = \sqrt{\frac{S}{c_c}}, \sigma_c = \sqrt{\frac{S}{c_c + c_p}}, \text{ and } \epsilon = \frac{\sigma_c}{\sigma} = \sqrt{\frac{1}{1 + c_p/c_c}}. \quad (7.5.34)$$

With increasing tread rubber stiffness the value of the parameter ϵ decreases until it vanishes when $c_p \rightarrow \infty$, which represents the case of no tread elements. When the quantities defined in eq (7.5.34) are introduced, one obtains the equations of equilibrium (7.5.31), (7.5.32), and (7.5.33) as

$$\sigma^2 \frac{\partial^2 v_c}{\partial x^2} - v_c = q_y / c_c, \quad (7.5.35)$$

$$\sigma^2 \frac{\partial^2 v_c}{\partial x^2} - v_c = 0 \quad \text{for } |x| > a, \quad (7.5.36)$$

$$\sigma_c^2 \frac{\partial^2 v_c}{\partial x^2} - v_c = -(1 - \epsilon^2)v \quad \text{for } |x| < a. \quad (7.5.37)$$

For large values of $|x|$ the deflection v_c tends to zero. Therefore the solution to eq (7.5.36) reads:

$$\begin{aligned} v_c &= C_1 e^{-x/\sigma} & \text{for } x > a \\ v_c &= C_2 e^{x/\sigma} & \text{for } x < -a \end{aligned} \quad (7.5.38)$$

At boundaries $x = \pm a$ we obtain:

$$\begin{aligned} v_c &= -\sigma \lim_{x \downarrow a} \frac{\partial v}{\partial x} & \text{for } x = a \\ v_c &= \sigma \lim_{x \uparrow -a} \frac{\partial v}{\partial x} & \text{for } x = -a \end{aligned} \quad (7.5.39)$$

Since for $x = \pm a$ the deflection v_c and its derivative $\partial v_c / \partial x$ vary continuously with x , the latter due to the fact that no finite concentrated forces can act on the strings, with finite deflection v_p and finite stiffness c_p (cf. also eqs (7.5.28) and (7.5.31)), in the expressions (7.5.39) the limit signs may be omitted, after which they can be used as boundary conditions for the solution of equation (7.5.37). For the determination of the integration constants occurring in the solutions of the first-order partial differential equations (7.5.9), the additional conditions are needed that the deflections v and u vary continuously at the leading edge, where $x = a$. That this continuity does take place can be proved in the following way.

For the real tire, where μ is finite and the vertical pressure gradually tends to zero at the leading and trailing edges of the contact area, it will be obvious that the tread elements show no deflection just after entering the contact area or just before leaving this area. Consequently the deflections vary continuously in the neighborhood of both edges in this case.

For the extreme case where finite shear stresses are available at the leading and trailing edge of the contact area ($\mu \rightarrow \infty$) a finite deflection may occur at these edges. It can be shown, however, that if we consider vanishing regions of sliding at both edges, at the leading edge sliding velocities would occur which produce friction forces directed opposite to the external forces required for maintaining the discontinuity, whereas at the trailing edge this will not occur. Similar findings are obtained for the model without tread rubber when kinks are assumed in the string at both edges. The conclusion must be that only at the trailing edge may a finite change in deflection of the tread rubber, or a kink in the string without tread rubber, occur in the extreme case as $\mu \rightarrow \infty$ (cf. [19] for detailed discussion).

The forces and the moment acting on the tire may be computed by

integration over the contact area A . The forces in the longitudinal and lateral directions become respectively:

$$F_x = - \int_A p_x dA, \quad F_y = - \int_A p_y dA. \quad (7.5.40a)$$

The moment about the vertical axis reads:

$$M_z = \int_A (p_x y - p_y x) dA. \quad (7.5.40b)$$

In case of purely lateral slip the tire model does not show longitudinal deformations, so that $p_x = F_x = 0$. The lateral force and the moment then, become:

$$F_y = - \int_{-a}^a q_y dx, \quad M_z = - \int_{-a}^a q_x x dx. \quad (7.5.41)$$

The general analysis derived above will be applied here for the case of steady state rectilinear side slip. As before, the vertical force distribution is assumed parabolic along the x -axis. We obtain for the lateral force distribution in the region of sliding:

$$2bp_y = q_y = \mu q_z \operatorname{sgn} V_{sy} \quad (7.5.42)$$

where

$$q_z = 2bp_z = \frac{3W}{4a} \left\{ 1 - \left(\frac{x}{a} \right)^2 \right\}. \quad (7.5.43)$$

When we reduce the slip angle from a large value, where total sliding occurs, we find a point of first adhesion which is situated somewhat behind the leading edge when the model parameter ϵ is smaller than a certain critical value depending on σ , i.e., when the lateral stiffness of the tread rubber exceeds a certain value. This means that when reducing the slip angle further, two regions of sliding occur: a small region in front of and a much larger one behind the region of adhesion. The critical value of ϵ above which adhesion occurs immediately at the leading edge is given by the following formula

$$\epsilon_{cr}^2 = \frac{1 - \left(\frac{\sigma}{a} \right) \tanh \left(\frac{\sigma}{a} \right)}{1 + \frac{\sigma}{a}}. \quad (7.5.44)$$

We shall discuss here only the results for a model with relatively low tread rubber stiffness exhibiting only one sliding region, and for a model without tread rubber elements ($c_p \rightarrow \infty$) showing two sliding regions. Figure 7.5.11 shows the deflected tire model of the former kind. Differential equations (7.5.13) and (7.5.37) are applicable for the adhesion region ($a_2 < x < a$) and (7.5.35) and (7.5.43) for the sliding region ($-a < x < a_2$).

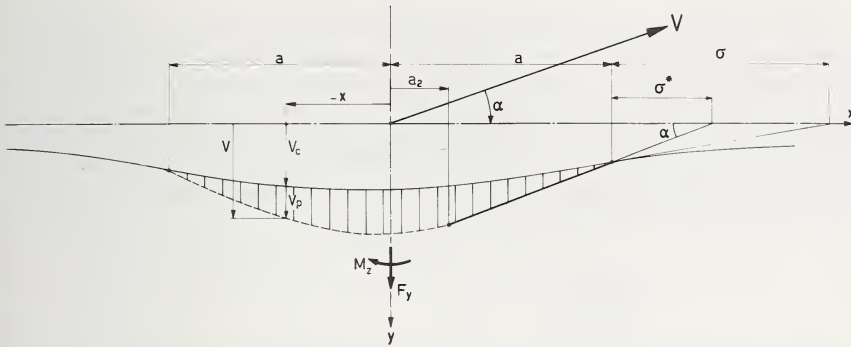


FIGURE 7.5.11. Deflected tire model provided with tread elements, showing an adhesion and a sliding region.

There are five constants of integration and one unknown a_2 . We therefore need six boundary conditions in order to find these.

These conditions follow from (7.5.39) and the discussions thereafter. The slip angle α and the shape of the deformation are calculated as a function of the distance a_2 for the special case $\epsilon = 1/7.5$ and $\sigma = 3.74 a$. Figure 7.5.12 shows the shape for a number of cases. The obliquely shaded area indicates the sliding regions, which grow with increasing slip angle until the whole contact line slides. Larger slip angles will not alter the shape anymore.

The relaxation length σ^* has been defined as the distance between the leading edge of the contact area and the point of intersection of the elongation of the straight portion of the contact line with the x -axis. The values of σ and ϵ mentioned above were chosen in such a way that σ^* tends to the value $3a$ for $\alpha \rightarrow 0$. Note that the relaxation length decreases from the value $3a$ to a value somewhat below $2a$ when total sliding starts. This property has been confirmed experimentally by Metcalf [55].

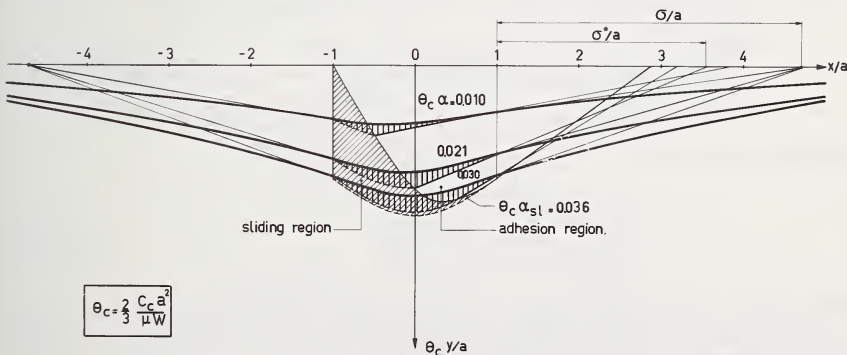


FIGURE 7.5.12. The tire model drifting at various slip angles α ($\sigma = 3.74a$, $\epsilon = 1/7.5$).

The shaded area indicates the regions where sliding occurs.

Once the deflection of the tire model is known, the force and moment can be calculated by the use of eqs (7.5.14) and (7.5.28). Integration over the contact length as indicated by eq (7.5.41) yields expressions for F_y and M_z in terms of a_2 . Figure 7.5.13 shows the calculated tire characteristics. As with Fromm's model, the slope of both curves becomes zero at the slip angle α_{sl} where total sliding starts. We shall see that this is not the case when the tread rubber is removed from the string ($c_p \rightarrow \infty$, $\epsilon = 0$, $\sigma^* = \sigma$, $v_p = 0$, $v = v_c$).

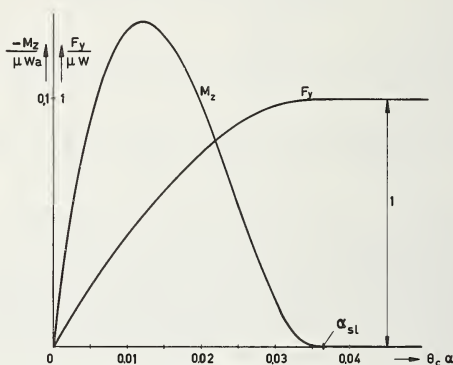


FIGURE 7.5.13. Tire cornering characteristic for the tire model with tread rubber ($\sigma = 3.47a$, $\epsilon = 1/7.5$).

String model without tread rubber elements.

Figure 7.5.14 shows this simple string model in a deflected situation. Two regions of sliding are expected to occur. In the region of adhesion ($a_2 < x_1 < a_1$) the stationary version of eq (7.5.13) holds. The sliding regions are governed by eqs (7.5.35) and (7.5.42). In the straight portion of the contact line where adhesion occurs, the following inequality holds according to eqs (7.5.35), (7.5.13), (7.5.42), and (7.5.43):

$$v < \frac{1}{2} \frac{a}{\theta_c} \left\{ 1 - \left(\frac{x}{a} \right)^2 \right\} \quad (7.5.45)$$

with the parameter

$$\theta_c = \frac{2}{3} \frac{c_c a^2}{\mu W}. \quad (7.5.45a)$$

This means that the straight portion of the contact line lies inside the parabola as indicated in figure 7.5.14. The points of inflection of the contact line are located on this parabola when $V_{su} < 0$ in these points. Near the edges $x = \pm a$ the available lateral force tends to zero. Since a finite deflection $v > 0$ is present in these places, the curvature of the

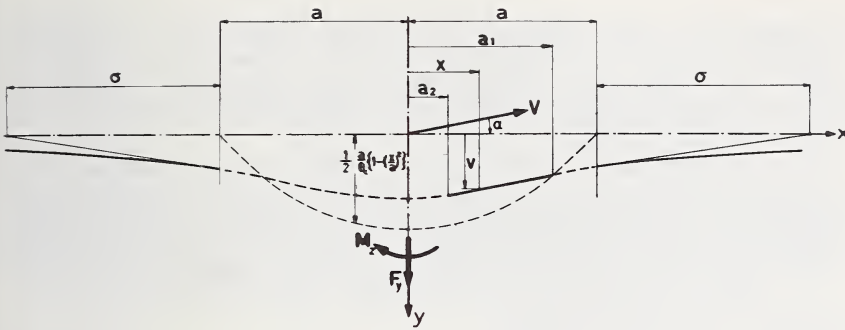


FIGURE 7.5.14. Deflected tire model without tread rubber showing two sliding regions.

string will be concave ($d^2v/dx^2 > 0$) according to (7.5.35). In the rear portion of the contact line we have $dv/dx > 0$, so that according to (7.5.14) $V_{sy} < 0$. Until the contact line intersects the parabola, the shape remains concave. Inside the parabola, however, the curve becomes convex. The boundary of the adhesion region is at $x = a_2$. The point of transition to the front sliding region is denoted by $x = a_1$. When this latter point lies inside the parabola, according to (7.5.35), the curve must be convex just in front of that point when the sliding velocity is negative. This shape, however, would lead to an increase in slope, so that according to (7.5.14) the sliding direction becomes positive in that case, which is in contradiction with the assumption. In the same way a concave shape can be shown to be impossible. The conclusion must be that this point of transition must lie on the parabola. The curve in the front sliding region can only be concave, so that $V_{sy} < 0$. Its curvature tends to zero when the parabola is approached. This forms one of the seven boundary conditions necessary for the calculation of a_1 and a_2 and the five constants

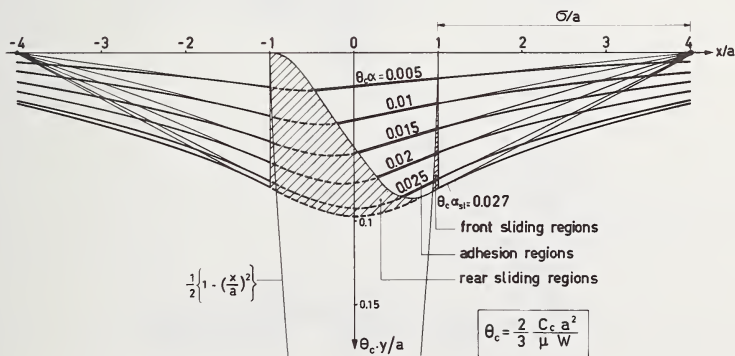


FIGURE 7.5.15. The tire model drifting at various slip angles α ($\sigma = 3a, \epsilon = 0$).

The shaded areas indicate the regions of sliding.

of integration in the solutions for the three differential equations. By means of iteration the contact line has been computed for a number of values of the slip angle α . Figure 7.5.15 shows the results. The variation of the relaxation length with slip angle will be extremely small for the model considered.

The cornering force and the aligning torque are found by integrating the external lateral forces along the contact line. The results of the computations are shown in figure 7.5.16. In contrast to the characteristics of the model with tread elements shown in figure 7.5.13, the curves show a discontinuity at the slip angle where total sliding starts.

Behavior at vanishing sliding.

It is of interest to know the behavior of both models with and without tread rubber in case of vanishing sliding, i.e., for coefficients of friction tending to infinity or for slip angles tending to zero (see fig. 7.5.17). The model without tread rubber and with vanishing sliding was originally treated by von Schlippe [9, 25, 26] and Temple [9]. Their theory is of particular importance for the study of nonsteady state motions as treated in section 7.5.3.

Omitting the detailed calculations, we obtain for the lateral deflection at the foreword contact point:

$$v_1 = \sigma^* \alpha \quad (7.5.46)$$

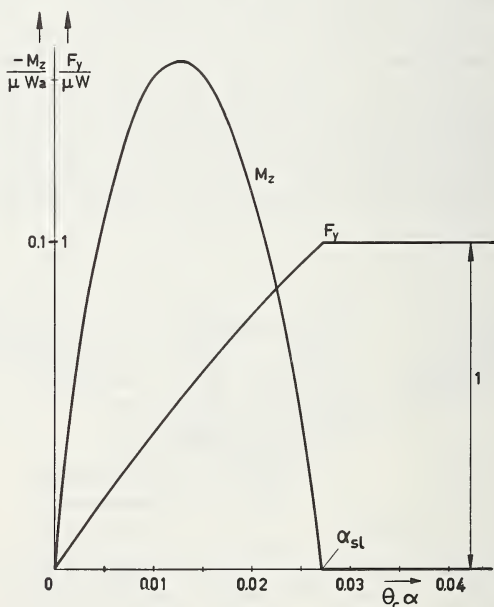


FIGURE 7.5.16. Tire cornering characteristics for tire model without tread elements ($\sigma = 3a$, $\epsilon = 0$).

where

$$\sigma^* = \frac{\sigma \{ (1 + \epsilon) e^{2a/\sigma_c} + (1 - \epsilon) e^{-2a/\sigma_c} - 2 \} - 4a}{\frac{1 + \epsilon}{1 - \epsilon} e^{2a/\sigma_c} + \frac{1 - \epsilon}{1 + \epsilon} e^{-2a/\sigma_c} + 2} \quad (7.5.47)$$

which is the expression for the relaxation length at zero slip angle as previously defined (see figure 7.5.17a). The relaxation length equals σ when the tread stiffness tends to infinity (see fig. 7.5.17b).

The cornering force and aligning torque becomes in this case:

$$F_y = C_{F\alpha} \alpha \text{ and } -M_z = C_{M\alpha} \alpha \quad (7.5.48)$$

with the stiffnesses $C_{F\alpha}$ and $C_{M\alpha}$ having the following values:

$$C_{F\alpha} = 2c_c(1 - \epsilon^2) \left[(\sigma^* + a)a - \frac{1}{4}\sigma\sigma^* \{ (1 + \epsilon) e^{2a/\sigma_c} + (1 - \epsilon) e^{-2a/\sigma_c} - 2 \} + \frac{1}{4}\sigma^2(1 - \epsilon^2)(e^{2a/\sigma_c} + e^{-2a/\sigma_c} - 2) \right], \quad (7.5.49)$$

$$C_{M\alpha} = 2c_c(1 - \epsilon^2) \left[\frac{1}{3}a^3 - \frac{1}{4}\sigma \{ \sigma^*(1 + \epsilon) - \sigma(1 - \epsilon^2) \} \{ a(1 + e^{2a/\sigma_c}) + \sigma_c(1 - e^{2a/\sigma_c}) \} - \frac{1}{4}\sigma \{ \sigma^*(1 - \epsilon) - \sigma(1 - \epsilon^2) \} \{ a(1 + e^{-2a/\sigma_c}) - \sigma_c(1 - e^{-2a/\sigma_c}) \} \right]$$

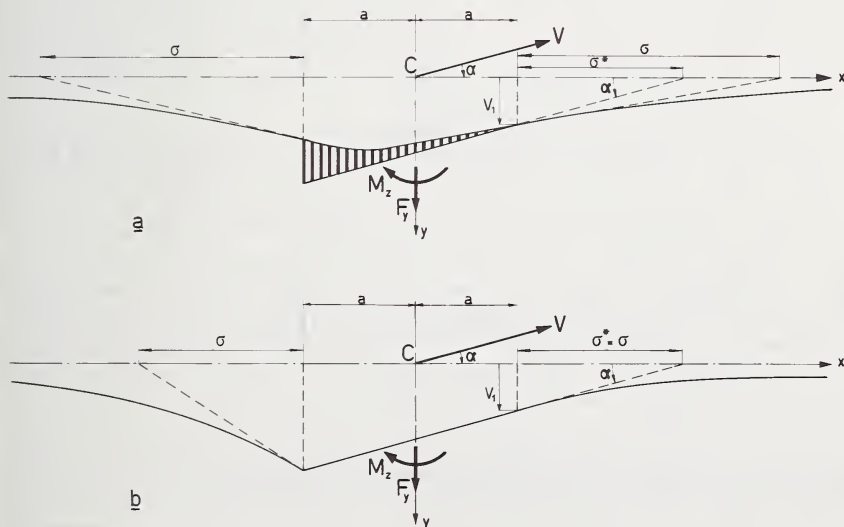


FIGURE 7.5.17. Drifting tire models at vanishing sliding; a. with tread rubber, b. without tread rubber.

in which σ_c and ϵ are defined by (7.5.34). When the tread elements are omitted ($\sigma_c = \epsilon = 0$), these equations reduce to:

$$C_{F\alpha} = 2c_c(\sigma + a)^2 \text{ and } C_{M\alpha} = 2c_c a \{ \sigma(\sigma + a) + \frac{1}{3}a^2 \}, \quad (7.5.50)$$

If the contact patch of a standing tire is moved sideways a lateral force will arise, which for small deformations is proportional to this lateral shift according to the relation

$$F_y = C_y v_o$$

where C_y denotes the lateral stiffness of the tire and v_o represents the lateral deformation of the contact patch relative to the wheel rim. In case of side slip, F_y assumes the same value when the center point of the contact line shows a lateral deflection equal to v_o . When taking into account that $v_o = (a + \sigma^*)\alpha$ the following relation appears to hold for the relaxation length of a tire

$$\sigma^* = \frac{C_{F\alpha}}{C_y} - a. \quad (7.5.51)$$

This expression may be used for the experimental determination of the relaxation length σ^* of a real tire.

For a number of values of σ and c_p/c_c the resulting relaxation length σ^* , pneumatic trail $t_o (= C_{M\alpha}/C_{F\alpha})$, and cornering stiffness $C_{F\alpha}$ are calculated and listed in table 7.5.1. The original value of the lateral carcass stiffness per unit length c_c has been designated with c_{c0} . It is remarkable that the inclusion of tread rubber of a relatively high stiffness ($c_p/c_c = 55$) does reduce σ^* , t_o and C_F so much. The model with tread rubber may give results close to those obtained experimentally (cf. Fonda and Radt [7, figs. 25, 34]).

In figure 7.5.18 for the same combinations of parameters (except $\sigma = 3a$) the variation of σ^* , $C_{F\alpha}$ and $C_{M\alpha}$ with vertical wheel load W is shown when a parabolic variation of the contact length $2a$ with W is assumed. The original values are designated with a_o and W_o . It is shown that relative to the behavior of Fromm's model ($c_c \rightarrow \infty$), the variation of the cornering stiffness with wheel load has improved somewhat due to the introduction of carcass elasticity. The case without tread rubber ($c_p \rightarrow \infty$), in turn, differs qualitatively from reality since the cornering stiffness $C_{F\alpha}$ remains finite for the vertical load W equal to zero. The drop sometimes observed at large values of W cannot be simulated with this model unless a c_c is varied. It is then necessary to introduce two different functions of average lateral foundation stiffness $c_{cF}(W)$ and $c_{cM}(W)$, one for the force and the other for the moment. This is plausible since for the force the lateral deformation of the center portion of the contact area is of primary importance, while for the moment the portions outside the contact area play the greatest role, and these show less radial deflection. As has been shown in section 7.3.1 the stiffness c_c decreases with increasing radial deflection. The variation of the relaxa-

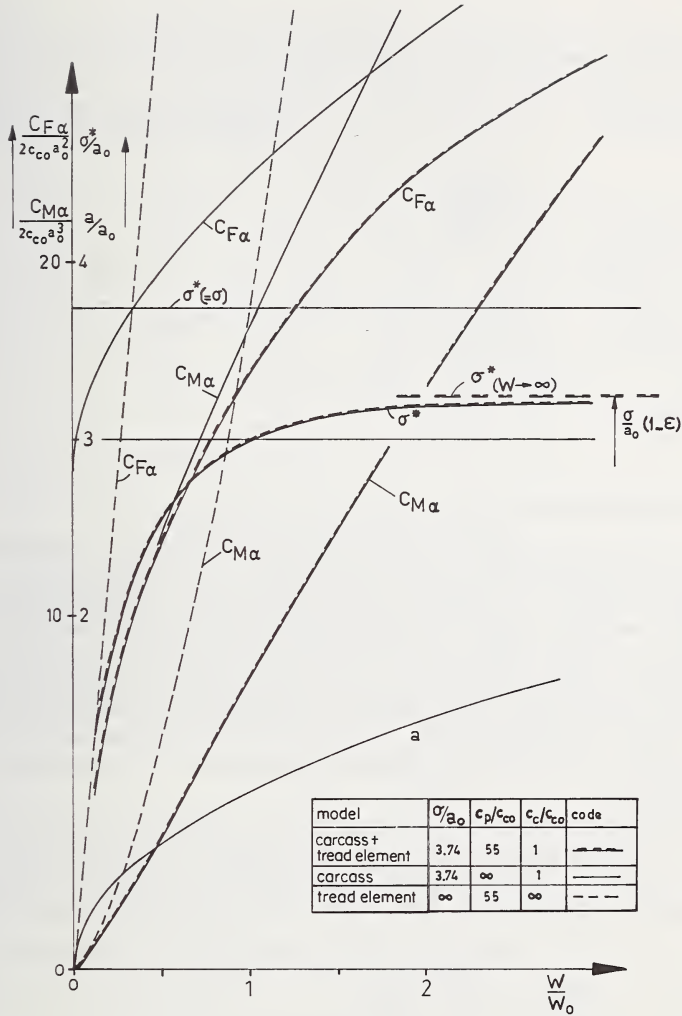


FIGURE 7.5.18. Influence of wheel load on theoretically obtained values of contact length a , relaxation length σ^* , and cornering force and moment stiffnesses $C_{F\alpha}$ and $C_{M\alpha}$ for three tire models.

a. carcass (string) + tread rubber ($c_p/c_r = 55$), b. carcass (string) only ($c_p \rightarrow \infty$), c. tread rubber only ($c_r \rightarrow \infty$).

tion length σ^* as indicated in figure 7.5.18 is of importance for the analysis of section 7.5.2, where the influence of a time-varying load is treated.

TABLE 7.5.1. Influence of model parameters

Tire model	Parameters			Relaxation length σ^*/a	Pneumatic trail t_0/a	Cornering stiffness $C_{Fa}/(c_{c0}a^2)$
	σ/a	c_p/c_{c0}	c_c/c_{c0}			
Stretched string with tread rubber	3.47	55	1	3	0.49	33.6
Stretched string without tread rubber	3.47	∞	1	3.74	.80	45
	3	∞	1	3	.77	32
Tread rubber only (rigid carcass)	∞	55	∞	0	.33	110

Camber and Turning

For antisymmetric steady state motion of automobiles, one must consider not only side slip but also the influence of two other effects, which in most cases are of much less importance than side slip. These two variables which complete the description of the antisymmetric motion are first the wheel camber, or tilt angle γ between the wheel plane and the normal to the road (cf. fig. 7.5.19), and second the spin or degree of turning. In the steady state case the spin equals the curvature $1/R$ of a circular path with radius R . In idealized form the mechanisms of camber and turning can be considered to be similar as has been enunciated in the following.

As indicated in figure 7.5.20, the wheel is considered to move tangentially to a circular horizontal path with radius R while the wheel plane has a constant camber angle γ . The wheel is assumed to be part of an imaginary ball. When lifted from the ground, the intersection of

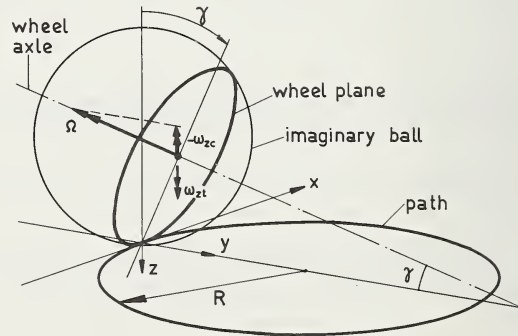


FIGURE 7.5.19. Camber and turning without side slip.

wheel plane and ball forms the peripheral line of the tire. When loaded vertically, the ball and consequently the peripheral line are assumed to show no horizontal deformations, which in reality will be the approximate case for a homogeneous ball showing a relatively small contact area (fig. 7.5.20).

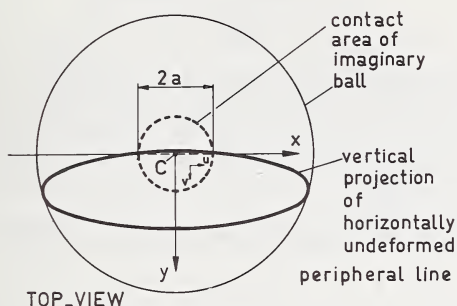


FIGURE 7.5.20. *Top-view of peripheral line of nonrolling tire considered as a part of imaginary ball pressed on flat surface.*

We apply the theory of rolling and slipping and consider equations (7.5.4). We assume:

$$V_{cx} = V_{cy} = V_{ry} = 0 \text{ and } V_{rx} = V.$$

Equations (7.5.4) become in the steady state case:

$$\left. \begin{aligned} V_{sx} &= -y\omega_z - V \frac{du}{dx}, \\ V_{sy} &= x\omega_z - V \frac{dv}{dx}. \end{aligned} \right\} \quad (7.5.52)$$

For the combination of turning and camber ω_z reads:

$$\omega_z = \omega_{zt} + \omega_{zc} = \frac{V}{R} - \Omega \sin \gamma. \quad (7.5.53)$$

The total spin ϕ consequently becomes (cf. eq (7.5.8):

$$\phi = \frac{\omega_z}{V} = \frac{1}{R} - \frac{1}{r_e} \sin \gamma \quad (7.5.54)$$

with r_e denoting the effective rolling radius. In case that complete adhesion occurs in the contact area eqs (7.5.52) become:

$$\frac{du}{dx} = -y\phi, \quad \frac{dv}{dx} = x\phi. \quad (7.5.55)$$

Integration yields the following expressions for the horizontal deformations in the contact area:

$$\left. \begin{aligned} u &= -\phi yx + \text{constant} \\ v &= 1/2 \phi x^2 + \text{constant} \end{aligned} \right\} \quad (7.5.56)$$

The constants of integrations follow from boundary conditions which depend on the tire model employed. As an example, consider a simple model corresponding to that of Fromm with horizontal deformations through elastic tread elements only. The contact area is assumed to be rectangular, of length $2a$ and width $2b$, and filled with an infinite number of tread elements. In figure 7.5.21 three rows of tread elements are shown in the deformed situation.

For this model the following boundary conditions apply:

$$x = a : v = u = 0.$$

With the use of (7.5.56) the formulae for the deformations read:

$$\left. \begin{aligned} u &= y(a - x)\phi, \\ v &= -1/2 (a^2 - x^2)\phi. \end{aligned} \right\} \quad (7.5.57)$$

After the introduction of c_{px} and c_{py} denoting the stiffness of the tread rubber per unit area in x and y direction respectively, we obtain for the lateral force and the moment about the vertical axis, by integration over the contact area:

$$\left. \begin{aligned} F_y &= -4/3 c_{py} a^3 b \phi = -C_{F\phi} \phi, \\ M_z &= -4/3 c_{px} a^2 b^3 \phi = -C_{M\phi} \phi. \end{aligned} \right\} \quad (7.5.58)$$

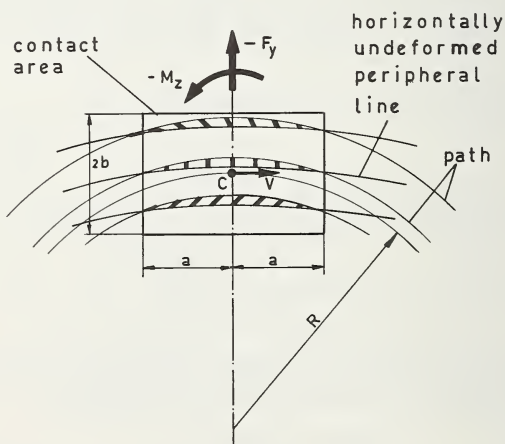


FIGURE 7.5.21. Top-view of cambered tire model rolling in a curve with radius R .

or in terms of camber and path curvature (γ small):

$$\left. \begin{aligned} F_y &= -C_{F\phi} \left(\frac{1}{R} - \frac{1}{r_e} \gamma \right), \\ M_z &= -C_{M\phi} \left(\frac{1}{R} - \frac{1}{r_e} \gamma \right). \end{aligned} \right\} \quad (7.5.59)$$

These expressions indicate that camber and path curvature have opposite effects when their signs are equal, according to the sign convention. In case of pure turning, the force on the tire is directed away from the path center and the moment acts opposite to the sense of turning. Consequently both the force and the moment try to reduce the curvature $1/R$. In case of pure camber, the force on the wheel is directed towards the point of intersection of the wheel axis and the road plane, while the moment tries to turn the rolling wheel towards this point of intersection. No resulting force or torque is expected to occur when $\gamma = r_e/R$, which is approximately the case when the point of intersection and the path center are the same. A number of authors explain the presence of a moment by considering two wheels rigidly connected to each other on one axle. In a curve the wheel centers travel different distances in a given time interval and when cambered, these distances are equal but the effective rolling radii are different. In both situations antisymmetric longitudinal creep must occur which produces the moment.

Up to now we have dealt with the relatively simple case of complete adhesion. When sliding is allowed by introducing a limited value of the coefficient of friction μ , the calculations become quite complicated. If, as before, a parabolic pressure distribution is assumed, it is obvious from eq (7.5.57), that for an infinitely thin tread ($b \rightarrow 0$) no sliding will occur up to a certain critical value of spin ϕ_{sl} , where the adhesion limit is reached throughout the contact length. Up to this point F_y varies linearly with ϕ .

According to eq (7.5.54), spin due to camber theoretically cannot exceed the value $1/r_e$, so that this discussion will be limited to the case of turning when higher values of spin are considered. Beyond the critical value ϕ_{sl} the situation becomes quite complex, as has been pointed out by Freudenstein [4]. In the front half of the contact line sliding will occur, whereas behind the contact center adhesion takes place up to a point B (cf. fig. 7.5.22) where the deformation v is opposite in sign and reaches a maximum, after which sliding occurs again. With increasing spin $\phi (= 1/R)$ this latter sliding zone grows while at the same time the side force $-F_y$ decreases and the torque $-M_z$, which arises for $\phi > \phi_{sl}$, increases until the situation has been reached where R and F_y vanish and $-M_z$ becomes maximum.

When a finite width $2b$ is introduced, complete adhesion will only occur for vanishing values of spin. We expect that sliding will start at the left and right rear corners of the contact area, since in these points the available horizontal contact forces reduce to zero and the longitudinal deformations u would become maximum for $\mu \rightarrow \infty$. The zones

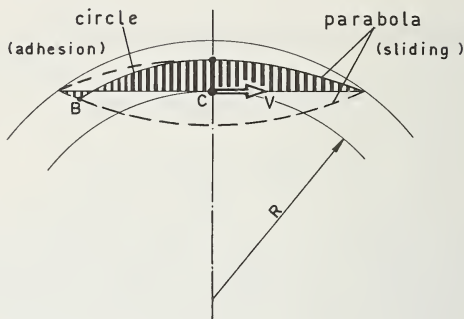


FIGURE 7.5.22. Simple tire model in sharp curve.

of sliding grow with increasing spin and will thereby cause a less than proportional variation of $-F_y$ and $-M_z$ with ϕ . The maximum lateral force will be lower than in case of line contact. A more or less exact theoretical treatment of the spin behavior of pneumatic tires with sliding taken into account has not been found in the literature. This behavior has been treated in great detail by Kalker [21] for the problem of rolling contact between elastic balls. Freudenstein [4] presents a rough theory for the turning behavior up to an approximate value of ϕ_{st} . He treats the longitudinal and lateral deformations as being uncoupled and introduces an effective coefficient of friction $\frac{1}{2} \mu \sqrt{2}$. In addition, Freudenstein gives an approximate value of the maximum torque occurring at $R=0$. For a parabolic pressure distribution in x -direction and a uniform distribution in y -direction, he obtains for contact areas with dimensions in the range $b < a < 2b$:

$$|M_{z \max}| \approx \frac{1}{4} \mu W (3/2 a + b) \quad (7.5.60)$$

Figure 7.5.23 (from [4]) gives the turning characteristics of a truck tire. A comparison with experimentally obtained cornering characteristics (cf. fig. 7.5.7) indicates that the values of both the lateral force and the moment reached at one degree slip angle roughly equal the force and moment obtained with the same tire when rolling in a curve with $R=3.5$ m. (according to experiments with bias ply truck tires). Reference [4] indicates, furthermore, that the cornering stiffnesses $C_{F\alpha}$ and $C_{M\alpha}$ are 20–30 percent higher for the radial ply (belted) tire. Analogously, the radial ply tire is expected to show greater resistance against turning than the diagonal ply tire.

From the discussion above it follows that the effect of spin due to a stationary turning may only be of importance with slow city driving. In theoretical investigations of automobile motions normally met in the literature, this effect has been neglected. Camber, however, which is the other variable associated with the spin effect, will be of particular importance for two-wheeled vehicles. The theoretical relationship between turning and camber has been used by many authors (Fiala [13], Freudenstein [4], Bergman [17] and Maier [9]). In fact, however, this

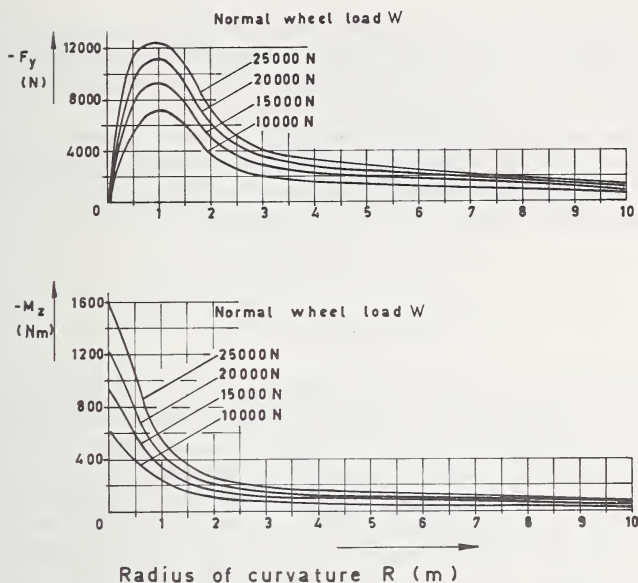


FIGURE 7.5.23. Measured turning characteristics for truck tire.

Lateral force F_y and moment M_z about vertical axis as a function of radius of curvature R . Tire cross-ply 9.00-20 eHD: $p_i=5.5$ bar. $V=1-3$ km/h on dry road (from Freudenstein [4]).

relationship is only exact in the case of a rolling ball. A cambered tire will behave somewhat differently since there exists a combination of radial and lateral stiffnesses of the tire which in general are not the same. We expect therefore that, unlike the ball, a cambered wheel loaded vertically through a purely vertical motion of the wheel axle (in which position the vertical projection of the peripheral line remains approximately unchanged), will show an initial horizontal lateral force before the wheel starts to roll. The camber force of a steady rolling tire may be obtained by superposition of the initial lateral force produced by the vertical displacement, and the change of this force during rolling due to the spinning action as treated in the theory above. In the final steady state stage, the cambered tire will show a straight contact line parallel to the wheel plane if sliding can be neglected. The complete process is very complicated and a fundamental treatment of the behavior of a rolling cambered wheel is needed.

In addition to the lateral (horizontal) force due to axial (i.e., normal to the wheel plane) deformation, we should take into account in such a theory the horizontal lateral force which arises when a standing tire is tilted about the line of intersection of wheel and road plane. From the difference in curvature of the tire side walls in the tire cross section, Rotta [20] calculates the side force which is necessary to balance the internal air pressure. Rotta states that this force is the main contribution to the camber thrust. Once the tire rolls, axial deformation may occur

due to, amongst other things, the torsional stiffness of the carcass and the finite width of the tread. These factors are responsible for the so-called overturning couple M_x about the x -axis (intersection of wheel and road plane).

For a tire model with line contact (for instance a single row of tread elements or a single elastically supported stretched string) there is no need for the peripheral line to move out of the wheel plane when it is tilted. The camber force and moments then simply read:

$$\left. \begin{aligned} F_y &= C_F \gamma = W \gamma, \\ M_x &= M_z = 0. \end{aligned} \right\} \quad (7.5.61)$$

These relationships appear to hold approximately for diagonal ply tires. Experiments indicate that radial ply tires produce less camber thrust than bias ply tires. This is in complete disagreement with the results deduced for turning, which reinforces the suspicion that the mechanism of camber and turning are not completely equivalent. As Freudenstein did not give the camber characteristics of the truck tires on which the turning behavior was measured, we are not able to compare the responses to camber and turning. According to Hadekel, for aircraft tires the lateral force due to turning is about four times higher than the camber force at equal values of spin. Evaluation of Freudenstein's truck tire data reveals that for bias ply tires (assuming that relation (7.5.61) holds for these tires) a lower ratio of about 1 is expected; for radial ply tires, however, Hadekel's value may be of the right order of magnitude. In figure 7.5.24 some experimental camber characteristics are shown. We furthermore refer to figures 7.3.37 and 7.3.38.

Influence of Braking and Traction Forces

According to experiment large longitudinal forces have considerable influence on tire cornering force and aligning torque. Theory on this subject is scarce. A significant paper is that of Bergman [17] which, however, is restricted to the influence of traction. Bergman had to simplify the system considerably, due to the exceedingly complex mechanism of the real tire. He employs the concept of interaction effect and effective lateral coefficient of friction. Bergman states that traction reduces the lateral stiffness of the standing tire, resulting in a reduction in cornering force. Similarly, one would expect that braking also would soften the tire in the lateral direction. However, experiments indicate that moderate braking increases the cornering force slightly. This contradicts Bergman's concept. The increasingly sharp reduction of the cornering force at high values of traction has been explained by Bergman by the introduction of the effective coefficient of friction in the lateral direction $\mu_y = \sqrt{\mu^2 - \mu_x^2}$, where μ_x represents the effective tractive coefficient F_x/W . It is obvious that this is a crude approximation to reality, although the results appear to fit some observations. However, for the description of the influence of the braking force, and especially

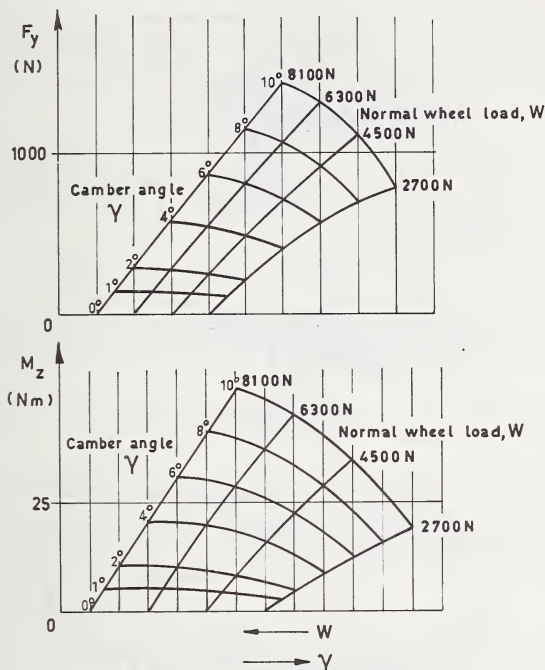


FIGURE 7.5.24. Measured camber characteristics.

Lateral force F_y and moment M_z as a function of camber angle γ and wheel load W . Same tire as in figure 7.5.6 ($\alpha = 0$) (from Nordeen and Cortese [5]).

for the influence of longitudinal forces on the aligning torque, Bergman's theory is inadequate.

A theory which is probably more widely applicable will be presented next. It is a further development of a first attempt of the author reported in [18]. It describes the behavior of a relatively simple model, which later on will be extended to a more advanced model.

Model without carcass elasticity.

The simple model is identical to Fromm's model, for which the steady state side slip behavior has been treated in section 7.5.1. The carcass is considered to be rigid, and the tread elements provide the necessary elastic properties of the tire. For purposes of mathematical simplicity it is assumed that the horizontal stiffnesses of the tread elements, of which several rows may be present, are equal in the lateral and longitudinal direction. We introduce:

$$c_p = 2bc_{px} = 2bc_{py} \quad (7.5.62)$$

with c_{px} and c_{py} denoting stiffnesses per unit area, and c_p the horizontal stiffness per unit of length.

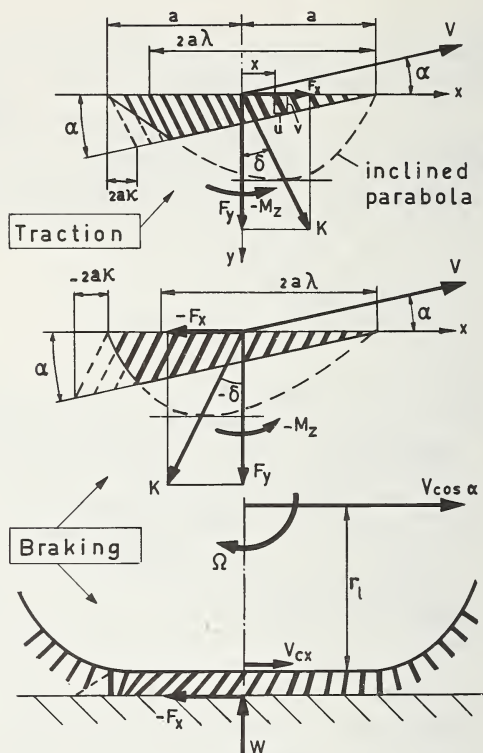


FIGURE 7.5.25. Deformations of the simple model due to side slip (α) and longitudinal slip (κ).

In figure 7.5.25 the deformations of the tread elements are shown for both the cases of traction ($F_x > 0$) and braking ($F_x < 0$). The longitudinal creep velocity V_{cx} obviously becomes:

$$V_{cx} = V \cos \alpha - \Omega r_l. \quad (7.5.63)$$

The longitudinal slip ratio has been defined as

$$\kappa = -\frac{V_{cx}}{\Omega r_l} = 1 - \frac{V \cos \alpha}{\Omega r_l} \quad (7.5.64)$$

The deformations due to longitudinal slip and side slip become, in case of full adhesion ($\mu \rightarrow \infty$):

$$\left. \begin{aligned} u &= (a-x)\kappa \\ v &= (a-x)(1-\kappa)\alpha \end{aligned} \right\} \quad (7.5.65)$$

where for simplicity α is assumed to be small. We introduce the angle δ , indicating the angular deviation of the total horizontal force from the lateral direction (cf. fig. 7.5.25). The following relations hold:

$$\sin \delta = F_x/K, \quad \cos \delta = F_y/K. \quad (7.5.66)$$

The relation between κ and α reads:

$$\tan \delta = \frac{\kappa}{(1-\kappa)\alpha}. \quad (7.5.67)$$

Analogous to eq (7.5.21), we solve with (7.5.20) for the point of initial sliding, but now with the presence of longitudinal slip ($\alpha > 0$):

$$\lambda = 1 - \frac{\theta(1-\kappa)\alpha}{\cos \delta} = 1 - \theta \frac{\kappa}{\sin \delta} = 1 - \frac{\theta\alpha}{\alpha \sin \delta + \cos \delta}. \quad (7.5.68)$$

For a given slip angle α , λ will be greater at positive δ (traction) than at negative δ (braking) for same absolute values of δ .

When for a combination of F_x and F_y total sliding begins ($\lambda=0$), the slip angle and the longitudinal slip ratio are:

$$\alpha_{sl} = \frac{\cos \delta}{\theta - \sin \delta}; \quad \kappa_{sl} = \frac{1}{\theta} \sin \delta \quad (7.5.69)$$

Integration over the contact length yields the total horizontal force:

$$K = \mu W (1 - \lambda^3) \quad (7.5.70)$$

and for the aligning torque:

$$M_z = -\mu W a \lambda^3 (1 - \lambda) \cos \delta. \quad (7.5.71)$$

From these formulae, for given α and κ , the tire forces and moment can be calculated with the use of eqs (7.5.66–68). In figure 7.5.26 a number of curves are shown for the parameter value $\theta=5$. For both the moment M_z and the force F_y plotted against F_x a slight asymmetry appears to occur.

In the (F_y, F_x) diagram curves for constant longitudinal slip values κ are also shown. From eqs (7.5.66, 68, 70) we obtain the following formula:

$$\frac{F_x}{\mu W} = \theta \kappa \left\{ \frac{3}{4} + \left(\frac{3}{2} - \frac{\theta \kappa}{\sin \delta} \right)^2 \right\}. \quad (7.5.72)$$

For $K < \mu W$, one finds that $0 < \theta \kappa / \sin \delta < 1$ and formula (7.5.72) indicates that for a given κ the absolute value of the longitudinal force $|F_x|$ decreases with increasing $\cos \delta$, and consequently with increasing slip angle α .

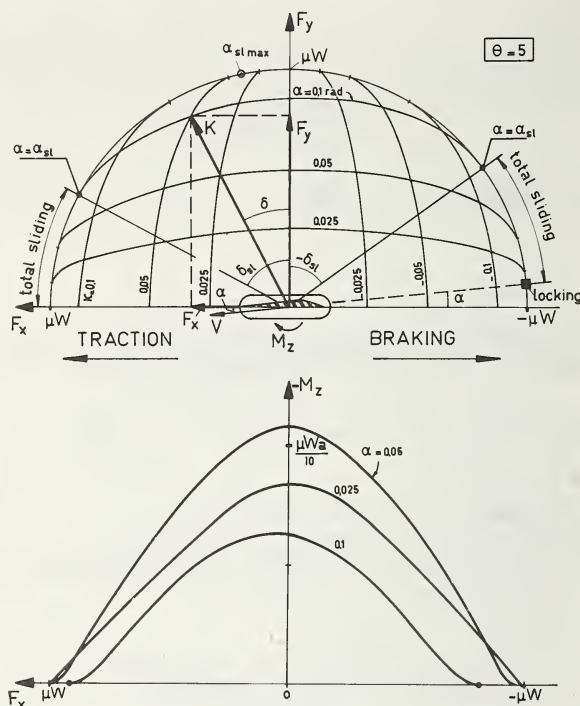


FIGURE 7.5.26. Variation of cornering force F_y and aligning torque M_z as a function of driving or braking force F_x for the tire model shown in figure 7.5.25.

These theoretical observations correspond to experiments carried out by, among others, Henker [6] on a rotating internal drum (dry, cf. fig. 7.5.27) and by Holmes and Stone [27] on wet pavement. The phenomenon that the curves on wet surfaces tend to end inwards may be due to the fact that at higher sliding velocities the coefficient of friction decreases (cf. fig. 7.3.49).

However, the variation of the aligning torque M_z with the longitudinal force F_x does deviate markedly from experimental results presented by Nordeen and Cortese [5] (cf. fig. 7.5.28). As shown, the force F_y varies as expected but the moment M_z does not agree with the theory. It appears the M_z changes its sign during heavy braking. This phenomenon cannot be explained with the simple model employed so far. Before we adopt a more advanced model, the cornering stiffnesses of the simple model will be derived as a function of F_x .

After elimination of λ from eqs (7.5.68) and (7.5.70) we obtain, for $F_y \rightarrow 0$, ($\alpha \rightarrow 0$, $K \rightarrow |F_x|$):

$$\sqrt[3]{1 - \frac{|F_x|}{\mu W}} = 1 - \theta \frac{|F_x|}{C_{F\alpha} + F_x} \quad (7.5.73)$$

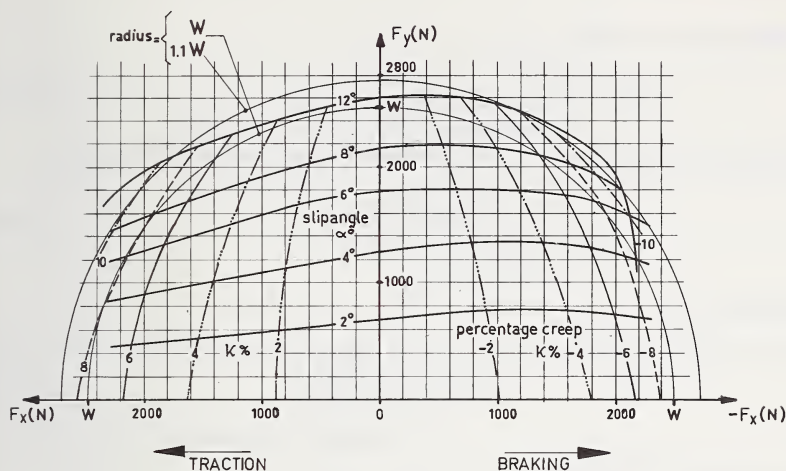


FIGURE 7.5.27. Measured side force (F_y)–longitudinal force (F_x) relationship for constant slip angle α (also shown for constant longitudinal slip value κ).

Same tire and conditions as in figure 7.5.8. ($W = 2500$ N) (from Henker [6]).

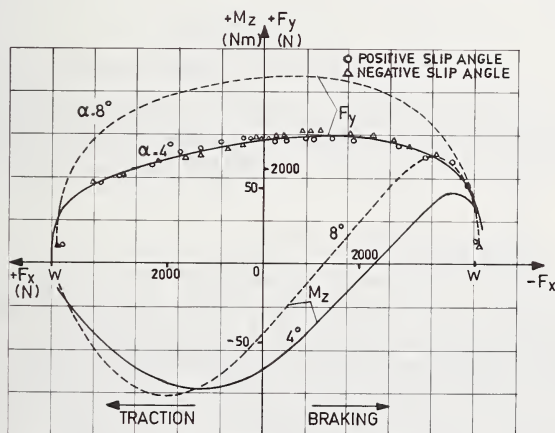


FIGURE 7.5.28. Measured variation of both F_y and M_z with F_x for constant slip angle α .

Same tire as in figure 7.5.6 ($W = 4500$ N, $\gamma = 0$). (from Nordeen and Cortese [5]).

which yields:

$$C_{F\alpha} = -F_x + \frac{\theta |F_x|}{1 - \sqrt[3]{1 - \frac{|F_x|}{\mu W}}} \quad (7.5.74)$$

which reduces, for $\mu \rightarrow \infty$, to

$$C_{F\alpha} \rightarrow 2c_p a^2 - F_x. \quad (7.5.75)$$

The pneumatic trail $t = -M_z/F_y$ becomes (using eqs (7.5.66, 68, 70)):

$$t = a \frac{\lambda^3(1-\lambda)}{1-\lambda^3} \quad (7.5.76)$$

or when $\alpha \rightarrow 0$:

$$t_0 = a\theta \frac{\mu W - |F_x|}{C_{F\alpha} + F_x} \quad (7.5.77)$$

from which is obtained:

$$C_{M\alpha} = t_0 \cdot C_{F\alpha} = a\theta C_{F\alpha} \frac{\mu W - |F_x|}{C_{F\alpha} + F_x} \quad (7.5.78)$$

and for $\mu \rightarrow \infty$:

$$C_{M\alpha} \rightarrow 1/3(2c_p a^3 - F_x a). \quad (7.5.79)$$

These results are not of direct importance since they deviate too much from experiment. They are, however, needed for the development of the theory of the more advanced model with carcass elasticity.

Model with carcass elasticity.

The simple model will now be extended by the introduction of lateral, longitudinal and torsional elasticity of the carcass. For simplicity we shall assume the carcass equatorial line to be straight in the contact region (see fig. 7.5.29). For the sake of distinction the quantities referring to the simple model of figure 7.5.25, which can be recognized as a part of the more advanced model, are indicated by upper bars. The quantities \bar{F}_y , \bar{M}_z , \bar{t} and $\bar{C}_{F\alpha}$ have been determined as a function of \bar{F}_x and $\bar{\alpha}$ in the preceding portion of this section.

The angles α and β (fig. 7.5.29) are assumed to be small. With the carcass stiffnesses C_{cx} , C_{cy} and $C_{c\beta}$ we obtain for the displacements of the straight carcass section:

$$\left. \begin{aligned} u_0 &= F_x/C_{cx} \\ v_0 &= F_y/C_{cy} \\ \beta &= -M_z/C_{c\beta} \end{aligned} \right\} \quad (7.5.80)$$

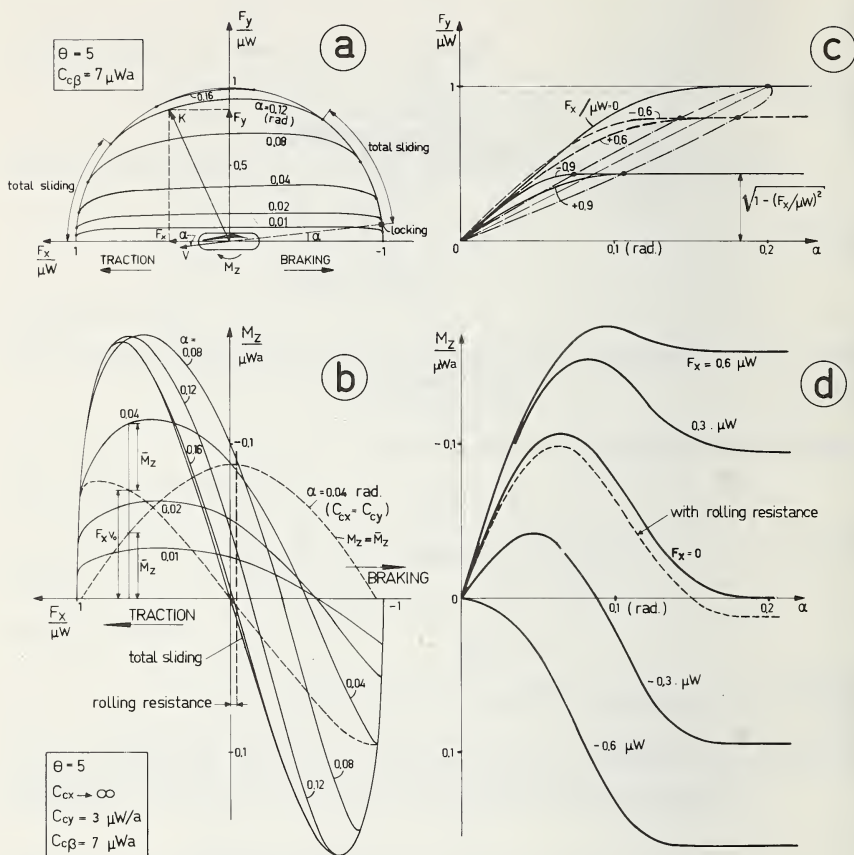


FIGURE 7.5.30. Tire force and moment characteristics as obtained for the more advanced tire model of figure 7.5.29.

which opposes the aligning torque $-M_z$ in case of braking, and thereby causes a change in sign of the aligning torque (diagram *b*) as has also been observed experimentally (cf. fig. 7.5.28). In the same figure 7.5.30*b*, the influence of equal stiffnesses $C_{cx} = C_{cy}$ has been indicated. In this case the torques produced by F_x and F_y about C balance each other so that no change in sign occurs. The influence of carcass elasticity may be smaller than predicted here because of the expected property that the displacements of the lines of action of F_x and F_y are smaller than the deflection v_o and u_o respectively. Smiley and Horne [8] give some information on the shift of the normal force relative to the horizontal deformations of a standing tire. They give figures of 80 percent and 25 percent respectively for aircraft tires.

The cornering stiffnesses valid for the more advanced model are derived as follows. With the relations (81, 82) we obtain for $\alpha \rightarrow 0$:

$$\left. \begin{aligned} C_{F\alpha} &= \frac{F_y}{\alpha} = \frac{\bar{F}_y - \bar{F}_x \beta}{\bar{\alpha} + \beta} = \bar{C}_{F\alpha} \frac{1 - F_x \bar{t}_0 / C_{c\beta}}{1 + \bar{C}_{F\alpha} \bar{t}_0 / C_{c\beta}}, \\ C_{M\alpha} &= \frac{-M_z}{\alpha} = \frac{-\bar{M}_z + F_x v_0 - F_y u_0}{\bar{\alpha} + \beta} \\ &= \frac{\bar{C}_{F\alpha} \bar{t}_0}{1 + \bar{C}_{F\alpha} \bar{t}_0 / C_{c\beta}} + C_{F\alpha} F_x \left(\frac{1}{C_{cy}} - \frac{1}{C_{cx}} \right) \end{aligned} \right\} \quad (7.5.84)$$

in which $\bar{C}_{F\alpha}$ and \bar{t}_0 are given by eqs (7.5.74) and (7.5.77). In figure 7.5.31 the functions (7.5.84) are plotted for the values given in eq (7.5.83), and in addition for two finite values of C_{cx} . It has been found that through the introduction of carcass elasticity considerable qualitative changes in characteristics can arise.

When braking, the cornering stiffness $C_{F\alpha}$ initially increases slightly, it then passes a maximum after which a sharp drop occurs, and finally complete sliding takes place. From this point $C_{F\alpha}$ decreases with increasing longitudinal slip velocity up to the point of a locked wheel. In case of traction $C_{F\alpha}$ decreases continuously and drops to zero in the range of complete sliding, when the slip velocity $-V_{cx}$ tends to infinity (wheel spin-up).

As indicated, the variation of $C_{M\alpha}$ depends on the ratio of longitudinal stiffness. For $C_{cx} \rightarrow \infty$, the aligning torque stiffness $C_{M\alpha}$ decreases with increasing braking force, becomes negative, passes a minimum and finally shows a small negative value when the wheel is locked. In case of traction $C_{M\alpha}$ first shows a slight rise after which $C_{M\alpha}$ tends to zero for $F_x \rightarrow \mu W$.

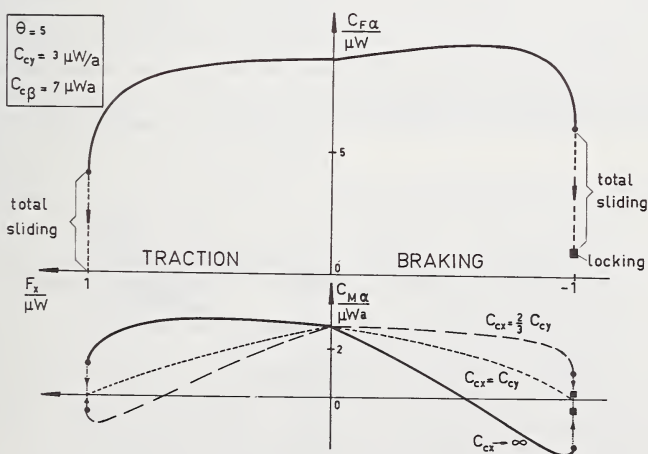


FIGURE 7.5.31. Cornering force and moment stiffness (at $\alpha = 0$) as a function of longitudinal force.

The influence of the longitudinal stiffness is of great importance as shown in the figure. In case of equal stiffnesses $C_{cx}=C_{cy}$, the variation of $C_{M\alpha}$ (and of the moment M_z , cf. fig. 7.5.30b) becomes more symmetrical, which corresponds to the experimental curves for radial ply tires. Bias ply tires, however, behave according to the theoretical curves for relatively large longitudinal carcass stiffness. The much lower longitudinal stiffness of radial tires might indeed be responsible for the great qualitative differences observed experimentally between diagonal and radial ply tires [28].

Limitations of theory.

The theory just developed is limited due to simplifications in the tire model. Probably the most questionable simplifications are the equal stiffnesses of the tread rubber elements in the lateral and longitudinal directions, and the assumption that the carcass remains straight in the contact zone. Furthermore, the theory assumes a constant coefficient of friction. As has been pointed out previously, the force and moment characteristics will change in shape due to the drop of the coefficient of friction with sliding velocity. Although a number of aspects may be clarified with the aid of this model, it is certain that important factors are not yet taken into account. One of these will be mentioned briefly. It is the influence of the change in tension force or effective tension force S in the carcass tread band due to braking or driving forces.

Influence of change in tension force, front and rear.

In order to investigate this influence, an alternative tire model must be adopted. Obviously, the simple stretched string model is most suitable. The slopes of the $C_{F\alpha}$ (F_x) and $C_{M\alpha}$ (F_x) curves at $F_x=0$ will be calculated while we restrict ourselves to the case of vanishing sliding ($\mu \rightarrow \infty$).

The slopes to be calculated, consequently, are purely due to the elastic properties of the tire and may be compared with the slopes obtained with the simple model for $\mu \rightarrow \infty$ (cf. eqs (7.5.75) and (7.5.79)). In figure 7.5.32 the stretched string model is shown subjected to lateral and longitudinal forces and the aligning torque. Like in the theory of steady state side slip (eq 7.5.31), the effective longitudinal tension force S is intro-

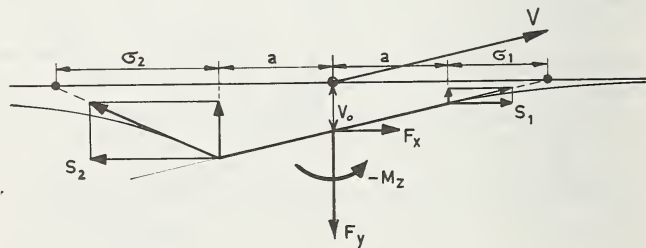


FIGURE 7.5.32. Stretched string model deformed due to side slip and traction (no sliding, $\mu \rightarrow \infty$).

duced, which, due to the longitudinal force F_x , will differ now at the trailing and leading edges. We assume the following relations to hold:

$$\left. \begin{aligned} S_1 &= S - 1/2 F_x, \\ S_2 &= S + 1/2 F_x. \end{aligned} \right\} \quad (7.5.85)$$

According to the definition of the relaxation length when tread elements are absent (σ , eq (7.5.34)) we obtain the following formulae for the relaxation length front and rear respectively:

$$\sigma_1^2 = (S - 1/2 F_x)/c_c, \quad \sigma_2^2 = (S + 1/2 F_x)/c_c. \quad (7.5.86)$$

Analogous to eq (7.5.50) the cornering stiffnesses read:

$$\begin{aligned} C_{Fa} &= c_c \{ (\sigma_1 + \sigma_2 + 2a)(\sigma_1 + a) + a(\sigma_2 - \sigma_1) \} \\ C_{Ma} &= c_c a \{ \sigma_2(\sigma_2 + a) + \sigma_1(\sigma_1 + a) \\ &\quad + 2/3 a^2 + (\sigma_2 - \sigma_1)(\sigma_1 + a) \}, \end{aligned} \quad (7.5.87)$$

which with the aid of (7.5.68) and with the assumption $F_x \ll S$ reduce to:

$$\left. \begin{aligned} C_{Fa} &= C_{Fa0} - 1/2 F_x, \\ C_{Ma} &= C_{Ma0} + 1/2 F_x a (\sigma_o + a) / \sigma_o, \end{aligned} \right\} \quad (7.5.88)$$

where index o refers to the situation without external longitudinal forces. The slope at $F_x = 0$ becomes:

$$\frac{dC_{Fa}}{dF_x} = -1/2; \quad \frac{dC_{Ma}}{dF_x} = 1/2 \frac{a}{\sigma_o} (\sigma_o + a). \quad (7.5.89)$$

It may be noted that the slopes of C_{Fa} and C_{Ma} differ in sign. The change in tension force due to traction or braking, consequently, intensifies the effect of lateral carcass elasticity.

The influence of a longitudinal force on camber force and moment has not been investigated properly as far as the author knows. Since the influence of camber itself is small relative to the influence of side slip, we may roughly approximate the effect of longitudinal forces on camber force and moment, as will be done in the next section.

Approximate Mathematical Representation of Combined Effects

In theories of steady state or quasi-steady state automobile motions, tire forces and moments must be introduced in an appropriate mathematical form. The complexity of this representation depends upon the object of the investigation. Many authors [29, 30, 31, 32, 33] restrict the motions to be investigated to relatively small deviations from the rectilinear path. In that case the equations of motion can be linearized and only coefficients like cornering stiffnesses are of importance. When,

in addition, longitudinal forces are not taken into account these coefficients depend only on the vertical wheel load, which may vary due to lateral load transfer. In the linear representation the latter effect is only of importance when initial steer or camber angles of the wheels front or rear are present. The change in rolling resistance (cf. part 7.2, fig. 7.2.56 and sec. 7.4.1) with wheel load will always enter the problem as soon as a finite height of the vehicle center of gravity is considered [31]. The order of magnitude of the cornering stiffness $C_{F\alpha}$ (force per radian), expressed in terms of the nominal vertical load, lies between $5W_o$ and $10W_o$; the pneumatic trail t_o expressed in terms of half the contact length lies in the range $0.4a$ to $0.7a$.

Theories which consider high lateral (cornering) accelerations (refs. [34] to [42]) need a more or less complete mathematical description of tire behavior. In these investigations most authors describe tire characteristics by means of simple mathematical expressions (parabola, sine, exponential) which correspond more or less to actual characteristics known from the literature. More sophisticated theories [38, 42] show the employment of actual tire characteristics in which the influence of vertical and longitudinal forces are also taken into account.

A complete, more or less exact, mathematical representation of measured data is difficult to accomplish. Fiala has combined his theories for side slip (with influence of W and μ) and camber. He presents explicit expressions for F_y and M_z for which we refer to the original paper [13].

We shall present a procedure with which the combination of most effects treated in this part 7.5 can be approximately represented. The principle of this method has been given in [18]. The philosophy is as follows. Consider the tire characteristics (F_y vs. α , M_z vs. α) measured at nominal wheel load W_o and zero camber and longitudinal force (except small rolling resistance force). From these basic tire characteristics we attempt, using the theoretical and experimental experience obtained, to derive F_y and M_z in cases where the conditions differ from basic conditions. These basic conditions are:

$$W = W_o, \mu = \mu_o, F_x = 0, \gamma = 0.$$

Under these circumstances we obtain

$$F_y = F_{y0}(\alpha), M_z = M_{z0}(\alpha), C_{F\alpha} = C_{F\alpha 0}, C_{M\alpha} = C_{M\alpha 0}.$$

The functions $F_{y0}(\alpha)$ and $M_{z0}(\alpha)$ may be approximated by antisymmetrical mathematical functions.

The influence of a variation of the vertical load W has two effects. First the cornering stiffnesses vary according to functions which may be measured (cf. fig. 7.5.6, low values of α). Secondly the maximum F_y changes proportionally with μW (experiments of Borgmann [16] show that in fact this variation is somewhat less than proportional). Through this effect the influence of μ has been taken into account. It is assumed that μ effects only the more or less horizontal level of the cornering force

characteristic. On slippery roads the shape of the curves may change considerably (fig. 7.3.26) and a different approach is needed.

The following equations hold approximately when only W and μ differ from the basic conditions:

$$\begin{aligned} F_y &= \frac{\mu W}{\mu_0 W_0} F_{y0}(\alpha_{Feq}), \\ M_z &= \frac{\mu W}{\mu_0 W_0} \frac{C_{M\alpha}(W)}{C_{M\alpha 0}} \frac{C_{Fa0}}{C_{Fa}(W)} M_{z0}(\alpha_{Meq}) \end{aligned} \quad (7.5.90)$$

with the equivalent slip angles

$$\alpha_{Feq} = \alpha_{Meq} = \frac{\mu_0 W_0}{\mu W} \frac{C_{Fa}(W)}{C_{Fa0}} \alpha. \quad (7.5.91)$$

The cornering stiffnesses C_{Fa} and $C_{M\alpha}$ are assumed to depend only on W , and are independent of μ . The functions $C_{Fa}(W)$ and $C_{M\alpha}(W)$ may be approximated by polynomials. In figure 7.5.33 the transformation of curves (0) (=basic) to curves (2), obtained by means of multiplication as indicated, result in the characteristics relevant for the new situation (μ , W).

The influence of camber can be approximated by shifting the curves (2) horizontally, so that for $\alpha=0$ the force F_y and the moment M_z equal $C_{F\gamma\gamma}$ and $C_{M\gamma\gamma}$ respectively. For experimental verification cf. Fonda [3, fig. 73], or Henker [6, fig. 98] and figure 7.3.40. Equations (7.5.94) can be applied but with different arguments.

$$\begin{aligned} \alpha_{Feq} &= \frac{\mu_0 W_0}{\mu W} \frac{C_{Fa}(W)}{C_{Fa0}} \left(\alpha + \frac{C_{F\gamma}(W)}{C_{Fa}(W)} \gamma \right), \\ \alpha_{Meq} &= \frac{\mu_0 W_0}{\mu W} \frac{C_{Fa}(W)}{C_{Fa0}} \left(\alpha - \frac{C_{M\gamma}(W)}{C_{M\alpha}(W)} \gamma \right). \end{aligned} \quad (7.5.92)$$

The functions $C_{F\gamma}(W)$ and $C_{M\gamma}(W)$ may be approximated by linear functions of W . The quantity $C_{M\gamma}$ is relatively small and might very well be neglected. The new curves (3) are shown in figure 7.5.33.

The influence of F_x is complicated. We propose the application of the following formulations which are expected to give reasonable results. With consideration of the theory of section 7.5.1 the cornering stiffnesses may be represented by:

$$\begin{aligned} C_{Fa}(\mu, W, F_x) &= \left(1 - \left| \frac{F_x}{\mu W} \right|^n \right) C_{Fa}(W) + \frac{1}{2} (F_x + |F_x|), \\ C_{M\alpha}(\mu, W, F_x) &= \left(1 - \left| \frac{F_x}{\mu W} \right|^m \right) C_{M\alpha}(W) + \left(\frac{\zeta_y}{C_{cy}} - \frac{\zeta_x}{C_{cx}} \right) F_x C_{Fa}(\mu, W, F_x) \end{aligned} \quad (7.5.93)$$

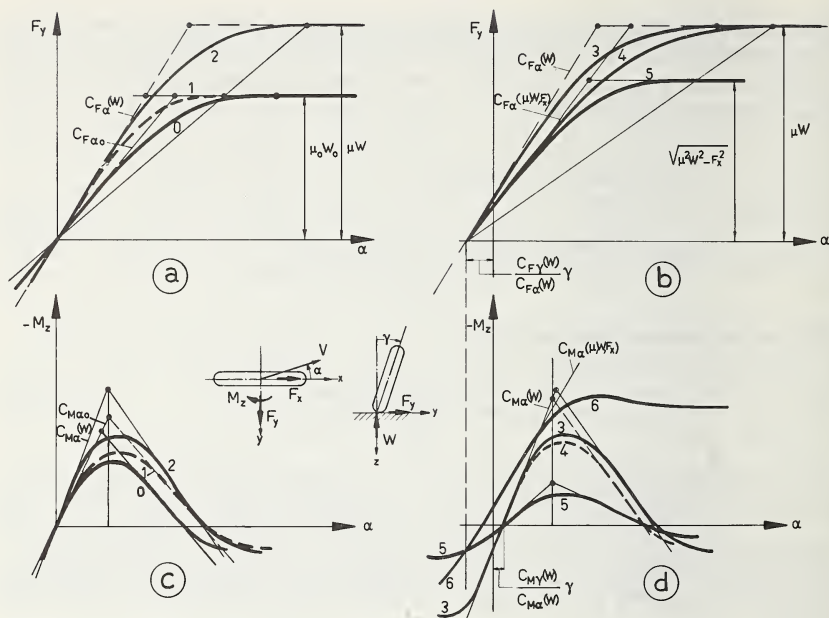


FIGURE 7.5.33. Illustration of characteristics obtained from the basic curves (0) according to formulae (7.5.90-95).

The following successive steps are carried out:

Diagram a:

- 0 : basic ($\mu_0, W_0, \gamma = F_z = 0$)
- 0-1 : horizontal mult. with $C_{Fa0}/C_{Fa}(W)$
- 1-2 : radial mult. with $\mu W/\mu_0 W_0$
- 2 : new conditions (μ, W)

Diagram c:

- 0 : basic ($\mu_0, W_0, \gamma = F_z = 0$)
- 0-1 : rad. mult. with $\frac{\mu W}{\mu_0 W_0} \frac{C_{Fa0}}{C_{Fa}(W)}$
- 1-2 : vertical mult. $C_{Ma0}(W)/C_{Ma0}$
- 2 : new conditions (μ, W)

Diagram b:

- 2-3 : horizontal shift
- 3 : new conditions (μ, W, γ)
- 3-4 : hor. mult. $C_{Fa}(W)/C_{Fa}(\mu, W, F_z)$
- 4-5 : rad. mult. $\sqrt{1 - (F_z/\mu W)^2}$
- 5 : new conditions (μ, W, γ, F_z)

Diagram d:

- 2-3 : horizontal shift
- 3 : new conditions (μ, W, γ)
- 3-4 : rad. m. $\frac{\sqrt{1 - (F_z/\mu W)^2} \cdot C_{Fa}(W)}{C_{Fa}(\mu, W, F_z)}$
- 4-5 : vert. mult. $(1 - |F_z/\mu W|^m)$
- 5-6 : vert. add. $\left(\frac{\zeta_y}{C_{cy}} - \frac{\zeta_x}{C_{cx}}\right) F_x F_y$
- 6 : new conditions (μ, W, γ, F_x)

in which C_{cx} and C_{cy} denote the lateral and longitudinal stiffnesses of the carcass relative to the wheel rim. The constant ζ_y and ζ_x represent the percentages of effectiveness of the carcass elasticity. They may be found experimentally or by curve fitting of the whole function $C_{Ma}(\mu, W, F_x)$.

The approximate formulations (7.5.93) in which the exponents are of the order of $n \approx 10-20$ and $m \approx 1-2$, do not take into account the theoretically exact vertical portions (dotted in fig. 7.5.31) where com-

plete sliding occurs at $|F_x| = \mu W$. In order to describe the variation of $C_{F\alpha}$ and $C_{M\alpha}$ in these portions, the longitudinal slip ratio actually should be introduced. We approximate this with a steep approach of the end-points (1, 0) and $(-1, 1)$ in the diagram ($C_{F\alpha}/\mu W$ vs. $F_x/\mu W$). Most authors [43, 41] approximate $C_{F\alpha}(\mu, W, F_x)$ by an ellipse. As a result of this, the curves (F_y vs. α) are merely multiplied in the vertical direction. This does not agree with theoretical findings (fig. 7.5.30c). A multiplication of the basic curve $F_{y0}(\alpha)$, mainly in the radial direction from the origin, is expected to occur. We obtain the following formulae:

$$\left. \begin{aligned} F_y &= \frac{\sqrt{\mu^2 W^2 - F_x^2}}{\mu_0 W_0} F_{y0}(\alpha_{F_{eq}}), \\ M_z &= \frac{\sqrt{\mu^2 W^2 - F_x^2}}{\mu_0 W_0} \left\{ 1 - \left| \frac{F_x}{\mu W} \right|^m \right\} \frac{C_{M\alpha}(W)}{C_{M\alpha 0}} \frac{C_{F\alpha 0}}{C_{F\alpha}(\mu, W, F_x)} M_{z0}(\alpha_{M_{eq}}) \\ &\quad - \left(\frac{\zeta_y}{C_{cy}} - \frac{\zeta_x}{C_{cx}} \right) F_x F_y \end{aligned} \right\} \quad (7.5.94)$$

in which the equivalent slip angles read:

$$\begin{aligned} \alpha_{F_{eq}} &= \frac{\mu_0 W_0}{\sqrt{\mu^2 W^2 - F_x^2}} \frac{C_{F\alpha}(\mu, W, F_x)}{C_{F\alpha 0}} \left(\alpha + \frac{C_{F\gamma}(W)}{C_{F\alpha}(W)} \gamma \right), \\ \alpha_{M_{eq}} &= \frac{\mu_0 W_0}{\sqrt{\mu^2 W^2 - F_x^2}} \frac{C_{F\alpha}(\mu, W, F_x)}{C_{F\alpha 0}} \left(\alpha - \frac{C_{M\gamma}(W)}{C_{M\alpha}(W)} \gamma \right). \end{aligned} \quad (7.5.95)$$

Figure 7.5.33 shows the change of the curves due to the introduction of the longitudinal force F_x . For F_y , curve (5) is the final curve and for M_z , curve (6) is the final curve, covering all effects of deviations from the basic conditions.

It should be pointed out finally that for the description of the unrestricted motion of a vehicle, tire characteristics must be used with the abscissa $\sin \alpha$, instead of α , extending from -1 to $+1$ (cf. [40]).

These final characteristics are ready for use in the theory of vehicle dynamics. It should be noted that the formulations above are but approximations of measured behavior. The basic curve measured under nominal conditions (average vertical load, zero camber, free rolling, actual road surface) depends on tire construction and inflation pressure. Quantitative experimental data is needed for the execution of each intermediate step. The simulation of wet traction behavior (fig. 7.3.49) is expected to be more complicated. In that case the influence of the speed of travel is appreciable.

7.5.2. Nonsteady State Motions

In this section two kinds of nonsteady state motion will be discussed. First, the response to nonsteady state horizontal motions of the wheel

axle and secondly, the influence of vertical oscillations of the wheel axle upon cornering force.

Horizontal Motions (Transient and Shimmy)

In the theories describing the horizontal nonsteady state behavior of tires one can identify two trends of theoretical development. One group of authors assumes a bending stiffness of the carcass and the other bases its theory on the string concept.

In principle, the string theory is simpler than the beam theory, since with the string model the deflection of the foremost point alone determines the path of the tread for certain wheel movements, whereas with the beam model the slope at the foremost point also has to be taken into account as an additional variable. The latter leads to an increase in order of the system by one.

Probably the first investigator who tried to describe tire behavior mathematically in the study of shimmy is Kantrowitz [44] (1937). In spite of his rough and theoretically unsatisfactory assumptions, the theory developed gave a fair correspondence with measured values of divergence of wheel deflections and frequency of the shimmy motion. Kantrowitz studied the damping effect of the gyroscopic couple due to lateral distortion of the rotating tire. Another theory, apparently inspired by Kantrowitz' work, was developed in 1942 by Greidanus [45]. Where Kantrowitz' work shows features of both the beam and the string, Greidanus is consistent in applying the bending concept in his interesting study. Besides the slope, the curvature of the peripheral line just in front of the contact point is also important for the further development of the motion. In Greidanus' model a vanishing area of contact was considered as may be deduced from his approach. In a discussion on Saito's paper [46] Pacejka has given the differential equations which govern the kinematical variations in lateral tire distortion for the beam type model with finite contact length. These equations appear to be identical to those given by Greidanus when the influence of camber is not considered, and when the contact length is taken equal to zero.

In 1962 Saito [46] presented a theory using a tire model consisting of an elastic beam of which a finite length makes contact with the road. The theory is based on an approximate treatment of the kinematic behavior of the contact line. Frequency response curves are given for the force and moment with respect to lateral and angular motions of the wheel plane. In order to obtain better agreement with experimental results, Saito introduced theoretically unjustifiable empirical corrections.

Besides this group of investigators which were inspired by the work of Kantrowitz, another group exists which has studied the problem with the aid of tire models more or less based on the string concept.

In 1941 Fromm [47] gave a simple theory where this model (although not mentioned by name) is investigated for the case of point contact. A similar theory was developed by Bourcier de Carbon [48] in 1948 together with an extension, somewhat unclear, which increases the order of the system by one. A similar simple theory originates from Böhm [49]. He

uses the nonlinear steady state cornering characteristics in order to find the amplitude of the periodic shimmy motion.

In 1941 von Schlippe [25] presented his well-known theory of the kinematics of a rolling tire, and introduced the concept of the stretched string model. For the first time a finite contact length was considered. In the same paper Dietrich applied this theory to the shimmy problem. Mathematical difficulties arose in the form of transcendental equations, due to the retardation effect of the assumption of a finite contact length. Later on, two papers of von Schlippe and Dietrich [50, 51] were published in which the effect of the width of the contact area is also considered. Two rigidly connected coaxial wheels, both approximated by a one-dimensional string model, are considered. The strings and their elastic supports are also supposed to be elastic in the circumferential direction.

Segel [52] derived the frequency response characteristics for the one-dimensional string model, and these are similar to response curves which arise in Saito's approximate theory for the beam model.

Smiley [10] gave a summary theory resembling the one-dimensional theory of von Schlippe [25]. He has correlated various known theories with several systematic approximations to his summary theory.

In [19] Pacejka gave the nonsteady state response of the string model of finite width provided with tread elements. The important gyroscopic effect has been introduced and the nonlinear behavior of the tire due to partial sliding has been discussed. Applications of the tire theory to the shimmy motion of automobiles have been presented.

Transfer functions.

We shall discuss here some theories of nonsteady state tire motion, based on the stretched string concept, starting with the relatively simple case where sliding in the contact area does not occur ($\mu \rightarrow \infty$ or $\alpha \rightarrow 0$ and $\phi \rightarrow 0$). The response of the force F_y and the moment M_z with respect to arbitrary variations of the slip angle α and the spin ϕ will be determined for models which are successive approximations of the stretched string model with tread rubber elements shown in figure 7.5.9, of which the steady state behavior has been treated in section 7.5.1.

The contact equations (7.5.9) apply when the velocities of sliding V_{sx} and V_{sy} are taken equal to zero. They read then:

$$\left. \begin{aligned} \frac{\partial u}{\partial x} - \frac{\partial u}{\partial s} &= -\gamma\phi, \\ \frac{\partial v}{\partial x} - \frac{\partial v}{\partial s} &= -\alpha + x\phi. \end{aligned} \right\} \quad (7.5.96)$$

These partial differential equations will be solved by using Laplace transformation. The Laplace transforms have been written in capitals. We will not transform with respect to time, as is done usually, but with respect to the distance travelled $s = Vt$, where V is a constant. The

Laplace transform of a variable quantity, generally indicated by q , is defined through:

$$\mathcal{L}\{q(s)\} = Q(p_s) = \int_0^\infty e^{-p_s s} q(s) ds. \quad (7.5.97)$$

With the initial condition $u(x, 0) = v(x, 0) = 0$ at $s = 0$ we obtain:

$$\frac{dU}{dx} - p_s U = -y\Phi, \quad (7.5.98a)$$

$$\frac{dV}{dx} - p_s V = -A + x\Phi. \quad (7.5.98b)$$

The solutions of these ordinary first-order differential equations read:

$$U = C_u e^{p_s x} + \frac{1}{p_s} y\Phi, \quad (7.5.99a)$$

$$V = C_v e^{p_s x} + \frac{1}{p_s} A - \frac{1}{p_s} \left(\frac{1}{p_s} + x \right) \Phi. \quad (7.5.99b)$$

The terms $C_u e^{p_s x}$ and $C_v e^{p_s x}$ point to a retardational behavior. The coefficients C_u and C_v are constants of integration. They are functions of p_s and depend on the tire construction, expressed for example by equation (7.5.37) and the boundary conditions (eqs. (7.5.39) and further). The conditions at the leading edge are:

$$x = a: \quad u = 0 \text{ or } U = 0 \quad (7.5.100)$$

leads to the following expression for C_u :

$$C_u = -\frac{1}{p_s} y\Phi e^{-p_s^q}. \quad (7.5.101)$$

For the determination of C_v we turn to eq. (7.5.37) whose transform is

$$\sigma_c^2 \frac{d^2 V_c}{dx^2} - V_c = -(1 - \epsilon^2) V. \quad (7.5.102)$$

With eq. (7.5.99b) the following solution is obtained:

$$V_c = C_+ e^{x/\sigma_c} + C_- e^{-x/\sigma_c} + (1 - \epsilon^2) \left\{ \frac{C_v e^{p_s x}}{1 - \sigma_c^2 p_s^2} + \frac{1}{p_s} A - \frac{1}{p_s} \left(\frac{1}{p_s} + x \right) \Phi \right\}. \quad (7.5.103)$$

The three constants of integration C_v , C_+ and C_- may be solved with the aid of boundary conditions discussed before (cf. eq (7.5.39) and further).

With the use of eqs (7.5.26–28) and (7.5.40) the Laplace transform of lateral force and moment can be obtained. For more details we refer to reference [19]. The discussion will be continued for the simpler model without lateral flexibility of the tread rubber elements ($c_p \rightarrow \infty$, $v = v_c$). The longitudinal flexibility of the tread elements will be maintained. The constant of integration C_v appearing in (7.5.99b) can now be found with the aid of the condition at $x = a$ expressed by (7.5.39), with $v = v_c$. Expression (7.5.99b) then becomes:

$$V = V_c = \frac{1}{p_s} \left[\frac{-A + (\sigma + a + 1/p_s)\Phi}{1 + \sigma p_s} e^{p_s(x-a)} + A - \left(x + \frac{1}{p_s} \right) \Phi \right] \quad (7.5.104)$$

At the leading edge the deflection becomes:

$$V_1 = \frac{\sigma}{1 + \sigma p_s} (A - a\Phi) \quad (7.5.105)$$

or transformed back:

$$\frac{dv_1}{ds} + \frac{v_1}{\sigma} = \alpha - a\phi = \psi - a \frac{d\psi}{ds}, \quad (7.5.106)$$

where use has been made of the relations (7.5.2–4).

The first-order differential equation may be found immediately from the original differential equation (7.5.10), when the condition that for $x = a$ the slope becomes $\partial v / \partial x = -v_1 / \sigma$ is taken into account.

For the calculation of the lateral force F_y and the moment M_z acting on the simple string model, two methods are encountered in the literature. The first method, employed by von Schlippe, makes use of integration of the internal lateral forces along the length of the string extending from minus to plus infinity. For the calculation of the moment, von Schlippe introduced a correction factor (ρ in [51, eq (77)]) with which the influence of the circular tire of radius r is meant to be expressed. It turns out that the effect of the circular tire upon the moment about the vertical z -axis through the contact center generated by the internal lateral forces $c_c v$ is completely cancelled out by the torque exerted by radial reactive forces S/r produced by tension in the string which is stretched around an imaginary cylinder and shifted laterally a distance v . Smiley [10] and Hadekel [9] adopted the same erroneous correction factor. Consequently, the circular shape of the tire (string) has no effect (except a small influence due to the finite length of the circular string (cf. Frank [12]) and the string can be considered to be developed in a plane (i.e., the road surface).

The other method which leads to the same results is due to Temple [9] who integrated the internal lateral forces only over the contact length and added the influence of the internal tension forces in the string just outside the contact region.

According to Temple's method we obtain for the lateral force:

$$F_y = c_c \int_{-a}^a v dx + S(v_1 + v_2)/\sigma \quad (7.5.107)$$

and for the moment due to lateral deformations denoted by M'_z :

$$M'_z = c_c \int_{-a}^a v x dx + S(a + \sigma)(v_1 - v_2)/\sigma \quad (7.5.108)$$

where v_1 and v_2 are the deflections at $x = a$ and $-a$ respectively, and $S = \sigma^2 c_c$ according to eq (7.5.34).

The moment due to longitudinal deformations of the tread elements u denoted by M_z^* becomes with eqs (7.5.26) and (7.5.40):

$$M_z^* = -c_{px} \int_{-a}^a \int_{-b}^b u y dx dy. \quad (7.5.109)$$

By adding up the contributions (7.5.108) and (7.5.109) the total moment about the z -axis is obtained

$$M_z = M'_z + M_z^*. \quad (7.5.110)$$

The Laplace transforms of F_y , M'_z and M_z^* can readily be obtained now with the aid of eqs (7.5.34), (7.5.104), and (7.5.99a). In general, these transforms can be written in the form:

$$\left. \begin{aligned} \mathcal{L}\{F_y\} &= F_\alpha A + F_\phi \Phi \\ \mathcal{L}\{M'_z\} &= M'_\alpha A + M'_\phi \Phi \\ \mathcal{L}\{M_z^*\} &= M_\alpha^* A + M_\phi^* \Phi \end{aligned} \right\} \quad (7.5.111)$$

in which F_α , F_ϕ , M'_α , M'_ϕ , M_α^* and M_ϕ^* represent the transfer functions of F_y , M'_z and M_z^* with respect to the slip angle α and the spin ϕ ($= d\psi/ds$). In order to avoid double subscripts, the subscripts y and z are omitted. We find the following transfer functions in vector form for the tire model considered

$$(F_\alpha, F_\phi) = \frac{c_c}{p_s} \left[2(\sigma + a) \left(1, -\frac{1}{p_s} \right) + \frac{1}{p_s} \left(1 + \frac{\sigma p_s - 1}{\sigma p_s + 1} e^{-2p_s a} \right) \right. \\ \left. \times \left(-1, \sigma + a + \frac{1}{p_s} \right) \right], \quad (7.5.112)$$

$$\begin{aligned}
 (M'_\alpha, M'_\phi) = \frac{c_c}{p_s} \left[2a\{\sigma(\sigma+a) + \frac{1}{3}a^2\} (0, -1) \right. \\
 \left. + \frac{a(1 + e^{-2\nu_s a}) + p_s\{\sigma(\sigma+a) - 1/p_s^2\} (1 - e^{-2\nu_s a})}{(\sigma p_s + 1)p_s} \right. \\
 \left. \times \left(-1, \sigma + a + \frac{1}{p_s} \right) \right], \quad (7.5.113)
 \end{aligned}$$

and furthermore

$$\begin{aligned}
 M_\alpha^* &= 0 \\
 M_\phi^* &= -\frac{\kappa^*}{ap_s} \left\{ 1 - \frac{1}{2ap_s} (1 - e^{-2\nu_s a}) \right\} \quad (7.5.114)
 \end{aligned}$$

in which the quantity has been introduced:

$$\kappa^* = \frac{4}{3} a^2 b^3 c_{px}. \quad (7.5.115)$$

By transforming back the above expressions, the deflection, the force and the moment can be found as a function of distance travelled for given variation of α and ϕ .

Response to step function of the slip angle.

An important characteristic aspect of tire behavior is the response of the lateral force to a stepwise variation of the slip angle α . The initial conditions at $s=0$ read: $v(x)=0$; for $s>0$ the slip angle becomes $\alpha=\alpha_0$. From (7.5.104) we obtain for the lateral deflection of the string in the contact region:

$$\frac{v}{\alpha_0} = a - x + \sigma \{1 - e^{-(s+x-a)/\sigma}\} \quad (\text{for } x > a - s) \quad (7.5.116)$$

while for the original points the following simple relation holds:

$$\frac{v}{\alpha_0} = s \quad (\text{for } x \leq a - s) \quad (7.5.117)$$

With (7.5.107), finally, the force has been calculated for the two intervals, with and without original contact points.

$$F_y = c_c \{2(\sigma+a)s - \frac{1}{2}s^2\} \alpha_0 \quad (s \leq 2a) \quad (7.5.118a)$$

$$F_y = c_c \{2(\sigma+a)^2 - 2\sigma^2 e^{-(s-2a)/\sigma}\} \alpha_0 \quad (s > 2a) \quad (7.5.118b)$$

The latter part (7.5.118b) could have been obtained immediately from (7.5.112). The variation of F_y , graphically shown in figure 7.5.34, may be used for an experimental determination of the relaxation length σ of the tire. For this purpose the ratio of the force attained at $s = 2a$ and the steady state value $C_{F\alpha}\alpha_0$ may serve. Another method for the determination of the relaxation length has been given in section 7.5.1, eq (7.5.51).

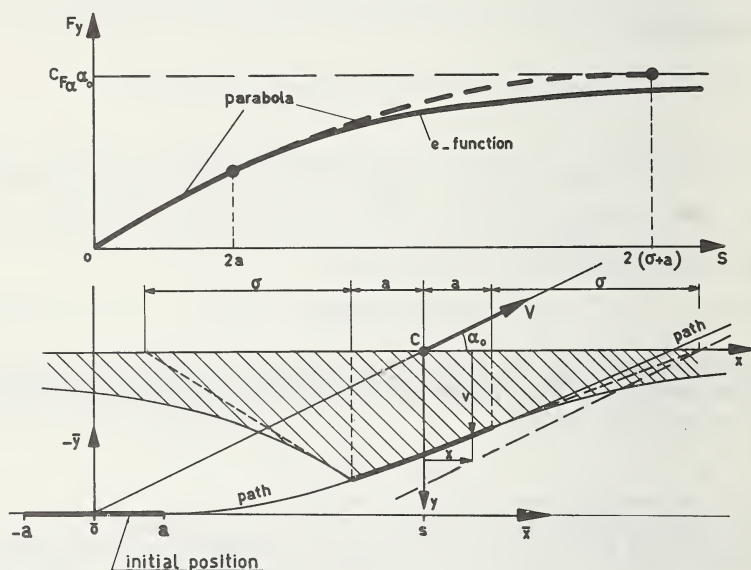


FIGURE 7.5.34. The response of the lateral force F_y on a step input of the slip angle α , calculated for the relaxation length $\sigma = 3a$.

Response to sinusoidal inputs (shimmy).

The frequency response functions for F_y and M_z can easily be found by replacing p_s by $i\omega_s$ in eqs (7.5.112–114). The path frequency ω_s equals $2\pi/\lambda$, where λ denotes the wavelength of the motion. When we are dealing with sinusoidal motions with the x -axis deviating only slightly from the \bar{x} -axis fixed to the road (cf. fig. 7.5.1), it is convenient to replace α and ϕ by the variables ψ and \bar{y} or $\beta (= d\bar{y}/ds$ for $\beta \ll 1$). With the aid of the relations (7.5.2), (7.5.3), and (7.5.8) we find for the transfer functions

with respect to ψ and β (or \bar{y}), expressed in terms of the transfer functions found before:

$$\left. \begin{aligned} F_{\psi} &= F_{\alpha} + p_s F_{\phi}, & F_{\beta} \left(= \frac{1}{p_s} F_{\bar{y}} \right) &= -F_{\alpha}, \\ M'_{\psi} &= M'_{\alpha} + p_s M'_{\phi}, & M'_{\beta} \left(= \frac{1}{p_s} M'_{\bar{y}} \right) &= -M'_{\alpha}, \\ M_{\psi}^* &= p_s M_{\phi}^*, & M_{\beta}^* \left(= \frac{1}{p_s} M_{\bar{y}}^* \right) &= 0. \end{aligned} \right\} \quad (7.5.119)$$

The frequency response functions, $F_{\psi}(i\omega_s)$ etc., are the complex ratios between output, F_y etc., and the input ψ etc. For the tire model with and without tread elements their absolute and phase relationship has been calculated. For shimmy analysis, the response of M_z to ψ is of great importance.

In figures 7.5.35a, b, c, d the various responses are shown, as a ratio to their steady state values as a function of the nondimensional path frequency, $\omega_s a$. Figure 7.5.35e shows the response M_{ψ}^* divided by the constant κ^*/a , the value of which M_{ψ}^* approaches when $\omega_s \rightarrow \infty$. The approximate responses treated below are also shown in these figures. The phase angles ϕ are taken as positive when the output lags behind the input, which appears to be the case with the force and moment due to lateral deformation. The moment M_z^* due to longitudinal deformation however, appears to lead in phase. The phase lead of M_z^* causes a reduction in phase lag of the total moment M_z with respect to ψ , as has been illustrated in the diagram of figure 7.5.36. This is a favorable effect for the suppression of shimmy.

In the complex plane shown in figure 7.5.36 the response curves are drawn for the moment M'_z , which applies for an infinitely thin tire, and for the moment $M_z = M'_z + M_z^*$ for a tire of finite width with $\kappa^* = C_{M\alpha} a$. The moments are made nondimensional by division by the steady state value M_{z0} , which occurs at $\alpha = \alpha_0 = \psi_0$. The curve for a tire with $\kappa^* = C_{M\alpha} a$ is obtained by vector addition of M'_z and M_z . Curves for other values of κ^* may be obtained by multiplying the vector of M_z by the factor $\kappa^*/C_{M\alpha} a$. The calculated behavior of the linear tire model has un mistakeable points of agreement with motions found experimentally at low values of the swivel frequency. At higher values of the frequency, the influence of the gyroscopic couple due to tire deformation, dealt with later on, is no longer negligible.

We may note, furthermore, that above a certain value of κ^* the curve for the total couple M_z/M_{z0} will not encircle the origin but will remain on the right-hand side of this point. This appears to be a typical property of curves obtained experimentally, which has not been explained before. The point of intersection of the curve for M_z and the real axis (fig. 7.5.36)

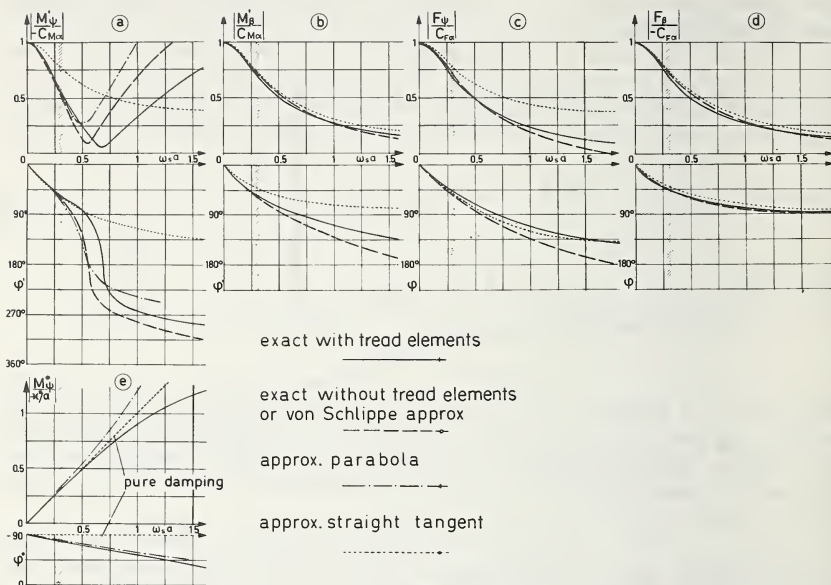


FIGURE 7.5.35. Exact and approximate response characteristics of force and moment with respect to ψ and β for string type models ($\sigma^* = 3a$, $\sigma = 3.74a$, $\epsilon = 1/7.5$; without profile elements: $\sigma = 3a$).

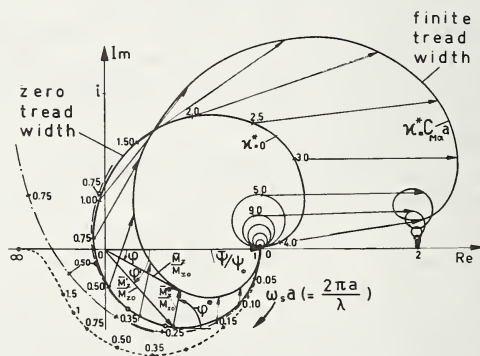


FIGURE 7.5.36. Response curves in the complex plane for the moment M_z with respect to yaw angle ψ .

represents the point of “kinematic” shimmy (cf. Kantrowitz [44] and Saito [46]). This sort of shimmy may occur at very low values of speed of travel, where the frequency and consequently the moments due to viscous damping and inertia acting about the king-pin axis become very small.

Dynamic tire tests at low values of the swivel frequency show good correspondence with the theory as will be shown after the introduction of the gyroscopic effect. Experiments with tires of different tread shapes indicate that tires with longitudinal ribs have a greater κ^* than tires with a block profile. Tests indeed show that ribbed tires are less sensitive to shimmy [19].

The response for $\omega_s \rightarrow \infty$ ($\lambda = 0$, standing tire) might be used for experimental determination of parameter κ^* . Torsion of a standing tire about the vertical axis over a small angle ψ_0 produces a moment:

$$-M_z = C_\psi \psi_0 = (C_{M\alpha} + \kappa^*/a) \psi_0 \quad (7.5.120)$$

from which the quantity κ^* can be obtained after the determination of the aligning torque stiffness.

Figure 7.5.35 shows that the exact responses of the models with and without tread elements are qualitatively the same. Quantitatively, the deviation from the response of the model with tread rubber becomes larger for shorter wavelengths (larger ω_s). In the region important for shimmy analysis, at the left-hand side of the hatched band, very good correspondence exists. The exact treatment of the simpler model, however, is still too complicated to be used in the actual shimmy analysis. We shall therefore consider three approximations for the response of the model without lateral tread rubber flexibility.

Approximations.

A first approximate description of the behavior of this model originates from von Schlippe [25]. The contact line is considered to be a straight line connecting the two endpoints of the real contact line (see fig. 7.5.37). Only the deflections v_1 and v_2 of these points are of importance now. For the transformed force and moment we obtain, after some manipulation and with the aid of expressions (7.5.50):

$$\begin{aligned} \mathcal{L}\{F_y\} &= c_c(\sigma + a)(V_1 + V_2) = C_{F\alpha} \frac{V_1 + V_2}{2(\sigma + a)}, \\ \mathcal{L}\{M_z\} &= c_c\{\sigma(\sigma + a) + 1/3a^2\}(V_1 - V_2) = C_{M\alpha} \frac{V_1 - V_2}{2a}. \end{aligned} \quad (7.5.121)$$

With the aid of (7.5.104) the transfer functions become:

$$(F_\alpha, F_\phi) = \frac{C_{F\alpha}}{2(\sigma + a)p_s} \left\{ 2\left(1, -\frac{1}{p_s}\right) + \frac{1 + e^{-2p_s a}}{\sigma p_s + 1} (-1, \sigma + a + 1/p_s) \right\}, \quad (7.5.122)$$

$$(M'_\alpha, M'_\phi) = \frac{C_{M\alpha}}{2ap_s} \left\{ 2a(0, -1) + \frac{1 - e^{-2p_s a}}{\sigma p_s + 1} (-1, \sigma + a + 1/p_s) \right\}. \quad (7.5.123)$$

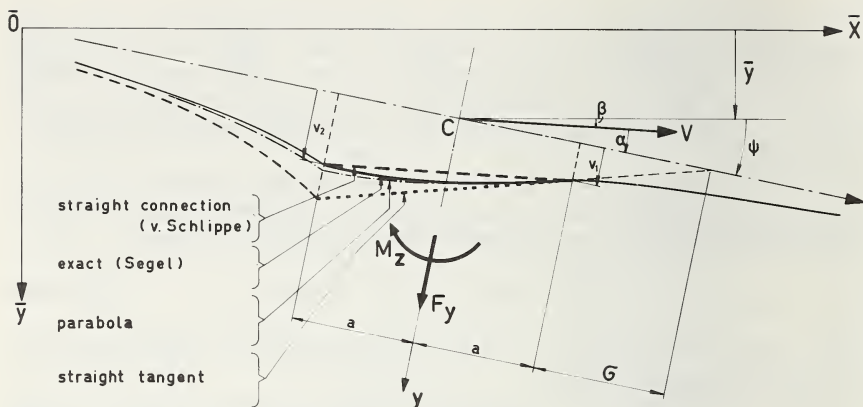


FIGURE 7.5.37. The exact deflection of the simple stretched string model and three approximations.

The responses with respect to ψ and β , obtained with the aid of formulae (7.5.119), appear to coincide practically with those obtained from formulae (7.5.112) and (7.5.113) in the range of wavelengths investigated for $\sigma = 3a$ (see curves "exact/v. Schlippe" in figs. 7.5.35–36).

Simulation of the von Schlippe representation by means of an analog computer appeared feasible although complicated (cf. [19]). In this simulation use has to be made of equation (7.5.106) for obtaining v_1 , and of the retardational behavior in order to generate v_2 . The latter may be carried out with the aid of a memory device (magnetic tape recorder or otherwise).

Simpler directly applicable approximations are obtained by expanding the exact response functions (7.5.112), (7.5.113) and also (7.5.114) into powers of p_s . With the use of relations (7.5.119) we find for the power series of the responses to the angular displacement ψ and the lateral displacement \bar{y} of the wheel plane:

$$\left. \begin{aligned}
 F_{\psi}(\sigma p_s + 1) &= C_{F\alpha}(1 - ap_s) + 2c_c a^2(\sigma + a) \left\{ (\sigma + \frac{2}{3}a)p_s^2 - \frac{1}{3}a^2 p_s^3 \right\} + \dots \\
 F_{\bar{y}}(\sigma p_s + 1) &= -C_{F\alpha} p_s + 2c_c a^2 \left\{ (\sigma + \frac{2}{3}a)p_s^2 - \frac{1}{3}a^2 p_s^3 \right\} + \dots \\
 M'_{\psi}(\sigma p_s + 1) &= -C_{M\alpha}(1 - ap_s) - (\sigma + a)aC_{M\alpha}p_s^2 \\
 &\quad + \frac{2}{3}(\sigma + a)a^2(C_{M\alpha} - 0.0667c_c a^3)p_s^3 + \dots \\
 M'_{\bar{y}}(\sigma p_s + 1) &= C_{M\alpha}p_s(1 - ap_s) \\
 &\quad + \frac{2}{3}a^2(C_{M\alpha} - 0.0667c_c a^3)p_s^3 + \dots
 \end{aligned} \right\} \quad (7.5.124)$$

$$\left. \begin{aligned} M_{\psi}^* &= -\kappa^* (p_s - 2/3 a p_s^2 + 1/3 a^2 p_s^3 + \dots) \\ M_s^* &= 0. \end{aligned} \right\} \quad (7.5.125)$$

In the periodic case we have: $p_s = i\omega_s = i\omega/V = 2\pi i/\lambda$. When in the power series (7.5.124) truncation is made to the second power of p_s , the shape of the contact line is approximated by a parabola and when the second and higher power are neglected, the contact line is approximated by a straight line, both touching the real contact line at the leading edge (cf. fig. 7.5.37). The larger the wavelength becomes relative to the contact length, the better the approximation will be. In the practical range of wavelengths, especially for the amplitude responses of M_z' to ψ , the parabolic approximation furnishes a great improvement with respect to the straight tangent approximation. The responses gotten from these approximation are shown in figure 7.5.35. Also, the response due to longitudinal deformations (7.5.125) has been approximated according to a quadratic and a linear variation of these deflections along the x -axis (see fig. 7.5.35e). The linear representation (up to p_s) corresponds to a viscous damping. The approximate differential equations for the force and the moment, directly applicable for shimmy analyses, which correspond to the quadratic approximation of the response functions (parabolic lateral deflection) read:

$$\left. \begin{aligned} \sigma \frac{dF_y}{ds} + F_y &= C_{F\alpha} \left\{ \psi - a \frac{d\psi}{ds} - \frac{d\bar{y}}{ds} \right\} \\ &\quad + \underline{2c_c a^2 (\sigma + 2/3 a) \left\{ (\sigma + a) \frac{d^2\psi}{ds^2} + \frac{d^2\bar{y}}{ds^2} \right\}} \\ \sigma \frac{dM_z'}{ds} + M_z' &= -C_{M\alpha} \left\{ \psi - a \frac{d\psi}{ds} - \frac{d\bar{y}}{ds} \right\} - \underline{C_{M\alpha} a \left\{ (\sigma + a) \frac{d^2\psi}{ds^2} + \frac{d^2\bar{y}}{ds^2} \right\}} \\ M_z^* &= -\kappa^* \frac{d\psi}{ds} + \underline{2/3 a \kappa^* \frac{d^2\psi}{ds^2}} \end{aligned} \right\} \quad (7.5.126)$$

When omitting the underlined portions of eqs (7.5.126), the linear approximation (lateral deflection according to straight tangent) is obtained. In that case F_y and M_z' only depend on v_1 (cf. eqs (7.5.106), (7.5.46) $\sigma^* = \sigma$, (7.5.49)), and M_z^* corresponds to a moment due to viscous damping (damping coefficient $= \kappa^*/V$).

A final approximation can be obtained by neglecting the dimensions of the contact area ($a = b = 0$). This leads to a representation of the nonsteady state tire behavior which has been used by various authors. Although the moment should vanish for the string model, some authors maintain M' and use the measured aligning torque stiffness $C_{M\alpha}$.

Nonlinear behavior due to partial sliding.

The general treatment of the combination of nonsteady state drift and turning is extremely difficult. We shall therefore restrict ourselves to the simple string type tire model without lateral tread rubber elasticity. The effect of tread width (M_z^*) may be treated separately when longitudinal sliding velocities are assumed to be small. From the above analysis it appears that for a wheel swivelling about a vertical axis through the wheel center, the two moments M^* and M' do not attain their maximum at the same time. A phase difference ranging from $\frac{1}{4}\pi$ to about $\frac{1}{2}\pi$ radians will occur in the practical range of wavelengths. In this range of wavelengths, many times larger than the contact length (order of 10 times), the shape of the deflection of the tire approaches the stationary shape, i.e., shows an almost straight contact line in case of complete adhesion (linear approximation mentioned above). If, furthermore, in figure 7.5.15 the front sliding region is neglected, the lateral deflection at the leading edge v_1 is the only quantity which governs the lateral tire deformation. As long as no total sliding occurs, v_1 varies according to the differential equation (7.5.106). Finally, for F_y and M_z^* , measured or calculated characteristics as a function of slip angle $\alpha = v_1/\sigma$ may be employed. According to the steady state side slip theory, the relaxation length of a tire with tread elements decreases somewhat with increasing slip angle (fig. 7.5.11). The introduction of a nonconstant σ , however, would lead to great mathematical complexity.

In [19] Pacejka uses an analog computer in connection with a tape recorder for the simulation of a more exact representation of the non-stationary behavior of the partially sliding tire, which can be seen as a nonlinear extension of von Schlippe's approximation of the behavior at complete adhesion.

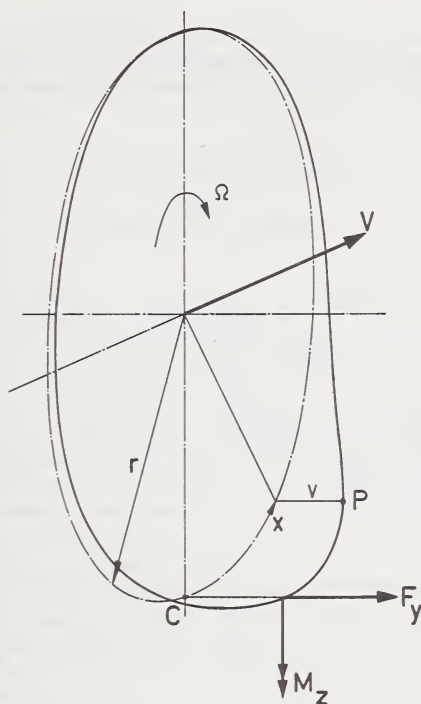
Gyroscopic couple due to lateral tire deformation.

In [19] it has been shown that inertial effects due to lateral vibrations of the peripheral line of the nonrolling tire may be neglected for frequencies lower than about 8 Hz. At higher frequencies tire inertial forces are expected to have considerable influence upon the tire deformation and consequently upon tire force and moment response. Approximate calculations indicate that the ratio of inertial and elastic forces amounts to 6 percent and 24 percent for a frequency of 7 c.p.s. and 14 c.p.s. respectively.

In case of a rolling tire we have to deal with the substantial acceleration of a material point of the tire. For a point P (fig. 7.5.38) of a tire with angular speed Ω and radius r we obtain:

$$\frac{d^2v}{dt^2} = \frac{\partial^2 v}{\partial t^2} - 2 \frac{\partial^2 v}{\partial x \partial t} r \Omega + \frac{\partial^2 v}{\partial x^2} r^2 \Omega^2. \quad (7.5.127)$$

The first term represents the inertial force discussed above. We shall neglect this term in the following. When calculating the moment about the vertical axis, taking into account the last two terms of (7.5.127) to

FIGURE 7.5.38. *The deflected tire peripheral line.*

gether with the centrifugal force acting on a tire element in radial direction, and furthermore a lateral deflection $v(x)$ of a massless tire model according to eqs (7.5.38) and (7.5.104), we find that only one term remains, which represents the gyroscopic couple. This couple corresponds to the gyroscopic couple which would arise when the circular peripheral line of the tire is tilted about the horizontal line which lies in the wheel plane and passes through the wheel axis. The lateral deflection of the tilted peripheral line represents the first odd harmonic of the Fourier expansion of the lateral tire deflection. This imaginary angle of tilt ($-\gamma_t$) will be approximately proportional to the lateral tire force F_y . We obtain, then, for the gyroscopic couple:

$$M_{\text{gyt}} = I'_t \Omega \dot{\gamma}_t = -C_{\text{gyt}} V \frac{dF_y}{dt}, \quad (7.5.128)$$

in which I'_t represents the effective fraction of the tire polar moment of inertia. C_{gyt} is a tire constant which is proportional to tire mass, m_t , and tire lateral compliance, $1/C_y$, and is furthermore influenced by the type of tire construction expressed by the dimensionless parameter c_{gyt} .

$$C_{\text{gyt}} = c_{\text{gyt}} m_t / C_y. \quad (7.5.129)$$

For a conventional tire we found that $c_{\text{gyr}}=0.12$ is a value which produces a good approximation to experimentally obtained responses.

From (7.5.128) we obtain the following expressions for the transfer functions of M_{gyr} :

$$M_{\text{gyr}, \psi} = -C_{\text{gyr}} V^2 p_s F_{\psi}, \quad (7.5.130)$$

$$M_{\text{gyr}, \dot{\psi}} = -C_{\text{gyr}} V^2 p_s F_{\dot{\psi}}.$$

from which we see that for a certain wavelength λ of the swivel motion, where $p_s = i\omega_s = 2\pi i/\lambda$ is a constant, the response increases quadratically with the speed of travel V . In the complex plane, the vector of M_{gyr} will be directed perpendicular to the vector of F_y . In figure 7.5.39 theoretically obtained response curves of the moment with respect to ψ are shown for the model with lateral tread rubber elasticity ($\sigma^*=2.4 a$, $\epsilon=1/7.5$). The value of σ^* has been experimentally determined with the aid of eq (7.5.51) for a tire whose experimental response curves are shown in figure 7.5.40. The value of ϵ has been estimated. Figures 7.5.35–36 show that the use of the simpler model without lateral tread rubber flexibility (exact or parabolic approximation) is expected to yield results which are close to the theoretical curves of figure 7.5.39 in the practical range of the dimensionless path frequency $\omega_s a < 0.35$. The straight tangent approximation needs longer wavelengths for acceptable results.

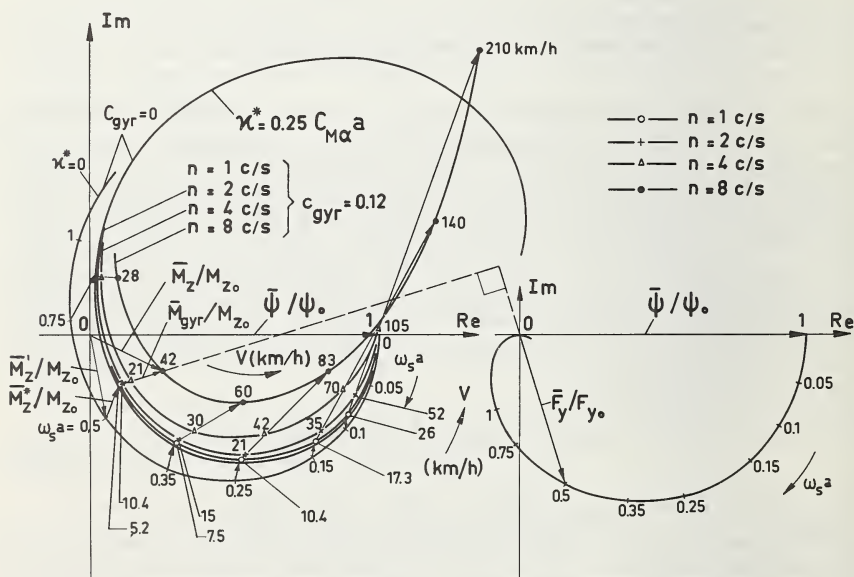


FIGURE 7.5.39. Influence of frequency of motion upon response (theoretical).

$\sigma^* = 2.4a$, $\epsilon = 1/7.5$, $a = 0.115$ m, $C_{Fa} = 64000$ N, $C_{M\alpha} = 3900$ Nm, $C_y = 165000$ N/m, $C_{\text{gyr}} = 2.5 \times 10^{-5}$ s², $m_t = 35$ kg.

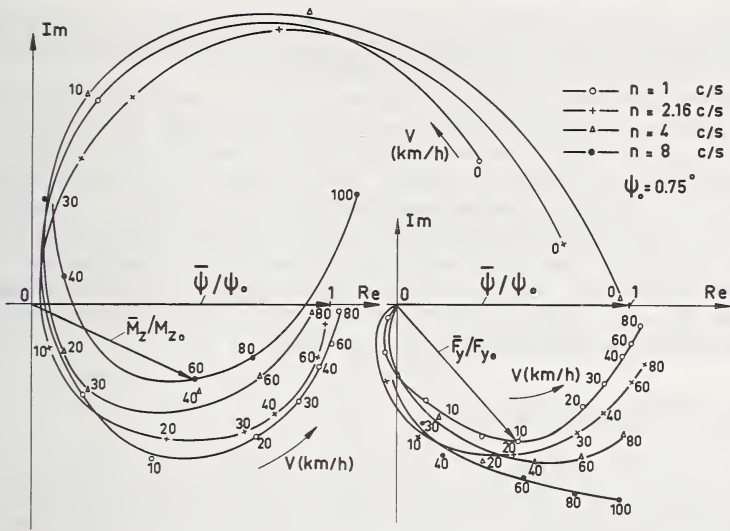


FIGURE 7.5.40. Influence of frequency of motion upon response (experimental).

Tests carried out on drum test stand (cf. figure 7.5.40a). Tire 9.00-16 block tread $p_1 = 1.75$ bar.

A reasonable correspondence between theory and experiment appears to exist. The figures clearly show that an important time influence exists. With increasing swivel frequency the curves of the moment rise, which means that the phase lag decreases and thus the degree of self-excitation of the system becomes less.

The points of the experimental curves obtained at $V = 0$ (standing tire) are situated above the real axis and become lower and further to the right at increasing frequencies. This may be due to the viscoelastic properties of the tire rubber, which shows larger stiffness and less damping at higher frequencies. The amplitude of the force F_y appears to

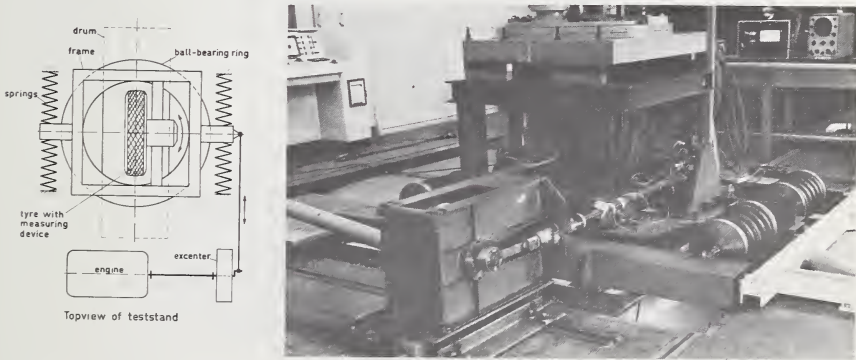


FIGURE 7.5.40a. Shimmy excitation test stand for measuring tire frequency response.

increase with increasing frequency. This property has not yet been explained theoretically. For shimmy analysis the effect of such an increase in amplitude appears to be of less importance.

The machine with which the shimmy response tests have been carried out is shown in figure 7.5.40a. The wheel is swivelled as it rolls over the drum, together with the whole structure in which the wheel axle is mounted. The structure is excited against four coil springs in the resonance frequency so that only a small force of excitation is needed. A special measuring hub (described in sec 7.2) has been used for the measurement of forces and moments. Because of the fact that the wheel inertia distorts the signal, a correction is needed in order to obtain the torque M_z acting from drum to tire. Results of other shimmy response tests can be found in references [46] and [57].

Effect of a Time-Varying Load

Due to road roughness, variations in vertical tire load occur which cause unfavorable changes in the tire cornering behavior. This has been found experimentally by, amongst others, Kurz [53]. The long wavelength phenomenon can be explained sufficiently by consideration of the steady state tire characteristics. As has been indicated by Kurz, the static loss of the average cornering force is due to the typical nonlinear variation of cornering force with normal load (cf. fig. 7.5.41). Tests carried out by Metcalf [55] (cf. also Endres [54]) reveal that short wave length motions show an additional loss in side force, which Metcalf has termed the dynamic loss, although the cause may be entirely of a kinematic nature.

In [56] Pacejka made mention of a theoretical study dealing with this problem. The essence of this theory, which has been restricted to small slip angles, will be enunciated below. After that, a semi-empirical theory

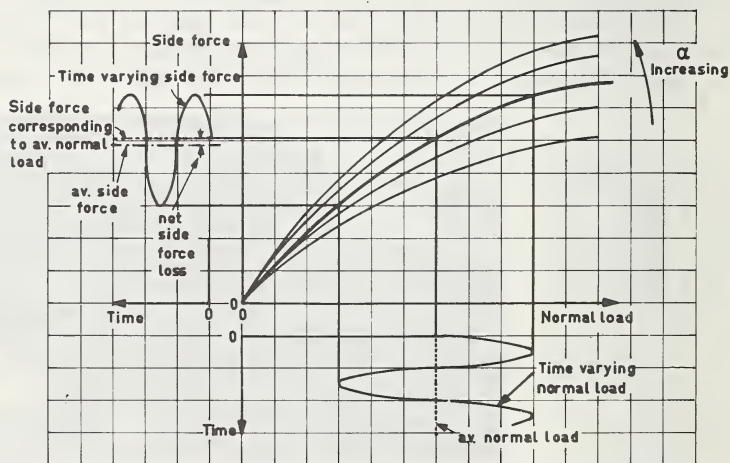


FIGURE 7.5.41. *Effect of slip angle and normal load on tire side force (from Kurz [53]).*

The changes in front and rear lateral deflection $v_{c1,2}$ are composed of contributions due to various causes. For the deflection at the front we obtain:

1. due to lateral wheel displacement ($\alpha\Delta_s$):

$$\Delta v_{c1} = A(a) \cdot \alpha \Delta_s$$

2. due to loss of contact rear ($\Delta \bar{x}_2 > 0$):

$$\Delta v_{c1} = -B(a) \frac{v_2 - v_{c2}}{\sigma_c} \bar{x}_2$$

3. due to loss of contact front ($\Delta \bar{x}_1 < 0$):

$$\Delta v_{c1} = B^*(a) \frac{v_1 - v_{c1}}{\sigma_c} \Delta \bar{x}_1$$

4. due to longitudinal displacement of leading edge ($\Delta \bar{x}_1$):

$$\Delta v_{c1} = -\frac{v_{c1}}{\sigma} \Delta \bar{x}_1$$

(7.5.133)

Similar expressions are obtained for the contributions to the change of the lateral deflection at the rear (v_{c2}). The contact-length-dependent coefficients appearing in the expressions are:

$$\left. \begin{aligned} A(a) &= \{-2\epsilon + (1 + \epsilon)e^{2a/\sigma_c} - (1 - \epsilon)e^{-2a/\sigma_c}\} / P(a) \\ B(a) &= 2/P(a) \\ B^*(a) &= \{(1 + \epsilon)e^{2a/\sigma_c} + (1 - \epsilon)e^{-2a/\sigma_c}\} / P(a) \\ P(a) &= \frac{1 + \epsilon}{1 - \epsilon} e^{2a/\sigma_c} - \frac{1 - \epsilon}{1 + \epsilon} e^{-2a/\sigma_c} \end{aligned} \right\} (7.5.134)$$

They are derived from solutions of the differential equation for the shape of the string (7.5.35). For the parameters employed we refer to expressions (7.5.34). From the differences shown above (7.5.132-133) the following differential equations for the unknowns v_{c1} and v_{c2} are formed:

$$\left. \begin{aligned} \frac{dv_{c1}}{ds} &= -\left(1 + \frac{da}{ds}\right) \frac{v_{c1}}{\sigma} - B(a) \left(1 - \frac{da}{ds}\right) \frac{v_2 - v_{c2}}{\sigma_c} \\ &\quad + B^*(a) \left(1 + \frac{da}{ds}\right) \frac{v_1 - v_{c1}}{\sigma_c} + A(a)\alpha, \\ \frac{dv_{c2}}{ds} &= \left(1 - \frac{da}{ds}\right) \frac{v_{c2}}{\sigma} - B^*(a) \left(1 - \frac{da}{ds}\right) \frac{v_2 - v_{c2}}{\sigma_c} \\ &\quad + B(a) \left(1 + \frac{da}{ds}\right) \frac{v_1 - v_{c1}}{\sigma_c} + A(a)\alpha. \end{aligned} \right\} (7.5.135)$$

The two remaining unknowns v_1 and v_2 , denoting the total lateral deflections and consequently the distance between wheel plane and contact line at the leading and trailing edges, are found by use of the following considerations. In the rolling process of a drifting tire with a continuously changing contact length, in general, three intervals can be distinguished during the contact phase of the loading cycle. In figure 7.5.43 a possible variation of the contact length $2a$ has been shown in the road plane (\bar{x} , \bar{y}). The tire touches the ground over a certain distance of travel. Immediately after the first point touches the road, the contact line will grow in two directions. This will continue until the second interval is reached, where growth of contact takes place only at the front, and at the rear loss of contact occurs. In the third interval, finally, loss of contact at both ends takes place until the tire leaves the road. When the tire does not leave the road, an additional interval II occurs before interval I is reached again and the cycle has started anew. In less severe cases, intervals I and III may not occur. We then have the relatively simple situation of continuous growth of contact at the front and loss of contact at the rear.

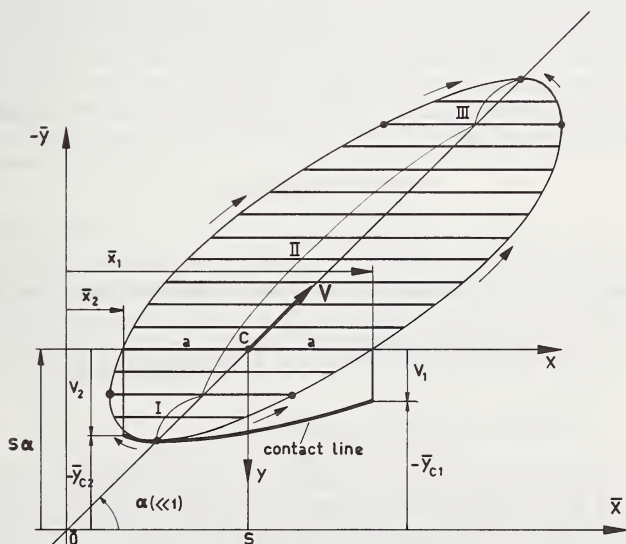


FIGURE 7.5.43. The development of the contact line of the tire model which periodically loses contact with the road.

Arrows indicate the directions in which the positions of the leading and trailing contact points change.

The unknowns v_1 and v_2 and the \bar{y} -coordinate of the contact points in the (\bar{x}, \bar{y}) plane are obtained as follows (cf. fig. 7.5.43).

$$\left. \begin{array}{l}
 \text{Interval I:} \quad \dot{\bar{x}}_1 > 0, \dot{\bar{x}}_2 < 0 \quad \left(\frac{da}{ds} > 1 \right) \\
 \quad \quad \quad v_1 = v_{c1}, v_2 = v_{c2} \\
 \quad \quad \quad -\bar{y}_{c1} = s\alpha - v_{c1}, -\bar{y}_{c2} = s\alpha - v_{c2} \\
 \\
 \text{Interval II:} \quad \dot{\bar{x}}_1 > 0, \dot{\bar{x}}_2 > 0 \quad \left(-1 < \frac{da}{ds} < 1 \right) \\
 \quad \quad \quad v_1 = v_{c1}, v_2 = s\alpha + \bar{y}_{c2} \\
 \quad \quad \quad -\bar{y}_{c1} = s\alpha - v_{c1} \\
 \\
 \text{Interval III:} \quad \dot{\bar{x}}_1 < 0, \dot{\bar{x}}_2 > 0 \quad \left(\frac{da}{ds} < -1 \right) \\
 \quad \quad \quad v_1 = s\alpha + \bar{y}_{c1}, v_2 = s\alpha + \bar{y}_{c1}
 \end{array} \right\} \quad (7.5.136)$$

By means of numerical integration equations (7.5.135) have been solved with the aid of the equations (7.5.136) and the expressions (7.5.134) for the case formulated below in which the vertical tire deflection δ has been given a periodic variation with amplitude δ_a greater than the static deflection δ_o , so that periodic loss of contact between tire and road occurs. The rated or static situation will be indicated with subscript o . The tire radius is denoted by r . The vertical deflection and the contact length are governed by the equations

$$\delta = \delta_o - \delta_a \sin \omega_s s, \quad (7.5.137)$$

$$a^2 = 2r\delta - \delta^2. \quad (7.5.138)$$

The numerical values of the system under consideration are as follows:

$$\left. \begin{array}{l}
 a_o = 0.25r, (\delta_o = 0.03175r), \delta_a = 0.1r, \omega_s = \frac{\pi}{4a_o} \\
 \sigma = 3a_o, \epsilon = 0.25, (\sigma_c = 0.75a_o).
 \end{array} \right\} \quad (7.5.139)$$

In figure 7.5.44 the calculated variation of contact length $2a$ (oval curve), the path of the contact points (lower curve AB) and the course of the points of the string at the leading and trailing edge (AC and BC) are indicated. Two positions of the tire are shown, one in interval II and one in interval III.

It is necessary that the calculations in the numerical integration process be carried out extremely accurately. A small error gives rise to a

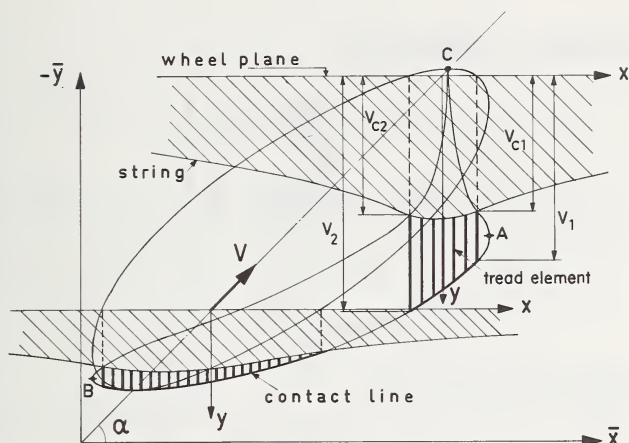


FIGURE 7.5.44. The deflected tire model in two positions during the interval of contact with the road.

rapid build up of deviation. In the case considered above, the integration time is limited and accurate results can be obtained. In cases, however, where continuous contact between tire and road exists, a very long integration time is needed before a steady state situation has been attained, which is due to the fact that the exact initial conditions of one loading cycle are not known. For this sort of situation, the exact method described above will be difficult to apply due to strong drift of v_{c2} in particular.

For further investigation of the effect of a time varying load we will turn to an approximate method based on the behavior of a string model without tread elements.

Simple string model.

The treatment of this model is much simpler since the deflections at both ends are independent of each other. Drift does not occur in the calculation process. In figure 7.5.45 the deflected model has been shown in interval II. In the three intervals the following sets of equations apply. Growth of contact at leading edge:

$$\left. \begin{aligned} \dot{\bar{x}}_1 &> 0 & \left(\frac{da}{ds} > -1 \right), \\ \frac{dv_1}{ds} &= \alpha - \frac{v_1}{s} \left(1 + \frac{da}{ds} \right), \\ \bar{x}_1 &= s + a, \\ -\bar{y}_{c1} &= s\alpha - v_1. \end{aligned} \right\} \quad (7.5.140)$$

Growth of contact at trailing edge:

$$\left. \begin{aligned} \dot{x}_2 &< 0 & \left(\frac{da}{ds} > 1 \right), \\ \frac{dv_2}{ds} &= \alpha + \frac{v_2}{\sigma} \left(\frac{da}{ds} - 1 \right), \\ \bar{x}_2 &= s - a, \\ -\bar{y}_{c2} &= s\alpha - v_2. \end{aligned} \right\} \quad (7.5.141)$$

Loss of contact at leading edge:

$$\left. \begin{aligned} \dot{x}_1 &< 0 & \left(\frac{da}{ds} < -1 \right), \\ \bar{y}_{c1} &= \bar{y}_{c, s+a}, \\ v_1 &= s\alpha + \bar{y}_{c1}. \end{aligned} \right\} \quad (7.5.142)$$

Loss of contact at trailing edge:

$$\left. \begin{aligned} \dot{x}_2 &> 0 & \left(\frac{da}{ds} < 1 \right), \\ \bar{y}_{c2} &= \bar{y}_{c, s-a}, \\ v_2 &= s\alpha + \bar{y}_{c2}. \end{aligned} \right\} \quad (7.5.143)$$

Solutions of the above equations show considerable differences from the results obtained using the more advanced model with tread elements. The most important difference is the fact that with the simple model the lateral force does not gradually drop to zero as the tire leaves the ground.

In order to get better agreement we introduce a relaxation length $\sigma = \sigma^*(a)$ which is a function of the contact length $2a$. We will take σ^* equal to the relaxation length of the more advanced model according to eq (7.5.47) and figure 7.5.18.

In figure 7.5.46 a comparison is made of the results for the three cases: without tread elements, with tread elements (exact) and according to the approximation with varying $\sigma = \sigma^*(a)$. The calculations are carried out for the values (7.5.139). The approximate path shows good agreement with the path of the contact points for the model with tread elements. When the tread elements are omitted the path becomes wider and the lateral deflections become greater.

The lateral force F_y and the moment M_z which act on the tire can be determined with good approximation by the following simplified for-

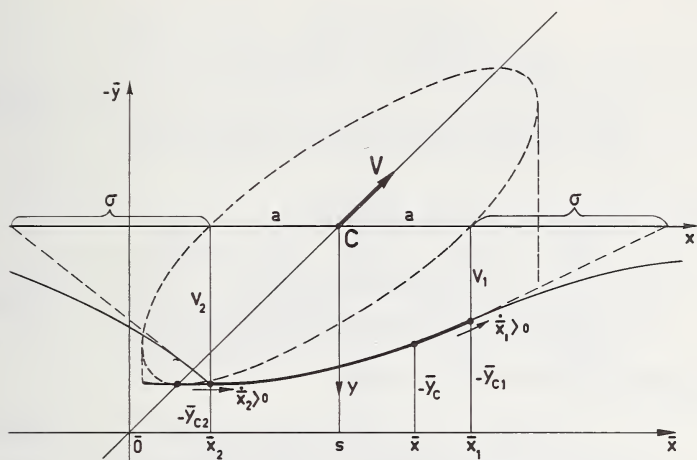


FIGURE 7.5.45. *The development of the contact line for the simple tire model without tread rubber.*

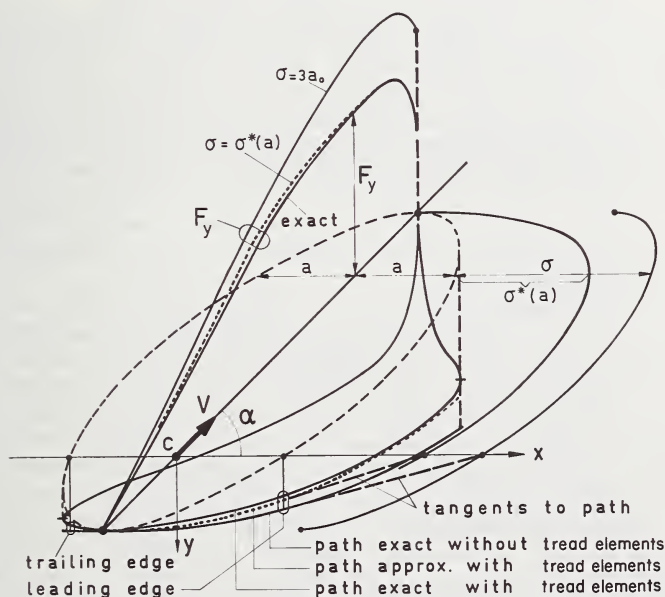


FIGURE 7.5.46. Paths of contact points and variations of lateral force F_y according to three theories.

mulae. In their derivations we have replaced the contact line by the straight line connecting the begin and end points of contact. For the model with tread rubber elements we obtain:

$$F_y = \frac{2c_c c_p}{c_c + c_p} \{a + \sigma A(a)\} v_o, \quad (7.5.144)$$

$$M_z = \frac{-2c_c c_p a}{c_c + c_p} \{1/3 a^2 + \sigma (\sigma + a) C(a)\} \alpha_o.$$

and for the model without tread elements:

$$F_y = 2c_c (a + \sigma) v_o, \quad (7.5.145)$$

$$M_z = -2c_c a \{1/3 a^2 + \sigma (\sigma + a)\} \alpha_o.$$

Here we have introduced the quantities

$$\text{and } v_o = 1/2 (v_1 + v_2), \alpha_o = 1/2 (v_1 - v_2)/a \quad (7.5.146)$$

$$C(a) = A(a) - \frac{\sigma}{a} \epsilon B^*(a) + \left(2 + \frac{\sigma}{a}\right) \epsilon B(a) \quad (7.5.147)$$

in which A , B and B^* are given by expressions (7.5.134).

For the sake of completeness the formulae for the moment have been given. We shall restrict ourselves to discussion of the variation of the force. For the three cases considered, the variation of the cornering force has been shown in the same figure 7.5.46. As expected, the approximate and exact theories drop to zero at the point of lift off, whereas the force acting on the simple string model remains finite, under the assumption of no sliding. The correspondence between exact and approximate solutions of the path and of the force are satisfactory, and we will henceforth use the approximate method exclusively for the investigation of the model with tread elements.

For a series of amplitudes δ_a and path frequencies ω_s the variation of the cornering force, or rather of the cornering stiffness, has been calculated. For illustration figure 7.5.47 gives the time histories of the cornering force acting upon the model without tread rubber elements. Four cases are considered. The upper figure shows the effect of a large amplitude, and it is clearly seen that oscillations with the larger wavelength (λ) attain a higher average side force. The effect of an amplitude equal to the static deflection is presented in the second figure. Two possibilities are considered. When contact is not lost, the tire lateral deflection does not need to be developed anew each cycle from the undeformed state, which happens when the tire leaves the ground. This causes the much lower level of the cornering force shown in the latter case. The lower figure gives the force variation which occurs at moderate values of the vertical amplitude.

Since during loss of contact negative vertical forces cannot be transmitted, the period of the total loading cycle must become greater in order to keep the average vertical load unchanged. This change in period has been taken into account in the calculation of the average side force or cornering stiffness $\bar{C}_{F\alpha}$.

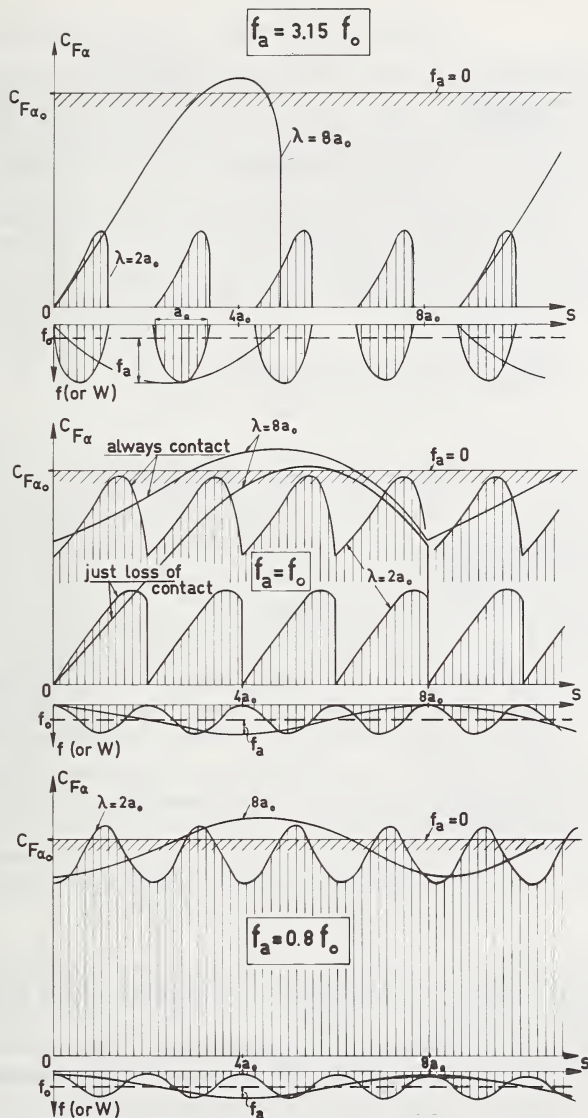


FIGURE 7.5.47. Calculated lateral force variation of the drifting simple string model (sliding not considered) due to a periodically changing vertical load W .

The lower figure represents the case of constant contact, the center figure the cases of just maintaining and losing contact and the upper figure the case of periodic loss of contact.

Figure 7.5.48 shows the final result of this investigation, viz the cornering stiffness averaged over one complete loading cycle as a function of vertical deflection amplitude δ_n and path frequency ω_s for both models with and without tread elements. With the values $\sigma = 3a_o$ and $\epsilon = 0.25$

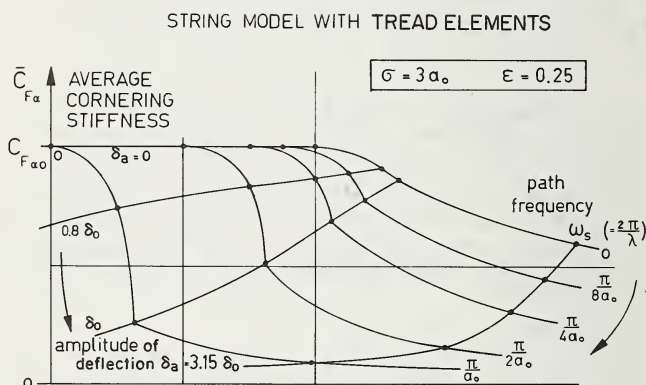
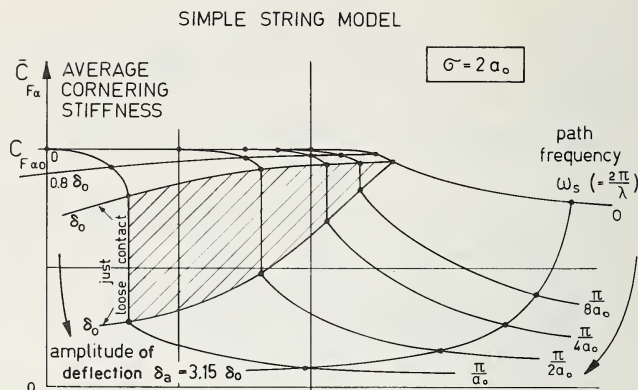


FIGURE 7.5.48. Calculated variation of average cornering stiffness \bar{C}_{Fa} with amplitude of tire normal deflection δ_a and path frequency.

the relaxation length of the more advanced model becomes $\sigma_0^* = 1.7a_0$. For the model without tread rubber a relaxation length has been considered equal to $\sigma = 2a_0$.

The figure clearly illustrates the unfavorable effect of increasing the amplitude and the path frequency. The curve at zero frequency is purely due to the nonlinear variation of the cornering stiffness as a function of vertical load shown in figures 7.5.18 and 7.5.41. A pronounced difference between the response of both types of models is the discontinuity which takes place in the curves for the simple string model. This is in contrast to the gradual variation in average cornering stiffness which occurs with the more advanced model, and no doubt also with the real tire. The more advanced model, furthermore, already shows a noticeable decrease in average cornering stiffness before the tire periodically leaves the ground. The very low level to which the average stiffness has been reduced, once loss of contact occurs, is of the same order of magnitude for both tire models.

Finite values of slip angle.

Thus far we have only discussed the behavior at small slip angles, where no sliding is assumed to occur. Larger slip angles will induce zones of sliding and cause a much more complicated situation. We have not attempted to extend this investigation into the nonlinear range of the problem.

For the analysis of automobile motions we might use the experimentally or theoretically determined average cornering stiffness function $\bar{C}_{F\alpha}(\delta_a, \omega_s)$ for the construction of the average tire characteristic $F_y(\alpha)$ from the basic characteristic $F_{y0}(\alpha_{eq})$ (cf. sec. 7.5.1) through the introduction of the equivalent slip angle.

$$\alpha_{eq} = \frac{\bar{C}_{F\alpha}(\delta_a, \omega_s)}{C_{F\alpha 0}} \alpha. \quad (7.5.148)$$

A semi-empirical theory of the effect of a time varying load has been developed by Metcalf [55]. In this theory large slip angles and the possibility of sliding have been included. Metcalf carried out a number of experiments with a 4.00-7 tire which was loaded against a rotating drum. During each loading cycle, induced by a sinusoidally changing axle displacement, two distinctly different phenomena were observed. First, as the normal load increases from a minimum value, the lateral force lags behind the applied vertical load. Secondly, after the vertical force has reached a maximum and has begun to decrease, a point is reached where the lateral force becomes equal to the instantaneous load on the tire multiplied by the friction coefficient between tire and drum.

This behavior has been simulated with the aid of an analog computer. A first-order filter has been employed for the generation of the phase lag. The response to a step change of the input corresponds to the lateral force response of the tire to a step change in vertical load (equal to the response shown in fig. 7.5.34) approximated by:

$$F_y = F_{y0}(1 - e^{-s/\sigma}). \quad (7.5.149)$$

Although Metcalf recognized that the relaxation length σ changes with vertical tire deflection, in the computations σ has been held constant for the sake of simplicity. By means of a "least selector," the lateral force has been limited to the friction coefficient multiplied by the normal load (μW).

In figures 7.5.49-54 Metcalf's computer and experimental results are presented. In the simulation a number of constant values of σ have been tried. In figure 7.5.49 the dynamic loss, which together with the static loss indicated in figure 7.5.41 forms the reduction in lateral force due to load variations, has been plotted against reduced or path frequency ω_s for three drum velocities. The test data from this figure support the hypothesis that the phenomenon is distance rather than time dependent. In figure 7.5.50 the average lateral force \bar{F}_y has been plotted against reduced frequency ω_s for two values of slip angle. The amplitude of the

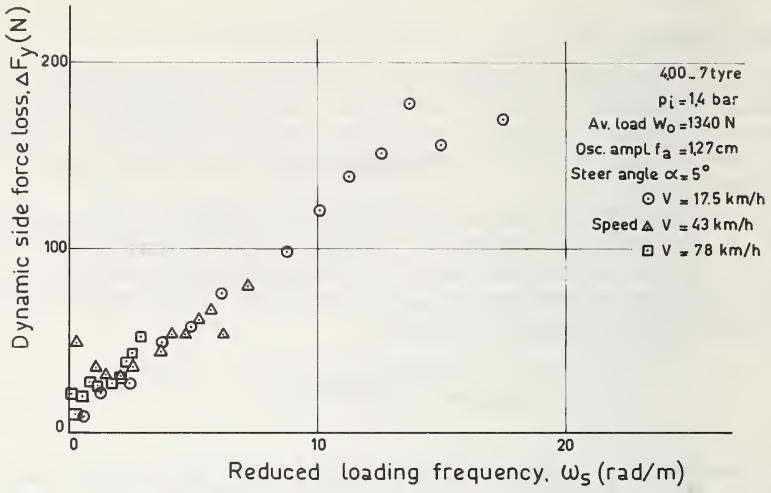


FIGURE 7.5.49. Dynamic side force loss versus reduced loading frequency for three drum velocities.
(Figs. 7.5.49-54 are taken from Metcalf [55]).

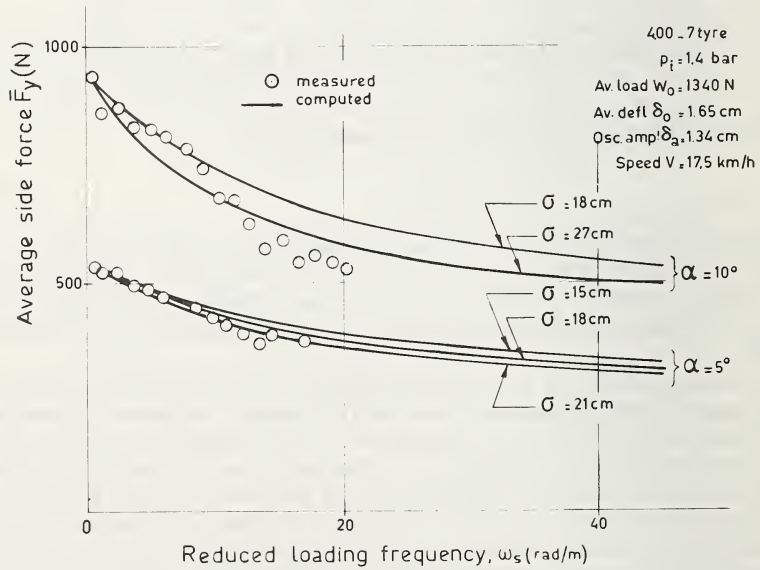


FIGURE 7.5.50. Average side force versus reduced loading frequency.

tire vertical deflection is lower than the static deflection so that contact between road and tire is maintained. In figure 7.5.51 results are plotted for the same tire but with higher inflation pressure and an amplitude greater than the static deflection, which results in a periodic loss of contact. Completely in accordance with the theory (cf. also fig. 7.5.48), the reduction with increasing reduced frequency ω_s becomes stronger for amplitudes in excess of the static tire deflection.

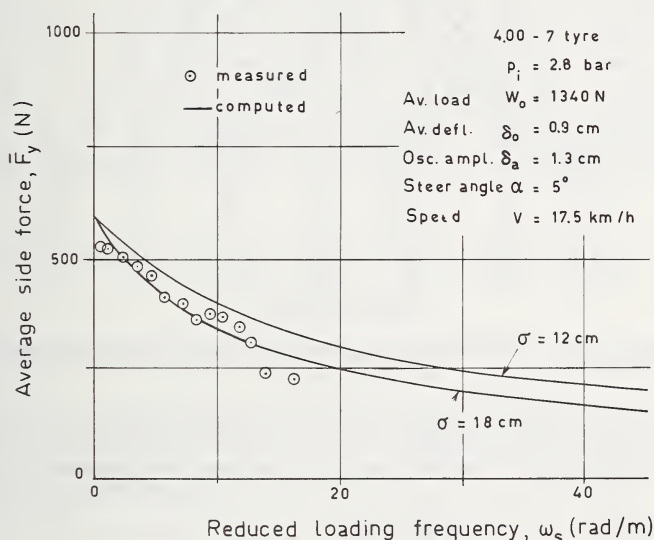


FIGURE 7.5.51. Average side force versus reduced loading frequency.

In figures 7.5.52–54 the time histories are shown for this latter configuration. These plots show agreement between test data and computed results. The lateral resonance of the measuring axle accounts for the high frequency oscillations present in the measured time histories.

The decrease of \bar{F}_y with ω_s has been reasonably well predicted by the analog computer results for $\sigma = 18$ cm. except at high values of slip angle where tests show that a sharper decrease of \bar{F}_y with ω_s occurs. This value $\sigma = 18$ cm. is approximately 20 percent larger than the value obtained experimentally at rated constant deflection W_0 and at small slip angles.

Interaction of vertical and horizontal motions.

Hitherto the slip angle of the tire has been considered as constant. In reality, however, the mass of the automobile is not infinitely large. Due to the variation of the lateral force being caused by a time-varying load, the wheel plane will move laterally. This brings us to the problem of combined nonstationary tire behavior influenced by both the vertical and horizontal wheel motions.

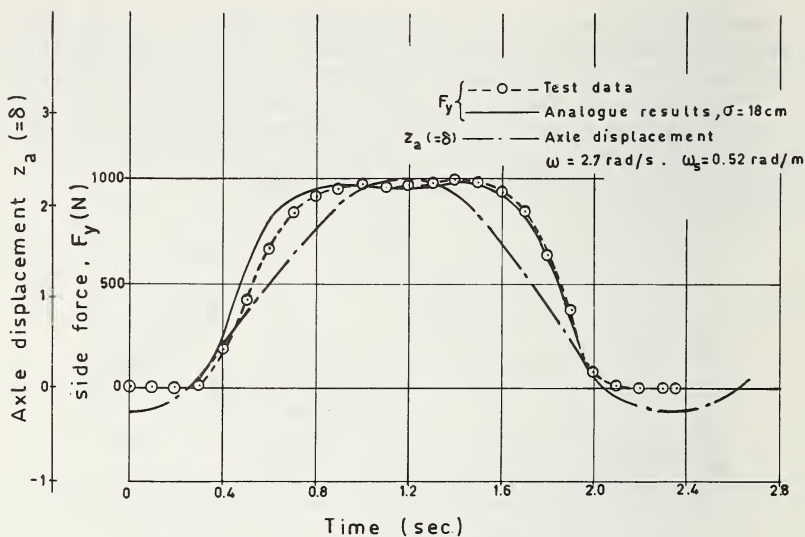


FIGURE 7.5.52. Time history, configuration of figure 7.5.51, low frequency.

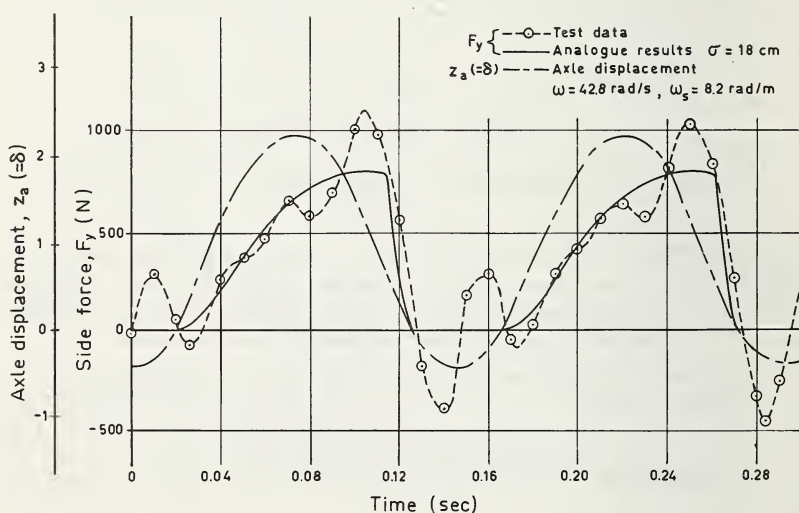


FIGURE 7.5.53. Time history, configuration of figure 7.5.51, moderate frequency.

In the literature, this problem has been touched at by Böhm [49]. He presents an approximate theory of the lateral motion of the mass m rigidly connected to the king-pin of the wheel which shows a constant steer angle ψ (cf. fig. 7.5.55). The mass is subjected to a constant lateral force K representing, for instance, the centrifugal force. Böhm considers

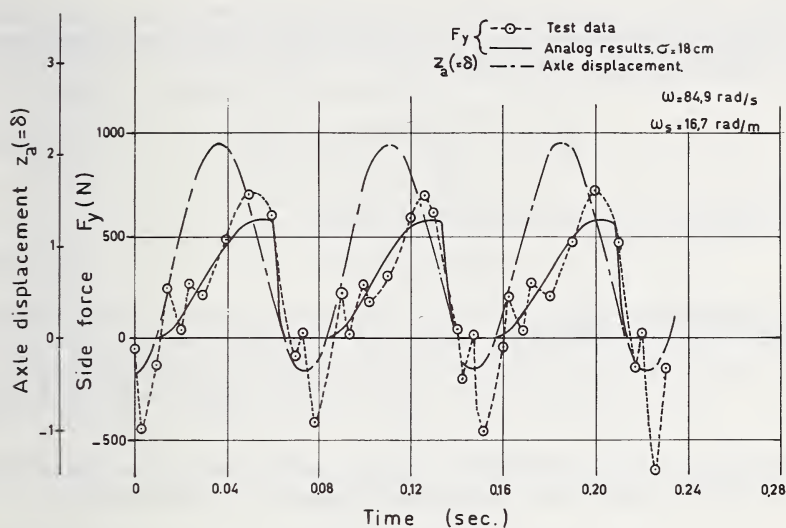


FIGURE 7.5.54. Time history, configuration of figure 7.5.51, high frequency.

a periodically changing vertical load and cornering stiffness, from which follows, according to eq (7.5.51), that for a constant lateral stiffness C_y the relaxation length σ^* also changes periodically. The following formulae are assumed to hold:

$$\left. \begin{aligned} W &= W_o / (1 + \zeta \sin \omega t), \\ C_{F\alpha} &= C_{F\alpha o} / (1 + \zeta \sin \omega t), \\ \sigma^* &= \sigma_o^* / (1 + \zeta \sin \omega t). \end{aligned} \right\} \quad (7.5.150)$$

From these assumptions it may be noted that the average values are not constant but increase with ζ !

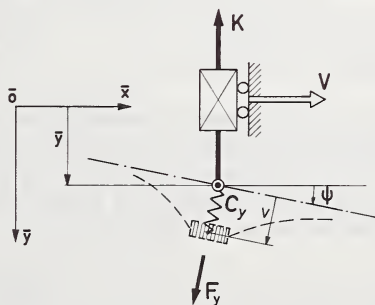


FIGURE 7.5.55. The simple tire model used for the analysis of interaction between vertical and lateral wheel motions.

The following simple differential equation for the nonsteady state variation of the lateral deflection v of the tire, valid for vanishing size of the contact area, has been applied:

$$\frac{1}{V} \dot{v} + \frac{1 + \zeta \sin \omega t}{\sigma_o^*} v = \psi - \frac{1}{V} \dot{y}. \quad (7.5.151)$$

The equation of motion for the mass reads:

$$m \ddot{y} = C_y v - K. \quad (7.5.152)$$

Elimination of \ddot{y} yields:

$$\ddot{v} + (1 + \zeta \sin \omega t) \frac{V}{\sigma_o^*} \dot{v} + \left(\frac{C_y}{m} + \zeta \frac{\omega V}{\sigma_o^*} \cos \omega t \right) v = \frac{K}{m}. \quad (7.5.153)$$

This equation with periodically changing coefficients may be solved with the aid of the perturbation method. We consider ζ small and put

$$v = v_0 + \zeta v_1(t) + \zeta^2 v_2(t) + \dots \quad (7.5.154)$$

After insertion of this power series in (7.5.153) another series arises which must vanish identically in ζ , hence the coefficients of the successive powers of ζ must vanish.

When we restrict ourselves to the second power of ζ the following form is obtained for the lateral tire deflection:

$$v = v_0 + \zeta A_1 \cos(\omega t - \phi_1) + \zeta^2 A_2 \cos(2\omega t - \phi_2) + \dots \quad (7.5.155)$$

For the factor of the first harmonic we obtain:

$$A_1 = - \frac{\frac{\omega V}{\sigma_o^*} v_0}{\sqrt{\left(\frac{C_y}{m} - \omega^2\right)^2 + \left(\frac{\omega V}{\sigma_o^*}\right)^2}}, \quad \tan \phi_1 = \frac{\frac{\omega V}{\sigma_o^*}}{\frac{C_y}{m} - \omega^2}. \quad (7.5.156)$$

It may be noted from these results that the maximum variations of lateral deflection are obtained at a frequency of the load variation equal to the natural frequency of the horizontal motion ($\omega^2 = C_y/m$). Insertion of this solution in equation (7.5.151) yields for the velocity of the mass in the lateral direction (assumed equal to zero for $\zeta=0$):

$$-\dot{y} = \zeta B_1 \sin(\omega t - \psi_1) + \zeta^2 \frac{V}{\sigma_o^*} A_1 \sin^2 \omega t \cdot \sin \phi_1 + \zeta^2 B_2 \sin(2\omega t - \psi_2) + \dots \quad (7.5.157)$$

The average of this expression does not vanish. As A_1 is negative (7.5.156) the average cornering stiffness apparently increases with ζ (this is in contradiction with the result of Böhm, presumably due to sign error). The maximum average lateral velocity

$$\dot{y}_{\max, \text{ave}} = 1/2 \zeta^2 \frac{V}{\sigma_o^*} v_o \quad (7.5.158)$$

exactly equals the decrease in side slip velocity resulting from the rise in average cornering stiffness due to the assumed variations (7.5.150). A better assumption keeping the average load constant no doubt will lead to different results.

References

- [1] Joy, T. J. P., and Hartley, D. C., Tire characteristics as applicable to vehicle stability problems, Proc. IME, Auto. Div. (1953-1954), p. 113.
- [2] Gausz, F., and Wolff, H., Ueber die Seitenführungskraft von Personen-wagen-Reifen, Deutsche Kraftf.forsch. und Str. verk. techn., Heft 133 (1959).
- [3] Fonda, A. G., Tire tests and interpretation of experimental data, Papers on research in automobile stability and control and in tire performance, Auto. Div. of IME, No. 7 (1956/57).
- [4] Freudenstein, G., Luftreifen bei Schräg- und Kurvenlauf, Deutsche Kraftf.forsch. und Str. verk. techn., Heft 152 (1961).
- [5] Nordeen, D. L., and Cortese, A. D., Force and moment characteristics of rolling tires, SAE Paper No. 713A (June 1963); SAE Trans., 325 (1964).
- [6] Henker, E., Dynamische Kennlinien von PKW-Reifen, Wissenschaftlich-Technische Veröffentlichungen aus dem Automobilbau (IFA-DDR) Heft 3 (1968).
- [7] Fonda, A. G., and Radt, H., Summary of Cornell Aeronautical Laboratory tire test data, CAL Report YD-1059-F-2 (1958).
- [8] Smiley, R. F., and Horne, W. B., Mechanical properties of pneumatic tires with special reference to modern aircraft tires, NACA (NASA) Tech. Note 4110 (1958).
- [9] Hadekel, R., The mechanical characteristics of pneumatic tires, S & T Memo No. 10/52 (British Ministry of Supply, TPA 3/TIB, 1952).
- [10] Smiley, R. F., Correlation, evaluation, and extension of linearized theories for tire motion and wheel shimmy, NACA (NASA) Tech. Note 3632 (June 1956).
- [11] Frank, F., Grundlagen zur Berechnung der Seitenführungskennlinien von Reifen, Kaut. Gummi 8 (18), 515 (1965).
- [12] Frank, F., Theorie des Reifenschräglaufts, Diss. T. H. Darmstadt (1965).
- [13] Fiala, E., Seitenkräfte am rollenden Luftreifen, VDI-Zeitschrift 96, 973 (1964).
- [14] Ellis, J. R., Frank, F., and Hinton, B. J., The experimental determination of tire model parameters, A.S.A.E. Report No. 2 (Sept. 1966).
- [15] Böhm, F., Der Rollvorgang des Automobil-Rades, ZAMM 43, T56-T60 (1963).
- [16] Borgmann, W., Theoretische und Experimentelle Untersuchungen an Luftreifen bei Schräglauflauf, Diss, Braunschweig (1963).
- [17] Bergman, W., Theoretical prediction of the effect of traction on cornering force, SAE Trans., 614 (1965).
- [18] Pacejka, H. B., Study of the lateral behaviour of an automobile moving upon a flat level road, Cornell Aeronautical Laboratory Report YC-857-F-23 (1958).
- [19] Pacejka, H. B., The wheel shimmy phenomenon, Diss., Tech. University of Delft (1966).

- [20] Rotta, J., Zur Statik des Luftreifens, *Ing. Archiv*, 129 (1949).
- [21] Kalker, J. J., On the rolling contact of two elastic bodies in the presence of dry friction, Diss., Delft (1967).
- [22] Nayak, P. R., and Paul, I. L., A new theory of rolling contact, *Engrg. Proj. Lab., Dept. of Mech. Engrg., M.I.T.* (1968).
- [23] Savkoor, A. R., The lateral flexibility of pneumatic tire and its application to the lateral rolling contact problem, SAE Paper No. 700378 (1970); FISITA Int. Auto. Safety Conf. Compendium, p. 367, New York (1970).
- [24] Savkoor, A. R., The relation of the adhesional friction of rubber to the friction between tire and ground, Paper B-12, FISITA, München (1966).
- [25] Schlippe, B. von, and Dietrich, R., Das Fattern eines bepneuten Rades, *Ber. Lilienthal Ges.* 140, p. 35 (1941).
- [26] Schlippe, B. von, and Dietrich, R., Shimmying of a pneumatic wheel (Translation of [25]), NACA (NASA) TM 1365, p. 125 (1954).
- [27] Holmes, K. E., and Stone, R. D., Tire forces as functions of cornering and braking slip on wet road surfaces, Paper 6 (IME Auto. Div. Symp., Handling of Vehicles under Emergency Conditions, Univ. of Technology, Loughborough, England, Jan. 8, 1969), *Proc. IME* 1968-69 **183** (Pt 3H), 35 (1969).
- [28] Gengenbach, W. (Private Communication).
- [29] Riekert, P., und Schunch, T. E., Zur Fahrmechanik des Gummi-bereiften Kraftfahrzeugs, *Ing. Archiv* **11**, 210 (1940).
- [30] Whitcomb, D. W., and Milliken, W. F., Design implications of a general theory of automobile stability and control, Papers on research in automobile stability, *Proc. Auto. Div. of IME*, No. 7 (1956-57), with many references.
- [31] Segel, L., Theoretical prediction and experimental substantiation of the response of the automobile to steering control, *Proc. Auto. Div. of IME*, No. 7 (1956-57).
- [32] Mitschke, M., Fahrtrichtungshaltung, Analyse der Theorien, *A.T.Z.* **70**(5), 157 (1968), with many references.
- [33] Fiala, E., Zur Fahrdynamik des Strassenfahrzeuges unter Berücksichtigung der Lenkungselastizität, *A.T.Z.*, 71 (1960).
- [34] Pevsner, Ja. M., Theory of the stability of automobile motions (in Russian), Masjgiz, Leningrad (1947).
- [35] Hoffmann, E. R., Note on vehicle stability, *Austral. Road Research* **1**, (1964) III, p. 15.
- [36] Antonov, D. A., Stability calculation of automobiles (in Russian), *Avtomobil'naja promislennost*, No. 9 (1963).
- [37] Apetaur, M., Beurteilung der Fahreigenschaften von Fahrzeugen nach der Ergebnissen der Prüfungen durch gleichmässige Fahrt auf einer Kreisbahn, Conference on Testing of Automobiles, Prague (Oct. 1965).
- [38] Radt, H. S., and Pacejka, H. B., Analysis of the steady-state turning behavior of an automobile, *Proc. Symp. Control of Vehicles* 1963, p. 66 (IME, London).
- [39] Böjm, F., Ueber den Fahrzustand des Kraftwagens auf einer ebenen Kreisbahn ohne Ueberhöhung, *Ing. Archiv* **32**, 112 (1963).
- [40] Koiter, W. T., and Pacejka, H. B., On the skidding of vehicles due to locked wheels, Paper 1 (IME Auto. Div. Symp., Handling of Vehicles under Emergency Conditions, Univ. of Technology, Loughborough, England, Jan. 8, 1969), *Proc. IME* 1968-69, **183** (Pt 3H), 3 (1969).
- [41] Chiesa, A., Rinonapoli, L., and Bergoni, P. I. R., A new loose inverse procedure for matching tires and car using a mathematical model, Paper 4 (IME Auto. Div. Symp., Handling of Vehicles under Emergency Conditions, Univ. of Technology, Loughborough, England, Jan. 8, 1969), *Proc. IME* 1968-69, **183** (Pt 3H), 93 (1969).
- [42] Harris, A. J., and Riley, B. S., Vehicle behavior in combined cornering and braking, Paper 5 (IME Auto. Div. Symp., Handling of Vehicles under Emergency Conditions, Univ. of Technology, Loughborough, England, Jan. 8, 1969), *Proc. IME* 1968-69 **183** (Pt 3H), 19 (1969).
- [43] Ellis, J. R., Understeer and oversteer, *Auto. Engr. (London)* (May 1963).
- [44] Kantrowitz, A., Stability of castering wheels for aircraft landing gears, NACA (NASA) Report 686 (1937).
- [45] Greidanus, J. H., Besturing en stabiliteit van het neuswielonderstel, NLL Report V 1038, Amsterdam (1942).
- [46] Saito, Y., A study of the dynamic steering properties of tires, FISITA London (1962), pp. 101. 246. 282.

- [47] Fromm, H., Kurzer Bericht ueber die Geschichte der Theorie des Radflatterns, Ber. Lilienthal Ges. 140, 53 (1941); or NACA (NASA) TM 1365, p. 181 (1954).
- [48] Bourcier de Carbon, C., Etude theorique due shimmy des roues d'avion, Off. Nat. d'Etude et de Rech. Aér. 7 (1948); or NACA (NASA) TM 1337 (1952).
- [49] Böhm, F., Reifenmechanik und fahreigenschaften des automobils, Paper B-3, FISITA München (1966).
- [50] Schlippe, B. von, and Dietrich, R., Zur Mechanik des Luftreifens, Zentral für Wiss. Ber., Berlin (1942).
- [51] Schlippe, B. von, and Dietrich, R., Das Flattern eines mit Luftreifen versehenes Rades, Jahrbuch Deutsche Luftfahrtforschung (1943).
- [52] Segel, L., Force and moment response of pneumatic tires to lateral motion inputs, Trans. ASME, J. Engr. for Ind. **88B**(1) (1966).
- [53] Kurz, H., Seitenführungskraft des Draftwagenrades bei wechselnder Radlast, A.T.Z. **60**(5) (1958).
- [54] Endres, W., Versuche über das Verhalten des Autorades in der Kurve, VDI-Zeitschrift **106**(4) (1964).
- [55] Metcalf, W. H., Effect of a time-varying load on side force generated by a tire operating at constant slip angle, SAE Paper No. 713C (1963).
- [56] Pacejka, H. B., Discussion, Proc. Symp. Control of Vehicles during Braking and Cornering 1963, p. 116 (IME, London).
- [57] Ginn, J. L., Miller, R. F., Marlow, R. L., and Heimovics, J. F., The B. F. Goodrich Tire Dynamics Machine. SAE preprint 490 B (March 1962).

Index

A

- Abrasion, rubber, tests for, 12
- Accelerating force, interaction with cornering, 507
- Adhesion
 - cord-to-rubber, RFL, 269
 - cord-stripping, 294
 - fabric stripping test, 295
 - H-test, 291
 - I-test, 293
 - polyester, 279
 - pop-test, 294
 - static tests of cord, 291
 - steel wire, 290
 - T-test, 291
 - testing of, 291
 - U-test, 291
- Adhesion tests, dynamic, 295
- Adhesive treatment
 - glass fiber, 291
 - polypropylene, 291
 - vinylon, 291
- Aging, rubber, 9
- Angles, helix yarn, 96
- Aquaplaning of tires, 534

B

- Bead, tire, 362
 - multiple, 366
- Belted tires, 373
- Bias ply tire, 372
- Braking, 515
- Braking force, interaction with cornering, 507, 669
- Breakers, tire, 360

C

- Camber, 663
- Camber and cornering, 664, 782
- Camber measurements, 665
- Carbon black
 - description, 4, 33
 - reinforcement of rubber with, 32
- Carcass elasticity, influence on string models of, 794
- Carcass construction, effect on friction of, 526

- Centrifugal loads on tire, 421
- Chafer, 366
- Chains, effect on friction of tire, 539
- Circumferential slip, 515
- Compression of cord, 172
- Compression in contact area, 375
- Compression test for adhesion, 295
- Composition, tire rubber compounds, 3
- Conditioning, tire, 595, 685
- Construction, tire, 360, 379
- Contact area
 - actual net, 457
 - membranes, 456
 - solid bodies, 454
 - tire, 447
 - cornering, influence of, 451
 - curved surfaces, influence of, 449
 - pressure, influence of, 449
 - velocity, influence of, 450
- Contact pressures
 - in soils, 480
 - influence on structure, 472
 - normal or vertical, 472
 - on hard surfaced roads, 480
 - tangential
 - in cornering, 494
 - lateral, 494
 - longitudinal, 487, 605
 - longitudinal during braking, 491
- Contraction, yarn, 71
- Cord
 - adhesion, static tests, 291
 - behavior in compression, 172, 186
 - bending, 191
 - bending rigidity, 196
 - bonding, 265
 - buckling, 172
 - efficiency, 177
 - fatigue resistance, 253
 - fatigue tests, 257
 - fiber glass, 241
 - friction, 190
 - geometric models, 67, 73
 - geometry, 65
 - heat-treating, 240
 - heat treatment after dipping for adhesion, 277

- Cord—Continued
 - impact resistance, 246
 - lubricants, 190, 222
 - nylon, 220
 - physical properties, 245
 - polyester, 238
 - radial tires, 244
 - rayon, 220
 - steel wire, 243
 - strain rate, effect of, 183
 - strength characteristics, 251
 - stress-strain curves, 186
 - stripping test for adhesion, 294
 - temperature, effect of, 183
 - tensile behavior, 111, 175
- Cord path, 385
 - tire, 414
- Cornering, definitions, 631
- Cornering force, 506, 649
 - braking and traction,
 - interaction with, 508, 669, 788
 - measurements, 639
 - with vehicles, 674
- Cosine law, 415
- Creep of rubber, 23
- Critical speed, tire, 424, 746

D

- Damping, cord-rubber laminates, 337
- Deformation
 - combined, 643
 - of laminates, 377
 - under braking, 603
 - under cornering, 639
- Degradation, cord-rubber laminates, 346
- Dynamic tire forces, vertical, 579
- Dynamic modulus, rubber, 26, 29

E

- Elastic constants
 - calendered cord-rubber, 319
 - composite bias laminates, 324
- Elasticity, theory of rubber, 14
- Energy loss, rubber, 16
- Energy loss, in tires, 31
- Enveloping properties, 702
- Equilibrium equations, shell, 408

F

- Fabric stripping test for adhesion, 295
- Fatigue, cord-rubber laminates, 341
- Fatigue of cords, 253
- Fatigue tests of cords, 257
- Failure, cord-rubber laminates, 341
- Fiber glass cord, 241
- Fibers, merged, 237
- Flange, rim, 367
- Flatspot index, 234
- Flatspotting, 233
- Flex cracking, rubber, 12

- Flexure tests for adhesion, 297
- Flipper, tire, 365
- Force response, longitudinal, 716
- Fracture, cord, 347
- Frequency method for tire stiffness, 580
- Frequency response, tire, 722
- Friction
 - definitions of, 44
 - influence of tread pattern and carcass construction, 526
 - measuring techniques, 611
 - on ice, 539
 - rubber
 - adhesive, 46
 - classification, 45
 - deformation, 49
 - dry, 54
 - tearing, 54
 - viscous, 52
 - wet, 56
 - speed dependence, 46, 518
 - tires, 525

G

- Geometry, cord, 65, 67, 73
- Glass fiber, adhesive treatment, 291
- Glass formulation, 241
- Groove depth, effect on braking, 470
- Gyroscopic effects, 816

H

- H-test for adhesion, 291
- Hardness, rubber, 11
- High frequency properties, tire, 726
- Hooke's Law, plane orthotropic materials, 313
- Hydrodynamic effects in skid, 468, 520
- Hydroplaning, 468, 534
- Hysteresis, effect on friction, 533

I

- I-test for adhesion, 293
- Ice, tire friction on, 539
- Impact resistance, cords, 246
- Inflation pressure
 - contact area, influence on, 449
 - cornering, influence on, 658
- Irregularity in tires, *see* Nonuniformity

K

- Kerfs, influence on tire friction, 528

- Lateral stiffness of tires, 576
- Lateral force distribution
 - in cornering, 646

Load-vertical deflection, tire, 567
 Load carrying, tire, 392, 398
 Longitudinal deformation of tire, 642
 Longitudinal slip, 711
 Longitudinal stiffness of tire, 575
 Lubricant, cord, 190

M

Membrane stress resultants in a tire, 408
 Migration, filament, 101
 Modulus, rubber, 6
 Molding, tire, 384
 Mooney material, model for rubber, 22

N

Nonsteady state motion, 803
 Nonuniformity
 effect on vehicles, 621
 grading machines, 624
 tire, 616, 690
 wheel, 621
 Normal load, *see* Vertical load
 Nylon cord, 220
 Nylon, high tenacity, 224
 Nylon 6 tire cord, 225
 Nylon 66, processing conditions, 228

O

Obstacles, 702
 Oversteer, 512, 638

P

Physical properties, fiber and
 filament, 241
 Polyester, adhesion, 279
 Polyester cord, 238
 Polyester, heat-treating, 240
 Polypropylene, adhesive treatment, 291
 Pop-test for adhesion, 294
 Power loss, tire, *see* Rolling resistance
 Pressure distribution, *see* Contact
 pressures

R

RFL, 269
 Radial tires, 244
 cord, 373
 Radius of curvature, tire, 414, 417
 Rayon
 extra high modulus, 224
 high tenacity, 221
 high tenacity, production processes, 222
 Rayon cord, 220
 Reduced flatspot materials, 236
 Relaxation length, cord in rubber, 336

Retraction, yarn, 88, 93
 Rims, tire, 366
 Road platform, 565
 Road surface roughness, 521
 measurement techniques, 676
 Rolling radius
 influence of carcass, 588
 influence of load and inflation, 589
 influence of speed, 589
 measurement of, 587
 tire, 584
 Rolling resistance
 effect of construction, 599
 effect of material, 596
 effect of operating conditions, 600
 effect of speed, 591
 measurement of, 592
 tire, 591
 Running-in of tires, 595

S

Self-aligning torque, 513
 Shear stress, cord-rubber in tire, 419
 Shear test for adhesion, 296
 Shimmy, 810
 Sipes, influence on tire friction, 528
 Skid testers, 683
 Slip angle, 631
 Slip
 definitions, 463, 503, 608, 757
 longitudinal, 711
 measurement of, 467
 Slip regions in cornering, 743
 Snow, tire friction on, 539
 Speed, influence on tire
 friction, 46, 518, 523
 Standing waves, *see* Critical speed
 Steering of vehicles, 636
 Strain energy functions, rubber, 21
 Strains, measurement of, 430, 437
 Strength loss, nylon cord, 230
 Stress relaxation, rubber, 26
 Stress resultants, tire, 417
 Stress-strain properties
 cord, 309
 cord-rubber laminates, 316
 rubber, 5, 309
 String models
 combined effects, 799
 generalized, 763
 limitations, 798
 Strip tests for adhesion, 296
 Studs, effect on friction, 539
 Superposition principle, rubber, 26

T

T-test for adhesion, 291
 Tear tests, rubber, 10
 Temperature, measurements, tire, 602
 Tenacity, 221

Tension
 cord, 418
 bead, 419
 Testing equipment, tire 553
 Texture, road surface, 521
 Thermal shrinkage, nylon 6 tire cord, 228
 Tire cords, *see* Cord
 Torsional stiffness of tire, 577
 Traction, 613
 interaction with cornering, 669
 Trailers, test, 686
 Transfer functions, cornering, 800
 Transient motion, *see* Nonsteady
 state motion
 Traveling waves, tire, 424
 Tread compound, effect on friction, 531
 Tread, function of, 369
 Tread pattern, effect on friction, 471, 526
 Tread wear, 648
 Turn-ups, tire, 364

U

U-test for adhesion, 291
 Understeering, 512, 638
 Uniformity, fiber, 129

V

Variable vertical load, influence of, 820
 Variability in singles yarn, 135
 Velocity effects on cornering force, 658
 Velocity effects on rolling radius, 589

Velocity effects on
 tire friction, 46, 518, 523
 Vertical load
 influence on cornering, 656
 variable, influence on cornering, 820
 Vertical stiffness, tire, 568, 695
 Vibration transmission of tire, 726
 Vibrations, tire tread
 normal, 733
 lateral, 741
 Vinylon, adhesive treatment, 291
 Viscoelasticity, rubber, 23
 Vulcanizing, tire, 385

W

Water films, 52, 521
 Wear, *see* Tread wear
 Wet roads, influence on cornering, 653
 Winter tires, 539

Y

Yarn
 analysis by energy, 127
 contraction, 70
 cross-sections, 100
 effect of transverse force, 121
 helix angles, 96
 large extension, 125
 migration of filaments, 101
 retraction, 88, 93
 structure, 87

U.S. DEPT. OF COMM. BIBLIOGRAPHIC DATA SHEET		1. PUBLICATION OR REPORT NO. NBS-MN-122	2. Gov't Accession No.	3. Recipient's Accession No.
4. TITLE AND SUBTITLE MECHANICS OF PNEUMATIC TIRES			5. Publication Date November 1971	
			6. Performing Organization Code	
7. AUTHOR(S) Samuel K. Clark, Editor			8. Performing Organization	
9. PERFORMING ORGANIZATION NAME AND ADDRESS University of Michigan Ann Arbor, Michigan 48104			10. Project/Task/Work Unit No. 4080401	
			11. Contract/Grant No. CST-386	
12. Sponsoring Organization Name and Address National Bureau of Standards Department of Commerce Washington, D. C. 20234			13. Type of Report & Period Covered	
			14. Sponsoring Agency Code	
15. SUPPLEMENTARY NOTES This publication was funded by the National Highway Traffic Safety Administration, Department of Transportation, through the NBS, Interagency Agreement FH--11-6090.				
16. ABSTRACT (A 200-word or less factual summary of most significant information. If document includes a significant bibliography or literature survey, mention it here.) The pneumatic tire has been an integral part of automotive transportation almost since its inception, yet it remains a product whose characteristics are not easily predictable or comprehensible by conventional engineering techniques. This treatise is an attempt to provide a rational descriptive and analytical basis for tire mechanics. Chapters of this book are contributed by active research workers in the fields of rubber and textile properties, friction, material properties, tire stress problems, tire design and construction, vehicle skid and handling, and tire mechanical properties.				
17. KEY WORDS (Alphabetical order, separated by semicolons) Friction; rubber; skid; tires; tire cord; tire contact; tire stress; tire structure, vehicles.				
18. AVAILABILITY STATEMENT <input checked="" type="checkbox"/> UNLIMITED. <input type="checkbox"/> FOR OFFICIAL DISTRIBUTION. DO NOT RELEASE TO NTIS.			19. SECURITY CLASS (THIS REPORT) UNCLASSIFIED	21. NO. OF PAGES 853
			20. SECURITY CLASS (THIS PAGE) UNCLASSIFIED	22. Price \$4.75



